12th INTERNATIONAL CONFERENCE ON THE STABILITY OF SHIPS AND OCEAN VEHICLES

STAB2015

UNIVERSITY OF STRATHCLYDE,
GLASGOW, 19-24 JUNE 2015

PROCEEDINGS

Volume 2

STAB2015

12th INTERNATIONAL CONFERENCE ON THE STABILITY OF SHIPS AND OCEAN VEHICLES

JUNE 14-19, 2015

GLASGOW, SCOTLAND

PROCEEDINGS

Edited by

Prof. Dracos Vassalos

Dr. Evangelos Boulougouris

The Department of Naval Architecture, Ocean and Marine Engineering

University of Strathclyde

Published and distributed by:

University of Strathclyde Publishing
Henry Dyer Building, 100 Montrose Street
Glasgow, G4 0LZ, UK

Telephone: +44 (0)141 548 4094

ISBN-13: 978-1-909522-13-8 (print)

ISBN-13: 978-1-909522-14-5 (ebook)

Session 9.1 – 2nd GENERATION INTACT STABILITY

An Approach to Assess the Excessive Acceleration based on Defining Roll Amplitude by Weather Criterion Formula with Modified Applicability Range

A Simplified Simulation Model for a Ship Steering in Regular Waves

Prediction of Wave-Induced Surge Force Using Overset Grid RANS Solver

This page is intentionally left blank

An Approach to Assess the Excessive Acceleration Based on Defining Roll Amplitude by Weather Criterion Formula with Modified Applicability Range

Prof. Rudolf Borisov, State Marine Technical University of St. Petersburg, rvborisov@mail.ru

Ph. D. Alexander Luzyanin State Marine Technical University of St. Petersburg,

aaluzyanin@rambler.ru

Dr. Michael Kuteynikov, Russian Maritime Register of Shipping, kuteynikov.ma@rs-class.org

Vladimir Samoylov, Russian Maritime Register of Shipping, samoylov.vr@rs-class.org

ABSTRACT

Development of the second-generation intact stability criteria is focused on five dynamical stability failure modes and three-level approach which indicates susceptibility and degree of susceptibility of a ship to a specific failure mode. The criteria of levels 1 and 2 are based on significant simplifications and have been developed considering substantial safety margins. Until now, the work has been concentrated on the development of levels 1 and 2 criteria and standards. The agreed proposal for excessive acceleration vulnerability criteria was generally made, but some undecided items regarding formulae of roll amplitude and period, formulae for effective wave slope and their applicability still exist. Besides, nonlinear components were not taken into account in the proposed level 1 vulnerability criteria for excessive accelerations, which could decrease the safety margin.

The purpose of the paper is to provide some additional information that can be used during finalization of the development of vulnerability criteria for excessive acceleration.

The possibility of application of a current IMO Weather Criterion to ships with ratio B/d > 3.5 and having restricted navigation area is considered. Some drawbacks of formulae for calculation of coefficient c that is necessary for calculation of roll period in the current IMO Weather Criterion are pointed out and the proposal for its correction is made. Criterion for excessive linear acceleration based on the assumptions of IMO Weather Criterion with modified applicability for several types of ships is presented and justification of the value 0.3g as a standard is made. The paper also includes information about the influence of nonlinear components on the value of acceleration and contribution of roll to the balance of horizontal accelerations.

Keywords: *acceleration, weather, stability*

1. INTRODUCTION

This paper contains some information about acceleration criterion, based on the assumptions of IMO Weather Criterion with modified applicability for ships with different navigation restrictions and ratios B/d > 3,5. Presumably it can be used during finalization of the development of vulnerability criterion for excessive acceleration in scope of the

development of second generation intact stability criteria. The proposed criterion is mostly suitable for the 1 level of the vulnerability criteria for excessive acceleration.

2. JUSTIFICATION OF ACCEPTABLE VERTICAL ACCELERATION VALUE 0,3g

There are several types of vessels which have acceleration limitations during roll on heavy sea. This limitations are connected with cargo type, vessel's purpose, or necessity of meeting certain conditions of operation safety.

Vertical accelerations due to roll are usually considered, but sometimes total vertical accelerations are normalized in different combinations of ship motions: roll + heave (on the upper decks and the bridge), pitch + heave (at fore perpendicular) [5]. Here are the main factors, which make normalizing of accelerations necessary.

Biological factors. Roll causes seasickness among crew and passengers. The main reason of seasickness is physiological influence of angular and linear roll accelerations on human body.

Operational factors. These include shifting of containers, bulk and timber cargo, swing of cargo suspended on crane hook, deterioration, and sometimes inoperability of main and auxiliary machinery.

Strength factors. Overall hull strength and strength of particular structures (stern and stem, constructions of cranes and cargo booms and etc.).

Operational and strength factors for transport vessels are basically considered in the appropriate sections of national and international rules [10], [4] for ensuring safe transport technology and marine operations. Stability standards envisage the assessment of bulk cargo safety conditions and indirectly take inertial forces during roll into account.

Developers of limitations for sea-river vessels [17] considered "… bulk cargo shift, loose cargo shift, especially deck cargo, deterioration of machinery operation conditions, seasickness of the crew, … dangerous stresses in ship's hull connections", i. e. it seems they created universal mean, that took into account all three groups of factors mentioned above.

Standards which take into account operational and strength factors is often less severe than standards which take into account biological factors. Therefore acceptable accelerations are usually chosen on the basis of biological factors.

Let's look at the factors in more detail. The threshold of human sensitivity to angular accelerations is within 2 – 3 deg./s^2, and to vertical accelerations – within 0,4 – 0,12 m/s^2. Seasickness is significantly increased when the vertical accelerations reach nearly 0,1g ≈ 1 m/s^2. Vertical accelerations in the specific point of vessel arises not only from linear but from angular ship motions. Therefore the greatest vertical accelerations occur near vessel's ends.

The majority of the medical scientists tend to think that seasickness is a result of vestibular apparatus malfunction caused by vertical accelerations [11].

The degree of ship motions influence on human body can be seen from the graph, shown in Fig. 1.

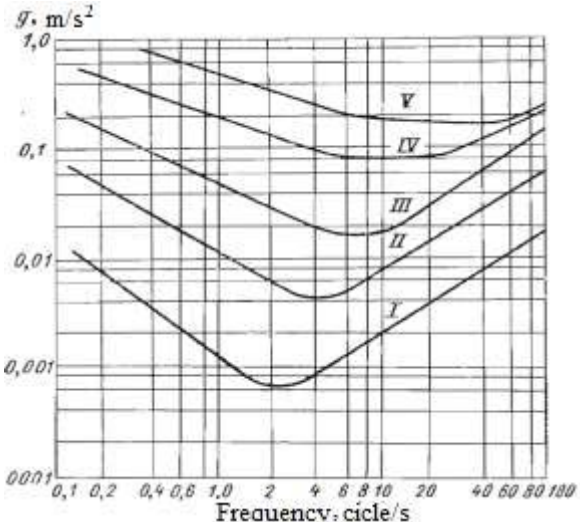

Fig. 1

Curve I marks the boundary of inceptive influence, curve II – boundary of sensible influence, curve III – strong influence, i. e. the beginning of seasickness and discomfort, curve IV – sensible discomfort and curve V – unbearable vibration. The diagram was obtained by Nieuwenhuysen [8]. The graph in Fig. 2 shows that the percentage of diseased passengers increases from 20% to 85% while accelerations increase from 0,1g to 0,4g.

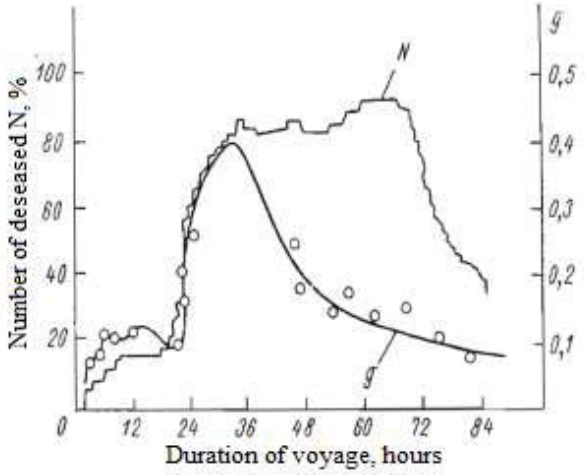

Fig. 2

Professional sailors adapt to seasickness, but this adaptation is not significant, as shown in Fig. 3. Therefore reduction of ship motions is necessary not only for passenger ships.

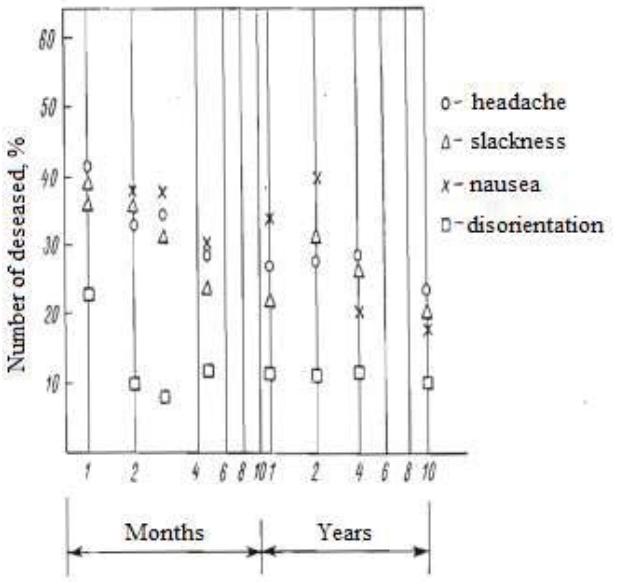

Fig. 3

Proceeding from the graph in Fig. 1 and collected data about the number of diseased people, shown in Figs. 2 and 3, the standard for vertical acceleration 0,3g was selected.

2. PROPOSAL FOR ACCELERATION CRITERION

Acceleration criterion is proposed taking into account the acceptable value of vertical accelerations mentioned above. It allows to input the operational limitations for acceptable wave height for ships with parameters $\frac{\sqrt{h_0}}{B} \geq$ 0,08 and $B/d \geq 2{,}5$ (where h_0 is initial transverse metacentric height without free surface correction; B is breadth of the vessel; d is draught).

Main proposals in the form of acceleration criterion were included in Rules for Classification and Construction of Sea-Going Ships of Russian Register in 1974 year. These ideas survived to the present day with slight changes in calculation procedure. Their point is as follows.

The stability is judged as satisfactory according to the acceleration criterion if

acceleration (in fractions of g) is not more than the permissible value, i. e. the following condition is fulfilled

$$K^* = 0{,}3/a_{cal} \geq 1, \quad (1)$$

Where K^* – is the acceleration criterion;
a_{cal} – is the calculated acceleration (in fractions of g) determined by the formula

$$a_{cal} = 0{,}0105\frac{h_0}{c^2 B}k_\theta \theta_r \quad (2)$$

Here, θ_r is the calculated amplitude of roll determined in accordance with [4]
$\theta_r = 109X_1X_2\sqrt{rS}$ as well as in case of weather criterion;
c – is the inertia coefficient determined during calculation of the weather criterion according to the formula
$c = 0{,}373+0{,}023B/d-0{,}043L_{wl}/100$; (3)
k_θ – coefficient that takes into account the peculiarities of roll for ships of river-sea navigation determined from Table 1.

Table 1

B/d	≤ 2,5	3	3,5	4	4,5	5	5,5	6	6,5
k_θ	1	1,08	1,11	1,11	1,2	1,3	1,45	1,56	1,61

In certain cases, it may be allowed the operation of the ship with the criterion K* < 1. In this case, an additional wave height restriction shall be introduced. The permissible wave height with 3 per cent probability of exceeding level is estimated proceeding from the value of the criterion K* as given in Table 2. The specific loading conditions with K* < 1 shall be stated in the Stability Booklet.

Table 2

K^*	1,0 and higher	1,0 – 0,75	0,75 and less
Permissible wave height with 3 per cent probability of exceeding level, m	6,0	5,0	4,0

The vessel is assumed to be in beam sea and undergoes rolling and heaving. Vertical accelerations are assessed on amidships at side and actual waterline intersection point.

The acceleration criteria mentioned above can be utilized as the basis for the revision of excessive acceleration vulnerability criterion of 1 level that is being created while developing the second generation intact stability criteria. The formula for calculation of roll amplitude can be used for the vessels with ratio B/d > 3,5, as shown below.

3. POSSIBILITY OF APPLICATION OF WEATHER CRITERION TO SHIPS WITH RATIO B/d > 3,5

It is well known, the formula for roll amplitude θ_r represents the formula of nonlinear roll theory that is reduced to handy calculation form and was used by authors of Japanese “Stability standards for passenger ships” and then corrected by SLF Subcommittee specialists in order to take into account the influence of B/d, C_B and bilge keels on roll damping in more detail. At the same time multipliers r and s in formula for θ_r are taken right from Japanese “Standards” and multipliers $X_1(B/d)$, $X_2(C_B)$ and k – from “Stability standards” of Russian Maritime Register of Shipping (in the editions published between 1970 and 1995) as noted in MSC.1/Circ. 1281 dated 9 December 2008.

The consideration of the value of r showed it to be a reduction coefficient, averaged on the

basis of the results of many calculations to the main part (Krilov's part) of disturbing moment. It is well known from the roll theory, this coefficient can't be more than one. This is how effective coefficient of wave slope changes (according to the terminology of Japanese "Standards"). It is calculated in compliance with Watanabe method for 60 passenger vessels of Japan and underlies linear statistical dependence of IMO IS Code: $r = 0{,}73 \pm 0{,}6OG / d$, where OG is the distance between center of gravity and waterline (+ if center of gravity is higher than the waterline).

Calculations for other types of ships with high center of gravity mainly cargo ships and industrial ships (for the purpose of this paper it means crane ships, drilling ships and dredgers) shows that in a number of cases the value of r becomes more than one, which is not in compliance with its physical meaning and leads to unreasonable overstating of roll amplitude θ_r. So, r = 1,06 for cargo ship (L = 65,0 m, B = 10,0 m, C_B = 0,66) with loading case "without cargo 10% consumables" (d = 2,42 m, OG = 1,34 m, GM = 0,88 m), and r = 1,29 for crane ship (L = 80,4 m, B = 25,4 m, C_B = 0,60) during voyage (d = 3,91 m, OG = 3,65 m, GM = 10,7 m) that leads to amplitude $\theta_r = 29^o$ which was not observed during operation of this ship in practice. Therefore it is proposed to take r = 1 during calculation of θ_r where r turns out to be more than one.

Analysis of dependence $X_1(B/d)$ showed that using scheme of roll calculation θ_r this dependence considers only increasing damping coefficient of rolling with growth of B/d. It is confirmed by results of numerous model tests carried out in different countries. Meanwhile the value of factor X_1 in Table 3 at any $B/d \geq$ 3,5 is limited by its marginal value X_1 = 0,8. Such limitation is not appropriate to calculation scheme for roll amplitude θ_r of IMO IS Code. Using of experimental data on damping coefficients of rolling gained in model basin of Saint-Petersburg State Marine Technical University (SPbSMTU) for different types of ships with wide range of B/d provided the justified prolongation of the dependence $X_1(B/d)$ in region of B/d > 3,5 till B/d = 7,0. It practically exhausts the real values of dependence B/d for wide range of classes of ships including cargo and industrial ships. Such dependence is presented in Table 3. It is gained by averaging of calculation results of factor X_1 for 15 types of cargo, fishing and industrial ships.

Table 3. The values of factor X_1.

B/d	X_1
≤ 2,4	1,0
2,5	0,98
2,6	0,96
2,7	0,95
2,8	0,93
2,9	0,91
3,0	0,90
3,1	0,88
3,2	0,86
3,3	0,84
3,4	0,82
3,5	0,80
3,6	0,79
4,0	0,78
4,5	0,76
5,0	0,72
5,5	0,68
6,0	0,64
≥ 6,5	0,62

It can be seen that using Table 3 for factor X_1 in roll amplitude formulae always leads to decreasing of value θ_r while B/d increases in accordance with physical nature of phenomenon. This decreasing becomes practically sensible starting from B/d > 4,0. Such ratios between breadth and draught as shown by statistical analysis of main dimensions of ships are typical for cargo ships with standard loading conditions "without cargo with ballast 10% consumables" (dry cargo, tankers), large fishing vessels (fish cannery ship, whale factory ship) with low production in holds and low consumables and for industrial ships during voyage, when B/d

often more than 5,0 – 6,0. The correction of Table 3 for them has the largest value and may reduce calculated roll amplitudes for 15 – 20%.

So, the formulae for roll amplitude from Weather Criterion can be applied for the vessels with ratio $B/d > 3{,}5$ which typically has excessive accelerations. Gained value of amplitude may be used in calculation of the acceleration.

4. SOME DRAWBACKS OF FORMULAE FOR CALCULATION OF COEFFICIENT *c* IN FORMULAE FOR CALCULATION OF ROLL AMPLITUDE

The following formulae is utilized in calculation of roll amplitude according to IMO method [4]:

$$c = 0{,}373 + 0{,}023B/d - 0{,}043L/100 \qquad (4)$$

It was obtained for ships of unrestricted service which usually have the ratio of breadth to draught $B/d < 3{,}5$ and relative metacentric height is $\frac{\sqrt{h_0}}{B} < 0{,}08$. Application of this dependence for sea-river ships, which typically have larger ratios B/d and metacentric heights leads to significant error.

The formulae (4) gives significantly discrepant values of coefficient c and consequently roll period for vessels with different length but with same B/d. So for the ship with length $L = 100$ m, $B/d = 2{,}5$, $\frac{\sqrt{h_0}}{B} = 0{,}06$ we will obtain: $c = 0{,}399$, $T = 12{,}9$ s, and for ship with length $L = 200$ m, with the same $B/d = 2{,}5$, $\frac{\sqrt{h_0}}{B} = 0{,}06$: $c = 0{,}345$, $T = 11{,}5$ s.

The difference is about 10%. It is obvious that with growth of length the error increases.

Taking into account the drawbacks mentioned above, the formulae for calculation of coefficient c also should be revised in order to avoid the above mentioned errors. Besides this, formulae for calculation of c does not take into account the influence of z-coordinate of center of gravity at natural roll period.

Natural roll period is defined by known formulae:

$$T = 2\pi\sqrt{\frac{I_{xx} + \lambda_{44}}{Dh}} \qquad (5)$$

Here I_{xx} – moment of inertia of ship's weight about central longitudinal axis;
λ_{44} – associated moment of inertia;
D – displacement.

Coefficient c can be defined from equality $T = \frac{2cB}{\sqrt{h}}$ taking into account (5) as follows

$$c = \frac{\pi}{B}\sqrt{\frac{I_{xx} + \lambda_{44}}{D}} \qquad (6)$$

Moment of inertia of ship's weight about central longitudinal axis and associated moment of inertia are necessary to define coefficient c.

Moment of inertia of ship's weight I_{xx} about central longitudinal axis OX can be determined most accurately by calculation of moments of inertia of the components of weight (shell plating, deck framing, superstructure, cargo, fuel, stores and etc.). The known formulae of theoretical mechanics is used for this purpose:

$$I_{xx} = \sum_i m_i \left[y_i^2 + (z_i - z_g)^2 \right] + \sum_i I_{xi}^c \qquad (7)$$

where m_i – weight of each i component from the whole weight;
y_i – ordinate of center of gravity of each m_i about centerline;
z_i – z-coordinate of its center of gravity about centerline;
I_{xi}^c – natural moment of inertia of each i component of weight.

Calculation according to the formulae (7) is rather laborious. So, approximate formulas are often used in practice. They are based on some facilitating assumptions about the hull form and its load distribution. The most appropriate formulae for many known authors is Duayer formulae [13]:

$$I_{xx} = \frac{D}{12g}(B^2 + 4z_g^2), \qquad (8)$$

and also formulae of Y. A. Shimanskiy, [13]:

$$I_{xx} = \frac{D}{g}\left(B^2 \frac{C_W^2}{11{,}4C_B} + \frac{H^2}{12}\right), \qquad (9)$$

where H – depth;
C_W – water plane area coefficient;
C_B – block coefficient.

Duayer formulae is more preferable because it gives the results close to calculation data according to (7) and describes the dependence from z-coordinate of ship's center of gravity.

Roll period of displacement ships which have large ratios *L/B* and small block coefficients can be calculated using data of V. A. Morenshildt which are obtained as a result of tests of systematic series of ship models [14]. Associated moment of inertia in dependence of *B/d*, *L/B*, C_W and C_B can be easily defined by nomograms for fishing vessels and transport ships proposed by V. V. Lugovskiy on the basis of tests of two systematic series (20 models in total), that were carried out in test basin of SPbSMTU [13, 6]. Later S. M. Panenko carried out model tests with larger block coefficients and ratios of *B/d* that are typical for industrial ships and proposed the nomogram for defining of λ_{44} [13, 9]. According to this data the associated moment of inertia is defined by the following expression:

$$\lambda_{44} = \frac{0{,}314}{C_B} I_{xx} \frac{\lambda_{44}}{I_{xe}} \quad , \qquad (10)$$

where I_{xe} – moment of inertia of underwater part of the ellipsoid, which has the same main dimensions, as the vessel under consideration (model).

The magnitude of λ_{44}/I_{xe} is defined by nomograms depending on *B/d*, *L/B*, C_W and C_B. The limits of changing of ships' characteristics for which those nomograms are provided in Table 4.

Table 4

No	Type of vessel	*L/B*	*B/d*	C_B	C_w
1	Transport ships	*≈7,3*	*2,4-3,5*	*0,59-0,74*	*0,7-0,82*
2	Fishing vessels and tugs	3,5-6,5	2,4-3,5	0,44-0,56	0,7-0,82
3	Industrial ships	4,5-6,5	3-5,6	-	0,75-0,9

The empirical formulae of G. K. Avdeev which is obtained by processing of the same results of model tests of different vessels in test basin of SPbSMTU can be utilized for defining of the associated moment of inertia for wide range of ships and inland-navigation vessels [1, 7].

$$I_{xx} + \lambda_{44} = \frac{I_{xx}}{0{,}28 + \dfrac{1{,}8}{BC_W\left(1 + \dfrac{1}{6}\dfrac{B}{d}\right)}\sqrt{\dfrac{I_{xx}g}{D}}}. \qquad (11)$$

It is necessary to know moment of inertia of ship's weight and associated moment of inertia to define natural roll period. Calculation of this moments are preferably to be carried out by approximate empirical methods.

The associated moment of inertia λ_{44} mainly depends on *B/d* and water plane area coefficient C_W and also moment of inertia of ship's weight I_{xx}. The formulae of G. K. Avdeev (11) and nomograms of V. V. Lugovskiy and S. M. Panenko most fully meets such dependences for wide range of ships and inland-navigation vessels.

Substitution of (11) in expression for coefficient c (6) will give us the following formulae:

$$c = \pi \sqrt{\frac{\left(1+4\,z_g^2/B^2\right)}{12g\left[0{,}28+\frac{1{,}8}{C_W\,(1+0{,}167\,B/d)}\sqrt{\frac{\left(1+4\,z_g^2/B^2\right)}{12}}\right]}}. \quad (14)$$

To facilitate calculations it can be reduced with enough for practice degree of accuracy (Fig. 4) to the form:

$$c = 0{,}114 + 0{,}012\frac{B}{d} + 0{,}26\frac{z_g}{B} + 0{,}195C_W \quad (15)$$

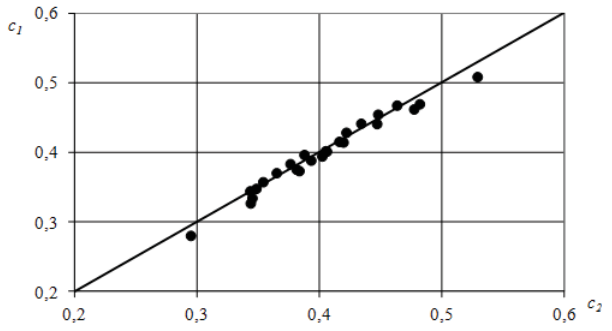

Fig.4 The comparison of the calculation results according to formulas (15) and (14)

Coefficient c can be determined utilizing nomograms of V. V. Lugovskiy and S. M. Panenko (moment of inertia of ship's weight is determined according to Duayer formulae):

$$c = 0{,}289\sqrt{\left(1+4\frac{z_g^2}{B^2}\right)\left(1+\frac{0{,}314}{C_B}\frac{\lambda_{44}}{I_{x\text{э}}}\right)} \quad (16)$$

Here the ratio λ_{44}/I_{xe} is determined by nomograms depending on ship's characteristics B/d, L/B, C_W, C_B. Based on the results of processing of these calculations the approximate dependence is obtained:

$$c = 0{,}121 + 0{,}10C_W + 0{,}025\frac{B}{d} + 0{,}35\frac{z_g}{B} + 0{,}001\frac{L}{B} \quad (17)$$

Calculations according to (17) give the results close to data that was obtained directly by nomograms. The error for all values of B/d, L/B, C_W, C_B does not exceed 5 – 7 % excluding C_W = 0,9. The error can reach 15 % for industrial ships where formulae gives understated results.

The results of calculation of coefficient c for determination of natural roll period by different methodologies are provided on Fig. 6:

1. IMO methodology, (2).
2. By formulae (15).
3. By formulae (17).

The calculations are carried out for sea-river vessel with different loading conditions. The ratio B/d is varied from 3.58 to 7,43; ratio z_g/B from 0,19 to 0,38; water plane area coefficient varied slightly ($C_W \approx 0{,}70 – 0{,}90$).

Analysis of provided dependences shows that nature of varying coefficient from $\frac{\sqrt{h_0}}{B}$ is practically the same for a number of methods: the value of coefficient c droningly reduces while $\frac{\sqrt{h_0}}{B}$ grows. The exclusion is method (2) (IMO) because coefficient c does not depend from $\frac{\sqrt{h_0}}{B}$.

The dependences of coefficient c which was calculated according to IMO formulae and proposed method (17) with widely varying parameters $B/$d, z_g/B, C_W are compared on Fig. 7. The range of varying of parameters B/d, z_g/B, C_W practically covers the whole varying range for real vessels: B/d = 2– 8; z_g/B = 0,2 – 0,6; C_W = 0,70 – 0,90. It can be seen from the provided dependences that proposed method of determination of coefficient c is practically in agreement with IMO method with $B/d \geq 4$ but has some advantages because it takes into account the influence of z-coordinate of center of gravity on natural roll period and takes into account more fully the ratio B/d.

Test calculations were carried out for 79 vessels of different types with different loading conditions (289 variants in total).

The difference in natural roll periods between IMO method and proposed method is small and does not exceed 11 % and when $z_g/B \approx 0{,}33 - 0{,}35$ they give practically the same results. When $z_g/B < 0{,}33$ roll period is less according to proposed method and when $z_g/B > 0{,}35$ it is larger than for IMO method.

Calculation method of natural roll period practically does not affect roll amplitudes for all loading conditions under consideration. It's obvious that Weather Criterion practically does not change when calculating period according to the proposed method.

The revised formulae (17) can be applied for vessels with ratio $B/d > 3{,}5$ and takes into account z-coordinate of center of gravity, but it practically does not affect roll amplitudes. So the existing formula for calculation of coefficient c can be applied to calculate roll amplitudes that are used for acceleration calculation for vessels with ratio $B/d > 3{,}5$.

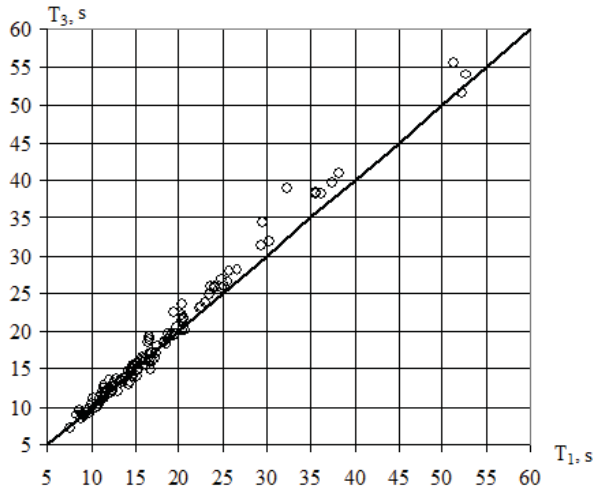

Fig. 5. Roll periods of ships of unrestricted service: T_1 – IMO , T_3 – proposed method

5. INFLUENCE OF NONLINEAR COMPONENTS ON THE VALUE OF ACCELERATION, DURING ROLLING

Calculation method for acceleration for other types of ship motions should be considered because of the influence of angular accelerations from roll and horizontal accelerations from sway on people health ("human element" in ship operation and carrying out of different work) [15].

Calculation method for acceleration for all types of roll except surge and yaw in linear and nonlinear formulation on regular waves is proposed in work [2]. This work notes that significant lateral horizontal accelerations are occurred because of the nonlinearity of roll especially at range of low frequencies $\omega < 0{,}8$. Herewith the acceleration amplitude can be greater on 30 – 50 % of the appropriate amplitudes that are calculated according to the linear theory.

The influence of nonlinear second order factors on the values of accelerations when sway occurs can reach 20 – 40 % at range of frequencies $\omega < 0{,}5$. The results of acceleration (from sway and roll) calculation in accordance with nonlinear theory at cross point of side and deck is also significantly differs from the same results in accordance with linear theory.

Contribution of roll in common balance of horizontal accelerations for usual loading cases (h_0 below 2 m) constitutes 15 – 20%. Accelerations themselves are 0,15 – 0,20g, but if metacentric height is greater it can reach 60% and summary accelerations significantly exceeds permissible values for horizontal accelerations.

The influence of nonlinear factors on accelerations in different points of vessel first of all depends on value of metacentric height h_0. Roll amplitudes for vessels with $h_0 < 1$ m which are calculated in accordance with nonlinear theory can exceed 50 – 60 % the

appropriate amplitudes which are calculated according to linear theory at range of main resonance. The influence of nonlinear factors at range of main resonance mode of rolling is practically absent for vessels with $h_0 > 2$ m, but it appears at range of super harmonic resonance.

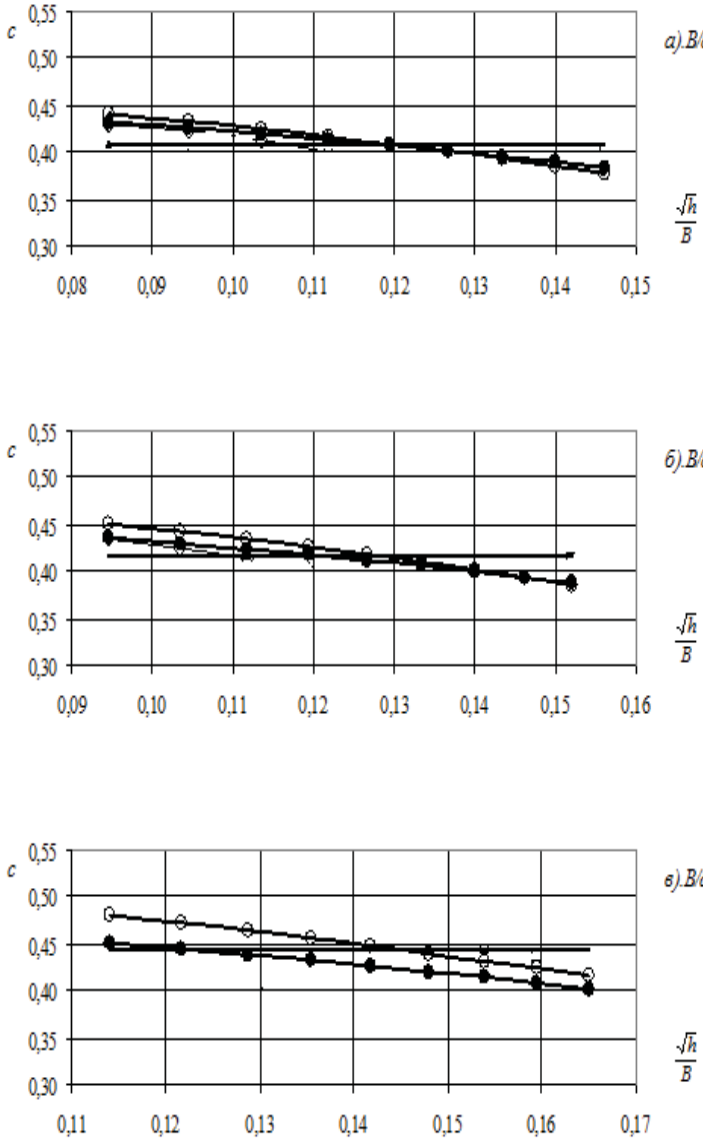

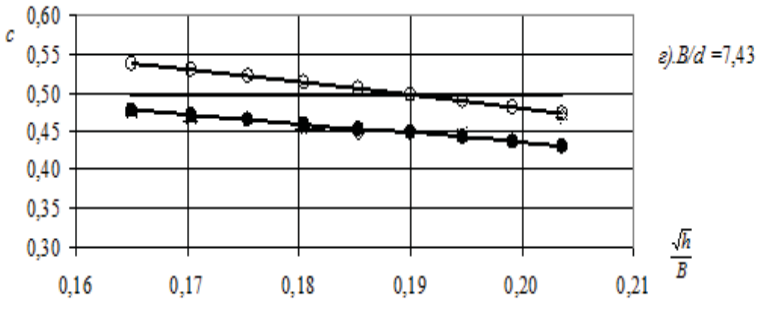

Fig. 6. Coefficient c, calculated according to methodologies:
—1, —●—2, —○—3,

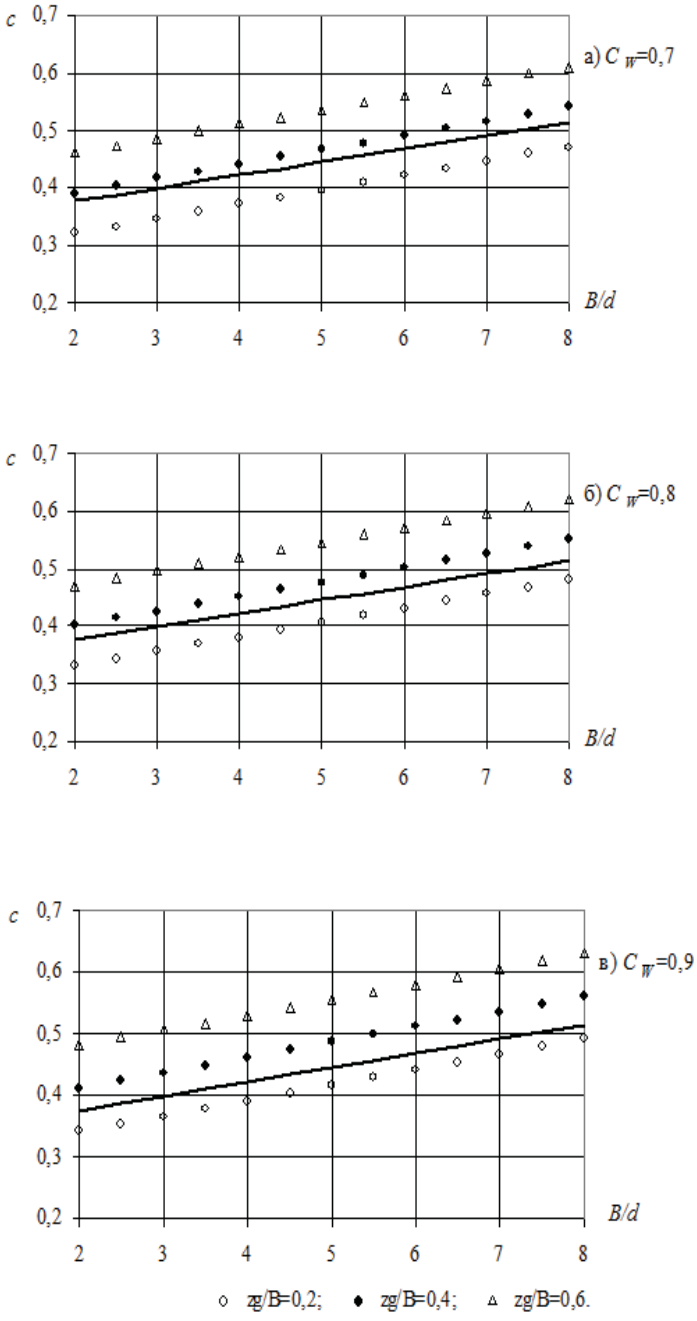

Fig. 7. Coefficient c

Main contribution to vertical accelerations at fore perpendicular is made by pitching (up to 80%) and contribution that is made by heaving is much less (up to 20%).

Significant influence of speed on acceleration should be noted. Its growth leads to drastic increase of amplitude of vertical accelerations and accelerations from surge at range of main resonance and super harmonic resonance. So the values of acceleration from heaving and surge when Fr = 0,306 are higher for 75% and 40% accordingly than when Fr = 0,2. The increment of the above mentioned values for 33 – 35 % occurs at range of super harmonic resonance modes.

6. CONCLUSION

Vulnerability criterion for excessive acceleration 1 level is proposed. The possibility of appliance of present formulae for roll calculation from Weather Criterion during acceleration calculation is showed. Data about the influence of nonlinear component on accelerations during rolling are presented. Formulae for calculation of coefficient c is proposed. Information that is contained in this paper can be used for additional work of vulnerability criterion for excessive accelerations 1 level.

7. REFERENCES

Anfimov V. N., Avdeev G. K. Hydrodynamic characteristics and calculation of roll amplitudes of inland-navigation vessels // Tr. CRI RF. – Ed. XXX. – L., 1955.

Borisov R. V., Kuteynikov M. A. Semenova V. Y., Luzyanin A. A. About the problem of standardizing of accelerations caused by roll. UDK 629.12.073.243.4 // Scientific and technical compilation No. 27. – SPb.: Russian Maritime Register of Shipping, 2004.

Borisov R. V., Kuteynikov M. A., Luzyanin A. A. Method of calculation assessment of natural roll period of marine vessels of different types. UDK 629.12.001.11 // Scientific and technical compilation No. 27. – SPb.: Russian Maritime Register of Shipping, 2004.

Code of Intact Stability for All Types of Ships. IMO Res. MSC.267(85). – 2008.

Kuteynikov M. A. The development and researching of theoretical basic foundation for setting of operational limitations when standardizing of marine vessels seaworthiness // Abstract for thesis for competition of Ph. D. science degree. – SPb.: SPbSMTU, 2001.

Lugovskiy V. V. Nonlinear tasks of seaworthiness. – L.: Shipbuilding, 1966.

Lugovskiy V. V. Roll of the ship. Text-book. – SPb.: Pub. Center SPbSMTU, 1999.

Nieuwenhuysen J. N. Experimental investigations on seasickness. Diss. Utrecht, 1958.

Panenko S. M. Hydrodynamic characteristics of roll of hopper dredgers // Scientific and technical compilation of USSR. Book 2. – L.: Transport, 1972.

Rules for the Classification and Construction of Sea-Going Ships. – SPb.: Russian Maritime Register of Shipping, 2015. – T. 1.

Semenov-Tyan-Shanskiy V. V., Blagoveshenskiy S. N., Holodilin A. N. Roll of the ship. L.: Shipbuilding, 1971.

Semenova V. Y. Research and development of programs for calculation of nonlinear hydrodynamic forces which are occurred due to roll of contour of ship form on the free surface of liquid // Thesis for competition of Ph. D. science degree. – SPb.: SPbSMTU, 1999.

Ship theory guide / Ed. Y. I. Voytkunskiy. – L.: Shipbuilding, 1985. – T.2.

Shmirev. A. N., Morenshildt V. A., Ilyina S. G. Anti-rolling devices of vessels. – L.: Transport, 1972.

Skorohodov D. A. Navigation and control of vessel movement. – SPb.: Almor, 2002.

Borisov R. V., Luzyanin A. A. The development of theoretical basic foundation for ships of different types when rolling //Report on theme. Baltic Engineering Center. – 2002.

Anfimov V. N., Vasilev A. I., Egorov G. A., Mamontov Y. N. The researching of seaworthiness of marine vessels with excessive stability and large block coefficient // Final report on theme 73-632. – L.: LIWT (Leningrad Institute of Water Transport), 1974.

A Simplified Simulation Model for a Ship Steering in Regular Waves

Xiechong Gu, *State Key Laboratory of Ocean Engineering, Shanghai Jiao Tong University* (*SJTU*), *Shanghai, China* xcgu@sjtu.edu.cn

Ning Ma, *State Key Laboratory of Ocean Engineering, SJTU, China* ningma@sjtu.edu.cn

Jing Xu, *China Ship Development and Design Centre, Wuhan, China* xujing.sjtu@gmail.com

Dongjian Zhu, *Shanghai Merchant Ship Design and Research Institute* tobya@sjtu.edu.cn

ABSTRACT

A simplified simulation model for a ship steering in regular waves is proposed. It combines the traditional MMG (mathematical manoeuvring group) model with seakeeping model. The former divides hydrodynamic forces into individual ones on the hull, from propeller and due to rudder operation. The latter treats wave forces as the first and second order ones. Impulse response functions, transformed from RAOs, are convoluted with ship motions. Manoeuvring of S175 container ship in regular waves is simulated, and validated by free running tests in regular waves of a S175 model in our ocean engineering basin. Validity and effectiveness of the simulation model are shown.

Keywords: *ship manoeuvring in waves, seakeeping, time domain simulation, impulse response function, second order wave force*

1. INTRODUCTION

Nowadays, manoeuvrability and seakeeping performance has begun to be wholly considered. In the past half a century, manoeuvrability is basically assessed in calm water. A MMG model, out of other theoretical models, was put forward by MMG group in Japan and showed very effective. In MMG model, hydrodynamic forces are split into individual parts, the ones on the ship hull, from the propeller and due to rudder operation, while interactions between them are implicitly, rather than explicitly, shown. Later, Hirano (1981) extended the calm water theory to operation in waves and added second order wave forces into the model. It takes water wave effects into account. Hirano (1981) measured second order wave forces and then calculated turning trajectory in waves. Kijima (1997) further improved the model, taking first order wave forces and roll response into account, and established a 4DOF MMG model. Kijima (1997) investigated effects of waves on turning trajectories. Yasukawa (2008) extended it to 6DOF motion. Accuracy of the simulated turning trajectory of a container ship in regular waves was apparently improved. On the other hand, Skejec (2008) established a unified manoeuvring and seakeeping model, where first order wave loads are evaluated by STF strip theory by Salvesen (1970). Skejec (2008) systematically investigated estimation methods for various hydrodynamic loads, and only those of suitable ones enter into the model. Turning trajectories simulated are much nice.

This paper presents a 6DOF model, of which manoeuvring and seakeeping are integrated. First order and second order wave loads in frequency domain are calculated in terms of

a code by three dimensional panel method. Impulse response functions are derived from the response amplitude operators (RAOs) by Fourier transformation. Motion equations are solved step by step in time domain. Turning trajectories and history of seakeeping motions are simultaneously obtained. For validation, free running tests of a S175 ship model are performed in our ocean engineering basin.

Below, a mathematical model is described at first, where coordinate systems, estimation method for various hydrodynamic loads, motion equations and solution method are shown. Next, numerical results, model ship specifications, simulated and measured turning trajectories and zigzag motions are given. Finally a brief conclusion is stated.

2. MATHEMATICAL MODEL

2.1 General Equations of Motion

Consider a ship travelling in regular waves. As Fig.1 shows, a global coordinate system, $O_0X_0Y_0Z_0$, is established. O_0X_0 coincides with wave propagation direction. Another coordinate system, $Gx_by_bz_b$, is fixed on the ship. G denotes the centre of gravity of the ship. Location G, (x_0, y_0, z_0), in $O_0X_0Y_0Z_0$ and attitude, (φ, θ, ψ), of the ship vary with time t. Heading angle, *i.e.* yaw angle, ψ, is measured from Gx_b to O_0X_0, pitching angle, θ, is from Gx_b to horizontal plane $O_0X_0Y_0$, and roll angle, φ, is from Gz_b to the vertical plane through longitudinal centreline of the ship. We denote (u, v, w) as the velocity at G in $Gx_by_bz_b$, and (p, q, r) as angular velocity of the ship. Relations of Eq.1 and Eq.2 can be derived. In these equations, dot over a symbol, say $\dot{x}_0$, means time derivative of that symbol, say x_0.

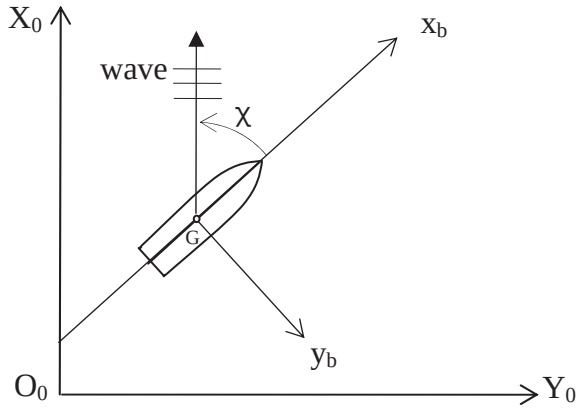

Figure 1 Coordinate Systems

$$\begin{bmatrix}\dot{x}_0\\ \dot{y}_0\\ \dot{z}_0\end{bmatrix}=\begin{bmatrix}\cos\psi\cos\theta & \begin{pmatrix}-\sin\psi\cos\phi+\\ +\cos\psi\sin\theta\sin\phi\end{pmatrix} & \begin{pmatrix}\sin\psi\sin\phi+\\ +\cos\psi\sin\theta\cos\phi\end{pmatrix}\\ \sin\psi\cos\theta & \begin{pmatrix}\cos\psi\cos\phi+\\ +\sin\psi\sin\theta\sin\phi\end{pmatrix} & \begin{pmatrix}-\cos\psi\sin\phi+\\ +\sin\psi\sin\theta\cos\phi\end{pmatrix}\\ -\sin\theta & \cos\theta\sin\phi & \cos\theta\cos\phi\end{bmatrix}\cdot\begin{bmatrix}u\\ v\\ w\end{bmatrix} \tag{1}$$

$$\begin{bmatrix}\dot{\phi}\\ \dot{\theta}\\ \dot{\psi}\end{bmatrix}=\begin{bmatrix}1 & \sin\phi\tan\theta & \cos\phi\tan\theta\\ 0 & \cos\phi & -\sin\phi\\ 0 & \sin\phi/\cos\theta & \cos\phi/\cos\theta\end{bmatrix}\begin{bmatrix}p\\ q\\ r\end{bmatrix} \tag{2}$$

According to MMG model, forces and moments on a ship are written as the sum of those due to ship hull, propeller, rudder where coupling effect between them is not explicitly shown. In addition, components due to wave, both the first order and the second order wave forces, are also added. This results Eq.3, a general equation of ship motions

$$\begin{cases} m(\dot{u}-vr+wq)=X_H+X_P+X_R+X_{1W}+X_{2W}\\ m(\dot{v}+ur-pw)=Y_H+Y_P+Y_R+Y_{1W}+Y_{2W}\\ m(\dot{w}-uq+vp)=Z_H+Z_{1W}\\ I_{xx}\dot{p}=K_H+K_R+K_{1W}\\ I_{yy}\dot{q}+(I_{xx}-I_{zz})pr=M_H+M_{1W}\\ I_{zz}\dot{r}+(I_{yy}-I_{xx})pq=N_H+N_P+N_R+N_{1W}+N_{2W}\end{cases} \tag{3}$$

where subscripts *H*, *P*, *R*, *1W* and *2W* stand for the forces or moments due to ship hull, propeller, rudder, the first order and the second order wave forces respectively. m is mass of the ship, and I_{xx}, I_{yy}, I_{zz} are moments of inertia of the ship with respect to axes Gx_b, Gy_b, Gz_b respectively, while other cross components are relatively small and ignored. Whenever general forces on the right hand side of Eq.3 are estimated step by step, motions of the ship are accordingly obtained by solving Eq.3. Estimations of these forces will be given below.

2.2 Propeller Forces

For simplicity, propeller is considered only producing either forward or backward forces,

$$X_P = (1-t_P)\cdot \rho n^2 {D_P}^4 \cdot K_T(J_P) \tag{4}$$

while Y_P and N_P are reasonably neglected. Here ρ is the water density, D_P diameter of the propeller, n rotational speed. Thrust deduction factor t_p is estimated from empirical formulas. $K_T(J_P)$ is open water propeller thrust coefficient, varies with advance coefficient J_P, where wake coefficient is also estimated from an empirical formula.

2.3 Rudder Forces

Rudder forces are dominantly due to the lift force, F_N, on the rudder. It causes mainly drag and drift forces, yawing and heel moments on the ship.

$$\begin{cases} X_R = (1-t_R)F_N \sin\delta \\ Y_R = (1+a_H)F_N \cos\delta \\ N_R = (x_R + a_H x_H)F_N \cos\delta \\ K_R = z_G Y_R \end{cases} \tag{5}$$

where δ is the rudder angle, t_R the rudder drag reduction factor, mainly due to the wake, a_H is drift force modification factor, x_H the distance from rudder centre to G, the centre of gravity of the ship, x_R is the horizontal distance from resultant rudder force to rudder centre, z_G is vertical coordinate of the resultant rudder force.

2.4 Hull Forces

This kind of forces is due to the ship moves advancing in calm water. It can be considered as two parts, one is due to pressures normal to the hull, the other is due to shear stress tangent to the hull.

Eq.6 is the contribution of pressure, which is evaluated by potential flow theory. Eq.7 shows the contribution of shear stress, which could be obtained either from captive model tests or from empirical formulas.

$$\begin{cases} -X_{HI} = A_{11}\dot{u} - A_{22}vr + A_{33}wq \\ -Y_{HI} = A_{22}\dot{v} + A_{11}ur - A_{33}pw \\ -Z_{HI} = A_{33}\dot{w} - A_{11}uq + A_{22}vp \\ -K_{HI} = A_{44}\dot{p} + (A_{66} - A_{55})qr + (A_{33} - A_{22})vw \\ -M_{HI} = A_{55}\dot{q} + (A_{44} - A_{66})pr + (A_{11} - A_{33})uw \\ -N_{HI} = A_{66}\dot{r} + (A_{55} - A_{44})pq + (A_{22} - A_{11})uv \end{cases} \tag{6}$$

$$\begin{cases} X_{HV} = X_{uu}u^2 + X_{vv}v^2 + X_{vr}vr + X_{rr}r^2 \\ Y_{HV} = Y_v v + Y_r r + Y_{|v|v}|v|v + Y_{|r|r}|r|r + Y_{vvr}v^2 r + Y_{vrr}vr^2 \\ Z_{HV} = -Z_w w - Z_q q - Z_{\dot{q}}\dot{q} - Z_\theta \theta \\ K_{HV} = -2K_p p - \rho g \nabla \overline{GM} \sin\varphi - Y_H z_H \\ M_{HV} = -M_w w - M_{\dot{w}}\dot{w} - M_q q - M_\theta \theta \\ N_{HV} = N_v v + N_r r + N_{|v|v}|v|v + N_{|r|r}|r|r + N_{vvr}v^2 r + N_{vrr}vr^2 + Y_H \cdot X_c \end{cases} \tag{7}$$

Subscript I in Eq.6 stands for those due to pressures, and subscript V in Eq.7 for those due to shear stresses, their sum gives the hull forces. For example, X_{HI}+X_{HV} gives out X_H. A_{ij} is the added mass of i-mode motion due to j-mode motion of the ship. ∇ is the volume displaced by the ship, GM the transverse metacentric height of the ship.

2.5 Wave Forces

Wave forces are decomposed into the first order and the second order ones. The former is further separated to the incident wave forces, *i.e.* Froude-Krylov forces, radiation ones and diffraction ones. Panel method is powerful in solution for velocity potential of radiation and diffraction. According to Cummins (1962), the radiation and diffraction forces are expressed as follows.

$$F_{jk}^R = -\mu_{jk}\ddot{\eta}_k(t) - b_{jk}\dot{\eta}_k(t) - c_{jk}\eta_k(t) - \int_0^t K_{jk}(t-\tau)\cdot\eta_k(\tau)d\tau \tag{8}$$

$$F_j(t) = F_j^D + F_j^I = -\int_{-\infty}^{t} H_j(t-\tau)h(\tau)d\tau \tag{9}$$

where superscript R stands for radiation, I and D are for incident wave and diffraction. $h(\tau)$ is the incident wave elevation at the instant τ. $\eta_k(\tau)$

is the moving displacement of mode k motion at the instant τ. The kernel function $K_{jk}(\tau)$ can be obtained from the damping coefficient $B_{jk}(\omega)$

$$K_{jk}(\tau)=\frac{2}{\pi}\int_0^{\infty}B_{jk}(\omega)\cdot\cos(\omega\tau)d\omega \tag{10}$$

$$\mu_{jk}=A_{jk}^{\infty} \tag{11}$$

$$b_{jk}=B_{jk}^{\infty} \tag{12}$$

that is, μ_{jk} and b_{jk} correspond to the added mass A_{jk} and damping coefficient B_{jk} at extremely high frequency, whereas c_{jk} is restoring forces with nonzero components follows

$$\begin{aligned} c_{33}&=\rho g A_{wp}\\ c_{35}&=c_{53}=-\rho g S_y\\ c_{44}&=\rho g\nabla\overline{GM}_T\\ c_{55}&=\rho g\nabla\overline{GM}_L \end{aligned} \tag{13}$$

where A_{wp} is the water plane area, S_y the first order moment of the water plane with respect to Gy_b axis, GM_T and GM_L are the transverse metacentric height and longitudinal metacentric height respectively.

Kernel function $H_j(t)$ is obtained from the wave force $f_{wj}(\omega)$ due to incident wave of unit amplitude and its corresponding diffraction as follows

$$H_j(t)=\frac{1}{2\pi}\int_{-\infty}^{\infty}f_{wj}(\omega)e^{-i\omega t}d\omega \tag{14}$$

As for the second order drift forces, at first we get the response amplitude operator (RAO) from panel method for different frequencies and heading angles, then at any instant the drift force is evaluated by interpolation of the RAO for the specified encounter frequency and heading angle.

2.6 Numerical Algorithm

In simulation, at first by means of the code based on panel method, radiation and diffraction problems are solved, then added mass and damping coefficient are evaluated, and kernel functions $K_{jk}(\tau)$ and $H_j(t)$ are calculated. At last, the 4th order Runge-Kutta method is applied to solve Eq.3 in time domain step by step.

3. NUMERICAL RESULTS

3.1 Ship for simulation

In simulation, the S175 container ship is used. Table 1 lists principal particulars of S175. Fig.2 shows meshes. In total 1968 quadrilateral meshes are used in calculation.

At first, linear wave force, added mass and damping coefficients, motion response and the second order wave force are calculated by the

Table 1. Principle particulars of S175

symbol	magnitude	unit
L_{OA}	183.0	m
L_{PP}	175.0	m
L_{WL}	178.2	m
B	25.4	m
D	15.0	m
d	9.5	m
∇	24380.6	m^3
C_B	0.5774	
KM	10.5	m
x_B (from AP)	80.64	m
k_{xx}	8.5852	m

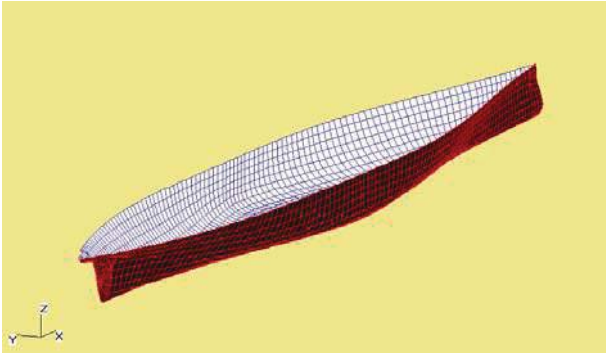

Figure 2 Meshes of S175 for Simulation

using the code based on panel method. In calculation, encounter wave frequency is in between 0.1 and 12 *rad/s*, with increment 0.1 *rad/s*. Heading angle relative to the wave is in between 0 to 360 *deg*, with increment 10 *deg*. It is found that results for 1968 meshes show almost no significant difference with those for more meshes, say 3156 meshes. Service speed corresponds Froude number 0.166. The second order wave force for specified encounter wave frequency and heading angle is evaluated from the computed results by applying Lagrange interpolation algorithm.

Fig.3 to 8 show response amplitude operators (RAOs) of motions. Fig.9 and 10 are the calculated added mass and damping coefficient. Fig.11 shows the first order wave forces and moments in beam waves. Fig.12 shows the second order wave forces and moments in beam waves.

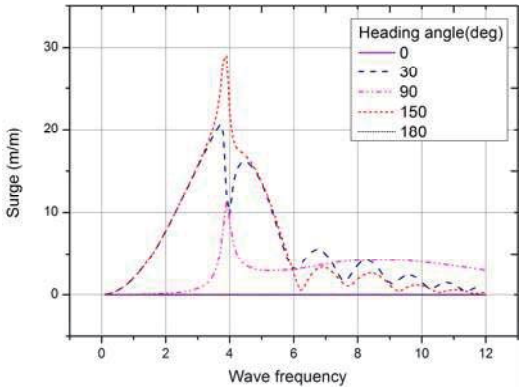

Figure 3 RAO of Surge

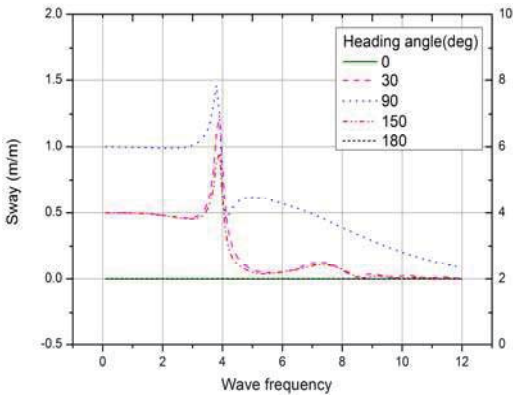

Figure 4 RAO of Sway

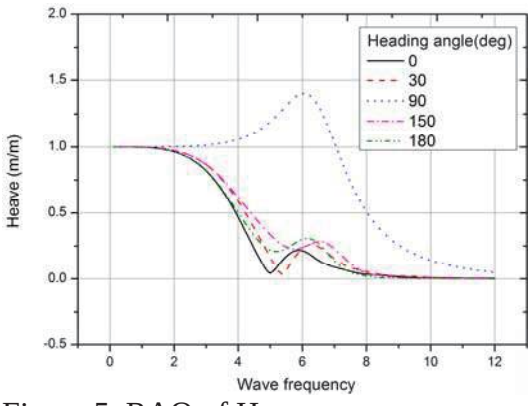

Figure 5 RAO of Heave

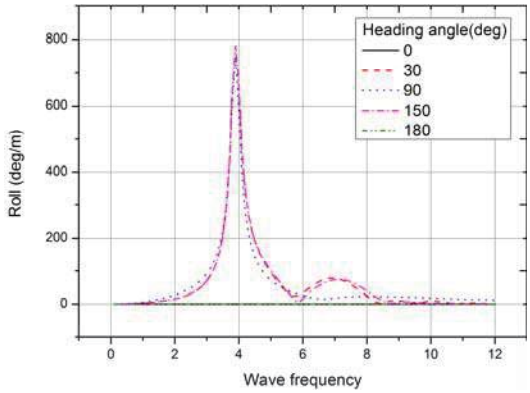

Figure 6 RAO of Roll

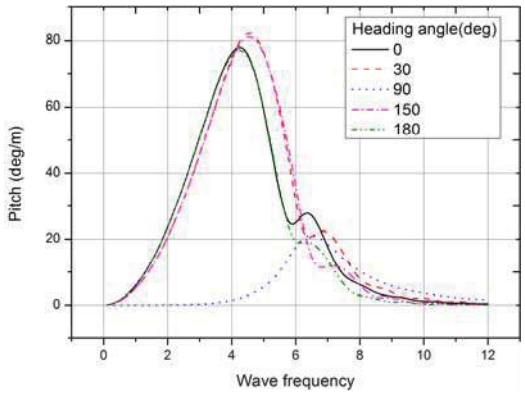

Figure 7 RAO of Pitch

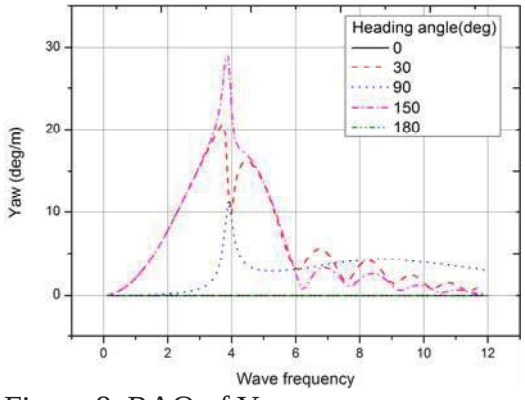

Figure 8 RAO of Yaw

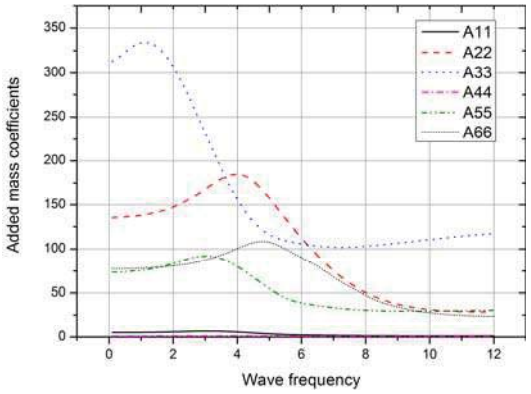

Figure 9 Added Mass

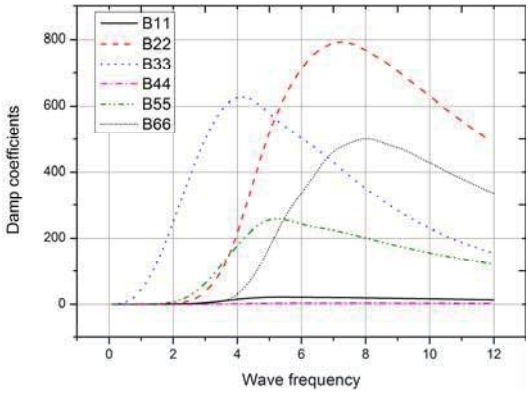

Figure 10 Damping Coefficient

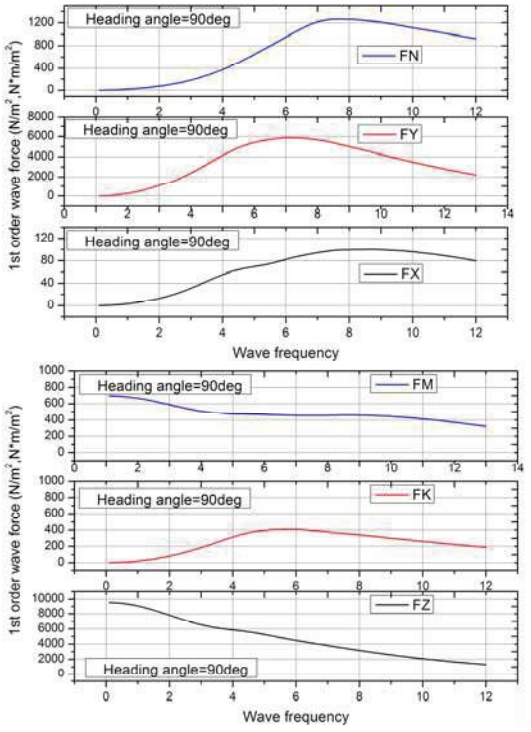

Figure 11 The First Order Wave Forces in Beam Waves

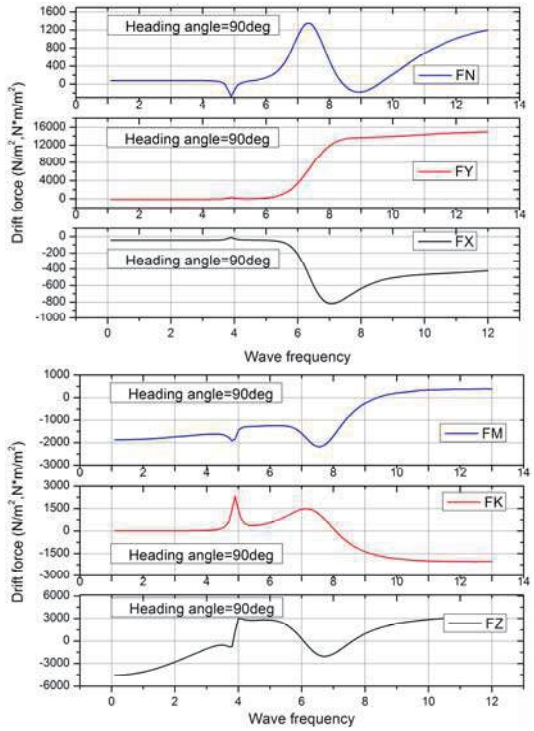

Figure 12 The Second Order Wave Forces in Beam Waves

Figure 13 Ship Model of S175

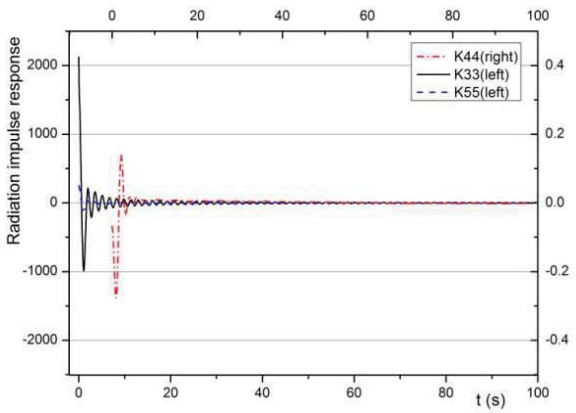

Figure 14 Radiation Impulse Responses

Equations of motion to be solved are summarized in Eq.15. In order to validate simulation method, a free running test for a S175 ship model, see Fig.13, with scale factor 57.69 was performed in the ocean engineering basin of Shanghai Jiao Tong University. Fig.14 shows the calculated radiation impulse responses.

$$
\begin{cases}
m(\dot{u}-vr+wq)+A_{11}\dot{u}-A_{22}vr+A_{33}wq+\int_0^t K_{11}(t-\tau)\cdot ud\tau+\int_{-\infty}^t H_{11}(t-\tau)\cdot h(\tau)d\tau \\
\quad = X_{HV}+X_P+X_R \\
m(\dot{v}+ur-pw)+A_{22}\dot{v}+A_{11}ur-A_{33}pw+\int_0^t K_{22}(t-\tau)\cdot vd\tau+\int_0^t K_{24}(t-\tau)\cdot pd\tau \\
\quad +\int_0^t K_{26}(t-\tau)\cdot rd\tau+\int_{-\infty}^t H_{22}(t-\tau)\cdot h(\tau)d\tau = Y_{HV}+Y_P+Y_R \\
m(\dot{w}-uq+vp)+A_{33}\dot{w}-A_{11}uq+A_{22}vp+C_{33}\cdot\eta_3(t)+C_{35}\cdot\eta_5(t)+B_{33}w+B_{35}q \\
\quad +\int_0^t K_{33}(t-\tau)\cdot wd\tau+\int_0^t K_{35}(t-\tau)\cdot qd\tau+\int_{-\infty}^t H_{33}(t-\tau)\cdot h(\tau)d\tau = Z_{HV} \\
I_{xx}\dot{p}+A_{44}\dot{p}+(A_{66}-A_{55})qr+(A_{33}-A_{22})vw+B_{44}\cdot p+C_{44}\cdot\eta_4(t)+\int_0^t K_{44}(t-\tau)\cdot pd\tau \\
\quad +\int_0^t K_{42}(t-\tau)\cdot vd\tau+\int_0^t K_{46}(t-\tau)\cdot rd\tau+\int_{-\infty}^t H_{44}(t-\tau)\cdot h(\tau)d\tau = K_{HV}+K_R \\
I_{yy}\dot{q}+(I_{xx}-I_{zz})pr+A_{55}\dot{q}+(A_{44}-A_{66})pr+(A_{11}-A_{33})uw+C_{55}\cdot\eta_5(t)+C_{53}\eta_3(t) \\
\quad +B_{53}\cdot w+B_{55}\cdot q+\int_0^t K_{55}(t-\tau)\cdot qd\tau+\int_0^t K_{53}(t-\tau)\cdot wd\tau+\int_{-\infty}^t H_{55}(t-\tau)\cdot h(\tau)d\tau = M_{HV} \\
I_{zz}\dot{r}+(I_{yy}-I_{xx})pq+A_{66}\dot{r}+(A_{55}-A_{44})pq+(A_{22}-A_{11})uv+\int_0^t K_{66}(t-\tau)\cdot rd\tau \\
\quad +\int_0^t K_{62}(t-\tau)\cdot vd\tau+\int_0^t K_{64}(t-\tau)\cdot pd\tau+\int_{-\infty}^t H_{66}(t-\tau)\cdot h(\tau)d\tau = N_{HV}+N_P+N_R-Y_{HV}\cdot x_c
\end{cases}
\tag{15}
$$

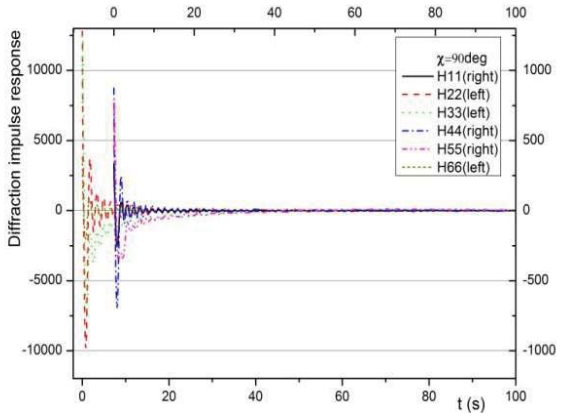

Figure 15 Diffraction Impulse Responses

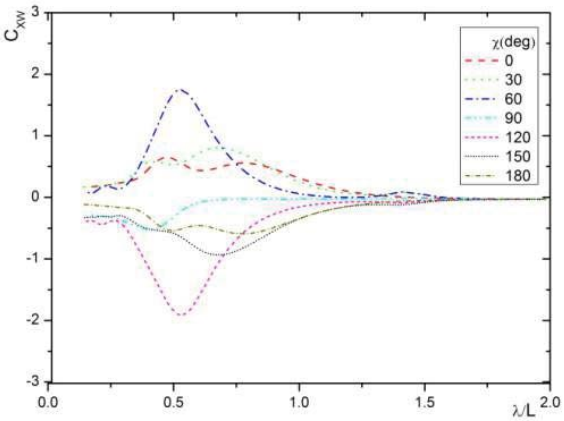

Figure 16 Longitudinal Second Order Wave Force Coefficients

Fig.15 gives out the calculated diffraction impulse responses at beam waves. Fig.16, 17 and 18 show the calculated results of longitudinal, lateral and yawing second order wave forces at various heading angles.

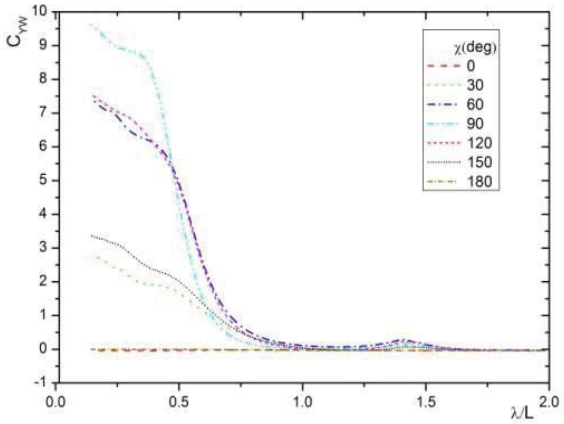

Figure 17 Lateral Second Order Wave Force Coefficients

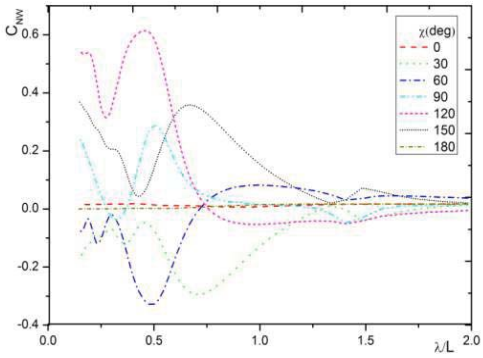

Figure 18 Yawing Second Order Wave Moment Coefficients

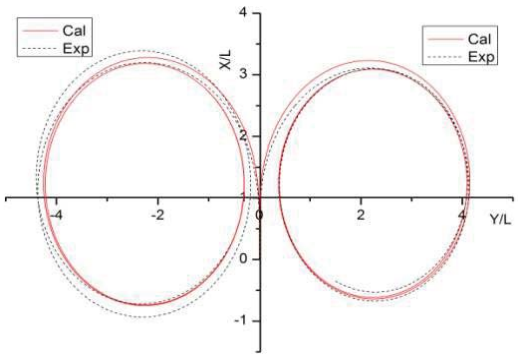

Figure 19 Turning Circle in Still Water with Rudder Angle ±35°

Based on the above results, turning circle and zigzag test are simulated by solving Eq.15 numerically. Fig.19 shows that in still water the simulated circles agree quite well to measured ones at rudder angles of left and right 35° . Fig.20 and 21 demonstrates that in still water the simulated zigzag results are very close to the measured records.

Now wave is introduced. As above, initial speed of the ship model is unchanged, also 0.72 *m/s*. Fig.22 is a comparison of the simulated turning circle in head wave with the test record.

Amplitude of the wave is 13.5 *mm*, and the ratio of wavelength to ship model length is 1.4. It can be seen that the turning circle drifts along the wave propagating direction downwards. The second order wave drift force seems the main cause of this phenomenon. Agreement of the simulated one with the test result is still quite good.

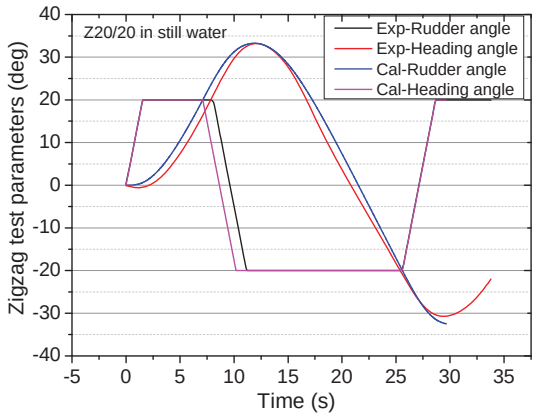

Figure 20 20/20° Zigzag in Still Water

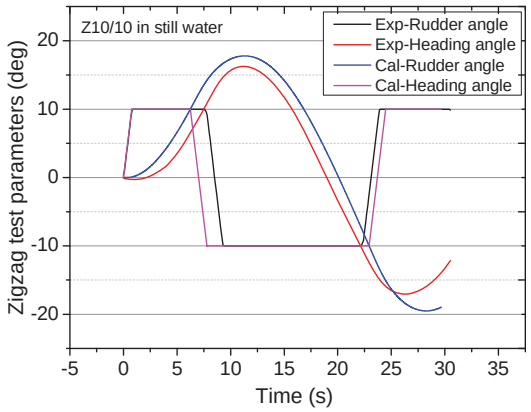

Figure 21 10/10° Zigzag in Still Water

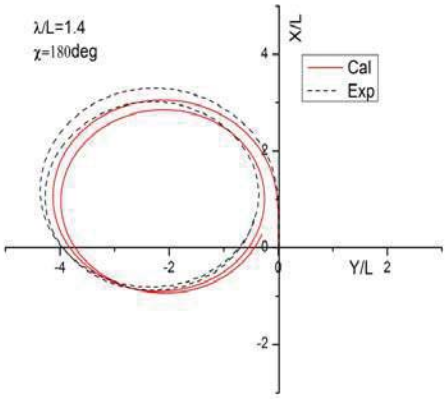

Figure 22 Turning Circle in a Head Wave

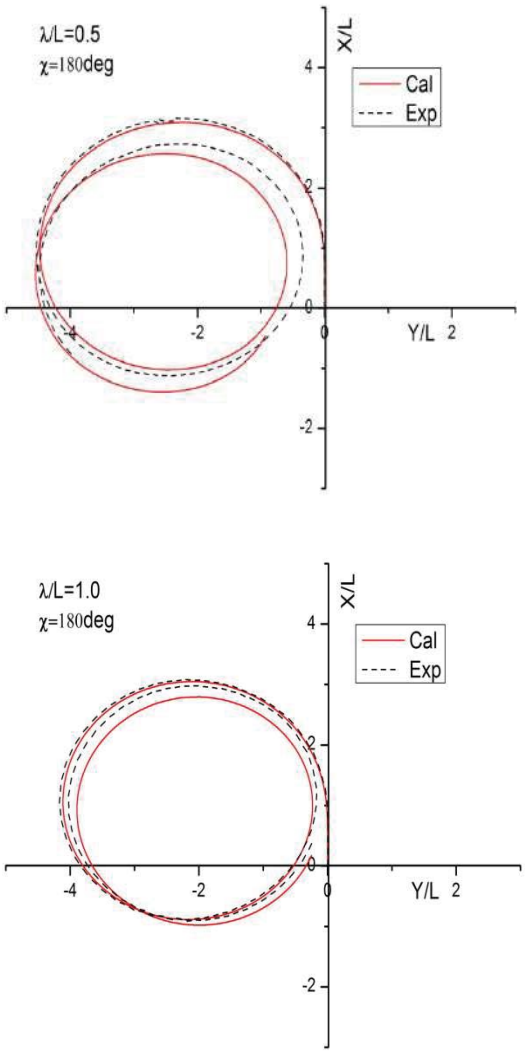

Figure 23 Turning Circle in Head Waves with Different Wave Lengths

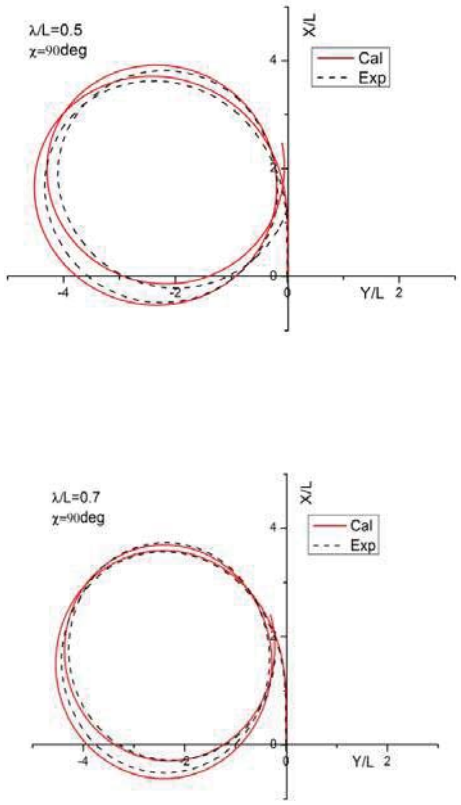

Figure 24 Turning Circle in Beam Waves with Different Wave Lengths

Fig.23 and 24 show turning circles in head and beam waves with different wavelengths. Agreement of the simulated ones with the test results is also quite good.

4. CONCLUSION

A simplified simulation method for a ship steering in regular waves is developed. The traditional MMG (mathematical manoeuvring group) model is combined with the Cummins seakeeping model. The former separates hydro-dynamic forces into several individual parts due to different causes, such as the ones on the ship hull, from propeller and due to rudder operation. The latter takes linear and second order wave forces into account.

Based on the investigation for S175 ship, this method seems valid and effective enough. Since a ship steering in waves is affected by a lot of factors, and their mechanisms are quite specific and complicated, further systematic investigations is needed and will be done later, especially for validation, model tests in steeper waves is urgent.

5. ACKNOWLEDMENTS

This study is a part of Project 51279105 which is financially supported by the National Foundation of China.

6. REFERENCES

Cummins W.E., 1962, “The Impulse Response Function and Ship Motions”, Schiffstechnik 9, pp. 101-109

Hirano, M., Takashima, J., Takeshi, K. and Saruta T., 1981, “Ship turning trajectory in regular waves”, West Japan Society of Naval Architects, Vol. 60, pp. 17-31

Kijima, K., Furukawa, Y., 1997, “Ship maneuvering performance in waves”, Proceedings of 3rd International Stability Workshop

Salvesen, N., Tuck, E. 0. and Faltinsen, 0., 1970, “Ship Motions and Ship Loads”, Trans. SNAME, Vol. 78, pp. 250-287

Skejec, R. and Faltinsen, O.M., 2008, “A Unified Seakeeping and Maneuvering Analysis of Ships in Regular Waves”, Journal of Marine Science Technology, Vol. 13, No. 4, pp. 371-394

Yasukawa, H., 2008, “Simulations of Ship Maneuvering in Waves”, Journal of the Japan Society of Naval Architects and Ocean Engineers, Vol. 7, pp. 163-170

This page is intentionally left blank

Prediction of Wave-Induced Surge Force Using Overset Grid RANS Solver

Hirotada Hashimoto, *Kobe University*, hashimoto@port.kobe-u.ac.jp

Shota Yoneda, *Kobe University*, s_yoneda@maritime.kobe-u.ac.jp

Yusuke Tahara, *National Maritime Research Institute*, tahara@nmri.go.jp

Eiichi Kobayashi, *Kobe University*, kobayasi@maritime.kobe-u.ac.jp

ABSTRACT

Prediction of the wave surging force acting on a ship in following seas is a key issue for the accurate prediction of surf-riding phenomenon. It is pointed out that the linear Froude-Krylov component generally overestimates the amplitude of wave-induced surge force. Therefore a simple correction formula for the Froud-Krylov force is proposed in the second-generation intact stability criteria under discussed at IMO. In this study, a RaNS solver with an overset grid system is used to realize more accurate prediction of the wave-induced surge force. Then the current correction formula is evaluated based on the CFD results for a series of hull forms with variety of hull form parameters.

Keywords: *Second-generation intact stability criteria, Broaching/Surf-riding, Wave-induced surge force, Overset grid RaNS Solver, Froude-Krylov force, Correction formula*

1. INTRODUCTION

The second-generation intact stability criteria are under development at International Maritime Organization (IMO). There are five stability failure modes to be discussed, and experimental/numerical prediction of the wave-induced surge force in following and quartering waves became an important issue for relatively high-speed vessels because it has big influence on the threshold of surf-riding and near surf-riding condition, which are triggers for dangerous situations of broaching and pure loss of stability. In a conventional way, the wave-induced surge force is calculated as the Froude-Krylov force. However its accuracy is not satisfactory for a criteria-use purpose because it generally provides the larger amplitude of the wave-induced surge force, and hence the danger of broaching and pure loss of stability could be overestimated. Therefore more reliable approach is needed for the second-generation intact stability criteria for surf-riding/broaching, i.e. alternative to captive model experiments to measure the wave-induced surge force. In the prediction of the wave-induced surge force for a ship running in following seas, considering the effects of diffraction and ship motion could be candidates to improve the prediction accuracy, and a three-dimensional hydrodynamic effect is also a possible element, which are missing in the linear Froude-Krylov calculation based on the strip theory.

Following these situations, CFD (Computational Fluid Dynamics) simulation to estimate the wave-induced surge force in following waves is executed using an overset grid RaNS Solver (CFDShip Iowa ver.4.5). In this study, the ONR tumblehome vessel is used as a sample ship and the CFD results are

compared with an existing experimental result. As a result, it is well confirmed that the CFD provides more accurate prediction than the Froude-Krylov component and the CFD results show fairy good agreement with the experimental results in a sense of practical uses. Then further CFD-based studies are done for a series of ONR-tumblehome hulls with varieties of fineness coefficients to investigate the influence of the hull form on the wave-induced surge force, and then the current correction formula for the Froude-Krylov component in the level 2 vulnerability criterion for broaching, is evaluated.

2. SECOND-GENERATION INTACT STABILITY CRITERIA

In the level 2 vulnerability criterion for broaching, the amplitude of the wave-induced surging force is calculated as the linear Froude-Krylov force by Eq.1 (IMO, 2014) to obtain the critical Froude number corresponding to the threshold of surf-riding for regular waves. However it is pointed out that the Froude-Krylov component has a tendency to overestimate the amplitude of the wave-induced surge force. If a captive model experiment in a towing tank or a numerical test using CFDs is available, more accurate and reliable prediction can be achieved. However they are time- and cost- consuming methods for the ship design in an early stage, so a simple formula for the correction of the Froude-Krylov force is useful. In this reason, one proposal was submitted to IMO, as an alternative to model experiments and CFD simulations in the second-generation intact stability criteria, to introduce an empirical correction coefficient, μ_x, for the linear Froude-Krylov calculation (see Eq.3). This coefficient is aimed to consider the diffraction effect missing in the Froude-Krylov assumption, and is expressed as functions of C_m and C_b as shown in Eq.(4) (Ito et al., 2014) (IMO, 2014).

$$f = \rho g k \frac{H}{2} \sqrt{F_C^2 + F_S^2} \tag{1}$$

$$F_c = \int_{AE}^{FE} S(x) e^{-kd(x)/2} \sin kx dx \tag{2}$$

$$F_S = \int_{AE}^{FE} S(x) e^{-kd(x)/2} \cos kx dx$$

ρ: density
g: gravity
k: wave number
H: wave height
AE: ship aft end
FE: ship fore end
$S(x)$: sectional under-water area
$d(x)$: sectional draught

$$f = \rho g k \frac{H}{2} \mu_x \sqrt{F_C^2 + F_S^2} \tag{3}$$

Here μ_x is an empirical correction coefficient derived from several captive model tests using different types of ship.

$$\begin{aligned} \mu_x &= 1.46 C_b - 0.05 && C_m < 0.86 \\ &= (5.76 - 5.00 C_m) C_b - 0.05 && 0.86 < C_m < 0.94 \\ &= 1.06 C_b - 0.05 && C_m \geq 0.94 \end{aligned} \tag{4}$$

C_b: block coefficient
C_m: midship section cefficient

3. SUBJECT SHIP

It is important to investigate the accuracy of CFD solvers when trying to discuss a hull form effect on the wave surging force with CFD results. The ONR tumblehome, which is a wave-piercing high-speed mono hull vessel and is prone to suffer surf-riding/broaching because of her small resistance, is selected as the subject ship because a comprehensive experimental data regarding the broaching phenomenon is available. (e.g. Umeda et al. (2008), Hashimoto et al. (2011)) The original hull of the ONR tumblehome is so slender that the midship coefficient, C_m, and the block coefficient, C_b, are small as compared to conventional commercial ships. Principal

particulars of the subject ship are shown in Table 1.

In this study, a naked hull that was not equipped with bilge keels, shaft brackets and rudders is used. The subject ship is designed for a twin screw propulsion system, so relatively large centre skeg is installed. In order to investigate the effect of ship fineness coefficients (C_m and C_b) used in the correction coefficient, a series of hulls are artificially generated by changing the under-water hull form systematically as shown in Fig.1 and Table 2. In the hull form generation, the original length, breadth and depth of the ship are kept. Since the sonar-dome and transom stern shapes are not simple/smooth, these parts are not modified from the original design.

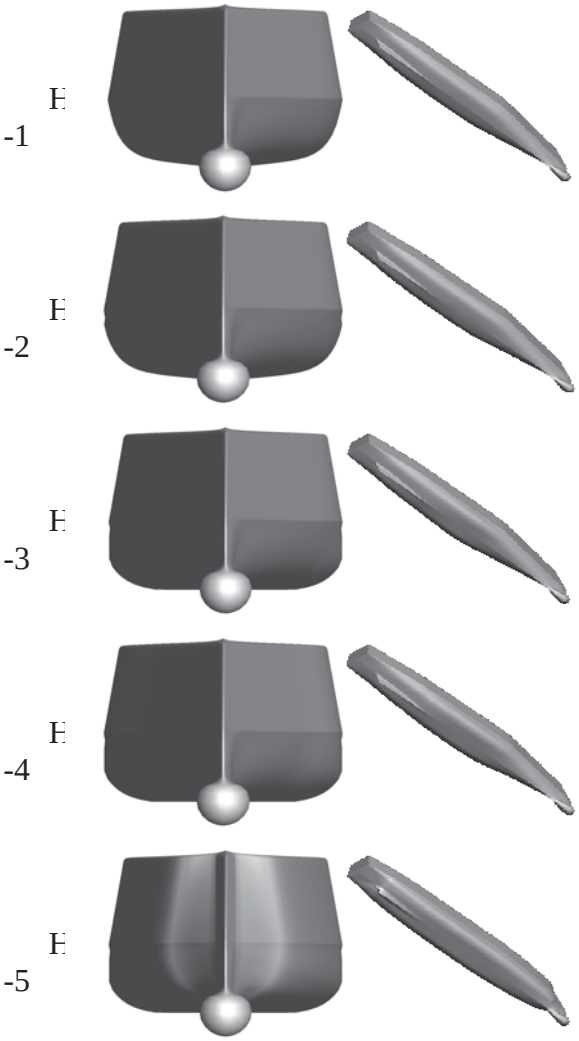

Figure 1 Geometry of the hulls

Table 1 Principal Particulars

Length: L	154.0 m
Breadth: B	18.8 m
Depth: D	14.5 m
Draught: d	5.5 m
Volume: V	8562 m^3
Block coefficient: C_b	0.535
Midship section cefficient: C_m	0.835
Radius of gyration in pitch: κ_{yy}/L	0.25

Table 2 Parameters of the hulls

name	C_m	C_b
H-1 (original hull)	0.835	0.539
H-2	0.880	0.546
H-3	0.950	0.556
H-4	0.950	0.571
H-5	0.950	0.695

4. CFD METHOD

4.1 RaNS solver

CFDShip Iowa ver.4.5 (Carrica et al., 2006) (Tahara et al., 2006) is used for numerical computation. CFDShip Iowa solves the RaNS equations using a blended k-ω/k-ε model for turbulence. The free surface is captured using a single-phase level set approach, in which the air/water interface is the zero level set distance function. The domain is discretized using multi-block structured grids. The capability of the overset is fully dynamic, which enables to simulate large amplitude motions in waves. Numerical methods include a finite difference discretization, with second-order upwind discretization for the convection term and second-order centered scheme for the viscous terms. The temporal terms are discretized using the second-order backwards Euler scheme. Incompressibility is imposed by the strong pressure/velocity coupling by using PISO. Regular waves are implemented through initial and boundary conditions. The fluid flow equations are solved in an earth-fixed inertial reference system, while the rigid body equations are done in the body-fixed system, so

forces and moments are projected to perform the integration of the rigid body equations of motion, which are solved iteratively. The SUGGAR module (Noack, 2007) is used for overset connectivity treatment and the PETSc (http://www.mcs.anl.gov/petsc/) is done to solve large simultaneous equations efficiently.

4.2 Grid

The overset grid design consists of 3 grids as shown in Fig.2. Two double-O boundary layer grids model the starboard and port sides of the hull to solve the asymmetric problem due to heeling. Cartesian grid is used as the background for the free surface and the wave propagation. Since the ship motion of heave and pitch is not small in steep waves even the encounter frequency is low, overset grids to accurately capture their effects might be needed to improve the prediction accuracy of the wave-induced surge force. The number of grid points is shown in Table 3. Since the total number is about 1 million, current laptop computers are sufficient enough to obtain CFD solutions. A mobile workstation of Dell Precision M6800 (Intel i7-4800MQ @2.7GHz) is used for this study.

4.3 Numerical condition

Numerical simulation using the overset grid RaNS solver is performed to obtain the wave-induced surge force acting on the subject ship running in pure following waves. Heave and pitch motions are solved in the CFD simulation, but other 4 degrees of surge, sway, roll, and yaw are fixed. Numerical conditions are shown in Table 4. Firstly the wave-induced surge force without heel is demonstrated to discuss the influence of hull form parameters, and then the influence of heel angle, ϕ, is also demonstrated. The wave length to ship length ratio, λ/L, of 1.25 is used in all the simulations because surf-riding and broaching phenomena are frequently observed in a free-running model experiment with this wave length to ship length ratio (Umeda et al., 2008), and the experimentally confirmed critical Froude number for the surf-riding was about 0.35 for λ/L of 1.25 and wave steepness, H/λ, of 0.05.

Table 3 Number of grid points

Domain	x*y*z direction	Grid points
Ship(S)	72*44*54	171,072
Ship(P)	72*44*54	171,072
Background	95*67*116	738,340
Total		1,080,484

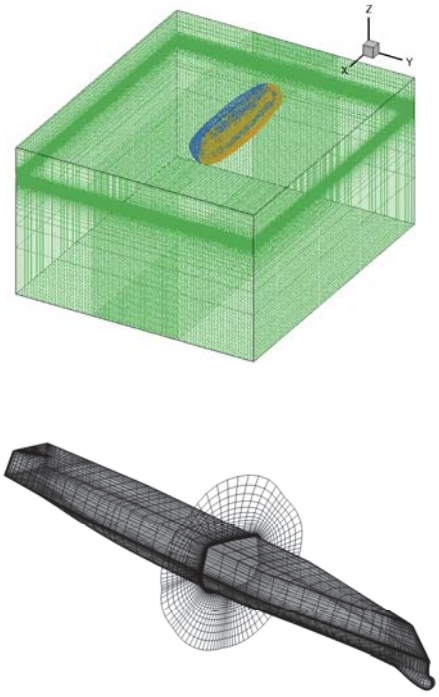

Figure 2 Computational grids

Table 4 Numerical condition

F_n	ϕ [deg]	λ/L	H/λ
0.35	0	1.25	1/40
0.35	0	1.25	1/20
0.35	10	1.25	1/40
0.35	10	1.25	1/20
0.35	20	1.25	1/40
0.35	20	1.25	1/20
0.35	30	1.25	1/40
0.35	30	1.25	1/20

5. RESULTS AND DISCUSSION

Prior to the investigation of the influence of hull form on the wave-induced surge force, the accuracy of the overset grid CFD solver is validated for the original hull (H-1) by comparing with an existing captive model experiment by Hashimoto et al. (2011). In this experiment, a two-meter ship model is used and all the appendages are removed as done in the CFD computation. Comparisons of time histories of wave-induced surge force, heave, and pitch for the wave steepness of 1/40 and 1/20 are shown in Figs.3-4. The non-dimensional time, $t'=t/T$, of 0 means the moment when the centre of ship gravity passes a wave trough. Here the wave-induced surge force is obtained by subtracting the resistance in calm water at the same Froude number from the measured/calculated surge force in following waves. The wave-induced heave and pitch motions are obtained by the same procedure.

The CFD results show fairly good agreement in the wave-induced surge force and in vertical motions for both wave steepness. Therefore it could be concluded that it is possible to use the same RaNS solver, overset grid treatment, numerical models, and computational grids, to investigate the influence of hull form parameters on the wave-induced surge force in regular following seas.

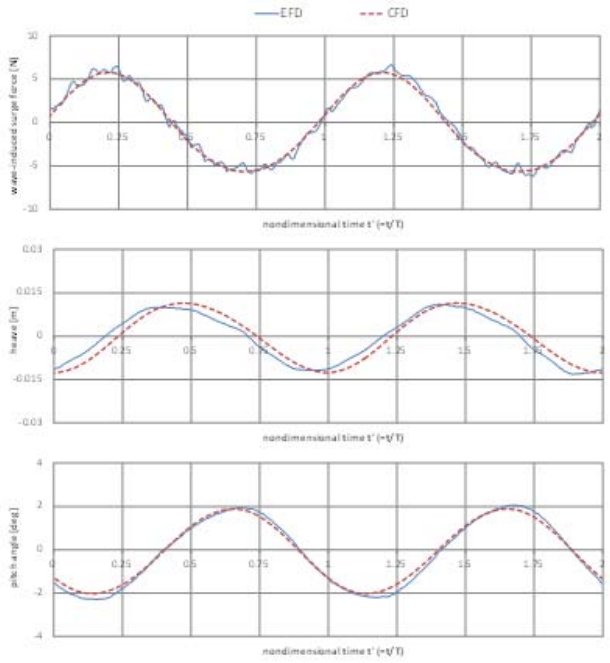

Figure 3 Comparison of wave-induced surge force, heave and pitch motions for the original hull form with H/λ=1/40

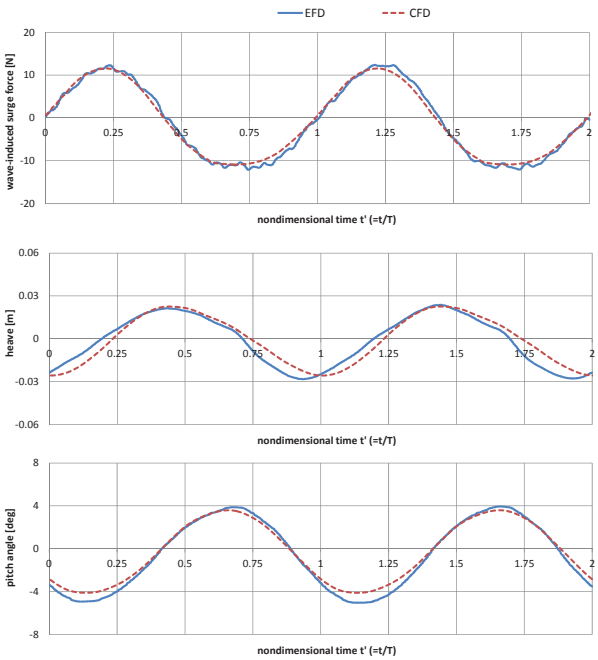

Figure 4 Comparison of wave-induced surge force, heave and pitch motions for the original hull form with H/λ=1/20

5.1 Influence of C_m and C_b

The CFD simulations are performed for the hull forms derived from the original one, i.e. H-2 to H-5 those have different C_m and C_b values. Because the underwater hull form is modified, the ship volume for the same draught is changed, but we impose the original draught for all hulls in the CFD simulation. Comparisons of CFD results of the wave-induced surge force are shown in Figs.5-6. Here the resistance in calm water of the original hull form in calm water is subtracted from all the calculated data. Therefore the vertical shift of the mean of the wave exciting force is regarded as the increase of the resistance in calm water due to the hull form modification, so the maximum shift can be found in the most-blunt hull (H-5). The amplitude of the wave surging force has a tendency to slightly increase with the fatness of the hull, but it is negligibly small. It is noted that the linearity of the wave-induced surge

force is not confirmed for the H-5 hull. Major difference between wave steepness of 1/40 and 1/20 can be found near wave up-slope position.

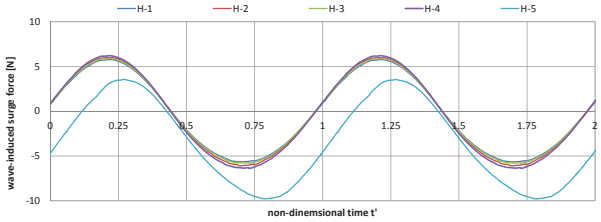

Figure 5 Comparison of wave-induced surge force for five different hull forms with H/λ=1/40

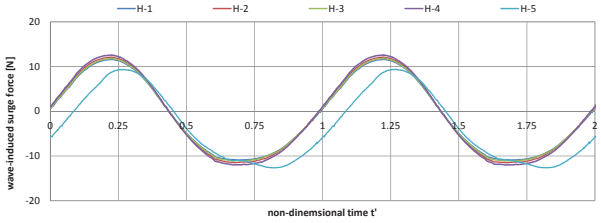

Figure 6 Comparison of wave-induced surge force for five different hull forms with H/λ=1/20

The CFD result of wave height and pressure on the underwater hull is shown in Fig.7. The ship is located in the wave down-slope potion where the wave presses the ship most strongly. It is difficult to find differences in the wave height distributions among H-1 to H-4. This means that the hull form modification, for H-1 to H-4, has few influences on the wave diffraction, ship-generated waves and their interference. In the result for the H-5 hull bloated over a considerable range, the wave diffraction and bow- and stern- generated waves are much prominent compared to H-1 to H-4 cases. Therefore the wave height distribution is different from the original sinusoidal wave. This might be a possible reason of significant change of the wave-induced surge force for the H-5 hull. The pressure distribution on the underwater hull looks not so different for H-1 to H-3. However, in the H-4 result, high-pressure region appears differently from those of H-1 to H-3, and the appearance of the pressure distribution becomes much different from others in the H-5 result. Regarding the H-5 hull, the different pattern of the pressure at bow and stern areas could be the reason to explain the phase difference of the wave-induced surge force found in Fig.6.

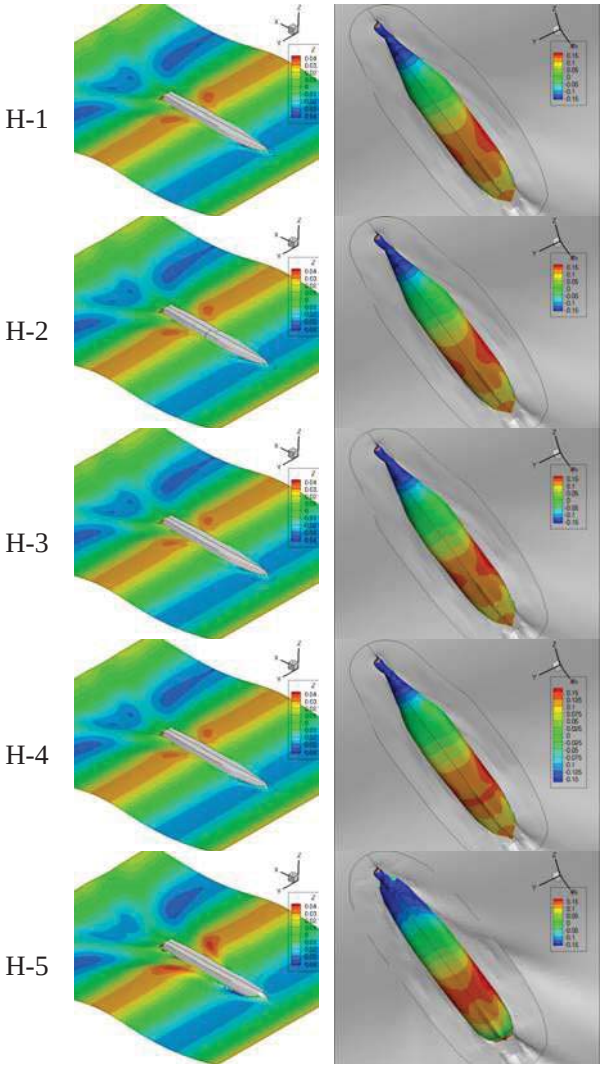

Figure 7 Contour maps of wave height and pressure with H/λ=1/20

Table 5 shows the non-dimensional amplitude of the wave-induced surge force in following seas, $X'_a = X_a / (\rho g V \times H / \lambda)$, obtained by the CFD and the linear Froude-Krylov calculations. Here the individual volume is used for each hull. The CFD simulation, which shows good agreement with the experimental result, provides much smaller values than the Froude-Krylov force in all

conditions. This means that the linear Froude-Krylov calculation would significantly overestimate the amplitude of the wave exciting force in following waves and hence the danger of surf-riding could be overestimated. Table 6 shows the correction coefficient for the linear Froude-Krylov calculation, which is calculated by the existing correction formula of Eq.4. It would be reasonable to assume the present CFD result is accurate enough, if so the correction coefficient μ_x should coincide with the value of CFD/FK. From the results of H-1 to H-3, in which C_m value is mainly changed, CFD/FK value does not always decrease with the increase of C_m while μ_x decreases monotonically. From the results of H-3 to H-5, with the same C_m but different C_b, the CFD/FK value decreases with the increase of C_b while μ_x increases oppositely.

Table 5 Estimated amplitude of the wave-induced surge force

hull	H/λ	X'a (CFD)	X'a (FK)	EFD/CFD	EFD/FK
H-1	0.025	1.246	1.546	1.024	0.826
H-2	0.025	1.231	1.557		
H-3	0.025	1.299	1.574		
H-4	0.025	1.291	1.585		
H-5	0.025	1.093	1.412		
H-1	0.05	1.234	1.546	1.055	0.842
H-2	0.05	1.211	1.557		
H-3	0.05	1.268	1.574		
H-4	0.05	1.258	1.585		
H-5	0.05	0.903	1.412		

Table 6 Evaluation of the correction coefficient

hull	H/λ	C_m	C_b	CFD/FK	μ_x
H-1	0.025	0.837	0.539	0.806	0.737
H-2	0.025	0.88	0.546	0.790	0.693
H-3	0.025	0.95	0.556	0.825	0.539
H-4	0.025	0.95	0.571	0.815	0.555
H-5	0.025	0.95	0.695	0.774	0.687
H-1	0.05	0.837	0.539	0.798	0.737
H-2	0.05	0.88	0.546	0.777	0.693
H-3	0.05	0.95	0.556	0.806	0.539
H-4	0.05	0.95	0.571	0.794	0.555
H-5	0.05	0.95	0.695	0.639	0.687

These results indicate that the existing correction formula, using C_m and C_b as variables, cannot reasonably explain the influence of the hull form on the wave-induced surge force. Although the current correction formula is based on several captive model tests, the correction coefficient would be only acceptable for the original hull (H-1) and the bluntest hull (H-5). This might be because there is a certain correlation between C_m and C_b values for well-designed ships while such correlation is neglected in the ship hull generation in the present study. However the comparison results show that the current correction formula would be only applicable for limited hull design and does not fully explain the influence of hull form on the wave-induced surge force. Therefore further efforts, to improve/reconstruct the formula using other hull form parameters or additional elements, are expected to realize more rational correction for the regulatory use in the second-generation intact stability criteria.

5.2 Influence of L/B

In order to find more appropriate hull form parameters and/or other elements missing in the current correction formula, the influence of L/B ratio is investigated because the diffraction force would be an important element to improve the prediction accuracy. For this purpose three fattening hulls are additionally generated by stretching the original hull in y-direction uniformly, and the stretched breadths are 1.1, 1.2 and 1.3 times of the original breadth as shown in Table 7 and Fig.8. The projected area to the y-z plane and the entrance angle of the bow becomes larger, so the diffraction effect becomes more significant. The CFD and Froude-Klyrov calculations as well as the correction coefficient are shown in Table 8. The correction coefficient is constant because the C_m and C_b values are the same, and the ratio of CFD and the Froudel-Krylov force shows the same tendency. Therefore it is confirmed that the diffraction effect is not a dominant, so L/B or bow entrance angle is not a candidate for the improvement of the correction formula. Further investigation is

desired to develop a reasonable correction formula to be applicable for any hull forms.

Table 7 Parameters of the hulls

Hull	*B*	*L/B*	Entrance angle [deg]
H-1 (original hull)	18.8	8.19	19.0
H-6	20.7	7.45	20.8
H-7	22.6	6.83	22.7
H-8	24.4	6.30	24.5

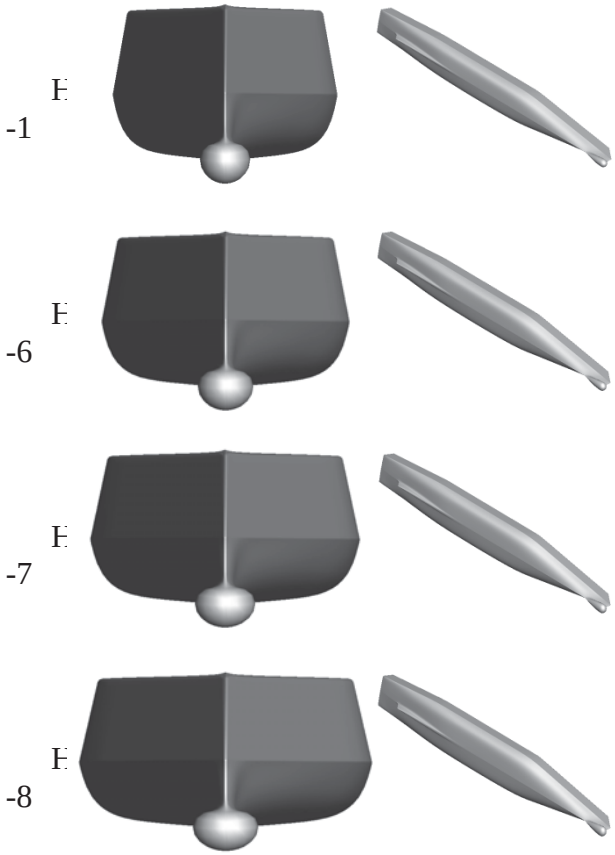

Figure 8 Geometry of the hulls

Table 8 Influence of *L/B*

hull No.	H/λ	X'a (CFD)	X'a (FK)	CFD/FK	μ_x
H-1	0.025	1.246	1.546	0.806	0.737
H-6	0.025	1.235	1.545	0.799	0.737
H-7	0.025	1.234	1.544	0.799	0.737
H-8	0.025	1.231	1.542	0.798	0.737
H-1	0.050	1.234	1.546	0.798	0.737
H-6	0.050	1.214	1.545	0.786	0.737
H-7	0.050	1.203	1.544	0.779	0.737
H-8	0.050	1.202	1.542	0.780	0.737

5.3 Influence of ship motion

In order to find out the major element to improve the prediction accuracy of wave-induced surge force, the influence of ship motion is examined. The CFD simulation is executed without solving the heave and pitch motions. Time histories of the calculated wave-induced surge force for the original hull is shown in Figs.9-10. Here the steady sinkage and trim in calm water at the same Froude number is neglected, but it is confirmed that their effect is negligibly small at least in the tested condition. These graphs clearly show the neglect of the ship vertical motion significantly affects both the amplitude and the phase of the wave-induced surge force. Therefore the heave and pitch motions should be included for the accurate prediction. However majority of the ship motion here is a component due to hydrostatic balancing in heave and pitch because the encounter frequency is very low and the ship length is comparable to the ship length. Therefore CFD simulation should be performed for the prescribed ship attitude obtained as hydrostatically balanced position in waves, to extract the dynamic effect of ship motion which is neglected in the Froude-Krylov calculation.

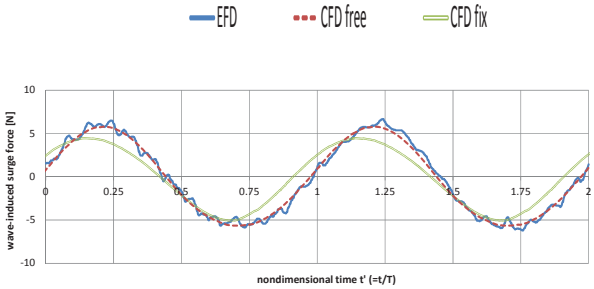

Figure 9 Influence of heave and pitch motions with H/λ=1/40

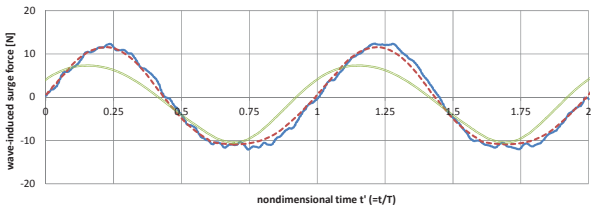

Figure 10 Influence of heave and pitch motions with H/λ= 1/20

5.4 Influence of heel angle

All the discussions until here are done for the ship in upright condition. Once broaching happens, violent yaw motion is induced so that a ship could largely heel due to the centrifugal force. For direct stability assessment of broaching, numerical prediction of the wave-induced surge force in largely heeled condition is also important to quantitatively assess the danger of broaching. Therefore the CFD simulation is executed for the original hull with 10, 20, and 30 degrees of heel angle. The estimated amplitudes of the wave-induced surge force are compared with an existing model experiment by Hashimoto et al. (2011) and their results are shown in Table 9. The experimental result of the amplitude of the wave-induced surge force does not change so much with the increase of heel angle up to 30 degrees. The CFD result can capture this trend and the maximum error is 8.2% and the mean error is 5.2%. The error does not increase with the heel angle, so the overset grid RaNS solver used in this study has possibility to be applicable for the direct stability assessment of surf-riding/broaching phenomenon as the third level of the direct stability assessment.

Table 9 Influence of heel angle

hull No.	H/λ	ϕ	X'a (CFD)	X'a (EFD)	EFD/CFD
H-1	0.025	0	1.246	1.277	1.024
H-1	0.05	0	1.234	1.302	1.055
H-1	0.025	10	1.248	1.328	1.064
H-1	0.05	10	1.228	1.329	1.082
H-1	0.025	20	1.187	1.262	1.062
H-1	0.05	20	1.222	1.261	1.032
H-1	0.025	30	1.181	1.237	1.047
H-1	0.05	30	1.228	1.197	0.975

6. CONCLUSIONS

The influence of hull parameters on the wave-induced surge force in following seas is investigated using an overset grid RaNS solver. The importance of C_m and C_b is investigated with a series of derived hull forms from the ONR-tumblehome vessel. It is recognized that increasing of C_b affects the amplitude of wave-induced surge force while C_m does not so. Since it is reconfirmed that the linear Froude-Krylov force significantly overestimates the amplitude of wave-induced surge force, reasonable correction formulae are highly desired to be used in the level two vulnerability criteria for broaching. Therefore current proposal of a correction formula is evaluated by CFD-based numerical tests. As a result, it is demonstrated that the current correction formula has limitation and cannot reasonably explain the influence of the hull form on the wave-induced surge force. Further investigation on the influence of L/B, heave and pitch motions, and heel angle is also performed. The L/B ratio and the heel angle are not influential but the consideration of ship motion is an important element for the accurate prediction of the wave-induced surge force at least for the subject ship. Further comprehensive research is necessary to develop and propose more valid and reliable correction formula to be applicable to any types of ship for the second-generation intact stability criteria for broaching.

7. ACKNOWLEDMENTS

This work was supported by JSPS KAKENHI Grant Number 25249128 and 24360355, and was also carried out as a research activity of Goal-Based Stability Criterion Project of Japan Ship Technology Research Association in the fiscal year of 2014, funded by the Nippon Foundation. The authors thank Prof. Naoya Umeda from Osaka University for his useful discussion.

8. REFERENCES

Carrica, P. M., Wilson, R.V., Noack, R., Xing, T., Kandasamy, M., Shao, J., Sakamoto, N., and Stern, F. 2006, “A Dynamic Overset, Single-Phase Level Set Approach for Viscous Ship Flows and Large Amplitude Motions and Maneuvering”, Proceedings of 26th Symposium on Naval Hydrodynamics,

Rome.

Hashimoto, H., Umeda, N., Matsuda, A. 2011, "Broaching prediction of a wave-piercing tumblehome vessel with twin screws and twin rudders", Journal of Marine Science and Technology, 16, pp.448-461.

IMO, "Proposed Amendments to Part B of the 2008 IS Code to Assess the Vulnerability of Ships to the Broaching Stability Failure Mode", SDC1 INF.8 ANNEX15.

IMO, "Proposal of working version of explanatory notes on the vulnerability of ships to the broaching stability failure mode", SDC1/5/4.

Ito, Y., Umeda, N. and Kubo, H., 2014, "Hydrodynamic Aspects on Vulnerability Criteria for Surf-Riding of Ships", Jurnal Teknologi, Vol. 66, No. 2, pp. 127-132.

Noack, R., 2007, "Enabling Large Amplitude and Relative Motions Through Overlapping Grids", Proceedings of 9th International Conference on Numerical Ship Hydrodynamics, Michigan.

Tahara, Y., Wilson, R.V., Carrica, P.M. and Stern, F. 2006, "RANS Simulation of a Container Ship Using a Single-Phase Level Set Method with Overset Grids and Prognosis for Extension to Self-Propulsion Simulator", Journal Marine Science and Technology, 11, pp. 209-228.

Umeda, N., Yamamura, S., Matsuda, A., Maki, A., Hashimoto, H., 2008, "Model Experiments on Extreme Motions of a Wave-Piercing Tumblehome Vessel in Following and Quartering Waves", Journal of the Japan Society of Naval Architects and Ocean Engineers, 8, pp.123-129.

Session 9.2 – DAMAGE STABILITY

Life-Cycle Risk (Damage Stability) Management of Passenger Ships

Free- Running Model Tests of a Damaged Ship in Head and Following Seas

Main Contributing Factors to the Stability Accidents in the Spanish Fishing Fleet

This page is intentionally left blank

Proceedings of the 12th International Conference on the Stability of Ships and Ocean Vehicles, 14-19 June 2015, Glasgow, UK.

Life-cycle Risk (Damage Stability) Management of Passenger Ships

Dracos, Vassalos, *Department of Naval Architecture, Ocean and Marine Engineering, University of Strathclyde*, d.vassalos@strath.ac.uk

Yu, Bi, *Department of Naval Architecture, Ocean and Marine Engineering, University of Strathclyde*, y.bi@strath.ac.uk

ABSTRACT

Inadequate damage stability, the Achilles heel of passenger ships, has been a critical research objective that industry and academia delved to improve every time following accidents with passenger ships. Most achievements focused on design phase, either for the new-made regulations or rather novel pro-active methodology of risk-based design, which ignored thousands of existing ships and wasted state-of-art knowledge on damage stability. Considering this situation, a framework of life-cycle risk (damage stability) management of passenger ship and its related damage stability verification framework were introduced and established in this paper.

Keywords: damage stability, risk management, damage control

1. INTRODUCTION

Accidents of passenger ships, involving thousands of lives on broad, are a matter of grave concern, consequences of which from time to time irritate and astonish the public. As a result, industry and academia's endeavour to improve safety of passenger ships never stops and much of it targets the inadequate damage stability, the Achilles heel of passenger ships. For centuries, traditional passive way of establishment and modification of safety regulations and rules in the aftermath of tragic accidents stays as the dominant method to help control the risk but nowadays it becomes difficult to catch up with the unrelenting pace of ship technology. In contrast, pro-active risk reduction ideas were put forward and various related methods are under development and tentatively expanding into the ship industry. The typical representative, risk-based ship design method, integrating safety assessment procedure into the ship design process, widens the design envelope and inspires innovations on the new specifications while proactively controlling the risk. Moreover, along with traditional regulations, it focuses on the improvement of damage stability in the design phase, which serves only for the newbuildings, leaving thousands of existing ships still confronted with uncontrollable risk and with state-of-art knowledge on damage stability wasted.

Given the background introduced above, it is not sensible to limit the research of damage stability improvement in ship design phase. Besides the risk control options (RCOs) in

design phase, throughout a ship's life, effective operational (active) measures and measures conducted during emergencies could also serve to improve damage stability and efficiently reduce the loss of lives. This gives birth to the idea of establishment of a complete framework for life-cycle risk (damage stability) management. Built on the life-cycle perspective, this framework is a holistic approach to improve damage stability cost-effectively through risk control measures in design, operation and emergency stages. As the building block of the framework, the risk reduction potential of risk control measures should be known. This could be accomplished by a damage stability verification framework which aims at the verification and measurement of the risk reduction measures in ship's whole life cycle via auditable and measurable means. And this paper would introduce the establishment of these two frameworks respectively.

2. SAFETY MANAGEMENT SYSTEM

The safety management system introduced by HSE (Health and Safety Excursive) in its guide -- *successful health and safety management* has served as a mainstream methodology for risk management and has been employed in various different industry fields managing risks and solving safety problem in a holistic view. The system comprises five steps, namely, policy, organizing, planning and implementing, measuring performance, reviewing and auditing (shown in figure 1). 'Policy' describes the corporate approach to safety; 'Organizing' describes the management hierarchy relating to safety with responsibilities defined at each level; 'Planning' shows the safety tasks to be targeted at each stage and 'Implementing' is to conducting measures to reduce or mitigate risks; 'Measuring performance' refers as measurement and verification of the effectiveness the implemented measures; 'Reviewing and Auditing' belongs to the system of continuous improvement, ensuring new hazards identified, near miss incidents considered and the SMS kept up to date. The importance of this safety management system lies on the classification of a rather complicated situation which includes huge numbers of different aspects into systematic and reasonable five steps.

Based on the HSE's Safety Management System (SMS) guideline, the damage stability risk management framework in this paper also followed the holistic idea of HSE's SMS and utilized the steps in the guideline. Given the particular situation of damage stability problems discussed in the paper, the main concerns of the framework focus on the last three steps which specifically are planning and implementation of risk control measures, measurement of the performance and effectiveness of implemented risk control measures, and acquisition of reviews and suggestions from the former two processes.

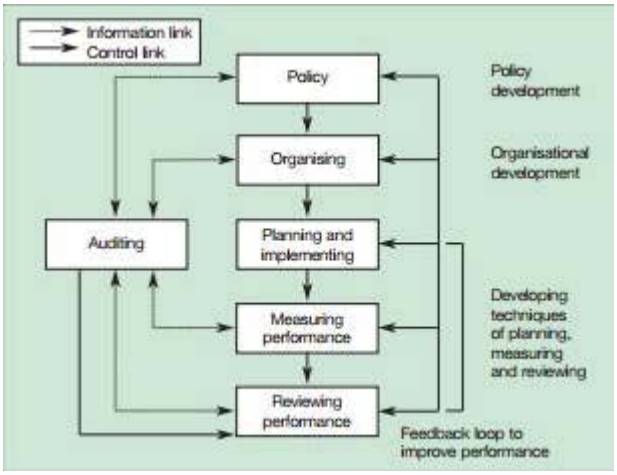

Figure 1: Key Elements of Successful safety management

3. LIFE-CYCLE RISK (DAMAGE STABILITY) MANAGEMENT FRAMEWORK

A literature review on life-cycle risk management (LCRM) for ships would tell us that LCRM is still a developing and immature

subject. Plenty of ideas merged and attempts of managing the overall risk from a life-cycle view have been made. The main target and challenging part of a primary thinking pattern is establishment of linkages among different life periods and among different risk control processes to order to integrate different life periods, safety essentials and risk-based methodologies together in a whole risk management system. A review and feedback system is prone to be established based on this kind of risk management system. However, it seems that this research direction builds on the hypothesis that appropriate measures would be conducted to reduce or mitigate risks and threats to tolerable level during operation and emergency stages, which is not often the case. Complementarily, the objective of the life-cycle risk management framework presented in this paper is assurance of risk being under control in every period of ship's life by managing the risk in ship's different life periods. Disassembly of this holistic goal indicates that target for each life period is the verification of risk reduction or mitigation in this period.

Establishing on a life-cycle perspective, the framework comprises three dominate phases in the life of a ship, namely design, operation, and emergency. The operation stage defined here is from an incident happened to the moment before the ship is going to be abandoned. And emergency stage starts from the moment ship is decided to be abandoned. Correspondingly, risks are divides in terms of life periods into three parts, risk in design, residual risk in operation and residual risk in emergency situation. In each life-cycle phase, three essential safety management steps mentioned in the first section are conducted respectively, reducing and mitigating the risk in every stage and ensuring an overall safety environment.

Verification of the risk control options in each life phase is most direct way to ensure risk reduction or mitigation in every life period. Risk control options in each stage are distinctive from each other. In design phase, traditionally rules always focus on design solutions, serving as passive risk control measures for damage stability improvement. Operational measures, referred as active risk control measures, are abundant in SOLAS Ch. II-2 (e.g. damage control). In emergency stage, effective risk control measures are mainly systems and measures focusing on emergency response, such as Decision Support Systems for Crisis Management, Evacuation, LSA (Life Saving Appliances), Escape and Rescue.

Whilst a substantial amount of options for planning and implementation of risk control measures exist, measurement of the performance and effectiveness of these risk control measures still remains as a big gap in this approach. Contrary to passive design solutions which has stayed as a primary research target for centuries, operational measures have not been rigorously validated yet. Moreover, the cost-effectiveness of emergency risk reduction potential was never measured nor verified before, since risk reduction of 'residual' risk in this stage falsely perceived to be small by definition. These problems need to be overcome before the overall risk management process can be formalized and adopted. This issue was considered in the next section.

4. DAMAGE STABILITY VERIFICATION FRAMEWORK

In addition to traditional design modifications, identification of alternative means and arrangements such as operational measures and emergency response measures gives credit to their benefit based on their verifiable contribution in improving stability levels. Damage stability verification framework is established, targeting on identification, quantification and validation of the risk-reduction potential of all such measures.

Damage stability verification framework encompasses one proposal for each life stage. The goal for design and operation stage is to assess the ship vulnerability to flooding, while

assessing effectiveness of emergency response is the target for emergency phase. To achieve the goal, objective of the proposal for design stage (Item 1) is establishment of baseline vulnerability and assessment of impact of design measures. Quantitative analysis, including damage stability statutory assessment and damage stability alternative method, are planned to conduct to acquire the effectiveness of various risk control options in design. Correspondingly, assessment of impact of active damage control measures by crew is the objective for operation proposal. Quantitative analysis to fulfill this objective includes damage stability alternative method and ship systems operability assessment, while qualitative analysis, namely assessment of crew performance, could serve as supplementary. Similarly, proposal objective for emergency stage is assessing impact of emergency responses measures. Escape and evacuation analysis and assessment of crew performance are the quantitative and qualitative analysis respectively.

4.1 Proposal for the design phase

The work in design phase comprises the following activities:

Statutory (SOLAS2009) damage stability assessment: The following actions describe in-house developments targeting design vulnerabilities and cost-effective design measures to reduce these.

1. Statutory A-value index calculation (basis calculations) in accordance with SOLAS Ch.II-1 (SOLAS 2009).

2. Vulnerability screening and identification of design modifications aimed at increasing the level of index A as high as it is practicably attainable.

3. The results of the vulnerability screening will be used to define appropriate design modifications on the basis of risk-reduction potential and cost effectiveness.

4. Taking into account the results of the vulnerability screening, simple solutions (such as closing openings) as well as a number of alternative ship watertight arrangements will be used for further analysis for each ship.

Operational data: The following actions target to identify ship specific data and conditions for use in the stability assessment (rather than the generalised average values used in the probabilistic rules)

5. Collection and analysis of real life on-board data for an agreed period of operation. The data relate to loading conditions, stability parameters, quantity and distribution of loads, etc. Use will be made of any data that already exists.

6. Readily available stability improvements can be specified by reviewing the quantity and distribution of fluid loads (fuel, ballast water, heeling water, fresh water, grey water).

7. Realistic operational data need to be used as a basis for numerical flooding simulations.

Alternative assessment of damage stability: The following actions describe the use of first-principles tools as a supplementary means to assessing damage stability.

8. Alternative assessment based on Monte Carlo (MC) sampling in conjunction with numerical flooding simulations (referred to subsequently as MC simulation). This approach reflects explicitly the damage statistics and accounts realistically for the physics of stability deterioration following a collision event. The MC simulation is a viable technique for stability assessment in accordance with SOLAS Chapter II Part B Regulation 4.2 (alternative method).

9. For the purposes of comparison, the

alternative assessment will be carried out for the same basis design and alternative watertight arrangements developed as part of the statutory damage stability assessment.

10. The MC simulations will allow identification of weak "spots" (e.g. local architecture) contributing to stability deterioration when subject to flooding as a result of water ingress following a large number of collision events.

11. The study will be performed for (a) three watertight arrangements per ship, and (b) two loading conditions, comprising one regulatory condition, and one real life loading condition. In total six cases per ship will be analysed.

4.2 Proposal for operation stage

The work comprises the following activities, carried out for the same sample ships referred to in Item 1. Measures related to damage stability assessment encompass active damage control which is STAGE 2 activity in a typical muster list.

<table>
<tr><th>STAGE 1</th><th>STAGE 2</th><th>STAGE 3</th></tr>
<tr><td rowspan="3">INCIDENT happens

(1) Detection & Alarm</td><td>(2) Damage control</td><td rowspan="3">(5) Abandon Ship
(6) Rescue</td></tr>
<tr><td>(3) Muster of Pax</td></tr>
<tr><td>(4) Preparation of LSA</td></tr>
</table>

Table 1 Generic sequence of events that may occur after a flooding event (typical muster list)

Qualitative analysis includes:

1. Definition of active damage control options by the crew. It is envisaged that for this, a one-day meeting with active crew members (Master, chief engineers, deck hands, etc.) involved in damage control duties on-board the vessels under evaluation will be conducted.

2. Definition of human and organizational (procedural) factors affecting the effectiveness of damage control actions.

3. Effectiveness of crew actions for flooding control will highly depend on the level of crew preparedness and competence necessary to carry out the actions safely, timely and effectively.

4. A qualitative measure reflecting the objective evidence in terms of crew competence and preparedness will be developed

Quantitative analysis includes:

1. One of the watertight arrangements defined in Item 2 will be used as platform to quantitatively assess the impact of possible active flooding control measures by crew when a flooding incident moves to damage control stage (see Table above).

2. The quantitative analysis will be based on the alternative MC simulation method described in Item 1. This entails identification of flooding scenarios where counter-ballasting is effective and feasible, the latter implying availability of ship systems to enable this action.

3. Crew actions to be analysed will comprise counter-ballasting operations. This is based on the premises that available options will be computed, defined and executed in a timely manner.

4. Effectiveness of crew actions for flooding control will depend, in addition

to the necessary ship systems being available, on the possibility of active reconfiguration for that purpose if the systems are impaired by the flooding.

5. The availability of relevant ship systems will be verified by using a design verification tool that allows modeling ship systems architecture, in topological and functional form. The tool is used for verification and analysis of essential ship systems redundancy when applying Safe Return to Port requirements of SOLAS Ch.II-2.

4.3 Proposal for emergency phase

The research comprises the following activities, carried out for the same sample ships referred to in Item 1. Measures related to evacuation include: muster of passengers, preparation of LSA, abandon ship and rescue operations, namely STAGE 2 and 3 activities in a typical muster list.

Qualitative analysis includes:

1. Definition of evacuation-related duties and activities by the crew. It is envisaged that for this, evacuation activities on-board the vessels under consideration will be conducted.

2. A hazard identification type of exercise needs to be conducted with a view to defining human and organisational (procedural) factors affecting the effectiveness of the evacuation process.

3. Effectiveness of crew actions for evacuation purposes will highly depend on the level of crew preparedness and competence necessary to carry out the actions safely, timely and effectively.

4. A qualitative measure reflecting the objective evidence in terms of crew competence and preparedness will be developed

Quantitative analysis (Evacuation analysis) includes:

5. Evacuation analyses of the ships in question will be conducted with an advanced evacuation analysis tool (as defined in MSC\Circ.1238)

6. The evacuation analysis will cover the mustering and ship abandonment process;

7. Human and LSA systems performance data for the analysis will be collected and validated prior to use on the basis of existing IMO instruments and operators experience

8. The evacuation time will be assessed in the context of the survival time (time to capsize) derived from the damage stability assessment (Items 1 and 2) for all critical emergency scenarios (where damage stability may be compromised)

9. Effectiveness of crew actions for evacuation will depend on the availability of necessary emergency ship systems or the possibility of active reconfiguration for that purpose if the systems are impaired by the flooding.

10. The availability of relevant ship systems will be verified as described in Item 2(9) above.

5. CASE STUDY

Here presented a simplified case study of the damage stability assessment for damage control process. The objective of the study is to identify and qualify the impact of damage control measures. The overall procedures are shown in Figure 2.

Firstly, the original geometry data and loading conditions of representative ship are given and recorded. Monte Carlo simulation

method is employed to generate different damage extents and sea states which would later be applied on the representative ship resulting piles of damage scenarios. By calculating the probabilities of survival under random sea states for each damage extent, critical scenarios that the probability of survival indicates an intolerable chance of capsize could be elected as research objects in the next step. For each critical scenario, corresponding risk control options are generated, with an alternative loading condition and geometry data comparing to the original one. Then Monte Carlo simulation needs to be employed again to generate random sea states, and with the help of PROTEUS program the motion responses of the damage ship under current circumstances could be obtained. Finally, the probabilities of survival under random sea states for three hours are calculated again, and the differences between the original and new survival probabilities could be counted as the impact of the related risk control options for a certain damage case.

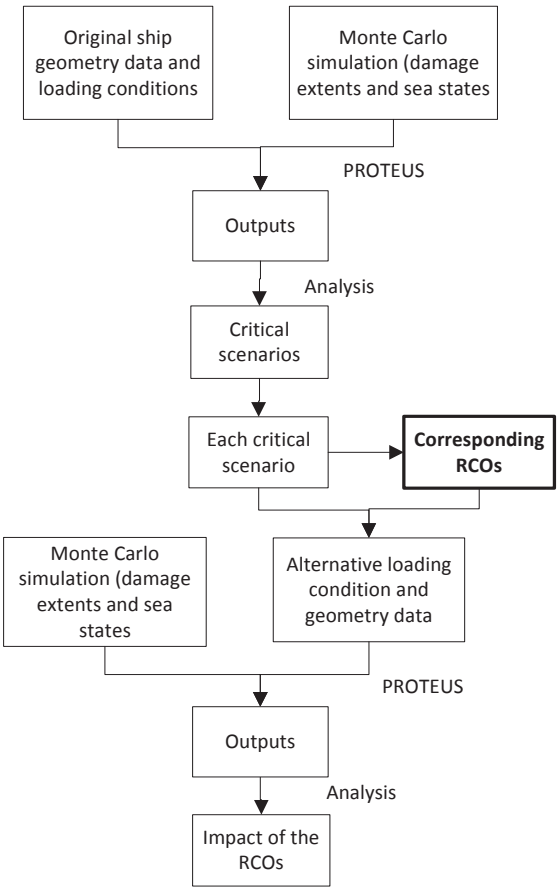

Figure 2 Overall procedures of damage control verification process

The damage control measures considered in this case study mainly include counter-ballasting plans. It is multi-objective optimisation process, and various algorithms could be proposed to determine the most effective risk control option based on both a list of performance and safety criteria.

6. CONCLUSIONS

This paper presented a hostile framework for life-cycle risk (damage stability) management of passenger ships which particularly emphasizes on the benefits and importance of identification and verification of the risk control measures in operation and emergency phases. Correspondingly, as the building block, a damage stability verification framework was established and specific proposals for each life stage were raised. And the last section of the paper outlined a related case study aiming at qualifying and verifying the impact of damage control measures. Further study might include development of the algorithms of generation of damage control measures under various performance and safety criteria at the same time.

7. REFERENCES

Vassalos, D., Konovessis, D., Jasionowski, A. (2013), “Life-cycle risk management: a safety case approach”, Proceedings of the IDFS 2013, pp. 37~42, 25-27 November, Shanghai, China

Martins, P.T. (2011), “Real-Time Decision Support system for managing ship stability under damage”, OCEANS, 2011 IEEE – Spain, ISBN: 978-1-4577-0086-6

Qi Chen (2012), “Uncertainty Quantification in Assessment of Damage Ship Survivability”,

University of Strathclyde, Glasgow, May 2013

Papanikolaou, Apostolos (Ed.) (2009), "Risk-based ship design – Methods, Tools and Applications", ISBN: 978-3-540-89041-6

Health and Safety Executive (1997), "Successful health and safety management", ISBN 978 07176 1276 5

Free-running Model Tests of a Damaged Ship in Head and Following Seas

Taegu, Lim, *Korea Research Institute of Ships and Ocean Engineering* ltg88@kriso.re.kr

Jeonghwa, Seo, *Seoul National University* thamjang@snu.ac.kr

Sung Taek, Park, *Seoul National University* probpst@snu.ac.kr

Shin Hyung, Rhee, *Seoul National University* shr@snu.ac.kr

ABSTRACT

A series of tests using a course-keeping model ship in a towing tank were carried out for research on Safe Return to Port (SRtP). A passenger ship model with a damaged compartment was modified to be equipped with propellers and rudders for a course-keeping maneuver by an onboard autopilot system. The 6DoF motion of the test model was measured by a wireless inertial measurement unit (IMU) and gyro sensors to achieve fully wireless model tests. Advance speed and motion response in various wave conditions were measured and analyzed to investigate the propulsion and maneuvering performances of the damaged ship model in head and following seas.

Keywords: *Free-running test, Safe Return to Port, Damaged ship stability*

1. INTRODUCTION

Recently the scale of damages in maritime accidents has grown with the increasing sizes of vessels. In the case of passenger ship accidents especially, a great number of casualties often results; thus, efforts to improve regulations and vessel designs to prevent casualties are required. The International Maritime Organization (IMO) effected a regulation on the Safe Return to Port (SRtP) of a passenger ship with a length over 120 m in July 2010 (Spanos and Papanikolaou, 2012).

SRtP regulations require the survivability of vessels after fire or flooding under a casualty threshold. After an accident occurs, the vessel must be able to return to a port nearby without external help. It also refers to the minimum requirements of the propulsion performance and maneuverability of the vessel in certain weather conditions; thus, assessing the stability and maneuverability of the vessel under various weather conditions is needed during the stage of designing the ship to judge whether the vessel follows SRtP regulations.

Traditionally ship stability was analyzed by model tests and analytic methods based on the potential flow theory. Analytic methods have been widely used, as they have the merits of high reliability and low computational resource requirements. For cases of unconventional hull geometry and nonlinear phenomena, however, applying analytic methods with the potential flow theory has limitations, and modifications to the methods are necessary.

Parametric roll and broaching are well-known nonlinear physical phenomena in ship stability. Model tests on those nonlinear vessel motions have been performed, and analytic methods are suggested (Bulian, 2005; Lee et al., 2007; Neves and Rodriguez, 2007).

To achieve an analysis of the nonlinear phenomena, an analysis of the fluid dynamics should precede, i.e., eddy-making, turbulent boundary layer, and viscous roll damping. These features are caused by the viscous nature of fluids; thus, approaching the analysis in consideration of the viscosity of fluid is in high demand and computational fluid dynamics (CFD) is the only viable method to treat the viscous flow field. In these days, CFD techniques have been applied to various fields of naval hydrodynamics: the self-propulsion performance of vessel (Seo et al., 2010; Carrica et al., 2011), the motions in waves (Carrica et al., 2007; Simonsen et al., 2013), and the prediction of maneuverability (Araki et al., 2012; Carrica et al., 2013). Approaches with CFD have produced good results, especially on the roll motion of vessels highly affected by the viscosity of fluid (Wilson et al., 2006). As roll motion is the most important criteria for judging the stability of a ship, it is obvious the CFD analysis will substitute traditional analytic methods based on the potential flow theory.

A CFD analysis also has been introduced to assess the issue of damaged ship stability. In the case of damaged ship stability, the interaction between flooded water and ship motion causes highly nonlinear phenomena (Gao et al., 2011). As damaged ship stability is one of the most important elements of SRtP conditions, approaches with CFD are expected to be essential during the design stage of passenger ships under SRtP regulation.

Before applying the CFD method to practical cases, it should be validated through existing experimental results. In the design of experiments for a validation database for CFD, the existence of nonlinear phenomena should be considered, as CFD approaches aim to predict the nonlinear motion of a vessel.

For experimental study on nonlinear motion of vessel, the motion response of a moored model in various waves was measured, and the parametric roll behavior was identified through a series of model tests (Begovic et al., 2013; Lee et al., 2012). Also, a gradual increase in the roll motion of a moored model in head seas has been reported and provided for the CFD validation database (Lim et al., 2014). In these tests, however, the restrained motion of the test model was measured, as the model was in a stationary condition with a mooring system.

To predict the stability of practical vessels with high fidelity, tests with a free-running model are required, as it does not require an external towing force. The free-running model has been used to test the seakeeping ability and maneuverability of vessels, but an intact model was used for most tests (Yoon et al., 2007; Sadat-Hosseini et al., 2010; Sadat-Hosseini et al., 2011). For the provision of a CFD validation database, free-running tests in waves must be achieved in damaged condition, and the results should be compared with those achieved in intact condition. Finally, the validated CFD methods can be applied to examine damaged ship stability problems.

In the present study, a free-running model of a passenger ship was used to carry out motion measurements in waves. Tests were designed by SRtP regulations, and the effects of wave conditions and flooded water behaviors on the motion of the test model were investigated.

2. EXPERIMENTAL METHODS

2.1 Test facility

Tests were carried out in the Seoul National University towing tank, the length, width, and depth of which are 110 m, 8 m, and 3.5 m, respectively. Figure 1 shows a schematic diagram of the towing tank, including the eight plunger-type wave makers located at the end of the towing tank. The initial locations of the test model in head seas and following seas were at 50 m and 20 m from the wave maker, respectively.

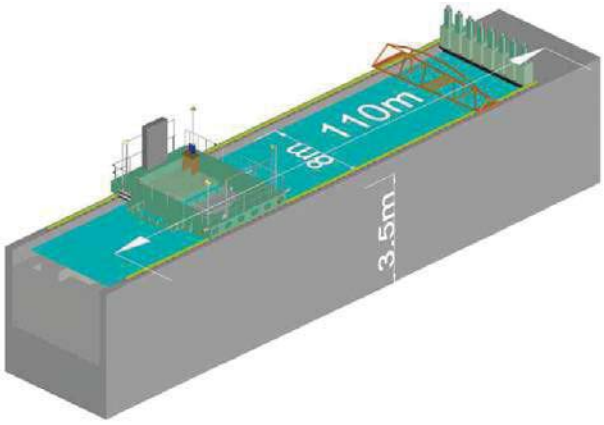

Figure 1 Schematic diagram of the Seoul National University towing tank.

2.2 Test model

A passenger ship hull designed by the Ship Stability Research Centre (SSRC) was used for the test model. It has a bulbous bow and a skeg on the stern. This hull was used for the study on damaged ship stability with a mooring system. Figure 2 shows the design of the test model.

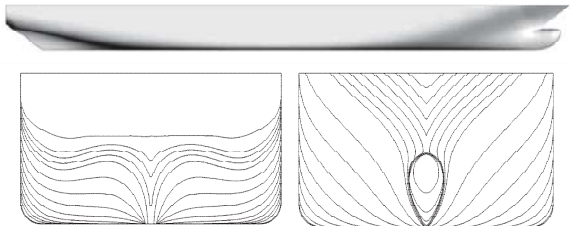

Figure 2 Lines and profile of the test model.

Following the test procedures and recommendations of the seakeeping tests presented by the International Towing Tank Conference (ITTC), the size of the towing tank limited the size of the model ship. The scale ratio of the model was 1/82.57, and the length of the model was 3 m. The principal particulars of the SSRC passenger ship are presented in Table 1. Arrays of studs were attached at station 19 and the bulbous bow to stimulate turbulent flow. Figure 3 shows the constructed test model.

Table 1 Principal particulars of the SSRC passenger ship and test model.

Item	Full Scale	Model Ship
Scale Ratio	1	1/82.57
Length between Perpendiculars (m)	247.7	3
Beam (m)	35.5	0.43
Draft (m)	8.3	0.1
Displacement (m^3)	56514.5	0.312
Propeller Diameter (m)	6	0.073
LCG from amidships (m)	-6.329	-0.077
KB (m)	4.085	0.049
KM (m)	18.781	0.227
KG (m)	16.393	0.199
GM (m)	2.388	0.029
k_{xx}	14.814	0.179
k_{yy}	61.925	0.750

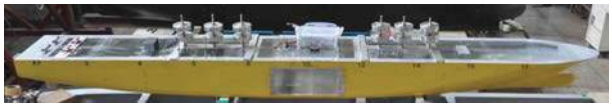

Figure 3 Test model.

A damaged compartment was installed amidships to represent the damaged condition. The location and design of the damaged compartment was identical to the experiments of Lee et al. (2012). Figure 4 shows the design and dimensions of the damaged compartment.

It consisted of two compartments: a damaged compartment located astern (Compartment 1) had an opening to the outside, and a damaged compartment located fore (Compartment 2) had only a connection with Compartment 1. The connection was on the free surface; thus, flooding to Compartment 2 was not expected in a static condition without severe motion. Every compartment had a ventilation hole to minimize the effects of air compression on the flooding behavior. If flooding to Compartment

1 occurred, the model ship gained 5.82 kg of flooded water and an initial heel angle of 2.83°.

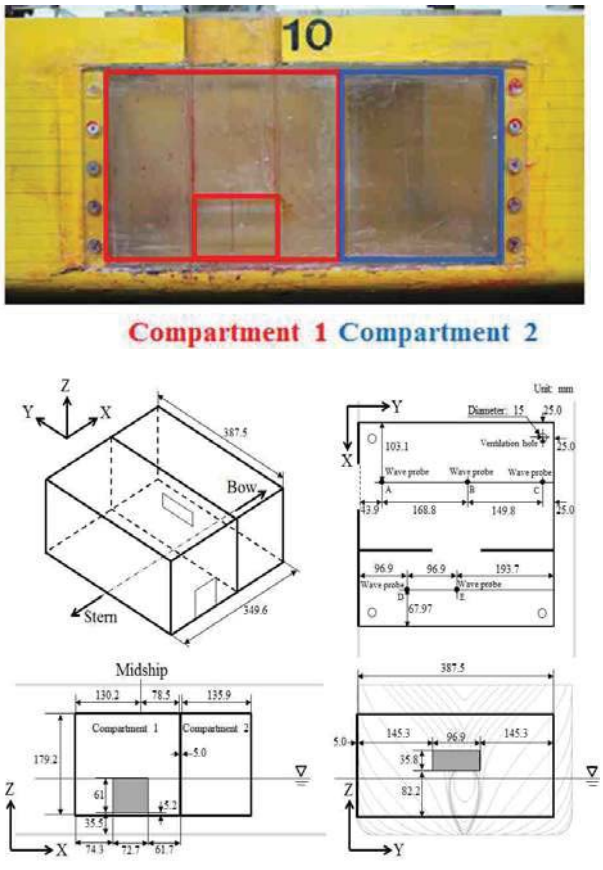

Figure 4 Geometry of the damaged compartment.

2.3 Autopilot system

Two propellers and rudders were appended on the test model to enable maneuverability. The design of a six-blade propeller in the present study was a modified design of the KP505 propeller, of which the design has been open (Paik et al., 2004; Seo et al., 2010). Its pitch ratio at 0.7 R was 0.997. Propeller shafts were supported by L-type struts, which were connected to the center skeg and stern. The profile of the rudder was NACA0012 hydrofoil. Figure 5 shows the fully appended stern of the test model.

Figure 5 Fully appended stern of the test model.

The autopilot system controlled the rudder angle and propeller revolution rate. The heading angle of the test model was measured by a gyro sensor, and the rudder angle was varied by a P controller, the parameter of which was 1.5. The propeller revolution rate was controlled by a PD controller, and the parameters of the P and D controllers were 20 and 8, respectively.

The motion of the model was measured by gyro sensors on the autopilot system and a wireless inertial measurement unit (IMU). Two measurement systems worked independently. The repetition rate of the wireless IMU was 100 Hz. The autopilot system transmitted motion and control signals to a laptop with a repetition rate of 16 Hz.

2.4 Test conditions

Based on the SRtP regulation suggested by Germanischer Lloyd (GL, 2009), the wave and propeller conditions were chosen. In the SRtP regulation, a vessel should achieve an advance speed of 7 knots or half of the design speed in normal weather conditions. In addition, the vessel should preserve maneuverability in unfavorable weather conditions. Normal and unfavorable weather conditions correspond to Sea states 5 and 6, respectively. Table 2 describes the wave conditions for the present SRtP tests.

Table 2 Wave conditions for SRtP tests.

		Normal weather conditions		Unfavorable weather conditions	
		Full scale	Model scale	Full scale	Model scale
Period (s)	T	6.7	0.737	8.3	0.913
Wave number (rad/m)	k	0.090	7.415	0.059	4.832
Wave length (m)	λ	69.9	0.847	107	1.300
Wave Amplitude (m)	A	2.8	0.034	5.4	0.066

To determine the minimum propulsion power, the propeller revolution rate at an advance speed that corresponds to 7 knots in the full scale (0.396 m/s) was investigated in calm water tests. It was 595 rpm, and the propeller revolution rate for tests was fixed at 615 rpm, considering the powering margin in the waves.

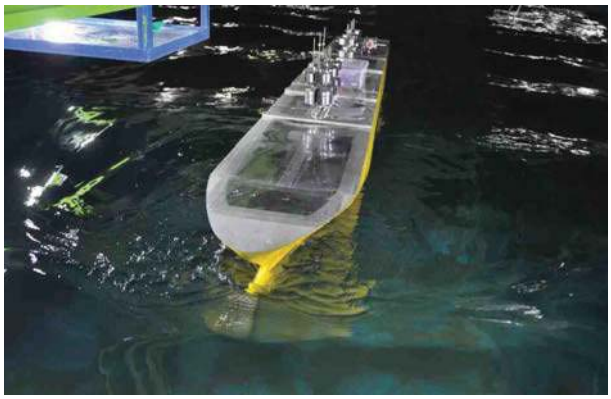

Figure 6 Snapshot of the free-running test.

Tests were performed in head and following seas conditions. The model was released in a stationary condition, and the motion in the time range with a converged speed was sampled and analyzed. Figure 6 shows the snapshot of the model test in head seas.

3. RESULTS AND DISCUSSIONS

3.1 Pitching motion

Figures 7 and 8 show the time history of the pitching motion of the test model. In normal weather conditions, the motion response in following seas was greater than that in head seas, while the pitching motion in head seas increased in unfavorable weather conditions.

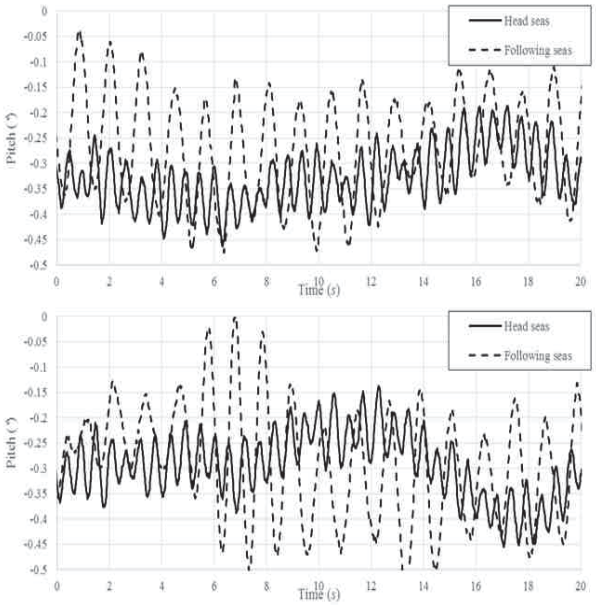

Figure 7 Time history of the pitching motion in normal weather conditions (top: intact condition; bottom: damaged condition).

When the pitching motion of a ship in waves occurs, the bow and stern of the ship move vertically in the water, resulting in slamming. Tendency of slamming, however, showed difference in cases of the bow and stern. As the bulbous bow and the bow flare was immersed, slamming occurred in all wave conditions. Slamming on the stern with flat transom, in contrast to the bow slamming, made high impact over certain wave height condition; thus, slamming on the stern restrained pitching motion in unfavorable weather condition only. In normal weather condition, slamming on the bow was dominant and pitching motion in head seas was smaller than that in following seas.

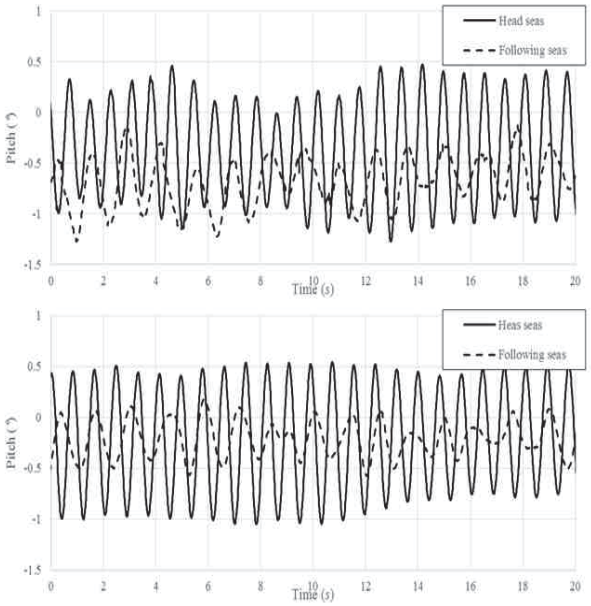

Figure 8 Time history of the pitching motion in unfavorable weather conditions (top: intact condition; bottom: damaged condition).

In all cases, the magnitude and period of the pitching motion in following seas was less regular than in head seas. In following seas, the incoming wave was disturbed by the Kelvin wave and propeller wake and could not maintain its waveform strictly.

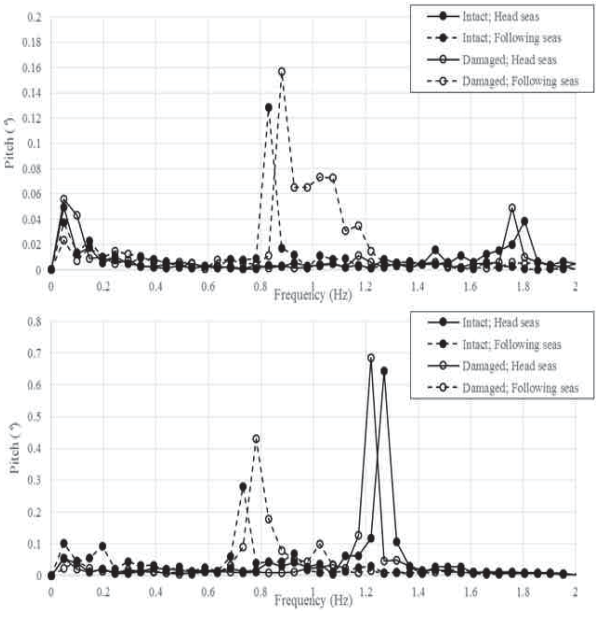

Figure 9 FFT analysis results of the pitching motion (top: normal weather conditions; bottom: unfavorable weather conditions).

Figure 9 shows the results of a fast Fourier transform (FFT) analysis of the pitching motion. The dominant frequency and magnitude of the pitching motion were identified. As stated above, the dominant frequency was clearer in head seas than in following seas due to clear waveform of incoming wave. Also, the magnitude of the pitching motion in damaged condition was greater, as the flooded water led to a loss of stability.

3.2 Speed measurement

The dominant frequency from the FFT analysis was identical to the wave encounter frequency, as the pitching motion was directly induced by waves. Using the incoming and encounter wave frequencies, the advance speed of the model could be derived by the Doppler effect. The derived advance speed of the intact free-running model is presented in Table 3.

Table 3 Advance speed of the intact model ship.

Wave condition		Wave encounter frequency (rad/s)	Advance speed (m/s)
Calm water		-	0.419
Normal weather condition (ω_0 = 8.52 rad/s)	Head seas	11.29	0.382
	Following seas	5.219	0.446
Unfavorable weather condition (ω_0 = 6.88 rad/s)	Head seas	7.933	0.227
	Following seas	4.699	0.471

Advance speed decreased significantly in head seas, while a small increase was observed in following seas because of the difference in the relative velocity of the waves. In head seas condition, the ship and waves were in the opposite direction; thus, the relative velocity of the incoming wave and test model increased,

resulting in large added resistance. As the group velocity of the wave was greater than the advance speed in following seas condition, the ship gained an additional propulsive force from the waves and the advance speed in following seas exceeds that in calm water.

Advance speed results in damaged condition are presented in Table 4. The flooding behavior that caused eddy-making and violent free surface in the damaged compartment was expected to create additional resistance, and a decrease in advance speed was observed in every wave condition. Retardation of the advance speed was more significant in unfavorable weather conditions, as strong flooding behavior occurred through the damaged hole.

Table 4 Advance speed of the damaged model ship.

Wave condition		Wave encounter frequency (rad/s)	Advance speed (m/s)
Calm water		-	0.410
Normal weather condition (ω_0 = 8.52 rad/s)	Head seas	11.12	0.340
	Following seas	5.322	0.404
Unfavorable weather condition (ω_0 = 6.88 rad/s)	Head seas	7.634	0.163
	Following seas	4.865	0.408

3.3 Roll motion

The flooding behavior in the damaged compartment induced roll motion, as well as the retardation of advance speed. Figures 10 and 11 shows the time history of the roll motion in normal weather conditions.

Roll motion was not expected in the ideal case when heading angle was perfectly aligned with wave direction. In the experiments, however, asymmetric flow field developed as the flow around the test model was not exactly symmetric, due to the slight yaw motion during autopilot course-keeping maneuver. Even small asymmetry caused coupled roll and pitching motion in head and following seas condition, and the roll motion period was expected to be identical to the wave encounter period.

In following seas condition, roll motion was regular and its period was identical to the wave encounter period. In normal weather condition, however, the roll motion period was identical to the natural roll period of the test model, although pitching motion period was identical to the wave encounter period. That implied existence of resonance of roll motion only. In the damaged condition, the resonance motion was interfered with by the flooded water; thus, the roll motion was not fully developed and irregular motion was observed.

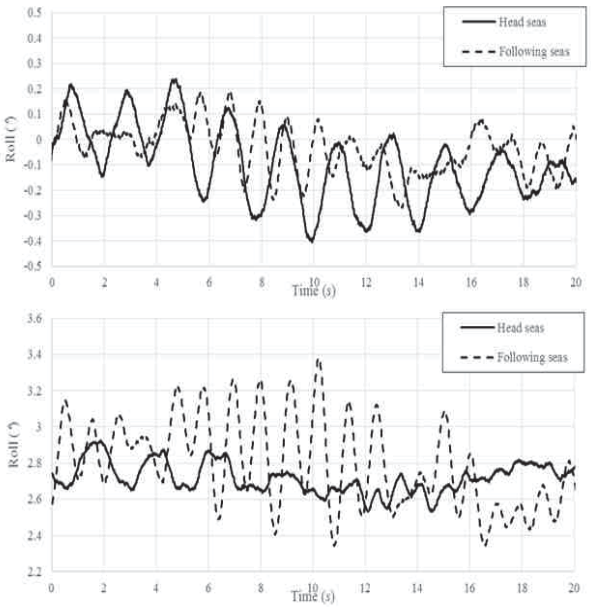

Figure 10 Time history of the roll motion in normal weather conditions (top: intact condition; bottom: damaged condition).

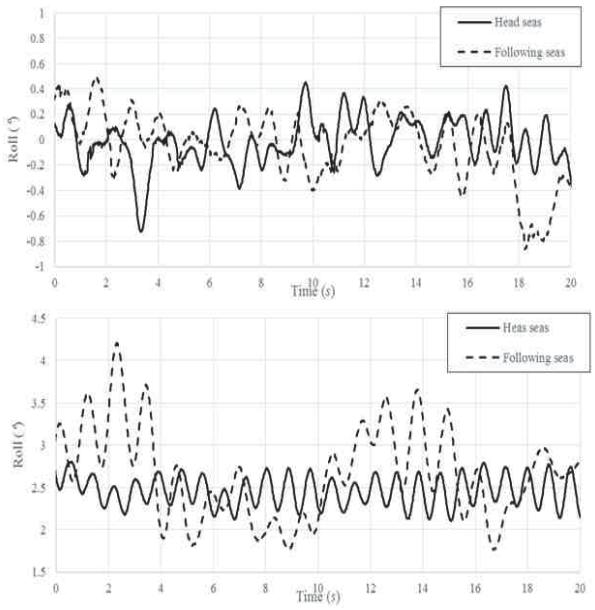

Figure 11 Time history of roll motion in unfavorable weather conditions (top: intact condition; bottom: damaged condition).

Figure 11 shows the time history of roll motion in unfavorable weather conditions. Strong flooding behaviors appear in unfavorable weather conditions; thus, roll motion was induced in damaged condition and its period was identical to the wave encounter period. In intact case, however, roll motion in head seas was irregular and the resonance motion in the natural roll period of the model was not observed, as there was no excitation force of the roll motion.

4. CONCLUSIONS

In the present study, a free-running model ship was constructed to perform experimental research on the SRtP of a damaged ship. Motion responses of the damaged ship model in head and following seas were measured, and the influences of the damaged compartment and wave conditions on the motion responses of the model were identified.

In the course-keeping tests in head and following seas, the characteristics of pitching motion were analyzed first. Slamming on the stern suppressed the pitching motion of the test model in unfavorable weather conditions; therefore, the pitching motion responses in following seas was less than those in head seas in unfavorable weather conditions.

The advance speed of the model was derived from the wave encounter frequency. In head seas, incoming waves generated additional resistance on the hull and caused the advance speed to decrease severely. In following seas, the phase velocity of the waves was faster than the advance speed of the free-running model; thus, the wave increased the advance speed slightly.

In damaged condition, the flooding behavior in the damaged compartment augmented resistance of the ship, resulting in a lower advance speed than in intact condition. In unfavorable weather conditions, retardation of the advance speed was 13% in following seas and 28% in head seas.

The roll motion responses of the ship in waves were also analyzed. The resonance of the roll motion in the natural roll period of the model was observed in intact and normal weather conditions. In damaged condition, however, the periodic flooding behavior stimulated roll motion, and the distinguishable roll period was identical to the wave encounter period.

Through free-running tests, the characteristics of the motion responses of a damaged ship model under SRtP regulations were identified. As future studies, a wireless measurement system for propulsion performance and wave heights in the damaged compartment will be installed on the free-running system to achieve the provision of a reliable validation database for CFD.

5. ACKNOWLEDMENTS

The present study is supported by the Office of Naval Research (ONR) under the supervision of Dr. Ki-Han Kim, the National Research

Foundation of Korea (Grant No. 2013R1A1A2012597), and the Multi-Phenomena CFD Research Center (Grant No. 20090093103), funded by the Ministry of Education, Science and Technology of the Korea Government.

6. REFERENCES

Araki, M., Sadat-Hosseini, H., Sanada, Y., Tanimoto, K., Umeda, N., and Stern, F., 2012, "Estimating Maneuvering Coefficients Using System Identification Methods with Experimental, System-based, and CFD Free-running Trial Data", Ocean Engineering, Vol. 51, pp. 63-84.

Ayaz, Z., Vassalos, D., and Spyrou, K. J., 2006, "Manoeuvring Behaviour of Ships in Extreme Astern Seas", Ocean Engineering, Vol. 33, pp. 2381-2434.

Begovic, E., Mortola, G., Incecik, A., and Day, A. H., 2013, "Experimental Assessment of Intact and Damaged Ship Motions in Head, Beam and Quartering Seas", Ocean Engineering, Vol. 72, pp. 209-226.

Bulian, G., 2005, "Nonlinear Parametric Rolling in Regular Waves-a General Procedure for the Analytical Approximation of the GZ Curve and Its Use in Time Domain Simulations", Ocean Engineering, Vol. 32, pp. 309-330.

Carrica, P. M., Wilson, R. V., Noack, R. W., and Stern, F., 2007, "Ship Motions Using Single-phase Level Set with Dynamic Overset Grids", Computers & Fluids, Vol. 36, pp. 1415-1433.

Carrica, P. M., Huiping, F., and Stern, F., 2011, "Computations of Self-propulsion Free to Sink and Trim and of Motions in Head Waves of the KRISO Container Ship (KCS) Model", Applied Ocean Research, Vol. 33, pp. 309-320.

Carrica, P. M., Ismail, F., Hyman, M., Bhushan, S., and Stern, F., 2013, "Turn and Zigzag maneuvers of a Surface Combatant Using a URANS Approach with Dynamic Overset Grids", Journal of Marine Science and Technology, Vol. 18, pp. 166-181.

Choi, J.E., Min, K.-S., Kim, J. H., Lee, S.B., and Seo, H. W., 2010, "Resistance and Propulsion Characteristics of Various Commercial Ships Based on CFD Results", Ocean Engineering, Vol. 37, pp. 549-566.

Gao, Z., Gao, Q., and Vassalos, D., 2011, "Numerical Simulation of Flooding of a Damaged Ship", Ocean Engineering, Vol. 38, pp. 1649-1662.

Germanischer Lloyd (GL), 2009, "Preliminary Guidelines of Safe Return to Port Capability of Passenger Ships", GL Rules for Classification and Construction, VI-11-02.

International Towing Tank Conference (ITTC), 2011, "Seakeeping Experiments", ITTC-Recommended Procedures and Guidelines, 7.5-02-07-02.1.

Lee, D., Hong, S. Y., and Lee, G.-J., 2007, "Theoretical and Experimental Study on Dynamic Behavior of a Damaged Ship in Waves", Ocean Engineering, Vol. 34, pp. 21-31.

Lee, S., You, J.-M., Lee, H.-H., Lim, T., Rhee, S. H., and Rhee, K.-P., 2012, "Preliminary Tests of a Damaged Ship for CFD Validation", International Journal of Naval Architecture and Ocean Engineering, Vol. 4, pp. 172-181.

Lim, T., Seo, J., Park, S. T., Rhee, S. H., 2014, "Experimental Study on the Safe-Return-to-Port of a Damaged Ship in Head Seas", Proceedings of 30th Symposium on Naval Hydrodynamics, Hobart, Australia.

Neves, M. A. S. and Rodriguez, C. A., 2007,

"Influence of Non-linearities on the Limits of Stability of Ships Rolling in Head Seas", Ocean Engineering, Vol. 34, pp. 1618-1630.

Paik, B. G., Lee, C. M., and Lee, S. J., 2004, "PIV Analysis of Flow around a Container Ship Model with a Rotating Propeller", Experiments in Fluids, Vol. 36, pp. 833-846.

Sadat-Hosseini, H., Stern, F., Olivieri, A., Campana, E., Hashimoto, H., Umeda, N., Bulian, G., and Francescutto, A., 2010, "Head-wave Parametric Rolling of a Surface Combatant", Ocean Engineering, Vol. 37. pp. 859-878.

Sadat-Hosseini, H., Carrica, P., Stern, F., Umeda, N., Hashimoto, H., Yamamura, S., and Mastuda, A., 2011, "CFD, System-based and EFD Study of Ship Dynamic Instability Events: Surf-riding, Periodic Motion, and Broaching", Ocean Engineering, Vol. 38, pp. 88-110.

Seo, J. H., Seol, D. M., Lee, J. H., and Rhee, S. H., 2010, "Flexible CFD Meshing Strategy for Prediction of Ship Resistance and Propulsion Performance", International Journal of Naval Architecture and Ocean Engineering, Vol. 2, pp. 139-145.

Simonsen, C. D., Otzen, J. F., Joncquez, S., and Stern, F., 2013, "EFD and CFD for KCS Heaving and Pitching In Regular Head Waves", Journal of Marine Science and Technology, Vol.18, pp. 435-459.

Spanos, D. A. and Papanikolaou, A. D., 2012, "On the Time Dependence of Survivability of ROPAX Ships", Journal of Marine Science and Technology, Vol. 17, pp. 40-46.

Wilson, R. V., Carrica, P. M., and Stern, F., 2006, "Unsteady RANS Method for Ship Motions with Application to Roll for a Surface Combatant", Computers & Fluids, Vol. 35, pp. 501-524.

Yoon, H. K., Son, N. S., and Lee, G. J., 2007, "Estimation of the Roll Hydrodynamic Moment Model of a Ship by Using the System Identification Method and the Free Running Model Test", IEEE Journal of Oceanic Engineering, Vol. 32, pp. 798-806.

Proceedings of the 12th International Conference on the Stability of Ships and Ocean Vehicles, 14-19 June 2015, Glasgow, UK.

Main Contributing Factors to the Stability Accidents in the Spanish Fishing Fleet

Francisco Mata-Álvarez-Santullano, *Maritime Accident and Incident Investigations Standing Commission, Government of Spain*, fmata@fomento.es

ABSTRACT

Between November 2008 and November 2014 a total of 28 stability accidents affecting to Spanish fishing vessels were investigated by the Spanish Marine Accident and Incident Investigation Standing Commission. A comprehensive review of these accidents allows determining the nature of the main contributing factors behind the high accident rates in the Spanish fishing sector.

Keywords: *fishing vessel, accident investigation, safety policies, training, complacency*

1. INTRODUCTION

The fishing sector ranks high in the list of mortality rates labor sectors. In Spain, figures published by INE (National Statistics Institute, *Instituto Nacional de Estadística*, http://www.ine.es/inebmenu/indice.htm) and various of its bodies (INSHT, 2011) shows the global rate of mortal accidents in 2011 to be 3 deaths for each 100000 workers in Spain (global rate: for all labour sectors). The global rate of severe accidents in Spain in the same year was 25 per 100000 workers. In the fishing sector only, the rate of mortal accidents in that year was of 33 deaths, that is to say, more than ten times the global rate. Similarly, the ratio of severe accidents in the fishing sector rose to 159 per 100000 workers (six times the global rate). According to these data, the fishing and aquiculture labour sector was the third with highest mortality rates in Spain, only behind silviculture1 (51 deaths per 100000 workers) and extractive industries2 (42 deaths per 100000 workers).

Several studies have been conducted studying the relation among fishing safety, research and public policies. Jin and Thunberg (Jin and Thunberg, 2005) established the importance of probability models in development and quantitative assessment of management mechanisms related to safety in the commercial fishing industry. Pérez-Labajos states (Pérez-Labajos, 2008) that the research work on the safety and accidents of commercial fishing vessels can be broken down into three clearly distinct frameworks of analysis: type of damage (personal and material), types of accidents, and accident inequalities applied to the fishing sector.

The present work belongs to the second type of analysis, but a new approach is proposed: instead of focusing in the type of accident of its consequences, proposes to research into the underlying causes which lead to the accidents.

In the fishing sector in Spain, the relation between type of accident and number of casualties (dead or missing person) shows clearly that the stability related accidents are, by far, the most dangerous.

Being clear that the loss of stability is one of the major risks a vessel may face, it is not so

obvious what can be done to prevent accidents due to loss of stability. For policy makers to develop effective policies to reduce the number of accidents is necessary the causes leading to these accidents be known. It is paradigmatic that accidents are due to multiple factors; not being common accidents which respond to a single cause. In any marine casualty is common to find personal factors (lack of training, fatigue ...), social factors (lack of safety culture, economic conditions ...), technical factors (design faults ...), regulatory factors (inadequate regulations …), etc.

Consequently the best policy to prevent stability accidents in the fishing fleet should be based on the incidence that each of the contributing factors has over the accidents rates. A possible way to approach such study is by establishing a maritime accident investigation policy with the following characteristics:

- Comprehensive, in the sense of examining accidents from multiple facets,
- Independent from other investigations. Not intended to establish blame or apportion liability.
- Providing a taxonomy which allows contributing factors to be classified for statistical analysis.

At European level, since 2011 there exists a regulation that harmonizes the investigation procedures and fulfils, in principle, those requirements. Directive 2009/18/EC of the European Parliament and of the Council (http://eur-lex.europa.eu/legal-content/EN/TXT/?uri=uriserv:OJ.L_.2009.131.01.0114.01.ENG), which entered into force in June 2011, establishes for European countries the obligation to investigate marine accidents and to notify the Commission on marine accidents and the data resulting from safety investigations in the European Marine Casualty Information Platform (EMCIP).

2. EMCIP ACCIDENT ANALYSIS MODEL

The EMCIP is built over a determined investigation analysis method. The accident analysis method lying below EMCIP is the ECFA (Events and Casual Factors Analysis) method, which is extensively described in the scientific literature of accident investigation.

The ECFA method in EMCIP depicts the necessary and sufficient events and causal factors for accident occurrence in a logical sequence (Buys and Clark, 1995). Under the ECFA scheme, behind the accidental events identified leading to the casualty there are contributing factors which must be identified and corrected to prevent the occurrence of similar accidents.

EMCIP provides taxonomy to classify contributing factors identified during an accident. However the EMCIP system has still to prove its value for accident analysis in the fishing sector, due to the following reasons:

- It is relatively recent; therefore it still does not store a significant amount of safety investigations.
- Fishing vessels with length below 15m are not included in the scope of Directive 2009/18/EC; therefore most countries are not notifying EMCIP with accidents in those vessels.
- EMCIP's taxonomy is adapted from existing models used in other transport modes and is oriented towards merchant marine traffic, but its use in the fishing sector is not always straightforward.

3. MARINE ACCIDENTS INVESTIGATED IN SPAIN

3. 1 CIAIM

In Spain the Maritime Accident and Incident Investigations Standing Commission (*Comisión Permanente de Investigación de*

Accidentes e Incidentes Marítimos, CIAIM) is an independent governmental body entrusted with the safety investigation of marine accidents. It acts pursuant to the provisions of Directive 2009/18/EC and the International Maritime Organization (IMO) Casualty Investigation Code. CIAIM was created in September 2008 and since then has received nearly 600 notifications of marine casualties, half of which affect fishing vessels (CIAIM, 2014, 2013, 2012, 2011, 2010, 2009).

3. 2 **Stability related accidents of fishing vessels**

The author has conducted a study of the stability related accidents of fishing vessels in Spain between September 2008 and December 2014. In this period CIAIM received 305 notifications of fishing vessels casualties, whose distribution according to type of accident and consequences is shown in Table 1.

Type of accident	Number of accidents	Number of dead / missing persons	Number of vessels lost
Capsizing / Listing	**32**	**30**	**28**
Collision	50	8	9
Contact	12	0	5
Damage to equipment	7	0	0
Grounding / Stranding	53	9	22
Fire / explosion	26	3	12
Flooding / foundering	74	8	53
Loss of control	10	1	3
Hull failure	4	0	2
Missing	1	3	1
Non accidental event	3	3	1
Occupational accident	33	27	0
Total	305	92	136

Table 1. Fishing vessel accidents between Sept'08 and Dec'14 in Spain

Definition for types of accidents listed in Table 1 is provided by the European Maritime Safety Agency in the EMCIP taxonomy:

Capsizing/listing: is a casualty where the ship no longer floats in the right-side-up mode due to: negative initial stability (negative metacentric height), or transversal shift of the centre of gravity, or the impact of external forces. When the ship is tipped over until disabled is called capsizing; when the ship has a permanent heel or angle of loll is called listing.

Collision: a casualty caused by ships striking or being struck by another ship, regardless of whether the ships are underway, anchored or moored. This type of casualty event does not include ships striking underwater wrecks. The collision can be with other ship or with multiple ships or ship not underway.

Contact: a casualty caused by ships striking or being struck by an external object. The objects can be: floating object (cargo, ice, other or unknown); fixed object, but not the sea bottom; or flying object.

Damage to equipment: damage to equipment, system or the ship not covered by any of the other casualty type.

Grounding / stranding: a moving navigating ship, either under command, under power, or not under command, drifting, striking the sea bottom, shore or underwater wrecks.

Fire / explosion: an uncontrolled ignition of flammable chemicals and other materials on board of a ship. Fire is the uncontrolled process of combustion characterized by heat or smoke or flame or any combination of these. Explosion is an uncontrolled release of energy which causes a pressure discontinuity or blast wave.

Flooding / foundering: is a casualty event when the ship is taking water on board. Foundering will be considered when the vessel has sunk. Foundering should only be regarded as the first casualty event if the details of the flooding which caused the vessel to founder are not known. Flooding refers to a casualty when a vessel takes water on board and can be: Progressive if the water flow is gradually; or Massive if the water flow is considerable.

Loss of control: a total or temporary loss of

the ability to operate or maneuver the ship, failure of electric power, or to contain on board cargo or other substances. Loss of electrical power is the loss of the electrical supply to the ship or facility. Loss of propulsion power is the loss of propulsion because of machinery failure. Loss of directional control is the loss of the ability to steer the ship. Loss of containment is an accidental spill or damage or loss of cargo or other substances carried on board a ship.

Hull failure: a failure affecting the general structural strength of the ship.

Missing: a casualty to a ship whose fate is undetermined with no information having being received on the loss and whereabouts after a reasonable period of time.

Non-accidental events: intentional events as a result of illegal or hostile acts. They are: Acts of war, criminal acts, illegal discharge, and others.

Occupational accident: Occupational accident type means the mode in which a person (crewmember, passenger or other person) was injured or killed, not involving in a ship casualty, which can be: accident, illness, suicide/homicide, or unknown.

It is to be noted the high risk of personal loss and vessel loss in stability related accidents in comparison with other types of accident. Focusing on stability related accidents, 28 out of the 32 accidents were investigated or are currently under investigation. These 28 accidents are listed in Table 2, in the appendix, including the following data:

Internal CIAIM accident code.

Vessel total length (Lt, m).

Indicator of the accident having occurred inside or outside territorial waters -12 miles off the coast (High seas, coast).

Mean wind speed (Vw, knots)

Significant wave height, wind and swell waves (Hs, m).

Primary cause of the accident. In the case of accidents still under investigation, the guessed cause is included.

Number of report published in CIAIM's website www.ciaim.es, in the case the report is published.

3. 3 Underlying causes

Behind the primary causes summarized in the previous table there are several underlying causes. When analysing deeply these 28 accidents the following list of underlying causes has been found.

These underlying causes are listed in Table 3 in the appendix.

3. 4 Contributing factors in the fishing sector

The listed underlying causes may be linked to one or several contributing factors in the EMCIP taxonomy. The individual study of the underlying cause and the specific circumstances of the accident allows for this distribution.

It is not in the scope of the present work to enter in details of the analysis performed in each of the accidents investigated. For the purposes of this study, the results are summarized below.

The results show that most underlying causes are linked to the same type of contributing factors that can be grouped in just six categories according to EMCIP taxonomy:

Type of contributing factor (CF)	Number of CF in CIAIM stability accidents
Lack of training	30
Economic conditions	14
Design error	4
Inadequate regulation	8
Lack of safety awareness	33
Lack of safety culture	20

Table 4. Type of contributing factor in 28 stability related accidents.

Graphically the previous results are presented in Figure 1.

4. ANALYSIS

Most of the contributing factors in the fishing vessel accidents are related to personal economic and social factors: lack of training of crewmembers, economic conditions putting press on the masters to navigate in dangerous areas looking for more abundant catches. Of special relevance is the lack of safety awareness among crew of fishing vessels and the lack of safety culture in fishing companies.

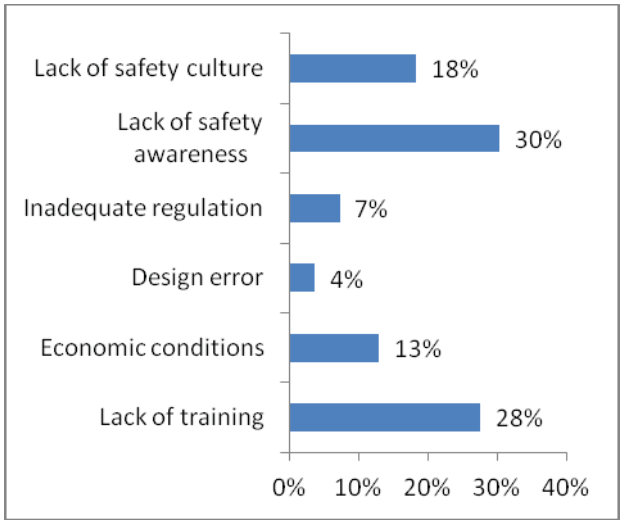

Figure 1 Type of contributing factor (percentage)

It is worth to mention the similarity of these results with those obtained in previous studies by Loughran et al. (Loughran et al, 2002) in their study of fishing vessel safety in the UK: they conclude that fishing industry lacks a safety culture and that more failure data needs to be collected in order to control risks.

Only in four accidents a design error was found to have contributed to the accident.

It is also significant that in 8 accidents the stability regulation has been found inadequate. While the ship fulfilled the stability criteria in force, these were found to be inadequate for correctly managing the stability on board: regulations which did not include any stability, loading or operating information for the master, therefore making impossible to adequately manage stability on board fishing vessels. This was especially true in small fishing vessels, with length below 15 m.

These data may be interpreted in different ways. First, they may indicate the need to design policies which address the basic problems detected: lack of safety awareness and training.

Being this true, the data also show that fishing vessels built and designed according to the approved standards (including safety and stability standards) could be prone to suffer accidents when personal and socio-economic factors are present. For instance, fishing in breaking waves and shoals could be forbidden, or training campaigns to inform about the risks associated to navigating in these areas could be established. Nevertheless it is a fact that fishing vessels will operate where catches can be captured.

This would support the idea of setting more exigent technical standards to fishing vessels, so they are capable to cope with inadequate operation from the crews and fishing companies.

5. CONCLUSIONS

Stability related accidents in Spain in the period September 2008 to December 2014 happened mainly for a combination of personal, social, economic and regulatory factors, being specially relevant the lack of training and lack of safety awareness (complacency) of crews. Marine safety policies in the fishing sector to prevent stability accidents must therefore address these problems.

In addition, the stability standards applicable to fishing vessels, in particular to small fishing vessels, are not capable to deal with the reality of the fishing sector. The maritime authorities should promote the revision of the stability standards applicable to those vessels, so they can bear inadequate operation derived from personal and socio-economic contributing factors present the fishing sector.

6. REFERENCES

Buys, J.R., Clark, J.L., 1995, "Events and Causal Factors Analysis (No. SCIE-DOE-01-TRAC-14-95)", Technical Research and Analysis Center.

CIAIM, 2009. Informe anual. Comisión permanente de investigación de accidentes e incidentes marítimos.

CIAIM, 2010. Informe anual. Comisión permanente de investigación de accidentes e incidentes marítimos.

CIAIM, 2011. Informe anual. Comisión permanente de investigación de accidentes e incidentes marítimos.

CIAIM, 2012. Informe anual. Comisión permanente de investigación de accidentes e incidentes marítimos.

CIAIM, 2013. Informe anual. Comisión permanente de investigación de accidentes e incidentes marítimos.

CIAIM, 2014. Informe anual. Comisión permanente de investigación de accidentes e incidentes marítimos.

Jin, Di and Thunberg, Eric, 2005, "An analysis of fishing vessel accidents in fishing áreas off the northeastern United States", Safety Science, Vol. 43, pp. 523-540.

INSHT, 2011. Análisis de mortalidad por accidente de trabajo en España, 2008-2009-2010. Instituto Nacional de Seguridad e Higiene en el Trabajo.

Loughran C. G., Pillay A., Wang J., Wall A. & Ruxton T., (2002) "A preliminary study of fishing vessel safety", Journal of Risk Research, 5:1, 3-21

Pérez-Labajos, Carlos, 2008, "Fishing safety policy and research", Marine Policy, Vol 32, pp. 40-45

APPENDIX

CIAIM accident code	Lt (m)		Vw (kt)	Hs (m)	Primary cause (summarized)	Report number
014/2008	27,85	High sea	25	2,7	Water ingress on main deck	A-05/2010
020/2008	34,5	High sea	25	6,5	Fishing gear stuck	A-15/2010
031/2009	39,3	High sea	20	3	Water ingress on main deck	S-28/2011
033/2009	9,6	Coast	30	1,5	Excessive weather conditions	S-41/2011
035/2009	17,7	High sea	5	1	Water ingress on main deck	A-06/2009
044/2009	10,53	Coast	12	0,25	Cargo shifting	S-20/2011
002/2010	27	High sea	35	3,5	Water ingress on main deck	A-10/2011
007/2010	37,35	High sea	17	4	Water ingress on main deck	S-27/2011
056/2010	7,18	Coast	12	0,25	Fishing gear stuck	S-14/2012
062/2010	24	High sea	20	1,25	Water ingress on main deck	A-01/2013
067/2010	28	High sea	30	4	Water ingress on main deck	A-10/2012
055/2011	14,83	High sea	22	3,5	Excessive weather conditions	A-08/2012
074/2011	5,76	Coast	19	1,4	Excessive weather conditions	S-26/2012
056/2012	15,5	High sea	11	1	Cargo shifting	S-23/2013
003/2013	7,2	Coast	5	1	Green seas	R-27/2013
008/2013	6,37	Coast	23	4,6	Excessive weather conditions	S-24/2013
039/2013	12,5	Coast	27	4,25	Excessive weather conditions	11/2014
047/2013	9,5	Coast	10	2	Green seas	S-42/2013
056/2013	8,45	Coast	11	2	Green seas	R-39/2013
016/2014	9,45	Coast	13	2	Fishing gear stuck	Investigation ongoing
028/2014	32	High sea	5	0,75	Cargo shifting	Investigation ongoing
056/2014	8,64	High sea	22	2	Water ingress on main deck	Investigation ongoing
057/2014	14,48	High sea	17	2	Water ingress on main deck	Investigation ongoing
079/2014	8,7	Coast	20	1	Green seas	Investigation ongoing
072/2014	11,85	Coast	n/a	2	Green seas	Investigation ongoing
088/2014	17,5	High sea	20	2	Water ingress on main deck	Investigation ongoing
089/2014	8,5	Coast	n/a	n/a	Green seas	Investigation ongoing
095/2014	18,6	Coast	20	1,25	Excessive weather conditions	Investigation ongoing

Table 2. Stability related accidents

CIAIM accident code	Contributing factor	CIAIM accident code	Contributing factor
035/2009	Freeing ports sealed	008/2013	Crew inexperienced
035/2009	Overloading: excess of fishing gear	008/2013	Inadequate stability regulation
035/2009	Non authorised modifications to vessel structure	008/2013	Excessive weather conditions
035/2009	Inadequate stability management on-board	003/2013	Loss of propulsion (dead ship)
014/2008	Overloading	003/2013	Fishing close to wave surf or shoal
014/2008	Watertight openings not closed	056/2013	Excessive weather conditions
020/2008	Watertight openings not closed	056/2013	Fishing close to wave surf or shoal
020/2008	Inadequate fishing winch operation	047/2013	Vessel undermanned
020/2008	Inaccessible fishing winch operation post	047/2013	Fishing close to wave surf or shoal
002/2010	Inadequate watertight opening design	047/2013	Excessive weather conditions
002/2010	Watertight openings not closed	039/2013	Excessive weather conditions
044/2009	Inadequate cargo lashing to deck and cargo shifting	039/2013	Fishing gear and catches shifting
044/2009	Overloading	039/2013	Freeing ports sealed
007/2010	Overloading	039/2013	Overloading
007/2010	Watertight openings not closed	016/2014	Excessive weather conditions
031/2009	Overloading	028/2014	Inadequate stability management on-board
031/2009	Watertight openings not closed	028/2014	Overloading
033/2009	Non authorised modifications to vessel structure	056/2014	Inadequate stability management on-board
033/2009	Overloading	056/2014	Inadequate stability regulation
033/2009	Inadequate stability regulation	056/2014	Navigating out of authorised area
055/2011	Inadequate stability regulation	057/2014	Excessive weather conditions
067/2010	Watertight openings not closed	057/2014	Inadequate stability regulation
067/2010	Gear hauling with stern seas	079/2014	Excessive weather conditions
067/2010	Bad watertight opening design	079/2014	Inadequate stability regulation
056/2010	Vessel undermanned	079/2014	Fishing close to wave surf or shoal
056/2010	Fishing winch lack of safety stop system	072/2014	Fishing close to wave surf or shoal
074/2011	Inadequate cargo lashing to deck	072/2014	Inadequate stability regulation
074/2011	Inadequate stability regulation	088/2014	Overloading
062/2010	Watertight openings not closed	088/2014	Bad watertight openings maintenance
062/2010	Navigating in quarter or stern waves	095/2014	Navigating out of authorised area
062/2010	Inadequate stability management on-board: excessive trim	095/2014	Inadequate cargo lashing to deck and cargo shifting
056/2012	Inadequate stowing and cargo shifting	089/2014	Fishing close to wave surf or shoal
056/2012	Inadequate stability management on-board		

Table 3. Underlying causes to 28 stability related accidents.

Session 9.3 – EXTREME BEHAVIOUR

A Time-Efficient Approach for Nonlinear Hydrostatic and Froude-Krylov Forces for Parametric Roll Assessment in Irregular Seas

Non-Stationary Ship Motion Analysis Using Discrete Wavelet Transform

A Study on the Effect of Parametric Rolling on Added Resistance in Regular Head Seas

This page is intentionally left blank

A Time-Efficient Approach for Nonlinear Hydrostatic and Froude-Krylov Forces for Parametric Roll Assessment in Irregular Seas

Claudio A. Rodríguez, *LabOceano, COPPE - Universidade Federal do Rio de Janeiro, Brazil*

claudiorc@laboceano.coppe.ufrj.br

Marcelo A. S. Neves, *LabOceano, COPPE - Universidade Federal do Rio de Janeiro, Brazil*

masn@laboceano.coppe.ufrj.br

Julio César F. Polo, *COPPE - Universidade Federal do Rio de Janeiro, Brazil*
jcfpolo@gmail.com

ABSTRACT

In the context of second generation stability criteria assessments, the present paper introduces a fast time domain algorithm for parametric roll assessment in irregular seas. Two features can be distinguished in the present proposal: a) it involves the essential heave-roll-pitch nonlinear coupling and b) it is a pre-calculated *derivative* model, convenient for the required systematic Monte Carlo simulations.

The main features of the model are described. The proposed methodology is based on a 3D panel method in which hydrostatic and wave-induced forces are computed on the actual body surface considering a set of systematic pre-defined hull positions. This set of data is preprocessed through polynomial fitting and the coefficients of the derivative model, corresponding to a Taylor series expansion defined up to the third order, are obtained. The methodology is applied to a container ship in head seas. The model is capable of reflecting the non-ergodicity of the head seas parametric rolling. At the same time, the heave and pitch motions display "weakly ergodic" responses.

KEYWORDS: *Head seas; Derivative model; Second generation stability criteria; Parametric rolling; Irregular seas.*

1. INTRODUCTION

Nowadays, several numerical methodologies exist for predicting the nonlinear behavior of parametric rolling of ships in waves in time domain. These procedures are usually categorized into fully nonlinear and weakly nonlinear codes. The first type considers nonlinearities in all the involved forces, whereas the second one introduces nonlinearities basically in the restoring and incident wave forces in a time domain integration scheme. Both approaches demand high computational effort and, as a consequence, appear prohibitive in terms of simulation time when assessing parametric roll motions in stochastic seas.

The first two authors have proposed an analytical derivative model which was

validated in regular waves, Neves and Rodríguez (2006) . In order to enhance the capabilities of the *derivative* model, i.e., by considering more general body geometries, the present paper uses an improved approach for the computation of the nonlinear restoring and Froude-Krylov coefficients. The proposed methodology is based on a 3D panel method in which hydrostatic and wave-induced forces are computed on the actual body surface considering a set of systematic pre-defined hull positions. This set of data is preprocessed through polynomial fitting and the coefficients of the derivative model, corresponding to a Taylor series expansion defined up to the third order are obtained. Such strategy does lead to an adequate hydrodynamic modeling capable of taking into consideration the essential nonlinear coupling effects between heave, roll and pitch, see Rodríguez et al. (2007).

In recent years, other authors have proposed mathematically similar approaches to achieve fast time domain algorithm in the context of second generation stability criteria assessments. Song and Kim (2011) used Fourier series decomposition applied to a one-degree-of-freedom roll model. Alternatively, Weems and Wundrow (2013) used a volume-based heave-roll-pitch hybrid model. Finally, Somayajula and Falzarano (2014) used a Volterra series model, again applied in a one degree of freedom model.

The present derivative model, derived in the context of Taylor series expansion is a very fast and reliable time domain algorithm which may be useful in the context of second generation stability criteria assessment. In the present paper the polynomial approach is described and applied in the context of irregular seas. The potentialities of the model are highlighted and some numerical results are presented. It is anticipated that one of the main advantages of the proposed methodology is that after all the derivatives are pre-computed, the equations of motion may be integrated in a very effective and fast way.

2. MATHEMATICAL MODEL

In order to simulate parametric rolling in irregular waves it is necessary to express forces and moments acting on the ship as time series. As these forces and moments depend on the submerged geometry which is governed by a random wave profile and irregular motions of the ship, the problem becomes very complex and costly in computer time. The “exact” approach of the problem implies in not only solving the ship hydrodynamic problem for the random submerged geometry but also the nonlinear hydrostatics in time domain, and additionally, to solve implicitly and iteratively the equations of motion.

To overcome these difficulties and make the solution of the parametric roll problem more practical, the paper proposes a hybrid method which combines some hypothesis from classical seakeeping with the solution of the nonlinear equations in time domain. The equations to be integrated are (Neves and Rodríguez, 2006):

$$\begin{aligned}&(m+Z_{\ddot z})\ddot z+Z_{\ddot\theta}\ddot\theta+Z_{\dot z}\dot z+Z_{\dot\theta}\dot\theta+\\&Z_z z+Z_\theta\theta+\frac{1}{2}Z_{zz}z^2+\frac{1}{2}Z_{\phi\phi}\phi^2+\frac{1}{2}Z_{\theta\theta}\theta^2+\\&Z_{z\theta}z\theta+\frac{1}{6}Z_{zzz}z^3+\frac{1}{2}Z_{zz\theta}z^2\theta+\frac{1}{2}Z_{\phi\phi z}\phi^2 z+\\&\frac{1}{2}Z_{\phi\phi\theta}\phi^2\theta+\frac{1}{2}Z_{\theta\theta z}\theta^2 z+\frac{1}{6}Z_{\theta\theta\theta}\theta^3+Z_{\zeta z}(t)z+\\&Z_{\zeta\theta}(t)\theta+Z_{\zeta\zeta z}(t)z+Z_{\zeta zz}(t)z^2+Z_{\zeta z\theta}(t)z\theta+\\&Z_{\zeta\varphi\varphi}(t)\varphi^2+Z_{\zeta\zeta\theta}(t)\theta+Z_{\zeta\theta\theta}(t)\theta^2\\&\qquad=Z_w(t)\end{aligned}\tag{1}$$

$$\begin{aligned}&(J_{xx}+K_{\ddot\varphi})\ddot\varphi+K_{\dot\varphi}\dot\varphi+K_{\dot\varphi|\dot\varphi|}\dot\varphi|\dot\varphi|+K_\varphi\varphi+K_{z\varphi}z\varphi+\\&K_{\varphi\theta}\varphi\theta+\frac{1}{2}K_{zz\varphi}z^2\varphi+\frac{1}{6}K_{\varphi\varphi\varphi}\varphi^3+\frac{1}{2}K_{\theta\theta\varphi}\theta^2\varphi+\\&K_{z\varphi\theta}z\varphi\theta+K_{\zeta\varphi}(t)\varphi+K_{\zeta\zeta\varphi}(t)\varphi+K_{\zeta z\varphi}(t)z\varphi+\\&K_{\zeta\varphi\theta}(t)\varphi\theta=K_w(t)\end{aligned}\tag{2}$$

$$(J_{yy}+M_{\ddot{\theta}})\ddot{\theta}+M_{\ddot{z}}\ddot{z}+M_{\dot{z}}\dot{z}+$$
$$M_{\dot{\theta}}\dot{\theta}+M_{z}z+M_{\theta}\theta+\frac{1}{2}M_{zz}z^2+$$
$$\frac{1}{2}M_{\phi\phi}\phi^2+\frac{1}{2}M_{\theta\theta}\theta^2+M_{z\theta}z\theta+\frac{1}{6}M_{zzz}z^3+$$
$$\frac{1}{2}M_{zz\theta}z^2\theta+\frac{1}{2}M_{\phi\phi z}\phi^2 z+\frac{1}{2}M_{\phi\phi\theta}\phi^2\theta+$$
$$\frac{1}{2}M_{\theta\theta z}\theta^2 z+\frac{1}{6}M_{\theta\theta\theta}\theta^3+M_{\zeta z}(t)z+M_{\zeta\theta}(t)\theta+$$
$$M_{\zeta\zeta z}(t)z+M_{\zeta zz}(t)z^2+M_{\zeta z\theta}(t)z\theta+M_{\zeta\phi\phi}(t)\phi^2+$$
$$M_{\zeta\zeta\theta}(t)\theta+M_{\zeta\theta\theta}(t)\theta^2=M_{w}(t) \qquad (3)$$

Definition of coefficients appearing in the set of equations (1-3) and how to obtain them have been described in Neves and Rodríguez (2007). The same paper demonstrates the good accuracy of the model in regular waves when compared to experimental results for a modern container ship.

3. METHODOLOGY FOR IRREGULAR SEAS

In irregular seas, functions that govern wave excitations lose their harmonic character, becoming random functions in time domain. One way of expressing these direct excitation forces and moments, as well as wave restoring actions associated to a given sea spectrum is through the transfer functions amplitude of excitations (or restoring) in regular waves in frequency domain. Therefore, for example, for the heave excitation force we have:

$$S_{Z_w}(\omega_e)=\left[RAO_{Z_w}(\omega_e)\right]^2 S_{\zeta}(\omega_e) \qquad (4)$$

and for the roll wave restoring coefficient $K_{\zeta\phi}(t)$:

$$S_{K_{\zeta\phi}}(\omega_e)=\left[RAO_{K_{\zeta\phi}}(\omega_e)\right]^2 S_{\zeta}(\omega_e) \qquad (5)$$

For the exciting forces and moments in the other degrees of freedom and for the other wave restoring coefficients the same logic as given in equations (4) and (5) follows. As observed in the structure of eqs. (1-3) the hydrodynamic coupling between the three modes is described by eight time-dependent contributions in the heave equation ($Z_{\zeta z}(t)$, $Z_{\zeta\theta}(t)$, $Z_{\zeta\zeta z}(t)$, $Z_{\zeta zz}(t)$, $Z_{\zeta z\theta}(t)$, $Z_{\zeta\phi\phi}(t)$, $Z_{\zeta\zeta\theta}(t)$, $Z_{\zeta\theta\theta}(t)$), four contributions in the roll mode ($K_{\zeta\phi}(t)$, $K_{\zeta\zeta\phi}(t)$, $K_{\zeta z\phi}(t)$, $K_{\zeta\phi\theta}(t)$) and eight contributions in the pitch mode ($M_{\zeta z}(t)$, $M_{\zeta\theta}(t)$, $M_{\zeta\zeta z}(t)$, $M_{\zeta zz}(t)$, $M_{\zeta z\theta}(t)$, $M_{\zeta\phi\phi}(t)$, $M_{\zeta\zeta\theta}(t)$, $M_{\zeta\theta\theta}(t)$). So, in total there are twenty functions to be pre-computed.

Added mass and damping in the directly excited modes (heave and pitch) may be computed using convolution (Cummins, 1962). However, based on Celis (2008) – which reports small influence of memory effects on the development of parametric rolling in regular waves – and given the aim of simplifying the proposed methodology, added mass and damping are computed at the frequency value corresponding to the peak value, as done by many authors. For roll mode these hydrodynamic coefficients are computed at the roll natural frequency, introducing also nonlinearities in roll damping (adopting the same approach proposed by the Authors in previous articles (Neves and Rodríguez, 2007) for parametric roll in regular waves. Hydrostatic restoring is introduced directly into the equations, as the respective coefficients are independent of time. These are pre-calculated for different hull positions defined around the hull mean position.

In summary, the proposed procedure for parametric roll simulation in irregular waves consists in:

a) Define a sea state, i.e. specify a sea spectrum $S_{\zeta}(\omega)$ for given basic parameters like significant wave height (H_s) and peak period (T_p).

b) Transform sea spectrum defined for wave frequency ω and heading χ into encounter frequency domain ω_e (see Bhattacharyya, 1978):

$$S_\zeta(\omega_e) = \frac{S_\zeta(\omega)}{1 - \frac{2\omega U}{g}\cos\chi} \qquad (6)$$

c) Compute amplitude operators of wave exciting forces and all wave restoring coefficients in frequency domain. The amplitude operators of wave exciting forces may be computed using well known softwares like WAMIT® or HANSEL. In the present paper, all twenty wave restoring coefficients are computed using DSSTAB (based on numeric calculation of numerical restoring coefficients based on polynomial fitting, as described in Rodríguez et al., 2007). These operators are computed for unit wave amplitude, analogous to ship RAOs.

d) Transform domains of amplitude operators defined in step (c) from wave frequency to encounter frequency:

$$\omega_e = \omega - \frac{\omega^2 U}{g}\cos\chi$$

e) Calculate spectra of exciting forces and all twenty restoring coefficients, as indicated in equations (4) and (5).

f) Use Fourier analysis to generate time series of all spectra defined in step (e). In the Fourier analysis, a general time series $\gamma(t)$ may be obtained from a given spectrum $S_\gamma(\omega)$ using the following well known expressions:

$$\gamma(t) = \sum_{n=1}^{N} \gamma_{a_n} \cos(k_n x - \omega_n t + \varepsilon_n) \qquad (7)$$

where: $\gamma_{a_n} = \sqrt{2S_\gamma(\omega_n).\delta\omega}$

g) Solve nonlinear equations of motion in time domain using, for example, the classical 4th order Runge-Kutta routine.

4. NUMERICAL SIMULATIONS

Now the above presented methodology is applied. A container ship is considered, here denominated SAFEDOR (ITTC A1), described in Spanos and Papanikolaou (2009). 3D lines of ship hull are shown in Figure 1.

Figure 1 SAFEDOR ship hull.

SAFEDOR hull was tested for a JONSWAP spectrum with significant height H_s = 5.00 m, peak period T_p = 10.63 s, γ = 3.3 , wave incidence is 180° (head seas). Ship speed corresponds to Fn = 0.12. Sea spectrum and transformed spectrum to Fn = 0.12 are shown in Figure 2.

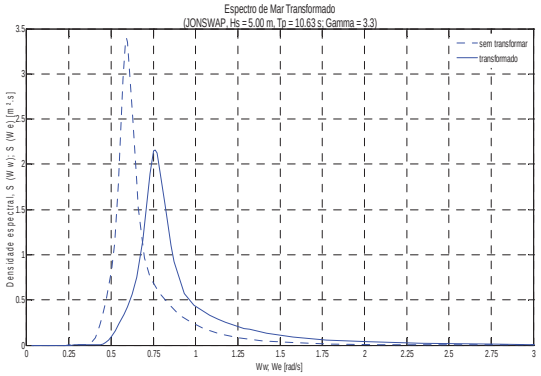

Figure 2 Sea spectrum, wave and encounter frequency domains

Transfer functions of external wave exciting force in heave and moment in pitch are given in Figures 3 e 4, respectively.

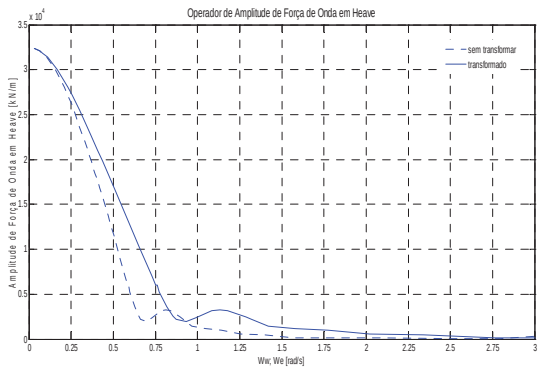

Figure 3 Transfer function, heave wave exciting force, Fn = 0.12

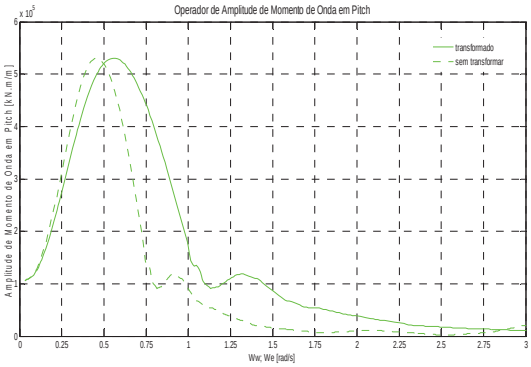

Figure 4 Transfer function, pitch wave exciting moment, Fn = 0.12

Transfer functions corresponding to roll wave restoring coefficients $K_{\zeta\varphi}$, $K_{\zeta z\varphi}$ and $K_{\zeta\varphi\theta}$ are shown in Figures 5 to 7.

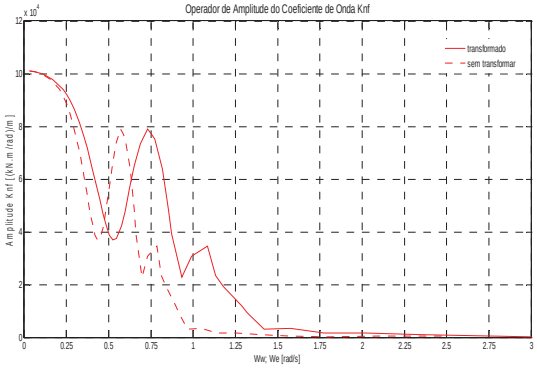

Figure 5 Transfer function, coefficient $K_{\zeta\varphi}$

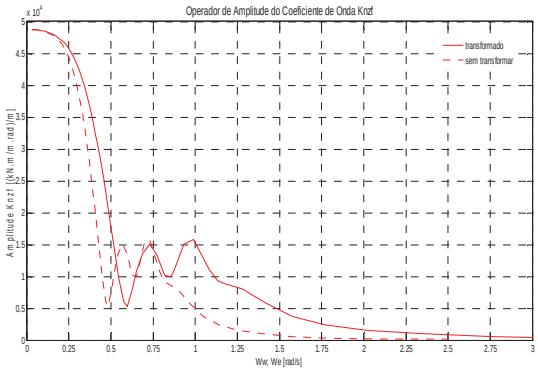

Figure 6 Transfer function, coefficient $K_{\zeta z\phi}$

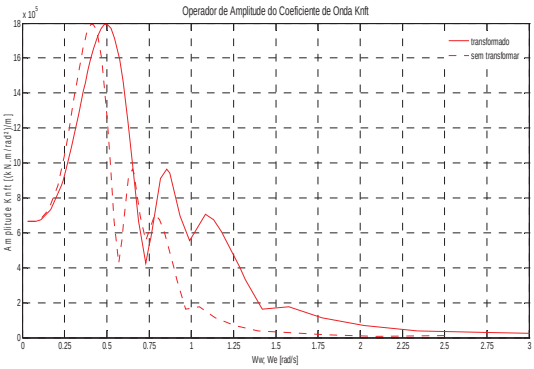

Figure 7 Transfer function, coefficient $K_{\zeta\phi\theta}$

With sea spectrum given in Figure 2 and the transfer functions the corresponding spectra for the specified sea condition are computed, as exemplified in equations (4) and (5). Some of these spectra are shown in Figures 8 to 10. Fourier analysis applied to the various spectra, corresponding time series are generated. Samples are given in Figures 11 to 13.

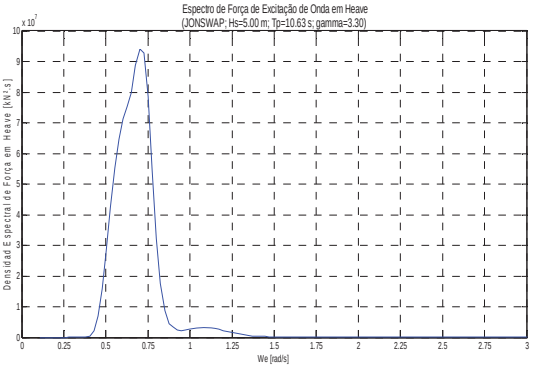

Figure 8 Heave exciting force spectrum

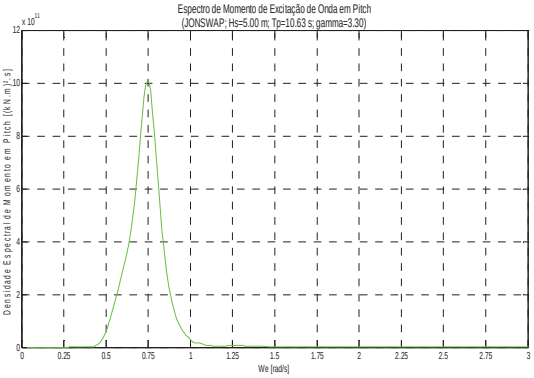

Figure 9 Pitch exciting moment spectrum

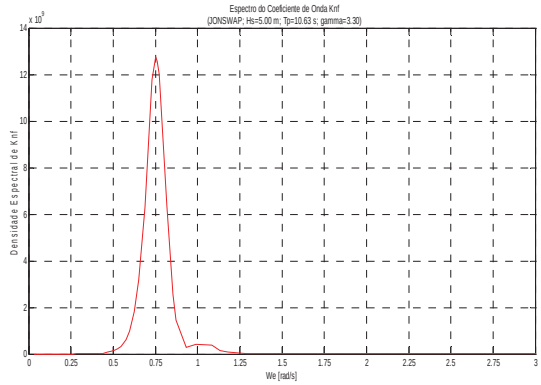

Figure 10 Roll restoring spectrum of $K_{\zeta\phi}$

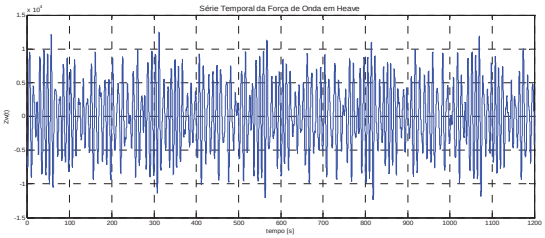

Figure 11 Heave force time series

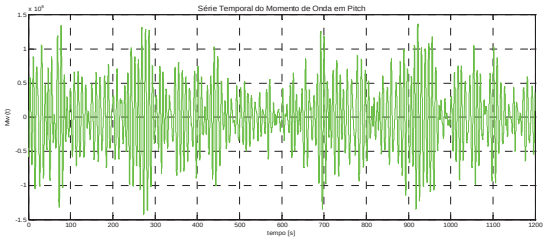

Figure 12 Pitch moment time series

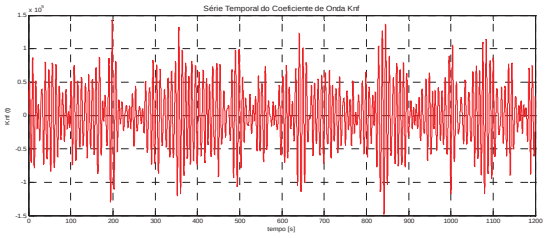

Figure 13 Wave coefficient $K_{\zeta\phi}$ time series

Time series obtained for the excitation forces and moments and all wave restoring coefficients are incorporated into the non linear equations of motion, eqs. (1-3), from which the time series of the heave-roll-pitch ship responses to the specified sea conditions result after integration.

To assess the ergodicity of responses in heave-roll-pitch modes, three realizations have been simulated (obtained from three different time series of wave excitations) for the specified sea conditions. These are shown in Figures 14 to 16.

Wave elevation is typically an ergodic process; additionally, transfer functions are linear. Therefore, even considering different time series (realizations) sufficiently long, wave excitation is statistically equivalent for the different realizations. In all cases the analyzed time series had a duration of 20', which in practice may be considered representative enough to describe the effects resulting from a given stochastic sea state.

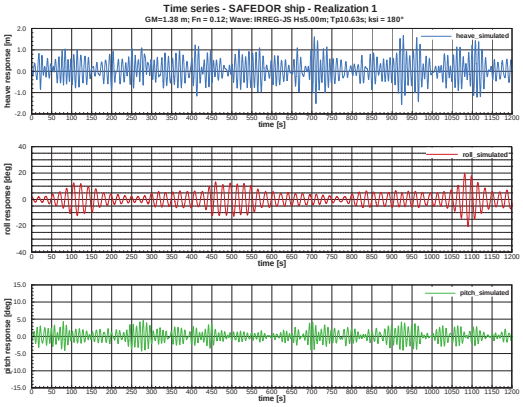

Figure 14 Heave, roll and pitch time series, realization #1

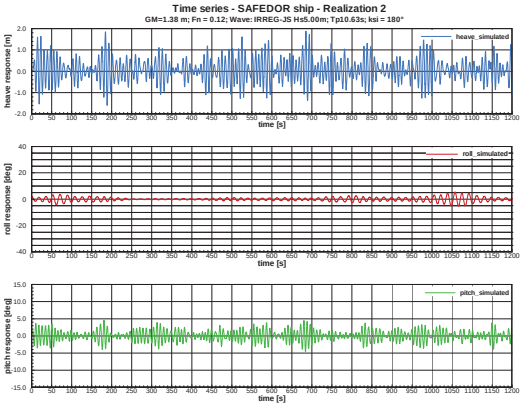

Figure 15 Heave, roll and pitch time series, realization #2

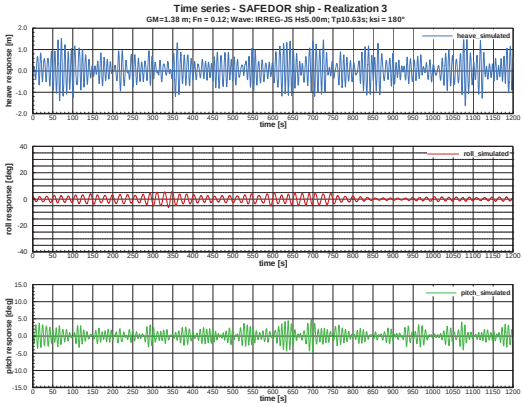

Figure 16 Heave, roll and pitch time series, realization #3

5. DISCUSSION OF NUMERICAL RESULTS

Despite the large frequency band with wave energy content, mainly the range of encounter frequency from 0.50 rad/s to 1.25 rad/s, wave excitation and restoring coefficients spectra are concentrated in a smaller band (0.50 to 0.85 rad/s) around the peak frequency of sea spectrum (0.76 rad/s) and outside the region of natural periods in heave (ω_{n3} = 0.82 rad/s), pitch (ω_{n5} = 0.85 rad/s) and roll (ω_{n4} = 0.33 rad/s).

Roll time series are distinct for the same tested condition. The first realization has moderate development of roll amplification, whereas the second and third realizations present quite small roll amplifications.

Roll responses have a larger period, corresponding typically to the characteristic 2:1 tuning, whereas both heave and pitch respond near encounter period.

Heave, roll and pitch spectra for the three realizations considered (see Figures 17 to 19) show the prevailing frequencies in each degree of freedom: heave and pitch present responses in the region of frequencies between 0.50 and 0.85 rad/s, which coincides with the main band of sea spectrum considered. On the other hand, roll responses are concentrated in a quite narrow band around the roll natural frequency, thus evidencing the occurrence of parametric rolling.

Roll spectra confirm the distinct character between the three realizations (see Figure 18). So, it is concluded that corresponding to the tested condition there two types of dynamic responses involved in roll: occurrence of parametric roll (realization #1) and non-occurrence of parametric roll (realizations #2 and #3). Thus, evidencing the influence of nonlinearities and the non-ergodicity in the responses.

Nonlinearities discussed in the above paragraph are also visible, but less intense in the heave and pitch spectra. It may be observed that spectral densities are smaller when there is parametric rolling (realization #1), whereas spectral densities are slightly larger in cases where parametric roll is very small (realizations #2 and #3). These results evidence the "weakly ergodic" character of heave and pitch motions, as has been pointed out by distinct authors (Belenky et al., 2003, Ogawa, 2007, Bulian et al., 2008).

It is important to notice here the great advantage in computing time when the derivative model is employed: running 50 time simulations of 10800 seconds with the corresponding 3100 frequency components (in order to avoid the *Self-Repeating Effect*) would take about 4 hours, whereas using full state-of-the art advanced hydrodynamic code DSSTAB in the same conditions would require about 3 days just to obtain a single realization of the random process on a normal desktop computer. On the other hand, running 20 simulations of 30 minutes with 220 frequency components, after pre-processing the derivative model will take nothing more than 12 seconds.

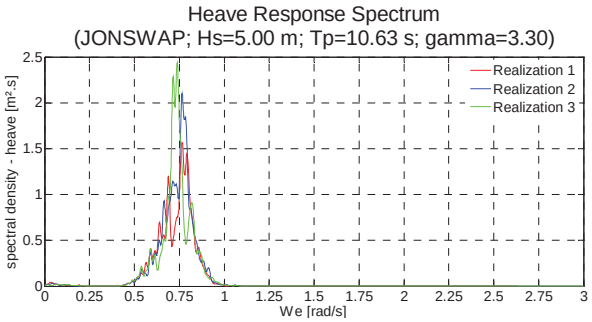

Figure 17 Heave motion spectra

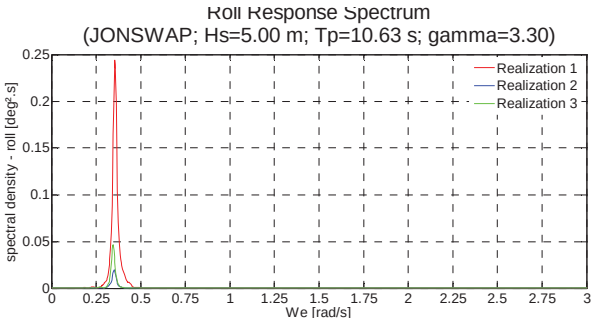

Figure 18 Roll motion spectra.

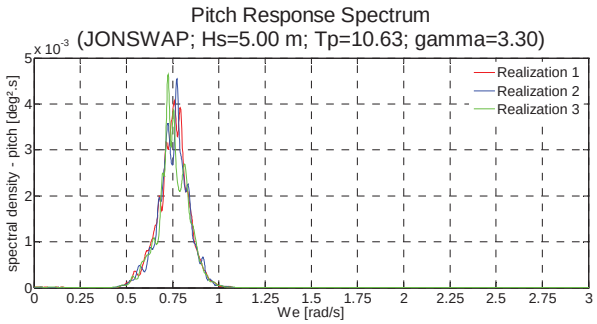

Figure 19 Pitch motion spectra

6. CONCLUSIONS

As previously mentioned, large series of time-domain simulations are required for realistic assessment of coupled heave, roll and pitch motions leading to extreme roll motion in irregular seas.

Some conclusions may be extracted based on the numerical results for the tested condition of SAFEDOR hull in head seas irregular seas.

It is shown that parametric roll affects the irregular responses in heave and pitch – as evidenced by the respective response spectra. In roll, the peak of responses is in the natural frequency, whereas in heave and pitch three peaks (or contributions) are observed, the larger at the encounter frequency and other two (much smaller) at the wave frequency and at the roll natural frequency.

Distinct realizations corresponding to a given test condition of SAFEDOR have produced qualitatively different responses with regard to occurrence of parametric rolling. This aspect confirms the capability of the proposed methodology to deal with strong nonlinearities, thus evidencing the non-ergodic character of roll responses when parametric rolling takes place.

For the heave and pitch modes the responses are "weakly ergodic".

The derivative model requires much less simulation time than full state-of-the art advanced hydrodynamic codes such as the DSSTAB code. This fact allows systematic Monte Carlo simulations in order to perform a realistic probabilistic assessment of parametric rolling of vessels.

7. ACKNOWLEDMENTS

The present investigation has been supported by CNPq, CAPES and ANP. Authors greatly acknowledge this crucial support.

8. REFERENCES

Belenky, V.L., Weems, K.M., Lin, W. and Paulling, J.R., 2003, “Probabilistic Analysis of Roll Parametric Resonance in Head Seas”. In: Proceedings of the 8th International Conference on Stability of Ships and Ocean Vehicles (STAB’2003), Madrid, Spain, pp. 325-340, Sep.

Bhattacharyya, R., 1978, Dynamics of Marine Vehicles. John Wiley & Sons, Inc., New York, United States of America.

Bulian, G., Francescutto, A., Umeda, N. and Hashimoto, H., 2008, "Experimental Investigation on Stochastic Parametric Rolling for a Post-Panamax Containership". In: Proceedings of the 6th Osaka Colloquium on Seakeeping and Stability of Ships (OC'2008), pp. 371-382, Osaka, Japan, Mar.

Celis, M.A.C., 2008, "Dynamic Stability of Ships: Influence of Memory Effects on Parametric Rolling" M.Sc. Dissertation, COPPE – Ocean Eng., Federal University of Rio de Janeiro, Brazil. (in Portuguese).

Cummins, W.E., 1962, "The Impulse Response Function and Ship Motions". In: International Symposium on Ship Theory, no. 8, Hamburg, Germany, pp. 101-109, Jun.

Neves, M.A.S. and Rodriguez, C.A., 2006, "An Investigation of Roll Parametric Resonance in Regular Waves". In: Proceedings of the 9th International Conference on Stability of Ships and Ocean Vehicles (STAB'2006), vol.1, Rio de Janeiro, Brazil, pp. 99-108, Sep.

Ogawa, Y. (2007): "An Examination for the Numerical Simulation of Parametric Roll in Head and Bow Seas", In: Proceedings of the 9th International Ship Stability Workshop (ISSW'2007), Hamburg, Germany, Aug.

Rodriguez, C.A., 2010, On the Nonlinear Dynamics of Parametric Rolling. D.Sc. Thesis, COPPE - Ocean Eng., Federal University of Rio de Janeiro, Brazil. (in Portuguese).

Rodríguez, C.A., Holden, C., Perez, T., Drummen, I., Neves, M.A.S. and Fossen, T.I., 2007, "Validation of a Container Ship Model for Parametric Rolling", In: Proceedings of the 9th International Ship Stability Workshop (ISSW'2007), Hamburg, Germany, Aug.

Somayajula, A.S. and Falzarano, J.M. 2014, "Non-linear Dynamics of Parametric Roll of Container Ship in Irregular Seas". OMAE2014-24186, San Francisco.

Song, K.H. and Kim, Y. 2011, "Quantitative Analysis of Parametric Roll and Operational Guidance", In: Proceedings of the 12th International Ship Stability Workshop (ISSW 2011), Washington DC.

Spanos, D., Papanikolaou, A., 2009, SAFEDOR International Benchmark Study on Numerical Simulation Methods for the Prediction of Parametric Rolling of Ships in Waves, NTUA-SDL Report, rev 1.

Weems, K.M. and Wundrow, D. 2013, "Hybrid Models for Fast Time Domain Simulation of Stability Failures in Irregular Waves With Volume-Based Calculations for Froude-Krilov and Hydrostatic Forces". In: Proceedings of the 13th International Ship Stability Workshop (ISSW 2013), Brest, France.

This page is intentionally left blank

Proceedings of the 12th International Conference on the Stability of Ships and Ocean Vehicles, 14-19 June 2015, Glasgow, UK.

Non-stationary Ship Motion Analysis Using Discrete Wavelet Transform

Toshio, ISEKI, *Tokyo University of Marine Science and Technology* iseki@kaiyodai.ac.jp

ABSTRACT

The discrete wavelet transform is applied to non-stationary ship motion data. The data was obtained by on-board measurements that were carried out under relatively severe sea conditions. In the full scale measurements, the ship travelled on several courses to investigate the change of frequency response relative to the encounter wave angle. Comparing to the results of Fourier analysis and time-varying autoregressive coefficient modelling, it is shown that the discrete wavelet transform can analyse non-stationary ship motions in the frequency and the time domain.

Keywords: *seakeeping, discrete wavelet transform, full-scale ship measurements, non-stationary time series*

1. INTRODUCTION

The author has been trying to develop a guidance system for heavy weather operation and investigating suitable signal processing methods under the necessity of analysing non-stationary stochastic process. Generally, the assumption of stationary stochastic processes is applied to the seaway, but not to ship response because it also depends on ship manoeuvres. Ship response is strongly affected by changes in the encounter angle and frequency of waves. Therefore, the method is needed to be a real-time algorithm that can deal with non-stationary stochastic processes. In the previous study (Iseki & Terada, 2002, Iseki, 2006), the instantaneous spectral analysis with the Time-Varying coefficient Vector Auto Regressive (TVVAR) model was introduced to deal with non-stationary ship motions. Some problems, however, were pointed out because the maximum likelihood method for determination of the trade-off parameter, which is the ratio of the observation noise and the system noise of Kalman filter, cannot be applied to the real-time algorithm.

On the other hand, the Discrete Wavelet Transform (DWT) is widely used recently in the field of signal processing (Percival and Walden 2000), image compression and analyses of non-stationary time series. In comparison with the Continuous Wavelet Trans-form (CWT), the process of DWT can be recognized as decomposition of a time series with use of digital filters while the CWT is defined by a convolution integral over entire time axis. In this sense, the DWT is suitable for digital computing and real-time analyses of non-stationary time series.

The author was also applied the Discrete Wavelet Packet Transform (DWPT) to non-stationary ship motion data (Kang and Iseki 2013). Comparing to the results of Discrete Fourier Transform (DFT) and the TVVAR modelling, it was confirmed that the locations of peaks of the DWPT coefficients agree well with the peak frequencies of the spectra estimated by DFT. However, the obvious advantage of DWPT was not observed in comparison with TVVAR modelling.

In this paper, both of DWT and DWPT are applied to analyses of non-stationary ship motion data which was measured during a large course alteration. Comparing to the results of DFT and TVVAR modelling, the validity of the DWT and DWPT is discussed in detail.

2. DISCRETE WAVELET TRANSFORM

2.1 Basic Properties

The DWT of a measured time series $\mathbf{X} = \{x_n : n = 0, 1, 2, \cdots, N-1\}$ is defined as follows:

$$\mathbf{W} = \mathbf{w}\mathbf{X} \tag{1}$$

where $\mathbf{W}$ denotes an N dimensional column vector of DWT coefficients, $\mathbf{w}$ an $N \times N$ real-valued matrix defining the DWT.

For the convenience, we assume that the sample size $N = 2^{J_0}$ for an integer J_0. The DWT coefficient $\mathbf{W}$ and matrix $\mathbf{w}$ could be separated as;

$$\mathbf{W} = \left[\mathbf{W}_1, \mathbf{W}_2, \cdots, \mathbf{W}_{J_0}, \mathbf{V}_{J_0}\right]^T \tag{2}$$

$$\mathbf{w} = \left[\mathbf{w}_1, \mathbf{w}_2, \cdots, \mathbf{w}_{J_0}, \mathbf{v}_{J_0}\right]^T \tag{3}$$

where

$$\mathbf{W}_i = \mathbf{w}_i \mathbf{X}^T, \quad \mathbf{V}_{J_0} = \mathbf{v}_{J_0} \mathbf{X}^T \tag{4}$$

The $\mathbf{W}_j$ and $\mathbf{V}_j$ are the wavelet coefficient sub-vector and the scaling coefficient sub-vector for the level j.

$$\mathbf{W}_i = \left[W_{i.1}, W_{i.2}, \cdots, W_{i.N_i}\right]^T \tag{5}$$

$$\mathbf{V}_i = \left[V_{i.1}, V_{i.2}, \cdots, V_{i.N_i}\right]^T \tag{6}$$

where $N_j \equiv N / 2^j$ denotes the number of components at the level j. Therefore, $\mathbf{V}_{J_0}$ contains only a scaling coefficient.

The "level j" is closely related to the scale $\tau_j \equiv 2^{j-1}$ $(j = 1, 2, \cdots, J_0)$ which is the sampling interval of the time series and denotes the number of times of "down-sampling by two". If the actual sampling time is denoted by Δt (sec), the physical scale can be expressed by $\tau_j \Delta t$.

By orthonormality of the DWT, we can synthesize the vector $\mathbf{X}$ from $\mathbf{W}$ by,

$$\begin{aligned} \mathbf{X} = \mathbf{w}^T \mathbf{W} &= \sum_{j=1}^{J_0} \mathbf{w}_j^T \mathbf{W}_j + \mathbf{v}_{J_0}^T \mathbf{V}_{J_0} \\ &= \sum_{j=1}^{J_0} \mathbf{D}_j + \mathbf{S}_{J_0} \end{aligned} \tag{7}$$

which is also a definition of Muti-Resolution Analysis (MRA) of $\mathbf{X}$. Here $\mathbf{D}_j$ and $\mathbf{S}_{J_0}$ are called as "details" for level j and "smooth" for level J_0, respectively. In the actual calculations, the DWT matrix $\mathbf{w}$ is not formed explicitly but rather $\mathbf{W}$ is computed using the "pyramid algorithm" which is effective and fast from the viewpoint of the computational process (Mallat 1989).

If we represent the actual wavelet filter by $\{h_l : l = 0, 1, 2, \cdots, L-1\}$, we can also derive the scaling filter by using "quadrature mirror" relationship,

$$g_l \equiv (-1)^{l+1} h_{L-1-l} \tag{8}$$

where L denotes the width of the wavelet filter.

In practice, the wavelet filter $\{h_l\}$ is a high-pass filter, while the scaling filter $\{g_l\}$ is a low-pass filter. Assuming $\mathbf{V}_0 = \mathbf{X}$ with defined $\{h_l\}$, $\{g_l\}$, general jth stage of the pyramid

algorithm yields the *n*th components of the sub-vector $\mathbf{W}_j$ and $\mathbf{V}_j$ as follows;

$$W_{j,n} \equiv \sum_{l=0}^{L-1} h_l V_{j-1,2n+1-l} \tag{9}$$

$$V_{j,n} \equiv \sum_{l=0}^{L-1} g_l V_{j-1,2n+1-l} \quad (n = 0, 1, 2, \cdots, N_j - 1) \tag{10}$$

Therefore, the DWT can be recognized as a decomposition of a time series **X** into coefficients that can be associated with different scales and times.

2.2 DWT spectrum

According to the decomposition described in the previous section, the power spectrum of DWT can be defined as follows;

$$P_W(\tau_j) \equiv \frac{1}{N}\left\|\mathbf{W}_j\right\|^2 \tag{11}$$

$$\sum_{j=1}^{J} P_W(\tau_j) = \frac{1}{N}\left\|\mathbf{W}_j\right\|^2 = \frac{1}{N}\left\|\mathbf{X}\right\|^2 - \overline{\mathbf{X}} = \sigma_{\mathbf{X}}^2 \tag{12}$$

where $\sigma_{\mathbf{X}}^2$ denotes the sample variance.

2.3 Wavelet Filters

The filter $\{h_{j,l}\}$ and $\{g_{j,l}\}$ are the band pass filters with pass band given by $1/\Delta t 2^{j+1} \le f \le 1/\Delta t 2^{j}$ and $0 \le f \le 1/\Delta t 2^{j+1}$ (Hz), respectively. Meanwhile, scaling filters as well as wavelet filters must satisfy the three basic properties, which are

$$\sum_{l=0}^{L-1} g_l = \sqrt{2}, \quad \sum_{l=0}^{L-1} g_l^2 = 1 \tag{13}$$

$$\sum_{l=0}^{L-1} g_l g_{l+2n} \equiv \sum_{l=-\infty}^{\infty} g_l g_{l+2n} = 0 \tag{14}$$

Additional to the above conditions, Daubechies (1988) specified vanishing moment conditions on the wavelet function and led to obtain the scaling filters which have minimum delay. In this study Daubechies filter of width 8 is used for the DWT. Actual value and the shape are expressed on Figure 1 and Table 1.

Table 1 Daubechies wavelet and scaling filters of width 8.

l	Wavelet filter (h_l)	Scaling filter (g_l)
0	-0.010597401785	0.230377813309
1	-0.032883011667	0.714846570553
2	0.030841381836	0.630880767930
3	0.187034811719	-0.027983769417
4	-0.027983769417	-0.187034811719
5	-0.630880767930	0.030841381836
6	0.714846570553	0.032883011667
7	-0.230377813309	-0.010597401785

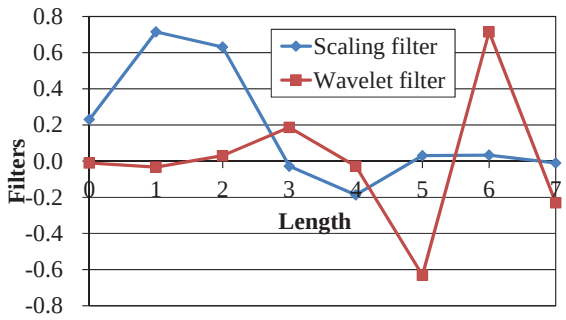

Figure 1 Daubechies wavelet and scaling filters of width 8.

3. DISCRETE WAVELET PACKET TRANSFORM

As shown in the previous section, the DWT decomposes the frequency interval $0 \le f \le 1/2\Delta t$ into adjacent individual intervals. The DWPT can be regarded as one of the extension of orthonormal transformation and decomposes the frequency into 2^j equal and individual intervals at the level j. The actual procedure of the calculation is readily

expressed using very simple modification of the pyramid algorithm (Percival and Walden 2000).

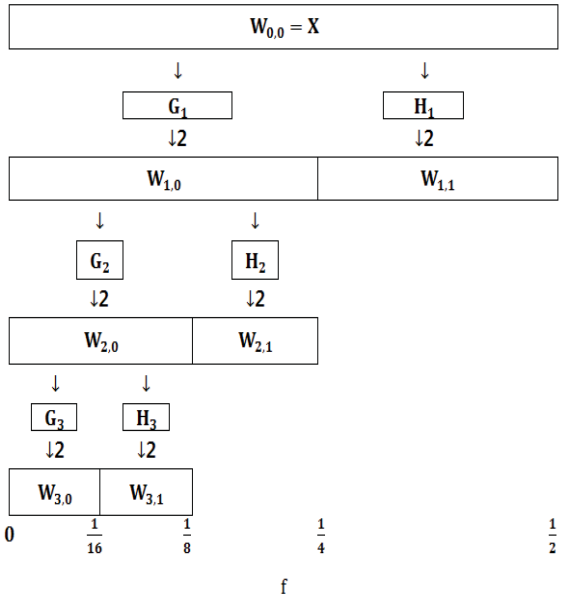

Figure 2 Flow diagram illustrating the analysis of $\mathbf{X}$ into $\mathbf{W}_{3,0}$, $\mathbf{W}_{3,1}$, $\mathbf{W}_{2,1}$ and $\mathbf{W}_{1,1}$ which is identical to partial DWT of level 3.

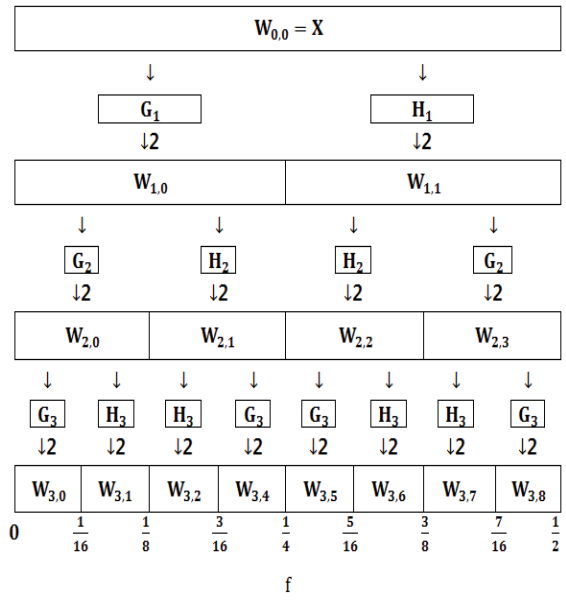

Figure 3 Flow diagram illustrating the analysis of $\mathbf{X}$ into $\mathbf{W}_{3,0}$, $\mathbf{W}_{3,1}$, …, $\mathbf{W}_{3,8}$ using DWPT of level 3.

Figure 2 shows the flow diagram of the DWT pyramid algorithm described in the previous section, where the level J_0=3. The starting point is defined as $\mathbf{W}_{0,0} = \mathbf{V}_0 = \mathbf{X}$ and other nodes represent $\mathbf{W}_{1,1} = \mathbf{W}_1$, $\mathbf{W}_{2,1} = \mathbf{W}_2$, $\mathbf{W}_{3,1} = \mathbf{W}_3$ and $\mathbf{W}_{3,0} = \mathbf{V}_3$. G_j and H_j represent filtering with use of the wavelet filter $\{h_l\}$ and the scaling filter $\{g_l\}$ at the level j. The '$\downarrow 2$' denotes the "down-sampling by two". The fractions at the lowest level denote the corresponding frequencies with Δt=1.

By using the low-pass and high-pass filters, the process of the decomposition of time series $\mathbf{X}$ is simply illustrated in the figure. It should be noted, however, that the nominal frequency intervals for these four nodes are not constant.

Figure 3 shows the flow diagram of the DWPT. It can be seen that the frequency intervals are constant and the resolution is improved by the iterative use of the low-pass and high-pass filters. This is the reason for the introduction of the DWPT.

4. FULL SCALE EXPERIMENT

The full scale ship experiment was carried out on January 25th 2012 using the training ship Shioji-maru of Tokyo University of Marine Science and Technology. A photo and principal particulars of the ship are shown in Figure 4 and Table 2. The location of the experimental area was off Sunosaki cape in Chiba Prefecture, Japan.

Figure 4 The training ship Shioji-maru.

Table 2 Principal particulars of the ship.

Length (P.P.)	46.00(m)
Breadth (M_{LD})	10.00(m)

Depth (M_{LD})	6.10(m)
Draught (M_{LD})	2.65(m)
Displacement	659.4(t)

Figure 5 shows the trajectory of the T.S. Shioji-maru during the experiment. The blue arrow denotes the main direction of waves. In order to measure changes in ship motions with respect to the encounter angle of waves, the angle of CPP was set to 10.5 degrees during 90 minute manoeuvres involving straight sections and changes in course.

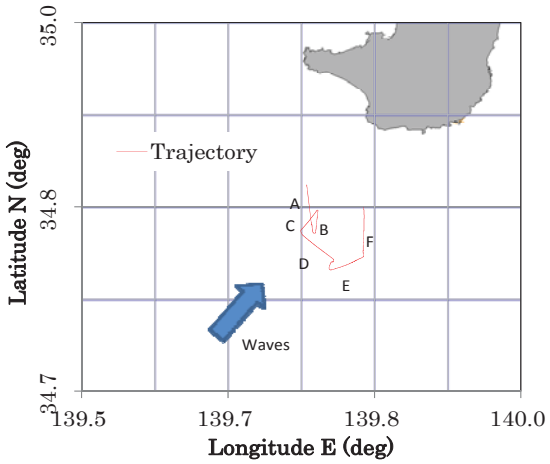

Figure 5 The experimental area at the south of Sunosaki cape and the ship trajectory.

Table 3 Ship course and the sea conditions.

Run	Ship course (deg)	Ship speed (knot)	Wind direction (deg)	Wind speed (m/s)
A	180	8.3	257	10.4
B	0	10.4	260	11.5
C	240	7.3	265	11.5
D	120	9.9	258	11.8
E	60	10.7	267	11.5
F	0	10.5	267	11.4

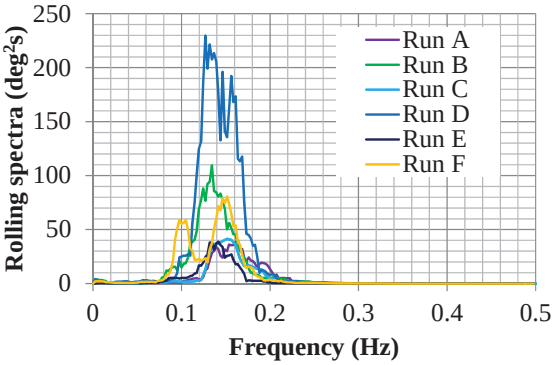

Figure 6 Power spectra of rolling motions.

Table 3 shows the courses and the mean speed-through-water of the ship, and true wind directions and the speeds are also summarized. During the experiment, observed wind waves were: height 1.0-1.5m, period 6-7 sec, direction 200-240 degrees, and swells were: height 2-3m, period 8-10 sec, direction 200 degrees. Note that the wave conditions listed in Table 3 can be recognized rather severe, since the ship is not a large ship (Table 2).

Figure 6 shows power spectra of the rolling motion calculated by FFT. It should be noted that the spectra “D” and “E” show the large difference in spite of adjacent run, because there is a large course alteration between them.

In this paper, the rolling time series between “D” and “E” are analysed in order to concentrate our attention on the non-stationarity. The trajectory is indicated in Figure 7 and seems to be a zigzag line because of beam seas. The analysed time span is 102.4s.

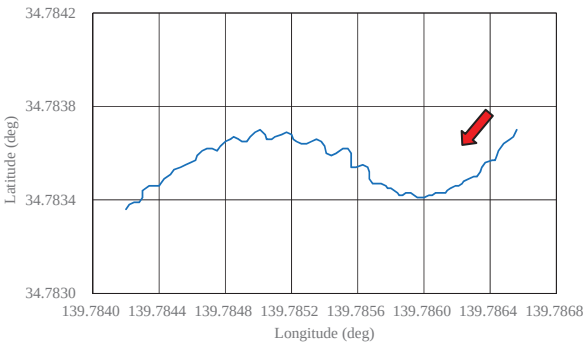

Figure 7 Time series of rolling motion. The red arrow denotes the starting side.

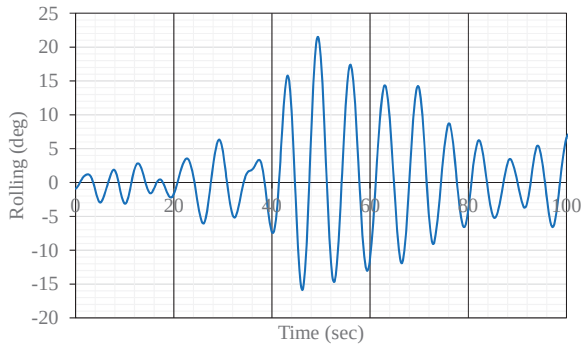

Figure 8 Time series of rolling motion.

Figure 8 shows the time history of the rolling motion that was analysed. The sampling time is 0.1s and 1024 observations are included. It can be seen that the ship was experienced rather large amplitude rolling during the beam seas condition (40 to 70 sec).

Figure 9 shows the power spectrum analysed by DFT ignoring the fact that the data is non-stationary. The peak frequency is 0.152Hz and coincides with the rolling natural frequency of the ship.

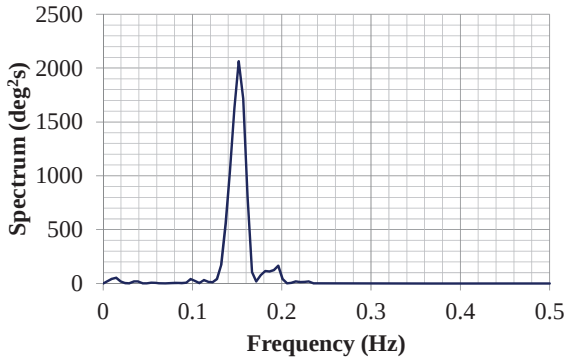

Figure 9 Power spectrum of rolling motion.

5. TVVAR MODEL ANALYSIS

TVVAR modelling was originally applied to analysis of the earthquake data (Kitagawa & Gersch, 1985, Jiang & Kitagawa, 1993). Generally, TVVAR models are transformed into state-space models, and the time varying coefficients can be evaluated by using the Kalman filter algorithm. Using the estimated time varying coefficients, the instantaneous power spectra of ship motions can be estimated at every moment.

Figure 10 shows the time evolution of the estimated auto spectra of roll angle from 0s to 100s. In this figure, the curves denote estimated instantaneous auto spectra and are superimposed on time axis with time increasing. In this estimation, the model order was set to 9. Comparing with the ship trajectory illustrated in Figure 8, it is found that the rolling motion becomes larger during the beam seas and the peak frequency coincides well with figure 9. On the other hand, it can be seen the "development period" at the beginning of analysis (from 0s to 30s). This comes from the initial conditions of the Kalman filter and means that the TVVAR modelling analysis requires a certain length of time series. In addition to this, some problems were pointed out in the TVVAR modelling. The maximum likelihood method for determination of the trade-off parameter, which is the ratio of the observation noise and the system noise of Kalman filter, cannot be applied to the real-time algorithm.

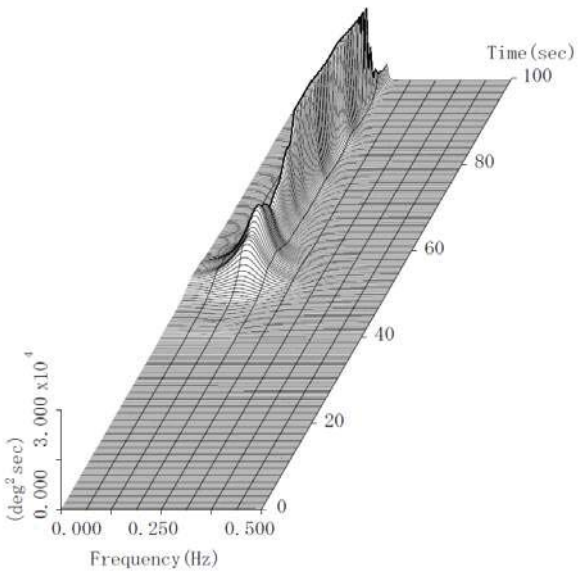

Figure 10 Instantaneous auto spectrum of rolling motions estimated by TVVAR modelling.

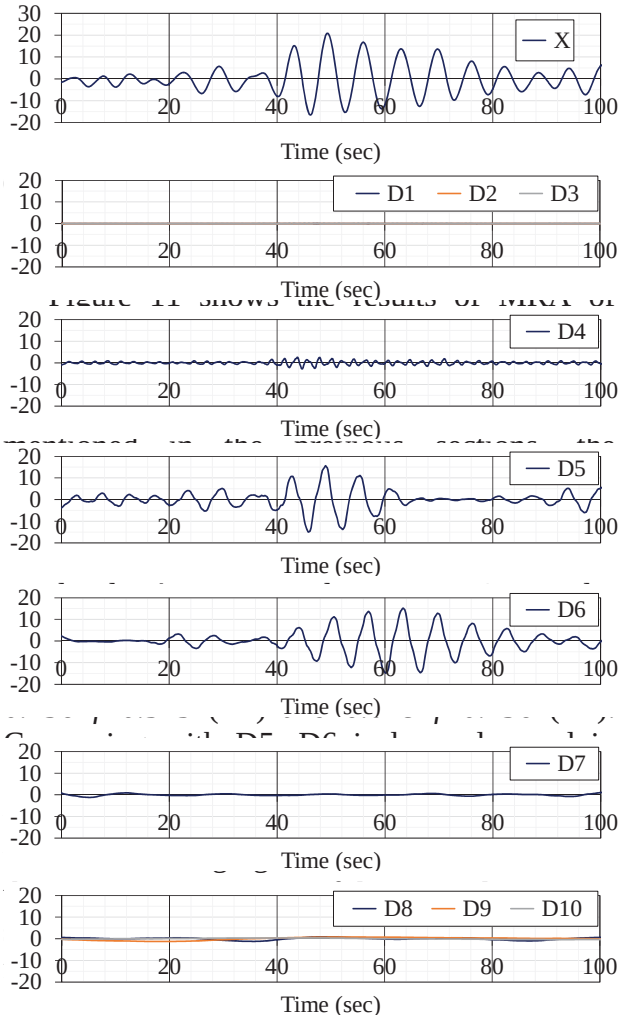

Figure 11 Results of multi-resolution analysis of rolling motion time series.

Figure 12 shows the time evolution of the estimated DWT spectrum from 0s to 100s. The DWT spectrum is expressed by discrete value, therefore, the graph is indicated in a stepwise shape. In this figure, levels of the DWT can be seen from 4 to 10 because frequencies of the smaller level are higher than 0.5Hz. The wide band on the centre (around 0.25Hz) denotes the power of D5 and the neighbouring left band denotes the power of D6. Similar to Figure 11, it can be observed that D6 is less advanced in development and has long duration, comparing with D5. This conclude that the DWT analysis is very useful for frequency/time analysis.

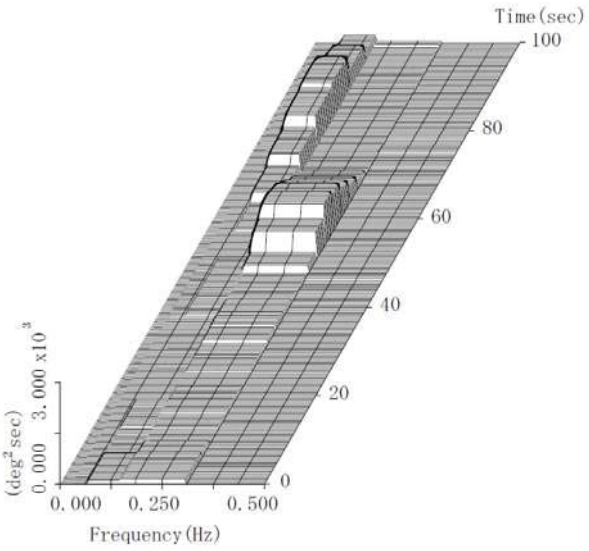

Figure 12 Results of DWT analysis of rolling motion.

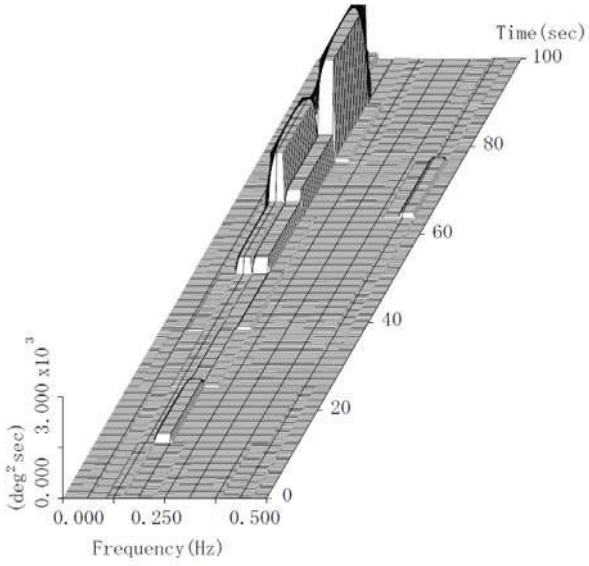

Figure 13 Results of DWPT analysis of level 7 of rolling motion.

Figure 13 shows the time evolution of the estimated DWPT spectrum of level 7. As described in the section 3, the frequency intervals are unified and the resolution is improved than DWT analysis. The peaks of the spectra were sharpened in the frequency-wise. Furthermore, the shape of spectra agree well

with the results of DFT and TVVAR modelling. However, it can be also seen that the resolution in time is worsened in comparison with Figure 12. Therefore, selection of the suitable level is very important for the effective DWPT analysis.

7. CONCULSIONS

The DWT and DWPT were applied to non-stationary ship motion data. Comparing to the spectra of DFT and the TVVAR modelling, the results obtained in this report can be summarized below:

(1) The MRA can be applied to analyses of non-stationary time series. It is very useful to extract the motion that has a certain frequency band.

(2) The locations of peaks of DWT spectra represent the time evolution of the rolling motion and agree well with the peaks of the spectra estimated by TVVAR modelling.

(3) Selecting a suitable level, the spectra estimated by the DWPT analysis agree well with the results of DFT and TVVAR modelling.

This concludes that the DWT and DWPT are powerful tools for analysing non-stationary ship motion data.

8. ACKNOWLEDMENTS

This work is partly supported by Grant-in-Aid for Scientific Research of the Japan Society for Promotion of Science (No. 26420822). The author expresses sincere gratitude to the above organizations and thanks the captain and crew of the training ship Shioji-maru.

9. REFERENCES

Daubechies, I., 1988, “Orthonormal Bases of Compactly Supported Wavelets”, Communications on Pure and Applied Mathematics, 41, pp.909-996.

Iseki, T., Terada, D, 2002, “Study on Real-time Estimation of the Ship Motion Cross Spectra,” Journal of Marine Science and Technology, Vol.7, pp.157-163.

Iseki, T., 2006, “Instantaneous Spectral Analysis of Non-stationary Ship Motion Data”, Proceedings of the 25th International Conference on Offshore Mechanics and Arctic Engineering, OMAE2006-92197.

Jiang, X. Q., Kitagawa, G., 1993, “A Time Varying Coefficient Vector AR Modeling of Non-stationary Covariance Time Series,” Signal Processing, 33, No.3, p.315-331.

Kang, B. and Iseki, T., 2013, “Application of Discrete Wavelet Transform to Ship Motion Analysis”, Proceedings of Asia Navigation Conference 2013(ANC2013), pp.20-26.

Kitagawa, G., Gersch, W., 1985, “A Smoothness Priors Time-Varying AR Coefficient Modeling of Nonstationary Covariance Time Series,” IEEE Trans. Automatic Control, AC-30, No.1, January, pp.48-56.

Mallat, S.G., 1989, “A Theory for Multiresolution Signal Decomposition”, The Wavelet Representation, IEEE Trans. Pattern Analysis and Machine Intelligence, 11, p.674-93.

Percival, D.B. and Walden, A.T., 2000, “Wavelet Methods for Time Series Analysis”, Cambridge Series in Statistical and Probabilistic Mathematics, Cambridge University press.

A Study on the Effect of Parametric Rolling on Added Resistance in Regular Head Seas

Jiang Lu, *China Ship Scientific Research Center, Wuxi, China*lujiang1980@aliyun.com

Min Gu, *China Ship Scientific Research Center, Wuxi, China* gumin702@163.com

Naoya Umeda, *Osaka University, Osaka, Japan,* umeda@naoe.eng.osaka-u.ac.jp

ABSTRACT

Both parametric rolling and added resistance in head seas are hot topics in ship hydrodynamics. Parametric rolling with half the encounter frequency is not taken into account in the calculation of added resistance in regular head seas. In order to study the correlation between parametric rolling and added resistance, firstly, a formula of added resistance in regular head seas with parametric rolling taken into account based on Maruo theory is developed to investigate the effect of parametric rolling on added resistance in regular head seas. Secondly, partially restrained free running experiments with and without roll motions are carried out respectively to investigate the effects of parametric rolling on added resistance in regular head seas. The results of experiments and simulations using the C11 containership show that added resistance is affected by parametric rolling, and the results of experiments also show that heave and pitch motions are distinctly affected by parametric rolling.

Keywords: *Parametric rolling, added resistance, heave, pitch, Maruo theory*

1. INTRODUCTION

The second generation intact stability criteria are under development at the International Maritime Organization (IMO) which covers five stability failure modes including parametric rolling as one of roll restoring variation problems, as a supplement to the existing prescriptive criteria (IMO SDC1, 2014).

In case of following waves, the encounter frequency is much lower than the natural frequencies of heave and pitch so that the coupling with dynamic heave and pitch is not important. In addition, added resistance due to waves is generally small in following waves. Thus several successful predictions of parametric rolling in following waves were reported (e.g. Munif and Umeda, 2000). In particular, clear experimental records of capsize due to parametric rolling in following waves were published by one of the present authors (Umeda et al., 1995).

In case of head seas, however, prediction of parametric rolling is not so easy because coupling with dynamic heave and pitch is significant. In addition, the added resistance and the resulting speed loss cannot be simply ignored. So far, the effect of dynamic heave and pitch motions on parametric rolling was investigated by many researchers and it was well established. The existing research revealed that restoring arm variation depending on dynamic heave and pitch motions is essential for accurately predicting parametric roll in head waves (Taguchi et al., 2006). However, these theoretical works do not deal with the effect of added resistance on parametric rolling.

Umeda et al (2008) and Umeda&Francescutto (2008) executed numerical simulations of parametric rolling in regular and irregular head seas with added resistance taken into account, but their hydrodynamic prediction method for added resistance is different from that for restoring variation. Two of the present authors (Lu et al., 2011a) executed numerical simulation of parametric rolling in head seas with added resistance taken into account, in which both the restoring variation and the Kochin function for added resistance are calculated by a strip theory.

Added resistance in waves is mainly caused by energy dissipation when a ship generates radiation waves and diffraction waves on the ship hull (Kashiwagi et al., 2010). Maruo obtained an well-established formula for added resistance in waves, within linear potential theory, based on the principle of momentum and energy conservation (Maruo, 1963). In linear ship dynamics, the frequency of ship oscillations is equal to encounter frequency, without the consideration of roll, sway and yaw motions in longitudinal waves. Hosoda (1973) and Maruo&Iwase (1980) extended these methods to oblique waves with roll, sway and yaw taken into account. Parametric rolling could occur in head seas with half the encounter frequency, and occasionally the amplitude of parametric rolling is more than 40 degrees. All calculation methods of added resistance mentioned above seem not to include wave radiations due to parametric rolling in head seas, and the effect of parametric rolling on added resistance cannot be discussed. Two of the present authors (Lu et al., 2011b)extended Maruo's theory to study the effect of parametric rolling on added resistance in regular head seas, while the effect of parametric rolling on heave and pitch motions was ignored and the experimental studies with and without parametric rolling were not conducted.

Therefore, the authors attempted to use the extended formula based on Maruo's theory for added resistance with parametric rolling taken into account to study the effect of parametric rolling on added resistance in regular head seas. Further, the model experiments were conducted to measure roll, heave, pitch motions and wave force in longitudinal direction with and without parametric rolling in regular head seas by a new experimental device.

2. THEORETICAL METHOD

The following formula based on Maruo's theory (Lu et al, 2011b) is used to calculate added resistance in regular head seas with parametric rolling taken into account.

$$\begin{aligned}\bar{R}=&\frac{\rho}{8\pi}\left[\int_{-\pi/2}^{-\alpha_0}+\int_{\pi/2}^{\alpha_0}-\int_{\pi/2}^{3\pi/2}\right]\times\left|H(k_1,\alpha)\right|^2\frac{k_1(k_1\cos\alpha-K\cos\chi)}{\sqrt{1-4\Omega\cos\alpha}}d\theta\\&+\frac{\rho}{8\pi}\left[\int_{\alpha_0}^{2\pi-\alpha_0}\right]\times\left|H(k_2,\alpha)\right|^2\frac{k_2(k_2\cos\alpha-K\cos\chi)}{\sqrt{1-4\Omega\cos\alpha}}d\alpha\\&+\frac{\rho}{8\pi}\left[\int_{-\pi/2}^{-\alpha_0'}+\int_{\pi/2}^{\alpha_0'}-\int_{\pi/2}^{3\pi/2}\right]\times\left|H(k_1',\alpha')\right|^2\frac{k_1'(k_1'\cos\alpha'-\frac{1}{2}K\cos\chi)}{\sqrt{1-4\Omega\cos\alpha'}}d\theta\\&+\frac{\rho}{8\pi}\left[\int_{\alpha_0'}^{2\pi-\alpha_0'}\right]\times\left|H(k_2',\alpha')\right|^2\frac{k_2'(k_2'\cos\alpha'-\frac{1}{2}K\cos\chi)}{\sqrt{1-4\Omega\cos\alpha'}}d\alpha'\\&\frac{E_1}{(\frac{\omega_e}{K})}\cos\chi\frac{E_2}{(\frac{\omega_e}{K})}\cos\chi\frac{E_3}{(\frac{\omega_e}{K})}\cos\chi\end{aligned}\tag{1}$$

where:

$$\alpha_0=\begin{cases}0 & (\Omega\le 1/4)\\ \cos^{-1}(\frac{1}{4\Omega}) & (\Omega>1/4)\end{cases};\quad \alpha_0'=\begin{cases}0 & (\Omega'\le 1/4)\\ \cos^{-1}(\frac{1}{4\Omega'}) & (\Omega'>1/4)\end{cases}\tag{2}$$

U is ship's forward velocity, $\omega_0$is wave circular frequency, K is wave number, χ is the angle of wave incidence, ρ is the water density and $\chi=\pi$ corresponds to the heading sea. Here we define that the encounter frequency is $\omega_e=\omega_0-kU\cos\chi$, the encounter period is T_e, the wavelength is λ for incident wave, diffraction wave and radiation waves due to heave, pitch and surge motions. At the same time, we also define that the frequency isω_{e2} =1/2ω_e, the period is T_{e2}, the wavelength is$\lambda_2$for radiation waves due to parametric roll, sway and yaw motions.

The added resistance can be obtained by averaging forces within the duration that is double the encounter period. According to energy dissipation by viscous roll damping force, the follow equations can be obtained:

$$\begin{aligned} E_1 &= 0 \\ E_2 &= 0 \\ E_3 &= \int_0^{2T_e} (B_{44\phi_a}\dot{\phi}_{roll})\dot{\phi}_{roll}\, dt \end{aligned} \quad (3)$$

where ϕ_a is the amplitude of parametric rolling, $B_{44}\dot{\phi}$ is the viscous roll damping force, $\dot{\phi}_{roll}$ is the angular velocity of parametric rolling. E_3 can be obtained by following formula (Katayama et al.,2010):

$$E_3 = \pi B_{44\phi_a}\phi_a^2(\frac{1}{2}\omega_e) \quad (4)$$

Both$k_1$wave and$k_2$wave are used for incident wave, diffraction wave and radiation waves due to heave, pitch and surge motions.

$$k_j = \frac{K_0\cdot(1-2\Omega\cos\alpha \pm \sqrt{1-4\Omega\cos\alpha})}{2\cos^2\alpha}$$
$$(+ for\ j=1, - for\ j=2, \Omega = \frac{\omega_e U}{g}, K = \frac{\omega_0^2}{g}, K_0 = \frac{g}{U^2}) \quad (5)$$

Both k_1'waveand k_2'wavesare used for radiation wavesdue to parametric roll, sway and yaw motions.

$$k_j' = \frac{K_0\cdot(1-2\Omega'\cos\alpha \pm \sqrt{1-4\Omega'\cos\alpha})}{2\cos^2\alpha}$$
$$(+ for\ j=1, - for\ j=2, \Omega' = \frac{\omega_{e2}U}{g} = \frac{1}{2}\frac{\omega_e U}{g} = \frac{1}{2}\Omega, K_0 = \frac{g}{U^2}) \quad (6)$$

The Kochin function can be calculated by formula (7), if singularity distributions ($\mu(x)$ and $\sigma(x)$) along the centre line of ship submerged with the depth of $z(x)$ are properly provided.

$$\begin{aligned} H(k_i,\alpha) = &\int_L \sigma(x) e^{-k_i z(x)} e^{ik_i x\cos\alpha}\, dx \\ &+ \int_L i\mu(x) e^{-k_i' z(x)} k_i' \sin\alpha\, e^{ik_i' x\cos\alpha}\, dx \end{aligned} \quad (7)$$

Based on the comparisons of calculated added resistance by different methods of source distribution $\sigma(x)$ for the modified Wigley model(Lu et al., 2011b), it can be concluded that Maruo and Ishii's method (Maruo and Ishii,1976)is the most appropriate for the region where parametric rolling could appear. Maruo and Ishii's formula can be described with the two-dimensional Kochin function of heave as follows:

$$\sigma(x) = -H_2^+(x)\times(i\omega_e - U\frac{\partial}{\partial x})(Z_G - x\Theta - \zeta_w) + H_2^+(x)\times U\frac{\dot{B}(x)}{B(x)}(Z_G - x\Theta - \zeta_w);\ z=0 \quad (8)$$

where $\sigma(x)$ is the source distribution, $Z_G e^{i\omega_e t}$ is the heaving, $\Theta e^{i\omega_e t}$ is the pitching, $\zeta_W e^{i\omega_e t}$ is the wave elevation , $H_2^+(x)$ is the two-dimensional Kochin function in heave, $B(x)$ is the ship breadth at x section and $\dot{B}(x) = \partial B(x)/\partial x$.

For calculating doublet distribution $\mu(x)$, Maruo and Iwase's method (Maruo and Iwase,1980)is used, which can be described with the two-dimensional Kochin function of sway($H_1^+(x)$) as follows:

$$\mu(x) = \frac{-1}{2k_e'}H_1^+(x)\times\{\frac{1}{B(x)}(\frac{\partial}{\partial t} - U\frac{\partial}{\partial x})[B(x)(Y_G - x\psi + |l_W|\varphi)] - V_W\} \quad (9)$$

where $Y_G e^{i\frac{1}{2}\omega_e t}$ is the swaying, $\psi_0 e^{i\frac{1}{2}\omega_e t}$ is the yawing, $\varphi_0 e^{i\frac{1}{2}\omega_e t}$ is the rolling and V_W is the wave particle velocity in y direction.

In this paper, however, the effect of only parametric rolling in head seas is investigated during numerical calculation. The doublet distribution $\mu(x)$ can be rewritten as follow:

$$\mu(x) = \frac{-1}{2k_e'}H_1^+(x)\times[i(\frac{1}{2}\omega_e)|l_W|\varphi_0 - U\frac{\dot{B}(x)}{B(x)}|l_W|\varphi_0] \quad (10)$$

3. EXPERIMENTS

The partially restrained experiment with a 1/65.5 scaled model of the post Panamax C11

class containership were conducted in the seakeeping basin (length: 69m, breadth: 46m, depth: 4m) of China Ship Scientific Research Center, which is equipped with flap wave makers at the two adjacent sides of the basin.

The partially restrained ship model was towed by the towing carriage in regular head seas and a newly designed equipment was used to measure ship motions including roll, pitch and heave motions and exciting wave moment/force including roll moment, yaw moment, sway force and surge force. Roll and pitch motions were measured by potentiometer sensor. Heave motion was measured by displacement sensor. Roll moment, yaw moment, sway force and surge force were measured by four sensors based on electromotive strain gauge.

The principal particulars and body plan of the C11 class containership are shown in Table1 and Fig.1, respectively. The ship model in partially restrained experiment is shown in Fig.2.

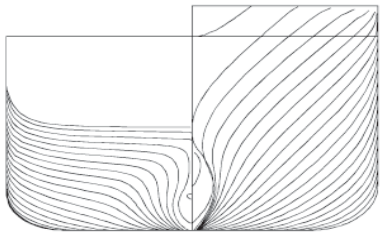

- Figure 1 Lines of C11 containership

Figure 2The ship model in partially restrained experiment

Table 1 Principal particulars of the C11 containership

Items	Ship	Model
Length:L	262.0m	4.000m
Draft:T	11.5m	0.176m
Breadth:B	40.0m	0.611m
Depth:D	24.45m	0.373m
Displ.:W	67508ton	240.2kg
C_B	0.560	0.560
GM	1.928m	0.029m
T_φ	24.68s	3.05s
K_{YY}	0.24L	0.24L

4. RESULTS AND DISCUSSION

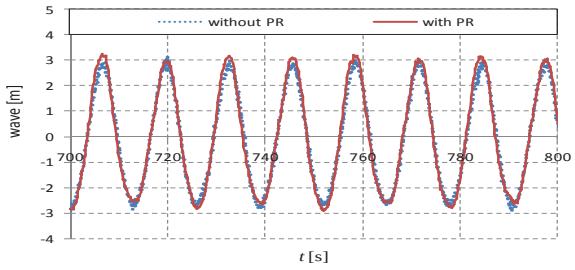

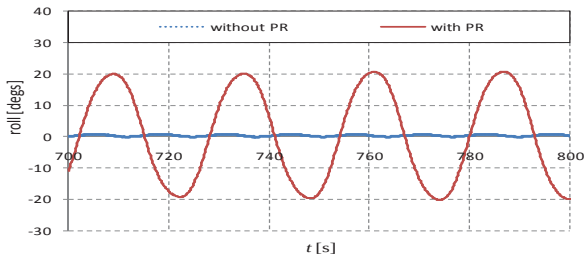

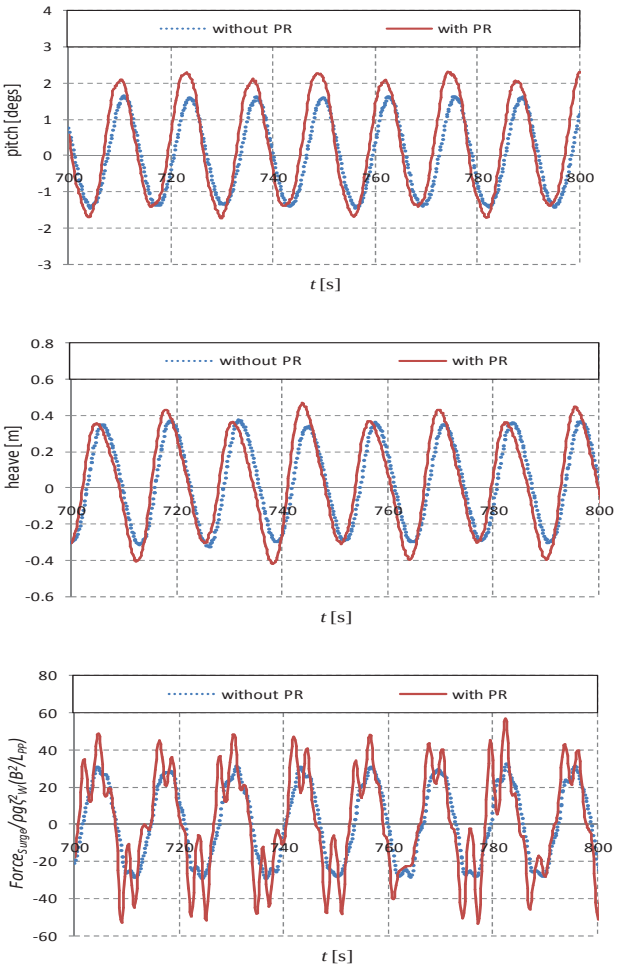

- Figure 3 Comparisons of wave, roll, pitch, heave and surge forcein time series between with and without parametric rolling in experiments, with Fn =0.0, H/λ=0.02, λ/Lpp=1.0 and χ=180 degs.

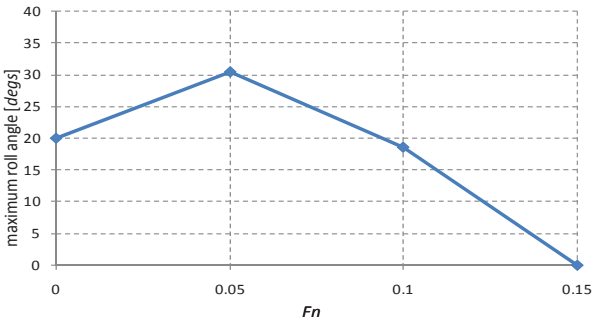

Figure 4 Parametric rolling in experiment as The function of Froude number with λ/L_{pp} =1.0, H/λ=0.02 and χ=180degs.

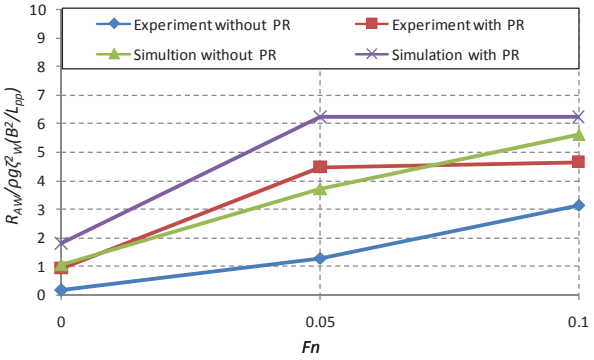

- Figure 5Added resistance with and without parametric rolling in experiments and simulations as the function of the Froude number with λ/L_{pp}=1.0,H/λ=0.02 and χ=180degs.

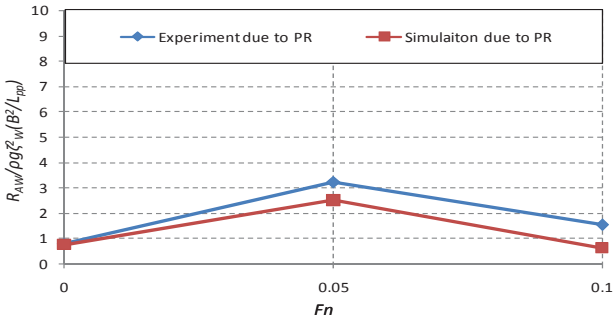

Figure 6The component of added resistance resulted from parametric rolling in experiments and simulations as the function of the Froude number with λ/L_{pp}=1.0,H/λ=0.02 and χ=180degs.

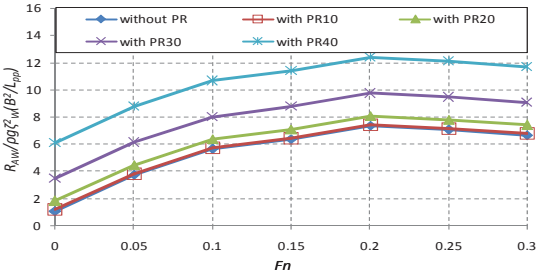

- Figure 7 Calculated added resistance with different amplitudes of parametric rolling as the function of the Froude number with λ/L_{pp}=1.0,H/λ=0.02 and χ=180degs.

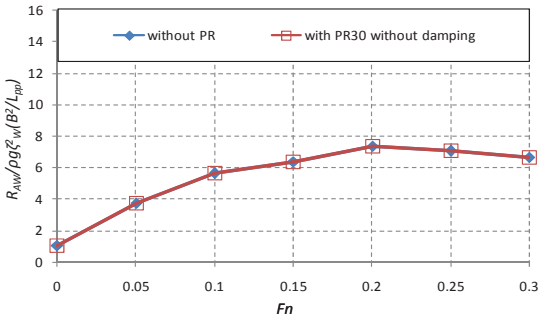

- Figure 8 Calculated added resistance with parametric rolling and without roll damping force, as the function of the Froude number with λ/L_{pp}=1.0,H/λ=0.02 and χ=180degs.

We compare heave, pitch, roll motions and surge force containing resistance with and without roll motion in experiment. An example of time series is shown in Fig. 3. When parametric rolling occurs with amplitudes of 20 degrees, heave and pitch motions are affected by parametric rolling and their large and small amplitudes alternatively appear. This phenomenon seems like “subharmonic pitch” and “subharmonic heave” (Neves et al., 2009; Lu et al., 2013, 2014). The phase difference of heave and pitch motion are also small changed as shown in Fig.3. This indicates that both the amplitude and phase difference of heave and pitch motions are distinctly affected by parametric rolling. The surge force is also affected when parametric rolling occurs with amplitudes of 20 degrees as shown in Fig.3.Heave and pitch motions are main cause of added resistance in waves. Therefore added resistance in waves could be affected by parametric rolling. Here we only show the experimental results of time series at zero speed, because the towing carriage has mechanical vibrations with forward speed.

Parametric rolling in regular head seas, as a function of the Froude number, was measured by the partially restrained experiment of C11 containership as shown in Fig.4, and the values of parametric rolling in experiments are used during the numerical simulations of added resistance in waves. The added resistance in experiments is obtained by subtracting the resistance in calm water from the averaged surge force. Both the experiment and numerical simulation show that the difference of added resistance with and without parametric rolling is not negligible, as shown in Fig.5. The component of added resistance resulted from parametric rolling in experiments and simulations is shown in Fig. 6. Although the calculated results are general larger than experimental results, the tendency of the effect of parametric rolling on added resistance in waves is the same. Here the viscous roll damping coefficient was estimated by roll decay test of the ship model.

In order to investigate the reason, the added resistance was calculated without parametric rolling and with different amplitudes of parametric rolling, as the function of the Froude number. The results shown in Fig.7 indicate that the effect of parametric rolling on added resistance in regular head seas becomes larger as the amplitude of parametric rolling becomes larger. The calculated added resistance with parametric rolling and without viscous roll damping force, as a function of the Froude number, is shown in Fig.8. The effect of parametric rolling on added resistance in regular head seas within a potential flow theory is very small, and it supports Maruo and Iwase’s(1980) conclusion in oblique waves, that is to say, the effect of rolling on added resistance is generally small. This means that the major effect of parametric rolling is viscous roll damping. It is noted here the effect of large parametric rolling on heave and pitch motions in simulations is ignored. Heave and pitch motion are main cause of added resistance in waves. Both the amplitude and phase difference of heave and pitch motions are distinctly affected by parametric rolling as show in Fig.3, which could be one of reasons why the added resistance in experiments is smaller than that in simulations as shown in Fig 6.

5. CONCLUSIONS

As a result of experimental and numerical study on the effect of parametric rolling on added resistance in regular head seas for a containership, the following remarks are noted:

1) An extended formula based on Maruo theory for added resistance in head seas with parametric rolling taken into account can be used to study the effect of parametric rolling on added resistance in regular head seas.

2) The effect of parametric rolling on added resistance in regular head seas mainly is due to viscous roll damping and it becomes larger as the amplitude of parametric rolling becomes larger.

Future research is desirable to validate the effect of heave and pitch motion on added resistance while parametric rolling occurs.

6. ACKNOWLEDGEMENTS

Part of this research was once supported by China Scholarship Council [No.2008606031] for the first author's visit to Osaka University. Prof. M. Kashiwagi from Osaka University provided the authors with his useful advice on the theoretical calculation of added resistance in waves. The research is supported by Ministry of Industry and Information Technology of China (No. [2012] 533). The authors sincerely thank the above organizations.

7. REFERENCES

Hosoda, R., 1973, "The Added Resistance in Oblique Waves", Journal of the Society of Naval Architects of Japan, Vol.133,pp.7-22.

Kashiwagi, M., Ikeda, T. and Sasagawa, T., 2010, "Effect of Forward Speed of a ship on Added Resistance in waves",International Journal of Offshore and Polar Engineering ",Vol.20(2),pp.1-8.

Katayama, T., Taniguchi, T., and Umeda, N., 2010, "An Experiment Study on Parametric Rolling of a High Speed Trimaran in Head Seas",Journal of the Society of Naval Architects of Japan, Vol. 10, pp.57-63.

Lu, J., Umeda, N. and Ma, K., 2011a. "Predicting parametric rolling in irregular head seas with added resistance taken into account",Journal of Marine Science and Technology,Vol.16, pp.462-471.

Lu, J., Umeda, N. and Ma, K., 2011b. "Theoretical Study on the Effect of Parametric Rolling on Added Resistance in Regular Head Seas",Journal of Marine Science and Technology, Vol.16,pp.283-293.

Lu, J., Min, G. and Umeda, N., 2013,"A Study on the Effect of Parametric Rolling on Heave and Pitch Motions in Head Seas",Proceedings 13th International Ship Stability Workshop, pp.185-191.

Lu, J., Min, G. and Umeda, N., 2014,"Experimental and Numerical Study on Predicting Method of Parametric Rolling in Regular Head Seas",Proceedings 14th International Ship Stability Workshop, pp.117-125.

Maruo, H., 1963. "Resistance in Waves", Chap.5 in Researches on Seakeeping Qualities of Ships in Japan, Soc. Nav. Arch. Japan 60th Anniv. Ser., No. 8, pp.67-102.

Maruo, H. and Ishii, T.,1976, "Calculation of Added Resistance in Head Sea Waves by Means of a Simplified Formula", Journal of the Society of Naval Architects of Japan, Vol.140,pp.136-141.

Maruo. H. and Iwase,K., 1980, "Calculation of Added Resistance in oblique Waves", Journal of the Society of Naval Architects of Japan, Vol.147,pp.79-84(in Japanese).

Munif, A. and Umeda, N. 2000,"Modeling Extreme Roll Motions and Capsizing of a

Moderate-Speed Ship in Astern Waves", Journal of the Society of Naval Architects of Japan, Vol. 187, pp. 405-408.

Neves, Ma.A.S., Vivanco, J.E.M. and Rodriguez, C.A., 2009,"Nonlinear Dynamics on Parametric Rolling of Ship in Head Seas", Proceedings 10th STAB, pp.509-520

Taguchi, H., Ishida, S., Sawada, H. and Minami, M., 2006, "Model Experiment on Parametric Rolling of a Post-Panamax Containership in Head Waves",Proceedings 9th STAB, pp.147-156.

Umeda, N., Hamamoto M., Takaishi, Y., Chiba, Y., Matsuda, A., Sera W. , Suzuki S. , Spyrou K. and Watanabe, K., 1995, " Model Experiments of Ship Capsize in Astern Seas", Journal of the Society of Naval Architects of Japan, Vol.177,pp.207-217.

Umeda, N., Hashimoto, H., Frederick, S., Nakamura, S., Seyed, H.S.H., Matsuda, A. and Pablo, C. 2008,"Comparison Study on Numerical Prediction Techniques for Parametric Roll", Proceedings of the 27th Symposium on Naval Hydrodynamics, Seoul,pp.5-10.

Umeda, N.and Francescutto, A., 2008, "Performance-Based Ship Operation",Proc 2nd International Workshop on Risk-Based Approaches in Maritime Industry,2.2.1-2.2.9.

Session 10.1 – 2nd GENERATION INTACT STABILITY

A Study on Roll Damping Time Domain Estimation for Non Periodic Motion

Investigation of the 2nd Generation of Intact Stability Criteria in Parametric Rolling and Pure Loss of Stability

Requirements for Computational Methods to be Used for the IMO Second Generation Intact Stability Criteria

This page is intentionally left blank

A Study on Roll Damping Time Domain Estimation for Non Periodic Motion

Toru Katayama, *Graduate school of Engineering, Osaka Prefecture University*

katayama@marine.osakafu-u.ac.jp

Jun Umeda, *National Maritime Research Institute, Japan*

umeda@nmri.go.jp

ABSTRACT

In this study, the memory effects of bilge keel component of roll damping in irregular rolling are investigated by numerically. First, in order to validate the results of numerical simulation, a forced irregular roll motion test is carried out, and the characteristics of the memory effects are also confirmed. Second, the mechanism of the memory effects is made clear by the numerical simulation. Finally, based on the simulation results, the roll damping time domain estimation, which is proposed by Katayama et al. (2013) based on the prediction method proposed by Ikeda et al. (1978), is improved.

Keywords: *Roll damping, Memory effects, Transient Effects, Previous Amplitude Effects, Time domain estimation, Non periodic motion*

1. INTRODUCTION

In order to guarantee the safety of vessels, it is important to estimate roll damping accurately. It is well known that there is a prediction method of the roll damping proposed by Ikeda et al. (1978). However, it is indicated by the previous studies that there are some problems in Ikeda's method. Ikeda's method is developed with theoretical and experimental backgrounds for periodical roll motion. Therefore, it is difficult to apply it to a time domain simulation of transitional and irregular roll motions.

In the previous studies (Ikeda et al., 1988, Katayama et al., 2010), it is pointed out that the memory effects of roll damping are necessary to consider for time domain simulations of non-periodical roll motions. Ikeda et al. (1988) show through experiments that the drag coefficient on flat plate increased in the first few oscillations when the flat plate is started rest (it is called the transient effects in this paper). An additional valuable observation reports from the experiments by Ikeda et al. (1988) is that the memory effects remain important in irregular motion. When an oscillation has a larger amplitude than the oscillation after it, then the drag coefficient is larger than at a steady oscillation amplitude (it is called the memory effects in this paper). Katayama et al. (2010) investigate the effects of transient motion on the drag force of a flat plate. In the region of KC < 250, the drag coefficient for acceleration in one direction is larger than the drag coefficient for acceleration in a uniform flow and smaller than that in a steady oscillatory flow. Moreover, in a transient condition under forced oscillation, the drag coefficients from the first to the third oscillation are smaller than that in a steady oscillatory flow. Katayama et al. (2013) propose a time domain estimation method

which is an improved Ikeda's method of bilge-keel component of roll damping based on the results of Katayama et al. (2010). However the improved method include only the transient effects and it is required to include the memory effects.

In this study, the bilge-keel component of roll damping for non-periodic motion is focused. The memory effects is investigated by numerically. First, a forced roll motion test with irregular motion is carried out, and the characteristics of the memory effects are confirmed and the numerical simulation is validated. Second, the mechanism of the memory effects is made clear by the numerical simulation. Finally, based on the CFD results, the roll damping time domain prediction method, which is proposed by Katayama et al. (2013) including the transient effects based on Ikeda's method (1978), is improved.

2. FORCED IRREGULAR ROLL MOTION TEST

2.1 Model and Measurement

In order to investigate the memory effects and take some validation data for the numerical simulation, forced roll motion measurements are carried out at the towing tank of Osaka Prefecture University (length 70m, breadth 3m, depth 1.5m).

Table 1 and Figure 1 show a body plan and principal particulars of a two dimensional model. The model is attached to end plate in order to remove three dimensional effects.

The model is given forced roll moment by the forced irregular roll motion device shown as figure 2, and it is putted on the centre line of the model. The device has three axis of rotation and three rods attached weights are rotated in the horizontal plane at different periods. In the measurement, roll motion and rotating positions of rods are measured in sampling frequency 100Hz.

Table 2 shows the conditions in the measurement. The measurements at systematically changed forced roll periods and drafts are carried out. In order to reduce wave making component, forced roll period is more than 1.2sec.

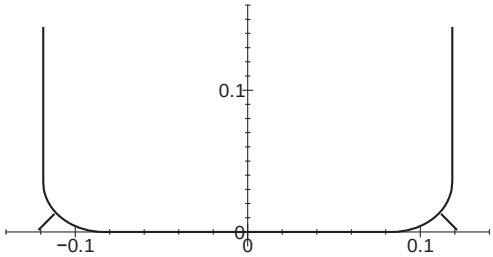

Figure 1 Section of the two dimensional model.

Table 1 Principal particulars of the two dimensional model.

L_{PP} [m]	0.80
B[m]	0.235
D[m]	0.145
Bilge radius[deg]	0.035
Bilge keel[m×m]	0.01×0.80

Figure 2 Forced irregular roll motion device.

Table 2 Conditions in the measurement.

height of roll axis [mm]	96
draft [mm]	96, 80, 72, 57
forced roll period [sec]	1.60-1.28, 1.80-1.44
device from roll axis [mm]	119
A mass of weight [g]	150
attached position of weight from centre of rotation[mm]	50

2.2 CFD Calculation

In the tank test, it is difficult to visualize flow around hull and divide the measured hydrodynamic forces into the each component, which are the normal component and the hull surface pressure component of the bilge keel component. In this study, bilge keel component calculated by CFD (Fluent) is divide into the each component and the memory effects on the each component is investigated.

In the calculation, the two dimensional model is given the roll motion expressed by Eq. (1), and roll moment acting on hull is calculated.

$$\phi(t) = \phi_{a1} f_1(t) \sin\omega_1 t + \phi_{a2} f_2(t) \sin\omega_2 t$$

$$f_i(t) = \begin{cases} \frac{1}{2}\sin\left(\frac{1}{4}\frac{\pi}{T_i}t - \frac{1}{2}\pi\right) + \frac{1}{2} & \left(for, t \le 4T_i\right) \\ 1 & \left(for, t > 4T_i\right) \end{cases} \quad (1)$$

Eq.(1) can almost express the measured roll motion in the forced irregular roll motion test in the limited cases, which is small amplitude irregular motion caused by two rods. Table 3 shows the calculation conditions and settings.

Table3 Calculation conditions.

Numerical solver	implicit unsteady first order
Viscous model	*k-ε* model
Solution algorithm	SIMPLE
Multiphase model	VOF, Geo-reconstructed
Gradient	Least Squares Cell Based
Discretization scheme	Second order Upwind
Interpolation scheme	PRESTO!
Draft[mm]	96
Forced roll period[sec] and amplitude[deg]	2.00-1.2sec and 8.0-5.0deg 1.20-0.67sec and 5.0-5.0deg 1.80-2.00sec and 10.0-8.0deg 1.60-2.00sec and 8.0-6.0deg 1.40-1.8sec and 8.0-6.0deg 1.60-1.28sec (measured) 1.80-1.44sec (measured)

2.3 Analysis of Roll Damping

The roll motion in the measurement and the calculation is expressed as Eq. (2).

$$A_{44}\ddot{\phi}(t) + B_{44}\dot{\phi}(t)\left|\dot{\phi}(t)\right| + C_{44}\phi(t) = M_E \quad (2)$$

Where the first term of left side of the equation is moment of inertia including added moment of inertia, the second term is the roll damping moment, the third term is the restoring moment and M_E is forced roll moment. It should be noted that A_{44}, B_{44} and C_{44} are not constant value for each time step.

In the measurement, the forced roll moment is given by the forced irregular roll motion device. The given moment can be calculated as follow. Figure 3 shows schematic view and coordinate system.

$$\begin{aligned} x &= r\cos\omega t \\ y &= r\sin\omega t\cos\phi + h\sin\phi \\ z &= h\cos\phi - r\sin\omega t\sin\phi \end{aligned} \quad (3)$$

Kinetic energy and potential energy of weights caused by rotation of weights and roll motion of hull are expressed as Eq. (4) and (5).

$$T = \frac{1}{2}m\{r^2\omega^2 + \left(h^2 + r^2\sin^2\omega t\right)\dot{\phi}^2 + 2hr\omega\dot{\phi}\cos\omega t\} \quad (4)$$

$$U = mg\left(h\cos\phi - r\sin\omega t\sin\phi\right) \quad (5)$$

The forced roll moment caused by weights can be obtained from applying Lagrange equation of motion to these energy.

$$\begin{aligned} m_{Ei} = &-mr^2\sin^2\omega t\ddot{\phi} \\ &- 2mr^2\omega_i\dot{\phi}\sin\omega_i t\cos\omega_t t \\ &+ mg\left(h\sin\phi + r\sin\omega_i t\cos\phi\right) \\ &+ mr\omega_i{}^2 h\sin\omega_i t \end{aligned} \quad (6)$$

C_{44} in Eq.(2) is obtained by the calculated *Gz* curve corresponding to the roll angle. The

roll angle removed noises by low-pass filter (10Hz) from the measured ones is used in Eq.(2). And roll angular velocity and acceleration obtained from differentiating numerically the filtered roll angle are used in Eq.(2). A_{44} and B_{44} in Eq. (2) are obtained to satisfy the Eq. (2). In concrete terms, the coefficients (A_{44} and B_{44}) at certain time t are decided by using least square method to time history data (data number n) from the starting position where angular velocity of roll is zero to a certain time. Roll damping is obtained in time domain due to decide the coefficients (A_{44} and B_{44}) changed in time step while increasing data number n.

On the other hand, in the calculation, the roll motion expressed by Eq. (1) is given, and the roll moment acting on hull M_E is calculated. The roll damping is obtained from the same way as the above-mentioned method.

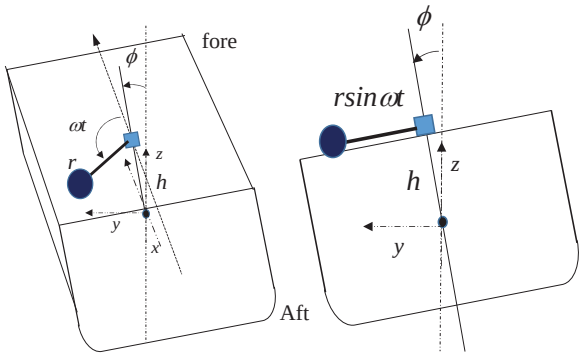

Figure 3 Schematic view of forced irregular motion test.

3. MEMORY EFFECTS

3.1 Comparison of Measured and Calculated results

An example of the comparison between measured and calculated roll damping is shown in Figure 4. The upper and bottom figures of Figure 4 show the time histories of roll angle and roll damping, respectively. The calculated result is good agreement with that of the measured result. It is confirm that roll damping under irregular motion can be calculated accurately by CFD.

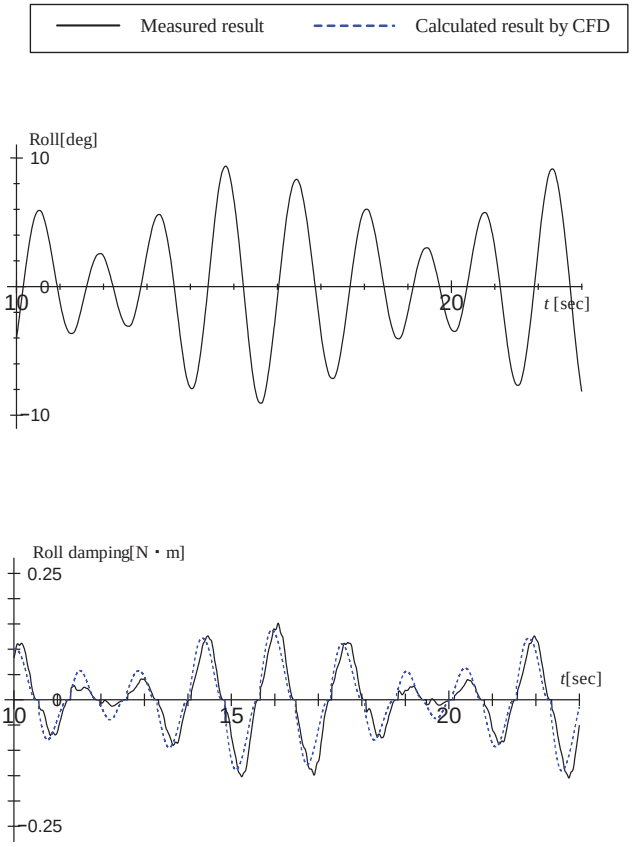

Figure 4 Comparison of measured and calculated roll damping.

3.2 Memory Effects on Normal Force Component

It is confirm that the vortex created by previous swing affects drag force acting on flat plate in present swing by Katayama et al. (2010) and it is assumed that bilge keel component may be affected by the memory effects.

In this section, bilge keel component calculated by CFD is divide into normal force component and hull surface pressure component and the memory effects on normal force component is investigated. Normal force component is the moment due to drag force acting on bilge keel. And the result by CFD is compared with the result estimated by the time

domain estimation proposed by Katayama (2013).

An example of the comparison between calculated and estimated roll damping is shown in Figure 5. The upper, middle and bottom figure of Figure 5 show time history of roll damping, time history of roll damping coefficient and *Kc* number for half cycle, respectively. When *Kc* number of the previous swing is larger than *Kc* number of the present swing, the calculated damping coefficient is larger than the estimated result. On the other hand, when *Kc* number of the previous swing is smaller than *Kc* number of the present swing, the calculated damping coefficient is good agreement with the estimated result. Therefore, when *Kc* number of the previous swing is larger than *Kc* number of the present swing, the memory effects must be considered in estimation method of normal force component.

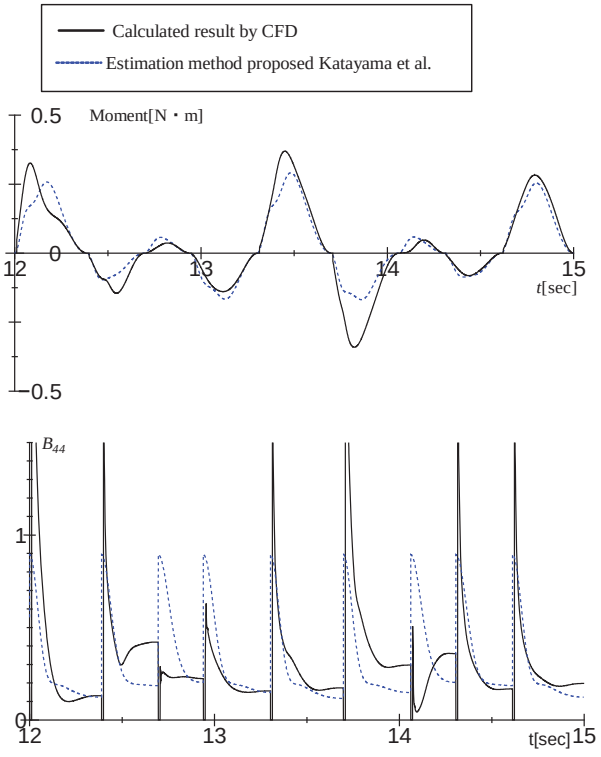

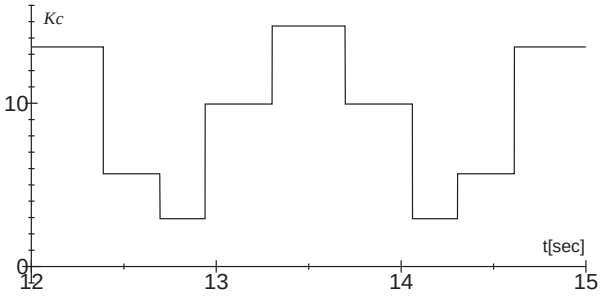

Figure 5 Previous amplitude effects on normal force component shown by comparison between the calculated result of CFD and the estimated result by the estimation method proposed by Katayama et al., (2014).

3.3 Memory Effects on Hull Surface Pressure Component

An example of roll damping coefficients of hull surface pressure component in time domain is shown in Figure 6. It is confirmed that the values are different even if *Kc* number of the present swing is the same. When *Kc* number of the previous swing is larger than *Kc* number of the present swing, the damping coefficient is larger. Therefore, it is also need to consider the memory effects on hull surface pressure component.

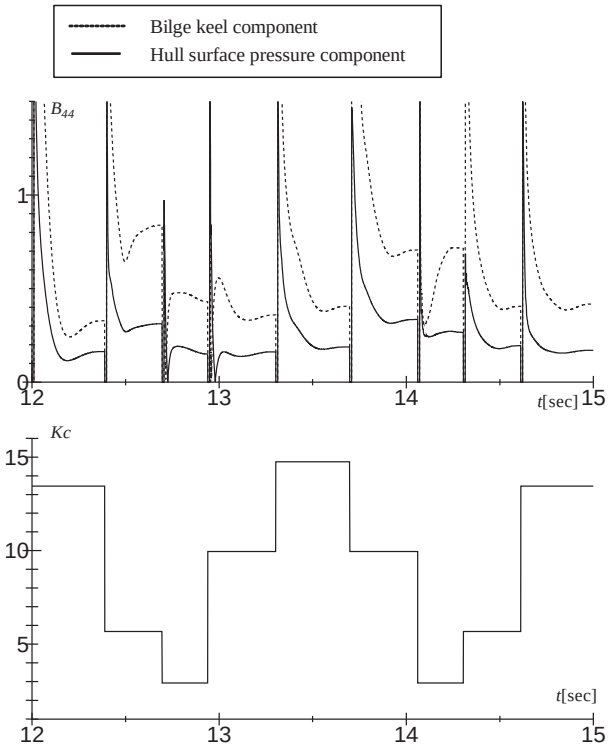

Figure 6 Memory effect for hull surface pressure component calculated by CFD.

3.4 Visualization of Flow around Hull

Flow field around hull is visualized in order to understand the mechanism of the memory effects. Figure 7 shows the velocity vectors around hull at the starting position of swing, and the direction of motion velocity of hull. The scales of these colour contour and arrow figures are the same and these show velocity magnitude. From figure 7(a) and (b), it is found that the fluid in front of bilge keels is given velocity due to the vortexes developed by the previous swing. The fluid velocity in front of bilge keel in the Figure 7 (a) is faster than that in the Figure 7 (b), because Kc number of previous swing of (a) is larger than Kc number of previous swing of (b) and the vortexes developed by previous swing of (a) are larger than that developed by the previous swing of (b). The moment due to the bilge keel is increased by increase of the relative velocity of the fluid in front of bilge keel. Therefore, the memory effects depends on Kc number in previous swing and in present swing.

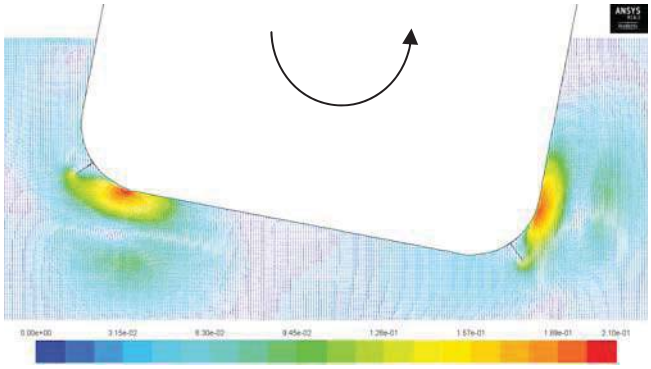

(a) *Kc* number of previous swing is 19.61

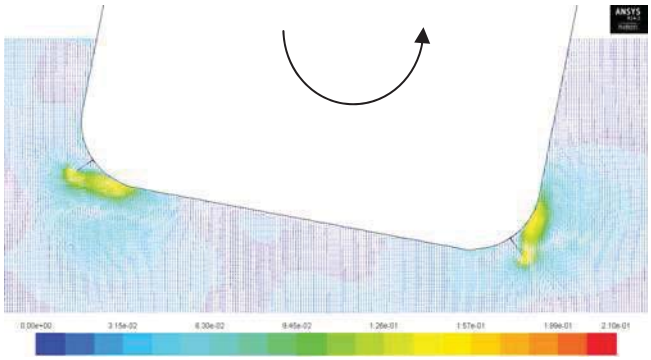

(b) *Kc* number of previous swing is 9.35

Figure 7 Calculated velocity vectors around hull starting position of swing for various *Kc* numbers of previous swing.

4. ROLL DAMPING TIMEDOMAIN ESTIMATION

4.1 Time domain Estimation Considering Memory effects

It is confirmed that the memory effects must be considered in time domain estimation of bilge keel component and the memory effects depends on Kc number in previous swing and in present swing. Therefore, the estimation method considering Kc number in previous swing and in present swing is proposed.

The normal force component is calculated by Eq.(7) using a drag coefficient of flat plate under one direction accelerating expressed by Eq.(11) (Katayama et al. (2010)). The hull surface pressure component is calculated by Eq.(8). The coefficient C_P in Eq.(8) is divided into the pressure coefficient C_P^+ on front face of bilge-keels and the pressure coefficient C_P^- on back face of bilge-keels. And the pressure coefficient C_P^- is calculated by Eq.(9) using CD expressed by Eq.(2). The hull surface pressure component can be obtained from the integration which is shown in Figure 8. Length of negative pressure region S_0, depends on the Kc number, and it is defined by Eq.(12).

$$M_{BKN} = \frac{1}{2}\rho l_{BK}\, b_{BK}\, mC_D l^2\, \dot{\phi}\left|\dot{\phi}\right|\, l\, f^2 \tag{7}$$

$$M_{BKH} = \frac{1}{2}\rho\, l^2 f^2\, \dot{\phi}\left|\dot{\phi}\right| \int_G C_p \cdot l_p dG \tag{8}$$

$$C_P^- = C_P^+ - mC_D = 1.2 - mC_D \tag{9}$$

$$S_0 / b_{\mathrm{BK}} = 0.3\left(\frac{\pi l\phi}{b_{\mathrm{BK}}}\right) f + 1.95 \tag{10}$$

$$C_D = \begin{pmatrix} 14.3e^{-1.80Kc_d} + 4.41e^{-0.37Kc_d} + \\ -10.4e^{-1.03Kc_d} - 0.30e^{-0.17Kc_d} + 1.0 \end{pmatrix} \times \left(0.908 + \frac{1.2}{1+1.01^{Kc_d}}\right) \times 2.1 \tag{11}$$

$$(0 < Kc_d \le 250)$$

$$Kc = Kc_d = \frac{\pi l\phi}{b_{BK}} \tag{12}$$

Where l_{BK} and b_{BK} is the length and breadth of the bilge-keel and l is the distance from the roll axis to the tip of the bilge-keel. f is a correction factor to take account of the increment of flow velocity at the bilge. m is a memory effect factor. The memory effects on normal force component is considered by the memory effect factor in Eq.(7) and the memory effects on hull surface pressure component is considered by the coefficient C_P^- in Eq.(9).

In order to investigate the memory effects factor, the ratio of roll damping coefficients estimated by using Eq. (11) to the coefficients of normal force component at the velocity is maximum are obtained. When Kc number of the previous swing is smaller than Kc number of the present swing, it is assumed that the memory effects factor equal 1.0.

Figure 9 shows the memory effects factor vs. difference of Kc number between previous swing and in present swing. In order to decide the memory effects factor, a fitting curve is obtained from the results. The memory effects factor is expressed as the following equation.

$$m = 0.0129(Kc_{previous} - Kc_{present})^2 + 0.0647(Kc_{previous} - Kc_{present}) + 1 \tag{12}$$

$$Kc_{previ} - Kc_{present} > 0$$

Where $Kc_{prev.}$ is Kc number in previous swing and Kc_a is Kc number in present swing.

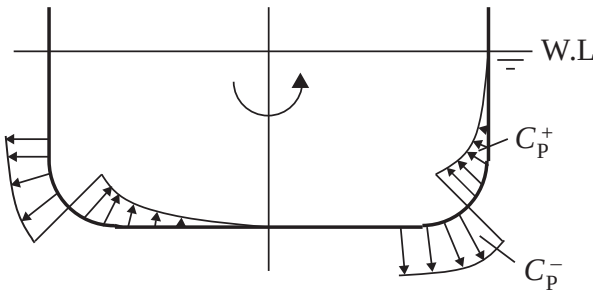

Figure 8 Assumed pressure distribution on the hull surface created by bilge-keels.

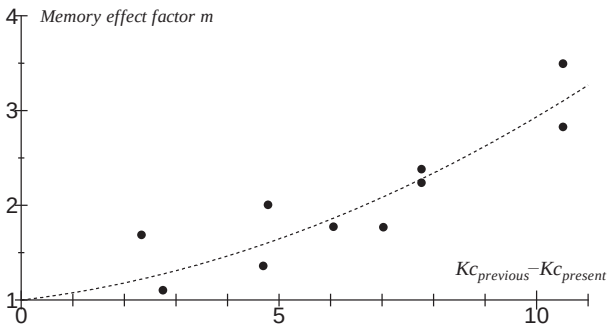

Figure 9 The memory effects factor vs. difference of Kc number between previous swing and in present swing.

4.2 Comparison with Measured Result

Figure 10 shows the result estimated by the proposed method and the result calculated by CFD and the measured result. In the case, the results show that the estimated result is good agreement with the measured and the calculated results. It is confirmed that roll damping can be estimated in time domain by using the method considering the memory effects.

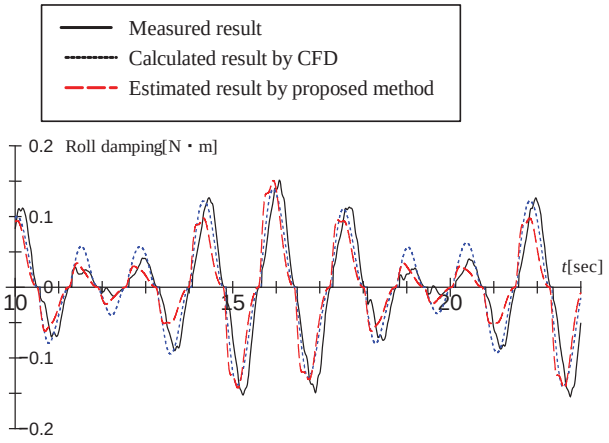

Figure 10 Comparison of estimated and calculated and measured result

5. NUMERICAL SIMULATION USING PROPOSED METHOD

5.1 The Subject Ship and Calculation method

By utilizing the numerical simulation model (H. Hashimoto et al., 2010), the effects of rolling in irregular waves is calculated to investigate the effects of the proposed method.

Fig.11 and Table 4 shows body plan and principal particulars of the subject ship.

In order to investigate effects of different roll damping estimation methods, in the simulation, roll damping component is estimated by two methods. The first one is a simplified method using Ikeda's original method which is used originally (the following section it is called the previous method) in the numerical simulation, and the other one is the proposed method in this study, which includes the estimation method for bilge-keel component by using the roll damping coefficient considering the memory effects in time-domain.

In the previous method, roll damping is estimated at changed roll amplitudes systematically in roll natural period by Ikeda's original method. And roll damping in the simulation is calculated by interpolation of the results. The roll amplitude is calculated by Eq.(13) with the roll angle and the roll angular velocity in each time step.

$$\phi_a = \sqrt{\phi^2 + \left(\frac{2\dot{\phi}}{\omega_e}\right)^2} \tag{13}$$

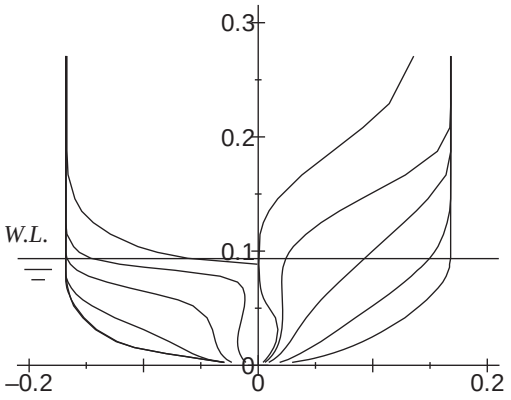

Figure 11 Body plan of the subject ship.

Table 4 Principal particulars of the subject ship.

L_{PP}	192.0 m
B	32.26 m
d	9.0 m
Speed	7knot
Height of gravity: KG	17.0 m
Metacentric height: GM	1.89 m
Natural roll period: T_ϕ	18.42 sec
Displacement: W	27205 ton
Breadth of bilge-keels	0.7 m
Position of bilge-keels	s.s. 3.34-s.s. 5.59

The simulation is carried out at F_n =0.083 in irregular head waves whose significant wave height is 6.0m for 120 minutes (real time scale). The spectrum of irregular wave is the ITTC spectrum expressed by Eq.(14).

$$S(\omega) = 0.0081 \times \frac{g^2}{\omega^5} \exp\left(\frac{-3.11}{H_{1/3}^2 \times \omega^4} \right) \quad (14)$$

The making irregular waves is same and roll motions in time histories are compared between two methods and the effect of the difference of estimation methods on prediction of the parametric rolling.

5.2 Results of Simulations

Figure 12 shows an example of the comparison between the two calculated roll motions in time. The bottom of figure 10 shows the wave elevation at the midship. In this figure, the ratios of mean encounter wave period to the roll natural period ($\overline{T_e}/T_\phi$) at T_1, T_2 and T_3 are also shown. From this figure, it is found that periodic rolling does not occur at T_2. In the result calculated by simplified method using Ikeda's original method, periodic rolling occurs at T_1. On the other hand, in the result calculated by proposed method, periodic rolling does not occur at T_1. In the two results, it is found that periodic rolling occurs at T_3. However, in the result calculated by the simplified method, roll amplitudes become large rapidly.

Therefore, it is confirmed that parametric rolling occurs more easily in simplified method than in the proposed method.

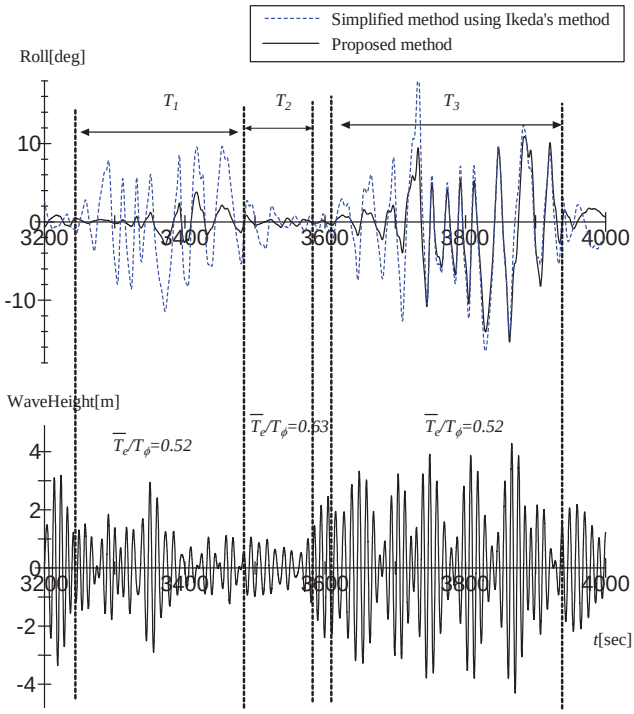

Figure 12 Calculation time history of roll angle and wave height in long crested head irregular waves.

6. CONCLUSIONS

In this study, the memory effects on roll damping is investigated by numerically. The following conclusions are obtained.

In order to take validation data for CFD, forced roll motion test with irregular motion is carried out and the analysis for the test. It is confirm that the proposed analysis can be applied roll damping under irregular motion and roll damping can be calculated accurately by CFD.

Bilge keel component is divide into normal force component and hull surface pressure component by using CFD and the memory effects is investigated. The memory effects depends on *Kc* number in previous swing and in present swing. Moreover, in order to clarify the mechanism of the memory effects, the flow filed around hull is investigated numerically. The relative fluid velocity in front of bilge keels is increased by the vortexes developed by

the previous swing. If Kc number of previous swing is larger, the vortexes developed by previous swing are larger. The moment due to the bilge keel is increased by increase of the relative velocity of the fluid in front of bilge keel.

The estimation method considering the memory effects is proposed. The result estimated by the proposed method is compared with the result calculated by CFD and measured in forced irregular motion test and roll damping can be estimated in time domain by using the method considering the memory effects.

The proposed estimation method is applied for a time domain simulation of parametric rolling in irregular head waves. It is confirmed that parametric rolling occurs more easily in previous method than in the proposed method.

7. REFERENCES

Ikeda Y., Himeno Y., Tanaka N., (1978). Components of Roll Damping of ship at Forward Speed, Report of Department of Naval Architecture University of Osaka Prefecture, 1978

Ikeda, Y., Osa, K., Tanaka, N. (1988). Viscous Forces Acting on Irregular Oscillating Circular Cylinders and Flat Plates, Trans. of the ASME, No. 140, Vol. 110, pp.140-147.

Katayama T., Yoshioka Y., Kakinoki T. and Ikeda Y., "Some Topics for Estimation of Bilge-keel Component of Roll Damping", Proceedings of the 11th International Ship Stability Workshop, 2010, pp.225-230.

Katayama, T., J. Umeda, H. Hashimoto & B.Yildiz (2013) "A study on roll damping estimation for non-periodic motion." Proc. 13rd Int'l. Ship Stability Workshop, Brest, France, pp. 44–49.

Hashimoto, H. and Umeda, N., 2010, "A Study on Quantitative Prediction of Parametric Roll in Regular Waves", Proceedings of the 11th International Ship Stability Workshop, Stability Workshop pp.295-301

Investigation of the 2nd Generation of Intact Stability Criteria in Parametric Rolling and Pure loss of Stability

Haipeng Liu, *University of Strathclyde*, h.liu@strath.ac.uk

Osman Turan, *University of Strathclyde*, o.turan@strath.ac.uk

Evangelos Boulougouris, *University of Strathclyde*, evangelos.boulougouris@strath.ac.uk

ABSTRACT

The International Maritime Organisation is developing the second generation intact stability criteria which include parametric rolling, pure loss of stability and the other three failure modes. This paper will focus on the application of the draft parametric rolling and pure loss of stability criteria on the well-known post-Panamax C11 class containership and a high speed containership developed in the FASTPOD project. The roll amplitude calculated from the proposed analytical method in level 2 parametric rolling criteria is compared to experiment results. The influence of the main particulars on the check by the criteria is investigated.

Keywords: *parametric rolling, pure loss of stability, new generation intact stability criteria*

1. INTRODUCTION

The phenomenon of parametric rolling has been known to naval architects for more than 50 years (Paulling & Rosenberg, 1959). The continued study from Paulling demonstrated parametric roll from a model test in following waves in San-Francisco Bay (Paulling, et al. 1972, 1975). In October 1998, a post-Panamax, C11 class containership experienced severe parametric rolling in the North Pacific Ocean and it confronted the largest container casualty in history (France, et al., 2003). After this accident, parametric rolling attracted increased attention from researchers, and since then, many more studies in parametric rolling prediction have been carried out.

Since the 1800s, the stability changes in waves compared with calm water is known to naval architects (Pollard & Dudebout, 1892; Krylov, 1958). Until the 1960s, a series of model tests were carried out in order to calculate the change of stability in waves. During the model experiments in San-Francisco Bay, pure loss of stability was identified (Paulling, et al., 1972, 1975).

Due to some similar accidents which occurred in the Pacific Ocean and the Atlantic Ocean, it was realised that the existing Intact Stability Code (IS Code) couldn't provide enough safety. Therefore, the International Maritime Organisation (IMO) initiated the revision of the existing regulatory framework with the development of the second generation intact stability criteria which will hopefully fill this safety gap. The new intact stability criteria include five stability failure modes as listed below (SLF, 2012)

- Dead ship condition in beam seas
- Surf riding and broaching-to
- Parametric rolling
- Pure loss of stability
- Excessive acceleration

After the new criteria were generated, the process of stability check is suggested in figure 1. In each stability failure mode, it is divided

into vulnerability layer of level 1 and level 2 and performance-based layer of level 3. With the level increasing, the procedure is more detailed and accurate. The lower the level it is, the more conservative it is. Currently, the IMO finished the simplest level 1 criterion and is developing level 2 criteria. In the following paragraphs a short description of the background and the procedure of vulnerability layer of the criteria will be presented.

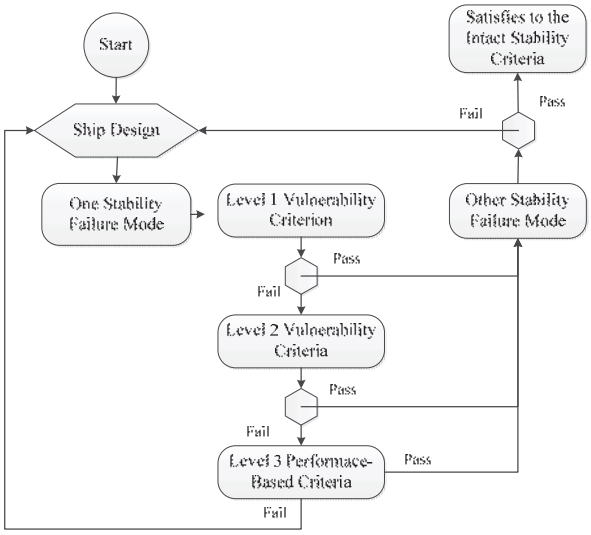

Figure 1 The proposed assessment process for next generation intact stability criteria

- Parametric Rolling

Parametric rolling is the roll amplification which is caused by the periodic change of metacentric height in longitudinal waves under specific conditions (ABS, 2004). The new parametric rolling vulnerability criteria with two levels included are described below.

Level 1 Vulnerability Criterion

As defined by current draft criteria (SDC, 2014), if the ratio of GM variation in reference wave (ΔGM/GM) is larger than the standard R_{PR}, the ship is temporary judged as vulnerable to parametric rolling; otherwise it means the vessel doesn't have any potential danger of parametric rolling. Here GM is the metacentric height of the loading condition in calm water including free surface correction and ΔGM is the change of metacentric height which can be estimated using two different methods. In the first method (Option A), two different drafts are used and Simpson's rule is applied to calculate the moment of inertia and the average GM variation is achieved. This method is not suitable for a tumblehome hullform but it is applicable to a ship without even keel design (SDC, 2014). In the second method (Option B), ΔGM may be determined as one-half difference between the maximum and minimum GM calculated in sinkage and trim on a series of waves with wave length equals to ship length and the wave height equals to 1/60 of wave length. Both of these two methods are utilised herein.

Level 2 Vulnerability Criteria

Level 2 criteria (SDC, 2014) will check the vessel in the aspects of ship speed, metacentric variation and roll amplitude. If either C_1 or C_2 is larger than safety standard R_{PR0} 0.06, the ship is judged to be in danger of parametric rolling (PR) and needs to be checked in performance-based layer, otherwise it passes the criteria. The aspects of speed and metacentric height variation constitute the first check and the aspect of roll angle computation constitutes the second check.

- First Check

The first check aims to test whether the vessel's speed is within the vulnerable region for PR and GM variation and satisfies the PR safety requirement. The probability of C_1 in the first check is a sum of the product of C_{1i} and the wave weighting factor W_i. The 16 wave series applied in this check are discretisation of the applied wave spectrum (SDC, 2014). The weighting factor is the occurrence probability among the wave series for each wave case. The wave lengths vary from 22.57m to 63.68m and the wave heights vary from 0.35m to 5.95m. The value for criterion 1 in each case, C_{1i} is 0 if both speed check and GM relevant check satisfy with the specific condition as the vessel is considered not vulnerable to PR; otherwise C_{1i} is 1.

Parametric rolling occurs when the encounter frequency is equal to double the natural roll frequency. The speed corresponds to the resonance speed V_{PRi} which is given by the following Equation 1.

$$V_{PRi} = \left| \frac{2\lambda_i}{T_\phi} \cdot \sqrt{\frac{GM(H_i, \lambda_i)}{GM}} - \sqrt{g \frac{\lambda_i}{2\pi}} \right| \quad [1]$$

For GM relevant conditions for avoiding the PR risk region are that $\Delta GM(H_i, \lambda_i)/GM(H_i, \lambda_i) < R_{PR}$ and $GM(H_i, \lambda_i) > 0$. Here, the average metacentric height corresponding to the loading condition under consideration, $GM(H_i, \lambda_i)$; and the one-half of the difference between the maximum and minimum values of the metacentric height GM in wave, $\Delta GM(H_i, \lambda_i)$; are calculated considering the ship balanced in sinkage and trim in the series of waves characteristic by H_i and λ_i.

If total probability of C_1 is greater or equal to the standard value R_{PR0} of 0.06 the ship is judged as potentially vulnerable and it needs to be checked by the second check; otherwise the vessel is not vulnerable and it passes the evaluation of parametric rolling problem.

- Second Check

When C_1 is not smaller than R_{PR0}, the designer should apply the second check. The ship performance is simulated under NO.34 standard wave cases (IACS, 2001). Each wave case has the corresponding weighting factor W_i, which represents the sample wave's occurrence probability among all the 306 wave cases. According to the criteria, if the vessel in each wave case experiences the roll angle which is larger than 25 degrees, the vessel is judged as vulnerable to parametric rolling and C_{2i} is 1, otherwise is 0. An analytical method based on the simplification of Mathieu's equation is used to predict the roll amplitude as given in equation [2] (CGIS, 2014). GM variation in waves is calculated quasi-statically. Ikeda's simplified method, based on an empirical formula, is used for the damping prediction (Kawahara et.al., 2009). It divides the roll damping into the frictional, the wave, the eddy, the bilge keel and the lift damping components.

$$(I_{xx} + J_{xx}) \cdot \ddot{\phi} + R \cdot (\dot{\phi}) + W \cdot GM \cdot \phi = 0 \quad [2]$$

Where Ixx+Jxx: virtual moment of inertia in roll;

R: nonlinear roll damping;

W: ship weight;

GM: metacentric height

For the second check, if the total probability sum C_2 which is the product of C_{2i} and wave weighting factor W_i, is greater than standard R_{PR0} 0.06, the ship is judged to be vulnerable to parametric rolling and the ship should be checked by level 3; if not, the ship passes the parametric rolling failure mode and it should be checked for the other stability failure modes.

- Pure Loss of Stability

If the stability is reduced for a sufficiently long time, a ship may experience a large roll angle or even capsize, as shown in figure 2 (Belenky, 2008). In the new generated pure loss of stability criteria (SDC, 2014), it mainly concerns the minimum GM value, the vanishing stability and the heel angle under action of specific heeling level. The criteria is proposed to apply to all ships with service speed larger than 0.24.

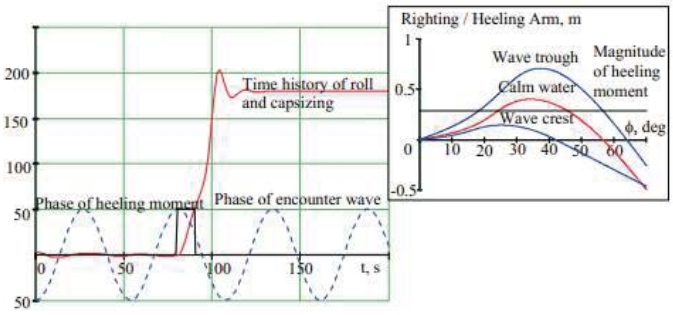

Figure 2: Capsizing due to Pure Loss of Stability (Belenky et.al., 2008)

Level 1 Vulnerability Criteria for Pure Loss of Stability

As proposed, if GM_{min} is greater than R_{PLA} 0.05, the ship is considered not vulnerable; otherwise it has to be checked by the next level (SDC, 2014).

Similar to the method of GM variation prediction in waves in parametric rolling criteria, the minimum value of metacentric height GM_{min} can be calculated either from the simplified method (Option A), or from considering the ship is balanced in sinkage and trim quasi-statically (Option B). In this case, the wave length is equal to the ship length and wave steepness is 0.0334 which is twice of that for parametric rolling.

Level 2 Vulnerability Criteria for Pure Loss of Stability

The procedure is quite similar to level 2 criteria for parametric rolling. It requires the stability calculations in a series of longitudinal sinusoidal waves. Here, the criteria totally include 2 checks which evaluate the ship in vanishing stability and the heel angle under action of specific heeling level. The target is for the angle of vanishing stability to be greater than 30 degrees (referred to C_{R1}), and the angle of heel under action of heeling level specified by R_{PL3} $8(H_i/\lambda)dF_n^2$ (referred to C_{R2}) to be larger than 15 degrees for passenger ship or 25 degrees for other ships. The total sum of probability according to corresponding wave probability in each criterion is C_{R1} and C_{R2}. The ship at its service speed is considered not to be vulnerable to pure loss of stability if the largest value among the two criteria, C_{R1} or C_{R2} is less than R_{PL0}; otherwise, performance-based layer should be applied for further check.

2. SAMPLE VESSELS

2.1 Reference Ship Data

The reference vessels applied with the draft criteria are C11 containership, ITTC ship A-1 and a high speed containership developed in Fastpod project (Turan et. al., 2008). The main particulars of these vessels and geometry are separately listed in table 1-3 and figure 3-5.

Table 1:
Main Parameters of C11 Containership

Item	Value	Unit
Length btw. waterline (L_{pp})	262.00	m
Breadth (B_{DWL})	40.00	m
Depth (D)	24.45	m
Draught (T)	11.50	m
Displacement (Δ)	69,034.40	tons
Block coefficient (C_B)	0.573	/
Transverse metacentric height (GM_T)	1.928	m
Vertical Centre of Gravity (VCG)	18.418	m
Service Speed (Vs)	12.86	m/s
Natural Roll period (T_Φ)	24.49	s

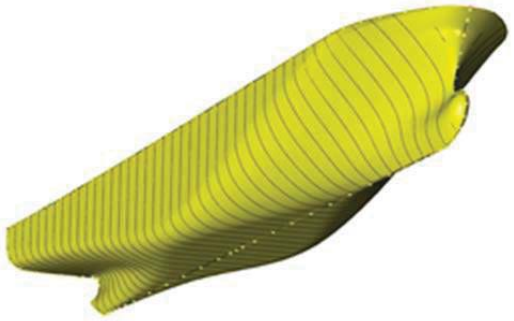

Figure 3: Geometry of C11 Containership

Table 2:
Main Parameters of Ship A-1

Item	Value	Unit
Length btw. Waterline (L_{pp})	150.00	m
Breadth (B_{DWL})	27.20	m
Depth (D)	13.50	m
Draught (T)	8.5	m
Displacement (Δ)	23,751.21	tons
Block coefficient (C_B)	0.668	/
Transverse metacentric height (GM_T)	0.15	m
Vertical Centre of Gravity (VCG)	11.475	m
Service Speed (Vs)	11.50	m/s
Natural Roll period (T_Φ)	43.30	s

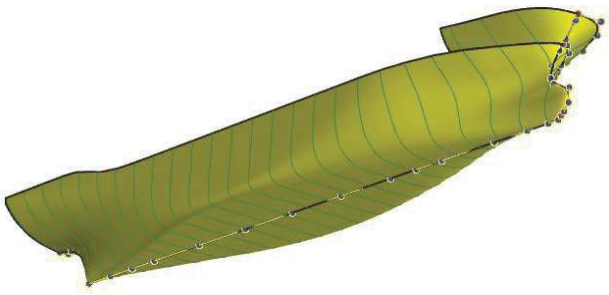

Figure 4: Geometry of ship A1

Table 3:
Main parameters of Fastpod Containership

Item	Value	Unit
Length btw. Waterline (L_{pp})	275.00	m
Breadth (B_{DWL})	30.00	m
Depth (D)	21.65	m
Draught (T)	10.30	m
Displacement (Δ)	49,580.28	tons
Block coefficient (C_B)	0.569	/
Transverse metacentric height (GM_T)	1.926	m
Vertical Centre of Gravity (VCG)	13.678	m
Service Speed (Vs)	18.00	m/s
Natural Roll period (T_Φ)	19.05	s

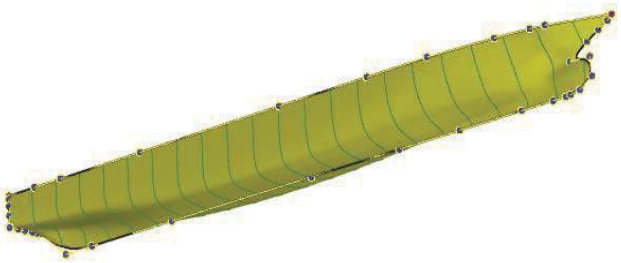

Figure 5: Geometry of Fastpod Containership

3. SECOND GENERATION INTACT STABILITY CRITERIA

The IMO is developing the second generation intact stability criteria of five failure stability modes. In this paper, the application of parametric rolling and pure loss of stability criteria will be introduced in section 3.1 and section 3.2 separately.

3.1 Parametric Rolling

The three sample vessels were tested according to the draft criteria. Roll amplitude results of C11 containership and Fastpod containership were calculated using the analytical methods proposed by the IMO working group and they were compared to model test results. The application of current parametric rolling criteria on the sample vessels is concluded. As C11 containership was tested in danger of parametric rolling, it is useful to investigate the influence of ship parameters on this issue.

- Analytical Method Vs. Experiment

In parametric rolling, the main part is to predict parametric roll amplitude. In level 2 vulnerability criteria, an analytical method is proposed to calculate roll angle (CGIS, 2014). As mentioned, level 2 is more conservative than level 3. If the vessel passes level 2, the vessel won't have any potential danger of parametric rolling. In other words, the roll amplitude calculated from the proposed method in level 2 should be larger than that of the vessel experiencing in practice.

Firstly, the well-known C11 containership is used to carry on the benchmark study. In wave length equals to ship length, wave steepness varies from 0.01 to 0.04 and Froude number changing from 0 to 0.15 in head sea, roll amplitude calculated from analytical method is compared to the experiment result shown in figures 6-9. All these results demonstrate that the analytical method provides a conservative estimate on roll amplitude which matches the purpose of level 2 criteria.

Secondly, the study is also applied to a high speed containership used in the Fastpod project (Turan, 2008). The model was tested for different wave heights for wave frequency 0.525 and vessel speed in 17 knots in head sea (Turan, 2008). The result comparison between analytical method and model test is plotted in figure 10. X axis represents the wave heights of regular wave while Y axis represents the roll amplitude. The data meet the conservative

purpose as well and the analytical method can achieve larger roll angle and provide a reasonable agreement to model test to some extent.

- Parametric Rolling Criteria Application

After validation of the analytical method, parametric rolling vulnerability criteria were applied to the three sample vessels. The results of level 1 and level 2 compared to the safety standard are shown in table 4. C11 is judged to be in potential danger of parametric rolling, while ship A-1 and Fastpod containership passes the criteria. The calculated result of C11 containership has a relative good agreement with IMO published result. Besides, The roll amplitude of most model tests of C11 containership are larger than the safety limit 25 degree while the largest roll amplitude of Fastpod containership reaches to 24.41 degree which is still smaller than the limit 25 degree. It therefore demonstrates that the parametric vulnerability criteria have good accuracy of parametric rolling occurrence prediction.

- Sensitivity Study

C11 containership was judged as being vulnerable to parametric rolling. It is important to investigate the influence of the main parameters on parametric rolling. To achieve the study, parametric transform method, based on Lackenby hull variation method (Lackenby, 1950) is used to generate new hullform. In this study, only one parameter was changed slightly (e.g. ΔL $\pm$2m; ΔB $\pm$0.4m; ΔT $\pm$0.4m; ΔC_b $\pm$0.01; ΔC_m $\pm$0.005; T_ϕ $\pm$0.5s), keeping the other main parameters constant and leaving the displacement free to vary. Among ship length Lwl, breadth B, draft T, block coefficient Cb, midship coefficient Cm and natural roll period T_ϕ, the small change to all the main parameters doesn't have any influence on C_1 of parametric rolling. In figure 11, it is clear that the small change of ship length doesn't have any influence on C_2 while in figure 12, the increase of breadth and block coefficient could slightly decrease the C_2 value. Compared to these three coefficients, C_m and T_ϕ have a relative larger influence on C_2 value. Overall, increasing draft could decrease the C_2 value but the vessel within this small change still in danger of parametric rolling, as shown in figure 13. From figure 14-15, it demonstrates that decreasing midship coefficient or natural roll period, could reduce the C_2 value and even avoid the vessel from parametric rolling occurrence

3.2 Pure Loss of Stability

In this part, the application of pure loss of stability to the three vessels is applied. The results are listed in table 5. In level 1, the simplified method (option A) seems more conservative. Although most results judged the ship as having a potential danger of pure loss of stability in level 1, all sample vessels still pass the level 2 criteria.

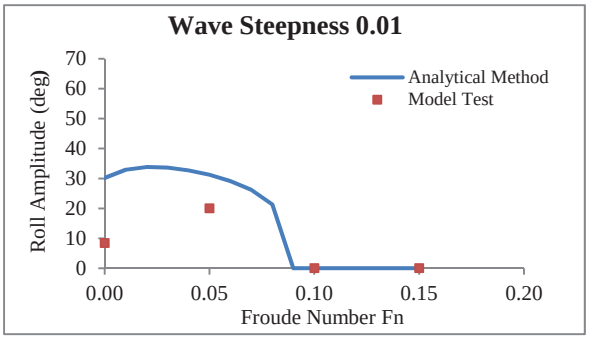

Figure 6 Comparison between Analytical Method and Experiment Result under Wave Steepness 0.01

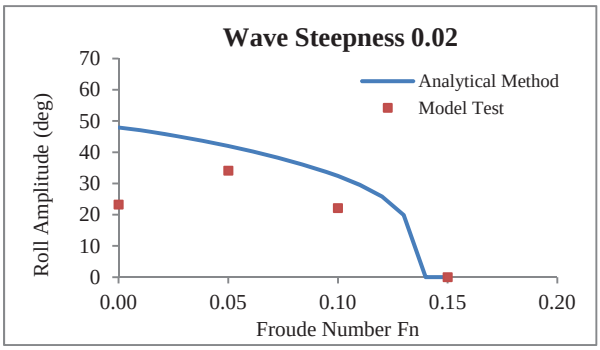

Figure 7 Comparison between Analytical Method and Experiment Result under Wave Steepness 0.02

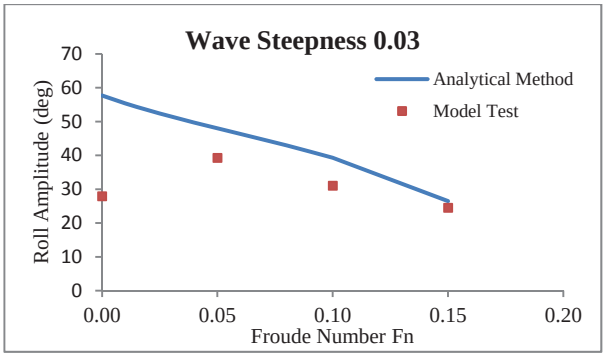

Figure 8 Comparison between Analytical Method and Experiment Result under Wave Steepness 0.03

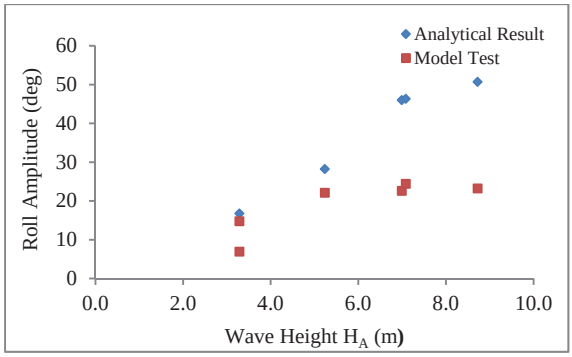

Figure 10 Roll Angle Comparison between the Analytical Method and Experiment Result with Different Wave Height

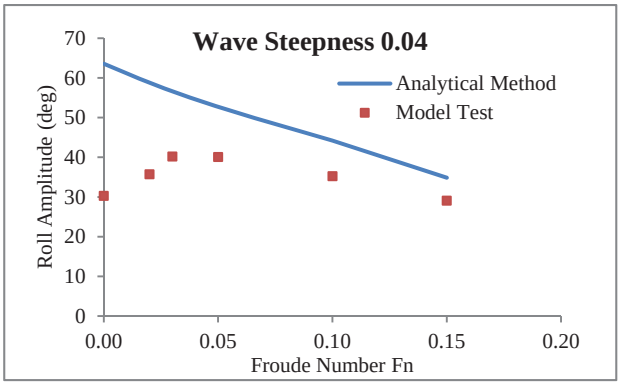

Figure 9 Comparison between Analytical Method and Experiment Result under Wave Steepness 0.04

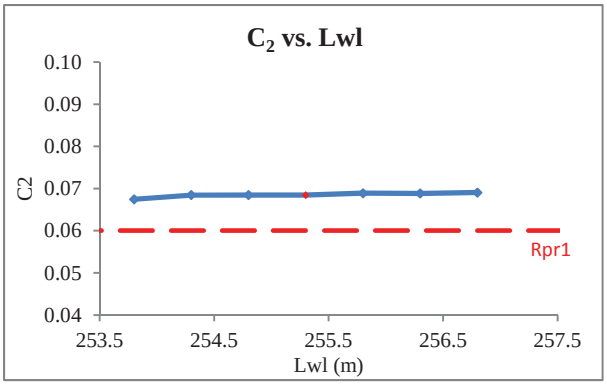

Figure 11 Relationship between ship length and C_2 of Parametric Rolling

Table 4:
Application of Parametric Rolling on Sample Vessels (Non-vulnerable; Vulnerable)

Ship Type	L_{pp} (m)	ΔGM/GM		R_{PR}	C_1	C_2
		Option A	Option B			
C11 from IMO	262	1.056	/	0.356	0.437	0.073
C11	262	1.067	0.852	0.400	0.436	0.068
Ship A-1	150	3.095	2.477	0.627	0.885	0.002
Containership 1	275	0.837	0.399	0.313	0.225	0.001

Table 5:
Application of Pure Loss of Stability on Sample Vessels (Non-vulnerable; Vulnerable)

Ship Type	L_{pp} (m)	F_n	Level 1		Level 2	
			Option 1-A	Option 1-B		
			GMmin-0.05(m)		C_{R1}	C_{R2}
C11	262	0.257	-1.969	-0.046	0.000	0.000
Ship A-1	150	0.3	-0.664	-0.201	0.000	0.000
Containership 1	275	0.345	-1.777	0.383	0.000	0.000

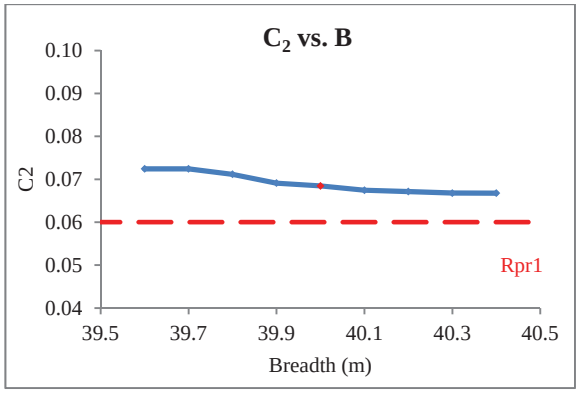

Figure 12 Relationship between Ship Breadth and C_2 of Parametric Rolling

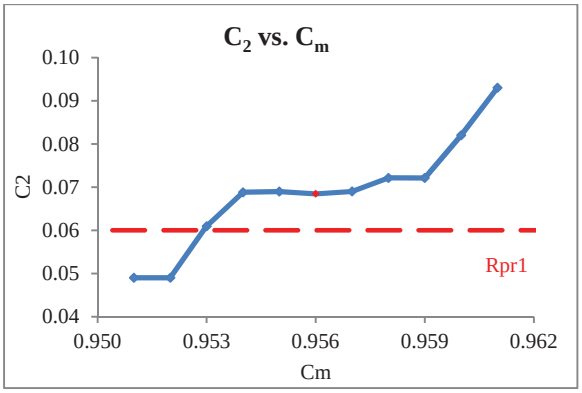

Figure 15 Relationship between Ship Midship Coefficient and C_2 of Parametric Rolling

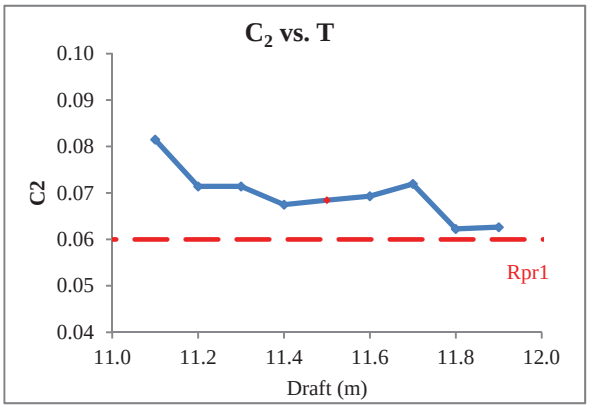

Figure 13 Relationship between Ship Draft and C_2 of Parametric Rolling

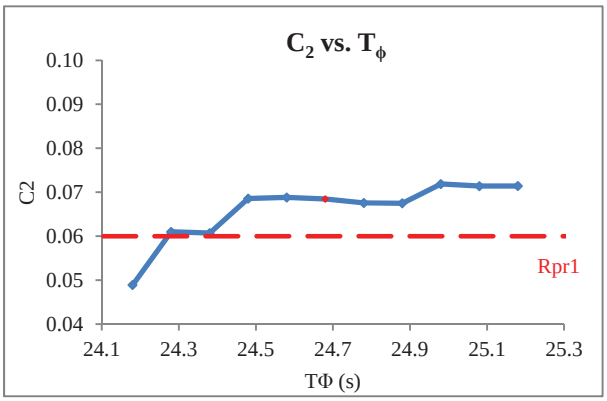

Figure 16 Relationship between Ship Natural Roll Period Coefficient and C_2 of Parametric Rolling

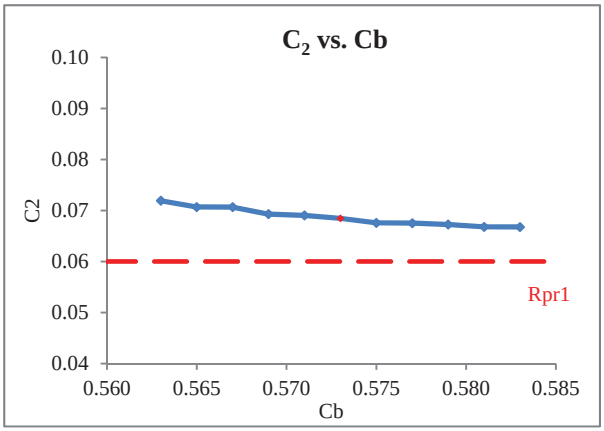

Figure 14 Relationship between Ship Block Coefficient and C_2 of Parametric Rolling

4. CONCLUSIONS

In this paper, the current parametric rolling and pure loss of stability criteria are applied to three sample vessels. C11 containership is judged as vulnerable to parametric rolling while ITTC ship A-1 and Fastpod containership are judged as non-vulnerable to parametric rolling. All the vessels passed the pure loss of stability criteria. Meanwhile, the analytical method from Mathieu equation provides a conservative estimate on the roll angle in comparison to experiments and to some extent; it has a relatively good prediction on the trend. Besides, the sensitivity study demonstrates that among ship length, breadth, draft, block coefficient, midship coefficient, natural roll period, when only one parameter is

changed and the other main parameters are left constant, C_1 is not sensitive but C_2 of parametric rolling is much influenced by draft, midship coefficient and natural period.

5. ACKNOWLEDMENTS

This project was funded by Lloyd's Register. All internal information relevant to second generation of intact stability was kindly provided by the Royal Institution of Naval Architects. The support from Lloyd's Register and the Royal Institution of Naval Architects is gratefully acknowledged.

The experiment of high speed containership was carried out under the European Commission Research Project FASTPOD (GRD2-2001-50063). The efforts from Dr Zafer Ayaz are very much appreciated.

6. REFERENCES

American Bureau of Shipping (ABS), 2004, "Guide for the Assessment of Parametric Roll Resonance in the Design of Container Carriers", Houston, Texas.

Belenky, V., Kat, H.O.D., and Umeda, N., 2008, "Toward Performance-Based Criteria for Intact Stability", Marine Technology, Vol.45, No.2, pp. 101-123.

Correspondence Group on Intact Stability (CGIS), 2014 "Working Version of Draft Explanatory Notes on the Vulnerability of Ships to the Parametric Rolling Stability Failure Mode", Sub-Committee on Ship Design and Construction, SDC 2/INF.10 Annex 17, pp. 59-74.

France, W.N., Levadou, M., Treakle, T.W., Paulling, J.R., Michel, R.K. and Moore, C., 2003, "An investigation of head-sea parametric rolling and its influence on container lashing systems", Marine Technology, Vol.40, Number 1, pp.1-19.

International Association of Classification Societies (IACS), 2001, "No.34 Standard Wave Data".

Lackenby, H., 1950, "On the Systematic Geometrical Variation of Ship Forms", RINA-Transaction, Vol 92, pp. 289-315.

Kawahara, Y., Maekawa, K., and Ikeda, Y., 2009, "A Simple Prediction Formula of Roll Damping of Conventional Cargo Ships on the Basis of Ikeda's Method and Its Limitation", The 10th International Conference on Stability of Ships and Ocean Vehicles, St. Petersburg, Russia.

Krylov, A.N., 1958, Selected Papers, USSR Academy of Sciences, Moscow.

Paulling, J.R., Kastner, S., and Schaffran, S., 1972, "Experimental Studies of Capsizing of Intact Ships in Heavy Seas", U.S. Coast Guard Technical Report

Paulling, J.R., Oakely, O.H., and Wood, P.D., 1975, "Ship Capsizing in Heavy Seas: The Correction of Theory and Experiments", Proceedings of 1st International Conference on Stability of Ships and Ocean Vehicles, Glasgow.

Paulling, J.R. and Rosenberg, R.M., 1959, "On Unstable Ship Motions Resulting from Nonlinear Coupling", Journal of Ship Research, Vol. 3, pp.36-46.

Pollard, J. and Dudebout, A., 1892, "Theorie Du Navire", Paris.

Sub-Committee on Stability and Load Lines and on Fishing Vessels Safety (SLF), 2012, "Summary of the Methodologies for the Second Generation Stability Criteria Available for SLF 54", SLF 54-WP, Annex 3.

Sub-Committee on Ship Design and Construction (SDC), 2014, "Draft Amendments to Part B of the IS Code with

Regard to Vulnerability Criteria of Levels 1 and 2 for the Parametric Rolling Failure Mode", Development of Second Generation Intact Stability Criteria – Development of Amendments to Part B of the 2008 IS Code on Towing and Anchor Handling Operations: Report of Working Group (Part 1), SDC 2/WP.4, Annex 2.

Turan, O., Ayaz, Z., Aksu, S., Kanar, J. and Bednarek, A., 2008, "Parametic Rolling Behaviour of Azimuthing Propulsion-driven Ships", Ocean Engineering, 35(13), pp. 1339-1356.

Requirements for Computational Methods to be Used for the IMO Second Generation Intact Stability Criteria

William Peters, *USCG Office of Design and Engineering Standards* william.s.peters@uscg.mil

Vadim Belenky, *Naval Surface Warfare Center Carderock Division*, vadim.belenky@navy.mil

Sotirios Chouliaras, *National Technical University of Athens*, sotchouliaras@gmail.com

Kostas Spyrou, National Technical University of Athens, k.spyrou@central.ntua.gr

ABSTRACT

Practical implementation of the second generation of IMO intact stability criteria is not possible without formulation of clear requirements for numerical or other computational methods. Probably, the highest priority should be given to the second-level vulnerability criteria. The first-level is simple enough and, as such, requirements may not be needed or will be obvious based on standard naval architectural practices. While scientifically mature, the application of numerical methods in the second-level may be more difficult as not all of these methods are familiar to practicing naval architects including those employed with administrations and classification societies. This paper focuses on requirements for use of the numerical method for the second-level vulnerability criteria for the parametric roll stability failure mode. Criteria for other modes of stability failure may have similar concerns. Use of a numerical solution of differential equations may be a good way to compute nonlinear ship motions. However, to ensure consistency of its application (i.e, results are reliably repeatable for the same ship in the same condition), all necessary parameters (such as the time increment, the number of steps, the initial conditions, etc.) must be explicitly defined. Further, special attention needs to be given to a ship response on very large waves, for which special procedures may be needed. Since the differential equation is nonlinear, the response to a very large excitation may be chaotic. Also, if capsized equilibrium is not modeled, special measures must be taken to prevent run-time related to a very large, unrealistic roll response.

Key Words: *IMO Second Generation Intact Stability Criteria, Parametric Roll*

1. INTRODUCTION

The development of the second generation IMO intact stability criteria has been an intense multi-year effort. Recognizing the fact that stability failure may be caused by different physical mechanisms, different modes of stability failure are explicitly considered in the new criteria:

- Restoring arm variation problems, such as parametric excitation and pure loss of stability;
- Stability under dead ship condition, as defined by SOLAS regulation II-1/3-8; and
- Maneuvering related problems in waves, such as broaching-to;
- Excessive accelerations (SLF 53/19, paragraph 3.28).

This development was partially motivated by the appearance of novel hull forms that renewed interest in dynamic stability, (see e.g. France, *et al*. 2003). As a result, the emphasis was made on adequate reflection of physics,

making new criteria based on performance (Belenky, *et al* 2008). This means that the assessment is based on hull geometry and physics of stability failure rather than past experience with similar ships.

The multi-tiered structure of new criteria addresses the potential complexity of the application of the new criteria. The first-level vulnerability check is very simple and quick, but conservative. If vulnerability to a particular stability failure mode is determined not to occur, no further assessments are needed. If not, then a more detailed, but less conservative analysis follows, which is the second-level vulnerability assessment.

The IMO Sub-committee on Ship Design and Construction, at its 2nd Session, finalized the first three elements of the criteria:

- Draft Amendments to Part B of The 2008 IS Code with Regard to Vulnerability Criteria of Levels 1 And 2 for the Pure Loss of Stability Failure Mode (Annex 1 of SDC 2/WP.4);
- Draft Amendments to Part B of The 2008 IS Code with Regard to Vulnerability Criteria of Levels 1 And 2 for the Parametric Rolling Failure Mode (Annex 2 of SDC 2/WP.4);
- Draft Amendments to Part B of The 2008 IS Code with Regard to Vulnerability Criteria of Levels 1 And 2 for the Surf-Riding / Broaching Failure Mode (Annex 3 of SDC 2/WP.4).

These documents describe the criteria, standards and contain general requirements for the calculation methods. The explanatory notes are expected to be developed to ensure uniform interpretations and application of the new criteria. The technical background of these criteria is described in Peters, *et. al.* (2011). A significant amount of information is being prepared for the explanatory notes, see SLF 53/3/3, Annexes 17, 19, 33, 34 of SDC 2/INF.10, Sections 2.1, 3.1 and 4.1 of Belenky, *et al*. (2011) and Peters, *et al*. (2014). The particular objective of this paper is to contribute towards the explanatory notes for second-level vulnerability assessment of the parametric roll stability failure mode.

2. MAXIMUM ROLL ANGLE

The second check for the second-level vulnerability criteria requires calculation of the maximum roll angle resulting from parametric roll. This calculation, while not too complex, is beyond the scope of traditional naval architectural calculations; why?

The conventional way to evaluate ship motions is with the use of Response Amplitude Operators (RAO). The RAO expresses dynamic properties of a ship. Its values are the characteristics of motions, multiplied by the values of sea spectrum and summed up to yield the characteristics of motion. RAO is an element or a form of a solution to the linear ship motion equation in waves.

The term “linear ship motion equation” means that the equation assumes that the motions are small and that non-linear parts of the full ship motion equation can be ignored because their effects are negligible (often because the waves are significantly longer than the ship). In particular, *GM*, which characterizes transverse stability, is used to represent roll stiffness. Indeed, stability at large roll angles cannot be characterized with *GM* alone.

The maximum angle of parametric roll also cannot be found just with *GM* even if its variation in waves is known. However, the responsibility for progressively growing roll angles, i.e. parametric roll, is associated with these *GM* variations together with a frequency ratio in which the encounter frequency is close to twice that of natural frequency (see e.g. SLF 54/3/3).

Once parametric roll motion starts, it grows to a certain maximum angle and the motion

repeats (i.e., it remains stable). This occurs because the *GZ* curve is not a straight line over the range of roll motion. As a result, the natural roll frequency changes with the increase of the roll angle (the instantaneous *GM* value also changes). Changing the roll frequency sooner or later will break the parametric roll condition because the supply of energy into roll motion will be stopped. The maximum roll angle is achieved during steady state parametric roll.

Thus, a large portion of the *GZ* curve is needed to find the maximum roll angle. While the GZ curve is known, the motion equation is no longer linear if *GZ* is included and a RAO-type of solution is no longer possible.

3. EQUATION OF MOTION

3.1 Overview of Forces Acting on a Ship

The equation of motion takes into account forces acting on the ship. The simplest mathematical model that is capable of evaluating the maximum roll angle includes four moments:

- Inertia, including added inertia (or added mass) as a part of hydrodynamic forces;
- Roll damping, which expresses energy loss from roll motions in creating waves, vortexes and skin friction;
- Roll restoring (stiffness) is modeled with the calm water *GZ* curve; the variation of stability in waves is included by *GM* represented with a sine function.
- Transverse wave forces are absent for a ship in exact following or head long-crested seas

3.2 Roll Inertia

The roll inertia of a ship as a solid body is measured by the transversal moment of inertia. In absence of ship specific data, it is recommended to assume the radius of gyration r_x as 40% of the molded breadth, *B*:

$$r_x = 0.4B \tag{1}$$

Then, the moment of inertia, I_x, is calculated as:

$$I_x = \rho \nabla r_x^2 \tag{2}$$

where ρ is the mass density of salt water; ∇ is the volume of displacement. Use of other approximation formulae may be helpful but only if the limits of their applicability are well known.

Inertial forces are proportional to accelerations. There are also hydrodynamic forces acting on a ship subject to accelerated motion that are also proportional to the accelerations. These hydrodynamic forces are usually expressed as an additional mass or a moment of inertia and referred as “added mass”. Again, in the absence of ship specific data, one can assume that the added mass in roll, A_{44}, as:

$$A_{44} = 0.25 I_x \tag{4}$$

Finally, the roll inertia is expressed as:

$$M_{IN} = (I_x + A_{44}) \cdot W_\phi \tag{5}$$

where W_ϕ is the angular acceleration in roll.

3.3 Roll Damping

Damping of roll motions is essentially a transfer of kinetic energy of a moving ship to the environment. It is a complex process, because this energy transfer occurs through different physical phenomena. Skin friction causes the layers of water nearest to the hull to move. The moving surface of the hull leads to formation of vortexes; the kinetic energy of the water moving in those vortexes is taken from the ship. Due to its motion, the ship also makes waves on the surface that also dissipate energy. The complexity of these physical phenomena is the reason why a model test is the most reliable source of information on roll damping. However, recent developments in computational fluid dynamics (CFD) holds

good promise for the availability of this computational method in the future.

In the absence of ship-specific or prototype data, the simplified Ikeda method can be recommended (Annex 3, SDC 1/INF.8). A moment of roll damping is presented in the following form:

$$M_D = (I_X + A_{44}) \cdot (\delta_1 V_\phi + \delta_3 V_\phi^3) \quad (6)$$

where δ_1 and δ_3 are coefficients computed with simplified Ikeda method and V_ϕ is the angular velocity of roll motions.

The simplified Ikeda method contains some empirical elements and, for this reason, the range of its applicability should be observed.

3.4 Roll Restoring

A proper representation of roll restoring is very important for the correct representation of parametric roll. The variation of stability in waves is a primary mechanism of development of parametric roll (an explanation is provide in SLF 54/3/3). The calculation of the instantaneous roll restoring, while straight forward, may be too complex for the level-two vulnerability check. (See the description of one of the simplest algorithms of direct calculation in Weems and Belenky, 2015). Hence, a quasi-static approach can be used instead.

The quasi-static approach means that the *GZ* curve for the ship on a wave is calculated using the "conventional" static algorithm (in which forces and moments are balanced in heave and pitch as required in Annex 2 of SDC 2/ WP.2), but the waterplane is not flat – it is determined from the intersection of a wave and the hull surface. Known also as "wave-pass" calculations, the capability for this calculation is provided by a number of commercially available hydrostatic software packages (see Figures 1 and 2). For the assessment of parametric roll, calculation of the *GZ* curve up to 180 degrees is recommended; it sets a natural maximum and prevents the numerical solution from growing too large and cause a numerical error.

Figures 1 shows the *GZ* variation in waves as a series of curves. Each curve is calculated for a particular position of the wave crest relative to the midship which results in a surface shown in Figure 2. For the intermediate values of heel angle and of the wave crest position, a bilinear or bi-cubic spline interpolation can be used. The definition of wave crest position is illustrated in Figure 3.

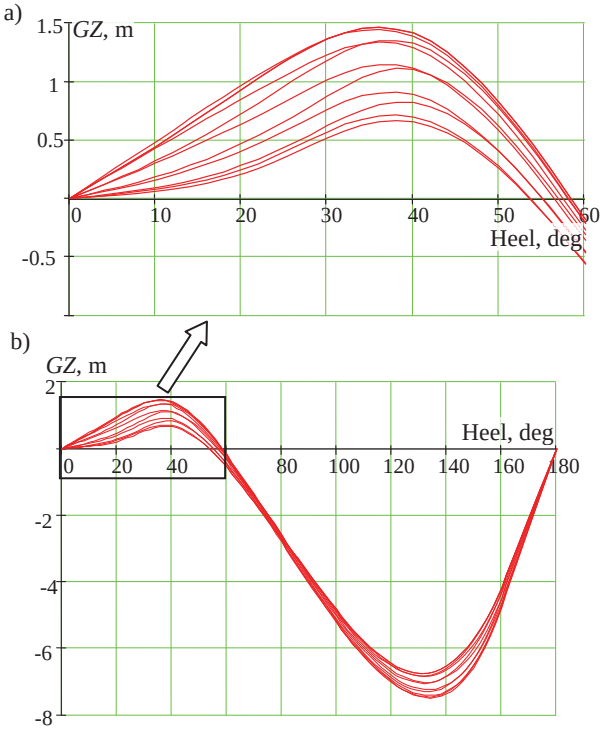

Figure 1: The *GZ* curve in waves (steepness 0.02, C11 class containership, full load) (a) positive range, (b) full range

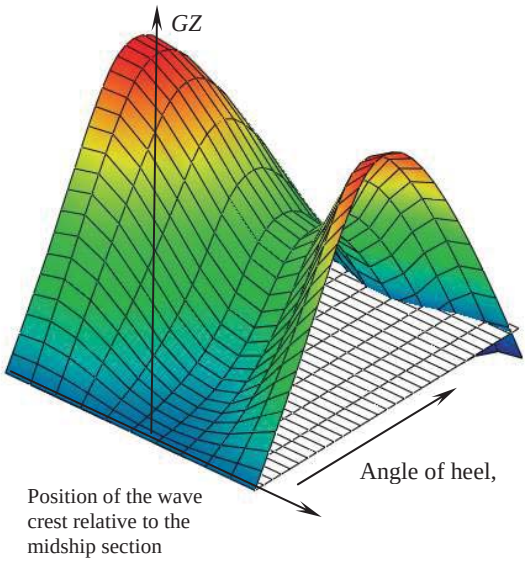

Figure 2: The *GZ* curve in waves as a surface (steepness 0.02, C11 class containership, full load)

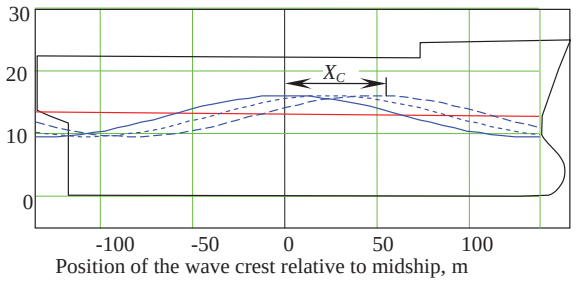

Figure 3: Definition of the position of the wave crest relative to the midship section

The position of the wave crest is a function of time:

$$X_C(t) = 0.5\lambda \sin(\omega_e t) \qquad (7)$$

where λ is the length of the wave and ω_e is the wave frequency of encounter:

$$\omega_e = \omega - \frac{\omega^2}{g} V_S \cos\beta \qquad (8)$$

where g is the gravity acceleration, β is the relative wave heading (0 degrees – following waves, 180 deg – head waves), and V_S is the forward speed in m/s. Thus, the value of the *GZ* curve in waves can be presented as a function of time and angle of heel, ϕ:

$$GZ = GZ(t, \phi) \qquad (9)$$

If, for some reason, the calculation software is not available, the *GZ* curve in a wave can be approximated using only the *GM* value that may be already available from the Level 1 vulnerability check. Indeed, as required by Annex 2 SDC 2/WP.2, the calculation of *GM* must be done with forces and moments balanced in heave and pitch. An example of the *GM* variation is shown in Figure 4:

Then, the *GZ* in waves may be approximated by the calm-water *GZ* "modulated" by the *GM* in waves

$$GZ(t, \phi) = \frac{GM(t)}{GM_0} GZ_0(\phi) \qquad (10)$$

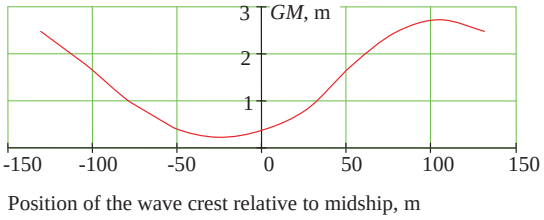

Figure 4: The *GM* value in waves as a function of wave crest position relative to midship (wave steepness 0.02, C11 class containership, full load)

Assuming that the *GZ* curve is symmetric, the total restoring moment is expressed as:

$$M_R = \text{sign}(\phi) \cdot \rho \nabla g \cdot GZ(t, |\phi|)$$
$$\text{sign}(\phi) = \begin{cases} 1 & \phi \geq 0 \\ -1 & \phi < 0 \end{cases} \qquad (11)$$

3.5 Equation of Motion and Its Solution

Following Newton's second law, the equation of roll motion is expressed as the inertial force equal to the sum of all other forces. Since the ship is in longitudinal waves, there is negligible or no direct forcing that comes from the waves:

$$M_{IN} = -M_D - M_R \tag{12}$$

In equation (12), the negative sign is inserted because both damping and restoring forces are directed against the roll motion or the rate of motion. The equation of roll motion can be re-written with each force as a function of motion parameters or time:

$$M_{IN}(W_\phi) + M_D(V_\phi) + M_R(t,\phi) = 0 \tag{13}$$

Equation (13) relates the roll motion with the roll rate and the angular roll acceleration. These quantities are related through differentiation: the angular velocity is a derivative of roll and the angular acceleration is a derivative of angular velocity. Thus, equation (13) is a differential equation.

The solution of a differential equation (13) is a time history of roll motions, similar to that shown in Figure 5.

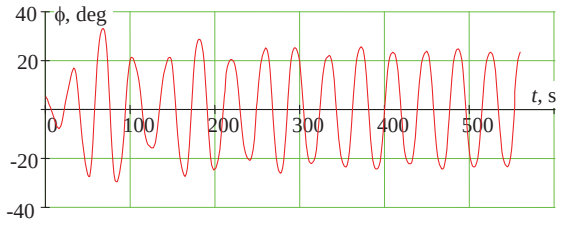

Figure 5 Time history of parametric roll

Figure 5, indeed, shows parametric roll. As the ship is sailing in longitudinal waves, there is no forcing in the transversal plane, so the observed rolling motion is a result of parametric resonance.

The equation (13) is solved by a standard program available from most numerical or engineering software packages. Numerical solvers of differential equation also are available in MS Excel in Visual Basic. To use the solver, the equation (13) must be presented in a form of a vector-valued function:

$$F\left(\begin{pmatrix}\phi\\ V_\phi\end{pmatrix}, t\right) = \frac{1}{I_X + A_{44}}\begin{pmatrix}V_\phi\\ -M_D(V_\phi) - M_R(t,\phi)\end{pmatrix} \tag{14}$$

Besides the vector-valued function (14), the solver requires initial conditions, *i.e.* values of roll angle and roll rate at the beginning (or at time step t = 0) of the calculations. The solution, as illustrated in Figure 5, was computed with assumed initial conditions (ϕ = 5 deg and V_ϕ = 0 deg/s). While the calculation can assume zero for both ϕ and V_ϕ, the development of parametric roll may not occur until a much longer duration is calculated.

To complete the inputs necessary for the calculation, two more parameters are needed: the time increment Δt and the total number of points N. These parameters can be related to the natural frequency of roll, ω_0, in calm water because a steady state parametric roll motion in longitudinal waves occurs with this frequency:

$$\omega_0 = \sqrt{\frac{\rho\nabla g \cdot GM_0}{I_X + A_{44}}} \tag{15}$$

Then, the period of the roll motion in calm water is expressed as:

$$T_0 = \frac{2\pi}{\omega_0} \tag{16}$$

The time increment Δt can be expressed in terms of the number of points per period N_{ppp}:

$$\Delta t = \frac{T_0}{N_{ppp}} \tag{17}$$

Thus, the number of points depends on the number of periods N_{per} to be reproduced:

$$N = N_{ppp} N_{per} \tag{18}$$

Practical experience recommends use of the following values:

$$N_{ppp} = 30; \quad N_{per} = 15$$

3.6 Calculation of Maximum Roll Angle

The parametric roll response has a transition from the state where the initial conditions still have an influence to the steady state where the amplitudes are similar or close to each other.

Different criteria for "closeness" can be used: relative (the difference is less than 3 - 5%) or absolute (say, less than one degree). Following this criteria, the steady state portion of the response can be extracted (see Figure 6) and the resultant maximum roll angle can be found as an average of steady state roll amplitudes.

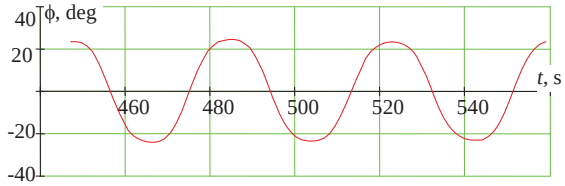

Figure 6 Steady-state portion of the roll motion in parametric resonance conditions

The steady state parametric roll is not the only possible type. If parametric roll is not possible for the given wave conditions, the response is represented by decaying roll oscillations – as shown in Figure 7. Indeed, the maximum roll angle here is the initial roll angle of 5 degrees. The response is not expected to look like a decaying sine function because of both the parametric excitation and nonlinearity of the equation (13).

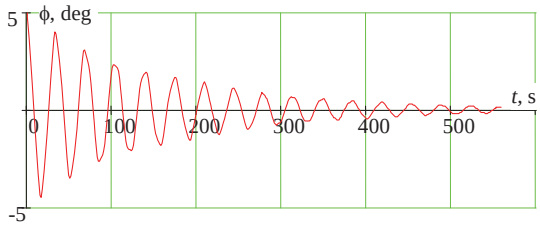

Figure 7 Roll response in absence of parametric roll

Another possible response may include "capsizing" (see Figure 8) if the *GZ* curve was computed for the entire range of 180 degrees (like in Figure 1). If the *GZ* curve is computed only for the positive stability range ($GZ > 0$), the calculation must be explicitly stopped once the roll angle exceeds the angle of vanishing stability.

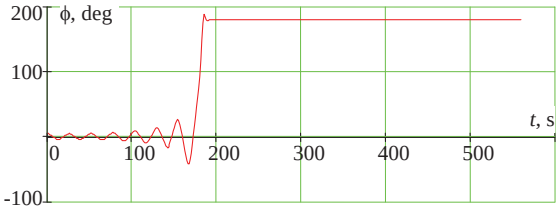

Figure 8 Roll response with parametric roll and capsizing

The mathematical model (13) is, probably, too simple to model actual capsizing, but the response, similar to that shown in Figure 8, indeed indicates a condition of strong parametric roll in which the maximum roll angle exceeds the standard level of 25 degrees as stipulated in Annex 2 of SDC 2/WP.4.

In rare cases, the user may observe response that does not stabilize. The roll amplitude may grow steadily or look like roll in irregular waves. These responses are not the result of an error, but of a known type of nonlinear behavior. In this case, the maximum achieved roll angle during N_{per} periods is used.

4. CALCULATION OF PARAMETRIC ROLL AMPLITUDE FOR A POST-PANAMAX CONTAINER SHIP

An example of a calculation of parametric roll amplitude, in compliance with the Level 2 criteria, is presented below. The investigated ship is a baby post-Panamax container ship with the characteristics as shown in Table 1:

Table 1: Main ship characteristics

Length L_{BP} (m)	238.35

Beam (m)	37.3
Depth (m)	19.6
Mean Draught (m)	11.5
Block Coefficient	0.657
GM (m)	0.84

The steady amplitude of parametric roll is calculated by using the following four methods:

a) a direct numerical solution of the non-linear differential equation of roll that is included in SDC 2/INF.10, Annex 17;
b) a numerical solution of the algebraic equation derived after applying the analytical method of averaging on the previous non-linear differential equation. (This algebraic equation is proposed in SDC 2/INF.10, Annex 17 to be used for obtaining the steady amplitude of parametric roll.)
c) a numerical solution of the non-linear roll equation used by Spyrou (2005); and
d) an analytical, closed-form, formula obtained by the method of harmonic balance, predicting the steady amplitude of parametric roll at principal resonance condition (Spyrou 2005).

The moment of inertia, I_x, and natural roll period T_0 are calculated through the roll radius of gyration by using Kato's formula, as proposed in SDC 2/INF.10-Annex 11. For the loading condition under investigation, T_0 = 39.3 s is assumed.

The linear damping coefficient is calculated by using Ikeda's method as proposed in the above IMO document, including the bilge keel component. While acknowledging that the criterion requires both linear and non-linear damping, at this stage, the comparison involves only linear damping.

The four methods use the same inertia and damping terms. Their main differences lie in the representation of the restoring terms. The SDC model (methods a and b above) is in the following form:

$$I_X\ddot{\phi} + B_{44}\dot{\phi} + mgGZ = 0 \qquad (19)$$

$$GZ = GM_0\phi + l_3\phi^3 + l_5\phi^5 + GZ_W \qquad (20)$$

$$GZ_W = GM_{mean}\phi + GM_{amp}\cos\omega_e t\left\{1-\left(\frac{\phi}{\pi}\right)^2\right\}\phi$$

where I_x is roll moment of inertia including added moment of inertia; B_{44} is linear damping coefficient; m is the ship's displacement; g is gravitational acceleration; l_3, l_5 are third and fifth order coefficients of GZ curve fit; ω_e is the encounter frequency; GM_{amp} is half the difference between the maximum and minimum value of GM on the span of a wave; GM_0 is the initial metacentric height in calm water. GM_{mean} is the mean of metacentric height variation on the span of the wave which, given the expressions in equation (20), and is interpreted to be the difference between the mean value of the GM in waves and the GM in calm water.

On the other hand, methods c) and d) (above) from Spyrou (2005) model parametric roll as follows:

$$\ddot{\phi} + 2\zeta\omega_0\dot{\phi} + \omega_0^2[1-h\cos(\omega_e t)]\phi - c_3\omega_0^2\phi^3 - c_5\omega_0^2\phi^5 = 0 \qquad (21)$$

where ζ is the damping ratio, ω_0 is roll natural frequency, c_3, c_5 are third and fifth order restoring coefficients and $h = GM_{amp}/GM_{mean}$.

The two differential equations for parametric roll, equations (19) and (21), are not identical and, therefore, the solutions are not expected to replicate on each other completely.

Roll amplitude is calculated for ten different cases where the ship is under the effect of following waves with $\lambda = L_{BP}$ and ten different heights with $H_j = 0.01jL$, where j = 1, 2,..., 10, as requested in SDC 2/INF.10, Annex 17. This leads to waves some of which are extremely steep and with extremely low probabilities of encounter. For each wave

height, hydrostatic calculations of GM_{mean} and GM_{amp} are carried out by using the well-known commercial software MAXSURF. The ratio of the calculated GM_{amp} to GM_{mean}, together with the corresponding wave heights, are shown in Table 2.

The encounter frequency for the ship when sailing in following waves of length equal to the ship length and with the design speed of 21 knots is 0.224 rad/s. This leads to a frequency index $a = 4\omega_0^2/\omega_e^2 = 2.04$, which is far to the right of the principal resonance value $a = 1$. The analytical manipulations that have been applied in the context of SDC and related literature on the parametric roll differential equation assume a condition very near to exact principal resonance. This may lead sometimes to questionable results if the detuning is large. Because the wave length is fixed to ship length, this discrepancy (i.e., a large difference between the frequency index and the principal resonance value) is quite likely to be present whenever a large ship is tested.

Table 2: Wave Height, Probability of Occurrence, and Ratio of GM_{amp} to GM_{mean}

Wave Length λ=238.35m			
N	Wave Height H(m)	$\frac{GM_{amp}}{GM_{mean}}$	Probability W
1	2.384	0.703	0.2367
2	4.767	1.155	0.1196
3	7.151	1.422	0.0336
4	9.534	1.571	0.006146
5	11.918	1.624	0.0009333
6	14.3	1.632	0.0001025
7	16.685	1.656	0
8	19.068	1.673	0
9	21.452	1.737	0
10	23.835	1.815	0

As said in SDC 2/INF.10, Annex 11, the roll amplitude is calculated by a numerical solution of an algebraic equation deduced through the averaging method. This equation is repeated below for linear damping only:

$$\left(\frac{8\pi^2\omega_e\alpha}{(2\pi^2-A^2)\omega_0^2}\right)^2+\left(\frac{6A^2-8\pi^2}{4(\pi^2-A^2)}\frac{GM_{mean}}{GM_0}+\frac{8\pi^2-5\pi^2A^4l_5-6\pi^2A^2l_3}{4(\pi^2-A^2)}+\frac{8\pi^2\omega_e^2}{4(\pi^2-A^2)\omega_0^2}\right)^2=\left(\frac{GM_{amp}}{GM_0}\right)^2 \quad (22)$$

where A is the roll amplitude and α is the linear damping term. Because the analytical solution of equation (22) is not provided in SDC 2/INF.10, Annex 17, the implementation of a numerical scheme to determine the solution cannot be avoided. However, since (22) is nonlinear with respect to amplitude A, more than one solution can exist. Therefore, guidance is required on the process of how to ensure that a solution identified is the correct one for use in the criterion. In general, a numerical calculation performed directly on the differential equation (19), which produces automatically a stable solution, is in many respects preferable to a calculation performed on the averaged form of equation (22), which produces also unstable solutions.

For completeness, the steady roll amplitude of the analytical solution of Spyrou (2005) is given in equation (23) also:

$$A^2=-\frac{3c_3}{5c_5}\pm\left(\left(\frac{3c_3}{5c_5}\right)^2-\frac{8}{5c_5}\left(\frac{1}{\alpha}-1\pm\sqrt{\frac{h^2}{4}-\frac{4k^2}{\omega_0^2\alpha}}\right)\right)^{0.5} \quad (23)$$

where k is a linear damping coefficient and $\alpha = 4\omega_0^2/\omega_e^2$

In Figure 9, the results obtained by each method, for the ten different wave heights discussed earlier, are shown. As each wave height corresponds to a specific value of GM_{amp}/GM_{mean}, this ratio is selected for the horizontal axis. The numerical simulations are initiated from an assumed roll angle of 0.01 rad (0.57 degrees).

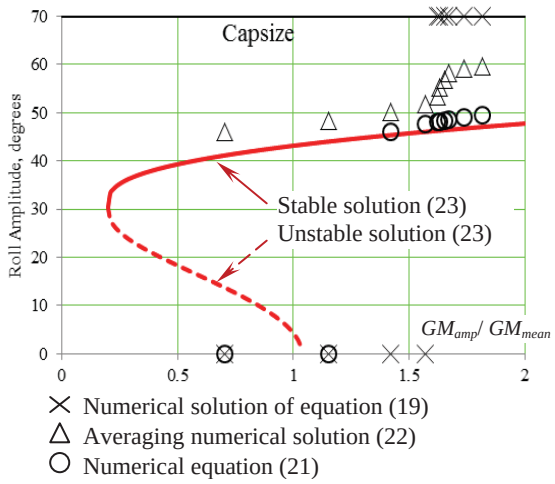

Figure 9: Parametric Rolling Amplitude for ten different wave heights

According to the analytical solution curve appearing in Figure 9, there are two possible responses by the ship: either a stable parametric resonance (continuous curve), similar to what was shown in Figure 6; or a decaying rolling that eventually leads to the upright position (as shown in Figure 7). Unstable solutions represented by the dashed curve cannot be physically realized. Nevertheless, they play the role of establishing a boundary between the coexisting solutions of zero and finite amplitude.

Figure 9 shows that all methods calculate a roll amplitude either close to the curve of parametric resonance or to the x-axis of decaying rolling. The numerical solutions of equation (19) for roll amplitude grow to infinity for the greater values of wave height which can be interpreted as a capsize event in mathematical terms.

When the solutions of parametric resonance and decaying roll coexist, the SDC method that uses equation (19) gives conflicting results. Also, the value of the parameter GM_{amp}/GM_{mean}, after which only parametric resonance occurs, is different for each method. These inconsistencies may lead to important differences between the index values of the second-level vulnerability check for parametric roll.

For greater values of wave height (and subsequently of the parameter GM_{amp}/GM_{mean}), the response becomes highly non-linear. One such example is shown in Figure 10 which corresponds to the numerical solution of equation (21) for H = 21.45m.

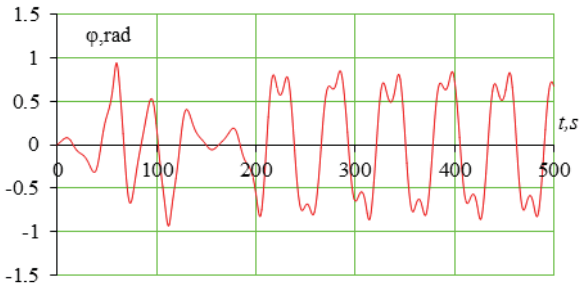

Figure 10: Highly non-linear parametric roll response

According to Figure 10, steady parametric rolling with very large amplitude (about 50 degrees) occurs. This essentially means that capsize is highly likely although the solution remains theoretically bounded. On the other hand, equation (19) for the same wave height detects capsizing, as can be seen from Figure 11. While the standard level of 25 degrees as stipulated in Annex 2 of SDC 2/WP.4 is exceeded in both cases, same order roll equations with similar terms show different dynamic characteristics for large waves.

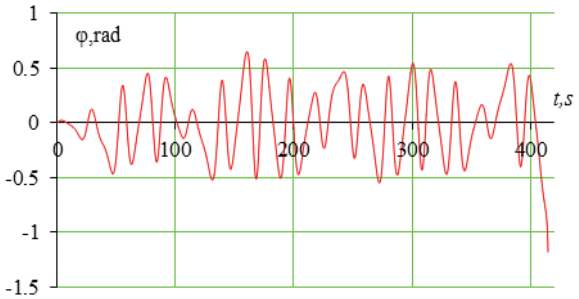

Figure 11: Non-linear parametric rolling that leads to capsize (19)

5. CONCLUSIONS

The second generation intact stability criteria presents new approaches for the assessment of ship stability failure. To perform these assessments, calculation methods are used that are not commonly used by practicing naval architects.

The equation of roll motion for the second check in the second-level of vulnerability criteria for parametric rolling is a differential equation. While the form of this equation may not be the same (see equations (19) and (21) above), a reliable solution of each requires a process to be followed if the solutions are to be replicated. The results show that such reliable solutions can be determined provided that the boundaries of application are respected.

6. REFERENCES

Belenky, V., J. O. de Kat and Umeda, N., 2008, "Towards Performance-Based Criteria for Intact Stability". Marine Tech., Vol. 45 No 2, pp:101–123.

Belenky, V., Bassler, C.C. and Spyrou K.J., 2011, Development of Second Generation Intact Stability Criteria, Naval Surface Warfare Center Carderock Division Report NSWCCD-50-TR-2011/065.

France, W. M, Levadou, M., Treakle, T. W., Paulling, J. R., Michel, K. and Moore, C., 2003, "An Investigation of Head-Sea Parametric Rolling and its Influence on Container Lashing Systems". Marine Tech., Vol 40, No 1, pp:1–19.

IMO SDC 2/INF.10, 2014, Second Generation Intact Stability Criteria. Information Collected by Correspondence Group on Intact Stability, Submitted by Japan, London, UK

IMO SDC 2/WP.2, 2015, Development of Second Generation Intact Stability Criteria. Report of the Working Group, London, UK.

IMO SDC 1/INF.8, 2013, Second Generation Intact Stability Criteria. Information Collected by Correspondence Group on Intact Stability, Submitted by Japan, London, UK

IMO SLF 54/3/3 2011, Summary of Research into Stability Failures Modes and associated Criteria Development, London, UK

IMO SLF 53/19, 2011, Report to Maritime Safety Committee, London, UK.

Peters, W., Belenky, V., Bassler C., Spyrou, K., Umeda, N., Bulian, G. and Altmayer, B., 2011, "The Second Generation of Intact Stability Criteria An Overview of Development", SNAME Trans. Vol. 119.

Peters, W., Belenky, V. and Spyrou, K., 2014 "Regulatory Use of Nonlinear Dynamics: An Overview" Proc. 14th Intl. Ship Stability Workshop, Kuala Lumpur, Malaysia, pp. 28-37

Spyrou, K., 2005, "Design Criteria for Parametric Rolling", Oceanic Engineering International, Vol. 9, No 1, pp. 11-27

Weems, K. and Belenky, V., 2015, "Rapid Ship Motion Simulations for Investigating Rare Stability Failures in Irregular Seas" Proc. 12th Intl. Conf. on Stability of Ships and Ocean Vehicles (STAB 2015), Glasgow, UK.

This page is intentionally left blank

Session 10.2 – NAVAL SHIP STABILITY

Analytical Study of the Capsize Probability of a Frigate

Aerodynamics Loads on a Heeled Ship

Validation of Time Domain Panel Codes for Prediction of Large Amplitude Motions of Ships

This page is intentionally left blank

Proceedings of the 12th International Conference on the Stability
of Ships and Ocean Vehicles, 14-19 June 2015, Glasgow, UK.

Analytical Study of the Capsize Probability of a Frigate

Frédéric Le Pivert, *Research Institute of the French Naval Academy*, *Brest, France*
frederic.le pivert@ecole-navale.fr

Abdelkader Tizaoui, *Institut Polytechnique des Sciences avancées, DRI, Paris, France*

Radjesvarane Alexandre, *ENSAM, Paristech, Paris, France*

ean-Yves Billard, *Research Institute of the French Naval Academy, Brest, France*

ABSTRACT

The roll motion for a ship in a transverse sea can be represented by a one degree of freedom model. Equations are derived to write analitycally the probability density function of roll angle, roll speed and roll excitation moment. Also a capsize cirterium is shown to have a whole process for a capsize probability calculation.

Keywords: roll motion, capsizing, Fokker-Planck-Kolmogorov equation, characteristic method.

1 INTRODUCTION

Ship stability is one of nowadays worries. The old criteria that were defined in the first part of the 20th century are based on static sta-bility. The new generation of criteria should be based on dynamical stability. These criteria are not simple evaluation but should be also quan-tification of the risks for a ship on any sea.

All ships are different but their behaviours on sea could be modelled with the same type of equations. Here the problem is limited to a ship sailing in transverse sea. It is assumed that in this case, roll motion could be represented by a one degree of freedom (1-DOF) model. So the goal of the paper is to solve the Fokker-Plank-Kolmogorov equation (FPK) associated to the dynamical problem and to obtain the probabil-ity density function of the three following vari-ables: roll angle, roll speed and roll excitation. The solution obtained has been tested on realis-tic situation. A capsize criterium is also added to have a full way to obtain a capsize probability.

Several methods have already been suggested to estimate large roll angles and stability fail-ures. The Peak Over Threshold Method (Mc-Taggart 2000) and Envelope Peak Over Thresh-old Method (Belenky & Campbell 2011) use statistical extrapolation on relatively small am-plitudes to find the largest motions probabil-ity (Campbell 2014). The extrapolation tech-nique is also a real issue for roll motion proba-bility. One way is the split-time method. The split-time method divides the problem in two

parts considering the ship behavior is different whether the roll angle is below or above a given threshold. The idea is to fit only the largest an-gles distribution (Belenky, 2014) and could be applicated for both Peak Over Threshold and Envelope Peak Over Threshold methods.

Melnikov methods have also been largely discussed in the 1990s and in the 2000s (Hsieh et al. 1994, Scolan, 1997, Jiang et al. 2000, McCue & Troesch 2005). Melnikov methods can deter-mine properly whether a sea state is dangerous or not. Markov methods use the dynamics of the system to find the complete expression of the roll motion probability by solving an FPK. The present paper uses one of these methods.

2 MATHEMATICAL ANALYSIS

2.1 Markov Methods

The aim of this group of methods is to consider roll motion as a Markovian process. In their paper Roberts and Vasta (Roberts & Vasta 2000) describe the time evolution of the energy of roll motion with a white noise as system perturbation.

More recent methods preserve the roll mo-tion equation and consider the perturbation as a filtered Gaussian white noise according to Spanos ARMA filters theory (Spanos 1983). This method was applied to uncoupled roll mo-tion by Francescutto and Naito (Francescutto & Naito 2004) and the method was fully developed by Su and Falzarano (Su & Falzarano 2011). This method overcomes the difficulty to deal with a noise which does not have any remark-able property. On the other hand the system becomes larger and new variables appear with-out any physical sense. By using this method, the FPK of the complete system for both old and new variables can be obtained. These previous authors derive numerically the equation.

In the present paper the FPK is derived analytically. This derivation needs in return some simplification of dynamics.

2.2 Derivation of the Methods

Consider the following adimensioned roll motion equation:

$$\ddot{\phi} + \lambda_1\dot{\phi} + \lambda_2\,\dot{\phi}|\dot{\phi}| + c(\phi) = f(t), \qquad (1)$$

where:

- φ is the roll angle,
- t is the time,
- ẏ means the time derivative of the quantity y,
- λ_1 is the linear damping coefficient,
- λ_2 is the quadratic damping coefficient,
- c is the restoring moment,
- f is the external random moment.

The equation (1) is the expression of the principle of dynamics applied to roll motion. To obtain (1), all the moments where divided by $I_{xx}\omega_0^2$, where I_{xx} is the total inertia in roll of the ship and ω_0 is the natural roll frequency of the ship.

The term f is supposed to be a filtered white noise. The considered filter is defined by the following equation:

$$\ddot{Z} + V_1\dot{Z} + V_0 Z = \gamma W, \tag{2}$$

where V_1, V_0, γ are constant. W is a Gaussian white noise. so it leads to the following system:

$$\begin{cases} \dot{x_1} = x_2, \\ \dot{x_2} = -\lambda_1 x_2 - \lambda_2 x_2|x_2| - c(x_1) + x_3, \\ \dot{x_3} = x_4, \\ \dot{x_4} = -V_1 x_4 - V_0 x_3 + \gamma W. \end{cases} \tag{3}$$

In (3), we have:

- $\varphi = x_1$,
- $\dot{\phi} = x_2$,
- $f = x_3$.

The system (3) is rewritten with vectors:

$$\dot{X} = F(X) + GW. \tag{4}$$

This can lead to the Fokker-Planck-Kolmogorov equation:

$$\partial_t P = -\nabla.(P\,F) + \frac{\gamma^2}{2}\partial_{x_4} P, \tag{5}$$

where P is the probability density function of the random variable X.

Remark: According to (Francescutto & Naito 2004), a 4th order-filter at least should be ap-plied. The present filter has a smaller order filter only to write an analytical formula for P . Here is one simplification to get the formula.

To integrate (5), it was chosen to take the space Fourier transform of this equation. Be-cause F_2 ($F_2 = -\lambda_1 x_2 - \lambda_2 x_2|x_2| - c(x_1) + x_3$) Fourier transform has no analytical expression, new hypotheses should be made:

- linearization around equilibrium $c(x_1) = c_i(x_1 - x_{eq})$,
- damping linearization, $\lambda_2 = 0$,

where c_i is the restoring coefficient around a considered point of equilibrium x_{eq}, x_{eq} is defined by $c(x_{eq}) = 0$. Here it is chosen to derive (5) assuming the hypotheses. It is assumed a boat has three heel angles of equilibrium on each side: $\varphi = 0$, $\varphi = \pm\varphi_V$, $\varphi = \pm\pi$. Choosing a lineariza-tion around these points is considering $c(x_1)$ as a 5th order polynom. The form of c is given by (6):

$$c(x_1) = C x_1 (x_1^2 - \varphi_V^2)(x_1^2 - \pi^2). \tag{6}$$

This method is equivalent to the piece-wise linearization method (Belenky 1993). The difference is: in the present method the roll motion is supposed to be fully forced by the external moment, whereas in (Belenky 1993) the roll angle is considered as a solution of (1). Using that method, a transition solution calculated by considering f = 0 should be taken into account.

The Fourier transform of (5) is:

$$\begin{aligned} \partial_t \hat{P} = \Big(& c_i \xi_2 \partial_{\xi_1} + (\xi_1 - \lambda_1 \xi_2)\partial_{\xi_2} \\ & + (\xi_2 - V_0 \xi_4)\partial_{\xi_3} \\ & + (\xi_3 - V_1 \xi_4)\partial_{\xi_4} \Big)\hat{P} + \frac{\gamma^2}{2}\xi_4^2 \hat{P} \end{aligned} \tag{7}$$

The equation (7) is a transport equation. So if we know an integrable solution $\hat{P}_0(\xi_1, \xi_2, \xi_3, \xi_4)$ at t = 0, there exists an integrable solu-tion $\hat{P}(t, \xi_1, \xi_2, \xi_3, \xi_4) = \hat{P}_t(\xi_1, \xi_2, \xi_3, \xi_4)$ with the same measure at every $t > 0$. Fourier transform make this property true for P solution of (5). Here to obtain (7) $\hat{P}$ has been supposed square-integrable. So P is square-integrable.

A method of characteristics is ap-plied: characteristic curves are curves

$s \rightarrow (t(s), \xi_1(s), \xi_2(s), \xi_3(s), \xi_4(s))$ who check the following condition:

$$\begin{cases} \frac{dt}{ds} = 1, \\ \frac{d\xi_1}{ds} = c_i\xi_2, \\ \frac{d\xi_2}{ds} = \lambda_1\xi_2 - \xi_1, \\ \frac{d\xi_3}{ds} = V_0\xi_4 - \xi_2, \\ \frac{d\xi_4}{ds} = V_1\xi_4 - \xi_3. \end{cases} \quad (8)$$

So t = s and

$$\begin{pmatrix} \dot{\xi}_1 \\ \dot{\xi}_2 \\ \dot{\xi}_3 \\ \dot{\xi}_4 \end{pmatrix} = \underbrace{\begin{pmatrix} 0 & c_i & 0 & 0 \\ -1 & \lambda_1 & 0 & 0 \\ 0 & 1 & 0 & V_0 \\ 0 & 0 & -1 & V_1 \end{pmatrix}}_{A} \begin{pmatrix} \xi_1 \\ \xi_2 \\ \xi_3 \\ \xi_4 \end{pmatrix} \quad (9)$$

The solution of (9) is written this way:

$$\begin{pmatrix} \xi_1 \\ \xi_2 \\ \xi_3 \\ \xi_4 \end{pmatrix} = \sum_{k=1}^{4} \kappa_k W_k e^{w_k s}, \quad (10)$$

where w_k are the eigenvalues of A, W_k are the eigenvectors of A and κ_k are determined by ini-tial conditions.

Remark: Now the choice for a second order filter can be justified. If a larger order filter had been chosen, this would have lead to a larger ma-trix A. Then it becomes impossible to calculate analytically the eigenvalues and the eigenvectors of A.

$$\begin{aligned} w_1 &= \frac{\lambda_1 + \sqrt{\lambda_1^2 - 4c_i}}{2}, \\ w_2 &= \frac{\lambda_1 - \sqrt{\lambda_1^2 - 4c_i}}{2}, \\ w_3 &= \frac{V_1 + \sqrt{V_1^2 - 4V_0}}{2}, \\ w_4 &= \frac{V_1 - \sqrt{V_1^2 - 4V_0}}{2}, \end{aligned} \quad (11)$$

and

$$\mathbf{W}_1 = \begin{pmatrix} -w_2(w_1(\lambda_1 - V_1) - c_i + V_0) \\ w_1(\lambda_1 - V_1) - c_i + V_0) \\ V_1 - w_1 \\ 1 \end{pmatrix}, \quad (12)$$

$$\mathbf{W}_2 = \begin{pmatrix} -w_1(w_2(\lambda_1 - V_1) - c_i + V_0) \\ w_2(\lambda_1 - V_1) - c_i + V_0) \\ V_1 - w_2 \\ 1 \end{pmatrix}$$

$$W_3 = \begin{pmatrix} 0 \\ 0 \\ w_3 \\ 1 \end{pmatrix}, W_4 = \begin{pmatrix} 0 \\ 0 \\ w_4 \\ 1 \end{pmatrix} \quad (13)$$

After calculation, a formulation of $\xi_1(s)$, $\xi_2(s)$, $\xi_3(s)$, $\xi_4(s)$ using $\xi_1(0)$, $\xi_2(0)$, $\xi_3(0)$, $\xi_4(0)$ is obtained. Along the characteristic curves, it can be written:

$$\frac{d\hat{P}}{ds} = \frac{\partial\hat{P}}{\partial t}\frac{dt}{ds} + \frac{\partial\hat{P}}{\partial\xi_1}\frac{d\xi_1}{ds} + \frac{\partial\hat{P}}{\partial\xi_2}\frac{d\xi_2}{ds} + \frac{\partial\hat{P}}{\partial\xi_3}\frac{d\xi_3}{ds} + \frac{\partial\hat{P}}{\partial\xi_4}\frac{d\xi_4}{ds} = -\frac{\gamma^2}{2}\xi_4^2\hat{P} \quad (14)$$

The only solution is:

$$\hat{P}(s) = \hat{P}(0)\exp\left(-\frac{\gamma^2}{2}\int_0^s \xi_4^2(u)du\right) \quad (15)$$

As the expression $\int_0^s \xi_4^2(u)du$ is difficult to understand written in this way, ξ_i are replaced by $\zeta_i = \kappa_i e^{w_i s}$.

So it leads to:

$$\xi_4 = \zeta_1 + \zeta_2 + \zeta_3 + \zeta_4. \qquad (16)$$

Let express the solution as a function of t:

$$\hat{P}_t \begin{pmatrix} \xi_1 \\ \xi_2 \\ \xi_3 \\ \xi_4 \end{pmatrix} = \hat{P}_0 \begin{pmatrix} \xi_1(0) \\ \xi_2(0) \\ \xi_3(0) \\ \xi_4(0) \end{pmatrix} .e^{\Psi} \qquad (17)$$

where $\xi_1(0)$, $\xi_2(0)$, $\xi_3(0)$, $\xi_4(0)$ could be expressed with ξ_1, ξ_2, ξ_3, ξ_4 and t.

$$\Psi = -\frac{\gamma^2}{2}\left(\begin{array}{c} \frac{\zeta_1^2}{2w_1} + \frac{\zeta_2^2}{2w_2} + \frac{\zeta_3^2}{2w_3} + \frac{\zeta_4^2}{2w_4} \\ + \frac{2\zeta_1\zeta_2}{w_1 + w_2} + \frac{2\zeta_1\zeta_3}{w_1 + w_3} + \frac{2\zeta_1\zeta_4}{w_1 + w_4} \\ + \frac{2\zeta_2\zeta_3}{w_2 + w_3} + \frac{2\zeta_2\zeta_4}{w_2 + w_4} + \frac{2\zeta_3\zeta_4}{w_3 + w_4} \end{array} \right) \qquad (18)$$

With (17) a complete formula for the time depending probability density function of the random variables ξ_1, ξ_2, ξ_3, ξ_4 is given at every time t. The function Ψ depends on the random vari-ables (18) and describes an ellipse. The term $\hat{P}_0$ is a displacement of the properties at t = 0 along the characteristic curves.

So the solution of (5) is:

$$P_t \begin{pmatrix} x_1 \\ x_2 \\ x_3 \\ x_4 \end{pmatrix} = P_0 \begin{pmatrix} x_1(0) \\ x_2(0) \\ x_3(0) \\ x_4(0) \end{pmatrix} * \chi \begin{pmatrix} x_1 \\ x_2 \\ x_3 \\ x_4 \end{pmatrix}, \qquad (19)$$

where $x_1(0)$, $x_2(0)$, $x_3(0)$, $x_4(0)$ can be expressed with x_1, x_2, x_3, x_4 and t and $*$ means the convolution product. The function χ is the in-verse Fourier transform e^{Ψ} and is a gaussian probability law for random variables y_1, y_2, y_3, y_4 which are derived from x_1, x_2, x_3, x_4 with an au-tomorphism. The following initial condition are apllied:

$$P_0 \begin{pmatrix} x_1(0) \\ x_2(0) \\ x_3(0) \\ x_4(0) \end{pmatrix} = \delta \begin{pmatrix} x_1 \\ x_2 \\ x_3 \\ x_4 \end{pmatrix}, \qquad (20)$$

where δ is the standard Dirac distributon.

So the final solution of (5) is:

$$P_t \begin{pmatrix} x_1 \\ x_2 \\ x_3 \\ x_4 \end{pmatrix} = \chi \begin{pmatrix} x_1 - x_1(0) \\ x_2 - x_2(0) \\ x_3 - x_3(0) \\ x_4 - x_4(0) \end{pmatrix} \qquad (21)$$

In this way, the solution does not depend on time.

The solution has a gaussian form for the 4 variables. This result is in accordance with (Belenky 1993) considering only forced oscillations.

3 RESULTS

3.1 Method

All results were obtained by generating a large number of simulations in which the sea state remain the same. The software used for the simulation is FREDYN. FREDYN calculate the 6-DOF dynamics of a given boat with the potential flow assumption. Here the boat used for simulation is the F70-frigate of the French Navy. The case tested is the frigate in trans-verse sea with 0 or 6 knots forward speed.

3.2 Time-independance Verification

The time-independance of the probability is tested with long simulations. The hypotheses of calculation used in the first part are not taken into account.

For a serie of 50 simulations lasting 5 hours in a sea state defined by a Pierson-Moskowitz spectrum with a significant wave height H_S = 12.4m and a mean wave period T_P = 12.7s, the max-imum of the roll angle for each simulation have been situated in time during the simulation. The number of maxima occuring before a certain time is counted and represented in Figure 1. The frigate's forward speed is 6 knots.

time of the maximum	number of maxima
< 2000s	8
< 4000s	11
< 6000s	23
< 8000s	27
< 10000s	31
< 12000s	33
< 14000s	37
< 16000s	46
< 18000s	50

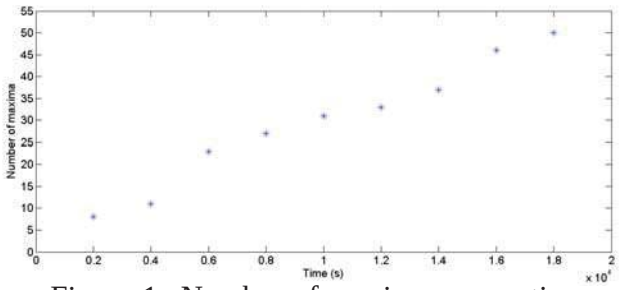

Figure 1: Number of maxima versus time

The number of maxima is linearly growing, so the probability associated to roll motion is time-independant.

3.3 Probability Density Function Esitimation

A direct estimation of the probability density function has been calculated for 0 forward speed frigate in 5 sea states. The estimation is made according that over a long time the probability is

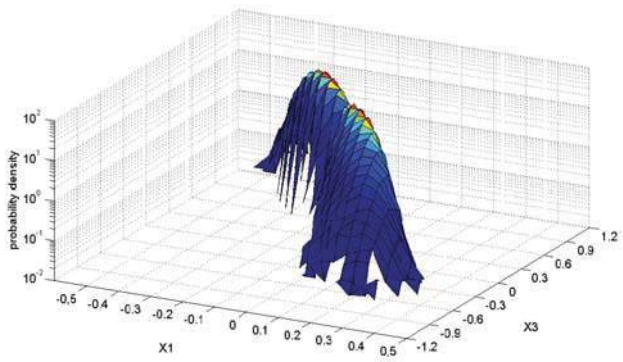

Figure 2: Conditional probability density function $P(x_1, x_2 = 0|x_3)$

stable. The first results showed a similar shape for the probability density function between sea states. To compare the sea states, Bayes' for-mula was used so:

$$P(x_1, x_2, x_3) = P(x_1, x_2|x_3).P(x_3), \qquad (22)$$

where | means knowing. The conditonal probability is supposed to be normal. For representa-tion, the results are taken at $x_2 = 0$. Figure 2 show a prefered axis of the (x_1, x_3)-plan. A for-mula is given with variable change: $Y_1 = kx_1+x_3$ and $Y_2 = kx_3 - x_1$. The variable Y_2 is describ-ing the evolution along the axis and Y_1 describes the evolution perpendicularly to the axis. The formula for $P(x_1, x_2 = 0|x_3)$ is of the following form:

$$P(x_1, x_2 = 0|x_3) = \exp\left(-\begin{pmatrix} h_0 + h_1Y_1 + h_2Y_1^2 \\ +g_1Y_2 + g_2Y_2^2 \\ +g_3Y_2^3 + g_4Y_2^4 \end{pmatrix}\right). \qquad (23)$$

The parameters k, h_0, h_1, h_2, g_1, g_2, g_3, g_4 are calculated for 5 different sea states and the re-sults are written in the following table.

H_S	T_P	h_0	h_1	h_2	k
9.270m	12.36s	-4.595	16.26	418.0	-0.4058
9.465m	12.57s	-5.981	15.96	422.6	-0.4141
9.660m	12.79s	-3.557	17.08	395.7	-0.4238
9.758m	12.90s	-3.963	15.68	418.6	-0.4256
10.448m	12.40s	2.994	16.96	401.5	-0.4140

H_S	T_P	g_1	g_2	g_3	g_4
9.270m	12.36s	0.8710	-10.680	-6.489	41.45
9.465m	12.57s	0.6514	-9.714	-4.792	34.70
9.660m	12.79s	0.5147	-9.380	-3.882	31.26
9.758m	12.90s	0.5350	-9.441	-3.870	31.63
10.448m	12.40s	0.1893	-2.475	-1.229	7.584

The parameters h_1, h_2, k have really similar values for all the sea state. For the other parameters, the last sea state (H_S = 10.448m, T_P = 12.40s) gives values contrastive in the other sea states. The significative wave height of the last sea state is significantly higher than the others and, in the same time, the mean wave period remains the same. This leads to a much more dangerous sea state and ex-plains why this sea state is associated to con-strative values for h_0, g_1, g_2, g_3, g_4. Nonetheless the value of h_0, g_1, g_2, g_3, g_4 are of close order. This could indicate a slight evolution of these parameters with the sea state. The similar val-ues for h_1, h_2, k indicate these parameters are almost constant. The parameter k gives the direction of the prefered axis at $x_2 = 0$ and h_1, h_2 the decrease of the probability for points of the (x_1, x_3)-plan which are not on the axis.

The form of the results obtained by numerical simulation is in accordance with the analytical developpement such as the gaussian probability law for the random variable Y_1.

3.4 Capsizing Criteria

The goal of the probability density estimation is to obtain a capsize probability. This leads to a search for criteria of capsizing.

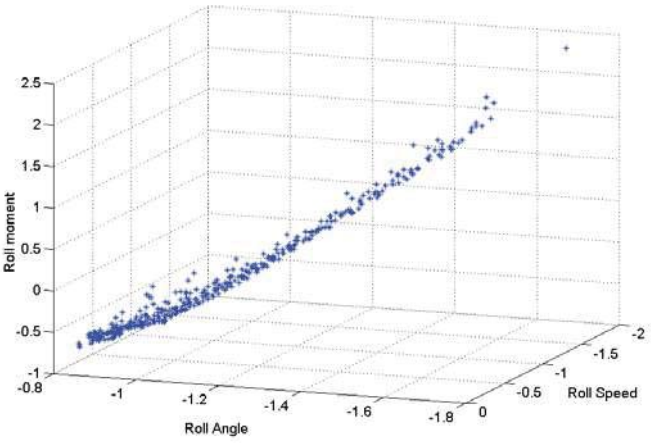

Figure 3: points of the angle-speed-moment-space with $\varphi > 48^\circ$, $\varphi.\dot{\varphi} > 0$

Here are compared simulations in which the roll angle has been really large and simulations leading to capsize. The sea state is still defined by a Pierson-Moskowitz spectrum, H_S = 12.5m and T_P = 12.6s. In the space defined by an-gle, speed and moment (x_1, x_2, x_3), points cor-responding to angle over 50° and speed of the same sign like angle (situations getting closer to capsize) are extracted Figure 3.

The points seem to get aligned in a same plan. Figure 4 show the points in this plan defined by two arbitrary variables V_1, V_2. Red points correspond to simulations getting to capsize and blue points correspond to simulations without capsizing.

A stable area can be defined with the trajectories which do not lead to capsize. So even for a large angle, the boat could escape such danger-ous situation. Then the probability of capsizing is the probability for the trajectory in the angle-speed-moment space to come out of the stable domain.

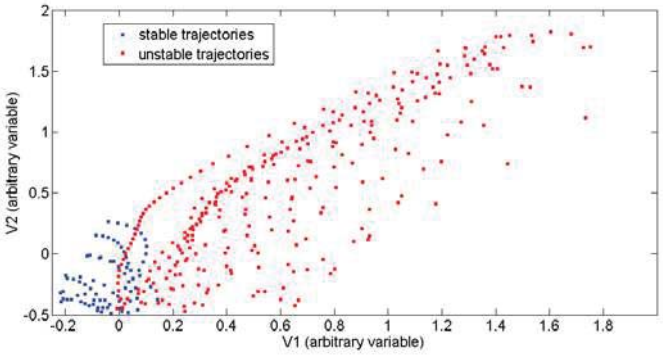

Figure 4: comparison of trajectories either stable or leading to capsize

4 CONCLUSION

In the paper an analytical formula of the probability density function of the linear roll motion has been obtained. The properties have been tested for simulations with realistic sea state. The results are partially in accordance, but the time independance remains exact both for linear and non-linear roll motion. In some case, the gaussian law proved for the linear motion remains exact for the non-linear motion. On top of that capsize criterium has been found for the calculation of a capsize probability with the probability density function of the roll angle, speed and moment.

5 REFERENCE

McTaggart, K.A., 2000, Ship Capsize risk in a Seaway Using Fitted Distributions to Roll Maxima, ASME Journal of O*ff*shore Mechanics and Artic Engineering, Vol. 122, No. 2, pp.141-146.

Belenky, V. and Campbell, B.L., 2011, Evaluation of the Exceedance Rate of a Stationary Stochastic Process by Statistical Extrapolation Using the Envelope Peaks over Threshold (EPOT) Method, Hydrodynamics Department Report, NSWCCD-50-TR-2011/032, Naval Surface Warfare Center Carderock Division, MD.

Hsieh, S.-R., et al., 1994, A Nonlinear Probabilistic Method for Predicting Vessel Capsizing in Random Beam Seas, Proceedings: Mathematical and Physical Sciences, Vol. 446, No. 1926, pp.195-211.

Scolan, Y.-M., 1997, Technical Note on ship rolling associated to high degree polynomial moment using Melnikov methods, Applied Ocean Research, Vol. 19, pp 225-234.

Jiang, C., et al., 2000, Capsize Criteria for Ship Models with Memory-Dependent Hydrodynamics and Random Excitation, Philosophical Transactions: Mathematical, Physical and Engineering Sciences, Vol. 358, No. 1771 The Nonlinear Dynamics of Ships, pp.1761-1791.

McCue, L. and Troesch, A., Probabilistic determination of critical wave height for a multi-degree of freedom capsize model, Ocean Engineering, Vol. 32, pp. 1608-1622.

Roberts, J.B., Vasta, M., 2000, Markov Mod-elling and Stochastic Identification for Nonlin-ear Ship Rolling in Random Waves, Philosoph-ical Transactions: Mathematical, Physical and engineering Sciences, Vol. 358, No. 1771 The Nonlinear Dynamics of Ships, pp. 1917-1941.

Spanos, P.-T.D., 1983, ARMA Algorithms for Ocean Wave Modelling, ASME Journal of Energy Resources Technology, Vol. 105, pp. 300-309.

Francescutto, A. and Naito, S., 2004, Large amplitude roll motion in a realistic seaway, International Shipbuilding Progress, Vol. 51, No. 2, pp. 221-235.

Su, Z. and Falzarano, J.M., 2011, Gaussian and non-Gaussian cumulant neglect application to

large amplitude rolling in random waves, International Shipbuilding Progress, Vol. 58, No. 2, pp. 97-113.

Campbell, B., et al., 2014, On the Application of Generalized Pareto Distribution for Statistical Extrapolation in the Assesment of Dynamic Stability in Irregular Waves, 14th International Ship Stability Workshop, Kuala Lumpur, Malaysia.

Belenky, V., et al., 2014, Extrapolation and Validation Aspects of the Split-Time Method, 30th Symposium on Naval Hydrodynamics, Hobart, Tasmania, Australia.

Belenky, V., 1993, A Capsizing Probability Computation Method, Journal of Ship Research, Vol. 37, No. 3

This page is intentionally left blank

Aerodynamics Loads on a Heeled Ship

Romain Luquet, *DGA Hydrodynamics, FRANCE*, romain.luquet@intradef.gouv.fr

Pierre Vonier *DGA Hydrodynamics, FRANCE*, pierre.vonier@intradef.gouv.fr

Andrew Prior, *Royal Canadian Navy, DGMEPM, DNPS 2-3*, andrew.prior@forces.gc.ca

Jean-François Leguen, *DGA Hydrodynamics, FRANCE*, jean-francois.leguen@intradef.gouv.fr

ABSTRACT

Verification of ship stability is based on rules which account for the effects of wind. Restrictive hypothesis are employed to define those rules and especially the influence of ship heeling. This study reviews some stability rules and applies them to the case of the F70 frigate. Then, two alternate approaches are considered: (i) accounting for the actual lateral areas and respective centroids of the heeled ship, and (ii) CFD calculations to determine aero and hydro dynamic coefficients at each heel angle. Finally, comparison is made between the results of these alternate approaches and the stability rules.

Keywords: *wind, CFD, rules, naval ships*

1. INTRODUCTION

Strong winds can increase the risk of capsizing, thus, stability assessment must account for wind effects. This study reviews some of the assumptions commonly embedded in stability rules and investigates two alternate approaches.

1.1 Stability Rules

The first phase of this study was a review of some stability rules (i.e. French Navy, Dutch Navy, IMO, Brown & Dreybach). The formulations defined in these rules were employed to calculate wind heeling moments for the French Navy F70 class frigate.

Whether it is because they are very old (sometimes established more than 50 years ago) or to facilitate the calculations, some of the assumptions common to stability rules are simplistic and do not reproduce faithfully the physics of the studied phenomenon. Examples of such assumptions include:

Fixed value for aerodynamic drag coefficient regardless of ship geometry or heel angle (e.g. $C_D = 1.12$).

Fixed locations (centroid of projected lateral areas) of application of aero and hydro dynamic forces.

Dead ship condition (zero forward speed with a beam wind) considered the worst case. Blendermann (1996) has shown that beam wind is not the worst case.

Constant wind speed. Gusting is accounted for as either an increase in wind lever arm (IMO) or by defining requirements for righting arm area ratios (naval stability rules).

No variation in amplitude of wind against altitude (IMO) or simple wind profile (naval stability rules). No variation in direction.

Simplified windage area.

1.2 Alternate Approaches

The second phase of this study was to address the first two assumptions of the previous section and investigate two alternate approaches:

AERODYNAMIC APPROACH: Uses the same basic wind moment formulation found in the stability rules. Except, the fixed distance between the upright centroid of windage area and half draft (along with cosine function) are replaced with calculated centroids for above waterline windage area and below waterline hull area (Zaero, Zhydro).

CFD APPROACH: Uses a CFD model to generate aerodynamic and hydrodynamic coefficients (C_Y, C_Z, Ck) for the ship at each heel angle.

1.3 Comparison

The last phase of this study was to compare wind heeling moment results to assess their consistency. The study focused only on the determination of the heeling moment on a ship exposed to a given constant wind speed. The relevance of the choice of speed and associated regulatory criteria is not discussed.

2. STABILITY RULES

1.1 French Naval Rules

The wind heeling moment formula in the French military regulations, IG 6018, (1999) is derived from the work of Sarchin and Goldberg (1962). It requires a reference wind speed (at 10 m height above waterline), assumes a wind speed profile (~ $h^{1/7}$) and integrates over the projected surface area exposed to wind. Integration is simplified by dividing this surface area into horizontal strips, each being subjected to a constant wind speed depending on the average height of the considered strip. The inclining lever arm in meters or BLI, due to wind (wind heeling moment divided by $\Delta.g$) is then obtained by summing the influence of each strip as follows:

$$B.L.I. = \sum_i \frac{0.0195\,.A_i.h_i.V_i^2}{1000.\Delta}\,cos^2\varphi \qquad (1)$$

Where:

V_i = Wind speed at strip center [knots]
A_i = Projected area of each strip [m²]
h_i = vertical distance between the center of the strip and the drift center (assumed immersed at T/2) [m]
φ = Heel Angle [deg]
Δ = Vessel displacement [t]

The coefficient 0.0195 is derived from the combination of physical constants and the units used for wind speed:

$$\frac{1}{2}\frac{\rho C_Y}{g}\left(\frac{1.852}{3.6}\right)^2 = 0.0195\ [\text{kg.m}^{-2}.\text{kts}^{-2}] \qquad (2)$$

Where:

C_Y = 1.12,
ρ = 1.29 kg/m³ and
g = 9.81 m²/s

The $\cos^2$ term, which is used in many other regulations, comes from historical studies of sail ships (Middendorf, 1903). Sail ships have a large windage area (upright) that decreases drastically with heel (Middendorf, 1903). The formulation is obviously flawed as at 90° heel a ship will still have a windage area.

1.2 Dutch Naval Rules

The formula used in naval regulations of the Netherlands is similar to the French regulations except that it utilizes a $\cos^3$ term and does not take into account the wind speed profile. These regulations are derived from Germany naval rules (Arndt 1982). The wind heeling arm formula is as follows:

$$B.L.I. = \frac{P.A.I}{1000.\Delta}.\frac{1+3\cos^3(\varphi)}{4}$$

$$P = \frac{C_W.\rho_l.V^2}{2} \qquad (3)$$

Where:
P = Wind pressure [Pa]
A = Windage surface area [m²]
I = Distance between the half-draft and the windage area center
C_W = 1.2
ρ_l = 0.125 kg.s².m^{-4}

The advantage of this formulation lies in its ability to model the decay of the heeling moment while maintaining a non-zero value at φ = 90 °. The choice to keep one quarter of the zero heel value seems somewhat arbitrary.

2.3 IMO

In the regulations established by the IMO, and therefore applicable to civilian vessels, the pressure applied on the windage surface is specified instead of the wind speed. In addition, the heeling moment is considered invariant with heel angle. The B.L.I. is calculated as follows:

$$B.L.I. = \frac{P.A.Z}{1000.\Delta.g} \qquad (4)$$

Where:
P = Pressure applied to windage surface [Pa]
Z = Distance between the center of the windage area and the center of the underwater lateral area (assumed by default located at T/2) [m]

This formulation is acceptable as it applies mainly to large commercial vessels like container ships or tankers, which by their shape, have a windage surface almost independent of the heel angle.

It is possible to compute an equivalent wind speed by comparing the IMO and naval formula at zero heel. Comparing with the French regulations, the relation obtained is:

$$V = \sqrt{\frac{P}{0.0195.g}} \qquad (5)$$

With the usual value of P = 504 Pa (IMO without gust) and assuming C_Y = 1.12, then V=51 knots or 63 knots (IMO with gust) instead of 100 knots generally used in naval stability rules for combatants.

2.4 Brown & Deybach

Brown & Deybach (1998) proposed a formula that considered the principal dimensions of the ship. Their wind heeling arm formula was as follows:

$$B.L.I. = \frac{\frac{1}{2}C_D\rho V^2.\left[C_W\frac{L_{PP}.B}{2}+\left(A-C_W\frac{L_{PP}.B}{2}\right)\cos(\varphi)\right]}{1000.g.\Delta}.\left[\frac{B}{2}+\left(L-\frac{B}{2}\right)\cos(\varphi)\right] \qquad (6)$$

Where:
C_D = Drag coefficient = 1.12
B = Ship beam
L_{pp} = Ship length
C_W = Water plane area coefficient

3. CASE STUDY

The ship chosen for this study is the French Navy F70 type anti-aircraft frigate shown in Figure 1. The CAD model of the ship used for this study has a simplified superstructure (masts and antennae are not considered) as shown in Figure 2. Blendermann (1999) provides guidance on the influence of the details of the superstructure on the

aerodynamic coefficients and its recommendations have been followed. The hydrostatic characteristics of the hull are presented in Table 1.

Figure 1: French frigate "Jean Bart"

Figure 2: CAD model of "Jean Bart"

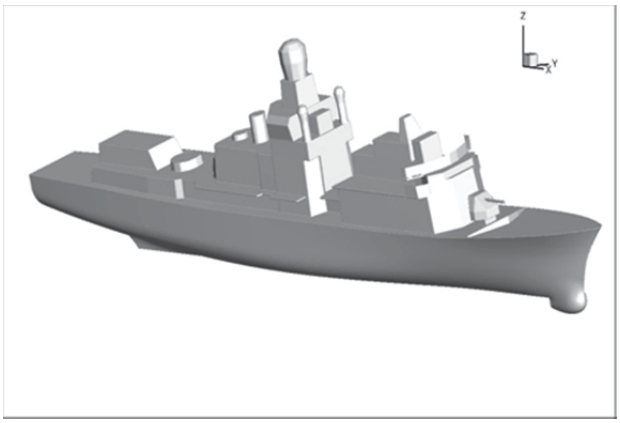

Table 1. Main characteristics

L_{pp}	m	129.00
BWL	m	14.00
T	m	4.82
Δ	t	4873
LCG	m	58.92
YG	m	0.00
VCG	m	5.96
Windage Area	m²	1346
Z_{aero}	m	6.24
Drift Area	m²	592
Z_{hydro} / calm water plane	m	-2.37

4. AERODYNAMIC APPROACH (I)

The formulae for wind heeling in the stability rules (other than IMO) use the aerodynamic drag at zero heel angle (or at best taking into account variation using $\cos^2$ or $\cos^3$ functions). In addition, they assume that the drift center is located at half draft.

One way to improve upon these formulae is to remove the assumption of an a priori law of decrease ($\cos^2$ or $\cos^3$) by calculating the actual projected windage area and centroid height (Z_{aero}) and immersed lateral area and centroid depth (Z_{hydro}) at each heel angle. The wind heel lever formula is thus:

$$B.L.I. = \frac{1}{2}\frac{C_Y.A.(Z_{aero} - Z_{hydro}).V^2}{1000.\Delta.g} \quad (6)$$

Where:
V = Wind speed [m/s] (at height Z_{aero})
C_Y = 1.12
ρ = 1.29kg/m^3

A, Z_{aero}, Z_{hydro} are calculated at each heel angle. This done by using FASTABI (DGA hydrodynamics code) to establish the hull equilibrium position (waterline position relative to hull) at each heel angle and then using the CAD model to calculate projected areas and centroids. Figure 3 illustrates this procedure.

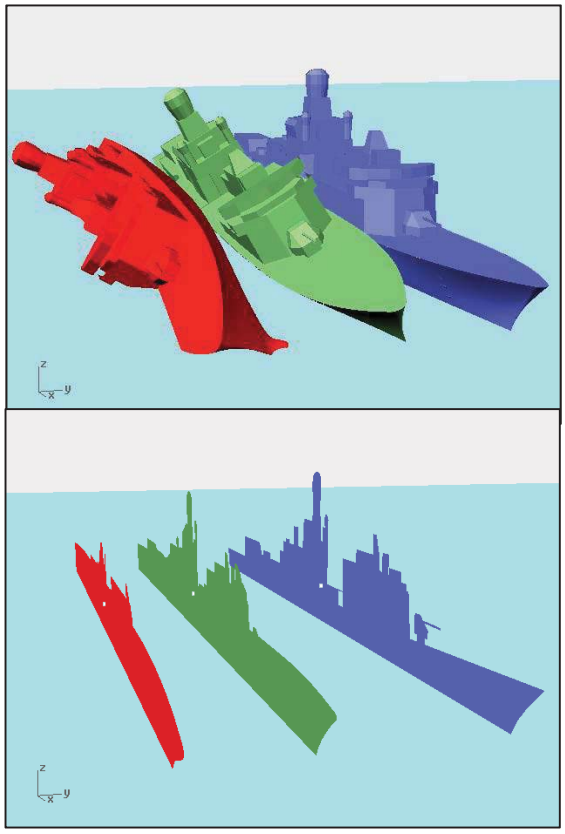

Figure 3: equilibrium and projected wind areas

Figure 4 plots wind lever results for this alternate approach along with the results obtained using the stability rule formula noted in Section 2. To ensure likewise comparison, a wind speed of 100 knots at 10m has been used in all cases, Equation (5) was used to calculate the corresponding pressure for the IMO formula.

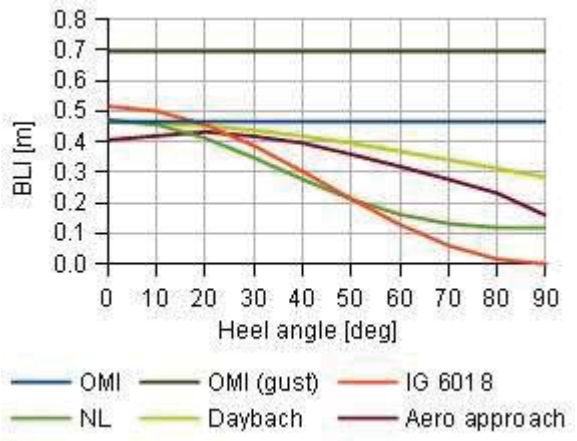

Figure 4: comparisons of BLI

At zero heel, BLI values are all quite similar. However, the shape of the lever arm curves (variance with heel) is very different. This alternative approach shows a maximum around 20° heel angle.

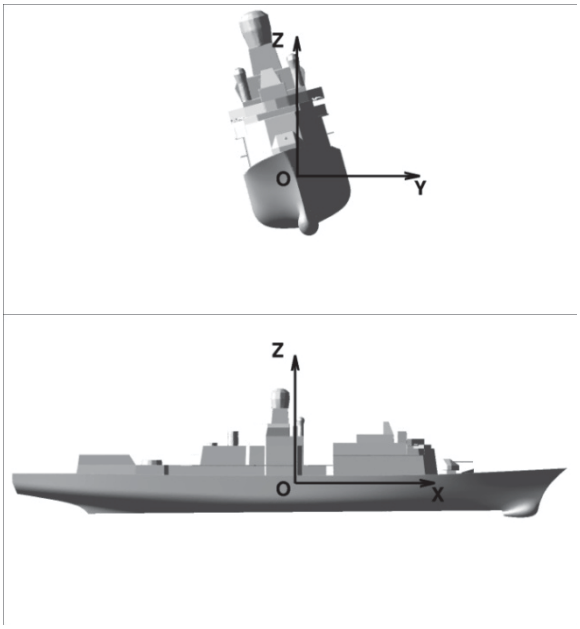

Figure 5: coordinate systems

5. CFD APPROACH (II)

CFD simulations were performed in a dead-ship condition to determine the aero and hydro dynamic forces acting on the ship.

5.1 Coordinate System & Coefficients

CFD work was conducted using the fixed coordinate system shown in Figure 5. The axes are independent of the heel angle, only the position of the origin is linked to the ship. The origin is located as follows:

Ox : At ship LCG (+ fwd, - aft)
Oy : At ship Centreline (+port, -starboard)
Oz : At the waterline (+above, -below)

The coefficients C_Y, C_Z and C_K are defined as:

$$C_Y = \frac{F_Y}{\frac{1}{2}\,\rho\, U_{ref}^2\, S_{ref}}$$

$$C_Z = \frac{F_Z}{\frac{1}{2}\,\rho\, U_{ref}^2\, S_{ref}}$$

$$C_K = \frac{M_X}{\frac{1}{2}\,\rho\, U_{ref}^2\, S_{ref}^2/L_{ref}} \qquad (7)$$

Where:

F_Y, F_Z = Force experienced by the ship in the y-axis and z-axis respectively.

M_X = Is the heeling moment acting on the ship (rotation about the x-axis).

L_{ref} = Ship length between perpendiculars.

Depending on whether aero or hydrodynamic forces are being considered:

S_{ref} = Either projected windage area or submersed hull area at zero heel angle.

U_{ref} = Wind speed or drift velocity.

ρ = Air or water density.

5.2 Computational domain and mesh

The computational domain is a parallelepiped as illustrated in Figure 6. A velocity-inlet condition (red) is applied on the upstream boundary and a pressure-outlet condition (blue) is applied at the downstream boundary. A no-slip condition (green) is imposed on the ship and a symmetry condition (gray) on the other boundaries. The computational domain covers 3 L_{pp} on each side and 1.5 L_{pp} above and below the ship.
The mesh consists of 17 million calculation points constituting 5 million polyhedral cells. The mesh near the walls is made of prisms to ensure proper computation of the boundary layer. The non–dimensional distance from the wall y^+ is fixed at 50 on the hull. The mesh is also made of prisms at the free surface to allow an accurate resolution in this crucial area. The rest of the mesh is covered by polyhedra.

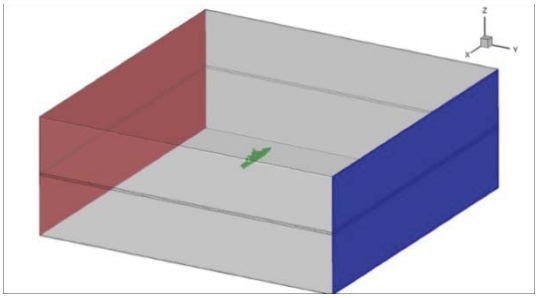

Figure 6: computational domain

5.3 Numerical Method

The calculations were performed using the commercial software FLUENT from ANSYS. It solves RANS equations (Reynolds Averaged Navier-Stokes equations). For these calculations, the Volume Of Fluid (VOF) model was used to simulate the coexistence of the two fluids (air and sea water). A kω-SST model was used to model the turbulence of the two fluids.

The simulations are unsteady using an adaptive time step beginning at 0.1s to reach 1s at the end of the calculation. High order discretization schemes have been applied to the momentum equations (MUSCL) and volume fraction (HRIC) to allow an accurate resolution of the air-water interface. The hull was considered to be hydraulically smooth (roughness was not taken into account).

5.4 Calculation Conditions

The simulations were performed on flat sea for a ship at zero forward speed in a fixed position according to the hydrostatic equilibrium at the selected heel angle (the equilibrium is only satisfied on the heave).
The characteristics of the two fluids simulated are shown in Table 2. The fluid properties were constant over the computation domain and the effects of temperature, pressure and air hygrometry were neglected.

Table 2. Main characteristics of fluid

Salt water (15°C)			
Dynamic viscosity	μ	(Pa.s)	$1.2200.10^{-03}$
Density	ρ	(kg/m^3)	1026
Speed	V_{hydro}	(m/s)	Such that Fy=0
Air (15°C, 1% RH, 1013 mbar)			
Dynamic viscosity	μ	(Pa.s)	$1.7894.10^{-05}$
Density	ρ	(kg/m^3)	1.225
Wind speed at 10m	V_{aero}	(knots)	100

A uniform lateral current was applied to the flow (water) to model the consecutive drift of the ship due to the efforts of the crosswind. The current speed was determined by balancing the drift forces sustained by the ship (aerodynamic and hydrodynamic loadings). The heeling moments balance is not verified.

Inlet condition imposed on the airflow was determined to correspond to a fully developed turbulent boundary layer profile. For a 100knot wind (at 10m reference height), the turbulent intensity at 10m is of the order of 10%. Theoretical profile, up- and down- stream computed profiles are shown in Figure 7.

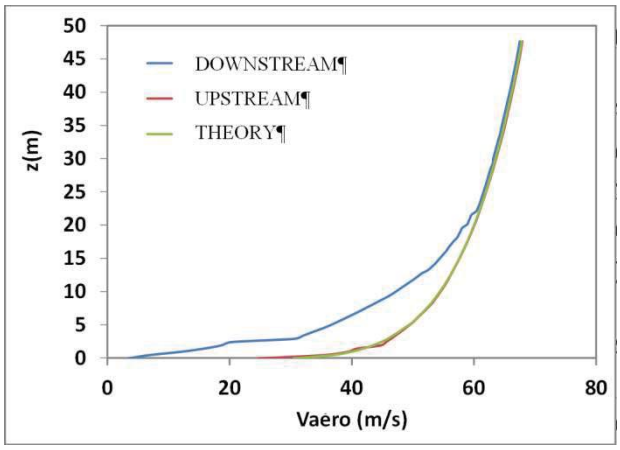

Figure 7: wind profile

5.5 Sensitivity and Convergence

A limited sensitivity analysis was performed. Firstly a higher density of mesh (10 million polyhedra) was tested to quantify the influence of the discretization of the computational domain. A maximum variation of about 3% was observed on the force coefficients. Then the upstream turbulence flow rate was multiplied and divided by two without observing any significant influence on the results. An evaluation of the influence of Reynolds number was also performed. Computations were performed for different wind speeds at zero heel angle, the results are shown in Table 3. There were no significant changes in the aerodynamic force coefficients; as expected since the Reynolds number remains greater than 10^7.

Table 3. Main characteristics of fluid

V knots	R_e	C_Y	C_Z	C_K
25	$1.23.10^{+07}$	0.86	0.65	0.44
50	$2.47.10^{+07}$	0.84	0.64	0.45
100	$4.93.10^{+07}$	0.83	0.62	0.47

The simulation duration was a period of 500 s which allowed good convergence of the force and moment coefficients as shown in Figure 8. Coefficient values reported in this study are the average over the last hundred seconds of simulation.

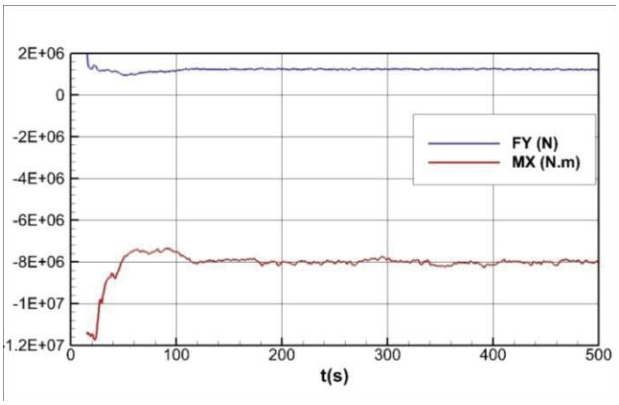

Figure 8: force and moment time trace

The CFD calculation methodology used for this study has not been validated using a

verification procedure. However, some confidence may be taken from comparison of the results obtained to data from wind tunnel tests. Blendermann (1996, 999) conducted zero heel angle tests for two ships with silhouettes similar to that of the F70 frigate (see Figure 9). Table 4 presents the C_Y and C_K coefficients from CFD and the Blendermann tests.

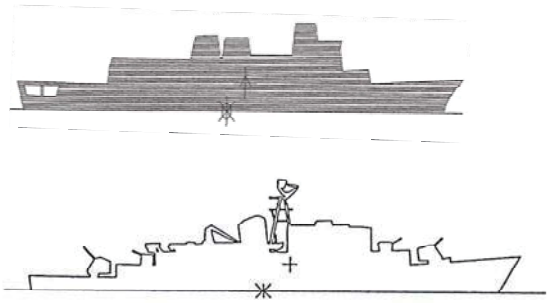

Figure 9: From Blendermann (1996 and 1999)

Table 4. Comparison with Blendermann

	F70 Present CFD	Blendermann Tests	
		1996	1999
C_Y	0.83	0.81	0.85
C_K	0.47	0.48	0.49

Finaly, a procedure for CFD simulation has been developed to evaluate the hydrodynamic and aerodynamic loads for vessel in the deadship condition (zero forward speed and drifting in a beam wind); see Figure 10 & 11."

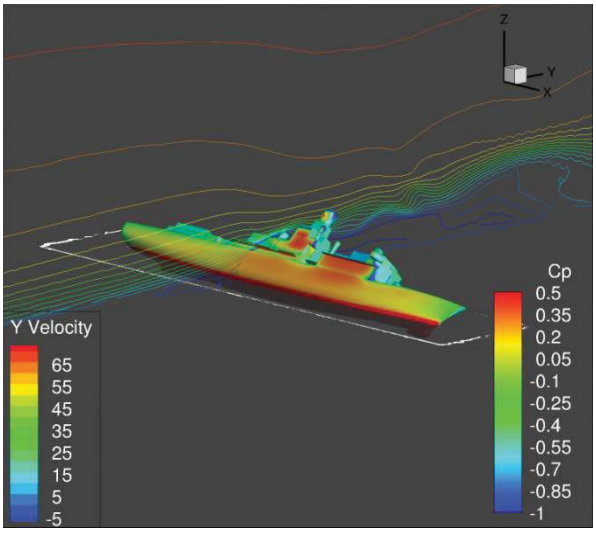

Figure 10: Iso-contours of C_P and iso-lines of transverse speed (m/s) around frigate F70 at +45° heel angle

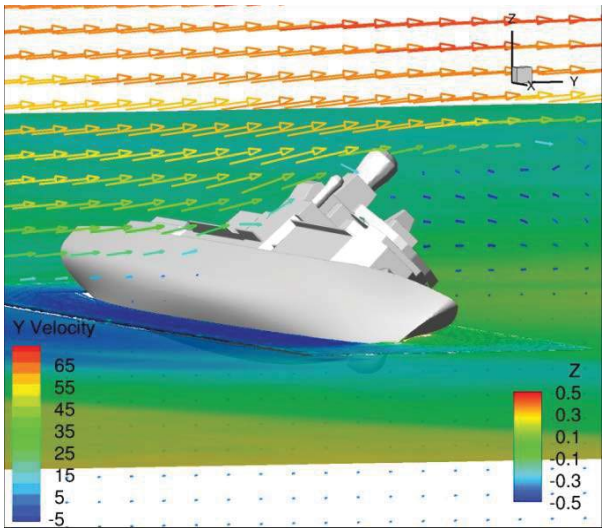

Figure 11: Iso-contours of Z(m) and transverse speed (m/s) around frigate F70 at +45° heel angle

5.6 Results

A series of simulations were performed for a wind speed of 100 knots and heel angles ranging from -60 ° to + 60 °; the positive heel angles correspond to the realistic situation where the ship leans towards leeward. The resulting force and moment coefficients are shown in Figure 12.There is a decrease in C_{Zaero}, C_{Yaero} and C_{Yhydro} with increasing heel angle. Note also that C_{Zaero} and C_{Yhydro} are of the same order of magnitude. C_{Zaero} will influence roll moment because the pressure field on the deck and superstructures of the ship is not symmetrical; this influence is not accounted for in the stability rules reviewed.

Figure 13 shows the vertical location of the point of application of the aerodynamic and hydrodynamic forces. As expected, the point of application of aerodynamic force is located near the centroid of the projected windage area and its height decreases with increasing heel angle. The position of the point of application

of hydrodynamic forces is above the free surface at zero heel but moves below with increasing heel angle to approach the mid-draft position. The heeling moment lever arm, z(aero) - z(hydro), does not change greatly with heel angle.

Table 5 presents drift velocity (V_{hydro}) and the lateral force coefficients C_{Yhydro} and C_{Yaero} for each heel angle. There are little variations in C_{Yhydro} and C_{Yaero} and thus V_{hydro} over the range of heel angles.

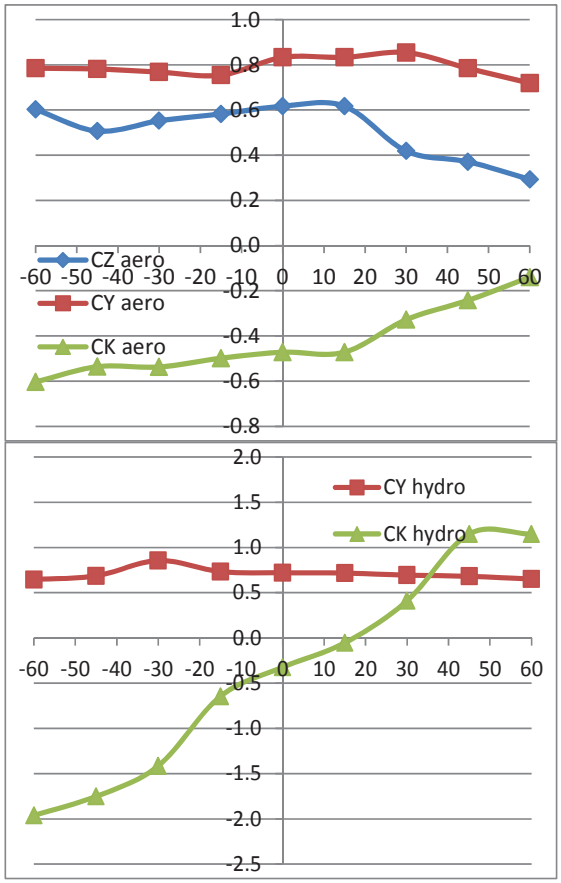

Figure 12: force and moment coefficients for different heel angles

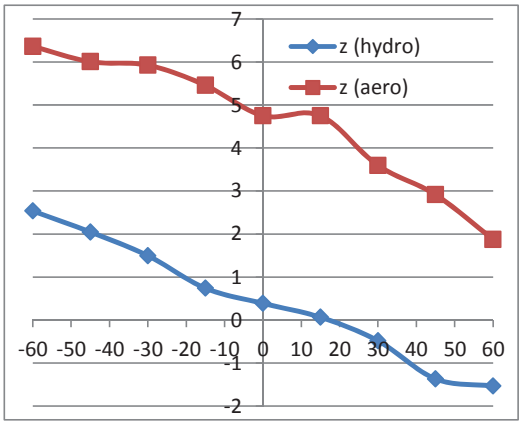

Figure 13: vertical location of hydro and aero forces

Table 5. Drifting speeds for 100 knots of wind

Heel (°)	CY hydro (-)	CY aero (-)	V hydro (knots)
-60	0.65	0.78	5.7
-45	0.69	0.78	5.6
-30	0.85	0.77	5.0
-15	0.73	0.75	5.3
0	0.72	0.83	5.6
15	0.72	0.83	5.6
30	0.69	0.85	5.8
45	0.68	0.78	5.6
60	0.65	0.72	5.5

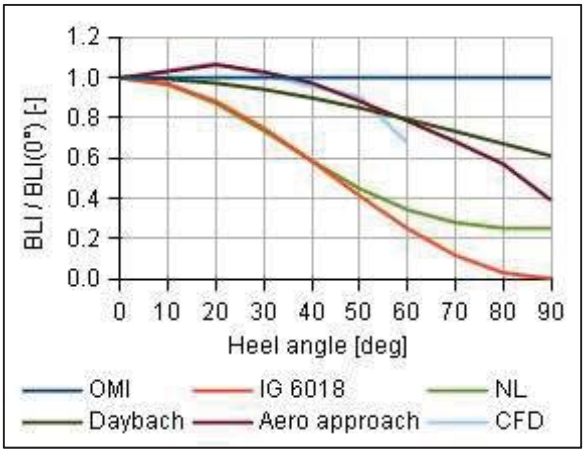

Figure 14: BLI comparisons

6. COMPARISON

Figure 14 presents comparison of the aerodynamic approach and the CFD approach to the stability rules reviewed. Since wind speed and formulation in the rules vary, the curves have been made non-dimensional using values for zero heel. The shape of the aerodynamic and CFD approach curves match well and show a maximums at 20° and 15° respectively. The decrease in BLI is much less pronounced than that obtained by the $\cos^2$ and $\cos^3$ function formulae found in the stability rules.

7. CONCLUSIONS

A review was made of different stability rule formulae to account for the effects of wind heeling. These formulae have been applied to the case of F70 frigate. The results obtained were compared to those derived from two alternate approaches. The first approach adopted the same basic formula of the stability rules but replaced the fixed upright windage area, centroids and $\cos^2$ terms with actual areas and centroids determined for each heel angle. The second approach employed CFD analysis to determine force and moment coefficients at each heel angle. A procedure for CFD simulation has been developed to evaluate the hydrodynamic and aerodynamic loads for vessel in the deadship condition (zero forward speed and drifting in a beam wind).

For the F70 frigate, the two alternate approaches produced similar BLI results. The BLI versus heel angle curves for both have a significantly different shape than that derived from stability rule formula based on a $\cos^2$ law. Of particular note is that both approaches show a peak in BLI (maximum destabilizing moment) in the 15° to 20° range of heel.

The alternate approaches presented here are interesting and deserves further study. In particular, further work can be done to improve the accuracy of the CFD simulations and validate the results obtained. This would provide the tool necessary for more comprehensive analysis leading to improved stability rule formulae.

ACKNOWLEDMENTS

This study was based on CRNAV (Cooperative Research Navies) discussions. Thanks also to Hélène Eudier who started the work in Val de Reuil during a training course. For the French part, the study is found by the French Ministry of Defence to support DGA Hydrodynamics in its research activities.

REFERENCES

Arndt B., H. Brandl and K. Vogt, 1982, 20 years of experience – Stability regulations of the West-German Navy, STAB'82, Tokyo pp. 111-121.

Blendermann W., 1999, Influence of model details on the wind loads demonstrated on a frigate, in Schiff & Hafen.

Blendermann W., 1996, Wind loadings of ships, - collected data from wind tunnel tests in uniform flow, Institute of Naval Architecture.

Brown A.J. and Deybach F., 1998, Towards a rational intact stability criteria for naval ships, Naval Engineers Journal.

DGA/DSA/SPN IG 6018 indice A, 1999, Stabilité des bâtiments de la Marine.

Middendorf, 1903, Bemastung und takelung des schiffe.

MSC.267(85).

Sarchin & Goldberg, 1962, Stability and buoyancy criteria for US naval surface ship, SNAME transactions, vol 70 pp418-434.

Validation of Time Domain Panel Codes for Prediction of Large Amplitude Motions of Ships

Erik Verboom, *Delft University of Technology*, emdverboom@gmail.com

Frans van Walree, *Maritime Research Institute Netherlands*, f.v.walree@marin.nl

ABSTRACT

The paper describes the validation of two time domain methods to simulate the behaviour of a frigate operating in stern quartering seas. The simulation methods differ in the way the seakeeping problem is linearized. The first method is partially body exact while the second method is fully body exact. The validation is based on a statistical analysis as well as a deterministic comparison of simulated and experimental motion time traces.

Keywords: *time domain panel method, statistics, deterministic validation*

1. INTRODUCTION

The operability and safety of a ship depends amongst others on its behaviour in waves. At higher speed in steep waves from aft ward directions dynamic stability risks may exist. These risks can be investigated by means of model tests. Provided these tests are properly executed, they offer the most reliable information on dynamic stability.

Issues in the use of model testing are the costs, the limited statistical reliability of the required tests in irregular waves, the limited flexibility, some limitations in representation of the physics of ship behaviour in waves from the stern quarter and the fact that the test results are not always easy to understand. The limitations in the physical representation relate to viscous effects in the components of the hull resistance with an effect on the propeller loading, in some of the smaller components of the roll damping, in components of the manoeuvring reaction forces and in the (dynamic) stall of the rudders. The neglect of wind on the roll damping and excitation, the wind heel and the propeller loading and related steerage has an effect. Issues that are modelled implicitly correctly are the natural peak-trough asymmetry in steep waves, the presence of breaking waves, the wave induced forces on the propeller and rudder, rudder and propeller ventilation and down-stream effects of vortices from the bilges and bilge keels on the rudder.

In order to understand the physics of dynamic stability, numerical modelling has been pursued for some time. Although the latest CFD techniques have undoubtedly the largest potential, they have not met the expectations yet. This is partly due to the problems of modelling the generation, propagation and absorption of steep waves in a limited computational domain and partly to the local physical character of issues like spilling wave crests on deck, roll damping from bilge keels and rudder stall and ventilation and the role of the propeller herein. In combination with the required domain size, this yields an extreme computational effort.

In between the above two techniques are hybrid calculation methods, which combine the efficiency of potential flow theory with empirical modules covering the non-linear aspects of manoeuvring and roll damping.

After validation, these models are particularly used in assessing capsize risk.

The present paper deals with validation and comparison of two such simulation methods for a frigate hull form operating in stern quartering seas. A brief description of the simulation methods is given first. Next, the experimental arrangement is described followed by a discussion on the effect of non-linear body boundary conditions on the simulation results.

The simulation methods have been partially developed in a joint industry project on high speed craft called FAST3. Participants are Damen Shipyards (NL), Delft University of Technology (NL), Defence Science Technology Organisation (AUS), MARIN (NL) and the Royal Netherlands Navy (NL).

2. SIMULATION METHODS

Predicting the motion performance of ships operating in stern quartering sea states is more complicated than that for beam or head seas. In stern quartering seas motion amplitudes may be large and both vertical and horizontal plane motions (course keeping) are important. Ideally, prediction methods should be capable of accounting for:

- Six degrees of freedom motions, especially the coupling between sway, yaw and roll,
- Large motion amplitudes,
- Non-linear waves: dynamic stability problems are generally most severe in steep waves for which non-linear effects are of importance,
- Time-varying wetted hull geometry and its effects on restoring forces, wave excitation, wave diffraction and wave radiation forces,
- Forward speed and the effects of friction and flow separation on hydrodynamic properties: in stern quartering seas the wave encounter frequency is low so that potential flow damping is relatively low,
- Propulsion and steering: the speed variations in the horizontal plane should be predicted adequately, and course keeping is important with respect to broaching,
- The contribution of the wind to the roll damping and the roll excitation.

Prediction methods that are capable of handling the above are in principle capable to simulate phenomena like capsize due to loss of stability in waves, surf riding and broaching. However, fully non-linear simulation methods are scarce and rather computationally intensive. When a large number of conditions needs to be investigated the required simulation times are impractical. Therefore, there is a need for fast(er) time simulation methods.

One approach that has been proven to lead to reasonable simulation results within a practical time frame is a time domain potential flow simulation. By inserting empirical and semi-empirical components, the errors due to neglecting viscosity, rotation and compressibility, can be minimized. However, also among the time domain potential flow simulations, choices have to be made between simulation time and accuracy. One of these choices is the handling of boundary conditions on the boundaries of the fluid domain.

In an attempt to quantify the effects of linearising boundary conditions, two simulation methods are compared that are identical except for the handling of body boundary conditions. Both simulations are implemented in Panship (Van Walree 2002, De Jong 2011, Van Walree and Turner 2013), a time domain panel method characterised by:

- 3D transient Green function to account for linearized free surface effects, exact forward speed effects, wetted surface, radiated and diffracted wave components along the hull and a Kutta condition for ventilated transoms,
- 3D panel method to account for Froude-Krylov forces on the instantaneous submerged body,
- Cross flow drag method for viscosity effects,

- Resistance (calm water and in waves) is obtained from pressure integration each time step,
- Propulsion and steering using propeller open water characteristics, semi-empirical lifting surface characteristics and propeller-rudder interaction coefficients,
- FDS (Blok and Aalbers 1991) viscous roll damping,
- Autopilot steering,
- Unsteady wind loading based on wind tunnel derived wind load coefficients.

It should be noted that apart from the cross flow drag method there are no “manoeuvring” terms present in Panship. For instance the sway force and yawing moment due to a drift angle or yaw rate are obtained from the potential flow panel method.

Panship is used at MARIN for seakeeping predictions for fast and unconventional ships. In the semi non-linear version, the transient Green function is solved for linearized free surface and body boundary conditions. Radiation and diffraction forces are then based on the mean wetted surface and the mean forward speed of the vessel. Since these are both known prior to the start of the time domain simulation, the Green function terms for all time steps can be calculated before the actual simulation starts, resulting in a significant reduction of the computational effort. Froude-Krylov forces are based on the exact wetted surface geometry including ship motions, incident and diffracted waves.

The purpose of the non-linear Panship version development is to determine wave impact loads on high speed ships. In the non-linear version of Panship, the Green functions are evaluated at each time step for the instantaneous position of the vessel in the incident and disturbed wave. Since the transient Green function relies on linear free surface boundary conditions, the wetted hull surface relative to the disturbed water surface ζ is used, i.e. the vertical coordinate z is replaced by z-ζ. For more detailed information on Panship see Van Walree and Turner (2013).

The present purpose is to investigate the merits of both Panship versions for a frigate operating in stern quartering seas. This is achieved by comparing simulation results of both methods with experimental results.

3. MODEL TESTS

Model tests were carried out on the parent hull of the FDS systematic hull form series; see Blok and Beukelman (1984). The tests have been performed in MARIN's Seakeeping and Manoeuvring Basin which measures 170x40x5 m in length, width and depth respectively. Table 1 shows the main particulars of the full scale vessel; Figure 1 shows the experimental setup. The model scale used was 15, resulting in a relatively large model.

L_{PP}	100.00	m
L_{WL}	99.982	m
B	12.502	m
T_F	3.125	m
T_A	3.125	m
C_b	0.401	-
Δ	1568.40	m^3
S	1212.30	m^2
GM	2.50	m

Table 1 Main particulars of frigate

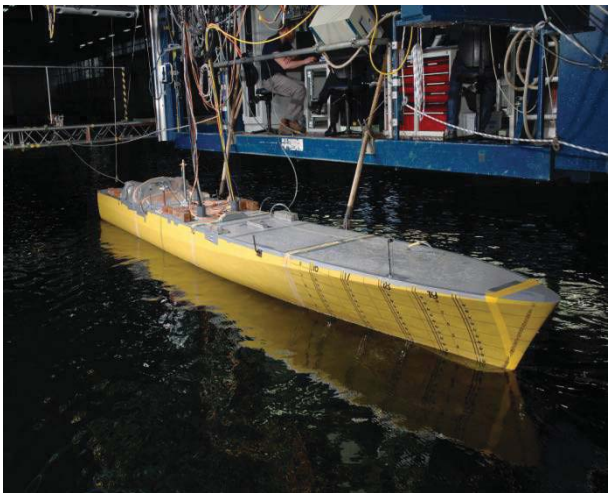

Figure 1 Experimental setup

During the tests the model was free sailing in six degrees of freedom and self propelled. Course keeping was realized by an autopilot actuating twin rudders. In order to ensure a negligible effect of the cables connecting vessel and towing carriage, the carriage was able to follow the vessel in its surge, sway and yaw motions.

4. VALIDATION

When validating simulation methods for (irregular) stern quartering waves, a number of aspects have to be taken into account. First, compared to head waves, accelerations, impact pressures and structural loads due to slamming are less relevant. Instead, course keeping and stability are the phenomena that are of interest. However, the low wave encounter frequencies combined with a large, strongly non-linear dependency of the vessels response on the initial speed and position in the wave make the acquisition of reliable statistical data time consuming and expensive.

In this paper two types of validation will be performed. First, a statistical comparison of simulations and model tests is shown. Next, individual model test runs will be used for a deterministic comparison of the vessels motions in stern quartering seas.

4.1 Statistical Validation

The main issue when it comes to validating statistical data for a vessel operating in stern-quartering waves is the acquisition of sufficient data. Due to the low encounter frequency, obtaining a reasonable number of wave encounters can be very time consuming. The model tests discussed here had a duration of 850 seconds (prototype value), obtained by performing 5 to 7 runs (depending on the operational speed) for every condition.

For the statistical validation of the simulation results, two conditions have been selected as shown in Table 2. In both conditions a JONSWAP spectrum has been used with a different wave train realization in each run. A 360 deg wave direction means following seas.

Test case	Speed [kt]	Wave direction [deg]	Wave height [m]	No. of wave encounters [-]
707	17	315	3.8	79
709	23	300	3.8	37

Table 2 Test conditions

As indicated in Table 2, the number of wave encounters during the model tests varied roughly between 40 and 80. In order to get an idea of the statistical significance of the data obtained, 10 simulations in identical conditions with different wave train realizations have been performed with the semi non-linear version of Panship. Each run had a duration of 850 seconds. Mean values and standard deviations of all six degrees of freedom have been determined for each run. An indication of the scatter in results can be obtained from Figures 2 through 5. Figures 2 and 3 show the mean values for all six degrees of freedom, Figures 4 and 5 the standard deviations. Note that for the x-direction the speed is shown instead of the surge motion. In the bar graphs, the left most (darkest) bar describes the values obtained during the model test, the next ten bars are values obtained from simulations for different

wave train realisations (seeds)

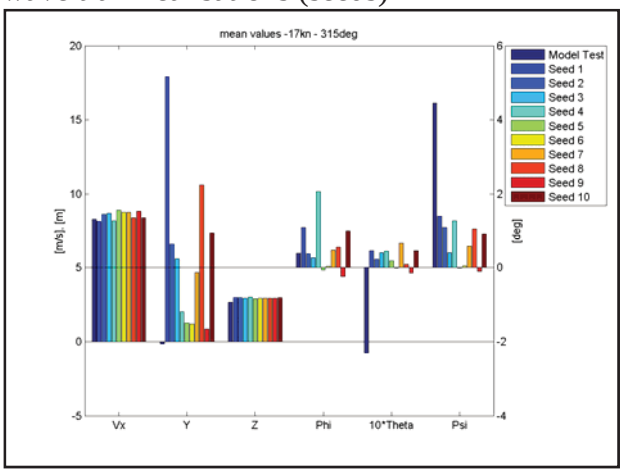

Figure 2 Mean values case 707

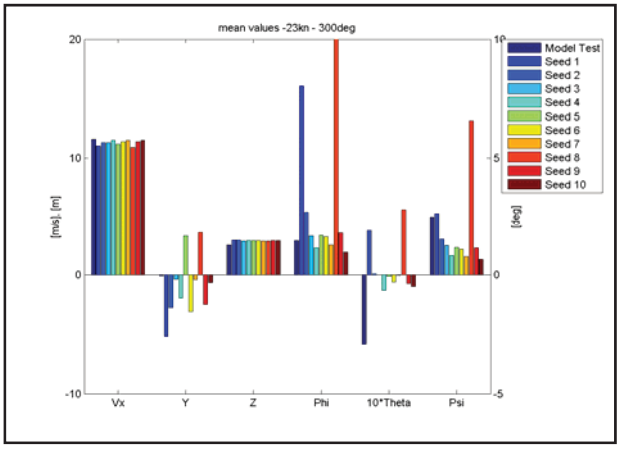

Figure 3 Mean values case 709

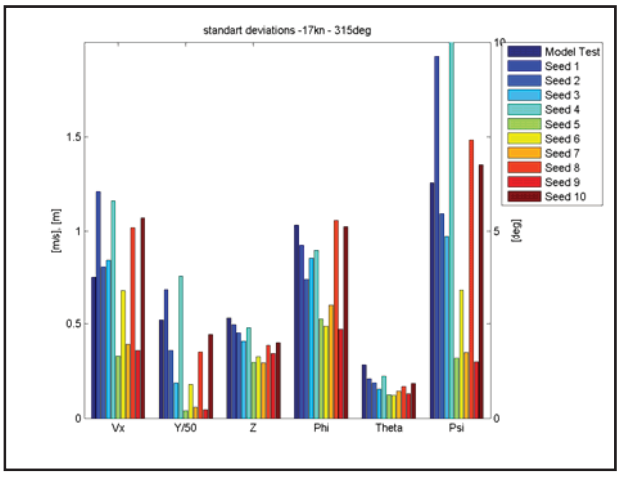

Figure 4 Standard deviations case 707

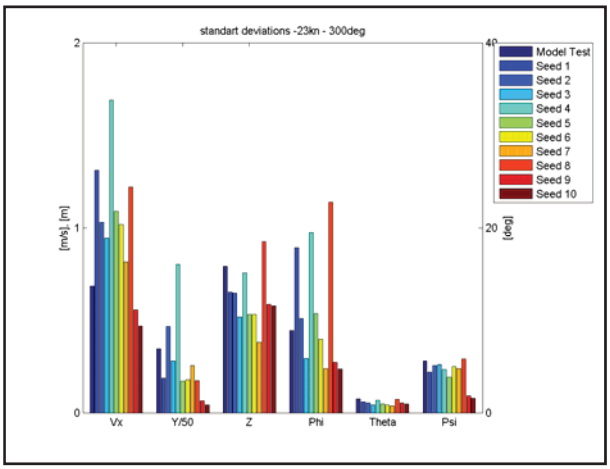

Figure 5 Standard deviations case 709

Individual runs show a significant variation in standard deviation for speed, heave and pitch. This is to be expected when between 40 and 80 waves are met per simulation run. The variation in mean value and standard deviation for sway, roll and yaw is quite large. The plots show that in almost all cases the model test results lie within the scatter of the simulations. The only conclusion that can be made about the validity of the simulation results on basis of these plots is that they are in the right order of magnitude.

In more detailed approach the 95% confidence bounds have been determined on basis of the variance of the variance of individual runs, following methods provided by Belenky et al (2007). Figures 6 through 11 show the mean standard deviation and 95% confidence intervals for sway, roll and yaw for the model tests and the simulations.

It can be seen that for all cases the mean standard deviation of the Panship simulations (indicated by the square symbol) is within the confidence bounds of the model test result. This suggests that Panship simulations are accurate in a statistical sense. The uncertainty in the model test results is expected to be much larger than that of the simulations since its duration is about 10 times lower. Apparently this is only so for case 709 for roll and yaw.

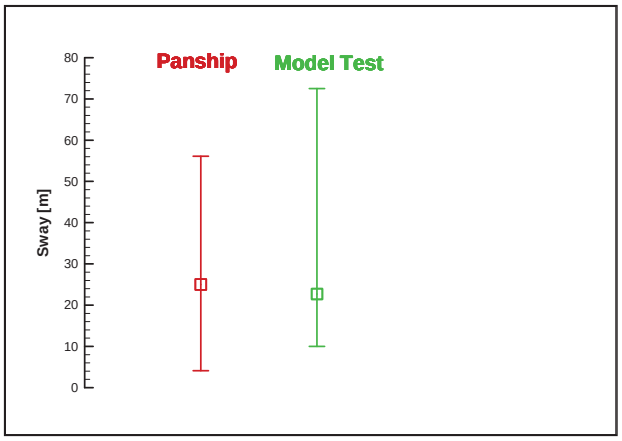

Figure 6 Confidence bounds for sway standard deviation, case 707

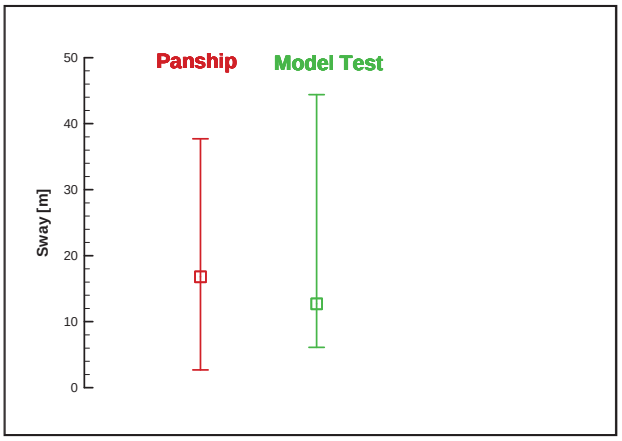

Figure 9 Confidence bounds for sway standard deviation, case 709

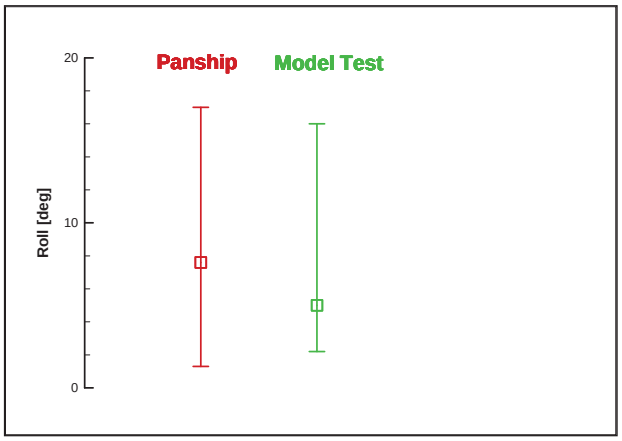

Figure 7 Confidence bounds for roll standard deviation, case 707

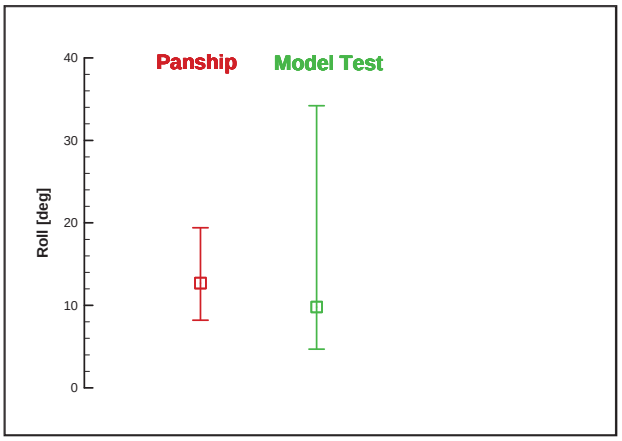

Figure 10 Confidence bounds for roll standard deviation, case 709

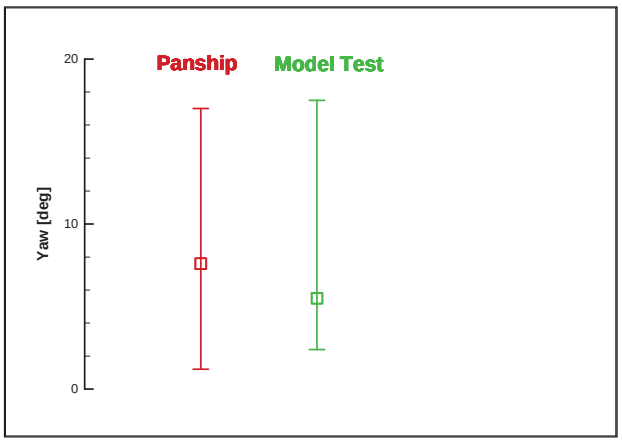

Figure 8 Confidence bounds for yaw standard deviation, case 707

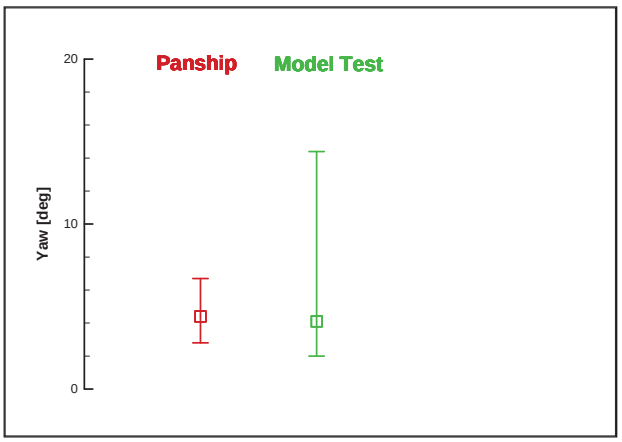

Figure 11 Confidence bounds for yaw standard deviation, case 709

4.2 Deterministic Validation

Next to the statistical method, a deterministic approach has been taken to validate the simulated responses of the vessel. First the experimental wave train needs to be reproduced in the simulations, so that time traces of motions can be compared. For this deterministic validation, single model test runs of about 175 seconds duration have been selected from the model tests runs for cases 707 and 709. For deterministic validation a number of aspects have to be taken into account.

The first point that has to be taken into account is the accumulation of errors over time. In stern quartering waves, the response of a vessel to a wave train is strongly dependent on its initial position, orientation and speed in that particular wave. Hence, in identical wave trains small errors in the simulated position would quickly accumulate, rendering the rest of the validation useless. In order to overcome this problem, during the simulation the vessel's X-Y position required to evaluate the wave kinematics is taken identical to that measured during the model test. In this way, for each time step the wave trains at the centre of gravity for model test and simulation are identical, provided the wave train reconstruction is perfect.

Secondly, attention should be paid to the initial conditions when the simulation is started. During the model tests, when the measurements are started the vessel has already sailed a number of ship lengths in the given conditions. During this period, any forward speed effects and the wave system are fully developed. However, when a simulation is started, there are no memory terms in the Green's function, creating the equivalent of the vessel being instantly accelerated from zero to operational speed the moment the simulation starts. For the deterministic simulations, this has been overcome by forcing the vessel to attain the velocity of the model test during the first 30 seconds of each run.

The process to reconstruct the experimental wave train in the simulation method is detailed by Van Walree and Carette (2011). Figure 12 shows a typical comparison between the measured and reconstructed wave trains. The reconstruction is reasonably good but not perfect, which will cause some differences between the measured and simulated motions.

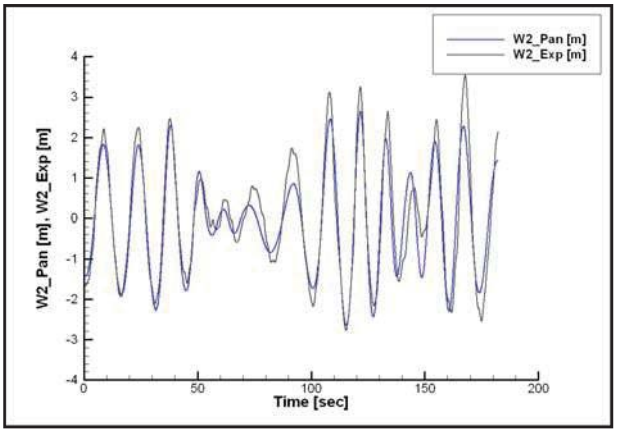

Figure 12 Comparison between reconstructed (blue) and experimental (black) wave trains

Figures 13 through 24 show a comparison between the measured and the simulated ship motions. The red signals denote the non-linear PanshipNL results, the green signals denote the semi-linear Panship results and the blue signal represents the experimental data.

Heave, roll and pitch are adequately predicted by both the semi non-linear and non-linear Panship methods for run 707005. For both methods the sway motion is off mainly due to a persisting difference in the yaw motion. The variations in forward speed are better predicted by the non-linear method.

For run 709003 differences between the semi non-linear and non-linear Panship versions are not large, except near the end of case 709 where relatively large roll and yaw motions occur which are better captured by the non-linear method. Again the speed loss is better predicted by the non-linear method.

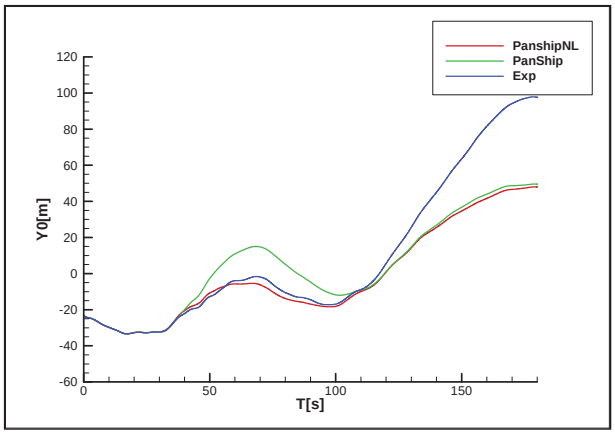

Figure 13 Comparison of sway for run 707005

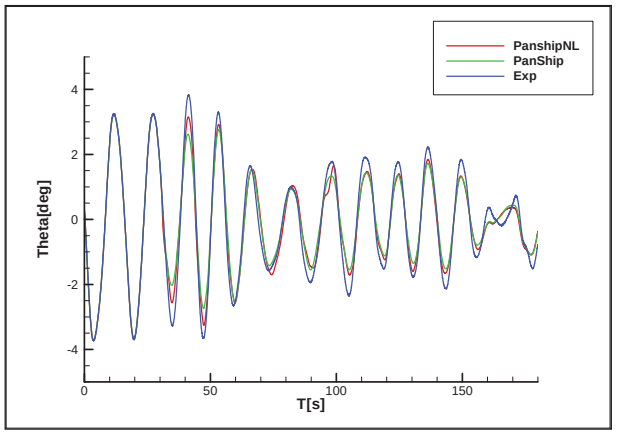

Figure 16 Comparison of pitch for run 707005

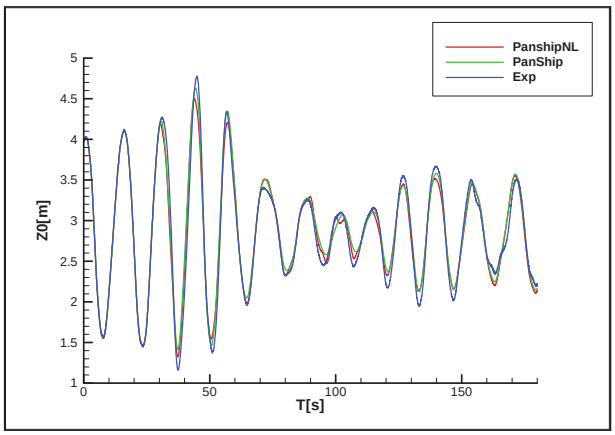

Figure 14 Comparison of heave for run 707005

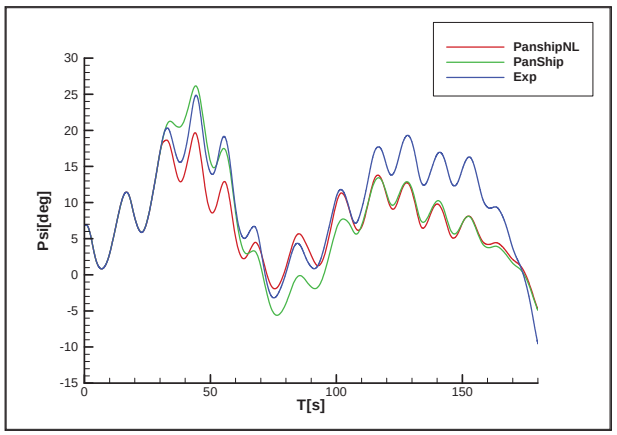

Figure 17 Comparison of yaw for run 707005

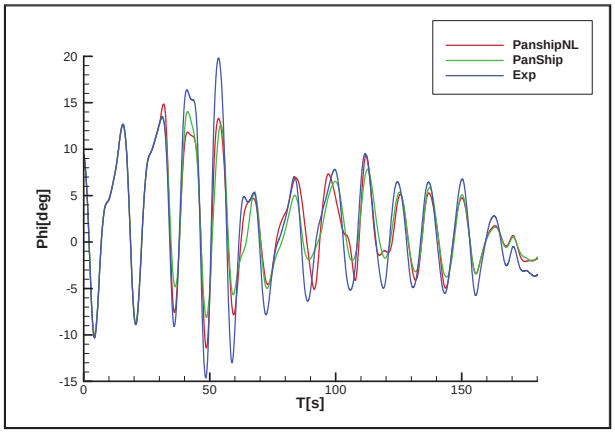

Figure 15 Comparison of roll for run 707005

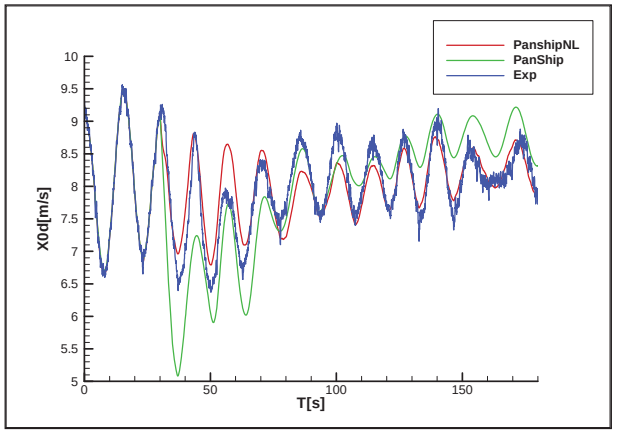

Figure 18 Comparison of speed for run 707005

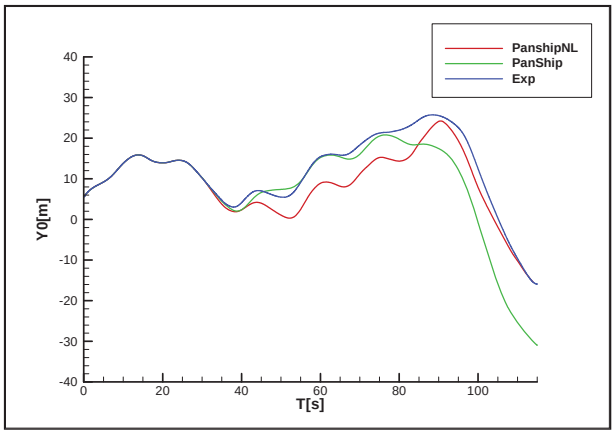

Figure 19 Comparison of sway for run 709003

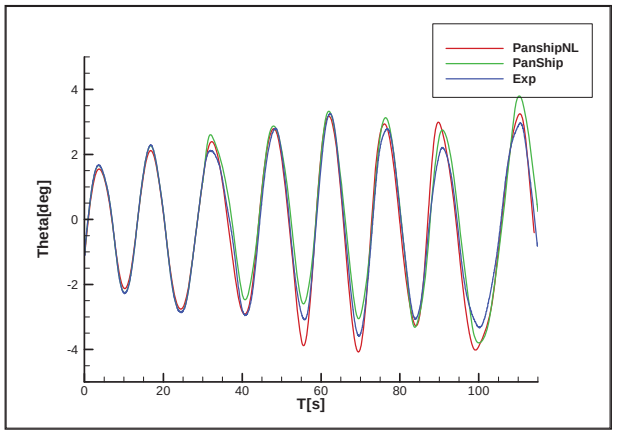

Figure 22 Comparison of pitch for run 709003

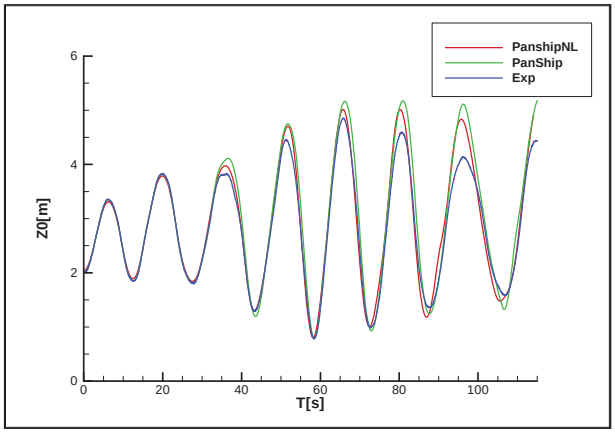

Figure 20 Comparison of heave for run 709003

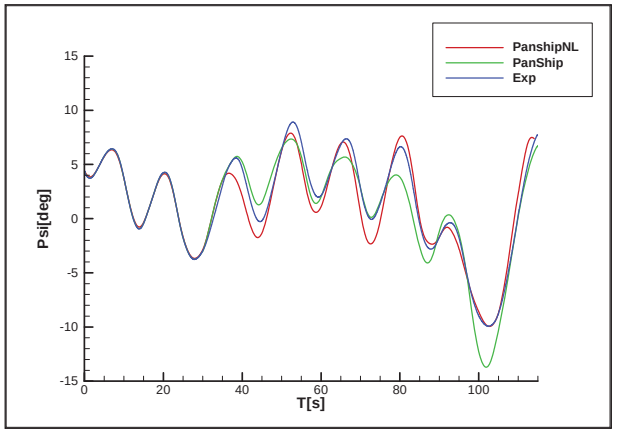

Figure 23 Comparison of yaw for run 709003

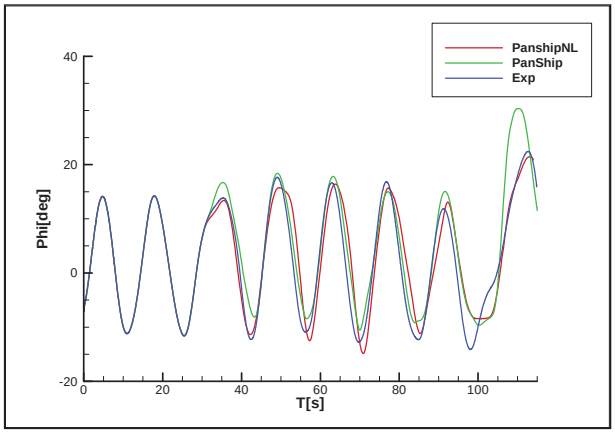

Figure 21 Comparison of roll for run 709003

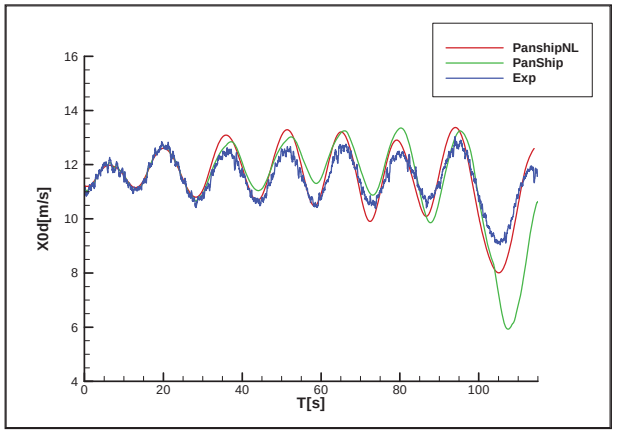

Figure 24 Comparison of speed for run 709003

7. CONCLUSIONS

As is well known for ships operating in stern quartering seas the horizontal plane motions show significant variation in mean value and standard deviation. The mean standard deviation of sway, roll and yaw motions of simulation results are found to be within the experimental confidence range for the standard deviation. Although the duration of the simulations is much greater than that of the model tests for most cases the confidence limits for simulations and model tests are quite similar.

Deterministic validation shows that both the semi non-linear and the non-linear simulation methods yield a fair prediction of motions and speed variations in stern quartering seas. This is not true for case 707 where the sway motion is offset due to a persistent difference in yaw motion. The non-linear simulation methods yield better predictions for the forward speed variations and the large amplitude roll and yaw motions, otherwise differences between the semi non-linear and non-linear simulation methods are small.

8. ACKNOWLEDMENTS

The authors acknowledge the permission of the FAST3 participants to use the experimental data.

9. REFERENCES

Belenky, V., Weems, K.M. and Lin, W-M., 2007, “A Probabilistic Procedure for Evaluating the Dynamic Stability and Capsizing of Naval Vessels, Phase 1: Technology Demonstration.” SAIC Report ASTD 08-017.

Blok J.J. and Aalbers A.B., 1991, “Roll damping due to lift effects on high speed monohulls”, Proceedings of 1st International Conference of High Speed Sea Transportation, FAST’91, Trondheim, Norway.

Blok J.J. and Beukelman W., 1984, “The High-Speed Displacement Ship Systematic Series Hull Forms – Seakeeping Characteristics”, Transactions SNAME, USA.

De Jong P. , 2011, “Seakeeping Behaviour of High Speed Ships”, Ph.D. Thesis, Delft University of Technology, Netherlands.

Walree F. van, 2002, “Development, validation and application of a time domain seakeeping method for high-speed craft with a ride control system”, Proceedings of 24th Symposium on Naval Hydrodynamics, Fukuoka, Japan.

Walree F. van and Carette N.F.A.J., 2011, “Validation of Time Domain Seakeeping Codes for a Destroyer Hull Form Operating in Steep Stern-quartering Seas”, International Journal Naval Architecture and Ocean Engineering, JNAOE, Vol. 1, pp 1-12.

Walree F. van and Turner T.G., 2013, “Development and Validation of a Time Domain panel Code for Prediction of Hydrodynamic Loads on High Speed Craft”, Proceedings of 12th International Conference of High Speed Sea Transportation, FAST’2013, Amsterdam, Netherlands.

Session 10.3 – EXTREME BEHAVIOUR

Surf-Riding in Multi-Chromatic Seas: “High-Runs” and the Role of Instantaneous Celerity

Stability and Roll Motion of a Ship with an Air Circulating Tank in Its Bottom

A Study on the Effects of Bilge Keels on Roll Damping Coefficient

This page is intentionally left blank

Surf-Riding in Multi-Chromatic Seas: "High-Runs" and the Role of Instantaneous Celerity

Nikos Themelis, *School of Naval Architecture and Marine Engineering, National Technical University of Athens*, nthemelis@naval.ntua.gr

Kostas J. Spyrou, *School of Naval Architecture and Marine Engineering, National Technical University of Athens*, k.spyrou@central.ntua.gr

Vadim Belenky, *David Taylor Model Basin / NSWCCD, Maryland, USA*, vadim.belenky@navy.mil

ABSTRACT

We investigate "high-run" events of ships in following seas. These are cases of ship motion when, due to waves' effect, a ship attains abnormally high speed. Investigations are carried out in three directions: firstly, the statistics of high-runs are calculated, exploring in particular their dependence on the wave spectrum and the sea state. Secondly, a rather neglected up to now method, proposed by Grim, for the quantification of the probability of high-run occurrence is implemented. Lastly, the focus is set on the connection of the instantaneous wave celerity with the mean surge velocity during high-run. For its evaluation, two different error metrics are implemented.

Keywords: *ship surging, surf-riding, high-run*

1. INTRODUCTION

A direct approach for calculating the probability of surf-riding of a ship operating in extreme irregular waves could be based on the identification of time intervals in which her speed is maintained at a level that is consistently above the normally expected range. Any individual realisation of such behaviour will be called hereafter "a high run" and it could be considered as generalisation of surf-riding for a multi-frequency wave environment. Whilst its inception requires careful consideration of system's phase-space, empirically it could be recognised by the up-crossing of an appropriate surge velocity threshold such as the instantaneous wave celerity. It is noted however that, for irregular seas, the role of wave celerity for surf-riding capture is still inferred from phenomenology rather than from proof (for some insights see Spyrou et al 2014a). A high-run's end could be similarly defined by the down-crossing of a suitable threshold, which however it is not easy to be uniquely defined through experience.

The literature in the topic is scarce. However, in a pioneering (but rather oversighted) work, Grim had attempted to determine how a ship could be accelerated by waves and then maintain a speed higher than her mean speed, for extended time intervals in irregular seas (Grim 1963). He had called such phenomena "long-runs". By a string of

eloquent and yet quite severe analytical approximations, he had produced statistical estimates of their existence (based on up-crossing of a speed level that he had considered as critical) and their duration.

In the current study the aim was the systematic examination of the probabilistic properties of the high-runs. It is well-known that, the longer a ship maintains a speed higher than normal, the more likely it is to experience the broaching-to instability (Spyrou 1995). The importance of the topic is thus prevalent. Firstly, a campaign of numerical simulations with direct counting of high-run durations was performed. Targeted quantities were: the mean duration of high-run; and the mean time between successive high-runs. Then, the key elements of Grim's approach were implemented, taking advantage however of current numerical calculation capability. Thus, alternative probability figures were derived which could be contrasted against those obtained by direct counting. Our final goal was to examine the correlation of instantaneous wave celerity with surge velocity during high-run incidents.

2. HIGH-RUN STATISTICS

2.1 Mathematical model

The mathematical model of surge motion in following seas was written for an earth-fixed observer, as follows:

$$\left(m-X_{\dot{u}}\right)\ddot{\xi}-\left(\tilde{\tau}_2\dot{\xi}^2+\tilde{\tau}_1 n\dot{\xi}+\tilde{\tau}_0 n^2\right)+\left(r_1\dot{\xi}+r_2\dot{\xi}^2+\right.$$
$$\left.+r_3\dot{\xi}^3\right)-\sum_{i=1}^{N}Fx_i\sin\left(k_i\xi-\omega_i t+\varepsilon_i+\varepsilon_{fi}\right)=0 \quad (1)$$

where ξ is the longitudinal position of the ship and m, $X_{\dot{u}}$ are her mass and "surge added mass" respectively. In the summation term denoting wave force, k_i, ω_i and ε_i stand respectively for the i harmonic's wave number, frequency and random phase. Fx_i denotes the amplitude and ε_{fi} the phase of the harmonic wave force component. Also, n is the propeller rate and r_i, $\tilde{\tau}_i$ are polynomial coefficients appearing in the resistance and thrust force expressions, respectively.

2.2 "High-run" definition

An apparent choice of a velocity threshold whose upcrossing would signal a high-run is the instantaneous wave celerity. Yet, it is known that attraction towards surf-riding is very likely to have started from a slightly earlier time (and thus from a lower velocity). If this early stage is neglected, a small underestimation of the probability should be expected. As down-crossing threshold was set, at first step, the nominal speed. This threshold should not be crossed by speed fluctuations occurring during surf-riding. The nominal speed is a safe choice from this point of view, although a conservative one, possibly contributing to a slight overestimation of probability. This may be statistically cancelled out, at least partly, with the underestimation linked with the beginning of the high-run. As an extra condition we request the surge velocity to be always higher than the nominal speed in order to exclude, in relatively short wave lengths and mild wave height conditions, cases that qualitatively, should not be counted as high runs. In Figure 1 are shown time segments of high-run in accordance to the presented definition. It is desired to obtain the statistics of the high-run's duration as well as of the time interval between successive events of this kind. The mean duration is obtained by summing up all individual durations and then dividing by the number of events:

$$\overline{t}_{\text{high run}}=\sum_{i=1}^{N}t_{\text{high-run}}^{(i)}\Big/\sum_{i=1}^{N}i \quad (2)$$

A similar formula is applied for the mean time between high-runs.

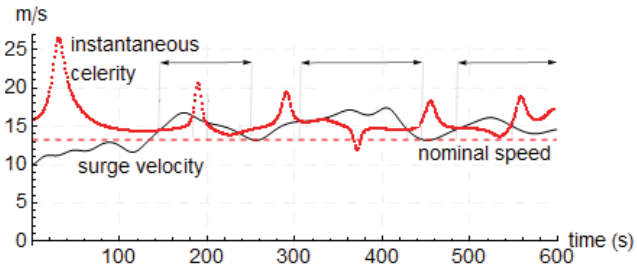

Figure 1 Schematic definition of high-run.

2.3 Simulation settings

The ship selected for applying the calculation schemes is the ONR "tumblehome topside", well-known from several previous studies (for example, Spyrou et al 2014a). A JONSWAP spectrum is considered, discretized by applying a fixed frequency increment $\delta\omega = 2\pi/t_{\text{sim}}$ where $t_{sim} = 300\ s$ is the so-called "basis simulation time". The total simulation time was a multiple of it (up to $40 \times t_{\text{sim}}$). Four ranges around spectrum's peak were separately examined, assumed containing the wave frequencies participated in the simulations. In Figure 2 are shown the wave amplitudes obtained from the spectrum, considering frequency ranges $0.2\omega_{\text{p}}$ and $0.4\omega_{\text{p}}$. A different choice would have been to modify the wave amplitude so that the variance remains constant. In that case the wave amplitudes obtained would be considerably higher (see again Figure 2). In the current study wave realizations were produced according to the first method, meaning that, the increase of the frequency range increased also the energy.

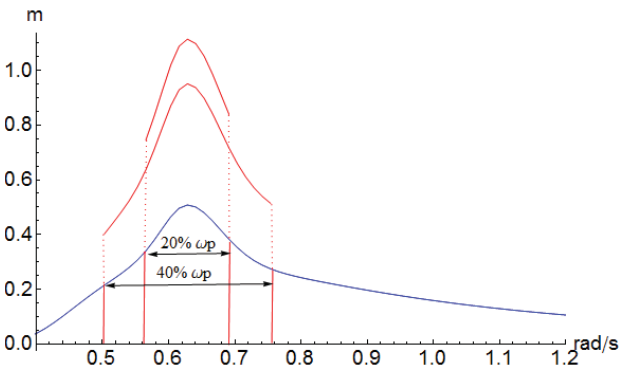

Figure 2 Wave amplitudes for 2 frequency ranges and their modified values when the variance is kept constant. H_S=6 m and T_P=10 s.

Lastly, in Table 1 appear the values of the remaining simulation parameters. Sensitivity studies in relation to the sea state, narrowness of the spectrum and the simulation time were carried out. We run 100 wave realizations per parameters' setting. The nominal and the initial speed of the ship, in each scenario, were not changed (for extra explanations see Spyrou et al 2014b).

2.4 Results

In Figure 3 appear characteristic high-run durations, obtained by simulation. Vast differences are noticed, some high-runs lasting just a few seconds and others reaching 1000 seconds! The probability density function (*pdf*) of the mean duration, based on 100 simulations, is shown in Figure 4. The effect of the sea condition on the mean, and also on certain percentiles, appear in Figures 5 and 6. Convergence with respect to the simulation time is confirmed from Figure 7.

Effect of wave frequency range on mean duration of high-run

When the frequency range is narrow, mean times are higher and they are concentrated around the lower peak periods (Figure 9).

Table 1 Range of the parameters of simulation

Parameter	Value
V_{nom} (m/s) - *Fn*	12 – 0.308
$V(0)$ (m/s)	10
wave realizations per scenario	100
H_S (m)	(3-6)
T_P (s)	(8.5-13)
(% ω_p one side)	(5-30)
Total simulation time (s)	(t_{sim} - 40xt_{sim})

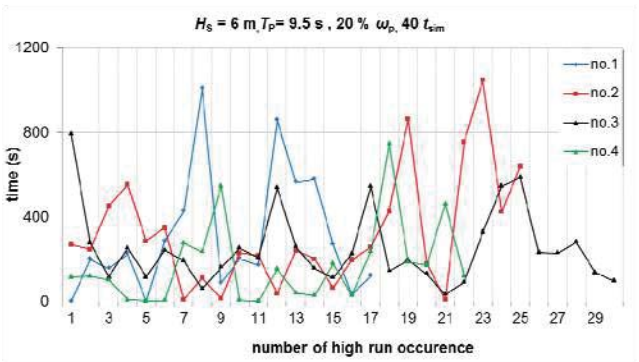

Figure 3 Recorded durations of high-run incidents in different simulations.

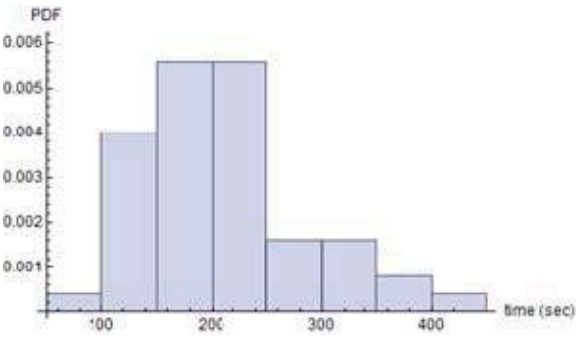

Figure 4 *pdf* of mean high-run duration [H_S=6 m, T_P=9.5 s, 40 t_{sim}, frequencies in 10% ω_P (one side)].

When the range is broadened, so do the peak values of the mean. The trend depends on the assumed significant wave height and it is more pronounced at higher significant wave heights.

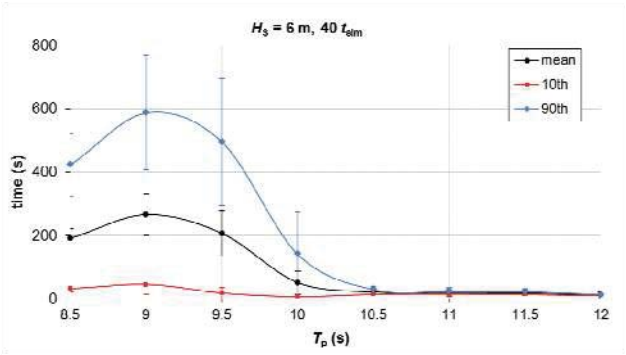

Figure 5 Mean value and percentile means (10th and 90th), as T_P is varied (H_S=6 m and simulation time 40 $t_{sim.}$). Standard deviations are included.

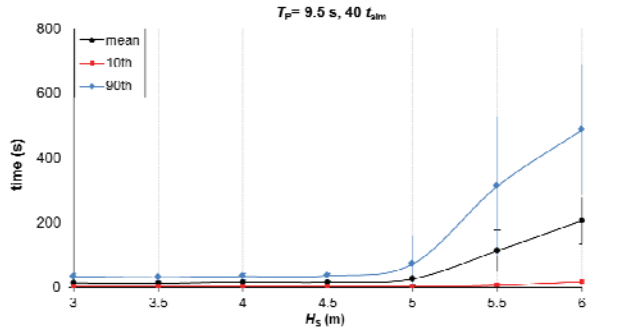

Figure 6 As in Figure 5, with varied significant wave height and fixed peak period.

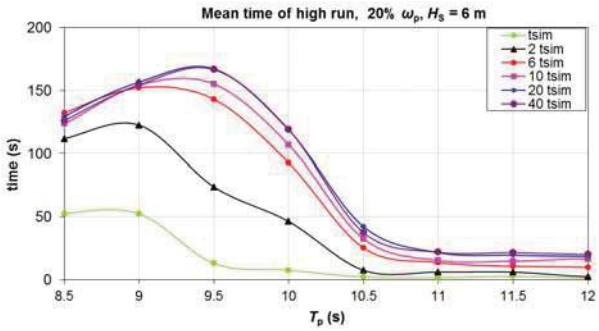

Figure 7 Convergence of statistics.

Effect of wave frequency range on mean time between high-runs

The mean time between successive high-runs is increased with the peak period (Figure 9). The effect of varying the significant wave height can be similarly assessed from Figure 10. The broader the frequency range, the more frequent the high-run occurrence. There seems to be a sharp increase of the mean time beyond a certain value of peak period. On the other

hand, the significant wave height seems more influential when the frequency range is narrow.

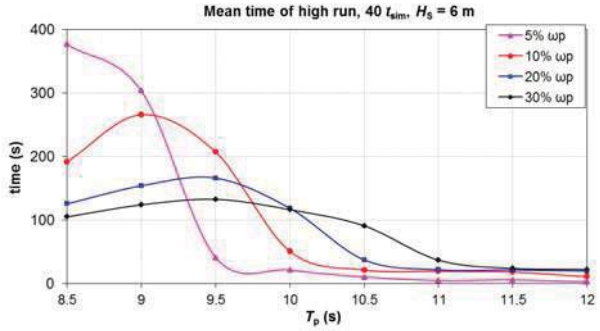

Figure 8 Mean duration of high-run for a gradually broader frequency range, as peak period is varied.

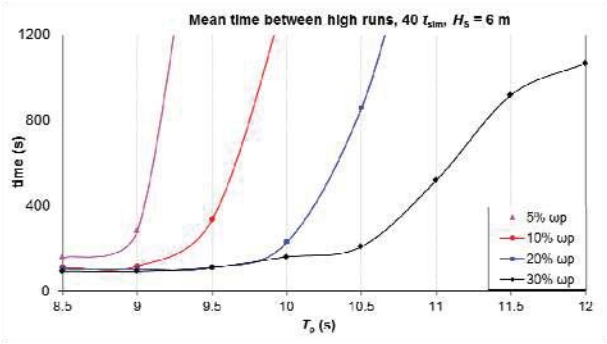

Figure 9 Mean time between successive high-runs as the peak period is varied.

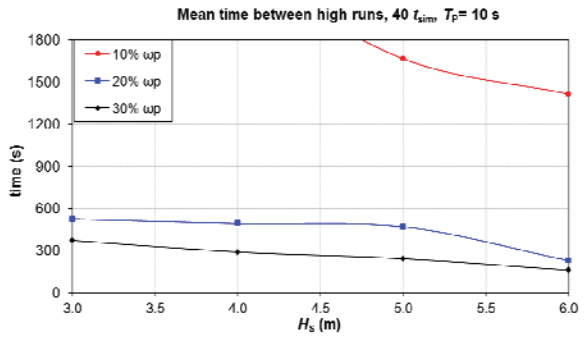

Figure 10 Mean time between high-runs as significant wave height is varied.

3. THE APPROACH OF GRIM

3.1 Key points

The main issue addressed by Grim was the probabilistic quantification of the occurrence and duration of high-run ("long run"), taking into account the strongly nonlinear character of surge motion when the phenomenon occurs, in a following irregular sea (Grim 1963). However, the lack of computer power for the demanding numerical calculations, together with the lack of a theory explaining surf-riding, at that time, had led him to incorporate several simplifying assumptions whose influence was unknown. Grim had focused on the condition generating unusually high surge acceleration and on the duration of the ensuing high speed run, which he assumed represented by a velocity plateau. Thus a simple, trapezoidal structure of ship speed was considered during such incidents. Next is presented a summary of Grim's method.

3.2 Mathematical model set-up

The surge equation is written with respect to an inertial system that moves with the ship's constant nominal speed V. The method assumes that the time is paused at the instant t when high-run's acceleration begins. Later time is measured through a new time variable τ:

$$\ddot{x}_0 + N\left(\dot{x}_0, x_0^2, x_0^3\right)/\left(m - X_{\dot{u}}\right) = \\ = \int_0^{\infty} \cos\left[\frac{\omega^2}{g} x_0 - \omega\left(1 - \frac{\omega \cdot V}{g}\right)(t+\tau) + \varepsilon\right] \sqrt{f_x^2(\omega) S(\omega) d\omega} \tag{3}$$

The distance variable x_0 determines ship's position. Function $N\left(\dot{x}_0, x_0^2, x_0^3\right)$ refers to the resistance and thrust forces, f_x is the RAO of the Froude-Krylov surge wave force [divided by the mass (including added mass) of the ship] and S is the wave spectrum. Consistently with the model of section 2, the term $N\left(\dot{x}_0, x_0^2, x_0^3\right)$ should take the following form:

$$N\left(\dot{x}_0, \dot{x}_0^2, \dot{x}_0^3\right) = \left[3r_3 V^2 + 2(r_2 - \tilde{\tau}_2)V + r_1 - \tilde{\tau}_1 n\right]\dot{x}_0 + \\ + \left(3r_3 V + r_2 - \tilde{\tau}_2\right)\dot{x}_0^2 + r_3 \dot{x}_0^3 + R(V) - T(V;n) \tag{4}$$

where resistance and thrust, at the nominal speed are, respectively:

$$R(V) = r_1 V + r_2 V^2 + r_3 V^3$$
$$T(V;n) = \tilde{\tau}_2 V^2 + \tilde{\tau}_1 V n + \tilde{\tau}_0 n^2 \quad (5)$$

At the critical stage, the ship is assumed under a constant acceleration for a time duration τ_1. When the critical velocity V_{crit} is reached the ship maintains this velocity for time $\tau_2 - \tau_1$ (see eq. 6). Thus, the required acceleration to realise the high run should be: $b = (V_{crit} - V)/\tau_1$.

$$\dot{x}_0 = \begin{cases} b \cdot \tau, & 0 \le \tau \le \tau_1 \\ b \cdot \tau_1, & \tau_1 \le \tau \le \tau_2 \end{cases} \quad (6)$$

We note that, whilst for the regular sea he identified celerity as the critical speed, he gave no similar indication for the choice of critical speed in an irregular sea.

The wave force in (3) is considered through its integral for a finite duration τ_1 (impulse function) – this leads to the key idea of producing an impulse spectrum. Integration of (3) in time leads to an equation based on momentum:

$$\int_0^{\tau_1} \left[\ddot{x}_0 + \frac{N\left(\dot{x}_0, x_0^2, x_0^3\right)}{(m - X_{\dot{u}})} \right] d\tau = \quad (7)$$
$$= \int_0^{\tau_1} \int_0^{\infty} \cos\left[\frac{\omega^2}{g} x_0 - \omega\left(1 - \frac{\omega \cdot V}{g}\right)(t+\tau) + \varepsilon \right] \sqrt{f_x^2(\omega) S(\omega) d\omega} d\tau$$

Calculating partly the force integral leads to the following expression of the impulse (for details see Grim 1963):

$$\int_0^{\infty} \cos\left[\omega\left(1 - \frac{\omega V}{g}\right) t + \varepsilon' \right] \sqrt{f_x^2(\omega) T^2 \left(I^2 + Y^2\right) S(\omega) d\omega} \quad (8)$$

where:

$$T^2\left(I^2 + U^2\right) = \left\| \int_0^{\tau_1} e^{i\left[-\omega\left(1 - \frac{\omega V}{g}\right)\tau + \frac{\omega^2}{g}\frac{b}{2}\tau^2 \right]} d\tau \right\|^2 \quad (8')$$

The term $f_x^2(\omega) T^2 \left(I^2 + Y^2\right) S(\omega)$ is the sought impulse spectrum, while ε' is another, but still random, phase. Since the maximum value of the impulse is of interest, the cosine term is set to 1. The impulse is a random function and Grim assumed that its amplitude follows the Rayleigh distribution. In analogy to the mean wave amplitude, the mean impulse amplitude (or some other percentile average of it) is obtained from the square root of the area under the impulse spectrum, for ω from 0 to ∞.

$$\bar{I}^{(1/n)} = \alpha_{1/n} \sqrt{\int_0^{\infty} f_x^2(\omega) T^2 \left(I^2 + \mathrm{Y}^2\right) S(\omega)\, d\omega} \quad (9)$$

where the coefficient $\alpha_{1/n}$ obtains specific values depending on the average of the impulse highest $1/n$ amplitudes. For example, $\alpha_{1/10} = 1.8$ corresponds to the average of the 1/10 highest amplitudes. Additionally, the probability to exceed this average value can be obtained from the Rayleigh density function (3.92%). So, eq. 7 is transformed to the next equation where one can solve for $\alpha_{1/n}$ in order to obtain the probability to reach a critical velocity within time τ_1:

$$b \cdot \tau_1 + \int_0^{\tau_1} \left[N\left(\dot{x}_0, x_0^2, x_0^3\right) / \left(m - X_{\dot{u}}\right) \right] d\tau = \bar{I}^{(1/n)} \quad (10)$$

By integrating eq. 3 up to $\tau = \tau_2$ and repeating the above procedure, a statistical estimate of the time duration of high-run can be obtained.

3.3 Application and results

The above methodology has been applied through the next steps:

- The critical velocity is set equal to the celerity of spectrum's peak frequency.
- The probability to exceed the targeted velocity in a given time τ_1 is calculated.
- Assuming that the critical velocity has been reached in τ_1, we calculate the probability to exceed certain durations $\tau_2 - \tau_1$ of high runs.
- The procedure is repeated by selecting various critical velocity levels, deriving from the nominal speed.

The nominal speed is 12 m/s and the spectrum is JONSWAP with its full frequency range.

Accelerated motion

In Figures 11 and 12 are shown plots of the calculated probability the ship speed to exceed the defined wave celerity. One could regard the time τ_1 as a fraction of the apparent wave period, i.e. it is comparable to the time, during an encounter wave cycle, when the ship is pushed by the wave. For the selected speed and peak periods, the τ_1 value should be somewhere in the range 18-26s. In Figure 13 several velocity thresholds have been tried. To be noted that the threshold $1.3V_{\text{nom}}$ corresponds to the wave celerity of $T_P = 10$ s.

Duration of high-run

The statistics of high-run duration depends on the time τ_1 (see Figure 14). It appears that, the sooner the threshold is reached the longer the high-run will last. However, according to Figure 11, the probability of a velocity threshold crossing becomes significant for $\tau_1 > 20$ s. Given that the threshold has been reached, we examine the effect of peak period and significant wave height on high-run's duration. Thus, Figures 15 and 16, showing the effect of peak period and significant wave height on high-run duration, were drawn for $\tau_1 = 20$ s.

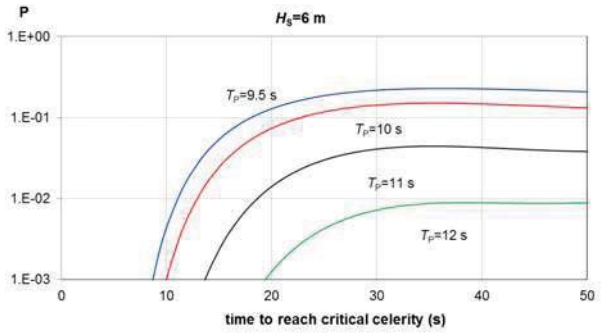

Figure 11 Probability to exceed the celerity value corresponding to the peak frequency, within a certain time, for H_S=6 m.

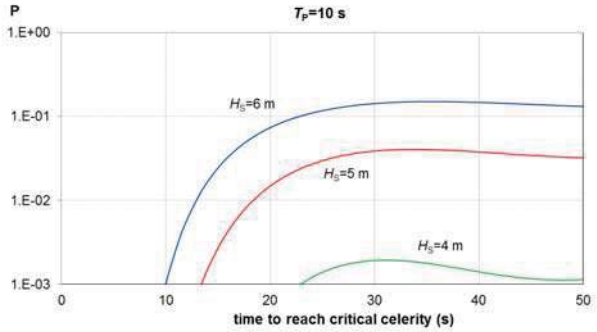

Figure 12 Probability to exceed the celerity value corresponding to the peak frequency, within a certain time, for T_P=10 s.

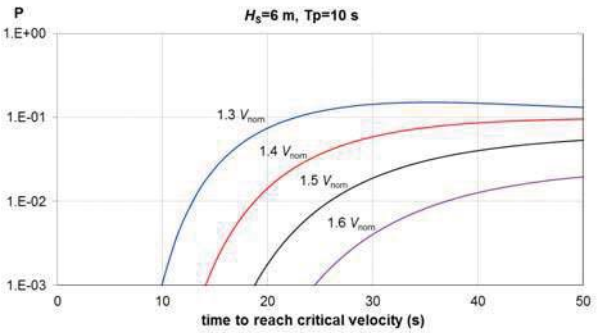

Figure 13 Probability to exceed various values of critical velocity (defined by a constant times the nominal speed) as a function of τ_1 (H_S=6 m and T_P=10 s).

By increasing the peak period, the high-run occur less frequently. One notes in Figure 16 the substantial decrease of the duration for lower significant wave heights. Also, from Figure 17 it is recovered that, setting a higher velocity threshold induces a significant reduction of probability.

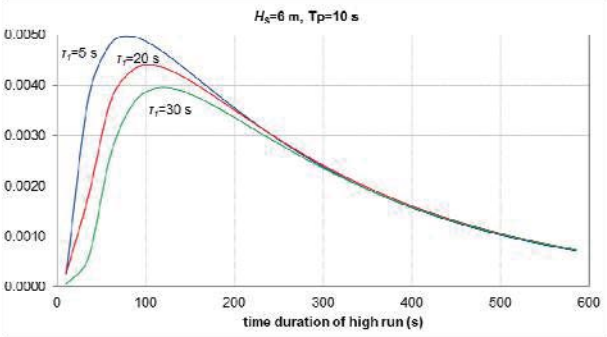

Figure 14 *pdf* of high-run duration for certain wave parameters (3 cases of τ_1).

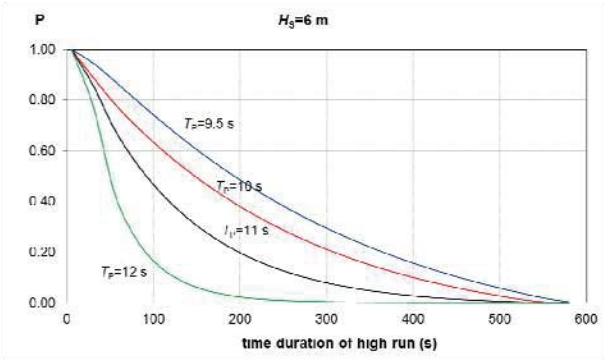

Figure 15 Probability of exceeding a duration value, for several peak periods ($\tau_1 = 20$ s).

3.4 Comparison with direct counting

We contrasted the statistics of high-run duration obtained with the method described in section 2, against the respective result based on Grim's approach (Figure 18). As observed, Grim's method suggests that the longer high-run are more probable (when compared with the mean durations obtained from simulation). This could be also verified by the fact that the mean duration derived from Grim's method (150 s) is approximately equal with the mean obtained for the 80th percentile. A qualitatively similar tendency was noticed also in other sea states.

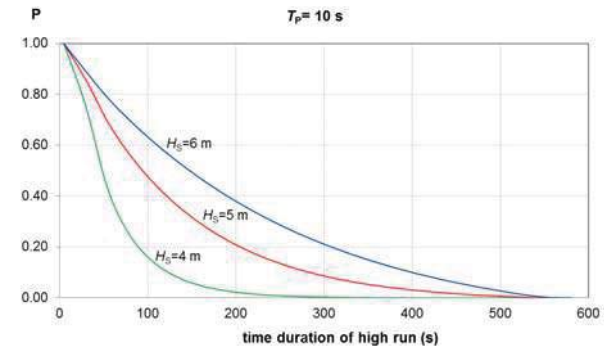

Figure 16 Probability to exceed a duration value. The threshold speed is the celerity corresponding to the peak frequency of the spectrum ($\tau_1 = 20$ s).

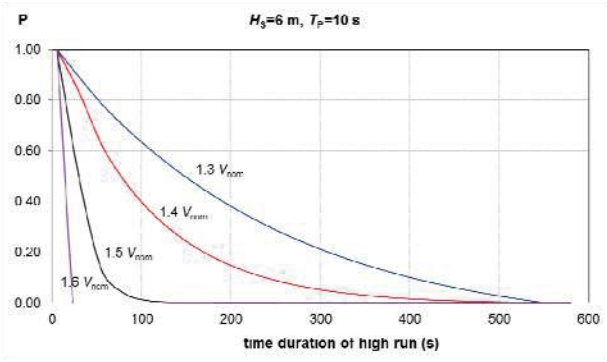

Figure 17 Probability of high-run duration for various velocity thresholds ($\tau_1 = 20$ s).

In interpreting any discrepancies between the results of the two methods, one should take into account their main differences: firstly, Grim's method assumes a constant (and equal to the targeted threshold) surge velocity during the high-run (possibly inspired by the regular wave case when surf-riding occurs). Nonetheless, we have observed fluctuations (sometimes strong) in high-runs. Furthermore, the velocity thresholds that bound the high-run in the two methods are different. In the direct counting, it is specified by the instantaneous wave celerity and the nominal speed while on Grim's approach the limit threshold is constant and equal to the celerity of peak frequency.

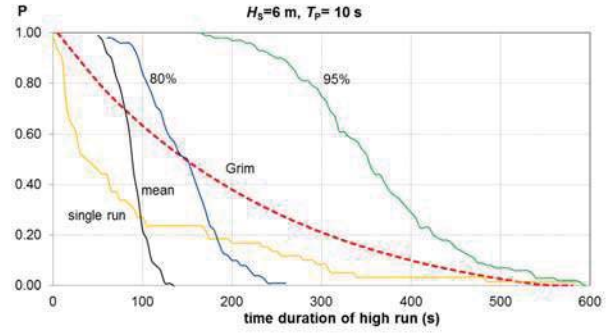

Figure 18 Comparison of probabilities of high-run duration between simulation statistics and Grim's method (H_S=6 m, T_P=10 s).

4. CORRELATION OF CELERITY AND MEAN SPEED IN HIGH-RUNS

4.1 Objectives of the study and error metrics

The aim of this final study is to examine whether could be objectively established that the instantaneous wave celerity truly dictates the mean surge velocity during high-run events. The frequency range is systematically varied in order to study the effect of a transition from a "narrow" to a "broad-band" spectrum. Methods of calculation of the instantaneous wave celerity $c(t)$ in irregular waves were discussed earlier (see Spyrou et al. 2014c). The one used here is derived from the concept of instantaneous frequency.

The mean speed $\bar{U}(t)$ is based on several speed values sampled between successive speed maxima and minima. Details of the calculation procedure are found in Spyrou and Themelis (2013). To quantify the difference between the two time-varying processes of interest (the instantaneous celerity and the mean speed), two error metrics commonly employed in studies addressing discrepancies of time histories will be used (Sarin et. al. 2010). The first metric is the well-known Euclidean vector norm:

$$L_2 = \left\| \mathbf{c} - \bar{\mathbf{U}} \right\| = \left(\sum_{i=1}^{N} \left| c_i - \bar{U}_i \right|^2 \right)^{1/2} \tag{11}$$

where $\mathbf{c}, \mathbf{U}$ are the discretised time histories (vectors of equal dimension N) of instantaneous celerity and mean speed, respectively. It should be noted that vector norms cannot distinguish an error due to phase difference from an error due to magnitude.

The second error metric has been proposed by Sprague and Geers (2004). It combines the error M due to magnitude differences (eq. 12) and the error P due to those of phase (eq.13):

$$M = \sqrt{\frac{\psi_{AA}}{\psi_{BB}}} - 1 \tag{12}$$

$$P = \frac{1}{\pi} \cos^{-1} \left(\frac{\psi_{AB}}{\sqrt{\psi_{AA} \cdot \psi_{BB}}} \right) \tag{13}$$

where

$$\psi_{\mathrm{AA}} = \frac{\sum_{i=1}^{\mathrm{N}} c_i^2}{N}, \; \psi_{BB} = \frac{\sum_{i=1}^{\mathrm{N}} \bar{U}_i^2}{N}, \; \psi_{\mathrm{AB}} = \frac{\sum_{i=1}^{\mathrm{N}} c_i \bar{U}_i}{N} \tag{14}$$

The combined error is:

$$C_{er} = \sqrt{M^2 + P^2} \tag{15}$$

These two error metrics will be applied not only to the instantaneous celerity versus the mean speed, but also to the celerity corresponding to the peak frequency versus the mean speed, because the latter is also a strong candidate for the critical speed of surf-riding.

4.2 Simulation settings

The "tumblehome" vessel is assumed operating at nominal speed 14 m/s. Ranges of wave frequency with gradually increasing width are tested (JONSWAP spectrum). Per frequency range, 10 realisations are generated. The significant wave height and the peak period are 6 m and 10 s, respectively. The total simulation time is 5000 s; however the first 2000 s of each run are excluded from further processing. The time step is 1 s.

4.3 Results

Error mean values according to the two applied metrics were obtained. To ensure that the comparison is carried out only during time segments of high run occurrence, we introduced a velocity condition requiring, the mean surge velocity to be greater than the nominal speed ($\bar{U}(t) > U_{\mathrm{nom}}$) ("1st velocity condition"). We tested also a slightly modified version of it: $\bar{U}(t) > 1.1 \cdot U_{\mathrm{nom}}$ ("2nd velocity condition"). Finally, we calculate the error values between the mean of the surge velocity and the mean of the instantaneous celerity. For

the latter, we follow the same calculation procedure as for the mean surge velocity.

Typical time histories on which the two metrics are applied are shown in Figure 19. Errors according to the Euclidean metric are seen in Figure 21 and 22, for the first and the second velocity condition, respectively. In contrast, Figures 23 and 24 show the errors according to the Sprague and Speers metric. The results based on the Euclidean metric suggest that, the discrepancy of mean speed from the celerity of peak frequency is consistently less than that of mean speed from instantaneous celerity. This trend appears too if the 2nd velocity condition ($\bar{U}(t) > 1.1 \cdot U_{\text{nom}}$) is imposed. The same conclusion is drawn when the Sprague-Geers metric is used, if the first velocity condition is applied.

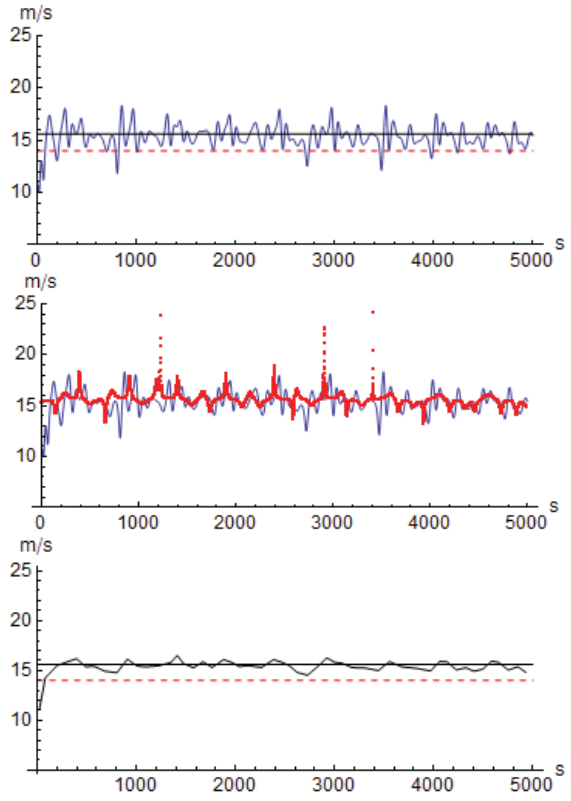

Figure 19 Time histories of surge velocity (upper diagram), instantaneous wave celerity (middle) and mean surge velocity (low). Continuous and dashed straight lines show the wave celerity of the peak frequency and the nominal speed, respectively. The simulations were based on a frequency range 20% ω_p (both sides).

However, for the second velocity condition the situation is reversed and the correlation of instantaneous celerity with mean speed is superior, for frequency ranges up to 45% ω_p. Even better correlation is achieved when the mean of the instantaneous celerity is taken, in place of the instantaneous celerity itself. In general, the error increases as the frequency range of the spectrum is broadened.

5. CONCLUDING REMARKS

The statistics of high-run occurrences in irregular seas were investigated by simulation–based direct counting and by an approximate semi-analytical method. The topic remains open since the dynamics behind these events is not completely understood yet. The velocity of the high-run shows good correlation with the mean instantaneous celerity when an error metric combining errors of amplitude and phase is applied.

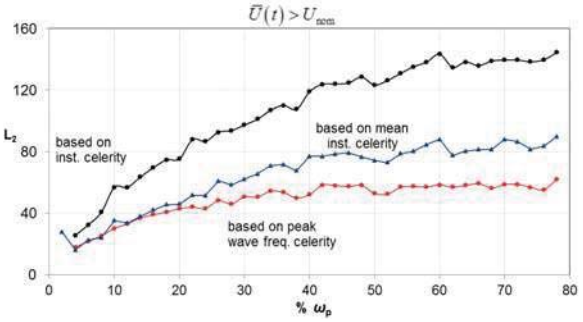

Figure 20 Calculated error according to Euclidean metric (1st velocity condition)

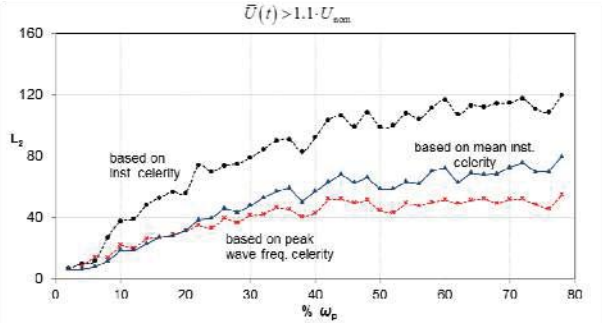

Figure 21 Calculated error according to Euclidean metric (1st velocity condition).

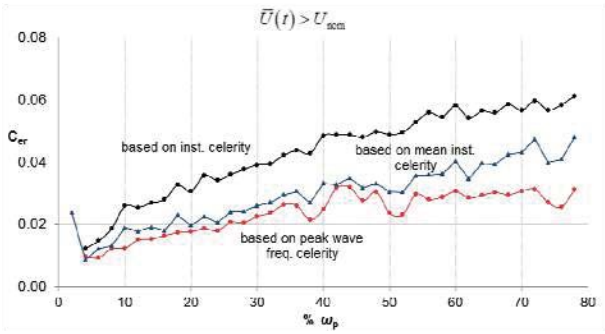

Figure 22 Error according to the Sprague and Geers metric, when satisfying the 1st velocity condition.

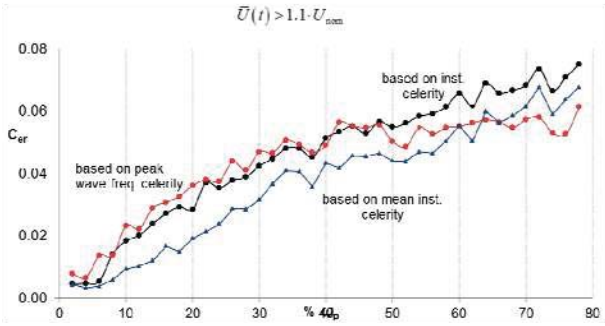

Figure 23 Error according to the Sprague and Geers metric when satisfying the 2nd velocity condition.

6. ACKNOWLEDGEMENTS

Parts of the work described in this paper (sections 2 and 3) have been funded by the Office of Naval Research under Dr. Ki-Han Kim and Dr. Woei-Min Lin. Section 4 has been supported by the Greek General Secretariat of Research and Technology under the General Program ARISTEIA I (contract reference number GSRT-252).

7. REFERENCES

Grim, O., 1963, "Surging motion and broaching tendencies in a severe irregular sea", Ocean Dynamics, Vol. 16, No 5, Springer Berlin/Heidelberg, pp. 201-231

Spyrou, K., 1995, Surf-riding, yaw instability and large heeling of ships in following/ quartering waves, Ship Technology Research/Schiffstechnik, 42 (2), 103-112

Spyrou, K., Themelis, N., 2013, "Wave celerity in a multi-chromatic sea: a comparative study", Proceedings, 13th International Ship Stability Workshop, Brest, France.

Spyrou, K., Belenky, V., Themelis, N., Weems, K., 2014a, "Detection of surf-riding behavior of ships in irregular seas", Nonlinear Dynamics, Vol. 78 (1), 649-667, Springer.

Spyrou, K., Themelis, N., Kontolefas, I., 2014b, "What is surf-riding in irregular seas?", Proceedings, 14th International Ship Stability Workshop, Kuala Lumpur, Malaysia, 29th September- 1st October 2014.

Spyrou, K., Belenky, V., Reed,A., Weems,K., Themelis,N., Kontolefas, I., 2014c, "Split-Time Method for Pure Loss of Stability and Broaching-To", Proceedings, 30th Symposium on Naval Hydrodynamics, Hobart, Tasmania, Australia, 2-7 November 2014.

Sarin, H., Kokkolaras, M., Hulbert, G., Papalambros, P., Barbat, S., Yang, R., 2010, "Comparing time histories for validation of simulation models: error measures and metrics", Journal of Dynamic Systems, Measurement, and Control, vol.132.

Sprague, M. A., and Geers, T. L., 2004, "A Spectral-Element Method for Modelling Cavitation in Transient Fluid-Structure Interaction," Int. J. of Numerical Methods Eng., vol. 60, pp. 2467–2499.

This page is intentionally left blank

Stability and Roll Motion of a Ship with an Air Circulating Tank in Its Bottom

Ikko Watanabe, *Osaka Prefecture University* sv103027@edu.osakafu-u.ac.jp

Satowa Ibata, *Osaka Prefecture University* ibata@marine.osakafu-u.ac.jp

Seijiro Miyake, *Osaka Prefecture University* miyake@marine.osakafu-u.ac.jp

Yoshiho Ikeda, *Osaka Prefecture University* ikeda@marine.osakafu-u.ac.jp

ABSTRACT

A ship with an air circulating tank in its bottom has been developed in Osaka Prefecture University with several Japanese shipyards to reduce the frictional resistance drastically and to save fuel consumption of the ship. It was pointed out that the moving air in the tank due to heel and roll motions may reduce the stability, and changes the roll motion characteristics of the ship.

In the present paper, at first, the effects of the moving air on the stability of a ship with an air circulating tank which has a single compartment are theoretically and experimentally investigated to confirm the loss of stability. To resolve the stability loss, the air circulating tank is divided into some transverse compartments. The stability calculation suggests that four compartments can keep enough stability in small roll angle. For the new tank, the stability, roll damping and roll motions are experimentally investigated.

Keywords: *air circulating tank, frictional resistance, stability, roll motions, roll damping*

1. INTRODUCTION

Reduction of the frictional resistance acting on a ship by using air has been studied in more than hundred years. In Russia (Soviet Union), Europe and Japan, research and development of ship drag reduction by using air were carried out from 1960's to 2000's. Comprehensive reviews were published (Gorbachev, Y, 2012 and Makiharju, S, 2012). For a large ship which runs in lower Froude number, drag reduction devices by using air-micro-bubbles were successively installed to module carriers, bulk carriers and a Ro-Ro ferry in Japan, and revealed that the devices gave a 3-12% reduction of fuel consumptions.

To get more effective drag reduction tools, the authors have been developing an air circulating tank (ACT) which is installed in the bottom of a ship and in which air is kept and circulates. Reduction of the frictional resistance can be more than the air micro-bubble method mentioned above. The experiments carried out by the authors showed that a 25-30% reduction of frictional resistance can be achieved in lower Froude numbers (Furuo, A, 2015). There are some problems to keep the drag reduction, for examples, how to keep the air in trim, heel and ship motions, how to reduce generated waves on the free surface between inside air and outside bottom water flow, how to keep the stability of the ship with the air circulating tank.

In the present study, fundamental characteristics of the stability of a ship with ACT are theoretically and experimentally studied, and an ACT to avoid the stability

reduction due to the bottom air is developed. Roll damping and roll motions in beam waves are also experimentally investigated.

2. STABILITY OF A SINGLE-COMPARTMENT ACT

Stability characteristics of a box shape model with a single-compartment ACT in the bottom are investigated. The cross section of the model are shown in Fig. 1. Air is accumulated in the ACT or the well.

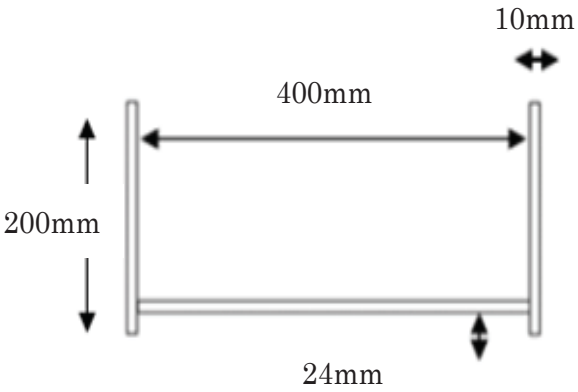

Figure 1 Cross section of the box shape model with a single-compartment ACT .

With increasing heel angle, the inside air shifts and generates a negative restoring moment as shown in Fig. 2. The inside air escapes from the tank in larger heel angle and the draft increases due to reduction of buoyancy as shown in the fourth figure in Fig. 2.

The stability reduction due to the air shift and escape in the ACT can be easily calculated. The results are shown in Fig. 3 with experimental results obtained by the authors. We can see that the air in ACT significantly reduces the stability of the model. It should be noted that the stability in small heel angle becomes very small as shown in Fig. 3. This means that the ship may be unstable in some degree, and needs appropriate GM to compensate the reduction of the stability due to the air. In larger heel angle, however, the inside air escapes from the ACT, and the stability may recover to the safety side.

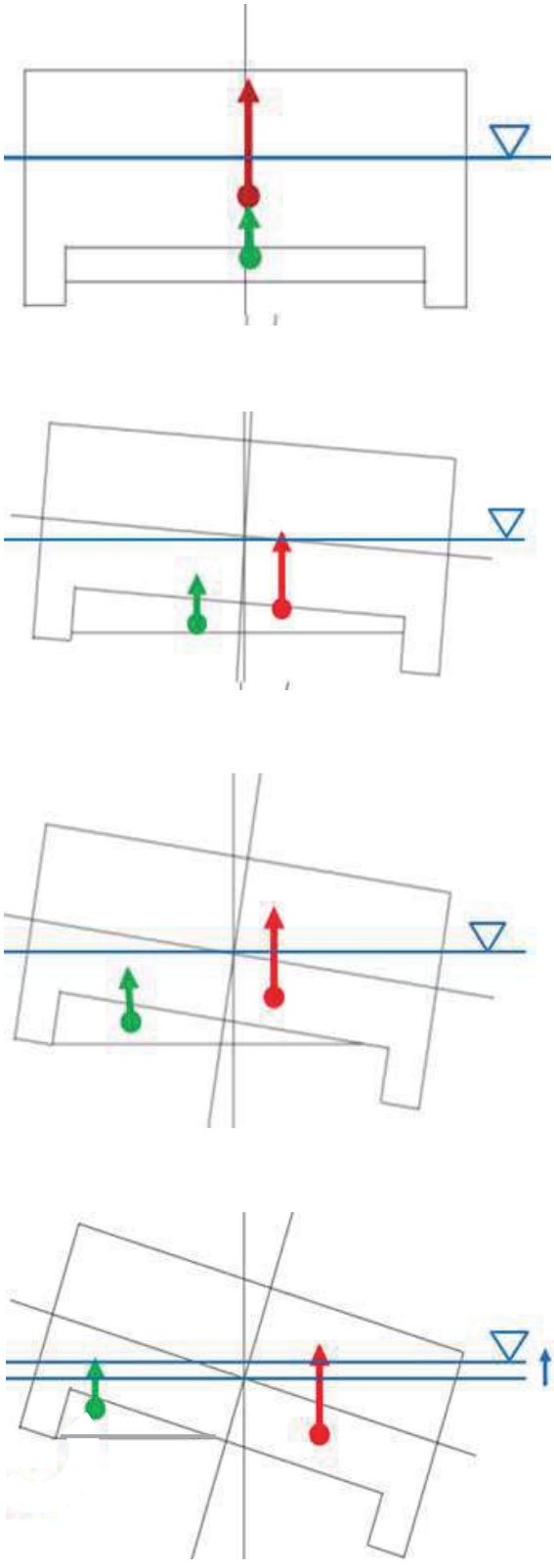

Figure 2 Inclining of a ship and air in ACT (red arrow: buoyancy acting on the body, green arrow: buoyancy by trapped air).

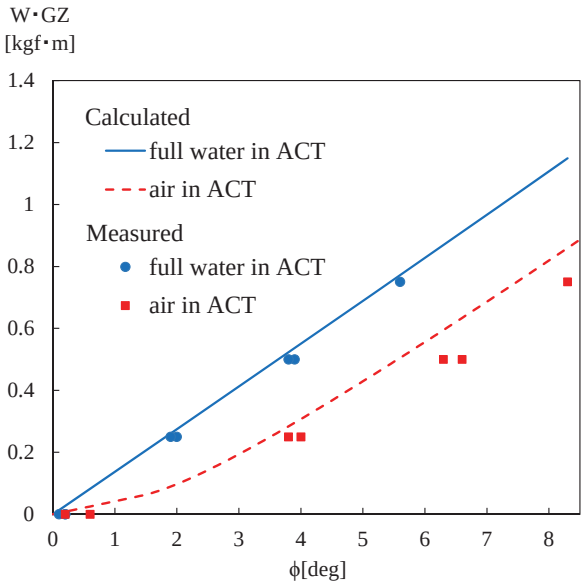

Figure 3 Reduction of stability of a box model due to air in a single-compartment ACT (lines: calculated, marks: measured)

3. IMPROVED ACT

The easiest way to resolve the reduction of the stability of a ship with ACT may be to transversely divide the tank into some compartments. Fig. 4 shows air shift in each compartments of the box model with a four-compartments ACT. Stability calculations for various numbers of the compartments are carried out, and the results are shown in Fig. 5. The results demonstrate that the transverse compartments drastically improve the stability, and the stability of a model with four compartments are almost same as that of the case of no air in the ACT. We can safely said that the four compartments can resolve the stability problem of a ship with an air circulating tank.

4. STABILITY AND ROLL MOTIONS OF ULCC

The authors developed a 20,000TEU ultra-large container carrier with shallow draft and wide beam. To reduce the frictional resistance of the ship, an ACT was developed for the ship as shown in Fig. 6.

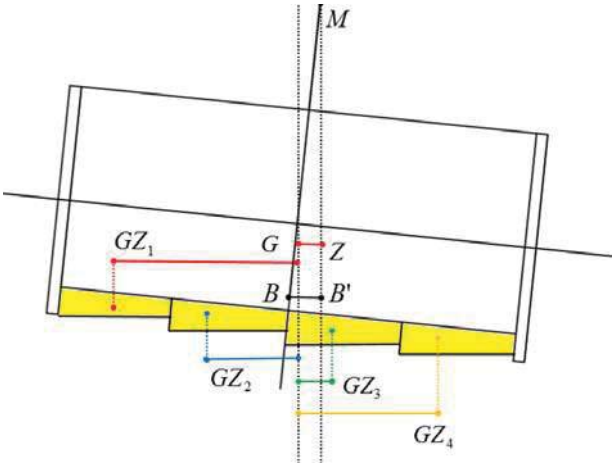

Figure 4 Schematic view of an inclining box model with an ACT with four-compartments.

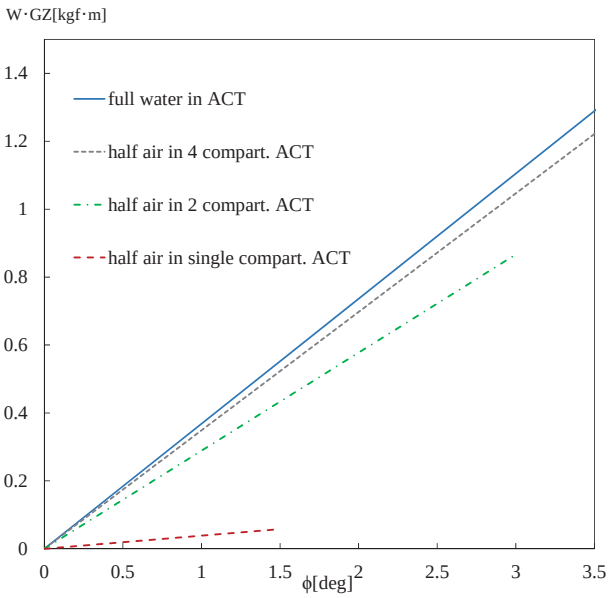

Figure 5 Calculated stability reduction of ACTs with single, two and four compartments.

Model experiments to measure the resistance acting on the model were carried out in a circulating water channel and a towing tank to find a 26% reduction of the frictional

resistance in low Froude number (Furuo, A, 2015).

In the present study, roll motions in beam waves are experimentally investigated. The body plan and the principal particulars of the model are shown in Fig. 7 and Table 1. The experimental results are shown in Figs. 8 and 9. The roll damping shown in Fig. 8 demonstrates that the air decreases the damping drastically. It can be seen that the damping for the case of no air in the ACT is much larger than those for the cases of air in the ACT and normal bottom. The increase of the roll damping may be because that the longitudinal walls which divide compartments in ACT works as the same as bilge keels of a ship. Roll amplitudes of the ship in beam waves shown in Fig. 9, however, suggest that the air in the ACT has only slight effects on the roll motions. The peak value at resonance of the case of air in the ACT is slightly larger than that full water in the ACT.

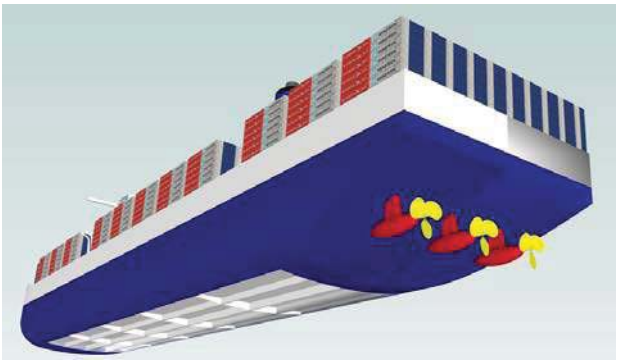

Figure 6 Artist impression of a 20,000TEU container ship with ACT.

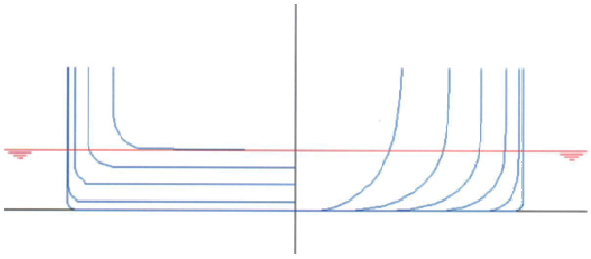

Figure 7 Body plan of the model without ACT

Table 1 Principal particulars of the model of ULCC

Model ship	Loa(m)	2.770
	Lwl(m)	2.670
	B(m)	0.500
	D(m)	0.150
	d(full load)(m)	0.063
	Wetted Surface Area (full load)(m^2)	1.549
	Cb	0.955
Air Circulating Tank	L(m)	2.000
	B'(m)	0.476
	H(m)	0.0125
	Surface Area (m^2)	0.952

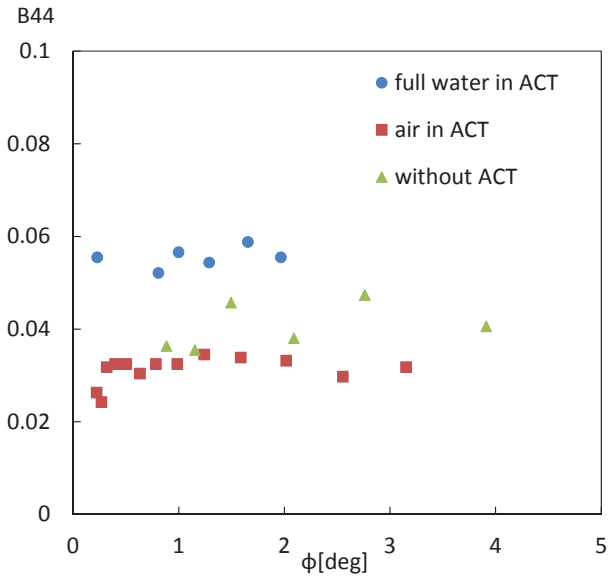

Figure 8 Measured roll damping coefficients by free decay tests

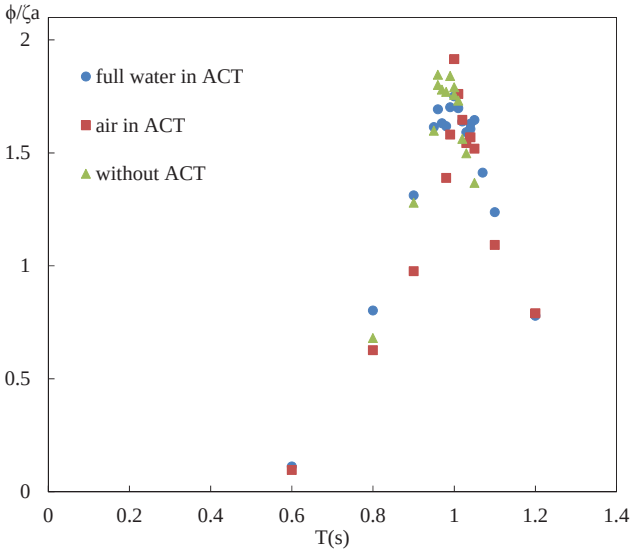

Figure 9 Measured roll amplitudes in beam waves of ULCC model with and without ACT

5. CONCLUSIONS

Effects of air in an air circulating tank (ACT) on the stability and the roll characteristics of a ship are theoretically and experimentally investigated, and following conclusions have been obtained.

1) Air in an air circulating tank of a single compartment reduces the transvers stability, particularly in small heel angle.
2) By dividing the ACT into some transverse compartments, the reduction of the stability decreases. The reduction disappears for four compartments.
3) Effects of the air in ACT on roll motions in beam waves are slight.

6. REFERENCES

Furuo, A, 2015, “A study on an air circulating tank to reduce the frictional resistance of a ship”, Master thesis, Osaka Prefecture University, Japan (in Japanese).

Furuo, A, 2015, “Development of an Air Circulating Tank to Reduce the Frictional Resistance of a Ship”, the 25th ISOPE Conference.

Gorbachev, Y, Amromin, E, 2012, “Ship Drag Reduction by Hull Ventilation from Lavel to Near Future”, Proc. of ATMA,

Makiharju. S, Ceccio. S. L, 2012, “Air Lubrication Drag Reduction on Great Lakes Ships”, Presentaion material at University of Michigan.

This page is intentionally left blank

A Study on the Effects of Bilge Keels on Roll Damping Coefficient

Yue Gu, *Department of Naval Architecture, Ocean and Marine Engineering, University of Strathclyde, Glasgow, UK*. yue.gu.2013@uni.strath.ac.uk

Prof. Sandy Day, *Department of Naval Architecture, Ocean and Marine Engineering, University of Strathclyde, Glasgow, UK*.sandy.day@strath.ac.uk

Dr. Evangelos Boulougouris, *Department of Naval Architecture, Ocean and Marine Engineering, University of Strathclyde, Glasgow, UK*. evangelos.boulougouris@strath.ac.uk

ABSTRACT

A study of the roll damping of a two-dimensional FPSO model produced by bilge keels using CFD method is presented in this paper. The tool to be utilized is the well-known code Star-CCM+, which uses the Volume of Fluid (VOF) approach to capture the free surface. The results are validated by comparison with experiments. Using the results from a number of simulations, the roll damping coefficient resulting from locating the bilge keels at different positions will be calculated. The analysis of the rolling damping coefficients for the different locations will provide a useful design tool for optimising the roll damping of vessels with bilge keels.

Keywords: roll damping coefficient, bilge keels, FPSO, 2-D, Star CCM+

1. INTRODUCTION

Roll motion although it is a significant parameter in the prediction of a ship's seakeeping performance, is one of the most difficult to calculate for seagoing vessels. This is due to fact that roll damping has a large influence on the roll motion up to the point that it may even cause the vessel's capsize (Haddara, 1989). It plays a dominant role on reducing the roll amplitude and that is why many researchers pay attention to the improvement of its prediction (Pesman at al, 2007). Since 1970s, many investigations have been carried out on the effects of bilge keels, which are used for many years on ships to enhance roll damping (Ikeda, 1977, Ikeda, 1978, Ikeda, 2004). However, due to the complicated nature of roll motion, mainly due to the influence of the viscosity, as well as other factors such as wind, waves and the interaction between the ship and the free surface, it is difficult to make accurate predictions using the potential theory or analytical solutions, which result in many cases in an over-estimation of the roll amplitude (ITTC, 2011). The most well-known and accepted empirical formula is Ikeda's method, but its limitations and inaccuracies have been revealed over time (Yuki, 2003a, Yuki, 2003b, Bassler, 2011). The most accurate way of predicting roll damping remains until today model testing. An efficient and low-cost method to minimise the number of model tests and improve the accuracy of the predictions is the roll damping simulation using CFD (Yang, 2012). Using such method the impact of bilge keels can be simulated and their roll damping coefficient can be predicted quite accurately.

2. BACKGROUND

A study on roll damping on a non-conventional 2-D cross-section was proposed by Yuck (2003a) to investigate the operational efficiency and stability of FPSO. Three kinds of models, namely bilge model, box model and step model, were established in the roll damping coefficient analysis under small roll angle. The results revealed a fact on midships cross-section that affects damping coefficient without bilge keels. Additional work was performed by Van't (2011) to predict the roll damping motion of a FPSO with bilge keels comparing experiment results with CFD simulations using Star CCM+, however, the entire work was limited on two bilge-keels positions.

Comparisons between experimental data and numerical results of roll damping decay for a FPSO with bilge keels was carried out by Avalos (2012, 2013, 2014) to validate accuracy of numerical methods.

Due to the limitation of Ikeda's method for large amplitude roll motions, a DTMB model with bilge keels has been developed by Bassler (2010a, 2010b, 2011) to increase the prediction accuracy of the ship's motions for design assessments.

A numerical model using RANS (Reynolds Averaged Navier Stokes) flow solver compared with experiments has been developed to improved predictions of the bilge keels effect on viscous roll damping coefficients (Querard, 2010). The results revealed that due to friction and eddy making, bilge keels have a dominant impact on the viscous roll damping coefficient.

Considering the effect of bilge keels on the roll damping, Chakrabarti (2001) investigated the features of roll damping with various ship hullform with experiments. Based on Ikeda's method, it was concluded that the impact of bilge keels on the roll damping depends on the locations of the bilge keels.

The effects of putting bilge keels at different positions on the a new non-ballast ship with rounder cross section was investigated by Miyake (2013), and results revealed that the effect of bilge keels on damping motion for a rounder cross-section are much smaller compared with a conventional square cross-section.

In this work, the effect of bilge keels at different locations for roll damping coefficients is investigated in a 2-dimensional FPSO model. Star CCM+ solver is used to simulate roll motion of the rectangular model and FPSO model. Initially, CFD simulations results are compared with previous work for validating the accuracy and feasibility of the scheme. Results obtained by Jung (2006) from roll decay tests on a rectangular structure in calm water and waves are used to be compared. Utilizing the FPSO model provided by Avalos (2012, 2013, 2014), an investigation is performed on the effects of bilge keels at different location on roll damping coefficients.

3. NUMERICAL FORMULAE

3.1 Rolling Motion

A simple equation for ship roll motion including single degree of freedom can be given by

$$A\ddot{\phi} + B(\dot{\phi}) + C\phi = M(\omega t) \quad (1)$$

However, the damping term $B(\dot{\phi})$ includes linear and nonlinear components

$$B(\dot{\phi}) = B_1\dot{\phi} + B_2\dot{\phi}|\dot{\phi}| + B_3\dot{\phi}^3 + \cdots \quad (2)$$

It can be assumed that the nonlinear component can be approximated by being linearized so that the damping term can become (Bassler, 2009)

$$B(\dot{\phi}) = B_{44}\dot{\phi} \quad (3)$$

3.2 Rolling in Calm Water

According to Bhattacharyya (1978), the equation of rolling motion in calm water can be expressed in a differential form given by

$$a\frac{d^2\phi}{dt^2} + b\frac{d\phi}{dt} + c\phi = 0 \qquad (4)$$

where,
a is the virtual mass moment of inertia
$d^2\phi/dt^2$ is the acceleration of rolling
a$(d^2\phi/dt^2)$ is the inertial moment
b is damping moment coefficient
$d\phi/dt$ is angular velocity
b$(d\phi/dt)$ is the damping moment
cϕ is the restoring moment
c is the restoring moment coefficient
ϕ is the angular displacement of rolling.

Parameters of ship roll motion are substituted into a, b and c, and the expression of roll motion in calm water can be given as

$$I'\frac{d^2\phi}{dt^2} + b\frac{d\phi}{dt} + \Delta GM\phi = 0 \qquad (5)$$

where I' is the virtual mass moment of inertia, which is the sum of the actual mass moment of inertia I and the added mass moment of inertia δI

$$I' = I + \delta I \qquad (6)$$

Equation (5) is divided by I', then the equation becomes

$$\frac{d^2\phi}{dt^2} + 2\zeta\omega_N\frac{d\phi}{dt} + \omega_N^2\phi = 0 \qquad (7)$$

where ζ is the damping factor, ω_N is the natural frequency given by

$$2\zeta\omega_N = \frac{b}{I'} \qquad (8)$$

$$\omega_N^2 = \frac{\Delta GM}{I'} \qquad (9)$$

4. METHODOLOGY VALIDATION AND ANALYSIS

The present work uses the experimental data provided by Jung (2006) for its validation. Roll decay simulations in calm water and waves use the same setup as the experiment.

4.1 Geometric Characteristics of Model

The model is a rectangular structure, which is 0.3m wide and 0.1m high with 0.05m draft shown as below

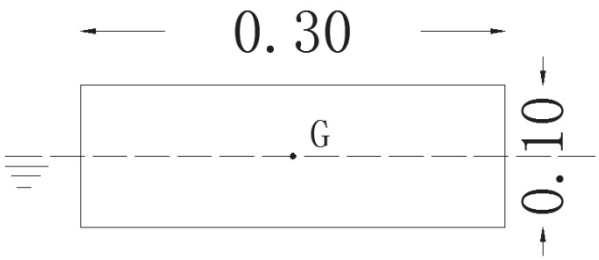

Figure 1 - Definition of geometric feature of model

4.2 Flow Domain in Free Decay Test

The roll decrement simulation is performed in a 2-D domain with the dimension of 5.7m long and 1.8m high with 0.9m water depth, shown as

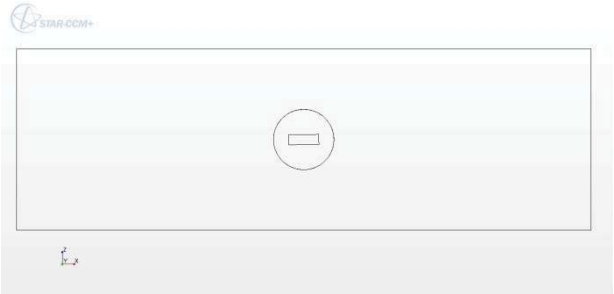

Figure 2 - Flow domain of free decay simulation

4.3 Generation of the Grid

As the body rolls in the domain, not all the mesh would be fixed. A mesh scheme is established by Manzke (2012) including deforming mesh, which changes shapes of grid

as the body rolls. However, deforming mesh is decreasing the quality of the calculations. In this work, a finer mesh scheme is utilized so that the mesh around the body can move rigidly with body without deformation. The trimmed mesh and prism layer mesher are used in the entire flow domain except the body itself. Fig.3 shows the distribution of grid through the whole domain, and Fig.4 gives the concentration of refined mesh around the free surface. Fig.5 demonstrates a refined mesh and prism layer mesh distribution around the body.

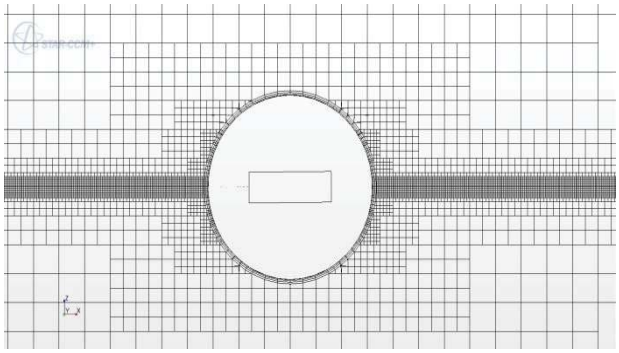

Figure 3 - Mesh scheme through the whole domain

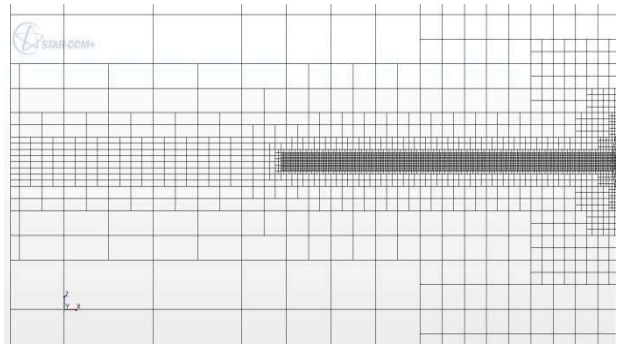

Figure 4 - Mesh distribution around free surface

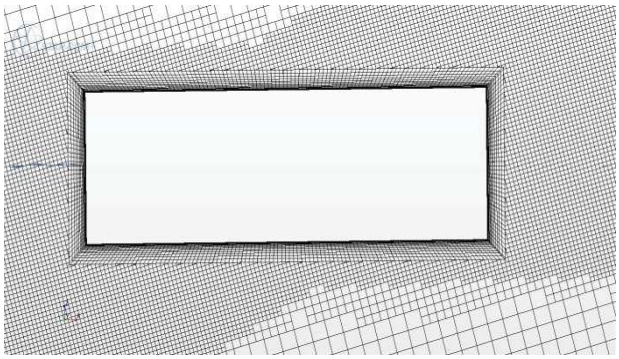

Figure 5 - Refined mesh around the body

4.4 Analysis of Free Decay Simulation

Fig.6 shows the time history of angle of inclination in the simulation of free decay. The body is initialized and released at 15 degree, inclination angle decreases after each time of roll.

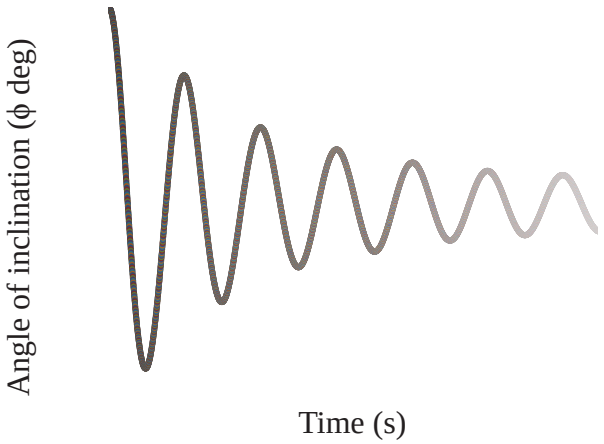

Figure 6 - Time history of angle of inclination

From Fig.6 the natural period of the structure can be obtained T_N= 0.931s, so that the natural frequency is ω_N=6.746rad/s, the virtual mass moment of inertia I'=0.364 kgm^2 and the added mass moment of inertia δI = 0.128 kgm^2, which gives a good agreement with experiment data provided (T_N= 0.93s, ω_N=6.78rad/s and δI =0.124 kgm^2). Fig.7 shows curve of the decrease of angles.

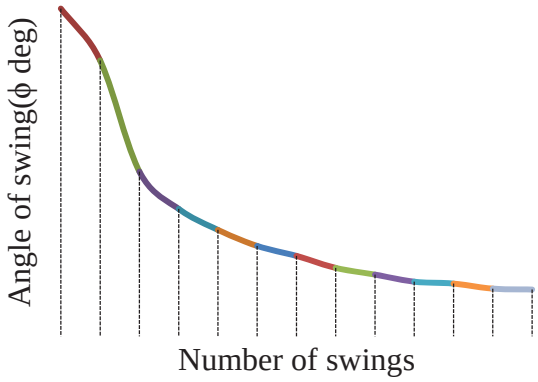

Figure 7- Curve of declining angles

According to the approach suggested by Bhattacharyya (1978), the coefficient K can be

found from the trendline of the curve of extinction that can be represented as

$$\delta\phi \text{ per swing} = K\,\phi_m \qquad (10)$$

Analysis of the calculated data gives K=0.3214. With the coefficient K obtained, the damping coefficient b can be obtained by the equation given below

$$b = \frac{KT_N\Delta GM}{\pi^2} \qquad (11)$$

So the damping coefficient b is 0.503kg-m-s. Compared with b=0.519kg-m-s from experiment data, the different percentage is 3.16%. And the damping factor ζ=0.103.

Since the simulation results demonstrate a good agreement with experiment data, the methodology can be considered valid for predicting the effect of bilge keels on the damping coefficients of FPSO model.

5. ROLL DECAY SIMULATIONS WITH BILGE KEELS

A FPSO model given by Avalos (2012, 2013, 2014) is used to investigate the damping effects of bilge keels at different locations through a series of roll decay simulations. The results demonstrate the correlation between bilge keels' locations and damping coefficients.

5.1 Characteristics of Models

Table 1 demonstrates the model features of FPSO in the present study, and bilge keels are distributed around the midship frame of FPSO at 10 positions (from position A to position J). Fig. 8 shows the distribution of bilge keels' positions at the cross-section of midships which can be given by

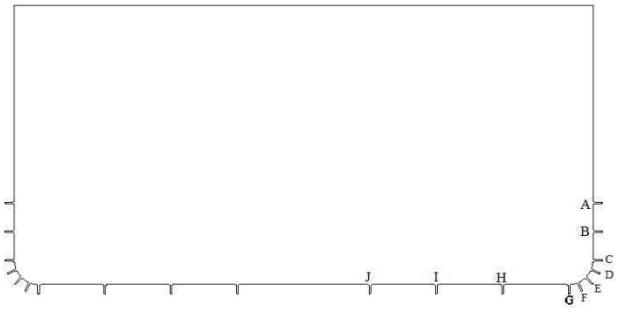

Figure 8 - Bilge keels distributions at midships cross-section

Characteristics of FPSO	Magnitude
Breath	0.725m
Draft	0.196m
Length	0.90m
Centre of gravity (KG)	0.175m
Radius of gyration (Rxx)	0.264m
Mass per unit length	169.76Kg/m
Transverse moment of inertia per unit length	13.269Kg/m
Bilge radius	0.03m
Bilge keel	0.016m

Table 1- Model characteristics of FPSO

5.2 Mesh Generation

Fig. 9 gives a view at the mesh generated based on the present scheme when the bilge keels are located at position E and refined mesh at bilge keels are illustrated by Fig.10.

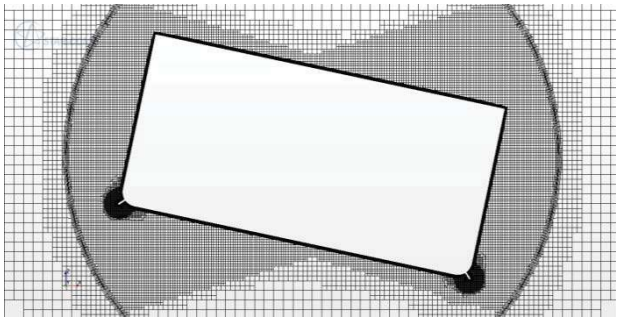

Figure 8 - Generated mesh at position E

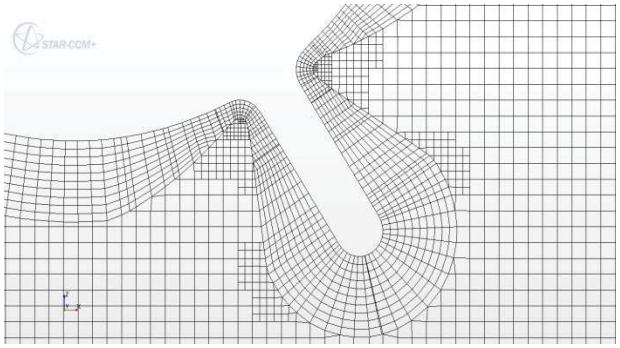

Figure 10 - Refined mesh at bilge keels

5.3 Results

Free decay simulations are carried out with each bilge keel's location (A to J). The results are compared with that of free decay without bilge keels. The initial rolling angle is 12 degree. All results are analysed to obtain the natural period T_N (s), natural frequency ω_N (rad/s), the coefficient Kn (n=1, 2, …, 10 corresponding to position A to J) based on Equ.(10) and the calculated damping coefficient b (kg-m-s) based on Equ.(11). The results can be given as Table 2. Comparison of rolling period between free decay with bilge keels and without bilge keels is shown in Fig.11. It should be noted that with bilge keels, rolling period increases obviously compared with that of the model without bilge keels (from 1.68s to approximately 1.87s).

The same effectiveness can be also seen from Fig.12 (a), which shows the time history of roll decay simulation without bilge keels and with bilge keels, which are located at position E (45° to the bilge). Fig.12 (b) is the result of roll decay test obtained by Avalos at the same position with the same magnitude of bilge keels. The comparison between Fig.12 (a) and Fig.12 (b) shows a good agreement. However, it should be noted that the decay rate is underestimated in both Fig. 12(a) and Fig. 12(b) for the smaller angles of roll oscillation. The phenomenon of under-estimated damping for smaller angle is recommended to be investigated further.

Fig.13 demonstrates the correlation between locations of bilge keels and damping coefficients based on Table 2.

Fig.14 (a) to Fig.14 (d) are the velocity distribution around the FPSO, and it can be clearly seen that the vortices at the bilge corners.

Positions	T_N	ω_N	Kn	b(kgms)
A (1)	1.8546	3.3861	0.0464	0.1818
B (2)	1.8661	3.3653	0.0617	0.2433
C (3)	1.8810	3.3386	0.1530	0.6080
D (4)	1.8748	3.3497	0.2225	0.8813
E (5)	1.8787	3.3428	0.2610	1.0360
F (6)	1.8737	3.3516	0.1850	0.7324
G (7)	1.8723	3.3541	0.1697	0.2790
H (8)	1.8375	3.4176	0.0024	0.0093
I (9)	1.8285	3.4345	0	0
J (10)	1.8276	3.4362	0	0
NO BK	1.6816	3.7345	0.0618	0.2196

Table 2 - Results of free decay simulations

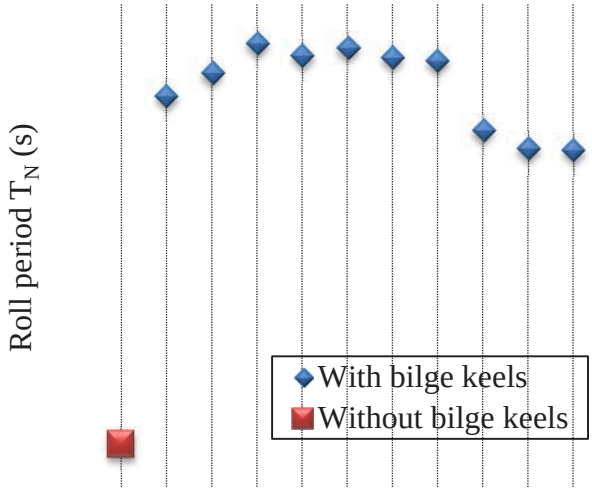

Figure 9 - Rolling period of free decay

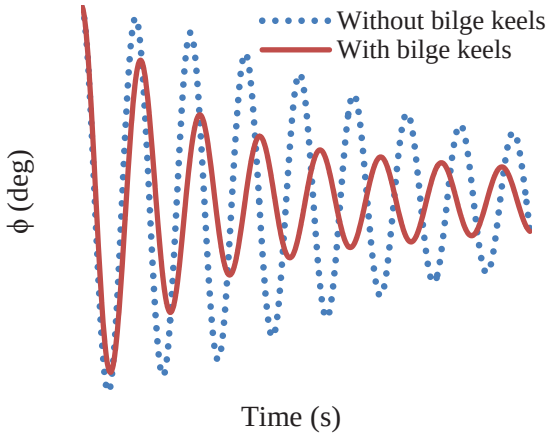

Figure 10 (a) – Results of angle of inclination at present study

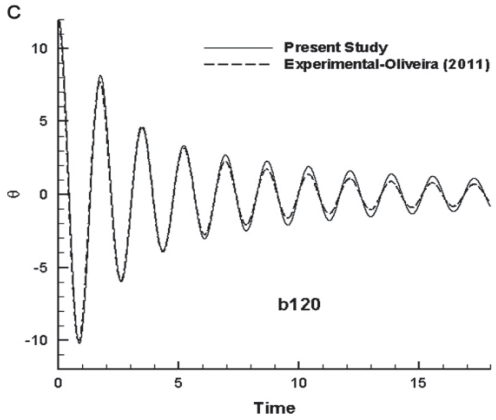

Figure 12 (b) - Result of roll decay test obtained by Avalos

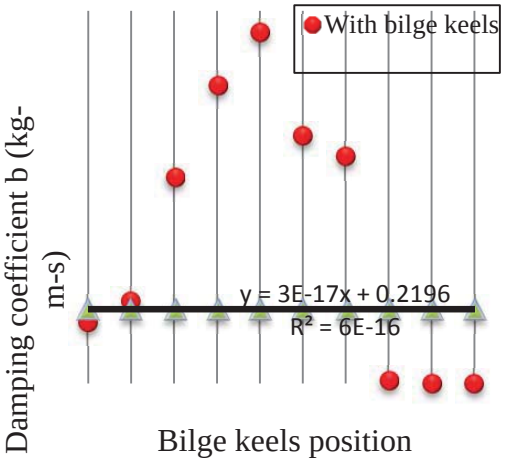

Figure 11 - Damping coefficient of FPSO model with bilge keels at each position (A to J) of bilge keels and without bilge keels

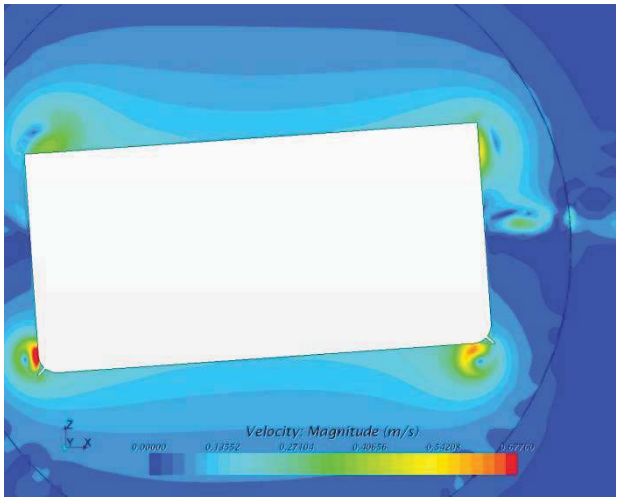

(a)

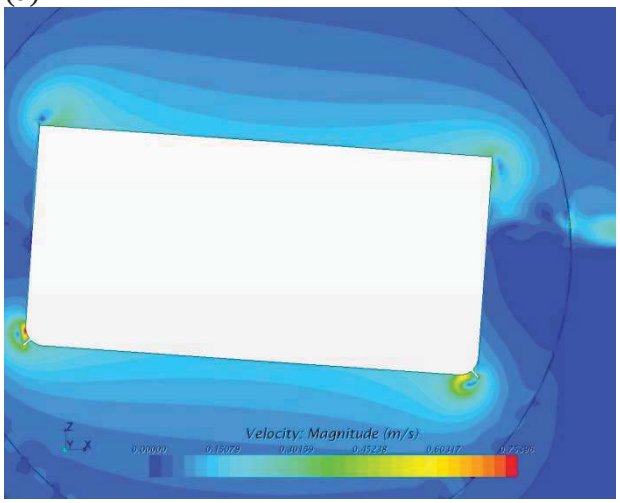

(b)

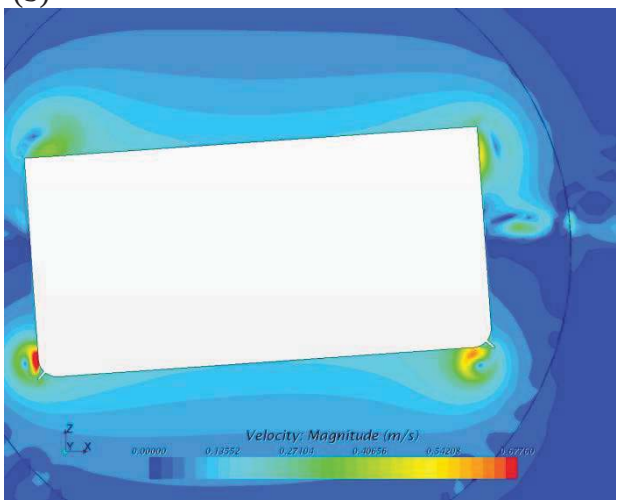

(c)

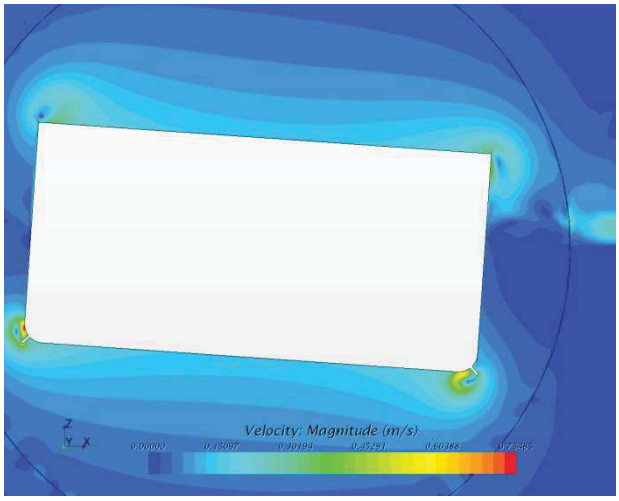

(d)

Figure 14 (a to d) – Velocity and vortex distributions

6. CONCLUSIONS

Table 2 and Fig.11 reveal that bilge keels, which located at ship side and bilge, do have an impact on damping the ship's roll motion. However, the effect can be negligible when bilge keels are positioned at ship bottom.

From Fig.13 it can be seen that bilge keels yield a larger damping coefficient when they are located at the bilge compared with other positions, which means when at the bilge, bilge keels can have a greater impact on the roll motion. Bilge keels at ship side and bottom also affect the damping, and the more they are close to the bilge the larger impact they have on the damping effectiveness.

Comparing results between side locations and bottom locations, bilge keels at the side have greater influence on the roll damping. Additionally, it can be seen from Table 2 that the coefficient K of position H, I and J are close to zero, so that bilge keels that are close to the ship keel are not effective in damping the motion.

Further work will be concentrated on investigating the effect of bilge keels on roll damping when the FPSO is rolling in waves.

7. REFERENCE

Avalos, G. O. G. & Wanderley, J. B., 2012, "A Two-Dimensional Numerical Simulation of Roll Damping Decay of a FPSO Using the Upwind TVD Scheme of Roe-Sweby", The 31st International Conference on Ocean, Offshore and Arctic Engineering, pp. 395-402.

Avalos, G. O. G., Wanderley, J. B. V. & Fernandes, A. C., 2013, "Roll Damping Decay of a FPSO With Bilge Keel", Proceedings of the ASME 2013 32nd International Conference on Ocean, Offshore and Arctic Engineering.

Avalos, G. O., Wanderley, J. B., Fernandes, A. C. & Oliveira, A. C., 2014, "Roll Damping Decay of a FPSO with Bilge Keel", Ocean Engineering, vol. 87(2014), pp. 111-120.

Bassler, C. C. & Reed, A. M., 2009, "An Analysis of the Bilge Keel Roll Damping Component Model", The 10th International Conference on Stability of Ships and Ocean Vehicles, pp. 369-386.

Bassler, C., Reed, A., & Brown, A., 2010, "Characterization of Physical Phenomena for Large Amplitude Ship Roll Motion", Proceedings of 29th American Towing Tank Conference.

Bassler, C. C., Reed, A. M., & Brown, A. J., 2010, "A Method to Model Large Amplitude Ship Roll Damping", Proceedings of the 11th International Ship Stability Workshop.

Bassler, C., Miller, R., Reed, A., Brown, A., 2011, "Considerations for Bilge Keel Force Models in Potential Flow Simulations of Ship Maneuvering in Waves", Proceedings of 12th International Ship Stability Workshop.

Bhattacharyya, R., 1978, "Dynamics of Marine Vehicles", John Wiley & Sons Inc., pp.75-95.

Chakrabarti, S., 2001, "Empirical Calculation of Roll Damping for Ships and Barges", Ocean Engineering, vol. 28(7), pp. 915-932.

Chan, H. S. Y., Xu, Z., & Huang, W. L., 1995, "Estimation of Nonlinear Damping Coefficients from Large-Amplitude Ship Rolling Motions", Applied Ocean Research, vol. 17(4), pp. 217-224.

Haddara, M. R., & Bennett, P., 1989, "A Study of the Angle Dependence of Roll Damping Moment", Ocean Engineering, vol. 16(4), pp. 411-427.

ITTC, 2011, "ITTC-Recommended Procedures: Numerical Estimation of Roll Damping", vol. 7.5-02-07-04.5, pp.1-33.

Ikeda, Y., 2004, "Prediction Methods of Roll Damping of Ships and Their Application to Determine Optimum Stabilization Devices". Marine Technology, vol. 41(2), pp. 89-93.

Ikeda, Y., Himeno, Y., & Tanaka, N., 1978, "A Prediction Method for Ship Roll Damping", Report of the Department of Naval Architecture, University of Osaka Prefecture.

Ikeda, Y., Komatsu, K., Himeno, Y., & Tanaka, N., 1977, "On Roll Damping Force of Ship, Effects of Hull Surface Pressure Created by Bilge Keels", Journal of Kansai Society of Naval Architects, vol. 165, pp. 31-40.

Jung, K. H., Chang, K.-A. & JO, H. J., 2006, "Viscous Effect on the Roll Motion of a Rectangular Structure", Journal of Engineering Mechanics, vol. 132**,** pp. 190-200.

Kawahara, Y., & Maekawa, K., 2012, "A Simple Prediction Formula of Roll Damping of Conventional Cargo Ships on the Basis of Ikeda's Method and its Limitation", Journal of Shipping and Ocean Engineering, vol. 2, pp. 201-210.

Miyake, T. & Ikeda, Y., 2013, "A Study on Roll Damping of Bilge Keels for New Non-Ballast Ship with Rounder Cross Section". Proceedings of the 13th International Ship Stability Workshop.

Manzke, M. & Rung, T., 2012, "Prediction of Roll Damping Using Viscous Flow Solvers", The 31st International Conference on Ocean, Offshore and Arctic Engineering, pp. 695-704.

Pesman, E., Bayraktar, D., & Taylan, M., 2007, "Influence of Damping on the Roll Motion of Ships", The 2nd International Conference on Marine Research and Transportation (ICMRT'07), pp. 28-30.

Querard, A. B. G., Temarel, P., & Turnock, S. R., 2010, "Application of RANS to Hydrodynamics of Bilge Keels and Baffles", William Froude Conference on Advances in theoretical and applied hydrodynamics – Past and Future.

Van't Veer, R., Fathi, F., & Kherian, J., 2011, "On Roll Hydrodynamics of FPSO's Fitted with Bilge Keels and Riser Balcony", ASME 30th International Conference on Ocean, Offshore and Arctic Engineering.

Yang, B., Wang, Z.-c., & Wu, M., 2012, "Numerical Simulation of Naval Ship's Roll Damping Based on CFD", Procedia Engineering, vol. 37, pp. 287-293.

Yuck, R. H., Lee, D. H., & Choi, H. S., 2003, "Estimation of Roll Damping Coefficients for Non-conventional Mid-ship Sections", The Thirteenth (2003) International Offshore and Polar Engineering Conference, pp. 540-543.

Yuck, R. H., Lee, D. H., Choi, H. S., Jin, Y. M., & Bang, C. S., 2003, "A Study on Roll Damping of 2-D Cylinders", International Journal of Offshore and Polar Engineering, vol. 13(03), pp. 205-208.

This page is intentionally left blank

Session 11.1 – RISK-BASED STABILITY

Influence of Linear Filters and Nonlinear Damping Models on the Stochastic Roll Response of a Ship in Random Seas

Risk Analysis of a Stability Failure for the Dead Ship Condition

Application of the Envelope Peaks over Threshold (EPOT) Method for Probabilistic Assessment of Dynamic Stability

Split-Time Method for Estimation of Probability of Capsizing Caused by Pure Loss of Stability

This page is intentionally left blank

Influence of Linear Filters and Nonlinear Damping Models on the Stochastic Roll Response of a Ship in Random Seas

Wei Chai, *Department of Marine Technology,*

Norwegian University of Science and Technology chai.wei@ntnu.no

Arvid Naess, *Centre for Ships and Ocean Structures & Department of Mathematical Sciences,*

Norwegian University of Science and Technology arvid.naess@ntnu.no

Bernt J. Leira, *Department of Marine Technology,*

Norwegian University of Science and Technology bernt.leira@ntnu.no

ABSTRACT

Roll motion is the most critical ship motion leading to capsizing. The single-degree-of-freedom (SDOF) model is applied in order to simulate the roll motion in random beam seas. The random wave excitation term in the SDOF model is approximated by a second-order linear filter or more accurately, by a fourth-order linear filter as a filtered white noise process. Then the original SDOF model would be extended into a four-dimensional (4D) or a six-dimensional (6D) dynamic system, respectively. For the 4D coupled system, it can be viewed as a Markov system whose probability properties are governed by the corresponding Fokker-Planck equation. With the advantage of Markov property, the stochastic roll response can be obtained by the efficient 4D path integration (PI) method. The effect of different damping models, i.e. the linear-plus-quadratic damping (LPQD) model and linear-plus-cubic damping (LPCD) model, on the stochastic roll response is investigated. Furthermore, Monte Carlo simulation is introduced in order to validate the stochastic roll responses calculated by the 4D PI method as well as to study the influence of two different linear filter models on the response statistics.

KEYWORDS: *stochastic roll response; path integration method; filtering technique; nonlinear damping; Monte Carlo simulation.*

1. INTRODUCTION

For large amplitude roll motion in random seas, ship motion is strongly nonlinear and the dynamic behaviour of the vessel as well as the stochastic nature of random wave excitation should be taken into consideration in ship stability analysis. Moreover, the problem of estimating the stochastic response of nonlinear dynamic system excited by random external loads has been a demanding challenge for several decades (Naess & Johnsen, 1993).

Markov models have been widely applied in the area of stochastic dynamic analysis of roll motion in random seas. The shaping filter technique is introduced in order to approximate the wave excitation as a filtered white noise process. Subsequently, an augmented dynamic system is created when the original dynamic system is coupled with the filter model. Under the Markov theory, the joint probability density function (PDF) of the roll response can be obtained by solving the governing equation, i.e.

the Fokker-Planck (FP) equation. However, extended dynamic system usually corresponds to a high-dimensional FP equation and analytical solutions to high-dimensional FP equations are only available for some linear systems and a very restricted class of nonlinear systems.

The path integration (PI) method is an efficient approximation for solving the high-dimensional FP equations with reliable accuracy. This method is based on the Markov property of the dynamic system and the global solution of the FP equation can be constructed by linking the explicitly known local solutions. Recently, this algorithm was successfully extended to 4D for studying the stochastic roll response of a ship in random beam seas (Chai et al. 2014).

Besides the efficient PI method, Monte Carlo simulation is another methodology to determine the response statistics of the nonlinear dynamic systems subjected to random external forcing. The nonlinear and time-dependent terms can be easily and directly dealt with. However, the main drawback of Monte Carlo simulation is the associated computational efficiency will be sacrificed for estimation of the extreme responses with low probability levels.

The nonlinearity of the roll damping has been recognized to be crucial for evaluating the ship stability since Froude's time (Bikdash et al., 1994). Since the quantitative evaluation of roll damping is difficult, empirical models are used to describe the roll damping term. The linear-plus-quadratic damping (LPQD) model has been verified by numerous studies of experimental data (Roberts & Vasta, 2000). On the other hand, the linear-plus-cubic damping (LPCD) model is infinitely differentiable, and mathematically preferable to the LPQD model. Bikdash et al (1994) derived a condition under which the LPCD model approximates well with the LPQD model in a least-squares sense.

In this paper, the wave excitation spectrum is modelled by a second-order linear filter and a more precise fourth-order linear filter. The effect of different linear filters on the stochastic roll response is investigated by comparison with the Monte Carlo data. The LPQD model is transformed into a LPCD model by the least square method. Then, the influence of two different damping models on the stochastic roll response, especially on the extreme response are evaluated. The accuracy of the 4D PI method is verified by means of the versatile Monte Carlo simulation technique.

2. THEORETICAL BACKGROUND

2.1 Mathematical model of roll motion

When the ship is excited by beam wave loads, the rolling behaviour can be represented by the following single-degree-of-freedom (SDOF) equation:

$$(I_{44} + A_{44})\ddot{\theta}(t) + B_{44}\dot{\theta}(t) + B_{44q}\dot{\theta}(t)\left|\dot{\theta}(t)\right| + \Delta(C_1\theta(t) - C_3\theta^3(t)) = M(t) \quad (1)$$

where $\theta(t)$ and $\dot{\theta}(t)$ are the roll angle and the roll velocity, respectively. I_{44} is the moment of inertia with respect to an axis through an assumed roll center, A_{44} denotes the added mass coefficient. B_{44} and B_{44q} are the linear and quadratic damping coefficients. Δ is the displacement of the vessel, C_1 and C_3 are the linear and nonlinear roll restoring coefficients of the restoring arm. $M(t)$ represents the random wave excitation moment.

The wave elevation and wave excitation moment are assumed to be stationary Gaussian stochastic processes. The wave excitation moment spectrum, $S_{MM}(\omega)$, can be determined as follows(Jiang et al., 1996):

$$S_{MM}(\omega) = \left|F_{roll}(\omega)\right|^2 S_{\zeta\zeta}(\omega) \quad (2)$$

in which $S_{\zeta\zeta}(\omega)$ is the wave energy spectrum, $|F_{roll}(\omega)|$ represents the roll excitation moment amplitude per unit wave height.

Dividing equation (1) by (I_{44} + A_{44}), the final form of the differential equation is obtained as:

$$\ddot{\theta}(t)+b_{44}\dot{\theta}(t)+b_{44q}\dot{\theta}(t)\left|\dot{\theta}(t)\right| + c_1\theta(t)-c_3\theta^3(t)=m(t) \tag{3}$$

where b_{44}, b_{44q}, c_1 and c_3 are relative roll parameters. The spectrum of the relative roll excitation moment, $S_{mm}(\omega)$, is expressed as:

$$S_{mm}(\omega)=\left|F_{roll}(\omega)\right|^2 S_{\zeta\zeta}(\omega)\big/(I_{44}+A_{44})^2 \tag{4}$$

Furthermore, the SDOF model (3) can be transformed into the following state-space equation:

$$\begin{cases} dx_1 = x_2 dt \\ dx_2 = (-b_{44}x_2 - b_{44q}x_2\left|x_2\right| - c_1x_1 + c_3x_1^3 + x_3)dt \end{cases} \tag{5}$$

where x_1= $\theta(t)$, x_2= $\dot{\theta}(t)$, x_3= $m(t)$.

2.2 Shaping filter technique

Dostal and Kreuzer (2011) proposed a second-order and a fourth-order linear filter to fit the desired narrow-banded spectrum. In this work, both of the linear filters can be applied in order to model the target spectrum, i.e. the relative wave excitation moment spectrum $S_{mm}(\omega)$. The second-order linear filter is given by the following differential equation

$$\begin{cases} dx_3 = (x_4 - \beta x_3)dt + \gamma dW \\ dx_4 = -\alpha x_3 dt \end{cases} \tag{6}$$

where x_3 and x_4 are the state variables in the filter equation with x_3 representing the output $m(t)$. dW(t)=W(t+dt)-W(t) is the increment of a Wiener process with E{dW(t)}=0 and E{dW(t) dW(t+dt)}=δ(dt), where $\delta(\cdot)$ represents the Dirac function. The spectrum generated by equation (6) is given by

$$S_{2nd}(\omega)=\frac{1}{2\pi}\frac{\gamma^2\omega^2}{(\alpha-\omega^2)^2+(\beta\omega)^2} \tag{7}$$

The fourth-order linear filter which represents a more accurate approximation is given by the following expression:

$$\begin{cases} dx_5 = (x_6 - \lambda_1 x_5)dt \\ dx_6 = (x_7 - \lambda_2 x_5)dt + \gamma_1 dW \\ dx_7 = (x_8 - \lambda_3 x_5)dt \\ dx_8 = -\lambda_4 x_5 dt \end{cases} \tag{8}$$

where x_5, x_6, x_7, x_8 are variables introduced for the state-space representation and x_5 represents the filter output $m(t)$. The spectrum generated by equation (11) will have the following form:

$$S_{4th}(\omega)=\frac{1}{2\pi}\frac{\gamma_1^2\omega^4}{[(\beta_1-\omega^2)^2+(\alpha_1\omega)^2][(\beta_2-\omega^2)^2+(\alpha_2\omega)^2]} \tag{9}$$

where the parameters λ_1, λ_2, λ_3, λ_4 in equation (9) can be determined by the following relationship: λ_1=α_1+α_2, λ_2=β_1+β_2+$\alpha_1\alpha_2$, λ_3=$\alpha_1\beta_2$ +$\alpha_2\beta_1$, λ_4= $\beta_1\beta_2$. The parameters α, β, γ in the second-order linear filter and the parameters α_1, α_2, β_1, β_2, γ_1 in the fourth-order filter are determined by a least-square algorithm which is utilized for fitting of the target spectrum, $S_{mm}(\omega)$. The bandwidth and the peak frequency of the filtered spectrum can easily be adjusted by changing the values of these parameters.

By combining the governing equation of the roll motion (5) with the linear filter equation (6) or (8), ship roll motion in random beam seas can be described by a 4D or a 6D state space equation, respectively.

2.3 Path integration method

The 4D state space equation can be expressed as follows:

$$\begin{cases} dx_1 = x_2 dt \\ dx_2 = (-b_{44}x_2 - b_{44q}x_2\left|x_2\right| - c_1x_1 + c_3x_1^3 + x_3)dt \\ dx_3 = (x_4 - \beta x_3)dt + \gamma dW \\ dx_4 = -\alpha x_3 dt \end{cases} \tag{10}$$

Equation (10) represents a Markov dynamic system driven by Gaussian white noise. It can be expressed as an *Itô* stochastic differential equation (SDE):

$$d\mathbf{x} = a(\mathbf{x},t)dt + b(t)d\mathbf{W}(t) \tag{11}$$

where $x(t)=(x_1(t),\ldots,x_4(t))^{\mathrm{T}}$ is a 4D state space vector process, the vector $a(\mathbf{x},t)$ represents the drift term and $b(t)\mathrm{d}\mathbf{W}(t)$ is the diffusive term. The vector $\mathrm{d}\mathbf{W}(t)=\mathbf{W}(t+\mathrm{d}t)-\mathbf{W}(t)$ denotes independent increments of a standard Wiener process.

The solution $\mathbf{x}(t)$ to equation (11) is a Markov process and its transition probability density (TPD), also known as the conditional PDF, $p(\mathbf{x},t|\mathbf{x}',t')$ satisfies the FP equation which is casted in the following form:

$$\begin{aligned}\frac{\partial}{\partial t}p(\mathbf{x},t\,|\,\mathbf{x}',t') &= -\sum_{i=1}^{4}\frac{\partial}{\partial x_i}a_i(\mathbf{x},t)\,p(\mathbf{x},t\,|\,\mathbf{x}',t') \\ &+\frac{1}{2}\sum_{i=1}^{4}\sum_{j=1}^{4}\frac{\partial^2}{\partial x_i\partial x_j}(b(t)\cdot b^T(t))_{ij}\,p(\mathbf{x},t\,|\,\mathbf{x}',t')\end{aligned} \tag{12}$$

Unlike direct numerical techniques, such as the finite-element method and the finite difference method, aiming to solve the FP equation (12) and obtain the TPD directly, the PI method captures the probabilistic evolution of the process $\mathbf{x}(t)$ by taking advantage of the Markov property of the dynamics system (11). In principle, the PI method is an approximation approach and the PDF of the process $\mathbf{x}(t)$ can be determined by the following basic equation:

$$p(\mathbf{x},t)=\int_{R^4}p(\mathbf{x},t\,|\,\mathbf{x}',t')p(\mathbf{x}',t')d\mathbf{x}' \tag{13}$$

where $d\mathbf{x}'=\prod_{i=1}^{4}dx_i'$.

Specifically, the value of the PDF at time t, $p(\mathbf{x},t)$, can be calculated by equation (13) with the value of previous PDF at time t' as well as the value of conditional PDF, $p(\mathbf{x},t|\mathbf{x}',t')$. For a numerical solution of the SDE (11), a time discrete approximation should be introduced. Naess and Moe (2000) proposed a fourth-order Runge-Kutta-Maruyama (RKM) discretization approximation:

$$\mathbf{x}(t)=\mathbf{x}(t')+r(\mathbf{x}(t'),t')\Delta t+b(t')\Delta\mathbf{W}(t') \tag{14}$$

where the vector $r(\mathbf{x}(t'),\,t')$ is the explicit fourth-order Runge-Kutta approximation or the Runge-Kutta increment. Since $\mathbf{W}(t)$ is a Wiener process, the independent increment $\Delta\mathbf{W}(t')=\mathbf{W}(t)-\mathbf{W}(t')$ is a Gaussian variable for every t'.

If we consider only the deterministic part of equation (11), the approximation (14) reduces to the fourth-order Runge-Kutta approximation $\mathbf{x}(t)=\mathbf{x}(t')+r(\mathbf{x}(t'),t')\Delta t$. Experiments have shown that, for the Markov systems, the accuracy associated with approximating the deterministic terms is the most important (Mo, 2008). In this regard, the accuracy of the fourth-order RKM approximation is satisfactory since the fourth-order Runge-Kutta approximation follows the time evolution of the deterministic part of equation (11) with an accuracy to the order of $O(\Delta t^5)$.

The time sequence $\{\mathbf{x}(i\cdot\Delta t)\}_{i=0}^{\infty}$ is a Markov chain and it can approximate the time-continuous Markov process solution of the SDE (11) when the time increment $\Delta t=t-t'$ is sufficiently small. Moreover, the conditional PDF of the process x(t), $p(\mathbf{x},t|\mathbf{x}',t')$, follows a (degenerate) Gaussian distribution and it can be written as (Naess & Johnsen, 1993):

$$\begin{aligned}p(\mathbf{x},t\,|\,\mathbf{x}',t') &= \delta(x_1-x_1'-r_1(\mathbf{x}',\Delta t)) \\ &\cdot\delta(x_2-x_2'-r_2(\mathbf{x}',\Delta t))\cdot\tilde{p}(x_3,t\,|\,x_3',t') \\ &\cdot\delta(x_4-x_4'-r_4(\mathbf{x}',\Delta t))\end{aligned} \tag{15}$$

where $\tilde{p}(x_3,t\,|\,x_3',t')$ is given by the relation:

$$\begin{aligned}\tilde{p}(x_3,t\,|\,x_3',t') &= \frac{1}{\sqrt{2\pi\gamma^2\Delta t}} \\ &\cdot\exp\left\{-\frac{(x_3-x_3'-r_3(\mathbf{x}',\Delta t))^2}{2\gamma^2\Delta t}\right\}\end{aligned} \tag{16}$$

in which $r_i(\mathbf{x}',\,\Delta t)$, i=1,2,3,4, are the Runge-Kutta increments for the state space variables.

Since the expression for the conditional PDF is known, the time evolution of the PDF of $\mathbf{x}(t)$ can be determined by the iterative algorithm (17) if an initial PDF $p(\mathbf{x}^{(0)}, t_0)$ is given

$$p(\mathbf{x},t)=\int_{R^4}\cdots\int_{R^4}\prod_{i=1}^{n}p(\mathbf{x}^{(i)},t_i\,|\,\mathbf{x}^{(i-1)},t_{i-1}) \cdot p(\mathbf{x}^{(0)},t_0)d\mathbf{x}^{(0)}\ldots d\mathbf{x}^{(n-1)} \tag{17}$$

where $\mathbf{x}=\mathbf{x}^{(n)}$, $t=t_n=t_0+n\cdot\Delta t$.

Equation (17) describes the mathematical principle of the PI approach. In this work, the initial PDF $p(\mathbf{x}^{(0)}, t_0)$ is chosen as a 4D Gaussian PDF with zero mean and variances evaluated by a simple Monte Carlo simulation. The straightforward Monte Carlo simulation ensures that the initial 4D Gaussian PDF includes all the information corresponding to the selected parameters of the dynamic system, and it also provides a rational computational domain for the subsequent simulation. For the numerical implementation of the iterative algorithm (17), it represents the PDF at the previous time t' as an interpolating spline surface via parabolic B-spline and then it evaluates the PDF at time t by several specific steps. The numerical iterative algorithm and the associated specific computational steps have been systematically described by Iourtchenko et al (2006) and Yurchenko et al (2013). Moreover, the capability of the PI method in producing accurate and reliable solutions for the stochastic dynamic systems has been demonstrated by numerous examples (Mo, 2008).

3. MEAN UPCROSSING RATE

The mean upcrossing rate is a key parameter for estimating the stochastic responses, especially the large and extreme responses. A nice aspect of the PI method is that the joint PDF of the roll angle and the roll velocity can be calculated directly. Then the mean upcrossing rate can be given by the Rice formula

$$v^{+}(\zeta;t)=\int_0^{\infty}\dot{\theta}\,f_{\theta\dot{\theta}}(\zeta,\dot{\theta};t)d\dot{\theta} \tag{18}$$

where $v^{+}(\zeta;t)$ denotes the expected number of upcrossing for the ζ-level per unit time at time t by the roll angle $\theta(t)$, $f_{\theta\dot{\theta}}(\theta,\dot{\theta};t)$ is the joint PDF of the roll angle and the roll velocity at the time instant t.

For nonlinear ship rolling in beam seas, due to the presence of negative nonlinear stiffness term in the SDOF model (1), ship capsizing may happen when the predetermined simulation time T is long enough or the intensity of the external excitation is strong enough. If the mean time to capsize is long enough, the dynamic system can be regarded as a highly reliable system and the corresponding roll response reaches stationarity in an approximate sense (Roberts & Vasta, 2000).

As for the four-dimensional dynamic system (10) or the six-dimensional dynamic system obtained by combing the equations (5) and (8), the fourth-order RKM method is adopted to solve the corresponding SDE. The mean upcrossing rates can be estimated from the time series of responses. Let $n_i^{+}(\xi;T_i)$ denote the counted number of upcrossing for the level ζ during the time interval (0, T_i) for simulated time history No. i. The appropriate sample mean value of averaged mean upcrossing rate, $\hat{v}^{+}(\xi)$ is then obtained as:

$$\hat{v}^{+}(\zeta)=\frac{\sum_{i=1}^{k}n_i^{+}(\zeta;T_i)}{\sum_{i=1}^{k}T_i} \tag{19}$$

A fair approximation of the 95% confidence interval, $CI_{0.95}$, for the value of $\hat{v}^{+}(\xi)$ can be obtained as (Naess et al, 2007):

$$CI_{0.95}(\zeta)=\left(\hat{v}^{+}(\zeta)-1.96\frac{\hat{s}(\zeta)}{\sqrt{k}},\hat{v}^{+}(\zeta)+1.96\frac{\hat{s}(\zeta)}{\sqrt{k}}\right) \tag{20}$$

Where the empirical standard deviation $\hat{s}(\xi)$ is given as

$$\hat{s}(\zeta)^2 = \frac{1}{k-1}\sum_{i=1}^{k}\left(\frac{n_i^+(\zeta;T_i)}{T_i} - \hat{v}^+(\zeta)\right)^2 \quad (21)$$

Moreover, the selection of the number of simulation, k, for the Monte Carlo simulation is selected according to the upcrossing rates in the tail region and the length of the predetermined simulation time T. Usually, low upcrossing rates and short time periods T corresponds to a large simulation number k.

Ship stability failure occurs when the roll angle exceeds some certain values, such as the angle of vanishing stability or some large roll angle leading to damage. Assume that the upcrossing events in the high level response region are statistically independent and the random process $\theta(t)$ is not extremely narrow-banded, the exceedance probability for a duration of exposure time T, $P_\Theta(T)$, can be approximated by a widely used Poisson estimate, which is given as follows:

$$\begin{aligned} P_\Theta(T) &= 1-\exp(-\int_0^T v^+(\zeta;t)dt) \\ &\approx 1-\exp(-v^+(\zeta)\cdot T) \end{aligned} \quad (22)$$

where $v^+(\zeta)$ represents the mean upcrossing rate of the level ζ at a suitable reference point in time, which can be determined directly by the 4D PI approach and the Rice formula (18).

4. SIMULATION RESULTS

4.1 Ship parameters and excitation spectrum

In this section, an ocean surveillance ship (Su, 2012), is selected for studying the stochastic responses of ship rolling. The parameters of the vessel and the natural roll frequency, ω_0, are given in Table 1.

The modified P-M spectrum, widely used for the fully developed ocean waves, is adopted in this analysis.

$$S_{\xi\xi}(\omega) = \frac{5.058g^2H_s^2}{T_p^4\omega^5}\exp(-1.25\frac{\omega_p^4}{\omega^4}) \quad (23)$$

in which H_s denotes the significant wave height, ω_p is the peak frequency at which the wave spectrum $S_{\xi\xi}(\omega)$ has its maximum, and T_p is the corresponding peak period.

Table 1 List of parameters for the vessel

Parameters	Dimensional value
$I_{44}+A_{44}$	5.540×10^7 kg·m^2
B_{44}	5.266×10^6 kg·m^2·s^{-1}
B_{44q}	2.877×10^6 kg·m^2
Δ	2.017×10^7 N
C_1	3.168 m
C_3	2.513 m
ω_0	1.074 rad/s

Three different sea states, i.e. different external excitations, are selected for analyzing the stochastic roll responses. The wave spectra and rolling excitation moment amplitude per unit wave height of the vessel are plotted in Figure 1.

The parameters α, β, γ in the second-order filter (6) and parameters λ_1, λ_2, λ_3, λ_4 in the fourth-order filter (8) can be determined by the least square scheme which is available in the curve fitting algorithms of MATLAB. The parameters in these two linear filters for different sea states are presented in Tables 2 and 3. Moreover, the fitting results of the relative wave excitation spectrum for sea state 1 are shown in Figure 2.

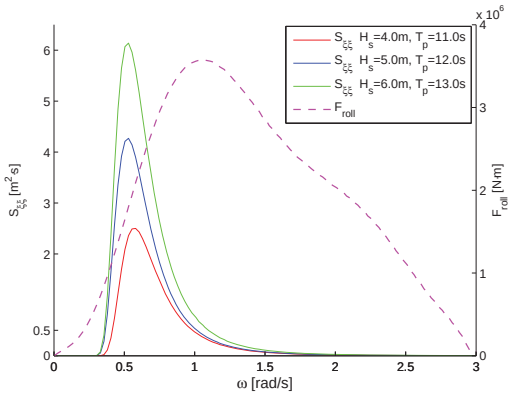

Figure 1 Wave spectra for different sea states and rolling excitation moment amplitude per unit wave height

Table 2 Parameters of the second-order linear filter for different sea states

Sea States	$H_s\,(m)$	$T_p\,(s)$	α	β	γ
Sea state 1	4.0	11.0	0.495	0.366	0.0432
Sea state 2	5.0	12.0	0.441	0.364	0.0498
Sea state 3	6.0	13.0	0.390	0.365	0.0555

Table 3 Parameters of the fourth-order linear filter for different sea states

$H_s\,(m)$	$T_p\,(s)$	λ_1	λ_2	λ_3	λ_4	γ_1
4.0	11.0	0.934	1.431	0.486	0.310	0.0363
5.0	12.0	0.924	1.309	0.429	0.249	0.0414
6.0	13.0	0.931	1.212	0.390	0.202	0.0461

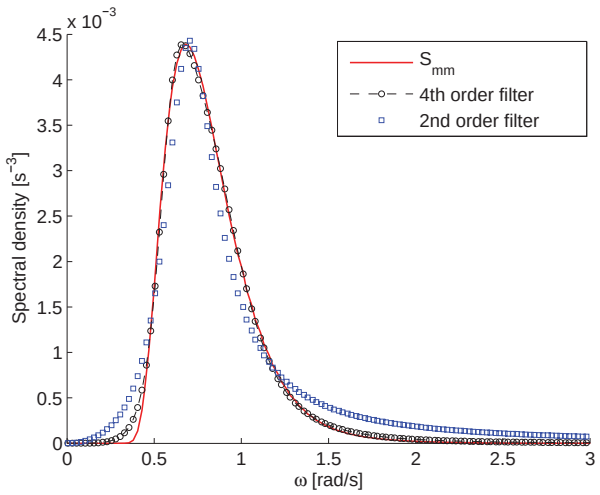

Figure 2 Relative wave excitation spectrum in equation (4) and filtered spectra for sea state 1

4.2 Influence of linear filter

The transfer function between wave excitation and roll response in the SDOF model (1) is narrow-banded due to the light roll damping. Thus, the fitting accuracy near the natural roll frequency, ω_0, has a significant effect on the subsequent rolling responses. However, there is a slight discrepancy between the spectral density generated by the second-order filter and the target spectral density in Figure 2. Therefore, a constant, c, should be introduced as a correction factor for the filtered spectral density to decrease the discrepancy in the critical region near roll frequency ω_0. The filtered spectrum (12) can be changed to:

$$S_{2nd}(\omega) = \frac{1}{2\pi}\frac{(c\cdot\gamma)^2\omega^2}{(\beta-\omega^2)^2+(\alpha\omega)^2} \tag{24}$$

The correction factor c is taken to be 1.07 by considering the mean difference of the two spectral densities in the critical frequency region. As mentioned in section 3, the joint probability density function (PDF) of the roll angle and the roll velocity can be obtained directly by the 4D PI method. The joint PDF of the roll response for sea state 1 is presented in Figure 3, while Figure 4 displays the contour lines of the joint PDF.

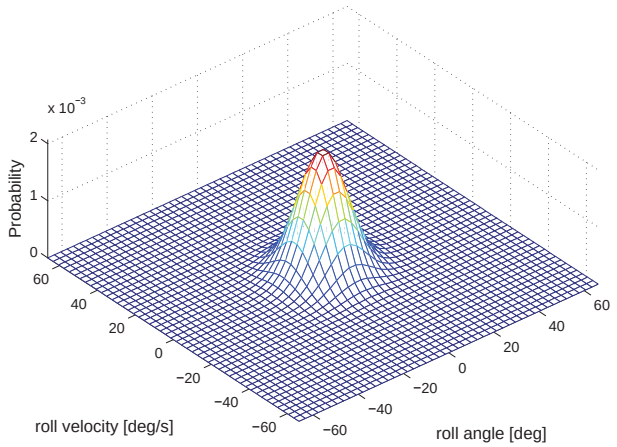

Figure 3 Joint PDF of the roll response for sea state 1 with H_s=4.0m, T_p=11.0s

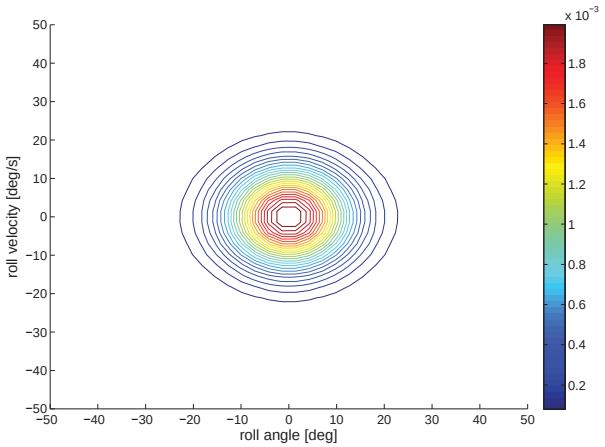

Figure 4 Contour lines of the joint PDF of the roll response for sea state 1

It can be observed in Figures 3 and 4 that the PDF of the roll response is symmetric. This is reasonable since the distribution of the random wave excitation, i.e. the filtered white noise process, and the vessel properties are symmetric with respect to the origin. Moreover, the marginal PDF of the roll angle process and the marginal PDF of the roll velocity process obtained by the 4D PI method and the 4D Monte Carlo simulation are plotted in Figure 5 and 6, respectively.

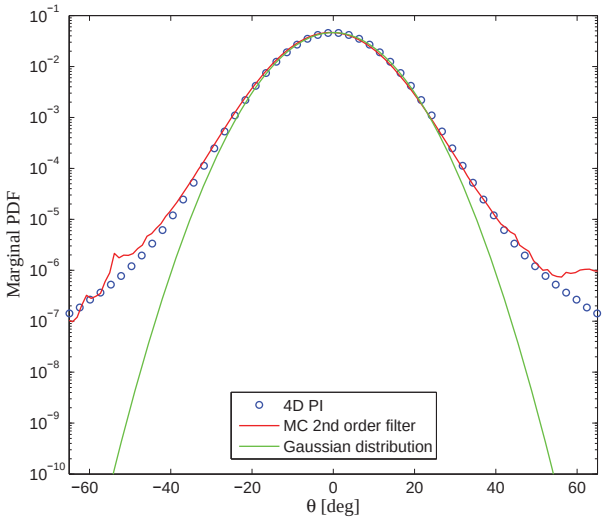

Figure 5 Marginal PDF of the roll angle process for sea state 1

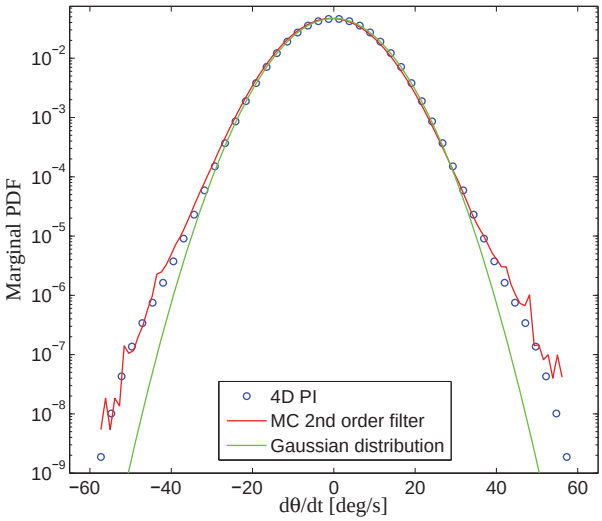

Figure 6 Marginal PDF of the roll velocity process for sea state 1

It is shown in Figures 5 and 6 that the Gaussian distribution gives a reasonable approximation of the statistics of small-amplitude roll motions. However, for the high-level responses, Gaussian distribution under-estimates the corresponding low probability levels in this region. Moreover, the 4D PI method provides nice results for the low probabilities, where the distributions obtained by the versatile Monte Carlo simulation are suffering from uncertainties.

The importance of the correction factor *c* for the stochastic roll response is illustrated in Figure 7. It can be observed that, the slight discrepancy between the second-order filtered spectrum and the target spectrum in the critical region, which is shown in Figure 2, results in noticeable influence on the subsequent roll response. If there is no correction factor for the second order linear filter, the stochastic roll response, will be significantly underestimated. In addition, the good agreement of the upcrossing rates obtained by 4D PI method and 6D Monte Carlo simulation (MCS) verify the rationality of the correction factor.

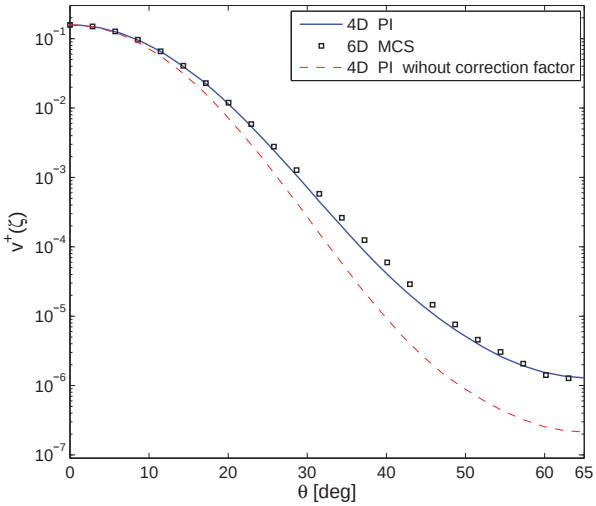

Figure 7 Influence of the correction factor, c, on the upcrossing rate for sea state 1 with H_s=4.0m, T_p=11.0s

The comparisons between the upcrossing rates calculated by the 4D PI method and the empirical estimation of the upcrossing rates as well as the 95% confidence intervals obtained by 4D Monte Carlo simulations for different sea states can be viewed in Figures 8, 9 and 10. It can be readily seen that the 4D PI approach yields accurate and reliable results for various external excitation cases. Next, the empirical estimation of the upcrossing rates computed by 6D Monte Carlo simulations are plotted in these Figures. The good agreement of the 4D results and 6D results extracted from Monte Carlo simulation verify the rationality of introducing the correction factor for all of the cases.

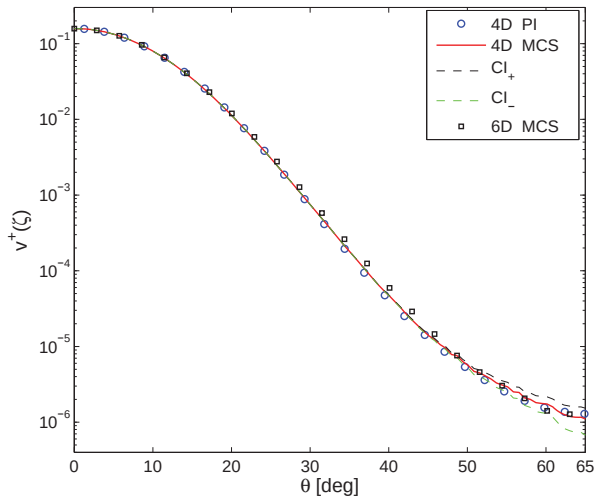

Figure 8 Upcrossing rate for sea state 1 with H_s=4.0m, T_p=11.0s (simulation number k =3000)

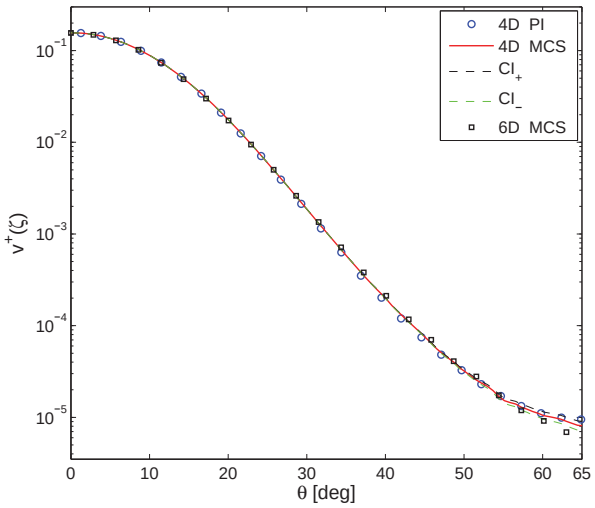

Figure 9 Upcrossing rate for sea state 2 with H_s=5.0m, T_p=12.0s (simulation number k = 1500)

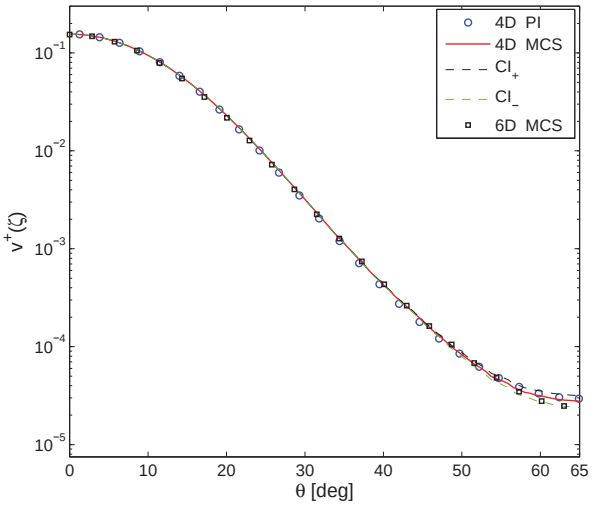

Figure 10 Upcrossing rate for sea state 3 with H_s=6.0m, T_p=13.0s (simulation number k = 1000)

4.3 Influence of nonlinear damping models

The roll damping is mainly due to three different sources: the free surface radiated wave damping, the damping caused by vortex shedding and flow separation and finally the

viscous friction damping. In general, these damping terms are coupled with each other. The linear-plus-quadratic damping (LPQD) model is one of the most common expressions used in the SDOF equation (1). This model is given as:

$$b_{44}\dot{\theta}(t) + b_{44q}\dot{\theta}(t)\left|\dot{\theta}(t)\right| \tag{25}$$

However, the LPQD model is only once continuously differentiable and mathematically inferior to the infinitely differentiable linear-plus-cubic damping (LPCD) model. The LPCD model is written as:

$$b'_{44}\dot{\theta}(t) + b_{44c}\dot{\theta}^3(t) \tag{26}$$

The least square method is a typical approach used to transform the LPQD model into the LPCD model. The result of fitting the two damping models is shown in Figure 11. Moreover, the roll response spectra for the dynamic systems with different damping models for sea state 1 are plotted in Figure 12.

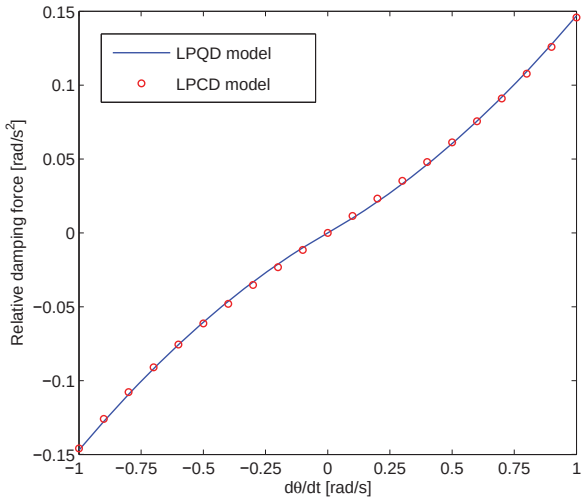

Figure 11 Fitting result for the LPQD and LPCD models

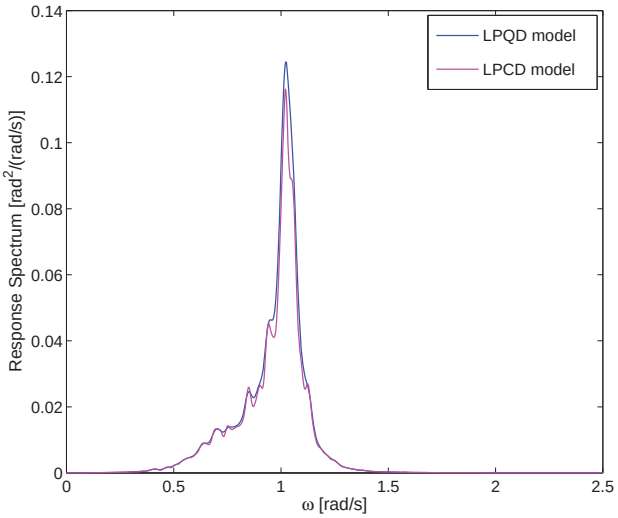

Figure 12 Roll response spectra for the LPQD and LPCD models for sea state 1

It is illustrated in Figure 11 that the two damping models have a good agreement in the least-square sense. Nevertheless, in Figure 12, there is still a slight discrepancy between the response spectra in the peak region, i.e. the critical frequency region near natural roll frequency ω_0. The upcrossing rates, obtained by the 4D PI method and the 4D Monte Carlo simulation, for the LPQD model versus the LPCD model for different sea states are plotted in Figures 13, 14 and 15, respectively.

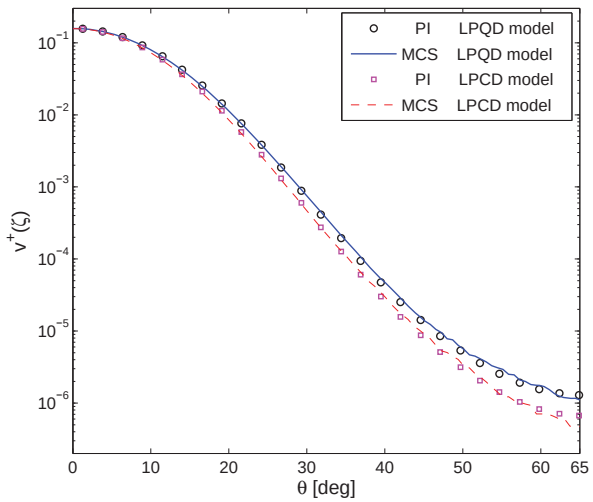

Figure 13 Upcrossing rate for different damping models for sea state 1

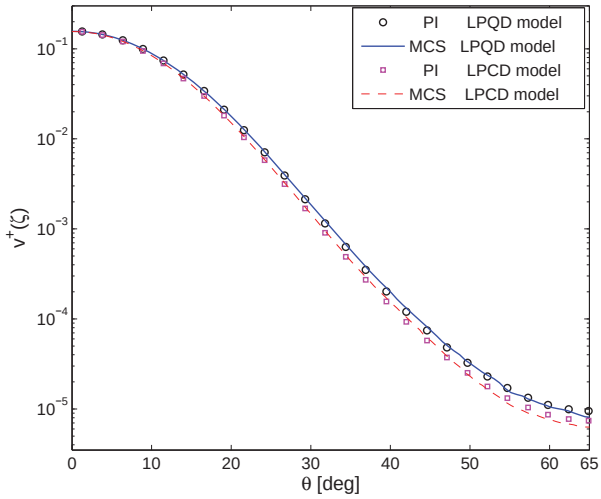

Figure 14 Upcrossing rate for different damping models for sea state 2

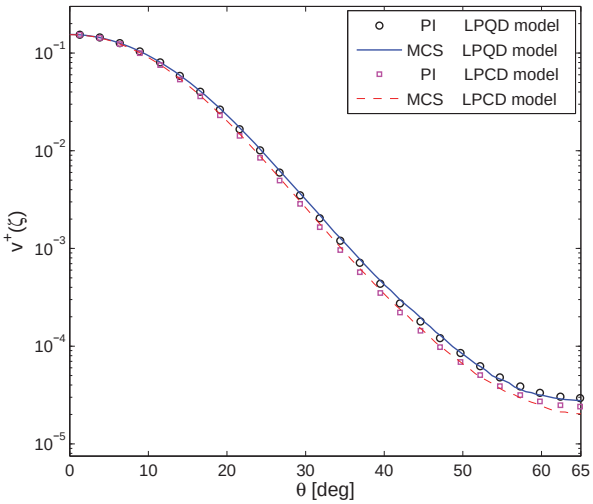

Figure 15 Upcrossing rate for different damping models for sea state 3

The 4D PI approach is available to provide high-accuracy results for both models when compared with the corresponding empirical estimations obtained by 4D Monte Carlo simulations. However, the corresponding upcrossing rates under the same sea sate are quite different, even though the two damping models match well in the least-square sense. The discrepancies between the upcrossing rates in the tail regions, suggest that the LPCD model might underestimate the extreme response of the dynamic system. Therefore, the traditional least square method, applied to transform the LPQD model into the LPCD model, cannot guarantee the accuracy of the subsequent stochastic roll response. Furthermore, from the observations in Figures 13-15, it can be predicted that when the stochastic linearization technique is applied in order to linearize the nonlinear damping term (25), even more significant discrepancy of the upcrossing rate would be observed in the tail region.

5. CONCLUSIONS

In this paper, the 4D path integration technique and Monte Carlo simulation were applied in order to investigate the influences of linear filter models and nonlinear damping models on the stochastic roll response of a vessel in random beam seas. From the numerical results and discussions above, some of the results can be summarized:

The correction factor, *c*, is important and reasonable to be introduced into the second-order linear filter. Moreover, the accuracy of the filtered spectrum in the critical frequency region is crucial for prediction of the response statistical. The 6D dynamic system can be simplified as a corresponding 4D dynamic system with a modified second-order linear filter due to the high-accuracy agreements for the upcrossing rates.

The typical least square method results in an underestimation of the upcrossing rate when it is used to transform a LPQD model into a LPCD model. The discrepancies between the upcrossing rates generated by different damping models should not be ignored.

It has been shown that the 4D PI approach yields reliable results for different damping

models and various excitation cases, even in the tail regions with low probability levels. Therefore, the 4D PI technique can be applied for the stochastic analysis of nonlinear ship rolling in random beam seas.

6. ACKNOWLEDMENTS

The first author would like to thank the financial support from the China Scholarship Council (CSC) (Grant No. 201306230077), affiliated with the Ministry of Education of the P.R. China. The funds from the Department of Marine Technology's budget for scientific travels and the "Norwegian ship-owners' association fund" at NTNU to scientific travels are gratefully acknowledged.

7. REFERENCES

Bikdash, M., Balachandran, B., Navfeh, A., 1994, "Melnikov analysis for a ship with a general roll-damping model", Nonlinear Dynamics, Vol. 6, pp. 101-124.

Chai, W., Naess, A., Leira, B. J., 2014, "Stochastic dynamic analysis of nonlinear ship rolling in random beam seas", Proceeding of the 7th International Conference on Computational Stochastic Mechanics, in press.

Dostal, L., Kreuzer, E., 2011, "Probabilistic approach to large amplitude ship rolling in random seas", Proceedings of the Institution of Mechanical Engineers, Part C: Journal of Mechanical Engineering Science, Vol. 225, pp. 2464-2476.

Iourtchenko, D.V., Mo, E., Naess, A., 2006, "Response probability density functions of strongly non-linear systems by the path integration method", International Journal of Non-Linear Mechanics, Vol. 41, pp. 693-705.

Jiang, C., Troesch, A.W., Shaw, S., 1996, "Highly nonlinear rolling motion of biased ships in random beam seas", Journal of ship research, Vol. 40, pp. 125-135.

Mo, E., 2008, "Nonlinear stochastic dynamics and chaos by numerical path integration", Ph.D. Thesis, Norwegian University of Science and Technology, Trondheim, Norway.

Naess, A., J. Johnsen, 1993, "Response statistics of nonlinear, compliant offshore structures by the path integral solution method", Probabilistic Engineering Mechanics, Vol. 8, pp. 91-106.

Naess, A., Gaidai, O., Teigen, P.S., 2007, "Extreme response prediction for nonlinear floating offshore structures by Monte Carlo simulation", Applied Ocean Research, Vol. 29, pp. 221-230.

Naess, A., Moe, V., 2000, "Efficient path integration methods for nonlinear dynamic systems", Probabilistic Engineering Mechanics, Vol. 15, pp. 221-231.

Roberts, J. and Vasta, M., 2000, "Markov modelling and stochastic identification for nonlinear ship rolling in random waves", Philosophical Transactions of the Royal Society of London. Series A: Mathematical, Physical and Engineering Sciences, Vol. 358, pp. 1917-1941.

Su, Z., 2012, "Nonlinear response and stability analysis of vessel rolling motion in random waves using stochastic dynamical systems", Ph.D. Thesis, Texas A & M University, Texas.

Yurchenko, D., Naess, A., Alevras P., 2013, "Pendulum's rotational motion governed by a stochastic Mathieu equation", Probabilistic Engineering Mechanics, Vol. 31, pp. 12-18.

Risk Analysis of a Stability Failure for the Dead Ship Condition

Tomasz Hinz, *Deltamarin LTD*, Tomasz.Hinz@deltamarin.com

ABSTRACT

In this article, the application of the risk analysis of a stability failure for the dead ship condition is presented. The analysis combines deterministic and probabilistic approach. First, the number of simulation runs is carried out for a specific RoPax ship with the use of LaiDyn model. Second, the obtained results were organized in a probabilistic meta model with the use of Bayesian Belief Network. Finally, the BBN-based model was used as a platform for risk assessment. The adopted measure of risk is a number of fatalities that results from an accident, when a ship is in Dead Ship Condition (DSC) capsizes. The results are presented in a form of F-N. Finally the sensitivity of the model is evaluated along with the assessment of associated uncertainties.

Keywords: *stability, Dead Ship Condition, risk, Bayesian Belief Network*

1. INTRODUCTION

Discussions on the improvement of the IS Code(Francescutto, 2007), which were conducted at IMO forum, resulted in the identification of several major stability accident scenarios(Umeda, 2013):

- events related to the changes of righting arm – the parametric resonance and the pure loss of stability
- Dead Ship Condition - ship losing propulsion and manoeuvring characteristics (DSC)
- Problems with manoeuvrability on the wave - broaching, surf-riding,
- Problems with excessive accelerations.

Because the scenarios proposed by the IMO, still do not provide all possible causes of the loss of stability, it is necessary to approach the problem in another way. Consequently, the new rules are loosing their passive and retroactive approach and shift towards active feature. Which are not the result of the study of the stability accidents, but are based on the previous in-depth analysis of the phenomena associated with the behaviour of a ship on a wave. Such an approach allows the extension of regulations of further scenarios more easily.

This means that when creating the next generation of rules, it is advisable to develop methods for assessing the safety of the ship, where they not only physical, but also the operational characteristics of vessels will be taken into account.

Well known methods, which take into account the above mentioned elements are methods based on analysis and risk assessment, such as the one based on Safety Cases(Wang, 2002), widely used in the offshore industry - or another one called Formal Safety Assessment (Psaraftis, 2012)(Montewka, Goerlandt, & Kujala, 2014), which is used in the shipbuilding industry to create new rules(IMO, 2002). There is also a Risk-Based Design methodology(Papanikolaou et al., 2009), which is more and more widely used in the design of ships in the damaged condition.

Risk-based methods allow taking into account even the most unlikely accident scenario, and also the interactions between the

scenarios, or some of their components. The probabilistic causal models (Bayesian networks (BN), Fault Tree (FT) and Event Tree (ET))(Goerlandt & Montewka, 2015; Montewka, Ehlers, et al., 2014; Pillay & Wang, 2003) are more and more frequently used as a tool in the risk assessment process.

The main objective of this project was to create a probabilistic risk model of the ship stability accident, which might be applied to the assessment of the intact stability safety with the usage of the probabilistic casual model. One of previously presented scenario, i.e. Dead Ship Conditions, was chosen for the further analysis. The following sections will present the risk model built with the usage of the Bayesian Network and its application in RoPax ship. They allow exploring easily the influence of particular elements on the other ones, and in both directions. Having BN at disposal, it is possible to conduct the casual analysis, examine the strength of the impact of some elements on the other ones and make decisions under conditions of uncertainty.

2. RISK MODEL OF DEAD SHIP CONDITION ACCIDENTS

The aim of the proposed method is to estimate the risk of the stability accidents in the intact condition for the loss of the propulsion and manoeuvrability scenario. Such scenario might results in ship drifting, increased rolling, which in turn may lead to the capsizing and the ensuing loss of life by passengers. For the given meteorological conditions, the probability of exceeding the limits of ship motions is determined with the usage of 'LaiDyn' model. The following factors are taken into account concerning: meteorological conditions, ship dynamic and ship loading conditions. The total number of fatalities (N) resulting from an accident is modelled using the concept of death rates. This factor is determined with the participation of evacuation time and time of capsizing. The number of passengers on board is modelled based on data from the operators of RoPax form the Gulf of Finland. All these elements together, also with the associated probabilities (P) of the number of victims, is shown in the graph FN. The risk is measured adopting societal measure pressed as the probability of a given number of fatalities.

3. DEFINING THE RISK MODEL

The risk model of the DSC accident for RoPax ship was built with the support of the probabilistic casual model, which is the Bayesian network (BBN). The BBN structure was built with the participation of experts. The parameters were developed with the participation of the PC classifier based on the training data. It was created using the GeNie software developed at the University of Pittsburgh(Drużdzel, 1999).

Due to the limited statistic data, it was primarily the knowledge of experts that was used to create the structure of the model.

The analysed system is quite wide and multidisciplinary, therefore the model is divided into sections associated with (i) stability, (ii) propulsion and manoeuvring system, and (iii) finally with the consequences of an accident.

Experts' knowledge about the domain was used during a brainstorming session and individual meetings. During the session, they were presented with a preliminary version of the structure. Then, based on their advice, the structure under went the further modifications. Once the final structure of the model was established, it was necessary to define the qualitative part of the model.

The structure of the risk model is shown in **Figure 1**.

Table 1 contains all the variables included in the model. If the variable is determined by means of literature, it is marked by reference.

Variables marked as E are determined with the support of experts' knowledge. Simulations were used for variables marked with the letter S. The letter N in the description of a variable indicates that it was obtained by numerical analysis.

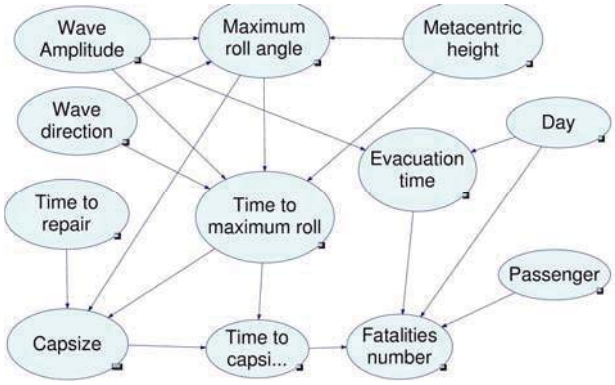

Figure 1 Structure of risk model

Table 1 Parameters of risk model

Name	Symbols	Source
Wave amplitude	Ampl	(IMO, 2013)
Wave direction	Beta	E
Maximum roll angle	$Roll_{max}$	S
Metacentric height	GM	E
Day	DAY	E
Time to repair	TTRep	(Ravn, 2006)
Evacuation time	TTE	(Montewka, Ehlers, et al., 2014)
Time to maximum roll angle	TTR	S
Capsize	Capsize	N
Time to capsize	TTC	S,N
Passenger	N_{PASS}	(Montewka et al., 2011), E
Fatalities number	N_{LOSA}	N

The simulation was conducted with the usage of the numerical model of the ship's movement on the wave. 17388 simulations of ship motions on the wave were performed. The simulation results were used to estimate the probability of exceeding the angle, which is considered to be the angle of capsizing. The results of simulations provided also data about the time at which the ship reaches the capsizing angle ('Maximum roll angle').

4. PARAMETERS OF THE RISK MODEL

This section describes the methods adopted to determine the parameters of the risk model.

The analysed accident scenario involves RoPax ship, which due to various reasons loses its propulsion and manoeuvring characteristics and enters a dead ship condition. This transition may be caused by a spontaneous failure of systems as well as the environment (large motions).

The basic elements of the model are:

- the probability of staying in a blackout state and time needed to exit this state,
- wave parameters,
- hydrostatic properties and ship loading conditions,
- ship's response to waves,
- the probability of capsizing of the ship in the DSC,
- elements related to the rescue of passengers, cargo and the ship,
- the number of victims of the stability accident.

Elements of the model presented in this paper relate to the ship RoPax, for unrestricted service area. However, the manner of use and modularity of the methodology allow its (this model) use for other types of ships, as well as for limited service areas.

The behaviour of the ship on waves was studied using a mathematical model developed by prof. Jerzy Matusiak(2007)(Acanfora & Matusiak, 2014). "LaiDyn" method is based on the assumption that the complete answer of a ship equals the sum of linear and non-linear parts. Such division results from the fact that

the linear computation methods are well-known. It causes the situation where the radiation and diffractive forces are presented by linear equations quite well(Kukkanen, 1995)(Journee & Adegeest, 2003). In this method, the main part of the first order load is calculated with the linear approximation, based on the current heading and location in relation to a wave. Defining the non-linear part, such elements as non-linearity as a result of ship shape, hydrostatics, wave force were taken into consideration.(Matusiak, 2011).

The LaiDyn program conducted over 17.000 simulations. The simulations conducted for four loading conditions. The wave statistics were taken from IACS documents(IACS, 2001). The information about the maximum roll angle and the time of reaching it, which were obtained as a result of conducted calculations, were applied to construct a risk model. When the time of reaching the critical angle was smaller then the time of repair, it was stated that the ship will capsize. The probability distributions of the variables, marked with references in **Table 1**, were prepared with the usage of the information included in various publications. The 'Fatalities number' variable includes information about the life lost probabilities of the N-passengers. BBN was created using the GeNie software developed at the University of Pittsburgh (Drużdzel, 1999).

5. RISK FRAMEWORK VALIDATION – SENSITIVITY ANALYSIS

The sensitivity analysis allows to investigate how sensitive the results obtained from the risk model are to changes of individual variables(Montewka et al., 2011). To do this, it is necessary to determine the function of the sensitivity for each individual node in the network(Chan & Darwiche, 2002):

$$f(t)=\frac{(c_1 t+c_2)}{(c_3 t+c_4)} \quad (1)$$

where f is the output probability of interest given observations, c1, c2, c3 and c4 which are identified based on the risk model(Goerlandt & Montewka, 2015). The effect of small changes in the input parameters on the result is called sensitivity. The sensitivity is determined from the first derivative of the sensitivity function (see eq. (1)).

Figure 2 provides a graphical result of the sensitivity model analysis, on the assumption that the resulting variable is the 'Fatalities number' of the accident.

The presented graph shows that these variables - 'Capsize', 'Time to capsize', and 'Evacuation time' – have the most crucial impact on the results from the risk model. The 'Capsize' and 'Time capsize' variables are considered as ones of the most important in the model constructed with the usage of the simulations and additional transformations. The 'Evacuation time' variable was created using data from the literature. So, if the Bayes network were to be applied in practice, it would be required to prepare a better model of the evacuation.

A similar analysis was performed for the 'Capsize' variable, as it is shown in **Figure 3**.

In the case where the 'Capsize' variable is analysed, it is impossible to observe any strong dominant variable. Concerning their dominant character, the average variables are the following ones: the 'Wave amplitude', 'Maximum roll angle', and 'Metacentric height'.

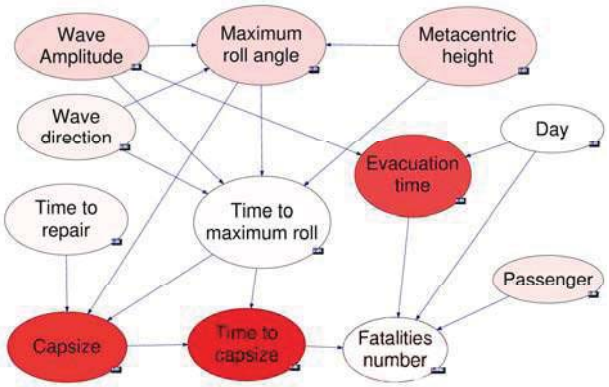

Figure 2 Sensitivity analysis – 'Fatalities number' variable

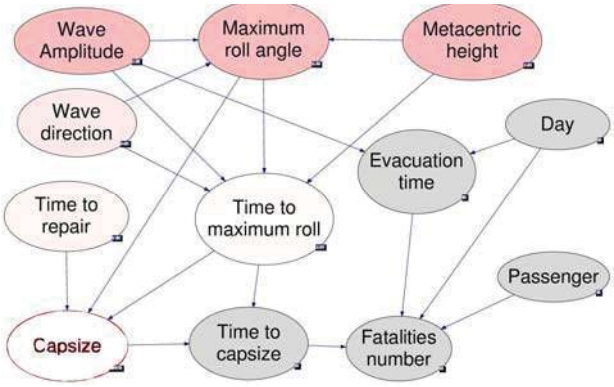

Figure 3 Sensitivity analysis - 'Capsize' variable

6. EXAMPLES

In this section, the methods currently applied to the assessment of stability safety are compared with the results obtained with the method based on risk analysis.

The comparison of two methods is used to show the applicability of the risk to the assessment of the ship stability safety. Such a comparison can also show the level of safety of ships built in accordance with modern requirements.

In the comparison, we used a RoPax type of ship, described below.

Table 2contains the basic dimensions and hydrostatic characteristics of a hull that was used in the risk analysis(Mattila, 1999). **Figure 4** presents the hull profile.

Table 2 Main dimension

Name	Symbol		
Length	Lpp	[m]	158
Breadth	B	[m]	25
Draft	T	[m]	6.1
Depth	H	[m]	15
Block Coefficient	C_b	[-]	0.571
Displacement		[ton]	13766
Wetted surface	S	[m2]	4356

Four different loading conditions for the draught of T=6.1 [m] were taken for the calculations.

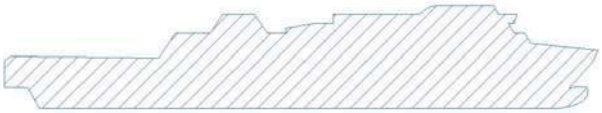

Figure 4 RoPax profile

The standard stability document created in the process of ship design takes a shape of a curve of minimum metacentric heights and maximal centres of gravity. It shows the loading conditions for which the ship complies with the criteria contained in the Code and for which the criteria are not met. The curve of the minimum GM is presented in the **Figure 5**. **Figure 6** shows the curve of the maximum centres of gravity. Both **Figure 5** and **Figure 6** also present the loading conditions used in the simulation.

The analysis of that graphs shows that LC1 condition does not meet the regulations, which are currently in force. Other loading conditions do meet the criteria defined by the rules, wherein LC2 condition is exactly on the limiting curve. According to the approach, that is used nowadays, LC1 condition cannot be considered as a safe one, whereas the remaining conditions are seen as safe ones.

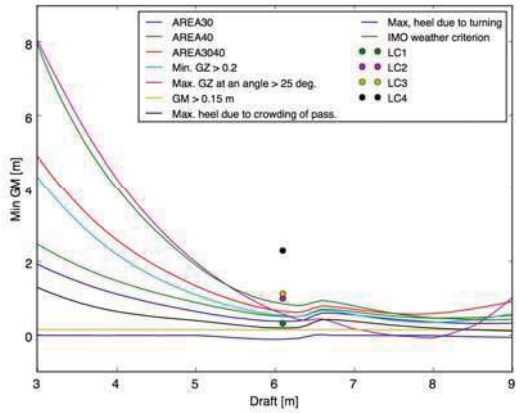

Figure 5 Minimum GM curve

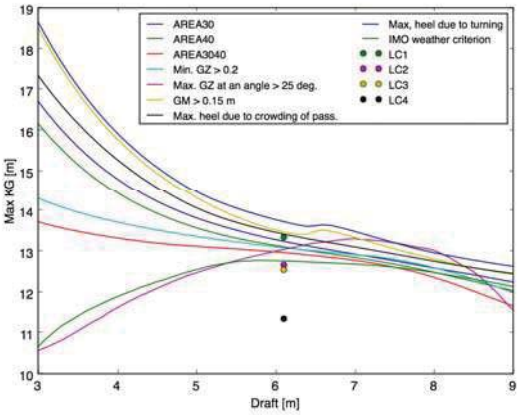

Figure 6 Maximum KG curve

Each FN curve in **Figure 7** corresponds to one load conditions (LC1-LC4). The horizontal position of each curve shows that the higher the GM is the fewer victims of the accident.

Loading condition coded LC4 has the highest GM. This condition meets current stability requirements with a large margin. Also the FN chart confirms this.

7. CONCLUSIONS

The assessment of the safety level has not been performed for the current legislation. So it is unknown how safe ships built with its use are.

Only by using the risk analysis it is possible to decide how safe a ship might be. The measure of safety is presented by the FN curve.

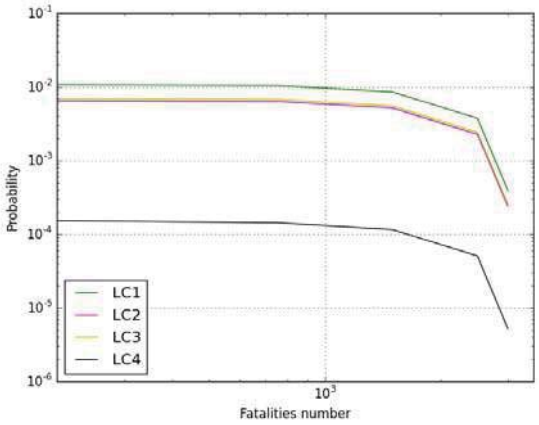

Figure 7 FN curves

Figure 8 is an extension of the graph in **Figure 7** and covers additional ALARP region(Pillay & Wang, 2003). According to the analysis of FN chart include the ALARP area, only LC4 loading condition is entirely included in the area or is located below it. Remaining loading conditions fall outside the area. One should assume that these conditions are not safe. In case of a real project, the group of experts should perform the third stage of

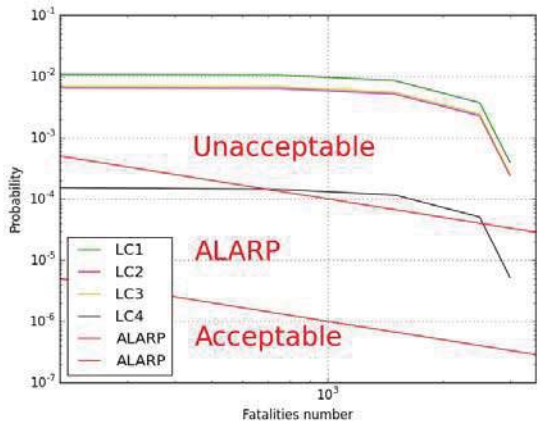

Figure 8 FN curve with ALARP region

According to the designers' experience it should be necessary to check the loading

conditions i.e. to verify whether these conditions are realistic. In the case of the situation where there are no results of the inclining experiment, at least not yet, one could verify the weight estimation. If the previous steps did not provide any appropriate outcome, it would be necessary to modify the shape of the hull. One could also develop an operation manual with the basic information about the limitations of loading conditions and the operating areas.

There are advantages and disadvantages of the risk analysis when used as a tool to assess the stability safety of the ship in the intact condition.

The great advantage of the methods based on the risk analysis is the fact that it might be applied in the new projects or even innovative ones, which cannot be compared to data taken from previous projects. In the process of designing modern vessels or offshore structures, it is possible to use model tests or computer simulations. Such an approach enables the prediction of certain properties in a much more accurate way than using a simple empirical formulas based on experience.

It is possible to use the risk analysis in the evaluation of only one of the scenarios; however such narrowing is not practical. Much better results are obtained by the application of a holistic approach using a variety of scenarios. The risk analysis can give an overall view of the causes and consequences of the accident, as well as examine the impact of the Risk Control Options (RCO) at risk.

The disadvantages of the risk analysis may include primarily large costs associated with the time-consuming experiment; regarding not only its financial side but also the issue of time and personnel. To perform a detail risk analysis, it is necessary to collect a group of experts what might be difficult to achieve in a small design office.

The lack of good probability models of the ship capsizing makes it more difficult to accurately estimate the risk. In many areas of technology, a rich statistic material replaces this lack of probability models of accidents. Concerning the stability accidents, such an approach cannot be applied because the statistical material is rather poor and the analysed accidents do not have any characteristics of repeatability.

8. ABBREVATIONS

ALARP – As Low As Reasonably Practicable

BBN - Bayesian (Belief) Network

FN – Fatalities number

LC – Loading Condition

RCO – Risk Control Option

9. REFERENCES

Acanfora, M., & Matusiak, J. (2014). Quantitative Assessment of Ship Behaviour in Critical Stern Quartering Seas. In 14th International Ship Stability Workshop (pp. 19–27).

Chan, H., & Darwiche, A. (2002). When do numbers really matter? Journal of Artificial Intelligence Research, 17, 265–287.

Drużdzel, M. (1999). Genie: A development environment for graphical decision-analytic models. In Annual Symposium of the American Medical Informatics Association (p. 1206). Washington, D.C., USA.

Francescutto, A. (2007). THE INTACT SHIP STABILITY CODE : PRESENT STATUS AND FUTURE. In 2nd

INTERNATIONAL CONFERENCE ON MARINE RESEARCH AND TRANSPORTATION (pp. 199–208). Ischia, Naples, Italy.

Goerlandt, F., & Montewka, J. (2015). An extended risk analysis approach for oil spill from tankers in a ship-ship collision. Safety Science, Submitted, 42–66. doi:10.1016/j.ssci.2015.02.009

IACS. (2001). Standard Wave Data. IACS (Vol. 34). IACS.

IMO. (2002). MSC/Circ.1023, MEPC/Circ.392 - GUIDELINES FOR FORMAL SAFETY ASSESSMENT (FSA) FOR USE IN THE IMO RULE-MAKING PROCESS. International Maritime Organization.

IMO. (2013). SDC 1/INF.6 - DEVELOPMENT OF SECOND-GENERATION INTACT STABILITY CRITERIA Vulnerability assessment for dead-ship stability failure mode Submitted by Italy and Japan. International Maaritime Organization (Vol. SDC 1/INF.). London, UK.

Journee, J. M. J., & Adegeest, L. J. M. (2003). Theoretical Manual of Strip Theory Program "SEAWAY for Windows." Technische Universiteit Delft. Delft, Nederlands.

Kukkanen, T. (1995). Sealoads version 6.0 - software manual. VTT Technical Research Centre of Finland. Espoo, Finland.

Mattila, M. (1999). Experimental study on transverse stability of fast Ropax vessels on waves. Helsinki University of Technology. Helsinki University of Technology.

Matusiak, J. (2007). On certain types of ship responses disclosed by the two-stage approach to ship dynamics. Archives of Civil and Mechanical Engineering, 7(4), 151–166. doi:10.1016/S1644-9665(12)60233-7

Matusiak, J. (2011). On the non-linearities of ship's restoring and the Froude-Krylov wave load part. International Journal of Naval Architecture and Ocean Engineering, 3(1), 111–115. doi:10.3744/JNAOE.2011.3.1.111

Montewka, J., Ehlers, S., Goerlandt, F., Hinz, T., Tabri, K., & Kujala, P. (2014). A framework for risk assessment for maritime transportation systems—A case study for open sea collisions involving RoPax vessels. Reliability Engineering & System Safety, 124, 142–157. doi:10.1016/j.ress.2013.11.014

Montewka, J., Goerlandt, F., Ehlers, S., Kujala, P., Erceg, S., Polic, D., … Tabri, K. (2011). A model for consequence evaluation of ship-ship collision based on Bayesian Belief Network. In E. Rizzuto & C. Guedes Soares (Eds.), Sustainable Maritime Transportation and Exploitation of Sea Resources (pp. 721–728). LONDON, UK: Taylor & Francis Group.

Montewka, J., Goerlandt, F., & Kujala, P. (2014). On a systematic perspective on risk for formal safety assessment (FSA). Reliability Engineering & System Safety, 127, 77–85. doi:10.1016/j.ress.2014.03.009

Papanikolaou, A. D., Guedes Soares, C., Andrzej Jasionowski, Jensen, J. J., McGeorge, D., Poylio, E., … Vassalos, D. (2009). Risk-Based Ship Design. (A. D. Papanikolaou, Ed.)Springer. Springer. doi:10.1007/978-3-540-89042-3

Pillay, A., & Wang, J. (2003). Technology and Safety of Marine Systems. (R. Bhattacharyya & M. E. McCormick, Eds.)Elsevier Ocean Engineering Series (Vol. 7). Elsevier.

Psaraftis, H. N. (2012). Formal Safety Assessment: an updated review. Journal of Marine Science and Technology, 17(3), 390–402. doi:10.1007/s00773-012-0175-0

Ravn, E. (2006). Risk based model for failure of propulsion and steering gear system. Safedor (Vol. 2.4.7).

Umeda, N. (2013). Current Status of Second Generation Intact Stability Criteria Development and Some Recent Efforts. In 13th International Ship Stability Workshop (pp. 138–157). Brest, Brittany, France.

Wang, J. (2002). Offshore safety case approach and formal safety assessment of ships. Journal of Safety Research, 33(1), 81–115.

This page is intentionally left blank

Application of the Envelope Peaks over Threshold (EPOT) Method for Probabilistic Assessment of Dynamic Stability

Bradley Campbell *NSWCCD (Naval Surface Warfare Center Carderock Division)*,

bradley.campbell@navy.mil

Vadim Belenky, *NSWCCD (Naval Surface Warfare Center Carderock Division)*,

vadim.belenky@navy.mil

Vladas Pipiras, *University of North Carolina at Chapel Hill*, pipiras@email.unc.edu

ABSTRACT

This paper reviews the research and development of the Envelope Peaks over Threshold (EPOT) method that has taken place since the previous STAB conference. The EPOT method is intended for the statistical extrapolation of ship motions and accelerations from time-domain numerical simulations, or possibly, from a model test. To model the relationship between probability and time, the large roll angle events must be independent, so Poisson flow can be used. The method uses the envelope of the signal to ensure the independence of large exceedances. The most significant development was application of the Generalized Pareto Distribution (GPD) for approximation of the tail, replacing the previously used Weibull distribution. This paper reviews the main aspects of modeling the GPD, including its mathematical justification, fitting the parameters of the distribution, and evaluating of the probability of exceedance and its confidence interval.

Keywords: *Large roll, Statistical extrapolation, Generalized Pareto Distribution, EPOT*

1. INTRODUDCTION

The rarity of dynamic stability failures in realistic sea condition makes the problem of extrapolation inevitable. This can be illustrated in the following example. If we assume an hourly stability failure rate of 10^{-6} hr^{-1} (Kobylinski and Kastner, 2003), then we can expect to see (on average) one failure every 1,000,000 hours. If we require 10 observations for a reliable statistical estimate; then we need to simulate 10,000,000 hours. Even if an advanced hydrodynamic code could run in a real time and a cluster with 1,000 processors is dedicated to the task, it would take 10,000 hours per condition (combination of seaway, speed and heading) to perform the assessment. The cost of the calculations prohibits direct simulation in this manner.

Additionally stability failure is associated with large-amplitude motions and is expected to be nonlinear. Indeed, capsize is related to the ultimate nonlinearity – transition to another equilibrium. In order to have enough fidelity to model this problem, the hydrodynamic code must be quite sophisticated (see a review by Reed, *et al.*, 2014). The probability of capsizing the topic of a multi-year ONR research project titled “A Probabilistic Procedure for Evaluating the Dynamic Stability

and Capsizing of Naval Vessels" (Belenky, *et al.*, 2015).

IMO document SLF 54/3/1 (Annex 1) defines intact stability failure as a state of inability of a ship to remain within design limits of roll (heel, list) angle combined with high rigid body accelerations. This includes also partial stability failure when a ship is subjected to a large roll angle or excessive accelerations, but does not capsizes. Following the same logic one could also include an excessive pitch angle. As this study focuses on partial stability failure, peak over threshold method (POT) was chosen (Pickands, 1975). Introducing a threshold allows considering the data that are more influenced by nonlinearity; this incorporates changing physics into the statistical estimates.

To satisfy the requirement of independent peaks over threshold, the peaks of envelope were used instead of the peaks of the process itself (Campbell and Belenky, 2010). The review of this research effort is available from Belenky and Campbell (2012). That work included consideration of the relationship between probability and time, the probabilistic properties of peaks, application of envelope theory and the extreme value distribution.

The relationship between time and probability is key to the proper treatment of the partial stability failures. It is modeled with Poisson flow and requires independence of the failures. In the case of capsizing, the enforcement of Poisson Flow is not required, since capsizing can only occur once per record (the possibility of several capsizings within one record can be safely ignored for practical cases). Belenky and Campbell (2012) also review different ways of statistical characterization of the rate of events, the only parameter of the Poisson flow.

Classical POT methods use the Generalized Pareto Distribution (GPD) to approximate the tail of the distribution above a threshold. However, under certain conditions the GPD may be right bounded, that is, there is some value above which the probability of exceedances is zero. This is not a problem for conventional statistical consideration, when we are interested in the quantiles of the (i.e. the probability is given and the level needs to be found). In ship stability generally the failure level is known and related to down flooding or cargo shifting angles and probability is to be found. The physical meaning of the right bound was not clear at that time (and still is not completely clear). As a result, the Weibull distribution was used for modeling the tail.

Normally distributed wave elevation was the subject of study in Belenky and Campbell (2012). This was a logical first test for these techniques. The study concluded that the distribution of large absolute values of peaks can be approximated by Rayleigh law. The Rayleigh distribution is a particular case of Weibull distribution when the shape parameter equals two. Thus, deviation of this parameter from two may be suitable for representing nonlinearity in a dynamical system.

To investigate the performance of a POT scheme based on the Weibull distribution, a model representing ship motions with realistic stability variation was used (Weems and Wundrow, 2013; Weems and Belenky, 2015). It was found that Weibull distribution does not have enough flexibility to approximate the tail of large-amplitude ship motions and the consideration of the GPD was started again.

Application of the GPD with EPOT produced very reasonable results (Smith and Zuzick, 2015). The techniques used to fit GPD, estimate the probability of exceedance of a given level and evaluate its uncertainty are described in Campbell, et al. (2014, 2014a) and Pipiras, et al. (2015) and briefly reviewed in the rest of this paper.

2. MATHEMATICAL BACKGROUND

2.1 Distribution of Order Statistics

In order to understand why statistical extrapolation is possible when the underlying distribution is unknown, we begin with order statistics.

Consider a set of *n* independent realizations of random variable *z*. Assume that the distribution is given in a form of a cumulative distribution function (CDF) and probability density function (PDF). Sorting the observed values from the largest to smallest we have:

$$y_i = sort(z_i) \quad i = 1,...n \tag{1}$$

Indeed, for a randomly selected values *y* and *z*:

$$pdf(y) = pdf(z); \quad CDF(y) = CDF(z) \tag{2}$$

Consider a value that happens to be *k*-th in the list ($1 \le k \le n$). It is a random number, because, if one generates another set of realizations of variable *z*, and sorts them, another value will be the *k*-th. This random number is referred as *k*-th order statistic. Like any other random variable, y_k has its own distribution. This distribution is (see, e.g. David and Nagaraja, 2003):

$$pdf(y \mid k) = pdf(y)\frac{n!}{(k-1)!(n-k)!} \cdot \left(CDF(y)\right)^{k-1}(1-CDF(y))^{n-k} \tag{3}$$

2.2 Generalized Extreme Value (GEV) Distribution

Consideration of distribution of the largest value (k=1) when the number of observations *n* grows, leads to a limit, known as Generalized Extreme Value (GEV) distribution (see e.g. Coles, 2001):

$$pdf(x) = \frac{1}{\sigma}\left(1+\xi\frac{x-\mu}{\sigma}\right)^{-\left(1+\frac{1}{\xi}\right)} \cdot \exp\left(-\left(1+\xi\frac{x-\mu}{\sigma}\right)^{\frac{1}{\xi}}\right) \tag{4}$$

ξ is a shape parameter, σ is scale parameter ($\sigma>0$); μ is a shift parameter, Equation (4) is non-zero for:

$$\begin{aligned} x &> \mu - \frac{\sigma}{\xi} \quad for \quad \xi > 0 \\ x &< \mu - \frac{\sigma}{\xi} \quad for \quad \xi < 0 \end{aligned} \tag{5}$$

and is zero otherwise. If the shape parameter ξ=0:

$$pdf(x) = \frac{1}{\sigma}\exp\left(\frac{x-\mu}{\sigma}\right) \cdot \exp\left(-\exp\left(\frac{x-\mu}{\sigma}\right)\right) \tag{6}$$

for any values of *x*.

It is important that the limit (4-6) does not depend on the distribution *z*. That means that all the extreme values have the same distribution if one considers a sample of sufficient volume. This is the essence of the extreme value theorem, sometimes referred to as the Fisher-Tippet-Gnedenko theorem (see, e.g. Coles, 2001).

Direct application of the extreme value theorem for probabilistic assessment of dynamic stability can be found in MacTaggart, (2000), MacTaggart and deKat (2000). However, several issues remained unresolved; including the question how large the sample should be (in terms of record length and number of records) to claim limiting properties of GEV.

2.3 Generalized Pareto Distribution (GPD)

The large sample volume needed for direct application of the GEV is partially driven by the fact that only a single value (the largest one

from the time window) is used to find the parameters of distribution. The desire to use more data leads to the idea of peaks over threshold methods.

Take μ as a threshold and find the distribution of the data exceeding this threshold, i.e. consider conditional probability. The Generalized Pareto distribution is derived from the GEV with the threshold condition applied. The basic logic of this derivation is available in Coles (2001). The GPD is expressed as

$$f(x)=\begin{cases}\dfrac{1}{\sigma}\left(1+\xi\dfrac{x-\mu}{\sigma}\right)^{-\left(1+\frac{1}{\xi}\right)}; \\ \quad if \quad \mu<x, \quad \xi>0, \quad or \\ \qquad \mu<x<\mu-\dfrac{\sigma}{\xi}, \quad \xi<0 \\ \dfrac{1}{\sigma}\exp\left(-\dfrac{x-\mu}{\sigma}\right) \quad ; \\ \quad if \quad \mu<x, \ \xi=0\end{cases} \qquad (7)$$

where ξ is the shape parameter, σ is the scale parameter (σ>0) and μ is the threshold, above which, the GPD is believed to be applicable.

Equation (7) expresses the second extreme value theorem, referred as Pickands-Balkema-de Haan theorem. It states that the tail of independent random variables can be approximated with the GPD.

3. FITTING THE GPD

3.1 Preparing Independent Data

Ship motions are characterized by strong dependence of the data points on each other, especially in following and stern quartering seas when a spectrum is narrow and autocorrelation function takes a long time to decay. However, the peaks of the piecewise linear envelope (see Figure 1) represent independent data points. The difference between piecewise linear and theoretical envelope is considered by Belenky and Campbell (2012). However, this technique may not work for the cases of parametric roll, where mutual dependence is much stronger. The method of collecting independent data for the case of parametric roll is described in Kim, *et al.* (2014).

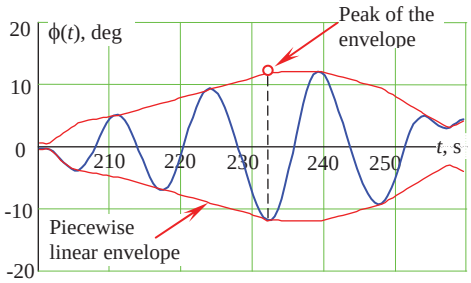

Figure 1: Piecewise linear envelope and its peak

3.2 Estimating Shape and Scale Parameters

To facilitate the choice of the threshold at a later step, fitting the shape and scale parameters are carried out for a series of prescribed thresholds. The maximum likelihood estimator (MLE) method is a standard way of estimating the parameters for the GPD. The idea of MLE method is quite intuitive: to find such values of parameters that are “most likely” to fit the data.

What is “most likely”? The data points that have been observed are the facts. At the same time they are instances of a random variable. Because these particular values were observed, they are more likely to occur than others. That means that the probability of observing these particular values reaches maximum when the correct parameters are used for distribution. The parameters are found by maximizing the value of the likelihood function. In practice this is made easier by taking the natural logarithm of the likelihood function (Equation 8 below).

$$l(\xi,\sigma) = -n\cdot\ln(\sigma) - \left(1+\frac{1}{\xi}\right) \cdot \sum_{i=1}^{n} \ln\left(1+\xi\cdot\frac{z_i}{\sigma}\right) \qquad (8)$$
$$z_i = x_i - \mu$$

Where n is the number of data points above a threshold μ, z_i are the sample data points above a threshold μ (sometimes referred to as *excesses*).

3.3 Distribution the GPD Parameters

Since the shape and scale parameters are estimated from the envelope peak data (which are random numbers), the estimated parameters are also random numbers. Their distribution can be approximated with a bivariate normal distribution (Smith, 1987).

$$f_N(\hat{\xi},\hat{\sigma}) = \frac{1}{2\pi V_\xi V_\sigma \sqrt{1-\rho_{\xi\sigma}^2}} \cdot\exp\left(-\frac{1}{2(1-\rho_{\xi\sigma}^2)}\cdot\left(\frac{(\hat{\xi}-E_\xi)^2}{V_\xi}+\frac{(\hat{\sigma}-E_\sigma)^2}{V_\sigma} - \frac{2\rho_{\xi\sigma}(\hat{\xi}-E_\xi)(\hat{\sigma}-E_\sigma)}{\sqrt{V_\xi V_\sigma}}\right)\right) \qquad (9)$$

Here $\hat{\xi}$ and $\hat{\sigma}$ are estimates of ξ and σ, E is used for expected (or mean) value, V is the variance and ρ is the correlation coefficient between ξ and σ. The parameter estimates produced by maximizing equation (8) are the mean values, while the covariance matrix M_C is found using the method outlined below.

$$M_C = \begin{pmatrix} V_\xi & \rho_{\xi\sigma}\sqrt{V_\xi V_\sigma} \\ \rho_{\xi\sigma}\sqrt{V_\xi V_\sigma} & V_\sigma \end{pmatrix} \qquad (10)$$

The delta method allows one to find the estimates of mean and variance of the output, if estimates of the input are known and the function that turns input into output can be linearized, such as by a Taylor series. Because of this the delta method is an approximation. Appling the delta method to maximization of equation (8) yields the Fisher information matrix M_F that is an inverse of the covariance matrix (10) (Boos and Stefanski, 2013):

$$M_F = \begin{pmatrix} -\frac{\partial^2 l(\xi,\sigma)}{\partial\xi^2} & -\frac{\partial^2 l(\xi,\sigma)}{\partial\xi\partial\xi\sigma} \\ -\frac{\partial^2 l(\xi,\sigma)}{\partial\xi\partial\xi\sigma} & -\frac{\partial^2 l(\xi,\sigma)}{\partial\sigma^2} \end{pmatrix} \qquad (11)$$

The derivatives in (11) are expressed as follows:

$$\frac{\partial^2 l(\xi,\sigma)}{\partial\xi^2} = \frac{2}{\xi^3}\sum_{i=1}^{n}\ln\left(1+\xi\cdot\frac{z_i}{\sigma}\right) - \frac{2}{\xi^2}\sum_{i=1}^{n}\frac{z_i}{\sigma+\xi\cdot z_i} - \left(1+\frac{1}{\xi}\right) \cdot\sum_{i=1}^{n}\frac{z_i^2}{(\sigma+\xi\cdot z_i)^2} \qquad (12)$$

$$\frac{\partial^2 l(\xi,\sigma)}{\partial\sigma^2} = \frac{n}{\xi\cdot\sigma^2} - \left(1+\frac{1}{\xi}\right) \cdot\sum_{i=1}^{n}\frac{1}{(\sigma+\xi\cdot z_i)^2} \qquad (13)$$

$$\frac{\partial^2 l(\xi,\sigma)}{\partial\xi\partial\sigma} = \frac{n}{\xi^2\cdot\sigma} - \frac{1}{\xi^2}\sum_{i=1}^{n}\frac{1}{\sigma+\xi\cdot z_i} - \left(1+\frac{1}{\xi}\right)\cdot\sum_{i=1}^{n}\frac{z_i}{(\sigma+\xi\cdot z_i)^2} \qquad (14)$$

The covariance matrix is finally found as:

$$M_C = M_F^{-1} \qquad (15)$$

Equations (10) through (14) completely define the bivariate normal distribution (9), as shown in Figure 2.

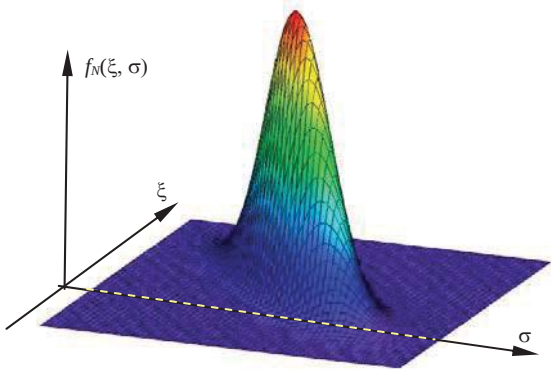

Figure 2: Joint distribution of GDP parameters

It is important to note that the scale parameter is by definition a positive quantity, while the bivariate normal distribution formally supports negative values for the scale parameter. To avoid negativity of σ as an artifact of approximation (9), Pipiras, et al. (2015) proposed using the $\hat{l}_\sigma = \ln\hat{\sigma}$ instead of σ. This leads to a new distribution:

$$f_{LN}(\hat{\xi},\hat{l}_\sigma) = \frac{1}{2\pi V_\xi V_{l\sigma}\sqrt{1-\rho_{\xi l\sigma}^2}} \cdot \exp\left(-\frac{1}{2(1-\rho_{\xi l\sigma}^2)}\cdot\left(\frac{(\hat{\xi}-E_\xi)^2}{V_\xi}+\frac{(\hat{l}_\sigma-E_{l\sigma})^2}{V_{l\sigma}} - \frac{2\rho_{\xi l\sigma}(\hat{\xi}-E_\xi)(\hat{l}_\sigma-E_{l\sigma})}{\sqrt{V_\xi V_{l\sigma}}}\right)\right) \quad (16)$$

$$E_{l\sigma} = \ln(E_\sigma);\quad V_{l\sigma} = \frac{V_\sigma}{E_\sigma^2};\quad \rho_{\xi l\sigma} = \frac{\rho_{\xi\sigma}}{E_\sigma} \quad (17)$$

Difference between distribution (16) and bivariate normal (9) is not very large (Pipiras, *et al.*, 2015).

3.4 Choice of the Threshold

Choosing a correct threshold is a critical to ensuring the applicability of the GPD. If the threshold is too low, the fitted GPD is not an approximation of the tail, because the conditions of the second extreme value theorem have not been met. If the threshold is too high, "eligible" data have been wasted and the result will more scatter or uncertainty than necessary.

The second extreme value theorem states that the GPD can be used for approximation of the tail of any distribution if the threshold is high enough. That means that above certain threshold the GPD approximation must be invariant to the threshold (Coles, 2001). The simplest way is to observe stabilization of the shape parameter, see Figure 3.

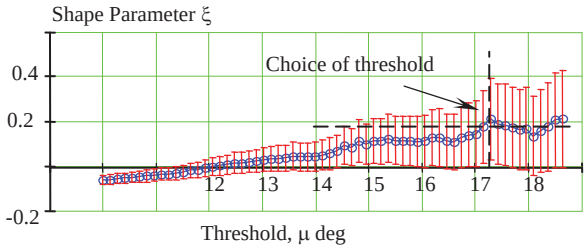

Figure 3 Choice of threshold by stabilization of the shape parameter

Campbell, *et al.* (2014) describes study of five different methods of setting the threshold:

1. Stabilization of shape parameter
2. Stabilization of modified scale parameter
3. Stabilization of mean residual life estimate
4. Ad-hoc method based on minimum absolute difference between the shape parameter and its median above the threshold
5. Ad-hoc method based on minimum squared difference in the shape from its mean above the threshold

The first three methods are taken from Coles (2001) and they were mostly intended for "manual" calculation with "a human in a loop". The methods 4 and 5 are similar to the methods proposed in Reiss and Thomas (2007) for automatic choice of the threshold. The referred study (Campbell, *et al.*, 2014) has shown that automation of the method 1 through 3 makes the threshold lower than the visual choice. For the example shown in Figure 3, these methods put the threshold somewhere

around 13~14 degrees, while the visual choice is somewhere above 17 degrees.

At the same time methods 4 and 5 have returned the threshold that is more close to the "visual" choice. The method 4 is quickly reviewed below. It is based on minimizing the following function:

$$f(\mu_k) = \frac{1}{N_{Tr} - 1 - k} \sum_{i=k}^{N_{Tr}-1} (N_{Tr} - i)^b \left| \hat{\xi}_i - \mathrm{median}(\hat{\xi}_k, .., \hat{\xi}_{N_{Tr}}) \right| \quad (18)$$

The value of b was taken as 0.5; N_{Tr} is the number of the thresholds considered. A plot of (16) is shown in Figure 4. A global minimum (ignoring that the function goes to zero at the right) occurs just below μ=17.4 deg, which is close to one of the visual choices made at Figure 3.

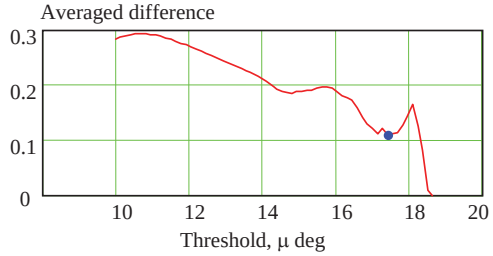

Figure 4 Choice of the Threshold based on the Global Minimum of the Equation (16)

4. EXTRAPOLATION AND UNCERTAINTY OF THE PROBABILITY OF EXCEEDANCE

4.1 Extrapolated Estimate

Using the GPD to extrapolate the probability of exceedance yields the conditional probability that the level of interest c has been exceeded if the threshold μ has been exceeded:

$$\hat{P} = \begin{cases} \left(1 + \hat{\xi} \cdot \frac{c - \mu}{\hat{\sigma}}\right)^{-\frac{1}{\hat{\xi}}} & if \quad \hat{\xi} > -\frac{\hat{\sigma}}{c - \mu} \\ 0 & if \quad \hat{\xi} \le -\frac{\hat{\sigma}}{c - \mu} \end{cases} \quad (19)$$

c is the limit that constitutes the stability failure. The probability that μ has been exceeded can be estimated statistically, since it has been exceeded often enough so that we have enough data to build the distribution of peaks above it.

Now let's consider the problem of the right bound. As can be seen from equation (19), the probability of exceedance is equal zero for negative shape parameters and $c \ge \mu - \hat{\sigma}/\hat{\xi}$. This has several implications.

First, the extrapolated estimate is a random number. The joint distribution of the shape and scale parameters is approximated using distribution (16). That also means that the mean values of the shape and scale parameters are the most probable values at the same time (because normal distribution has a maximum at its mean value). Thus, one could expect that the most probable values used for formulae (19) returns the most probable value of extrapolated estimate.

So if the formula (19) returns zero, it is the most probable answer, but not the only one possible. In fact, the formula (19) must be accompanied with confidence interval that may be seen as a "range of answers".

4.2 Mean and Distribution of the Extrapolated Estimate

In contrast to the most probable value of the extrapolated estimate, the mean value is never zero for a finite volume of data. Consider formula (19) as a deterministic function of random arguments:

$$\hat{P} = g\left(\hat{\xi}, \hat{\sigma}\right) \quad (20)$$

Its mean value can be found as using well known formula for the mean value of deterministic function of random arguments:

$$E(\hat{P}) = \int_0^{\infty} \int_{-\infty}^{\infty} g(\xi,\sigma)\, f_{LN}(\xi,\sigma) d\xi d\sigma \qquad (21)$$

Using (21) the PDF of the extrapolated estimate is derived as:

$$f_p(x) = \int_{-\infty}^{\infty} f_{LN}\left(\xi, \frac{\xi(c-\mu)}{x^{-\xi}-1}\right) \cdot \frac{\xi^2 x^{-\xi-1}}{\left(x^{-\xi}-1\right)^2}(c-\mu) d\xi \qquad (22)$$

Figure 5 depicts the PDF of the extrapolated estimate

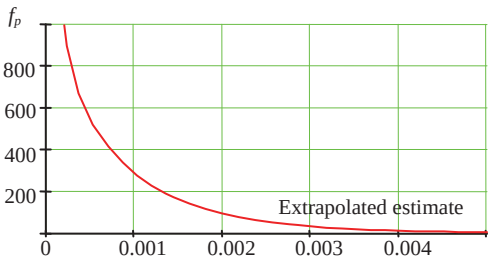

Figure 5: PDF of the Extrapolate Estimate (Campbell, *et al.*, 2014).

More details are available from Campbell *et al.* (2014). The formula (22) also can be written using the bivariate normal distribution (9).

4.3 Confidence Interval of the Extrapolated Estimate

Quantiles of distribution (22) can be used to evaluate the confidence interval of the extrapolated estimate. The profile log likelihood PLL method (Coles, 2001) adapted for the extrapolated estimate is another way to find the confidence interval (Campbell, *et al.*, 2014). The log likelihood estimator (8) is expressed in terms of the extrapolated estimate $\hat{P}$ (19):

$$l_p(\hat{\xi},\hat{P}) = -n\ln\left(\frac{\hat{\xi}\cdot c}{\hat{P}^{-\xi}-1}\right) - \left(1+\frac{1}{\hat{\xi}}\right)\sum_{i=1}^{n}\ln\left(1+\frac{z_i\left(\hat{P}^{-\xi}-1\right)}{c}\right) \qquad (23)$$

and maximized by the shape parameter:

$$l_m(\hat{P}_x) = \arg\max_{\hat{\xi}} l_p(\hat{\xi},\hat{P}_x) \qquad (24)$$

and the extrapolated estimate:

$$\hat{P} = \arg\max_{\hat{P}_x} l_m(\hat{P}_x) \qquad (25)$$

The difference between them, referred as deviance statistic D and is assumed to have χ^2 distribution:

$$D(\hat{P}_x) = l_m(\hat{P}) - l_m(\hat{P}_x) \qquad (26)$$

The confidence interval includes the space where:

$$D(p) < 0.5 Q_{\chi 2}(P_\beta, dof = 1) \qquad (27)$$

P_β is the confidence probability and $Q_{\chi 2}$ is the quantile function of the χ^2 distribution. The boundaries are found as the limits of P_x that satisfy the condition (27), see Figure 6.

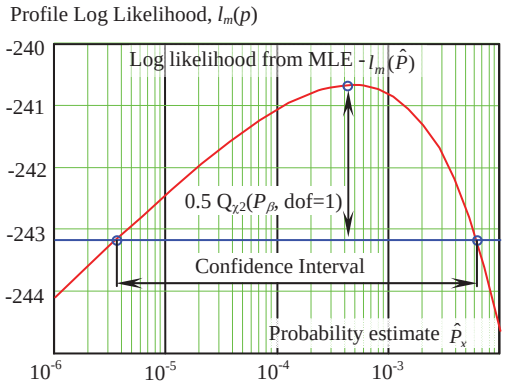

Figure 6. Profile Log Likelihood Method for Confidence Interval (Campbell, *et al.* 2014)

Pipiras, *et al.* (2015) systematically studied and compared different methods of calculating the confidence interval for the extrapolated

estimate. The following methods were considered:

1. Delta method
2. "Normal" method (distribution 9)
3. "Lognormal" method (distribution 22)
4. "Boundary" method
5. Standard bootstrap method
6. Profile likelihood method (as briefly described above)

In addition to those six methods, three more techniques, termed indirect techniques, investigated were based on quantiles rather than extrapolated estimate for exceedance probability. Any of the methods mentioned above can be used to construct a confidence interval for the return level (the level to be exceeded with given probability p):

$$x_p = \frac{\sigma}{\xi}\left(p^{-\xi} - 1\right) \qquad (28)$$

The general scheme of calculations of the confidence interval through quantiles / return level is shown in Figure 7. The three methods adapted to the indirect approach using quantiles were:

7. Indirect "Lognormal" method
8. Indirect "Boundary" method
9. Indirect Profile likelihood method

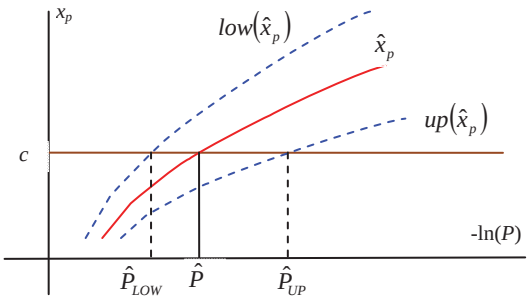

Figure 7 On Calculation of Confidence Interval using quantiles (Pipiras, *et al.*, 2015)

A comparison study was performed on simulated data sampled from a GPD distribution. The performance was judged based on the percentage of cases where the confidence interval contained the true value (coverage). An accurate method should have the coverage close to the given confidence probability (P_β=0.95). There were two series of calculations with 100 and 50 samples each.

The indirect profile likelihood method was shown to have the best performance, see Pipiras, *et al.* (2015). The delta method does not perform well for probability estimates and should not be used. The "normal", "log-normal", and indirect "log-normal" methods are slightly anticonservative (coverage < 95%) with the log-normal method preferred among the tree. The boundary method and indirect boundary methods are slightly conservative (coverage > 95%). The bootstrap and profile likelihood methods performed poorly for negative and near-zero shape parameters.

4.4 Convergence Study

Campbell, *et al.* (2014) describes convergence study for the EPOT method, using of the datasets from Smith *et al.* (2014) and Smith and Zuzick (2015). The results are shown in Figure 8.

The convergence test uses a moving average for 100 extrapolation data sets; the moving average is performed for the most probable value, mean value, and the upper boundary of the confidence interval calculated with the "log-normal" method. The most probable value is a better estimator when the sample volume is large, while the mean shows better (and more conservative) performance for smaller sample volumes. More details are available from Campbell, *et al.*, (2014).

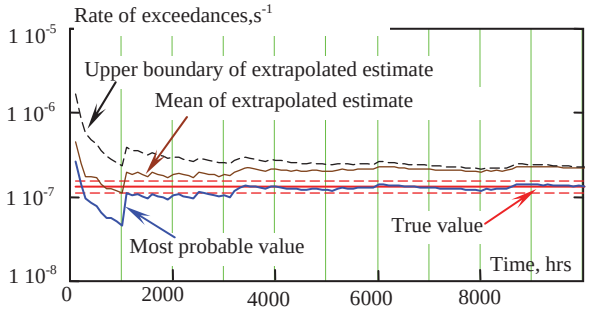

Figure 8 Convergence Test Using Moving

Averages to Approximate Extrapolated Estimates (Campbell, *et al.*, 2014)

4.5 On the Validation of EPOT

A comprehensive validation study of the EPOT method is reported by Smith and Zuzick (2015). Motions of the ONR Tumblehome topsides (Bishop *et al.*, 2005) configuration were simulated with a 3-DOF volume-based simulation (Weems and Wundrow, 2013; Weems and Belenky, 2015) for hundreds of thousands of hours to produce "true" values on rare exceedances. Than small subsets (100 hrs each) was used by EPOT extrapolation. Smith and Zuzick (2015) used log-normal and boundary methods in carrying out their validation procedure for six relative wave headings considering roll, pitch, lateral and vertical accelerations. Using the same data set, Pipiras, *et al.* (2015) reported results for heave and pitch only for 30 and 45 degrees of heading, but used methods 2 through 9 for the confidence interval.

Total number of conditions reported by Smith and Zuzick (2015) was 23. The minimal acceptable coverage was set to 90%. With log-normal confidence interval six conditions failed, while all the conditions are passed using the boundary method. These results could be expected as the log-normal method is slightly anti-conservative and the boundary method is slightly conservative, as mentioned above. Smith and Zuzick (2015) noted that all the conditions show acceptable results for restricted range of headings – aft of the beam seas. Similar conclusions were reached by Pipiras, *et al.* (2015).

5. CURRENT STATUS AND FUTURE WORK

The EPOT method has evolved significantly in the three years since the previous STAB conference. The main idea remains the same, however: extrapolate peaks over a threshold and use the envelope to ensure independence. The idea of threshold was originally aimed to emphasize influence of nonlinearity. Now it is also has a mathematical interpretation – it ensures the applicability of the second extreme value theorem.

Use of the second extreme value theorem leads to use of the Generalized Pareto distribution (GPD) to approximate the distribution above a certain large threshold. The selection of the threshold is done based on applicability of GPD approximation above the chosen threshold. Five different techniques for selecting the threshold have been considered.

Fitting the GPD is performed with the maximum likelihood estimation (MLE) method. These parameter estimates from the MLE fit are assumed to follow a normal distribution. Several methods were considered for estimating the confidence interval of the extrapolated probability of exceedance. Some of them we anti-conservative and some were conservative. A definitive recommendation on which to use is still outstanding.

Significant progress has been achieved in the validation techniques of EPOT and the problems of extreme rarity in general. A very fast simulation code has been developed that is capable of producing statistics for events that occur only a few times during millions of hours. The simulation was shown to be qualitatively similar to higher fidelity codes like LAMP (Weems and Belenky, 2015). A procedure for the validation of statistical extrapolation techniques has been developed and applied to EPOT (Smith and Zuzick, 2015). While not all the tested environmental conditions satisfied the currently proposed requirements, the EPOT method shows promise and potential to be acceptable.

In addition to finalizing the confidence interval formulation, attention needs to be paid to reducing the uncertainty in the extrapolated probability of exceedance estimates. It may be possible to reduce the uncertainty if a

relationship between the GPD parameters and physical considerations can be established. Pipiras, *et al.* (2015) investigated fixing the ratio between the GPD parameters for the case of pitch based on shape of the longitudinal GZ curve. This resulted in decreasing of width of the confidence interval and spread of the estimates around the "true" value. Such a decrease of uncertainty was the result of introducing additional physical information into the problem. The idea of a limiting roll angle is discussed by Campbell, *et al* (2015) and may lead to a similar result for roll. It is anticipated that further study into the nature of the tail of the distribution of large ship motions will lead to an application-ready EPOT method.

6. ACKNOWLEDGEMENTS

The work described in this paper has been funded by the Office of Naval Research, under Dr. Patrick Purtell, Dr. Ki-Han Kim and Dr. Thomas Fu. The authors greatly appreciate their support. The participation of Prof. Pipiras was facilitated by the Summer Faculty Program supported by ONR and NSWCCD under Dr. Jack Price (David Taylor Model Basin, NSWCCD). The authors would like to acknowledge fruitful discussions with Prof. Pol Spanos (Rice University), Dr. Art Reed, Mr. Tim Smith (David Taylor Model Basin, NSWCCD), and Prof. Ross Leadbetter (University of North Carolina ,Chapel Hill).

7. REFERENCES

Belenky, V. and Campbell, B.L., 2012 "Statistical Extrapolation for Direct Stability Assessment", Proc. 11th Intl. Conf. on Stability of Ships and Ocean Vehicles STAB 2012, 243-256, Athens, Greece.

Belenky, V., Weems, K. and Lin, W.M., 2015 "Split-time Method for Estimation of Probability of Capsizing Caused by Pure Loss of Stability" in Proc. 12th Intl. Conf. on Stability of Ships and Ocean Vehicles STAB 2015, Glasgow, UK.

Bishop, R. C., W. Belknap, C. Turner, B. Simon, and Kim J. H., 2005 "Parametric Investigation on the Influence of GM, Roll damping, and Above-Water Form on the Roll Response of Model 5613." Report NSWCCD-50-TR-2005/027.

Boos, D. D. and Stefanski, L. D., 2013 Essential Statistical Inference: Theory and Method. Springer.

Campbell, B. and Belenky, V., 2010 "Assessment of Short-Term Risk with Monte-Carlo Method" Proc. 11th Int. Ship Stability Workshop, Wageningen, the Netherlands.

Campbell, B., Belenky, V. and Pipiras, V., 2014 "Properties of the Tail of Envelope Peaks and their Use for the Prediction of the Probability of Exceedance for Ship Motions in Irregular Waves" CSM7 Computational Stochastic Mechanics, Deodatis, G. and P. D. Spanos, eds. (accepted).

Campbell, B., Belenky, V. and Pipiras V., 2014a "On the Application of the Generalized Pareto Distribution for Statistical Extrapolation in the Assessment of Dynamic Stability in Irregular Waves" Proc. 14th Intl. Ship Stability Workshop, Kuala Lumpur, Malaysia, pp. 144-148.

Coles, S., 2001 An Introduction to Statistical Modeling of Extreme Values. Springer, London.

David, H. A. and Nagaraja, H. N., 2003. Order Statistics. Wiley Series in Probability and Statistics

IMO SLF 54/3/1 Development of Second Generation Intact Stability Criteria. Report of the Working Group at SLF 53 (part 2). Submitted by the Chairman of the Working Group, 2011, London, UK.

Kim, D.H., Belenky, V., Campbell, B. L. and Troesch, A. W., 2014 "Statistical Estimation of Extreme Roll in Head Seas" in Proc. of 33rd Intl. Conf. on Ocean, Offshore and Arctic Engineering OMAE 2014, San-Francisco, USA.

Kobylinski, L. and Kastner, S. 2003 Stability and Safety of Ships. Regulation and Operation, Elsevier.

McTaggart, K. A., 2000 "Ongoing Work Examining Capsize Risk of Intact Frigates Using Time Domain Simulation". In Contemporary Ideas of Ship Stability, D. Vassalos, et al. (eds), Elsevier Science, pp. 587–595.

McTaggart, K. A., de Kat J.O., 2000 "Capsize Risk of Intact Frigates in Irregular Seas". Trans. SNAME, Vol. 108, pp 147–177.

Pickands, J., 1975 "Statistical Inference Using Extreme Order Statistics". The Annals of Statistics Vol. 3, No 1, pp. 119-131.

Pipiras, V., Glotzer, D., Belenky, V., Campbell, B., Smith, T., 2015 "Confidence Interval for Exceedance Probabilities with Application to Extreme Ship Motions", J. of Statistical Planning and Inference (Submitted)

Reed, A., Beck, R. and Belknap, W., 2014 "Advances in Predictive Capability of Ship Dynamics in Waves", Invited Lecture at 30th Symposium of Naval Hydrodynamics, Hobart, Australia.

Reiss, R.-D. and Thomas, M., 2007 Statistical Analysis of Extreme Values with Application to Insurance, Finance, Hydrology and Other Fields. 3rd Edition, Basel: Birkhäuser Verlag.

Smith, R. L., 1987 "Estimating tails of probability distributions." The Annals of Statistics Vol 15, pp.1174–1207.

Smith, T. C., 2014 "Example of Validation of Statistical Extrapolation Example of Validation of Statistical Extrapolation," Proc. of the 14th Intl. Ship Stability Workshop, Kuala Lumpur, Malaysia.

Smith, T. C., and Zuzick, A., 2015 "Validation of Statistical Extrapolation Methods for Large Motion Prediction" in Proc. 12th Intl. Conf. on Stability of Ships and Ocean Vehicles (STAB 2015), Glasgow, UK.

Weems, K., and Wundrow, D., 2013 "Hybrid Models for Fast Time-Domain Simulation of Stability Failures in Irregular Waves with Volume-Based Calculations for Froude-Krylov and Hydrostatic Forces", Proc. 13th Intl. Ship Stability Workshop, Brest, France.

Weems, K. and Belenky, V., 2015 "Fast Time-Domain Simulation in Irregular Waves With Volume-Based Calculations for Froude-Krylov and Hydrostatic Force" in Proc. 12th Intl. Conf. on Stability of Ships and Ocean Vehicles (STAB 2015), Glasgow, UK.

Split-time Method for Estimation of Probability of Capsizing Caused by Pure Loss of Stability

Vadim Belenky, *NSWCCD (David Taylor Model Basin)*, vadim.belenky@navy.mil

Kenneth Weems, *NSWCCD (David Taylor Model Basin)*, kenneth.weems@navy.mil

Woei-Min Lin, *Office of Naval Research – Global*, woei-min.lin.civ@mail.mil

ABSTRACT

The paper reviews a multi-year research effort for using the split-time method to calculate the probability of ship capsizing due to pure loss of stability in irregular waves. The idea of the split-time method is to separate the complex problem of the probability of capsizing into two less complex problems: a non-rare problem that involves the upcrossing of an intermediate level of roll and a rare problem that focuses on capsizing after an upcrossing. An initial implementation using a dynamic model with piecewise linear stiffness, which can be considered to be the simplest model of capsizing in beam seas, led to the concept of critical roll rate as the smallest roll rate at the instant of upcrossing that inevitably leads to capsizing. The piecewise linear system allows a closed-form solution for the critical roll rate, but a more general approach using perturbations can be used for numerical models including advanced hydrodynamic simulation codes. The extension of the split-time method to pure loss of stability required the consideration of the change of roll stiffness in waves and led to calculating the critical roll rate at each upcrossing. A metric of the likelihood of capsizing has been defined as the difference between the observed and critical roll rate at the instances of upcrossing. The probability of capsizing after upcrossing becomes an extrapolation problem for the value of the metric, which can be performed by approximating the tail of the metric's distribution with the Generalized Pareto Distribution. This probability is combined with the observed rate of upcrossings to estimate the rate of capsizing in irregular seas.

Keywords: *Capsizing, Probability, Pure Loss of Stability, Split-Time Method*

1. INTRODUCTION

The dynamic capsizing of a ship is a complex phenomenon dominated by the nonlinearity of the large amplitude roll response, so that linearized mathematical models cannot retain the phenomenon's essential properties. Capsizing of an intact ship in realistic irregular waves represents an even bigger challenge, as this extreme nonlinearity is combined with extreme rarity, leaving no chance for using brute-force Monte-Carlo simulation with hydrodynamic codes of sufficient fidelity.

This challenge has been taken up by the US Office of Naval Research (ONR) project "A Probabilistic Procedure for Evaluating the Dynamic Stability and Capsizing of Naval Vessels". The objective of the project is to create a robust theory of probabilistic capsizing in irregular waves and a numerical procedure based on this theory.

As is well known, an intact ship in realistic ocean waves can capsize in a number of different scenarios or modes. The physical mechanism is different for each scenario, so the

theory must be mode-specific. The pure loss of stability is, in a sense, a simplest scenario. It can be modeled in a basin just with waves, assuming that roll damping is high enough to prevent parametric roll resonance and the forward speed is too low for surf-riding and broaching-to.

The split-time method has been developed to simultaneously address the phenomenon's extreme nonlinearity and rarity by providing an evaluation of the probability of capsizing from a relatively small volume of irregular sea response data, perhaps hundreds of hours of simulation rather than the millions of hours required for a Monte-Carlo approach. Numerical implementation has largely been carried out using the Large Amplitude Motion Program (LAMP), although the procedure is fundamentally code-independent.

The split-time method is being developed in phases. The initial phase considered a ship with time-invariant stiffness. While this can be considered to be a model of capsizing at zero speed in beam seas, the primary objective was to develop a basic theory of the method for both a simplified mathematical model and numerical simulation codes. The second phase of the development has extended the theories to the problem of pure loss of stability by considering the ship's change of stiffness as it moves in waves. This paper discusses the development of the theory for these initial two phases.

2. BASIC THEORY OF RARE RANDOM TRANSITIONS

2.1 Piecewise Linear System

Capsizing can be considered as a transition of a ship moving about its stable upright equilibrium to motions about its stable "mast down" equilibrium. A dynamical system with a piecewise linear stiffness is, possibly, the simplest way to describe a transition between two stable equilibria:

$$\ddot{\phi} + \omega_\phi^2 f_L^*(\phi) = 0 \qquad (1)$$

ω_ϕ is a natural frequency of roll and f_L^* is a piecewise linear stiffness function. As illustrated in Figure 1, equation (1) models the phase plane topology of a ship in calm water, and has a closed-form solution for each range.

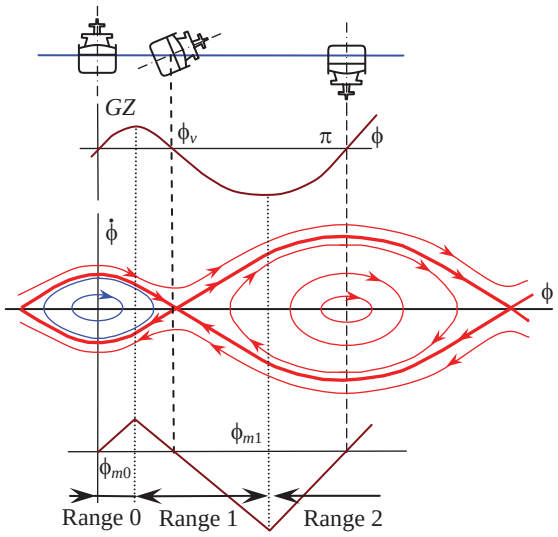

Figure 1: Phase plane topology of capsize and piecewise linear stiffness (Belenky, 1993)

Adding linear damping and random excitation to the dynamical system (1) makes it a model of random transition between stable equilibria:

$$\ddot{\phi} + 2\delta\dot{\phi} + \omega_\phi^2 f_L^*(\phi) = f_{E\phi}(t) \qquad (2)$$

δ is a linear damping coefficient and $f_{E\phi}$ is a stochastic process of roll excitation, modeled as:

$$f_{E\phi}(t) = \sum_{i=1}^{N_\omega} \alpha_{Ei} \sin(\omega_i t + \varphi_{0i}) \qquad (3)$$

α_{Ei} are amplitudes, ω_i are frequencies and φ_{0i} are initial phases of the i^{th} component of an excitation process presented as a Fourier series with N_ω frequencies. Equation (2) has a known closed-form solution in each range:

$$\phi = \begin{cases} \phi_a e^{-\delta t}\sin(\omega_{d0}t + \varepsilon) + p_0(t) \\ \qquad if \qquad -\phi_{m0} \le \phi \le \phi_{m0} \\ Ae^{\lambda_1 t} + Be^{\lambda_2 t} + p_1(t) \\ \qquad if \qquad \phi_{m0} < \phi \le \phi_{m1} \\ \phi_{a2} e^{-\delta t}\sin(\omega_{d2}t + \varepsilon_2) + p_2(t) \\ \qquad if \qquad \phi > \phi_{m0} \end{cases} \quad (4)$$

ϕ_a, ε, A, B, ϕ_{a2} and ε_2 are arbitrary constants that are dependent on the initial conditions at the "switching" of the ranges; ω_{d0} and ω_{d2} are frequencies of the damped oscillation in ranges 0 and 2, respectively; λ_1 and λ_2 are eigenvalues for the solution in Range 1. The particular solutions for each range are expressed as:

$$p_j(t) = \sum_{i=1}^{N_\omega} p_{ij}\sin(\omega_i t + \beta_{ij} + \varphi_{0i}) + E_j \quad (5)$$

j=0, 1, 2 is a range number, p_{ij} is an amplitude and β_{ij} is a phase shift of the i^{th} component of the response. E_j is a position of equilibria for each range:

$$E_0 = 0; \quad E_1 = \phi_V; \quad E_2 = \pi \quad (6)$$

ϕ_v is the angle of vanishing stability. One of the eigenvalues for the Range 1 is positive while another is negative:

$$\lambda_1 = -\delta + \sqrt{\omega_\phi^2 k_{f1} + \delta^2} > 0$$
$$\lambda_2 = -\delta - \sqrt{\omega_\phi^2 k_{f1} + \delta^2} < 0 \quad (7)$$

k_{f1} is the slope coefficient for Range 1 taken with opposite sign.

2.2 Condition of the Transition

Whether the transition to the "mast down" equilibrium (*i.e.* capsize) occurs is determined by the sign of the arbitrary constant A, as the first term in Range 1 in solution (4) is unlimited (for non-zero A):

$$A = \frac{(\dot\phi_1 - \dot p_{01}) - \lambda_2(\phi_{m0} - p_{01} - \phi_V)}{\lambda_1 - \lambda_2} \quad (8)$$

$\dot\phi_1$ and ϕ_{m0} are initial conditions, and $\dot p_{01}$ and p_{01} are values of particular solution (5) at the instant of crossing from Range 0 into Range 1. If A>0, the transition occurs immediately, as illustrated in Figure 2. One can express the condition of transition in terms of the roll rate at the instant of upcrossing ϕ_{m0}:

$$\dot\phi_{cr} = \lambda_2(\phi_{m0} - p_{01} - \phi_V) + \dot p_{01} \approx -\lambda_2\phi_V \quad (9)$$

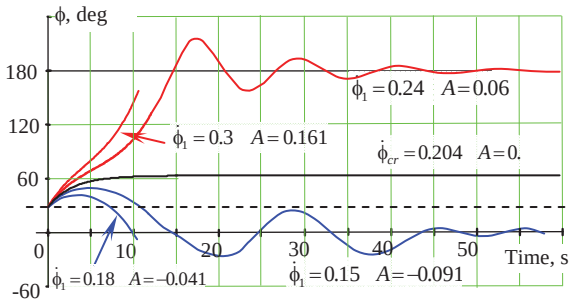

Figure 2: General solution of homogenous equation (2), the derivative values are expressed in rad/s

Values of a particular solution and its derivative at the instant of upcrossing are small and can be neglected. The dynamical system (4) is a repeller in Range 1, so resonance is impossible and the particular solution is small; see Figure 3. The same argument can be applied to the value of the derivative of the particular solution in Range 1 (Belenky, 1993).

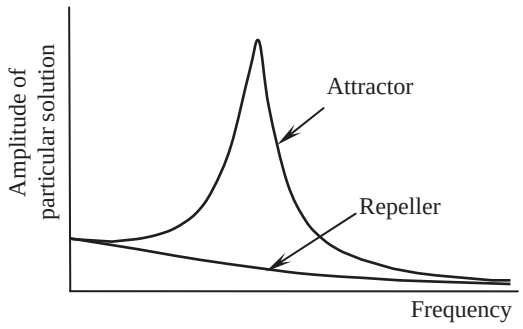

Figure 3: Amplitudes of frequency-domain response of attractor and repeller (Belenky *et al.*, 2008)

Thus, the random transition occurs whenever the process upcrosses the threshold ϕ_{m0} and its derivative exceeds the critical value (9) at the instant of upcrossing. Some upcrossings will result in the transition, while other will not. The transition can be seen as an upcrossing, with its rate reduced by the probability of the derivative's exceeding the critical value (9):

$$\xi_C = \xi_U(\phi_{m0}) \cdot P(\dot{\phi}_1 > \dot{\phi}_{Cr}) \qquad (10)$$

where $\xi_U(\phi_{m0})$ is the upcrossing rate through the threshold ϕ_{m0}.

Formula (10) expresses the main idea of the split-time method. The complex problem of transition has been divided into two less complex problems: characterizing the upcrossing of the intermediate level (non-rare problem) and finding the probability of transition if the upcrossing has occurred (rare problem).

2.3 The Non-Rare Problem

The random transitions (capsizings) are expected to be rare. If one assumes that upcrossings of the threshold ϕ_{m0} are also rare, then influence from the general solution of the homogenous equation on Range 1 can be neglected. For this model, the process of the particular solution is normal and the rate of upcrossing can be expressed as:

$$\xi_U(\phi_{m0}) = \frac{1}{2\pi}\sqrt{\frac{V_{\dot{\phi}}}{V_{\phi}}}\exp\left(-\frac{\phi_{m0}^2}{2V_{\phi}}\right) \qquad (11)$$

$V_{\phi} = V_{p0}$ and $V_{\dot{\phi}} = V_{\dot{p}0}$ are the variances of the particular solution and its derivative in Range 0, and can be found from formula (5):

$$V_{p0} = \sum_{i=1}^{N_\omega} p_{0i}^2 \quad ; \quad V_{\dot{p}0} = \sum_{i=1}^{N_\omega} \omega_i p_{0i}^2 \qquad (12)$$

The calculation of these variances does not present a problem.

2.4 The Rare Problem

The difference between the observed and critical values of the derivative is the metric of the transition's likelihood. Since the critical value for the derivative is constant, it is only necessary to find the distribution of the value of the derivative at upcrossing. The original derivation was published in Appendix 3 of Belenky *et al.* (2008), while the abridged and updated version is given below.

The upcrossing event is defined as follows (Kramer and Leadbetter, 1967):

$$U = \begin{cases} \phi(t) < \phi_{m0} \\ \phi(t+dt) > \phi_{m0} \end{cases} = \begin{cases} \phi(t) < \phi_{m0} \\ \phi(t) > \phi_{m0} - \dot{\phi}(t)dt \end{cases} \qquad (13)$$

The probability that U occurs at time t is

$$P(U) = \int_0^{\infty} \int_{\phi_{m0}-\dot{\phi}dt}^{\phi_{m0}} pdf(\phi,\dot{\phi})d\phi d\dot{\phi} = dt\int_0^{\infty} \dot{\phi} \cdot pdf(\phi = \phi_{m0}, \dot{\phi})d\phi d\dot{\phi} \qquad (13)$$

$pdf(\phi,\dot{\phi})$ is the joint probability distribution function of the process and its derivative.

Consider a random event V such that:

$$V = \begin{cases} \dot{\phi}(t) \le \dot{\phi}_1 \\ \dot{\phi}(t) > 0 \end{cases} \qquad (15)$$

A random event that the events U and V occur simultaneously:

$$U \cap V = \begin{cases} \phi(t) < \phi_{m0} \\ \phi(t) > \phi_{m0} - \dot{\phi}(t)dt \\ \dot{\phi}(t) \le \dot{\phi}_1 \\ \dot{\phi}(t) > 0 \end{cases} \qquad (16)$$

The probability that U and V occur simultaneously at time t is:

$$P(U \cap V) = \int_0^{\dot{\phi}_1} \int_{\phi_{m0}-\dot{\phi}dt}^{\phi_{m0}} pdf(\phi, \dot{\phi}) d\phi d\dot{\phi} = dt \int_0^{\dot{\phi}_1} \dot{\phi} \cdot pdf(\phi = \phi_{m0}, \dot{\phi}) d\dot{\phi} \quad (17)$$

By definition, the Cumulative Distribution Function (*CDF*) is:

$$CDF\left(\dot{\phi}_1 \mid \phi_{m0}\right) = P\left(\dot{\phi}(t) < \dot{\phi}_1 \mid \phi_{m0}\right) = \frac{P(V \cap U)}{P(U)} = \frac{\int_0^{\dot{\phi}_1} \dot{\phi} \cdot pdf(\phi = \phi_{m0}, \dot{\phi}) d\dot{\phi}}{\int_0^{\infty} \dot{\phi} \cdot pdf(\phi = \phi_{m0}, \dot{\phi}) d\dot{\phi}} \quad (18)$$

Differentiation of (18) yields the *pdf* of the derivative value at the instant of upcrossing:

$$pdf(\dot{\phi}_1 \mid \phi_{m0}) = \frac{\dot{\phi}_1 \cdot pdf(\phi = \phi_{m0}, \dot{\phi}_1)}{\int_0^{\infty} \dot{\phi} \cdot pdf(\phi = \phi_{m0}, \dot{\phi}) d\dot{\phi}} \quad (19)$$

If upcrossings are rare, the response process and its derivative can be assumed to be normal. This also means that they are independent, as the stationary process is not correlated with its first derivative and two uncorrelated normal processes are independent. Substitution of the normal distribution into (19) yields:

$$pdf(\dot{\phi}_1) = \frac{\dot{\phi}_1}{V_{\dot{\phi}}} \exp\left(-\frac{\dot{\phi}_1^2}{2V_{\dot{\phi}}}\right) \quad (20)$$

Formula (20) is the Raleigh distribution.

The distribution of the derivative at the instant of upcrossing is different from the distribution of the derivative in general. The distribution "in general" is obtained if the sampling is done in "any" (or random) instant. The instant of upcrossing of the primitive is not a random instant. A condition when the upcrossing is occurred is expressed by equation (13). Thus, the distribution of the derivative at upcrossing is not equivalent to the distribution of the derivative "in general".

Finally, the conditional probability of the transition after upcrossing has occurred is derived using equations (9) and (20):

$$P\left(\dot{\phi}_1 > \dot{\phi}_{Cr}\right) = \exp\left(-\frac{(\lambda_2 \phi_V)^2}{2V_{\dot{\phi}}}\right) \quad (21)$$

Equation (20) is the solution of the rare problem.

2.5 Probability of Rare Transitions

The combination of equations (10) and (20) yields the solution for the rate of rare random transitions:

$$\xi_C = \frac{1}{2\pi} \sqrt{\frac{V_{\dot{\phi}}}{V_{\phi}}} \exp\left(-\frac{1}{2}\left(\frac{\phi_{m0}^2}{V_{\phi}} + \frac{(\lambda_2 \phi_V)^2}{V_{\dot{\phi}}}\right)\right) \quad (21)$$

For the ship-like dynamical system with piecewise linear stiffness (Figure 1), the domain of attraction to the capsized equilibrium is larger than for the one with "mast up". Thus, while the transition to capsized equilibrium is rare, the probability of transition in the opposite direction can be neglected. It is safe to assume that once transition has occurred, the dynamical system will stay capsized. That means that any two transitions are independent, as they must occur in two independent records. This means the transition meets the requirement of Poisson flow (Sevastianov, 1963, 1994), which leads to the following formula for the probability of transition (capsizing) during a given time *T*:

$$P(T) = 1 - \exp\left(-\xi_C T\right) \quad (22)$$

2.6 Summary of the Basic Theory

The original solution for random rare transitions in a dynamical system with

piecewise linear stiffness was found in the late 1980s (Belenky, 1993). It has been applied to the probability of capsizing of a ship in beam wind and seas (Paroka and Umeda, 2006; Paroka *et al*., 2006). Some verification of self-consistency was carried out within the framework of the ONR project, which resulted in the refinement of the solution; the distribution of the derivative value at the instant of upcrossing was found to be Rayleigh (Belenky *et al*., 2008).

The dynamical system with the piecewise linear stiffness likely represents the simplest model of a rare random transition between two stable equilibria. Nevertheless, considering this simple model, the following conclusions can be reached:

- A "critical derivative" ("critical roll rate") can be defined as the value of the derivative which, if exceeded at upcrossing, inevitably leads to transition (capsizing)
- The difference between the observed and critical derivatives (roll rates) can be used as a metric of the likelihood of transition (capsizing)
- The rate of transitions (capsizings) can be defined as the rate of upcrossings of a maximum stiffness level in which the observed derivative (roll rate) exceeds the critical derivative (roll rate)
- The calculations of upcrossings and critical roll rate can be considered separately as non-rare and rare problems, respectively.

3. NUMERICAL EXTENSION OF THE BASIC THEORY OF RARE RANDOM TRANSITIONS

3.1 Toward a Time-Domain Solution

The dynamical system with piecewise linear restoring (2) yields a closed-form solution for the probability of random rare transition (21), which is the simplest mathematical model of a ship capsizing in waves. Is it possible to apply the split-time method if a dynamical system is represented by a time-domain hydrodynamic simulation code?

The non-rare problem can be readily solved in the time domain, as long as the code can provide a sufficient statistical sample. If the intermediate threshold is set appropriately, one can count the upcrossings and estimate the upcrossing rate and an average number of events per unit of time.

The rare problem can also be recast in the time domain. If one assumes that roll stiffness of the dynamical system does not change in time and can be represented by the calm water GZ curve, then the critical roll rate can be found by an iterative set of numerical simulations. The calculations start at the intermediate level and the initial roll rate is perturbed for each run until capsizing is observed. The iteration scheme will create a picture similar to the one in Figure 2.

The distribution of the roll rate at upcrossing can be estimated statistically. Because capsizing is a rare event, the observed roll rates are expected to be smaller than the critical roll rate. The solution of the rare problem in the numerical case therefore involves statistical extrapolation, so only the tail of the distribution needs to be modeled. Generalized Pareto Distribution can be used for this purpose.

3.2 Numerical Non-Rare Problem

The non-rare problem will be solved using a set of time-domain simulations in "random" realizations of stationary irregular waves, which will typically be derived by discretizing an ocean wave spectrum into a set of component wave frequencies with pseudo-random phases. For the upcrossing rate to be estimated correctly, this model of wave excitation should be statistically representative for the duration of each record. To ensure this, the frequency set must be selected so as to

avoid a possible self-repeating effect (Belenky, 2011). Since long records require a very large number of incident wave frequencies to avoid this effect, it is generally more efficient to use a number of relatively short records – about 30 minutes each – than a smaller number of long records.

Following the approach developed for the model with piecewise linear stiffness, the level of the intermediate threshold is set to the maximum of the roll restoring (GZ) curve, where the slope of the curve becomes small enough that the corresponding instantaneous frequency does not support resonance under realistic wave excitation. Wave excitation will then add little energy to the dynamical system after this threshold is exceeded, which justifies the solution of the rare problem for the critical roll rate value without excitation, *i.e.* in clam water.

Once the non-rare simulations are completed, the upcrossing rate is estimated as:

$$\hat{\xi} = \frac{N_U}{N_T \Delta t} \tag{23}$$

N_U is the observed number of upcrossings, N_T is total number of data points in all records, and Δt is the time increment (data sampling rate), which is assumed to be the same for all records.

This estimate is a random number and requires an evaluation of statistical uncertainty. Assuming independence of upcrossings (for the purposes of statistical uncertainty assessment only), the occurrence of an upcrossing at a particular time step can be seen as a Bernoulli trial. The number of observed upcrossings then has a binomial distribution:

$$pmf\left(N_U\right) = \binom{N_T}{N_U} p^{N_U} (1-p)^{N_T - N_U} \tag{24}$$

p is a parameter of binomial distribution that has the meaning of the probability of a "success" (*i.e.* upcrossing) at a particular time increment. It can be estimated as:

$$\hat{p} = \frac{N_U}{N_T} \tag{25}$$

The boundary of the confidence interval corresponding to a confidence probability P_β can be computed as:

$$\hat{\xi}(low, up) = \frac{Q_{Bin}\left(0.5(1 \mp P_\beta) \mid \hat{p}\right)}{N_T \Delta t} \tag{26}$$

Q_{Bin} is the quantile of the binomial distribution. Its calculation, however, may encounter numerical difficulties as the total number of points N_T may be large. If this is the case, a normal approximation of the binomial distribution can be used with the following variance estimate:

$$\hat{Var}\left(\hat{\xi}\right) = \frac{\hat{\xi} \cdot \left(1 - \hat{\xi}\right)}{N_T \Delta t} \tag{27}$$

The boundaries of the confidence interval are then expressed as:

$$\hat{\xi}(low, up) = \hat{\xi} \pm K_\beta \sqrt{\hat{Var}\left(\hat{\xi}\right)} \tag{28}$$

K_β is $0.5(1+ P_\beta)$ quantile of a standard normal distribution. Further details may be found in Belenky *et al.* (2008) and Campbell and Belenky (2010).

3.3 Numerical Rare Problem

As described above, the numerical solution of the rare problem starts with an iterative set of simulations with different initial conditions to compute the critical roll rate at upcrossing that leads to capsizing. These simulations must include an accurate calculation of the restoring at large roll angles.

The numerical solution of the rare problem was implemented using the Large Amplitude Motion Program (LAMP). LAMP is a mature hybrid time-domain code (Lin and Yu, 1990) incorporating a number of hydrodynamic modeling options of different fidelity.

Figure 4 shows a sample rare solution using a simplest option based on hydrostatics only solution (LAMP-0) with the following features:

- 3-D hydrostatics up to the instantaneous waterline
- Does *not* solve the wave-body disturbance problem
- "Tunable" terms for viscous damping and wave interaction effects (*e.g.* added mass)
- CPU time per 2.5-minute simulation: ~3 seconds.

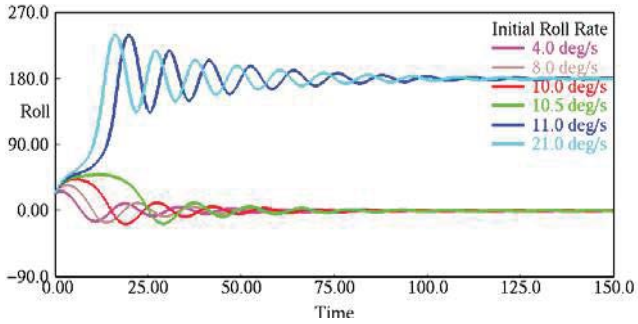

Figure 4: Calculation of critical roll rate via iterative numerical simulation (LAMP-0)

Figure 5 shows the next level of complexity: the approximate body-nonlinear solution (LAMP-2). LAMP-2 is characterized by the following features:

- 3-D hydrostatics up to the instantaneous waterline
- Solves the wave-body disturbance potential over the mean wetted hull surface
- "Tunable" damping terms for viscous effects
- CPU time per 2.5-minute simulation: ~2 minutes (Direct) or ~8 seconds (pre-computed impulse response functions for disturbance potential).

Figure 6 shows the complete body-nonlinear solution (LAMP-4), which is characterized by the following features:

- 3-D hydrostatics up to the instantaneous waterline
- Solves the wave-body disturbance potential over the instantaneous wetted hull surface
- "Tunable" damping terms for viscous effects
- CPU time per 2.5 minute simulation: ~3 hours.

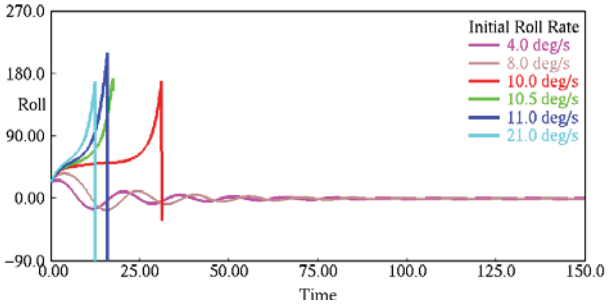

Figure 5: Calculation of critical roll rate via iterative numerical simulation (LAMP-2)

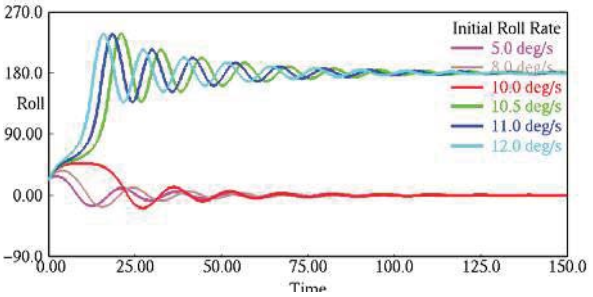

Figure 6: Calculation of critical roll rate via iterative numerical simulation (LAMP-4)

The next step in solving the rare problem is estimating the probability of capsizing after upcrossing. It is associated with exceedance of the critical value by the roll rate at the instant of upcrossing. Its distribution is not known, however, and must be modeled based on the time-domain results. If a good model were available for the joint distribution of roll and roll rate, formula (19) could be used to derive the distribution of the roll rate at the instant of upcrossing; however, no such model is available. Instead, one can attempt to directly model this distribution using the upcrossing data. As the critical roll rate is relatively large, only the tail of the distribution needs to be modeled. Since direct observation of capsizing is not expected, modeling the tail of the

distribution is, in fact, a statistical extrapolation problem.

The mathematical background of statistical extrapolation is based on two extreme value theorems (Coles, 2001):

- Fisher-Tippet-Gnedenko theorem states that the largest value of independent identically distributed (IID) random variables asymptotically tends to the Generalized Extreme Value (GEV) distribution
- Pickands-Balkema-de Haan theorem states that the tail of IID random variables can be approximated with the Generalized Pareto Distribution (GPD).

The *pdf* of the GPD is expressed as:

$$pdf(\dot{\phi}_1) = \begin{cases} \frac{1}{\sigma}\left(1+k\frac{\dot{\phi}_1-\mu}{\sigma}\right)^{-\left(1+\frac{1}{k}\right)}; \\ if \quad \mu < \dot{\phi}_1, \quad k>0, \quad or \\ \qquad \mu < \dot{\phi}_1 < \mu - \frac{\sigma}{k}, \quad k<0 \\ \frac{1}{\sigma}\exp\left(-\frac{\dot{\phi}_1-\mu}{\sigma}\right); \\ if \quad \mu < \dot{\phi}_1, \; k=0 \end{cases} \tag{29}$$

k is the shape parameter, σ is the scale parameter, and μ is the threshold above which GPD is applicable.

These three parameters must be estimated in order to approximate the tail. Belenky *et al.* (2014) describes the technique for fitting the GPD for the more complex case that accounts for stability variation, which will be reviewed later in this paper. One can see that the constant stiffness is the particular case where the critical roll rate remains the same for each upcrossing. There seems to be no reason to believe that the fitting technique will not work for this particular case, as it worked for more general case.

The fitting procedure consists of the following steps (see Belenky *et al.* (2014) for details):

- Set a series of thresholds μ for the observed roll rates at upcrossing – this threshold is the value of the roll rate at which the GPD becomes valid (*i.e.* the start of the tail) and is not to be confused with the intermediate threshold for roll angle
- Use the log-likelihood method (Grimshaw, 1991) to find the estimate of shape and scale parameter for each threshold μ
- Using the Delta method, find variances and covariances of the shape and scale parameter for each threshold μ (Boos and Stefanski, 2013)
- Find the minimum threshold μ providing applicability of GPD, using techniques described in Coles (2001) and based on Reiss and Thomas (2007).

The probability of capsizing if the threshold μ is exceeded is then expressed as:

$$\hat{P}_1 = \begin{cases} \left(1+\hat{k}\cdot\hat{\sigma}^{-1}\cdot\left(\dot{\phi}_{cr}-\mu\right)\right)^{-\hat{k}^{-1}} \\ \qquad if \;\; \hat{k} > -\frac{\hat{\sigma}}{\dot{\phi}_{cr}-\mu} \\ 0 \quad otherwise \end{cases} \tag{30}$$

The probability (30) is computed using estimates, which are random numbers, so the result of (30) is also an estimate and a random number. It can also be considered as the most probable value, because the scale and shape parameters were estimated with the log likelihood method, *i.e.* they are the most probable values for the parameters.

The next step is evaluating the confidence interval for the probability estimate (30). This is done by considering it as a deterministic function of random arguments. Assuming a normal distribution for the estimates of shape parameter and the logarithm of scale parameter (scale parameter is always positive), the

following formula was derived for the distribution of the estimate of probability of capsizing after upcrossing:

$$pdf_{P1}(P_1) = \int_{-\infty}^{\infty} f_N\left(k, \frac{k\left(\dot{\phi}_{cr}-\mu\right)}{P_1^{-k}-1}\right)\cdot\frac{k^2 P_1^{-k-1}}{\left(P_1^{-k}-1\right)^2}\left(\dot{\phi}_{cr}-\mu\right)dk \quad (31)$$

where $f_N(k,\ln(\sigma))$ is a normal joint distribution of the shape parameter and the logarithm of the scale parameter. The boundaries of the confidence interval are computed with the quantiles of the distribution (31). The most probable value of P_1 may be zero; however, this does not necessarily mean that the upper boundary of the confidence interval is zero.

The GPD distribution approximates a tail of the distribution when it exceeds the threshold μ. Equation (31) therefore estimates a conditional probability under the condition that the threshold was exceeded, so the solution of the rare problem is expressed as:

$$\hat{P}\left(\dot{\phi}_1 > \dot{\phi}_{Cr}\right) = \frac{N_\mu}{N_U}\hat{P}_1 \quad (32)$$

N_μ is the number of upcrossings when the roll rate has exceeded the threshold μ. The complete estimate of the capsizing rate is:

$$\hat{\xi}_C = \frac{N_U}{N_T\Delta t}\cdot\frac{N_\mu}{N_U}\hat{P}_1 = \frac{N_\mu}{N_T\Delta t}\cdot\hat{P}_1 \quad (33)$$

The number of upcrossings of the intermediate threshold has disappeared from equation (33). Thus, the choice of the intermediate threshold μ can only affect the independence of the upcrossings as a condition of the GPD's applicability.

The fraction in equation (33) is the estimate of the rate of events: upcrossings of the intermediate level when the roll rate has exceeded μ. The confidence interval of this estimate can be computed using formula (26), but N_U must be substituted N_μ:

$$\hat{\xi}_\mu(low, up) = \frac{Q_{Bin}\left(0.5(1\mp P_{\beta1}) \mid \hat{p}_\mu\right)}{N_T\Delta t}$$
$$\hat{p}_\mu = \frac{N_\mu}{N_T} \quad (34)$$

$P_{\beta1}$ is the "new" confidence probability; it reflects the fact that the estimate of capsizing rate is a product of two random numbers, each of which has its own confidence interval. As these numbers are independent,

$$P_{\beta1} = \sqrt{P_\beta} \quad (35)$$

The confidence interval of the estimate P_1 must therefore use $P_{\beta1}$ as a confidence probability:

$$\hat{P}_1(low, up) = Q_{P1}\left(0.5(1\mp P_{\beta1})\right) \quad (36)$$

Q_{P1} is the quantile of the distribution (29). Finally, the boundaries of the confidence interval for the capsizing rate estimate (33) are:

$$low(\hat{\xi}_C) = low(\hat{\xi}_\mu)\cdot low\left(\hat{P}_1\right)$$
$$high(\hat{\xi}_C) = high(\hat{\xi}_\mu)\cdot high\left(\hat{P}_1\right) \quad (37)$$

3.4 Summary for the Numerical Extension of the Basic Theory

The numerical extension of the basic probabilistic theory of capsizing was published in Belenky *et al*. (2008), where most of the numerical problem's specifics were formulated. However, the problem of modeling the distribution of the roll rate remained without practical solution until the applicability of the GPD was fully appreciated (Belenky *et al*., 2014).

The extension demonstrated that the split-time method is applicable for a dynamical system presented by an advanced hydrodynamic simulation code instead of an ordinary differential equation (ODE). The simplest numerical extension involves:

- Assuming that the roll stiffness of the dynamical system can be modeled by the GZ curve in calm water
- Finding the critical roll rate by a series of iterative simulations starting from an intermediate threshold with different rates; the critical roll rate is defined as the largest roll rate not leading to capsizing
- Modeling the tail of the distribution of roll rate at upcrossing with GPD
- Evaluating the statistical uncertainty for the estimates of upcrossing rate and probability of capsizing after upcrossing.

The transition to the numerical solution involves working with time-domain data and requires statistical methods to handle the results of numerical simulation, including the modeling of distributions and the assessment of statistical uncertainty.

4. BASIC THEORY OF RARE RANDOM TRANSITIONS WITH RANDOM STIFFNESS

4.1 Piecewise Linear System

The next step is to find out if the assumption of time-invariant stiffness may be abolished and if a solution can still be obtained in the simplest case with random stiffness. Consider the dynamical system (2), but with the stiffness in Range 1 now time dependent; its intercept is random, but the slope remains the same, as shown in Figure 7.

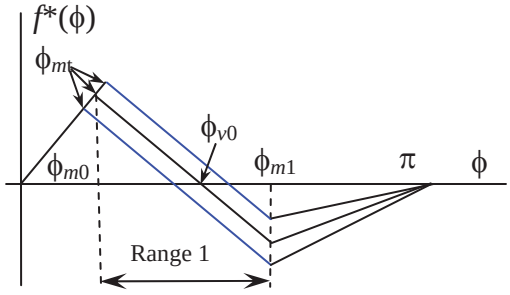

Figure 7: Time-variant piecewise linear stiffness

The variation of the stiffness in waves can be caused by the wave pass effect and ship motions. Both phenomena have certain inertia, so the parameters of time-varying stability are described by stochastic processes rather than random variables. Belenky *et al.* (2011) describes a simple mathematical model where the intercept in Range 1 is a linear function of heave:

$$\ddot{\phi} + 2\delta_\phi \dot{\phi} + \omega_\phi^2 f^*(\phi, \zeta_G) = f_{E\phi}(t) \qquad (38)$$

ζ_G is the heave displacement modeled with a linear ODE. The boundary ϕ_m between Ranges 0 and 1 in equation (38) now depends on time. However, within Range 0 equation (38) is identical to equation (2). The difference caused by the stiffness variation in Range 1 makes equation (38) appear as follows:

$$\begin{aligned} &\ddot{\phi} + 2\delta\dot{\phi} + \omega_\phi^2 k_{f1}\phi \\ &\quad = \omega_\phi^2 k_b \zeta_G(t) + \omega_\phi^2 k_{f1}\phi_{v0} + f_{E\phi}(t) \end{aligned} \qquad (39)$$

- Coefficient k_b reflects the dependence of the intercept on the heave displacement ζ_G. The term containing ζ_G is the only difference between (39) and (2).

Taking into account that the slope coefficient k_{f1} has been taken with the opposite sign, equation (39) describes a repeller and its general solution is:

$$\begin{aligned} \phi(t) = &A\exp(\lambda_1 t) + B\exp(\lambda_2 t) \\ &+ p_1(t) + \phi_{v0} \end{aligned} \qquad (40)$$

The difference between solutions (40) and (4) in Range 1 is the particular solution that now includes the influence of the random variation of stiffness.

4.2 Condition of Transition

The homogenous part of equation (39) does differ from the homogenous part of equation (2) in Range 1, but the condition of transition at the instant of upcrossing t_1 is still the same:

$$A(t_1) > 0 \quad \Rightarrow \quad \dot{\phi}(t_1) > \dot{\phi}_{cr}(t_1) \qquad (41)$$

The critical roll rate is still defined by the same formula (9), but the particular solution can no longer be neglected. As a result, the critical roll rate becomes a function of time, *i.e.* it is a stochastic process:

$$\dot{\phi}_{cr}(t) = \lambda_2\left(\phi_m(t) - p_1(t) - \phi_{v0}\right) + \dot{p}_1(t) \qquad (42)$$

4.3 Non-Rare Problem

The boundary between Ranges 0 and 1 is now time-dependent, so it makes sense to formulate the non-rare problem for a difference between the boundary and the roll motion, introducing a new stochastic process:

$$x(t) = \phi(t) - \phi_m(t) + \phi_{m0} \qquad (43)$$

Upcrossing of the process $x(t)$ through the threshold ϕ_{m0} makes the switch from Range 0 to Range 1.

The time-dependent boundary $\phi_m(t)$ is a linear function of the heave motion, which is also linear. A Fourier series presentation for $x(t)$ is available from Belenky *et al.* (2011), which allows the upcrossing rate to be expressed using formula (11):

$$\xi_U\left(\phi_{m0}\right) = \frac{1}{2\pi}\sqrt{\frac{V_{\dot{x}}}{V_x}}\exp\left(-\frac{\phi_{m0}^2}{2V_x}\right) \qquad (44)$$

V_x and $V_{\dot{x}}$ are variances of the process $x(t)$ and its derivative.

4.4 Rare Problem

To formulate the rare problem, consider a difference between the critical roll rate and the instantaneous roll rate $y(t)$:

$$y(t) = \dot{\phi}_{cr}(t) - \dot{\phi}(t) \qquad (45)$$

The process $y(t)$ is a linear combination of normal processes and can be presented with a Fourier series (Belenky *et al.*, 2011). The capsizing event is associated with a negative value of y at the instant of upcrossing. One therefore needs to find the distribution of the process $y(t)$ at the instant when the dependent process x(t) has an upcrossing. The problem is similar to the one considered in Section 2.4, but instead of a derivative, a dependent process is considered.

To derive the distribution of the process $y(t)$ at the instant of upcrossing, consider a random event W:

$$W = \left(y(t) \le y_C\right) \qquad (46)$$

The events of U (defined by equation (13), but re-formulated for the process $x(t)$) and W occur simultaneously:

$$U \cap W = \begin{cases} x(t) < \phi_{m0} \\ x(t) > \phi_{m0} - \dot{x}(t)dt \\ \dot{x}(t) > 0 \\ y(t) \le y_C \end{cases} \qquad (47)$$

The probability that U and W occur simultaneously at time t is:

$$\begin{aligned} P(U \cap W) &= \int_{-\infty}^{y_C}\int_{0}^{\infty}\int_{a-\dot{x}dt}^{\phi_{m0}} pdf(x,\dot{x},y)dxd\dot{x}dy \\ &= dt\int_{-\infty}^{\phi_{m0}}\int_{0}^{\infty}\dot{x}\cdot pdf\left(x=\phi_{m0},\dot{x},y\right)d\dot{x}dy \end{aligned} \qquad (48)$$

By definition, the *CDF* is:

$$\begin{aligned} CDF\left(y_C \mid \phi_{m0}\right) &= \frac{P(W \cap U)}{P(U)} \\ &= \frac{\int_{-\infty}^{\phi_{m0}}\int_{0}^{\infty}\dot{x}\cdot pdf\left(x=\phi_{m0},\dot{x},y\right)d\dot{x}dy}{\int_{0}^{\infty}\dot{x}\cdot pdf\left(x=\phi_{m0},\dot{x}\right)d\dot{x}} \end{aligned} \qquad (49)$$

Differentiation of (49) yields a *pdf* of the value of the dependent process at the instant of upcrossing:

$$pdf(y_C) = \frac{\int_0^\infty \dot{x} \cdot pdf\left(x = \phi_{m0}, \dot{x}, y_C\right) d\dot{x}}{\int_0^\infty \dot{x} \cdot pdf\left(x = \phi_{m0}, \dot{x}\right) d\dot{x}} \qquad (50)$$

For the considered case of a dynamical system with piecewise linear term, all of the processes are normal and their mutual dependence is completely described by the appropriate covariance moments. This information is available as all of these processes are presented by Fourier series. The integrals in equation (50) can be evaluated symbolically:

$$pdf(y_C) = \frac{\sigma_{\dot{x}|xy}}{\sqrt{2\pi}} \exp\left(-\frac{\left(m_{\dot{x}|xy}(y_C)\right)^2}{2\sigma^2_{\dot{x}|xy}}\right) + \frac{m_{\dot{x}|xy}(y_C)}{2}\left(1 - \mathrm{erf}\left(-\frac{m_{\dot{x}|xy}(y_C)}{\sqrt{2}\sigma_{\dot{x}|xy}}\right)\right) \qquad (51)$$

- $m_{\dot{x}|xy}$ and $\sigma_{\dot{x}|xy}$ are the conditional mean and the conditional standard deviation of the derivative of the process $x(t)$ if the processes $x(t)$ and $y(t)$ took particular values. Note that the conditional mean is a function of the value of the process y at upcrossing, while the standard deviation is a constant; erf is the standard error function (see Belenky *et al.* (2013) for details).

The probability of capsizing after an upcrossing event is expressed as:

$$P(y_C < 0) = \int_{-\infty}^{0} pdf(y_C) dy_C \qquad (52)$$

Equation (52) completes the solution of the rare problem.

4.5 Probability of Rare Transitions

The final result of the rate of transitions (capsizes) can only be resolved using quadratures:

$$\xi_C = \frac{1}{2\pi}\frac{\sigma_{\dot{x}}}{\sigma_x}\exp\left(-\frac{\phi^2_{m0}}{2\sigma^2_x}\right)\int_{-\infty}^{0} f_C(y_C) dy_C \qquad (53)$$

- σ_x and $\sigma_{\dot{x}}$ are the standard deviation of process x and its derivative.

Most of the basic theory of rare transitions with random stiffness was published in Belenky *et al.* (2010, 2011). The assumption of the independence of the process x and its derivative, which appeared in those publications, was abolished in order to obtain a more general solution (Belenky *et al.*, 2013, 2013a). The latter works also contain a closed-form solution to (51), which was not available in the earlier publications.

The main outcome of the basic study of rare transitions in dynamical system with random stiffness is that the critical roll rate becomes time variant and random as well. As part of this study, the distribution of the value of dependent process at the instant of upcrossing was derived.

5. NUMERICAL EXTENSION OF BASIC THEORY OF RARE RANDOM TRANSITIONS WITH RANDOM STIFFNESS

5.1 Towards a Time-Domain Solution

A comparison of a basic theory of random transition (Section 2) with its numerical extension (Section 3) shows a commonality in their approaches but some significant differences in technique. The understanding that numerical techniques may be quite different from the solution for the simpler piecewise linear system came from a number of

studies, where "theoretical" methods were attempted in a more direct way.

The calculation of instantaneous GZ curve in waves was described in Belenky and Weems (2008). Belenky *et al.* (2010) describe a method of tracking the maximum of the GZ curve in waves. However, an attempt to use the theoretical formula for upcrossing rate, as proposed in Belenky *et al.* (2008), showed a significant discrepancy from statistical estimates for stern quartering seas. This discrepancy was not observed in beam seas.

The reason for this discrepancy is the dependence between roll angles and roll rate in stern quartering seas (Belenky and Weems, 2012; Belenky *et al.*, 2013). The roll angles and rates are not correlated (see, for example, Bendat and Piersol, 1986). However, the absence of correlation means independence only for a normal process. Since large-amplitude roll motions may be not normal, independence cannot be assumed based on an absence of correlation. In this case, dependence can be characterized through the joint moments of higher order, say the fourth joint moment (covariance is the second joint moment). It is possible that the dependence is somehow related with stability variation in stern quartering seas, as it was not observed in beam seas.

The probabilistic properties of the elements of GZ curve in waves was found to be quite complex (Belenky and Weems, 2008). As a result, the modeling of a threshold distribution is difficult. Difficulty is further increased by the necessity to include all dependencies in order to get the joint distribution required in formula (50). Even if such a distribution fit is proposed, it may be reasonable only near the mean value, while the distribution needs to be evaluated on the tail. It was concluded that this approach did not offer a practical solution.

The difficulties fundamentally originated from the necessity to model tails of multi-dimensional distributions. These distributions are needed for characterizing the values at the instant of upcrossing. Why not get this information directly from the simulated data?

This simple question has led to understanding that numerical methods may be quite specific and should be based on direct data analysis, *i.e.* statistics. This motivated a revision of the original work on the evaluation of probability of capsizing in beam seas. The description in Section 3 reflects the authors' current understanding of how the problem should be handled, which has evolved significantly since its first publication in Belenky *et al.* (2008).

5.2 Numerical Non-Rare Problem

The formulation of the non-rare problem for the case of time-dependent stiffness is almost identical to the case of constant stiffness. However, the requirement of the independence of upcrossings can be removed. Dependent crossing events will be addressed as a part of rare problem as will be described in the next subsection. As a result, the choice of the intermediate threshold becomes a matter of computational efficiency only.

5.3 Numerical Rare Problem

The solution for a dynamical system with random piecewise stiffness has shown that the critical roll rate depends on time. To account for the stability changes in wave in the numerical case, the critical roll rate is calculated at each upcrossing, and the effect of the wave is included in the rare simulations. The calculations start from the instant of upcrossing; and roll rate is perturbed until capsizing is reached; see Figure 8.

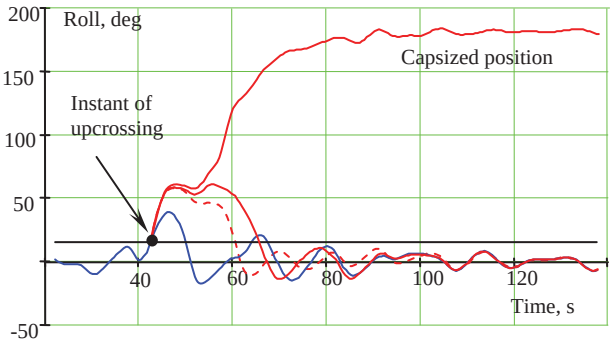

Figure 8: Calculation of critical roll rate

A detailed discussion of this algorithm, further referred as the Motion Perturbation Method (MPM), can be found in Spyrou *et al.* (2014). A particularly important point is how MPM is related to the definition of motion stability and the classic definition of ship stability given by Euler (1749). The result of the MPM calculation is a value of the metric of likelihood of capsizing (Belenky *et al.*, 2014):

$$y_i = 1 - \dot{\phi}_{Ui} + \dot{\phi}_{Cri}\ ; \quad i = 1,\ldots, N_U \qquad (54)$$

- $\dot{\phi}_{Crj}$ is the critical roll rate calculated for the i^{th} upcrossing, and $\dot{\phi}_{Ui}$ is the roll rate observed at the i^{th} upcrossing.

The next step should be the GPD extrapolation of the metric y to find the probability of exceeding 1, which is the value associated with capsizing per equation (54). However, GPD requires independent data and the independence of upcrossings is no longer required when choosing the intermediate threshold. To resolve this, the dependence or independence of successive upcrossings must be determined.

If capsizing does not occur, the perturbed time history returns to the unperturbed state after some time ("time of convergence"); see Figures 9. If the next upcrossing occurs within this time of convergence, it is considered to be dependent. If the effect of perturbation has no further influence, the next upcrossing is considered to be independent; see Figure 9. The critical roll rate is calculated for all upcrossings, but only the largest value in each set of dependent upcrossings is retained for further processing; see Spyrou *et al.* (2014) for further details.

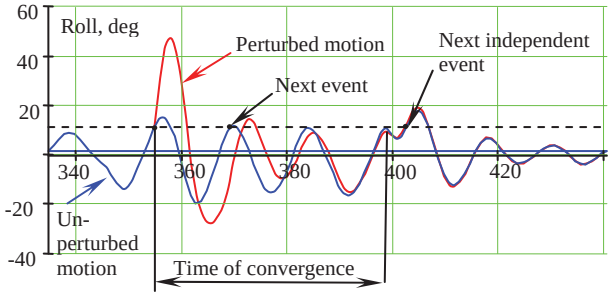

Figure 9: Dependent and independent upcrossings

The procedure for GPD extrapolation is similar to the constant stiffness case that was reviewed in Section 3.3. The only difference is that metric y is extrapolated and the target value associated with capsizing equals 1.

5.4 Initial Validation

As with any analytical method, validation is required if the method is to be put to practical use. But what would constitute validation of the split-time method of probability of capsizing? The split-time method is essentially the method of extrapolation; it is intended to evaluate the probability of capsizing based on a limited simulation data set. Thus, the validation of extrapolation is the more general question.

A statistical extrapolation method can be considered valid if its prediction is identical to value directly estimated from a sample. To do this, the sample must be large enough to support the estimation of the predicted event. To estimate the probability of capsizing, a sample must contain a number of capsizes so that the rate of capsizing can be estimated by direct counting. The extrapolation can then be applied to one or more small sub-samples of the data, each of which may or may not contain any capsizing events. If the estimates from the extrapolations and direct counting match, then the extrapolation method is valid.

While this idea seems straightforward, many issues need to be resolved to create a procedure of extrapolation. The development of this procedure is described by Smith and Campbell (2013), Smith (2014), and Smith *et al.* (2014) and summarized in Smith and Zuzick (2015). A key idea of the procedure is that the validation must be repeated systematically for the same condition in order to verify the confidence interval as well as for different speed, heading and wave environment in order to verify the robustness of the method.

Another question is how to get a sample that is large enough to capture such a rare event while retaining the essential nonlinear physics? For realistic wave conditions, millions of hours of simulation may be required to see capsizing. A particular problem is how to model stability variations in waves that play the central role in capsizing caused by pure loss of stability. ODE solvers may be fast enough to provided required simulation time, but ODE models may be quite questionable in terms of reproducing the stability variation.

For the present study, simulations were made with a 3 degree-of-freedom (heave, roll, pitch) time-domain simulation code which incorporates a novel volume-based calculation of the body-nonlinear Froude-Krylov and hydrostatic pressure forces. The algorithm is almost as fast as an ODE solver, but it captures the key features of the nonlinear wave forcing and restoring, allowing large, realistic irregular sea motion data sets to be generated. Description of the algorithm, implementation and verification is available from Weems and Wundrow (2013) and Weems and Belenky (2015).

The code was used to generate 1,000,000 hours of motion data for the ONR Topsides Tumblehome hull in random realizations of large, irregular stern quartering seas. 157 capsizes were observed, which allows a “true” value to be estimated. The split-time method was applied to 50 different sub-sets of the data, each of which consisted of 100 hours of data. The observed and extrapolated capsizing rates, with confidence intervals, are plotted in Figure 10. The percentage of successful extrapolations is 96%, which is very close to 95% of confidence probability. Details of the validation can be found in Belenky *et al.* (2014).

5.5 Summary on the Numerical Extension of the Basic Theory for Random Stiffness

Numerical extension of the basic theory of random transition in a dynamical system with random stiffness was initially published in Belenky *et al.* (2013), with an exponential distribution as a model for the tail of the metric. Subsequent publications (Belenky *et al.*, 2014; Spyrou *et al.*, 2014) include the switch to GPD, which has led to a successful initial validation.

The development of this numerical extension can be summarized as follows:

- It is possible to estimate the probability of capsizing numerically without any assumption on roll stiffness
- The problem can be solved by GPD extrapolation of the metric of likelihood of capsizing (equation 54)
- The metric fully accounts for the nonlinearity of dynamical system; it contains a critical roll rate computed by perturbations
- The metric can be seen as an implementation of both the classical definition of ship stability and the general definition of motion stability
- Roll rate and angles may be dependent in stern quartering seas, while remaining uncorrelated.

The method has been successfully tested using a large volume of ship motion generated with a volume-based 3-DOF simulation code. This test provides a very promising but limited validation of the method, as the results of the 3-DOF simulation should be considered to be a

qualitatively rather than a quantitatively correct representation of ship capsizing. The numerical extension cannot be considered complete until it has been fully implemented and validated with a more complete time-domain simulation code such as LAMP.

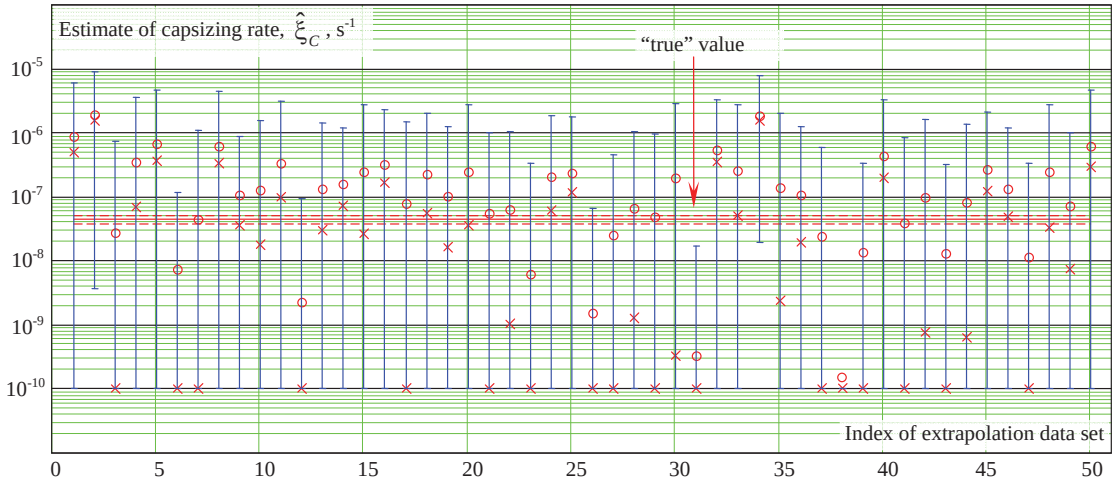

Figure 10: Results of initial validation performed for 50 validation data sets for ONR tumblehome

6. CONCLUSIONS AND FUTURE WORK

This paper has reviewed work under the ONR project "A Probabilistic Procedure for Evaluating the Dynamic Stability and Capsizing of Naval Vessels". The review was limited to the results related to pure loss of stability, without consideration of effects from wind, surge, sway, or yaw. The main focus of the study was on the effect of random stability variations in waves. The research was reviewed in four following steps:

- Basic theory of rare random transitions
- Numerical extension of the basic theory of rare random transition
- Basic theory of rare random transition in a dynamical system with random stiffness
- Numerical extension of the theory of rare random transition in a dynamical system with random stiffness.

The result of the study is a procedure of physics-based statistical extrapolation using a limited data set from nonlinear time-domain numerical simulation. The procedure consists of the following steps:

- Prepare an extrapolation data set of simulation data; typically about 100 hours of total duration and consisting of a number of records approximately 30 minutes each
- Set an intermediate threshold providing a reasonable number (thousands) of upcrossings to be observed
- For each upcrossing, use perturbation simulations to find the critical roll rate leading to capsize, and then use the difference between the observed and critical roll rate to calculate the value of the metric of the likelihood of capsizing; then remove dependent data from the dataset
- Fit GPD with the metric data; evaluate the estimate of the capsizing rate and its confidence interval.

So far, this procedure has had a very limited validation for one condition and has not been fully implemented with LAMP or other advanced hydrodynamic code. The following are the next steps in the development of the method:

- Bring the validation to reasonable completion by considering more conditions
- Address implementation issues related with the consideration of 6 DOF in the solution of the non-rare and rare problems
- Consider the inclusion of hydrodynamic diffraction and radiation forces in the solution of the rare problem.

7. ACKNOWLEDGEMENTS

The work described in this paper has been funded by the Office of Naval Research, under Dr. Patrick Purtell, Dr. Ki-Han Kim, and Dr. Thomas Fu. The authors greatly appreciate their support.

Over the years of the development, many colleagues have influenced and contributed to our work. The authors would like acknowledge Prof. Pol Spanos (Rice University), Dr. Art Reed, Mr. Tim Smith, Mr. Brad Campbell (NSWCCD, David Taylor Model Basin), Prof. Kostas Spyrou (National Technical University of Athens), and Profs. Ross Leadbetter and Vladas Pipiras (University of North Carolina Chapel Hill).

The participation of Prof. Pipiras was facilitated by the Summer Faculty Program supported by ONR and managed by Dr. Jack Price (NSWCCD, David Taylor Model Basin).

8. REFERENCES

Belenky, V. L. 1993, "A Capsizing Probability Computation Method", J. Ship Research, Vol. 37, pp. 200- 207.

Belenky, V. and Weems K. M. 2008, "Probabilistic Qualities of Stability Change in Waves", Proc. 10th Intl. Ship Stability Workshop, Daejon, Korea, pp. 95-108.

Belenky, V. L., Weems, K. M., and Lin, W.-M. 2008, "Numerical Procedure for Evaluation of Capsizing Probability with Split Time Method", Proc. 27th Symp. Naval Hydrodynamics, Seoul, Korea.

Belenky, V. L., Weems, K. M., Lin, W.-M., and Spyrou, K. J. 2010, "Numerical Evaluation of Capsizing Probability in Quartering Seas with Split Time Method", Proc. 28th Symp. Naval Hydrodynamics, Pasadena, California, USA.

Belenky, V., Reed, A.M., and Weems K. M. 2011, "Probability of Capsizing in Beam Seas with Piecewise Linear Stochastic GZ Curve", Chapter 30 of "Contemporary Ideas on Ship Stability", edited by M.A.S. Neves, V. L. Belenky, J. O. de Kat, K. Spyrou, and N. Umeda, Springer, pp. 531-554.

Belenky, V. L. 2011, "On Self-Repeating Effect in Reconstruction of Irregular Waves", Chapter 33 of "*Contemporary Ideas on Ship Stability*", edited by M.A.S. Neves, V. Belenky, J. O. de Kat, K. Spyrou, and N. Umeda, Springer, pp. 589-598.

Belenky, V., and Weems, K. 2012, "Dependence of Roll and Roll Rate in Nonlinear Ship Motions in Following and Stern Quartering Seas", Proc. 11th Intl. Conf. on Stability of Ships and Ocean Vehicles (STAB 2012), Athens, Greece, pp. 59-66.

Belenky, V., Weems, K. M., and Pipiras, V. 2013, "Split-time Method for Calculation of Probability of Capsizing Due to Pure Loss of Stability", Proc. 13th Intl. Ship Stability Workshop, Brest, France, pp. 70-78.

Belenky, V., Spyrou, J., Weems, K. M., and Lin W.-M. 2013a, "Split-time Method for the Probabilistic Characterization of Stability Failures in Quartering Waves", Intl. Shipbuilding Progress, Vol. 60, No. 1-4, pp. 579-612.

Belenky, V., Weems, K., Campbell, B., and

Pipiras, V. 2014, "Extrapolation and Validation Aspects of the Split-Time Method", Proc. 30th Symp. Naval Hydrodynamics, Hobart, Tasmania, Australia.

Bendat, J. S., and Piersol, A.G., 1986, Random Data: Analysis and Measurement Procedures, 2nd edition, New York: John Wiley & Sons.

Boos, D. D. and Stefanski L. D. 2013, Essential Statistical Inference: Theory and Method, Springer.

Campbell, B. and Belenky, V. 2010, "Assessment of Short-Term Risk with Monte-Carlo Method", Proc. 11th Intl. Ship Stability Workshop, Wageningen, Netherlands, pp. 85-92.

Coles, S. 2001, An Introduction to Statistical Modeling of Extreme Values. London: Springer-Verlag.

Euler, L. 1749, Scientea Navalis, St.Petersburg, Russia.

Grimshaw, S. D. 1991, "Calculating Maximum Likelihood Estimates for the Generalized Pareto Distribution", Proc. 23rd Symp. Interface of Computing Science and Statistics, Seattle, Washington, USA, pp 616–619.

Kramer, H., and Leadbetter, M. R. 1967, Stationary and Related Stochastic Processes, New York: John Wiley.

Lin, W.-M., and Yue, D.K.P. 1990, "Numerical Solutions for Large Amplitude Ship Motions in the Time-Domain" Proc. 18th Symp. on Naval Hydrodynamics, Ann Arbor, Michigan, USA, pp. 41–66.

Paroka, D., Okura, Y., and Umeda, N. 2006, "Analytical prediction of capsizing probability of a ship in beam wind and waves", J. Ship Research, Vol. 50, No. 2, pp. 187-195.

Paroka, D. and Umeda, N. 2006, "Capsizing probability prediction of the large passenger ship in irregular beam wind and waves: comparison of analytical and numerical methods" J. Ship Research, Vol. 50, No. 4, pp. 371-377.

Reiss, R.-D., and Thomas, M. 2007, *Statistical* Analysis of Extreme Values with Application to Insurance, Finance, Hydrology and Other Fields, 3rd Edition, Basel: Birkhäuser Verlag.

Sevastianov, N. B. 1963, "On Probabilistic Approach to Setting Stability Standards". Trans. of Kaliningrad Institute of Technology, Vol. 18 (in Russian).

Sevastianov, N. B. 1994, "An Algorithm of Probabilistic Stability Assessment and Standards", Proc. 5th Intl. Conf. on Stability of Ships and Ocean Vehicles (STAB 1994), Melbourne, Florida, USA, Vol. 5.

Smith, T. C. and Campbell, B. L. 2013, "On the Validation of Statistical Extrapolation for Stability Failure Rate" in Proc. of 13th Intl. Ship Stability Workshop, Brest, France, pp. 79-87.

Smith, T. C., Campbell, B. L., Zuzick, A. V., Belknap, W. F., and Reed, A. M. 2014, "Approaches to Validation of Ship Motion Predictions Tools and Extrapolation Procedures for Large Excursions of Ship Motions in Irregular Seas" in Computational Stochastic Mechanics – Proc. of the 7th Intl. Conference *(CSM-7)*, edited by G. Deodatis and P. Spanos, Santorini, Greece.

Smith, T. C. 2014, "Example of Validation of Statistical Extrapolation," in Proceedings of the 14th Intl. Ship Stability Workshop, Kuala Lumpur, Malaysia.

Smith, T. C., and Zuzick, A. 2015, "Validation of Statistical Extrapolation Methods for Large Motion Prediction" in Proc. 12th Intl. Conf. on Stability of Ships and Ocean Vehicles (STAB 2015), Glasgow, UK.

Spyrou, K. J., Belenky, V., Reed, A., Weems, K., Themelis, N., and Kontolefas, I. 2014, "Split-Time Method for Pure Loss of Stability and Broaching-To", Proc. 30th Symp. Naval Hydrodynamics, Hobart, Tasmania, Australia.

Weems, K., and Wundrow, D., 2013, "Hybrid Models for Fast Time-Domain Simulation of Stability Failures in Irregular Waves with Volume-Based Calculations for Froude-Krylov and Hydrostatic Forces", Proc. 13th Intl. Ship Stability Workshop, Brest, France.

Weems, K. and Belenky, V. 2015, "Fast Time-Domain Simulation in Irregular Waves With Volume-Based Calculations for Froude-Krylov and Hydrostatic Force" in *Proc. 12th Intl. Conf. on Stability of Ships and Ocean Vehicles (STAB 2015),* Glasgow, UK.

Session 11.2 – NAVAL SHIP STABILITY

Beyond the Wall

Exploration of the Probabilities of Extreme Roll of Naval Vessels

Comparative Stability Analysis of a Frigate According to the Different Navy Rules in Waves

Towing Test and Motion Analysis of a Motion-Controlled Ship - Based on an Application of Skyhook Theory

This page is intentionally left blank

Beyond the Wall

Richard Dunworth, *Department of Defence, Australia* richard.dunworth@defence.gov.au

ABSTRACT

Inaccuracy in evaluation of inclining experiments by the application of the wall-sided concept was discussed by Dunworth (2014). KG can be significantly underestimated for V-bottomed hull forms when relying on GM to evaluate inclining experiments. A solution was proposed which derived KG and TCG to align heeling and righting moments without reference to the metacentre.

Looking beyond the theory, this paper describes practical model testing to explore the accuracy of the new method, reviews experiences in its use by the Australian Department of Defence and offers guidance in its application.

Keywords: *Stability; Inclining; Metacentre; Wall-sided*

NOMENCLATURE

Δ	Displacement of the system (ship plus inclining masses) (t)
d	Distance of inclining mass shift (m)
φ	Angle of heel (degrees)
GG'	Shift of centre of gravity (m)
GM_0	Transverse metacentric height when upright (m)
GZ	Righting arm (m)
GZ'	Righting arm corrected for TCG_I (m)
HZ	Heeling arm (m)
HZ_0	Heeling arm when upright (m)
KG	Height of vertical centre of gravity above baseline (m)
KG_I	Estimated height of vertical centre of gravity above the origin, in global coordinates, with inclining masses in their initial position (m)
KG_L	Estimated height of vertical centre of gravity above baseline, in local (ship) coordinates, with inclining masses in their initial position (m)
KM_0	Height of transverse metacentre above baseline (m)
KN	Righting arm about the origin (m)
KN_0	Righting arm about the origin when upright (m)
TCB_0	Transverse centre of buoyancy when upright (m)
TCG	Transverse centre of gravity (m)
TCG_0	Estimated transverse centre of gravity when in upright equilibrium (m)
TCG_I	Estimated transverse centre of gravity of the system with inclining masses in their initial position (m)
w	Inclining mass (t)

1. INTRODUCTION

The concept of an inclining experiment was first proposed by Hoste (1697), a professor of mathematics at the Royal Naval College in Toulon, France. However it was nearly fifty years before a practical method of conducting an inclining experiment was described by Bouguer (1746).

The traditional calculation associated with an inclining experiment led directly to a value of GM_0 and, as this was the primary measure of

stability, it was not necessary to know *KG* itself until the development of the concept of *GZ*. By that time, Bouguer's calculation method was well established and continues to be used to this day.

Growth in displacement and *KG* is common on naval ships. Communication, navigation and armament equipment increase with time and tend to be placed high up. Conversely, when heavy machinery low down in the ship is upgraded, it is often replaced with more efficient, lighter equipment. Without compensation, these effects almost guarantee that *KG* will rise over time. Growth must be captured and updated regularly in the stability information provided to ships.

For RAN ships, stability is managed by comparison of a load condition's *KG* with a curve of limiting *KG*. If *KG* has been over-estimated, then unnecessary operational restrictions may result but, if *KG* has been under-estimated, then the vessel may be at risk if it encounters the environment and/or damage which underlie the curve of limiting *KG*.

The lightship characteristics of RAN ships are regularly checked by inclining experiments with the interval determined by the expected time before any standard load condition will exceed the limiting *KG*, due to growth. Over the whole fleet, there is about one ship checked every three or four months.

Although there is ample guidance available on the conduct of an inclining, Administrations rarely, if ever, prescribe the method of deriving *KG* from the recorded data.

2. THE CLASSIC METHOD

2.1 Relying on the Metacentre

It has previously been assumed that the metacentre does not move significantly at small angles of heel. On this premise, the wall-sided concept has been used to derive GM from inclining experiment results using the relationship:

$$GM = \frac{w\ d}{\Delta\ \tan\varphi} \tag{1}$$

and *KG* is then calculated as:

$$KG = KM - GM \tag{2}$$

The derivation of GM is most commonly performed by fitting a line of best fit (trendline) through the plot of $w\ d$ against $\Delta\ \tan\varphi$. GM is then equal to the slope of that trendline.

2.2 The Moving Metacentre

Even for a wall-sided ship, the metacentre moves at small angles of heel and, for some hull forms, the movement is significant. Where a hull has a relatively shallow V-bottom over a significant proportion of its length, reliance on *GM* for determining *KG* is unsafe.

3. THE NEW METHOD

3.1 Balancing Heeling and Righting Arms

The new method recognises that, after each weight move, the vessel is in equilibrium and that there must be a righting arm, GZ, equal and opposite to the heeling arm HZ developed by the shift of inclining weights. With the vessel's trim and displacement known from draught readings, it is possible to calculate the corresponding value of KN for each weight move. *GZ* is derived from *KN* by the relationship:

$$GZ = KN - KG\ \sin\varphi - TCG\ \cos\varphi \tag{3}$$

In the absence of experimental error, there is a pair of unique values for TCG and VCG which will result in values of GZ for each heel which exactly match the corresponding HZ

values. Similarly, even when there are experimental errors present, there will be a pair of unique values for TCG and KG which will result in the trendlines through HZ and GZ against heel being coincident. When close to upright, TCG can be considered to raise or lower the trendline, while VCG skews the trendline about zero heel.

A method for deriving *TCG* and *KG* has been proposed (Dunworth, 2014) and is briefly described below.

3.2 The Solution for TCG_I

When $\varphi = 0$, $\sin\varphi = 0$ and $\cos\varphi = 1.0$, so Equation 3 reduces to:

$$HZ_0 = KN_0 - TCG_\mathrm{I} \tag{4}$$

Equation 4 can be re-arranged to give a solution for TCG_I:

$$TCG_\mathrm{I} = KN_0 - HZ_0 \tag{5}$$

KN_0 is identical to TCB_0 and could therefore be found from upright hydrostatics. However, it is more convenient to calculate KN_0 with the other *KN* values which will be required. KN_0 can be expected to be close to zero, but will only be exactly so if both hull and appendages are truly symmetric about the centreline. The actual value should generally be calculated.

HZ_0 can be found from the trendline through the *HZ* points when plotted against heel angle and is the value of *HZ* when heel = 0, i.e. the intercept of the trendline.

A third-order polynomial trendline should be used because it can closely match non-linear data sets which include a point of inflection - which generally occur near equilibrium in *GZ* plots.

When there is known to be a discontinuity in *GZ* within the range of heels at the inclining experiment, the points should be divided into two sets, either side of the discontinuity, and only the set which spans upright used to determine HZ_0. If the discontinuity is exactly at upright, both sets may be used and HZ_0 taken to be the mean of the two intersections.

3.3 The Solution for KG_I

Equation 3 can be re-arranged as:

$$KG_\mathrm{I} \sin\varphi = KN - HZ - TCG_\mathrm{I} \cos\varphi \tag{6}$$

and the solution for KG_1 is therefore:

$$KG_\mathrm{I} = \frac{KN - HZ - TCG_\mathrm{I} \cos\varphi}{\sin\varphi} \tag{7}$$

For each mass move, $KG_\mathrm{I} \sin\varphi$ (from Equation 6) is plotted against $\sin\varphi$. All points should lie on a straight line and the value of KG_I is then equal to the slope of the linear line of best fit through the points.

KG_I is a vertical measure and, to account for trim, G_I will need to be rotated about the ship's origin to give VCG in ship coordinates.

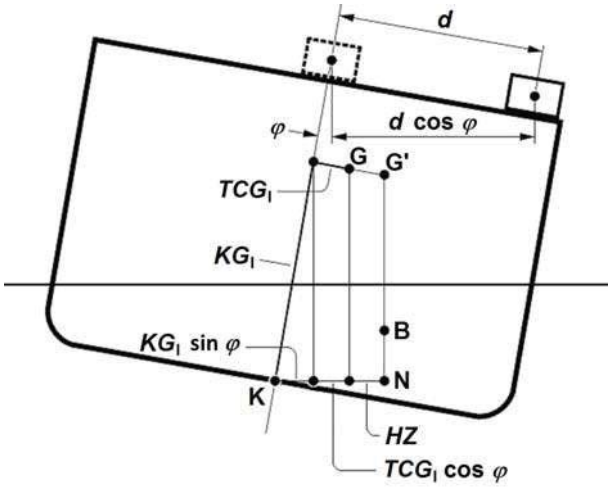

Figure 1 Illustration of Equation 6

4. VALIDATING THE NEW METHOD BY MODEL TESTING

4.1 Selection of the Hull Form

As part of the validation process for the new method, a scale model of a hull section was built and tested. The model was sized to fit into an existing trough used for teaching inclining experiments and was a practical size and weight to handle. As will be shown, there was sufficient difference between *KG*s calculated by the two methods for the result to be conclusive and not lost within variations caused by experimental error.

Being representative of a hull section only, the model is considerably wider than it is long with a beam of 1.2 m and length of only 0.3 m. Details are shown in Table 1 and Figure 2.

Table 1 Model particulars

Length	0.3	m
Beam	1.2	m
Displacement	17.560	kg
Inclining weight	3.098	kg
KM_0	1.073	m
Forward pendulum length	1086.35	mm
Aft pendulum length	1085.25	mm

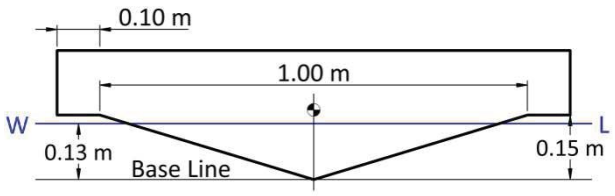

Figure 2 Model section

The model is not intended to accurately reflect any particular vessel, with the shape having been chosen specifically to demonstrate the difference in results between the classic and new methods. It is, however, geometrically similar to a section through the aft portion of the small aluminium survey boats operated by RAN.

On one occasion, one of these craft was presented for inclining with a list of just under three degrees. This would not normally be acceptable, in part because of the unreliability of tank dips at that angle, but it was decided to proceed with the experiment so that the results could be used in planning appropriate remedial measures. A heel of over two degrees each way was developed, but the vessel never came upright during the experiment. This inclining is of interest and will be referred to later at 5.5.

4.2 Model Construction

The model was of plywood construction and subsequent measurements showed it to be generally quite accurate.

Aluminium angle rails, forward and aft, were pre-drilled at 50 mm centres out to 550 mm either side of the centreline. This allowed quick and accurate movement of the inclining weight without having to measure the shift at each weight move and also provided a secure mounting for a pair of ballast weights.

Figure 3 Model Arrangement

The ballast weights were suspended on threaded rods and could be wound up and

down to vary *KG*. A disadvantage of this arrangement is that two pairs of the pre-drilled holes were occupied by the ballast and were therefore not available for inclining weight shifts. Ballast was chocked to prevent any movement.

To date, only one set of readings has been taken: at a single displacement and with ballast in its lowest position.

As ballasted, the model floated close to level trim (0.07^o) and heel (0.05^o) with the chine flat about 19 mm clear above the waterplane. The chine outer edge touched the waterplane at a heel of 1.9 degrees and the chine flat was completely immersed beyond 2.2 degrees. The significance of the small trim was not realised until the inclining results were analysed and is discussed later at 5.1.

4.3 Determining the Model Weight

An unexpected difficulty came with the determination of the model weight.

For the first measurement, a pair of scales, each with an upper limit of 5 kg, was used to weigh the bare hull and individual components. It was immediately apparent that the two scales gave different readings, but there was no way of determining which, if either, was correct.

A second measurement was taken by measuring the rise of water in the trough; from the trough dimensions and water density (0.9985 kg/l), the weight of the model could be calculated. Once the model was in the trough, the depth of water and height to gunwale were used to determine the freeboard at each corner. Both methods required measurement of water depths, but the height of the meniscus where the water surface met the measuring scale was difficult to determine. This was a concern as the effect of change of draught for the model is about 0.265 kg/mm.

A set of as-built offsets was lifted so that a new numerical model could be generated and the results re-worked.

Finally, a larger set of scales was used to weigh the entire model. Although the scales were not calibrated, this was thought likely to be the most accurate measurement and differs by less than 0.5 percent from the mean value of 17.560 kg which was taken to be the model weight for calculation purposes. Results are shown in Table 2.

Table 2 Results of the methods used to determine model weight

Method	Weight
Weigh parts	17.473 kg
Weigh whole	17.575 kg
Freeboards	17.928 kg
Draughts	17.223 kg
Displaced volume	17.698 kg
Mean weight	17.560 kg

4.4 Establishing *KG*

Six strong points were incorporated in the model to allow it to be freely suspended from a spreader bar, via solid wire strops, onto large washers; pendulums were hung from the same points – see Figures 4 and 5. On one face, all three pendulum lines intersected at a single point: on the other, they formed a very small triangle or ‘cocked hat’.

Values forward and aft of 162.0 mm and 161.5 mm respectively were found and the mean value of 161.75 mm was taken to be the model *KG*.

4.5 Inclining the Model

By sighting across the two pendulums, both during the measurement of *KG* and during the inclining at each weight move, parallax errors in the readings were minimised. All readings were photographed for later analysis. A short video of each would have been useful as it

Figure 4 Establishing *KG* by suspension

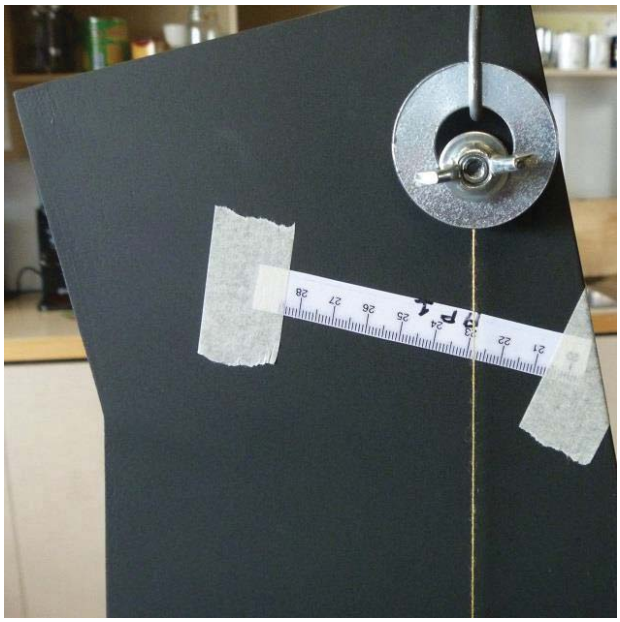

Figure 5 Suspension point detail

would have shown the extent of any movement at pendulum readings.

The inclining weight was then moved progressively along the rails with pendulum readings taken at each move. In addition to the pre-determined positions, the weight was also placed as close as practicable to either side of each ballast weight (moves 11, 12, 14 & 15), and the positions measured, to give additional readings close to upright.

In analysing the results, deflections were normalised to the respective mean zero readings. The full set of inclining readings is shown in Table A–1.

For the classic workup, $w\ d$ and $\tan\varphi$ are calculated and the derived data over all weight moves is included in Table A–1.

Table A–2 shows the derived data for the new method over all weight moves. There was a small initial list of 0.054 degrees measured by freeboards. This was added to each heel determined by pendulum deflection to give actual heels. *KN*s were then calculated from the numerical hull mesh model.

5. INTERPRETING THE MODEL TEST RESULTS

5.1 Balancing Heeling and Righting Arms

The concept of the new method is based on heeling and righting arms being equal after each weight shift. Knowing KG_I, upright TCG_I can be calculated and a set of righting arms developed from the *KN* values. These righting arms are, in effect, *GZ* values shifted to take account of TCG_I. The comparison between experimental heeling arms and calculated righting arms is included in Table A–2.

It can be seen that the greatest differences occur at weight moves 9 and 17. These are symmetrical port and starboard and it is possible that they resulted from the small initial trim. This would have caused the low corners of the chine flats to touch the water surface early, generating small additional righting moments at those weight moves.

The use of readings with large differences between heeling and righting arms should be avoided in further calculations if practicable.

5.2 Simulating Actual Inclining Experiments

The full data set was analysed, together with four combinations of weight moves to represent inclining experiment scenarios. Not all sets use the same number of weight moves.

5.3 Case 1: Full Data Set

Using the full set of results the new method gives an accurate *KG* of 0.162 m. Despite a high coefficient of determination of 0.998, the classic method is significantly in error with *KG* of 0.010 m. See Figure 6 and Table 3.

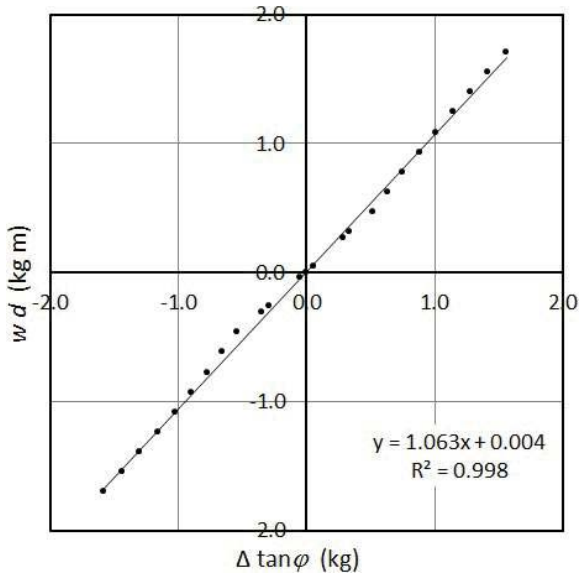

Figure 6 Plot of full data set $w\,d$ vs. $\Delta \tan\varphi$

Table 3 Results using the full data set

Classic – Full Set		
GM_0	(m)	1.063
KG_I	(m)	0.010

New – Full Set		
TCG_I	(m)	0.001
KG_I	(m)	0.162

5.4 Case 2: Typical

A typical set of inclining results can be selected with a heel range a little over two degrees each way. Results are shown in Table A–3. *KG* by the new method is 2 mm low, but significantly better than by the classic method.

5.5 Case 3: Large Initial List to Port

A set can be selected which is similar to the inclining experiment on the survey boat described previously at 4.1. *TCG* is known to be −0.053 m from the inclining weight shift at the initial state (move 20) and values for the classic method have been adjusted to reflect this.

The resulting *KG* is 0.163 m by the new method (1 mm error) with *TCG* slightly in error at −0.050 m. The small error in *TCG* may been caused by extrapolation of the trendline through *HZ* vs. Heel to obtain the intersection at upright. *KG* is −0.063 m by the classic method – placing the centre of gravity below the baseline. Results are shown in Table A–4.

The fact that the classic method can give a negative *KG*, well below the underside of keel, is alarming – though hopefully would not go unnoticed.

5.6 Case 4: Restricted Heel

It has been pointed out that, since the new method relies on division by $\sin\varphi$, the results can be erratic when measurement of heels close to upright is not completely accurate. When calculating individual results, division by zero would occur at upright.

This is not an issue with a reasonable range of heels to either side of upright. By using the slope of a trendline, values close to the mean have little effect as they tend to shift, rather than skew, the line of best fit. However a set of inclining values over a small range near upright may cause a problem. In fact, the model test shows a good result by the new method, even with less than one degree heel to either side of upright.

Though still a little low, the result for the classic method is almost correct – as would be expected with such a small range of heel. Results are shown in Table A–5.

5.7 Case 5: One Extreme Heel Close to Upright

Division by $\sin\varphi$ may also result in error if one of the extreme heels is close to upright.

The current set of model results cannot be used to reliably illustrate the problem. Upright was the starting point for model readings and the mean of three readings (0, 13 & 26) gives better accuracy than would be expected in practice. Results in Table A–6 show that the new method has an error of 2 mm but, as in Case 3, the classic method gives a nonsensical result with *KG* below the baseline!

5.8 Summary of the Simulation Cases

Figure 7 shows the *KG*s for the five cases by each method. The horizontal line is at the *KG* found by suspending the model. Clearly the new method is the more reliable for this model.

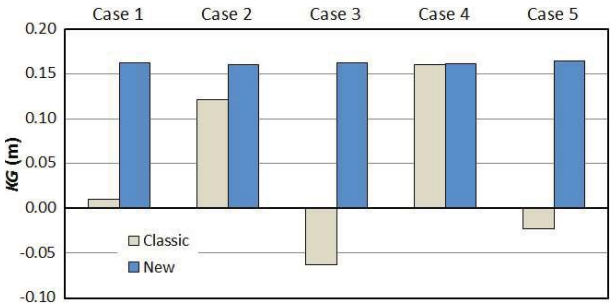

Figure 7 Comparison of inclining simulations

6. GENERAL OBSERVATIONS

6.1 Discarding Readings Near Upright

The new workup method benefits from values near upright for calculating *TCG* but, in the subsequent calculation of *KG*, there may be justification for discarding any readings with the vessel close to upright unless good accuracy in the measurements of those heel angles can be assured.

6.2 Measuring Pendulum Deflections

The problem of measuring small pendulum deflections can be overcome to some extent by the use of longer pendulums. However, these can often fail to settle at a measurable point and are influenced by ship movement transmitted through the pivot point. The practice of hanging pendulums high in the ship is not helpful and, wherever practicable, they should be low down with the pivot point close to the waterline for best results.

Damping of the pendulum bob in a trough of viscous fluid will assist. In the past, DNPS has recommended the use of spent oil as a damping medium, but now advocates the use of a thin wallpaper paste – about 5 g/l. This has several advantages: it is readily available, light (it can be taken in powder form to the inclining) and, being basically starch, is more environmentally friendly. There are no special precautions or equipment required for disposal.

7. EXPERIENCES WITH THE NEW METHOD

7.1 Applying the New Method

RAN generally employs contractors to conduct inclining experiments and to produce the associated reports. Since the use of the new workup method was introduced in 2013, a number of inclining experiments have been conducted on RAN ships and the new method used with varying degrees of success.

Some contractors have chosen to use the resources of DNPS to provide the as-inclined characteristics, but several have used the new method for themselves. DNPS offers an Excel spreadsheet which will perform the necessary calculations.

Apart from *KN*s, the data input required is the same as for the classic method.

7.2 Generating *KN* Values

The calculation of *KN* values is clearly an issue. Few contractors hold good numerical models of our ships and even those who do so are not necessarily able to produce *KN*s at the specific heel angles, and to sufficient accuracy, to be of use.

One solution has been to provide *KN* data tabulated at fine intervals of heel, trim and volume which can be interrogated by linear interpolation. Volume is used rather than displacement as it is independent of the water density at the time of the inclining experiment. Considerable effort has gone into determining how fine the intervals need to be and experience has shown that the requirements are specific to each hull form. To date, no general rules have been found which will enable the intervals to be determined by simple inspection of the hull characteristics.

8. CONCLUSIONS

Although some issues, particularly the generation of accurate *KN* values, need to be resolved before the new method can be readily and universally applied, the practical model inclining has shown how robust and versatile it is. By comparison, on only one occasion did the classic method come closer than 0.04 m (25%) to the correct *KG* in the scenarios which were simulated for this particular model.

It has been clearly demonstrated that this is a superior method for application to non- wall-sided hull forms, even when they are inclined to extreme angles, and its adoption is strongly recommended.

9. ACKNOWLEDMENTS

The author is grateful for the assistance given by members of the Stability and Hydrodynamics Sections of DNPS in the conduct of the model testing described above.

10. FUTURE WORK

10.1 Extending the Experimental Data Set

To date, only a single set of readings has been taken on this model at one displacement and *KG*. The work should be extended to cover a range of hull forms, displacements and *KG*s. This should include a true wall-sided model.

10.2 Investigating Sensitivity

The sensitivity of the new method to both hull type, and to inaccuracies in measurements taken at the inclining experiment, needs to be investigated.

10.3 Deviations in Hull Form

Deviations of the hull from the original design and errors in numerical modelling may be significant. Work is needed to establish the extent of this problem in practice and the influence it has on inclining experiment results.

11. REFERENCES

Bouguer, P., 1746, Traité du Navire, de sa Construction et de ses Mouvemens (Treatise of the Ship, its Construction and its Movements), Jombert, Paris.

Dunworth, R.J., 2014, “Back Against the Wall”, The Transactions of The Royal Institution of Naval Architects, vol. 156, part B2 (International Journal of Small Craft Technology), pp. 99-106.

Hoste, P., 1697, Théorie de la Construction des Vaisseaux (Theory of the Construction of Vessels), Arisson & Posule, Lyon.

Appendix A – Tables of Data and Results

Table A–1 Pendulum deflections and classic workup

Move No.	Weight Shift mm	Forward Pendulum			Aft Pendulum			Mean Heel (φ) deg.	$w\,d$ kg m	$\Delta \tan\varphi$ kg
		Reading mm	Deflection mm	Heel (φ) deg.	Reading mm	Deflection mm	Heel (φ) deg.			
0	0	151.5	0.00	0.000	153.2	0.00	0.000	0.000	0.0000	0.0000
1	550	54.4	96.90	5.097	249.9	96.73	5.094	5.095	1.7039	1.5658
2	500	63.7	87.60	4.610	241.0	87.83	4.627	4.619	1.5490	1.4186
3	450	72.0	79.30	4.175	232.2	79.03	4.165	4.170	1.3941	1.2803
4	400	80.5	70.80	3.729	223.8	70.63	3.724	3.726	1.2392	1.1437
5	350	88.6	62.70	3.303	215.5	62.33	3.287	3.295	1.0843	1.0110
6	300	96.6	54.70	2.883	207.8	54.63	2.882	2.882	0.9294	0.8841
7	250	104.5	46.80	2.467	200.0	46.83	2.471	2.469	0.7745	0.7571
8	200	111.8	39.50	2.082	192.5	39.33	2.076	2.079	0.6196	0.6375
9	150	119.0	32.30	1.703	185.2	32.03	1.691	1.697	0.4647	0.5202
10	100	130.2	21.10	1.113	174.1	20.93	1.105	1.109	0.3098	0.3399
11	84.50	133.5	17.80	0.939	171.0	17.83	0.941	0.940	0.2618	0.2881
12	16.00	147.8	3.50	0.185	156.5	3.33	0.176	0.180	0.0496	0.0553
13	0	151.2	0.00	0.000	153.2	0.00	0.000	0.000	0.0000	0.0000
14	-14.00	154.2	-2.90	-0.153	150.3	-2.87	-0.151	-0.152	-0.0434	-0.0466
15	-84.25	168.9	-17.60	-0.928	135.5	-17.67	-0.933	-0.930	-0.2610	-0.2852
16	-100	172.3	-21.00	-1.107	132.0	-21.17	-1.117	-1.112	-0.3098	-0.3410
17	-150	184.5	-33.20	-1.750	120.3	-32.87	-1.735	-1.743	-0.4647	-0.5342
18	-200	191.5	-40.20	-2.119	113.2	-39.97	-2.109	-2.114	-0.6196	-0.6482
19	-250	198.8	-47.50	-2.504	105.8	-47.37	-2.499	-2.501	-0.7745	-0.7671
20	-300	206.5	-55.20	-2.909	98.2	-54.97	-2.899	-2.904	-0.9294	-0.8908
21	-350	214.5	-63.20	-3.330	90.4	-62.77	-3.310	-3.320	-1.0843	-1.0186
22	-400	222.4	-71.10	-3.745	82.0	-71.17	-3.752	-3.748	-1.2392	-1.1504
23	-450	231.2	-79.90	-4.206	73.1	-80.07	-4.219	-4.213	-1.3941	-1.2935
24	-500	239.8	-88.50	-4.657	64.8	-88.37	-4.655	-4.656	-1.5490	-1.4302
25	-550	248.9	-97.60	-5.134	55.8	-97.37	-5.127	-5.130	-1.7039	-1.5765
26	0	151.2	0.00	0.000	153.1	0.00	0.000	0.000	0.0000	0.0000
Mean Zero		151.30			153.17					

Table A–2 New workup and heeling / righting arm comparison

Move No.	Actual Heel (φ) deg.	*KN* m	sin φ	cos φ	*HZ* m	*KG* sin φ m	*HZ* mm	*GZ'* mm	Delta mm
0	0.054	0.0013	0.0009	1.0000	0.0000	0.0002	0.00	0.00	0.00
1	5.149	0.1123	0.0898	0.9960	0.0966	0.0146	96.64	96.65	0.01
2	4.673	0.1022	0.0815	0.9967	0.0879	0.0131	87.92	87.85	-0.07
3	4.224	0.0924	0.0737	0.9973	0.0792	0.0121	79.18	79.30	0.12
4	3.780	0.0824	0.0659	0.9978	0.0704	0.0108	70.42	70.55	0.14
5	3.349	0.0724	0.0584	0.9983	0.0616	0.0096	61.64	61.78	0.14
6	2.936	0.0625	0.0512	0.9987	0.0529	0.0085	52.86	53.11	0.25
7	2.523	0.0524	0.0440	0.9990	0.0441	0.0072	44.06	44.14	0.08
8	2.133	0.0426	0.0372	0.9993	0.0353	0.0062	35.26	35.41	0.15
9	1.751	0.0334	0.0306	0.9995	0.0265	0.0058	26.45	27.27	0.82
10	1.163	0.0221	0.0203	0.9998	0.0176	0.0033	17.64	17.69	0.05
11	0.994	0.0189	0.0173	0.9998	0.0149	0.0029	14.91	14.99	0.08
12	0.234	0.0047	0.0041	1.0000	0.0028	0.0007	2.82	2.87	0.04
13	0.054	0.0013	0.0009	1.0000	0.0000	0.0002	0.00	0.00	0.00
14	-0.098	-0.0016	-0.0017	1.0000	-0.0025	-0.0002	-2.47	-2.42	0.05
15	-0.876	-0.0162	-0.0153	0.9999	-0.0149	-0.0024	-14.51	-14.81	-0.30
16	-1.058	-0.0196	-0.0185	0.9998	-0.0176	-0.0031	-17.64	-17.72	-0.08
17	-1.689	-0.0315	-0.0295	0.9996	-0.0265	-0.0062	-26.45	-27.84	-1.39
18	-2.060	-0.0396	-0.0359	0.9994	-0.0353	-0.0055	-35.26	-34.89	0.37
19	-2.447	-0.0494	-0.0427	0.9991	-0.0441	-0.0064	-44.07	-43.59	0.48
20	-2.850	-0.0593	-0.0497	0.9988	-0.0529	-0.0076	-52.86	-52.41	0.46
21	-3.266	-0.0693	-0.0570	0.9984	-0.0616	-0.0088	-61.65	-61.22	0.42
22	-3.694	-0.0793	-0.0644	0.9979	-0.0704	-0.0100	-70.42	-70.02	0.40
23	-4.159	-0.0899	-0.0725	0.9974	-0.0792	-0.0118	-79.18	-79.26	-0.08
24	-4.602	-0.0996	-0.0802	0.9968	-0.0879	-0.0129	-87.93	-87.78	0.15
25	-5.076	-0.1098	-0.0885	0.9961	-0.0967	-0.0143	-96.65	-96.60	0.05
26	0.054	0.0013	0.0009	1.0000	0.0000	0.0002	0.00	0.00	0.00

Table A–3 Case 2: Data set representing a typical inclining experiment

Move No.	Shift m	*w d* kg m	Δ tanφ kg	Heel (φ) deg.	*KN* m	sinφ	cosφ	*HZ* m	*KG* sinφ m
13	0.000	0.0000	0.0000	0.0540	0.0013	0.0009	1.0000	0.0000	0.0004
10	0.100	0.3098	0.3399	1.1629	0.0221	0.0203	0.9998	0.0176	0.0036
8	0.200	0.6196	0.6375	2.1330	0.0426	0.0372	0.9993	0.0353	0.0065
13	0.000	0.0000	0.0000	0.0540	0.0013	0.0009	1.0000	0.0000	0.0004
16	-0.100	-0.3098	-0.3410	-1.0584	-0.0196	-0.0185	0.9998	-0.0176	-0.0028
18	-0.200	-0.6196	-0.6482	-2.0602	-0.0396	-0.0359	0.9994	-0.0353	-0.0052
13	0.000	0.0000	0.0000	0.0540	0.0013	0.0009	1.0000	0.0000	0.0004
		GM_0	0.952		TCG_I	0.001			
		KG_I	0.121		KG_I	0.160			

Table A–4 Case 3: Data set representing an inclining experiment with large initial list

Move No.	Shift m	$w\,d$ kg m	$\Delta \tan\varphi$ kg	Heel (φ) deg.	KN m	$\sin\varphi$	$\cos\varphi$	HZ m	$KG \sin\varphi$ m
20	0.000	0.0000	0.0000	-2.8502	-0.0593	-0.0497	0.9988	0.0000	-0.0094
22	-0.100	-0.3098	-0.2587	-3.6942	-0.0793	-0.0644	0.9979	-0.0176	-0.0118
25	-0.250	-0.7745	-0.6826	-5.0763	-0.1098	-0.0885	0.9961	-0.0439	-0.0161
20	0.000	0.0000	0.0000	-2.8502	-0.0593	-0.0497	0.9988	0.0000	-0.0094
18	0.100	0.3098	0.2421	-2.0602	-0.0396	-0.0359	0.9994	0.0176	-0.0072
15	0.216	0.6676	0.6052	-0.8764	-0.0162	-0.0153	0.9999	0.0380	-0.0042
20	0.000	0.0000	0.0000	-2.8502	-0.0593	-0.0497	0.9988	0.0000	-0.0094
		GM_0	1.136		TCG_I	-0.050			
		KG_I	-0.063		KG_I	0.163			

Table A–5 Case 4: Data set representing an inclining experiment with restricted heel

Move No.	Shift m	$w\,d$ kg m	$\Delta \tan\varphi$ kg	Heel (φ) deg.	KN m	$\sin\varphi$	$\cos\varphi$	HZ m	$KG \sin\varphi$ m
13	0.000	0.0000	0.0000	0.0540	0.0013	0.0009	1.0000	0.0000	0.0002
11	0.085	0.2618	0.2881	0.9941	0.0189	0.0173	0.9998	0.0149	0.0029
13	0.000	0.0000	0.0000	0.0540	0.0013	0.0009	1.0000	0.0000	0.0002
15	-0.084	-0.2610	-0.2852	-0.8764	-0.0162	-0.0153	0.9999	-0.0149	-0.0024
11	0.000	0.0000	0.0000	0.0540	0.0013	0.0009	1.0000	0.0000	0.0002
		GM_0	0.912		TCG_I	0.001			
		KG_I	0.161		KG_I	0.163			

Table A–6 Case 5: Data set representing an inclining experiment with an extreme heel close to upright

Move No.	Shift m	$w\,d$ kg m	$\Delta \tan\varphi$ kg	Heel (φ) deg.	KN m	$\sin\varphi$	$\cos\varphi$	HZ m	$KG \sin\varphi$ m
8	0.000	0.0000	0.0000	2.1330	0.0426	0.0372	0.9993	0.0000	0.0142
6	0.100	0.3098	0.2462	2.9362	0.0625	0.0512	0.9987	0.0176	0.0166
3	0.250	0.7745	0.6412	4.2241	0.0924	0.0737	0.9973	0.0440	0.0201
8	0.000	0.0000	0.0000	2.1330	0.0426	0.0372	0.9993	0.0000	0.0142
11	-0.116	-0.3578	-0.3491	0.9941	0.0189	0.0173	0.9998	-0.0204	0.0110
13	-0.200	-0.6196	-0.6375	0.0540	0.0013	0.0009	1.0000	-0.0353	0.0082
8	0.000	0.0000	0.0000	2.1330	0.0426	0.0372	0.9993	0.0000	0.0142
		GM_0	1.096		TCG_I	0.028			
		KG_I	-0.023		KG_I	0.164			

Proceedings of the 12th International Conference on the Stability of Ships and Ocean Vehicles, 14-19 June 2015, Glasgow, UK.

Exploration of the Probabilities of Extreme Roll of Naval Vessels

Douglas Perrault, *Defence Research and Development Canada – Atlantic Research Centre* Doug.Perrault@DRDC-RDDC.GC.Ca

ABSTRACT

Dynamic stability simulation tools developed by the Cooperative Research Navies have been used to investigate the relationship between a number of stability criteria and the probability of exceeding a critical roll angle. Multiple roll response time series for several ships in various seaway conditions are generated to provide the probabilities. This paper describes the investigation into the probability results themselves, as a precursor to regression against GZ curve parameters. Specifically, it examines the effects of modelling choices and of variation and range in the input control variables.

Keywords: *Dynamic Stability, Probability of Capsize, Simulation*

1. INTRODUCTION

Tools for assessing dynamic stability of intact ships have been developed within the Cooperative Research Navies (CRNav) Dynamic Stability Project. Under tasking from the Naval Stability Standards Working Group (NSSWG), the tools were employed to investigate the relationship between risk of capsize and various geometry and stability parameters. The risk of capsize is characterized by the probability of exceeding a critical roll angle (PECRA), and although in the present case it is related to capsize, the critical roll angle may also take on a number of other important connotations, such as machinery or weapon limits.

The probability of exceeding a critical roll angle (PECRA) is determined by running multiple, time-domain simulations of a ship in a specific loading condition at a mean speed and heading (the operating point of the vessel) in waves of a given significant height and modal period (the environmental condition). The time series of roll responses are used to determine the PECRA. The probability outcomes are later used as the regressands (response variables) in regression analysis investigating relationships with parameters associated with ship stability.

This paper records the study into how the PECRA vary with the input control variables of ship speed (V), ship heading relative to the wave system (β), significant wave height (H), and modal wave period (τ). It also looks into the differences between ships and between loading conditions. It further seeks to address the issue of the range and resolution of the sets of input control variables that will fully characterize the total probability of exceeding a critical roll angle (TPECRA) across all input variables for each load condition of each ship.

The next section will discuss the scope of work to date, looking at the similarities and differences between three phases of work, each with slightly different goals. Following that will be a look at the different geometries of the ships used in Phase 2. The next section will briefly examine the effects of load conditions,

operating points, and environmental conditions. After that will be a study into the consequences of choices relating to range and resolution of the input control variables (V, β, H, τ). This will be followed by a discussion on the use of Operational Overlays. Finally conclusions will be presented.

2. SCOPE OF WORK – 3 PHASES

2.1 Determination of Probabilities

FREDYN is a non-linear, semi-empirical, time-domain software for simulating ship motions in environmental conditions from calm water to severe wind and waves. It allows for studies in stability, seakeeping and manoeuvring. FREDYN is appropriate for any type of a relatively slender mono-hull with a Froude number less than 0.5. Specific to the current study, FREDYN is capable of predicting a range of capsize modes in regular and irregular waves.

Since 1999, the objectives of the NSSWG have been pursued through three phases of study for intact ships. Phase 1 (FREDYN version 8.2) used a strip theory approach to look at relationships between the risk of capsize and various stability-related and ship-form parameters. Phase 2 (FREDYN version 9.9) used panel methods and the emphasis of the study shifted to looking for the level of safety inherent in the current naval stability standards. In addition to using a panel method for the Froude-Krylov forces, the Frank Close Fit Method was implemented to replace a conformal mapping method, the roll damping method was improved, and the ship motion algorithm was upgraded. Phase 3 (FREDYN version 10.2) was conducted after a complete rewrite of the software to modularize the code. The Phase 3 study still used panel methods, but included a more accurate modelling of the effects of deck-edge immersion, as well as an automatic determination of the retardation function time interval and time step. The focus in Phase 3 was narrowed to finding criteria that would be suitable for stability standards, in particular the Naval Ship Code (ANEP 77, 2012).

The set of ships investigated was largely the same for all three phases, and included slender hulls with twin propellers and one or two rudders. Several different load conditions are explored for each ship, with each load condition delineated by draft (T) and vertical position of the centre of gravity (KG). The radii of gyration were held constant for a given ship for all load conditions (TKG). Some of the load conditions were common in two or more phases, but most were not.

What is common to all three phases is the general approach to determining the probability of exceeding the critical roll angle (PECRA). Simulations were run for each ship in specific load conditions, at standard operating points and environmental conditions.

The standard operating points are three speeds chosen by the NSSWG as typical for frigates, and 7 headings covering 0° to 180°, following the standard assumption that the symmetry of the ship will make the results from 180° to 360° a mirror image of those from 0° to 180°. In fact the 0° and 180° headings were changed to 1° and 179° to mimic the asymmetry of real vessels. The standard environmental conditions were taken as those define by the Bales North Atlantic scattergram (see Bales, Lee, and Voelker, 1981) as modified by McTaggart and De Kat (2000).

The same set of operating points and environmental conditions was used in Phase 2 as in Phase 1, but in Phase 3 there were fewer wave heights and periods and only one ship speed.

To be conservative, a single sea direction was assumed and wave spreading was not used, so that all the energy associated with the sea spectrum would be concentrated in the

unidirectional wave train. This is expected to result in a more pessimistic estimate of risk.

Wind was modelled as a function of wave height and was set to be collinear with the wave, again to be conservative. No currents were included in the simulations.

Each environmental condition was modelled as a Bretschneider spectrum defined by the significant wave height and modal wave period. The spectrum is built by summing regular waves of different amplitudes, wavelengths and phase angles, and there are an infinite number of ways to realize (achieve) the spectrum, with each realization accomplished by a different choice of the pseudo-random seed number used to generate the component wave phase angles. Each realization is capable of producing a unique time series of wave conditions, and thus ship responses. This is the key to generating probabilistic results: under the assumption that any one of the unique realizations is equally likely to occur, performing multiple simulation runs (where each run is a unique realization) generates a statistical sample leading to the probability of exceeding the critical roll angle (PECRA).

The same operating points and environmental conditions were used in all cases within a given phase, but the number of seaway realizations was not necessarily the same for each ship, or even for each load condition for the same ship. The number of realizations depended on the quality of the probability result; (small) batches of simulations were added when the uncertainty in the probability result was higher than acceptable.

2.2 Post-Analysis

For Phases 1 and 2 a block maxima method called PCAPSIZE (see McTaggart and De Kat, 2000) was used to determine the probability of exceeding the critical roll angle (which for Phases 1 and 2 was 90°) within one hour.

For Phase 3 an envelope-peaks-over-threshold (EPOT) method called LORELEI (see Ypma and Harmsen, 2012) was developed to obtain the probability of exceeding the critical roll angle (which for Phase 3 was 70°) within an hour. This method makes fuller use of the time-series data and thus theoretically provides a more accurate value.

2.3 Current Investigation

For each load condition, the simulation results can be stored as a 4-dimensional hyper-cube with each dimension representing a single input control variable. While this makes it easy to index into the data, as well as to partition the data along any subset of variable ranges, for visually examining the data, it is necessary to "flatten" the data into at most 2 dimensions. It is intuitive to group the speed and heading together, and the wave height and period together. For each ship loading condition there can be up to 148 speed-heading tables or plots and up to 21 height-period tables or plots. Each phase has at least 37 loading conditions to consider, and over all 3 phases there are a total of 152 distinct loading conditions (i.e., not including repeated loading conditions) over 14 ships. The number of tables and/or plots to examine is large, so generalizations will be made by looking at single speed-heading plots that represents a sum of PECRA over all wave heights and periods for a given ship loading condition, and single height-period plot that represents a sum of PECRA over all ship speeds and headings for a given ship loading condition. These summations are known as marginal sums and can be denoted as MPECRA-HT and MPECRA-VB respectively. Each of these marginal summations can be further summed to a common number representing the total probability of exceeding the critical roll angel (TPECRA) for the load condition.

The marginal sums and the total sum are only possible by applying suitable probability distributions for the wave conditions, and/or

ship's speed and heading. The choice of probability distributions for the input control variables will be discussed more fully under Operator Overlays. For this paper, uniform distributions were used to make it easy to investigate the relationships without any weighting issues.

The probability results vary across several orders of magnitude. It is arguably more intuitive to talk about these probabilities in terms of their order of magnitude than about the values themselves. Therefore the remainder of this paper concerns itself with the data in terms of the base-10 logarithm of the probabilities; i.e., O(PECRA), O(MPECRA-HT), O(MPECRA-VB), O(TPECRA).

2.4 Data Presentation

Typically, the data with respect to the operating point (ship speed and heading) would be plotted on a polar plot, or a half-polar plot given an assumption of symmetry of the ship leading to similar results for relative headings from 180° to 360° as for 0° to 180°. In this paper, a contour plot of the order of magnitude of TPECRA with respect to speed and heading will be given in the form of a rectangular contour plot.

Figure 1 shows the more complicated contour plot in terms of environmental conditions (wave height and period), in this case for the order of magnitude of the probability of observing the wave height-period combination according to Bales as modified by McTaggart and De Kat (2000). The plot is more complicated because of several features. Wave steepness (significant wave height divided by wavelength) is taken into account so that waves that are too steep to exist are not included. This results in the lower left corner being empty; other empty areas are the result of not having data for the height-period combination. Overlaid on the plot are wave steepness contours (lines sweeping down from the top left corner). Stokes wave theory predicts a limit of steepness of 1/7, while Buckley (see McTaggart and De Kat, 2000) gives an observed limit of about 0.049, based on significant wave height and peak wave period. Note that the Bales data only has valid elements below both limits (i.e. above those contours in the figure). The lines crossing the steepness contours are contours of constant (normalized) energy due to the incident wave.

The average energy per unit meter along the wave[1] (perpendicular to the direction of wave travel) is given by:

$$E = (1/16\pi)\rho g^2 H^2 \tau^2 \quad \textbf{(1)}$$

This is clearly a function of the wave height and period only (for a given density of water). The energy is normalized by the highest value, which would be at the largest values of height and period; hence the contours show an increase towards the lower right corner.

The dashed boxes added to this particular figure indicate the NATO STANAG 4194 (1994) Sea State definitions for reference (see also Bales, Lee, and Voelker, 1981).

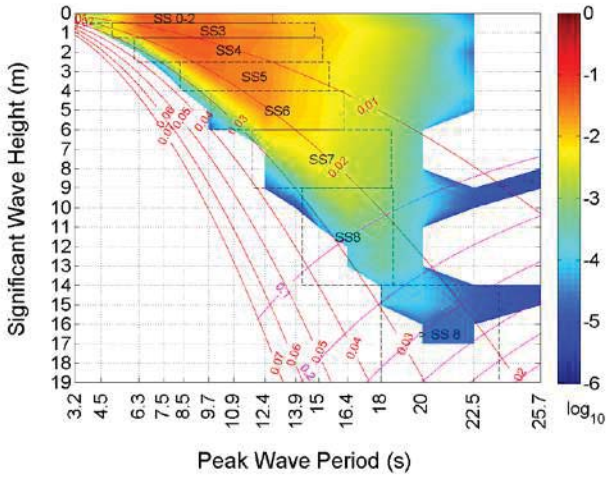

Figure 1. Order of Magnitude of Probabilities of Occurrence in Bales (modified) North Atlantic Wave Table.

[1] An estimate of the total energy imparted to the ship by the incident wave can be calculated by multiplying E by the waterline length of the ship times the sin of the relative heading to the wave. This estimate does not take into account radiation, diffraction, or other physical phenomena – only the energy in the incident wave.

2.5 Effects of Modelling and Analysis Choices

An attempt was made to track the changes between the phases of the intact stability study, in order to establish the effects of specific modelling choices, like the difference between strip theory and panel methods.

Across the set of ships and loading conditions in the three phases, there were 9 common loading conditions, representing 5 different ships. Some ships have one common condition and others have more. The loading conditions are numbered from 1 to 9 without regard to which ship they are associated with. Figures 2 through 4 show an example of the same loading condition in each phase. They show the maximum order of magnitude of PECRA over all speeds and headings, and do not, therefore, represent any particular operating point, nor are they marginal sums.

Because the ranges of wave heights and periods in phase 3 were reduced, Figures 2 and 3 have been cropped to show the Phase 3 Equivalent (P3E) ranges.

It is clear that each phase shows different orders of magnitude of the probabilities for the same conditions. Unfortunately, there were too many changes to the software in between phases to definitively assign changes in the probability results to specific modelling choices. Phase 2 data was chosen for this analysis because, as will be seen later, the ranges of input control variables provide for a more accurate characterization of the TPECRA.

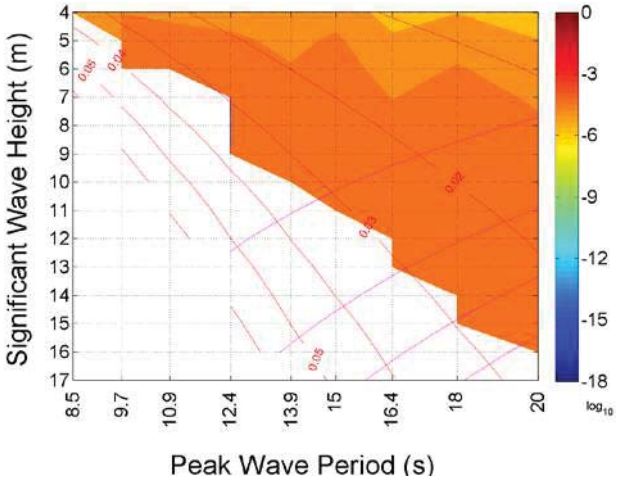

Figure 2. Maximum O(PECRA-VB) by Wave Height and Period – Phase 1 Load Condition 6.

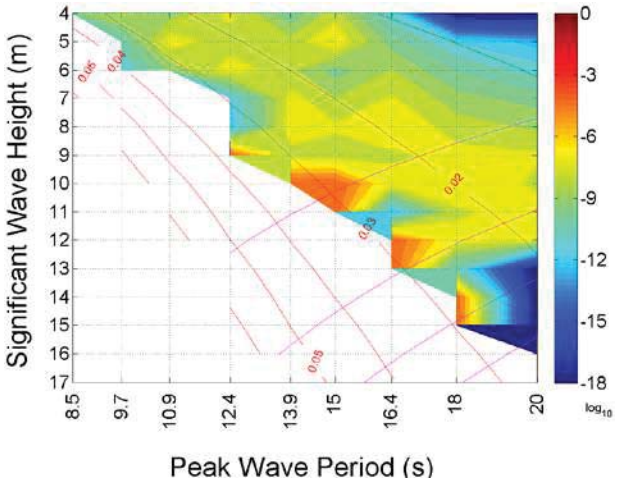

Figure 3. Maximum O(PECRA-VB) by Wave Height and Period – Phase 2 Load Condition 6.

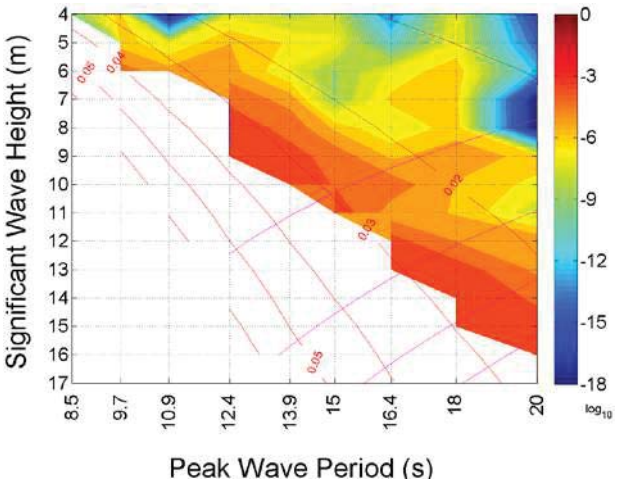

Figure 4. Maximum O(PECRA-VB) by Wave Height and Period – Phase 3 Load Condition 6.

3. SHIP GEOMETRY

The study looked at three forms of geometry:

1. A binary factor defining appendages
    a. Single vs double rudders
    b. Presence vs absence of skeg
    c. Presence vs absence of stabilizing fins
2. Dimensional geometry
3. Non-dimensional geometry

Scatter plots of TPECRA are used to investigate the effects of ship geometry.

3.1 Appendages

Within the set of ships simulated there are vessels with a skeg and/or fins, and some ships have a single rudder rather than twin rudders. The set of ships can be partitioned into groups having the various features:

Skeg Exclusively: ship(s) with skegs and double rudders, but no fins vs. all ships with a single rudder and/or fins and/or no skeg.

Fins Exclusively: ship(s) with fins and double rudders, but no skeg vs. all ships with a single rudder and/or a skeg and/or no fins.

Single Rudder Exclusively: ship(s) with a single rudder, but no skeg or fins vs all ships with a skeg and/or fins and/or double rudders.

Skeg Inclusive: ship(s) with skegs, with or without double rudders and/or fins vs. all ships without a skeg.

Fins Inclusive: ship(s) with fins, with or without double rudders and/or a skeg vs. all ships without fins.

Single Rudder Inclusive: ship(s) with a single rudder, with or without a skeg and/or fins vs. all ships with double rudders.

Skeg and Fins and Single Rudder: ship(s) with a skeg, fins, and double rudders vs. all ships not having all three features.

Other partitions are possible, but either the ship subsets already exist in the partitions above, or the ships used do not support them; i.e., one of the partitions is a null set and the other is the set of all ships.

Figure 5 shows a typical result. The filled markers in this figure indicate the load conditions of those ships with a single rudder only, but no fins, and no skeg, while the unfilled markers represent load conditions of all other ships. Although all the load conditions for the single-rudder ships are in one corner of the grouping, there is no definitive distinction between the filled and unfilled markers, at least in terms of the KG and O(TPECRA). Figure 6 shows that when ships with single rudders and fins or skegs are included, there is even less distinction. Figures 7 and 8 show the same thing when O(TPECRA) is plotted against the draft of the ship.

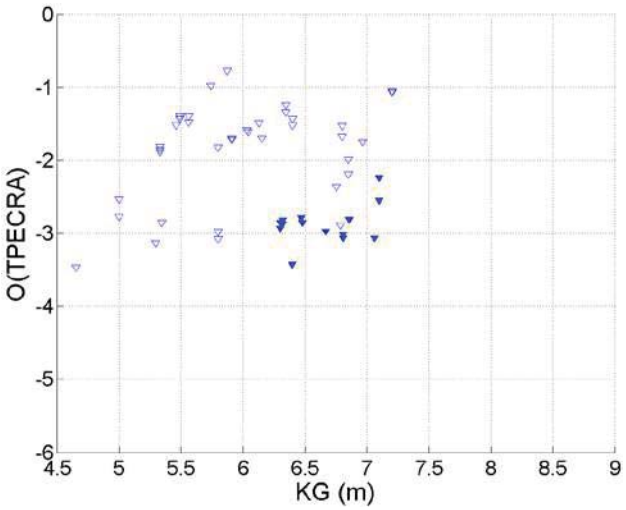

Figure 5. O(TPECRA) for each KG grouped by Single Rudder Exclusively (Phase 2).

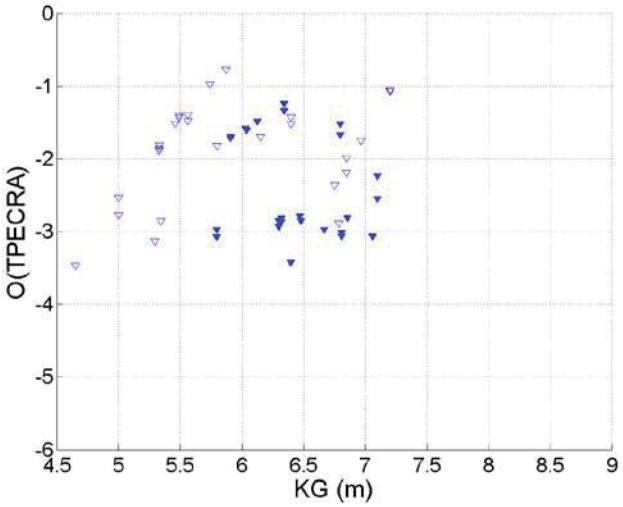

Figure 6. O(TPECRA) for each KG grouped by Single Rudder Inclusively (Phase 2).

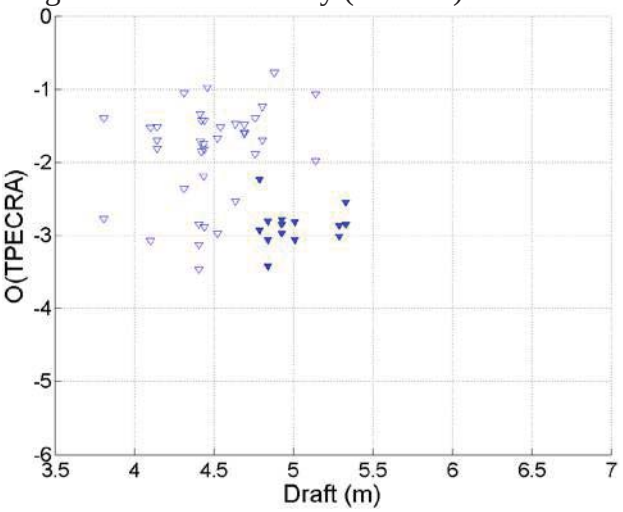

Figure 7. O(TPECRA) for each Draft grouped by Single Rudder Exclusively (Phase 2).

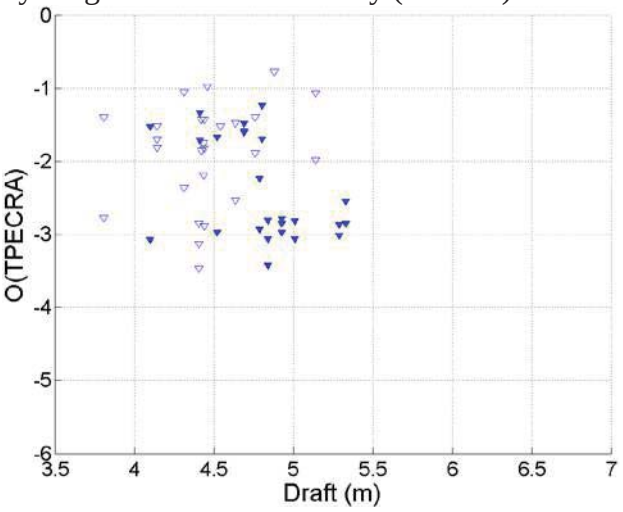

Figure 8. O(TPECRA) for each Draft grouped by Single Rudder Inclusively (Phase 2).

3.2 Dimensional Geometry

Dimensional measures of lengths, areas, and volumes were also examined to find any trends in the probability data. For some typical measures it is possible to look at the fore-aft differences as well.

LWL:	Length along waterline[2], L_{WL}.
BMSWL:	Beam at midships on the waterline.
BmaxWL:	Maximum beam on the waterline[3]
TMS:	Draft at midships.
AMS:	Area of the (immersed) midship section.
AWP:	Area of the waterplane.
VDisp:	Volume of displacement, ∇.

The length (LWL), waterplane area (AWP) and volume of displacement (VDisp) can be examined for fore-aft variations. The following postscripts are added to distinguish each case:

FWDMS/AFTMS:	Forward/aft of midships.
FWDLCF/AFTLCF:	Forward/aft of the center of flotation.
FWDLCB/AFTLCB:	Forward/aft of the center of buoyancy.

Midships (MS) represents a division in two based on ship length; the longitudinal center of floatation (LCF) represents division on the basis of waterplane area; and the longitudinal center of buoyancy (LCB) represents a division in two on the basis of volume.

The relationships between dimensional geometry (lengths, areas, volumes) are very similar to those for non-dimensional geometry, with lengths behaving like the ratios and

[2] The waterline is at the draft associated with the specific load condition, which is not necessarily the design draft.
[3] Because the maximum beam typically exists for some distance along the length of a ship, rather than only at a single, specific point, it is not suitable for dividing the ship into clear fore and aft parts.

coefficients in Figures 9 through 12, and areas and volumes more like Figure 13.

3.3 Non-Dimensional Geometry

Non-dimensional measures are ratios of dimensional measures, including classical form coefficients.

LWLoverTMS:	Length to draft ratio.
LWLoverBMS	Length to beam ratio.
WL:	
BMSWLoverT	Beam to draft ratio.
MS:	
CM:	Midship coefficient AMS/(BMSWL*TMS).
CW:	Waterplane coefficient AWP/(LWL*BMSWL).
CB:	Block coefficient Vdisp/(LWL*BMSWL*TMS).
CLP:	(Longitudinal) prismatic coefficient Vdisp/(AMS*LWL) = CB/CM.
CVP:	Vertical prismatic coefficient Vdisp/(AWP*TMS = CB/CW.

Length over beam, length over draft, the waterplane area coefficient, the block coefficient, and both prismatic coefficients allow for fore-aft versions, which are delineated by the same suffixes as the dimensional measures.

The O(TPECRA) was plotted against each of the geometry parameters to look for obvious trends. Figure 9 shows both forms of the typical results. On the left, the L/B ratios are tight-banded, while the more wide-banded data are like those of the B/T data on the right. None of the geometry parameters show a trend with the O(TPECRA); they were all vertical bands like those in Figure 9.

Figure 10 shows that the most common form coefficients do not have a meaningful relationship with O(TPECRA) either.

Figure 11 and Figure 12 show the situation is not changed by splitting the coefficients into fore and aft measures at midships (equal length halves). The results for division at the LCF (equal area halves) and the LCB (equal volume halves) show the same (lack of) trend.

Finally the freeboard is examined via the volume of reserve of buoyancy in Figure 13. It does not show any clear trend with O(TPECRA) either.

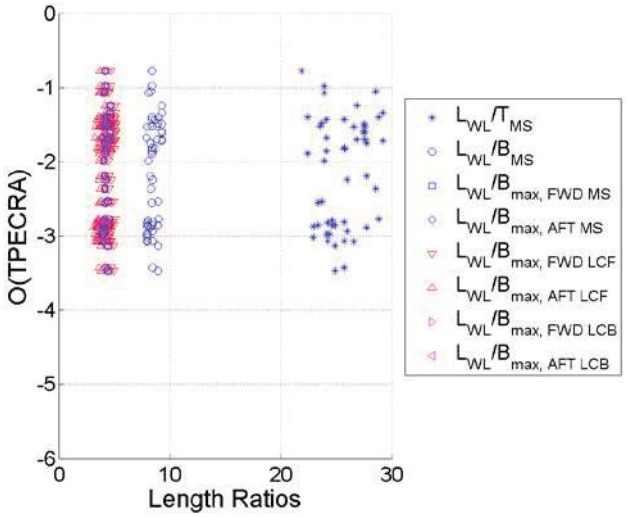

Figure 9. O(TPECRA) vs. Non-Dimensional Length (Beam) Ratios

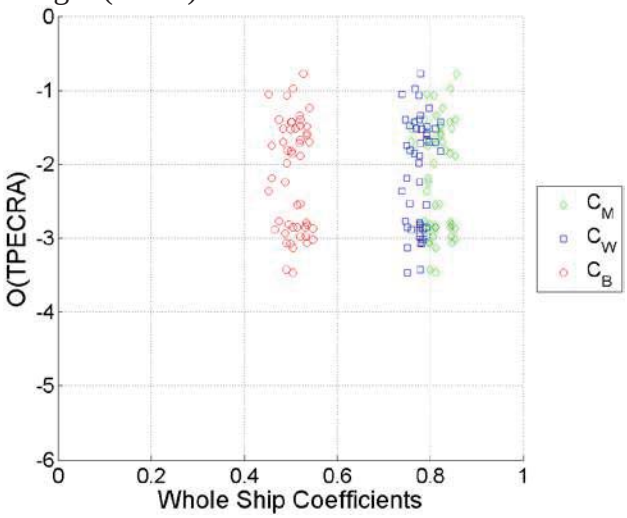

Figure 10. O(TPECRA) vs. Coefficients of Form for the Ship as a Whole.

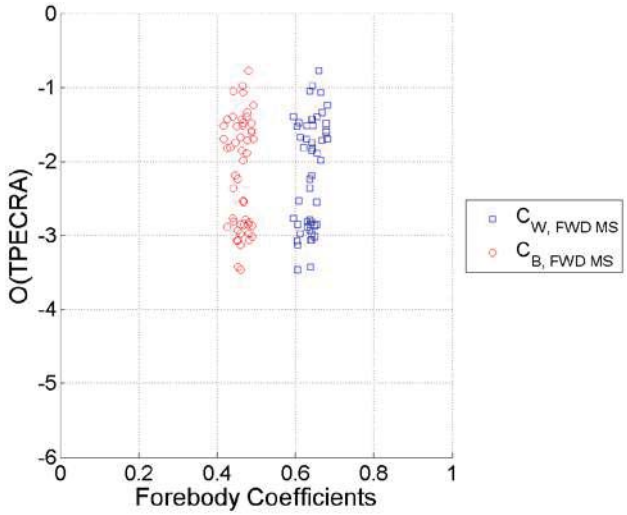

Figure 11. O(TPECRA) vs. Coefficients of Form for the Fore Body.

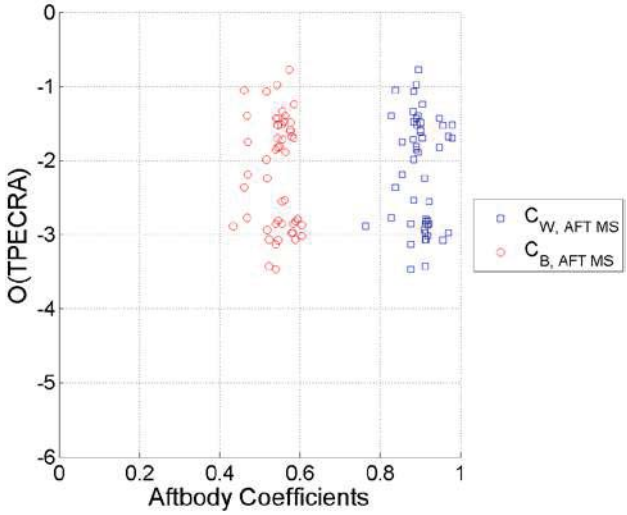

Figure 12. O(TPECRA) vs. Coefficients of Form for the Aft Body.

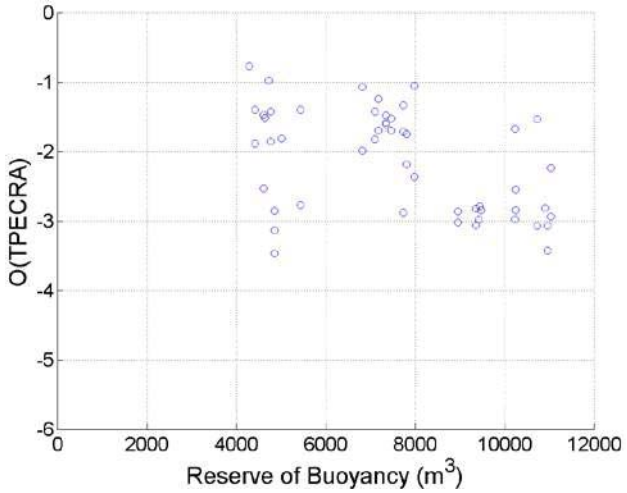

Figure 13. O(TPECRA) vs. Volume Reserve of Buoyancy

4. LOADING CONDITIONS, OPERATING POINTS, AND ENVIRONMENTAL CONDITIONS

In Phases 1 and 2, the loading conditions were picked such that for each ship at least four T-KG combinations constituted a matrix where two KG were simulated at two (or more) values of draft. This was not the case in Phase 3.

Contour plots over environmental conditions have been generated where the order of magnitude of the highest PECRA for all speeds and headings are shown for each height-period combination. For example, see Figure 14. Note that these plots show maxima results rather than marginal summations. Examination of contour plots for each loading condition of a ship will show that there can be a wide variation in the TPECRA for different loading conditions. Typically the effect of change in KG is more pronounced than that of a change in draft; however, this is not always true. Arguably, the expected outcome within each matrix is that the combination of the highest T and lowest KG would have the least O(PECRA), while the lowest T and the highest KG would have the greatest O(PECRA), with the other two combinations between the two extremes. Out of 8 ships, only 2 showed the expected outcome.

Contour plots over operating points were also generated where the order of magnitude of the highest PECRA for all heights and periods are shown for each speed-heading combination. Out of 8 ships, only 1 ship shows the expected outcome described above. These results indicate that the relationship between O(PECRA) and the draft and KG is complex and likely is affected by other factors, including the environmental conditions and the ship operating point.

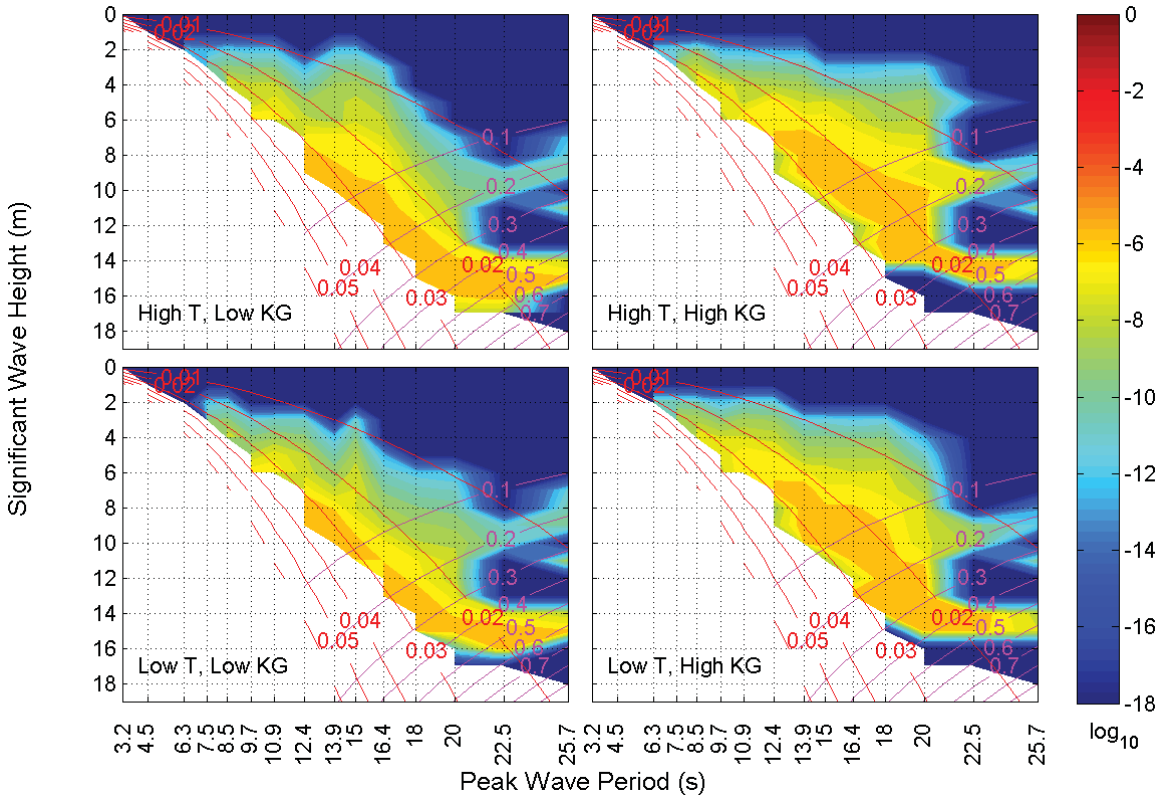

Figure 14. Typical Set of Environmental Relationships for Matrix of Load Conditions.

5. RANGE AND RESOLUTION OF INPUT CONTROL VARIABLES

The amount of data generated for each ship loading condition is sizeable, such that it is an onerous task to examine it all. It would be useful to reduce the number of conditions/points that need to be simulated. On the other hand, it is necessary to ensure that a sufficient number of conditions/points are simulated that an accurate characterization of the ship's behaviour is captured.

The idea of reduced data sets suggests that fewer simulations can be run to obtain the needed results. This was in fact practiced for the Phase 3 study, based on an educated guess of the new ranges of ship speed, and wave height and period. The question naturally arises as to whether or not the guess is reasonable, and further, how far the variable ranges can be reduced before the characterization of extreme roll probability is significantly affected.

Before either of these questions can be answered "significant" must be quantified. As stated above, when dealing with probabilities it is reasonable to speak in terms of orders of magnitude, and "significantly affected" can be thought of in terms of the difference between the order of magnitude of the sum of probabilities (TPECRA) for the reduced range and that for the full range. Five levels of significance have been examined in this study: 0.01, 0.05, 0.1, 0.5, and 1.0. These values represent approximately 2%, 12%, 26%, 300%, and 1000% changes respectively. The first level is very demanding, while the last level allows a 10x difference, and should be considered to be at or near the limit of acceptable difference, and in some cases may be too much of a difference.

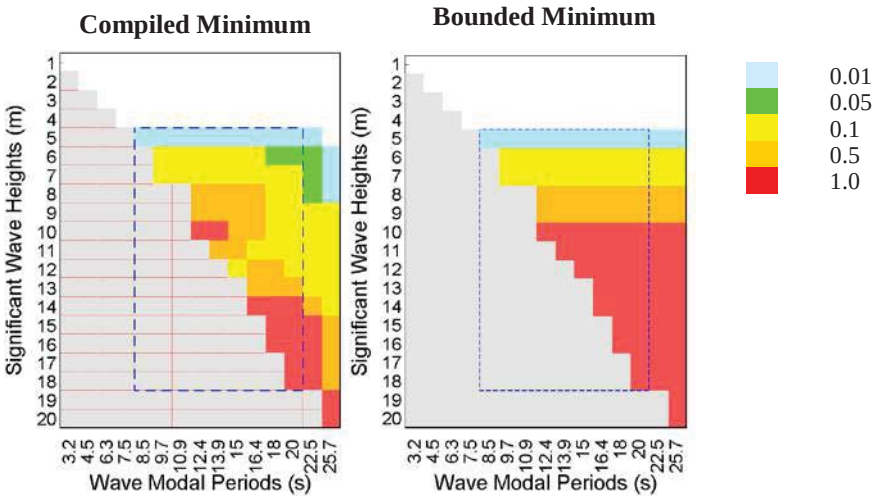

Figure 15. Minimum ranges of Wave Height and Period.

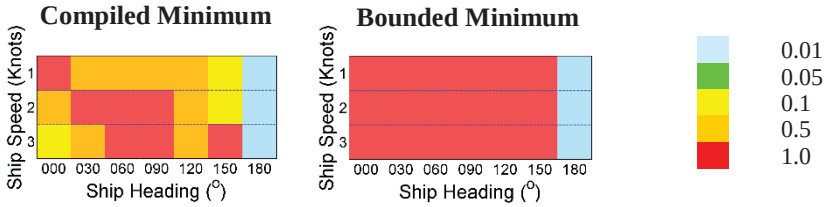

Figure 16. Minimum ranges of Ship Speeds and Headings.

The effect of reducing the range of the variables was investigated via a set of systematic reductions of the marginal sums over every possible range of the input control variables, leading to range-specific PECRA (RPECRA).

Figure 15 shows a compilation of results of the minimum-height-period-range search for all ship load conditions in Phase 2. The figure shows two wave height-period tables, each with all the possible wave conditions as non-greyed-out cells. The left-hand table shows the actual compilation of ranges; i.e., the minimum required range of environmental conditions for each load condition of all ships is included in the same figure, with the ranges corresponding to the less demanding levels of significance overlaid on the more demanding levels. Each level of significance is depicted in a different colour, with blue as the most demanding level and red as the least demanding level; the blue cells show the ranges of conditions required to provide a probability of exceeding the critical roll angle with an order of magnitude within 0.01, while the green cells represent a difference in the order of magnitudes of 0.05, the yellow cells a difference of 0.1 order of magnitude, the orange cells represent a difference in the order of magnitudes of 0.5, and the red cells a difference of 1 order of magnitude. The right-hand side shows the single contiguous range for each level needed to capture all the individual load condition ranges indicated in the left-hand side. These contiguous ranges represent the number of simulations that would be required if there was no prior knowledge of the individual constituent ranges. The blue dashed lines indicate the range of speeds and headings in the P3E (reduced) set.

Figure 15 shows that as the margin of difference is reduced, the ranges of conditions

must increase. It also indicates that, based on the compilation of results from all ship load conditions, the range of wave heights go from 4 to 20 m and the range of wave periods is from 8.5 to 25.7 s to ensure that extreme roll probability is within 0.01 order of magnitude of the full-table value. The range of wave heights go from 10 to 20 m and the range of wave periods is from 12.4 to 25.7 s to ensure that extreme roll probability is within 1 order of magnitude of the full-table value.

Figure 16 shows a compilation of results of the minimum-speed-heading-range search. At the 0.01 level of significance, the whole range of speeds and headings are necessary, while at levels of significance of 0.05 and greater all speeds and most headings are still required. Note that a heading of 0° represents the ship in following seas.

Figures 15 and 16 indicate that the Phase 3 range reductions are somewhat reasonable in terms of wave height and period, but are not appropriate for ship speed. The results in Figures 15 and 16 do not necessarily reflect the characteristics of the individual ships used in the compilation.

Table 1 summarizes the check on the validity of reducing the ranges of ship speeds and wave heights and periods as done in Phase 3. The table shows that the reduction in wave conditions will still give results within half an order of magnitude of the full table, for most ships. However, reducing the range of speeds will lead to a difference in extreme roll probability of up to an order of magnitude for most ships, and greater for some ships.

Table 1. Adequacy of Phase 2 data when ranges reduced to those of Phase 3.

	Reduced Environmental Profile			Reduced Operational Profile		
	0.1	0.5	1.0	0.1	0.5	1.0
Ship A	×	✓	✓	×	×	✓
Ship B	×	✓	✓	×	×	✓
Ship C	×	✓	✓	×	×	✓
Ship D	✓	✓	✓	×	×	✓
Ship E	×	✓	✓	×	×	✓
Ship F	×	✓	✓	×	×	✓
Ship G	×	×	×	×	×	×
Ship H	×	✓	✓	×	×	✓

The ranges of environmental conditions and operating points are not the only determining factors for ensuring coverage of the phenomena that accurately characterizes the ship behaviour. The number of simulations required is also dependent on the resolution of the environmental condition and operating point sets. The resolution for the operating points was arbitrarily assigned by the NSSWG. The resolution of the environmental conditions is that of the Bales scattergram.

Figure 17 is an example of a Phase 2 contour plot over environmental conditions. Figure 18 shows the data cropped to the Phase-3-Equivalent range of wave headings and periods; that is, all the data is available but the axes scales are reduced to show only the ranges similar to the Phase 3 plots. Figure 19 shows the same data set when only the data from the heights and periods that are common to Phase 3 are kept. Figure 19 is different from Figure 18, indicating that the range and resolution of the data affects the plot. If the resolution were sufficient, the plots would be similar. Essentially, the contours are being affected by "far field" values. Better resolution would make it more difficult for the "far field" to affect the results.

6. OPERATIONAL OVERLAYS

Advice to the designer or operator would have to take into account the probabilities of being at each loading condition, operating point, and in each environment.

For the sake of the current work however, because summation across input variables required the use of probability distributions, the probabilities for the operating points and environmental conditions were taken as

uniformly distributed over the ranges employed, while the probability of the load condition has not been considered. This was done to avoid obscuring relationships between the conditional probabilities and the conditions.

Naval Administrations can replace the uniform distributions with distributions more representative of their own particular pattern of use for the vessel. The replacement may require some interpolation. Any extrapolation must be limited to values very near the original data.

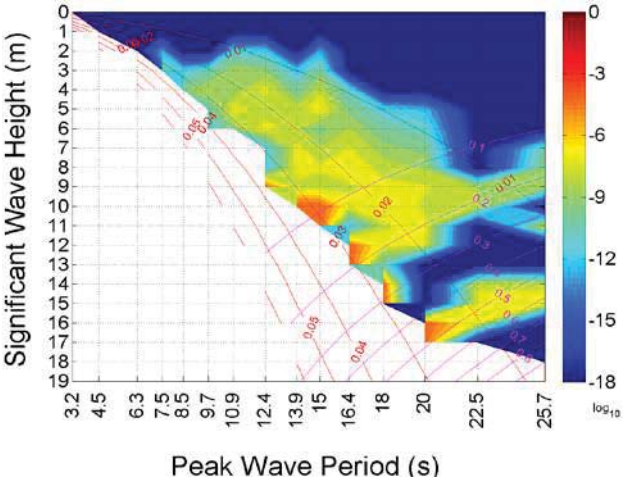

Figure 17. O(MPECRA-VB) by Wave Height and Period in Phase 2 Load Condition 6 (Full Range of Height and Period).

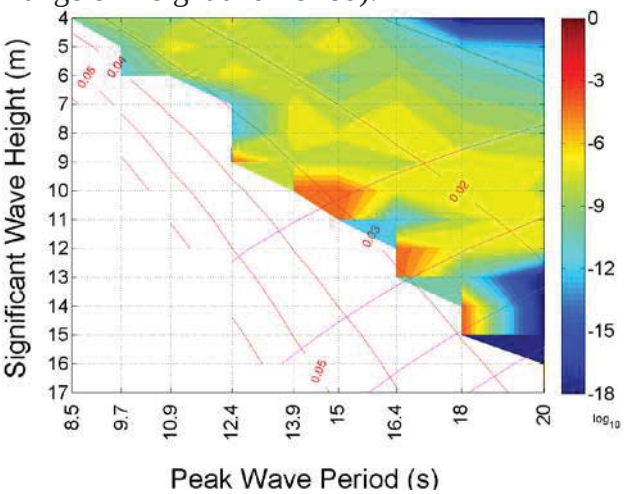

Figure 18. O(MPECRA-VB) by Wave Height and Period in Phase 2 Load Condition 6 (Full Range of Height and Period Cropped).

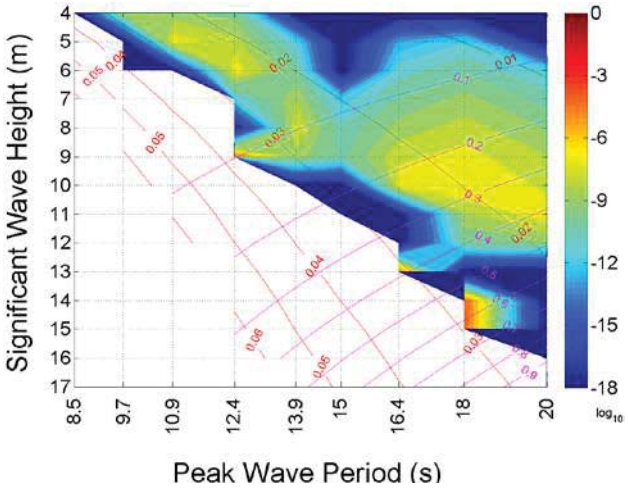

Figure 19. O(MPECRA-VB) by Wave Height and Period in Phase 2 Load Condition 6 (Phase 3 Equivalent Range of Height and Period).

For the main work of regression against stability parameters, the ships were assumed to be equally likely to take on any heading relative to the waves, but a generic 3-speed profile based on experience was agreed on and used (Phases 1 and 2; reduced to the most common speed for Phase 3). Further, the Bales' scattergram for the North Atlantic (see Bales, Lee, and Voelker [1981]) as modified by McTaggart and De Kat [2000] was used as the joint probability distribution of wave heights and periods.

Other options for operational overlays include the capability to use different wave height-and/or wave period distributions (e.g., the North Pacific scattergram) with the same underlying PECRA (via interpolation), and the ability to rule out certain environmental conditions based on restrictions due to design or change of vessel state. Operational overlays may also be used to account for operator influence, such as voluntary speed reductions and course changes in more severe seas.

7. CONCLUSIONS

This study has looked at probability data generated to investigate relationship between the probability of exceeding a critical roll angle (PECRA) and ship form and stability

parameters. The probabilities were produced for several ships at a number of loading conditions, and for a standard set of operating points (speeds and headings) and environmental conditions (wave heights and periods).

Similar simulations were run for each of 3 phases which each had a different goal. There are notable differences in the results between the 3 phases of the intact stability project. Unfortunately, because of the number of changes in modelling capabilities and choices between the phases, it is not possible to attribute the changes to specific choices.

Within each phase, a careful examination of the probabilities for each ship did not provide any clear patterns related to the typical appendages, or due to geometric parameters, whether expressed in dimensional or non-dimensional form. However, the set of ships used represents a relatively small sample of closely related hull forms with similar features, and it is possible that a larger sample, using more divergent ship types may identify relationships between PECRA and geometry.

When differences between loading conditions for each ship were studied, there was clear evidence of the expected variation due to draft and, more strongly, vertical center of gravity, but these expected variations were not observed in all cases. This suggests greater complexity, and perhaps the influence of other factors. More investigation is warranted.

The study did not investigate the data at the level of each combination of control input variables, because the number of combinations is essentially too large to manually observe. Instead, marginal sums and maxima over operating points and/or environmental conditions provided the basis of analysis. It is possible that there may be some method to examine the large data set, but it is thought that such an investigation would be more suitable when a specific behaviour or anomaly is in view. It was noted that the O(PECRA) contours tended to align with wave steepness, indicating that future work with wave steepness and energy is needed.

The question of how to efficiently and accurately characterize PECRA was addressed by looking at the range and resolution pf the input control variables. It was found that the environmental conditions might be reduced in range, but probably need to be increased in resolution. It was also found that the both the range and resolution of the operating points may need to be increased, particularly in terms of the range of speeds. Further investigation is required.

Finally, the utility of Operational Overlays was introduced as a means of extending usefulness of underlying probability data for all users, from the designer to the operator.

8. REFERENCES

ANEP-77, Naval Ship Code, NATO, Ed. 4, December 2012

Bales, S.L., Lee, W.T., and Voelker, J.M. ‘Standardized Wave and Wind Environments for NATO Operational Areas’. DTNSRDC, (Report DTNSRDC/SPD-0919-01), 1981.

McTaggart, K.A., De Kat, J. O., ‘Capsize Risk of Intact Frigates in Irregular Seas’, SNAME Transactions, 2000.

STANAG 4194, Standardized Wave and Wind Environments and Shipboard Reporting of Sea Conditions, Ed. 2, 1994.

Ypma, E., Harmsen, E., Development of a new methodology to predict the capsize risk of ships, 11th International Conference on the Stability of Ships and Ocean Vehicles, Athens, Greece, 2012.

Comparative Stability Analysis of a Frigate According to the Different Navy Rules in Waves

Emre Kahramanoğlu, *Yıldız Technical University*, emrek@yildiz.edu.tr

Hüseyin Yılmaz, *Yıldız Technical University*, hyilmaz@yildiz.edu.tr

Burak Yıldız, *Yıldız Technical University*, buraky@yildiz.edu.tr

ABSTRACT

As it is known, the naval ships are vulnerable to be damaged because of their mission. Therefore the most important parameter is survivability for them. This parameter is directly related to damaged stability analysis. In this study, the intact and damaged stability analysis of a frigate which is partially modernized have been carried out in waves according to three different navy rules. In addition to its conformity with these three different groups of rules, it has been examined that whether there are conflicting and varying points of different group of rules with each other and it has been tried to determine which one is more realistic.

Keywords: *damage stability, frigate, naval ship stability*

1. INTRODUCTION

Probability of damaging is very high for naval ships and it is related to their vocation. Therefore survivability is one of the most important parameter for them. Thereby intact and damaged stability analyses are so important for these ships in every circumstance.

Up to today there are many the studies which include the ships' intact and damaged stability analysis in waves. Some of them are mentioned.

A ship's intact and damaged stability analyses were made by Lee et al. (2012) via 2D linear method to determine the response of the ship in waves. On another study the waves were sent to model in different directions by Begovic et al. (2013). In that study the different scale of models' results were compared by the investigators. The global wave loads on ship which has zero speed was tried to determine by Chan et al. (2003). The analyses were made intact and damaged situations. An algorithm was developed by Hu et al (2013) to determine the optimum response when a naval ship has damage. A study about second generation intact stability criteria was done by Belenky et al (2011). It also included the effect of wave crest or through which were on the amidships on stability. A study about parametric roll motion of ships which come across a longitudinal wave was carried out by Taylan et al (2012).

In this study, the intact and damaged stability analyses of a frigate which is designed conceptually are implemented in waves according to three different navy rules. Also the results are compared with each other.

2. NAVY RULES

Basically, the stability analyses are made depend on two curves with regard to navy rules. One of them is the righting arm and the other is heeling arm. The heeling arm curve can

be made by beam winds, icing, lifting of heavy weights over the side, crowding passengers on one side or high speed turning.

2.1 American Navy Rules (DDS079)

Basically, in reference to DDS079 stability criteria depend on the areas under the righting and the heeling arm curves, the ratio of these areas, the equilibrium angle of the two curves and the ratio of arm's value at the equilibrium angle and the maximum righting arm (GZmax) (DDS079,2002). On the Figure 1 classically, the areas and the curves are shown.

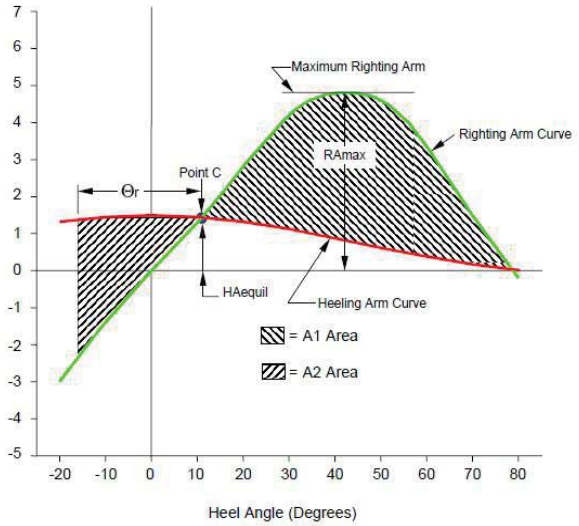

Figure 1. The areas and the curves with reference to DDS079 (2002)

With respect to the DDS079 the heeling arms are calculated by using these formulas:

Caused by beam winds:

$$HA = \frac{0.0195 * V_w^2 * A * z * \cos^2 \varphi}{1000 * \Delta} \quad (1)$$

9.

Caused by lifting of heavy weights or crowding passengers over the side:

$$HA = \frac{w * a * \cos \varphi}{\Delta} \quad (2)$$

Caused by high speed turning:

$$HA = \frac{V^2 * a_1 * \cos \varphi}{g * R} \quad (3)$$

In here,

A: projected sail area

V_W: wind speed

z: lever arm from half draft to centroid of sail area

a: transverse distance from centreline to end of boom

a_1: distance between ship's centre of gravity (KG) and centre of lateral resistance with ship upright

g: acceleration due to gravity

R: radius of turning circle

φ: angle of inclination

Δ: displacement

2.2 German Navy Rules (BV1030)

10. Basically, with reference BV1030 stability criteria depend on the equilibrium angle of the two curves. By using this angle a reference angle is determined. At the reference angle the residual arm must be greater than the minimum value (BV1030, 2001). In the Figure 2, the residual arm and the equilibrium angle are shown.

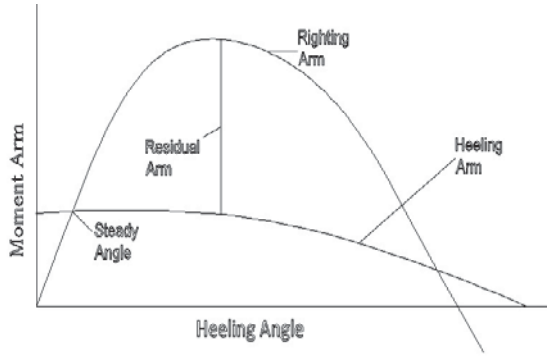

Figure 2. In regard to BV1030 (2001) the arm curves

With respect to the BV1030 (2001) some of the heeling arms can be calculated by using these formulas:

Caused by beam winds:

$$HA = \frac{A_w * (A_{WOH} - 0.5 * T)}{\Delta * g} * P_W * (0.25 + 0.75 * \cos^3 \varphi) \quad (4)$$

Caused by free surface effect:

$$HA = \frac{\sum(\rho * i)}{\Delta} * \sin \varphi \quad (5)$$

Caused by high speed turning

$$HA = \frac{C_D * V^2 * (KG - 0.5 * T)}{g * LWL} * \cos \varphi \quad (6)$$

Caused by crowding passenger over the side:

$$HA = \frac{P * Y}{\Delta * g} * \cos \varphi \quad (7)$$

In here,

A_W: projected sail area

$A_{WOH:}$ centroid of sail area

P_W: wind pressure

ρ: density of liquids in the tanks

Y: transverse distance from centreline to centroid of passengers

i: moment of inertia of liquids in tanks

g: acceleration due to gravity

C_D: coefficient for turning

V: vessel speed

KG: centre of gravity

T: draft of vessel

φ: angle of inclination

Δ: displacement

LWL: length of waterline

P: weight of passenger

2.3 English Navy Rules (NES109)

Basically, in accordance with NES109 stability criteria depend on the areas under righting and heeling arm curves, the ratio of these areas, the equilibrium angle of the two curves and the ratio of arm's value at the equilibrium angle and the maximum righting arm (GZmax). In addition of these criteria it has some other requirements. For example the value of GM, GZ_{MAX}, and the area of from 30° to 40° etc. (NES109, 2000)

Formulas in order to calculate heeling arms are same as the DDS079. But it has different notations and different limitations. In the Figure 3 classically; the areas and the curves are shown.

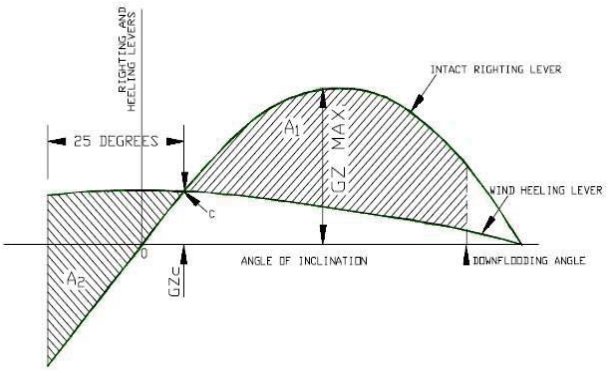

11. Figure 3. In regard to NES109 (2000) the areas and the arm curves

3. SPECIFICATIONS OF THE SHIP

12. Form used in analyses was designed by Sener (2012). This form has been designed conceptually in this study. During the design, from steel weight to weapon and electronic systems lots of parameters have been chosen, calculated and placed originally. In Table 1 the main values of the frigate are shown.

13. Table 1. Main values of the vessel

LOA	145	*m*
LPP	139	*m*
B_{MAX}	18,2	*m*
D	11,2	*m*
T	5,05	*m*
C_B	0,49	-
V	18	*knot*
V_{MAX}	30	*knot*

14. Figure 4 Subdivision of the frigate (Kahramanoglu, 2015)

15. In the Figure 3 the watertight bulkheads are shown on the vessel. The location of them has been settled by originally via taking into consideration experiments and other frigates (Kahramanoglu, 2015). But the damaged stability criteria are not considered when the locations are specified. Just the effect of this localization has been tried to observe on the different navy rules.

4. COMPARATIVE STABILITY ANALYSES IN WAVES

Calculations are made considering each navy rules. On the intact stability analysis, initially, all calculations are made for the calm water. Then a sinus wave which has the same length and direction with the vessel is sent to the vessel. The wave crest is moved from fore to aft step by step. The same methodology is also used for the damaged stability analyses. On the damaged stability analyses, the wave crest is also considered.

4.1 Basic Differences Between Navy Rules

There are some differences between the navy rules. The calculation method of heeling arms and the assumptions are different. Therefore the results of the same analyses differentiate for each navy. The effects of the basic differences on the results are the main aim of this study.

Table 2. Basic differences among navy rules

Parameter	DDS079	NES109	BV1030
Wind speed (intact) (knot)	100	90	90
Wind speed (damaged) (knot)	35	34	40
Roll back (intact)(deg.)	25	25	-
Roll back (damaged) (deg.)	10,5	15	-
Damage length (m)	20,58	25	18
Wave height (m)	7,126	7,126	8,2
Limit of Initial heeling angle (damaged) (deg.)	15	20	25

In the Table 2, the values are demonstrated. Some of them are calculated and some of them are assumed such as wave height with regard to navy rules. Wave height has been assumed equal to DDS079 because of their methodology's similarity.

Damage cases are directly related to damage extents. The damage length values can be seen Table 2.So, as it is seen in Table 3, the damage compartments are different for each navy rules for some damage cases. Thereby the damage cases differentiate. It is assumed that the longitudinal extent of damage starts the near of the bulkhead shown in Figure 2 and moved towards to fore of the vessel. The transverse extent of damage is limited by centre line. The vertical extent of damage is limited by main decks. These limitations are chosen with regard to all navy rules.

Table 3. Damage scenarios

Damage Scenario	Damaged Compartments		
	BV1030	NES109	DDS079
D1	1-2	1-2-3	1-2-3
D2	2-3	2-3-4	2-3
D3	3-4	3-4	3-4
D4	4-5	4-5	4-5
D5	5-6	5-6	5-6
D6	6-7	6-7-8	6-7
D7	7-8	7-8-9	7-8-9
D8	8-9	8-9	8-9
D9	9-10	9-10	9-10
D10	10-11	10-11	10-11

4.2 Intact Stability Analysis

All analyses are made for full load case. Firstly, analyses are carried out for calm water. Then they are repeated in waves. From fore to aft wave crest is moved 0.1*L step by step (Kahramanoglu, 2015).

16. In this section, effects of the beam winds, lifting of heavy weights and crowding passenger over the side, high speed turning and icing are investigated. In the figures some of the most critical results are shown. In Figure 5 effects of beam winds are shown. With respect to NES109 and DDS079 the ratios of areas are compared for different location of the wave crest.

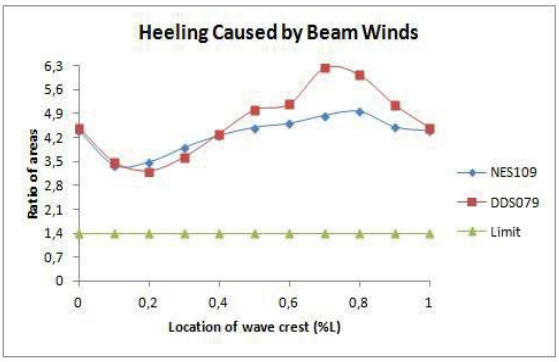

17. Figure 5. Ratio of areas when beam winds cause heeling

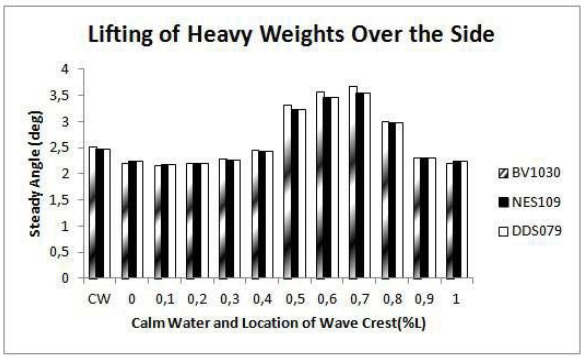

18. Figure 6. Effects of lifting of heavy weights over the side on the steady angle

In figure 6 the effects of lifting of heavy weights on steady angle are shown. In this figure the results of DDS079 and NES109 are the same because their calculation methods of heeling arm caused by lifting of heavy weights are the same. However, there are some differences for BV1030. The reason is that, the calculation method is different for BV1030. (2) and (7)

19. Effect of icing has similarities. For this section the calculation method and assumptions are different between NES109 and DDS079.

Therefore, the results differentiate. There are no extra criteria for BV1030 for icing. In Figure 7 and Figure 8 the differences of effects of icing are shown.

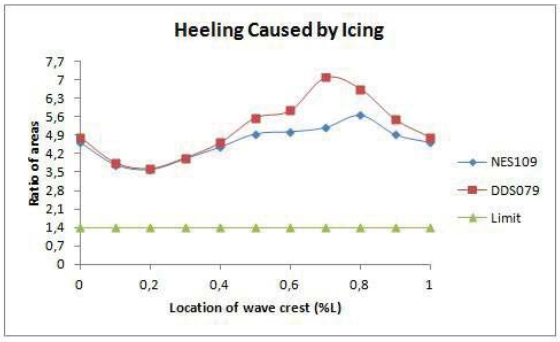

20. Figure 7. Ratio of areas when icing causes heeling

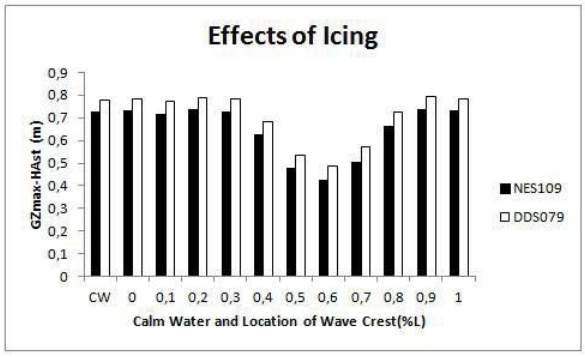

21. Figure 8. The differences about the arms when icing causes heeling

4.3 Damaged Stability Analyses

For damaged stability analysis the scenarios in Table 3 are used. The analyses are carried out for each navy rules. At first, all calculations are performed for calm water alike intact stability analyses. Then they are repeated for different location of the wave crest (Kahramanoglu, 2015).

In both intact and damaged stability analyses, it is considered that ship is operating in head wave condition in addition to calm water. With respect to all of three navies the damaged stability analyses are performed for damaged conditions. Wind is coming to the ship from beam direction in all cases while the wind velocity differs in regard to the navy rules. However, wind velocities are different from intact ones (Table 2). The criteria are about the angles, areas and the ratio of GZ_{MAX} and GZ_{ST} (=HA_{ST}) for NES109 and DDS079. However, for BV1030 the criteria of damaged stability are about the angles and residual arm alike intact one.

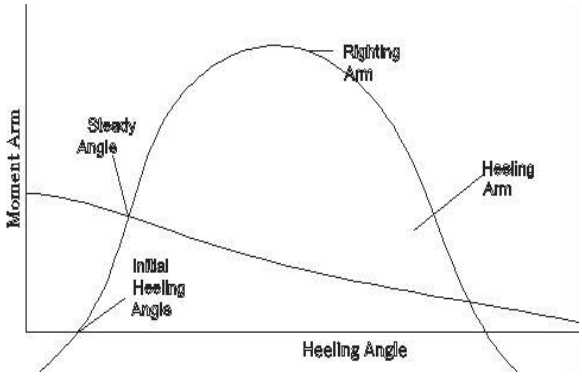

Figure 9. Initial heeling angle and steady angle in damaged stability analysis

In Figure 9 steady angle and the initial heeling angle are shown. These two parameters are crucial for each navy rules.

In Figure 10 and Figure 11, the steady angles and the initial heeling angles are shown for each navy rules and each damaged scenarios in calm water.

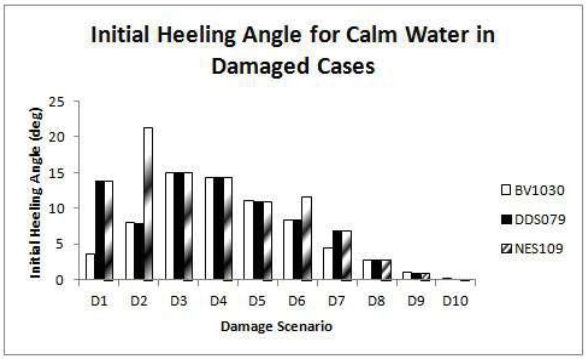

Figure 10. Initial heeling angle for calm water in damaged cases

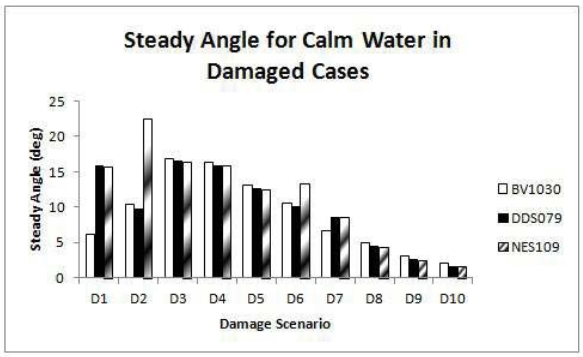

Figure 11. Steady angle for calm water in damaged cases

22. As can be seen from Figure 10 when number of damaged compartments is also same, the initial heeling angles are the same because this is related to vessel's hull form and distribution of weights. Figure 11 shows some differences for steady angles. This is related to the calculation of heeling arm in addition to vessel's hull form and distribution of weights.

Results of D1, D2, D6 and D7 scenarios are shown with more detail. Because these scenarios have differences in terms of initial heeling angle and steady angle and also they are more critic than the others (Kahramanoglu, 2015).

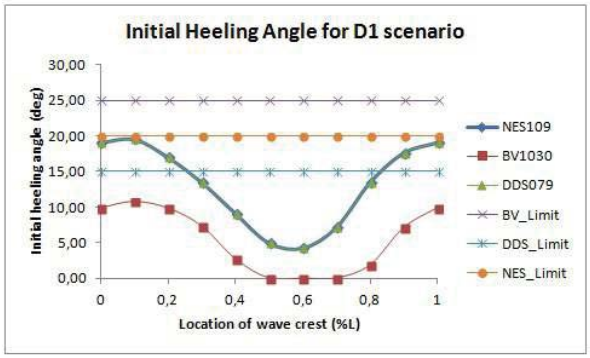

Figure 12. Initial heeling angle for D1 scenario

In Figure 12, initial heeling angles are shown for D1 scenario. It is observed that, the results of NES109 and DDS079 are the same. However, results of BV1030 are different and it can be also realised that the results of BV1030 are less than the others. All these results are just related to number of damaged compartments. For D1 scenario, NES109 and DDS079 have same number of damaged compartments which is more than BV1030 (Table 3).

In Figure 13, initial heeling angles are shown for D2 scenario. For this scenario, because NES109 has more damaged compartments than BV1030 and DDS079, its results are higher. Moreover when the location of the wave crest is between 0,6*L and 0,8*L, the criteria of damaged stability for NES109 is not adequate. The reason of differences between DDS079 and BV1030 is the wave height for this scenario (Table 2).

There are similarities between Figure 13 and Figure 14. As before the number of damaged compartments is higher for NES109. Because of this reason, the initial heeling angle values are higher. In addition to NES109, the criteria of damaged stability for DDS079 for D6 scenario are not adequate for some location of wave crest, too.

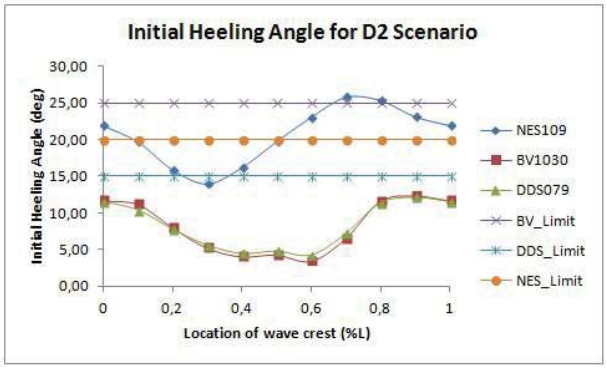

Figure 13. Initial heeling angle for D2 scenario

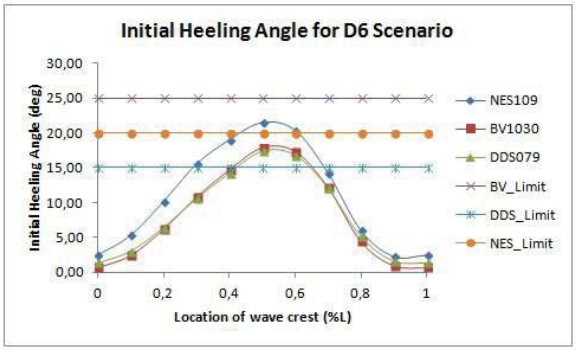

Figure 14. Initial heeling angle for D6 scenario

The results of other scenarios for initial heeling angle do not have significant differences between each other. The little differences' reason is the wave height (Kahramanoglu, 2015).

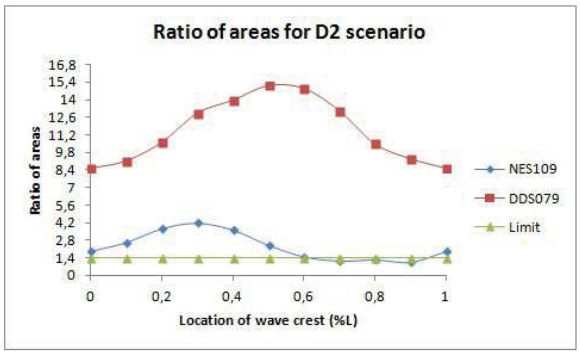

Figure 15. Ratio of areas for D2 scenario

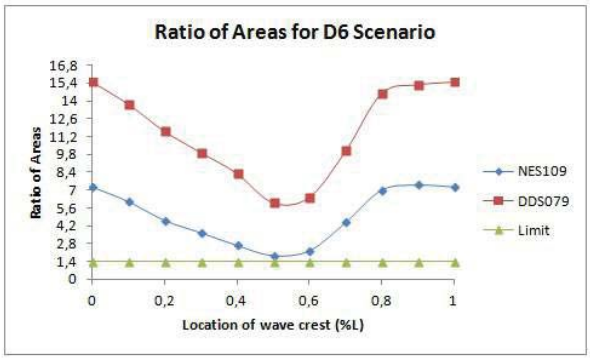

Figure 16. Ratio of areas for D6 scenario

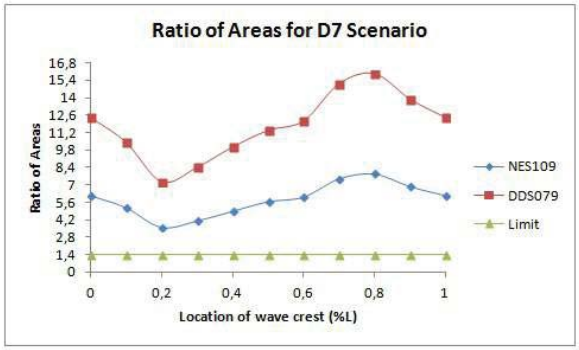

Figure 17. Ratio of areas for D7 scenario

When Figure 15 is examined, it can be realised that when the location of crest is between 0,6*L and 0,7*L the ratios of areas are lower than minimum value for NES109. It means that the stability requirements are not satisfied for NES109 when the location of crest is between 0,6*L and 0,7*L. However, according to DDS079 all the points satisfy the criteria. The reason of these differences is same as before ones. The calculation method of areas and the number of damaged compartment are different so the results differ.

In Figure 16, the reasons of differences are same with Figure 15. Moreover, the ratios are lower for NES109 for both figures.

In Figure 17, one of the reasons mentioned just before is disappeared. The number of compartments is the same for NES109 and DDS079 for D7 scenario. However, the values of NES109 are again lower. At this point, while it is known that the only difference is the calculation method of areas. The effects of the method can be picked out easily. The other scenarios' results for ratios are just same with D7 scenario.

5. CONCLUSIONS

For each navy rules, effects of beam winds are more important than the others for intact stability analysis. NES109 and DDS079 have more strict rules than BV1030 for intact stability.

For damaged stability analysis the most important parameter was length of damage. In this respect, NES109 had the maximum value and BV1030 is the minimum. Therefore, sometimes NES109 had more damaged compartments than BV1030 and sometimes it had more damaged compartments than BV1030 and DDS079. This has made it difficult to meet adequate stability criteria.

When present form and load case are taken into consideration;

- Satisfying criteria of initial heeling angle was more difficult than criteria of ratio of areas.
- Among three navy rules, BV1030 was the simplest to meet criteria.
- Because considering areas and being limit values higher, NES109 was the most suitable one (just for this form and loadcase)
- Location of wave crest was very important for stability analyses and the most critical points of it were a little bit forward from amidships and it is thought that it could be related to vessel's form.
- When damage was near amidships, it could be more critical for each navy rules.

6. REFERENCES

Lee, Y., Chan, H.S., Pu, Y., Incecik, A. and Dow, R.S., (2012). "Global Wave Loads on a Damaged Ship", Ship and Offshore Structures, 7:237-268.

Begovic, E., Mortola, G., Incecik, A. and Day, A.H.,(2013). "Experimental Assessment of Intact and Damaged Ship Motions in Head, Beam and Quartering Seas", Ocean Engineering, 72:229-236.

Chan, H.S., Atlar, M. and Incecik, A., (2003). "Global Wave Loads on Intact and Damaged Ro-Ro Ships in Regular Oblique Waves", Marine Structures, 16:323-344.

Hu, L.F., Ma, K. and Ji, Z., (2013). "A M-H Method-Based Decision Support System for Flooding Emergencies Onboard Warship", Ocean Engineering, 58:192-200.

Belenky, V., Bassler, C.C. and Spyrou, K.J., (2011). "Development of Second Generation Intact Stability Criteria", NSWCCD, 3-24.

Peşman, E. and Taylan, M., (2012). "Influence of Varying Restoring Moment Curve on Parametric Roll Motion of Ships in Regular Longitudinal Waves", Marine Science and Technology, 17:511-522

DDS 079-1, (2002). Stability and Buoyancy of U.S. Naval Surface Ships, Department of The Navy, Version 1.2.

NES 109, (2000). Stability Standards for Surface Ships, Ministry of Defence, Bristol.

BV1030, (2001). Construction Regulations for German Vessels 1030-1 Stability of Surface Combatants, Koblenz.

Sener, B., (2012). Developing of frigate type hull form series and hydrodynamic form optimization, PhD Thesis, YTU Institute of Science, Istanbul (in Turkish).

Kahramanoglu, E. (2015). Naval ships' intact and damaged stability analysis in waves, MSc. Thesis, YTU Institute of Science, Istanbul (in Turkish).

This page is intentionally left blank

Proceedings of the 12th International Conference on the Stability of Ships and Ocean Vehicles, 14-19 June 2015, Glasgow, UK.

Towing Test and Motion Analysis of a Motion-Controlled Ship - Based on an Application of Skyhook Theory

Jialin Han, *Doctoral Student, Department of Systems Innovation, School of Engineering, the University of Tokyo, Japan* kankarin@iis.u-tokyo.ac.jp
Teruo Maeda, *OPD Research Center* t-maeda@theia.ocn.ne.jp
Takeshi Kinoshita, *Adjunct Professor, Department of Oceanic Architecture and Engineering, College of Science and Technology, Nihon University, Japan* kinoshit@iis.u-tokyo.ac.jp
Daisuke Kitazawa, *Associate Professor, Institute of Industrial Science, the University of Tokyo, Japan* dkita@iis.u-tokyo.ac.jp

ABSTRACT

A novel–concept catamaran called the Motion-Controlled Ship (MCS) Type-6 is proposed. It consists of a cabin, two hulls, four suspension setting units as well as four relative dependence control system units. The cabin and hulls are separated by suspensions. By implementing adaptive control algorithms, the motion modulation of the cabin is realized. A hull-excited bench test is conducted to validate the function of the control systems, following which a model ship towing test is performed in regular wave conditions. The motion responses of the MCS in terms of heave, pitch and roll are analysed under five control algorithms at two different towing speeds. Compared to a rigid body catamaran (in which suspension systems are invalid), pitch is eliminated by a maximum of 93% and an average of 74.8% under certain test conditions.

Key Words: *Catamaran, Motion Control, Stability, Skyhook, Suspension System*

1. INTRODUCTION

Ride comfort plays an important role in ground vehicle evaluation. Numerous researchers have dedicated themselves to the investigation and improvement of devices for shock absorption or vibration elimination. Currently, suspension setting, which comprises springs and dampers, is commonly applied in such motion control systems.

Comparing road profiles to the ocean surface, one finds that the latter is much rougher and can easily lead to violent shaking; however, suspension settings have seldom been used in ocean vehicles to improve ride comfort and stability.

The development of a Motion-Controlled Ship (MCS) has been ongoing since 2008. The MCS Type-1, shaped similar to a tricycle, had

three small hulls and one big submerged float (Figure 1). One suspension setting, which consisted of a spring and an oil damper, was equipped between the cabin and one of the hulls. It was found that strong dampers had a relatively high efficiency in reducing the motion of the small hulls but had less effect on the cabin (Lu. 2010).

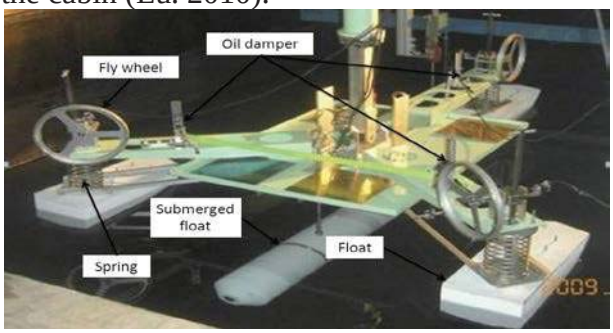

Figure 1 Structure of the MCS Type-1

The MSC Type-2 was a catamaran. It had two suspension setting units on each hull, located at the front and rear (Figure 2). The test results indicated that the reduction of the heave and pitch motions of the cabin was improved along with the increase of the damping coefficient when the towing speed was $1.5 m/s$. The results also suggested that the relative displacement between the cabin and hulls could produce sufficient kinetic energy to be reused (Tsukamoto. 2012).

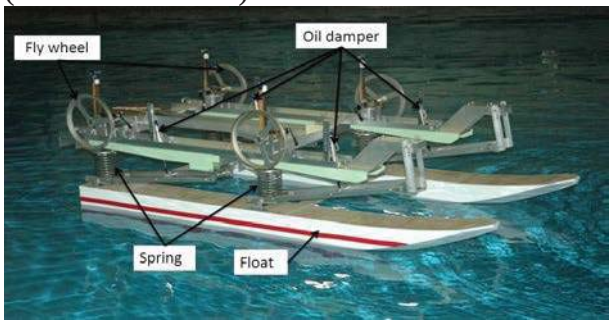

Figure 2 Structure of the MCS Type-2

Instead of oil dampers, the so-called electronic damper was formed and applied to the MCS Type-3 (Figure 3). A stepping motor was connected to a load resistor in series to construct an electrical circuit; by tuning the value of the resistance, the current in the circuit was made to vary and therefore the rotations of the motor shafts were adjusted. This affected the angular velocity of a pinion that meshed with a rack, leading to a change in the relative velocity between the cabin and hulls. This can be seen as an equivalent result of that obtained by damper tuning. A towing test was performed; it was shown that the ability of motion elimination increased along with the reduction of load resistance, which meant an increase in the damper coefficient. It also implied that a strategy of simultaneously enhancing motion control and energy harvesting is possible. A compromise between those aims is necessary and should be made according to the use of the ship (Han. 2013a).

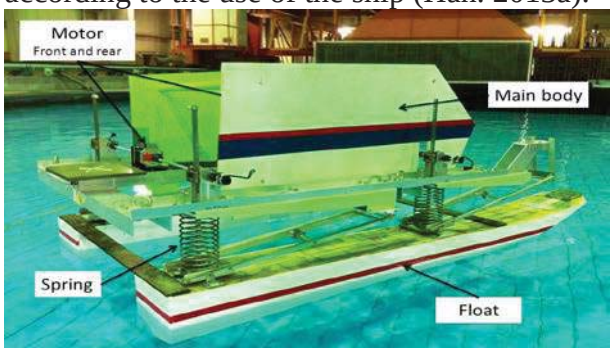

Figure 3 Structure of the MCS Type-3

A semi-active motion control system was developed for the MCS Type-4. The ship structure was similar to the Type-3, except the number of motors in one control system was increased from one to two. The control system analysed the feedback signals of the acceleration of the cabin as well as the relative velocity between the cabin and hulls, then determined whether or not to trigger the motion-control system. Through the inductive force generated by the motors, the heave and pitch of the cabin could be reduced. This was proved by a towing test. In the wave energy harvesting phase, the motors acted as generators, and a wave energy harvesting potential (defined as the ratio of the harvested energy to the wave energy contained by the crest over the width of the hulls) of 110% was achieved (Han. 2013b).

Between Type-2 and Type-4, the MCS can be seen as a high speed ship with hulls that planed on the sea surface. Type-5 adopted displacement type hulls.

In this paper, the MCS Type-6, which is equipped with a pair of displacement hulls, is introduced. The suspension settings are improved so as to yield roll motion. Based on an application of skyhook control theory, the model ship is tested and evaluated for its potential to eliminate heave, pitch and roll motion.

2. CHALLENGES OF THE MODEL

There are three challenges facing the design of the proposed novel catamaran. The first is motion separation between the cabin and hulls. A traditional ship has a rigid body, which generates motion in six degrees of freedom: translational motion—surge, yaw and heave; rotational motion—roll, pitch and sway. In our design, the two hulls are connected rigidly. By means of springs which are mounted between the cabin and hulls, the motion of the ship increases by up to 12 degrees of freedom. Considering the stability of the ship, the suspension supports are designed to refrain from generating phase differences in surge, sway and yaw between the cabin and hulls. Hence, a 9 degree-of-freedom model is proposed, the heave, pitch and roll of the cabin as well as those motion of the hulls; surge, sway and yaw of the whole ship. A blueprint for this design is given in Figure 4. It shows how the relative forward and lateral motions between the cabin and hulls are restricted.

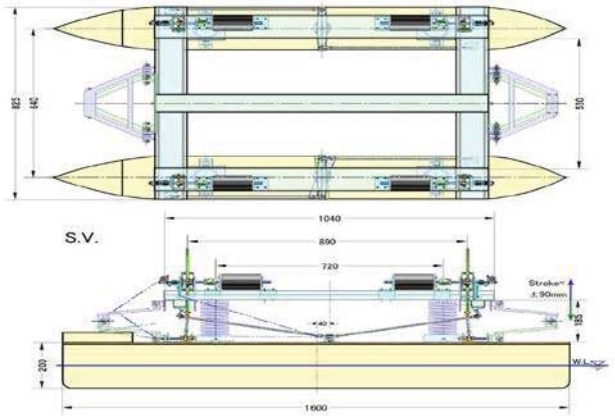

Figure 4 Blueprint of the MCS Type-6

The second challenge is effective power transfer between mechanical and electrical forms. To solve this, a crank and connecting rod (con-rod)-type mechanism is at first considered. A con-rod is connected to one of the hulls, while a crank rotates the motor shaft. Through testing, we find that the transmission efficiency from electrical to mechanical energy is unexpectedly low. Thus, we return to the former rack-pinion mechanism and attempt to make a modification. The final proposal, which adds an adding ball joint to the bottom of the rack to offer another degree of freedom for the roll motion of the cabin, is given in Figure 5.

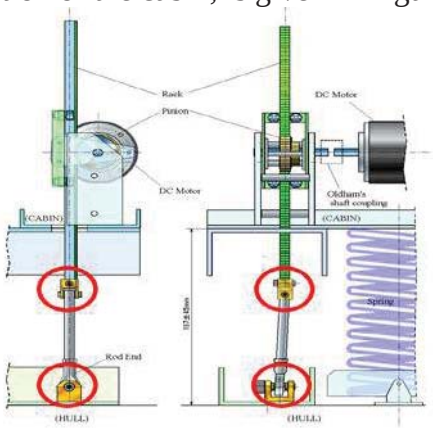

Figure 5 Configuration of the revised rack

The third challenge is high feasibility of motion-control system to achieve a certain level of stability of the cabin. In the model ship, there are four control spots, which work dependently along with the input signal of the acceleration at each spot. We assume that the cabin could simultaneously obtain its pre-concerted motion state, if the four control sports achieve their. More specific details will be introduced in the next section.

3. CONTROL ALGORITHMS

3.1. Skyhook Control Theory

For an ideal skyhook control, we consider a design consisting of a damper connected to a suspended mass and an inertial reference which is fixed in the sky. When the base reference is excited, the damper will provide a force to eliminate the motion of the mass. Although this is a purely imaginary configuration, it serves as

an inspiration for the design concept of the proposed motion control system.

In the model ship, the hulls are excited by waves. The wave force can be illustrated as a combination of a spring force (K_W) and a damping force (C_W). Meanwhile, the suspension system, set between the cabin and hulls, provides another spring force (K), while the motor fit on the cabin produces a reaction force meant to counteract the force that acts on the cabin. This skyhook-like dynamic configuration is shown in Figure 6.

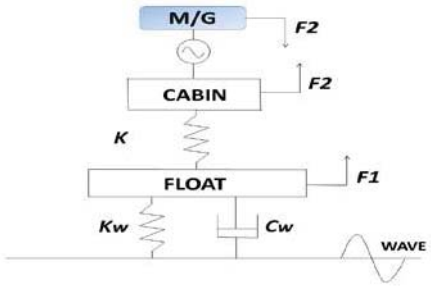

Figure 6 Configuration of the model ship dynamic

Specifically, when a spring starts to expand or contract from its neutral length, the motor applies power to restrain it (motor mode); when the spring expands or contracts to the normal length, the generator absorbs the spring power and converts it into electricity (generator mode); hence, the external force acting on the cabin is supposed to be zero.

3.2. DC Motor and Sensor

Considering the affordability of the control system, a brushed DC motor Maxon-353300, made by Maxon Japan Co. Ltd, is selected and tested. The stall torque of the motor is $1.41Nm$, the terminal resistance is 1.06Ω. The sensitivity of the G-sensor is $1.2V$ per gravitational acceleration.

3.3. PI Control System

Our control contains both proportional and integral elements and is therefore known as PI control. In P control the system acts in such a manner that the control effort is proportional to the error, while which of I control is proportional to the integral of the error.

In the current study, only I control is activated. The acceleration of the cabin is detected by a G-sensor and transferred to an integral operator to calculate the cabin's absolute velocity. The difference between the reference velocity (set to zero) and the cabin absolute velocity is analysed. By tuning the gain of the I control, the instruction signal measured in voltage (V_{out}) is varied. This signal is fed to the motor and determines the value of the torque force it generates. Such torque force acts on the hull through a rack-pinion unit that eventually restrains the motion of the cabin. Therefore a new acceleration is generated, and causes the control circle to repeat until the current velocity of the cabin reaches 0m/s, this procedure is shown in Figure 7.

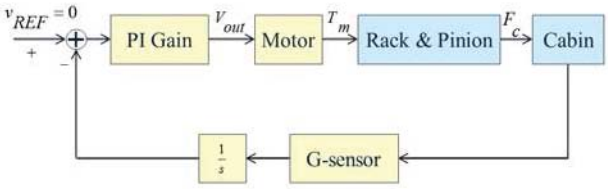

Figure 7 PI control procedure

4. HULL-EXCITED BENCH TEST AND SIMULATION

A hull-excited bench test is performed to validate the proposed skyhook control system, simplified to one degree of freedom.

4.1 Experiment Setting

An oscillation machine is settled on a heavy steel framework (Figure 8). The oscillation operator is connected to a metal support on which the model ship rides. The hulls are tightly tied to the bottom of the metal support, when the oscillation machine exerts a force at the centre of gravity of the frame-ship structure, the hulls move along with the metal support,

therefore yielding heave motion in the cabin.

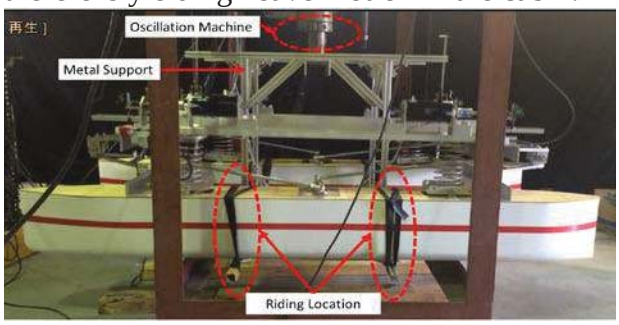

Figure 8 Experimental set-up of the bench test

4.2 Experiment Conditions

A simulation model with one degree of freedom is built in LTspice®, which is an open source analogue electronic circuit simulator produced by the semiconductor manufacturer Linear Technology (LTC).

The value of the mechanical friction is estimated in two steps. First, the skyhook control system is eliminated; therefore a simple mass-spring-mass structure is constructed. Under this condition a bench test is implemented and the heave response of the cabin is recorded. Second, tuning the value of the friction in the simulation program until the similar motion response of the cabin is obtained. The value of friction is determined at this point.

The I-gain (G_I) based on the design of our PI control system is expressed as a multiplication of several components, shown in Equation (1):

$$G_I = G_G \times G_{IC} \times G_{PA} \times G_A \tag{1}$$

where G_G is the gain of the G-sensor, equal to $0.122V/(m/s^2)$; G_{IC} is the gain of the integrator circuit, expressed as $25s^{-1}$ (s is the Laplace Operator); G_{PA} is the gain of a power amplifier, equal to 4; G_A is the gain of an adjusting unit, which is a ratio of a reference resistance ($47k\Omega$) to R_{sky}. Note that R_{sky} is an adjustable resistance, so G_I therefore can be described as

$$G_I = 573.4 / (s \cdot R_{sky}) \tag{2}$$

Here, R_{sky} can be seen as a medium for modulating the magnitude of the PI control system. According to the test results, we find that if R_{sky} is smaller than $4k\Omega$, an unstable motion is observed for the cabin. Therefore, we consider that $4k\Omega$ is the threshold value of R_{sky}. In order to make a comparison between the performance of several skyhook control conditions, another two R_{sky} are decided: $10k\Omega$ and $20k\Omega$. The equivalent I-gains of these cases are 143.35, 57.34 and 28.67, respectively.

The stroke amplitude of the hulls is set as $3cm$, while frequency is $0.8Hz$, $1.0Hz$, $1.2Hz$ and $1.4Hz$.

4.1 Experimental Results

The results of the bench test and the simulation for the dimensionless heave and power consumption are shown in Figure 9 to Figure 12. The x-axis represents stroke frequency, while y-axis is either dimensionless heave or power consumption.

In Figure 9, it is found that among the three resistances, $R_{sky} = 4k\Omega$ shows the strongest motion-elimination ability, reducing the heave by more than 50%. When R_{sky} gets bigger, such elimination ability gets weaker. Moreover, in the same control algorithm, a higher stroke frequency achieves better motion elimination. The heave motion is mitigated to 20.5% when $R_{sky} = 4k\Omega$ and $f = 1.4Hz$.

In Figure 10, the simulation results show the same trend, along with the variety of R_{sky} and f. However, compared to Figure 9, a significant deviation of the magnitude of heave is observed, which might be caused by the rough estimation of the friction or other unconsidered factors.

In Figures 11 and 12, it is easy to determine

that when $R_{sky} = 4k\Omega$, the power consumption maintains its highest level, which decays if R_{sky} grows bigger. This proves that in order to achieve better motion control, more power consumption is necessary. The power can be seen as partially used to maintain the stability of the cabin and partially devoted to overcoming friction. Note that the stability in the bench test is worse than that in the simulation, which implies that the power consumption should be smaller. However, the overall power consumption in the bench test is higher than that in the simulation, suggesting that more power is consumed in overcoming friction during the test than the simulation. This conclusion agrees with the inference in the above motion analysis.

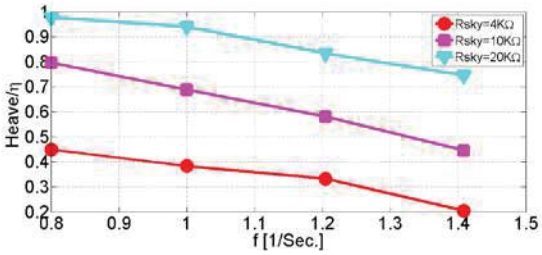

Figure 9 Dimensionless heave in bench test

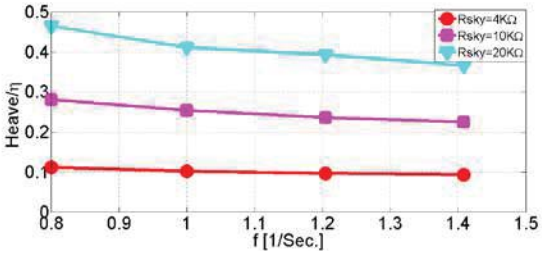

Figure 10 Dimensionless heave in simulation

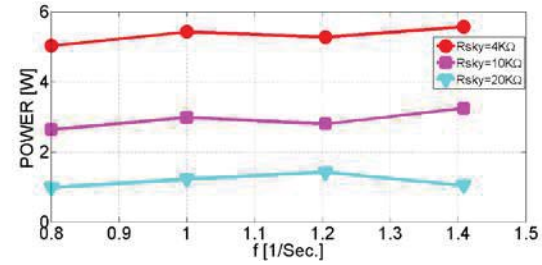

Figure 11 Power consumption of bench test

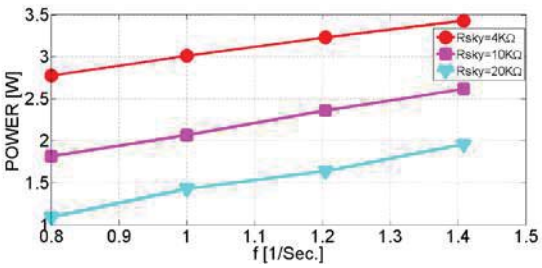

Figure 12 Power consumption of simulation

4.3 Conclusions

Through the comparison between the simulation and the bench test, the one-degree of-freedom control system was evaluated. Conclusions can be summarized as:

- The control circuit and control panel are well-designed and the blushed DC motor is well functioned. Four one-degree-of-freedom control system sets perform reasonably.
- Higher I-gain produces better heave motion reduction. $R_{sky} = 4k\Omega$ is currently the optimal skyhook control condition and could be adopted as a test condition in the towing tank test.
- A better motion control strategy consumes more power.
- The friction of the ship structure should be discussed further so as to improve the accuracy of the simulation program.

5. TOWING TEST AND RESULTS

5.1 Model Ship Specifications

The components and the structure of MCS Type-6 are given in Figure 13. The model ship is $1.6m$ in length and $0.83m$ in width. The weight of the cabin session is $34.71kg$, which of the hulls session is $13.14kg$. The mass of the suspension parts is equally distributed into those two sessions. The spring constant is $615N/m$ and water surface is $0.498m^2$. The locations of the four control spots are arranged symmetrically $0.445m$ from the centre of gravity of the hulls from bow to stern.

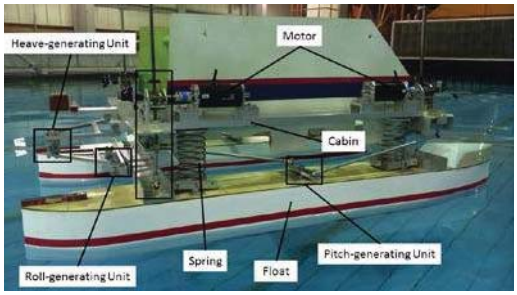

Figure 13 Structure of the MCS Type-6

5.2 Experiment Descriptions

A towing test was performed in December 2014, at Ocean Engineering Basin in the Chiba Campus of the University of Tokyo.

In order to evaluate the efficiency of the skyhook control system, a rigid body catamaran is used as a reference model. By connecting the cabin and the hulls with four metal plates, the suspension system was invalid, therefore an equivalent model of rigid body catamaran is formed, called Rigid Body mode.

Control OFF mode, is a test condition when the skyhook control system is turned off, by only letting springs be functioned.

Skyhook control algorithms are $R_{sky} = 4k\Omega$, $10k\Omega$ and $20k\Omega$, which are the same as the bench test.

The towing test is performed in regular wave conditions which are listed in Table 1 and Table 2. The direction of wave propagation β is $180°$ and $90°$ .. Due to the limitation of the towing tank, the towing speed is chosen as 0.0m/s and 1.5m/s .

Table 1 Regular wave conditions $\beta = 180°$

Wave Period [sec]	Frequency [Hz]	Wave Amplitude [cm]	Wave slope
0.67	1.5	1.12	
0.77	1.3	1.47	
0.83	1.2	1.71	0.100
0.91	1.1	2.06	
1.00	1.0	2.48	
1.11	0.9	3.06	
1.25	0.8	1.94	
1.43	0.7	2.54	0.050
2.00	0.5	4.97	

Table 2 Regular wave conditions $\beta = 90°$

Wave Period [sec]	Frequency [Hz]	Wave Amplitude [cm]	Wave slope
0.67	1.5	1.12	
0.77	1.3	1.47	
0.83	1.2	1.71	
0.91	1.1	2.06	0.100
1.00	1.0	2.48	
1.11	0.9	3.06	
1.25	0.8	3.88	
1.43	0.7	5.08	
2.00	0.5	4.97	0.050

5.3 Motion Responses

The results of the heave, pitch and roll of the cabin are given from Figure 14 to Figure 19. The x-axis represents the encounter wave frequency, while the y-axis represents dimensionless value.

When $\beta = 180°$, Control OFF mode shows the biggest motion response and significant resonances are observed. Compared to the rigid body mode, control modes show several levels of reduction in heave and pitch motion, the potential of which increases along with the decrease of R_{sky} . In other words, $R_{sky} = 4k\Omega$ shows the best motion elimination. It agrees with the conclusion in the bench test.

When $\beta = 90°$, only the control mode in $R_{sky} = 4k\Omega$ is tested. Comparing the control mode to the rigid body mode, heave motion is greatly reduced, especially around the resonance frequency. However, in roll motion such reduction only appears around the resonance frequency. In other wave frequencies, rigid body shows relatively smaller motion response. In general, Control OFF mode

generates the largest motion magnitude.

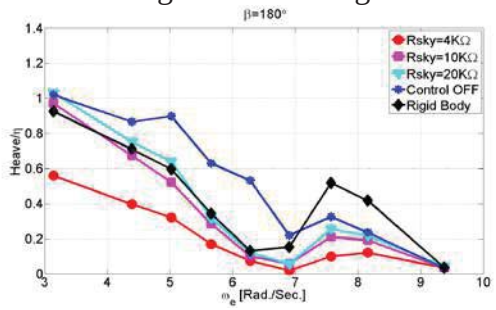

Figure 14 Dimensionless heave when $V = 0.0\text{m/s}$ at $\beta = 180°$

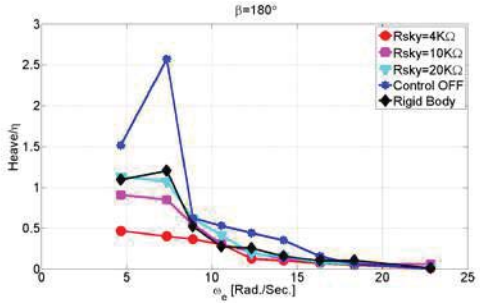

Figure 15 Dimensionless heave when $V = 1.5\text{m/s}$ at $\beta = 180°$

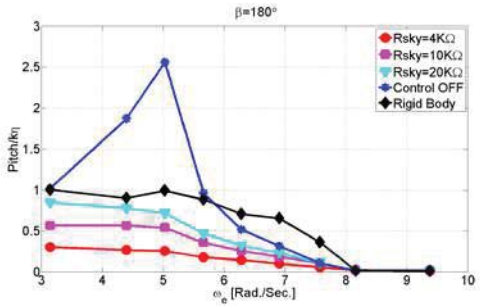

Figure 16 Dimensionless pitch when $V = 0.0\text{m/s}$ at $\beta = 180°$

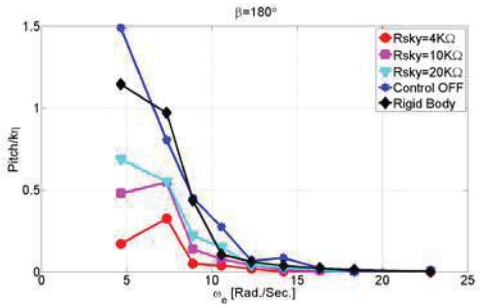

Figure 17 Dimensionless pitch when $V = 1.5\text{m/s}$ at $\beta = 180°$

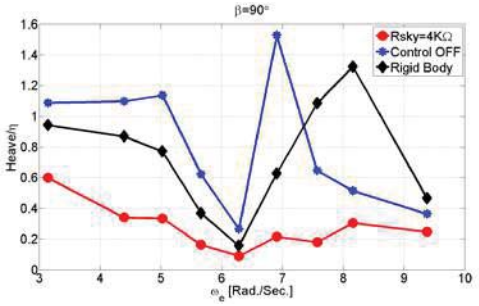

Figure 18 Dimensionless heave when $V = 0.0\text{m/s}$ at $\beta = 90°$

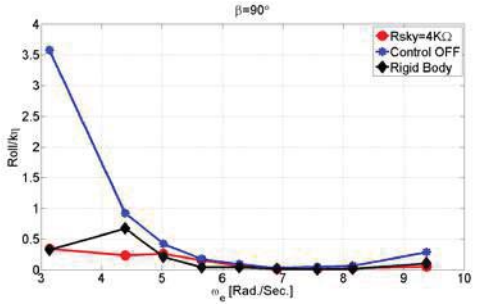

Figure 19 Dimensionless roll when $V = 0.0\text{m/s}$ at $\beta = 90°$

5.4 Stability Evaluation of the Cabin

A ratio of motion response in Control Mode against Rigid Body mode is applied as an index of stability evaluation, which is expressed as

$$Ratio = {ControlMode}/{RigidBodyMode} \times 100 \qquad (3)$$

The lower the ratio is, the better the stability represents. Assuming the benefit of a control mode is expressed in Equation (4). When the value is positive, a certain benefit is gained, otherwise a certain loss is obtained.

$$B = 100 - Ratio \qquad (4)$$

The results of the ratio are shown from Figure 20 to Figure 24. When $\beta = 180°$, in most of cases benefits are obtained. The highest benefit reaches up to 93% in pitch when $R_{sky} = 4k\Omega$, $V = 1.5\text{m/s}$, $\omega_e = 14.19\text{Rad/Sec}$.

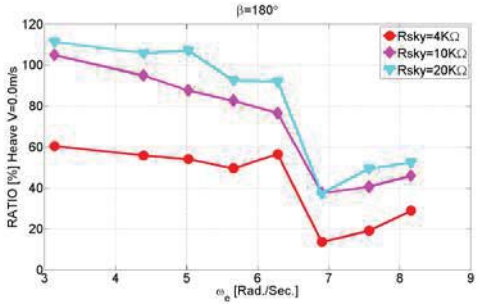

Figure 20 Stability of heave when $V = 0.0\text{m/s}$ at $\beta = 180°$

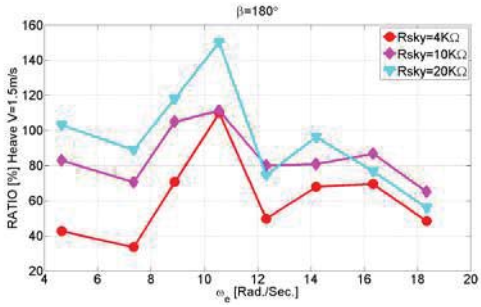

Figure 21 Stability of heave when $V = 1.5\text{m/s}$ at $\beta = 180°$

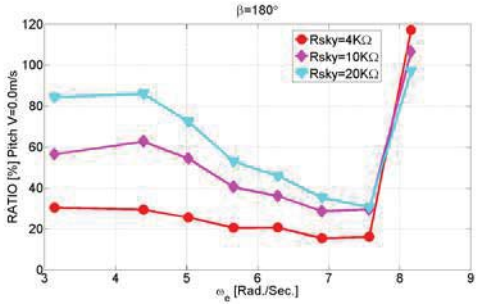

Figure 22 Stability of pitch when $V = 0.0\text{m/s}$ at $\beta = 180°$

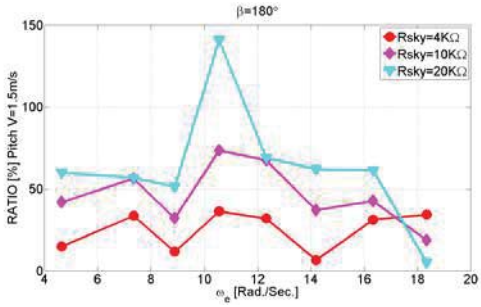

Figure 23 Stability of pitch when $V = 1.5\text{m/s}$ at $\beta = 180°$

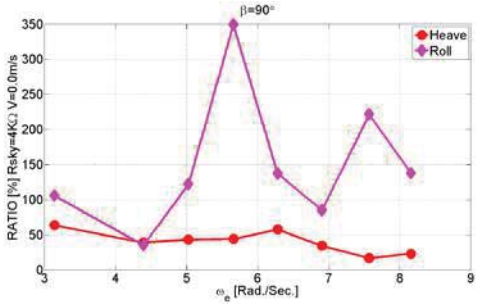

Figure 24 Stability of the cabin when $V = 0.0\text{m/s}$ at $\beta = 90°$

If the average benefit is given by

$$B_{avg} = \sum_{n=1}^{n=8} (100 - Ratio_n) \tag{5}$$

Then the B_{avg} at $R_{sky} = 4k\Omega$ can be summarized and shown in Table 3. An average benefit in pitch reaches up to 74.8%, when the towing speed $V = 1.5\text{m/s}$ and $\beta = 180°$. However, an average loss of 49.35% in roll is obtained when $V = 0.0\text{m/s}$ and $\beta = 90°$.

Table 3 Average benefit level at $R_{sky} = 4k\Omega$

$\beta = 180°$			$\beta = 90°$	
	0.0m/s	1.5m/s		0.0m/s
heave	57.7	38.5	heave	59.7
pitch	65.5	74.8	roll	-49.35

6. CONCLUSIONS

In the current study, a 1/5-scale model ship that contains suspension systems and brushed DC motors was tested and evaluated. A hull-excited bench test and a tank towing test were performed. The motion reduction of the heave, pitch and roll of the cabin under several control modes were validated.

The bench test showed that a reasonable heave motion reduction was obtained and the highest level reached up to 79.5% of reduction. A higher I gain in PI control algorithm, generated stronger motion elimination ability. However, because of the friction of the structure, extra power consumption was unavoidable. Further work will be required to understand friction control.

In the towing test, the optimal control algorithm agreed with the bench test, with an average benefit level of 74.8% in pitch when towing velocity is 1.5m/s. The peak reduction of pitch reached to 93% at a certain wave and control condition. However, this reduction was

not reproduced in roll motion.

In next step, the research might focus on improving the motion control system by developing an absolute position control model, and evaluating the motion responses in irregular wave conditions.

7. ACKNOWLEDGEMENT

I am sincerely grateful, to Mr. Yukitsugu Hirota who is a responsible, sophisticated and enthusiastic electro-dynamics expert and taught me a lot of principles about system controls and motors and to Mr. Hiroshi Itakura, an excellent technical staff member, who gave me sufficient support about parts manufacture and ship building.

The major part of this paper is based on results obtained from a project commissioned by the New Energy and Industrial Technology Development Organization (NEDO). A part of the paper was supported by Japan Society for the Promotion of Science (JSPS), Grant-in-Aid for Challenging Exploratory Research, 25630399.

8. REFERENCE

Jialin Han, Teruo Maeda, Takeshi Kinoshita, Daisuke Kitazawa, 2013a, “Towing Test and Analysis of an Oscillation Controlled Small Ship with Wave Energy Converters”, World NAOE Forum 2013 & International Symposium on Marine and Offshore Renewable Energy, Tokyo, Japan.

Jialin Han, Teruo Maeda, Takeshi Kinoshita, Daisuke Kitazawa, 2013b, “Research on a Motion-Controlled Ship by Harvesting Wave Energy–Based on a Semi-Active Control System”, The 6th East Asia Workshop for Marine Environment and Energy, Qingdao, China.

Chenliang Lu, 2010, “A Comfortable Boat with Suspensions Absorbing Wave Power”, Master Thesis, Department of Systems Innovation, School of Engineering, the University of Tokyo.

Daisuke Tsukamoto, 2012, “Basic research on a wave energy absorbing and motion-controlled ship”, Master Thesis, Department of Systems Innovation, School of Engineering, the University of Tokyo. (In Japanese)

Session 11.3 – EXTREME BEHAVIOUR

Statistical Uncertainty of Ship Motion Data

An Investigation into the Capsizing Accident of a Pusher Tug Boat

Rapid Ship Motion Simulations for Investigating Rare Stability Failures in Irregular Seas

Dynamic Instability of Taut Mooring Lines Subjected to Parametric Excitation

This page is intentionally left blank

Statistical Uncertainty of Ship Motion Data

Vadim Belenky, *NSWCCD (David Taylor Model Basin)*, vadim.belenky@navy.mil

Vladas Pipiras, *University of North Carolina at Chapel Hill*, pipiras@email.unc.edu

Kenneth Weems, *NSWCCD (David Taylor Model Basin)*, kenneth.weems@navy.mil

ABSTRACT

Records of nonlinear ship motion data, which are the basis for a probabilistic assessment of dynamic stability of a ship in irregular waves, are produced by time-domain numerical simulations or model tests in a basin. The volume of such samples is finite, so any statistical estimates calculated from a sample are random numbers and need to have a confidence interval, which quantifies the statistical uncertainty of the estimate. Ship motion data samples generally come in the form of an ensemble of records for a given condition, in which dependence may be very strong within the record, while the records themselves are independent of one another.

Since multiple data points describe the same feature of the process, statistically dependent data usually contains less information in comparison to independent data, so the confidence interval is wider for a set of dependent data than for the same amount of independent data. The paper revisits known mathematical methods to account for data dependency in computing the variance of the mean estimate and the variance of the variance estimate, which are the basis for computing a confidence interval of these estimates. The paper also addresses the calculation of the variance of the mean and variance of the variance for an ensemble of independent records of different length. The issue of minimum record length is considered and it is shown that a record of any length can contribute to the ensemble estimates of mean and variance.

Keywords: *Confidence interval, Statistical estimate*

1. INTRODUCTION

The development of probabilistic models for the assessment of the dynamic stability of a ship requires a characterization of the nonlinear response of the ship to severe sea conditions. This characterization is generally based on time-domain numerical simulations or model-scale experiments in large, “random” waves derived from theoretical or experimental representations of severe ocean waves. The direct results of such model test or numerical simulation campaigns are presented as a set of time histories of ship motion in large amplitude, irregular waves.

As the waves are irregular, the time histories are records of a stochastic process of ship motions. The most basic statistical processing includes the estimation of the mean value and variance or standard deviation. These estimates are essentially random numbers, which tend to the true value as the volume of data increases. A confidence interval is a measure of how close the estimate is likely to be to the true value, and is presented as a range of values and a probability, $P_{\beta,}$ that the true value is within that range. For example, an estimate of standard deviation with its confidence interval can be presented as:

$$\hat{\sigma} = [\sigma_{low}; \sigma_{up} \mid P_{\beta}] \qquad (1)$$

It means that there is a P_β chance that the true value of the standard deviation is between the lower boundary σ_{low} and upper boundary σ_{up}. The confidence probability P_β is an *a priori* given or agreed value; P_β=0.95 is widely used for engineering purposes. The "hat" above a symbol indicates an "estimate", which is a random value. The absence of a "hat" indicates that the value is deterministic.

Engineering calculations will typically use the upper and/or lower values of the confidence interval as a bound of the actual expected value. For example, if a measure of the intensity of ship motion is needed for further assessment or calculation, the upper boundary of confidence interval can be used as a conservative value. A change to the confidence probability P_β allows the conservatism of the assessment to be "tuned" to a level appropriate for the task in hand. A larger P_β will result in a wider confidence interval for an estimate and a wider range of values for assessments based on that estimate, but reduce the likelihood that the true value of the assessment is outside of the computed range.

Confidence intervals are heavily used in validation as they enable the comparison of two estimates; this application aspect (among others) is considered in Smith and Zuzick (2015) and is outside of the scope of this paper. Another use for the confidence interval is in the planning of model tests and numerical simulations, as it can help to determine the number and length of model tests or simulation runs that are needed to achieve required accuracy; this type of application is also outside the scope of this paper.

The uncertainty of statistical estimates is of particular concern for assessments, which involve the prediction of extreme responses or low-probability events form non-linear time domain data. Since these assessments are fundamentally extrapolations, the uncertainty in the results will tend to be very sensitive to the uncertainty in the statistical characterization of the data. For this reason, the consideration of the statistical uncertainty of ship motions is an important part of the ONR project "A Probabilistic Procedure for Evaluating the Dynamic Stability and Capsizing of Naval Vessels" (Belenky, *et al.*, 2015).

2. CONCEPT OF ENSEMBLE

The ensemble is a set of ship motion data records which represent a single or narrow range of sea and operating conditions. By its definition, it presumes that more than one record may be needed. Why is this so?

- Limitations on record length; for model tests in a seakeeping basin, the limited size of the facility will limit the duration of any test run with forward speed. As a result, a single record may have too few wave encounters to assess motions. This will particularly be true for cases with high speed and/or following or quartering seas.

- Practical non-ergodicity; the nonlinearity of ship behavior may cause one run to be insufficient for a complete assessment, even if it is relatively long. A typical example is parametric roll in head seas (Reed 2011), for which a typical run in a linear basin did not provide the necessary variation in initial conditions for proper statistical characterization of parametric roll.

- Valid modeling of irregular waves for numerical simulation. The elevation, pressure and velocity field of the incident wave is generally modeled using Fourier series, where amplitudes are defined by spectra and phases are random. The duration for which such a model will produce statistically independent waves will depend on the number of frequencies used for the discretization of a spectrum (Belenky, 2011). Increasing the number of frequencies in the wave model incurs a significant computational cost, so a set of

relatively short records, each of which requires fewer wave frequencies, is computationally more efficient than one long record requiring many frequencies.

The records in ensemble are not necessarily of the same length. It is both difficult and unnecessary to ensure that experimental runs have exactly the same duration.

In the analysis of irregular wave motion data, the processes of waves and ship motions are assumed to be stationary. If the ship capsizes, the response of the "mast-down" ship will be fundamentally different for its upright response, which has to be considered as a violation of the stationarity of the motion process. Attempting to include pre-capsize, capsize and post-capsize motion as part of a single stationary process will make the required volume of the data impractical. As a result, the record has to be cut immediately prior to capsizing. Similarly, it may be necessary to truncate a model test run if variations in the speed or relative heading of the ship become too large. Both of these scenarios may result in records of different lengths.

Thus, the ensemble for a particular wave environment, speed and heading is an irregular data structure that can be described by a "nested array" defined as an array that contains other arrays as elements. To avoid confusion with typical matrix notation, the following nomenclature will be used:

$$X = [x_i]_j \; ; \quad i = 1,...Np_j \; ; \quad j = 1,..Nr \qquad (2)$$

The index within the square bracket refers to a data point within a record while the index outside of the square brackets relates to the record number. An example data structure is illustrated in Figure 1.

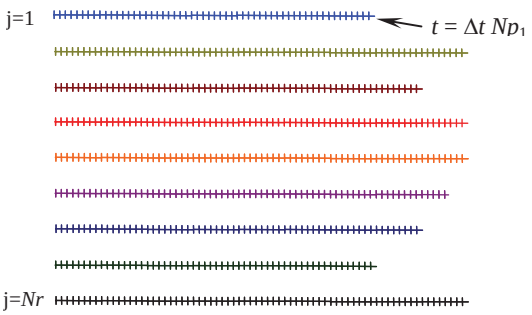

Figure 1: Illustration of a nested array

The data points within each record are dependent, while no dependence in expected between the records. Dependence between the data points is a result of inertia of ship motions, hydrodynamic memory and inertia of water particles in wave. Independence between simulation records is ensured by using different pseudo-random sets of initial phases in the model of the irregular waves. Independence between model test records is supported by the pseudo-random actuation of the wave maker and by the time lag between runs; this time usually is sufficient for the waves to be radiated and decay on the damping beach of a basin.

The combination of dependent and independent data within a single sample is specific to ship motion data.

3. ESTIMATES FOR A SINGLE RECORD

The consideration starts with examining mean value and variance estimates and their confidence interval for a single record. To simplify the notation, the square brackets and record index are not used in this section.

3.1 Dependence and Uncertainty

Consider the mean value and variance estimates.

$$\hat{E} = \frac{1}{Np} \sum_{i=1}^{Np} x_i \qquad (3)$$

$$\hat{V} = \frac{1}{Np-1}\sum_{i=1}^{Np}\left(x_i - \hat{E}\right)^2 \qquad (4)$$

The dependency within a record does not matter for these estimates. Changing the sampling rate or time increment will change the number of data points, but it will be reflected in the number *Np*. As long as the time increment remains within the reasonable range, *e.g.* it does not become large compared to the response period of the ship, the estimates (3) and (4) are affected very little.

This is not true for the confidence interval. The confidence interval is a metric of statistical uncertainty, which generally decreases with an increased volume of the sample. Theoretically, the width of the confidence interval goes to zero when the volume of the sample becomes infinite, because the estimate becomes a true value. Increasing the sampling rate does not increase the amount of information available in the sample; however the number of data points becomes larger. The data points become closer to each other. Since the same information is carried by more points, the dependence between data points becomes stronger, and the contribution of each of them is decreased.

Conversely, if the increment between the data points is increased, their dependence is decreased and the contribution of each individual data point becomes larger. Further increase of the increment (decrease of the sampling rate) should lead to independence. Once the independence is achieved, the contribution of each data point can no longer be affected by other points. This means that the number of independent points will define the amount of information available in the sample. The dependence between the data points may therefore have a serious effect on uncertainty and the width of the confidence interval. The mathematical treatment of this influence is considered further.

3.2 Variance of the Mean Value

Estimates of the mean value and variance of the process *X* are random numbers and, as any other random numbers, may have a variance. Priestley (1981) gives a general direction for the derivation of the formulae for the variance of mean value and variance estimates. That derivation was reproduced in Belenky *et al.* (2013) in order to examine the role of the assumption of normal distribution for *X*. An abridged version of this derivation in included below for the sake of completeness.

Apply a variance operator to both sides of equation (3) and treat the sum as if the values are dependent, so the variance of the sum is a sum of all of the terms of the covariance matrix:

$$\mathrm{var}\left(\hat{E}\right) = \mathrm{var}\left(\frac{1}{Np}\sum_{i=1}^{Np} x_i\right) = \frac{1}{Np^2}\sum_{i=1}^{Np}\sum_{j=1}^{Np} Cov(x_i, x_j) \qquad (5)$$

Var(..) is the variance operator and *Cov*(..) is the covariance operator. Since the process *X* is assumed to be stationary, its auto-covariance function depends only on the difference in time (time lag) between the two points and does not depend on particular time instances:

$$Cov(x_i, x_j) = R(t_{i-j}) = R(\tau_k) \qquad k = 0, 1..., Np-1 \qquad (6)$$

Consider a sum of all the elements of the covariance matrix in Equation (5):

$$\sum_{i=1}^{Np}\sum_{j=1}^{Np} Cov(x_i, x_j) = \qquad (7)$$

$$\sum \begin{pmatrix} R(\tau_0) & R(\tau_1) & \dots & R(\tau_{N-2}) & R(\tau_{N-1}) \\ R(\tau_1) & R(\tau_0) & \dots & R(\tau_{N-3}) & R(\tau_{N-2}) \\ \dots & \dots & \dots & \dots & .. \\ R(\tau_{N-2}) & R(\tau_{N-3}) & \dots & R(\tau_0) & R(\tau_1) \\ R(\tau_{N-1}) & R(\tau_{N-2}) & \dots & R(\tau_1) & R(\tau_0) \end{pmatrix}$$

The elements of the main diagonal are variances:

$$R(\tau_0) = R(0) = V \tag{8}$$

The other elements on the line parallel to the main diagonal are also the same; the next element to the term $R(\tau_0)=V$ is always $R(\tau_1)$, then $R(\tau_2)$ and so forth. The main diagonal of a $Np \times Np$ square matrix contains Np elements. The lines of elements parallel to the main diagonal and located next to it contain only Np-1 elements. Each subsequent line will have one fewer element, until diagonals at the low-left or upper-right corner have only one element. Having in mind that the covariance matrix is symmetric relative to its main diagonal and all the "lines of elements" except the main diagonal are encountered twice:

$$\sum_{i=1}^{Np}\sum_{j=1}^{Np} Cov(x_i, x_j) = Np \cdot V + 2\left((Np-1)R(\tau_1) + (N-2)R(\tau_2) + \ldots + R(\tau_{N-1})\right) = Np \cdot V + 2 \cdot \sum_{i=1}^{Np-1}(N-i)R(\tau_i) \tag{9}$$

Substitution of Equation (9) into Equation (5) leads to the standard formula for the variance of the mean value estimate (see *e.g.* Priestly 1981):

$$\mathrm{var}\left(\hat{E}\right) = \frac{V}{Np} + \frac{2}{Np} \cdot \sum_{i=1}^{Np-1}\left(1 - \frac{i}{Np}\right) \cdot R(\tau_i) \tag{10}$$

The first term in Equation (10) is actually the variance of the mean estimate of a random variable, while the second term accounts for the dependence between the data points of a stochastic process. As expected, if the process X is uncorrelated white noise (Wiener process), the result is identical to the one for a random variable, because the auto-covariance function of the white noise equals zero for all non-zero time lags.

3.3 Variance of the Variance

Variance is, by definition, the average of centered squares, so a process Y is introduced as:

$$y_i = \left(x_i - E\right)^2 \approx \left(x_i - \hat{E}\right)^2 \tag{11}$$

The estimate of the mean value of the process Y is the estimate of the variance of the original process x:

$$\hat{E}_y = \hat{V} \tag{12}$$

The variance of the mean estimate of the process Y is then the variance of the variance estimate of the process X:

$$\mathrm{var}\left(\hat{V}\right) = \frac{V_y}{Np} + \frac{2}{Np} \cdot \sum_{i=1}^{Np-1}\left(1 - \frac{i}{Np}\right) \cdot R_y(\tau_i) \tag{13}$$

V_y and R_y are, respectively, the variance and the auto-covariance function of the process of centered squares Y.

The standard formula for the variance of the variance (*e.g.* Priestley 1981) uses the assumption that the process X is normal, which leads to

$$\mathrm{var}\left(\hat{V}\right) = \frac{2V^2}{Np} + \frac{4}{Np}\sum_{i=1}^{Np-1}\left(1 - \frac{i}{Np}\right)\left(R(\tau_i)\right)^2 \tag{14}$$

Because for the normal process

$$V_y = 2 \cdot V^2 \; ; \quad R_y(\tau) = 2 \cdot \left(R(\tau)\right)^2 \tag{15}$$

Reed (2011) uses an alterative form of (14):

$$\mathrm{var}\left(\hat{V}\right) = \frac{2}{Np}\sum_{i=-(Np-1)}^{Np-1}\left(1 - \frac{|i|}{Np}\right)\left(R(\tau_{|i|})\right)^2 \tag{16}$$

As noted in Belenky, *et al*. (2013), there is no apparent reason to use the normal assumption for the process X. The calculation of the auto-covariance function of the centered squares requires little additional computation effort in comparison with the straight auto-covariance function.

3.4 Estimate of Auto-Covariance

To use Equations (10) and (13), it is necessary to estimate the auto-covariance functions of the processes *X* and *Y*. The estimate is expressed as:

$$\hat{R}'(\tau_i) = \frac{1}{Np-i}\sum_{j=1}^{Np-i}(x_j - \hat{E})(x_{j+i} - \hat{E}) \qquad (17)$$

Accuracy of the estimate (17) deteriorates very quickly for larger time lags due to insufficient data – as the time lag gets larger there are fewer pairs of data points with that time lag. This leads to statistical "noise" as shown Figure 2. This is obviously noise as there is no reason why the dependence could that strong after 500 seconds.

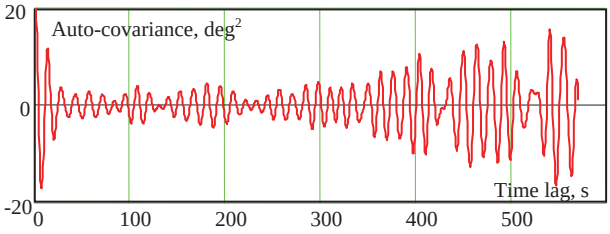

Figure 2 Estimate of auto-covariance function

This loss of accuracy can be alleviated by a simple weighting factor: (*Np*-*i*)/*Np*. Such weighting results in little change to the auto-covariance function for small time lags as the difference between *Np* and *Np*-*i* is not significant for small *i*. When the index *i* becomes large, the amount of available data decreases and therefore the influence of its contribution also decreases. The weighted estimate is expressed as:

$$\hat{R}(\tau_i) = \frac{1}{Np}\sum_{j=1}^{Np-i}(x_j - \hat{E})(x_{j+i} - \hat{E}) \qquad (18)$$

The result of weighting the estimate of the auto-covariance function is shown in Figure 3. It is apparent that the amount of "noise" has subsided, while the initial part (first 100 seconds) has not changed very much. Details on the numerical example can be found in Belenky *et al.* (2013).

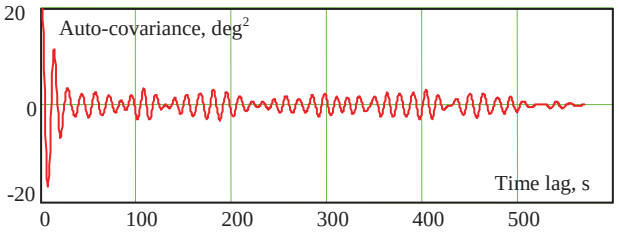

Figure 3 Weighted estimate of auto-covariance function

However, weighting the estimate may not be sufficient to get rid of all of the "noise". Cases are still possible when the "noise" makes the calculations completely senseless (*e.g.* producing negative value of the variance of the mean) if one uses the estimate (18) in formulae (10) or (13). Since the auto-covariance estimates at large lags are still not very reliable, they can be cut off, at a point designated *M*. Equations (10) and (13) are re-written as:

$$\hat{\mathrm{var}}(\hat{E}) = \frac{V}{Np} + \frac{2}{Np}\cdot\sum_{i=1}^{M-1}\left(1-\frac{i}{M}\right)\cdot\hat{R}(\tau_i) \qquad (19)$$

$$\hat{\mathrm{var}}(\hat{V}) = \frac{V_y}{Np} + \frac{2}{Np}\cdot\sum_{i=1}^{M-1}\left(1-\frac{i}{M}\right)\cdot\hat{R}_y(\tau_i) \qquad (20)$$

Belenky, *et al.* (2013) considered *M*=*Np*/2, which works well if the estimate of the auto-covariance is fairly accurate. Further review of the literature has led to (Priestly, 1981; Brockwell and Davis, 2008):

$$M = \sqrt{Np} \qquad (21)$$

Some sources also suggest $2\sqrt{Np}$ or $\sqrt{Np}/2$. The origin of this formula is optimality of spectral smoothing. The range $[0.5Np^{0.5}; 2Np^{0.5}]$ appears to represent an area where the result is not very sensitive to the specific value of *M*. The operation of cutting off the autocorrelation function is essentially the same as smoothing the spectral estimate. Spectral representations are a traditional way of processing ship motion information and can also be used for the estimate of the auto-covariance. However, the discussion of estimation of spectra is outside of the scope of this paper.

4. ESTIMATES OF AN ENSAMBLE

4.1 Estimate of Mean and Variance

Consider an ensemble of *Nr* records, each of which has Np_j data points. The time increment Δt is assumed to be the same for all the records, which is the usual practice for both numerical simulations and model tests. The statistical weight for each record is expressed as follows:

$$W_j = \frac{Np_j}{Nt} \tag{22}$$

Nt is the total number of points in the ensemble:

$$Nt = \sum_{j=1}^{Nr} Np_j \tag{23}$$

The ensemble estimate for the mean value is calculated for all of the points:

$$\hat{E}_a = \frac{1}{Nt}\sum_{j=1}^{Nr}\sum_{i=1}^{Np_j}[x_i]_j = \frac{1}{Nt}\sum_{j=1}^{Nr}\frac{Np_j}{Np_j}\sum_{i=1}^{Np_j}[x_i]_j = \sum_{i=1}^{Nr} W_i\left(\frac{1}{Np_j}\sum_{i=1}^{Np_j}[x_i]_j\right) = \sum_{i=1}^{Nr} W_i\hat{E}_i \tag{24}$$

$\hat{E}_j$ is the mean value estimate for a record *j*. The ensemble estimate of the variance is:

$$\hat{V}_a = \frac{1}{Nt-1}\sum_{j=1}^{Nr}\sum_{i=1}^{Np_j}\left([x_i]_j - \hat{E}_a\right)^2 = \sum_{i=1}^{Nr} W_j'\hat{V}_j' \tag{25}$$

$$\hat{V}_j' = \frac{1}{Np_j - 1}\sum_{i=1}^{Np_j}\left([x_i]_j - \hat{E}_a\right)^2 \tag{26}$$

$$W_j' = \frac{Np_j - 1}{Nt - 1} \tag{27}$$

The weights (27) are slightly different from (22). However, as the number of points is quite large (thousands and tens of thousands), one can state that

$$W_j \approx W_j' \tag{28}$$

Note that the variance estimate in (26) is not exactly the same as the record variance estimate from (4), as it uses the ensemble mean estimate instead of record mean estimate.

4.2 Estimate of Auto-Covariance Function

As the records may have different length, the estimate of the auto-covariance function (18) is padded with zeros to facilitate averaging across the record:

$$[\hat{R}_m]_j = \frac{1}{Np_j}\begin{cases}\sum_{i=1}^{Np_j-m}([x_i]_j - \hat{E}_a)([x_{i+m}]_j - \hat{E}_a) & i+m < Np_j \\ 0 & i+m \geq Np_j\end{cases} \qquad m = 1,..,\max\left(Np_j\right) \tag{29}$$

Like the data, the record estimate of the auto-covariance is presented in a form of nested array, with *j* being the index of record, while *m* is the index of the time lag. Since they have been padded by zeros, all of the record estimates of the auto-covariance function have the same length.

The ensemble estimate of the auto-covariance function is obtained by averaging across the records (assuming that if very short records are present in the ensemble, their statistical weight is small):

$$\hat{R}_a(\tau_m) = \sum_{j=1}^{Nr} W_j[\hat{R}_m]_j = \frac{1}{Nt}\sum_{j=1}^{Nr}\sum_{i=1}^{Np_j-m}\begin{cases}([x_i]_j - \hat{E}_a)([x_{i+m}]_j - \hat{E}_a) & i+m < Np_j \\ 0 & i+m \geq Np_j\end{cases} \tag{30}$$

Note that for *m*=0, equation (30) yields an expression identical to the formula for ensemble averaged variance. The averaging procedure significantly decreases the amount of "noise", as illustrated in Figure 4.

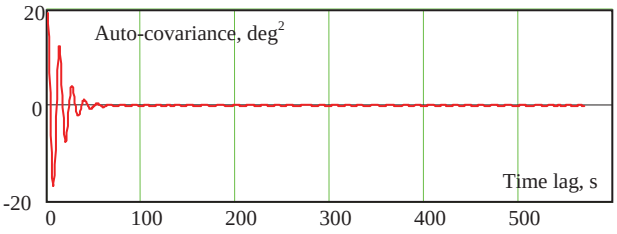

Figure 4 Ensemble-averaged estimate of auto-covariance function (Belenky *et al.*, 2013)

The formula for the ensemble averaged estimate for the process Y (the process of the centered squares) is similar to equation (30):

$$\hat{R}_{Ya}(\tau_m) = \frac{1}{Nt}\sum_{j=1}^{Nr}\sum_{i=1}^{Np_j-m}\begin{cases}([y_i]_j - \hat{V}_a)([y_{i+m}]_j - \hat{V}_a) & i+m < Np_j \\ 0 & i+m \geq Np_j\end{cases} \quad (31)$$

The ensemble-averaged estimate of auto-covariance function of centered squared for an example set of roll data is plotted in Figure 5.

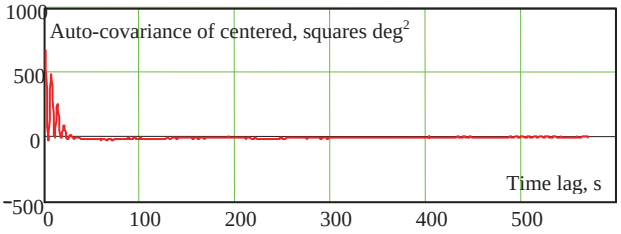

Figure 5: Ensemble-averaged estimate of auto-covariance function of centered squares (Belenky *et al.*, 2013)

4.3 Variances of Mean and Variance

In order to get the variance of the ensemble-averaged mean estimate, the variance operator is applied to both sides of equation (24):

$$\mathrm{var}\left(\hat{E}_a\right) = \mathrm{var}\left(\sum_{j=1}^{Nr} W_j \hat{E}_j\right) = \sum_{j=1}^{Nr} W_j^2 \,\mathrm{var}\left(\hat{E}_j\right) \quad (32)$$

$\mathrm{var}\left(\hat{E}_j\right)$ is the variance of the record mean value estimate, expressed with equation (19) where the auto-covariance function is estimated by equation (29). The cut-off point M can be taken for the ensemble:

$$M = \sqrt{\max(Np_j)} \quad (33)$$

Substitution of equations (19), (22) and (29) into (32) leads to:

$$\hat{\mathrm{var}}\left(\hat{E}_a\right) = \frac{1}{Nt}\sum_{j=1}^{Nr} W_j \hat{V}_j' + \frac{2}{Nt}\sum_{m=1}^{M}\left(1-\frac{m}{M}\right)\cdot\sum_{j=1}^{Nr} W_j [\hat{R}_m]_j \quad (34)$$

Here, the variance estimate (26) is used instead of the record estimate (4) for consistency with the auto-covariance estimate (29), so the ensemble mean estimate is used instead of record mean estimate.

Equations (25), (28) and (30) can be used to re-write equation (34) in terms of ensemble-averaged estimates:

$$\hat{\mathrm{var}}\left(\hat{E}_a\right) = \frac{\hat{V}_a}{Nt} + \frac{2}{Nt}\sum_{m=1}^{M}\left(1-\frac{m}{M}\right)\cdot\hat{R}_a(\tau_m) \quad (35)$$

A similar argument can be made for the ensemble-averaged variance of the variance estimate:

$$\hat{\mathrm{var}}\left(\hat{V}_a\right) = \sum_{i=1}^{Nr}\left(W_j'\right)^2 \mathrm{var}\left(V_j\right) \quad (36)$$

$$\hat{\mathrm{var}}\left(\hat{V}_a\right) = \frac{\hat{V}_{Ya}}{Nt} + \frac{2}{Nt}\sum_{m=1}^{M}\left(1-\frac{m}{M}\right)\cdot\hat{R}_{Ya}(\tau_m) \quad (37)$$

$\hat{V}_{Ya}$ is the ensemble-averaged estimate of the variance estimate of the process Y (centered squares) based on the ensemble-averaged mean value estimate:

$$\hat{V}_{Ya} = \hat{R}_{Ya}(0) = \frac{1}{Nt}\sum_{j=1}^{Nr}\sum_{i=1}^{Np_j}([y_i]_j - \hat{V}_a)^2 \quad (38)$$

4.4 Alternative Method for Variances of Mean and Variance

If the number of records is large enough, the variances of the mean and variance estimates can be computed without an auto-covariance estimate. Consider equation (32) for the special case where all of the records have the same length, so all the weights are the same and equal to 1/*Nr*. The theoretical values of the variances of the mean estimates $\mathrm{var}\left(\hat{E}_j\right)$ are the same for all the records. The variance of ensemble-averaged mean estimate for the records of the same length is expressed as:

$$\mathrm{var}\left(\hat{E}_a\right)=\frac{\mathrm{var}\left(\hat{E}_j\right)}{Nr} \tag{39}$$

If the bias is assumed to be small, the estimate can be used instead of theoretical value:

$$\hat{\mathrm{var}}\left(\hat{E}_a\right)=\frac{1}{Nr^2}\sum_{j=1}^{Nr}\left(\hat{E}_i-\hat{E}_a\right)^2 \tag{40}$$

Equation (40) can then be presented as:

$$\begin{aligned}&\hat{\mathrm{var}}\left(\hat{E}_a\right)=\sum_{j=1}^{Nr}W^2\left(\hat{E}_i-\hat{E}_a\right)^2\\&W=\frac{1}{Nr}\end{aligned} \tag{41}$$

The weight lacks a record index as all of the records are of the same length. However, this requirement is no longer necessary as the weight is inside the summation sign, so the record index *j* can be brought back:

$$\hat{\mathrm{var}}\left(\hat{E}_a\right)=\sum_{j=1}^{Nr}W_j^2\left(\hat{E}_i-\hat{E}_a\right)^2 \tag{42}$$

Formula (42) is equivalent to formula (35). To prove this, start by substituting (3) into (39):

$$\begin{aligned}&\hat{\mathrm{var}}\left(\hat{E}_a\right)=\sum_{j=1}^{Nr}W_j^2\left(\frac{1}{Np_j}\sum_{i=1}^{Np_j}[x_i]_j-\hat{E}_a\right)^2=\\&\sum_{j=1}^{Nr}W_j^2\left(\frac{1}{Np_j}\sum_{i=1}^{Np_j}[x_i]_j-\frac{1}{Np_j}\sum_{i=1}^{Np_j}\hat{E}_a\right)^2=\\&\sum_{j=1}^{Nr}\frac{W_j^2}{Np_j^2}\left(\sum_{i=1}^{Np_j}\left([x_i]_j-\hat{E}_a\right)\right)^2\end{aligned} \tag{43}$$

Using the well-known formula for the square of a sum:

$$\begin{aligned}&\left(\sum_{i=1}^{N}a_i\right)^2=\sum_{i=1}^{N}\sum_{j=1}^{N}a_ia_j=\\&\sum_{i=1}^{N}a_i^2+\sum_{i=1}^{N}\sum_{j=1\,j\neq i}^{N}a_ia_j=\\&\sum_{i=1}^{N}a_i^2+2\sum_{i=1}^{N}\sum_{j=1}^{N-i}a_ia_{i+j}\end{aligned} \tag{44}$$

Note the algebraic equivalence of the structure of equations (44) and (7). Applying the expansion (44) to equation (43) leads to:

$$\begin{aligned}&\hat{\mathrm{var}}\left(\hat{E}_a\right)=\sum_{j=1}^{Nr}\frac{W_j^2}{Np_j^2}\left(\sum_{i=1}^{Np_j}\left([x_i]_j-\hat{E}_a\right)^2+\right.\\&\left.2\sum_{m=1}^{Np_j}\sum_{i=1}^{Np_j-m}\left([x_i]_j-\hat{E}_a\right)\left([x_{i+m}]_j-\hat{E}_a\right)\right)\end{aligned} \tag{45}$$

The first term of (45) can be converted into a biased estimate of the record estimate and the second term can be converted into a non-weighted estimate of the auto-covariance function (17):

$$\begin{aligned}&\hat{\mathrm{var}}\left(\hat{E}_a\right)=\sum_{j=1}^{Nr}\frac{W_j^2}{Np_j}\left(V_j''+\right.\\&2\sum_{i=1}^{Np_j}\frac{Np_j-i}{Np_j}\cdot\frac{1}{Np_j-i}\sum_{k=1}^{Np_j-i}\left([x_i]_j-\hat{E}_a\right)\times\\&\left.\left([x_{i+k}]_j-\hat{E}_a\right)\right)=\\&\sum_{j=1}^{Nr}W_j^2\left(\frac{\hat{V}_j''}{Np_j}+\frac{1}{Np_j}\sum_{m=1}^{Np_j}\left(1-\frac{m}{Np_j}\right)\cdot[\hat{R}_m']_j\right)\end{aligned} \tag{46}$$

$\hat{V}_j''$ is the biased estimate of record variance.

$$\hat{V}_j'' = \frac{Np_j - 1}{Np_j}\hat{V}_j' \approx \hat{V}_j' \tag{47}$$

$$[\hat{R}_m']_j = \frac{1}{Np_j - m}\begin{cases} \sum_{i=1}^{Np_j - m}([x_i]_j - \hat{E}_a)([x_{i+m}]_j - \hat{E}_a) & i + m < Np_j \\ 0 & i + m \geq Np_j \end{cases} \tag{48}$$

$$m = 1,.., \max(Np_j)$$

Substitution of equation (22) into (46) yields

$$\hat{\text{var}}(\hat{E}_a) = \frac{1}{Nt}\sum_{j=1}^{Nr} W_j \hat{V}_j'' + \frac{1}{Nt}\sum_{j=1}^{Nr} W_j \sum_{m=1}^{Np_j}\left(1 - \frac{m}{Np_j}\right)\cdot[\hat{R}_m']_j \tag{49}$$

Introducing the cut-off point M defined by equation (33) completes the derivation

$$\hat{\text{var}}(\hat{E}_a) = \frac{\hat{V}_a''}{Nt} + \frac{1}{Nt}\sum_{m=1}^{M}\left(1 - \frac{m}{M}\right)\cdot \hat{R}_a'(\tau_m) \tag{50}$$

Equation (50) is identical to equation (35), taking into account that the large number of points and insignificant bias:

$$\hat{V}_a'' = \sum_{j=1}^{Nr} W_j \hat{V}_j'' \approx \hat{V}_a \tag{51}$$

Estimates of auto-covariance (29) and (48) differ by weighting. However, they can still be considered to be approximately equal because the cut-off limits the influence of weighting, so

$$\hat{R}_a'(\tau_m) = \sum_{j=1}^{Nr} W_j [\hat{R}_m']_j \approx \hat{R}_a(\tau_m) \tag{52}$$

A similar argument can be made for the variance of the variance, allowing the following formula to be used for the calculation of the variance of the ensemble-averaged variance estimate:

$$\hat{Var}(\hat{V}_a) = \sum_{j=1}^{Nr} W_j^2 (\hat{V}'_i - \hat{V}_a)^2 \tag{53}$$

Further consideration of equation (53) can be found in Belenky *et al.*, (2013).

4.5 Confidence Interval for Mean and Variance Estimates

The calculation of the boundaries of the confidence interval requires knowledge of the distribution of the estimates. This information is rarely available as distribution of the estimate is related with the distribution of the process itself. For example, if a sample of independent random variables is known to have normal distribution, the estimate of the mean will have student-t distribution and the distribution of variance estimate is related to 2 distribution.

The distributions of the processes of ship motion are not known. Even if the central part of the distribution can be approximated with normal for some motions and some ships, the mutual dependence of data points creates difficulties with using Student-t and 2 distribution. On the other hand, the sample, i.e. ensemble of records, is presented with large number of points. The calculations of the estimates involve mostly summation, so it seems appropriate to invoke the Central Limit Theorem, which allows the distribution of the estimates to be assumed to be normal.

This assumption presents no difficulties for the mean value, but may be a problem with variance estimate. The normal distribution supports negative values, while the variance and its estimate cannot be negative. Practical experience, however, shows that the confidence interval of variance is usually small enough to keep the low boundary of the variance far from zero. Nevertheless, the

possibility of numerical difficulties does exist, especially for smaller ensemble data volume.

Once the assumption of normality of distribution of the estimate is accepted, the calculation of the boundaries of confidence interval is trivial:

$$E_{low} = \hat{E}_a - K_\beta \sqrt{Var(\hat{E}_a)}$$
$$E_{up} = \hat{E}_a + K_\beta \sqrt{Var(\hat{E}_a)} \qquad (50)$$

$$V_{low} = \hat{V}_a - K_\beta \sqrt{Var(\hat{V}_a)}$$
$$V_{up} = \hat{V}_a + K_\beta \sqrt{Var(\hat{V}_a)} \qquad (51)$$

K_β is the $0.5(1+P_\beta)$ quantile of a standard normal distribution (with zero mean and unity variance):

$$K_\beta(P_\beta) = Q_N\left(\frac{1+P_\beta}{2}\right)$$
$$K_\beta(0.95) = 1.959964.. \approx 1.96 \qquad (52)$$

The confidence interval for standard deviation can be calculated using the "boundary" method (Bickel and Doksum, 2001):

$$\sigma_{low} = \sqrt{V_{low}} \quad ; \quad \sigma_{up} = \sqrt{V_{up}} \qquad (53)$$

5. CONCLUSIONS AND FUTURE WORK

The analysis of dynamic stability in ocean waves is based primarily on irregular sea ship motion data obtained from model tests in the basin or time-domain nonlinear numerical simulations. As the volume of data from these sources is, by necessity, limited, such analyses must account for uncertainties that result from the finite volume of data. The present paper presents robust and easy-to-use formulae for the calculation of estimates of the mean value and variance, with confidence intervals, from such data.

Ship motions in irregular waves are generally presented as an "ensemble" of records of time-domain data which has been computed or measured for the same environmental conditions, loading conditions, speed and heading. The records are independent of each other, but there is a strong dependence between data points within each record. Different records may have different length, so the natural data structure for an ensemble is a nested array (*i.e.* an array containing other arrays).

The structure of the dependence (strong dependence within each record and independence of records to each other) does not affect the ensemble-averaged estimates of mean value and variance, but must be accounted for when evaluating the statistical uncertainty of those estimates. The dependence within each record is accounted for through estimates of the auto-covariance function of the value of ship motion processes and their centered squares. As these quantities are estimated from a finite-length time series, a cut-off point is introduced to limit the possible influence of statistical "noise" caused by a deterioration of accuracy for large time lags. The estimation of the auto-covariance functions may be avoided if an ensemble contains a sufficient number of independent records.

Future development may be expected in the relation of the statistical uncertainty with spectral characteristics. In particular, the smoothed spectral estimate can be seen as a natural source for the estimate of auto-covariance function. Further test calculations are desirable in order to determine how many independent records are "sufficient" to use formulae (39) and (48) instead of (32) and (37).

Future work may also include further testing of the formulae. This would include creating or collecting a large set of ensembles from different experimental and numerical sources in order to see how well the computed confidence interval captures the expected

values of the ensemble estimates. The fraction of estimates falling within the confidence interval should be close to the given confidence probability.

6. ACKNOWLEDGEMENTS

The work described in this paper has been funded by the Office of Naval Research, under Dr. Patrick Purtell, Dr. Ki-Han Kim and Dr. Thomas Fu. The authors greatly appreciate their support. The participation of Prof. Pipiras was facilitated by the Summer Faculty Program supported by ONR and managed by Dr. Jack Price (David Taylor Model Basin, NSWCCD). The authors are grateful to Dr. Mike Levine for internal support of this work.

Over the years of the development, many colleagues have influenced and contributed to our work. The authors would like acknowledge Prof. Pol Spanos (Rice University), Dr. Art Reed, Mr. Tim Smith, Mr. Brad Campbell, Dr. Mike Hughes (David Taylor Model Basin, NSWCCD), and Prof. Ross Leadbetter (University of North Carolina Chapel Hill).

7. REFERENCES

Belenky, V.L. 2011, "On Self-Repeating Effect in Reconstruction of Irregular Waves", Chapter 33 of "Contemporary Ideas on Ship Stability", Neves, M.A.S., *et al.* eds., Springer, pp. 589-598.

Belenky, V., Pipiras, V., Kent, C., Hughes, M., Campbell, B. and Smith, T. 2013, "On the Statistical Uncertainties of Time-domain-based Assessment of Stability Failures: Confidence Interval for the Mean and Variance of a Time Series", Proc. 13th Intl. Ship Stability Workshop, Brest, France, pp. 251-258.

Belenky, V., Weems, K. and Lin, W.M., 2015 "Split-time Method for Estimation of Probability of Capsizing Caused by Pure Loss of Stability" in Proc. 12th Intl. Conf. on Stability of Ships *and Ocean Vehicles STAB 2015*, Glasgow, UK

Bickel, J. P. and Doksum, K. A., 2001 Mathematical Statistics: Basic Ideas and Selected Topics. Vol. 1, Prentice-Hall, Upper Saddle River, NJ.

Brockwell, P. J. and Davis, R. A., 2006, Time Series: Theory and Methods, Springer, 2nd edition.

Priestley, M. B., 1981, Spectral Analysis and Time Series, Vol. 1, Academic Press, New York.

Reed, A., 2011, "26th ITTC Parametric Roll Benchmark Study", Proc. 12th Intl. Ship Stability Workshop, Washington DC, USA pp 195-204.

Smith, T. C. and Zuzick A. 2015, "Validation of Statistical Extrapolation Methods for Large Motion Prediction" in Proc. 12th Intl. Conf. on Stability of Ships and Ocean Vehicles STAB 2015, Glasgow, UK.

An Investigation into the Capsizing Accident of a Pusher Tug Boat

Harukuni Taguchi, *National Maritime Research Institute (NMRI)* taguchi@nmri.go.jp

Tomihiro Haraguchi, *National Maritime Research Institute (NMRI)* haraguch@nmri.go.jp

Makiko Minami, *Japan Transport Safety Board (JTSB)* mminami@nmri.go.jp

Hidetaka Houtani, *National Maritime Research Institute (NMRI)* houtani@nmri.go.jp

ABSTRACT

This paper outlines a technical investigation into an accident of a pusher tug boat, which capsized whilst navigating near the outer boundary of Seto Inland Sea, Japan on 27 May 2013. In order to clarify the relation between rudder angle and heel angle in the manoeuvring motion of the capsized boat, an experiment using an actual similar boat was carried out. Utilising the experimental results and a stability calculation of the boat at the accident along with a statistically estimated roll angle in the waves at that time, a mechanism of capsizing was identified from energy balance like the IMO weather criterion concept.

Keywords: *accident investigation, pusher tug boat, capsizing, experiment with an actual boat, heel due to manoeuvring*

1. INTRODUCTION

A typical Japanese pusher tug boat “No. 38 Sankyo Maru” capsized off Awaji Island in Seto Inland Sea on 27 May 2013. The accident claimed two lives of crew on board. The Japan Transport Safety Board (JTSB) had investigated this accident and identified probable causes of the accident. The results of the investigations were compiled into an investigation report and submitted to the Minister of Land, Infrastructure, Transport and Tourism and publicized (JTSB, 2014).

As a technical part of the investigation, the National Maritime Research Institute (NMRI) carried out a manoeuvring experiment using an actual similar boat and utilising the experimental results a mechanism of capsizing was examined along with a stability calculation. Based on the technical investigation the JTSB concluded the probable causes of the accident and issued recommendations in order to prevent similar accidents.

In this paper the main points of technical investigation are presented.

2. OUTLINE OF THE ACCIDENT

2.1 Summary of the Accident

“No. 38 Sankyo Maru” whilst returning to Osaka from Tokushima without a box barge capsized off Awaji Island around 15 o’clock on 27 May 2013. Two members of the crew in the bridge died and a skipper in the cabin inside the hull was rescued from the capsized boat. A high sea warning was issued at that time. The estimated wind and sea conditions at the time of the accident are summarised in Table 1.

According to the skipper, who took a nap at the accident, the boat suddenly heeled to the port side largely then capsized in a short time. But sequence and mechanism of the accident were not clear.

Table 1. Wind and Sea Conditions at the Accident.

Average wind speed	about 7 m/s ~ 8 m/s
Wind direction	SSW
Significant wave height	about 2 m ~ 3 m
Average wave period	about 5 s
Wave direction	S

2.2 Capsized Pusher Tug Boat "No. 38 Sankyo Maru"

"No. 38 Sankyo Maru" (Lr = 16.00 m, B = 5.50 m and D = 2.00 m) constructed in 2007 was a twin-propeller and twin-rudder pusher tug boat of 19 gross tons. The general arrangement of the boat is shown in Figure 1.

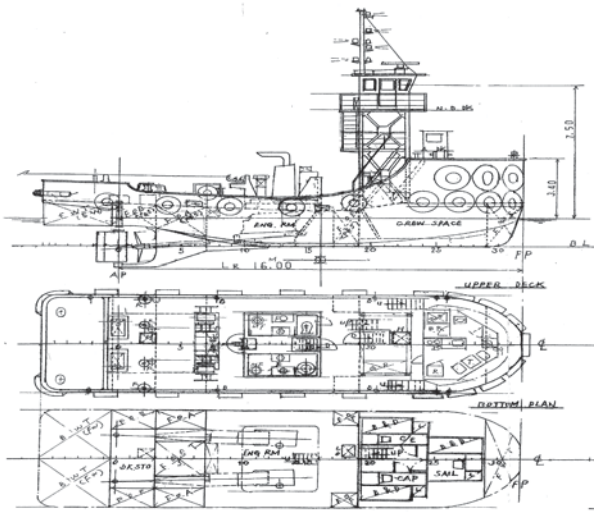

Figure 1 General Arrangement of "No. 38 Sankyo Maru".

In order to secure enough manoeuvrability during linking with a box barge the rudder area ratio of the boat was relatively large and even with small rudder angle its steering quality was good. However, relatively large rudder area also led to inducing large heeling moment in manoeuvring motion. Therefore, during navigating without a box barge in order to prevent large heel in changing course the skipper used to limit the rudder angle to about 5 degrees and ease the wheel immediately. And he instructed the crew to follow his way of steering the boat.

3. AT-SEA EXPERIMENT

Due to the above mentioned feature of the capsized boat it was presumed that heel angle in manoeuvring motion might be related to the occurrence of the accident but its characteristic was unknown. Therefore, in order to clarify the relation between rudder angle and heel angle in manoeuvring motion of the capsized boat, an experiment using an actual similar boat was carried out. From the experimental results an estimation method for heel angle of the capsized boat in manoeuvring motion was derived.

3.1 Outline of the Experiment

A twin-propeller and twin-rudder pusher tug boat "No. 58 Sankyo Maru" whose principal particulars, rudder area and output of main engines were the same as for the capsized boat was used in the experiment. At the experiment the boat was almost full loaded with fuel oil and fresh water.

Table 2. Hull Condition at the Experiment.

Displacement: W	141.31 t
Mean draft: d	1.69 m
Trim by stern: τ	1.11 m
Vertical C.G.: KG	1.99 m
Metacentric height: GM	0.76 m

An inclining test was carried out first to clarify the condition of the boat at the experiment and the result (Table 2) was used to estimate the condition of the capsized boat at the accident. Then, a manoeuvring experiment

was carried out and the boat motion (roll angle, yaw angle, yaw rate and so on) and the boat speed were measured. In the experiment not only rudder angle but also way of steering was changed (Table 3).

Table 3. Summary of the experiment

Kind of test	Turning test, weave manoeuver test.
Approach speed	9 kn, the same as the presumed speed of the capsized boat at the accident.
Rudder angle (degrees)	(1)Turning test 5, 8, 10 (port), 10 (stbd.).
	(2) Weave manoeuver test 7(port)-7(stbd.)-8(port)-6(stbd.), 9(stbd.)-8(port)-9(stbd.)-9(port), 10(port)-9(stbd.)-12(port)-12(stbd.), 13(port)-10(stbd.)-10(port)-13(stbd.), 22(stbd.)-17(port)-23(stbd.)-7(port).

3.2 Experimental Results

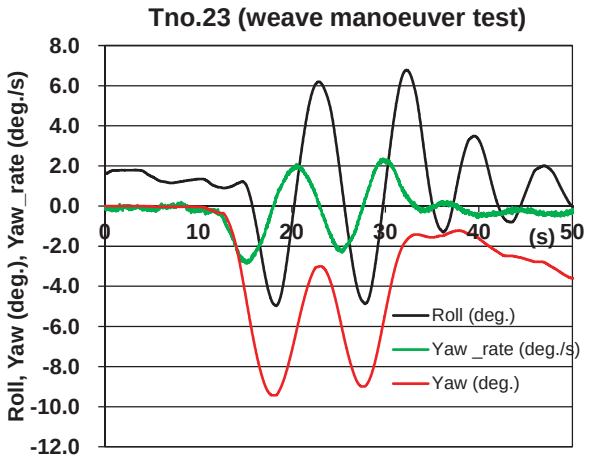

Figure 2 Measured roll angle, yaw angle and yaw rate in a weave manoeuver test with a series of rudder angles of 13(port)-10(stbd.)-10 (port)-13(stbd.) degrees.

Figure 2 shows an example of measured time histories of roll angle, yaw angle and yaw rate in a weave manoeuver. Roll angle is positive for the port side down and yaw angle and yaw rate are positive for a starboard turn. From the measured boat motion and observation during the experiment the characteristic of heel angle in manoeuvring motion of the similar boat could be summarised as follows (refer to Figure 2).

(1)No clear inward heel occurs in the initial stage of manoeuvring motion.

(2)Corresponding to the magnitude of rudder angle relatively large outward heel occurs during manoeuvring motion.

(3)Response speed of heel to steering is relatively fast and outward heel develops quickly.

Heel Angle. Figure 3 shows relation between heel angles and rudder angles measured in the experiment. The horizontal axis is rudder angle δ, positive for the starboard side, and the vertical axis is outward heel angle ϕ_2, positive for the port side down. From Figure 3 it is noticed that within the measured extent the relation between heel angles and rudder angles is approximated by a linear function (showed in the dotted line) and in manoeuvring motion of the similar boat outward heel of almost half as large as rudder angle is induced.

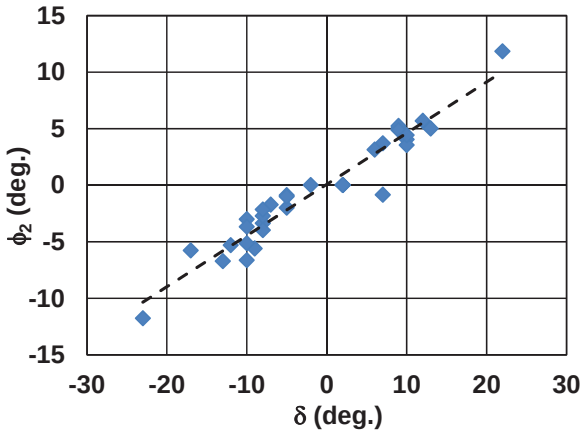

Figure 3 Measured heel angles and rudder angles in the experiment.

Turning Rate. Figure 4 shows the relation between turning rates (yaw rates) and rudder angles measured in the experiment. The vertical axis is normalised turning rate *r'*, which is positive for a starboard turn. The normalised turning rate *r'* was calculated with equation (1).

$$r' = \frac{L_{pp}}{r} = \frac{\omega \cdot L_{pp}}{V} \quad (1)$$

where ω is the measured turning rate, V is the measured boat speed, r is the local radius of trajectory and L_{pp} is the length between perpendiculars of the boat.

From Figure 4 it is noticed that within the measured extent the relation between normalised turning rates and rudder angles is approximated by a linear function as equation (2) (the dotted line in Figure 4).

$$r' = 0.0122 \times \delta - 0.0078 \quad (2)$$

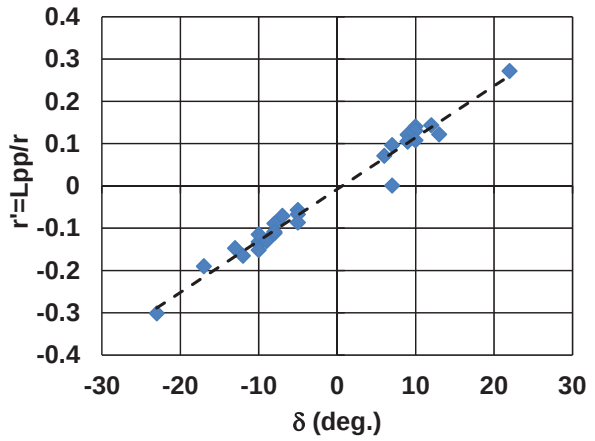

Figure 4 Measured turning rates and rudder angles in the experiment.

3.3 Estimation of Outward Heel Angle of the Capsized Boat

Outward heel in manoeuvring motion is induced by a couple consisting of a centrifugal force acting on the centre of gravity and a fluid reaction force acting on the side of hull. If the fluid reaction force is assumed to act at half the mean draft (d/2), outward heeling moment M is estimated with equation (3) (Morita, 1985).

$$M = \frac{W}{g}\frac{V^2}{r}\left(\overline{KG} - \frac{d}{2}\right) \quad (3)$$

where W is the displacement of the boat, g is the gravitational acceleration, KG is the vertical centre of gravity of the boat.

Figure 5 shows a comparison between the outward heeling moments estimated by substituting experimental data in equation (3) and the righting moments corresponding the measured heel angle, $W \bullet GM \bullet \sin\phi_2$. From Figure 5 it is noticed that the righting moment is almost 2.77 times (the dotted line in Figure 5) larger than the outward heeling moment estimated with equation (3). This indicates that for the similar boat the fluid reaction force acts at a position, which differs largely from half draft (d/2). And in addition to this due to inertia of the boat and change in rudder force at reversing rudder angle in weave manoeuver might increase the outward heel angle.

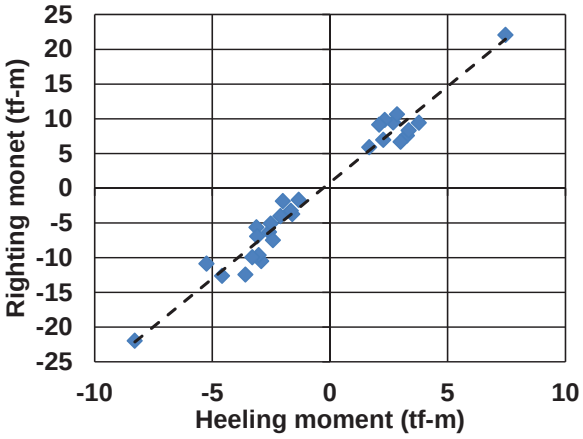

Figure 5 Outward heeling moments estimated with equation (3) and righting moments corresponding to measured heel angles.

If the following are supposed, outward heel angle ϕ_2 of the capsized boat in manoeuvring motion for given rudder angle δ can be estimated with equations (2), (4) and (5).

(1)Turning characteristics, the relation between rudder angle and turning rate, of the capsized boat at the accident is the same as the similar boat at the experiment (Figure 4).

(2)Speed reduction in manoeuvring motion is negligible.

(3)Feature of outward heeling moment of the similar boat at the experiment (Figure 5) is

applicable to the capsized boat at the accident.

$$r = \frac{L_{pp}}{r'} \tag{4}$$

$$\sin\phi_2 = 2.77 \times \frac{V^2}{g \cdot r \cdot \overline{GM}} \left(\overline{KG} - \frac{d}{2} \right) \tag{5}$$

4. CONSIDERATION ON CAPSIZING MECHANISM

As the high sea warning was issued at the time of the accident and for the capsized boat quite careful steering was necessary to prevent large heel in changing course during navigating without a box barge , it is presumed that the following factors, wind and waves at the accident and careless steering of the boat, were related to the accident. As the skipper explained that the boat suddenly heeled to the port side largely then capsized in a short time, the situation of occurrence of the capsizing was supposed to be similar to that of the IMO weather criterion. Therefore, with calculating maximum heel angle based on an energy balance concept like the weather criterion, the capsizing mechanism was examined.

4.1 Stability at the Accident

Table 4 shows the estimated loading condition of the boat at the time of the accident, which is based on the inclining test result of the similar boat and the fuel oil and fresh water, supposed to be loaded into the capsized boat at the accident. Stability calculation was carried out with trim free condition. Figure 6 shows the stability curve at the time of the accident and Table 5 shows the estimated draft, trim, metacentric height and angle of bulwark top immersion. In Figure 6 the stability curve of the similar boat at the experiment is also shown.

From Figure 6 and Tables 2, 4 and 5 it is noticed that as the full loaded fuel oil and fresh water increase the draft and trim of the boat, for large heel angle the stability of the similar boat at the experiment is smaller than that of the capsized boat at the accident. Therefore, for pusher tug boats of similar type to the capsized one, in order to maintain sufficient stability special attention is needed in loading fuel oil and fresh water.

Table 4. Loading condition at the accident.

Displacement: W	129.21 t
Vertical C.G.: KG	2.03 m
Longitudinal C.G.: mid-G	-1.19 m
Free surface effect: GG_0	0.11 m

Table 5. Draft, trim, metacentric height and angle of bulwark top immersion at the accident.

Mean draft: d	1.66 m
Trim by stern: τ	0.37 m
Metacentric height: G_0M	0.70 m
Angle of bulwark top immersion: ϕ_b	20.7 deg.

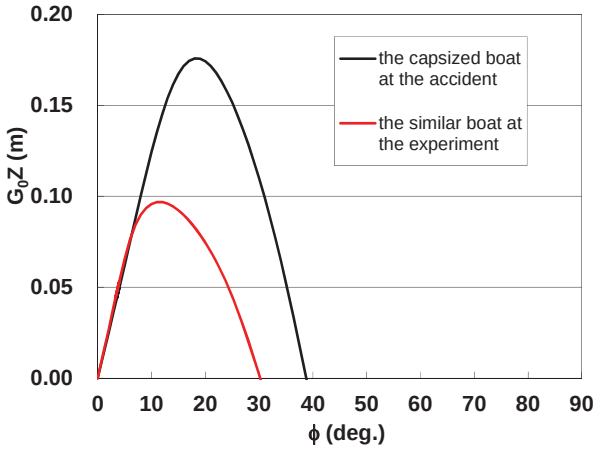

Figure 6 Stability curves at the accident and at the experiment.

4.2 Influence of Wind and Waves

Heel due to the Wind at the Accident. Assuming beam wind condition, heel angle under action of steady wind and gust wind at

the accident were estimated with the same method as the weather criterion except wind pressure at 8 m/s. Table 6 shows the estimated heel angles due to the wind at the accident. Even gustiness considered, the heel angle due to the wind at the accident is estimated to be less than 1 degree. Taking the stability curve at the accident, Figure 6, into account, influence of the heel due to the wind at that time on the capsizing of the boat would be quite small. Therefore, the influence of the wind was excluded from consideration on capsizing mechanism.

Table 6. Heel angle due to the wind at accident (steady wind speed of 8 m/s).

Lateral windage area: A	49.06 m^2
Vertical distance from centre of "A" to a point at half the mean draft: Z	2.82 m
Wind pressure at 8 m/s: P	47.7
Heeling lever due to steady wind: $l_{w1} = PAZ/1000gW$	0.005 m
Heeling lever due to gust wind: $l_{w2} = 1.5l_{w1}$	0.008 m
Heel angle due to steady wind: ϕ_0	0.44 deg.
Heel angle due to gust wind:$1.5\phi_0$	0.65 deg.

Roll due to the Waves at the Accident. It was presumed that the speed of the boat was 9 knots and its heading angle was about 60 degrees at the time of the accident. Based on this information and the estimated sea condition at the time of the accident, Table 1, roll response of the capsized boat in a short crested sea was statistically estimated with the condition that the significant wave height was 2 m, the average wave period was 4.8 s and the mean encounter angle was 60 degrees. As a result, the expected largest in 200 successive roll amplitudes, ϕ_1 of the capsized boat is estimated to be 15.6 degrees (Table 7). Considering the stability at the accident, the estimated roll in the waves at the accident should be one of main factors related the capsizing of the boat.

As shown in Table 7, the expected largest in 200 successive roll amplitudes of the similar boat in the wave at the accident is 6.2 degrees, which is less than half that of the capsized boat. However, considering the stability of the similar boat at the experiment, the estimated roll angle in the waves at the accident might impair its safety.

Table 7. Roll angle of 1/200 maximum expectation in waves at the accident.

The capsized boat at the accident	15.6 deg.
The similar boat at the experiment	6.2 deg.

4.3 Influence of Steering

No information on the way of steering the capsized boat at the accident was provided. Therefore, outward heel angle ϕ_2 of the capsized boat at speed of 9 knots in manoeuvring motion with rudder angle of 5 to 15 degrees was estimated with equations (2), (4) and (5). Figure 7 shows the estimated outward heel angle due to steering of the capsized boat along with that of the similar boat at the experiment.

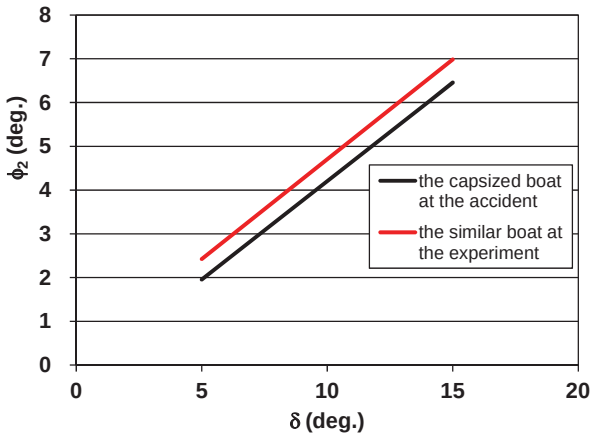

Figure 7 Outward heel angle due to steering.

The outward heel angle of the capsized boat at the accident is smaller than that of the similar boat at the experiment. At the condition of the accident the outward heel angle of the capsized boat with rudder angle of 10 degrees is estimated to be 4.2 degrees, which is much

smaller than the estimated roll angle in the waves at the accident. However, during steering the capsized boat outward heeling moment was supposed to keep working at the accident. In that case the outward heeling moment should reduce the residual dynamical stability of the capsized boat significantly.

4.4 Consideration on Capsizing Mechanism

As mentioned above it was presumed that rolling in waves at the accident and outward heel due to steering played a key role to the capsizing of the boat. Therefore, assuming that the capsized boat rolling in waves was carelessly steered at the accident, the mechanism of the capsizing was examined by calculating maximum heel angle with an energy balance concept like the weather criterion. In the examination as the worst case, the capsized boat was assumed to suffer outward heeling moment induced by starboard steering when it rolled to starboard side at an angle corresponding to the 1/200 maximum expectation in the waves at the accident and energy balance between rolling energy and dynamical stability was calculated. As no information on the steering of the capsized boat at the accident was available, the energy balance calculation was carried out at various rudder angles. The rudder angles, which induced the bulwark top immersion and the capsizing, were estimated and their feasibility was considered.

Table 8. Calculation results

δ (deg.)	ϕ_2 (deg.)	$b(\phi_b)/a$	b/a	$\phi_{\_1}$ (deg.)
4.7	1.8	1.00	1.77	20.7
5.0	2.0	0.97	1.70	21.1
9.7	4.1	0.58	1.00	34.9

Calculation results are shown in Table 8 and graphs used for calculation are shown in Figure 8. In Table 8, ϕ_2 is the outward heel angle due to starboard steering with rudder angle of δ, “a” and “b” are the rolling energy to the port side (the capsizing direction) and the residual dynamical stability respectively (refer to Figure 8), “b (ϕ_b)” is the residual dynamical stability up to the angle of bulwark top immersion (refer to Figure 8) and $\phi_{\_1}$ is the maximum heel angle to the port side.

From Table 8 it is noticed that if the outward heeling moment induced by the steering with rudder angle of 4.7 degrees is assumed to act on the boat when it rolls to the starboard side at the maximum, the resultant port side heel reaches the angle of bulwark top immersion (ϕ_b), 20.7 degrees. If the assumed rudder angle is larger than 4.7 degrees, the maximum heel angle to the port side exceeds the angle of bulwark top immersion. For example with the assumed rudder angle of 5.0 degrees the maximum heel angle to the port side is 21.1 degrees, and the bulwark top is considered to be immersed. After the top of bulwark is immersed, it should induce a resistance force against up-righting the boat. Therefore, if the bulwark top is immersed the boat would not upright readily and the successive waves might capsize it. Table 8 also shows that if the assumed rudder angle of starboard steering at the accident is larger than 10 degrees, the boat is considered to capsize immediately to port.

Although during navigating without a box barge in order to prevent large heel in changing course steering with small rudder angle used to be carried out for the capsized boat, it seems not unrealistic to assume that steering with rudder angle of about 5 degrees was carried out at the accident. In any case the calculation results indicate that if the worst case that when the boat rolls to one side at the maximum heeling moment due to steering to the same side is assume to act on the boat, steering with rudder angle of less than 10 degrees could lead the boat to capsize. Therefore it seems that for pusher tug boats of similar type to the capsized one, careful steering with small rudder angle is indispensable to ensure safety during navigating without a box barge.

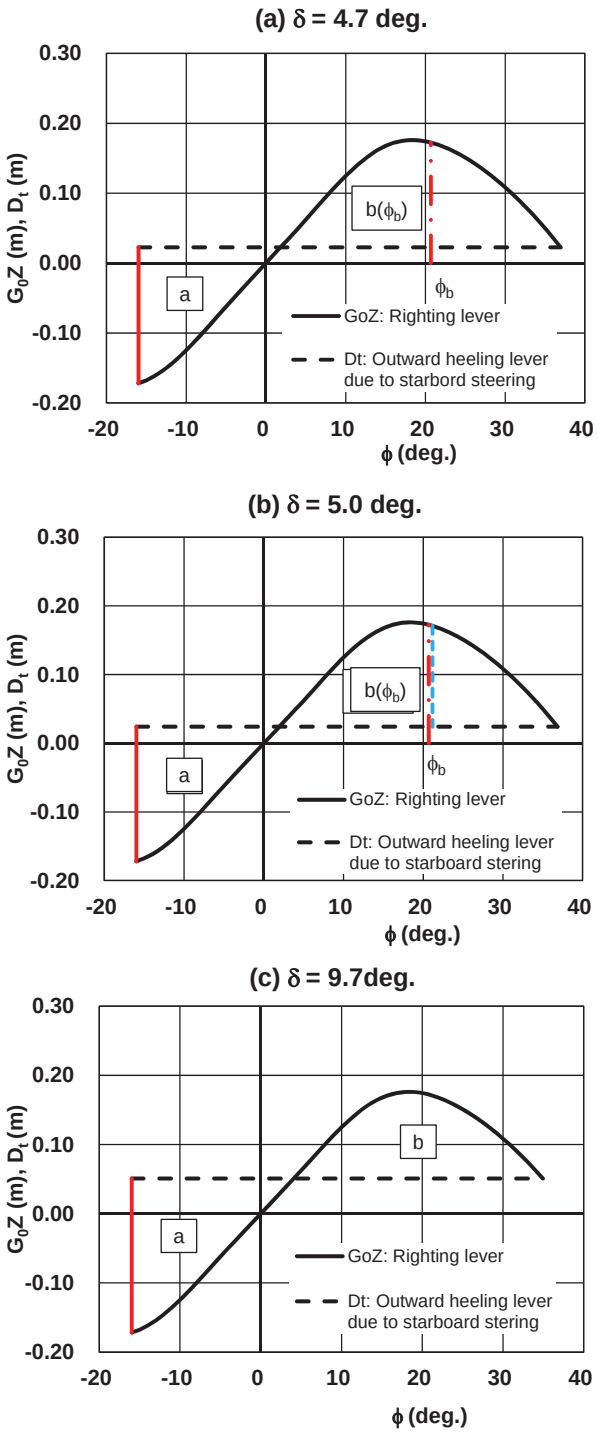

Figure 8 Comparison between dynamical stability and heeling energy with various rudder angles.

5. CONCLUSIONS

With the above mentioned technical investigation and so on the JTSB compiled the investigation report on the capsizing accident of "No. 38 Sankyo Maru" and publicised it (JTSB, 2014). In the report, the probable cause of the accident is summarised as follows. Due to the steering with rudder angle of larger than 4.7 degrees the capsized boat navigating without a box barge at speed of about 9 knots with suffering starboard waves of about 2 ~ 3 meters in significant wave height and about 5 seconds in average wave period was forced to heel beyond the angle of bulwark top immersion to the port side and fell into a difficult situation for up-righting. Then with successive waves action the boat might have capsized.

In the report the following feature of pusher tug boats of similar type to the capsized one are pointed out too.

(1) Depending on the loading condition of fuel oil and so on, the stability of these boats tends to reduce considerably.
(2) In rough weather large rolling due to waves may occur easily in these boats.
(3) As the rudders of these boats are designed to secure enough manoeuvrability during linking with a box barge, in case of navigating solely these boats are liable to heel largely by the action of rudders.

In order to prevent similar accident, the operating company is instructed to prepare a manual, which explains precautions for pusher tug boats in navigating solely, limitation on loading fuel oil and so on, wind and sea conditions where planed navigation should be abandoned, appropriate way of steering etc. and advise skippers to follow it.

6. REFERENCES

Japan Transport Safety Board, 2014, "Push boat SANKYO MARU No. 38 Capsizing", Marine Accident Investigation Report, MA2014-3 (in Japanese).

Morita, T., 1985, "Theory of Ship Stability - Basis and Application -", Kaibun-do, pp. 134-136 (in Japanese).

Rapid Ship Motion Simulations for Investigating Rare Stability Failures in Irregular Seas

Kenneth Weems, *NSWCCD (Naval Surface Warfare Centre Carderock Division)*,

kenneth.weems@navy.mil

Vadim Belenky, *NSWCCD (Naval Surface Warfare Centre Carderock Division)*,

vadim.belenky@navy.mil

ABSTRACT

The use of time-domain numerical simulations for the investigation of stability failures and other rare events in random, irregular seas requires a challenging combination of speed and accuracy. Simulations must be fast enough to observe a statistically significant number of failure or near failure events in order to build a reliable stochastic model of the event or conditions leading up to the event, while also being accurate and complete enough to capture the physical behavior that drives the event. Of particular importance are the body-nonlinear hydrostatic and Froude-Krylov forces, which are critical for large-amplitude roll motion and may also play a significant role in the surge and sway forces involved in surf-riding and broaching.

This paper presents a volume-based evaluation of the body-linear Froude-Krylov and hydrostatic pressure forces, which retains the inseparability of hydrostatic and Froude-Krylov forces and the effects of large-amplitude relative motion along the length of a ship. Implementation of the method requires a minimum number of evaluations of the incident wave, so it can run at a fraction of the computational cost for traditional surface pressure integration schemes. The calculation has been implemented in a hybrid numerical method that incorporates ordinary different equation (ODE) like models for wave-body perturbation forces. The hybrid method has been used to produce a very large number of realizations of irregular sea responses, including a statistically significant number of stability failures, for validating schemes for the extrapolation of extreme motion responses.

Keywords: *Seakeeping, Nonlinear Restoring, Froude-Krylov Forces*

1. INTRODUCTION

The use of time-domain numerical simulations for the investigation of stability failures and other rare events in random, irregular seas requires a challenging combination of speed and accuracy. The rarity of such events requires an extremely long set of simulations in order to observe a statistically significant number of events, while the complexity of the physics precludes the use of excessively simple models.

Of particular importance are the body-nonlinear restoring (hydrostatic) and incident wave (Froude-Krylov) forces, which are critical for large-amplitude roll motions and may also play a significant role in the surge and sway forces involved in surf-riding and broaching. France *et al.* (2003) described how these forces were key to describing parametric roll, while Spyrou *et al.* (2014) and others have linked the change of roll stability in waves to

large roll events and capsizing in pure loss-of-stability events.

Hybrid time-domain simulation codes, which generally combine a body-nonlinear calculation of the hydrostatic and Froude-Krylov forces with a potential-flow solution of the wave-body hydrodynamic disturbance forces (radiation, diffraction, etc.) and theoretical or semi-empirical models of viscous and lift forces, have become the principal tool for simulating non-linear ship motion in irregular waves. These tools provide a reasonable compromise between accuracy and speed, and they can readily generate hundreds or thousands of hours of motion data for different realizations of ocean waves.

This, of course, is not nearly enough simulation time to observe a statistically significant number of failure or near failure events; building a reliable stochastic model of the event or conditions leading up to the event may require millions of hours of simulation for a single wave and operating condition. This has led to the development of extrapolation methods that attempt to characterize the probability of rare events from limited motion data (see, for example, Belenky et al. 2015 and Campbell et al. 2015). However, the development, testing, and validation of such methods still require extremely large simulation data sets of motions in extreme conditions.

Faster methods, therefore, are needed. For the development and validation (or at least testing) of extrapolation methods, they need not be quantitatively accurate to a high degree, but they do need to be qualitatively accurate in that they capture the key physics of the large-amplitude roll motion (Smith and Zuzick 2015). As mentioned above, a key part of such a calculation is the body-nonlinear hydrostatic and Froude-Kyrlov forces. While it is relatively straightforward to calculate these forces via direct pressure integration, they can be computationally expensive: they require a very large number of evaluations of the incident wave, and a very large number of component frequencies are required for a statistically valid representation of the irregular wave field for long simulations (Belenky 2011).

To provide a fast but complete calculation of the body-nonlinear Froude-Krylov and hydrostatic pressure forces, a sectional, volume-based evaluation has been developed that retains the inseparability of hydrostatic and Froude-Krylov forces and the effects of large-amplitude relative motion along a ship's length. Implementing the method requires a minimum number of evaluations of the incident wave, so it can run at a fraction of the computational cost of traditional surface pressure integration schemes. The calculation has been implemented in a hybrid numerical method that incorporates ordinary differential equation (ODE) like models for wave-body perturbation forces. The hybrid method has been used to produce a very large number of realizations of irregular sea responses, including a statistically significant number of stability failures, for validating schemes to extrapolate extreme motion responses (Weems and Wundrow 2013).

In this initial implementation, the simplified model of wave-body hydrodynamics prevents this simulation from being considered as quantitatively accurate. In the future, however, rapid, quantitatively accurate simulations may be possible by combining volume-based restoring and wave forces with a more complex but still fast model of the wave-body hydrodynamics, perhaps based on impulse response potentials or a more sophisticated coefficient representation.

2. FORMULATION OF VOLUME-BASED CALCULATIONS

The non-linear wave forcing and restoring forces can generally be computed by integrating the incident wave and hydrostatic pressure over the instantaneous wetted hull surface (in the Earth-fixed frame):

$$\mathbf{F}_{FK+HS}(t) = -\rho\iint_{S_B(t)}\left(\frac{\partial\phi_0(x,y,z,t)}{\partial t} + gz\right)\hat{\mathbf{n}}\,ds \quad (1)$$

$\partial\phi_0(x,y,z,t)/\partial t$ is the pressure of the undisturbed incident wave field (Froude-Krylov pressure) and $S_B(t)$ is the instantaneous wetted portion of the hull surface up to the incident wave waterline $\eta(x,y,t)$. The key element of this expression is that it captures the geometric non-linearity due to large vertical motion relative to the wave surface, ranging from the effect of bow flare to full emergence or submergence of the bow and stern.

It should be noted that this expression can be used with linear or nonlinear incident wave models as long as the incident wave model expresses a pressure and velocity field in the body-nonlinear domain, that is up to $z=\eta(x,y,t)$. For the typical linear wave model – in which the wave is represented by a superposition of sinusoidal components – this can be accomplished by applying the Wheeler stretching technique, in which the exponential decay term in the expressions for pressure, velocity, and their derivatives is expressed as $e^{k(\eta-z)}$.

As noted above, this expression is relatively straightforward to evaluate but can be expensive to generate, as it generally involves a large number of evaluations of the incident wave. To provide a much faster calculation, a volume-based calculation scheme is considered, using the submerged volume at each instant in time, which can be calculated with a minimal number of incident wave evaluations. It is, however, imperative that the scheme capture the effect of the longitudinal variation of the relative motion, as this is a principle driver in dynamic stability phenomena such as parametric roll and pure loss of stability in waves. To do so, Equation (1) is expressed as the sum of incremental forces calculated on a set of incremental sections distributed along the ship's length:

$$\mathbf{F}_{FK+HS}(t) = \sum \delta\mathbf{F}_{FK+HS}(x_i,t) \quad (2)$$

$\delta\mathbf{F}_{FK+HS}(x_i,t)$ is the force *computed* over the incremental submerged portion of the hull's surface running from $x_i-\Delta x/2$ to $x_i+\Delta x/2$, which is designated $\delta S_B(x_i,t)$:

$$\delta\mathbf{F}_{FK+HS}(x_i,t) = -\rho\iint_{\delta S_B(x_i,t)}\left(\frac{\partial\phi_0(x,y,z,t)}{\partial t} + gz\right)\hat{\mathbf{n}}\,ds \quad (3)$$

Note that the incremental hull surface $\delta S_B(x_i,t)$ is *considered* to include the wetted portion of the hull for that section as well as the wetted (below the incident wave) portions of the planes (cross-sections) separating this section from adjacent sections.

Within each section, a Taylor series expansion (neglecting higher-order derivatives) can be used to approximate the distribution of the incident wave pressure over an incremental hull section in terms of the value and derivatives of the pressure at a nominal point (x_0,y_0,z_0) on the section:

$$\begin{aligned}\frac{\partial\phi_0(x,y,z,t)}{\partial t} \cong\ & \frac{\partial\phi_0(x_0,y_0,z_0,t)}{\partial t} + \\ & \frac{\partial^2\phi_0(x_0,y_0,z_0,t)}{\partial t\partial x}(x-x_0) + \\ & \frac{\partial^2\phi_0(x_0,y_0,z_0,t)}{\partial t\partial y}(y-y_0) + \\ & \frac{\partial^2\phi_0(x_0,y_0,z_0,t)}{\partial t\partial z}(z-z_0)\end{aligned} \quad (4)$$

The dynamic free surface *boundary* condition can be used to relate the Froude-Krylov pressure at the free surface to the incident wave elevation:

$$\frac{\partial\phi_0(x,y,\eta,t)}{\partial t} = -g\eta(x,y,t) \quad (5)$$

If the *evaluation* point is chosen to be on the incident wave surface, $z_0=\eta$, Equation (4) can be written as:

$$\begin{aligned}\frac{\partial\phi_0(x,y,z,t)}{\partial t} &\cong -g\eta(x_0,y_0,t)\\ &-g\frac{\partial\eta(x_0,y_0,t)}{\partial x}(x-x_0)\\ &-g\frac{\partial\eta(x_0,y_0,t)}{\partial y}(y-y_0)\\ &+\frac{\partial^2\phi_0(x_0,y_0,\eta,t)}{\partial t\partial z}(z-\eta)\end{aligned} \quad (6)$$

Using an overbar to *designate* the mean or nominal value of the elevation, etc. for a section, the sectional force can be written as:

$$\begin{aligned}\delta\mathbf{F}_{FK+HS}(x_i,t) \cong \rho\iint_{\delta S_B(t)} &(g\overline{\eta}-gz\\ &+g\overline{\frac{\partial\eta}{\partial x}}(x-x_0)+g\overline{\frac{\partial\eta}{\partial y}}(y-y_0)\\ &+\overline{\frac{\partial^2\phi_0}{\partial z\partial t}}(z-z_0))\hat{\mathbf{n}}\,ds\end{aligned} \quad (7)$$

Since the incremental surface $\delta S_B(x_i,t)$ includes x=constant plane separating adjacent sections and the pressure over the free surface above the section will be zero, the RHS of (7) complete encompasses the submerged portion of the section. Gauss's theorem can then be applied in order to define the sectional force in terms of the integral of the gradient of the approximated pressure field over the incremental volume:

$$\delta\mathbf{F}(t)=\iint_{\delta S_B(t)}P\hat{\mathbf{n}}\,ds=-\iiint_{\delta V(t)}\nabla P dv \quad (8)$$

This results in a volume-based formula for the sectional incident wave and restoring force:

$$\begin{aligned}\delta\mathbf{F}_{FK+HS}(x_,t) \cong &\rho g\delta V(x_i,t)\hat{\mathbf{k}}\\ &-\rho g\delta V(x_i,t)\overline{\frac{\partial\eta}{\partial x}}\hat{\mathbf{i}}\\ &-\rho g\delta V(x_i,t)\overline{\frac{\partial\eta}{\partial y}}\hat{\mathbf{j}}\\ &+\rho g\delta V(x_i,t)\overline{\frac{\partial^2\phi_0}{\partial z\partial t}}\hat{\mathbf{k}}\end{aligned} \quad (9)$$

$\delta V(x_i,t)$ is the instantaneous volume of the submerged portion of the i^{th} section up to the incident wave surface. The first term in Equation (9) is the familiar buoyancy term, but with the volume integrated up to the incident wave surface. The second and third terms are longitudinal and side forces from the gradient of the incident wave pressure field, evaluated in terms of the incident wave slope. The final term can be considered to be a "correction" to the vertical incident wave force, using a linear approximation of the exponential decay of the incident wave pressure field with depth.

Similarly, expressions for the moments can be derived by applying the relation:

$$-\iint_S(\hat{\mathbf{n}}\times P\mathbf{r})\,ds=\iiint_V\nabla\times P\mathbf{r}dv \quad (10)$$

This gives the following formula for the roll and pitch moments:

$$\begin{aligned}\delta Mx_{FK+HS}(x_i,t) \cong &\rho g\delta V(x_i,t)y_{CV}(x_i,t)\\ &-\rho g\delta V(x_i,t)\overline{\frac{\partial\eta}{\partial y}}z_{CV}(x_i,t)\\ &+\rho g\delta V(x_i,t)\overline{\frac{\partial^2\phi_0}{\partial z\partial t}}y_{CV}(x_i,t)\end{aligned} \quad (11)$$

$$\begin{aligned}\delta My_{FK+HS}(x_i,t) \cong &-\rho g\delta V(x_i,t)x_{CV}(x_i,t)\\ &+\rho g\delta V(x_i,t)\overline{\frac{\partial\eta}{\partial x}}z_{CV}(x_i,t)\\ &-\rho g\delta V(x_i,t)\overline{\frac{\partial^2\phi_0}{\partial z\partial t}}x_{CV}(x_i,t)\end{aligned} \quad (12)$$

$x_{cv}(x_i,t)$, $y_{cv}(x_i,t)$ and $z_{cv}(x_i,t)$ are coordinates for the center of the instantaneous submerged volume for the i^{th} section up to the incident wave waterline. The sectional roll and pitch moments can be summed to get the total moments on the ship:

$$Mx_{FK+HS}(t)=\sum\delta Mx_{FK+HS}(x_i,t) \quad (13)$$

$$My_{FK+HS}(t)=\sum\delta My_{FK+HS}(x_i,t) \quad (14)$$

The yaw moment can be computed from the sectional lateral forces as:

$$Mz_{FK+HS}(t) = \sum -\rho g \delta V(x_i,t)\overline{\frac{\partial \eta}{\partial y}}(x_i - x_{cg}) \quad (15)$$

With these formulae, the body-nonlinear Froude-Krylov and hydrostatic restoring forces can be computed with a single evaluation of the incident wave per section. The only major assumption in the derivation of these formulae is the Taylor series expansion of the incident wave pressure in Equation (4). This expansion assumes that the wave slope is constant over the beam and the incremental length of each section Δx, and can be considered a long-wavelength assumption in which the wave length is assumed to be long with respect to the beam and increment section length. This assumption should be quite reasonable for waves, or wave components in an irregular sea model, that are longer than two or three times the beam, but the linear approximation of the sinusoidal wave profile will become inaccurate for shorter waves. However, the section-based derivation retains the variation of elevation and slopes from section to section, so the waves are not assumed to be long relative to the ship length and the variation of relative motion along the ship's length, which the primary driver of the change of stability in waves, is considered.

The expansion considers the vertical pressure gradient to be, at most, linear with depth, so the wave is also assumed to be long compared to the draft of the ship. The linear approximation of the exponential pressure decay will become quite inaccurate for shorter waves, so any implementation of the $\partial^2\phi_0/\partial z\partial t$ term will need to treat of short waves or wave components carefully.

3. IMPLEMENTATION OF VOLUME-BASED CALCULATIONS

The implementation of these volume-based formulae in a time-domain numerical code requires the calculation of the submerged volume, up to the incident wave, and volume center for a set of ship hull sections at each time step. In order to accommodate extreme motion problems, these sectional volume calculations should accommodate large amplitude heave and pitch including fully submerged and emerged sections, and large amplitude roll motions including a fully inverted ship.

In the initial implementation, the sectional volume calculations were implemented using an approach similar to the Bonjean curves used for classic stability analysis. Prior to starting the simulation, a set of x=constant stations are cut through the hull and the volume and volume moments for the $y>0$ half of the hull section are pre-computed for 0 heel up to each station offset point.

At each time of a simulation (or heel angle of a restoring curve calculation), the Froude-Krylov and hydrostatic restoring force for each section is computed as follows:

1. Evaluate the incident wave elevation and slope at the centerline of each station
2. Find the intersection of the incident wave surface and the section centerline considering the wave elevation and vertical motion of the station due to the ship's heave and pitch
3. Find the port and starboard waterline points from the incident wave/center intersection and an effective heel angle, which is the sum of the ship's roll angle and the lateral wave slope at the centerline
4. Interpolate the volume and volume moments up to the waterline point for each side of the hull (dark blue in Figure 1)
5. Correct the volume and volume moments for the effective heel angle by adding or subtracting the contribution of the light blue triangular regions in Figure 1
6. Combine the volume and volume moments for the two sides to determine the volume and volume center for the section

7. Compute sectional forces and moments via Equations (9), (11), and (12).

The sectional forces and moments are then integrated along the length of the ship to get the total forces and moments.

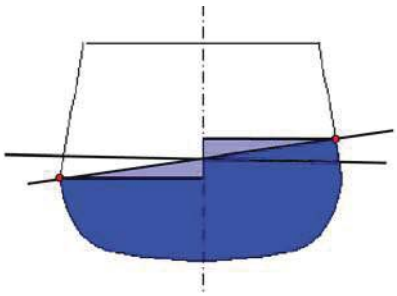

Figure 1: Sample sectional volume calculation for a midships section of the ONR Topsides Series Tumblehome hull

Figure 2 shows the station offsets and the waterline intersection points of each station for a time instant from a simulation in stern oblique irregular waves.

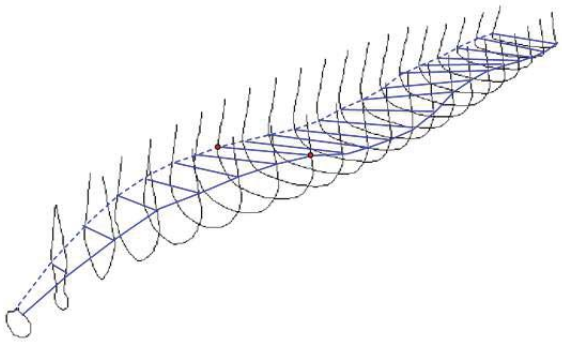

Figure 2: Station/incident wave intersection points for the ONR Tumblehome hull in stern oblique seas

In the initial implementation of the volume-based calculation, the $\partial^2\phi_0/\partial z\partial t$ term has *not* been included. Further work may be required to explore the $\partial^2\phi_0/\partial z\partial t$ term and to develop a robust and accurate handling for shorter waves and irregular wave representation, including short wave components.

The procedure is very fast, since it requires only a single evaluation of the incident wave elevation and its derivatives for each station at each time step. Even this effort can be mitigated by interpolating the wave in space and/or time. For a 3-DOF (heave, roll, pitch) simulation in which surge, sway, and yaw are prescribed based on constant forward speed, the global position of the sections is known *a priori*, so the incident wave values can be pre-computed at a larger time increment and interpolated to the simulation time step.

4. RESTORING CURVE CHECK

In order to verify the formulation and implementation of the sectional volume-based calculation, the roll restoring arm (GZ) curve was computed in both calm water and for the quasi-static wave-pass problem, and the results were compared to results from 3-D surface pressure integration in the Large Amplitude Motions Program (LAMP) and to results from a standard statics code. Figure 3 compares the calm water restoring arm of the different calculations for a 100m x 20m x 6m rectangular barge, while Figure 4 presents a similar comparison for the ONR Topsides Series Tumblehome hull.

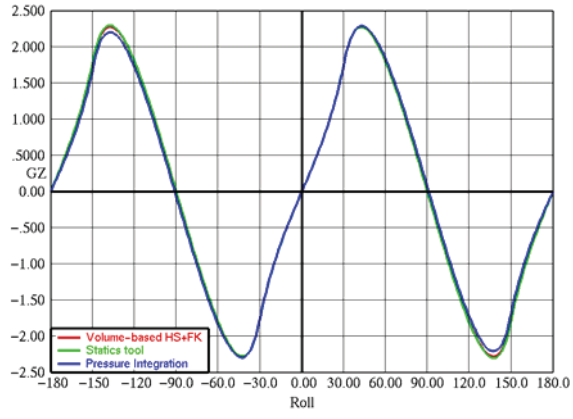

Figure 3: Calm water restoring curve for rectangular barge

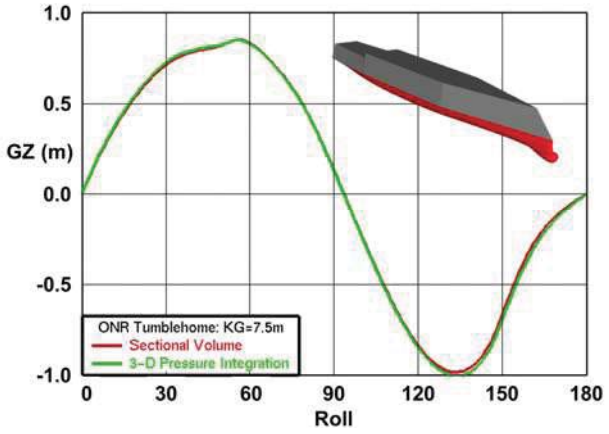

Figure 4: Calm water roll restoring arm (GZ) curve for ONR Tumblehome hull

As expected, the curves are nearly identical. As the calculation of the restoring moment is based on a volume calculation that is nearly exact, the incremental restoring moment about its static or instantaneous dynamic position, which is to say its restoring curve in calm water or in waves, will be nearly exact as well.

5. MOTIONS IN REGULAR WAVES

The volume-based Froude-Krylov and hydrostatic force calculation has been implemented in a 3-DOF (heave, pitch, roll) hybrid numerical simulation tool that incorporates ODE-like models for wave-body perturbation forces and viscous roll damping. In order to test the tool, the predicted response in regular waves was compared to LAMP simulations. LAMP is a general hybrid time-domain ship motions prediction tool that incorporates a conventional surface pressure integration of the hydrostatic and Froude-Krylov pressures with several different options for the wave-body hydrodynamic force (Shin *et al.*, 2003). Most LAMP simulations use its 3-D potential flow solution of the wave-body hydrodynamics, but LAMP also has the option, sometimes referred to as LAMP-0, of substituting coefficient-based added mass and damping terms for the potential flow solution. LAMP's Froude-Krylov pressure terms can also be evaluated without the pressure decay term (e^{kz}).

Figures 5 and 6 show the roll and heave response for a 3-DOF (heave, roll, pitch) simulation of a 100m x 20m x 6m rectangular barge in regular quartering waves with wave length equal to ship length and wave height equal to 1/3rd of the draft. The roll and pitch responses are nearly identical, as was heave (not plotted).

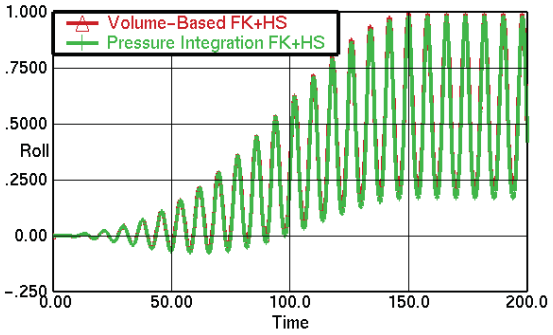

Figure 5: Roll motion for rectangular barge in quartering regular waves, λ=L h=d/3

The "Pressure Integration" results in Figures 5 and 6 are LAMP-0 results in which the incident wave decay (e^{kz}) has been turned off. As such, the incident wave and hydrostatic forces will differ only by the calculation method: volume vs. pressure integration. The viscous damping models and implementation of the hydrodynamic coefficient are similar but not identical. The results indicate that for a wave that is equal to the ship length and long relative to the beam, the magnitude and phase of the wave forcing and restoring, including the coupling that results in the asymmetric roll response, is well represented in the volume-based calculation.

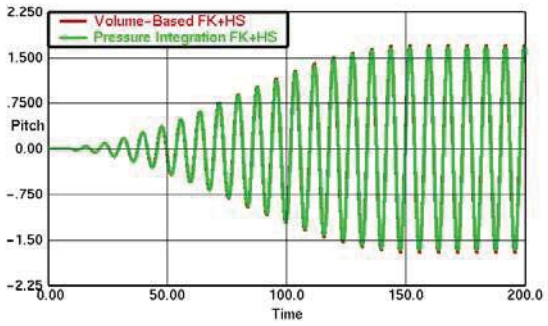

Figure 6: Pitch motion for rectangular barge in quartering regular waves, λ=L h=d/3

In order to evaluate the effects of wave length and calculation options, a series of regular wave response calculations were made for the ONR Topsides Series Tumblehome hull in regular, quartering seas at zero speed. Figures 7 through 9 plot the normalized response amplitude vs. the ratio of ship length to wave length for a wave slope of H/λ=50. The heave response is normalized by wave amplitude while the roll and pitch response are normalized by wave slope (ka).

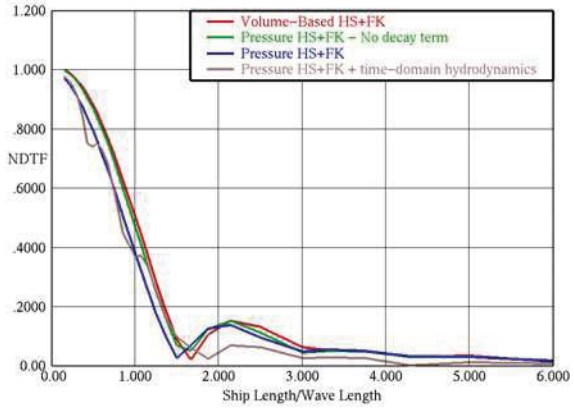

Figure 7: Heave response of ONR Tumblehome in regular, stern quartering waves, 0 knots

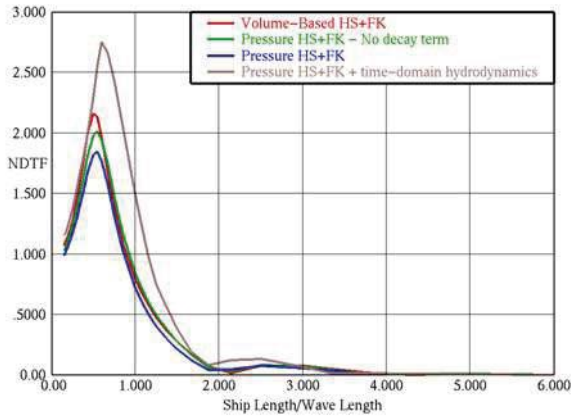

Figure 8: Roll response of ONR Tumblehome in regular, stern quartering waves, 0 knots

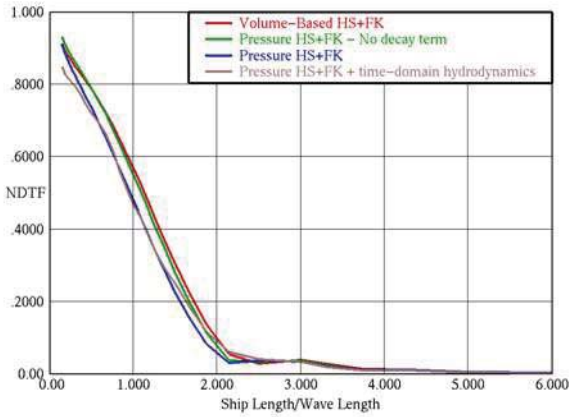

Figure 9: Pitch response of ONR Tumblehome in regular, stern quartering waves, 0 knots

These calculations were made with four different methods, labeled as:

- Volume-Based HS+FK is the simulation tool incorporating the new, volume-based calculation (red line)
- Pressure HS+FK – No decay term is a LAMP-0 simulation with surface pressure integration of HS+FK pressure neglecting the decay (e^{kz}) term (green line)
- Pressure HS+FK is a LAMP-0 simulation with surface pressure integration of HS+FK pressure including the decay (e^{kz}) term (blue line)
- Pressure HS+FK + time-domain hydrodynamics is a regular LAMP simulation with 3-D potential flow solution of the wave-body interaction. (brown line)

The difference between the red and green curves is primarily the difference between the new, volume-based calculation of the HS+FK forces vs. the traditional, pressure integration calculation, but with the effect of the pressure decay removed. There is also some difference in the coefficient-based hydrodynamics and damping models, which is most likely responsible for the difference in the roll response peak. The largest difference between the two calculations is expected to be for the

shorter waves, but the response there is equally small for both.

The difference between the green and blue curves is entirely the effect of the decay (e^{kz}) term in the Froude-Krylov pressure integration. The effect is evident, especially in heave and pitch, but does not dominant the results. It is probably worth investigating the $\partial^2\phi_0/\partial z\partial t$ term in Equations (9), (11), and (12), which has been neglected in the initial implementation over the method, to correct for this difference.

The difference between blue and the brown curves is the effect of the more accurate hydrodynamics in the regular LAMP calculation. The effect is large enough that volume-based method must be coupled with a more complete model of hydrodynamics in order to create a quantitative tool for ship motions.

6. MOTIONS IN IRREGULAR SEAS

As described above, the primary purpose for developing the volume-based calculation of the hydrostatic restoring and incident wave forcing was to produce a tool capable of creating very large data sets of ship motions in severe, irregular seas that are at least qualitatively representative of actual, nonlinear data. These data would be used in developing and testing of extrapolation methods for severe roll motion including capsizing.

Figure 10 shows 20 records of the roll response for the ONR Tumblehome ship at a low GM condition (GM=1.5m) in large (Sea State 8) steep stern quartering waves. The seaway is modeled by 220 wave components to provide a statistically independent wave representation over each 30-minute realization. The total calculation time for these 20 realizations was about 7 seconds on a single processor laptop computer. 2,000,000 realizations comprising 1,000,000 hours of data can be generated in a day or so on a modest sized cluster.

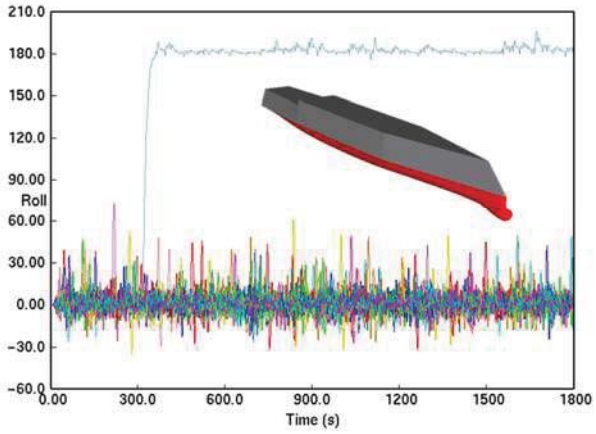

Figure 10: Roll motion for 20 realizations of ONR Tumblehome hull in steep Sea State 8

This example shows that the code is fast enough, but does it reproduce the significant nonlinearities of realistic severe ship motion, especially roll? Since the method captures the key features of the change of stability in waves, it should, at least to some extent. But how does one demonstrate, let alone prove, that it does?

For the present, we look at the distribution of predicted roll motion for the ONR Tumblehome hull at 6 knots in long-crested quartering seas with a significant wave height ($H^{1/3}$) of 9.5m, which is one of the cases used to test the extrapolation methods described in Belenky *et al.* (2015). Figures 11 through 13 compare a histogram of the roll angle from 15 hours of regular (with potential flow hydrodynamics) LAMP simulations (30 30-minute realizations) to a curve derived from 500 hours of simulations using the volume-based HS+FK calculation with simplified hydrodynamics. The horizontal axis is the roll angle divided by its standard deviation (σ). A normal distribution is overlaid for reference.

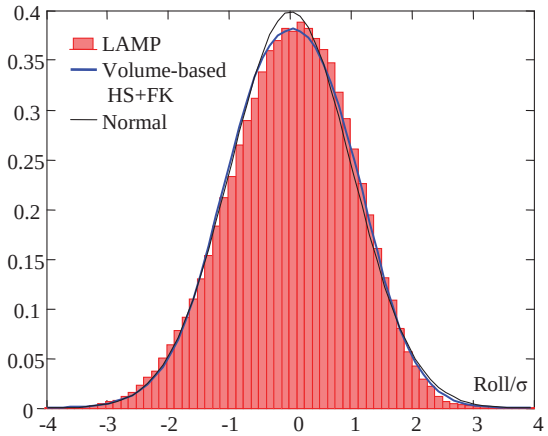

Figure 11: Distribution of Roll Angle for ONR Tumblehome at 6 knots in quartering seas, $H^{1/3}$=9.5m

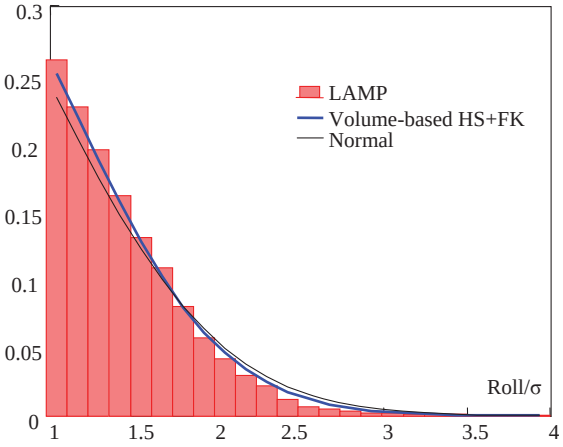

Figure 12: Distribution of Roll Angle – positive tail

The difference between the normal distribution and the LAMP results is not huge, but it has been shown that this difference is important, especially at the tail. Most important is the relative thinness of the positive tail (Figure 12) thickness of the negative tail (Figure 13). The trending of the volume-based result follows the LAMP results rather well. This result is not conclusive by any means, but it is encouraging and provides justification for using the results of the volume-based simulations for the testing of the extrapolation techniques.

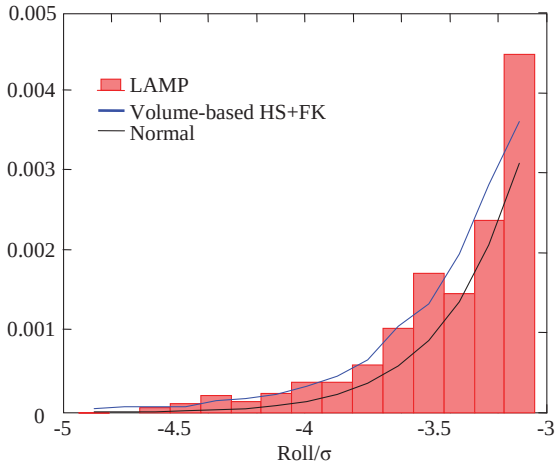

Figure 13: Distribution of Roll Angle – negative tail

7. CONCLUSIONS AND FUTURE WORK

The analysis of rare dynamic stability failures, including extreme roll events and capsizing, can gain considerable benefit from very rapid numerical simulations in irregular waves, as long as the simulations capture the principal physical phenomenon of the events. The very large data sets of irregular sea ship motion generated by such methods would allow the direct observation of rare events or near events and provide a basis for building and testing probabilistic models. Simulations that are even qualitatively correct have potential application for testing such models, especially those which are based on the extrapolation of smaller data sets.

In order to enable the development of such a numerical simulation tool, a very fast calculation method has been developed for the body-nonlinear hydrostatic restoring and incident wave (Froude-Krylov) forcing, which has been identified as a principal contributor to parametric roll and pure-loss-of-stability events. The calculation method uses volume-based formulae for the forces and moments on a series of hull stations as a function of the local relative motion and effective heel angle. The method is very accurate in the assessment of roll restoring and its changes due to relative motions in waves, but is approximate in the

evaluation of the incident wave forcing. By requiring only one evaluation of the incident wave per section, it is far faster than traditional methods based on the integration of pressure over the hull surface.

The method has been implemented in a 3-DOF (heave, roll, pitch) hybrid simulation tool which incorporates simple, coefficient-based models for wave-body hydrodynamics and viscous damping. The tool is capable of practically generating very large data sets, *e.g.* millions of hours, but can be considered only qualitatively accurate with its simplified hydrodynamic model. Future work will include an investigation of the vertical derivative term in the formulae, a more complete verification that the method provides a qualitatively accurate representation of ship motion in large waves and the integration of the volume-based calculation with more complete models for the wave-body hydrodynamics, maneuvering forces such as propulsion and hull lift, and other effects.

8. ACKNOWLEDGEMENTS

The work described in this paper has been funded by the Office of Naval Research, under Dr. Patrick Purtell and Dr. Ki-Han Kim. The authors greatly appreciate their support.

The authors would like to recognize the contributions of Dr. A. Reed, B. Campbell, Dr. D. Wundrow and T. Smith of NSWCCD during the development and testing of this method.

9. REFERENCES

Belenky, V. L., 2011, "On Self-Repeating Effect in Reconstruction of Irregular Waves", Chapter 33 of Contemporary Ideas on Ship Stability" edited by M.A.S. Neves, V. L. Belenky, J. O. de Kat, K. Spyrou, and N. Umeda, Springer, pp. 589-598.

Belenky, V., Weems, K. and Lin, W.M., 2015, "Split-time Method for Estimation of Probability of Capsizing Caused by Pure Loss of Stability," Proc. 12th Intl. Conf. on Stability of Ships and Ocean Vehicles (STAB 2015), Glasgow, UK.

Campbell, B., Belenky, V. and Pipiras, V. 2015 "Statistical Extrapolation in the Assessment of Dynamic Stabilityin Irregular Waves" Proc. 12th Intl. Conf. on Stability of Ships and Ocean Vehicles (STAB 2015), Glasgow, UK

France, W.M, Levadou, M, Treakle, T.W., Paulling, J. R., Michel, K. and Moore, C. (2003). "An Investigation of Head-Sea Parametric Rolling and its Influence on Container Lashing Systems," Marine Technology, Vol. 40, No. 1, pp. 1-19.

Shin, Y.S., Belenky, V., Lin, W.M., Weems, K. and Engle, A. (2003), "Nonlinear Time Domain Simulation Technology for Seakeeping and Wave-Load Analysis for Modern Ship Design,"SNAME Transactions, Vol. 111.

Smith, T., and Zuzick, A., 2015, "Validation of Statistical Extrapolation Methods for Large Motion Prediction," Proc. 12th Intl. Conf. on Stability of Ships and Ocean Vehicles (STAB 2015), Glasgow, UK.

Spyrou, K. J., Belenky, V., Reed, A., Weems, K., Themelis, N., and Kontolefas, I., 2014, "Split-Time Method for Pure Loss of Stability and Broaching-To," Proc. 30th Symp. Naval Hydrodynamics, Hobart, Tasmania, Australia.

Weems, K. and Wundrow, D. 2013, "Hybrid Models for Fast Time-Domain Simulation of Stability Failures in Irregular Waves with Volume-Based Calculations for Froude-Krylov and Hydrostatic Force", Proc. 13th Intl. Ship Stability Workshop, Brest, France.

This page is intentionally left blank

Dynamic Instability of Taut Mooring Lines Subjected to Bi-frequency Parametric Excitation

Aijun Wang, *University of Strathclyde*

Hezhen Yang , *State Key Laboratory of Ocean Engineering, Shanghai Jiao Tong University*

Nigel Barltrop, *University of Strathclyde*

Shan Huang, *University of Strathclyde*

ABSTRACT

Parametric excitation or parametric resonance occurs when the offshore structure system parameter varies with time and meets a certain condition. Moored structure during the swell sea states causes the taut mooring line tension fluctuation which may induce very large dynamic motion of mooring lines. In this work, the taut mooring lines subjected to bi-frequency parametric excitation are studied. The parametric excitation equation of mooring lines is derived. The Bubnov-Galerkin approach is employed to obtain stability chart when consider the bi-frequency excitation. The responses of the mooring lines subjected to single- and bi-frequency excitation are discussed.

Keywords: *dynamic instability; mooring line; parametric excitation； Mathieu; bi-frequency*

1. INTRODUCTION

The dynamic instability is the oscillatory motion of dynamic system due to time-dependent variation of structure parameters e.g. inertia or stiffness due to the influence of externally applied force. Different the forced excitation, the parametric excitation is nonautonomous system. It can have catastrophic effects on the structures. The study indicated parametric excitation would cause very large increase in lateral dynamic motion of mooring lines due to the variation of axial tension. (Rönnquist et al., 2010). It is beneficial to avoid the mooring line design to locate in the unstable zone. Recently, some researchers have studied the dynamic instability due to parametric excitation such as parametric rolling of ships, spar and risers (Falzarano et. al 2003, Yang et al. 2015, and Zhang et. al 2010). However, previous work all focused on the single frequency excitation. Actually, the offshore structure is exposed to random waves which are multi-frequency excitation. So, it is necessary and beneficial to study the taut mooring lines subjected to bi-frequency parametric excitation.

2. THEORY AND MATHEMATICAL MODEL

The general dynamic equation of Bernoulli-Euler beam can be expressed as follow.

$$EI\frac{\partial^4 y}{\partial x^4}-T\frac{\partial^2 y}{\partial x^2}+m\frac{\partial^2 y}{\partial t^2}=f(x,t) \qquad (1)$$

Where EI is the bending stiffness, T is the axial tension, m is mass per unit length, $f(x,t)$ is external force on the beam.

For the mooring lines, the bending stiffness often can be neglected and the axial tension can be expressed by

$$T=T_0+T_A\phi(t) \qquad (2)$$

Where $\phi(t)=\sum_{n=0}^{\infty}A_n\cos(\omega_n t+\theta_n)$.

T_0 is the mean tension of the line.

T_A is the amplitude of lines dynamic tension.

ω_n is the tension variation frequency of the line.

θ_n is the random phase.

The hydrodynamic on the lines are calculated by Morison equation. It is nonlinear and can be linearized as the follows.

$$f(x,t)=-\frac{1}{2}\rho DC_D\left|\frac{\partial y}{\partial t}\right|\frac{\partial y}{\partial t}=-\sqrt{\frac{2}{\pi}}C_D\rho D\sigma\frac{\partial y}{\partial t} \tag{3}$$

Combing equations (1)-(3) leads to

$$m\frac{\partial^2 y}{\partial t^2}+\sqrt{\frac{2}{\pi}}C_D\rho D\sigma\frac{\partial y}{\partial t}-\left(T_0+T_A\sum_{n=0}^{\infty}A_n\cos(\omega_n t+\theta_n)\right)\frac{\partial^2 y}{\partial x^2}=0 \tag{4}$$

Assumed that the ends are pinned, the lateral motion of lines can be written as

$$y(x,t)=\sum_{n=1}^{\infty}y_n(t)\sin\frac{n\pi x}{l} \tag{5}$$

Submit Eq. (2) into Eq. (1), it follows that

$$\sum_{n=1}^{\infty}[m\frac{d^2y_n(t)}{dt^2}+\sqrt{\frac{2}{\pi}}C_D\rho D\sigma\frac{dy_n(t)}{dt}+\left(T_0+T_A\sum_{n=0}^{\infty}A_n\cos(\omega_n t+\theta_n)\right)(\frac{n\pi}{l})^2y_n(t)]\sin\frac{n\pi x}{l}=0 \tag{6}$$

The above equation can be rewritten into the general form,

$$\frac{d^2y_n(\tau)}{d\tau^2}+2c_n\frac{dy_n(\tau)}{d\tau}+\left(a_n+2q_n\sum_{n=0}^{\infty}A_n\cos(k\tau+\theta_n)\right)y_n(\tau)=0 \tag{7}$$

where $\tau=\omega_0 t$, ω_0 is the basic frequency.

$k=\frac{\omega_n}{\omega_0}$, $a_n=(\frac{\bar{\omega}_n}{\omega_0})^2$, $q_n=\frac{1}{2}\frac{T_A}{T_0}(\frac{\bar{\omega}_n}{\omega_0})^2$,

$c_n=\sqrt{\frac{1}{2\pi}}\frac{C_D\rho D\sigma}{m\omega_0}$.

$\bar{\omega}_n=\frac{n\pi}{l}\sqrt{\frac{T_0}{m}}$ n=1, 2, $\cdots$

$\bar{\omega}_n$ is the natural frequency of the line.

This is the second order homogenous equation which named Hill equation.

3. SINGLE-FREQUENCY EXCITATION CASE

In this section, only single-frequency excitation is taken into account, and then the Eq. (7) can be expressed as follow. It is the well-known Mathieu equation.

$$\ddot{y}+2c\dot{y}+\left(a+2q\cos(2\tau)\right)y=0 \tag{8}$$

For the single-frequency excitation, the top end motion of mooring lines corresponds to the floating structure during the regular sea.

3.1 Stability chart of single-frequency excitation

The stability chart is often used to identify the unstable and stable zones of dynamic instability due to parametric excitation. The stability chart can show the change instability as the parameters are varied and are very useful for the design guidance. It can be solved by Floquet theory or perturbation method. The stability chart of single-frequency excitation for

the taut mooring lines is shown in the Fig.1. It can be seen that the unstable zone will shrink as the damping increases. The resonance will occur when excitation is integral or sub multiple of fundamental frequency.

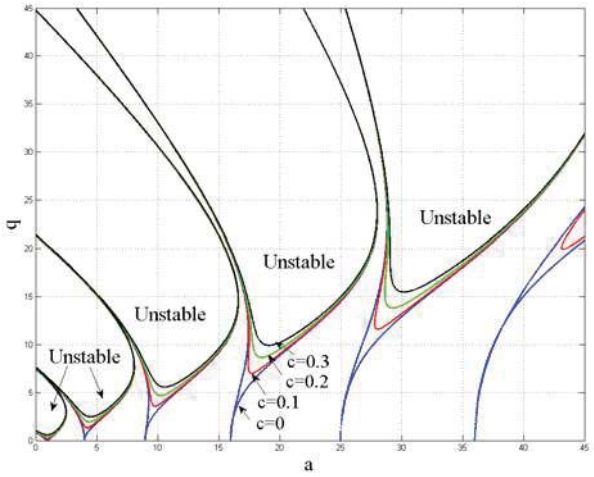

Fig.1 Stability chart of single-frequency excitation
(Blue line--c=0; red line--c=0.1; green line--c=0.2; black line--c=0.3)

3.2 Dynamic response due to single-frequency excitation in time domain

Fig.2 present two case for the lateral dynamic response at the midpoint of the mooring line (Case I locate at stable zone and case II locate at unstable zone). The direction of response is orthogonal to the direction of the excitation. For the case II, It can be seen that the response will increase exponentially. This case should be removed for the design.

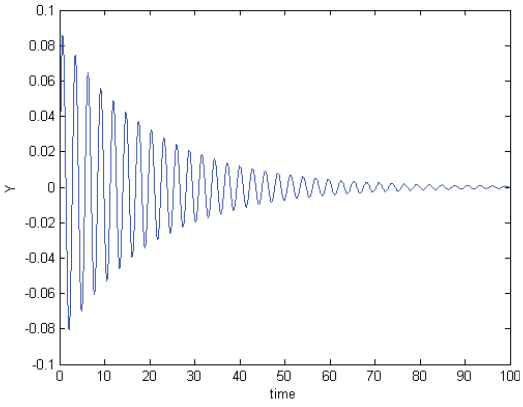

Response

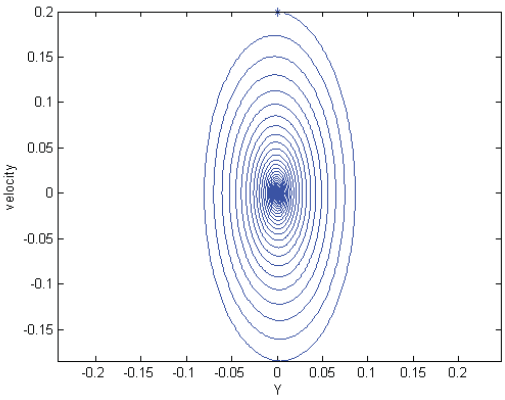

Phase plane trajectory

(Case I)

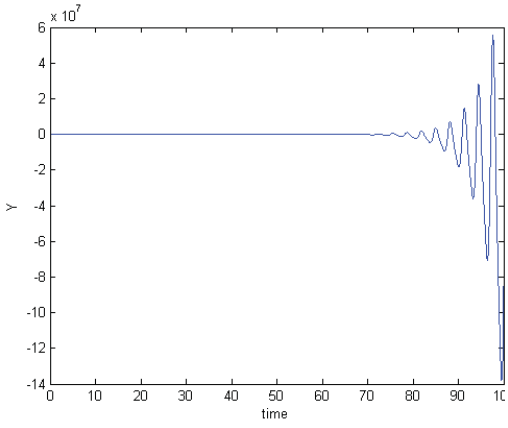

Response

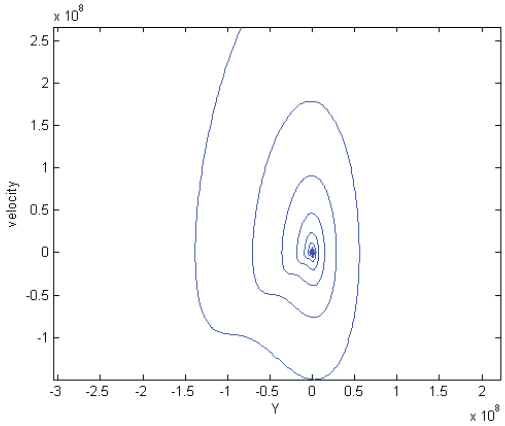

Phase plane trajectory

(Case II)

Fig.2 Dynamic response due to single-frequency excitation in time domain
(Case I: a=5; q=0.04; c=0.1; Case II: a=5; q=2.5; c=0.1)

4. BI-FREQUENCY EXCITATION CASE

For real sea conditions, the top end of mooring line is subjected to multi-frequency excitation from floating motions in the random waves. The parametric instability property of mooring line has great effects on the safety of the design case and it can cause the lateral motion exponential increase in the oscillation. Here, the parametric instability due to bi-frequency excitation is studied which is conducive to understand the mechanism of the dynamic instability.

$$\ddot{y} + 2c\dot{y} + \left(a + 2q(\cos(2\tau) + d\cos(4\tau)\right) y = 0 \tag{9}$$

The dynamic instability for the bi-frequency excitation is obtained by the Bubnov-Galerkin approach (Perdesen, 1980). Fig.3 shows the stability chart for the bi-frequency excitation. It can be seen that the unstable zone for the bi-frequency excitation is obviously different from the single-frequency excitation.

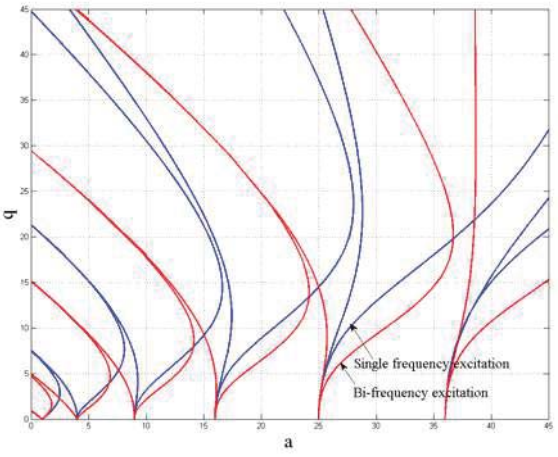

Fig.3 Stability chart for single- and bi-frequency excitation (d=-0.5)
(Blue line- single-frequency excitation; red line- bi-frequency excitation)

4.1 Effects of different d

Fig.4 and 5 give the stability charts for different d =0.5 and -0.5 respectively. The sign of d mean the different phase between the two excitations. The unstable zone changes when d turns into negative and the shape is also different. It is interesting to find that the closed zone exists.

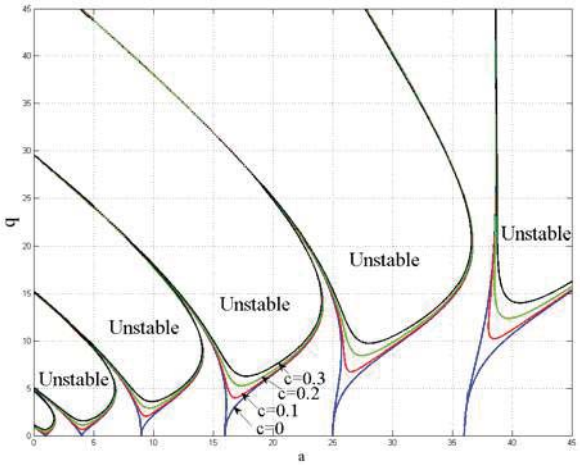

Fig.4 Stability chart for bi-frequency excitation for different damping (d=-0.5)
(Blue line--c=0; red line--c=0.1; green line--c=0.2; black line--c=0.3)

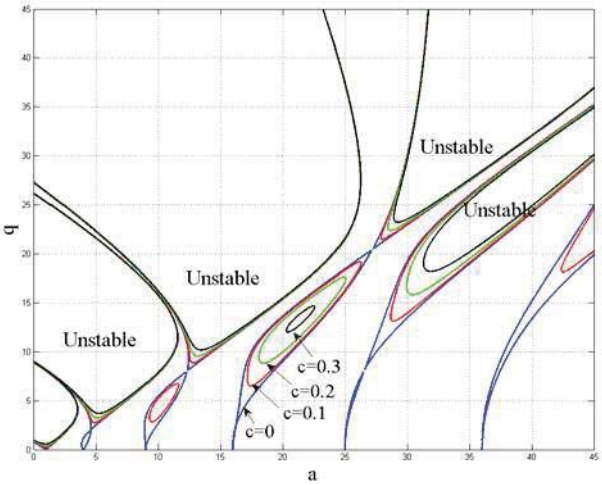

Fig.5 Stability chart for bi-frequency excitation for different damping (d=0.5)
(Blue line--c=0; red line--c=0.1; green line--c=0.2; black line--c=0.3)

4.2 Effects of different damping for positive d

The effects of different damping for positive d are compared in the Fig.6-8. The damping varies from 0 to 0.3. It can be seen that the unstable zone of bi-frequency excitation is more sensitive than the single-frequency excitation. The unstable zone changes more as the damping varies.

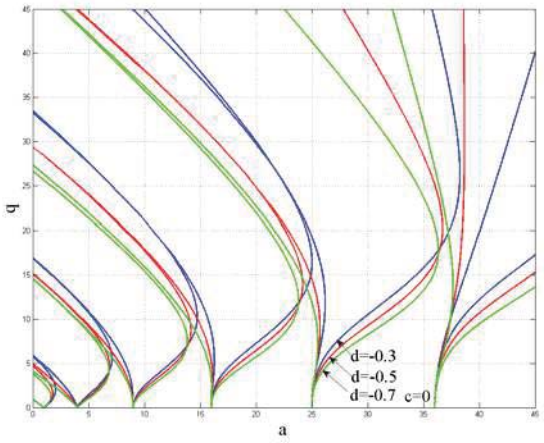

Fig.6 Stability chart for bi-frequency excitation for different damping (c=0.0)
(Blue line--d=-0.3; red line--d=-0.5; green line--d=-0.7)

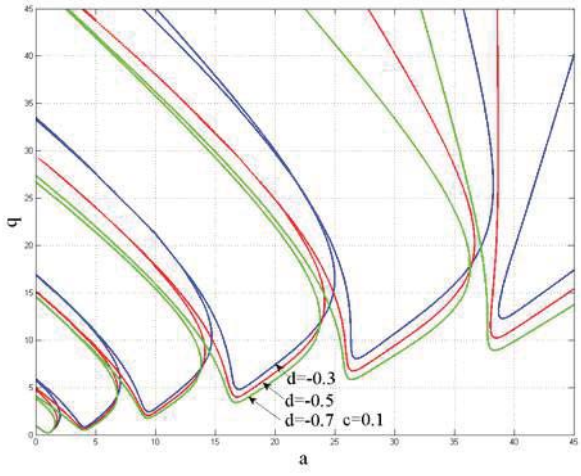

Fig.7 Stability chart for bi-frequency excitation for different d (c=0.1)
(Blue line--d=-0.3; red line--d=-0.5; green line--d=-0.7)

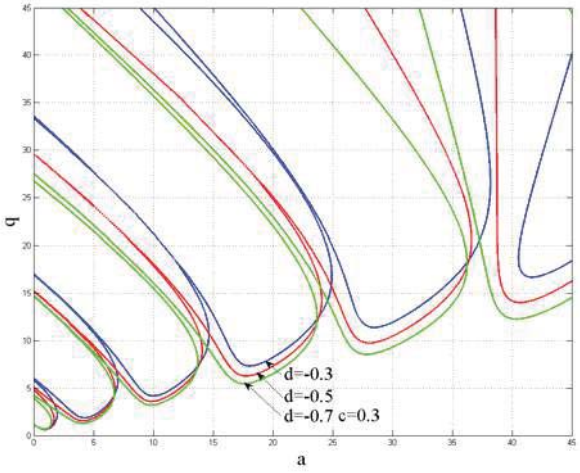

Fig.8 Stability chart for bi-frequency excitation for different d (c=0.3)
(Blue line--d=-0.3; red line--d=-0.5; green line--d=-0.7)

4.3 Effects of different damping for negative d

Fig.9-11 present the effects of different damping for negative d on the dynamic instability zone. The damping varies from 0 to 0.3. It can be seen that the unstable zone of bi-frequency excitation is completely different from the single-frequency excitation. The unstable zone changes more as the damping varies. The safety case will turn into unsafely when damping varies or the sign of d changes.

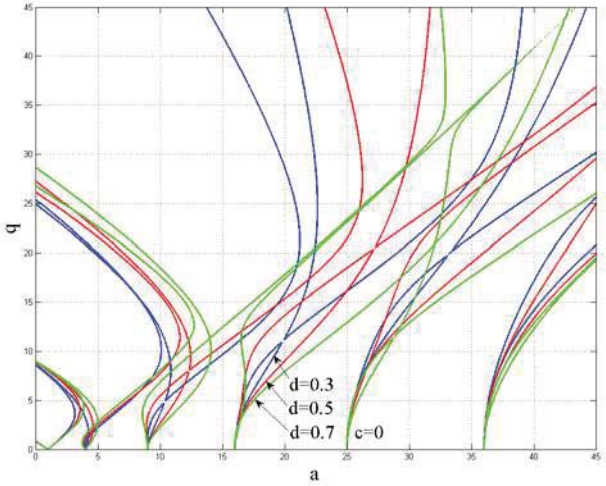

Fig.9 Stability chart for bi-frequency excitation for different d (c=0.0)

(Blue line--d=0.3; red line--d=0.5; green line--d=0.7)

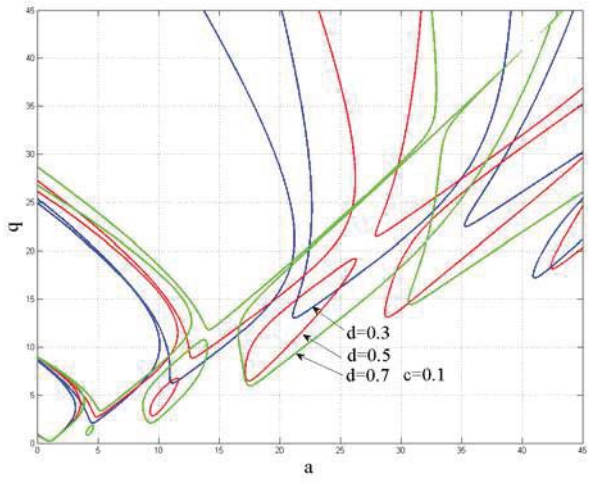

Fig.10 Stability chart for bi-frequency excitation for different d (c=0.1)
(Blue line--d=0.3; red line--d=0.5; green line--d=0.7)

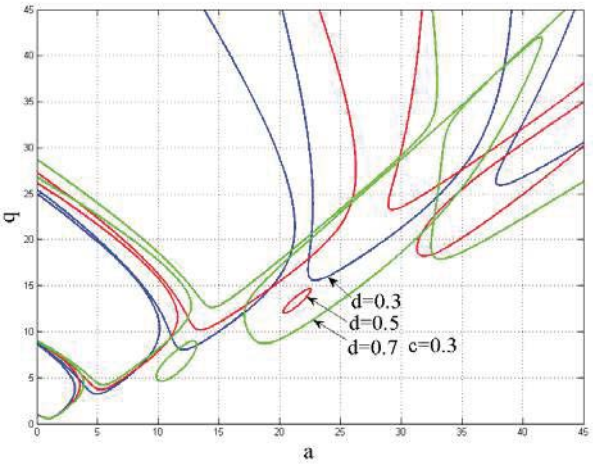

Fig.11 Stability chart for bi-frequency excitation for different d (c=0.3)
(Blue line--d=0.3; red line--d=0.5; green line--d=0.7)

5. CONCLUSIONS

In this work, the taut mooring lines subjected to single and bi-frequency parametric excitation were studied. The responses of the mooring lines subjected to single- and bi-frequency excitation were discussed. The unstable zone of bi-frequency excitation is obviously different from the single-frequency excitation. The safety case in the single-frequency excitation may become unsafely in the bi-frequency excitation. The effects of different parameters on the stability chart were discussed. The results indicate that multi-frequency should be given consideration in a more accurate prediction of parametric excitation.

ACKNOWLEDGEMENTS

This work was financially supported by the National Natural Science Foundation of China (Grant No. 51379005).

6. REFERENCES

Rönnquist, A. Remseth, S. and Udahl, G. 2010. Unstable Non-Linear Dynamic Response Investigation of Submerged Tunnel Taut Mooring Elements Due to Parametric Excitation. 23rd Nordic Seminar on Computational Mechanics.

Jeffrey Falzarano, Jun Cheng, and Samrat Das. 2003. Parametric excitation of floating offshore platforms. 8th International Conference on the Stability of Ships and Ocean Vehicles.

Yang H.Z., Xu P. , 2015. Effect of hull geometry on parametric resonances of spar in irregular waves. Ocean Engineering. 99:14-22.

Libang Zhang, Ayman Eltaher, Paul Jukes. 2010. Mathieu instability of TTR due to VIV. Proceedings of the 5th International Offshore Pipeline Forum.

Pedersen, P. 1980. Stability of the solutions to Mathieu-Hill equations with damping. Ingenieur-Archiv, 149 (1),15-29.

Session 12.1 – DAMAGE STABILITY

Flow Model for Flooding Simulation of a Damaged Ship

An Overview of Warships Damage Data from 1967 to 2013

Advanced Damaged Stability Assessment for Surface Combatants

Dynamic Stability Assessment of Naval Ships in Early-Stage Design

This page is intentionally left blank

Flow Model for Flooding Simulation of a Damaged Ship

Gyeong Joong Lee, *KRISO*, gjlee@kriso.re.kr

ABSTRACT

In this paper, new models for vented compartments and an accumulator model were proposed, which can adjust the inner pressure automatically, even for systems with many compartments and openings. The dynamic-orifice equation was investigated for use in the case of large openings, so that the ripples in the air pressure that had been caused by the square-root singularity of the existing orifice equation could be eliminated. In addition, some models of flow between compartments were investigated, so that the simulation could reflect more realistic situations. Application to a recent real accident validated the effectiveness of the proposed models.

Keywords: *orifice equation, flooding, air compressibility, damaged ship*

1. INTRODUCTION

While the number of flooding and sinking accidents is relatively small, they often lead to the tragic loss of personnel. Therefore, better knowledge about the processes that occur during flooding and sinking is required, and optimal response measures should be prepared according to the results of the study. For this purpose, a great deal of research about flooding has been conducted for specific real accidents, and safety assessments have been conducted during ship design, in anticipation of possible damage in the field.

The flooding simulation of a damaged ship seems to have been started by Spouge (1986), when he investigated the Ro-Ro Ferry sinking. He used a hydraulic-flow model to calculate the flood rate, and used an empirical formula to determine the center-of-gravity of the floodwater and its movement. Sen and Konstantinidis (1987) developed his method further, and they obtained the position of the center-of-gravity by assuming the free surface always remains horizontal. Later, to take into account the dynamic effect of the floodwater, Papanikolaou et al. (2000) developed the method of lumped mass. A flow equation for shallow water and the movement of point mass followed (Chang and Blume, 1998; Chang, 1999). These two papers were cited in Ruponen (2007). Computational fluid dynamics followed (van't Veer and de Kat, 2000; Woodburn et al., 2002; Cho et al., 2005); then the depth-averaged Euler equation was introduced (Lee, 2010a).

Until now, the hydraulic orifice equation has been used to obtain the flow between compartments. For the application of this equation, the following assumptions are required: incompressible fluid, inviscid fluid, steady conditions, and small openings (area). The most troublesome assumption is that steady state: the flow velocity can change instantly as the pressure changes. Lee (2014) newly derived the dynamic-orifice equation from the basic equations of fluid mechanics. In this study, the property of this dynamic-orifice equation was investigated, and the sample calculations with analysis were given.

Another problem that occurs in the simulation of ship flooding, involves the calculation of the pressure in each compartment, when many compartments are connected to each other in complicated ways. This problem has been addressed previously (van't Veer et al., 2002, 2004; Ikeda et al.,

2004; Vassalos et al., 2005). The most important thing is the determining a reference pressure for use in each compartment. Ruponen (2007) made a comprehensive study of this problem and proposed a pressure-correction method that satisfied the mass-conservation law. In this study, a new compartment model was proposed that adjusts the reference pressure simply, even for systems with many compartments and openings. And a method that takes into consideration the dynamic effect for quasi-static analysis was investigated.

2. RE-ANALYSIS OF THE ORIFICE EQUATION

In many studies, the following 'orifice equation' has been used in calculating the flow through an opening.

$$q = \rho C_D A v = \rho C_D A \sqrt{\frac{2\Delta p}{\rho}} \tag{1}$$

where, q and ρ are the mass flux and density of the flow through the opening, A is the area of the opening, Δp the pressure difference, and C_D the discharge coefficient. The above orifice equation was derived from the steady Bernoulli's equation.

2.1 Hydraulic Orifice Equation

Let us derive the hydraulic orifice equation. Bernoulli's equation can be applied to the flow of an incompressible, inviscid fluid in steady state along a stream line. Bernoulli's equation and the continuity equation used for Fig. 1 are Equations 2 and 3, respectively.

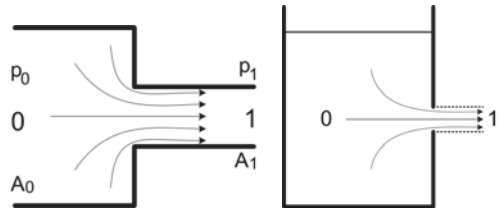

Fig. 1 Orifice and stream lines

$$\frac{p_0}{\rho} + \frac{1}{2}V_0^2 + gz_0 = \frac{p_0}{\rho} + \frac{1}{2}V_1^2 + gz_1 \tag{2}$$

$$A_0 V_0 = A_1 V_1 \tag{3}$$

where, g is the gravitational acceleration, z the height of the position, the subscripts '0' and '1' indicate the orientation (position), the fluid flows from side '0' to side '1'. The total speed of the flow is the square root of the component velocity squared, $V = \sqrt{u^2 + v^2 + w^2}$. From Equations 2 and 3, the flow velocity through the orifice can be expressed as in Equation 4.

$$V_1 = \sqrt{\frac{2}{\rho}\frac{(\Delta P + \rho g \Delta z)}{1 - (A_1/A_0)^2}} \tag{4}$$

If the area of side '0' is large, and the height difference vanishes, then Equation 4 can be reduced to the simpler form below.

$$V_1 = \sqrt{\frac{2}{\rho}\Delta p} \tag{5}$$

The flux can then be obtained by multiplying the area of orifice and fluid density.

$$q = C_D \rho A V_1 = C_D \rho A \sqrt{\frac{2\Delta p}{\rho}} \tag{6}$$

where, the discharge coefficient C_D is related to the inlet/outlet shape, and the Reynolds number. Usually for an orifice with right-angled edges, a discharge coefficient of 0.6–0.7 is used.

Equation 6 has a singular behavior of the square root function for small pressure differences. The rate of change with respect to the pressure difference, goes to infinity as the pressure difference goes to zero. Because of this, an unrealistic oscillation takes place when the pressure difference is small (as for an opening between two compartments with no

other openings), while there is no problem when the pressure difference is large. This phenomenon of square root instability is explained in detail in Appendix A. Thus, the hydraulic orifice equation (6) is for a large pressure difference, subject to the assumptions stated previously.

2.2 Dynamic Orifice Equation

There are two problems with the hydraulic orifice equation. One is that it applies to steady state conditions. The second is that it applied orifices of small cross-section (area). In order to conduct a time-domain flooding simulation, it is required to include the dynamic effect, and to expand the applicability to include orifices of large area. Let us shortly introduce the work of Lee (2014), derivation of a new dynamic orifice equation. The momentum conservation law can be represented by the Euler equation for an incompressible, inviscid fluid (Equations 7 and 7′).

$$\frac{\partial \vec{v}}{\partial t} + (\vec{v} \cdot \nabla)\vec{v} = \vec{F} - \frac{1}{\rho}\nabla p \tag{7}$$

$$\frac{\partial \vec{v}}{\partial t} + \frac{1}{2}\nabla(\vec{v} \cdot \vec{v}) = \vec{F} - \frac{1}{\rho}\nabla p \tag{7′}$$

where, $\vec{v}$ is a velocity vector, p the pressure, ρ the density of fluid, and $\vec{F}$ is the body force, including gravity. The above two equations are the same for incompressible and inviscid fluid. In this study, the integral version of the Euler equation will be used, so the momentum conservation law can be represented as in Equations 8 and 8′ for a specific control volume.

$$\int_{\Omega} \frac{\partial}{\partial t}(\rho\vec{v})dV + \int_{\partial\Omega} \rho\vec{v}(\vec{v} \cdot \vec{n})dS = \int_{\Omega} \rho\vec{F}dV - \int_{\partial\Omega} p\vec{n}dS \tag{8}$$

$$\int_{\Omega} \frac{\partial}{\partial t}(\rho\vec{v})dV + \frac{1}{2}\int_{\partial\Omega} \rho(\vec{v} \cdot \vec{v})\vec{n}dS = \int_{\Omega} \rho\vec{F}dV - \int_{\partial\Omega} p\vec{n}dS \tag{8′}$$

where, Ω is the control volume of concern, and $\partial\Omega$ is the boundary of the control volume. The orientation of the normal vector is outward normal.

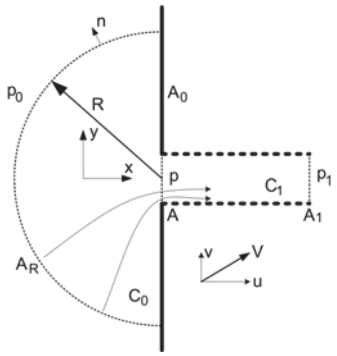

Fig. 2 Orifice, control volumes and related parameters

Fig. 2 shows the orifice and the overall shape of the control volume, where R is the distance from the center of orifice and is chosen to be large so that the flow velocity at that distance will be small enough. On the boundary, A_R, the pressure is constant as p_0, and the flow velocity is parallel to the normal vector. Let us represent the velocity vector as $\vec{v}$, the velocity normal to orifice as u, and the total velocity as $V = \sqrt{u^2 + v^2 + w^2}$, here and after. At the right side of the orifice, the velocity and pressure are assumed to be constantly distributed. The area of the orifice is $A = A_1$, the area of the wall in which the orifice exists is A_0. The control volumes on the left and right are C_0 and C_1, respectively. The velocity components, excluding u, are asymmetric about the centerline of the orifice.

Applying the mass and momentum conservation law to the control volume C_0 and C_1, we can obtain the resulting equation (9) which relates the velocity at the orifice and the pressure difference. (Lee (2014) finally got Equation 9 for the dynamic-orifice equation.)

$$\frac{\sqrt{A}}{2}\frac{\partial \bar{u}}{\partial t}+\frac{7}{8}(\bar{u})^2=\frac{(p_0-p_1)}{\rho} \tag{9}$$

where, $\bar{u}$ is the average normal velocity at the orifice. The final velocity for a steady state of the above equation is:

$$\bar{u}_f=\sqrt{\frac{8}{7}\frac{(p_0-p_1)}{\rho}} \tag{10}$$

This final steady state value is less than that provided by Equation 5. As briefly explained previously, the velocity from Equation 5 is the total velocity, and that of Equation 10 is the normal velocity at the orifice. It is reasonable to use the normal velocity for the calculation of flux through an orifice. Comparing Equations 5 and 10, it can be seen that the theoretical value of the contraction coefficient of a circular orifice with right-angle edge, is $\sqrt{4/7}\cong 0.756$ for an inviscid fluid. We can obtain the initial rate of velocity (i.e., initial acceleration) from rest using Equation 9.

$$\left.\frac{\partial \bar{u}}{\partial t}\right|_{t=0}=\frac{1}{\sqrt{A}}\frac{2(p_0-p_1)}{\rho} \tag{11}$$

The time to reach final velocity using the initial rate of change would be:

$$T=\frac{\bar{u}_f}{d\bar{u}/dt|_{t=0}}=2\sqrt{\frac{A}{7}}\sqrt{\frac{\rho}{2(p_0-p_1)}} \tag{12}$$

Fig. 3 shows the velocity rise with respect to time, when the pressure difference is a step-function.

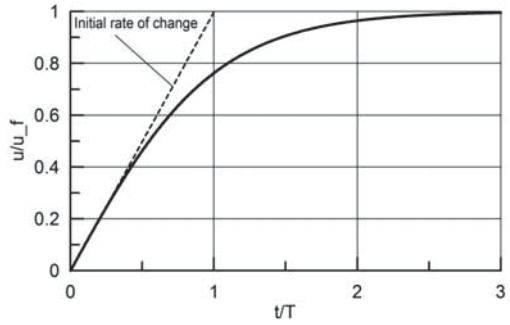

Fig. 3 Orifice velocity behavior when the pressure difference is a step function

The velocity reaches 0.765 of the final velocity at $t=T$, 0.965 at $t=2T$, and 0.99 at $t=3T$. From Fig. 3, the numerical time integration using Equation 9 seems not to be desirable if the size of time step of the simulation is less than T. For that case, one can use Equation 10 rather than 9. Here, T (from Equation 12) becomes larger as the pressure difference becomes smaller. This means that the dynamic model works for the case of small pressure differences, even if we use a fixed size of time step.

For the discharge coefficient, the use of $C_D/\sqrt{4/7}$ is desirable because of the difference between the normal velocity and total velocity in Equations 10 and 5. The density in Equation 10 should be determined according to the sign of the velocity, not the sign of the pressure difference. Equation 9 stands for positive velocity only, and we can modify the equation a little bit for both directions.

$$\begin{aligned}&\frac{\sqrt{A}}{2}\frac{\partial \bar{u}}{\partial t}+\frac{7}{8}\bar{u}|\bar{u}|=\frac{(p_0-p_1)}{\rho}\\ &\text{if } \bar{u}\geq 0, \quad \rho=\rho_0\\ &\text{if } \bar{u}<0, \quad \rho=\rho_1\end{aligned} \tag{13}$$

2.3 Large Opening

The pressure difference can vary across the orifice when it is large. If the pressure difference is constant over the orifice area, Equations 5 and 14 can give the flow velocity, but if it varies; it is possible to obtain the flow by solving the Euler equation or the Navier-Stokes equation. However, this is impractical for a system with many compartments and orifices. A more practical way is to integrate the expression over the orifice area in order to obtain the flux through the orifice. The hydraulic orifice equations (5 and 6) do not include the concept of average velocity, but for practical calculation, one can use the average concept of velocity by integrating them over

the orifice area. Meanwhile, the dynamic orifice equation (13) uses the average velocity, so it creates no logical problem to integrate the pressure difference in order to get the forces acting on the surrounding fluid. Therefore, the average velocities could be obtained using the following equations, and multiplying the orifice area gives the flux.

$$V = \frac{1}{A}\int_A \sqrt{\frac{2}{\rho}\Delta p}\, dA = \frac{1}{A}\sqrt{\frac{2}{\rho}}\int_A \sqrt{\Delta p} dA \qquad (14)$$

$$\frac{\sqrt{A}}{2}\frac{\partial \bar{u}}{\partial t} + \frac{7}{8}\bar{u}|\bar{u}| = \frac{1}{\rho A}\int_A \Delta p dA \qquad (15)$$

where, $\Delta p = p_0 - p_1$ is the pressure difference across the orifice. The mass flux can be obtained by the following equations. (The subscripts 'h' and 'd' mean the flux from the hydraulic orifice equation and dynamic orifice equation, respectively.)

$$q_h = \rho C_D A V \qquad (16)$$

$$q_d = \rho C_D{}' A \bar{u} \qquad (17)$$

where the value of C_D is from the hydraulic experiment, so use $C_D{}'$ as $C_D/\sqrt{4/7}$.

Another big problem with larger openings is the fact that the free surface may lie upon cross section of the orifice. Followings are a number of cases (Fig. 4) that could occur, depending on the height of the free surface, and the substances on both sides of the orifice.

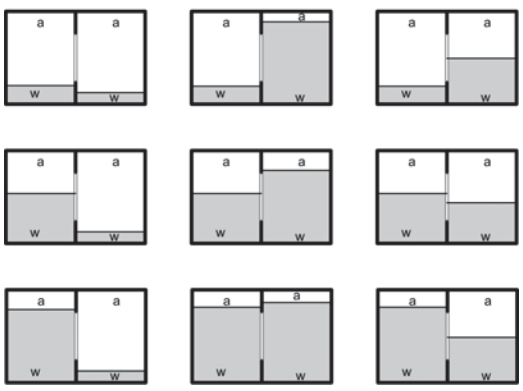

Fig. 4 Orifice and adjacent substances ('a' is air, 'w' is water)

These cases can be classified into four boundary types (within the orifice) according to the substances in contact: Air-Air, Air-Water, Water-Air, and Water-Water. The integration of Equations 14 and 15 can be obtained by dividing the orifice area into sub-regions so that each sub-region has one type of material boundary, then integrating the equations (14, 15) over each sub-region, and adding the results.

Regarding the shape of the openings, many have long, narrow shapes (e.g., doors and gaps). In these cases, one-dimensional (1-D) integration may be helpful, but for other cases the integration should be done in 2-D.

In order to calculate the flow through an opening, there is a need for several definitions. First, the identification of the compartment of interest is needed because the opening connects two compartments; thus, we have Compartment 0 and Compartment 1. This identification may be provided by adding the subscript '0' or '1'. The velocity is defined as positive when the flow is from Compartment 0 to Compartment 1; whereas, negative velocity means flow in the opposite direction. Compartment 0 is called the 'donor'; Compartment 1 is the 'acceptor'. The subscripts 'w' and 'a' refer to the substances water and air, respectively.

The two substances can flow through the opening simultaneously, so the flux may be identified by adding subscript as follows,

q_{ha} : mass flux of air using hydraulic orifice equation
q_{hw} : mass flux of water using hydraulic orifice equation
q_{da} : mass flux of air using dynamic orifice equation
q_{dw} : mass flux of water using dynamic orifice equation

First, let us divide the opening area into sub-regions with one of the four types of boundary (i.e., 'air-air', 'air-water', 'water-air', and 'water-water'). If the sign of the pressure difference changes in any sub-region, this sub-region is divided into two sub-regions so that each sub-region has a distinct sign of pressure

difference, and one boundary type. For each sub-region, calculate the following integrals,

$$I_i = \int_{A_i} sgn(\Delta p)\sqrt{|\Delta p|}\,dA \tag{18}$$

$$J_i = \int_{A_i} \Delta p\,dA \tag{19}$$

$$A_i = \int_{A_i} dA \tag{20}$$

where, $sgn(\Delta p)$ is the sign of Δp. Because the integrand has one sign, the sign of the integral is the same as the sign of the pressure difference.

The mass flux can be calculated using the above integrals, if we use the hydraulic orifice equation (21 and 22).

$$q_{ha} = \sum_i \begin{cases} \rho_{a0} C_D \sqrt{2/\rho_{a0}}\; I_i & for\ I_i \geq 0, and\ donor\ is\ air \\ \rho_{a1} C_D \sqrt{2/\rho_{a1}}\; I_i & for\ I_i < 0, and\ acceptor\ is\ air \end{cases} \tag{21}$$

$$q_{hw} = \sum_i \begin{cases} \rho_{w0} C_D \sqrt{2/\rho_{w0}}\; I_i & for\ I_i \geq 0, and\ donor\ is\ water \\ \rho_{w1} C_D \sqrt{2/\rho_{w1}}\; I_i & for\ I_i < 0, and\ acceptor\ is\ water \end{cases} \tag{22}$$

To use the dynamic orifice equation (15), the calculation should be done according to the sign of the velocity not the sign of the pressure difference. Because the velocity is the unknown, two cases (positive and negative) should be prepared. Thus,

For air-air, $J_{Pa} = \sum_i J_i\ ,\ A_{Pa} = \sum_i A_i$

$J_{Ma} = \sum_i J_i\ ,\ A_{Ma} = \sum_i A_i$

For water-water, $J_{Pw} = \sum_i J_i\ ,\ A_{Pw} = \sum_i A_i$

$J_{Mw} = \sum_i J_i\ ,\ A_{Mw} = \sum_i A_i$

For air-water, $J_{Pa} = \sum_i J_i\ ,\ A_{Pa} = \sum_i A_i$ if $J_i \geq 0$

$J_{Mw} = \sum_i J_i\ ,\ A_{Mw} = \sum_i A_i$ if $J_i < 0$

For water-air, $J_{Pw} = \sum_i J_i\ ,\ A_{Pw} = \sum_i A_i$ if $J_i \geq 0$

$J_{Ma} = \sum_i J_i\ ,\ A_{Ma} = \sum_i A_i$ if $J_i < 0$

According to the sign of the velocity, the following equations give the averaged water and air velocities.

$$\frac{\sqrt{A_{Xa}}}{2}\frac{\partial(\bar{u})_a}{\partial t} + \frac{7}{8}\bar{u}|\bar{u}|_a = \frac{1}{\rho A_{Xa}} J_{Xa} \tag{23}$$

$$\frac{\sqrt{A_{Xw}}}{2}\frac{\partial(\bar{u})_w}{\partial t} + \frac{7}{8}\bar{u}|\bar{u}|_w = \frac{1}{\rho A_{Xw}} J_{Xw} \tag{23′}$$

Equation 23 is for the air flow, and 23′ is for the water flow. In the above equation 'X' is 'P' if the velocity is positive; while 'M' is negative. The mass flux can be obtained by the following equations.

$$q_{da} = \rho_a C_D' A_a (\bar{u})_a \tag{24}$$

$$q_{dw} = \rho_w C_D' A_w (\bar{u})_w \tag{24′}$$

In some cases, the force acing on a door is required to determine when the door will collapse; the force can be obtained by simply adding all J_i.

1-D Opening

Sometimes, it is convenient to neglect the variation of the pressure difference along width and to integrate it along the height, for a door or its gap, as shown in Fig. 5.

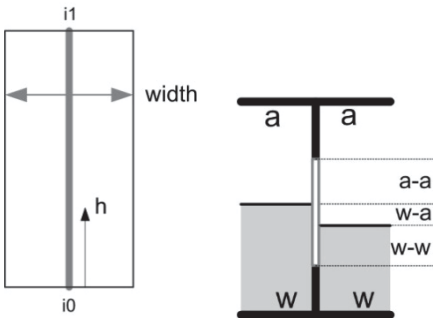

Fig. 5 Shape of 1-D opening and sub-regions of orifice

The integration of Equations (18), (19), (20) can be carried out analytically by assuming the linear variation of pressure difference in each sub-region. For the i-th sub-region, $(h_i \leq h < h_{i+1})$ the pressure difference can be represented as,

$$\Delta p = a_i(h - h_i) + b_i$$

$$b_i = \Delta p_i\ ,\ a_i = (\Delta p_{i+1} - \Delta p_i)/(h_{i+1} - h_i)$$

Then, substitute the above into Equations 18 and 19, and integrate them analytically. The results of the integrations for $a_i = 0$ are:

$$I_i = sgn(\Delta p_i) w_0 \int_{h_i}^{h_{i+1}} (|\Delta p|)^{\frac{1}{2}} dh = sgn(\Delta p_i) w_0 (|\Delta p|)^{\frac{1}{2}} (h_{i+1} - h_i) \quad (25)$$

$$J_i = w_0 \int_{h_i}^{h_{i+1}} \Delta p dh = w_0 \Delta p (h_{i+1} - h_i) \quad (26)$$

$$A_i = w_0 \int_{h_i}^{h_{i+1}} dh = w_0 (h_{i+1} - h_i) \quad (27)$$

and for $a_i \neq 0$,

$$I_i = sgn(\Delta p_i) w_0 \int_{h_i}^{h_{i+1}} (|\Delta p|)^{\frac{1}{2}} dh = sgn(\Delta p_i) w_0 \frac{2}{3a_i} \left[\Delta p (|\Delta p|)^{\frac{1}{2}} \right]_i^{i+1} \quad (28)$$

$$J_i = w_0 \int_{h_i}^{h_{i+1}} \Delta p dh = w_0 \frac{1}{2a_i} [(\Delta p)^2]_i^{i+1} \quad (29)$$

$$A_i = w_0 \int_{h_i}^{h_{i+1}} dh = w_0 (h_{i+1} - h_i) \quad (30)$$

where, $[\ ]_i^{i+1}$ means the subtraction of i indexed value from i+1 indexed value. The above expression was drawn to be independent of the sign of the pressure difference.

2-D Opening

For the general shape of an opening, the integration would be carried out in 2-D. Let us divide the opening area into sub-regions as explained previously, which can be represented as a closed polynomial. Next, integrate them over each sub-region using the Stokes theorem. Let us fit the pressure difference by bi-linear interpolation as in Equation 31.

$$\Delta p = ax + by + c \quad (31)$$

Three constants a, b, and c can be found from three conditions at three vertices of that polynomial.

Let us change the area integral to the contour integral, along the contour C_i using Stokes theorem.

$$I_i = sgn(\Delta p) \iint_{R_i} \sqrt{|\Delta p|} dx dy = \frac{2}{3a} \oint_{C_i} |\Delta p|^{2/3} dy \quad (32)$$

$$J_i = \iint_{R_i} \Delta p dx dy = \frac{1}{2a} \oint_{C_i} (\Delta p)^2 dy \quad (33)$$

$$A_i = \iint_{R_i} dx dy = \oint_{C_i} x dy \quad (34)$$

On the j-th line segment of the i-th sub-region, the following geometric relation exists.

$$x = b_{xj} y + c_{xj}, \qquad b_{xj} = \frac{x_{j+1} - x_j}{y_{j+1} - y_j}, \qquad c_{xj} = x_j - \frac{x_{j+1} - x_j}{y_{j+1} - y_j} y_j$$

Therefore, the pressure difference (31) can be expressed as follows on the j-th line segment.

$$\Delta p = ax + by + c = b_j' y + c_j'$$
$$b_j' = b + a b_{xj}, \ c_j' = c + a c_{xj}$$

If we integrate Equation 32, the results are (for $a \neq 0$),

$$I_i = sgn(\Delta p) \frac{2}{3a} \times \sum_j \begin{cases} \frac{2}{5b_j'} \left[(\Delta p)^2 (|\Delta p|)^{\frac{1}{2}} \right]_j^{j+1} & for\ b_j' \neq 0 \\ (\Delta p)(|\Delta p|)^{\frac{1}{2}} (y_{j+1} - y_j) & for\ b_j' = 0 \end{cases} \quad (35)$$

and for $a = 0$, ($b_j' = b$, $c_j' = c$)

$$I_i = sgn(\Delta p) \times \sum_j \begin{cases} \frac{2}{15b^2} \left[(5bx - 2b_{xj}\Delta p)(\Delta p)(|\Delta p|)^{\frac{1}{2}} \right]_j^{j+1} & for\ b \neq 0 \\ \frac{1}{2} (|\Delta p|)^{\frac{1}{2}} (x_{j+1} + x_j)(y_{j+1} - y_j) & for\ b = 0 \end{cases} \quad (36)$$

The results of equation (33) are (for $a \neq 0$),

$$J_i = \frac{1}{2a}\sum_j \begin{cases} \frac{1}{3b_j'}[(\Delta p)^3]_j^{j+1} & for\ b_j' \neq 0 \\ (\Delta p)^2(y_{j+1} - y_j) & for\ b_j' = 0 \end{cases} \quad (37)$$

and for $a = 0$, $(b_j' = b\ , c_j' = c)$

$$J_i = \sum_j \begin{cases} \frac{1}{6b^2}[(3bx - b_x\Delta p)(\Delta p)^2]_j^{j+1} \\ for\ b \neq 0 \\ \frac{1}{2}(\Delta p)(x_{j+1} + x_j)(y_{j+1} - y_j) \\ for\ b = 0 \end{cases} \quad (38)$$

The area, from Equation 34, can be rewritten as follows.

$$A_i = \sum_j \frac{1}{2}(x_{j+1} + x_j)(y_{j+1} - y_j) \quad (39)$$

2.4 Sample Applications

Let us consider the case in which two compartments are adjacent, and an opening is located in the wall between them. The size of the compartment is 5 m (L) x 5 m (W) x 5 m (H), and there is no vent. The sample calculations were carried out for a point and a 1-D opening, the compressibility of air was included, and an iso-thermal process was assumed. The result from the dynamic orifice equation was compared with that from the hydraulic orifice equation.

For a point opening, the area of the opening is 1 m^2 and the location of the orifice 1 m from the bottom. A 1-D calculation was also made for the comparison. The calculation cases are shown in Fig.6. The results are shown in Fig. 7 in comparison with 1-D calculation.

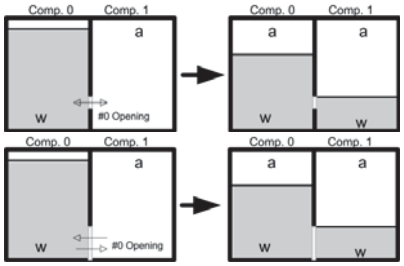

Fig. 6 Sample model for point opening (upper two) and equivalent 1-D opening (below two) (In each pair of figures, the left figure shows the initial state, and the right figure shows the expected final state.)

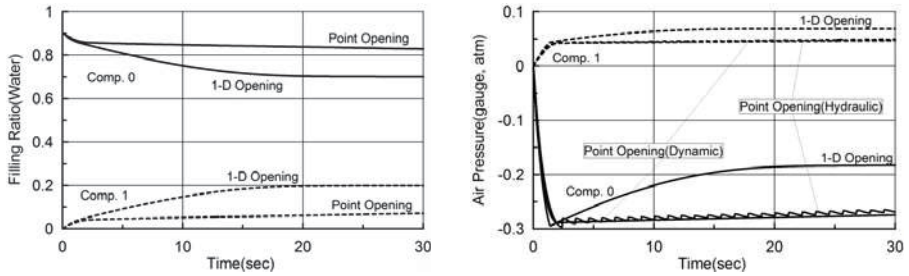

Fig.7 Filling ratio (left) and the air pressure (right) in compartments with a point-opening

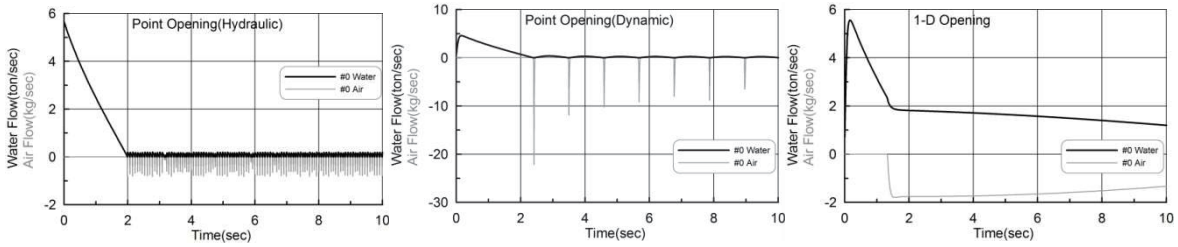

Fig. 8 Flow rates of water and air for point (left and center) and 1-D openings (right)

The filling ratio of Compartment 0 decreases with time, and the filling ratio of Compartment 1 increases. However, the results for the point-opening vary slowly, except in the initial stage, and the pressure in Compartment 0 oscillates. The flows of water and air are shown in Fig. 8.

The flow of air exhibits many rapid small oscillations with the hydraulic orifice equation, while it exhibits intermittent large oscillations with the dynamic orifice equation. This affects the pressure fluctuation in Fig. 7. This is because a point opening can only allow the flow of one substance at a time. For 1-D openings, the water and air can flow simultaneously in opposite directions, the flow is smoother, and the filling ratio reaches the value we anticipated. From these results, we now know that point-openings should not be used when there is only one opening in a compartment.

1-D opening

The next sample calculations were made with 1-D openings. The sample cases were for situations with a low opening (Case 1), a centered opening (Case 2), and two openings, one upper and one lower (Case 3). The results with a 2-D opening would be the same as the results with a 1-D opening of the same shape, if the compartments were not inclined. Here, the focus is on the comparison of the results of the hydraulic and dynamic orifice equations.

For Case 1, the model was set as in Fig. 9; the opening was located in the lower part of the wall, the height of opening was 1m and the area was $1m^2$.

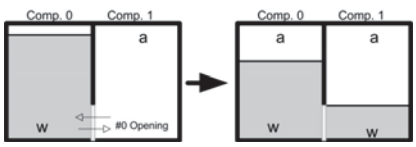

Fig. 9 Sample Case 1: low 1-D opening (The left figure shows the initial state, and the right figure shows the expected final state.)

As can be seen in Fig. 10, the calculation results for the hydraulic-orifice and dynamic-orifice equations are similar. There was no oscillation phenomenon in the results. This might be because the water totally covers the opening in the final steady stage.

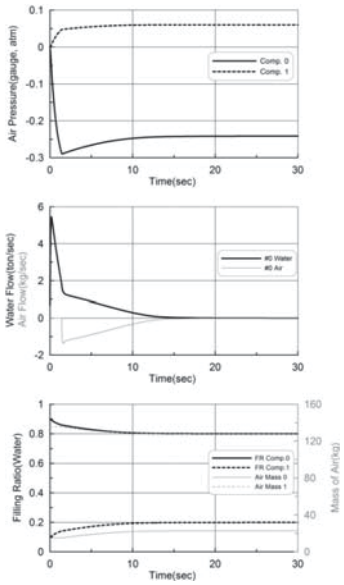

Fig. 10 Time simulation results for Sample Case 1 (low 1-D opening)

Next was Case 2, involving a 1-D opening in the middle of the wall (Fig. 11).

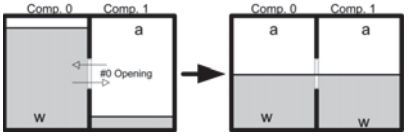

Fig. 11 Sample Case 2: centered 1-D opening (The left figure shows the initial state, and the right figure shows the expected final state.)

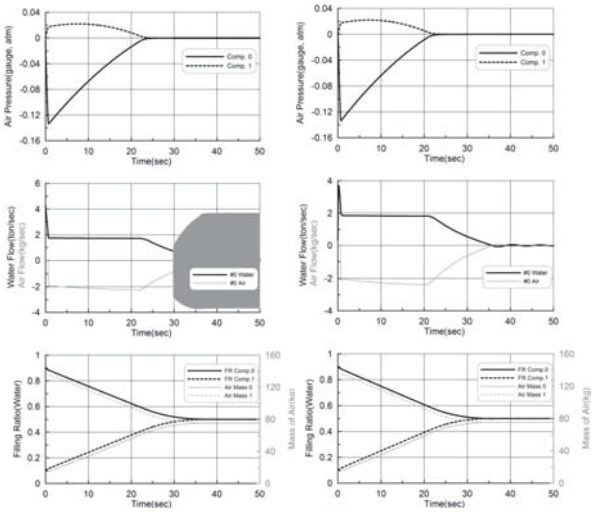

Fig. 12 Time simulation results for Sample Case 2 (centered 1-D opening), left–results from the hydraulic orifice equation, right–results from the dynamic one

The Case 2 results are shown in Fig. 12. The filling ratios are similar, but the air flows after 30 seconds are quite different from each other. The result from the hydraulic orifice equation starts to oscillate highly around 30 seconds; an enlarged view of this oscillation was drawn in Fig. 13. This oscillation is due to the numerical stability of the square root. However, the results from the dynamic orifice equation oscillated smoothly. This might be from an inertia effect.

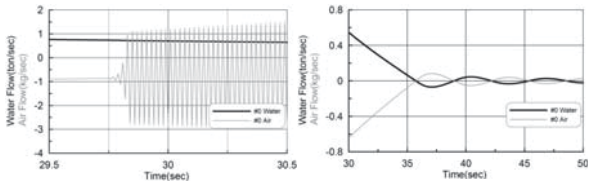

Fig. 13 Enlarged view of the flow rates of water and air: left–for hydraulic orifice equation, right–for the dynamic one)

The third sample, Case 3, involves two openings, one upper and one lower. The height of both openings is 1 m, and both openings are 1 m^2, the model was set in Fig. 14.

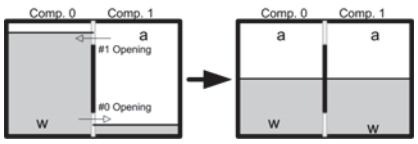

Fig. 14 Sample Case 3: two 1-D openings, one upper and one lower (The left figure shows the initial state, and the right figure shows the expected final state.)

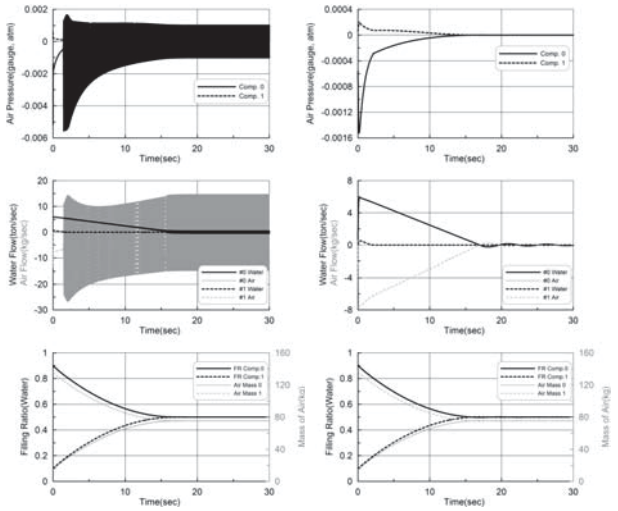

Fig. 15 Time simulation results for Sample Case 3 (two 1-D openings, one upper and one lower), left–for hydraulic orifice equation, right–for dynamic one

In this case also, the filling ratios were similar. However, the air pressure and air flow through the upper opening started to oscillate from an early stage, as in Fig. 15. Fig. 16 shows the enlarged view of the air flow and air pressure around the start of oscillation.

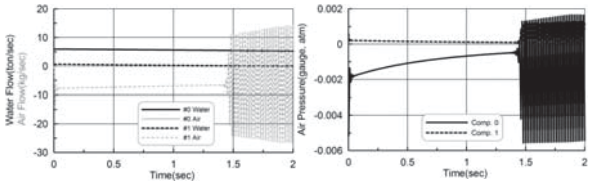

Fig. 16 Enlarged view of flow rates of water and air, and air pressure (around the starting point of the oscillation)

The results from the three sample calculations above show that the point opening should not be used for the cases with one opening in a compartment, and that the numerical instability takes place when the air in both compartments is connected through an opening. Surely, for the case of many compartments, the numerical instability due to the square-root function can ruin the flooding simulation. The dynamic orifice equation can solve this problem as it did in the above calculations.

3. COMPARTMENT MODEL

If damage occurs in a ship with many rooms, like a passenger ship, the flows of floodwater and air through the inside passages is quite complicated. The air could block the flow of water into some compartments, and retard the flooding rate. Thus, the compressibility of air plays a crucial role in the transient stage of flooding. Moreover, it is necessary to provide a reference pressure for every compartment. If a compartment is partially filled with water, the reference pressure is the one on the free surface, i.e. the air pressure. In fully water-filled compartment, there exist no free surface; so no air pressure. In such cases, selection of the reference pressure is a problem.

For a fully water-filled compartment, there is no reference pressure, while the reference pressure in a partially filled compartment is the air pressure. Ruponen (2007) introduced the idea of water height at each compartment to play the role of reference pressure in fully filled compartments. He used a method in which the pressure should be determined to satisfy the mass conservation law for each compartment, by pressure-correction. However, this method is complex and he had no choice but to use iteration to solve the pressure-correction equation

However, there is no need to focus on mass conservation. It can be satisfied automatically if we calculate the mass flux in the right way. For steady state, there is no choice but to use the iteration method to solve the non-linear pressure-correction equation. On the other hand, for unsteady problems, dynamics gives the relation between mass flow and pressure, so that the mass flow and pressure vary continuously with time, in order to maintain mass and momentum balance (i.e., via the law of conservation of mass and momentum). Therefore, if we solve the dynamic equation derived from the conservation law, the conservation will be satisfied intrinsically. The compartment that can be fully flooded is usually one with a vent. For this compartment, the mass conservation law will be satisfied if we count on the mass flowing through the air vent, that is, mass conservation for the compartment and vent, not the compartment only.

In this section, the compartment model was adapted. Then the mass of water and air, the calculation of flow in and out, and the reference pressure of the compartment, were analyzed for vented and unvented compartments.

3.1 Basic Compartment Model

Consider a compartment in which all the openings, including vents, are well defined. The mass of water and air can be calculated as,

$$\begin{aligned} \dot{m}_w &= q_w \\ \dot{m}_a &= q_a \quad (for\ m_a \geq 0) \end{aligned} \tag{40}$$

where, m_w, m_a are the mass of water and air; q_w, q_a are the mass flux of each substance into the compartment through all openings. The volume charged by water V_w is calculated by m_w/ρ_w, then the remaining volume of the compartment is the volume charged by air.

$$\begin{aligned} V_w &= m_w/\rho_w \\ V_a &= V_{max} - V_w \end{aligned} \tag{41}$$

The above equation (41) can be applied for ($V_w \leq V_{max}$) only. The state equation of ideal gas gives the pressure of the air. The state equation using pressure and density is

$$pV^\gamma = const. \quad \rightarrow \quad p/\rho^\gamma = const. \tag{42}$$

where, γ is the ratio of specific heat of ideal air, for the iso-thermal process its value is '1', and for the iso-entropic process its value is 7/5. The pressure of the air can be calculated as

$$p_a = k_{atm}\rho_a^\gamma - p_{atm} \tag{43}$$

where, the density of air $\rho_a = m_a/V_a$, and the constant coefficient of the atmospheric condition $k_{atm} = p_{atm}/\rho_{atm}^{\gamma}$. The pressure p_a is the gauge pressure, and p_{atm} is the atmospheric pressure. About the ratio of specific heat γ, the value '1' is adequate for the case that the flooding is proceeded slowly (i.e., the slow compression), and 7/5 for the case of rapid compression.

3.2 Vented Compartment Model

A vented compartment is one from which the air can flow out, if the water flows into it, without actually describing the vent duct. If the vent area (cross-section) is large enough, the pressure will remain at atmospheric. However, for a small vent area, the air would become compressed, so that the pressure of the air inside is greater than atmospheric pressure. There is no problem in calculating the flows of water and air, and the pressure, if air remains in the compartment, as in Fig. 17 (left). If, however, all the air flows out (Fig. 17, right) there is no means to calculate the pressure in it without comparing the surrounding pressure (i.e., there is no reference pressure). In this case, water can enter the compartment; the mass conservation law seems to be violated without considering the flow through the vent. If the same amount of water is understood to flow out through the vent, the mass conservation law is satisfied. We found a way to designate a reference pressure, considering the pressure at the position of the vent. For this purpose, we propose the following compartment model (Fig. 18).

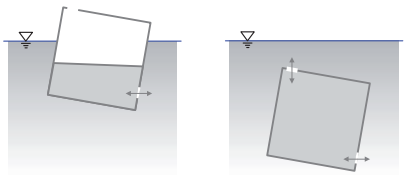

Fig. 17 Previous vented-compartment concept: floating (left) and submerged (right)

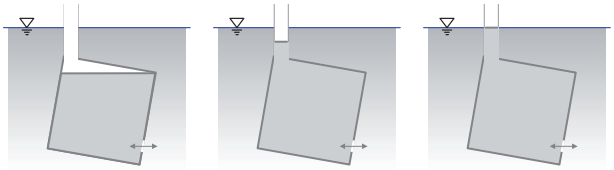

Fig. 18 Alternative air-water column concept for vented compartments

For the real vent duct (or ducts) substitute a simple vertical (virtual) vent (i.e., introduce a vertical air-water column at the top of the compartment). For the case of partial filling, there is no problem, and the reference pressure is the air pressure. Even for the case of full filling, the water can flow into the compartment; the surplus water flows up through the vertical vent. The surplus water fills the vertical vent and the top surface goes up to the free surface, and the reference pressure will be set to the pressure corresponding to the height of the water column in the vertical vent. If more water flows into it, the height of water column will be higher than the free surface, and the reference pressure will be higher than the surrounding compartment. If so, the water in that compartment could flow out to another compartment, and the water column could be reduced (that is, the reference pressure will be set to the correct value automatically as the event progresses). The above assumptions explain real situations well, and the conservation of mass is satisfied.

To continue, the compartments can then be categorized into partially vented and fully vented compartments. If the vent area is large, the air is easily vented if the water flows in, so the air pressure is almost the same as atmospheric pressure. If the vent area is small, the air will be compressed. From these, the criterion for a fully vented compartment can be drawn. It seems reasonable that a fully vented compartment has a virtual vent area greater than 1/100 of the top area. A compartment with a vent area less than 1/100 of the top area would be classified as a partially vented compartment.

Fully Vented Compartment

Let us assume the vent area $A_v = 0.01 \times (V_{max})^{2/3}$ or the area of water flow in. Then air compressibility is nearly absent. For fully vented compartments, the flow model can be described for V_w/V_{max} <1, i.e., the case in which air remains,

$$\begin{aligned} \dot{m}_w &= q_w \\ V_w &= m_w/\rho_w \\ p_a &= 0 \end{aligned} \tag{44}$$

for $V_w/V_{max} \geq 1$, i.e. fully water-filled, $(V_v \geq 0)$

$$\begin{aligned} V_w &= V_{max} \\ \dot{V}_v &= q_w/\rho_w \\ h_v &= V_v/A_v \\ p_a &= \rho_w g h_v \end{aligned} \tag{45}$$

where, h_v, V_v are the height and volume of the water column in the vertical vent, respectively.

Partially Vented Compartment

In this model, the air pressure is sought. Suppose that A_v is given.

For V_w/V_{max}<1,

$$\begin{aligned} q_{av} &= \begin{cases} C_D \rho_a A_v \sqrt{2p_a/\rho_a} & for\ p_a \geq 0 \\ -C_D \rho_{atm} A_v \sqrt{-2p_a/\rho_{atm}} & for\ p_a < 0 \end{cases} \\ \dot{m}_w &= q_w \\ \dot{m}_a &= q_a + q_{av} \\ V_w &= m_w/\rho_w \\ V_a &= V_{max} - V_w \\ \rho_a &= m_a/V_a \\ p_a &= k_{atm}\rho_a - p_{atm} \end{aligned} \tag{46}$$

For $V_w/V_{max} \geq 1$, i.e. fully filled, $(V_v \geq 0)$

$$\begin{aligned} V_w &= V_{max} \\ \dot{V}_v &= q_w/\rho_w \\ h_v &= V_v/A_v \end{aligned} \tag{47}$$

$$p_a = \rho_w g h_v + p_{vent}$$

where, in the last equation p_{vent} is the pressure loss due to the flow through the vent. It can be represented by the equation $p_{vent} = 1/2\ \rho\ v^2$, in which the velocity and density is assumed to be those of the air flowing through the vent.

When the filling ratio (V_w/V_{max}) reaches '1' (i.e., the substance that flows through the inlet of the vent changes from air the water), the volume of the air (V_a) vanishes. So, we have trouble in calculating the density of air. To remedy this, it is required to add the volume of the vent to V_a, and the mass of air in the vent to the air mass of the compartment. At the moment when the compartment is just fully filled, the pressure of air (i.e., the reference pressure) has a jump to p_{vent}. If we use the density and velocity of the water, this gives very large value at that moment, whereas it will soon be balanced with the adjacent compartment. So it is recommended to use the density and velocity of the air through the vent, and add some damping to it.

3.3 Accumulator Model

If a compartment is not vented, usually all the air does not flow out. Of course, all the air could flow out if there were any openings at the top of the compartment. If air remains in the compartment, the air pressure can be calculated using the state equation of air (Equation 43). On the other hand, if the amount of air is very small, the air pressure is so largely affected by the amount of water inflow, that it is difficult to calculate the air pressure. Furthermore, if all the air flows through an opening, there is no means to calculate the air density, thus a problem arises in calculating the reference pressure. In fact, a compartment in a ship might have machinery, freight, and many other things in it, so that there might be many small spaces that could contain air. This means that all the air in a compartment seldom flows out. Let us

introduce a virtual accumulator that could solve this problem.

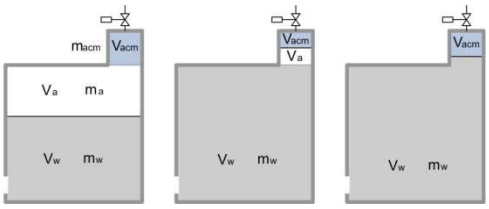

Fig. 19 Virtual Accumulator Model

Fig. 19 shows the concept of a virtual accumulator for several cases: a case with remaining air, a case with a very small amount of remaining air, and a case without air. Air fills the accumulator, and its maximum volume is represented as V_{acmmax} , the operating volume is V_{acm} , and the air mass in the accumulator is m_{acm}.

A simple way to apply the accumulator is by adding the extra air volume without pre-charged pressure to the compartment volume, which cannot flow out. This is a passive accumulator, and its mathematical model is Equation 48.

$$\begin{aligned}
&\dot{m}_w = q_w \\
&\dot{m}_a = q_a \ (for\ m_a \geq 0) \\
&V_w = m_w/\rho_w \\
&V_a + V_{acm} = V_{max} + V_{acmmax} - V_w \\
&\rho_a = \frac{m_a + m_{acm}}{V_a + V_{acm}} \\
&p_a = k_{atm}\rho_a - p_{atm} \\
&V_a = m_a/\rho_a \\
&V_{acm} = m_{acm}/\rho_a
\end{aligned} \tag{48}$$

The virtual accumulator has the effect of enlargement of the volume. Even when there is no air the accumulator can provide a reference pressure and stabilize pressure fluctuation. If a passive accumulator is used, the mass conservation law is violated a little. However, if we want to conserve mass strictly, the active accumulator ensures it. An active accumulator makes the accumulator volume constant by controlling the amount of air. If the water flows in, the air in the accumulator is compressed so that the reference pressure rises and blocks the inflow of water. In this way, the active accumulator can give the reference pressure and ensures the mass conservation law in that compartment. A sudden inflow violates the mass conservation law, but in a short time, the appropriate amount of water flows out, so that the inner mass of compartment remains constant in reference to the concept of time average. The active accumulator model simply adds a feedback control law to regulate the volume of the accumulator. This allows the accumulator to maintain a nearly constant volume, and this feedback control changes the mass of the accumulator as in Equation 49.

$$\begin{aligned}
&V_{in} = V_{acmmax} - V_{acm} \\
&\dot{m}_{acm} = k_P V_{in} + k_D \dot{V}_{in}
\end{aligned} \tag{49}$$

where, k_P , k_D are the proportional and differential gains respectively, V_{in} means the change of the accumulator volume from its initial one (i.e., the volume that enters the accumulator). Through many calculations, we found that 5% of the compartment volume is reasonable for a maximum accumulator volume, and $k_P = 1$, $k_D = 10$ are adequate for almost all the cases with $\Delta t = 0.01s$. For other values of Δt, the adequate values of control gains may differ, of course.

3.4 Floodwater Dynamics

In this study, the movement of the center-of-gravity was analyzed using quasi-static analysis. This analysis has no dynamics, so that the center-of-gravity moves instantly to a new position if a compartment inclines. However, in real situations, time is required for the floodwater to accumulate in new locations, and some complicated flow motions arise, typically waves. Quasi-static analysis has no dynamics effect, so it cannot reflect this reality. In flooding simulation, this effect is large for a ship like a Ro-Ro ferry, which has a large car deck. Suppose that a ship contains floodwater, even if it is inclined only a little bit, the shift in the floodwater center-of-gravity is largely

instantaneous (by previous methods). Therefore, the calculated motions of the ship include unrealistic motions because of the instant large shifts in the center-of-gravity. In this study, a simple method is proposed that considers the dynamics of the floodwater.

The center-of-gravity moves toward the geometric center as time goes, so we want a method that provides a force toward the static center-of-gravity, and that also provides adequate damping. The appropriate mathematical model for the movement of floodwater might be a second-order differential equation in the form of Equation 50.

$$m\dot{v} + bv = f \times (x_S - x) \tag{50}$$

where, x is the center-of-gravity of floodwater, while x_S is the static one; m is the mass of floodwater, and v the moving velocity of the center-of-gravity. If the static center-of-gravity does not move, the center-of-gravity moves toward the static one.

The forcing factor f seems to be proportional to the mass and gravity, and be a function of the filling ratio f_r. So, we propose the equation of motion of the center-of-gravity as follows,

$$m\dot{v} + bv = mg\frac{1 + 2f_r}{l/2}(x_S - x) \tag{51}$$

where, l is a characteristic length of the compartment. Dividing the above equation by the mass, the equation can be represented as a typical second-order differential equation.

$$\begin{aligned} &\ddot{x} + b'\dot{x} + \omega_n^2 x = \omega_n^2 x_S \\ &\omega_n^2 = \frac{2(1 + 2f_r)g}{l} \\ &b' = \omega_n \end{aligned} \tag{52}$$

Let us also consider the damping coefficient b'. If the damping is critical, it is $b'_c = 2\omega_n$. In order to reflect more realistic situations, it is better to have an overshoot, so let us take 1/2 of the critical value. If we take this value, the amplitude of RAO at resonance is '1'. The above equation shows that the center-of-gravity moves slowly if the characteristic length is long, and moves quickly if the length is short. This reflects reality. Consider the natural frequency of Equation 52. The natural frequency of the first resonance mode of a standing wave in a tank whose length is l can be found in Equation 53.

$$\begin{aligned} &\omega_n^2 = \frac{\pi g}{l} \\ &\text{from } (\frac{1}{2}\lambda = l\,, k = \frac{2\pi}{\lambda} = \frac{\pi}{l}) \end{aligned} \tag{53}$$

Comparing the two resonance frequencies (52, 53), if the filling ratio is about 0.3, the two frequencies are similar. As the filling ratio decreases, the effect of shallow water makes the natural frequency lower, and as the filling ratio increases, the natural frequency becomes higher. This characteristic is already included, approximately, in Equation 52.

The advantage of this equation is the fact that we can consider the effect of the filling ratio in a simple manner. If we can determine the static center-of-gravity, Equation 52 gives the motion of the center-of-gravity without involving complex fluid dynamics.

4. VALIDATION

Recently, there was a sinking accident with the loss of many people in Korea. The ship, MV Sewol, was a Ro-Ro ferry of 132m length, 22m breath, and 9,610ton displacement. It has two car decks and a freight deck in it. The simulation team in KRISO was launched in order to make data to reasonably explain the cause and effect of the accident (KRISO, 2014). The main reason of the accident turned out to be the lack of restoring and the movement of freight during its turn. The ship was modeled

with 27 internal compartments and 81 openings for flooding simulation. Figure 20 shows the shape of the ship and compartments in it. The flooding simulation team had tried to tune up the parameters (especially related with openings, the gap of doors and ramps) so that the simulation results resemble the official data from the cooperative investigation headquarter for MV Sewol. Then, the team provided explanations about the process of the flooding and sinking.

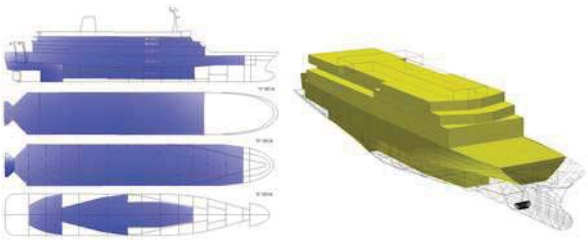

Fig. 20 Shape and the internal compartments of MV Sewol

It was presumed that the ship tumbled down due to an excessive steering and the resulting movement of freight in it. It was reported the initial angle of heel was 30 degrees port after its tumble and there was no collision accident. The flooding simulation started from the condition in which the roll angle was negative 30 degree (i.e., the left side of the ship went down). Fig. 21 shows the roll angle (inclination) compared with the official data provided by the cooperative investigation headquarter for MV Sewol. Fig. 22 shows the pitch and heave motion during flooding and sinking.

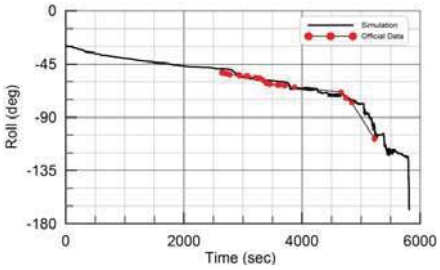

Fig. 21 Inclination angle(roll) compared with the official data

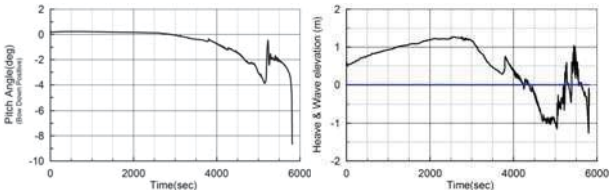

Fig. 22 Pitch(left) and heave(right)

Fig. 23 shows the flow rate through some important openings from outside. And Fig. 24 shows the filling ratios in compartments below the main deck. At the start, the flow-in took place only through the side door located at D deck. As the inclination went larger, the flow-in through the stern ramps began to grow. There were only 3 openings through which the sea water flows in before 2,700 seconds. The resulting floodwater was piled up in D deck and E deck (these decks is located under the main deck). After 2,700 seconds, the sea water flowed in through the vent of the left stabilizer room. And after, many other compartments flooded.

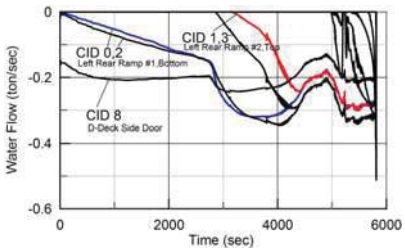

Fig. 23 Flow rate of water through important openings

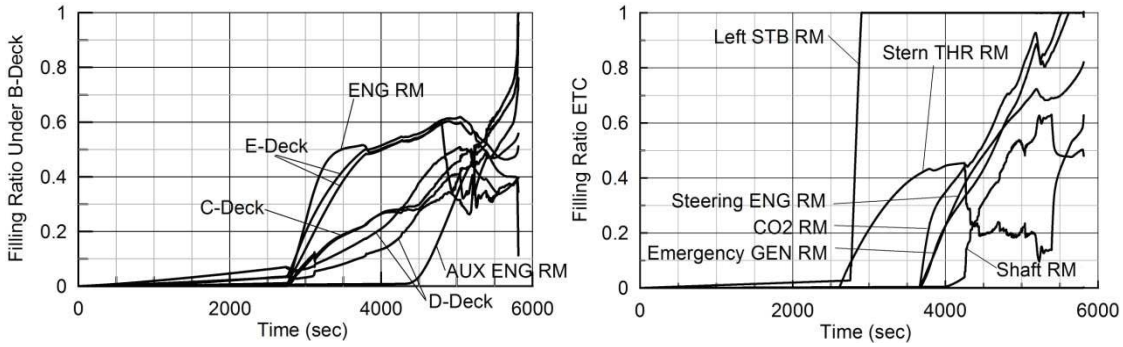

Fig. 24 Filling ratios of the lower compartments (below main deck)

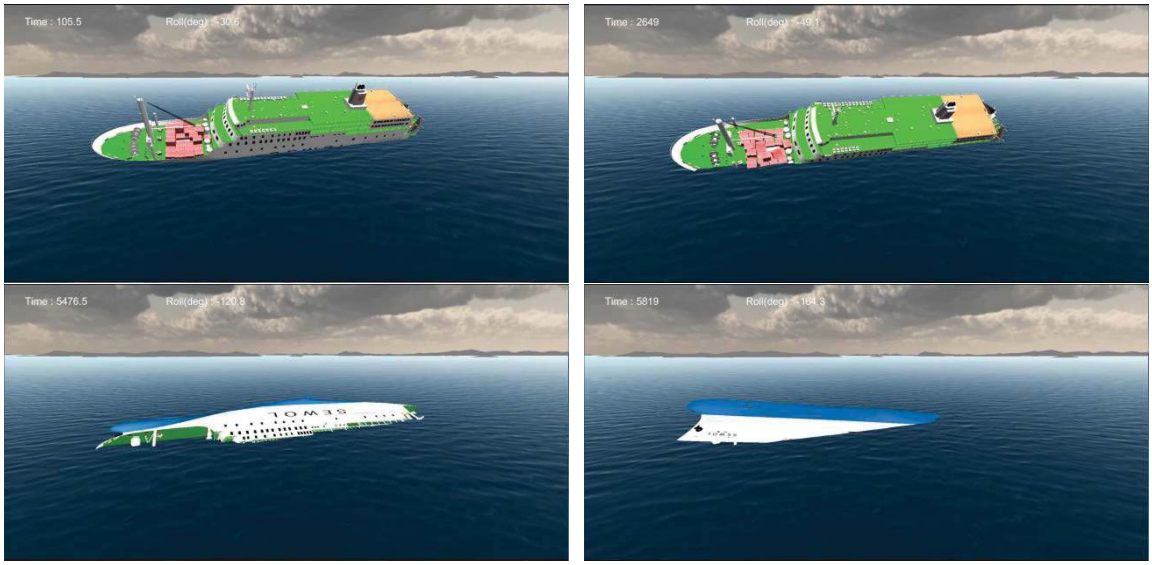

Fig. 25 Visualizations of the simulation results (upper left: initial state, upper right: when the coast guard arrived, lower left: when the last rescue action, lower right: final state)

The side door located at D deck and the rear ramps are assumed to be closed. The simulation team assumed gap of 0.01m along the edge of the door and ramps. It could be said that the only 0.01m of gap size of a side door and rear car ramp are sufficient to flooding and sinking of Ro-Ro ferry.

Fig. 25 shows the important situations to be noticed: initial condition of flooding simulation, the ship when coast guard arrived, when the last rescue action played, finally capsized. The results reflect the actual situations well, in comparison with the pictures that have shown in many mass medias.

5. CONCLUSIONS

In this study, flow models for simulation of ship flooding were investigated. The most important matters were the orifice equations and the compartment models. For the orifice equation, it was shown that numerical instability could occur involving the air flow, if the hydraulic orifice equation is used to calculate the flow through an opening. A newly derived dynamic orifice equation by Lee (2014) was investigated that could resolve the numerical instability that comes from the square root of the pressure difference. A new compartment model that can provide pressure balance automatically was proposed. It reduces the computational burden and difficulty in applying the pressure-correction method.

Furthermore, practical models indispensable for application to realistic situations were investigated. These included down flooding and a simple method for giving the dynamic effect of floodwater in quasi-static analysis.

Using these models, the flooding simulation of a recent actual accident was carried out. When the results were compared with official data, the process of the flooding and sinking could be explained approximately, but reasonably.

6. ACKNOWLEDMENTS

In the accident mentioned in this study, the ship sank with the loss of many people, dead or missing. The data included in section 5 are parts of the report of the simulation team for the accident of Ro-Ro ferry. The writer feels sorry for not adding the details of the report of the simulation team of this accident in this paper. The writer hopes that this study helps to make ships safer. This study was partially supported through a basic project of KRISO(PES1990).

7. REFERENCES

Chang, B.-C., Blume, P., 1998. "Survivability of Damaged Ro-Ro Passenger Vessels", Schiffstechnik – Ship Technology Research, Vol. 45, pp. 105-112.

Chang, B.-C., 1999. "On the Damage Survivability of Ro-Ro Ships Investigated by Motion Simulation in a Seaway", Schiffstechnik – Ship Technology Research, Vol. 46, pp. 192-207.

Cho, S. K., Hong, S. Y., Kim, Y. H., and Lee, K. J., 2005. "Investigation of dynamic characteristics of the flooding water of the damaged compartment of an ITTC RORO Passenger Ship", Proceedings of the 8th International Ship Stability Workshop, Istanbul, Turkey, 6-7 October 2005.

Clift, R., Grace, J.R., and Weber, M.E., 1978. Bubbles, Drops, and Particles, Academic Press Inc., New York, p.205.

FLOODSTAND Project Consortium, 2011. WP2 - Flooding Progression Modelling, Deliverable No. D2.3, D2.4a, D2.4b, FLOODSTAND Project Consortium, EU.

Ikeda, Y., Ishida, S., Katayama, T., and Takeuchi, Y., 2004. "Experimental and Numerical Studies on Roll Motion of a Damaged Large Passenger Ship in Intermediate Stages of Flooding", Proceedings of the 7th International Ship Stability Workshop, Shanghai, China, 1-3 November 2004, pp. 42-46.

ITTC, 2011. "Final Report and Recommendations to the 26th ITTC, The Specialist Committee on Stability in Waves", Proceedings of 26th ITTC, Rio de Janeiro, Brazil, 28 August - 3 September 2011, pp.523-560.

KRISO, 2014. Analysis of the cause of a sinking accident of MV Sewol (Simulation of Maneuvering, Flooding, and Sinking), Report No. UCPGS2750-10546-6. KRISO, Korea, pp.114-129. (in Korean)

Lamb, H., 1945. Hydrodynamics, Dover Publications, Inc., New York. (republication of the 6th(1932) edition by Cambridge University Press), p.164.

Lee, G. J., 2010a. "Simplified Modelling of Floodwater Dynamics", Proceedings of the Annual Autumn Meeting, SNAK, Changwon, 21-22 October 2010, pp.969-974. (in Korean)

Lee, G. J., 2010b. "Flow through Openings for Flooding Calculation", Proceedings of the Annual Autumn Meeting, SNAK, Changwon, 21-22 October 2010, pp.979-990. (in Korean)

Lee, G. J., 2014. "A Study on the Dynamic Orifice Equation for the Flooding Simulation of a Ship", Journal of Ships & Ocean Engineering, vol. 55., pp.17-27. (in Korean)

Lee, G. J., 2015. "Dynamic orifice flow model and compartment models for flooding simulation of a damaged ship", Ocean Engineering (submitted).

Papanikolaou, A., Zaraphonitis, G., Spanos, D., Boulougouris, E., and Eliopoulou, E., 2000. "Investigation into the Capsizing of Damaged Ro-Ro Passenger Ships in Waves", Proceedings of the 7th International Conference on Stability of Ships and Ocean Vehicles, Launceston, Tasmania, Australia, 7-11. February 2000, pp. 351-362.

Ruponen, P., 2007. Progressive Flooding of a

Damaged Passenger Ship, Doctoral Dissertation, Helsinki University of Technology, Finland.

Spouge, J. R., 1986. "The Technical Investigation of the Sinking of the Ro-Ro Ferry European Gateway", Transactions of Royal Institute of Naval Architects, RINA, Vol. 128, pp. 49-72.

Sen, P. and Konstantinidis, C., 1987. "A Time Simulation Approach to the Assessment of Damage Survivability of Ro/Ro Cargo Ships", Transactions of Society of Naval Architects and Marine Engineers, SNAME, Vol. 95, pp. 337-355

van't Veer, R. and de Kat, O., 2000. "Experimental and Numerical Investigation on Progressive Flooding in Complex Compartment Geometries", Proceedings of the 7th International Conference on Stability of Ships and Ocean Vehicles, Launceston, Tasmania, Australia, 7-11 February 2000, pp. 305-321.

van't Veer, R., de Kat, O., and Cojeen, P., 2002. "Large Passenger Ship Safety: Time to Sink", Proceedings of the 6th International Ship Stability Workshop, New York, U.S.A, 13-16 October, 2002.

van't Veer, R., Peters, W., Rimpelä, A-L., and de Kat, J., 2004. "Exploring the Influence of Different Arrangements of Semi-Watertight Spaces on Survivability of a Damaged Large Passenger Ship", Proceedings of the 7th International Ship Stability Workshop, Shanghai, China, 1-3 November 2004.

Vassalos, D., Jasionowski, A., and Guerin, L., 2005. "Passenger Ship Safety – Science Paving the Way", Proceedings of the 8th International Ship Stability Workshop, Istanbul, Turkey, 6-7 October 2005.

White, F. M., 1979. Fluid Mechanics, McGraw-Hill, New York, pp. 159-163, Chapter 6,10.

Woodburn, P., Gallagher, P., and Letizia, L., 2002. "Fundamentals of Damage Ship Survivability", Transactions of Royal Institute of Naval Architects, RINA, Vol. 144, pp.143-163.

APPENDIX A. Square Root Instability

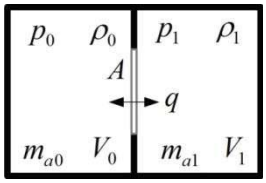

Fig. A-1 Arrangement of the sample problem

The hydraulic orifice equation was originally for steady state, let us see what happens if we apply it for an unsteady case. Here, the point of focus is the fact that the flow velocity is represented using the square root of the pressure difference. Consider the situation in Fig. A-1, in which both sides are filled with air, and there is an opening between them. The final state is the one in which the pressures on both sides are the same, so the pressure difference is zero.

Let us formulate the above situation. The flow could be represented as

$$q = sgn(\Delta p)\rho A\sqrt{\frac{2|\Delta p|}{\rho}} = sgn(\Delta p)A\sqrt{2\rho}\sqrt{|\Delta p|} \quad \text{(A-1)}$$

The mass would change to

$$\dot{m}_{a0} = -q \qquad \dot{m}_{a1} = q \quad \text{(A-2)}$$

The density at each compartment could be represented by

$$\rho_0 = m_{a0}/V_0 \qquad \rho_1 = m_{a1}/V_1 \quad \text{(A-3)}$$

The pressure in each compartment can be determined under the assumption of iso-entropic process of air. (γ is the specific heat, 7/5 for an iso-entropic process, and 1 for an iso-thermal process)

$$p_0 = k_a\rho_0^\gamma - p_{atm} = k_a\left(\frac{m_{a0}}{V_0}\right)^\gamma - p_{atm}$$
$$p_1 = k_a\rho_1^\gamma - p_{atm} = k_a\left(\frac{m_{a1}}{V_1}\right)^\gamma - p_{atm} \quad \text{(A-4)}$$
where $k_a = p_{atm}/\rho_{atm}^\gamma$.

Take the time differentiation of the above equations,

$$\dot{p_0} = \gamma\frac{k_a}{V_0}(m_{a0})^{\gamma-1}\dot{m}_{a0} = -\gamma\frac{k_a}{V_0}(m_{a0})^{\gamma-1}q$$
$$\dot{p_1} = \gamma\frac{k_a}{V_1}(m_{a1})^{\gamma-1}\dot{m}_{a1} = \gamma\frac{k_a}{V_1}(m_{a1})^{\gamma-1}q \quad \text{(A-5)}$$

Here, we assume the same volume of compartments (i.e., $V_0 = V_1$). If the pressures are the same initially, then air masses in both compartments are the same initially. Assume the change of air masses is small, and the mass could be assumed as constant m_a for the last expression of Equation A-5. If the flow through an opening increases the pressure of one compartment, the pressure of the other compartment goes down, so that $p_1 = -p_0$.

$$\dot{p_0} = -\gamma\frac{k_a}{V}(m_a)^{\gamma-1}sgn(p_0)A\sqrt{2\rho}\sqrt{2|p_0|} \quad \text{(A-6)}$$

The atmospheric pressure is large enough so that the density is nearly constant, so Equation A-6 can be rewritten as

$$\dot{p_0} = -\gamma\frac{k_a}{V}(m_a)^{\gamma-1}sgn(p_0)2A\sqrt{\rho_{atm}}\sqrt{|p_0|}$$
$$= -2\gamma\frac{A}{V^{2-\gamma}}\frac{p_{atm}}{\sqrt{\rho_{atm}}}sgn(p_0)\sqrt{|p_0|} \quad \text{(A-7)}$$

Let us rewrite this into a simpler form.

$$\dot{p} = -Ksgn(p_0)\sqrt{|p_0|} \quad \text{(A-8)}$$
where $K = 2\gamma\frac{A}{V^{2-\gamma}}\frac{p_{atm}}{\sqrt{\rho_{atm}}}$

The value of K is very large. One solution of the above equation is $p = 0$, which is what we want. Let us examine the numerical solution, using the Euler method,

$$p^{n+1} = p^n - Ksgn(p)\sqrt{|p^n|}\Delta t \quad \text{(A-9)}$$

We know the pressure would bounce around zero, because of the large value of K. Let us seek the amplitude of oscillation p^*.

$$-p^* = p^* - K\sqrt{p^*}\Delta t \;\rightarrow\; 2p^* = K\sqrt{p^*}\Delta t$$
$$\therefore\; p^* = 0 \;\; or \; p^* = \frac{(K\Delta t)^2}{4} \quad \text{(A-10)}$$

The oscillating solution is as follows.

$$p^n = (-1)^n\,(K\Delta t)^2/4 \quad \text{(A-11)}$$

No matter what the absolute value of the pressure was initially, the amplitude of pressure oscillation converges to p^*. That is a type of self-sustained oscillation (or self-excited). Even though we use the predictor-corrector, or Runge-Kutta method, the pressure will not go to zero, and does not oscillate as in Fig. A-2.

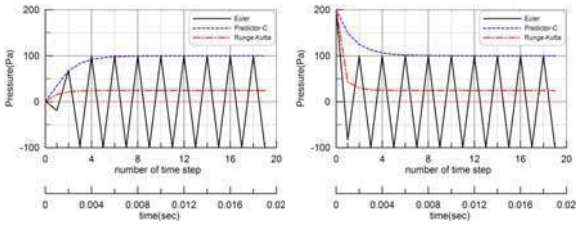

Fig. A-2 Numerical solution of the air pressure revealing the square root instability. (K=20000, Δt=0.001, p^*=100)

The above figure shows that even if the initial value is infinitesimally small (not zero) or larger than p^*, the result of the Euler method oscillates back and forth around zero and the amplitude grows to p^*. However, the results of the predictor-corrector do not oscillate and go to the value of p^*. Even for the Runge-Kutta method, it goes to about 1/4 p^*, not zero. This is numerically unstable. Because the predictor-corrector and Runge-Kutta methods give non-zero solutions, they are dangerous compared with the Euler method. The result of the Euler method gives values whose average is zero. We expected the solution to go to zero, but it does not, so this phenomenon can be called numerical instability.

Let us investigate the value of K,

$$K = 2\gamma \frac{A}{V^{2-\gamma}} \frac{p_{atm}}{\sqrt{\rho_{atm}}}$$

Substitute the real values except A and V(ρ_{atm}=1.26 , p_{atm} ≅100,000)

$$K = 178{,}174 \times \gamma \frac{A}{V^{2-\gamma}} = 356{,}348 \times \frac{A}{V^{0.6}} \quad \text{(A-12)}$$

In order to maintain p^* as less than 100 Pa (i.e., 1/1000 of atmospheric pressure; this would be accepted as a negligible amount in the engineering sense) the time interval of simulation should be the following value.

$$\Delta t^* = 20/K = 5.6 \times 10^{-6} \frac{V^{0.6}}{A}$$

For example, a passenger ship has many rooms in which the dimensions are about 4m(depth), 3m(width), and 2.5m(height), for which the area of door is 2m^2, and for that room Δt=0.00022. This is not practical. For a larger compartment of 10m x 10m x 5m, with a 2m^2 door, the time interval should be Δt =0.001. Therefore, this is impractical because of the numerical instability of the square root.

This page is intentionally left blank

An Overview of Warships Damage Data from 1967 to 2013

Andrea Ungaro, *CETENA spa, Genoa, ITALY* andrea.ungaro@cetena.it

Paola Gualeni, DITEN University of Genoa, ITALY paola.gualeni@unige.it

ABSTRACT

In the last decade, in the field of merchant ships, a long harmonization process has taken place at IMO, resulting in the enforcement of the so called probabilistic SOLAS2009 for the residual buoyancy and stability assessment of a ship in a damaged condition.

In the warships design process, the probabilistic methodology might represent a consistent approach to complement the fundamental overall ship survivability assessment. Nevertheless among the most critical issues, while discussing the possible implementation of this innovative approach, are the lack of a damage database and the significantly different threat typology.

In this perspective, significant damage cases in the field of warships are investigated and critically analyzed. The observed time period will regard the period from 1967 (sinking of the Eilat) to 2013.

Keywords: *warships, damage, survivability assessment*

1. INTRODUCTION

In the field of merchant ships, the rules for stability assessment of a damaged ship have been renewed a few years ago by the International Maritime Organization (IMO).

The new requirements are based on the probabilistic approach and represent a significant change in one of the most long-established safety issues i.e. the ship subdivision criteria.

They are the result of a prolonged process having its roots in the sixties (IMO, 1960) and passing by the adoption of the mandatory probabilistic regulation for cargo ships (IMO, 1990). An harmonization process has subsequently originated, leading to a comprehensive SOLAS Convention text for both passenger and cargo ships that has been enforced from January 1st 2009 (IMO, 2007), the reason why in the following it is going to be mentioned as SOLAS2009.

This paper is developed in the perspective that the probabilistic approach might represent an interesting hint also within the warship design context (Harmsen & Krikke, 2000; Papanikolaou & Boulougouris, 2000). In fact, in principle, it is particularly suitable to address the vulnerability characteristics of the ship in terms of survivability after damage and it can be exploited also in terms of risk assessment, for the discussion of ship survival attitude after damage due to a weapon hit (Boulougouris & Papanikolaou, 2012).

At the same time, some critical points can be raised, for example in relation with the totally different context in terms of threat and operational situations.

Moreover the lack of a rational and comprehensive damage database is another fundamental issue in order to define the statistical characteristics of hull damages.

2. PRESENT CRITERIA FOR THE DAMAGED SHIP: NAVAL AND MERCHANT FIELD

At present, major Navies in the world apply the so called "determistic" approach for the design and assessment of the appropriate ship subdivision, derived from the World War II experience and form the Sarchin and Goldberg studies (1962).

Damaged stability criteria are based on standard extents of damage, margin line and V-line concepts for buoyancy assessment and progressive flooding prevention; for the residual stability assessment, criteria are developed processing the righting arm characteristics in comparison with standard.

A remarkable overview about the current warship damaged stability criteria is given in Surko (1994), where a compared analysis is carried out among the deterministic criteria applied by Canada, France, Germany, Israel, Italy, United Kingdom, United States, Australia. In the same paper many interesting hints for improvement are suggested for example the need to treat the survivability and the damage control as a single issue in the 21st century. The same author raise the attention toward the residual strength after damage, in a comprehensive performance assessment perspective (Surko, 1988).

In the field of merchant ships, before the SOLAS2009 enforcement the "deterministic" approach was the general SOLAS damage stability paradigm. At present, the traditional set of rules has been replaced by the probabilistic approach that in principle can be described as a rational, comprehensive and able to deliver a synthetic final score parameter, representative of the damaged ship survivability global attitude. Furthermore it has the characteristic of being a versatile instrument, able to deal with innovative and peculiar ship typologies.

Notwithstanding many positive conceptual features, its implementation in actual design poses a number of problems. In general, among the less encouraging features, is the extremely long, elaborate and intricate procedure it requires (only the significant increase and availability of cheap calculation power have practically allowed the introduction of this new methodology). At the same time, a critical aspect is represented by the feeble chance to appreciate intuitively the effects of even a light modification in the ship general layout in terms of damage stability compliance. This in turn could mean that in case the investigated ship doesn't satisfy the requirements, the designer's options to improve the situation are not so clear and straightforward.

3. CRITICAL ISSUES FOR PROBABILISTIC APPROACH TRANSFERABILITY FROM MERCHANT TO WARSHIP DESIGN

A very short and not exhaustive description of the SOLAS 2009 probabilistic methodology is given in the following. The methodology is based on a calculation of the attained subdivision index A and the required subdivision index R. The ship is sufficiently subdivided when

$$A > R, \quad R = R\left(L_S, N_1, N_2\right) \quad (1)$$

In particular coefficient R, besides its dependence on the ship length (L_S), is defined as a function of the number of people for whom lifeboats are provided (N_1) and of the number of people (including officers and crew) the ship is permitted to carry in excess of N_1.

The formulation of the attained coefficient A is more complex, it is obtained after relevant calculations for three different draughts: the deepest subdivision draught (*ds*, the waterline which corresponds to the summer load line), the light service draught (*dl*, related with the lightest loading condition of the vessel) and the partial subdivision draught (*dp*, the light service draught plus 60% of the difference between the light service draught and the deepest subdivision draught). For each of the aforementioned calculation draughts *ds*, *dp* and *dl*, partial indices respectively *As*, *Ap*, *Al*, are to be found. The global attained coefficient *A* is calculated as the linear combination of the partial subdivision indices at each defined draught:

$$A = 0.4A_s + 0.4A_p + 0.2A_l \qquad (2)$$

Every partial index *As*, *Ap*, *Al* is the summation of the products of two parameters (*pi* and *si*) representing respectively, the probability that only the compartment or group of compartments under consideration may be flooded *pi*, (disregarding any horizontal subdivision) and the probability of survival *si* after flooding of the compartment or group of compartments under consideration, (including the effect of any horizontal subdivision). Each partial index *Aj* is therefore calculated as follows:

$$A_j = \left[\Sigma_i \; p_i \quad s_i\right]_j \qquad (3)$$

The formulation of the pi coefficients is based on the damage length and on its longitudinal position along the ship. As a matter of fact when dealing with a certain zone within two transversal bulkheads it is possible to take into account different transversal damage penetrations, correcting *pi* by the *ri* coefficient, that accounts for the probability not to damage the longitudinal bulkhead.

The *si*, parameter the survivability index, is calculated with reference to the residual buoyancy and stability characteristics of the ship after damage and accounts also for intermediate stages of flooding and external heeling moments such as wind, movement of passengers and launch of a survival craft. Moreover the survivability index coefficient can be corrected by the factor *vi* in case the horizontal watertight boundaries are fitted above the waterline under consideration and they are limiting superiorly the damage: the *vi* factor in fact, represents the probability that the spaces above the horizontal subdivision will not be flooded. The attended index *A* takes therefore the following form,

$$A_j = \left[\Sigma_i \left(p_i \quad r_i\right) \quad \left(v_i \quad s_i\right)\right]_j \qquad (4)$$

In order to avoid that global index *A* is attained also in case of extremely unbalanced situations some corollary requirements have been introduced: for passenger ships, prescriptions on the *si* values are imposed regarding some specific damage scenarios defined in terms of position and extensions, depending on the number of passengers onboard. Moreover a minimum value of for partial *As*, *Ap*, *Al* indices is imposed (at least 0.5•*R* for cargo ships and 0.9•*R* for passengers ships).

To discuss the opportunity of the probabilistic approach application in the field of warship design it is worth mentioning that "survivability" in such cases is a very wide concept and also includes the concepts of vulnerability and susceptibility (Ball & Calvano, 1994).

The possible application, moreover, would imply an extensive work of re-formulation of the probabilistic parameters characterizing the damage scenario probability and of the survivability index.

In fact, one of the biggest issues for the probabilistic approach application in the warship field is the redefinition of coefficients exploited in the methodology. In this process it would be necessary to take into account the different environmental, operational scenarios

and the boundary conditions the naval ship has to operate in.

Two points should be properly considered: the first one is the different performances required after damage and the second is the origin and nature of the damage.

The ship performances after damage should be tackled through the definition of a new *si* survivability factor within the probabilistic methodology.

The nature of the damage should be introduced with the definition of damage probability factors i.e. *pi*, *ri*, *vi*, respectively representing the longitudinal transverse and vertical extents of damage.

The occurrence of a damage has different features in case of a merchant ship or a naval ship: in general the first suffers damage due to collision and grounding while the second suffers damage due to offensive /aggressive threats (weapons) put in act to destroy the ship herself and characterized by more devastating effects.

Moreover a new definition of the required index R is necessary, since in the SOLAS 2009 it has a statistical origin too; the harmonized SOLAS has been applied to several ships which complied with the old deterministic rules and their attained indexes A have been calculated. The index R has been defined by means of a regression of such set of values with the aim to keep an equivalent level of safety. A similar approach should be followed with a proper set of naval ships to define its naval formulation.

From what above, the critical points for probabilistic approach transferability to navy ships are summarized below:

- Definition of suitable probabilistic terms to evaluate damage extensions statistics and damage effects
- Definition of survivability index
- Definition of a new R factor, i.e. the level of sufficient subdivision

Unfortunately a database of damage cases for ships in the military context with all the necessary data for a statistical analysis is not available.

In the following paragraph an overview about the damage scenario of warships in the latest decades is carried out; the aim is to investigate what kind of framework and information would be useful in the perspective of a possible probabilistic approach for damage stability assessment for warship design. A special attention is given also to the threat typology as a fundamental parameter to class the damage size and typology.

4. A TAXONOMY FOR A WARSHIP DAMAGE DATA OVERVIEW

Year 1967 marks a breakthrough in naval warfare, specifically the sinking of INS Eilat by means of guided ship-launched anti-ship missiles (ASMs) a few months after the Six-Day War.

Guided weapons had already been used during the Second World War: the German Luftwaffe used several kinds of remotely-controlled glide bombs, such as the Henschel Hs293 and the so-called “Fritz-X”; two hits from the latter in fact sunk the RN Roma in 1944. All of these weapons were however dropped by a bomber and usually controlled via radio signals by an operator within visual range, following the smoke trail left by the bomb to help steering.

When INS Eilat was sunk in October 21st, 1967, the three hits were by P-15 Termit (NATO name: SS-N-2 Styx) missiles, fired from two Komar-class missile boats, carrying their own radar sensors, and attacking well outside visual range (17 nm as reported).

From 1967 to 2013, 45 hits by guided anti-ship missiles, both surface- and aircraft-launched, have been suffered by naval ships. Of these hits, 16 concerned 9 different naval ships with a displacement larger than 1000 t (corvette-sized or bigger) and are therefore interesting for our study; hits on smaller ships are less interesting because smaller platforms can hardly survive missile impacts. In those cases, specific details are also hard to come by (the ship, typically a missile boat, is usually listed as "sunk", without other information).

Of these 16 hits, 6 were by P-15 Termit (3 of those during the Eilat attack and 3 during Operation Trident), 4 by some versions of the Exocet, 3 by Harpoon missiles, 2 by Sea Sparrow missiles (a "blue-on-blue" incident) and 1 by a YJ-82. 4 out of 9 of the hit ships were sunk. In 7 cases out of 9, the ships were clearly mission-killed, i.e. lost the capability to carry out their operational tasking.

In 6 out of 9 ships, and in 3 out of 4 ships being sunk, fire is mentioned as a significant damage mechanism; specifically, HMS Sheffield and IRS Sahand were lost due to incontrollable fires, even though the first one eventually sunk due to flooding and the second due to secondary ammunition explosions. INS Eilat on the other hand suffered a complete loss of integrity of the hull girder (i.e. "broke in two") after the third hit whereas the fate of PNS Khaibar was probably caused by extensive flooding.

Note that this statistic doesn't include non-naval ships (several oil carriers were hit by ASMs during the so-called Tanker War, for example) and doesn't include merchant ships in military use such as the Atlantic Conveyor, which despite being a container ship was in military use during the 1982 Falklands War, and the Venus Challenger, which was reportedly carrying ammunition (this is contested) when sunk during the 1971 Operation Trident.

In the same historical period, 15 ships larger than 1000 t sustained hits from weapons other than guided missiles: 3 were torpedoed, 8 were hit by bombs, 3 struck a mine and 1 was struck by a suicide boat. One of the ships hit by bombs (IIS Sahand) was also hit by missiles, and therefore our list below is composed of 23 entries rather than 24.

The three ships that were hit by torpedoes all sunk, in a quite short time frame and with large loss of life.

The three ships that were hit by mines received severe damage and were mission-killed in two cases, whereas USS Tripoli, undoubtedly also due to her large displacement, remained mission-capable. Casualties were low.

USS Cole, struck by a suicide boat, was certainly unable to continue her mission, and was ultimately drydocked and brought back to the US for repairs.

Finally, the 8 ships that were struck by bombs: 3 were hit by multiple bombs and sunk (HMS Ardent during defusing operations); 3 were struck by unexploding bombs only and survived (HMS Argonaut suffered a partial missile magazine explosion and fire and had to be towed away); 1 was struck by a single bomb and lost propulsion but survived (IIS Sabalan) and 1 was struck by multiple bombs and missiles and sunk (IIS Sahand).

In 4 out of 5 cases of ships struck by bombs which exploded successfully, and in 1 case out of 3 of unexploded bomb hits only, fire is mentioned as a significant factor. Only HMS Coventry was lost mainly due to loss of stability.

The following review goes into some detail, as available from unclassified or de-classified sources, about the damage sustained by the ships as listed in table 1.

It appears evident that the definition of damage as described in the SOLAS2009 (i.e. in terms of longitudinal, transverse and vertical extension) is not commonly available, and that the damage is usually described in terms of source (i.e. kind of weapon) and effects (i.e. residual buoyancy, total loss, fire, fatalities).

INS Eilat (1967)

INS Eilat (ex HMS Zealous) was a WWII Z-class destroyer with a displacement of about 1700 t. She received three hits (sources report anything from 2 to 4 hits), all by P-15 Termit missiles (carrying 454 kg warheads), which sunk her.

Reports are unclear on the location of the hits but it's clear that after the two first hits the ship was dead in the water (boiler rooms out of order) and with severe structural damage; some sources report one hit very close to the waterline (and therefore flooding) and fire is reported as well.

The ship was still floating when two hours later the third hit finished her by splitting the already damaged hull into two parts. Further underwater damage from a near-miss by a 4th missile was reported (the ship was attacked by two Osa missile boats carrying two missiles each).

PNS Khaibar (1971)

PNS Khaibar (ex HMS Cadiz) was a WWII Battle class destroyer with a displacement of about 2300 t standard (3300 full load). She received two hits by P-15 Termit missiles which sunk her (Harry, 2002).

The first hit was on the starboard side, low on the water; propulsion and electrical power were lost (possibly due to shock?) Boiler room 1 was lost and the ship was engulfed in thick black smoke, with spreading fires reported. The second subsequent hit was on the same side and destroyed boiler room 2 as well as some boats, causing a heavy list. The ship sunk shortly thereafter.

Name	Year	Country	Weapons	Final status
INS Eilat	1967	Israel	3 x P-15 Termit	Sunk
PNS Khaibar	1971	Pakistan	2 x P-15 Termit	Sunk
PNS Shah Jahan	1971	Pakistan	1 x P-15 Termit	Unknown, did not sink
INS Khukri	1971	India	1 x 550-mm torpedo	Sunk
ARA General Belgrano	1982	Argentina	2 x Mk 8 torpedo	Sunk
HMS Sheffield	1982	UK	1 x Exocet (did not explode)	Sunk
HMS Ardent	1982	UK	Multiple aircraft bombs	Sunk
HMS Antelope	1982	UK	2 aircraft bombs	Sunk during defusing operations
HMS Coventry	1982	UK	Multiple aircraft bombs	Sunk
HMS Broadsword	1982	UK	1 unexploded bomb	Mission capable
HMS Argonaut	1982	UK	2 unexploded bombs	Towed away
HMS Antrim	1982	UK	1 unexploded bomb	Unknown

HMS Glamorgan	1982	UK	1 x Exocet	Mission capable after damage recovery
USS Stark	1987	USA	2 x Exocet (1 did not explode)	Severe damage, mantained propulsion
USS Samuel B. Roberts	1988	USA	1 x M-08 contact mine	Severe damage, reduced propulsion
IIS Sahand	1988	Iran	3 x Harpoon, 2 x CBU, 2 x LGB	Sunk
IIS Sabalan	1988	Iran	1 x LGB	Severe damage, towed away
USS Tripoli	1991	USA	1 x LUGM-145 contact mine	Mission capable after damage recovery
USS Princeton	1991	USA	1 x MN-103 influence mine	Severe damage, towed away
TCG Muavenet	1992	Turkey	2 x Sea Sparrow	Crippled by loss of staff
USS Cole	1999	USA	1 x suicide boat	Severe damage, drydocked
INS Hanit	2006	Israel	1 x YJ-82 missile	Moved away from the area
ROKS Cheonan	2010	South Korea	1 x unknown torpedo	Sunk

Table 1: List of the analyzed ships with some summarized details

PNS Shah Jahan (1971)

PNS Shah Jahan (ex HMS Charity) was a C-class destroyer with a displacement of about 2500 t. She received one hit by a P-15 Termit missile.

Not much is known about this attack, except that the ship did not sunk but was eventually scrapped due to the extensive damage.

INS Khukri (1971)

INS Khukri was a Type 14 (Blackwood-class) frigate with a displacement of about 1450 t (full load). She received one hit by a 550-mm torpedo which sunk her.

According to open literature accounts, the torpedo hit “exploded under the oil tanks”. This apparent fact, taken together with the small displacement of the ship, explains the reportedly quick sinking of the ship and proportionally large loss of life.

ARA General Belgrano (1982)

ARA General Belgrano was a WWII Brooklyn-class light cruiser with a displacement of about 12200 t at full load. She was hit by two Mk 8 torpedoes which sunk her, earning her the dubious distinction of being the first and only ship to be killed by a nuclear submarine in history.

The torpedoes hitting the Belgrano had a 363 kg warhead. The first hit came very close to the bow, outside both the armored belt and the anti-torpedo bulge, and blew it up; the damage was however ultimately very small as the ship water integrity was preserved.

The second hit was sustained aft, again outside the armored area, and proved catastrophic: the aft machinery room and two mess rooms were immolated causing about 275 casualties, and subsequently the explosion vented through the main deck.

The ship very quickly filled with smoke. Electrical power was lost due to the explosion

and the list that the ship soon developed could not be countered by pumping. Twenty minutes later the order to abandon ship was given and she eventually slipped beneath the waves.

HMS Sheffield (1982)

HMS Sheffield was a Type 42 destroyer with a displacement of about 4800 t. She received one hit by an Exocet which sunk her.

This is probably the missile attack that has been discussed most in the brief history of naval missile combat. According to the official RN account (UK-MOD 1982a) Sheffield sustained the hit on her second deck, 2.4 meters above the waterline. Immediate damage included the control room, fire main, forward auxiliary and machinery room being lost. Fire spread and could not be fought due to heavy smoke and no fire main, so eventually the ship was abandoned. Sheffield then sunk during towing due to flooding through the side hole, but fire (and smoke) was definitely the primary damage mechanism in this attack.

It is significant that the missile with its 165 kg warhead did not detonate, according to official statements, though this is contested by some.

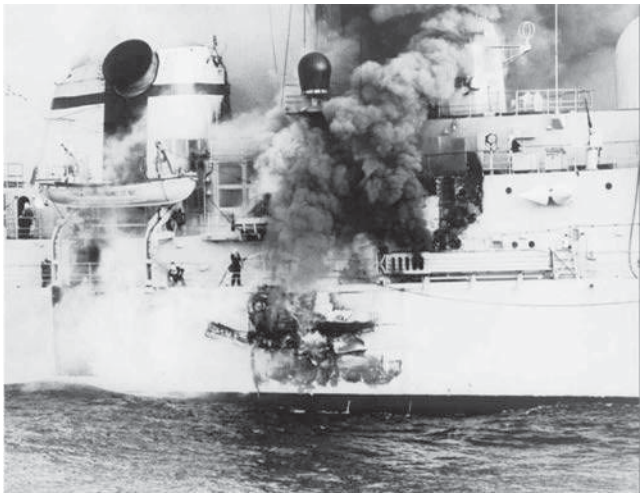

Figure 1: HMS Sheffield on fire after the Exocet hit
(photo credit: UK MoD - believed to be in the public domain)

HMS Ardent (1982)

HMS Ardent was a Type 21 frigate with a displacement of about 3200 t. She received several bomb hits which sunk her (UK-MOD 1983).

Ardent was hit by several waves of air attacks.

The first three hits were sustained in the hangar (two weapons) and aft auxiliary machinery room (one weapon, which failed to explode but caused significant damage nonetheless by destroying a switchboard which left, among other things, the main gun inoperative). The hangar hits destroyed the helicopter and a missile launcher, as well as started a large fire and caused significant crew casualties.

A subsequent wave of attackers hit the ship in the aft area with an unknown number of weapons, estimates range from two to four bombs. There are reports of more weapon hitting the ship at the same time but failing to explode, which was fairly common due to the low altitude the attacks were performed at. These attacks caused many casualties and the ship lost steering as well. Fires aft grew out of control and a list was developed from flooding due to underwater explosions of near misses. The ship was abandoned and sunk about 12 hours later.

According to Argentine sources both Mk 83 (450 kg) and Mk 82 (230 kg) bombs were used, in the normal and retarded type.

HMS Antelope (1982)

HMS Antelope was a Type 21 frigate with a displacement of about 3200 t. She was sunk when the defusing attempts on two bombs that she had received failed (UK-MOD, 1982b).

Antelope sustained two bomb hits, the first in the starboard side, the second close to the

main mast, from an aircraft that crashed through it. No one of the bombs exploded.

Defusing attempts on the aft bomb failed and the ship was torn open from waterline to funnel. Major fires were started in both engine rooms. Electrical power was lost and the starboard fire main was fractured as well, making fire fighting all but impossible.

The ship was abandoned and shortly thereafter missile magazines began exploding. The ship was still afloat, her keel broken and her substructure all but melted, the following day, but eventually sunk after breaking in half.

HMS Coventry (1982)

HMS Coventry was a Type 42 destroyer with a displacement of about 4800 t. She received four hits by bombs, two of which exploded, and eventually sunk.

Coventry was hit a first time on her flight deck by a 450-kg bomb which destroyed her helicopter but did not explode. Then, she was hit by three 225-kg bombs on her port side, just above the waterline: two of the bombs exploded, one putting the computer room and most of the senior staff out of commission; the second in the forward engine room. The latter hit destroyed the bulkhead separating the two engine rooms, causing an incontrollable flooding (the ship could survive two compartments being flooded but not the two engine rooms as they were too large).

The ship capsized in about twenty minutes and sunk shortly thereafter.

HMS Broadsword (1982)

HMS Broadsword was a Type 22 frigate with a displacement of about 4400 t. She received one hit by a bomb which did not explode.

During the same action in which Coventry was sunk, Broadsword was hit by a bomb of unknown weight, which bounced on her flight deck, destroying her helicopter (similarly to Coventry) and then exploded harmlessly in the water.

The ship remained mission capable (but for the loss of her helicopter of course) and in fact was instrumental in rescuing most of the crew of Coventry.

HMS Argonaut (1982)

HMS Argonaut was a Leander-class frigate with a displacement of about 3250 t at full load. She received two hits by bombs which did not explode.

HMS Argonaut was hit by two bombs which did not explode; however, one of them entered a missile magazine, detonating two missiles and causing some casualties and a fire.

The ship moved away from the area under tow, which suggests some internal damage for which however documentation is lacking.

HMS Antrim (1982)

HMS Antrim was a County-class destroyer with a displacement of about 6850 t at full load. She received one hit by a bomb which did not explode.

HMS Antrim was hit by one 450-kg bomb which did not explode.

Information is lacking about what damage, if any, was caused by the impact.

HMS Glamorgan (1982)

HMS Glamorgan was a County class destroyer with a displacement of about 5400 t (6200 full load). She received one hit by an Exocet which she survived despite some extensive fire damage.

The hit was sustained on the port side of the hangar deck, close to the Sea Cat launcher, and

deflected upwards (the ship was violently maneuvering to present the stern to the missile). The hangar deck was holed by the explosion, fire spread in the galley below; the missile body kept going and penetrated the hangar, destroying the ship helicopter. Eventually the crew managed to contain the spread of fire but there was extensive damage in the hangar area (Inskip, 2012). The ship was definitely able to float, though there was some list caused by the extensive quantity of water used in firefighting, and moved away at high speed soon after the attack; her fighting capabilities are unclear, but her main sensors were probably still active. The following day however saw the ship in sheltered waters for repairs. After the end of the war the ship traveled back to the UK under her own power.

USS Stark (1987)

USS Stark was a Perry class frigate with a displacement of about 4200 t (full load). She received two hits by Exocet missiles which she survived despite significant, fire, flooding and crew losses.

The ship received two hits in the same location, on the port side close to the waterline (more or less below the bridge); the first missile did not detonate but started a fire, the second exploded in crew quarters causing large losses among the crew.

Official statements (USN, 1987) indicate that the first hit was more damaging as a large quantity of propellant was injected further inside the ship, whereas the second hit is estimated to have occurred about 1 m inside the ship and vented some of its energy outside her.

Energic damage control carried out for several hours with the help of nearby ships managed to contain the spreading of fires and saved the ship, which at a point had an extensive list, reported as 15° (USN, 1987). The ship eventually made it to Bahrain where she sustained temporary repairs before returning home.

While propulsion was maintained, it took a while before the ship was able to move safely; also, the Standard launcher was reportedly down and the ship could not retaliate nor defend herself (except with the CIWS) from further attacks.

USS Samuel B. Roberts (1988)

USS Samuel B. Roberts was a Perry class frigate with a displacement of about 4200 t (full load). She sustained one hit by a contact mine which caused extreme damage but did not sink her.

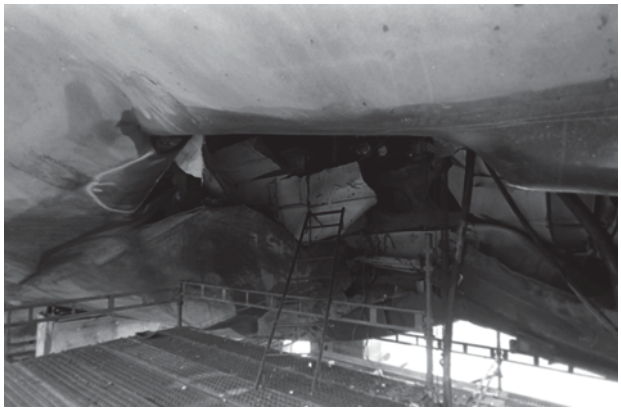

Figure 2: The damaged hull of USS Samuel B. Roberts
(photo credit: PH2 Rudy D. Pahoyo - USN - public domain)

Samuel B. Roberts struck an M-08 contact mine with a nominal charge of about 115 kg (Watts, 1991). Literature suggests however that some of the mines encountered in the Persian Gulf had a higher than normal charge in exchange for flimsier chains, which could explain the fact that the mine was encountered in a commercial shipping lane.

The hit broke the keel of the ship and blew a 5 m hole in the hull, flooding the engine room and knocking the two gas turbines from their mounts; a large fire was also initiated. Heroic damage control managed to contain the damage and save the ship, which then moved away under the power of her auxiliary thruster and reportedly maintained (or quickly

regained) radar coverage and weapon readiness; however her extreme structural damage as well as her much reduced mobility still qualifies this hit as a mission-kill.

IIS Sahand (1988)

IIS Sahand was a British-made Alvand-class 1500 t full load frigate that was sunk after sustaining 3 Harpoon hits plus further hits by 2 cluster bombs and at least 2 laser guided bombs.

It is reported that either of the first two Harpoon shots (with a 220 kg warhead) hit the superstructure in the command area, effectively disabling the fighting capabilities of the ship; further hits had the ship ablaze from bow to stern, dead in the water and listing; eventually the ship blew up when the flames reached her ammunition magazines.

IIS Sabalan (1988)

IIS Sabalan was a British-made Alvand-class 1500 t full load frigate that was hit by 1 225-kg laser-guided bomb.

Sabalan sustained a hit by a Mark 82 bomb, reportedly close to her exhaust stack, which caused the ship to lose propulsion and set her on fire. It was eventually towed back to port and repaired. Not much more is known about this event.

USS Tripoli (1991)

USS Tripoli was a Ivo Jima-class amphibious assault ship with a displacement of 19300 t that was hit by a contact mine (USN 1992, Atkinson 1994).

Tripoli was hit on her starboard bow by an LUGM-145 mine carrying about 145 kg of explosives, the effect of the hit being magnified by the close bottom. The explosion ripped a 5 by 7 m hole in the hull and caused damage throughout the bow, including an artillery magazine being flooded with JP5 kerosene and water and a mixture of paint and thinner being vaporized and filling part of the hull with its toxic vapors.

Damage control managed to contain the effects of the damage; the ship resumed operations after 20 hours, remaining in the combat area for several days until relieved, though she was unable to deploy her mine-hunting helicopter due to the relevant fuel tanks having been damaged by the hit.

USS Princeton (1991)

USS Princeton is a Ticonderoga-class cruiser with a displacement of 9800 t at full load. She was hit by two influence mines (USN 1992, Atkinson 1994).

Princeton was hit by the blast of an Italian-made MN-103 Manta, a bottom-mounted influence mine, which exploded under the port rudder; immediately thereafter a second mine of the same type (probably in a sympathetic detonation) exploded forward of the starboard bow. The whipping induced by the detonations caused the ship to suffer severe structural damage.

The fantail nearly separated from the rest of the ship. Cracks developed in the hull and in the superstructure which was nearly divided in two parts by a crack going completely through its sides. The port rudder was jammed and the starboard propeller shaft was damaged. A fire main was damaged, flooding part of the ship and shorting one of the main switchboards.

The AEGIS system was brought back online in a short while and the forward weapons were still operational, but the ship could not be safely moved due to the severe structural damage and eventually had to be towed away, so as in the case of Samuel B.

Roberts this must be considered a mission-kill as well.

TCG Muavenet (1992)

TCG Muavenet (ex USS Gwin) was a mine layer destroyer that was hit by two Sea Sparrow missiles fired inadvertently by USS Saratoga.

The missiles were meant for AA use and therefore had smaller 40-kg warheads; however the first hit destroyed the bridge and the CIC, whereas the second struck the aft magazine but did not detonate.

Damage control operations saved the ship which was still capable of floating and moving, but she had been effectively crippled due to the loss of most of her bridge crew and command rooms.

USS Cole (1999)

USS Cole is an Arleigh Burke-class destroyer with a displacement of 9000 t at full load. She was hit by a suicide small boat on her port side. It is estimated that 200-300 kg of explosives, possibly formed in a shaped charge, were used. The attack was probably the most successful attempt at asymmetric warfare in the post Cold War era and has influenced naval thinking and design in recent times.

The hit opened an 18 by 12 m gash in the ship at the waterline, driving two lower decks upward toward the main deck and opening the room containing the starboard main engine to the sea. Fuel lines were ruptured and power throughout the vessel went out as well. Damage control took three days until the situation was stabilized enough for the ship to be towed and then dry-docked.

INS Hanit (2006)

INS Hanit is a Sa'ar 5 class corvette with a displacement of 1300 t (full load) which received a single hit by what has been reported as a YJ-82 missile.

The hit was sustained in the stern area of the ship; the explosion split the helo deck, caused crew casualties and reportedly extensive damage to propulsion. Despite this the ship made it back to a safe port under her own power; her fighting capabilities after the impact remain however unknown.

ROKS Cheonan (2010)

ROKS Cheonan was a Pohang-class corvette with a displacement of 1200 t which, according to the official investigation, received a single torpedo hit which sunk her.

The matter is contested, but what is clear is that a medium-sized explosive charge, estimated as 250 kg of TNT equivalent, detonated just below the hull in the stern area, somewhat off to port; the resulting bubble jet broke the ship in half, separating the stern, and the ship capsized and sunk in a very short time frame.

5. CONCLUSIONS

At the base of this paper there is the opinion that the SOLAS2009 probabilistic approach might represent and interesting methodology to be implemented in the warship survivability assessment. After the indication of the main critical points for the approach transferability to the warship design process, attention is given to the need of a consistent and comprehensive investigation, about the different damage scenario characteristics..

As an initial approach to the problem an overview is carried out evidencing the importance to discuss about the ship characteristics, the kind of threat, the primary effects (hull damage and flooding), the secondary effects (for example fire or systems failures) and the final evolution of the situation.

It appears evident that the damage size description in terms of length, penetration and height is not a straightforward activity and that some further studies are necessary in the perspective of a probabilistic approach, SOLAS2009 like, the field of naval ship assessment. Actually some analytical probability density function derived from literature (Przemieniecki, 2000) able to describe the ship damage statistics, might represent a more suitable way to move forward, as already proposed by some authors.

The efficiency that the watertight subdivision can express is of course in close relation with the weapon overall power intensity that in some occasions is really devastating. To this regard, it might be more interesting to focus on a possible optimization of the ship subdivision considering the effect of an asymmetric threat, characterized by a lower power, but usually oriented to possibly offend a sensitive part of the ship. However there is growing attention to the assessment of a warship performance not only to survive a hostile damage, but also in relation with typical merchant fleet accidents like collision and grounding (Smith & Heywood, 2009) and in this sense the possible application of the probabilistic approach for the warship design might find its exploitation.

6. REFERENCES

Atkinson, R. 1994 “Crusade: The Untold Story of the Persian Gulf War” Mariner Books

Ball, R.E.; Calvano, C.N. (1994), “Establishing the fundamentals of a surface ship Survivability Design Discipline”, Naval Engineers Journal, Vol. 106, No. 1, pp. 71-74

Boulougouris E., Papanikolaou A., 2012, “Risk-based Design of Naval Combatants” 11th International Marine Design Conference IMDC 2012 Glasgow UK

Harmsen, E., Krikke, M., 2000, “A probabilistic damage stability calculation method for naval vessels”, 7th International Conference on Stability of Ships and Ocean Vehicles (STAB ’00), Tasmania, Australia.

Harry, B. 2002 "Trident, Grandslam and Python: Attacks on Karachi". Pages from History. Bharat Rakshak Monitor - Volume 4 (4) IMO, 1960, “Resolution A.265 (VIII) - Regulations on Subdivision and Stability of Passenger Ships as an Equivalent to Part B of Chapter II of the International Convention for Safety of Life at Sea”, London, UK.

IMO, 1990, “Resolution MSC 19 (58) on the Adoption of Amendments to the SOLAS 1974 Convention, regarding the Subdivision and Damage Stability of Dry Cargo – MSC 58/25 Annex 2” London, UK.

IMO, 2007, “MSC 82/24/Add.1 Report of the Maritime Safety Committee on its eighty-second Session - ANNEX 2 MSC.Res.216(82)” London UK.

Inskip, I., 2012 “Ordeal by Exocet: HMS Glamorgan and the Falklands War 1982” Frontline Books

Papanikolaou, A.; Boulougouris, E., 2000, “On a rational approach to the assessment of survivability of surface naval and merchant ships”, Proc. 9th congress of the Int. Maritime Association of Mediterranean, IMAM 2000, Ischia, April 2000

Przemieniecki, J.S. (2000), “Mathematical Methods in Defense Anlyses”, Third Edition, American Institute of Aeronautics and Astronautics, Reston VA, USA.

Sarchin T.H., Goldberg, L.L., 1962 “Stability and Buoyancy Criteria for U. S. Naval Surface Ships” Transactions SNAME Vol. 70.

Smith, D., Heywood, M., 2009 “Accidental

Damage Templates (ADTs) A basis for the future of Naval Ship Safety Certification?" Proceedings of the 10th International Conference on Stability of Ships and Ocean Vehicles, STAB 2009 St. Petersburg Russia

Surko, S.W., 1994, "An Assessment of Current Warship Damaged Stability Criteria", Naval Engineers Journal, Vol. 106, No. 3, pp. 120-131.

Surko, S.W., 1988, "The residual strength of a ship after an internal explosion" Thesis (M.S.)--Massachusetts Institute of Technology, Dept. of Ocean Engineering, 1988, and (M.S.)--Massachusetts Institute of Technology, Dept. of Mechanical Engineering.

UK MOD, 1982a "Loss of HMS Sheffield – Board of Enquiry" reference 520/237.L

UK MOD, 1982b "Loss of HMS Antelope – Board of Enquiry" reference 520/4.X

UK MOD, 1983 "Loss of HMS Ardent – Board of Enquiry" reference 520/241L

USN, 1987 "Formal investigation into the circumstances surrounding the attack on the USS Stark (FFG 31)"

USN 1992 "Salvage Report Operations Desert Shield / Desert Storm" Volume I. Naval Sea System Command.

Watts A.J., 1991 "Jane's Underwater Warfare Systems 1991-1992" Jane's Information Group

Advanced Damaged Stability Assessment for Surface Combatants

Evangelos Boulougouris, *University of Strathclyde*, evangelos.boulougouris@strath.ac.uk

Stuart Winnie, *University of Strathclyde*

Apostolos Papanikolaou, *National Technical University of Athens*

ABSTRACT

One of the major contributors to survivability of a surface combatant is her vulnerability to weapon effects and as such the damage stability characteristics have a direct influence on vulnerability. There are serious concerns about the limitations of the current semi-empirical deterministic criteria in which a combatant's damage stability is assessed upon. This paper details a comparison between the current approach and a newly presented probabilistic approach with the aim of determining which will result in a more accurate way of estimating the level of survivability of a particular design. A study is also presented in which the damage length used is increased to merchant standards of $0.24L_{bp}$.

Keywords: *naval ships, damage stability, probabilistic, survivability*

1. INTRODUCTION

Surface warships differ from other categories of ships in that they are designed to operate in a man-made hostile environment. In addition to being able to withstand damage from collision and grounding a surface combatant must be able to avoid and withstand the effects of modern anti-ship weapons. As warships are designed and built to support high-end combat operations, survivability and the ability to 'fight hurt' is a vital design objective.

One of the main contributors to a surface combatants survivability is her vulnerability to weapon effects and as such the damage stability and floatation characteristics of the vessel determine the vulnerability of the vessel. Therefore it is critical for the designer to minimise the vulnerability of the vessel from the early design stages in order to maximise its survivability. This can be achieved through the use of optimal subdivision and by considering a large number of damage scenarios and operational /environmental conditions.

The majority of modern warship stability criteria used is based on a set of empirically defined stability criteria proposed by Sarchin and Goldberg (1962). The survivable damage lengths and criteria are based largely on WWII battle damage experience. The criteria used by major navies such as the U.S Navy (USN) and Royal Navy (RN) have been reviewed over the years however, there have been no significant changes. Although the criteria have served their purpose for many years, they now appear to be outdated and there are serious concerns about their limitations and applicability to modern naval ship designs. Some of the shortfalls of the criteria incluide (Surko, 1994);

- Capability of modern warships to survive damage from current threats, in demanding environmental conditions, is not known
- Modern hull forms and construction techniques differ greatly from the ships

used to determine the criteria
- Assumption of moderate wind and sea conditions at the time of damage

This suggests that even though a vessel may comply with the standards outlined, the designer and operator may not have a clear understanding of the survivability performance and operational limits of their vessel.

In contrast the International Maritime Organisation (IMO) have made significant advances in terms of upgrading safety standards of merchant vessels. The acceptance of the new harmonized probabilistic damage stability framework of SOLAS 2009 for the damage stability assessment of passenger and dry cargo vessels shows that the maritime industry and regulatory bodies are convinced this is the only way forward. Boulougouris and Papanikolaou (2004) previously presented a methodology for the probabilistic damaged stability assessment of naval combatants and its application to design optimisation. The methodology allows the risk that the vessel will be lost as a result of damage to be quantified. Therefore minimal risk can become a design objective and the surface ship can be optimised for minimum risk while still being efficient and economical.

This paper details a comparative study of the currently used semi-empirical deterministic approach and the proposed quasi-static probabilistic approach to assessing the damage stability of a surface combatant. Each approach is applied to a generic frigate and the merits and shortcomings of each method along with the results are presented. In addition, a study was carried out to observe the effects of increasing the damage length on a frigate which meets the current deterministic criteria.

2. SURVIVABILITY

The survivability of a naval combatant can be defined as *"the capability of a (naval) ship and its shipboard systems to avoid and withstand a weapons effects environment without sustaining impairment of their ability to accomplish designated missions"* (Said, 1995). Survivability consists of two main aspects;

- Susceptibility – Inability of the ship to avoid being damaged in operation and is also referred to as the probability of being hit (P_H)
- Vulnerability – Inability of the ship to withstand the effects of a threat weapon and is also referred to as the probability of serious damage or loss when hit ($P_{K/H}$)

Survivability is the opposite of killability which is the probability that the ship will be lost due to enemy action. Killability can be described mathematically as the product of susceptibility and vulnerability. A ship kill can be expressed in many different ways, in this case the definition given by Ball & Calvano (1994) is referred to;

- System Kill – damage of one or more compartments which leads to the failure of a ship system.
- Mission Area Kill – damage which leads to the loss of a mission critical area such as AAW
- Mobility Kill – damage which leads to the ship being immobilised through the loss of propulsion or steering.
- Total Ship Kill – damage which leads to the loss of the ship through insufficient buoyancy, loss of transverse stability or abandonment due to fire.

The mathematical relationship between survivability (P_s), susceptibility and vulnerability is as follows (Ball & Calvano, 1994);

$$P_s = 1 - (P_H x P_{K/H}) \quad (1)$$

The relationship highlights that both susceptibility and vulnerability are of equal importance to the survivability of the vessel.

Some naval design philosophies have included to 'design for peace' as the probability of being damaged in operation is very low. They will therefore accept that in the event of a hit that the vessel will be out of action or have limited participation in the operation. Thus their focus has been to minimise the susceptibility of the vessel. Most of the scenario simulations ran would assume a single hit has a kill probability equal to one for smaller vessels and two hits would be sufficient to sink a larger vessel. Although modern surface ships are powerful military assets on the open ocean, they lose their advantage near shore. Even the stealthiest vessel is susceptible to asymmetrical threats. By treating the vulnerability as a property with a deterministic outcome, pass or fail, it is not possible to truly quantify the survivability of the vessel.

3. DETERMINISITC

Currently both the USN and RN use deterministic criteria to assess the stability of naval ships after damage. The stability standards previously used by the UK MOD, NES 109, was recently reissued in DEFSTAN 02-900 part 1: Ship safety & Environmental Protection (UK MOD, 2013). However the criteria used in the assessment of stability and reserve buoyancy after damage remain unchanged. Table 1 shows the semi-empirical damage stability criteria currently used by the USN and RN for surface combatants. Both use a damage length of 15% L_{wl} for larger vessels however the UK also implements a minimum damage length of 21m. Although the survivability requirements between naval ships and merchant vessels differ significantly it is of interest to note that the current IMO probabilistic damage approach considers damage extents up to 24%.

Although both criteria are very similar the UK criteria is slightly more demanding, the use of a 15 degree roll back angle requires that UK warships have a greater righting energy to achieve the same reserve dynamic stability criteria. In addition the use of a minimum length of damage shows progress towards a threat based standard for damage length.

4. PROBABILISTIC ASSESSMENT

Boulougouris and Papanikolaou (2004, 2013) previously presented a methodology for the probabilistic damaged stability assessment and its application to design optimisation. It is based on the fundamentals of the probabilistic damage stability concept for passenger vessels introduced by Wendel (1960) and its derivatives (IMO Resolution A.265; IMO MSC.19 (58); IMO MSC.216 (82)) which are used to assess the ships level of safety after damage. The probabilistic approach uses the probability of survival after damage as a measure of the ships safety when damaged. The approach considers the following probabilities of events as being relevant to the ships damage stability;

- The probability that a compartment or group of compartments i may be flooded (damaged), p_i.
- The probability that the ship will survive after flooding of the compartment or group of compartments i under consideration, s_i.

Table 1
Current UK and US damage stability criteria for surface combatants

Criteria	UK Defstan 02-900		U.S.N DDS 079-1	
Damage Length	LWL < 30m	1 Compartment	LWL < 100ft	1 Compartment
	30m < LWL < 92m	2 comp of at least 6m	100ft < LWL < 300ft	2 comp of at least 6m
	LWL > 92m	max{15%LWL or 21m}	300ft < LWL	15% LWL
Permeability	Watertight void	97%	Watertight void	95%
	Accomodation	95%	Accomodation	95%
	Machinery	85%	Machinery	85-95%
	Stores etc.	80-95%	Stores etc.	60-95%
Angle of list or loll	< 20°		List < 15°	
GZ at C	60% of Gzmax		-	
Area A1	> 1.4 A2		> 1.4 A2	
Longitudinal GM	> 0			
Buoyancy	longitudinal trim less than required to cause down-flooding		3 in margin line	

The total probability of survival is expressed by the attained subdivision index, A, and is the given by the sum of the product of p_i and s_i for each compartment and compartment group, i along the ships length.

$$A = \sum_i p_i . s_i \tag{2}$$

In order for a vessel to comply with the IMO probabilistic method for passenger and cargo ships (IMO MSC.216 (82)) the attained subdivision index must be greater than or equal to the required index. This ensures that the vessel is designed with an acceptable level of risk. The required attained index is based on the number of passengers carried, safety equipment on-board and the length of subdivision. The calculated required index (R) of the ship is consistent with the mean value of the attained index (A) from a sample of ships which in theory face a similar level of risk. This consists of ships of a similar size and number of passengers which have acceptable damage stability/ survival characteristics. Similarly for warships an acceptable level of risk should be specified by either the owner (navy) or approval authority (NATO/ classification society).

For naval vessels there is a probability that the ship will be targeted and engaged leading to the flooding of one or more compartments. The damage can occur at any point along the ship's hull and can vary extensively is magnitude. The extent of damage is dependent on both the characteristics of the target (ship) and the threat weapon. As the survivability of the vessel is determined by the vulnerability and susceptibility, the probability distribution for damage of a naval ship relates these characteristics.

The probability of survival of a particular function of the ship can be extracted from the total attained index, which represents ship's floatability and stability after damage. If j*={j1, j2, j3,.., jn} is the set of compartments that host all systems of the particular function F, then the damage of any set j that includes j* will impair the ship from function F. Therefore the probability of survival of the particular function is calculated using the following formula:

$$S_f = \sum_i p_i . s_i - \sum_j p_j . s_j \tag{3}$$

where j are all damage cases, which include the compartment set j*.

4.1 Determining p_i

During the initial stages of a naval ship's design, when there is a lack of refined information for the threat's signature distribution along the ship it can be assumed that the probability of weapon impact along the hull follows a basic mathematical distribution, such as the piecewise linear distribution. Boulougouris and Papanikolaou (2004) propose that for air-to-surface missile (ASM) threats, a piecewise linear distribution with maximum probability amidships can be used. As both the ships radar profile and heat emissions due to machinery and exhaust are highest at amidships this is the most likely aim point of the weapon. For contact mines a linear distribution can be assumed (Harmsen & Krikke, 2000). Thus the impact point probability density function in the missile's case with a piecewise linear distribution is;

$$imp(x) = \begin{cases} 4x & x \le 0.5 \\ -4x + 4 & x \ge 0.5 \end{cases} \tag{4}$$

The damage length probability density distribution is based on the concept of the Damage Function used in the theory of Defence Analysis (Przemieniecki, 1994). The well-known log-normal distribution considered the most appropriate for this case. Therefore the damage length probability density distribution is given by the following formula;

$$Dam(y) = \frac{1}{\sqrt{2.\pi}.\beta.y}.\exp\left[-\frac{\ln^2(y-\alpha)}{2\beta^2}\right] \quad (5)$$

Where;

$$\alpha = \sqrt{L_{SS}L_{SK}}, \beta = \frac{1}{2\sqrt{2}z_{ss}}\ln\left(\frac{L_{SS}}{L_{SK}}\right) \quad (6)$$

Where L_{SK} is the sure kill length which means that d (L_{SK}) =0.98, L_{SS} is the sure save length which means d (L_{SS}) =0.02 and z_{SS} is a constant equal to 1.45222.

For defining the damage extent range, it is a common approach in naval ship design to consider 2 or 3 damaged compartments around the detonation compartment especially in case of absence of blast resistant bulkheads (Erkel & Galle, 2003). More detailed estimates may result from a careful risk assessment based on live firing tests analysis, the analysis of data from actual engagements, empirical formulas linking the damage range with the type and weight of the warhead or from the use of damage lengths/extents defined in current deterministic damage stability regulations for naval ships. In the latter case, which is the one proposed by Boulougouris and Papanikolaou (2004), a first approximation of the L_{SS} can be taken according to naval codes DefStan 02-900 and DDS-079 and it would be 0.15L (see Table 1). The author's state that the L_{SK} has can be assumed equal to 0.02L.

By combining the impact point and damage length density functions the probability of damage lying between the boundaries x1 and x2 or a naval ships compartments is;

$$p_i = \int_0^y Dam(y) \int_{x_1+\frac{y}{2}}^{x_2-\frac{y}{2}} imp(x)dxdy \quad (7)$$

The equations resulting from substituting Dam(y) and Imp(x) into equation (7) were presented in Boulougouris and Papanikolaou (2004).

Similar to collision damage the extent from a threat weapon will vary in magnitude transversely and vertically. The transverse damage penetration especially from ASM threats can vary extensively and in cases can extend across the full hull. Weapons fitted with time-delay fuses will penetrate the hull to an optimum position before detonating. However the damage penetration distribution is not an 'issue' for surface combatants as longitudinal subdivision which would lead to asymmetrical flooding is avoided by design.

For the assessment carried out a piecewise linear distribution with maximum probability at the centreline was utilised for the damage penetration distribution in order to calculate reduction factors for various damage cases. The vertical extent of damage may also vary depending on the weapon's characteristics. In a surface combatant such as a frigate or a destroyer there are 3 vertical watertight boundaries, namely the tanktop, the damage control deck and the main deck. Excessive vertical watertight boundaries are avoided by design as high flooding can lead to poor stability thus it can be favourable to allow lower decks to flood. In the case of an air delivered weapon (e.g. Anti-Ship Cruise Missile) it will generally detonate close to the waterline causing greater damage above the waterline and the tank top will most likely remain intact. However in the case of an underwater weapon (e.g. contact mine or torpedo) which detonates close to the keel, the damage control deck will likely remain intact. The problem with an underwater explosion is that modern under-keel torpedoes are capable of causing extensive damage to the keel girder of even a cruiser sized ship, often this is sufficient to cause breaking and sinking of the ship. Such cases are not covered in the proposed methodology as the maintenance of structural integrity is a perquisite for the assessment of the ships damage stability.

For a hit by an air-delivered weapon, a linear distribution for the probability density function of the vertical extent of damage can be

used. Its maximum is at the main deck and the minimum at the keel, the opposite is valid for an underwater weapon (see Figure 1) (Boulougouris & Papanikolaou, 2013). By considering the vertical extent of damage the effect of the position of vertical watertight boundaries on the overall survivability of the vessel can be observed. In order to take into account both threats a weighting factor can be applied according to an operational analysis of the potential threats.

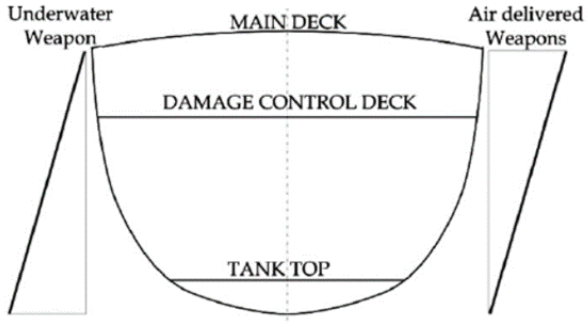

Figure 1 Naval Ship Vertical Watertight Boundaries

4.2 Survival index S_i

The approach used to assess the probability of survival after damage is a probabilistic quasi-static approach adjusted for the currently valid, semi-empirical deterministic criteria for naval ships (Boulougouris & Papanikolaou, 2013). The approach considers the probability of survival after damage and is based on quasi-static survival criteria such as those used by the Royal Navy and US Navy. The criteria were developed from real life damage incidences of WWII and although the current criteria have been under criticism as being outdated they have proved reliable over the years and thus there have been no significant changes. One of the main criticisms of the current criteria is the fundamental assumption that the sea conditions at the time of damage are "moderate." This constraint was lifted in the proposed methodology with the requirement for a specific survival sea state in case of damage.

This allows the correction of these requirements by consideration of the probability of exceedance of the wave height considered as basis for the current deterministic RN and USN criteria, namely a significant wave height H_S of merely 8 ft. The wave height is used in the criteria in order to define φ_{roll}, the roll amplitude due to wave action. It was also the underlying assumption behind the guidelines for establishing the watertight features/closures to prevent progressive flooding. Thus, any attempt to change the wave amplitude must take into account changes in both φ_{roll} as well as the margin line or equivalent.

The wind speed is another important parameter which needs to be considered, however given the small probability of exceeding the values given by RN and U.S Navy standards, the values were left unchanged (approximately 33 knots for a 3500t frigate). Table 2 shows the criteria which were applied in the frame of a probabilistic approach to assess the survivability of a generic frigate.

Table 2
Probabilistic damage stability criteria for naval combatants

$s_i = 1$	Θ_{roll} = 25 deg	Wind Speed = According to Defstan 02-900
	$A_1 \geq 1.4\ A_2$	Min Freeboard ≥ 3in + 0.5(H_s(0.99) - 8ft)
$s_i = P(H_s \leq 8ft)$	Ship meets Defstan 02-900 damage Stability Criteria	
$s_i = 0$	Θ_{roll} = 15 deg	Wind Speed = According to Defstan 02-900
	$A_1 \leq 1.05\ A_2$	Longitudinal trim < required to cause downflooding

For intermediate stages, interpolant values can be used. Figure 2 shows the meaning of various notions of the righting arm curve.

Implementing the above criteria for ships operating in North Atlantic P($H_S \leq 8$ ft) would be 0.56 and for East Mediterranean Sea 0.90 (Athanassoulis & Skarsoulis, 1992). For the North Pacific P ($H_S \leq 8$ ft) would be 0.42 (Lee, 1995) and for the South China Sea 0.71 (Haveman et al, 2006).

Therefore, a combatant, meeting the U.S. Navy criteria for warships, should have according to the proposed criteria a 56% probability of survival in the North Atlantic for a damage length not exceeding the current regulations (Ochi, 1978). This probability will increase to 90% probability of survival in the Mediterranean Sea and to 71% in the South China Sea. However in the case of the North Pacific the probability of survival will decrease to 42%. Obviously a similar methodology can be introduced for auxiliary naval vessels. The minimum required values for compliance could be estimated after application of the above procedure to sample/existing ships.

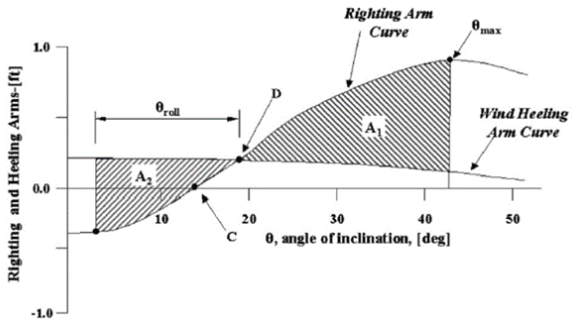

Figure 2 Damaged ship GZ criteria

5. CASE STUDY

Both the current deterministic approach and proposed probabilistic approach were applied to a generic frigate model which was defined in the Maxsurf package (Bentley Systems, 2013). The stability of the vessel was assessed using Maxsurf stability advanced. The ships main particulars are given in Table 3 and the 3D hull model is shown in Figure 3.

Table 3

Main Particulars	
Loa (m)	148.1
Lwl (m)	137
Twl (m)	4.31
Depth (m)	9.3
Displacement (tons)	4528

Figure 3 Frigate 3D hull model

The arrangement is typical for a frigate of this size with a centreline passageway providing an un-flooded route across the full length of the damage control deck. The ship has two main engine rooms, one for two cruise gas turbines and the other for two boost gas turbines. In addition there are two auxiliary machinery rooms forward and aft of the GT rooms.

The internal layout of the frigate consisted of 13 watertight transverse bulkheads which subdivide the hull into 14 main compartments. Three decks form the horizontal watertight boundaries, namely the main deck (1st deck), damage control deck (2nd deck) and the tank top (4th deck).

The ship has a 4528t displacement at full load condition without a growth margin and has a VCG of 5.53m resulting in a GMcorr of 1.097m. At this condition the ship fulfils the intact stability criteria outlined in DefStan 02-900.

Initially the deterministic assessment was carried out in which all damage cases had to meet the criteria outlined in DefStan 02-900. The damage length specified (15%Lwl) resulted in a damaged length of 20.55m, thus the minimum length of 21m was used to define the damage cases. This resulted in mainly 3 compartment damage cases. Several different transverse extents were taken for each damage case including B/5, B/2 and penetration across the full beam to ensure to worst possible cases were considered. As the frigate model was designed to this standard all damage cases fulfilled the criteria.

For the quasi-static probabilistic approach damage cases up to 6 adjacent zones were initially considered, however the probability of occurrence of both 5 and 6 compartment damage extents was found to be insignificant.

A total of 226 damage cases extending up to 4 adjacent damage zone were defined in Maxsurf stability. The formulas for the calculation of the probability of damage occurring, p_i, from equation (7), were applied to the basis ship and results for single compartment damage are given in Table 4.

Table 4 p_i for frigate 1-comp damages

Room	NZ	x_1	x_2	x_1u	x2u	y	Pi
1	1	0	13.06	0.000	0.095	0.095	0.0071
2	1	13.06	23.53	0.095	0.172	0.076	0.0117
3	1	23.53	29.32	0.172	0.214	0.042	0.0024
4	1	29.32	41.19	0.214	0.301	0.087	0.0309
5	1	41.19	51.61	0.301	0.377	0.076	0.0293
6	1	51.61	62.06	0.377	0.453	0.076	0.0362
7	1	62.06	72.5	0.453	0.529	0.076	0.0421
8	1	72.5	79.58	0.529	0.581	0.052	0.0118
9	1	79.58	89.11	0.581	0.650	0.070	0.0261
10	1	89.11	102.37	0.650	0.747	0.097	0.0466
11	1	102.37	109.01	0.747	0.796	0.048	0.0048
12	1	109.01	117.64	0.796	0.859	0.063	0.0088
13	1	117.64	128.06	0.859	0.935	0.076	0.0089
14	1	128.06	137	0.935	1.000	0.065	0.0018

For the given subdivision arrangement, damage length and longitudinal distribution, 1 compartment damage cases contribute approximately 0.27 whereas 2, 3 and 4 compartment cases contribute 0.6, 0.11 and 0.01 respectively.

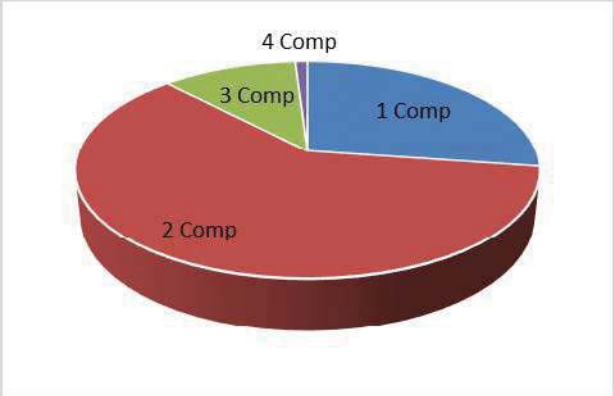

Figure 4 Contribution of various damage cases to attained index

Two different operational areas were considered in order to determine the influence of sea state on survivability, considering the criteria given in Table 2. For the North Atlantic Scenario, we assume P (Hs≤8ft) = 0.56 and Hs (0.99) =10m, for the North Pacific P (Hs≤8ft) = 0.42 and Hs (0.99) =11.2m.

For the frigate under consideration at full load condition the attained index was found to be A=0.98 for the North Atlantic and A=0.95 for the North Pacific Scenario. The survivability of the mobility function was calculated using equation (3) where j are all the main engine room compartments; in this case 5, 6 and 7. This resulted in a mobility survivability index of 0.87.

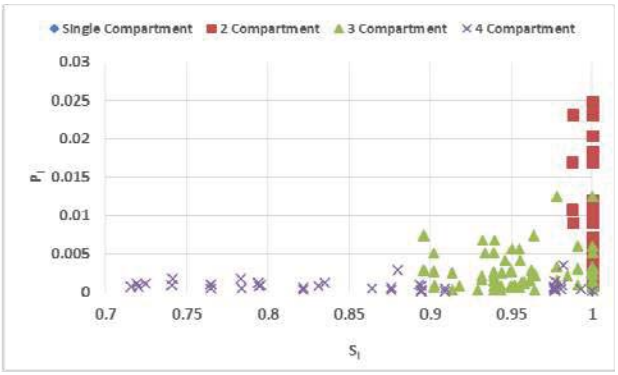

Figure 5 North Pacific pi against si

Figure 5 shows that for the given damage length and longitudinal distribution, the damage cases which are most likely to occur and their corresponding probability of survival. The results illustrate that the vessel has a low risk of being lost due to damage up to two compartments. Due to the length of damage utilised, up to two adjacent compartments contributes approximately 0.87 to the attained index. The risk increases significantly for four or more adjacent compartments however the probability of occurrence of this extent of damage is too low to affect the overall attained index.

It was readily observed that the probabilistic approach can result in minimising the vulnerability of the vessel in the early stages of the design. The results from this approach can be easily visualised making the comparison of many different designs more concise for the designer. As the result of a deterministic assessment is simply a 'pass or fail' for each of the damage cases, it is difficult to quantify the effect of any major design changes on the overall survivability of the vessel. The use of the attained survivability index in the probabilistic approach enables the designer to adopt a holistic approach to naval ship survivability and allows him to easily monitor the influence of his decisions on the survivability.

The defined deterministic length of damage criteria directly influences the position of transverse watertight bulkheads; the specified length of damage implies that the length of either two or three compartments should be slightly larger than the damage length. This results in larger ships being designed with longer compartments to limit the extent of flooding in fewer compartments. Therefore the subdivision methodology simply following the concept of compliance with a set of deterministic criteria, as opposed to an optimisation for maximum survivability. The use of the probabilistic approach in a formal, multi-objective optimisation procedure allows the designer to achieve the optimum level of survivability, while keeping ship's weight and shaft length to a minimum (Boulougouris & Papanikolaou, 2013).

Relaxing the assumption for a moderate sea state (Hs=2.4m or 8ft) at the time of damage, it gives a more demanding and realistic set of criteria, which can ultimately result in a higher level of survivability. The currently used significant wave height in the deterministic approach has a 58% chance of exceedance in the North Pacific and a 44% chance of exceedance in the North Atlantic. Thus, it does not properly reflect the harsh environments, which modern surface combatants are expected to operate in.

5.1 Damage Length

The current IMO regulations for dry cargo and passenger ships (IMO MSC.216 (82)) consider collision damage lengths of up to 24% L_{bp}, thus any length of damage over 24% L_{bp} is considered as statistically insignificant. This means that collision damage extents of less than 24% L_{bp} (but still greater than 15% weapon damage length) are statistically significant.

In order to develop a proper set of probabilistic criteria for naval ships extensive calculations must be carried out on a sample of ships, which comply with the current damage stability regulations. A study was carried out in order to explore the effects of the damage length in which the ship is expected to survive on the overall survivability. This will provide insight regarding the extent of damage modern naval ships are capable of surviving. This can therefore lead to a more rational approach of basing the damage extent on an assessment of threat while still having a set of criteria which can be reasonably met resulting in a higher level of survivability.

Initially the maximum length of damage was increased from 15% L_{wl} (or 21m) to 20% L_{bp} for the deterministic assessment. This led to a damage length of 27m resulting in a majority of four compartment damage cases. The new length of damage fulfilled the deterministic criteria for all cases; however, the criteria were met with a much lower margin for the 4 compartment cases. A single 5 compartment case at the bow of the vessel was also assessed in which it passed the reserve buoyancy criteria by 0.17m.

Similarly for the quasi-static probabilistic assessment the maximum length of damage in the distribution was increased from 15% L_{wl}. The value of L_{ss} was set to 20% L_{bp} which altered the damage length distribution. For the new damage length, 1 compartment cases now contribute 0.22 and 2, 3 and 4 compartment damage cases contribute 0.57, 0.17 and 0.03 respectively. For a 15% damage length, 1 and 2 compartment cases contributed 0.87 to the attained index; however that has fallen to 0.79 for a 0.2L damage. An attained index of A=0.96 was obtained for the North Atlantic scenario and A=0.93 for the North Pacific scenario. Finally the damage length was increased to 0.24L. As collision damage extents over 0.24L are considered to be statistically insignificant this was taken as the maximum value for the study. At approximately ¼ of the ships lengths this resulted in a large number of 5 compartment damages for the deterministic assessment. At this point the basis frigate failed the assessment in several cases due to both insufficient transverse stability and reserve buoyancy.

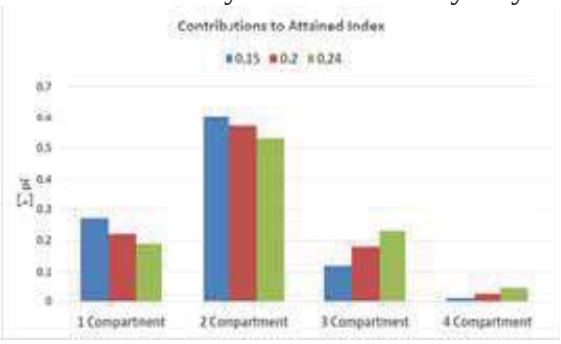

Figure 6 Contributions to attained index

For the probabilistic assessment the 0.24L damage length led to an attained index of A=0.94 for the North Atlantic and A=0.90 for the North Pacific Scenario. The 4 and 5 compartment cases now contribute a maximum of 0.05 to the attained index as opposed to approximately 0.01 for the 0.15L case.

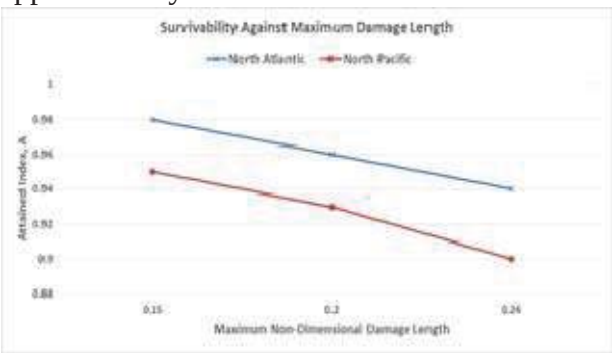

Figure 7 Survivability against max damage length

Figure 6 and 7 show the difference in contribution to the attained index for various damage cases and the effect on the attained index for each of the maximum damage lengths investigated.

Figure 8 illustrates the different contributions to the attained index for the frigate under consideration in the outlined probabilistic approach and also when considering IMO MSC.216 (82); both assessments are for a damage length of 0.24L.

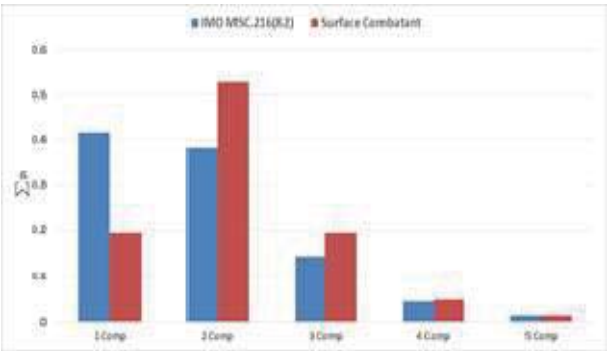

Figure 8 Comparison of damage length distributions

As a damage from a threat weapon will result in greater damage extent than from collision, there is a peak at two compartment damage as opposed to one compartment damage in the case of the linear distribution of SOLAS.

Although SOLAS considers damage lengths up to $0.24L_{bp}$, the use of the linear damage length distribution results in a more conservative estimate of the level of survivability. The linear distribution from SOLAS 2009 was applied and an attained index of A=0.97 was obtained for the North Atlantic and A=0.94 for the North Pacific. Using the log-normal distribution with the same maximum length of damage (0.24L) the values obtained where A=0.94 for the North Atlantic and A=0.90 for the North Pacific.

It is observed that the log-normal distribution is more practical for naval ships as it can accurately represent the extent of damage associated with weapon effects. The use of the log-normal distribution will increase the likelihood of occurrence of damage cases involving multiple adjacent zones, therefore resulting in a more accurate estimate of survivability.

6. CONCLUSION

The use of a probabilistic approach to assess the damage stability of a naval combatant can lead to a higher level of survivability. The use of the probabilistic assessment through the attained subdivision index allows a holistic approach to be taken to surface ship survivability. This allows ship's subdivision to be optimised for *minimum risk* (or *maximum Attained Index*) making survivability a distinct feature of the naval ship design and no longer a requirement. In addition, the use of more realistic operating conditions such as sea state at the time of damage will give the designer a better understanding of the damaged ship's performance and limitations.

The conducted study on the damage length margin for a naval ship shows that the length can be readily increased to more accurately represent damages reflecting possible weapon threats and without compromising the position of bulkheads. It illustrates that current naval vessels are capable of surviving greater damage lengths than previously specified. Thus, altering the damage length distribution for naval ships appears to be fully justified, whereas the impact on design is not anticipated to be drastic. In any case, the length of damage can be more rationally refined, namely based on current weapon threats which a combatant may face in its life cycle, resulting in a more realistic representation of the ship's survivability.

7. REFERENCES

Athanassoulis, G., & Skarsoulis, M. (1992). Wind and wave atlas of the North-Eastern Mediterranean Sea. NTUA-SMHL.

Ball, R. E., & Calvano, C. N. (1994). Establishing th fundamentals of a surface ship Survivability Design Discipline. Naval Engineers Journal 106, 71-74.

Bentley Systems. (2013). Maxsurf Marine Vessel Analysis and Design Software. Retrieved from http://www.bentley.com/en-US/Products/Maxsurf/Marine+Vessel+Analysis+and+Design.htm

Boulougouris, E. K., & Papanikolaou, A. D. (2004). Optimisation of the Survivability of Naval Ships by Genetic Algorithms. 3rd Int. EuroConference of Computer Applications and Information technologies in the Maritime Industries.

Boulougouris, E., & Papanikolaou, A. (2013). Risk-based design of naval combatants. Ocean Engineering 65, 49-61.

Department of US Navy. (2002). DDS 079-1 Stability and Buoyancy of U.S Naval Surface Ships. Department of US Navy.

Erkel, A. v., & Galle, L. F. (2003). TNO-PML Developments of Blast Resistant Doors and Walls. 8th International Marine Design Conference, (pp. 753-764). Athens.

Ferreiro, L. D., & Stonehouse, M. H. (1991). A Comparative Study of US and UK Frigate Design. SNAME Transactions Vol. 99, 147-175.

Harmsen, E., & Krikke, M. (2000). A probabilistic damage stability calculation method for naval vessels. 7th International Conference on Stability of Ships and Ocean Vehicles (STAB'00). Tasmania.

Haveman, C., Parliament, J., Sokol, J., Swenson, J., & Wagner, T. (2006). Design of a Floating, Production, Storage, and Offloading Vessel for Operation in the South China Sea. Texas: Texas A&M University.

IMO. (2007). MSC.1/Circ.1226 Interim Explanatory Notes to the Solas Chapter II-1 Subdivision and Damage Stability Regulations. IMO.

Lee, W. T. (1995). Global Wave Statistics for Structural Design. Maryland: Naval Surface Warfare Center.

MOD. (2010). MAP 01-024 Stability of Surface Ships part 1.

NATO/PfP. (2004). NATO/PfP Working Paper on Small Ship Design (Unclassified). NATO.

Perrault, D. E., Hughes, T., & Marshall, S. (2010). Naval ship stability guidelines: developing a shared vision for naval stability assessment. Trans. RINA. Inr. J Marit. Eng., 99-118.

Przemieniecki, J. S. (1994). Mathematical Methods in Defence Analysis. American Institure of Aeronautics and Astronautics.

Rawson, K. J., & Tupper, E. C. (2001). Basic Ship Theory Vol 2.

Said, M. O. (1995). Theory and Practice of Total Ship Survivability for Ship Design. pp 191-203.

Sarchin, T. H., & Goldberg, L. L. (1962). Stability and buoyancy Criteria for U.S. Naval Surface Ships.

Surko, S. W. (1994). An Assessment of Current Warship Damaged Stability Criteria. Naval Engineers Journal, 120-131.

UK MOD. (2013). DEFSTAN 02-900 Part 1.

Walree, F. v., & Carette, N. (2011). Validation of time domain seakeeping codes for a destroyer hull form operating in steep stern-quartering seas. JNAOE, 9-19.

Wendel, K. (1960). Die Wahrscheinlichkeit des Überstehens von Verletzungen. Journal of Ship Technology Research, 47-61.

Dynamic Stability Assessment of Naval Ships in Early-Stage Design

Heather A. Tomaszek, *Naval Surface Warfare Center Carderock Division*
heather.tomaszek@navy.mil
Christopher C. Bassler, *Naval Surface Warfare Center Carderock Division*
christopher.bassler@navy.mil

ABSTRACT

A method is currently under development at the International Maritime Organization (IMO) to assess dynamic stability susceptibility during early-stage ship design. The method is intended to provide a physics-based, preliminary analysis of relative risk for ship designs to dynamic stability phenomena, including parametric roll and surf-riding and broaching, with only minimal information about the ship design of interest for evaluation. The method uses a two-stage approach to determine the susceptibility to dynamic intact stability failure modes. This approach can be used to identify designs with increased susceptibility to dynamic stability behavior, which will then require a more detailed analysis and possibly the development of ship-specific operator guidance. Using the mature method developed specifically to assess parametric roll and surf-riding, and to demonstrate the robustness of the method, results for eight naval ship types are presented and discussed. These results were also used to establish an estimate of the criteria corresponding to the second threshold for a sample population of eight notional naval vessels.

Keywords: *Early-stage design, Dynamic Stability, Parametric Roll, Surf-riding / Broaching-to*

1. INTRODUCTION

The International Maritime Organization (IMO) is currently developing the second generation intact stability criteria - SGISC (IMO SDC 2/WP.4). The new criteria are focused on dynamic stability and have a multi-tiered structure. The first two tiers are susceptibility checks that are suitable for early stage ship design (Peters, et al. 2011). In early stage ship design many detailed parameters of a ship design are unknown. The method to evaluate these criteria relies on basic hull geometry defined by a table of offsets, design speed, and basic dimensions such as length, beam, and draft. The results of dynamic stability assessment provide additional information to the ship designer to aid in decision making for either down selection or design modification.

The criteria are being developed for ships covered by IMO instruments. The complex designs typically associated with naval ships differ from typical commercial vessels. To demonstrate the robustness of the criteria and the applicability to naval vessels, a notional naval fleet of eight ships was assessed using the susceptibility criteria from IMO SGISC. The benefits of early identification of dynamic stability failure susceptibilities in naval ship design are discussed. Further discussion of the mathematical models and criteria can be found in the references, and are discussed only briefly here.

Other IMO efforts on dynamic stability criteria include failures related to pure loss of stability, dead ship conditions and excessive accelerations. A study of methods for early-stage design evaluation of pure loss of stability of notional navy ships has been performed earlier by Belenky and Bassler (2010). This

paper can be seen as a continuation of those efforts.

2. PARAMETRIC ROLL

2.1 Physical Description

Periodic stability changes at certain frequencies resulting from the changing hull submergence while operating in waves causes the development of parametric roll. Increased stability from roll on the wave trough increases the restoring moment causing greater angles and increased roll rate. With stability decreasing as the ship is restored to upright, the ship rolls further to the opposite side due to the increased roll rate, see Figure 1 (SLF 54/3/3). The roll period during this phenomenon is generally about two times the wave period.

2.2 Sample Notional Naval Ship Calculations

The level 1 susceptibility check uses the Mathieu equation to check if both the frequency is within the necessary range and the magnitude of the stability change is above the threshold (Belenky, et al. 2011). The level 1 assessment accounts for bilge keels. The calculations were done following the requirement identified in Annex 2 of SDC 2.WP.4.

The level 2 susceptibility check increases the fidelity by accounting for certain aspects of irregular waves. The first check accounts for the possibility of encountering waves of different lengths. The second check accounts for roll damping and maximum roll angle during parametric roll. The standard for the criterion used in the level 2 calculations was 0.06 (Annex 2 of SDC 2/WP.4).

Calculations generally follow Annex 3 of SDC 1/INF.8. A wave scatter diagram from IACS Recommendation 34 was used as a data source for wave cases. Representative wave characteristics were calculated using Grimm Effective Wave as described in the document referred to above. As a result, the length of the representative wave equals to ship length. The height of the representative wave depends on spectral characteristics and roughly reflects the likelihood of encountering a wave of that length in a given sea conditions. Roll damping was calculated with a simplified Ikeda method as described in Annex 3 SDC 1/INF.8.

Three options to apply the second check of the level 2 criteria are considered in the calculations:

- Option 1. Numerical solution of a 1 degree of freedom (DOF) for the equation of roll motion, using the interpolated GZ curve defined by the user (as in Annex 22 of SDC-2/INF.10)
- Option 2. The *GZ* curve is fitted with a 5th order polynomial, then the maximum roll angle is evaluated by the averaging method as described in paragraph 2.6 of Annex 3 of SDC 1/INF.8.
- Option 3. The *GZ* curve is fitted with a 5th order polynomial, but the maximum roll angle is found by numerical solution of 1 DOF for the equation of roll motion (the result is expected to be close to the result in option 2)

Results are shown in Table 1. All calculations assume the ship is at the storm draft loading condition.

2.3 Discussion of Results

Several of the results are consistent with expected results. Where the second level shows susceptibility, the first level does as well. The level 1 criterion indicates susceptibility for more ships. This provides a conservative filtering method to identify ships with potential susceptibility to this dynamic stability failure mode. Some inconsistencies among the methods are discussed below.

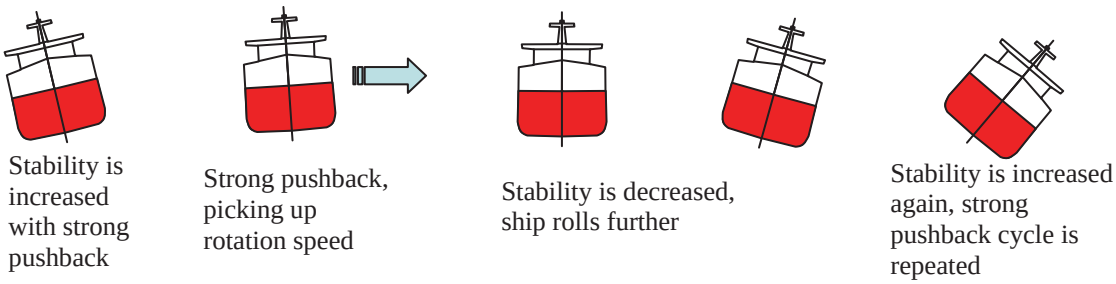

Figure 1. Development of Parametric Roll Resonance (Parametric Roll)

Table 1 Results of Susceptibility Check on Notional Navy Ships for Parametric Roll

				Level 1			Level 2				
Notional Ship	L, m	GM	Vs, kts	Criterion	Standard	Y/N	Criterion Check 1	Criterion Check 2 Option 1	Criterion Check 2 Option 2	Criterion Check 2 Option 3	Y/N
Amphib	200	4.6	20	0.390	0.297	Y	0	0	0.1385	0	N
Carrier	317	3.0	30	0.287	0.334	N	0	0.0224	0.1031	0	N
Cruiser	161	0.8	30	0.401	0.386	Y	0	0.0015	0.0008	0.0011	N
Destroyer	142	1.4	30	0.599	0.378	Y	0	0.0007	0.0003	0.0004	N
Frigate	127	1.1	30	0.459	0.378	Y	0	0.0003	0.0003	0.0003	N
Minehunter	53	4.9	20	0.125	0.474	N	0	0	0	0	N
Patrol Craft	48	1.2	20	0.312	0.578	N	0	0	0	0	N
Small Combatant	98	1.5	30	0.696	0.170	Y	0.5634	0	0	0	Y

Two of the options to check parametric roll susceptibility rely on an approximated GZ curve, so the approximation method should match well with the calculated curve. Two examples are shown below where the approximated curve closely mimics the calculated curve past the useful range to 25~30 degrees of heel before deviating substantially (see Figures 2, 3). Because the offsets of the ship must be known for the calculation the preferred method for naval ship designs is to use actual GZ curve, due to the sensitivity of the hull forms the fitted curve may not always be accurate.

Additionally for the amphibious ship and the carrier, ship specific data indicates that the two ships would not be susceptible to parametric roll. The geometry of these ships indicates that the change in stability would not be significant enough along the length of the ship to produce parametric roll. The simplified Ikeda method for predicting roll damping may be under-predicting the damping. Similarly, the small combatant indicates a very low standard on the level 1 check. Hard chines on the small combatant may provide greater damping than estimated. The under-predicted damping indicates a susceptibility that isn't supported by the specific information of the ships. Consideration to the applicability of the Ikeda method for roll damping should be made by the designer. Additional research for a more accurate prediction of damping in naval ships is still needed.

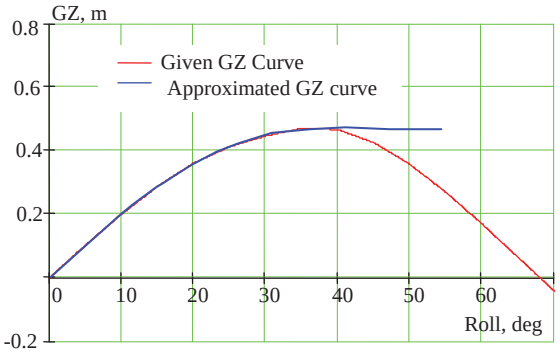

Figure 2. GZ Curve of a Notional Cruiser

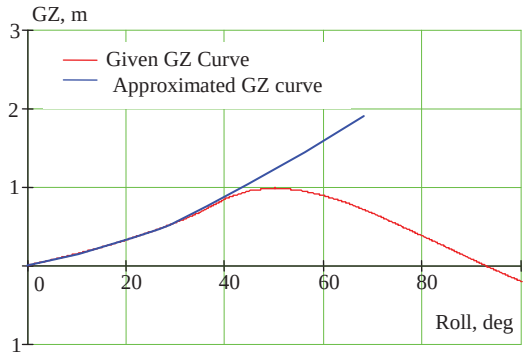

Figure 3. GZ Curve of a Notional Patrol Craft

3. SURF-RIDING AND BROACHING-TO

3.1 Physical Description of Broaching-to

Broaching-to is an operational phenomenon, which results in an uncontrolled turn, which is associated with unsuccessful efforts to reverse direction with maximum steering to the opposite direction. The result of a broaching-to event is often an excessive heel angle resulting from the sharp turn. This excessive heeling of the ship may cause a ship to sustain damage or even capsize. Surf-riding precedes the most common case of broaching-to. As the calculation of likelihood of surf-riding in early stages of design is easier than broaching-to, the susceptibility criteria use probability of surf-riding (Belenky, et al. 2011).

3.2 Sample Naval Ship Calculations

The level 1 susceptibility check assumes the possibility of surf-riding occurs when Froude number is greater than or equal to 0.3, while ship length is less than 200 m. If the length of the ship more than 200 m, then the ship is not considered susceptible even if Froude number exceeds 0.3 (Annex 3 of SDC 2/WP.4). Length is considered due to surf-riding being caused by steep waves with the length equal to about ship length. Encountering a long and steep wave is not very likely.

The level 2 criterion is based on the critical Froude number. If the critical Froude number is exceeded, surf-riding occurs from any location on the wave and with any initial speed. Melnikov's method is applied to calculate the critical Froude number as described in Annex 35 of SDC 2/INF.10; theoretical background can be found in (Spyrou, 2006). Melnikov's analysis is applied to a single wave; the probability of encounter of the wave where the critical Froude number is exceeded by the service Froude number is associated with the probability of the ship surf-riding. The standard criterion used in the level 2 calculations was 0.005 (Annex 3 of SDC 2/WP.4).

Two options for the method of calculation were used in determining the probability surf-riding. Option 1 uses a cubic polynomial fit for resistance in calm water, while option 2 uses a 5th degree polynomial fit.

Results are shown in Table 2. All calculations assume the ship is at the storm draft loading condition.

3.3 Discussion of Results

There was consistency among the criterion. Additionally, the calculations were consistent with what a designer would expect. Relatively short, fast ships are most susceptible to surf-riding and broaching-to. Short steep waves are more likely to occur naturally than long steep waves. Because surf-riding and broaching-to is most likely to occur on steep waves where the ship is similar in speed and length to the wave, shorter ships with significant speed are intuitively more susceptible to surf-riding.

Table 2 Results of Susceptibility Check on Notional Navy Ships on Surf-riding /Broaching-to

Notional Ship	L, m	Vs, kts	Fn	Criterion, option 1	Criterion, option 2	Y/N
Amphib	200	20	0.23	0	0	N
Carrier	317	30	0.28	0.0005	0	N
Cruiser	161	30	0.39	0.0186	0.0183	Y
Destroyer	142	30	0.41	0.0278	0.0276	Y
Frigate	127	30	0.44	0.0386	0.0386	Y
Minehunter	53	20	0.45	0.1094	0.1094	Y
Patrol Craft	48	20	0.47	0.1090	0.1090	Y
Small Combatant	98	30	0.50	0.0640	0.0640	Y

4. DESIGN CHANGES OR OPERATIONAL GUIDANCE

As with all early stage design calculations, the accuracy of the susceptibility assessments here are not significantly high, because of the minimal information available to make the assessment. The ship designer must take into account the limited accuracy of the calculation when making decisions to modify hull geometry or make recommendations for operational limitations guidance.

The information gained from the above calculations in early stage design can lead the ship designer to either modify the hull geometry design to reduce the susceptibility to parametric roll or broaching, or develop operational guidance to avoid parametric roll or broaching events. In some cases other ship design requirements may outweigh the risk of stability failure events and the hull geometry is not able to be changed. Other considerations for hull geometry can be signature, hydrodynamic, or weapons systems related. In the case that signature reduction or speed will be compromised to reduce the risk of dynamic stability failure, often the ship designer will assume the risk in favor of a more capable warship in the safe operating environment. If the risk of dynamic stability is identified but the hull geometry is unable to be modified the early stage design calculations still provide significant value to the ship designer.

The ship designer is able to identify early on an operational limitation of the ship in certain seaways. From a naval fleet perspective, the early identification of operational limitation offers a gap which may be filled by several other ships in the fleet already.

If greater operational area is a higher priority for a certain class of naval ship than speed or signature reduction, the susceptibility assessment allows the designer to modify geometry early in the design when modifications are most cost effective. In cases where these susceptibilities may not be identified until much later in the design process through computational fluid dynamics modelling or model testing, the design may be too mature to allow for significant modifications. Later designs changes in hull geometry can lead to changes in other aspects of the design leading to schedule delays.

5. CONCLUSIONS

Not all methods used in commercial ship designs are viable for assessing naval ship designs. Use of actual GZ curve is preferable over the fitted GZ curve, unless, there are some substantial benefits like use of closed-form solutions. The simplified Ikeda method for roll damping is also may be not applicable to all types of Naval ships.

While there are some limitations, the sample calculations shown indicate that provide a realistic susceptibility checks for naval ship designs. The accuracy of the assessment should be considered in relation to the accuracy and fidelity of the available information to be input to the models. The assessments discussed provide an advantage of additional decision making information to early stage naval ship designers.

6. ACKNOWLEDMENTS

Portions of the dynamic stability criteria research was sponsored by the Office of Naval Research under Dr. Ki-Han Kim.

The authors of this paper would like to acknowledge all those involved in the development of the criteria used in this assessment, especially Dr. Vadim Belenky (NSWCCD). The second author would like to express his gratitude to Prof. Kostas Spyrou (National Technical University of Athens, Greece) for many fruitful discussions on dynamic stability.

7. REFERENCES

Belenky, V. and Bassler, C. 2010, "Procedures for Early-Stage Naval Ship Design Evaluation of Dynamic Stability: Influence of the Wave Crest," Naval Engineers Journal, 122(2), pp.93-106

Belenky, V., Bassler, C. C. and Spyrou, K. J. (2011), "Development of Second Generation Intact Stability Criteria," Hydromechanics Dept. Report, NSWCCD-50-TR-2011/065, December

IMO SDC 2/INF.10, 2014 Second Generation Intact Stability Criteria. Information Collected by Correspondence Group on Intact Stability, Submitted by Japan, London, UK

IMO SDC 2/WP.4, 2015, Development of Second Generation Intact Stability Criteria. Report of the Working Group, London, UK.

IMO SDC 1/INF.8, 2013 Second Generation Intact Stability Criteria. Information Collected by Correspondence Group on Intact Stability, Submitted by Japan, London, UK

IMO SLF 54/3/3 2011 Summary of Research into Stability Failures Modes and associated Criteria Development, London, UK.

Peters, W., Belenky, V., Bassler C., Spyrou, K., Umeda, N., Bulian, G. and B. Altmayer, 2011 "The Second Generation of Intact Stability Criteria An Overview of Development", SNAME Trans. Vol. 119.

Spyrou, K. J., 2006 Asymmetric Surging of Ships in Following Seas and its Repercussion for Safety. Nonlinear Dynamics, Vol 43, pp. 149–172.

Session 12.2 – DECISION SUPPORT

Prediction of Survivability for Decision Support in Ship Flooding Emergency

Crew Comfort Investigation for Vertical and Lateral Responses of a Container Ship

Novel Statistical Prediction on Parametric Roll Resonance by Using Onboard Monitoring Data for Officers

Target Ship Design and Features of Navigation for Motion Stabilization and High Propulsion in Strong Storms and Icing

This page is intentionally left blank

Prediction of Survivability for Decision Support in Ship Flooding Emergency

Pekka Ruponen *NAPA Ltd* pekka.ruponen@napa.fi

Daniel Lindroth, *NAPA Ltd* daniel.lindroth@napa.fi

Petri Pennanen, *NAPA Ltd* petri.pennanen@napa.fi

ABSTRACT

Several recent flooding emergencies on passenger ships have pointed out the need to quickly get a better assessment of the survivability onboard a damaged ship. The development of time-domain flooding prediction methods has enabled advanced decision support tools. In this paper a method for assessment of the survivability of the people onboard a damaged ship is presented. The level sensor data is used to detect the breach and calculate progressive flooding in time-domain. The predictions are constantly updated to increase the reliability of the results. The method is tested with two realistic damage scenarios for a large cruise ship.

Keywords: *damage stability, flooding simulation, decision support*

1. INTRODUCTION

Several recent flooding emergencies concerning passenger ships, such as the Costa Concordia incident, have clearly pointed out the need to quickly get an accurate assessment of the survivability onboard a damaged ship. It is essential for the crew of the ship to know the extent of the damage and how the situation will develop. If the ship will survive the damage with sufficient reserve stability, the ship is likely the safest place for the passengers and the crew. On the other hand, if the ship is expected to capsize or sink, evacuation and abandonment of the ship should be started as soon as possible. Every minute counts when a large number of persons needs to be evacuated in a safe manner. In this context the term survivability is associated with the survivability of the people onboard the damaged ship, not the survivability of the ship itself, as it is in the damage stability calculations in ship design.

Several different methods have been presented for decision support for flooding emergencies onboard a damaged ship. *Ölcer and Majumder (2006)* presented a method based on pre-calculated damage cases. *Jasionowski (2011)* presented a method for assessing the safety level of an intact ship, based on increased vulnerability due to open watertight doors. A fast time-domain flooding prediction method was introduced by *Ruponen et al. (2012)*, and more recently, also *Varela et al. (2014)* have described a tool for decision support for damaged ships.

Recent developments in the time-domain prediction of progressive flooding now enable a new kind of decision support system that produces more detailed information on the damage case. The actual loading condition and flood level sensors can provide input data for predicting the progress of flooding. Yet the interpretation of the results is a challenge. One major question that remains is how to assess the survivability of the people onboard a damaged ship, even when the actual damage case is known with a fairly good accuracy.

Spanos and Papanikolaou (2014) have concluded that for actual damage incidents a reliable assessment onboard is still a technical

challenge as the identification of the damage extent and related survivability suffers from uncertainty. This paper describes a new approach, where information from systems already available is utilized for fast time-domain flooding predictions. The results are continuously updated in an attempt to improve the accuracy. As the flooding progresses, more information is collected by the level sensors that can be used to update the breach definitions for the calculations. This approach will decrease the uncertainty in the results.

The key factors that affect the survivability are reviewed. These include the extent of flooding, stability and possibility for an orderly evacuation and abandonment. Based on these, a method for assessing the survivability on the basis of a time-domain flooding prediction is presented. Finally, the developed method is tested with a large passenger ship design and two realistic damage scenarios.

2. FLOODING PREDICTION

2.1 Progressive Flooding

Over the past two decades, several time-domain flooding simulation tools have been developed and successfully validated. Most of these are based on an application of Bernoulli's equation. However, for use onboard a damaged ship, the computational performance is of utmost importance. This combined with the fact that the available input data is never fully accurate, justifies the use of a more approximate and robust method with good computational performance.

In this study a time-domain simulation method, *Ruponen (2007)*, is used with a long time step of 30 s. The implicit time integration of the pressure-correction method ensures numerical stability, even with such a long time step. However, this means that the results are not as time-accurate, as they would be with a shorter time step. Consequently, the word "prediction" is used instead of "simulation". The applied method has been validated also against full-scale measurements, *Ruponen et al. (2010)*. Updating the flooding predictions at certain intervals will provide better information of the situation at hand. The actual measured floodwater is added to the initial condition. For rooms without level sensors, the volumes obtained from the previous prediction can be used as input for the updated prediction.

2.2 Ship Motions

Ship motions are considered to be quasi-static, so that at each time step a static floating position of the ship is calculated based on the distribution of floodwater inside the ship. It is also assumed that the sea is calm. This simplification allows for purely deterministic approach, based on the real flooding scenario. On the other hand, the increased flooding due to waves is disregarded. However, the HARDER statistics indicate that over 90% of the collision damages occur in a sea state, where the significant wave height is less than 2.0 m, *Tagg and Tuzcu (2003)*. For a large passenger ship with a dense internal subdivision, the effect of waves on the flooding process can be considered as minimal.

2.3 Ship Model

The flooding prediction requires a detailed 3D model of the rooms and openings. For non-watertight doors, additional parameters are needed for modelling leakage or collapsing due to floodwater pressure. Results from the FLOODSTAND, *IMO SLF54/INF.8/Rev.1*, can here be used as the best available approximation for this data.

The status of the watertight (WT) doors (open/closed) is obtained from the automation system. For most of the non-watertight doors this information may not be available. The cold room doors can be assumed as closed, while fire doors to staircases and along the service

corridor may be open. In order to achieve some level of conservativeness, all fire doors are assumed to be open, unless the status is available from the automation system.

3. BREACH DETECTION

A breach in the hull of the ship is detected by the floodwater level sensors. Both the size and the location of the breach need to be estimated based on this sensor data. Thus every WT compartment should have sensors on all deck levels on both sides of the ship, *IMO SDC2 INF.6*. Problems related to breach detection has previously been studied by *Penttilä and Ruponen (2010)*.

The rooms, where floodwater is initially detected within the first 30…60 s, are considered to be breached. Based on the measured water level rate and the floating position of the ship, a rough approximation of the breach size is done. If the room is limited to the hull surface the breach is modelled on the side, Fig. 1. Otherwise the breach is placed on the bottom of the room.

The ship is assumed to heel towards the breached side, and the area of the breach is approximated based on Bernoulli's equation:

$$A \approx \frac{\mu S \dfrac{dH}{dt}}{C_d \sqrt{2g(T-H)}} \qquad (1)$$

where H is floodwater level, S is the surface area of the room corresponding the level, μ is the permeability, g is gravitational acceleration, T is the draft of the ship and t is time. A constant discharge coefficient C_d = 0.6 can be used.

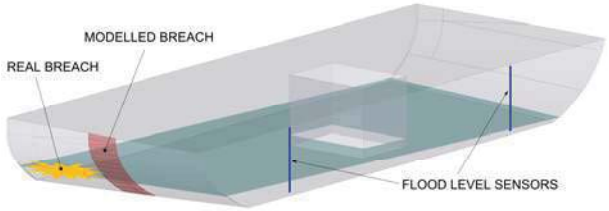

Figure 1: Approximated breach based on level sensor data

For an updated flooding prediction, the original breach is by default unchanged. Other flooded rooms are checked against the result of the previous prediction. If the room is not predicted to be flooded, the water may come from a previously undetected breach or through unknown progressive flooding (e.g. broken pipelines). For the updated prediction, these rooms are also modelled as breached in addition to the original breaches, Fig. 2.

The detected breaches and the door statuses from the automation system form the basis for the time-domain flooding prediction. The main challenge is to separate progressive flooding through the modelled openings from the flooding through breaches in the hull. This is essential since too many breaches will result in too fast flooding.

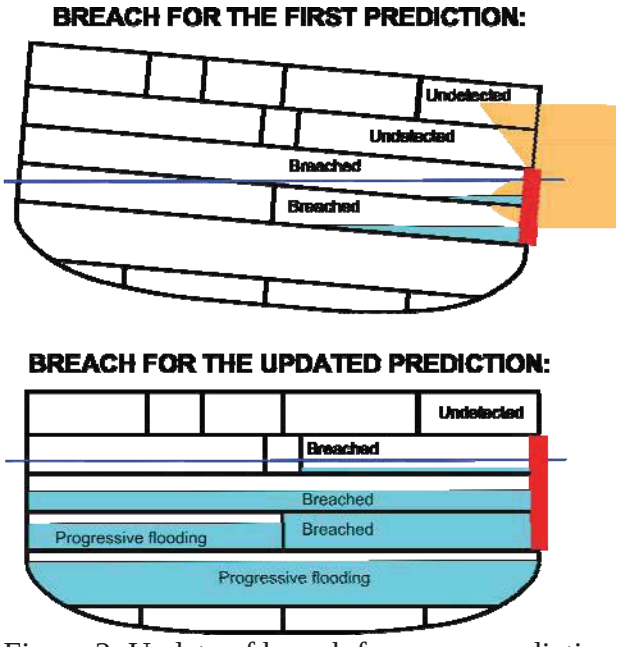

Figure 2: Update of breach for a new prediction

4. ASSESSMENT OF SURVIVABILITY

4.1 Methodology

In this study the survivability level is evaluated with the following equation:

$$F_{tot} = \min\left(F_{ext}, F_{stab}, F_{evac}\right) \quad (2)$$

The sub factors for flooding extent, stability and evacuation (F_{ext}, F_{stab} and F_{evac}) are presented in detail in the following sections. Each of them is a function of time, and the applied value is the minimum during a time window extending from the current time to the approximate maximum required evacuation time, see Fig. 3.

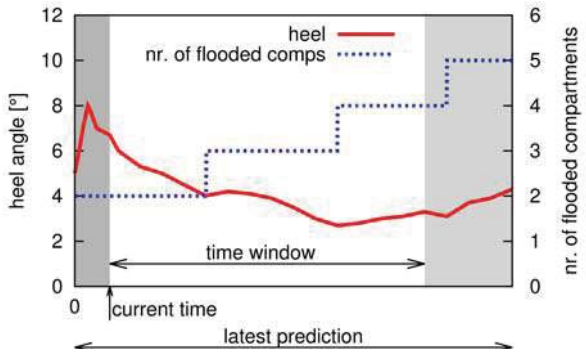

Figure 3: Time window for evaluation of the survivability level from the prediction results

4.2 Floating Position

Heel angle is considered to be the most important factor that affects the survivability level. At large heel angles launching of the lifeboats becomes impossible. Moreover, large heeling also increases the required evacuation time. Consequently, the predicted development of the heel is a primary information to the master for decision making. However, in the presented approach heel angle is only considered indirectly through its effects on stability and evacuation.

4.3 Damage Extent

The new probabilistic damage stability regulations do not set any specific requirements on how many watertight compartments can be flooded without a risk of sinking or capsizing. Despite of this, it is considered to be of the utmost importance to clearly identify how many WT compartments are flooded, since this is vital information for the decision making. If water is detected on the bulkhead deck, or at the time when floodwater is predicted to reach the bulkhead deck, the survivability level is significantly decreased. The reason for this is the increased risk of progressive flooding to undamaged WT compartments. In this study, the following approach is used:

$$\begin{aligned} F_{ext} &= 1.0 && \text{when } N_f \le N_1 \\ F_{ext} &= C \cdot \frac{N_0 - N_f}{N_0 - N_1} && \text{when } N_1 < N_f < N_0 \\ F_{ext} &= 0.0 && \text{when } N_f \ge N_0 \end{aligned} \quad (3)$$

where N_f is the number of flooded WT compartments during the time window (see Fig. 3), i.e. the flooding extent at the end of prediction. N_1 is the number of compartments that can be flooded without significant risk and N_0 is the number of flooded compartments when the survivability level is set to zero. The additional coefficient C is 0.5 if the bulkhead deck is flooded, otherwise 1.0. The function is illustrated in Fig. 4.

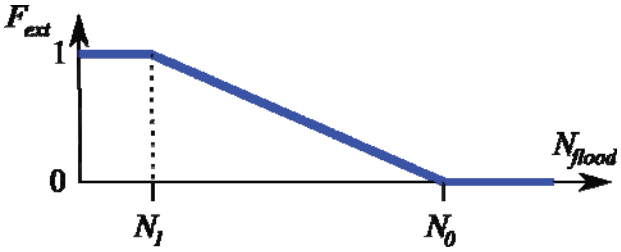

Figure 4: Flooding extent factor

In the present study N_1 = 1 and N_0 = 6 are used. However, N_0 should also be considered to depend on the size of the ship, i.e. the total number of WT compartments or the length of the ship. With N_1 = 1 it is ensured that F_{tot} = 1.0 only for one compartment flooding cases.

4.4 Stability

Even with a small heel angle the risk of capsizing can be significant if the stability of the ship is not good enough. The s-factor in SOLAS II-1 Part II-1 Regulation 7 is applied:

$$s_{final} = K \cdot \left(\frac{GZ_{\max}}{0.12} \cdot \frac{range}{16} \right)^{\frac{1}{4}} \quad (4)$$

where GZ_{max} is limited to 0.12 m and *range* to 16°. The effect of the heel angle ϕ is accounted with the coefficient:

$$K = \sqrt{\frac{15° - \phi}{15° - 7°}} \quad (5)$$

when the heeling angle is between 7° and 15°. If the heeling exceeds 15° the effective s-factor is taken as zero.

The *range* is limited to the angle where the first unprotected opening is immersed, Fig. 5. Only real unprotected openings above the bulkhead deck should be considered in order to avoid too conservative approach that limits the reserve buoyancy of the hull. On the other hand, if no limitation of the range is used, the results could be too optimistic. This approach also allows for a simple inclusion of the external heeling moments through the factor:

$$s_{mom} = \min\left(\frac{(GZ_{\max} - 0.04) \cdot \Delta}{M_{heel}}, 1.0 \right) \quad (6)$$

where Δ is the intact displacement of the loading condition and M_{heel} is the maximum external heeling moment caused either by crowding of passengers, launching of survival craft or wind. In the present study the SOLAS wind pressure is applied.

The stability factor in the survivability assessment is taken as the smallest value during the time window t_{window} (see Fig. 3):

$$F_{stab} = \min\left(s_{final}(t_i) \cdot s_{mom}(t_i) \right), \; t_i \in t_{window} \quad (7)$$

Although in SOLAS there is a separate, less stringent, s-factor formula for intermediate flooding stages, it is believed that the application of the s-final formula is more suitable for the assessment of damage stability onboard a damaged ship, since the flooding process can be slow.

For better computational performance, the s-factor does not need to be evaluated at every time step, but frequently enough, e.g. every 5 min. Still, for each intermediate time step without the stability curve calculated, the effect of the heeling angle can still be taken into account through the *K*-factor, eq. (5).

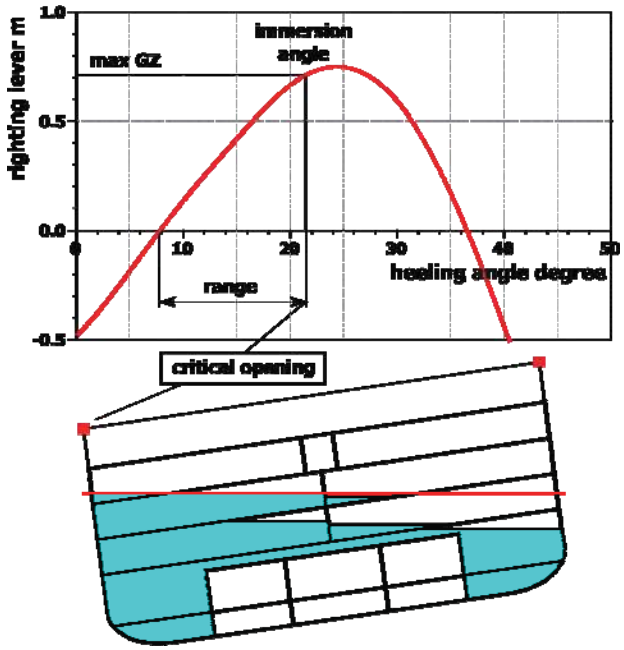

Figure 5: Effect of unprotected openings above the bulkhead deck on the GZ curve

For the survivability assessment onboard a damaged ship, the calculation of stability is somewhat different since the flooding process still continues. The traditional approach with the lost buoyancy method cannot be applied. Instead, the volumes of floodwater in the flooded rooms are kept constant for the calculation of the GZ curve. However, contrary to the added weight method, a constant displacement is used. With this approach also the so-called multiple free surface effect, see Fig. 5, is properly taken into account in the intermediate phases of flooding.

4.5 Evacuation Time

A key factor for evaluation of the survivability is the relation between the required evacuation time T_R and available evacuation time T_A. The following simple formula, providing some safety margin, is applied:

$$F_{evac} = 1.0 \quad \text{when } T_R/T_A \le R_{evac}$$
$$F_{evac} = \frac{\left(1 - \frac{T_R}{T_A}\right)}{1 - R_{evac}} \quad \text{when } R_{evac} < T_R/T_A < 1.0 \quad (8)$$
$$F_{evac} = 0.0 \quad \text{when } T_R/T_A \ge 1.0$$

This function is illustrated in Fig 6. The applied critical ratio of evacuation times was R_{evac} = 0.75. The available time is limited by maximum allowed heel of 15°.

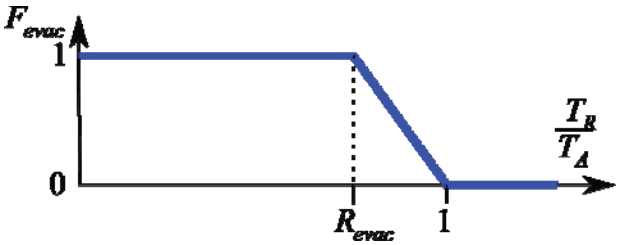

Figure 6: Evacuation time factor

The *IMO MSC.1/Circ.1238* gives the required evacuation time as 80 min for a passenger ship with more than three vertical fire zones. In the absence of more accurate data this value can be used as the best approximation.

Adverse conditions, such as extensive heel, will increase the required evacuation time. The simplest approach is to integrate over the predicted development of heel angle:

$$\int_0^{T_R} r\left(\left|\phi(\tau)\right|\right) d\tau = T_0 \quad (9)$$

where $r(\phi)$ is the reduction factor due to the heel/trim angle and T_0 is the required evacuation time at zero heel and trim. The latter can also include the time of the day and other factors such as the number of passengers onboard. *Bles at al. (2002)* have concluded that the walking speed is linearly decreased with an increasing heel angle. In the presented calculations, it is assumed that the reduction factor is 0.5 at a heel angle of 20°. This is somewhat more conservative than in previous studies, *Meyer-König et al. (2005)*, but even more radical decrease was initially presented by *Vassalos et al. (2002)*, Fig. 7.

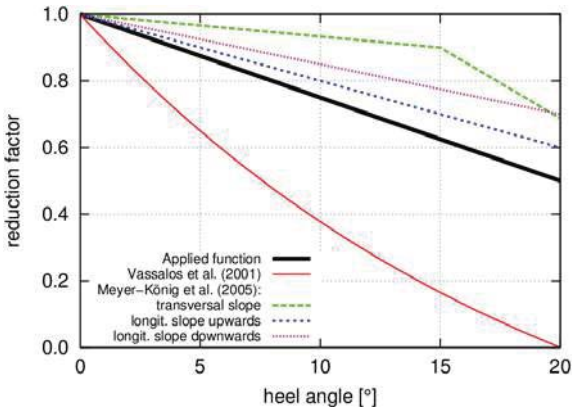

Figure 7: Reduction factor due to heel angle

4.6 Survivability Level

The vessel TRIAGE categorization[1] can be used to present the survivability level with color codes. This is very important in communication with the MRCC (Maritime Rescue Coordination Centre). A similar three-level categorization for stability of a damaged ship was presented by *Lee et al. (2005)*. The present approach is shown in Table 1. The limit between yellow and red was set on the basis of equation (5), corresponding to a heel angle of 10°. Also eq. (3) results in F_{ext} = 0.8 when flooding is limited to two compartments.

[1] http://www.raja.fi/vesseltriage

Table 1: Color coding for survivability level

Color	Description	*F*
green	• flooding is limited • ship is stable enough • orderly evacuation can be done	1.0
yellow	• ship is still safe but flooding is extensive • notable heeling can occur • orderly evacuation can be done	≥ 0.8 & < 1.0
red	• very extensive flooding • progressive flooding to undamaged WT compartments • very large heel angles • orderly evacuation may not be possible	< 0.8
black	• ship has capsized or sunk	-

5. TEST CASES

5.1 Testing Methodology

The 125 000 GT large cruise ship design, *Kujanpää and Routi (2009)*, developed in the FLOODSTAND project, is used. The actual breach geometry was first modelled, and the damage scenarios were calculated using an accurate time-domain flooding simulation, *Ruponen (2007)*, with a short time step of 2.0 s. The simulation results were then used to generate the level sensor data in the flooded rooms.

Total of 292 rooms, including the tanks, were modelled, as well as 313 internal openings, Fig. 8. A typical loading condition with GM_0 of 2.72 m, draft of 8.45 m and small bow trim of 0.05 m was used as an initial intact condition.

All cold room doors and WT doors were closed. 169 of the 227 fire doors were open. These open doors were located either in the passenger areas on Deck 5 or in locations where the crew frequently passes the door. Random variation, based on the Raleigh distribution, was applied to the leaking and collapsing parameters of the non-watertight doors in the accurate simulations of the reference data. In the flooding predictions the standard values were used.

The ship was considered to be equipped with 123 level sensors in the dry spaces, following the guidelines provided in *IMO SDC2/INF.6*. This represents 66 % of the rooms below the bulkhead deck and 50 % of the rooms on the bulkhead deck.

The first flooding prediction and analysis of the survivability level is done by using the sensor data from the first 60 s after the damage. The results are then updated by performing new predictions with a measured floodwater volumes as input for rooms with a level sensor. For the rooms without a sensor, the volumes of floodwater from the previous prediction were used as an initial condition. The predictions were repeated at the interval of 5…10 min. Calculation time for each prediction was about 2 min.

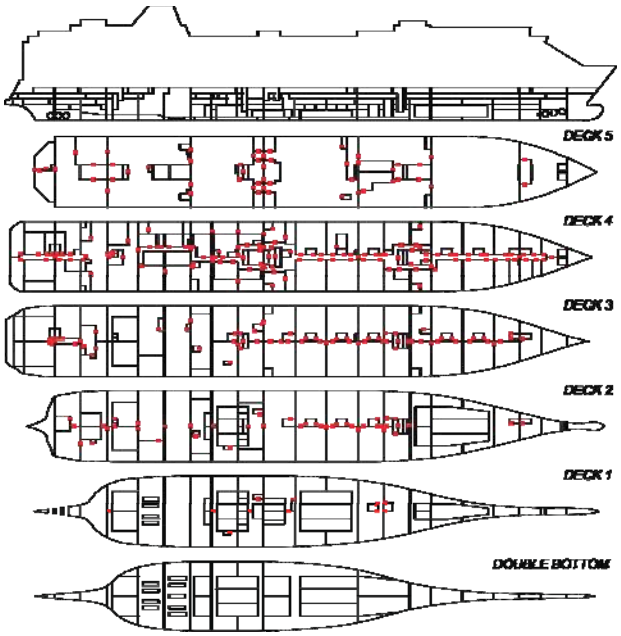

Figure 8: Modelled room arrangement and openings for the studied large passenger ship

5.2 Extensive Side Grounding Damage

This damage scenario is similar to the Costa Concordia accident. The grounding causes a 61

m long very narrow breach on the starboard side of the ship about 6 m below the sea level, Fig. 9. The damage extends over six WT compartments, including both engine rooms. Also part of the double bottom is breached.

Figure 9: Damage case for extensive side grounding

The damage is so extensive that the bulkhead deck is flooded within 32 min, and water progresses also to undamaged WT compartments. In the reference simulation the ship capsizes after 3 h. The predictions indicate somewhat faster flooding, where the critical heel angle of 15° is achieved in about 2 h after the damage, Fig. 10. By this time there is already floodwater in nine WT compartments. The predictions assume that all A-class fire doors are open, whereas in reality the closed doors slow down the progress of floodwater, especially on the bulkhead deck. Thus also in the updated predictions the flooding rates are immediately somewhat faster than measured, Fig. 11. Consequently, the updated predictions indicate slightly faster time-to-capsize.

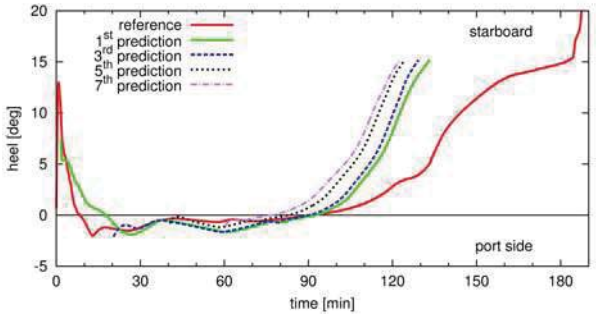

Figure 10: Comparison of heel angle for the initial and updated predictions against the simulated reference result

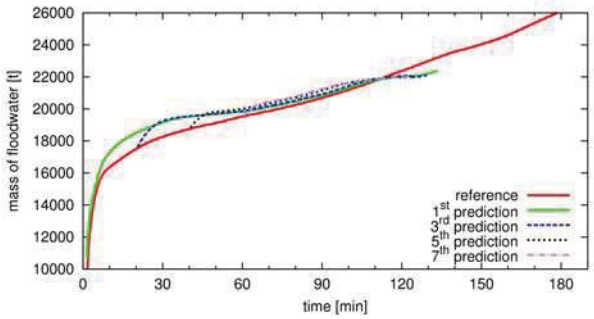

Figure 11: Comparison of the total mass of floodwater

Due to the very extensive damage, the survivability level is very poor. The color code is red (see Table 1) instantly since F_{ext} = 0. From the start, the prediction results provide important information to the crew that evacuation needs to be started immediately after the initial transient heeling has equalized. For a time frame of about 90 min the heeling is predicted to be less than 5°. And since the required evacuation time is about 85 min, there should be just enough time for orderly evacuation and abandonment before the ship is predicted to capsize.

5.3 Collision Damage

The second scenario is a typical collision damage, breaking two WT compartments. The breach extents above the waterline, but it is vertically limited so that the double bottom remains intact. Here however, one transverse bulkhead is not fully watertight, and also a third compartment is eventually flooded. This is accounted for in the reference simulation results by modelling a small additional internal opening in the bulkhead, Fig. 12.

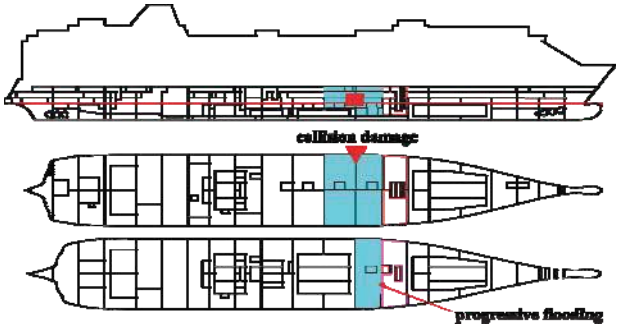

Figure 12: Collision damage case with progressive flooding

The first prediction that is started 60 s after the damage properly estimates the equalization of the initial heel towards the damaged side, Fig. 13. The predicted survivability level is fairly good with only the two damaged compartments rapidly filled up with water. The flooding extent factor is F_{ext} = 0.8, corresponding to a yellow color code, Table 1. Thus the initial result is too optimistic when compared to the reference simulation results for total amount of floodwater, Fig. 14.

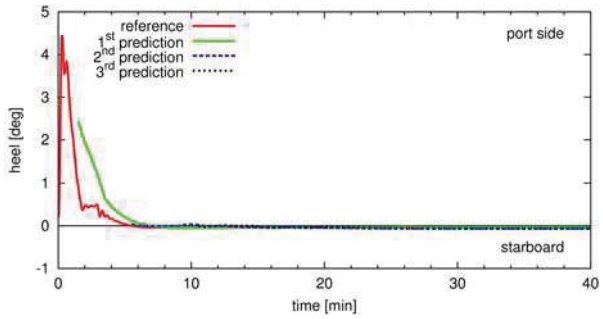

Figure 13: Comparison of initial and updated prediction against the simulated reference result

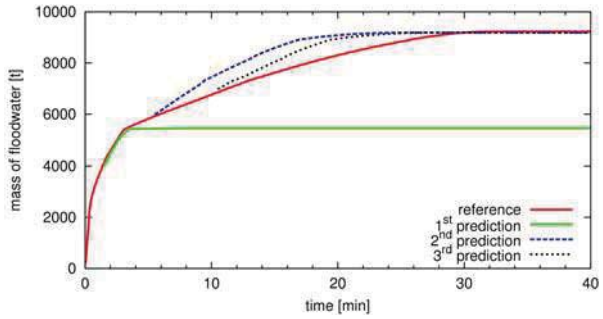

Figure 14: Comparison of the total mass of floodwater for collision damage

The updated prediction, starting 5 min later, accounts for the progressive flooding through the WT bulkhead and results in the same equilibrium as the reference result, Figs. 13 and 14. Now only the time-to-flood is somewhat shorter. The origin of the floodwater in the third compartment remains unknown, but an additional breach to one room is modelled, see Fig. 15.

The increased flooding extent results in F_{ext} = 0.6, and the color code changes to red. The ship is still very stable (F_{stab} = 1.0) and there is plenty of time for an orderly evacuation. Still, the fact that there is progressive flooding to a new undamaged WT compartment means that the situation could become more severe.

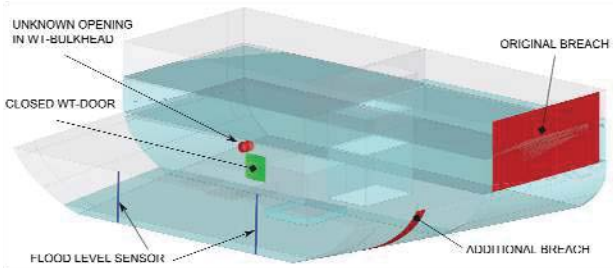

Figure 15: Additional breach in the hull to model detected flooding from an unknown source

6. CONCLUSIONS

A new approach has been developed for assessing the survivability of people onboard a damaged ship. Critical factors, such as stability of the ship and the evacuation time are accounted for. Data from level sensors is utilized and a fast time-domain flooding prediction method is used to assess the progressive flooding and the development of heel. Following the suggested principles for vessel TRIAGE, a color code representation for the severity of the situation can be determined based on the calculated factors for flooding extent, stability and available evacuation time.

The developed method has been tested with two realistic damage cases. The predicted time-to-capsize or time-to-flood is in general shorter than in the reference simulation due to the assumption that all A-class fire doors are open.

Thus the prediction results are normally somewhat more conservative. Fine-tuning of the presented criteria for the survivability level may still be needed, but the present approach forms a solid basis for further work.

It must be noted that a sufficient number of properly located flood level sensors is a prerequisite for a reliable assessment of the survivability. The combination of available measurement data from the sensors and the results from the previous prediction is a challenge. Based on the presented case studies the applied method seems to work well, but some improvements may still be needed.

Further studies are needed to ensure that the developed method works also in other damage scenarios. These cases could include also real accidents. In addition, the impact of inaccuracies in flood level sensor data needs to be further investigated.

The developed method for a fast analysis of the survivability onboard a damaged ship seems to work well in both tested scenarios. The results provide essential information on how the flooding will progress and how serious the situation is. The updated predictions can also account for additional breaches or unknown sources of flooding. This information is very useful and support the master in the decision making.

7. REFERENCES

Bles, W., Nooy, S., Boer, L.C. 2002 Influence of Ship Listing and Ship Motions on Walking Speed, Pedestrian and Evacuation Dynamics, Springer Verlag, pp. 437-452.

IMO MSC.1/Circ.1238 Guidelines for Evacuation Analysis for New and Existing Passenger Ships, 30 October 2007.

IMO SDC2/INF.6 Guidelines for Flood Sensor Placement and Technical Requirements, submitted by Finland, 2014.

IMO SLF/54/INF.8/Rev.1 Modelling of leaking and collapsing of closed non-watertight doors, submitted by Finland, 28 Oct. 2011.

Jasionowski, A. 2011. Decision Support for Ship Flooding Crisis Management, Ocean Engineering, Vol. 38, pp. 1568-1581.

Kujanpää, J. Routi, A-L. 2009. Concept Ship Design A, FLOODSTAND Deliverable D1.1a.

Lee, D., Lee, S-S., Park, B-J., Kim, S-Y. 2005. A Study on the Framework for Survivability Assessment System of Damaged Ships, Ocean Engineering, Vol. 32, pp. 1122-1132.

Meyer-König, T., Valanto, P., Povel, D. 2005. Implementing Ship Motion in AENEAS – Model Development and First Results, Pedestrian and Evacuation Dynamics 2005, pp. 429-441.

Ölcer, A. I., Majumder, J. 2006. A Case-Based Decision Support System for Flooding Crises Onboard Ships, Quality and Reliability Engineering International, Vol. 22, pp. 59-78.

Penttilä, P., Ruponen, P. 2010. Use of Level Sensors in Breach Estimation for Damaged Ship, Proceedings of the 5th International Conference on Collision and Grounding of Ships *ICCGS 2010*, Finland, pp. 80-87.

Ruponen, P. 2007. Progressive Flooding of a Damaged Passenger Ship, TKK Dissertations 94.

Ruponen, P., Kurvinen, P., Saisto, I., Harras, J. 2010. Experimental and numerical study on progressive flooding in full-scale, Transactions of the Royal Institute of Naval Architects, Vol. 152. pp., A197–A207.

Ruponen, P., Larmela, M., Pennanen, P. 2012. Flooding Prediction Onboard a Damaged Ship, *Proceedings of the 11h International* Conference on Stability of Ships and Ocean Vehicles STAB2012, Athens, Greece, pp. 391-400.

Spanos, D., Papanikolaou, A. 2014. On the time for the abandonment of flooded passenger ships due to collision damages, Journal of Marine Science and Technology, Vol. 19, pp. 327-337.

Tagg, R., Tuzcu, C. 2003. A Performance-Based Assessment of the Survival of Damaged Ships: Final Outcome of the EU Research Project HARDER, Marine Technology, Vol. 40, No. 4, pp.288-295.

Varela, J.M., Rodrigues, J.M., Guedes Soares, C. 2014. On-board Decision Support System for Ship Flooding Emergency Response, Procedia Computer Science, Vol. 29, pp. 1688-1700.

Vassalos, D., Kim, H., Christiansen, G., Majumder, J. 2002. A Mesoscopic Model for Passenger Evacuation in a Virtual Ship-Sea Environment and Performance-Based Evaluation, Pedestrian and Evacuation Dynamics, Springer Verlag, pp. 437-452.

Vessel TRIAGE project: http://www.raja.fi/vesseltriage

This page is intentionally left blank

Crew Comfort Investigation for Vertical and Lateral Responses of a Container Ship

Ferdi Çakıcı, *Yildiz Technical University, fcakici@yildiz.edu.tr*

Burak Yıldız, *Yildiz Technical University, buraky@yildiz.edu.tr*

Ahmet Dursun Alkan, *Yildiz Technical University, alkanad@yildiz.edu.tr*

ABSTRACT

This study deals with the crew comfort on board analyses based on vertical and lateral responses of a container ship in sea states 4, 5 and 6. Crew on board might be affected by excessive motions of the ship where fatigue and lack of morale might began gradually and it leads to low concentration for deck operations. This is all called as seasickness phenomena and it should be investigated/evaluated influence on conceptual design decisions. Vertical and lateral responses calculations of the ship are carried out by using strip theory and short statistical method. The total roll damping coefficient is defined using Ikeda's estimation method. The obtained results are combined with the published seakeeping criteria in terms of human factor. In the end of study, operability indices of the container ship are shown with respect to sea states and selected criteria in polar diagrams and tables.

Key Words: *Operability, Ikeda's Method, Potential Theory, Human Factor*

1. INTRODUCTION

It always has been a significant issue to have seakeeping characteristics of ships in waves during design stage. It is very important to obtain the responses in waves due to the effects of the ship motions on human. Minimization for responses can definitely advance the operability and safety of the crew on deck. Reducing motions and accelerations in several sea states is necessary for the sake of crew on ship. Operability index (OI) for the bridge and bow operations should be increased. Intensive operability calculations on board for the commercial ships have to be evaluated during design stage.

It is very common to evaluate container ships as regard to their mobility in terms of seakeeping. However seakeeping performance of commercial ship in terms of crew morale has an important impact on overall performance and it is a measure of being under the specified seakeeping criterion. Absolute vertical and lateral accelerations are significant responses for the safety of crew. People who are not familiar with the excessive responses easily may get seasick.

Seakeeping analysis has been widely used after the development of the first practical strip theory. It is mainly based on the evaluation of the hydrodynamic characteristics of hull sections by using Lewis conformal mapping technique or Frank Close-

Fit approach (Frank, 1967). Although the strip theory is the quickest and relatively most accurate one it has main restrictions due to its theoretical assumptions. It has been most preferred tool during conceptual design stage for calculation of motions. Due to its theory is linear; solutions are more realistic for slender hulls and low Froude numbers. However, strip theory has been widely accepted and a large number of computer codes are developed.

A large number of researches could be found in the seakeeping literature. In the study of Sarıöz and Narlı (2005), they showed that the chosen criterion directly affects seakeeping performance of a ship and they calculated operability index values for selected criteria for sea state 5 and 6. In another study, they tabulated the operability performance indices for a passenger ship by using wave distribution scatter (Sarıöz and Sarıöz, 2005). In both studies, they deal with the vertical accelerations and obtain the limiting values by the help of ISO 2631 standards. In addition to what is mentioned above, seakeeping computations and comfort analyses for three different mono hull yachts are investigated by Nabergoj (2006). On the other hand, Scamardella and Piscopo obtained the overall motion sickness incidence for passenger ships (Scamardella and Piscopo, 2014). Cakici and Aydin discovered the overall seakeeping properties up to several sea states for the gulet type pleasure boats (2014). In another study, Cakici et al. presented the MSI and HI percentages of mega yacht and catamaran hulls for their general arrangements (2014).

In this study, a container ship model is taken as a sample for seakeeping calculations with 2-D strip method. It is shown the OI values of the ship model via polar diagrams according to specified sea conditions and suggested criteria. Selected responses are vertical-lateral accelerations and roll motion. For this responses, criteria are selected as regards to NORDFORSK project (1987) and Ferdinande V. (1969).

2. SEAKEEPING PERFORMANCE PREDICTION

The seakeeping performance of a ship in a particular sea environment depends on 4 main factors. These are:

- Response in regular waves (RAO)
- Sea state (SS)
- Vessel's speed and heading
- Standardized seakeeping criteria.

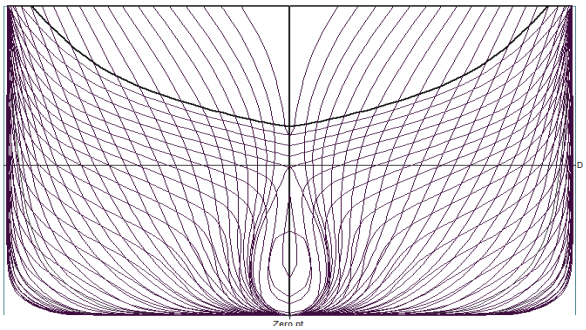

Figure 1 Body plan of the vessel

Body plan and geometric features of the chosen container ship is shown in Fig.1 and Table 1 respectively.

Table 1 Geometric properties of the vessel

Ship	**Figures**
Displacement, Δ (kN)	48562.16
Draft, T (m)	5.250
Waterline length, L_{OA} (m)	104.321
Waterline length, L_{WL} (m)	100.453
Waterline beam, B_{WL} (m)	16.495
Prismatic coefficient, C_P	0.582
Block coefficient, C_B	0.570
Waterplane area coefficient, C_{WP}	0.698
LCB from FP, LCB, %LWL	-53.871 (+fwd)
Vertical center of buoyancy, KB (m)	2.852
Vertical center of gravity, KG (m)	6.562
Cruise Speed (kts)	18.26
GM_T (m)	0 824

While the behaviour of a ship in regular waves depends on its weight, main dimensions, hull form parameters and weight distribution, the sea state information is based on annual measurements and it may differ for each sea states. Vertical and lateral plane accelerations in regular waves can be

calculated by using 2D strip methods in conceptual design phase. Typical RAO, wave spectrum and response spectrum curve is shown in Fig.2, 3 and 4, respectively, for seakeeping calculations.

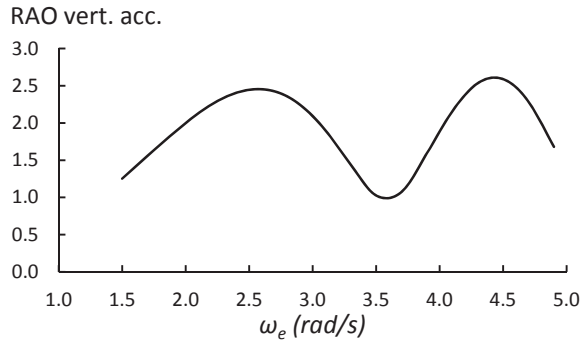

Figure 2 Typical RAO curve

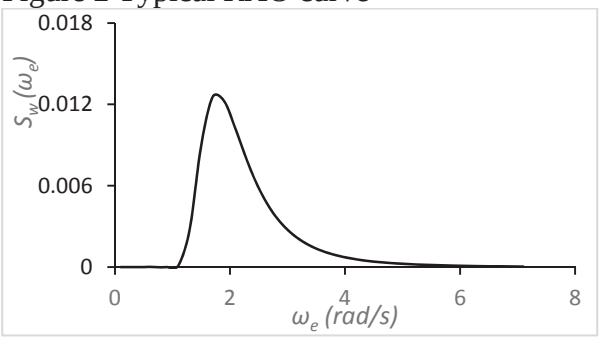

Figure 3 Typical wave spectrum curve

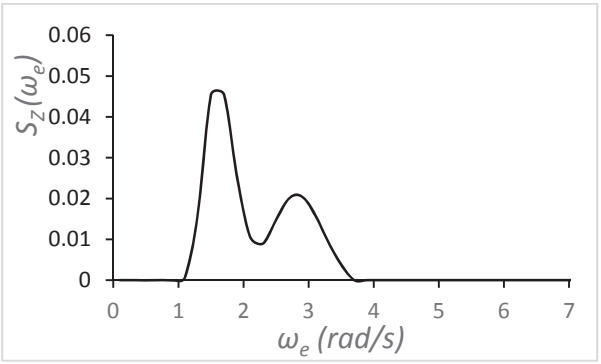

Figure 4 Response spectrum curve

Roll motion is the most critical response of a ship in waves among ship motions and it is important to calculate the roll motion during design stage. Roll motion affects the crew performance, ship habitability, limits the operability, causes the cargo shift, loss of deck cargo and even leads to ship capsize. Accurate prediction of roll motion is necessary for operational and safety considerations, especially for container ships. Roll damping coefficient has to be determined correctly for an exact prediction of the roll motion. One of the most used methods to determine roll damping is Ikeda's estimation method. According to Ikeda (1978), see also Himeno (1981), the total equivalent linear roll damping coefficient can be divided into five components. These components are composed of skin friction damping, eddy damping, wave damping, lift damping and bilge keel damping. These are indicated in equation 1.

$$B_e = B_F + B_E + B_W + B_L + B_{BK} \quad (1)$$

In this study, Ikeda's method is used for the prediction of roll damping coefficient.

2.1 Definition of environmental conditions

Motion responses in irregular waves are significant since there are almost no regular waves in nature. Irregular sea surfaces can be defined by the help of wave spectra that is composed through a probabilistic distribution model. This function must be adoptable with the characteristics of the seaway. In this study, the seaway is taken on one parameter Pierson –Moskowitz formulation. The analyses are performed at sea states 4, 5 and 6 and the corresponding characteristic wave heights and modal periods of North Atlantic are shown in Table 2.

Table 2 Wave heights of North Atlantic

Sea State	Significant wave height (m)
4	1.88
5	3.25
6	5.00

2.2 Operability Index Based on Ship Motions

A typical seakeeping polar diagram involves wave heading and sea state for a

given seakeeping limit by using the results of ship motion analyses in irregular seas. Thus polar diagram shows an area where human tolerance is valid and the rest of area refers at least one seakeeping limit criterion is violated. The percentage rate between human tolerant or safer area to violating area of any seakeeping limiting criterion of a seakeeping polar diagram is so-called as Operability Index (OI). This one is defined by both mechanical vibrations from various sources and vibrations resulting from ship motions in waves. In this study OI values are computed by integrating the limiting speeds from stationary speed to cruise speed for all headings, specified sea conditions and seakeeping criterion by employing

$$OI = \frac{1}{2\pi V_0}\int_0^{2\pi} V_{lim}(H_{\frac{1}{3}}, \mu)d\mu \quad (2)$$

Where:
OI: Operability Index based on ship motions (-)
V_o: Ship Speed (m/s)
V_{lim}: Limiting Criterion Speed (m/s)
μ: Heading (rad)
$H_{1/3}$: Characteristic Wave Height (m)

Operability indices of the container ship are computed for sea state four to six at speeds from zero to cruise speed. OI gives a robust idea according to limit vertical and lateral accelerations defined by existing studies. Safety of crew is closely related to vertical and lateral accelerations. In Figure 5-8, one can easily have an idea for safer places at bridge and bow of the container ship and as well as roll motion in terms of speed and route. The coloured zones show safer regions. Selected criteria are shown with Table 3.

Table 3 Selected Criteria

RMS Lat. Acc. (m/s^2)	RMS Vert. Acc. (m/s^2)	RMS roll motion (deg)
0.12g (bridge)	0.15g (bridge)	6°
	0.20g (bow)	

2.3 Limiting Wave Height for all heading and speed range

The limiting significant wave heights are computed based on each criterion. The results are displayed in Fig. 10. This figure clearly illustrates the influence of the selected response on the maximum allowed significant wave heights.
Necessary computation method is presented in Eq.3.

$$LSWH = Max\ H_{1/3}\{R_i(V_j\mu_k) \leq R_i^{cr}\} \quad (3)$$

Where:
LSWH: Limiting Significant Wave Heights (m)
μ_k: Heading 0:π° (rad)
$H_{1/3}$: Characteristic Wave Height (m)
$R_{i:}$ Computed Response
R_i^{cr}: Criterion Defined Response
V_j: Ship speed 0: V_{cruise} (m/s)

3. SEAKEEPING CALCULATIONS AND RESULTS

In this part of the study calculated polar diagrams for lateral and vertical responses are presented with figures.

For sea state four and five, polar diagrams are all safe due to there is no exceed values of specified responses in accordance with selected criteria. Therefore, this sea conditions are not dangerous for crew on deck. However, in sea state six, polar diagrams give two different regions. While coloured zone is safe for the operetion; the non-coloured zone is critical. Figure 5-8 show the polar diagrams for selected responses.

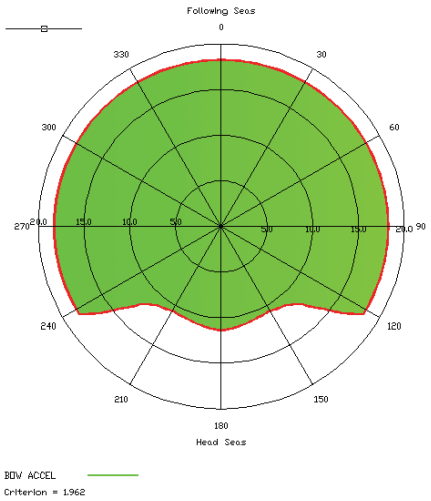

Fig.5 Bow Vert. Acc. Operability Diagram for SS6

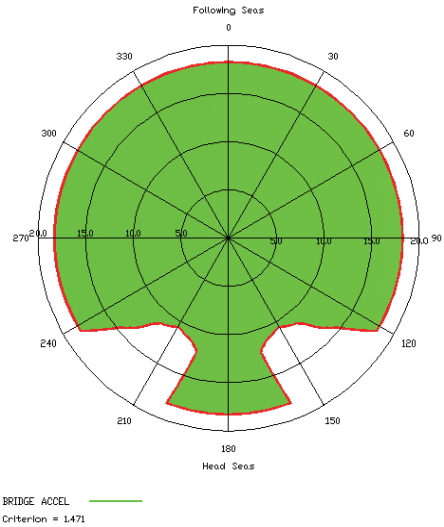

Fig.6 Bridge Vert. Acc. Operability Diagram for SS6

Table 4 Exceeding routes and limiting speeds (knots) for Bow Vert. Acc.

μ	**V_{lim} @150°**	**V_{lim} @180°**
122°-180°	**11.1 knot**	**11.3 knot**

Table 5 Exceeding routes and limiting cruise speed for Bridge Vert. Acc.

μ	**V_{lim}@150°**	**V_{lim} @160°**
123°-160°	**11.2 knot**	**11.9 knot**

While figure 5 shows the bow vertical acceleration polar diagram, figure 6 shows the bridge vertical acceleration polar diagram for SS6. Exceeding routes and limiting cruise speed for specified responses are shown in Table 4-6.

Table 6 Exceeding routes and limiting cruise speed for Roll Motion

μ	**V_{lim} @60°**	**V_{lim} @70°**
55°-70°	**6.9 knot**	**6.9 knot**

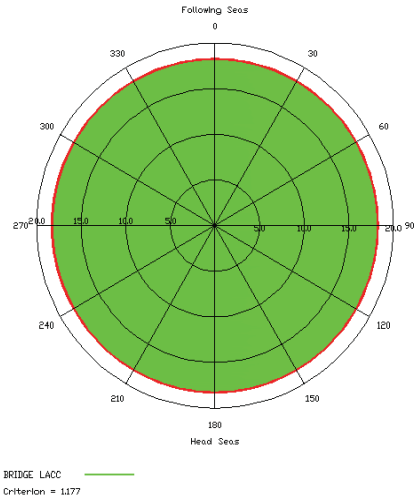

Fig.7 Bridge Lat. Acc. Operability Diagram for SS6

Bridge lateral acceleration polar diagram in Fig. 7 gives an idea that calculated lateral acceleration values are under the selected criterion. There is no exceeding route and limiting cruise speed value for this response.

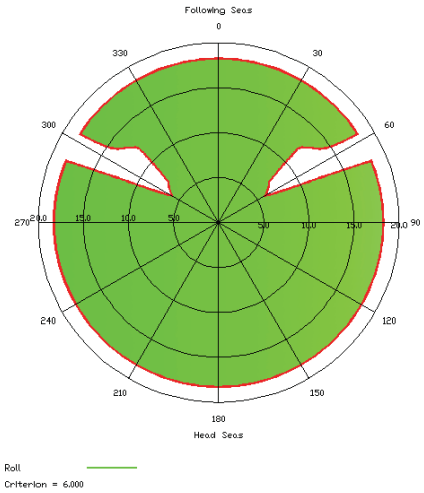

Fig.8 Roll Motion Operability Diagram for SS6

Roll motions of chosen container ship are calculated in irregular waves for sea states 4, 5 and 6. Safe regions are shown in polar diagram as seen in Fig. 8.

Fig. 9 can be obtained by the help of figures 5 -8. OI values are shown between 0-1 for the three sea states.

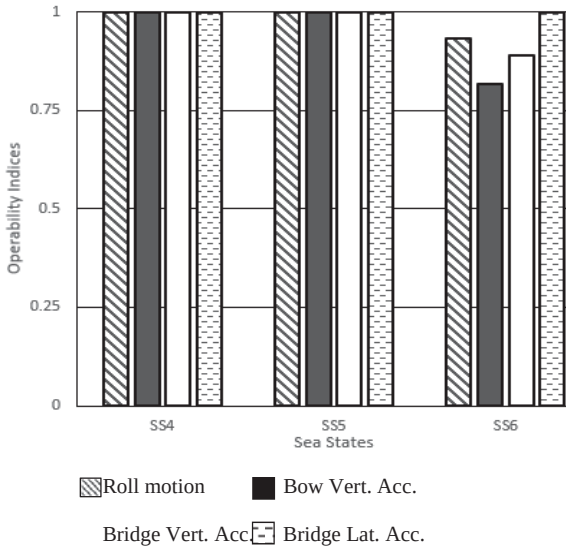

Fig.9 Comparison of Operability Indices

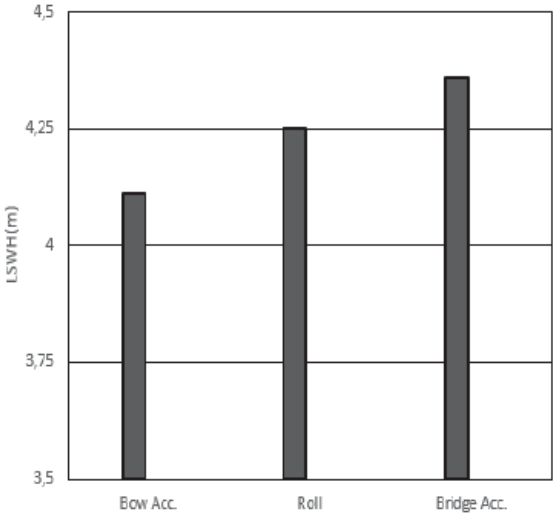

Fig.10 Limiting Significant Wave Heights for Selected Responses

4. CONCLUSIONS

Operability indices regarding crew comfort on board for a container ship are investigated with respect to different sea states, seakeeping phenomena and criteria. The study underlines the crew comfort operability percentages under the lateral and vertical responses for a given seaway and sea state. The limiting wave heights are calculated for each response.

The authors suggest that seakeeping analyses on crew comfort on board as well as

on vessel behavior are remarkably important that must be considered during concept design level. Such analyses will gain useful information on optimal positioning of bridge and accommodation locations as well as defining seakeeping ship.

5. REFERENCES

K. Sarioz, E. Narli, "Effect of Criterion on Seakeeping Performance Assessment", Ocean Engineering 32, (2005) 1161–1173.

K. Sarioz, E. Narli, "Effect of Criterion on Seakeeping Performance Assessment", Ocean Engineering 32, (2005) 1161–1173.

Nabergoj, R. (2006). "Passenger comfort and seakeeping: A new challenge for high-tech ship design", Proceedings of SMALL CRAFT: An International Conference on Small Craft Related Sciences and Technology, Bodrum, Muğla.

Scamardella, A. and Piscopo, V. (2014), "Passenger ship seakeeping optimization by the Overall Motion Sickness Incidence", Ocean Engineering, Vol:76, pp: 86-97.

Cakici F. and Aydın M., (2014) "Investigation of Habitability Indices of YTU Gulet Series in Various Sea States", Brodogradnja/ Shipbuilding.

Çakici, F., Sukas, O. F. and Alkan, A. D., (2014) "An Investigation of Comfort on Board Calculations for a Passenger Catamaran and Mega Yacht Hulls", 2nd International Symposium on Naval Architecture and Maritime. INT-NAM 2014, (pp. 589-594).

NORDFORSK 1987, "The Nordic Cooperative Project, Seakeeping Performance of Ships Assessment of a Ship's Performance in a Seaway", Marintek, Trondheim.

Ferdinande V. 1969, "Analysis of Slamming Phenomena on a Model of a Cargo Ship in Irregular Waves", International Shipbuilding Progress, November

Ikeda, Y., Y. Himeno, and N. Tanaka,"A Prediction Method for Ship Roll Damping", Report of the Department of Naval Architecture, University of Osaka Prefecture, 1978e, No. 00405.

Himeno, Y., "Prediction of Ship Roll Damping-State of the Art", U. Michigan Dept. of Naval Arch. and Marine Engineering, 1981, Report 239

This page is intentionally left blank

Proceedings of the 12th International Conference on the Stability of Ships and Ocean Vehicles, 14–19 June 2015, Glasgow, UK.

Novel Statistical Prediction on Parametric Roll Resonance by Using Onboard Monitoring Data for Officers

Daisuke Terada, *Fisheries Research Agency* dterada@affrc.go.jp
Hirotada Hashimoto, *Kobe University* hashimoto@maritime.kobe.ac.jp
Akihiko Matsuda, *Fisheries Research Agency* amatsuda@affrc.go.jp

ABSTRACT

A novel statistical prediction method on occurrence of roll with large amplitude is proposed based on a methodology applied exponential autoregressive (ExpAR) modeling procedure, which is a kind of nonlinear time series analysis. The verification of the proposed method is implemented by using results of model experiments concerning the parametric roll resonance. It can be con-firmed that the large amplitude roll motion can be predicted based on the predictive probability distribution calculated by using the statistically optimum ExpAR model determined by Akaike Information Criterion (AIC).

Keywords: *Parametric roll resonance, ExpAR model, AIC, Predictive probability distribution*

1 INTRODUCTION

There are many studies concerning a parametric roll resonance that have been published in the past Stability of Ships and Ocean Vehi-cles (STAB) conference and the International Ship Stability Workshop (ISSW) (e.g. Belenky & Campbell 2012; Bulian & Francescutto 2012; Cooper & McCue 2012; Katayama *et. al.* 2012; Miguez-Gonzalez *et. al.* 2012; Hashimoto & Umeda 2012; Ovegard *et. al.* 2012; and so on) from the viewpoint of naval architecture. And excellent knowledges concerning this issue has been showed. However, they are not enough from the viewpoint of ship officers, since ship motions under navigation are big different due to lording conditions of cargoes and external forces such as waves, wind, current and so on. Therefore, it is very important for officers to understand the state of roll motion in which it is the steady or the unstable.

From this background, one of authors (Terada, 2014) suggested that during navigation, officers should keep monitoring the roll motion. In that study, the dynamical system on roll mo-tion can be approximated by an exponential autoregressive (ExpAR) model that is a kind of a nonlinear time series model, and it showed that roots of a characteristic equation on the ExpAR model are an evaluation index useful as the method to confirm the state of roll mo-tion. In short, if all characteristic roots lie in-side of the unit circle, then the system is sta-tionary and stable. Moreover, when the real part of the characteristic root changes from pos-itive/ negative to negative/positive, the dynam-ical system for the roll motion can be evaluated as nonlinear for the damping force. Moreover, when the imaginary part of the characteristic root changes from positive/negative to nega-tive/ positive, the dynamical system for the roll motion can be evaluated as nonlinear for the restoring force. Therefore, since officers can un-derstand the detailed dynamics of the roll mo-tion under navigation, it is considered that the proposed method is useful for promoting safer

navigation. However, we has been pointed out that it is very difficult for officers to understand the result, and we need to solve this issue.

On the other hand, it is possible to consider that the ExpAR model is one class of the ra-dial basis function (RBF) approximation model in the neural network approach. Ueno & Han (2013) attempted to predict the time series of the roll motion, they showed it's effectiveness. Note that this kind of approach cannot use in actual navigation, since officers do not steer confirming the time series of the roll motion and serious accidents occur with the failure of the prediction.

In this study, we attempt to establish a novel statistical prediction method, which uses an upper and lower endpoint of a pre-dictive probability distribution calculated from a stochastic simulation based on the ExpAR model, in order to give the significant infor-mation concerning the roll motion to officers. To confirm the effectiveness of the proposed method, we analyzed the data of the paramet-ric roll resonance. The obtained findings are reported.

2 RELATIONSHIP BETWEEN NONLINEAR STOCHASTIC DYNAMICAL SYS-TEM AND TIME SERIES MODEL

Firstly, we mention a relationship be-tween nonlinear stochastic dynamical system and time series model according to Terada& Matsuda (2011) and Terada (2014).

Consider the following nonlinear stochastic dynamical system concerning the roll motion:

$$\ddot{x}(t) + f\big(\dot{x}(t)\big) + g\big(x(t)\big) = u(t) \tag{1}$$

where $x(t)$ indicates a roll angle, the notation $(\cdot)$ and $(\cdot\cdot)$ indicate the 1st and the 2nd or-der deferential operator with time, $f(*)$ indi-cates the nonlinear mapping function concern-ing the damping force, $g(*)$ indicates the non-linear mapping function concerning the restor-ing force and $u(t)$ indicates an external distur-bance that is treated with the random variable, respectively. Note that $u(t)$ has the finite vari-ance, but is not white noise sequence. And Equation 1 can be written in the following vec-tor form:

$$\dot{\boldsymbol{x}}_t = \mathcal{F}\big(\boldsymbol{x}_t\big) + \boldsymbol{u}_t \tag{2}$$

where, as the notation (T) means the transpose,

$$\boldsymbol{x}_t = \big[\dot{x}(t), x(t)\big]^T,$$
$$\mathcal{F}\big(\boldsymbol{x}_t\big) = \Big(-f\big(\dot{x}(t)\big) - g\big(x(t)\big), \dot{x}(t)\Big)^T,$$
$$\boldsymbol{u}_t = \big[u(t), 0\big]^T.$$

According to the locally linearization method (Ozaki, 1986), Equation 2 can be discretized as follows:

$$\boldsymbol{x}_n = \mathrm{EXP}\big[\boldsymbol{K}_{n-1}\Delta t\big] \cdot \boldsymbol{x}_{n-1} + \boldsymbol{B}_{n-1}\boldsymbol{u}_n \tag{3}$$

where,

$$\boldsymbol{x}_n = \big[\dot{x}_n, x_n\big]^T,$$
$$\boldsymbol{K}_n = \frac{1}{\Delta t}\mathrm{LOG}\big(\boldsymbol{A}_n\big),$$
$$\boldsymbol{A}_n = \boldsymbol{I} + \boldsymbol{J}_n^{-1}\Big\{\mathrm{EXP}\big[\boldsymbol{J}_n\Delta t\big]\Big\}\boldsymbol{F}_n,$$
$$\mathrm{LOG}\big(\boldsymbol{A}_n\big) = \sum_{k=1}^{\infty}\frac{(-1)^k}{k}\big(\boldsymbol{A}_n - \boldsymbol{I}\big)^k,$$
$$\boldsymbol{J}_n = \frac{\partial\mathcal{F}\big(\boldsymbol{x}_n\big)}{\partial\boldsymbol{x}_n},$$
$$\boldsymbol{F}_n\boldsymbol{x}_n = \begin{pmatrix} -f(\dot{x}_n) & -g(x_n) \\ \dot{x}_n & 0 \end{pmatrix},$$

and, Δt indicates a discrete interval and $B_{n-1}u_n$ is a two-dimensional colored noise se-quence, which is obtained by the stochastic in-tegral.

In Equation 3, since the term of the noise is not the white noise sequence, it is necessary to transform the colored noise sequence into a white noise sequence in order to deal with the problem stochastically. To do the whitening,

Yamanouchi (1956) showed how to use the discrete autoregressive process: in Equation 3, let

$$\boldsymbol{\varepsilon}_n \equiv \boldsymbol{B}_{n-1}\boldsymbol{u}_n. \tag{4}$$

Then this can be approximated by the following m–th order discrete autoregressive process.

$$\boldsymbol{\varepsilon}_n = \sum_{i=1}^{m} \boldsymbol{D}_i \boldsymbol{\varepsilon}_{n-i} + \boldsymbol{w}_n, \quad (\boldsymbol{\varepsilon}_n = \boldsymbol{w}_n \ \text{ for } i = 0), \tag{5}$$

where w_n is a 2×2 Gaussian white noise se-quence with $N(0,\ \mathrm{diag}(\sigma_1^2,\ \sigma_2^2))$ and D_n indi-cates a 2×2 autoregressive coefficient matrix. On the other hand, the following relation is ev-ident.

$$\begin{aligned}
\boldsymbol{\varepsilon}_n &= \boldsymbol{x}_n - \boldsymbol{A}_{n-1}\boldsymbol{x}_{n-1} \\
\boldsymbol{\varepsilon}_{n-1} &= \boldsymbol{x}_{n-1} - \boldsymbol{A}_{n-2}\boldsymbol{x}_{n-2} \\
&\vdots \\
\boldsymbol{\varepsilon}_{n-m} &= \boldsymbol{x}_{n-m} - \boldsymbol{A}_{n-m-1}\boldsymbol{x}_{n-m-1}.
\end{aligned} \tag{6}$$

Therefore, by substituting Equations 6 into Equation 5, we can obtain the following two dimensional (m + 1)–th order time-varying autoregressive model.

$$\boldsymbol{x}_n = \sum_{i=1}^{m+1} \boldsymbol{C}_i \boldsymbol{x}_{n-i} + \boldsymbol{w}_n. \tag{7}$$

Here C_i (i = 1, · · · , m + 1) is the time-varying autoregressive coefficient matrix, which is expressed as follows:

$$\begin{aligned}
\boldsymbol{C}_1 &= \boldsymbol{D}_1 + \boldsymbol{A}_{n-1}, \\
\boldsymbol{C}_2 &= \boldsymbol{D}_2 - \boldsymbol{D}_1\boldsymbol{A}_{n-2}, \\
&\vdots \\
\boldsymbol{C}_m &= \boldsymbol{D}_m - \boldsymbol{D}_{m-1}\boldsymbol{A}_{n-m}, \\
\boldsymbol{C}_{m+1} &= -\boldsymbol{D}_m\boldsymbol{A}_{n-m-1}.
\end{aligned}$$

Moreover, by using the following relation

$$\dot{x}_n \cong \frac{1}{\Delta t}\big(x_n - x_{n-1}\big), \tag{8}$$

Equation 7 can be approximated by the following the M(= m + 2)–th order scalar time-varying autoregressive model

$$x_n = \sum_{i=1}^{M} a_{n,i} x_{n-i} + w_n. \tag{9}$$

where $a_{n,i}$ indicates time-varying autoregres-sive coefficients, w_n is the Gaussian white noise sequence with $N(0,\ \sigma_2^2)$. Now, since $a_{n,i}$ is time-varying autoregressive coefficients, sup-pose that the following relation

$$\sum_{i=1}^{M} a_{n,i} \cong \sum_{i=1}^{M} \big\{\phi_i + \pi_i \exp[-\gamma x_{n-1}^2]\big\} \tag{10}$$

where φ_i is a linear term of autoregressive coefficients, π_i is a time-varying term of autoregres-sive coefficients and γ is a scaling parameter. Thus, Equation 9 can be written as follows:

$$x_n = \sum_{i=1}^{M} \big\{\phi_i + \pi_i \exp[-\gamma x_{n-1}^2]\big\} x_{n-i} + w_n \tag{11}$$

This time series model, which is called an exponential autoregressive(ExpAR) model, was first introduced by Ozaki & Oda (1978). And then characteristics are investigated by Hag-gan & Ozaki (1981). According to Haggan & Ozaki (1981), consider the following character-istic equations of Equation 11:

$$\lambda^M - \phi_1\lambda^{M-1} - \cdots - \phi_{M-1}\lambda - \phi_M = 0 \tag{12}$$

$$\begin{aligned}
&\lambda^M - \big(\phi_1 + \pi_1\big)\lambda^{M-1} - \cdots - \\
&\qquad \big(\phi_{M-1} + \pi_{M-1}\big)\lambda - \big(\phi_M + \pi_M\big) = 0
\end{aligned} \tag{13}$$

If all roots of these equations lie inside of the unit circle, then the nonlinear stochastic dynamical system is stationary and stable. Moreover, when the real part of the characteristic root changes from positive/negative to negative/positive, the dynamical system for the roll motion can be evaluated as nonlinear for the damping force. And also, when the imaginary part of the characteristic root changes from positive/negative to negative/positive, the dynam-ical system for the roll motion can be evaluated as nonlinear for the restoring force.

3 FITTING OF THE ExpAR MODEL AND PARAMETER ESTIMATION

As to the estimation of the model order M and the coefficients γ, (φ_i, π_i; $i = 1, \cdots, M$) in the ExpAR model, for simplicity, by fixing the parameter γ at one of a grid of values, we estimated the model order M and the corresponding φ_i, π_i parameters as well as Haggan & Ozaki (1981). As N is the total number of observations, after fixing $\gamma = \gamma_0$, the ExpAR model for $n = M + 1, \cdots, N$; $i = 1, \cdots, M$ can be written as follows:

$$x_n = \sum_{i=1}^{M} \left\{\phi_i + \pi_i \exp[-\gamma_0 x_{n-1}^2]\right\} x_{n-i} + w_n. \quad (14)$$

So the matrix form of Equation 14 can be written as

$$\boldsymbol{X}^{(n)} = \boldsymbol{H}\boldsymbol{\beta} + \boldsymbol{w}. \quad (15)$$

where, $n = N - M, \cdots, N$ and

$$\begin{aligned}
\boldsymbol{X}^{(n)} &= \left(x_n, x_{n-1}, \cdots, x_{n-(N-M-1)}\right)^T, \\
\boldsymbol{Y}^{(n)} &= \left(\exp[-\gamma_0 x_n^2]x_n, \exp[-\gamma_0 x_n^2]x_{n-1}, \cdots, \right. \\
&\qquad \left. \exp[-\gamma_0 x_n^2]x_{n-(N-M-1)}\right)^T, \\
\boldsymbol{H} &= \left(\boldsymbol{X}^{(n-1)}, \boldsymbol{Y}^{(n-1)}, \boldsymbol{X}^{(n-2)}, \boldsymbol{Y}^{(n-2)}, \cdots, \right. \\
&\qquad \left. \boldsymbol{X}^{(n-i)}, \boldsymbol{Y}^{(n-i)}\right), \\
\boldsymbol{\beta} &= \left(\phi_1, \pi_1, \phi_2, \pi_2, \cdots, \phi_i, \pi_i\right)^T, \\
\boldsymbol{w} &= \left(w_n, w_{n-1}, \cdots, w_{M+1}\right)^T,
\end{aligned}$$

so that the normal equations for β become $X^{(n)} = H\beta$, hence β can be found from

$$\hat{\boldsymbol{\beta}} = \left(\boldsymbol{H}^T\boldsymbol{H}\right)^{-1}\boldsymbol{H}\boldsymbol{X}^{(n)}. \quad (16)$$

The model order M of the fitted model is se-lected by using the Akaike Information Cri-terion(AIC) for nonlinear time series(Ozaki & Oda, 1978)

$$\mathrm{AIC}(M) = (N - M)\log\hat{\sigma}_{2,M}^2 + 2(2M + 1), \quad (17)$$

where,

$$\hat{\sigma}_{2,M}^2 = \frac{\left(\hat{w}_N^2 + \hat{w}_N^2 + \cdots + \hat{w}_M^2\right)}{N - M} \quad (18)$$

is the least squares estimate of the residual variance of the model.

4 STATISTICAL PREDICTION OF ROLL WITH LARGE AMPLITUDE

As mentioned before, we can evaluate the stability of the dynamical system by using the characteristic roots calculated from Equation 12 and 13. However, it is impossible to un-derstand the absolute amount of roll ampli-tude based on this method, and we cannot give the accurate information concerning the future roll motion to officers. Therefore, we propose a novel procedure to solve this prob-lem. In this procedure, We firstly consider a predictive probability distribution calculated from a stochastic simulation based on the op-timum ExpAR model determined by Equation 17. Then, as the results we can estimate the

upper and lower endpoint of the probability distribution, and can use them as evaluation index concerning the absolute amount of roll amplitude.

The concrete procedure is as follows:

Step 1:
Fit the ExpAR model to the data of N samples, and the model order, and estimate parameters such as the model order, the scaling factor and so on based on Equation 16 to 18.

Step 2:
Reduce the model order M from the data of N samples.

Step 3:
Prepare the $N - M$ sequence, and give the data of $N - M$ samples as the ini-tial values of their sequence. After that, perform the stochastic simulation of roll motion based on the ExpAR model deter-mined by the AIC.

Step 4:
Calculate the histogram by using the obtained realizations at [Step 1]. Estimate the predictive probability distribution of roll motion by normalization of the his-togram. In this case, the the upper and lower endpoint of the probability distri-bution are simultaneously obtained.

Step 5:
Evaluate the safety level of the roll amplitude based on the upper and lower end-point of the probability distribution. If values exist within the safety level of the roll amplitude then return to [Step 1] to consider next data set. Otherwise, in-form officers the information in which the present state is danger.

Step 6:
Return to [Step 1] to consider next data set.

5 VERIFICATION

To verify the proposed procedure, we analyzed the two kinds of data of the paramet-ric roll resonance concerning a container model ship obtained by Hashimoto *et. al.* (2005). First one is regular waves, and other one is ir-regular waves. They were measured at sam-pling interval 0.1[sec] when the ship was run-ning in head seas.

Figure 1 shows a time series of roll motion in regular waves. We analyzed 1,200 samples every 300 samples, namely every 30[sec], con-cerning this data. In this figure, we defined them as form ”Data set 1” to ”Data set 4”. As shown this figure, the amplitude of roll motion is small in ”Data set 1”, and becomes gradually large after ”Data set 1”.

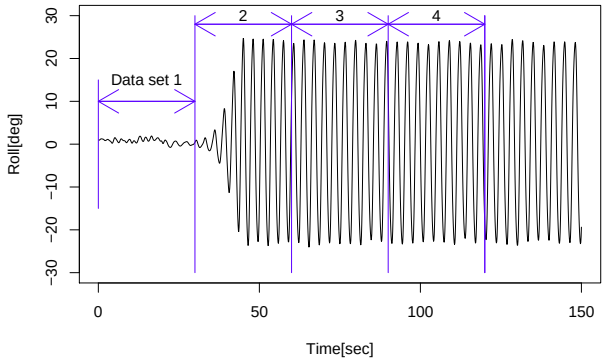

Figure 1 Time series in the case of regular waves

Results of the ExpAR modeling are summa-rized in Table 1. The probability distribution are calculated based on values shown in this table.

As to the regular waves shown in Figure 1, the predictive probability distribution of next data set calculated from optimum ExpAR model determined by AIC concerning present data set is shown in from Figure 2 to Figure 5.

Table 1 Results of the ExpAR modeling concerning the data of Fig.1

Data	1	2	3	4
Order	3	6	2	2
AIC	-4462.8	-3309.4	-2555.1	-2507.9
γ	8321.8	49.6	51.1	51.7
$\hat{\sigma}^2$	1.04×10^{-7}	4.32×10^{-6}	6.68×10^{-5}	7.82×10^{-5}
ϕ_1	2.79	2.31	1.88	1.86
π_1	0.0419	-0.0545	-0.0344	-0.0358
ϕ_2	-2.70	-1.15	-0.935	-0.933
π_2	-0.0827	0.177	0.0322	0.0332
ϕ_3	0.910	-0.809	–	–
π_3	0.0428	-0.164	–	–
ϕ_4	–	0.373	–	–
π_4	–	0.00175	–	–
ϕ_5	–	0.653	–	–
π_5	–	0.0519	–	–
ϕ_6	–	-0.395	–	–
π_6	–	-0.0110	–	–

In these figures, the horizontal axis indicates the roll angle and the vertical axis indicates the density of the probability, respectively. As you can see from Figure 2, the predictive probabil-ity distribution of ”Data set 2” calculated from optimum ExpAR model of ”Data set 1” shows that the amplitude of roll motion has danger of growing in the future, since the density of the probability exists in the range of from -30[deg] to 30[deg]. In actual, the amplitude of roll motion is growing in ”Data set 2”. There-fore, it is considered that it is possible to predict the absolute amount of roll amplitude based on this method. As to the results of from Figure 3 to Figure 5, the predictive probability distribu-tion is nearly normal distribution, since time series is stationary, although their amplitude are large.

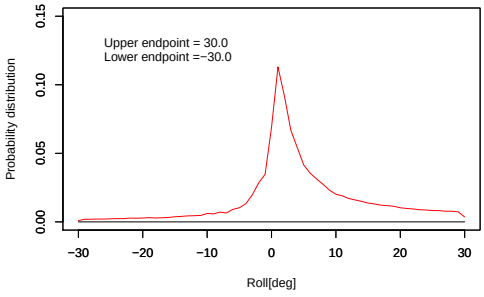

Figure 2 Probability distribution in Data 2 predicted by using ”Data set 1” of Fig.1

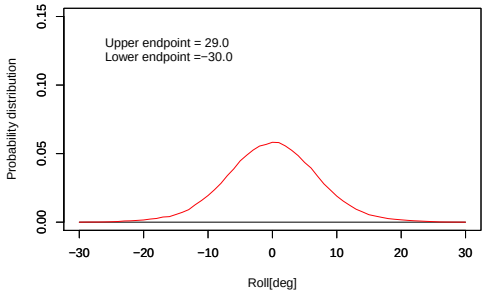

Figure 3 Probability distribution in Data 3 predicted by using ”Data set 2” of Fig.1

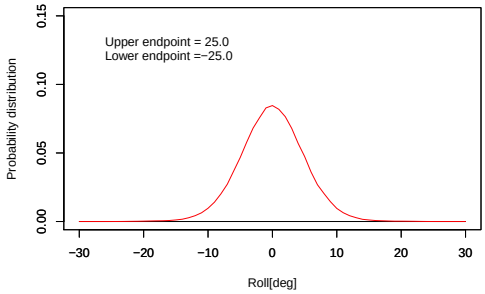

Figure 4 Probability distribution in Data 4 predicted by using ”Data set 3” of Fig.1

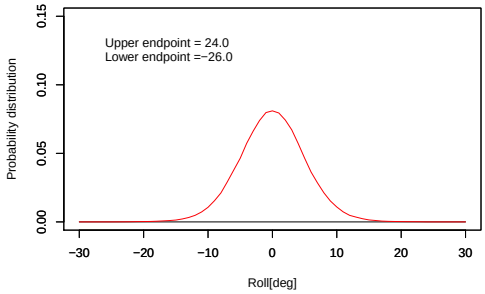

Figure 5 Probability distribution in after Data 5 predicted by using ”Data set 4” of Fig.1

Figure 6 shows a time series of roll motion in irregular waves. We analyzed 1,500 samples every 300 samples, namely every 30[sec], con-cerning this data. In this figure, we defined them as form ”Data set 1” to ”Data set 5”. As shown this figure, the amplitude of roll motion becomes large in after ”Data set 5”.

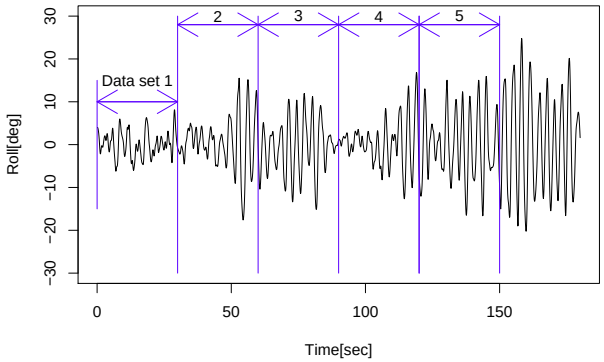

Figure 6 Time series in the case of irregular waves

Results of the ExpAR modeling are summa-rized in Table 2. The probability distribution are calculated based on values shown in this table.

Table 2 Results of the ExpAR modeling concerning the data of Fig.6

Data	1	2	3	4	5
Order	4	4	6	4	5
AIC	-3306.1	-3389.7	-3335.4	-3255.9	-3172.385
γ	458.7	97.7	132.1	106.4	109.5
$\hat{\sigma}^2$	4.85×10^{-6}	3.66×10^{-6}	3.96×10^{-6}	5.75×10^{-6}	7.25×10^{-6}
ϕ_1	3.02	3.21	2.97	3.06	2.69
π_1	0.0162	-0.0361	-0.00426	0.0373	-0.0273
ϕ_2	-3.61	-4.09	-3.14	-3.66	-2.16
π_2	-0.00978	0.126	-0.0263	-0.0749	0.125
ϕ_3	2.06	2.48	0.824	2.05	-0.391
π_3	-0.0184	-0.150	0.128	0.0258	-0.219
ϕ_4	-0.487	-0.617	1.02	-0.468	1.41
π_4	0.0125	0.0607	-0.181	0.0148	0.178
ϕ_5	–	–	-0.918	–	-0.574
π_5	–	–	0.105	–	-0.0567
ϕ_6	–	–	0.222	–	–
π_6	–	–	-0.0207	–	–

As to the irregular waves shown in Fig-ure 6, the predictive probability distribution of next data set calculated from optimum ExpAR model determined by AIC concerning present data set is shown in from Figure 7 to Figure 11. In these figures, as well as the case of regular waves, the horizontal axis indicates the roll an-gle and the vertical axis indicates the density of the probability, respectively. As you can see from Figure 11, the predictive probability dis-tribution in after ”Data set 5” calculated from optimum ExpAR model of ”Data set 5” shows that the amplitude of roll motion has danger of growing in the future, since the density of the probability exists in the range of from -30[deg] to 30[deg]. It means that it is possible to predict the absolute amount of roll amplitude based on this method even the case of irregular waves. As to the results of from Figure 7 to Figure 10, the upper and lower endpoint of the probabil-ity distribution is from about -20[deg] to about 20[deg]. Thus, we can judge that this experi-mental condition is overall dangerous. For of-ficers, this information is very important from the view point to remain safe navigation.

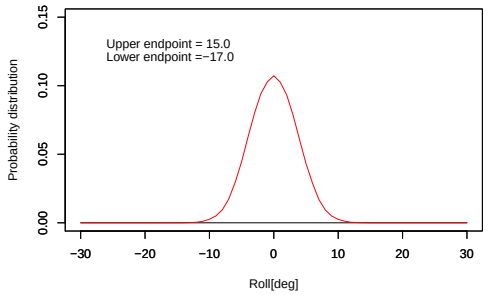

Figure 7 Probability distribution in Data 2 predicted by using ”Data set 1” of Fig.6

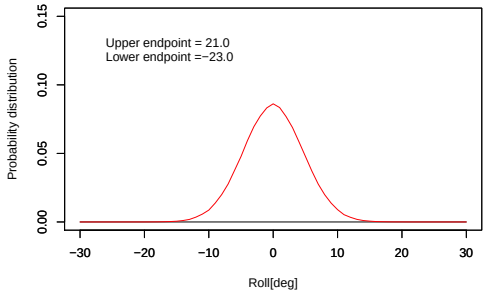

Figure 8 Probability distribution in Data 3 predicted by using ”Data set 2” of Fig.6

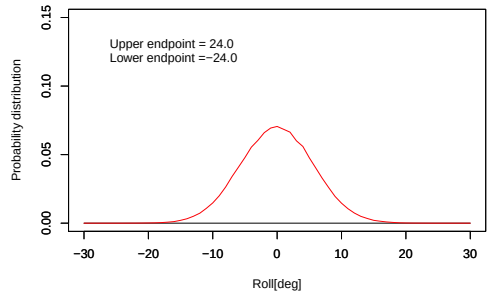

Figure 9 Probability distribution in Data 4 predicted by using ”Data set 3” of Fig.6

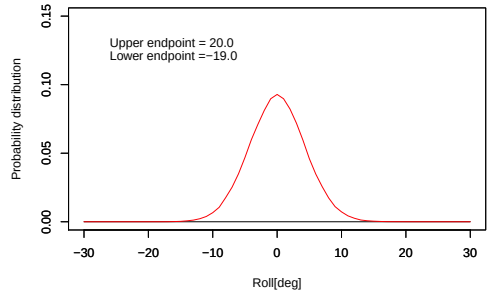

Figure 10 Probability distribution in Data 5 predicted by using ”Data set 4” of Fig.6

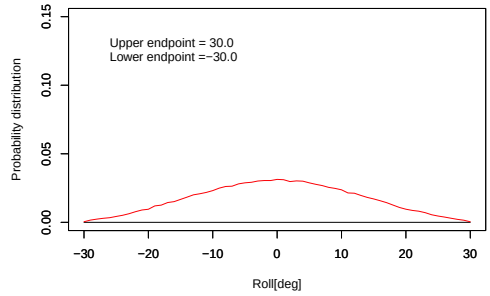

Figure 11 Probability distribution in after Data 5 predicted by using ”Data set 5” of Fig.6

6 CONCLUSIONS

In this study, we attempt to establish a novel statistical prediction method, which uses an upper and lower endpoint of a predic-tive probability distribution calculated from a stochastic simulation based on the exponential autoregressive (ExpAR) model, in order to give the significant information concerning the roll motion to officers. To confirm the effectiveness of the proposed method, we analyzed the data of the parametric roll resonance. Main conclu-sions are summarized as follows:

1. As to the regular waves, it is roughly possible to predict the absolute amount of roll amplitude based on this method.

2. It is roughly possible to predict the absolute amount of roll amplitude based on this method even the case of irregular waves.

As mentioned before, it is very important for officer to obtain the predictive information concerning the parametric roll resonance from the view point to remain safe navigation, and we confirmed that the proposed procedure is possible to realize it. Therefore, we consider that the proposed procedure is practical use-fulness, and can be used as a powerful tool to remain safe navigation.

Note that we need to verify the proposed procedure more concerning many kind of ships as future task.

7 ACKNOWLEDMENTS

This work was supported by JSPS KAKENHI Grant Number 25289328. Authors would like to thank President Genshiro KITAGAWA (Research Organization of Information and System) and Prof. Kohei OHTSU (Tokyo University of Marine Science and Technology) for helpful suggestions.

8 REFERENCES

Belenky, V. and Campbell, B. (2012): Statistical extrapolation for direct stability assessment, Proc. of 11th International conference on STAB, pp.243–256.

Bulian, G. and Francescutto, A. (2012): Roll motion of a ship with low metacentric height in bi-chromatic beam waves, Proc. of 11th International conference on STAB, pp.187– 200.

Cooper, M D, and McCue, L S. (2012): Effectiveness of chaotic system measures for the validation of ship dynamics simulation, Proc. of 11th International conference on STAB, pp.363–372.

Katayama, T., Miyamoto, S., Hashimoto, H. and Tai, Y. (2012): An experimental study on characteristics of rolling in head waves for a vessel with non-linear GZ-curve, Proc. of 11th International conference on STAB, pp.281–290.

Miguez-Gonzalez, M., Diaz-Casas, V., Lopez-Pena, F. and Perez-Rojas, L. (2012): Experimental parametric roll resonance characterization of a stern trawler in head seas, Proc. of 11th International conference on STAB, pp.625–634.

Haggan, V. and Ozaki, T. (1981): Modelling nonlinear random vibrations using an amplitude-dependent autoregressive time series model, Biometrika, 68, 1, pp.189–196.

Hashimoto, H., Matsuda, A. and Umeda, N. (2005): Model Experiment on Parametric Roll of a Post-Panamax Container Ship in Short-Crested Irregular Seas, Conference Proc. of the Japan society of naval architects and Ocean Engineers, vol.1, pp.71–74.

Hashimoto, H. and Umeda, N. (2012): Validation of a numerical simulation model for parametric rolling prediction using a PCTC, Proc. of 11th International conference on STAB, pp.141–150.

Ovegard, E., Rosen, A., Palmquist, M. and Huss, M. (2012): Operational quidance with pure loss of stability and parametoric rolling, Proc. of 11th International conference on STAB, pp.363–372.

Ozaki, T. and Oda, H. (1978): Nonlinear time series model identification by Akaike's information criterion, Information and Systems, Dubuisson (eds) (1978), Pergamon Press, pp.83–91.

Ozaki, T. (1986): Local Gaussian modelling of stochastic dynamical systems in the analysis of nonlinear random vibrations, Essays in Time Series and Allied Processes, Festshrift in honour of Prof.E.J.Hannan (1986), Probability Trust, pp.241–255.

Terada, D. and Matsuda, A. (2011): Study on a relationship between nonlinear dynamical system and stochastic model - Application to stability judgment system of ships - (in Japanese), Journal of the Japan Society of Naval Architects and Ocean Engineers, 14, pp.75–84.

Ueno, K. and Fan, C. (2013): Quasi-chaotic behaviors of narrow-band response of a non-deterministic resonant System -Application to analysis of ship motion in irregular seas, Japan Journal of Industrial and Applied Mathematic, Vol.30, No.1, pp.203–225.

Yamanouchi, Y. (1956): On the Analysis of ships, Oscillations as a Time Series, Journal of zosen kyokai, Vol. 99, pp.47–64.

This page is intentionally left blank

Target Ship Design and Features of Navigation for Motion Stabilization and High Propulsion in Strong Storms and Icing

Vasily N. Khramushin,
Applied mathematics and control processes faculty, St. Petersburg State University,
Russian science-engineering society of shipbuilders of Alexey Krylov, Yuzhno-Sakhalinsk,
V.Khram@Gmail.com

ABSTRACT

Statement of the design problem for ocean vessel of unlimited sailing can be based on the active use of the historical experience of designing of the good-quality ships. Such experience includes good sea practice of the most authoritative seafarers. It is reflected in the navigational instructions on achievement of efficient operation of ships, in pilot recommendations of practical navigation and unwritten rules of carrying out dangerous and hard sea work in the complicated, storm and ice conditions. Particular specialization of the ship for a concrete type of sea activity in the originally specified geographical and navigational conditions allows the use of achievements of noncontradictory design. It is formally reduced to global optimization (as well as in mathematician) under the terms of minimum external impact on a ship hull. Such approach certainly requires special navigator skills or adaptation of the automated navigation complexes in a variety of special or emergency situations, unpredictable in long ocean voyages. Each new design solution of the vessel of the improved seaworthiness should be complemented by the corresponding techniques on efficient carry out of sea works in storm conditions. In this paper, various examples show how to implement this concept in order to address the engineering problem of the highest efficiency of maritime activities of specialized ships. As target parameters are considered safety of navigation (including in extreme situations), achievement of optimum propulsion in strong storms and severe icing.

Keywords: *seafaring, shipbuilding, sensible target design, trochoidal wave, ninth wave, propulsive and pitching quality of the ship*

1. INTRODUCTION

Seamanship and maritime infrastructure development is an important indicator of efficiency of use of high technologies, general geographic knowledge and creative art marine engineers and navigators authoritative, in general, forming the foundation of "good seamanship" and exclude the possibility "of vainly invention not for mariners".

The concept of a consistent target of ship design is aimed at full harmonization of engineering solutions to well-defined geographical, navigational and meteorological conditions of navigation; for a given level arrangement of regional marine infrastructure and adequate competence shore-based and ship crews. Priority in the selection of design decisions and responsible for the formation of sailors ship's architecture; for the layout of ship equipment and mechanisms, as a consequence, lead to a mismatch of formal methods model shipbuilding and claim new research to test the special in-

structions on the efficacy and safety of navigation and marine operations for the intended purpose of the vessel.

A sensible design of the ship means the execution of the whole complex of marine research to optimize engineering solutions in shipbuilding for extremely accurate and complete realization of the real operating experience and good seamanship all-weather control of the ship in specific geographical areas of the ocean, that the Russian Far East is the need of understanding all aspects of navigation in complex, ice and storm conditions navigation ensuring with all-season and all-weather works maintenance of ship for its original purpose, and without the possibility of reliable shelter while waiting for the sea "fair weather".

2. THE EVOLUTIONARY GENESIS OF THE SHIP'S AFFAIRS AND GOOD SEAMANSHIP

Appearance, contours and architecture of the historic ship uniquely determine the possibility of its maneuvering in a storm winds and waves (Khramushin, 2011). Historically, as well as in real engineering and seamanship, seaworthiness of ships predetermined by relative strength of the shiphull and reserves its weighting to achieve the best propulsion in rough weather, or to keep the storm safe course in any one of the three historically verified modes storming, relying only on the ability of the crew to provide maneuvering in complex and storm sailing conditions:

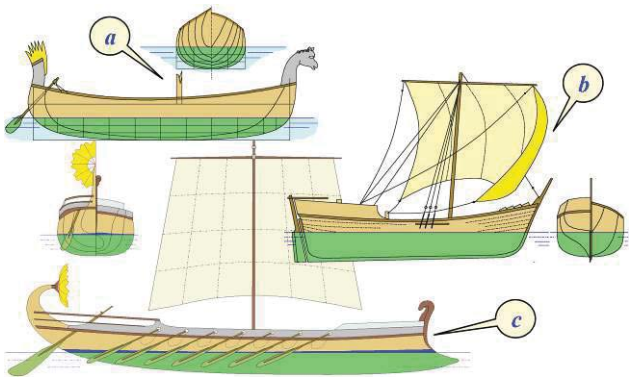

Figure 1 Design solutions ancient shipbuilding

techniques associated storm navigation:
a) - with a course along to a wave;
b) - active move in the wind and wave;
c) - passive storming bow on a wave.

a) – course of along to a wave (Figure 1-***a***) so far implemented on a wooden boat on the Volga river; previously used by the ancient Egyptian ships on the Nile river; as well as the broad Norwegian boats for shallow water areas, including long-range maritime and ocean navigation. Such vessels have excessive initial stability, why are experiencing intense rolling and pitching in the tempo of fast surface slope of storm waves, and, of course, need to be active course correction to keep the shiphull along the ridge for largest and most dangerous storm waves that ancient vessels was performed with a feed fin oars. This mode of stormy navigation fundamentally unacceptable to consider as the base for the vessels with a large displacement;

b) – active storm course on a wave fronts (Figure 1-***b***) is sometimes used by modern sailing yachts with a broad stern, as well as quite large rescue tugs with advanced bow superstructure; previously been used extensively the sloops Russian Pomors on a northen latitudes of the Arctic Ocean. The vessel medium displacement on the course with the wind must feels smooth pitching with a significant reduction in power loads on the shiphull by large ridges for passing storm waves, that provided the maintenance of sustainability and maneuverability via hinged aft rudder, effectively operating at a relatively high speed movement under the bow square sail;

c) – storming the course bow on a wave (Figure 1-***c***), unfortunately, has now become is practically the sole means of aimless containment of forward propulsion to provide its safety in heavy weather at extreme external loads on the host machine and the steering gear. This method has historically inherited from the ancient Phoenician warships with bulbous bowram; in the Middle Ages storming by a bow wave created conditions for safety far ocean sailing expeditions of the Geographical Dis-

covery Age. Asymmetry forms of fore and aft ends shiphull gives the ship weathervanes properties in relation to the wind and the waves, which is achieved by the creation of special contours and perfecting form a surface part shiphull to minimize power influence on the intensity of the storm loads on the hull of the vessel by the oncoming wave fronts, and this asymmetry is quite enough to safely the sea waiting for good weather with no active of the crew.

Last method of a stormy timelessness on course "bow on a wave" is a special captain's ability to save the ship in a stormy sea, which often require a hazard to pull by the main engines, with extremely high overloading mechanisms of steering device, that ship changes a favorable course before impact with each storm wave ridges – with the dangerous ninth wave. This ability does not correct the disastrous mistakes shipbuilders, and the use of such "skills" in a large vessel is limited by the fact that the crew and passengers survive unbearable conditions of habitability; until main deck sheer strake belt of shiphull is not broken under the blows of the ship's cargo in the cycles of rise in weightlessness - to fold multiplication of forces under the influence of the weight onboard and heaving; and immense overload onboard mechanisms do not overpower the technical capabilities and resources efficiency of main machine and control systems.

3. TARGET SHIP DESIGN AND EFFECTIVENESS OF STORM NAVIGATION

Modern fleet with the current power availability by each ocean ships can be used in combination regimens of maneuvering in heavy weather, and steady maintenance of propulsion by arbitrary course throw hurricane winds on stormy waves, if the original design of the ship provides a thorough engineering study of ship contours, the hull shape and the ship's architecture for specific geographic conditions, with the obligatory agreement of all the navigator's requirements and practical methods of seafaring and exploitations of perspective fleet in a predetermined maritime area. Search and optimization of technical solutions determines are "sensible target ship design", is the key results of which are discussed in this paper.

At the time the Great Geographical Discoveries ocean fleet (Figure 2-***a***) has gained universal understanding of good seamanship for a far transoceanic expeditions, which was supported by a universal ship's architecture for reducing impacts to ship from stormy waves, and provides passive storming on the course bow on a wave. Draught becomes comparable with half the width of the shiphull and freeboard tumblehome inwardly to compensate for the hydrodynamic force action of storm waves. The external appearance of ocean ship has a high aft superstructure – as storm weather vane, and very low deck of bow under privy head and vessel there (knee of the head)), dived under the ridges of counterpropagating waves for a hydrodynamic compensation of pitching, and as a result, prevent the wave impact loads on a wooden shiphull and deck superstructures, which has a relatively lower strength.

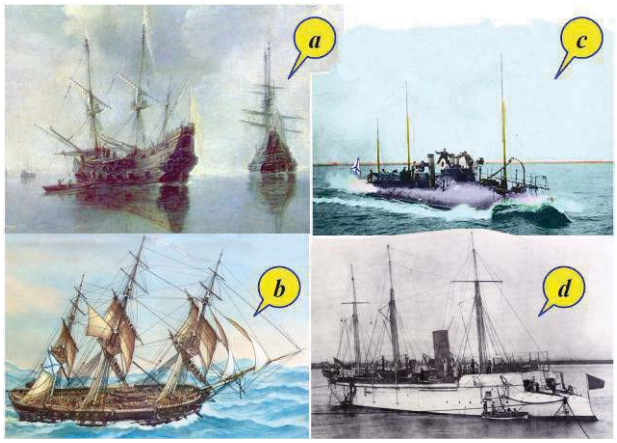

Figure 2 The optimal design for a ocean sailing ships: left side – ***a***) and ***b***); and their evolutionary improvement to a ships with enhanced stormy seaworthiness by using the power-driven propulsion: right side – ***c***) and ***d***).

By the beginning of the XIX century a structure and governance by sailing equipments

was up to the highest technical perfection, and, as evidence of optimal engineering solutions – there is a universal uniformity of sailing fleets all over the world. In the latest projects of sailing ships begins traceable target concept of designing to achieve the highest efficiency seafaring in a fresh ocean winds and intense stormy waving for specific geographical conditions maritime communications. On the example of the cruiser-frigate "Pallada" (Figure 2-***b***) there is a decrease of height and alignment of the continuous upper deck, which indicates assurance of the crew in the adequacy of sailing equipments for all-weather control and manoeuvrable of yours best ship. Noncontradictory design concept, however, keep it up in using the old method of passive support storming course by the "bow on a wave", that enables the use of storm the aft mizzen instead of high aft superstructure, and in the event of the hazard of hurricane force winds, and still foremast can go overboard as a drogue anchor, which also weighting and stabilizing the ship bow on a stormy waves.

Evolutionary perfection design of contours, hull shapes and ship's architecture in general for new fleet is achieved by implementation of steam engines, propeller screws and highly durable steel hulls of ships and vessels at the end of XIX – beginning of XX centuries (Figure 2-***c***, ***d***). In the external appearance the newest ships disappear multitude bulky devices except the mizzen mast gaff on, indicates the possibility of quickly setting the mizzen storm sail to bring the ship on course bow on a wave during storm strong wind. Draught of ship hull was remains relatively deep, and the freeboard has a tumblehome form to compensation force action of the waves and reduce roll. The bow deck is very low, the stem to the stern tumblehome, or is almost vertical stem, it is necessary to sharpen the waterlines and reduce the risk of intense pitching.

4. KEY TECHNICAL SOLUTIONS TO ACHIEVE THE BEST STORM SEAWORTHINESS

The main engineering solutions to achieve efficiency of navigation in heavy weather, and especially their involvement in good seamanship outlining maritime forum STAB-2009 in St-Petersburg in the report "Key design solutions and specifics of operation in heavy weather, fluid mechanics approach to stabilization of ship in heavy seas" (Khramushin). And we restrict ourselves the illustrations and brief explanations necessary in subsequent submissions by the refined of geometric constructions ship contours and shape of the hull of ships and vessels enhanced storm seaworthiness and ice passability, which is very important for navigation on the Russian Far East seas.

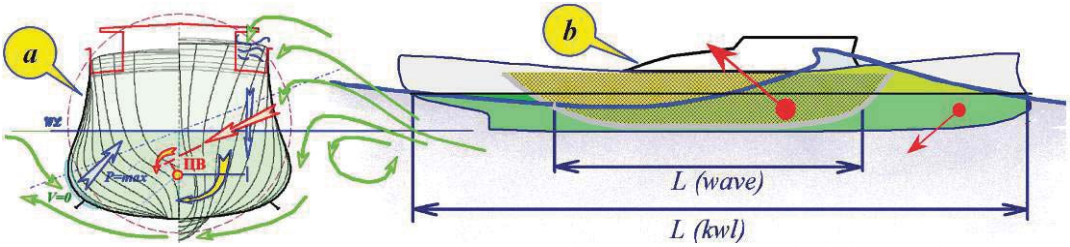

Figure 3 The hull form must given the hydrodynamic compensation: ***a***) – a rolling using by minimizing height of tumblehome board in the middle, and: ***b***) – pitching of ship through the redistribution of pressures in trochoidal wave on board.

In real navigating practice are preserving the tradition visual interpretation the force distribution and hydrostatic pressure changes of flow field (by Bernoulli's law) in the hydrodynamics ascent by account of water flows near the hull and outboard stabilizers, also under the influence of sea waves, which performed by analogy of engineering decision-making for maneuvering using of spatial images and laws ship fluid mechanics, generally accepted in the international language of navigator communication on duty watches, with pilots, marine res-

cuers and captain's mentors from a coastal services. The scheme of hydrodynamic effects of storm waves impact to the shipboard, was built on navigator's principles, mentioned (Figure 3) in the design and optimization of contours and shape of the hull to minimize rolling (Patent of invention № 2360827, 2009) (Figure 3-***a***) and pitching (Order of invention 2007133625, 2007) (Figure 3-***b***), found experimentally confirmed for almost complete compensation rolling under the influence of extremely high ridges storm waves (Figure 3-***a***), which free passing under the tumblehome shiphull, and emerging from the other board with little or no shape distortion and intensity collapsing wave's ridges, as well as visually complete transformation pitching hull in the heaving (Figure 3-b), which helps to maintain the best propulsion and better habitability conditions in the active movement of the ship relatively an arbitrary course of progressive wave ridges and ninth wave, resulting in packages trochoidal wave structures.

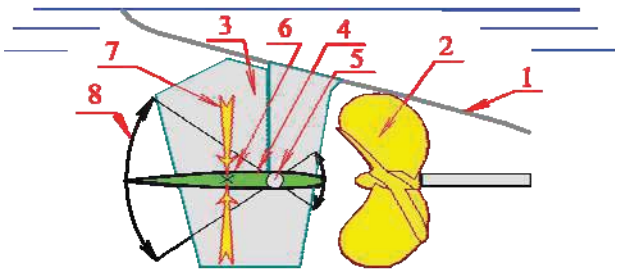

Figure 4 Screw steering system (2, 3) with stabilizing wings (4) - storm emergency propulsion. 1 – the ship's hull; 5 – axis of blow in the stream behind the propeller-driven and allows the elastic rotation of the wings; 6 – the abscissa of summary forces (7) of the heaving motion of a stern extremity; 8 – the turn angles for the plane of stabilizing – propulsion wing.

Hydrodynamic compensation effects on the hull by storm trochoidal waves in deep water is formally responsible solution of the inverse problem of the project is minimal body reaction to external force is well-defined wave nature. If the ship would be under the influence of any other roll and different forces, such as in the circulation; mode porpoise on a wave; or in the zone of cnoidal wave ridges in shallow water; et al., the ship may be subject to unacceptably large angles of roll or different of uncontrollably increasing, with a sweeping flow of water on upper decks on the bow and aft decks; and the like. Assuming that the external forces of nature nonwave have significantly lower intensity may direct opposition to their negative impact with active wing devices to compensate for residual pitch and roll (Patent 2384457, at 2010).

In stormy conditions stabilized in the direction of flow of the water near the ship's hull, going full speed ahead, there is only a flow of working propellers (Figure 4-4). There is also is possible to obtain the greatest moments of forces for active roll stabilization and pitch of the ship in stormy weather on the fast circulation et al.

In case of loss of ship way ahead, the influence of storm waves may there are heave for aft in a large amplitude, which will lead to the wing unit with elastic axis shaft to mode flapping fin propulsion, which auto activating in a dangerous conditions on stormy sailing of the ship with the machine stopped. Passive fin propulsion requires no additional power or control actions on the wing device, and elastic rotation (backlash) on the rudder angle of ± 30 ° to protect the ship from hitting the surface of the water that is no less important and active stabilization mode on the fly pitching ship.

5. GEOMETRIC CREATION OF LINE CONTOURS AND FORM OF THE HULL FOR A NEW SEAFARING VESSEL

The result of research into the historical evolution of shipbuilding, it is possible to formulate the main design features of construction contours and form of the hull of the typical ship and a low-speed vessel, which considering the need to achieve effective navigation in ice and storm on the Far Eastern seas.

Stem and bilge contours of the high-speed surface ship (Figure 5) or relatively low-speed commercial vessel (Figure 6) determine the conditions of preservation of the storm propulsion at arbitrary courses; lessening all kinds of stormy hull motions; prevent dangerous icing upper decks; and to enable autonomous navigation in ice conditions. A large series of computational and towing experiments with models of ships and vessels of different classes, has identified the most important geometric elements and design features of the stem and hull lines in the bow:

– slope to aft (*tumblehome*) or vertical (*plumb*) and arrow-headed stem (Figures 5, 6–3) in the range of variables waterlines when sailing at a moderate sea state (about one-third or one-half of the draught) for non-impact cutting of a stormy waves ridges and rising the edge of breaking ice by ship under way, from the ice fields diving under the bilge or the bottom of the hull;

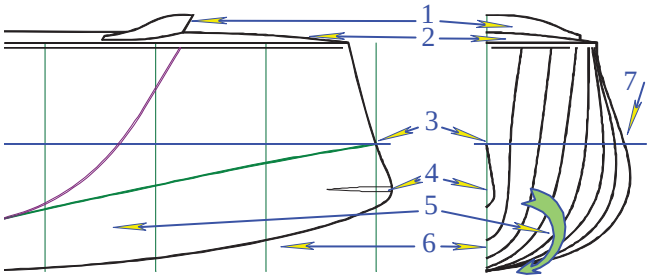

Figure 5 The bow with tumblehome stem of fast ship hull, capable to actively maneuvering in a gale-force winds, stormy waves, and also for autonomous navigation in the ice conditions with average continuity.

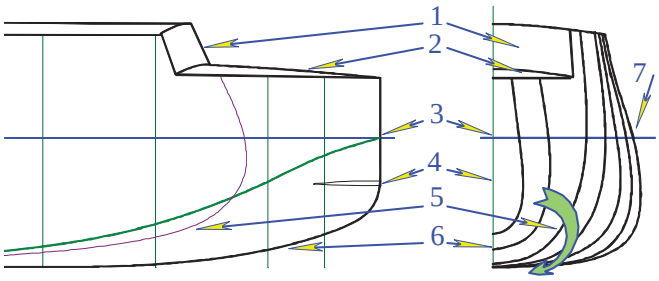

Figure 6 The bow with plumb stem of slow-speed vessel hull, capable to keep a given course with relative slowly way under hurricane-force winds and waves, and for autonomous sailing throw average continuity ice fields.

– stormy undercut at bottom to stem (Figure 5, 6–6) with an average slope of 20°–30° from the keel line, which need to allow free yaw under heavy rolling and pitching with the active movement of the ship on a stormy seaway;

– with a special strengthening of the collision part of stem (Figure 5, 6–4) to an impact load for splitting of medium ice fields on the speed way up to 6 knots, or with immediately stop the ship at speeds up to 3 – 4 knots, with the ability to create maximum force thrust to lower part of large ice floes and ridges, where the ice is warmed up to a temperature of the water, with the vector force on a small rise of the ice edge to prevent of diving an ice fragments to a bilge and under bottom of the ship;

– branches of a bow freeboard frames may have little rake for hydrodynamic compensate of possible burrowing the bow deck under oncoming storm waves ridges for speed movement ship at high speed ahead (Figure 5), or have a tumblehome upper part of the all frame's height contours with descent of connection point with sheerstrake belt under forecastle deck of slow-speed vessels (Figure 6), that is required to compensate for pitching and heaving due to admission to bow deck big flows of water from storm waves ridges;

– wave screen of fast ship (Figure 5-1) and the shelterdeck's superstructure bulkhead of a slow-speed vessel (Figure 6-1) to protect crew on the upper deck of the direct impacts of waves in rough weather;

– at the expense of the bulb-board shell in the range of variables waterplanes (Figure 5, 6-3) creates screw surface on the length of the stem to the area of divergent ship waves breakaway, including comparable in length with external storm waves to tighten the counter-flow

and wave ridges under the bow and bilge bottom of the hull;

– just behind the plot waterlines at diverging ship-waves in break-away zone, can begin a convex bend in the frame's loops to form a boules and tumblehome boards in the middle part of the shiphull (Figure 5, 6–7), that it is necessary for the hydrodynamics compensation of rolling when sailing an arbitrary course relative on storm waves, and also creates the conditions for the repulsion of large ice floes floating under the large around ice fields, and, as a consequence, prevent tightening of ice fragments to the zone with propeller-rudder system at the astern part of the shiphull.

Stern-post, bottom bilge, aft quarter and valance above propeller-rudder system, are arranged in a single or twin-screw in the propulsion options, including the ability to install stabilizers residual pitching and rolling in a stabilized flow directly behind the propeller propellers (Figure 7), and optimized under the terms of the hydrodynamic stabilization running trim at movement in calm water and in heavy storm waves, for which:

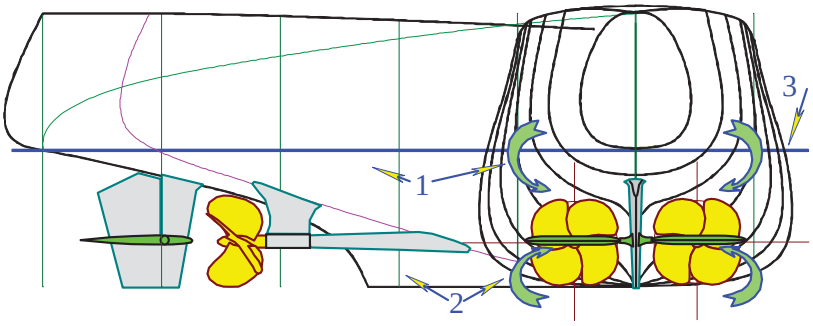

Figure 7 Aft valance, quarter, bottom bilge and stern-post of twin-screw ship, optimized to minimal trim on calm water way

– at the level of a heaving variables waterplanes must created helical surface along from boules on middle board (Figure 7–3) to the astern overhangs (Figure 7–1) for tightening and partial redirection of water flow near the side plating up, thereby compensating cocurrent (hydrostatic) slipstream and break away prevent of the high-frequency component of the ship's wave, followed by the dispersion concentration of wave energy in long-end of the spectrum, with phase shift for damping of interference with the main component of wave – a wave of cross-ship;

– helical surface in variable waterplanes will reduce the volume of the aft freeboard, and natural sharpening shell for cruising ship over astern overhangs, thereby reducing external force by storm waves and corresponding of slowing to heaving and pitching; not least to prevent shock and danger of capture the stern of the ship (*broaching*) by the ridges of ninth waves and especially on dangerous courses to wave moves by slow speed way, and in the case of an emergency loss of moving;

– a pointed cruising stern does not deform hydrodynamic field in storm waves water flows under the aft shell and astern overhangs hull, when stopping the main machinery, which automatically switches from regime of active wing stabilizers for pitching and rolling, to new mode of the passive storm emergency, which thrusters to bring the ship to a safe course of the storm, bringing the total for the device and the shape of the aft end must be optimized in order to maintain control, even at the minimum power, which arises as a result of the elastic reaction on the rudder passive wing propellers;

– on extended from bottom bilge shell to pairing with stern contour must created a second helical surface (Figure 7-2) to the oncoming flow rotation with over waterplanes (supporting) depth, thus allowing for the mutual compensation of the lower and upper flow vorticity in the area aft overhangs and in the scope of the rudder and horizontal stabilizers of residual (non-linear) pitching and rolling of the ship, as well as through the creation of a total vertical component of flow at small distance from the side shell plating is prevented delays in broken ice from the area of on-board bulls in the area aft propeller-steering and stabilizing the complex, including the possibility of creat-

ing a sustainable ice channel at the astern of the ship;

– tumblehome board in the middle of the hull at the level of current waterplane (Figure 7-3) promotes hydrodynamic compensation of the ship rolling, as well as the raised ridge intercepts ship waves ice fields and does not allow them to flooding and diving the area of propeller-rudder system and wing stabilizers under stern overhand.

6. CONCLUSIONS

The paper presents some special engineering solutions for ships and vessels average displacement, showing features of "design target" for storm conditions in the cold polar seas, with options "consistent design" based on matching the experience of good seamanship, navigation practices to achieve efficient and all-weather safe navigation in the precarious waters of the Russian Far East - in the polar latitudes storm the North and South Pacific Ocean, historically successfully develop Sakhalin sailors, fishermen.

Usage target consistent design is characterized by the search for geometric shapes in order to reduce the external power load on the ship from the storm waves, high winds and ice hazards, followed by naturally developing are ship mechanisms, devices, and the appearance of the ship as a whole as it appears in the light engineering the evolution of the best shipbuilding solutions for ocean and coastal fleet – for the effective conduct of offshore operations in specific geographic conditions.

Due to the involvement of competent seafarers to design and build a new and prospective fleet, what allowed to return to seafarers practice a natural concern for the safety of navigation in difficult, storm and emergency conditions using proven captain and boatswain's methods, such as: installation of storm mizzen or staging sea anchor and all other useful nautical fittings to achieve sustainable and safe navigation in all seasons in all meteorological and weather conditions.

7. ACKNOWLEDMENTS

This study summarizes the results of many years of discussion on the creation of contours and ship's architecture and historical perspective ships, covering the time period from the 60s to the ship-modeling studios mentors students in the city of Syzran on the Volga (*Vladimir and Alexander Lagutin, Arkady Aksenov*). followed by the formulation of principles of good seamanship on the authority of mariners and confirmation of the advantages of ships late XIX – early XX centuries from older teachers and navy officers of the Kaliningrad Marine College, insisted on the experimental verification of the historical merits of the steam fleet in the 70s (*Alexander Kamyshev, Gregory Malenko , Dalen Bronstein*). Special gratitude for chair teachers of fluid mechanics and the theory of the ship of the Leningrad Shipbuilding Institute, delivered the first professional seaworthiness experiments for historical views on good-quality design of the ship in the 80s (*Alexander Kholodilin, Walter Amphilokhiev*), and put on the path of the present study thirty years approbation with the sailors and shipbuilders of the Far East of Russia (*Sergey Antonenko, Igor Tikhonov, Nikolai Mytnyk, Sergey Chizhiumov* and *Nikolay Taranukha* et al.), and then - St. Petersburg (Sergey Krolenko, Alexander Promyslov and Alexander Degtyarev).

8. REFERENCES

Khramushin V. N. Exploratory studies of storm seaworthiness of the ship (History of evolutionary engineering solutions and architecture of the contours of the ship, of the unity of marine science and good seamanship). Lambert Academic Publishing, Germany. (2011-01-20). 288 c, in Russian: ShipDesign.ru/Khram/History-II.pdf

Khramushin V. Key Design Solutions and Specifics of Operation in Heavy Weather (Fluid Mechanics Approach to Stabilization of Ship in Heavy Seas) // Proceedings. 10th International Conference on Stability of Ships and Ocean Vehicles. STAB-2009, June 22-26, 2009. S-Petersburg, Russia. P. 473-482. ShipDesign.ru/Khram/Art/STAB2009-eng.html

Khramushin V. N. Ship without rolling in rough seas. Patent 2360827 on July-10, 2009. ShipDesign.ru/Invent/01.html

Khramushin V. N. Ship without pitching under way on seaway. Order for invention № 2007133625, 2007.09.07, Bull.N 8 on 2009.03.20. Shipdesign.ru/Invent/02.html

Khramushin V. N. Active stabilizer pitching and rolling of the ship - a storm emergency propulsion. Patent number 2384457 to 2010.03.20. Shipdesign.ru/Invent/04.html

This page is intentionally left blank

Session 12.3 – INSTABILITY OTHER THAN ROLL MOTION

Prediction of Parametric Rolling of Ships in Single Frequency Regular and Group Waves

Probabilistic Response of Mathieu Equation Excited by Correlated Parametric Excitation

Coupled Simulation of Nonlinear Ship Motions and Free Surface Tanks

Modelling Sailing Yachts Course Instabilities Considering Sail Shape Deformations

This page is intentionally left blank

Prediction of Parametric Rolling of Ships in Single Frequency Regular and Group Waves

Shukui Liu, *National Technical University of Athens*, liushukui@deslab.ntua.gr

Apostolos Papanikolaou, *National Technical University of Athens*, papa@deslab.ntua.gr

ABSTRACT

In this paper, a 3D nonlinear time domain numerical simulation method, which is based on the impulse response function concept, is applied to the investigation of parametric rolling of the ITTC-A1 ship. During the simulation, the hydrodynamic coefficients are determined by 3D panel code on the basis of linear potential theory, whereas several nonlinear terms are considered in the equations of motion, such as the excitation by large amplitude waves, the exact restoring forces and moments resulting from the actual wetting of the ship hull geometry and the semi-empirical nonlinear viscous damping. In addition, nonlinear inertia terms are retained when considering motions of large angles. The parametric rolling of the ship is predicted by simulating 6 degree of freedom (DoF) nonlinear motions in response to single frequency regular waves and triple frequency group waves. The obtained numerical results are compared with corresponding experimental measurements and good agreement has been observed.

Keywords: *numerical simulation, parametric resonance, roll motion, non-linear dynamics, ship safety*

1. INTRODUCTION

Parametric rolling is the induced roll motion of a ship due to the periodic change of the restoring characteristics as the ship advances in waves. This phenomenon is often observed on ships with excessive bow flares and very flat sterns, such as modern containerships, car carriers etc. Typically it takes place when the wave frequency of encounter is close to twice of the natural roll frequency of the ship and near the heave/pitch resonance frequency. Under such condition, the occurrence of the parametric roll phenomenon, which is a strongly nonlinear oscillatory motion phenomenon, is actually subject to the incident wave amplitude, the ship's loading condition, ship's speed and roll damping feature.

The prediction of parametric rolling has high practical value, as it can lead to not only the loss of cargo, but also to the loss of the ship, thus it is an important safety issue already considered in IMO regulations (Peters et al, 2011). It is, also, a popular research subject, because of the complexity of the associated nonlinear ship dynamics and hydrodynamic phenomena; thus the correct prediction of parametric rolling, in terms of likelihood of *occurrence and resulting roll amplitude*, in regular waves and irregular seas remains a challenge to state-of-the-art numerical simulation methods and software tools.

The investigation of parametric rolling by numerical and experimental methods has a long history, dating back to the 1930s (see Paulling, 2006 for historical review). The phenomenon attracted special interest only in the last few decades with the serious accidents on large

ships, for instance, the containership APL CHINA casualty in 1998 (France et al, 2003).

Several approaches are being employed to analyze and understand the parametric roll phenomenon, ranging from the uncoupled, one degree of freedom non-linear roll equation, adjusted with appropriate parameters, for instance, Paulling (1961), Francescutto (2002), Umeda et al. (2003), to models of multi degrees of freedom, where the roll motion and ship hydrodynamics are appropriately coupled with the other degrees of freedom, Ribeiro et al. (2005), Neves, (2005), Krueger (2006), Spanos and Papanikolaou (2006). Parametric rolling has been investigated for both regular and irregular seaways (Belenky, 2003), as well as for following and head seas conditions. A thorough review of the related literature has been carried out by ITTC (2005).

In this paper, a nonlinear time domain method based on the impulse response function concept (Liu et al., 2014), is applied to the simulation of parametric rolling. This method has been developed (independently of earlier work by Spanos and Papanikolaou, 2006) at the Ship Design Laboratory of National Technical University of Athens in the frame of NTUA-SDL's HYBRID software system, aiming to facilitate the analysis of the seakeeping performance and safety of ships in complex environmental and/or adverse sea conditions. In the framework of potential theory, the wave excitation is decomposed into Froude-Krylov, radiation and diffraction forces. Incident wave forces (both hydrodynamic and hydrostatic parts) are calculated through direct integration of the corresponding pressures over the instantaneous wetted surface, which is defined by the undisturbed incident wave and the instant position of the ship. The radiation forces are calculated using the added mass and damping coefficients calculated by a 3D frequency domain code NEWDRIFT (Papanikolaou et al. 1985, 1990) and transformed in the time domain by application of the impulse response function concept. Diffraction forces are obtained in a similar manner, using corresponding results obtained by NEWDRIFT. Solving the six coupled nonlinear integro-differential equations of motion by a time integration method, the six DOF motions of the ship are obtained in the time domain.

2. MATHEMATICAL MODEL

In order to study the nonlinear ship motion problem, three coordinate systems are defined: the earth-fixed *OXYZ* system, a system *O'X'Y'Z'* travelling with the mean ship speed, always parallel to *OXYZ* and a body-fixed *Gxyz* system, with its origin *G* at the center of gravity. It is assumed that at t=0 both *O* and *O'* coincide with *G*. The two coordinate systems, *O'X'Y'Z'* and *Gxyz* are connected by the three Euler angles: θ (roll), ψ (pitch), and φ (yaw). If *O'X'Y'Z'* is rotated by the three Euler angles, it becomes parallel with *Gxyz*. The order of rotation is θ, ψ, and φ. A vector $\vec{x}$ in the *Gxyz* system may be expressed as $\vec{X}'$ in *O'X'Y'Z'* system as follows:

$$\vec{X}' = \mathbf{T}\vec{x} \qquad \textbf{(1)}$$

where **T** is the transformation matrix:

$$\mathbf{T} = \begin{bmatrix} \cos\psi\cos\phi & \sin\theta\sin\psi\cos\phi - \cos\theta\sin\phi & \cos\theta\sin\psi\cos\phi + \sin\theta\sin\phi \\ \cos\psi\sin\phi & \sin\theta\sin\psi\sin\phi + \cos\theta\cos\phi & \cos\theta\sin\psi\sin\phi - \sin\theta\sin\phi \\ -\sin\psi & \sin\theta\cos\psi & \cos\theta\cos\psi \end{bmatrix} \qquad \textbf{(2)}$$

The ship is assumed travelling on the free-surface with a mean speed $\vec{V}_{O'} = [U,0,0]^{\mathrm{T}}$ parallel to the *OX* axis, subject to incident regular waves. The location of the ship in the *OXYZ* system is expressed by the location of the center of gravity (*G*) and the three Euler angles. The location of the center of gravity is defined by $\vec{X}_G(t) = [X_G(t), Y_G(t), Z_G(t)]^{\mathrm{T}}$ and it's velocity $\vec{V}_G(t)$ by the time derivative of $\vec{X}_G(t)$. The relationship between the absolute velocity of the ship and the relative velocity (both

expressed in the earth-fixed coordinate system) is:

$$\vec{V}_G^R = \vec{V}_G - \vec{V}_{O'} = \vec{V}_G - [U,0,0]^T \quad \textbf{(3)}$$

The angular velocities about the ship-fixed coordinate axes given by $\vec{\omega}$ are related to the time derivatives of the Euler angles as follows:

$$\vec{\omega} = \begin{bmatrix} \omega_1 \\ \omega_2 \\ \omega_3 \end{bmatrix} = \begin{bmatrix} 1 & 0 & -\sin\psi \\ 0 & \cos\theta & \sin\theta\cos\psi \\ 0 & -\sin\theta & \cos\theta\cos\psi \end{bmatrix} \begin{bmatrix} \dot{\theta} \\ \dot{\psi} \\ \dot{\phi} \end{bmatrix} = \mathbf{B} \begin{bmatrix} \dot{\theta} \\ \dot{\psi} \\ \dot{\phi} \end{bmatrix} \quad \textbf{(4)}$$

where:

$$\mathbf{B} = \begin{bmatrix} 1 & 0 & -\sin\psi \\ 0 & \cos\theta & \sin\theta\cos\psi \\ 0 & -\sin\theta & \cos\theta\cos\psi \end{bmatrix} \quad \textbf{(5)}$$

Let $\vec{a}_G$ be the (total) acceleration vector of the center of gravity *G*, expressed in the body-fixed system; $\vec{a}_G$ may be expressed as follows:

$$\vec{a}_G = \dot{\vec{v}}_G + \vec{\omega} \times \vec{v}_G \quad \textbf{(6)}$$

The first term in the above equation corresponds to the rate of change of the translational velocity of the ship, while the second one takes into account the effect of rotation of the body-fixed coordinate system.

The equations of motion are given by application of Newton's second law:

$$m(\dot{\vec{v}}_G + \vec{\omega} \times \vec{v}_G) = \vec{F} \quad \textbf{(7)}$$

$$\mathbf{I}\dot{\vec{\omega}} + \vec{\omega} \times \mathbf{I}\vec{\omega} = \vec{M} \quad \textbf{(8)}$$

In the above equations, the external forces and moments are expressed in the body-fixed system of coordinates and they consist of the gravitational, radiation, diffraction, incident wave force, restoring forces and possible viscous terms, while **I** is the moment of inertial matrix of the ship.

2.1 Diffraction forces

For weakly nonlinear motions, assuming the ship in the upright/mean position when calculating the diffraction forces due to the incoming waves is a reasonable approach. However, as the motions increase and particularly when the dimensions of the ship are small compared to the wave length (e.g. the case of a small boat in large waves), the effect of the oscillatory ship motions on the diffraction forces increases, and their calculation assuming the ship at its instantaneous position may be considered. On the other hand, in this latter case, diffraction effects will tend to zero, due to the small disturbance to the incoming waves, caused by the presence of the ship.

In the current study, diffraction forces and moments are calculated assuming the ship in the upright/mean position using the velocity potential results obtained by NEWDRIFT. This code is based on a 3D panel method for the evaluation of the responses (ship motions, structural loads and drift forces) of arbitrarily shaped marine structures and shiplike bodies subject to the excitation of incident regular waves; it has been widely benchmarked over the last 35 years and applied to a variety of problems and ship types by marine industry professionals and university researchers. NEWDRIFT was initially developed for the zero speed case (Papanikolaou, 1985), based on the distribution of zero-speed pulsating Green sources over the mean wetted body surface to express the radiation and diffraction potentials and was subsequently extended to the case of shiplike bodies advancing with forward speed in waves (Papanikolaou et al. 1990).

2.2 Incident wave forces

The Froude-Krylov and restoring forces/moments are calculated by integrating the pressure over the *instantaneous* wetted surface of the ship. The incident wave pressure

is herein defined by the sum of linear dynamic pressure and hydrostatic pressure:

$$p = -\rho \frac{\partial \Phi_I}{\partial t} - \rho g Z \qquad \textbf{(9)}$$

According to the linear wave theory, the dynamic pressure is assumed constant from the mean free surface to the actual free surface, whereas the hydrostatic component increases linearly from zero at the actual water surface and is being added to the dynamic component.

2.3 Radiation forces

Following Cummins (1962), the radiation forces and moments in the body-fixed coordinate system are evaluated by:

$$F_i(t) = -\sum_{j=1}^{6}\left[A_{ij}\dot{v}_j + \int_0^t L_{ij}(t-\tau)v_j(\tau)\mathrm{d}\tau \right] \quad i = 1 \sim 6 \qquad \textbf{(10)}$$

where A_{ij} are the added mass coefficients, v_j stand for the velocities of the ship in 6DOF, while the kernel functions L_{ij} may be calculated from the damping coefficients B_{ij}:

$$L_{ij}(\tau) = \frac{2}{\pi}\int_0^\infty B_{ij}(\omega)\cos\omega\tau\,\mathrm{d}\omega \qquad \textbf{(11)}$$

The added mass and damping coefficients appearing in (10) and (11) are calculated by NEWDRIFT.

2.4 Time domain integration

In order to smoothly introduce the incident wave disturbance into the numerical scheme and to mitigate the effect of initial transients on the steady response to an incident regular wave, the velocity potential of the incident wave is defined as following:

$$\Phi_0 = \frac{g\zeta}{\omega} e^{kz} \sin\left[k(x\cos\beta + y\sin\beta) - \omega t\right] \qquad \textbf{(12)}$$

$$\zeta = \begin{cases} \zeta_a \left[\frac{1}{2}\left(1 - \cos\frac{t\pi}{nT}\right)\right]^2 & t < nT \\ \zeta_a & t \geq nT \end{cases} \qquad \textbf{(13)}$$

where ω is the wave frequency, ζ_a the wave amplitude, k the wave number, β the angle of incidence (with 180deg corresponding to head waves) and n is a pre-defined integer parameter.

During the numerical simulation of the motion of the ship, the determination of the instantaneous wetted surface, considering the ship motions as well as the actual wave elevation is required. This is done according to the following procedure:

1. Prepare a panelization for the ship, including the part of the outer shell above the waterline, up to and including the deck;

2. At each time instant, check the position of each panel in relation to the instantaneous wave surface, mark the panels that are fully wetted, partially wetted, or non-wetted;

3. The non-wetted panels are skipped. Regarding the partially wetted panels, if only one node is immerged, a new triangular panel will be formed; if 2 nodes are immerged, a new rectangular panel will be formed; if 3 nodes are immerged, the wetted area will be split into 2 panels.

3. THE EXPERIMENT

In order to investigate the occurrence of roll resonance and its dependence on the basic parameters of the problem, tank tests have been conducted within SAFEDOR project for the validation of numerical simulation methods in an international benchmark study, coordinated by NTUA-SDL (Spanos and Papanikolaou, 2009).

This benchmark study was based on parametric roll investigations of the

standardized containership ITTC-A1. The principal particulars and body plans of these ships are shown in Table 1 and Figure 1. The two ship loading conditions investigated are shown in Table 2, while in Table 3 the matrix of simulated tests which will be described and discussed in the following section is presented.

The ship model has been investigated with a constant forward speed in head waves. The model was free to move in 3 DoF, namely, in heave, roll and pitch. Tests were independent of any course keeping mechanism. The model was tested both in regular and irregular waves. Free decay tests were also performed in order to evaluate the damping properties of the ship model. The motion of the model, the restraining forces and moments and the wave elevation have been measured. This type of semi-captive tests can be considered "ideal" for the benchmarking of numerical simulation methods (even deviating from the actual, free to move ship performance), as the uncertainties related to the speed and course keeping are suppressed. The experimental results as well as the numerical results of the benchmark study have been extensively reported by Spanos D. (2009) within SAFEDOR framework.

Table 1 Main Particulars of ITTC-A1 ship

Items	***Ship***
length : L_{pp}	150.0 m
breadth : B	27.2 m
depth : D	13.5 m
draught at FP : T_f	8.5 m
mean draught : T	8.5 m
draught at AP : T_a	8.5 m
block coefficient : C_b	0.667
prismatic coefficient : C_p	0.678
water plane coefficient : C_w	0.787
wetted surface area : S	5065 m^2

Table 2. Loading conditions tested in benchmark study

Tests 01 ~ 11	GM	=	1.38 m
	i_{xx}	=	10.33 m
	i_{yy}	=	37.5 m
Tests 12 ~ 22	GM	=	1.00 m
	i_{xx}	=	10.33 m
	i_{yy}	=	38.2 m

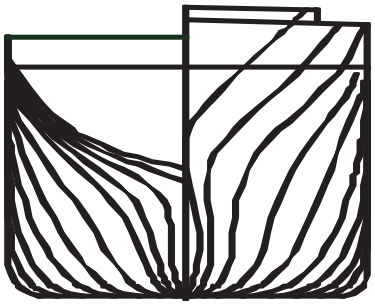

Figure 1. Body plan of ITTC-A1 Ship

Table 3. Matrix of simulated tests from SAFEDOR benchmark study

TEST	GM (m)	Heading (deg)	Fn	H (m)	T (sec)	Comment
T01	1.38	180	0.00	-	-	Roll decay
T02	»	»	0.08	3.6	10.63	Regular
T03	»	»	»	5.7	»	»
T04	»	»	0.12	3.6	»	»
T05	»	»	»	5.7	»	»
T06	»	»	»	2.4 2.4 2.4	10.63 9.66 11.55	Group
T07	»	»	»	4.0 1.0 1.0	10.63 9.66 11.55	»
T09	»	160	»	3.6	»	Regular
T10	»	»	»	5.7	»	»
T11	»	»	»	4.0 1.0 1.0	10.63 9.66 11.55	Group
T20	1.00	180	0.08	5.0	12.12	Regular
T21	»	»	0.12	5.0	»	»
T22	»	»	0.08	4.0 1.0 1.0	12.12 10.77 13.47	Group

4. NUMERICAL RESULTS AND DISCUSSION

In this section we apply the 6 DoF model described, outlined in section 2, to the simulation of parametric rolling phenomenon.

Before proceeding to the parametric rolling simulation, it is necessary to calibrate the roll damping and gyration properties of the model according to the decay test results. Figure 2 shows the tuned decay simulation for Test 01. Using this result, the actual roll viscous damping may be adjusted, as well as the radius of gyration.

For simulating the parametric roll phenomenon in a longitudinal, symmetric wave load condition, we need to introduce a small roll disturbance (by a small initial roll displacement of 1-2 degrees), upon the excitation of which the ship will start rolling with a continuously decreasing roll amplitude, unless the condition for the occurrence of a parametric roll instability is met. This initial disturbance corresponds in practice to the excitation by a sudden side wind or other acting transverse force, while the ship is sailing in exactly head or following sea condition.

When analysing the roll amplitude time records, the mean roll amplitude of the stationary response is used for the quantification of the performance of the numerical method in terms of the predictability of the roll motion magnitude, which is the mean value of successive amplitudes.

Figure 3 shows the overall results for the mean roll amplitude from the present method against the tank tests. In general, numerical predictions of the roll amplitude are consistently higher than experimentally measured amplitudes. Examining the testing conditions, it is noted that going from Test 02 to Test 03, or from Test 04 to Test 05, or from Test 09 to Test 10, the only difference has been the *increase of wave amplitude*, while the wave frequency remained the same. The results for such an *increase of incident wave amplitude* were the *decrease of resonance amplitude*, both in the experimental and numerical simulation. *This is a clear indication of a rare nonlinear motion phenomenon, for which an increase of the excitation amplitude leads to a decrease of the response amplitude* (or even to zero response, see Spanos D. and Papanikolaou A. 2009b). Commenting on conducted Test 20 and Test 21, the only difference in testing conditions is the increase of speed from Fn=0.08 to Fn=0.12; this change has induced the disappearance of the roll resonance, as could be also numerically predicted.

Figure 4-11 show the time histories and tank results of several test cases. It is observed that for regular waves, after the initial transient time (depending on the numerical set-up), the ship response is fully developed and a stationary rolling behaviour (constant amplitude) is achieved. Another observation is that the period of roll resonance is twice that of the encounter wave period, which shows the essentially different mechanism of the parametric rolling from a normal (prime resonance) rolling motion excited by incident waves.

At last in Figure 12 the mean roll amplitude results based on the present method are plotted against the simulations of the four best performing methods from the SAFEDOR benchmark study together with the experimental data (full diamond symbols). Interestingly the present method correctly simulated the outcome of Test 21, where no parametric rolling has been observed in tank test, but even the four best performers of SAFEDOR benchmark participants failed to properly simulate it. Comparing the conditions for Test 20 and Test 21, which only differ slightly with respect to ship's speed of advance, but are associated with the initiation of parametric rolling or not, it proves that the sensitivity of prediction methods with respect to the ensuing parameters is very crucial for the reliable prediction if the parametric roll phenomenon.

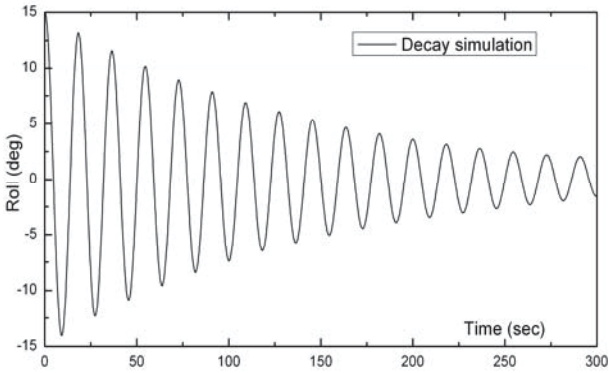

Figure 2. Roll decay simulation GM=1.38m

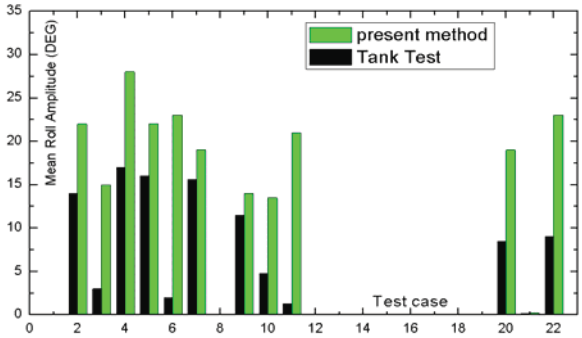

Figure 3. Predicted mean roll amplitude by present method against the experimental results

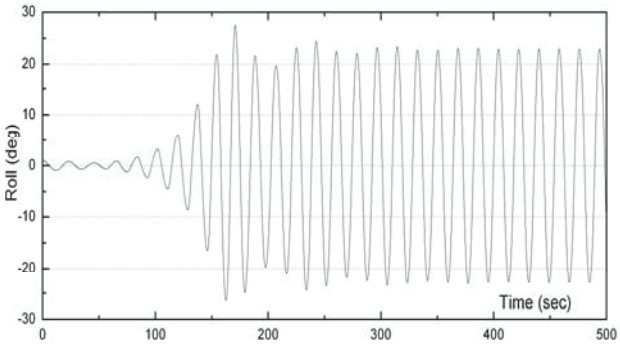

Figure 4. Simulated roll angle history, Test 02

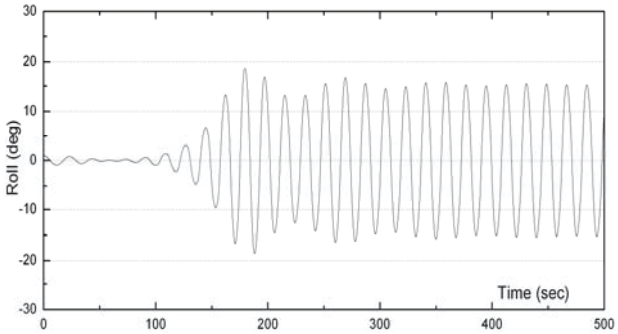

Figure 5. Simulated roll angle history, Test 03

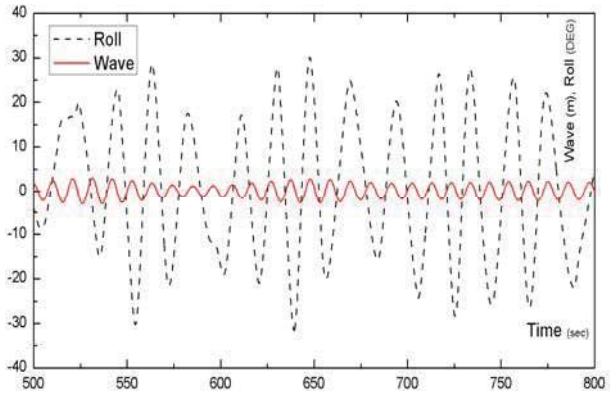

Figure 6.Time history of roll angle simulation in test case T07, head sea, group wave

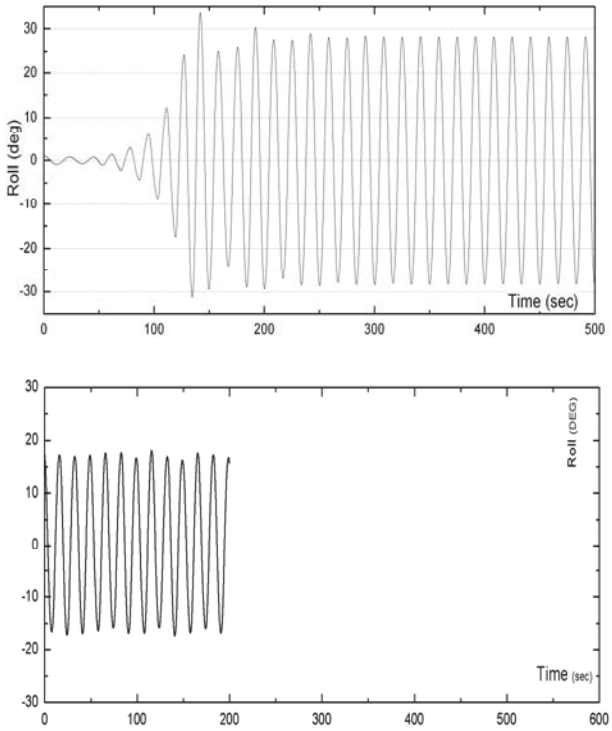

Figure 7. Time history of roll angle of Test 04, simulation (above) vs experiment (below)

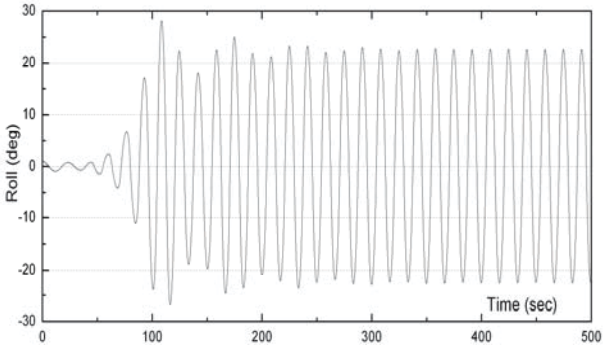

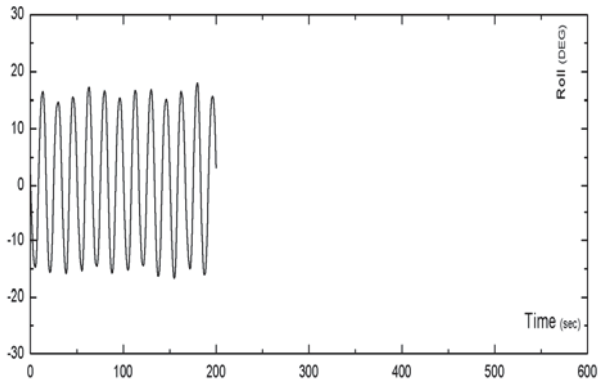

Figure 8. Time history of roll angle of Test 05, simulation (above) vs experiment (below)

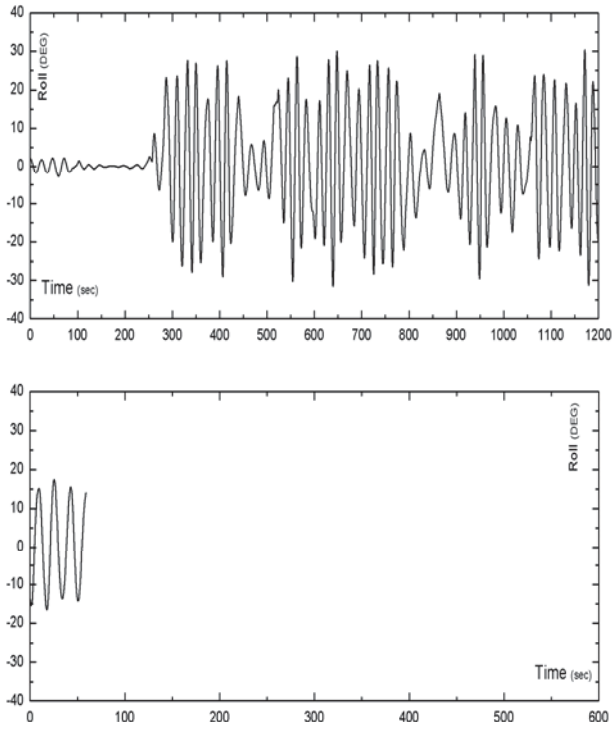

Figure 9. Time history of roll angle of Test 07, simulation (above) vs experiment (below)

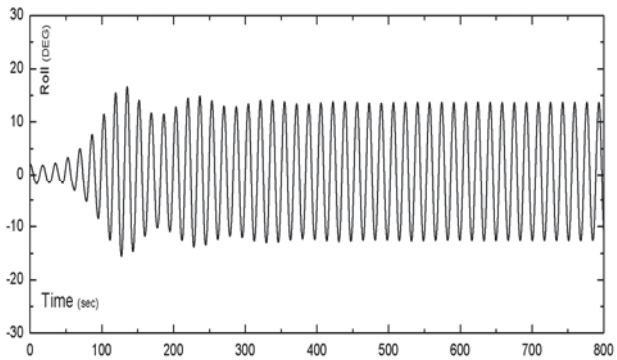

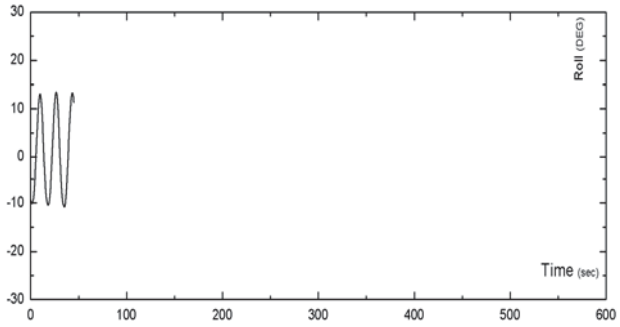

Figure 10. Time history of roll angle of Test 09, simulation (above) vs experiment (below)

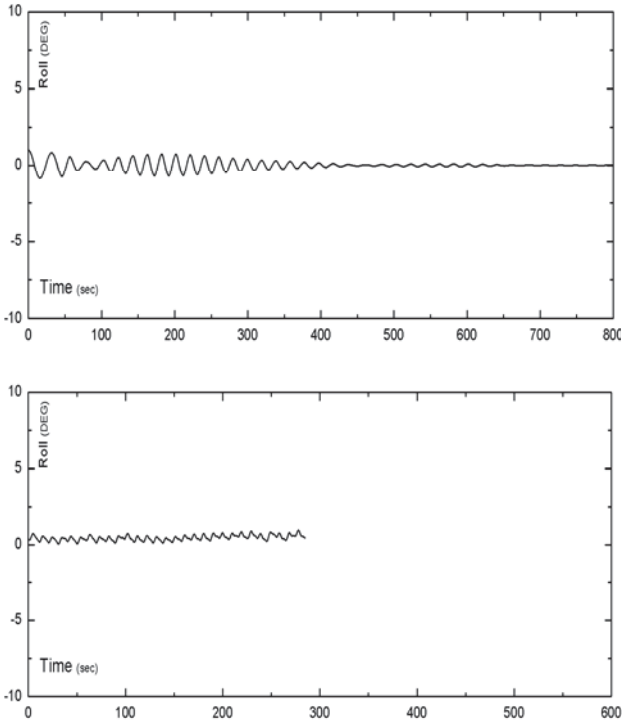

Figure 11. Time history of roll angle of Test 21, simulation (above) vs experiment (below)

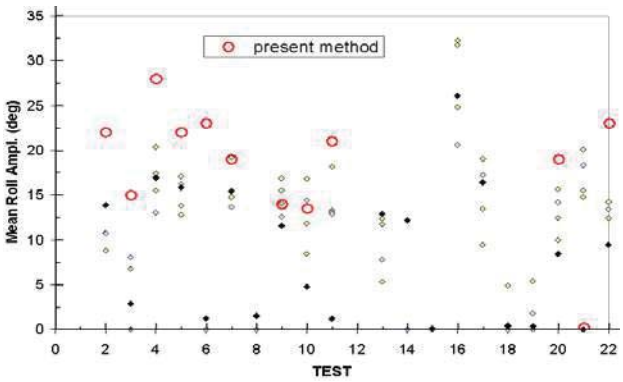

Figure 12 Mean roll amplitude as estimated from current method and the best performing

(four) methods of SAFEDOR benchmark, as well as experimental results

5. CONCLUSIONS

The prediction of parametric roll resonance is inherently a difficult subject, as revealed by the large scattering of numerical results presented in the SAFEDOR benchmark study. Hence it is a good test case for any under development numerical method and software tool to test its performance in such conditions. The quality of the numerical results should be judged by two criteria, as suggested by the SAFEDOR benchmark study:

1. Is the occurrence of resonance correctly captured?

2. Is the amplitude correctly predicted?

Based on these two criteria, we may draw a preliminary conclusion regarding the performance of the herein presented method.

1. The current method has been successfully applied to the prediction of parametric rolling phenomenon of ships in regular waves and triple-frequency group waves. For the 8 tested regular wave cases and 4 tested triple-frequency group wave cases, parametric rolling phenomenon has been correctly predicted in all tested cases (100%).

2. The importance of proper prediction in triple frequency wave group excitation is highlighted, noting that the predictability of parametric roll in natural irregular seas is inherently related to the occurrence of dominating wave groups within the multi-frequency wave ensemble.

3. The amplitude of roll resonance has been in general over-predicted. This is due to the employed linear viscous roll damping model. Despite this, the fact is, as shown in Test Cases 2 3, Test Case 4 and 5, that the gradient of predicted amplitude change against the incident wave amplitude, has been correctly captured.

3. The correction of the potential theory linear damping by an equivalent viscous damping that may be deduced from roll decay tests, appears to have little effect on the correct prediction of the parametric rolling amplitude. Hence, it is advisable to test higher order roll damping models and to consider in addition the enhanced damping in other modes of motion (heave and pitch), before concluding.

6. ACKNOWLEDMENTS

The work presented in this paper is supported by the Collaborative Project (Grant Agreement number 605221) SHOPERA (Energy Efficient Safe **SH**ip **OPERA**tion) co-funded by the Research DG of the European Commission within the RTD activities of the FP7 Thematic Priority Transport / FP7-SST-2013-RTD-1/ Activity 7.2.4 Improving Safety and Security / SST.2013.4-1: Ships in operation. The European Community and the authors shall not in any way be liable or responsible for the use of any knowledge, information or data of the present paper, or of the consequences thereof. The views expressed in this paper are those of the authors and do not necessary reflect the views and policies of the European Community.

7. REFERENCES

Cummins, W., 1962, “The impulse response function and ship motions”, Journal Schiffstechnik, Vol. 9, no. 47, pp. 101-109.

France W. N., Levadou M., Treakle T. W., Paulling J. R., Michel R. K., Moore C. (2003), “An investigation of head-sea

parametric rolling and its influence on container lashing systems", Marine Technology, *40*(1), 1-19.

Francescutto, A., Bulian G., 2002, Nonlinear and Stochastic Aspects of Parametric Rolling Modeling., Proceedings of International Ship Stability Workshop, Webb Institute, USA.

ITTC, The specialist committee on Stability in Waves, 2005, Final report and recommendations to the 24th ITTC.

Krueger S., Kluwe, F., 2006, "Development of Dynamic Stability Criteria from Direct Seakeeping Simulations", Proc. of the 9th Inter. Marine Design Conference, Ann Ardor, USA.

Liu S., Papanikolaou A. and Zaraphonitis G., 2014, "Time domain simulation of nonlinear ship motions using an impulse response function method", Proceeding of ICMT2014, 7th-9th July, Glasgow, UK

Neves M. A. S. and Rodriguez C.A., 2005, "Stability Analysis of Ship Undergoing Strong Roll Amplifications in Head Seas", Proceedings of the 8th International Ship Stability Workshop, Istanbul, Turkey.

Papanikolaou A., 1985, "On Integral-Equation-Methods for the Evaluation of Motions and Loads of Arbitrary Bodies in Waves," Journal Ingenieur - Archiv., 55:17-29.

Papanikolaou A. and Schellin Th., "A Three Dimensional Panel Method for Motions and Loads of Ships with Forward Speed", Journal Schiffstechnik - Ship Technology Research, Vol. 39, No. 4, pp.147-156,1992

Papanikolaou A. and Spanos D., 2008, "SPECIFICATION OF SAFEDOR BENCHMARK SHIP MODEL TESTS", Rev.00, SAFEDOR technical document.

Peters W., Belenky V., Bassler C., Spyrou K. J., Umeda N., Bulian G. and Altmayer B., 2011, "The Second Generation Intact Stability Criteria: An Overview of Development", SNAME Transactions, 121, Houston.

Paulling J. R., 1961, "The transverse stability of a ship in a longitudinal Seaway", Journal of Ship Research, V 4:4

Paulling J. R., 2006, "Parametric resonance in head seas – Then and Now", Proc. 9th International Conference on Stability of Ships and Ocean Vehicles, Rio de Janeiro-Brazil

Spanos D., 2009, "SAFEDOR International Benchmark Study on Numerical Simulation Methods for the Prediction of Parametric Rolling of Ships in Wave", Document Id. SAFEDOR-R-7.3.9-2009-02-13

Spanos D., Papanikolaou A., 2006a, "Numerical Simulation of a Fishing vessel in Parametric Roll in Head Seas", Journal of Marine Systems & Ocean Technology, SOBENA, Vol. 2, No. 1-2, pp. 39-44.

Spanos D. and Papanikolaou A., 2006b, "Numerical Simulation of Parametric Roll in Head Seas", Proc. 9th International Conference on Stability of Ships and Ocean Vehicles, Rio de Janeiro-Brazil

Spanos D. and Papanikolaou A., 2009a, "Benchmark Study on Numerical Simulation Methods for the Prediction of Parametric Roll of Ships in Waves", Proceedings of the 10th International Conference on Stability of Ships and Ocean Vehicles, St. Petersburg, Russia

Spanos D., Papanikolaou A., 2009b, "On the Decay and Disappearance of Parametric Roll of Ships in Head Steep Waves", Proc. 10th International Conference on Stability of Ships and Offshore Vehicles, St. Petersburg, Russia,.

Umeda N., 2001, "Final Report on the benchmark tests for intact ships (Ships A-1 & A-2)", ITTC Specialist Committee on Prediction of Extreme Ship Motions and Capsizing.

Umeda N., Hashimoto H., Vassalos D., Urano S., Okou K., 2003, "Nonlinear Dynamics on Parametric Roll Resonance with Realistic Numerical Modeling", Proc. of 8th Inter. Conference on the Stability of Ships and Ocean Vehicles STAB03.

This page is intentionally left blank

Proceedings of the 12th International Conference on the Stability of Ships and Ocean Vehicles, 14-19 June 2015, Glasgow, UK.

Probabilistic Response of Mathieu Equation Excited by Correlated Parametric Excitation

Mustafa A. Mohamad, *Massachusetts Institute of Technology*,

Themistoklis P. Sapsis, *Massachusetts Institute of Technology*,

Abstract

We derive analytical approximations for the probability distribution function (pdf) for the response of the Mathieu equation with random parametric excitation at the main resonant frequency. The inclusion of stochastic excitation renders the otherwise straightforward response into a system exhibiting intermittent resonance. Due to the random amplitude term the system may momentarily cross into the instability region, triggering an intermittent system resonance. As a result, the statistics of the response are characterized by heavy-tails. We develop a mathematical approach to study this problem by conditioning the density of the system response on the occurrence of an instability, and analyze separately the stable and the unstable regimes.

Keywords: *Mathieu equation, random excitation, heavy-tails quantification, intermittent instabilities.*

1 INTRODUCTION

In this work we consider a Mathieu type stochastic differential equation of the form

$$\ddot{x}(t) + 2\varepsilon\zeta_0\omega_0\dot{x}(t) + \omega_0^2(1 + \varepsilon\beta(t)\sin\Omega t)x(t) = \sqrt{\varepsilon}\xi(t), \quad (1)$$

where ζ_0 is the damping ratio, ω_0 is the undamped natural frequency of the system, Ω is the frequency of the harmonic excitation term and $\beta(t)$ its (random) amplitude, ε is a small positive parameter, and $\xi(t)$ is a broadband weakly stationary random excitation. It is well known that the Mathieu equation

$$\ddot{x}(t) + 2\zeta_0\omega_0\dot{x}(t) + \omega_0^2(1 + \lambda\sin\Omega t)x = 0, \quad (2)$$

displays instability due to resonance depending upon the parametric excitation frequency and amplitude parameters in the (Ω, λ) plane. Near $\Omega/2\omega_0 = 1/n$ for positive integers n, we have regions of instabilities, with the widest instability region being for $n = 1$. Damping has the effect of raising the instability regions from the $\Omega/2\omega_0$ axis by $2(2\zeta)^{1/n}$. Therefore, for $\zeta \ll 1$ the instability region near $n = 1$ is of greatest practical importance (Lin & Cai, 1995, Nayfeh & Mook, 1984). In the following we consider (1) tuned to the important resonant frequency $\Omega = 2\omega_0$. The case, where the frequency is slightly detuned can be generalized following exactly the same approach, but for simplicity of the presentation we consider no detuning. In realistic systems the parameter λ in (2) that controls the stability of the system for a fixed Ω and ζ_0 may be a random quantity and not necessarily deterministic. If this is the case, intermittent resonant instabilities may occur due to the randomly varying parameter $\beta(t)$ in (1) crossing momentarily into the instability region which induces a short-lived large amplitude spike in the response after which the system is relaxed back to its stable response (Fig. 1). In other words, we are interested in the case where $\beta(t)$ is on average stable, but can momentarily transition into the instability region due to randomness. From an applications standpoint ignoring randomness in

$\beta(t)$, woud severely underestimate the probability for extreme events since the corresponding averaged equation would lead to Gaussian statistics, whereas the original system features heavy-tailed statistics. It is the purpose of this work to quantify the probabilistic response of (1), in other words the probability distribution function (pdf), for the case when $\beta(t)$ is a random quantity. The strategy we employ utilizes a decomposition of the probabilistic system response into stable and unstable regimes, which are then individually analyzed and combined to construct the full distribution of the response.

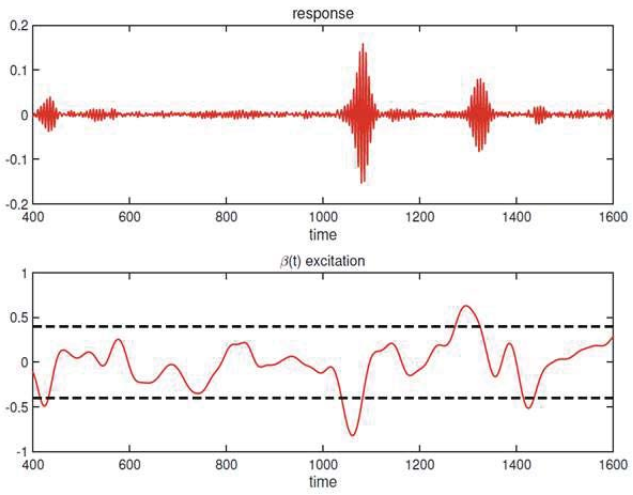

Figure 1 Sample realization of the Mathieu equation (3) (top). The parametric amplitude stochastic excitation term β(t) (bottom) triggers intermittent resonance when it crossing above or below the instability threshold (dashed lines).

2 PROBLEM STATEMENT

We consider the following equation

$$\ddot{x}(t) + 2\zeta_0\omega_0\dot{x}(t) + \omega_0^2(1 + \beta(t)\sin 2\omega_0 t)x(t) = \xi(t), \qquad (3)$$

where it is understood that the order of the terms are as in (1), $\xi(t)$ is a broadband weakly stationary excitation, and $\beta(t)$ is a correlated weakly stationary Gaussian process. To derive the probability distribution of (3) the standard approach is by a coordinate transformation to a pair of slowly varying variables and then to apply the stochastic averaging procedure to arrive at a set of Ito stochastic differential equations for the transformed coordinates. The Fokker-Plank equation can then be used to solve for the response pdf (Lin & Cai, 1995, Floris 2012). This standard approach, applied to the problem (3) leads to Gaussian statistics. In reality, randomness in the amplitude $\beta(t)$ leads to intermittent parametric instabilities, and therefore non-Gaussian statistics. To account for the statistics due to intermittent events triggered by $\beta(t)$ we decompose the probabilistic system response into the stable regime and unstable regime according to

$$\mathbf{P}(X) = \mathbf{P}(X \mid \text{stable regime})\mathbf{P}(\text{stable regime}) + \mathbf{P}(X \mid \text{unstable regime})\mathbf{P}(\text{unstable regime}), \qquad (4)$$

and derive the corresponding distributions for each term in (4). We assume that instabilities are statistically independent so that the decomposition is applicable; in other words that the frequency of $\beta(t)$ crossing into the instability region is sufficiently rare. We remark that for the system to feature intermittent instabilities it is required that the correlation length of the process $\beta(t)$ must be sufficiently large compared the time scale of damping $\approx 1/\zeta_0$ so that instabilities develop. In the following sections our attention will be aimed for the case where the excitation $\beta(t)$ is described by a *Gaussian* process to facilitate the analytic determination of the terms in (4). However, the ideas developed can be generalized to the case when $\beta(t)$ is a non-Gaussian process by carrying out the procedure using numerically generated realization of the excitation process.

To proceed we will average the governing system (3) over the fast frequency ω_0. We assume that correlation length of the stochastic process $\beta(t)$ varies slowly over the systems natural period $2\pi/\omega_0$ so that $\beta(t)$ can be treated constant over the period, which will be the case in order for (3) to exhibit intermittent instabilities. To apply the method of averaging to (3) we introduce the following transformation

$$x(t) = x_1(t)\cos(\omega_0 t) + x_2(t)\sin(\omega_0 t)$$
$$\dot{x}(t) = -\omega_0 x_1(t)\sin(\omega_0 t) + \omega_0 x_2(t)\cos(\omega_0 t) \quad (5)$$

for the slowly varying variables $x_1(t)$ and $x_2(t)$. Inserting (5) into (3) and using the additional relation $\dot{x}_1\cos(\omega_0 t) + \dot{x}_2\sin(\omega_0 t) = 0$ gives the following pair of differential equations

$$\dot{x}_1(t) = -[2\zeta_0\omega_0(x_1\sin^2(\omega_0 t) - \frac{1}{2}x_2\sin(2\omega_0 t)) - \frac{\omega_0\beta}{2}x_1\sin^2(2\omega t) - \omega_0\beta x_2\sin^2(\omega_0 t)\sin(2\omega t)] - \frac{1}{\omega_0}\sin(\omega_0 t)\xi(t) \quad (6)$$

$$\dot{x}_2(t) = [2\zeta_0\omega_0(\frac{1}{2}x_1\sin(2\omega_0 t) - x_2\cos^2(\omega_0 t)) - \frac{\omega_0\beta}{2}x_2\sin^2(2\omega t) - \omega_0\beta x_1\cos^2(\omega_0 t)\sin(2\omega t)] + \frac{1}{\omega_0}\cos(\omega_0 t)\xi(t) \quad (7)$$

Averaging the deterministic terms in brackets in (6) and (7) over the fast frequency $\frac{\omega_0}{2\pi}\int_0^{2\pi/\omega_0} d\,t$ we have

$$\dot{x}_1 = -\left(\zeta_0 - \frac{\beta}{4}\right)\omega_0 x_1 - \frac{1}{\omega_0}\sin(\omega_0 t)\,\xi(t) \quad (8)$$

$$\dot{x}_2 = -\left(\zeta_0 + \frac{\beta}{4}\right)\omega_0 x_2 + \frac{1}{\omega_0}\cos(\omega_0 t)\,\xi(t). \quad (9)$$

The averaged variables x_1 and x_2 provide an excellent statistical and pathwise approximation to the original system. Applying the stochastic averaging procedure to the random forcing gives the following set of Ito stochastic differential equations for the transformed coordinates

$$\dot{x}_1 = -\left(\zeta_0 - \frac{\beta(t)}{4}\right)\omega_0 x_1 + \sqrt{2\pi K}\,\dot{W}_1(t) \quad (10)$$

$$\dot{x}_2 = -\left(\zeta_0 + \frac{\beta(t)}{4}\right)\omega_0 x_2 + \sqrt{2\pi K}\,\dot{W}_2(t), \quad (11)$$

with $K = S_{\xi\xi}(\omega_0)/2\omega_0^2$, where $S_{\xi\xi}(\omega_0)$ is the spectral density of the additive excitation $\xi(t)$ at frequency ω_0, and $\dot{W}_1$ and $\dot{W}_2$ are independent white noise of unit intensity (Lin & Cai, 1995). The slowly varying coordinates after averaging transform into two decoupled Ornstein-Uhlenbeck (OU) processes. While averaging the forcing term provides poor pathwise agreement with the original system, it does however provide excellent statistical agreement.

3 PROBABILITY DISTRIBUTION OF THE SLOW VARIABLES

Here we will present the main results on how the heavy-tailed statistics of the averaged slowly varying variables in (10) can be approximated by separating the response into stable and unstable regimes according to (4). If $\beta(t)$ is a zero mean process both x_1 and x_2 will follow the same distribution. Incorporating bias in the amplitude excitation term $\beta(t)$ is straightforward. We will however concentrate on a zero mean process which we write as $\beta(t) = k\tilde{\gamma}(t)$, where $\tilde{\gamma}(t)$ is a Gaussian process with zero mean and unit variance. We consider the following OU process which represents x_1 or x_2

$$\dot{x} = -\left(\zeta_0 - \frac{\beta(t)}{4}\right)\omega_0\, x + \sigma\,\dot{W}(t) \quad (12)$$

We write (12) as

$$\dot{x} = -\gamma(t)\,x + \sigma\,\dot{W}(t), \quad (13)$$

so that $\gamma(t) = \tilde{m} - \tilde{k}\tilde{\gamma}(t)$ is a Gaussian process with mean $\tilde{m} = \zeta_0\omega_0$ and standard deviation $\tilde{k} = k\omega_0/4$. From (13) it is clear that intermittency is triggered when γ has zero downcrossings.

We define the threshold of an instability by $\eta = \tilde{m}/\tilde{k}$. So that the probability of γ being in a regime that does not trigger instabilities is given by $\mathbf{P}(\gamma > 0) = \Phi(\eta)$ and otherwise by $\mathbf{P}(\gamma < 0) = 1 - \Phi(\eta)$ (where $\phi(\cdot)$ denotes the standard normal pdf and $\Phi(\cdot)$ denotes the standard normal cdf). However due to the relaxation phase after an instability the probability $\mathbf{P}$(unstable regime) is not exactly $1 - \Phi(\eta)$. To determine the typical duration of

the decay phase, we note that during the growth phase the dynamics are approximately given by $x_p = x_0 e^{-\overline{\gamma}|_{\gamma<0} T_{\gamma<0}}$, where $T_{\gamma<0}$ is the duration for which $\gamma < 0$, x_p is the peak value of x during the instability, and $\overline{\gamma}|_{\gamma<0}$ is the conditional mean of γ given $\gamma < 0$. Similarly, for the decay phase $x_0 = x_p e^{-\overline{\gamma}|_{\gamma>0} T_{\text{decay}}}$. Combining these two results we have that the typical ratio between the growth and decay phase is given by

$$\frac{T_{\text{decay}}}{T_{\gamma<0}} = -\frac{\overline{\gamma}|_{\gamma<0}}{\overline{\gamma}|_{\gamma>0}} = -\frac{\tilde{m} - \tilde{k}\frac{\phi(\eta)}{1-\Phi(\eta)}}{\tilde{m} + \tilde{k}\frac{\phi(\eta)}{\Phi(\eta)}} = \nu. \quad (14)$$

The total duration of an unstable event is thus given by the sum of the duration of $T_{\gamma<0}$ and T_{decay}: $T_{\text{inst}} = (1+\nu)T_{\alpha<0}$. Making this modification we have

$$\mathbf{P}(\text{unstable regime}) = (1+\nu)\mathbf{P}(\gamma < 0), \quad (15)$$

$$\mathbf{P}(\text{stable regime}) = 1 - (1+\nu)\mathbf{P}(\gamma < 0). \quad (16)$$

3.1 Stable Regime Distribution

In the stable regime we have by definition no intermittent events. The dynamics can therefore be well approximated by replacing $\gamma(t)$ by its conditionally stable average $\overline{\gamma}|_{\gamma>0} = \tilde{m} + \tilde{k}\frac{\phi(\eta)}{\Phi(\eta)}$ so that

$$\dot{x} = -\overline{\gamma}|_{\gamma>0}\, x + \sigma\, \dot{W}(t). \quad (17)$$

The corresponding stationary pdf of (17) is a Gaussian distribution by the Fokker-Planck equation (Soong & Grigoriu, 1993). This gives us the following distribution for the conditionally stable dynamics

$$\mathbf{P}(X = x \mid \text{stable regime}) = \sqrt{\frac{\overline{\gamma}|_{\gamma>0}}{\pi\sigma^2}}\, e^{-\frac{\overline{\gamma}|_{\gamma>0} x^2}{\sigma^2}}. \quad (18)$$

3.2 Unstable Regime Distribution

Next we will derive the pdf for the system response for the unstable regime. In the unstable regime there is a growth phase due to the stochastic process $\gamma(t)$ crossing below the zero level, which triggers the instability. During this stage we assume that the parametric excitation is the primary mechanism driving the instability and ignore the small white noise forcing term which has a negligible minimal impact on the pdf of the response. We characterize the growth phase by the envelope of the response $u \simeq u_0 e^{\Lambda T_{\gamma<0}}$, where u_0 is a random variable that characterizes the stable envelope pdf, Λ is a random variable that represents the Lyapunov exponent, and $T_{\gamma<0}$ is the random length of time that the stochastic process γ spends below the zero level.

We first determine the energy growth distribution $Q = \Lambda T_{\gamma<0}$. By substituting the representation $u \simeq u_0 e^{\Lambda T_{\gamma<0}}$ into (13) we obtain that the eigenvalue is given by $\Lambda = -\gamma$ so that

$$f_\Lambda(x) = \mathbf{P}(-\gamma \mid \gamma < 0) = \frac{1}{k(1-\Phi(\eta))}\phi\left(\frac{x+\tilde{m}}{\tilde{k}}\right). \quad (19)$$

To determine analytically the distribution of the time that the stochastic process $\tilde{\gamma}$ spends below an arbitrary threshold level η is not in general possible. However an asymptotic expression is available for the case of rare crossings $\eta \to \infty$ (Rice 1958)

$$f_{T_{\gamma<0}}(t) = \frac{\pi t}{2\overline{T}^2} e^{-\frac{\pi t^2}{4\overline{T}^2}}, \quad (20)$$

which in our case provides a very good approximation since we assume that instabilities are rare so that η is relatively large. In (20) $\overline{T}$ represents the average length of an instability which for a Gaussian process is given by the ratio between the probability of $\gamma < 0$ and the average number of upcrossings of level η per unit time $\overline{N}^+(\eta)$ (Rice 1958)

$$\overline{T}_{\gamma<0} = \frac{\mathbf{P}(\tilde{\gamma}>\eta)}{\overline{N}^+(\eta)} = \frac{1-\Phi(\eta)}{\frac{1}{2\pi}\sqrt{-R''_{\tilde{\gamma}}(0)}\exp\left(-\frac{\eta^2}{2}\right)}, \quad (21)$$

where we have used Rice's formula for the expected number of upcrossings (Blake & Lindsey, 1973, Kratz 2006) and where $R_{\tilde{\gamma}}(x)$ represents the correlation of the process $\tilde{\gamma}$. With these results we can determine the

distribution of the energy excitation statistics by the product distribution

$$f_Q(z) = \int_0^\infty f_\Lambda(x) f_{T_{Y<0}}(z/x) \frac{1}{|x|}\, dx. \quad (22)$$

With the distribution of the energy excitation statistics from (22) we can now derive the pdf for the unstable response. For simplicity let $U = Ye^Q$ and $\Lambda = Q$, so that by a random variable transformation we have

$$\begin{aligned} f_{U\Lambda}(u,\lambda) &= f_{YQ}(y,q)\det|\partial(y,q)/\partial(u,\lambda)| \\ &= \frac{1}{e^Q} f_Y(y) f_Q(q) \\ &= \frac{1}{e^\lambda} f_Y(u/e^\lambda) f_Q(\lambda). \end{aligned} \quad (23)$$

Therefore the general form of the system pdf is given by

$$f_U(u) = \int_0^\infty \frac{1}{e^\lambda} f_Y(u/e^\lambda) f_Q(\lambda)\, d\lambda. \quad (24)$$

Where the pdf f_Y corresponds to the pdf of the initial point of the instability. We note that the OU process has the property that its interaction with the parametric excitation gives rise to "instabilities" of very small intensity which are indistinguishable from the typical stable state response. To enforce the separation of the unstable response from the stable state requires we introduce the following correction to the initial point of the instability $Y = |x_s| + c$, where $|\tilde{x}_s|$ is the pdf of the envelope of the stable response (Rayleigh) and c is a constant that enforces the separation. We find that choosing c such that it is one standard deviation of the typical stable response is sufficient to enforce this separation and works well in practice. In addition, this choice is associated with very robust performance over different parametric regimes. Therefore we have that the distribution of the initial point of an instability is given by

$$f_Y(x) = \frac{2\overline{\gamma}|_{\gamma>0}}{\sigma^2}(x-c)\exp(-\frac{\overline{\gamma}|_{\gamma>0}}{\sigma^2}(x-c)^2), \quad (25)$$

for $x \geq c$.

Thus after transforming the envelope representation into the full response distribution by a narrowbanded argument we finally have the conditionally unstable distribution

$$\mathbf{P}(X = x \mid \text{unstable regime}) = \frac{1}{2} f_U(|x|) \quad (26)$$

4 COMPARISON WITH MONTE-CARLO EXPERIMENTS

With the results from Section 3 constructing the full probability distribution for the slow variable is straightforward and requires using the result from the unstable regime (26) and stable regime (18) and combining them with the appropriate weights (15) according to the decomposition (4). Since we considered that the noise term $\beta(t)$ is unbiased with zero mean the corresponding distribution for the response of the Mathieu equation (3) will be given by the distribution of the average of the slow variable x_1 and x_2 (which are equivalent) since the response is a narrowbanded process according to $x(t) = x_1(t)\cos(\omega_0 t) + x_2(t)\sin(\omega_0 t)$. This can be seen by considering the probability distribution for $\cos(\varphi)$, where φ is a uniform random variable between 0 and 2π. The pdf for $z = \cos(\varphi)$ is given by $f_z(x) = 1/(\pi\sqrt{(1-x^2)})$, $x \in [-1,1]$, which we approximate by $f_z(x) = \frac{1}{2}(\delta(z+1) + \delta(z-1))$.

For the Monte-Carlo experiments we solve (3) with white noise forcing and non-dimensionalize time by ω_0 so that

$$\ddot{x}(t) + 2\zeta_0\, \dot{x}(t) + (1 + \beta(t)\sin 2t)x(t) = \delta\dot{W}(t), \quad (27)$$

for 2500 realization using forward-Euler integration with a time step $dt = 5 \times 10^{-3}$ from $t = 0$ to $t = 3500$ and discard the first 500 time units to ensure statistical steady states from any initial transients. Moreover we simulate the stochastic process $\beta(t)$ according to the method presented in Percival 1992.

For comparisons we present three cases. Moreover, even in very turbulent regimes with frequent instabilities our results capture the

trend of the tails. We set the damping at $\zeta_0 = 0.1$, $\delta = 0.002$, the correlation length of $\beta(t)$ to be 50 times the time scale of damping $L_{\text{corr}} = 500$, and show three cases with varying frequency of instabilities by changing the variance of β. For the most intermittent regime we set the standard deviation of $\beta(t) = k\tilde{\gamma}(t)$ to $k = 0.229$ so that rare event crossings occur with a 4.0% chance, for the middle regime $k = 0.200$ with a 2.3% chance of rare event crossings, and finally for the least intermittent regime $k = 0.178$ with a 1.2% rare event crossing frequency, see Fig. 2. Overall we have good agreement between the analytic distribution and Monte-Carlo results for these three cases, we stress that the results are robust across a range of parameters that satisfy the assumptions.

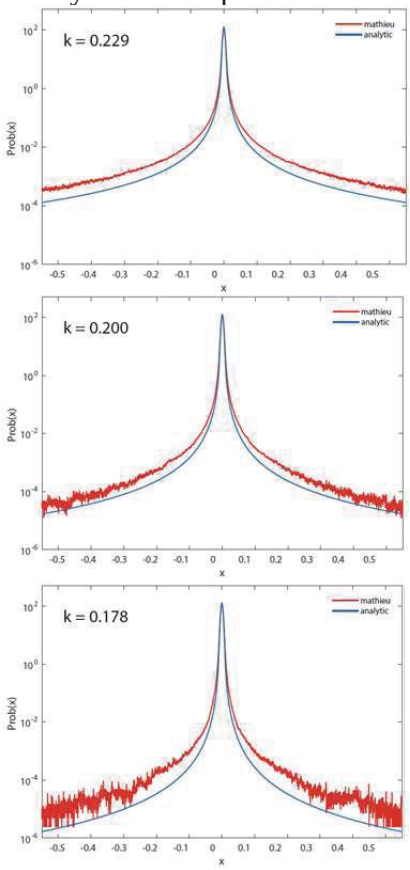

Figure 2 Comparison of Monte-Carlo results of the Mathieu equation (27) (red curve) and analytic probability distribution (blue curve) for various intermittency levels with (left) being most intermittent and (right) least intermittent (semilogarithmic y-axis scale).

5 CONCLUSIONS

In this work we derive an analytic approximation to the pdf for the damped Mathieu equation tuned to the main resonant frequency with random amplitude on the harmonic parametric excitation term. This system features intermittent resonance due the random nature of the amplitude term that triggers intermittent resonance and these intermittent events lead to complex heavy-tailed statistics. To derive the pdf for the response we average the governing equation over the fast frequency to arive at a set of parametrically excited OU processes. We then decompose the response for the slow variables by conditioning on the stable regime and the unstable (transient) state. In the stable regime we employ classical results to describe the pdf of the statistical steady state. In the unstable regime we capture the response by characterizing the transients bursts by an exponential representation with a random Lyapnuov exponent and growth duration. This method allows us to capture the statistics associated with the dynamics that give rise to the heavy-tailed distributions and the resulting analytical approximations compare favorably with direct numerical simulations for a large parameter range.

Acknowledgments

This research has been partially supported by the Naval Engineering Education Center (NEEC) grant 3002883706 and by the Office of Naval Research (ONR) grant ONR N00014-14-1-0520. The authors thank Dr. Craig Merrill (NEEC Technical Point of Contact), Dr. Vadim Belenky, and Prof. Andrew Majda for numerous stimulating discussions.

6. REFERENCES

Blake, Ian F. and William C. Lindsey (1973). "Level-crossing problems for random processes". In: IEEE Trans. Information Theory IT-19, pp. 295–315.

Floris, Claudio (2012). "Stochastic Stability of Damped Mathieu Oscillator Parametrically Excited by a Gaussian Noise." In: Mathematical Problems in Engineering 2012, pp. 1–18.

Kratz, Marie F. (2006). "Level crossings and other level functionals of stationary Gaussian processes". In: Probab. Surv. 3, pp. 230–288.

Lin, Y. K. and C. Q. Cai (1995). Probabilistic Structural Dynamics. McGraw-Hill, Inc.

Nayfeh, A. H. and D. T. Mook (1984). Nonlinear Oscillations. New York: Wiley-Interscience.

Percival, D. B. (1992). "Simulating Gaussian Random Processes with Specified Spectra". In: Computing Science and Statistics 24, pp. 534–538.

Rice, S. O. (1958). "Distribution of the duration of fades in radio transmission: Gaussian noise model". In: Bell System Tech. J. 37, pp. 581–635.

Soong, T. and M. Grigoriu (1993). Random Vibration of Mechanical and Structural Systems. PTR Prentice Hall.

This page is intentionally left blank

Coupled Simulation of Nonlinear Ship Motions and Free Surface Tanks

Jose Luis Cercos-Pita, *Technical University of Madrid*, Spain, jl.cercos@upm.es

Gabriele Bulian, *University of Trieste*, Italy, gbulian@units.it

Luis Pérez-Rojas, *Technical University of Madrid*, Spain, luis.perezrojas@upm.es

Alberto Francescutto, *University of Trieste*, Italy, francesc@units.it

ABSTRACT

This paper investigates the coupled nonlinear dynamics of a vessel with a free surface tank onboard. To this end, a 6-DOF ship motions simulation code is coupled with a CFD solver addressing the behaviour of the fluid in the tank. The nonlinear ship motions code is of the blended (hybrid) type, intended for the simulation of free running vessels in waves. The nonlinear CFD solver is a GPU-based 3D Weakly-Compressible Smoothed-Particle Hydrodynamic (WCSPH) solver. Numerical results are presented for the nonlinear roll motion of a vessel with and without a free surface tank in regular beam waves with different steepnesses.

Keywords: *nonlinear ship motions; sloshing; smoothed-particle hydrodynamics (SPH); GPU; anti-rolling tanks; 6-DOF simulations; blended codes; coupling*

1. INTRODUCTION

Tanks characterised by the presence of a free surface are almost invariably present onboard vessels, with different scopes: fuel tanks, ballast tanks, cargo tanks, anti-rolling devices, etc. While taking exactly into account their effect on static restoring is, nowadays, a matter of routine stability calculations, the same cannot be said when ship dynamics and fluid cargo dynamics are to be accounted for in a coupled way. Due to the complexity of the involved phenomena, a coupled dynamic approach is particularly challenging when nonlinear effects are to be considered in both ship motions and fluid dynamics in the free surface tanks.

Different approaches have been used in the past to simulate the behaviour of a vessel in presence of liquid tanks onboard. Fully linear approaches for ship motions, internal hydrodynamics and external hydrodynamics, have been developed by Malenica et al. (2003) and Kim & Shin (2008). Such approaches are very suitable for design purposes in mild sea conditions. However, when sloshing within the tanks becomes violent and/or ship motions become large, the linearity assumption become too restrictive and the underlying models fail to reproduce the actual fluid and ship dynamics. As a result, nonlinearities need to be introduced, and different authors, recognising this need in certain conditions, have tackled the problem with approaches having different levels of sophistication.

In case ship motions can be considered small enough to be treated linearly, nonlinear effects can be introduced only in the numerical solution of the sloshing problem. Approaches along this line can be found, for instance, in

(Kim et al. ,2007, Zhao et al., 2014), where nonlinear time domain potential flow approaches are used under the assumption of a free surface retaining a single-valued behaviour. However, this assumption does not allow taking into account strong nonlinear phenomena such as free surface fragmentation or wave breaking, which characterise violent sloshing. The possibility of handling complex, non-single valued, free surface dynamics was instead introduced in the work of Bunnik & Veldman (2010), where a VOF solver for the internal sloshing flow was coupled in time domain with a linear ship motions model handling the linear potential external fluid-structure interaction and the linearized rigid body dynamics.

However, there are many situations when linear approaches to ship motions are insufficient. This is, for instance the case when the interest is on the assessment of ship behaviour in severe environmental conditions, or when the interest is on typically nonlinear dynamic stability phenomena in waves (e.g. parametric roll, pure loss of stability, surf riding and broaching, large rolling amplitudes in beam waves – see IMO (2009)), or when the interest is on the simulation of the behaviour of a vessel, having free surface tanks onboard, and which is free running in waves. In all such, and other, cases, nonlinear models need to be used for simulating the dynamics of the vessel. Approaches making use of nonlinear ship motions models together with simplified models for the behaviour of the fluid in the tank can be found in Francescutto & Contento (1999) for the beam sea case, and in Neves et al. (2009) for the case of longitudinal sea and, in particular, parametric roll. 6-DOF ship motions models coupled with 1-DOF U-tube tank models have been reported by Youssef et al. (2003) and Holden & Fossen (2012).

More sophisticated models are required when nonlinear effects are to be introduced in both ship motions and in the solution of the fluid flow in the tank. Nonlinear effects in the fluid flow can become particularly relevant in case of tanks featuring large free surfaces. Along the line of increasing the accuracy of the CFD solver for the internal flow, Hashimoto et al. (2012) coupled a nonlinear 1-DOF roll motion model for the simulation of parametrically excited roll motion, with a fully nonlinear solution of the fluid flow in the tank using the Moving Particle Semi-implicit (MPS) method, which is able to take into account strongly nonlinear free surface flows. In Mitra et al. (2012) a nonlinear potential flow model was solved by FEM for the internal tank, assuming the free surface to be single valued (therefore, also in this case, free surface fragmentation, breaking and strong nonlinearities cannot be accounted for), and the coupling was done with a partially nonlinear 6-DOF ship motions model.

In this study an approach is used where a 6-DOF ship motions simulation code is coupled with a CFD solver addressing the behaviour of the fluid in the tank. The nonlinear ship motions code is of the blended (hybrid) type, intended for the simulation of free running vessels in waves. The nonlinear CFD solver is a 3D Weakly-Compressible Smoothed-Particle Hydrodynamic (WCSPH) solver, allowing the use of graphical processing units (GPUs). In the following, the simulation tool is firstly described. Then, numerical results are presented for the nonlinear roll motion of a vessel with and without a free surface tank in regular beam waves with different steepnesses.

2. SIMULATION TOOL

The tool developed in the present study is intended to be able to simulate the general case of nonlinear motions for a free running ship sailing in regular or irregular waves, with a liquid tank onboard. Since nonlinear motions and nonlinear fluid flow inside the tank are of interest, and since the tool is expected to be able to deal with the general case of a ship free running in waves, linear frequency domain approaches (Malenica et al., 2003, Kim & Shin, 2008) do not represent a relevant option

for the scope of the study. Although research is ongoing (Sadat-Hossein et al., 2010, Carrica et al., 2012) regarding the use of direct computational fluid dynamics approaches for nonlinear ship motions of, possibly free running, ships in waves, the required computational time and resources are still prohibitive for practical applications.

Considering the situation, herein an intermediate approach has been followed, where the nonlinear rigid body dynamics and the ship-waves interaction is dealt with by means of a blended (hybrid) nonlinear 6-DOF approach, while the internal fluid-structure interaction, i.e. the fluid dynamics within the tank, is handled through a CFD approach based on a fully nonlinear SPH solver. The two tools are then coupled, in order to incorporate the tank effects in the solution of ship motions.

In particular, the ship dynamics is handled by the 6-DOF blended simulation code SHIXDOF ("nonlinear SHIp motion simulation program with siX Degrees Of Freedom"), under development at the University of Trieste. The code has been described and applied previously in (Bulian et al., 2012, Bulian & Francescutto, 2013) and herein some main details are reported.

The simulation approach used in SHIXDOF is a typical hybrid approach along the line of de Kat & Paulling (1989). To date, approaches of such type have been considered suitable for practical assessment of nonlinear ship motions in waves, and their suitability for such purpose has been stated also in the framework of IMO "Second Generation Intact stability Criteria" (Bulian & Francescutto, 2013, IMO, 2010, 2013). As described in some more details by Bulian et al. (2012) and Bulian & Francescutto (2013), SHIXODF solves nonlinear rigid body motions equations with respect to the ship-fixed reference system:

$$\begin{cases} m\cdot\left[\begin{array}{l}\underline{u}_O{}' + \underline{\omega}\wedge\underline{u}_O + \\ +\underline{\omega}'\wedge\underline{x}_G + \underline{\omega}\wedge\left(\underline{\omega}\wedge\underline{x}_G\right)\end{array}\right] = \underline{F}_{ext}\left(t\right) \\ \underline{\underline{I}}_O\cdot\underline{\omega}' + \underline{\omega}\wedge\left(\underline{\underline{I}}_O\cdot\underline{\omega}\right) + m\cdot\underline{x}_G\wedge\underline{u}_O{}' + \\ +m\cdot\underline{x}_G\wedge\left(\underline{\omega}\wedge\underline{u}_O\right) = \underline{M}_{ext,O}\left(t\right) \end{cases} \quad (1)$$

The vessel is then moved and oriented with respect to an earth-fixed reference system. The external force $\underline{F}_{ext}\left(t\right)$ and moment $\underline{M}_{ext,O}\left(t\right)$ comprise the following main effects: Froude-Krylov pressure, including hydrostatic term, calculated up to the instantaneous wetted surface of the hull (to catch geometrical nonlinearities); linear hydrodynamic radiation terms through convolution of kernel functions and infinite frequency added mass terms obtained from linear potential flow pre-calculations; instantaneous diffraction forces from linear frequency domain pre-calculations; manoeuvring forces, comprising a cross-flow model. Furthermore, it is possible to consider: constant and gusty wind effects; additional empirical damping terms (typically for, but not limited to, roll); linear/nonlinear, mooring-like springs; propulsors; lifting surfaces (rudders, fins).

In addition to the abovementioned effects, in the simulation tool developed herein, $\underline{F}_{ext}\left(t\right)$ and $\underline{M}_{ext,O}\left(t\right)$ also contain the instantaneous action, on the vessel, of the fluid in the tank. Such actions are calculated by the coupled CFD solver, which is based on the numerical solution of the 3D fluid field through a meshless Smoothed-Particle Hydrodynamics (SPH) approach.

The SPH approach has become very popular in CFD field thanks to the adaptability to complex geometries, and the capability of dealing with heavily fragmented fluids, while keeping a reasonable computational cost. The particular solver used herein is AQUAgpusph (Cercos-Pita et al., 2013, Cercos-Pita, 2015), developed at University of Madrid. To address the actually incompressible flow,

AQUAgpusph uses the commonly employed weakly-compressible SPH approach (WCSPH) (Monaghan, 2005, Colagrossi et al., 2009), which is based on the solution of the Navier-Stokes equations, where an artificial weak compressibility is considered through a pressure-density state equation which provides small density variations:

$$\begin{cases} \dfrac{d\rho_a}{dt} = -\rho_a \nabla \cdot \underline{u}_a \\ \dfrac{d\underline{u}_a}{dt} = -\dfrac{\nabla p_a}{\rho_a} + \dfrac{\mu}{\rho_a}\Delta \underline{u}_a + \underline{g} \\ p_a = p_a(\rho_a) \end{cases} \quad (2)$$

AQUAgpusph solves the discretised version of (2) using the Lagrangian kernel-based SPH formalism. Other formulations can be found in order to perform truly incompressible SPH simulations (e.g. Cummins & Rudman, 1999, Souto-Iglesias et al., 2014), but the WCSPH formulation has the main benefit that a purely explicit scheme can be used to perform the integration, and hence, no linear system of equations needs to be solved in order to compute the pressure field at each time step. In order to speed up the computation, AQUAgpusph can exploit, through OpenCL, the parallel computing capabilities of graphical processing units (GPUs), if such hardware, as in the present application, is available (Cercos-Pita et al., 2013, Cercos-Pita, 2015).

To allow coupled simulations, an explicit coupling strategy has been implemented, where SHIXDOF performs the time stepping by means of an explicit integration scheme, receiving force and moment from AQUAgpusph at the beginning of each step, and passing to AQUAgpusph the updated ship and tank motions at the end of the step. With such information, AQUAgpusph simulates the fluid motion in the tank within the considered time step, while SHIXDOF waits to receive the force and moment at the beginning of the next time step. The integration in SHIXDOF is carried out by means of a 4th-order Adams-Bashforth integration scheme with fixed time step. On the other hand, AQUAgpusph integrates in time by means of a Leap-Frog method (Souto-Iglesias et al., 2006) with variable time step controlled by a Courant condition.

3. APPLICATION

An application of the developed nonlinear coupled simulation tool has been carried out using a freely available and well-known hull form geometry. This allows present results to serve as possible comparison cases for other researchers developing similar tools. Furthermore, the considered hull has been selected because experimental data regarding nonlinear rolling motion without tank were available from previous studies.

The geometry and positioning of the tank in the simulations was chosen, and constraint, to be compatible with an already existing 1:100 scale model of the hull. As a result of such choice, the positioning of the tank in the simulations is quite high above the waterline and above the centre of gravity.

Simulations have been targeted at assessing nonlinear effects on the roll response curve, coming from external hydrodynamics (ship-wave interaction) and internal hydrodynamics (ship-tank interaction). To this end, numerical experiments have been carried out, for one specific tank geometry, in regular beam waves having different steepnesses (ratio between wave height and wave length).

3.1 Sample hull and free surface tank

The simulation tool has been used for simulating the behaviour of a Series 60 hull form, in bare hull condition, and equipped with a box-shaped free surface tank. The bodyplan

of the hull, together with a transversal view of the tank geometry is shown in Figure 1, while the main characteristics of the hull and the loading condition (with empty tank) are reported in Table 1. Such hull form, without any tank onboard, was used in previous numerical and experimental studies regarding nonlinear roll motion in beam regular, bi-chromatic and irregular waves (Tzamtzis, 2004, Bulian et al., 2012, Bulian & Francescutto, 2013). As a result, a certain amount of reference experimental data was available for the present study.

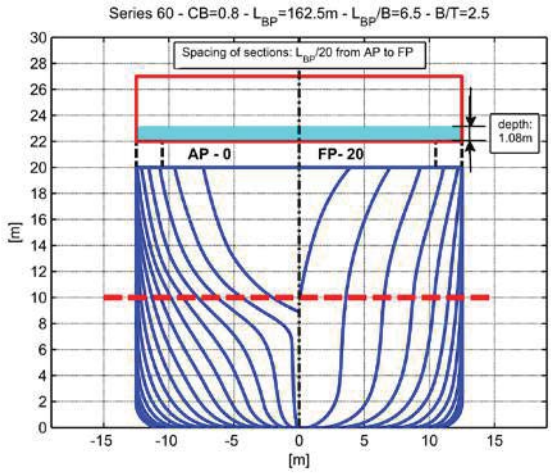

Figure 1: Hull bodyplan and tank geometry.

Table 1: Main data of hull and loading condition (without tank).

L_{BP}	[m]	162.5	Length b.p.
B	[m]	25.0	Beam
T	[m]	10.0	Draught
C_B	[-]	0.8	Block coefficient
$\overline{GM}$	[m]	1.65	Transversal metacentric height
$\overline{KG}$	[m]	8.59	Height of CoG above baseline
ω_0	[rad/s]	0.408	Roll natural frequency
$R_{xx,G}$	[m]	9.1	Dry roll radius of inertia (w.r.t. CoG)
$R_{yy,G}$	[m]	40.6	Dry pitch radius of inertia (w.r.t. CoG)
$R_{zz,G}$	[m]	40.6	Dry yaw radius of inertia (w.r.t. CoG)

The tested tank has the main characteristics reported in Table 2. The tank is longitudinally positioned at the mid perpendicular, spanning a total length of 10m in longitudinal direction (5m aft and 5m forward of the mid perpendicular). The transversal width of the tank corresponds to the ship breadth, and the fluid depth is set in such a way to obtain a first transversal linear natural sloshing mode matching the roll natural frequency of the vessel with empty tank. In such configuration, the ratio between the mass of the fluid in the tank and the mass of the vessel with empty tank is 0.83%. The increase of draught due to the additional weight loaded in the tank is 76mm, i.e. 0.76% of the ship draught without fluid in the tank. It is also to be noted that the depth to width ratio for the fluid in the tank is 0.0432, meaning that sloshing occurs in a shallow water regime. Even under purely static inclinations, the bilge corner of the tank becomes dry at a heel angle of just 4.9deg. It is herein assumed that the hull without tank has the same mechanical properties (mass, position of centre of gravity, radii of inertia) of the hull equipped with the empty tank. As a result, the indications “without tank” and “empty tank” are to be assumed, herein, as synonymous.

The righting lever ($\overline{GZ}$) curve has been calculated for the vessel without tank and with the tank. For sake of comparison, the calculation of the righting lever with the tank was carried out considering the cargo as both solid (frozen) and fluid. Results are shown in Figure 2. Since the liquid cargo is loaded high above the baseline, part of the reduction in the righting lever is due to the increase of $\overline{KG}$ (the variation of $\overline{KM}$ due to the small variation of draught, associated with the loading of the fluid in the tank, is very small). Then, the majority of the reduction in the restoring is due to the free surface effect. As a consequence of the large fluid depth to tank width ratio, free surface effects are practically linear with respect to the heeling angle until the tank bilge corner gets dry (abt. 5deg) then the overall free surface effect reduces as the heeling increases.

Table 2: Main characteristics of the tank.

Tank dimensions L_{tank} x W_{tank} x H_{tank}	10m x 25m x 5m
Longitudinal position	Centre at mid perpendicular
Height of tank bottom from baseline	22m
Fluid depth - d_{fluid}	1.08m
d_{fluid} / W_{tank}	0.0432
Filling ratio	0.2160

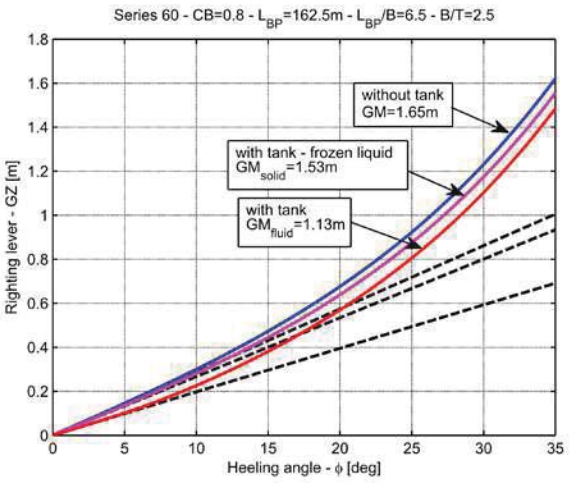

Figure 2: Righting lever curves without tank, with frozen liquid in the tank and with fluid in the tank.

3.2 Roll motion in regular beam waves without free surface tank

Before running a set of coupled simulations, the 6-DOF software tool has been compared and tuned, in terms of additional roll damping coefficients. The tuning has been performed making reference to a set of experimental data without tank for roll motion in regular beam waves at zero speed (Tzamtzis, 2004). A first tuning of the 6-DOF code on roll decay experimental data for the considered loading condition was carried out by Bulian & Francescutto (2013). Herein the tuning has been improved to achieve a better matching between simulations and experimental roll response at large forcing wave steepnesses in beam regular waves, while still keeping a good matching with roll decay data and experiments in milder regular beam waves.

In the tuning process, the drag coefficient used in the cross flow model has been kept constant to a value equal to 0.8, which is in line with typical lateral drag coefficients for quite full vessels with similar beam to draught ratios (e.g. Kijima, 2003, Faltinsen, 1990). In view of the experimentally observed behaviour of equivalent linear roll damping coefficient as a function of the oscillation amplitude from roll decays, the tuning of damping in roll was carried out through an additional empirical linear-in-velocity term ($-B_{L,add}\cdot\dot{\phi}$) and an additional cubic-in-velocity term ($-B_{C,add}\cdot\dot{\phi}^3$). Such terms have been added to the moment acting on the vessel around the longitudinal axis of the ship-fixed reference system. It is to be noted that, as a result, such additional damping terms are not independent from the considered reference system.

Simulations have then been carried out in regular beam waves, without tank, for different frequencies close to the roll natural one, and considering two wave steepnesses, 1/100 and 1/30, as in the experimental conditions (Tzamtzis, 2004, Bulian & Francescutto, 2013). In both experiments and simulations the vessel was free to drift. In the experiments the beam sea condition was maintained by manual control, while in the simulations a linear, with respect to yaw, restoring moment directed along the earth-fixed vertical axis and with spring constant equal to $5.3\cdot10^8\,N\cdot m/rad$ was used in order to keep the heading at about 90deg. The introduction of this artificial spring leads to a yaw natural frequency, as measured from yaw decays, of $0.0673 rad/s$, which is far enough from the roll natural frequency to reduce the risk of spurious couplings. The comparison between experimental results and results from simulations is shown in Figure 3 (at ship scale). Although there is still a small overestimation of the experimental roll amplitude at the larger forcing steepness, the re-tuning of additional roll damping has led to a reduction in the difference between

experimental and numerical maximum roll response at $s_W = 1/30$, from about 15% in Bulian & Francescutto (2013), to about 9% herein. The difference in the peak roll between experiments and simulations for $s_W = 1/100$ is, instead, 2%. It can be noticed that the bending towards high frequencies of the roll response curve, associated with the hardening roll restoring, is well captured by the simulations.

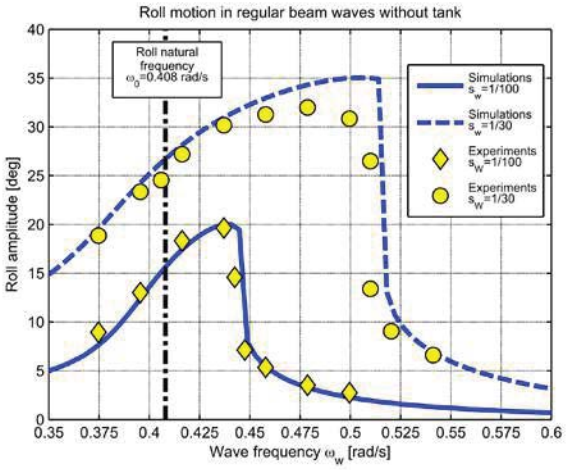

Figure 3: Roll motion in regular beam waves, without tank.

In order to analyse the obtained roll dissipation level in calm water after tuning the ship motions code, a numerical roll decay has been simulated. The resulting roll time history has then been analysed on the basis of the classical 1-DOF nonlinear model:

$$\ddot{\phi} + 2 \cdot \mu \cdot \dot{\phi} + \beta \cdot \dot{\phi} \left| \dot{\phi} \right| + \delta \cdot \dot{\phi}^3 + \omega_0^2 \cdot r(\phi) = 0 \quad \text{with} \quad r(\phi) = \phi + \gamma_3 \cdot \phi^3 + \gamma_5 \cdot \phi^5 + \ldots \tag{3}$$

Results from the roll decrement analysis according to the methodology described by Bulian et al. (2009), lead to $\omega_0 = 0.408 rad/s$, $\mu = 0.00340 s^{-1}$, $\beta = 0.0994 rad^{-1}$ and $\delta = 0.554 s \cdot rad^{-2}$.

On the basis of the reported results, it can therefore be concluded that the 6-DOF nonlinear ship motions code can be considered validated for the intended scope of this study.

3.3 Validation of the SPH solver

The SPH solver has been validated by simulating the SPHERIC validation test 9 (Botia-Vera et al., 2010, Bulian et al., 2010), for which data are available from https://wiki.manchester.ac.uk/spheric/ under the "Validation Tests" section.

The validation test 9 consists in a simplified 1-DOF mechanical model of a tuned liquid damper (TLD), where a rectangular tank is allowed to rotate around a fixed point under the forcing of a translating mass with prescribed oscillatory motion. The motion of the mass is rectilinear in the tank-fixed reference system. The tank is partially filled with liquid, and the resulting system is, therefore, a 1-DOF mechanical system coupled with the action of the fluid inside the tank. Such system, can also be considered as a simplified model relevant for the dynamics of a vessel equipped with a free surface tank.

The equation of motion of the coupled system, in such condition, and the values for the model parameters can be found in (Pérez-Rojas et al., 2011, Botia-Vera et al., 2010, Bulian et al., 2010) and can also be obtained from the already mentioned SPHERIC website.

Figure 4 shows a comparison between experiments and simulations carried out with a total of about 100000 particles. The very good agreement between predictions and experimental outcomes can be noticed. The SPH solver can therefore be considered suitable for the intended purpose of this study.

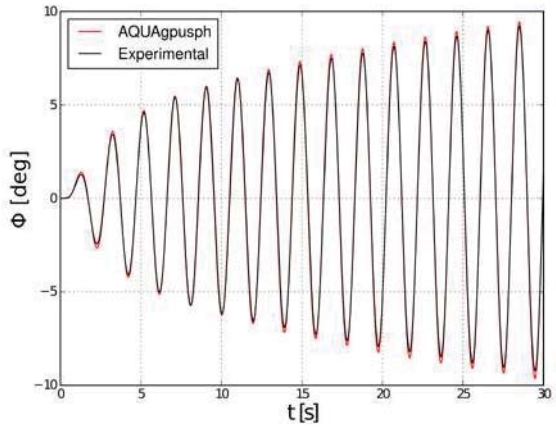

Figure 4: Roll angle of the tuned liquid damper. Comparison between SPH simulation and experiments. Amplitude of the motion for the moving mass: 100 *mm*. Forcing frequency equal to natural frequency of the dry system.

3.4 Roll motion in regular beam waves with free surface tank

After checking the capability of the 6-DOF nonlinear ship motions code to reproduce experimental data without the effect of the free surface tank, and after checking the capability of the SPH solver to properly reproduce the fluid action in a simplified 1-DOF coupled TLD model, a series of 6-DOF coupled ship-tank simulations have been carried out considering the tank partially filled with fluid as reported in Table 2.

Coupled 6-DOF simulations have been carried out in beam regular waves at zero speed, with the same numerical setup used for simulating the motion of the vessel without tank. The ship was free to drift, but rotations around the earth fixed vertical axis were partially restrained as in the case without tank. The number of particles used for the fluid discretisation in the SPH solver was set to about 12000.

The primary scope of the simulations described herein was to analyse the behaviour of the coupled system for different levels of the wave forcing. Roll motion is known to behave nonlinearly as the wave forcing increases. Similarly, it can be expected to observe a nonlinear behaviour also for the action on the vessel of the fluid inside the tank as the motion of the tank boundaries, which are forcing the fluid, increases. For the considered tank this is particularly expectable, as a consequence of the small depth to width ratio, and the associated very shallow water regime in which the tank is working. To this end, four wave steepnesses have been tested, namely: 1/80, 1/67, 1/57 and 1/50. A specific set of wave frequencies was simulated for each steepness in order to have a clear representation of the roll response curve.

To allow an assessment of the effectiveness of the tank as a passive anti-rolling device, simulations have been carried out for the same four steepnesses also for the vessel without tank.

The total length of each simulation was set to 500s, with an initial ramp of 50s on the wave forcing. A 2s pre-stabilization of the SPH solver is performed before starting each simulation. The average roll amplitude was measured considering the final part of each simulation. Herein, the roll amplitude is defined as half of the difference between maximum and minimum roll within each cycle. The roll response curves resulting from the simulations are shown in Figure 5.

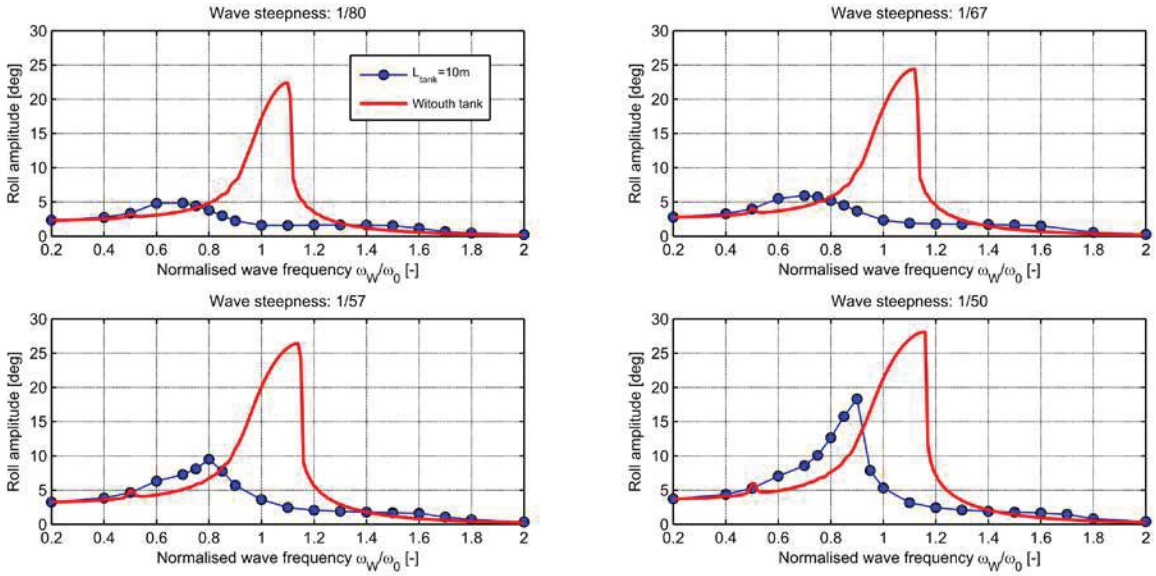

Figure 5: Roll response in regular beam waves with different steepnesses, with and without tank.

From the results reported in Figure 5, it can be noticed that the vessel without the tank follows the classical well-known nonlinear behaviour in regular beam waves, with a peak roll response which increases less-than-linearly as a function of the wave steepness, and a bending of the response curve towards the region of high frequencies, in accordance with the hardening behaviour of the roll righting moment in calm water. A small secondary peak is also visible at $\omega_W \approx 0.5\omega_0$, particularly for the largest steepnesses. Such small peak is associated with the inception of ultra-harmonic roll motions (Cardo et al., 1981), where the roll response, in addition to the harmonic at the encounter frequency, features a significant harmonic at twice the encounter frequency of the forcing.

Looking at the behaviour of the roll response with the tank partially filled with fluid, it can be noticed that the effect of the tank, as an anti-rolling device, is very significant in case of the two lowest forcing steepnesses ($s_W = 1/80$ and $s_W = 1/67$). In such cases the roll response shows the well-known double-peak shape (e.g., Field & Martin, 1976, Lee & Vassalos, 1996, Francescutto & Contento, 1999, Kim et al., 2007, and discussion by Bell in van den Bosch & Vugts, 1966): in the frequency region close to the roll natural frequency the roll motion is strongly suppressed, while, on the other hand, the roll response with the tank is larger than without the tank in the frequency regions close to the two peaks appearing at low and high frequency.

However, the roll motion has a totally different behaviour for the largest forcing steepness ($s_W = 1/50$). In such case, the maximum roll amplitude with tank is much closer to the maximum roll amplitude without tank, and the effectiveness of the tank, as an anti-rolling device, is very significantly reduced. Looking at the shape of the response curve, although a small high-frequency peak is still present, the roll response with tank approximately resembles the one without tank, with a shifting towards lower frequencies and a reduction in the maximum peak. A small but noticeable hump is still present in the frequency region corresponding to the low frequency peak for at $s_W = 1/80$ and $s_W = 1/67$, as a reminiscence of the behaviour of the roll response curve for small wave forcing. The case of forcing steepness $s_W = 1/57$ seems to represent, instead, a sort of transition case. In this case, the roll response behaves, in part, similarly to the case of small wave forcing. However the inception of the peak which will then become dominant at $s_W = 1/50$, is already noticeable at wave frequencies around $0.8\omega_0$. In the same

frequency region, the transitional character of this forcing condition manifests also in time domain, as long transients before stationarity.

The behaviour described above on the basis of Figure 5 is more evident when plotting the roll response curves with tank for different steepnesses, on the same graph, as shown in Figure 6. From the response curves in Figure 6 it is also interesting to note that, similarly to the case without tank, also in case of vessel equipped with the tank the roll response curve, in the region of the low-frequency peak, tends to bend towards higher frequencies. Furthermore, it is also interesting to report that the observation of the time histories at $\omega_W = 0.5\omega_0$ indicates that, for all forcing steepnesses, the presence of the tank is able to suppress the inception of the small ultra-harmonic response which was instead observed in the simulations without tank.

Finally, Figure 7 shows the simulated fluid behaviour inside the tank for two example cases. The two cases correspond to the frequency ratio $\omega_W / \omega_0 = 0.9$ for the minimum and maximum simulated wave steepness, i.e. $s_W = 1/80$ and $s_W = 1/50$ respectively. The reported snapshots are taken at four representative time instants within the last available roll cycle, corresponding to: minimum roll, up-zero-crossing for roll, maximum roll and down-zero-crossing for roll. It can be noticed that impacts on the tank side take place at the lowest steepness. At the highest steepness, where the rolling amplitude exceeds 18deg, the fluid also impacts the top of the tank.

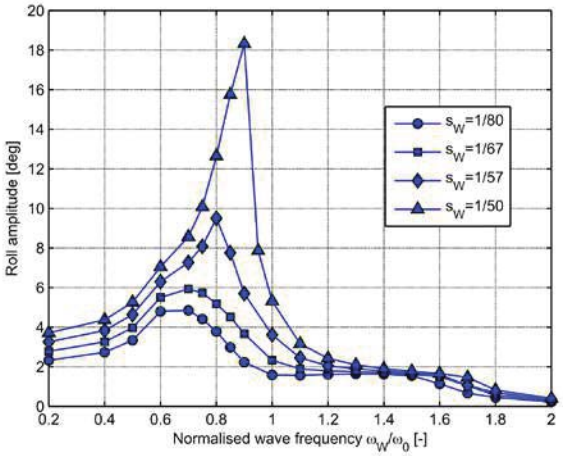

Figure 6: Roll response in regular beam waves with different steepnesses, with tank.

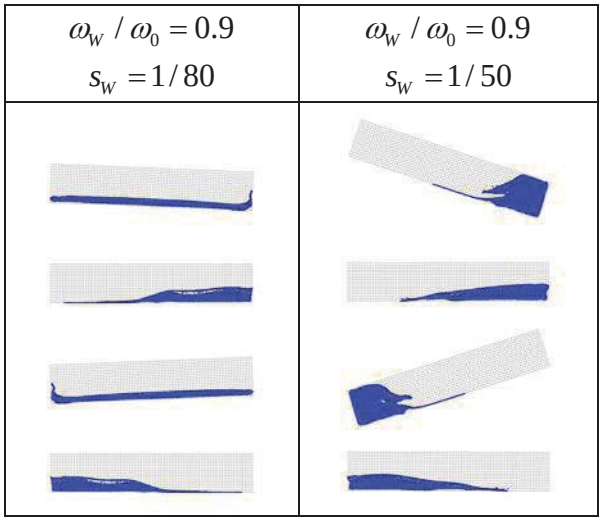

Figure 7: Representative snapshots of fluid inside the tank for two example cases.

4. FINAL REMARKS

Since vessels almost invariably sail with tanks partially filled by liquids, the analysis of ship motions in presence of free surface tanks onboard represents an interesting research topic, having also significant practical implications.

In this paper a time domain simulation approach has been presented where a blended (hybrid) nonlinear 6-DOF ship motions simulation code has been coupled with a nonlinear SPH solver intended to address the flow in the internal tank.

An application of the developed tool has been carried out for a Series-60 hull, with one rectangular tank meant to act as anti-rolling device. The tuning of the tank with the roll natural frequency of the vessel led to a small fluid depth to tank width ratio, and therefore a shallow water fluid regime.

The primary scope of the simulations described in the paper was to analyse the

behaviour of the coupled system for different levels of the wave forcing, in order to highlight the possible occurrence of nonlinear behaviours. To this end, simulations have been carried out in regular beam waves with different steepnesses.

Before carrying out coupled ship-tank simulations, the 6-DOF ship motions code was tuned, in terms of roll dissipation, using available experimental data. Validation comparisons between simulations without tank and available experimental data indicated a good agreement. Similarly, the SPH solver was separately validated on the basis of available experimental data for a 1-DOF coupled mechanical system representing a tuned liquid damper.

Results of coupled ship-tank simulations have been reported in terms of roll response curves, with and without tank, for a range of frequencies. Outcomes from simulations have clearly shown the occurrence of nonlinear phenomena. The most notable behaviour was found to be a reduction of effectiveness of the anti-rolling tank as the wave forcing, and the consequent motions, increase. Also, simulations without tank showed the occurrence of a small ultra-harmonic roll response at wave frequencies close to half the roll natural frequency. Such type of response, instead, did not appear with the tank partially filled by fluid. Also, bending of the response curves, with and without tank, was observed, in line with the hardening restoring of the vessel.

Although the developed approach has been tested herein at zero forward speed in beam regular waves with a box-shaped tank, the software architecture is more flexible. Indeed, the 6-DOF code allows simulating ship motions in case of the vessel manoeuvring in regular/irregular waves, considering the coupling with the tank. Furthermore, the SPH solver allows taking into account more complex tank geometries (e.g. non box-shaped tanks, presence of baffles and obstructions, etc.). As a result, in addition to representing a valuable tool for research purposes, there are potentialities for this approach to be used for more practical engineering applications. Research is presently ongoing regarding the application of the present approach in different conditions and, in particular, in cases associated with different tank dimensions.

5. REFERENCES

Bosch, J.J. van den, Vugts, J.H., 1966 “On roll damping by free-surface tanks” Transactions of the Institution of Naval Architects, Vol. 69, pp. 345-361.

Botia-Vera, E., Souto-Iglesias, A., Bulian, G., Lobovský, L., 2010, “Three SPH novel benchmark test cases for free surface flows”, Proc. 5th ERCOFTAC SPHERIC workshop on SPH applications, pp. 146–155

Bulian, G., Francescutto, A., 2013, ”Second Generation Intact Stability Criteria: on the validation of codes for direct stability assessment in the framework of an example application”, Polish Maritime Research, Vol.20, Issue 4, pp. 52-61

Bulian, G., Francescutto, A., Fucile, F., 2009, "Determination of Relevant Parameters for the Alternative Assessment of Intact Stability Weather Criterion on Experimental Basis", Final report HYD-III-CEH-5, University of Trieste

Bulian, G., Francescutto, A., Sinibaldi, M., 2012, "Roll motion of a ship with low metacentric height in bi-chromatic beam waves", Proc. 11th International Conference on the Stability of Ships and Ocean Vehicles (STAB2012), 23-28 September, Athens, Greece, pp. 187-200

Bulian, G., Souto-Iglesias, A., Delorme, L. , Botia-Vera, E., 2010, “SPH simulation of a tuned liquid damper with angular motion,”

Journal of Hydraulic Research, Vol. 48, Extra Issue, pp. 28–39

Bunnik, T., Veldman, A., 2010, “Modelling the effect of sloshing on ship motions”, Proc. 29th International Conference on Ocean, Offshore and Arctic Engineering (OMAE2010), June 6-11, Shanghai, China, paper OMAE2010-20458

Cardo, A., Francescutto, A., Nabergoj, R., 1981, “Ultraharmonics and Subharmonics in the Rolling Motion of a Ship: Steady-State Solution”, International Shipbuilding Progress, Vol. 28, pp. 234-251

Carrica, P.M., Sadat-Hosseini, H., Stern, F., 2012, “CFD analysis of broaching for a model surface combatant with explicit simulation of moving rudders and rotating propellers”, Computers & Fluids, Vol. 53, pp. 117–132

Cercos-Pita, J.L., 2015, "AQUAgpusph, a new free 3D SPH solver accelerated with OpenCL", Accepted for publication in Computer Physics Communications.

Cercos-Pita, J.L., Souto-Iglesias, A., Gonzalez, L.M., Macià, F., 2013, “AQUAgpusph, a free 3D SPH solver accelerated with OpenCL”, Proc. 8th International SPHERIC Workshop, 4-6 June, Trondheim, Norway

Colagrossi, A., Antuono, M., Touzé, D.L. 2009, “Theoretical considerations on the free-surface role in the Smoothed-particle-hydrodynamics model”, Physical Review E (Statistical, Nonlinear, and Soft Matter Physics), vol. 79(5), 056701

Cummins, S., Rudman,M., 1999, “An SPH projection method”, Journal of Computational Physics, Vol. 152 (2), July, pp. 584–607

de Kat, J.O., Paulling, J.R., 1989, “The Simulation of Ship Motions and Capsizing in Severe Seas”, Trans. SNAME, Vol. 97, pp. 139-168

Faltinsen, O.M., 1990, "Sea Loads on Ships and Offshore Structures", Cambridge University Press

Field, S.B., Martin, J.P., 1976, “Comparative effects of U-tube and free surface type passive roll stabilization systems”, Transactions of the Royal Institution of Naval Architects, Vol. 118, pp. 73-92.

Francescutto, A., Contento, G., 1999, “An Investigation on the Applicability of Simplified Mathematical Models to the Roll-Sloshing Problem”, International Journal of Offshore and Polar Engineering, Vol. 9, pp. 97-104

Hashimoto, H., Ito, Y., Kawakami, N., Sueyoshi, M., 2012, “Numerical Simulation Method for Coupling of Tank Fluid and Ship Roll Motions”, Proc. 11th International Conference on the Stability of Ships and Ocean Vehicles (STAB2012), 23-28 September, Athens, Greece, pp. 477-485

Holden, C., Fossen, T.I., 2012, “A nonlinear 7-DOF model for U-tanks of arbitrary shape”, Ocean Engineering, Vol. 45, pp. 22–37

IMO SDC1/INF.8-Annex 27, 2013, “Draft Guidelines of Direct Stability Assessment Procedures as a Part of the Second Generation Intact Stability Criteria – Submitted by Japan and United States”, in SDC1/INF.8 submitted by Japan, 15 November, London, UK

IMO SLF52/WP.1-Annex 2, 2010, “Preliminary Specifications for the New Generation Intact Stability Criteria”, 28 January, London, UK

IMO, 2009, "International Code on Intact Stability, 2008 - 2009 Edition"

Kijima, K., 2003, "Some studies on the prediction for ship manoeuvrability", Proc. International Conference on Marine Simulation and Ship Maneuverability (MARSIM'03), pp. KN-3-1 – KN-3-10.

Kim, B., Shin. Y.S., 2008, "Coupled seakeeping with liquid sloshing in ship tanks", Proc. 27th ASME International Conference on Offshore Mechanics and Arctic Engineering, 15-20 June, Vol. 6, pp. 247-257

Kim, Y., Nam, B.W., Kim, D.W., Kim, Y.S., 2007, "Study on coupling effects of ship motion and sloshing", Ocean Engineering, Vol. 34, pp. 2176–2187

Lee, B.S., Vassalos, D., 1996, "An investigation into the stabilization effects of anti-roll tanks with flow obstructions", International Shipbuilding Progress, Vol. 43, No. 433, pp. 70-88

Malenica, Š., Zalar, M., Chen, X.B., 2003, "Dynamic coupling of seakeeping and sloshing", Proc. 13th International Offshore and Polar Engineering Conference, 25-30 May, Honolulu, Vol. III, pp. 486-492

Mitra, S., Wang, C.Z., Hai, L.V., Reddy, J.N., Khoo, B.C., 2012, "A 3D fully coupled analysis of nonlinear sloshing and ship motion", Ocean Engineering, Vol. 39, pp. 1–13 (see also Corrigendum Ocean Engineering, Vol. 52, 2012, p. 128)

Monaghan, J.J., 2005, "Smoothed particle hydrodynamics", Reports on Progress in Physics, vol. 68, pp. 1703–1759

Neves, M.A.S., Merino, J.A., Rodríguez, C.A., 2009, "A nonlinear model of parametric rolling stabilization by anti-roll tanks", Ocean Engineering, Vol. 36, pp. 1048–1059

Pérez-Rojas, L., Botia-Vera, E., Cercos-Pita, J.L., Souto-Iglesias, A., Bulian, G., Delorme, L., 2011, "A combined Experimental and SPH Approach to Sloshing and Ship Roll Motions", in "Contemporary Ideas on Ship Stability and Capsizing in Waves", Fluid Mechanics and Its Applications, Springer, Volume 96, Part 10, pp. 735-749 (see also Proc. STAB2009, pp. 261-270)

Sadat-Hosseini, H., Stern, F., Olivieri, A., Campana, E.F., Hashimoto, H., Umeda, N., Bulian, G., Francescutto, A., 2010, "Head-wave parametric rolling of a surface combatant", Ocean Engineering, Vol. 37, pp.859–878

Souto-Iglesias, A., Delorme, L., Pérez-Rojas, L., Abril-Pérez, S., 2006, "Liquid moment amplitude assessment in sloshing type problems with smooth particle hydrodynamics", Ocean Engineering, vol. 33, , pp. 1462–1484

Souto-Iglesias, A., Macìa, F., González, L.M., Cercos-Pita, J. L., 2014, "Addendum to on the consistency of MPS", Computer Physics Communications, Vol. 185(2), pp. 595 – 598

Tzamtzis, S., 2004, "Development and testing of a procedure for the alternative assessment of Weather Criterion on experimental basis", Thesis, University of Trieste and National Technical University of Athens.

Youssef, K.S, Mook, D.T., Nayfeh, A.H., Ragab, S.A., 2003, "Roll Stabilization by Passive Anti-Rolling Tanks Using an Improved Model of the Tank-Liquid Motion", Journal of Vibration and Control, Vol. 9, pp. 839-862

Zhao, W., Yang, J., Hu, Z., Tao, L., 2014, "Coupled analysis of nonlinear sloshing and ship motions", Applied Ocean Research, Vol. 47, pp.85–97

This page is intentionally left blank

Modeling Sailing Yachts' Course Instabilities Considering Sail Shape Deformations

Emmanouil Angelou, *National Technical University of Athens,*angeloum@mail.ntua.gr

Kostas J. Spyrou, *National Technical University of Athens,* k.spyrou@central.ntua.gr

ABSTRACT

The performance of sailing yachts depends partly on the fluctuating pressure field around the sails which causes continual change of the shape of the sails. The present study focuses on the development of a mathematical model for predicting the behaviour of sailing yachts, with a twofold purpose: to evaluate the variations of forces and moments sustained by the sails due to wind induced sails-shape deformations; and to assess the impact of these variations on the development of course-keeping instability phenomena during downwind sailing conditions. The fluid-structure interaction problem of the sails is handled by coupling, in an iterative way, a Vorticity-Stream Function formulation to a Finite Element Method for flexure elements.

Keywords: *Sailing Yachts, Sail Modeling, Downwind Course*

1. INTRODUCTION

The course stability of sailing yachts is a topic that has not attracted much attention, although, historically, several records exist referring to broaching-to incidents of ships with sails (Spyrou 2010). The present study is a first step towards setting up a systematic study of the course stability of sailing yachts operating in wind and waves. A mathematical model is under development, consisted of two major components: an aerodynamic one, addressing the forces on the sails and the variation of their shape due to wind flow; and a hydrodynamic, handling the hull and its appendages.

Sails produce the aerodynamic forces exploited for propulsion. However, because they are very thin, they have their shape continually adapted according to the locally developing pressures. Thus the flying shape of a sail in real sailing conditions differs from its design shape and it is basically unknown. In terms of physical modelling, one can distinguish sailing cases as *upwind* (running to the wind) where the flow is characterized as lifting and can be assumed as attached to the sails; and as *downwind* (running away from the wind) where viscous effects cannot be disregarded and drag effects are dominant. Recently, the fluid-structure interaction problem of the sails in the upwind case has been tackled, by coupling a low order Boundary Element Method for the aerodynamic part (Lifting Surface) to a Finite Element Method for the structural part (Shell Elements), in combination with an iterative scheme that provided the converged flying shape of the sail and the sustained forces and moments (Angelou & Spyrou 2013).

In the current paper, the sails model is expanded to a wider operational range of inflow angles, from the outskirts of upwind sailing, to beam and fully downwind cases. The method is a pseudo-3d approach, based on the evaluation of vorticity of the flow field around certain cross sections of the sails in order to obtain the force and moment coefficients, while the deformed shape of each sail is obtained using a finite element formulation for flexure

elements. The hydrodynamic part is not complete yet. However, in order to qualitatively evaluate our aerodynamic model we coupled it with a typical semi-empirical manoeuvring model accounting qualitatively for hull reaction and wave forces.

2. MATHEMATICAL MODEL

2.1 Equations of Motion and Coordinate Systems

Since downwind following seas are the cases of main interest, the model includes 4 degrees of freedom, surge, sway, roll and yaw and it used three different coordinate systems: an earth-fixed non-rotating coordinate system (X_0,Y_0,Z_0), a wave fixed body system that travels with the wave celerity (x_w,y_w,z_w) and a body fixed system (x,y,z) with its origin fixed on the midship point where the centerplane and waterplane intersect (Fig. 1);

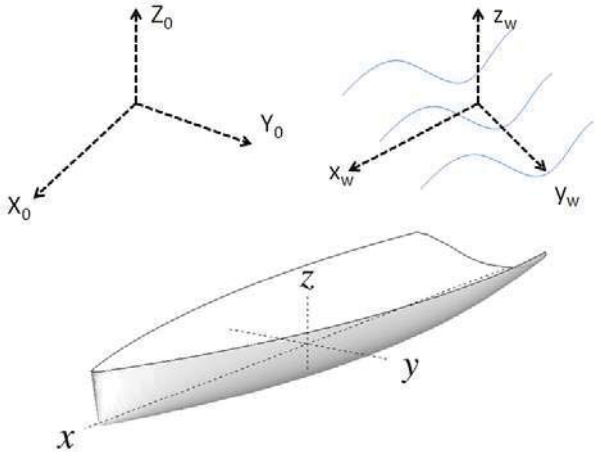

Figure 1: Coordinate Systems.

The systems are in accordance with the right hand rule where ‘x’ axis points positive forward, having on its left the positive ‘y’ axis, while positive ‘z’ axis points upwards.

Assuming the hull as a rigid body, the equations of motions for the 4 degrees of freedom are as in Masuyama & Fukasawa (2011)

$$\left(m+m_x\right)\ddot{x}-\left(m+m_y\cos^2\varphi+m_z\sin^2\varphi\right)\dot{y}\cdot\dot{\psi}= X_{\mathrm{HR}}+X_{\mathrm{R}}+X_{\mathrm{W}}+X_{\mathrm{S}} \tag{1}$$

$$\left(m+m_y\cos^2\varphi+m_z\sin^2\varphi\right)\ddot{y}+ \left(m+m_x\right)\dot{x}\cdot\dot{\psi}+2\left(m_z-m_y\right)\sin\varphi\cos\varphi\cdot\dot{y}\cdot\dot{\varphi}= Y_{\mathrm{HR}}+Y_{\mathrm{R}}+Y_{\mathrm{W}}+Y_{\mathrm{S}} \tag{2}$$

$$\left(I_{xx}+J_{xx}\right)\ddot{\varphi}- \left[\left(I_{yy}+J_{yy}\right)-\left(I_{zz}+J_{zz}\right)\right]\sin\varphi\cos\varphi\cdot\dot{\psi}^2= K_{\mathrm{HR}}+K_{\mathrm{R}}+K_{\mathrm{W}}+K_{\mathrm{S}} \tag{3}$$

$$\left[\left(I_{yy}+J_{yy}\right)\sin^2\varphi+\left(I_{zz}+J_{zz}\right)\cos^2\varphi\right]\ddot{\psi}+ 2\left[\left(I_{yy}+J_{yy}\right)-\left(I_{zz}+J_{zz}\right)\right]\sin\varphi\cos\varphi\cdot\dot{\psi}\cdot\dot{\varphi}= N_{\mathrm{HR}}+N_{\mathrm{R}}+N_{\mathrm{W}}+N_{\mathrm{S}} \tag{4}$$

The subscripts on the right-hand-side of the equations indicate force contribution from *Hull Reaction*, *Rudder*, *Waves* and *Sails*. These terms are grouped into two modules, named *Hull* and *Sails Model* respectively, in accordance with the excitation being of hydrodynamic or aerodynamic origin.

3. SAILS MODEL

3.1 Sails Variation

Sails are surfaces of very small thickness and while this allows a major simplification in the fluid modelling, it simultaneously induces a drawback. This insignificant thickness makes the sail to be a very flexible surface, subjected to deformations due to the pressure forces it sustains under wind flow. Calculating the flow around them then is not enough, as one should

be able to account for the difference between the design shape of the sail and the flying shape it adopts. Moreover, it is important to know the effect this bears to the forces and moments on the sail. Excluding wind tunnel tests and real-time measurements at sea, a common computational approach is to combine a fluid solver for the flow field around the sail with a structural solver for the transition of the initial to the new shape.

Regarding the *upwind* case and in terms of the aforementioned simplification, the small thickness of the sail makes it ideal for being modelled with a potential flow method, such as the one using the Lifting Surface Theory (L.S.T.) (Angelou & Spyrou 2013). This is a formulation for lifting flows that allows the effects of camber and thickness to be decoupled and it is usually applied through a numerical scheme based on the Vortex Lattice Method (V.L.M.). While the lifting surface bears minimal computational cost, it requires that the flow always remains attached to the surface, thus restraining L.S.T.'s applicability to a relatively narrow range of fluid inflow angles.

To examine the behaviour of a sail in a wider operational range, notably *downwind*, as is the scope of this study, the use of viscous flows methods is unavoidable as drag effects become dominant. These methods provide great detail of the flow field, yet they induce a considerable computational cost.

The numerical schemes involving the solution of the Vorticity Transport – Stream Function equations in a computational mesh may appear at first instance outdated compared to modern schemes that handle the primitive variable form of the Navier-Stokes equations. However as the long term objective of this study is directional stability analysis using 6 degrees of freedom while taking into account the instant position and shape of the sail(s), this method was chosen as an intermediate step towards a Lagrangian "free" vorticity formulation, where remeshing of the domain and the induced computational cost can be avoided.

3.2 Sails Modelling

Considering wind flow velocity V_{TW} and a sailing yacht that moves with boat velocity V_B, then the apparent wind, i.e., the wind that actually excites the sails, is defined as in Fossati (2009):

$$V_{AW}^2 = \left(V_{TW} \cdot \cos a_{TW} + V_B\right)^2 + V_{TW} \sin a_{TW} \cos^2 \varphi \tag{5}$$

$$a_{AW} = \operatorname{atan}\left(\frac{V_{TW} \sin a_{TW} \cos\varphi}{V_{TW} \cos a_{TW} + V_B}\right) \tag{6}$$

where a_{TW} is true wind angle and a_{AW} is the apparent wind angle.

The sail forces are obtained in terms of *drag* (C_D) and *lift* (C_L) coefficients, where *drag* (D) is the resulting force on the direction of the free stream flow (apparent wind), while *lift* (L) is normal to it:

$$D = \frac{1}{2}\rho \cdot V_{wind}^2 \cdot S \cdot C_D \tag{7}$$

$$L = \frac{1}{2}\rho \cdot V_{wind}^2 \cdot S \cdot C_L \tag{8}$$

Through transformation to the ship coordinate system the surge and sway forces are obtained:

$$X_S = D \cdot \cos a_{AW} + L \cdot \sin a_{AW} \tag{9}$$

$$Y_S = D \cdot \sin a_{AW} + L \cdot \cos a_{AW} \cdot \cos\varphi \tag{10}$$

Roll and yaw sail induced moments are:

$$K_S = -Y_S \cdot z_{cef} \cdot \cos\varphi \tag{11}$$

$$N_S = \left(Y_S \cdot xcef + X_S \cdot ycef\right) \qquad (12)$$

In this study, the method of aerodynamic force calculation is pseudo-transient, meaning that calculations are performed on certain sections of the sails, and vertical flow interaction effects are ignored. Every section has a computational flow field constructed around it, in the form of an unstructured meshed domain of triangular elements. A Finite Volume numerical scheme is applied on these elements for the solution of the Vorticity Transport and Stream Function equations.

Once the velocity and pressure fields are computed, pressure loads are transformed to nodal forces and they are used for deriving the deformation of the sail via a Finite Element Formulation for flexure beams. When the sail shape has converged, lift and drag coefficients of the section are used in order to calculate total sail excitation. Each section sail coefficient (red lines Fig. 2) is averaged over a surface that extends bilaterally off the section's vertical position (black lines Fig. 2). Total Drag and Lift forces of the sail are defined as

$$D = \frac{1}{2}\rho \cdot V_{wind}^2 \cdot \sum\left\{S_i \cdot C_{Di}\right\} \qquad (13)$$

$$L = \frac{1}{2}\rho \cdot V_{wind}^2 \cdot \sum\left\{S_i \cdot C_{Li}\right\} \qquad (14)$$

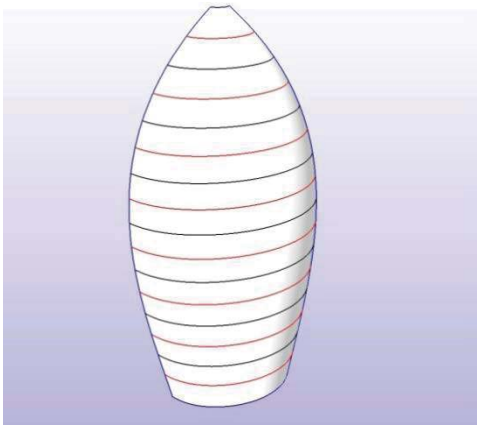

Figure 2: Spinnaker Sail and sections.

3.3 Meshing

The mesh is constructed using the Advancing Front Method – AFV (Peraire et al 1987), which was chosen due to its ability to handle complex geometries whilst its implementation is straightforward. Given the boundary of an outer domain Ω and any internal boundaries Ω_i, this formulation creates an initial front of connected segments, each of which is used as the edge of a candidate triangle element to be added. With every triangle addition, the respective initial segment is replaced by the new edge or edge(s), and the front is reduced until the domain is completely meshed.

However, the obtained mesh may contain triangles with highly acute angles, prone to cause numerical errors during the solution. To overcome this, the smoothing technique of Zhou & Shimada (2000) is applied on the domain. This method treats all triangle edges as springs, either on a compressed or on an elongated state. By iterating through probable nodal positions, this method seeks to find an optimized set, where the torsional energy of every spring is minimized. All non-boundary nodes are moved accordingly and each triangle tends to reach an equilateral shape (Fig. 3).

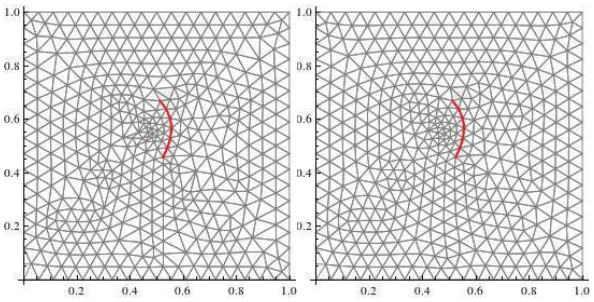

Figure 3: Initial (left) and Smoothed (Right) Mesh around a Sail Section (Bold Red).

While the obtained mesh is smoothed, the size of the triangles in regions away from the given boundaries tends to increase. This is a drawback in accuracy, especially in case the triangles are located in areas where state variables are characterized by large gradients.

A future step is the local refinement in these areas using mesh enrichment techniques.

3.4 Aerodynamic Component

The fluid domain around the sails is obtained by solving the non-conservative Vorticity Transport Equation (15) and the Stream Function Equation (16) using a Finite Volume scheme on an unstructured triangular meshed domain. The triangles are virtually treated as P2 elements, meaning that mid-edge point values of vorticity are included in the calculations, but only in order to update the vorticity on the centres and vertices.

$$\frac{\partial \omega}{\partial t}+u\frac{\partial \omega}{\partial x}+v\frac{\partial \omega}{\partial y}=\nu\left(\frac{\partial^2 \omega}{\partial x^2}+\frac{\partial^2 \omega}{\partial y^2}\right) \quad (15)$$

$$\frac{\partial^2 \psi}{\partial x^2}+\frac{\partial^2 \psi}{\partial y^2}=-\omega \quad (16)$$

The numerical solution of the Vorticity Transport equation is dictated by the viscous split technique where the advection and diffusion terms are treated separately (e.g. see Cottet & Koumoutsakos, 2000) :

$$\frac{\partial \omega}{\partial t}+u\frac{\partial \omega}{\partial x}+v\frac{\partial \omega}{\partial y}=0 \quad (17)$$

$$\frac{\partial \omega}{\partial t}=\nu\left(\frac{\partial^2 \omega}{\partial x^2}+\frac{\partial^2 \omega}{\partial y^2}\right) \quad (18)$$

The pure advection part (17) of the Vorticity Transport equation is treated using the fluctuation-splitting scheme of Nishikawa & Roe (2005). This method provides a way for the calculation of the fraction of the fluctuation of a variable inside any triangle, as that fluctuation is directed to the triangle's downstream nodes. The nodes are characterized as upwind or downwind, according to the triangle's orientation in relation with the local convection velocity vector $\vec{V}$. Thus, in every triangle, transport effects are accounted for, by updating only the downstream nodes.

The pure diffusion equation (18) is treated as in Hoffman & Chiang (2000). Considering any triangle T, by applying Green's theorem on the surface integral of the diffusion equation, the right hand side is transformed to a line integral that can be calculated using the mid-point vorticity values of the triangle edges. These are obtained by interpolation of vorticity value that is assigned on the neighbouring triangles centres, as also on the common nodes they share with triangle T.

The Stream Function, as in Hoffman & Chiang (2000), can be transformed from an elliptic (16) to a pseudo-transient (19) parabolic equation:

$$\frac{\partial \psi}{\partial t}=-\left(\frac{\partial^2 \psi}{\partial x^2}+\frac{\partial^2 \psi}{\partial y^2}+\omega\right) \quad (19)$$

Equation (19) is treated as the diffusion equation (18) with the addition of the calculated vorticity during the current time step as a source term.

The free stream flow is considered to enter a rectangular computational domain from the left side bearing horizontal velocity of constant magnitude u_0, and exit from the right side far downstream of the sails. The same value of inflow velocity is considered at the top and bottom domain boundaries in order to simulate infinite fluid extent normal to them. The stream function is assigned a constant value across the bottom boundary and gradually increases with increasing height according to $u=\partial\psi/\partial y$ so as to provide a constant velocity u_0. The stream function value on the top boundary remains constant until the end of the domain. Initial vorticity values have been set to zero all over the domain. When the wind vector has a non-zero angle of attack then inflow conditions for the velocity remain the same and it is the initial geometry of the sail that is rotated accordingly.

3.5 Aeroelastic Component

The structural response of every discrete sail section to wind loads is modelled using a Finite Element Method for *flexures*. A flexure is an enriched beam element, capable of being subjected to both axial and bending loading. Each section is divided to small segments that correspond to all triangle edges that consist of sail nodes explicitly. Considering a linearly elastic, isotropic and homogeneous material, the displacements **U** of the nodes are calculated by solving the linear system

$$K_{STIFF} \cdot \boldsymbol{U} = \vec{\boldsymbol{F}} \tag{20}$$

The total stiffness matrix K_{STIFF} is composed by superposition of all element stiffness matrices k_E according to their connectivity. The matrix k_E is a joint matrix of a bar and a flexure element, for axial and bending loads respectively without considering any coupling between them. The formation of the bending flexure stiffness matrix for each segment is obtained through the application of the first theorem of Castigliano, with respect to nodal translational and rotational displacements, to the strain energy function U_E of the element (Hutton 2004).

$$U_E = \frac{1}{2}\int \sigma_x \varepsilon_x \mathrm{d}V \tag{21}$$

Assuming that each segment can be considered as an elastic bar of constant cross section, the axial stiffness matrix of the element is formulated by analyzing the axial forces using the stress and strain formulae (Hutton 2004). After solving the linear system, nodal positions are adjusted according to the displacements vector of the solution and the domain is re-meshed.

4. HULL MODEL

As the scope of this study is to emphasize on the sail-induced impact on the development of instabilities, the hull modular parts of the mathematical model have been treated so far using methods that do not necessarily lead to a precise quantification of hull responses. In addition, as the appendages have been approximated by simplified geometries and in the general case flow interaction effects between them have been omitted, hull realistic modelling is underacted. However as this manoeuvring model is still under development and bears a potential for growth of modelling detail regarding the modular parts it consists of, compromising with low level analysis on these components has been tolerated.

4.1 Inertia Terms

The calculation of the moments of inertia is based on the mass distribution of the yacht. For the canoe body, the added masses along y and z axes are calculated by considering sections along the hull and approximating their corresponding added mass coefficients from Korotkin (2008), while for the x axis and added moments of inertia around all axes as in Ridder (2004). The appendages are treated as elongated ellipsoids and their added masses as also their added moments of inertia are approximated as in Korotkin (2008).

4.2 Resistance

The resistance of the yacht can be decomposed to viscous, induced (which is the lift-induced Drag force component that is developing on the body and appendages due to the inflow angle) and wave-making parts. Viscous and induced terms are calculated as in Oossanen (1993) with some modifications regarding the contribution of the canoe body of the hull and the bulbous part of the keel, where a drag coefficient and a form factor have been added respectively, as in Nesteruk & Cartwright (2011) and in Scragg & Nelson (1993). Wherever included in the above formulation, the wetted surface is calculated from the summation of the areas of the hull

panels (Fig. 4) that are immersed at that instant under heel, if any. Lastly, the wave-making resistance of the yacht is calculated as in Pascual (2007).

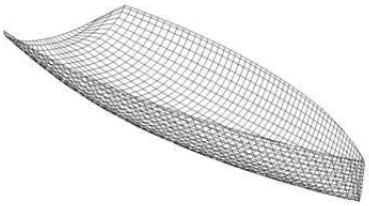

Figure 4: Canoe Body Panels.

4.3 Other Hull Reaction and Rudder

Other hull reaction forces and moments for sway and yaw modes are taken into account using the model of Inoue et al (1979), where the linear hydrodynamic coefficients are as in Clarke (1983) and the nonlinear as in Inoue et al(1979). Heel effects for the same modes have been added as in Hirano & Takashina (1980). Though the aforementioned references provide coefficients suitable for much larger hulls and need treatment regarding appendages effects, they were chosen as a rough indication due to our lack of data regarding the hydrodynamic responses of the studied sailing yacht. Roll terms are limited to damping and restoring moments. Rudder forces and moments in the model are accounted for as in Masuyama&Fukasawa (2011).

4.4 Waves

Considering an undisturbed pressure field around the yacht, the wave excitation is limited to Froude-Krylov forces and moments. These are calculated by integrating the unit potential φ_0 (e.g. Belenky & Sevastianov 2003) on every immersed panel of the hull up to the elevated running waterline, after the panel coordinates have been transformed suitably for the relative position of the hull on the encountered wave.

5. CASE STUDY– RESULTS

5.1 Principal Dimensions

Problems of course stability in strong wind are well known for motorships (e.g. Spyrou 1995, Spyrou et al 2007), while for sailing yachts the available studies are only a few (e.g. Harris et al 2000). The yacht used as a case study is a one-mast modern cruiser, carrying a mail and a jib sail, or a main and a spinnaker sail, for upwind and downwind courses respectively. Principal dimensions of the hull are on table 1.

HULL	
Length Overall	13.90 m
Length Waterline	12.86 m
Beam Waterline	2.79 m
Draught [Canoe Body | Total]	0.525 m | 3.45 m
Displacement	7830 kg

Table 1.Hull and Sails Dimensions.

The concept of the first two “trial” simulated scenarios is to apprehend the sensitivity of the model. The first scenario handles a case where the yacht is sailing under the influence of constant wind of 10 knots speed and $a_{TW}=0^o$ direction off the stern (*true* wind angle) while wave excitation is omitted.

After a small simulated time (t =10sec) the wind direction is considered to change to $a_{TW}=10^o$ off the stern while the rudder angle is kept fixed to zero position. On both cases counter-rotating vortices develop in front and back of the sail (Fig.5). This vorticity trend was expected, as compared with a bluff canopy body, bearing strong similarity to a sail (Johari & Desabrais 2005). As the wind angle changes, the yacht commences a turn. Trajectory and responses for 30 seconds of simulation are depicted in Figures 6 to 8.

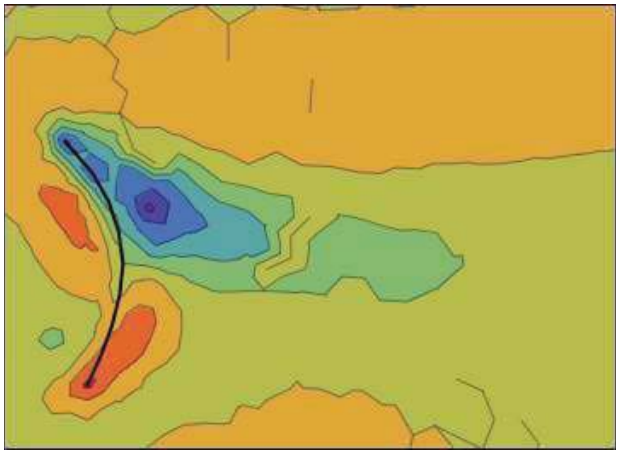

Figure 5a: Vorticity field, V_{wind}: 10kn, a_{TW}: 0°

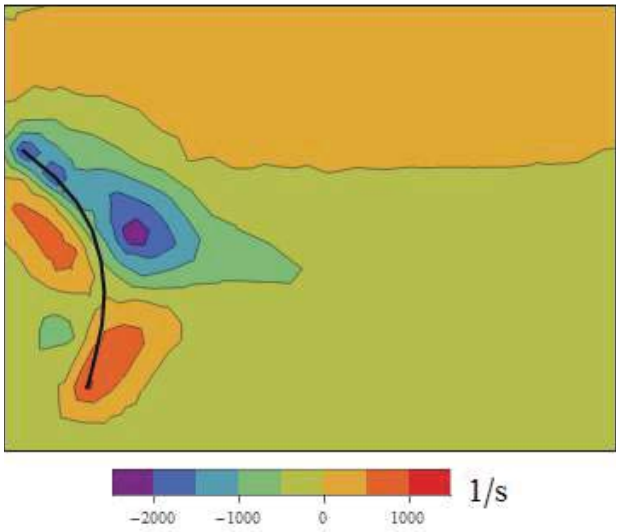

Figure 5b: Vorticity field, V_{wind}: 10kn, a_{TW}: 10°

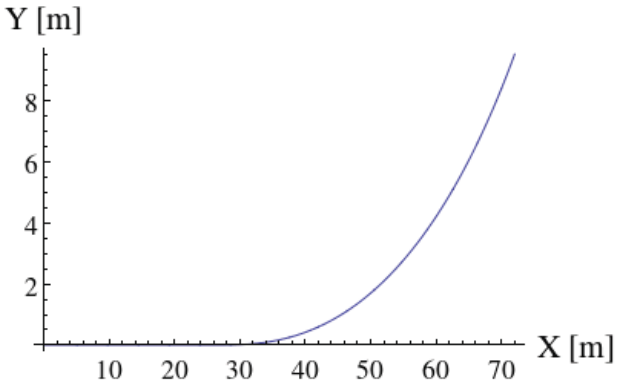

Figure 6: Course trajectory: scenario 1.

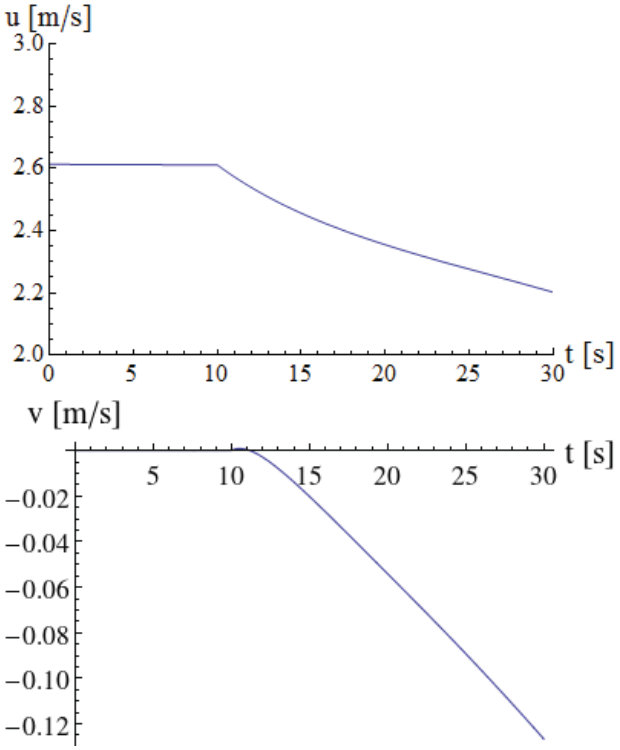

Figure 7: Surge (top) and sway (bottom) velocity.

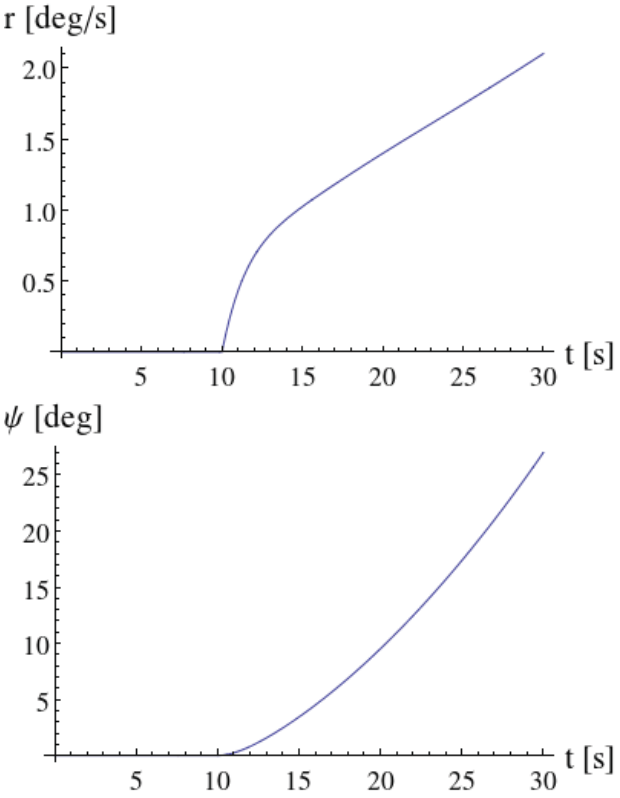

Figure 8: Yaw turning rate (top) and angle (bottom).

In the second scenario the yacht is sailing under the influence of a purely following *true* wind (0^o off the stern) of constant speed of 10 knots. Simultaneously it is excited by following harmonic waves of $\lambda = 1.5\ L_{wl}$ with steepness H/λ=0.036. As shown in Fig. 9, the yacht experiences asymmetric surging. Moreover, for a very steep wave (H/λ=0.051) it adopts surf-riding behaviour (Fig. 9).

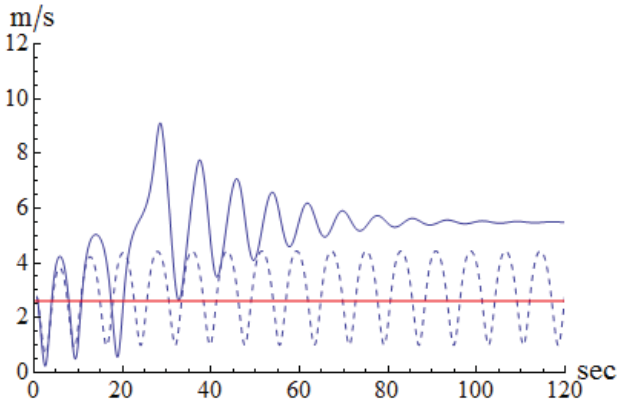

Figure 9: Asymmetric surging and surf-riding.

6. CONCLUSIONS – FUTURE WORK

This study is the first step towards a mathematical model suitable for the analysis of directional instabilities phenomena of sailing yachts. As the authors' intention is to evaluate the impact of sail shape deformations and sail forces variations on the behaviour of yachts, the hull model has been formulated inside the context of low level detail analysis, while the sails have been modelled by coupling two relatively simple models, among the family of the finest advanced methods: a pseudo-3d Vorticity-Stream function formulation and a Finite Element Method for flexure elements.

The performance of the sails model seems realistic, in qualitative terms. Future steps include further development by implementing turbulence effects and by moving towards a full 3d method for both the fluid and structural formulations.

The hull model has proved to be hypersensitive to excitations. This was expected and it is attributed to the choice of handling (in lack of any full scale data or of a more appropriate formulation) the performance of a small sailing yacht using methods intended for hulls of significant greater displacement; doing so, the influence of the appendages was underacted and the damping of the hull underestimated.

The same method used for the fluid part of the sails model can be modified to tackle the problem of finding a realistic pattern of hull reaction forces and moments.

7. ACKNOWLEDMENTS

Mr. Angelou acknowledges with gratitude his support by NTUA's PhD Research Fund for Doctoral Candidates (ΕΛΚΕ).

8. REFERENCES

Angelou, E. and Spyrou, K.J., 2013, "Simulations of Sails of a Yacht Using a Fluid-Structure Interaction Model", 10th HSTAM International Congress on Mechanics, Chania, Greece.

Belenky, V.L. and Sevastianof, N.B., 2003, "Stability and Safety of Ships, Vol. II : Risk of Capsizing", Elsevier Ocean Engineering Book Series, Vol.10-II, pp. 83-86.

Clarke D., Gedling P. and Hine G., 1983, "The Application of Manoeuvring criteria in Hull Design using Linear Theory", RINA Transactions, Vol. 125, pp. 45-68.

Cottet, G.H., Koumoutsakos, P.D., 2000, "Vortex Methods: Theory and Practice", Cambridge University Press, Cambridge, UK.

Fossati, F.,2009, "Aero-Hydrodynamics and the Performance of Sailing Yachts", Adlard Coles Nautical, London, pp. 265-287.

Harris, D., Thomas, G., Renilson, M., 2000, "Towards Predicting the Behaviour of Yachts in Following Seas", 7th International Conference on Stability of Ships and Ocean Vehicles, pp. 595-608.

Hirano, M. and Takashina, J., 1980, "A Calculation of Ship Turning Motion Taking Coupling Effect Due to Heel into Consideration", Journal of the West-Japan Society of Naval Architects and Ocean Engineers, Vol. 59, March 1980, pp. 71-81.

Hoffmann, K.A. and Chiang, S.T., 2000, "Computational Fluid Dynamics", Vol. II, Engineering Education System, pp. 391-402.

Hutton, D.V., 2004, "Fundamentals of Finite Element Analysis", Mc-Graw Hill, pp. 91-131.

Inoue, S., Hirano, M. and Mukai, K., 1979, "The Non-linear Terms of Lateral Force and Moment Acting on Ship Hull in Case of Maneuvering", The Japan Society of Naval Architects and Ocean Engineers, Vol 58, August 1979, pp. 153-160.

Johari, H. and Desabrais, J.K., 2005, "Vortex Shedding in the Near Wake of a Parachute Canopy", Journal of Fluid Mechanics, vol. 536, pp.185-207.

Korotkin, A.I., 2008, "Added Masses of Ships Structures, Springer, Series of Fluid Mechanics and its Applications, Vol.88, pp. 82.

Masuyama, Y. andFukasawa T., 2011, "Tacking Simulation of Sailing Yachts with New Model of Aerodynamic Force Variation During Tacking Maneuver", SNAME Journal of Sailboat Technology, Article 2011-01.

Nesteruk, I. and Cartwright, J.H.E., 2011, "Turbulent Skin-Friction Drag on a Slender Body of Revolution and Gray's Paradox", 13th European Turbulence Conference (ETC13), Journal of Physics: Conference Series 318.

Nishikawa, H. and Roe, L.P., 2005, "Towards High-Order Fluctuation-Splitting Schemes for Navier-Stokes Equations", 17th AIAA CFD Conference, Toronto.

van Oossanen, P., 1993, "Predicting the Speed of Sailing Yachts", SNAME Transactions, Vol. 101, pp. 337-397.

Pascual, E., 2007, "Revised Approached to Khaskind'sMethod to Calculate the Wave-Making Resistance Depending on the Sectional Area Curve of the Ship", Journal of Ship Research, Vol. 51, September 2007, pp. 259-266.

Peraire, J., Vahdati, M., Morgan, K. and Zienkiewicz, O.J., 1987, "Adaptive Remeshing for Compressible Flow Computations", Journal of Computational Physics, Vol. 72, pp. 449-466.

Ridder, E.J., Vermeulen, K.J. and Keuning, J.A., 2004, "A Mathematical Model for the Tacking Maneuver of a Sailing Yacht", The International HISWA Symposium on Yacht Design and Yacht Construction, Amsterdam, Netherlands.

Scragg C.A. and Nelson B.D., 1993, "The Design of an Eight-Oared Rowing Shell", SNAME Marine Technology, Vol. 30, No.2, April 1993, pp. 84-49.

Spyrou K., 1995, "Yaw Stability of Ships in Stationary Wind", Ship Technology Research/Schiffstechnik, 42, No.1, pp. 21-30.

Spyrou K., Tigkas, I., Hatzis, A., 2007, "Dynamics of a Ship Steering in Wind

Revisited", Journal of Ship Research, 51, pp. 160-173.

Spyrou, K.J., 2010, "Historical Trails of Ship Broaching-To", The Transactions of the Royal Institution of Naval Architects: Part A - International Journal of Maritime Engineering, 152, Part A4, pp. 163-173.

Zhou, T. and Shimadi, K., 2000, "An Angle-Based Approach to Two-Dimensional Mesh Smoothing", Proceedings of the Ninth International Meshing Roundtable, New Orleans, pp. 373–384.

This page is intentionally left blank

Session 13.1 – STABILITY IN ASTERN SEAS

Coherent Phase-Space Structures Governing Surge Dynamics in Astern Seas

Toward a Split-Time Method for Estimation of Probability of Surf-Riding in Irregular Seas

The Effect of Ship Speed, Heading Angle and Wave Steepness on the Likelihood of Broaching-To in Astern Quartering Seas

This page is intentionally left blank

Coherent Phase-Space Structures Governing Surge Dynamics in Astern Seas

Ioannis Kontolefas, *National Technical University of Athens*, ikon@central.ntua.gr

Kostas J. Spyrou, *National Technical University of Athens*, spyrou@deslab.ntua.gr

ABSTRACT

Consideration of a steep multi-chromatic wave field greatly increases the complexity of ship surge dynamics as it renders the underlying strongly nonlinear system also time-dependent. Consequently, conventional concepts used for the analysis of stationary phase-space flows are no longer sufficient to support an in-depth investigation of ship dynamics. To overcome this hindrance, the concept of hyperbolic Lagrangian Coherent Structures (LCSs) is employed. These phase-space objects can be regarded as finite-time generalizations of the stable and unstable manifolds of hyperbolic trajectories defined in dynamical systems with special (such as periodic or quasiperiodic) time dependencies. LCSs represent, locally, the strongest repelling or attracting material surfaces (curves in the case of 2-dimensional systems) advected with the phase flow. We identify hyperbolic LCSs that are intrinsic to the phase flow associated with the surge motion of a ship in astern seas. To the global approach of LCSs is incorporated a scheme aiming to track in space-time "local features" of the flow. The emerging new toolset can enhance substantially current efforts towards a rigorous assessment of ship dynamic stability in steep following seas.

Keywords: *Surf-riding, Multi-frequency Waves, Lagrangian Coherent Structures*

1. INTRODUCTION

The mechanisms generating surf-riding for a ship in regular seas have been extensively studied in the past (Kan 1990; Spyrou 1996). However, gaining understanding beyond the context of harmonic waves has been considered as a daunting task, till recently. The consideration of a multi-frequency wave field brings in new concepts accruing from the time-dependent nature of the problem.

For the regular sea scenario, it is well known that surf-riding can be identified as an equilibrium solution of the surge equation of motion. The consideration, though, of more general wave forms introduces profound complications. For an irregular seaway, this key definition needs to be revised, since stationary states are not likely to exist; i.e., one cannot assume that the underlying non-autonomous dynamical system will admit constant solutions. Therefore, a broader definition of surf-riding needs to be sought.

These difficulties have been recognized and a phenomenological approach to surf-riding in irregular seas has been proposed, expanding upon the notion of wave celerity and its role in signaling the capture to surf-riding (Spyrou et al. 2012, 2014a). In particular, definition and methods for the calculation of wave celeri-

ty for an irregular seaway were proposed and their relevance to the problem of surf-riding was examined. The appeal of such an approach is that it can permit the evaluation of the probability of surf-riding in irregular seas, by setting up the latter as a threshold exceedance problem.

Through the identification of "surf-riding equilibria", i.e. points on the wave where the equilibrium of forces in the longitudinal direction of the ship is instantaneously satisfied, Belenky et al. (2012) endeavoured to gain insight into the dynamics of surge equation in multi-frequency following waves. It is noted that for the calculation of such points, celerity of irregular waves needs to be evaluated.

In another study, Spyrou et al. (2014b) examined the possibility of extracting and tracking "features" related to the surge dynamics in irregular seas (the term is used to characterize objects that are relevant to the problem considered). It was concluded that meaningful features are found among the elements of the zero set of the "acceleration field" i.e., points on the phase space where the acceleration and its time derivative attain, instantly, zero values. Moreover, it was conjectured that certain points satisfying such a condition correlate with surf-riding events.

In the current work, new methods with potential to yield further insights into the dynamics of the surge motion in multi-chromatic astern seas are applied. In particular, the concept of hyperbolic Lagrangian Coherent Structures (LCSs) is tested for unveiling the changing-in-time organization of system's phase-space. Through their organizing role, these structures can be considered as analogues of the stable and unstable manifolds of hyperbolic fixed points, defined in autonomous dynamical systems. For their identification different methods can be applied. Here, a popular, in the nonlinear dynamics literature, numerical scheme is applied, based on the calculation of the spatial distribution of the largest finite-time Lyapunov Exponent of system's trajectories.

2. LAGRANGIAN COHERENT STRUCTURES

2.1 General

The concept of Lagrangian Coherent Structures seems to have emerged as result of the interbreeding of ideas originating from the fields of dynamical systems theory and fluid dynamics. Although the term was first introduced by Haller & Yuan (2000) many people have contributed in the development of computational strategies – for a short review see Shadden (2011). In the context of fluid flows, LCSs can be physically observed as the cores of emergent trajectory patterns and are identified as, locally, the strongest attracting/repelling material surfaces advected with the flow. LCSs have been extensively used during the last years in a wide range of applications concerning physical and biological flows, while the theory, as well as efficient calculation methods, are still developing.

2.2 Identification of LCSs

Although one can choose among different identification schemes (such as the finite size Lyapunov Exponent (FSLE) approach, or the variational theory of hyperbolic LCSs developed recently by Haller (2011) that enables a more rigorous computation) for the needs of the current study we will consider a widely used computational procedure, which involves the calculation of the largest finite-time Lyapunov Exponent (FTLE) field.

Let us consider the following dynamical system that defines a flow on the plane,

$$\dot{x} = f(x,t), \qquad x \in D \subset \mathbb{R}^2, \quad t \in \left[t^-, t^+\right] \qquad (1)$$

A trajectory of system (1) at time t, starting from the initial condition x_0 at t_0, will be denoted by $x(t;t_0,x_0)$. We can write for the flow map $F_{t_0}^{t}(x_0)$ of (1),

$$\begin{aligned} F_{t_0}^{t}: \quad & D \to D \\ & x_0 \mapsto x(t;t_0,x_0) \end{aligned} \tag{2}$$

Through (2), the phase-particle passing from x_0 at time t_0, is associated with its position $x(t;t_0,x_0)$ at time t. If we furthermore consider two phase-particles, located at x_0 and $x_0+\xi_0$ at time t_0, we can write for their distance $\|\xi_t\|$, in a first order approximation with respect to $\|\xi_0\| \ll 1$,

$$\begin{aligned} \|\xi_t\| &\approx \left\|\nabla F_{t_0}^{t}(x_0)\,\xi_0\right\| = \\ &= \|\xi_0\|\sqrt{\hat{\xi}_0^T\left[\nabla F_{t_0}^{t}(x_0)\right]^T \nabla F_{t_0}^{t}(x_0)\,\hat{\xi}_0} \end{aligned} \tag{3}$$

In the above $\hat{\xi}_0$ is the unit vector along the direction of ξ_0, A^T denotes the transpose of A, while $\nabla F_{t_0}^{t}(x_0)$ is the deformation gradient and $C_{t_0}^{t}(x_0)=\left[\nabla F_{t_0}^{t}(x_0)\right]^T \nabla F_{t_0}^{t}(x_0)$ the right Cauchy-Green deformation tensor, both evaluated at x_0. $C_{t_0}^{t}(x_0)$ is a real symmetric, positive definite tensor and as such has real positive eigenvalues,

$$0 < \lambda_1 \le \lambda_2 \tag{4}$$

Moreover, the corresponding eigenvectors e_i, $i=1,2$ form an orthonormal basis. The Cauchy-Green deformation tensor provides a measure of how line elements in the neighbourhood of x_0 deform under the flow i.e., how the lengths and the angles between line elements change, when considering the configuration in the close vicinity of $x(t;t_0,x_0)$ at times t_0 and t. A circular blob of initial conditions centred at x_0 will evolve into an ellipse, with the major (minor) axis aligned with the direction of the eigenvector e_2 (e_1). The coefficients of expansion along these directions will be given by $\sqrt{\lambda_i}$, $i=1,2$.

The finite-time Lyapunov exponents (FTLEs) are defined as follows,

$$\Lambda_i = \frac{1}{|t-t_0|}\ln\sqrt{\lambda_i}, \qquad i=1,2 \tag{5}$$

The largest FTLE, Λ_2, is usually referred to as "FTLE" without distinction. By virtue of (5) Λ_2 can be regarded as a time-averaged measure of stretching and therefore, as a (rough) measure of a trajectory's hyperbolicity. Yet, as noted by Shadden (2011) and Haller (2011), this does not hold in general.

Through the calculation of the spatial FTLE distribution, the identification of LCSs can be made possible. The latter will appear as local maximizing curves of the FTLE field. Typically, the calculation of the field is performed on the basis of a structured grid of initial conditions spanning a considered domain at a given time t_0. The grid is integrated over a specified time interval, $\tau = t - t_0$, using a numerical integration algorithm. Once the final position of each grid point is calculated, the deformation gradient is obtained by implementing a finite difference scheme on the nodes of the initial grid. In the final step of the procedure, the largest eigenvalue of the deformation gradient is computed and the FTLE field is calculated directly from expression (5). The location of repelling/attracting LCSs can be identified as ridges of the FTLE field when forward/backward integration times are considered – contraction can be viewed as expansion in reverse time.

3. MATHEMATICAL MODEL OF SURGE MOTION

Consider the following unidirectional waveform comprised of *N* propagating, harmonic wave components,

$$\zeta(x;t) = \sum_{i=1}^{N} A_i \cos\left[k_i x - \omega_i t + \varepsilon_i^{(r)}\right] \tag{6}$$

In the above, x is the distance from an earth-fixed point of reference, while A_i, k_i and ω_i are the amplitude, wave number and frequency, respectively, of the distinct wave component i; $\varepsilon_i^{(r)}$ denotes the random phase of the latter, uniformly distributed in the range $[0, 2\pi)$.

We, furthermore, consider an elementary mathematical model that can reproduce asymmetric surging and surf-riding occurrences in following waves of the form (6) – Spyrou et. al. (2012, 2014a),

$$\underbrace{\left(m - X_{\dot{u}}\right)\ddot{\xi}}_{inertia} = \underbrace{\left(\tau_0 n^2 + \tau_1 n \dot{\xi} + \tau_2 \dot{\xi}^2\right)}_{thrust} - \underbrace{\left(r_1 \dot{\xi} + r_2 \dot{\xi}^2 + r_3 \dot{\xi}^3\right)}_{resistance} + \underbrace{\sum_{i=1}^{N} A_i RAO_i \sin\left[k_i \xi - \omega_i t + \varepsilon_i^{(r)} + \varepsilon_{fi}\right]}_{wave\ force} \tag{7}$$

In the equation above, ξ is the position of a ship-fixed point of reference with respect to the earth-fixed origin, while RAO_i and ε_{fi} denote the response-amplitude-operator and phase, respectively, of the surging force corresponding to the wave component i; n corresponds to the propeller revolutions. The overdot denotes differentiation with respect to time t. Setting,

$$x_1 = \xi \ , \quad x_2 = \dot{\xi} \tag{8}$$

equation (7) can be written in normal form,

$$\begin{aligned} \dot{x}_1 &= x_2 \\ \dot{x}_2 &= \Big\{ \tau_0 n^2 + \\ &\quad + \sum_{i=1}^{N} f_i \sin\left[k_i x_1 - \omega_i t + \varepsilon_i^{(r)} + \varepsilon_{fi}\right] - \\ &\quad - \left(r_1 - \tau_1 n\right) x_2 - \left(r_2 - \tau_2\right) x_2^2 - r_3 x_2^3 \Big\} \Big/ \left(m - X_{\dot{u}}\right) \end{aligned} \tag{9}$$

where in the above $f_i = A_i RAO_i$.

4. APPLICATION

We select, as a case study, the tumblehome hull from the ONR topside series with $L = 154\ m$, $B = 18.8\ m$ and $T = 5.5\ m$. To test the applicability of the method in the problem considered, we first write system (9) for $N = 1$ (regular waves),

$$\begin{aligned} \dot{x}_1 &= x_2 \\ \dot{x}_2 &= \left(m - X_{\dot{u}}\right)^{-1} \\ &\quad \Big[\left(\tau_1 n - r_1\right) x_2 + \left(\tau_2 - r_2\right) x_2^2 - r_3 x_2^3 + \\ &\quad + f \sin\left(k x_1 - \omega t + \varepsilon\right) + \tau_0 n^2 \Big] \end{aligned} \tag{10}$$

We set the wave length and steepness values to $\lambda = L$ and $H / \lambda = 0.04$, respectively, where H the wave height. Deep water is assumed. For the calculation of the FTLE field, a grid is considered at $t_0 = 300\ s$ on a (x_1, x_2) domain. Integration time is set to $\tau = 45\ s$. The graph of the resulting field can be seen on the left part of figure 1. On the right part of the same figure, we visualize loci of points where the field surpasses a selected threshold of $0.85 \mathrm{Max}\left(\Lambda_2\right)$. The emergent curves correspond to repelling LCSs over the interval $[t_0, t_0 + \tau]$.

To further examine the relevance of these structures with the stable and unstable manifolds of hyperbolic fixed points arising in the context of surf-riding in regular waves, we render (10) in autonomous form by considering the following transformations,

$$x_1 = x_1^w + ct \ , \quad x_2 = x_2^w + c \tag{11}$$

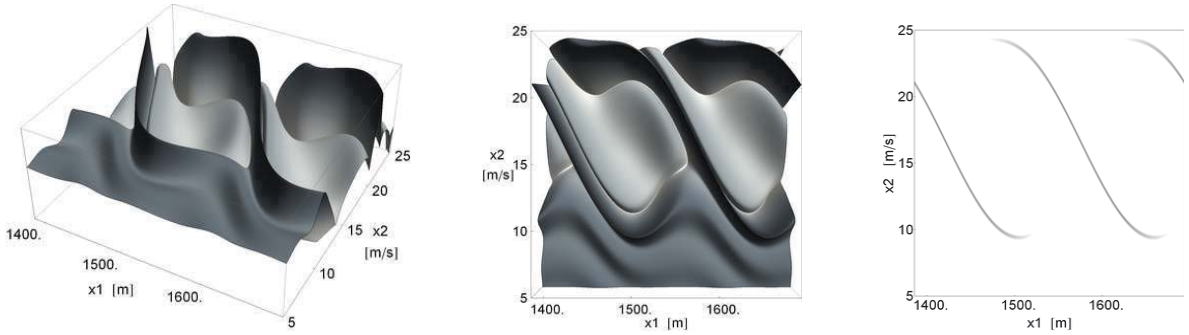

Figure 1 Harmonic excitation: The graph of the forward FTLE field over a (x_1, x_2) domain (left, middle). Loci of points where the field surpasses a selected threshold (right).

In the above, x_1^w and x_2^w is the longitudinal position and velocity, respectively, of the ship with respect to a frame located at a wave crest, translating with the wave celerity c.

Applying expressions (11) to system (10) we obtain, after rearranging, the following set of equations,

$$\begin{aligned}
\dot{x}_1^w &= x_2^w \\
\dot{x}_2^w &= \left(m - X_{\dot{u}}\right)^{-1} \\
&\left\{ \left[\tau_1 n - r_1 + 2c\left(\tau_2 - r_2\right) - 3r_3 c^2\right] x_2^w + \right. \\
&\quad + \left(\tau_2 - r_2 - 3r_3 c\right)\left(x_2^w\right)^2 - r_3\left(x_2^w\right)^3 + \\
&\quad \left. + f\sin\left(k x_1^w + \varepsilon\right) + g\left(c, n\right)\right\}
\end{aligned} \tag{12}$$

where,

$$\begin{aligned}
g\left(c,n\right) &= \tau_0 n^2 + \\
&+ \left(\tau_1 n - r_1\right)c + \left(\tau_2 - r_2\right)c^2 - r_3 c^3
\end{aligned} \tag{13}$$

It can be seen that system (12) does not depend (explicitly) on time. Stationary solutions can be obtained by setting the right hand side to be equal to zero and solving with respect to x_1^w and x_2^w. In the upper part of figure 2, a number of saddle points are identified and the unstable/stable manifolds are "grown" by integrating perturbed, with respect to the fixed points and along the eigendirections, initial conditions forward and backward in time. Wave length and nominal speed are set to $\lambda = L$ and $u_{nom} = 12.5\ m/s$. The figure on the left (right) correspond to a wave steepness of $s = 0.015\ \ (s = 0.04)$.

We, consequently, consider system (10) and calculate, for the same settings, the forward ($\tau = 420\ s$) and backward ($\tau = -240\ s$) FTLE field at $t_0 = 0\ s$. LCSs are identified as in the case of figure 1. Results are presented in the lower part of figure 2; grey (black) lines correspond to repelling (attracting) LCSs. We note that the arrangement of the structures revealed is, substantially, identical to the arrangement of manifolds integrated from the saddle points. The only difference is that the former are translating with the wave celerity – as system (10) is expressed with respect to an earth-fixed frame.

We now introduce a second wave component i.e., system (9) is considered with $N = 2$. The length and steepness of the reference wave are set to $\lambda_1 = L$ and $s_1 = 0.04$. The parameters of the second wave component are fixed such that $\omega_2/\omega_1 = 0.91$ and $s_2/s_1 = 0.4$. Nominal speed is set to $u_{nom} = 12\ m/s$. FTLE fields are calculated at $258\ s$ and $282\ s$ (figure 3). As it can be noticed, LCSs seem to persist while their arrangement resembles, in a sense, to that observed in the regular case. This time though, the image is somehow "distorted" – as expected.

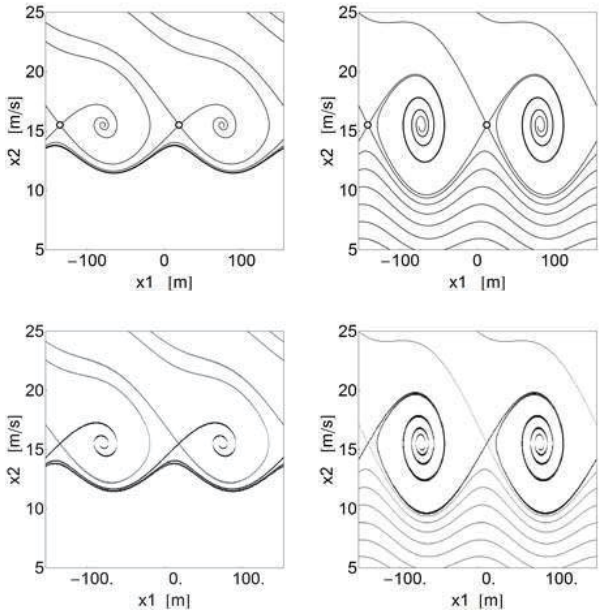

Figure 2 Top: Manifolds of hyperbolic points of (12). Bottom: LCSs of (10) obtained from forward (grey) and backward (black) FTLE fields.

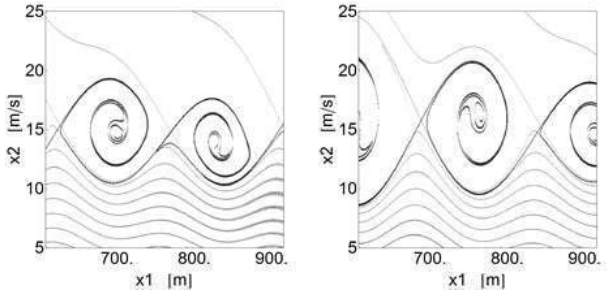

Figure 3 Bi-chromatic excitation: Attracting (black) and repelling (grey) LCSs.

The same procedure is repeated for the case of a JONSWAP spectrum with a peak period and significant height of $T_p = 10\ s$ and $H_s = 5.5\ m$, respectively. A frequency range of $0.5\omega_p$ is considered around the peak value ω_p and a 51-component wave is produced. Nominal speed is set to $u_{nom} = 12\ m/s$. Results are displayed in figure 4. As it can be seen, the arrangement of the identified structures appears to be fairly complicated.

Returning to the bi-chromatic scenario, we attempt, this time, to ascertain the organizing

role of LCSs on the time-varying phase-flow. We set $\lambda = L$, $s_1 = 0.025$, $\omega_2/\omega_1 = 0.76$, $s_2/s_1 = 0.4$ and $u_{nom} = 12\ m/s$. In figure 5 a parcel of particles is integrated – these correspond to different initial conditions for the ship. The evolution of the parcel under the flow reveals different "long-term" behaviour of particle trajectories, as the former, after some time, splits in two. Some particles seem to respond in a surging-like manner (figure 5, particles on the left part of the last snapshot), while others seem to be engaged to surf-riding (same snapshot, right part).

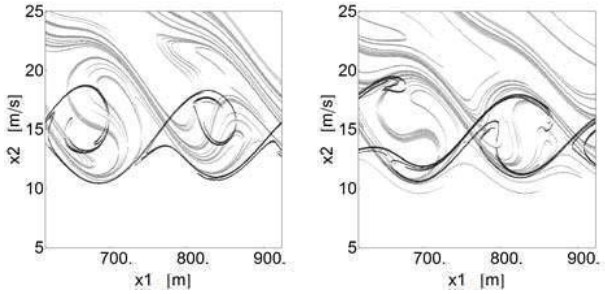

Figure 4 Attracting (black) and repelling (grey) LCSs for the case of a JONSWAP spectrum (51 wave components).

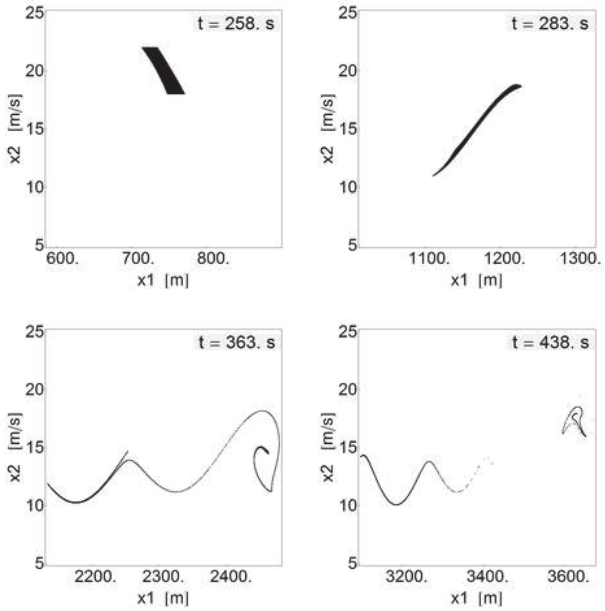

Figure 5 Bi-chromatic excitation: Integration of a dense patch of initial conditions reveals qualitatively different "long-term" behaviour of particle trajectories.

We keep the same setting and calculate the FTLE field on a domain containing the initial conditions ($t = 258\ s$). It seems that the "sus-

pect" for the situation depicted above can be identified among the repelling LCSs of the phase flow. Specifically, the repelling LCS associating with the hyperbolic trajectory passing near (790,16) at time $t = 258\ s$ (figure 6, snapshots on the left), acts as a transport barrier between regions of the flow with distinct dynamics. In fact, particles travel along this repelling structure towards the hyperbolic trajectory, where they are redirected towards different branches of the attracting LCS correlating with the same trajectory (figure 6, last three snapshots, top and bottom row).

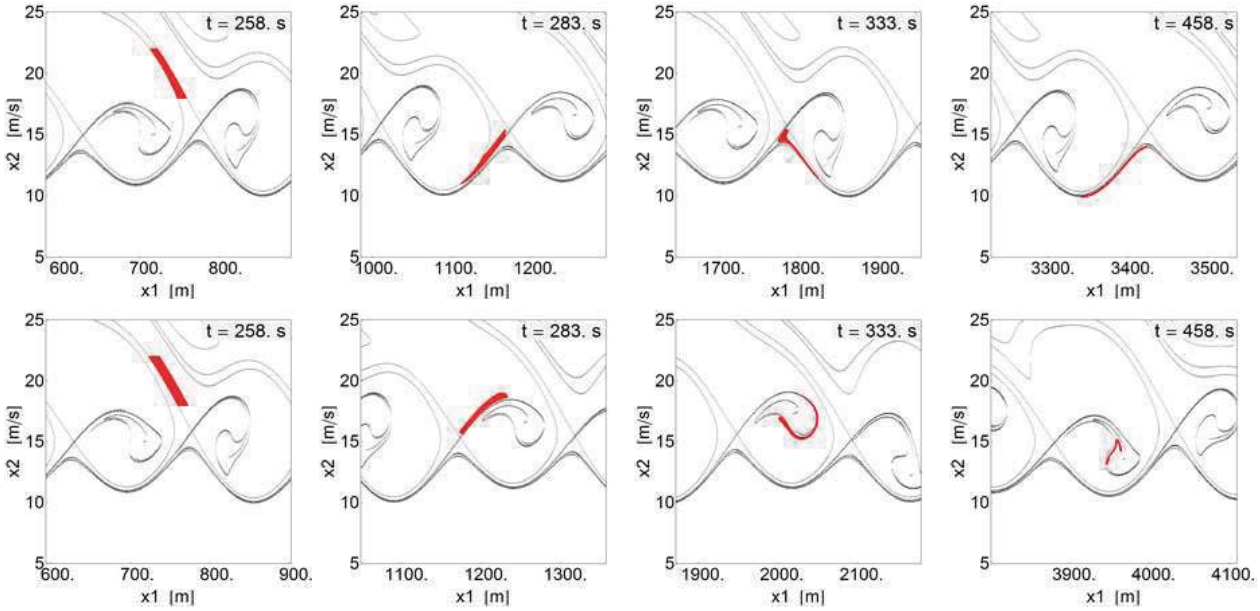

Figure 6 Same setting as in figure 5. Advection of two adjacent phase-particle parcels (red); integration of 91.000 and 118.000 (approx.) initial conditions, top and bottom row respectively.

Lastly, a bi-chromatic scenario is considered, with the frequency and steepness ratio of the two related wave components set to $\omega_2/\omega_1 = 0.93$ and $s_2/s_1 = 0.5$, respectively. The reference wave has been chosen such that $\lambda_1 = L$ and $s_1 = 1/30$, while nominal speed is set to $u_{nom} = 12\ m/s$.

We differentiate (9) with respect to time to obtain the acceleration field $a = (\ddot{x}_1, \ddot{x}_2)$ – the use of this term is justified from the fact that one can interpret (9) as a velocity field on the phase plane. Our objective is to track critical points of a i.e., points where the acceleration vector vanishes. In Spyrou et al. (2014b) it has been conjectured that certain critical points of this field correlate with surf-riding events. Furthermore, in Spyrou et al. (2015) it has been argued that critical points of a moving along paths that "resemble" to solutions of (9) seem to mark regions in the extended phase space where ensembles of trajectories are engaged to surf-riding.

In figure 7, a simulation corresponding to the aforementioned scenario can be seen (red line). Distance is measured from amidships (x-axis) while u-axis refers to velocity as measured by an on-shore observer. Three critical points of the acceleration field have been detected at around $t = 220\ s$ (these have been selected as they are related to the calculated trajectory; one could find more critical points at different space-time intervals). Their paths (grey and black lines) have been computed using the Feature Flow Field method (Theisel & Seidel 2003). In the same figure, we have included sections depicting LCSs that have been identified on phase-space windows around the ship at selected time instants. There seems to be a strong correspondence between the paths

of two critical points (denoted with grey lines) and hyperbolic trajectories revealed via the FTLE fields. The third critical point, on the other hand, appears near the core of an attracting LCS, in a region of the phase flow where a surf-riding state can be revealed (Spyrou et al. 2015). It is noted that for the considered arrangement, this would be a periodic trajectory with an attracting character.

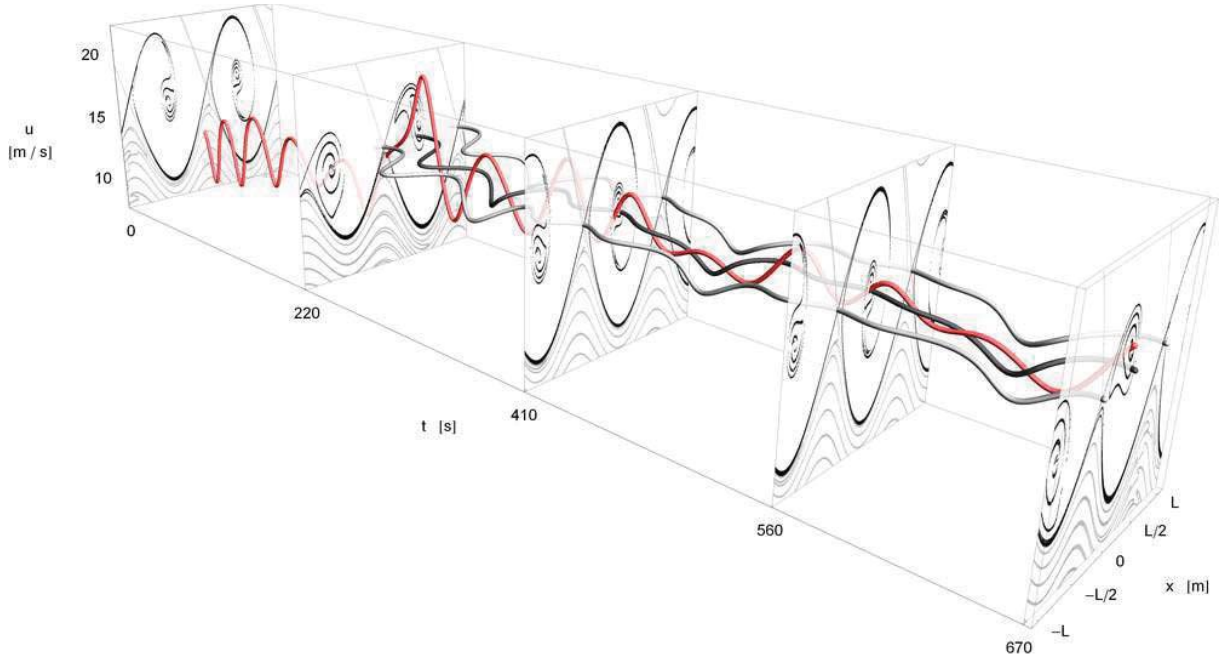

Figure 7 Bi-chromatic excitation: Ship trajectory (red line), LCSs at selected time instants and paths of three critical points of the acceleration field (black and gray lines).

5. CONCLUDING REMARKS

Methods for gaining insight into the dynamics of ship surge motion in astern multi-chromatic seas are introduced. Specifically, an identification method for Lagrangian Coherent Structures (LCSs) is applied on the phase flow defined by the surge equation of motion. It is based on a well-known scheme with a wide range of applications in the literature, which involves the calculation of the spatial distribution of the largest finite-time Lyapunov exponent (FTLE). Through the FTLE field, LCSs i.e., influential material lines shaping the pattern of the time-dependent flow, were obtained. Their role as phase-flow organizing structures was examined. It was found that, for the case of a bi-chromatic scenario, LCSs can help to understand the evolution of ensembles of initial conditions, by providing the location of transport barriers, as well as the final destinations of particle trajectories.

Furthermore, the Feature Flow Field method was implemented for the tracking of features, corresponding to elements of the zero set of the acceleration field defined by the surge equation of motion. Results obtained from the tracking of such features and the LCSs identification procedure were combined. It has been shown that the paths of certain features correlate to hyperbolic trajectories of the surge equation, while others to trajectories with attracting character that seem to evolve in the core of specific branches of attracting LCSs.

6. ACKNOWLEDGEMENTS

The calculation and testing of LCSs for surging and surf-riding behaviour described in this paper have been funded by the Greek General Secretariat of Research and Technology under the General Program ARISTEIA I (contract reference number GSRT-252). The work regarding the feature tracking method applied in Section 4 has been funded by the Office of Naval Research, ONRG grant number N62909-13-1-7, under Dr. Ki-Han Kim, Dr. Tom Fu and Dr. Woei-Min Lin.

7. REFERENCES

Belenky, V., Spyrou, K., & Weems, K., 2012, "Evaluation of the probability of surf-riding in irregular waves with the time-split method", Proceedings of 11th International Conference on the Stability of Ships and Ocean Vehicles, Athens, Greece, pp. 29-37.

Haller, G. and Yuan, G., 2000, "Lagrangian coherent structures and mixing in two-dimensional turbulence", Physica D, 147, pp. 352-370.

Haller, G., 2011, "A variational theory of hyperbolic Lagrangian Coherent Structures", Physica D, 240, pp. 574-598.

Kan, M., 1990, "Surging of Large Amplitude and Surf-riding of Ships in Following Seas", Selected Papers in Naval Architecture and Ocean Engineering, The Society of Naval Architects of Japan, 28.

Shadden, S. C., 2011, "Lagrangian Coherent Structures", Transport and Mixing in Laminar Flows: From Microfluidics to Oceanic Currents, Roman Grigoriev, Ed., Wiley-VCH.

Spyrou, K., 1996, "Dynamic instability in quartering seas: The behaviour of a ship during broaching", Journal of Ship Research, SNAME, 40, No 1, pp. 46-59.

Spyrou, K., Belenky, V., Themelis, N., & Weems, K., 2012, "Conditions of surf-riding in an irregular seaway", Proceedings of 11th International Conference on Stability of Ships and Ocean Vehicles, Athens, Greece, pp. 323-336.

Spyrou, K., Belenky, V., Themelis, N., & Weems, K., 2014a, "Detection of surf-riding behaviour of ships in irregular seas", Nonlinear Dynamics, DOI 10.1007/s11071-014-1466-2.

Spyrou, K., Belenky, V., Reed, A., Weems, K., Themelis, N., Kontolefas, I., 2014b, "Split-Time Method for Pure Loss of Stability and Broaching-To", Proceedings of 30th Symposium on Naval Hydrodynamics, Hobart, Tasmania, Australia.

Spyrou, K., Themelis, N., Kontolefas, I., 2015, "Development of Probabilistic Models for Evaluating the Dynamic Stability and Capsizing Tendency of Naval Vessels with Respect to Broaching-to", Technical Report to the Office of Naval Research (2015), ONRG grant number: N62909-13-1-7.

Theisel, H., Seidel, H-P., 2003, "Feature flow fields", Data Visualization 2003, Proc. VisSym 03, 2003, pp. 141-148.

This page is intentionally left blank

Toward a Split-Time Method for Estimation of Probability of Surf-Riding in Irregular Seas

Vadim Belenky, *Naval Surface Warfare Center Carderock Division*, vadim.belenky@navy.mil

Kenneth Weems, *Naval Surface Warfare Center Carderock Division*, kenneth.weems@navy.mil

Kostas Spyrou, *National Technical University of Athens*, k.spyrou@central.ntua.gr

ABSTRACT

The paper reviews the status of a multi-year research effort for using the split-time method to calculate the probability of ship capsizing due to broaching-to in irregular waves. The present work focuses on extending the existing theory of surf-riding and broaching-to from regular waves to irregular waves and applying it to numerical simulation codes. Extending the theory for irregular waves leads to the formulation of a spatial-temporal framework for considering surf-riding where the celerity of irregular waves must be defined. An approximate metric for the likelihood of surf-riding in irregular waves has been proposed as the distance, in the phase plane, between the instantaneous position of a ship and the stable surf-riding equilibrium at that instant. Further work includes studying the properties of the surf-riding phase plane in irregular waves and statistics of surf-riding occurrences.

Keywords: *Probability, Surf-Riding, Celerity, Split-Time Method*

1. INTRODUCTION

Surf-riding and broaching-to are associated, complex phenomena linked through the generation of attraction towards a point of equilibrium located near a wave trough, appearing to be stable in surge but unstable in yaw. This yaw instability leads to a rapid, uncontrollable turn which can induce a large roll angle or capsize. The standing theory of surf-riding and broaching-to was proposed on the basis of the nonlinear dynamics theory (Spyrou 1996, 1997). It used an ordinary differential equations (ODE) model of ship motion in regular following/quartering waves. The minimal mathematical model for describing these phenomena includes surge-sway-yaw for modeling broaching-to plus a roll motion equation to model capsize. An auto-pilot equation also must be included for the directional control of the ship. The resulting system has a 10-dimensional phase space.

This already complex description becomes even more complex if one considers the fact that large-amplitude ship motions are described by integro-differential equations, where wave excitation cannot be separated from stiffness and hydrodynamic memory effects, such as radiation and diffraction forces, are present. Furthermore, the irregularity of realistic ocean introduces new physical qualities to the phenomenon.

The challenge to include surf-riding and broaching into a probabilistic assessment of stability based on advanced hydrodynamic codes has been taken up by the US Office of Naval Research (ONR) project “A Probabilistic Procedure for Evaluating the Dynamic Stability and Capsizing of Naval Vessels”. The project’s main objective is to create a robust theory of probabilistic capsizing in irregular waves and a numerical procedure based on this theory.

The split-time method is the probabilistic framework of this project. The idea of the split-time method is to separate the complex problem of the probability of a rare, extreme event in two problems that may be less complex. The “non-rare” problem is associated with an intermediate random event, statistics of which can be obtained by running an advanced code for sufficient time. This “non-rare”

problem ensures a correct relation between time and probability in irregular waves. The "rare" problem is responsible for modeling the physics of the rare event. Its core is a metric of the danger of the severe event, for example capsizing or large roll angle caused by broaching, that is computed when the intermediate random event occurs. The procedure is repeated for each intermediate random event observed during the non-rare simulations. The sample of metric values is then statistically extrapolated to determine the likelihood of the rare event. Since the metric value is expected to include the physics of the extreme event, actual observations of the event are not required, so the method is expected to work for conditions (sea states, speed, loading) where extreme events are rare.

2. SURF-RIDING AND BROACHING-TO IN LAMP

2.1 Objective and Approach

As the current theory of surf-riding and broaching-to was developed using ODE, application to more general models raises certain questions. Can this theory be extended to the cases when ship motions are presented with integro-differential equations with 6 degrees of freedom and hydrodynamic memory effects? How well will the analysis tools of nonlinear dynamics work with the dynamical system represented by the advanced hydrodynamic code? The results of a study of these issues are presented in Spyrou *et al.* (2009) and Belenky *et al*. (2010).

While the Large-Amplitude Motion program (LAMP) was used as the main hydrodynamic code for this study, the results are meant to be code-independent and applicable to any code capable of reproducing surf-riding, broaching-to, and capsizing. LAMP is a based on a boundary value problem for radiation and diffraction (potential flow), a body non-linear evaluation of the hydrostatic and Froude-Krylov forces, and force models for vortex and viscous effects (Lin and Yue 1990). The use of LAMP for the simulation of ship maneuvering is described in Lin *et al*. (2006) and Yen *et al*. (2010).

The ship configuration used for demonstrating the surf-riding and broaching phenomena is the "tumblehome" form of the ONR Topsides Study (Bishop *et al*. 2005).

2.2 Time-Domain Simulations

The study first looked at the modeling of large heel angle (up to capsize) caused by a sharp turn. Figure 1 shows predicted time histories of roll with two values of the transverse metacentric height (GM) after a 30° rudder application while sailing at 38 knots in calm water. At the higher GM value, the ship attains a large heel angle before recovering. At the lower GM value, the ship capsizes.

The study then looked at surf-riding in combinations of wave frequency and height and ship speed for which the theory predicts a co-existence of surging and surf-riding. Figure 2 shows different responses depending on the initial conditions. Systematic simulations were performed for a nominal Froude number (*Fn)* from 0.3 to 0.41 and commanded headings relative to the wave direction from 10 to 32 degrees. A summary of the results is presented in Figure 3.

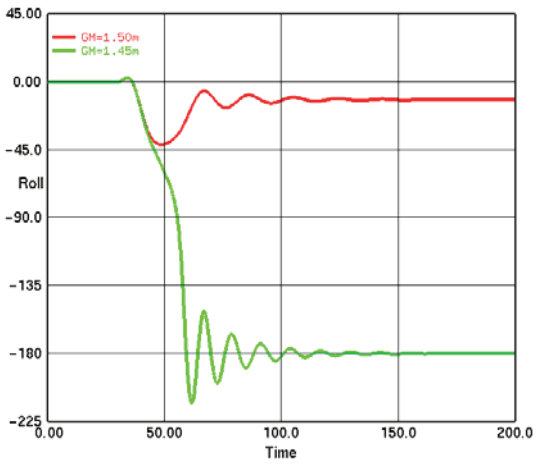

Figure 1: Large heel angle and capsizing due to sharp turn in calm water (Belenky *et al*. 2010)

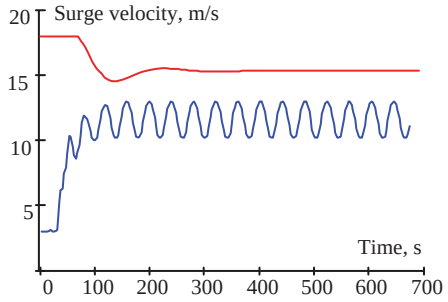

Figure 2: LAMP simulations showing coexistence of surging and surf-riding (Belenky *et al*. 2010)

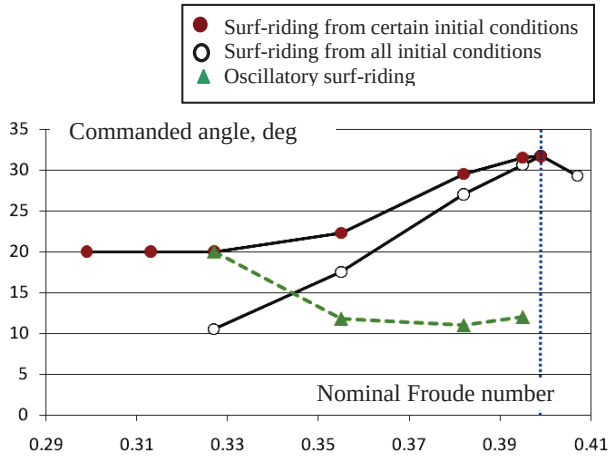

Figure 3: Boundaries of surf-riding in terms of commanded heading as a function of nominal Froude number (Spyrou *et al.* 2009)

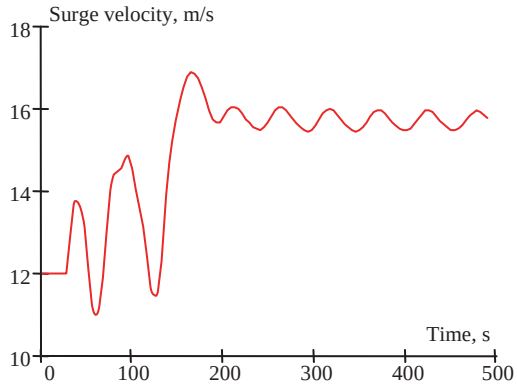

Figure 4: Capture into oscillatory surf-riding for commanded relative heading of 12 deg, Fn=0.36; notice the upward jump of mean speed (Spyrou *et al*. 2009)

A remarkable feature that appeared at the higher nominal speeds (*Fn*>0.33) was a stable oscillatory type of surf-riding, for which the time history of ship speed is shown in Figure 4. As the ship is carried along by a single wave, it is also oscillating up-and-down the wave face. This fascinating occurrence has been observed in the past and has been explained as being due to a Hopf bifurcation (Spyrou 1996).

2.3 The Continuation Method

The continuation method is a powerful approach for studying the behavior of nonlinear systems by mapping and characterizing equilibria. However, continuation techniques were developed for dynamical systems described by ODE, and the application of continuation with advanced hydrodynamic codes presents many challenges, mostly caused by hydrodynamic hysteresis (memory effect). The first use of the continuation method (DERPAR) with a potential flow code (LAMP) was described by Spyrou *et al.* (2009). To avoid excessive complexity associated with the memory effect, the diffraction and radiation forces have been approximated with constant added mass and damping coefficient.

A sample result from LAMP-based continuation analysis is given in Figure 5. The curve shows the positions of surf-riding equilibria in the coordinates as yaw vs. rudder angle, and follows the similar curve from Spyrou (1996). This curve contains both stable and unstable surf-riding equilibria. That is why the continuation method is necessary, as direct time-domain simulations are not capable of capturing unstable equilibria.

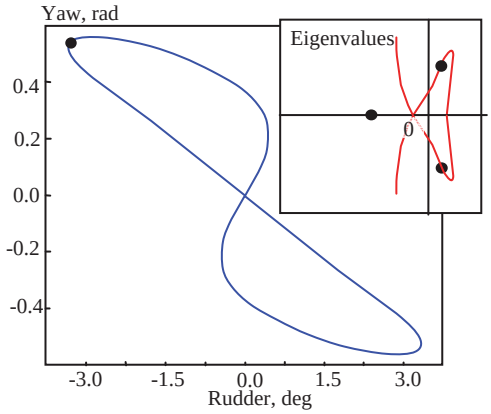

Figure 5: Curve of yaw *vs.* rudder angle for surf-riding equilibria calculation with DERPAR and LAMP (Belenky *et al*. 2010)

The stability of regions of the equilibrium curve was analyzed by examining the eigenvalues. The inset plot shows eigenvalues in the complex plane for a point on the curve at which the Hopf bifurcation (Figure 4) can be expected. Further development has led to the inclusion of hydrodynamic memory effects into the continuation analysis (Spyrou and Tigkas 2011).

2.4 The Theory and Code

The analysis carried out by Spyrou *et al.* (2009) demonstrated that the LAMP-simulated behavior is consistent with the current theory of broaching-to and surf-riding. It also confirmed the generic nature of the phenomena that had been identified independently and for a very different configuration in earlier research. In particular, the consideration of all six degrees does not change the qualitative picture of the phenomenon.

LAMP-based continuation analysis produced results that are consistent with direct simulation of the stable equilibria as well as the results of previous continuation research of a more theoretical nature.

These results lead to the conclusion that the current theory can be used to explain the outcomes of time-domain simulation with advanced hydrodynamic codes and that advanced hydrodynamic codes can describe a nonlinear dynamical system.

3. SPATIAL-TEMPORAL FRAMEWORK FOR SURF-RIDING

In regular waves, a sliding coordinate system with its origin on the wave crest (or any other point fixed to the wave) allows a space-only consideration for surf-riding, as the next or previous wave in space and time is exactly the same. Figure 6 illustrates this approach; the upper part (Figure 6a) shows the balance of thrust and resistance plotted with the spatial representation of the surging wave force. The intersections of these two lines correspond to surf-riding equilibria, which define the topology of the phase plane shown in the lower part (Figure 6b). As the wave is regular, shifting coordinates in space corresponds to shifting coordinates in time, so only one coordinate − usually space − has to be considered.

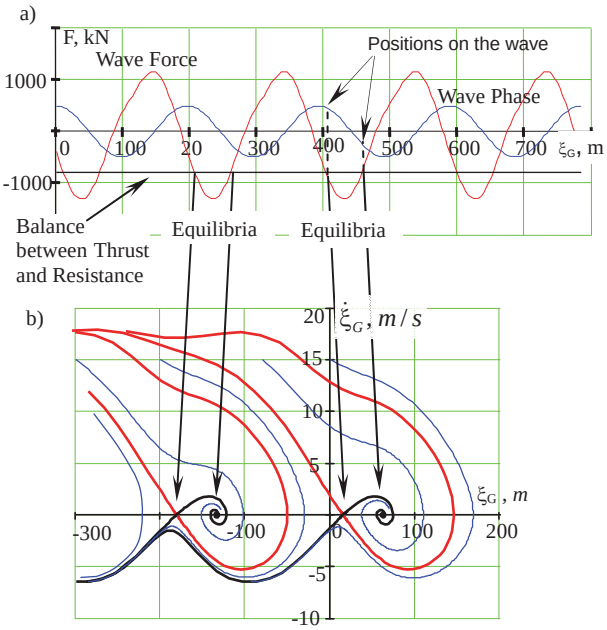

Figure 6: Surf-riding in regular waves – space consideration only: (a) balance of forces and (b) phase plane

In irregular seas, the waves are changing in both space and time. Consider an Earth-fixed coordinate system and imagine Figure 6 slowly changing in space for a fixed instant of time. The picture then changes slightly for the next time instant. As the waves change, surf-riding equilibria (actually quasi-equilibria) appear and disappear at different instances of time and points in space. This qualitative description is illustrated in Figure 7.

This rather qualitative consideration produces two main outcomes:

- Celerity of irregular waves must be defined in order to find the equilibria
- All elements of the mathematical model of surf-riding in irregular waves must be functions of position (x-coordinate) and time.

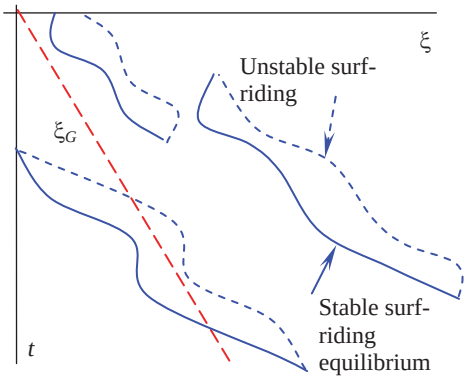

Figure 7: Spatial-temporary framework for surf-riding in irregular seas (Belenky *et al.* 2011)

4. CELERITY OF IRREGULAR WAVES

4.1 Velocity of a Profile

The most evident idea for irregular wave celerity was to find characteristic points in the profile, track them in time, and take their velocity as an approximation of wave celerity at these points. Belenky *et al.* (2012) proposed the tracking of zero-crossing points as illustrated in Figure 8. Each curve in Figure 9 is a spatial wave profile plotted at a time instant. Three zero-crossing points, marked by circles, are tracked. The celerity calculated by this method is generally reasonable, but at times can become negative or jump to a very large value.

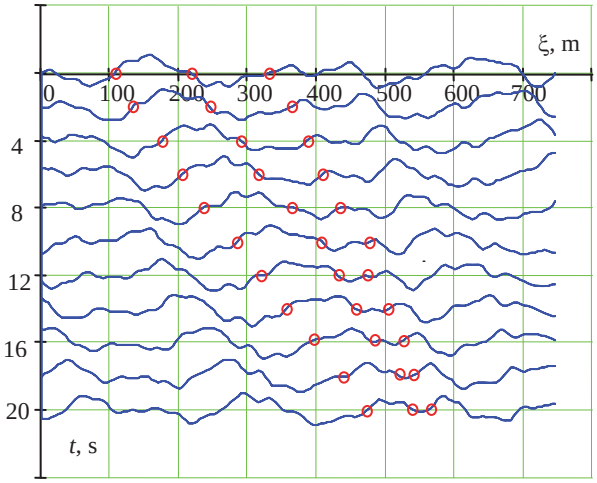

Figure 8: Celerity based on zero-crossing points (Belenky *et al.* 2012)

To gain a better understanding of the nature of this behavior, simplified cases were created with only two and three components (bi- and tri-chromatic waves), as shown in Figures 9 and 10. The tendency for large peaks can be seen even for two frequencies, and is even more dramatic for three frequencies.

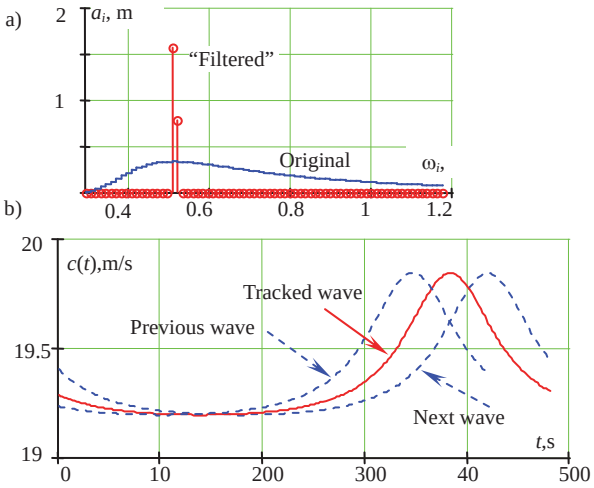

Figure 9: Bi-chromatic waves: (a) spectrum and (b) time history of celerity (Belenky *et al.* 2012)

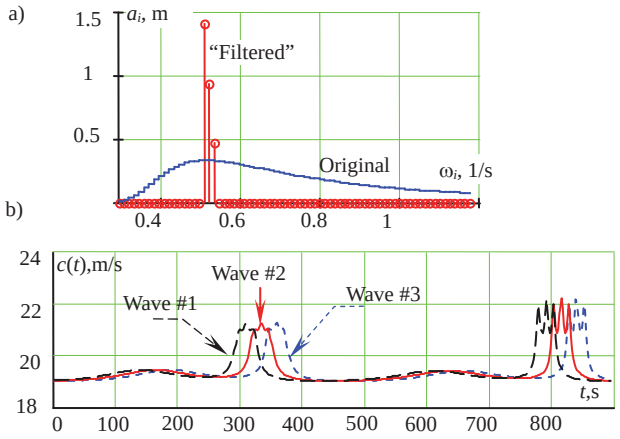

Figure 10: Tri-chromatic waves: (a) spectrum and (b) time history of celerity (Belenky *et al.* 2012)

Spyrou *et al*. (2012) had preferred to track the points of constant wave slope, proposing the concept of instantaneous celerity which can be calculated at the exact ship position at each time step. Figure 11 shows the celerity curves calculated for seaway derived from a JONSWAP spectrum. In a further development, they also proposed calculating a characteristic local celerity value corresponding to the point of maximum wave slope that is found in the vicinity of the ship. All these methods converged to the finding that the peaks in the celerity curve are intrinsic to the problem.

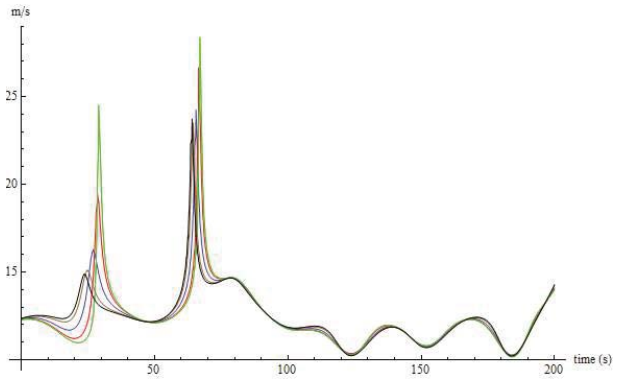

Figure 11: Celerity curves corresponding to wave slopes 1/75, 1/100, 0, -1/100, -1/75 (Spyrou *et al*. 2012)

The peaks appear to be related to changes in the local wave features, as when one wave overtakes another. As this occurs, a local wave feature may cease to exist and the tracked points disappear and appear in another place, leading to a "spike" in the velocity of those points. Several candidate wave features were considered as points to track, and the smoothest behavior was found for the point of the maximum wave slope on the forward face. As this point can also be associated with the maximum surging force on a ship, it has a physical meaning with regard to surf-riding.

The calculation of wave celerity by tracking the points of maximum wave slope has been implemented in LAMP. In order to consider oblique and short-crested (multi-directional) seas, the algorithm searches for zeros of the derivative of the wave slope in the ship's direction of travel,

$$\frac{\partial^3 \zeta_W(\xi_{\alpha\max}, t)}{\partial \xi^3} = 0 \qquad (1)$$

with the condition that they are on the down-slope:

$$\frac{\partial^2 \zeta(\xi_{\alpha\max}, t)}{\partial \xi^2} < 0 \qquad (2)$$

ζ_W is wave elevation, ξ is a coordinate in the mean direction of travel, and $\xi_{\alpha\max}$ is a position of maximum wave slope angle. ξ is related to this Earth-fixed coordinate system as:

$$\begin{aligned} x &= x_G(t) + \xi\cos\psi \\ y &= y_G(t) + \xi\sin\psi \end{aligned} \qquad (3)$$

(x_G, y_G) is the current position of the center of gravity of the ship and ψ is the mean heading angle with respect to the global frame.

For efficiency, the algorithm computes the elevation and its derivatives on a line of points within a characteristic wave length of the ship, then iterates within intervals containing a maximum slope point. The local maximum slope points are tracked in time and the propagation speed of the point closest to the ship provides a practical celerity.

Figure 12 shows a snapshot of a LAMP simulation for the ONR tumblehome hull form running in long-crested irregular waves. The plot shows the wave profile at that time instance along the ship's travel direction with marks for the points of maximum down slope and elevation (crest). The wave in this case is derived from a Bretschneider spectrum with H_s=7m and T_m=12.0s. A portion of the time history of the ship speed and the local wave celerity is shown in Figure 13.

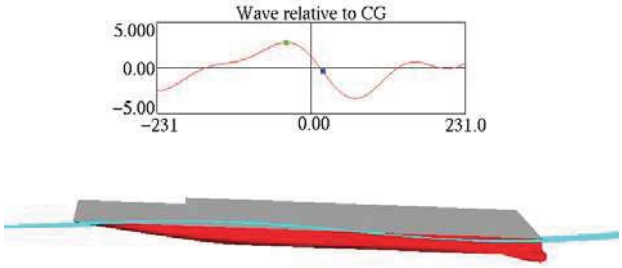

Figure 12: LAMP simulation of ONR Topsides tumblehome hull in irregular following seas (Spyrou *et al*. 2012)

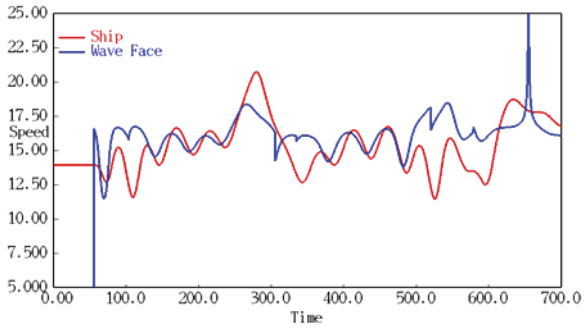

Figure 13: Ship speed and wave celerity for case with significant surf-riding in irregular waves (Spyrou *et al*. 2012)

The comparison of ship speed and local wave celerity clearly shows periods of surf-riding (*e.g. t*=380-480) and periods where the wave is overtaking the ship (*e.g. t*=480-600). While the initial wave celerity jump at 60 seconds is an artifact of ramping-up the wave, the "spike" in wave speed at t=675 is a case where the phasing of the wave component produces a very rapid local translation of the point of maximum slope and is related to a "merging" of wave faces. However, other discontinuities in the celerity, such as the one at t=530, are simply cases where the closest point of maximum slope switches from one face to another as the waves overtake the ship.

In general, the problem of celerity in irregular waves and how it can affect ship motion is a very deep problem. Spyrou *et al*. (2014) provided a comprehensive theoretical analysis with an emphasis on the detection of surf-riding.

4.2 Celerity Based on Instantaneous Frequency

Looking for a method capable of producing a smoother celerity curve, Spyrou *et al*. (2014a) proposed an alternate scheme based on the instantaneous frequency derived from an envelope presentation of the wave elevation:

$$\zeta(t,\xi) = A(t,\xi)\cos\left(\vartheta(t,\xi)\right) \tag{4}$$

For a case where the wave elevation ζ_W is presented as typical cosine series, the amplitude $A(t,\xi)$ and phase $\vartheta(t,\xi)$ functions are computed from the wave elevations ζ_W and the Hilbert transform of the wave elevations $H(\zeta_W)$:

$$\begin{aligned} A(t,\xi) &= \sqrt{\zeta_W^2 + \left(H\left(\zeta_W\right)\right)^2} \\ \vartheta(t,\xi) &= \arctan\frac{\zeta_W}{H\left(\zeta_W\right)} \end{aligned} \tag{5}$$

$$\begin{aligned} \zeta_W(t,\xi) &= \sum_{i=1}^{N_\omega} a_i \cos\left(k_i\xi - \omega_i t + \varphi_i\right) \\ H\left(\zeta_W(t,\xi)\right) &= \sum_{i=1}^{N_\omega} a_i \sin\left(k_i\xi - \omega_i t + \varphi_i\right) \end{aligned} \tag{6}$$

a_i, ω_i, and k_i are the amplitude, frequency, and wave number of the i^{th} component, while φ_i is a random phase shift.

The instantaneous frequency ω_W and the instantaneous wave number k_W are then computed as:

$$\omega_W(t,\xi) = -\frac{\partial \vartheta(t,\xi)}{\partial t} \tag{7}$$

$$k_W(t,\xi) = \frac{\partial \vartheta(t,\xi)}{\partial \xi} \tag{8}$$

This leads to the following definition of the wave celerity:

$$c(t,\xi) = \frac{\omega_W(t,\xi)}{k_W(t,\xi)} \tag{9}$$

For numerical calculations, it is convenient to substitute equations (5, 7, 8) into equation (9) and perform differentiation:

$$c(t,\xi) = -\frac{\frac{\partial H(\zeta_W)}{\partial t}\zeta_W - \frac{\partial \zeta_W}{\partial t}H(\zeta_W)}{\frac{\partial H(\zeta_W)}{\partial \xi}\zeta_W - \frac{\partial \zeta_W}{\partial \xi}H(\zeta_W)} \tag{10}$$

Equation (10) presents the wave celerity as a function of time and space that can be computed everywhere. The result can be compared against the instantaneous celerity calculated through the tracking method. Spyrou *et al.* (2014a) shows a series of comparisons between the "wave profile" and "instantaneous frequency" calculation schemes, an example of which is reproduced in Figure 14. The two calculations are generally very similar and both show "spikes" in celerity, although there is significant difference at the second spike at 440 s. What causes the "spikes" in formula (10)?

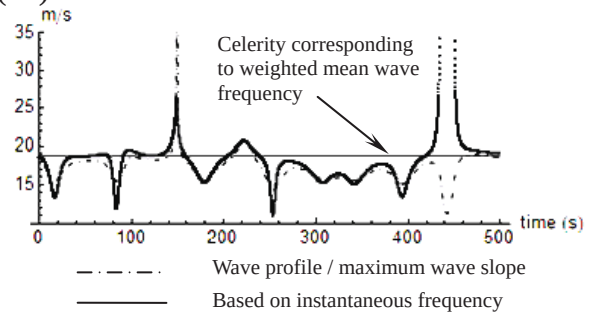

Figure 14: Instantaneous celerity for the bandwidth limited to 20% of the peak period (Spyrou *et al.* 2014a)

Figure 15 shows the spatial profile of the wave celerity calculated for Sea State 7 (Significant wave height 7.5 m, modal period 15 s) using a full-bandwidth Bretschneider spectrum and random phases. At this instant in time, there are four spikes at around 1500 m.

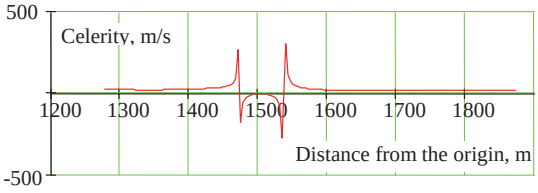

Figure 15: Spatial profile of wave celerity

One of the advantages of the present scheme of celerity calculation is that the origin of a spike can be analyzed. Consider the instantaneous wave number, which is the denominator in formula (9):

$$k_W(t,\xi) = \frac{\partial \vartheta(t,\xi)}{\partial \xi} = \frac{\frac{\partial H(\zeta_W)}{\partial \xi}\zeta_W - \frac{\partial \zeta_W}{\partial \xi}H(\zeta_W)}{\zeta_W^2 + \left(H(\zeta_W)\right)^2} \tag{11}$$

The spatial profile of the instantaneous wave number is shown in Figure 16. It has a minimum around 1500 m and this minimum is negative. The curve of the instantaneous wave number crosses zero twice, which results in spikes in the value of instantaneous wave celerity. Figure 17 plots the spatial profile of wave elevations and shows that the minimum of the wave number and spikes of the celerity occur near the secondary maximum, *i.e.* the local maximum without crossing the line of calm water.

The secondary maxima and minima are related to the origination of new waves. If the local maximum at 1500 m raises and crosses the calm water line, the new wave will appear. Appearance of the new wave will lead to appearance of a new point of maximum of the wave slope and new zero-crossing. At the instance the new wave appears, the tracked points will make a finite "jump" in the infinitely small period of time causing a

theoretically infinite "spike" in celerity. Limiting the smallest value of the instantaneous wave number will limit the value "spike" and will make the celerity equation (10) into a practical formula for calculation.

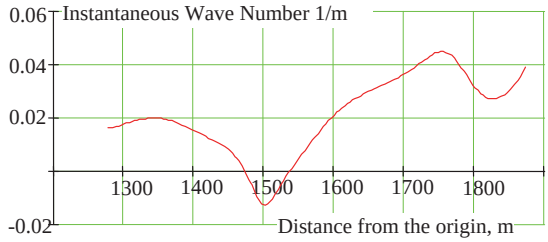

Figure 16: Spatial profile of the instantaneous wave number

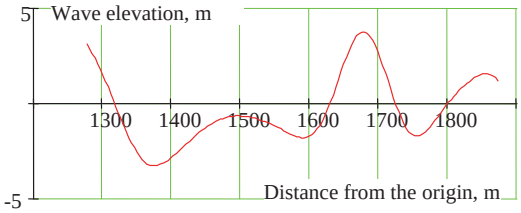

Figure 17: Spatial profile of the wave elevation

5. SURF-RIDING IN IRREGULAR WAVES

5.1 Simple Mathematical Model of Surging and Surf-Riding in Irregular Waves

A simple model for one-degree-of-freedom nonlinear surging was proposed in Belenky *et al*. (2011):

$$\left(M + A_{11}\right)\ddot{\xi}_G + R\left(\dot{\xi}_G\right) - T\left(\dot{\xi}_G, n\right) + F_X\left(t, \xi_G\right) = 0 \tag{12}$$

M is mass of the ship, A_{11} is the longitudinal added mass, R is resistance in calm water, T is the thrust in calm water, n is the propeller rotation rate, F_X is the surging component of the Froude-Krylov wave force, and ξ_G is longitudinal position of the center of gravity in the Earth-fixed coordinate system. The dot above the symbol indicates temporal derivative. Following Spyrou (2006), a polynomial approximation for thrust and resistance are used:

$$\begin{aligned} R(U) &= r_1 U + r_2 U^2 + r_3 U^3 \\ T(U,n) &= \tau_1 n^2 + \tau_2 n U + \tau_3 U^2 \end{aligned} \tag{13}$$

As the model is meant at this stage to be qualitative, a linear wave-body formulation seems to be appropriate for the case. Therefore:

$$F_X\left(t, \xi_G\right) = \sum_{i=1}^{N} A_{Xi} \cos\left(k_i \xi - \omega_i t + \varphi_i + \gamma_i\right) \tag{14}$$

As a body-linear formulation is adopted, the amplitude A_{Xi} and phase shift γ_i are available via response amplitude and phase operators:

$$A_{Xi} = a_i RAO(k_i) \tag{15}$$

$$RAO(k_i) = \rho g k_i \left(\left(\int_{-0.5L}^{0.5L} C(x,k_i)\cos\left(k_i x\right)dx \right)^2 + \left(\int_{-0.5L}^{0.5L} C(x,k_i)\sin\left(k_i x\right)dx \right)^2 \right)^{1/2} \tag{16}$$

$$C(x,k_i) = 2\int_{-d}^{0} \exp\left(k_i z\right) b(x, z+d)\,dz \tag{17}$$

Here x and z are measured in the ship-fixed coordinate system (positive forwards of amidships and upward from the baseline), $b(x, z)$ is the molded local half-breadth, and d is the draft amidships. The surging phase shift is expressed as:

$$\gamma_i = \arctan\left(\frac{\int_{-0.5L}^{0.5L} C(x,k_i)\sin\left(k_i x\right)dx}{\int_{-0.5L}^{0.5L} C(x,k_i)\cos\left(k_i x\right)dx} \right) \tag{18}$$

The mathematical model described by equations (12 through 18) is essentially an

extended time domain version of the model presented in Spyrou (2006). It is expected to reproduce nonlinear surging and surf-riding, which is illustrated in Figure 18.

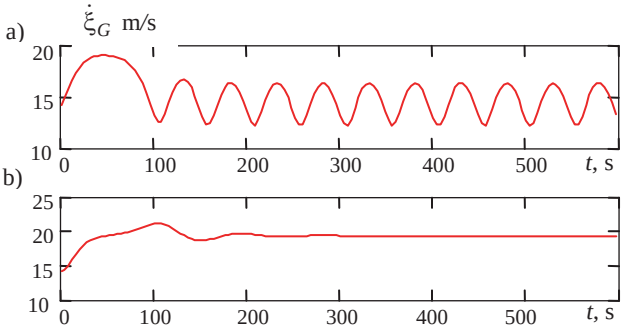

Figure 18: Solution in regular waves: co-existence of (a) surging and (b) surf-riding (Belenky *et al.* 2011)

5.2 Identification of Surf-Riding Instances in Irregular Waves

There are two aspects to the problem of identifying instances of surf-riding. The first is that surf-riding in irregular seas is not visually evident from the ship speed, as was illustrated in Figure 13. Without the wave celerity plotted alongside, an observer sees just a periodic stochastic process. The second aspect is to see how well definition of the wave celerity in irregular seas can explain the observed behavior. In a sense, the identification of surf-riding can be used as qualitative validation of the celerity calculation scheme.

A very basic example of such identification is described by Belenky *et al*. (2012), using tri-chromatic waves and zero-crossing wave celerity (see Figure 10). The time histories of surging speed and celerity are shown in Figure 19. The evolution of the surging speed for the first hundred seconds suggests attraction to a surf-riding equilibrium. But is this really the case?

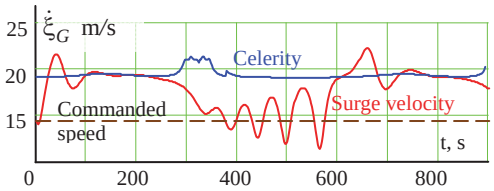

Figure 19: Time histories of surging velocity and celerity for tri-chromatic waves (Belenky *et al.* 2012)

Figure 20 shows a "spatial snapshot" of the forces (surging force vs. balance of thrust and resistance) superimposed with a spatial profile of the wave and its zero-crossing points. The time instant is t=150 s. The instantaneous position of the ship is indicated via the x-coordinate of the diamond, while the balance between thrust and resistance is indicated by its y-coordinate. The diamond is located at the intersection of the surging force and the balance of the thrust and resistance at the wave celerity. This means that the ship is in equilibrium and surf-riding is observed.

This simple example shows how wave celerity allows an interpretation of the observed motion and establishes the fact of surf-riding. The example also verifies the physical relevance of the calculated wave celerity. The method of calculating celerity based on maximum wave slope was successfully tested for identification of surf-riding by Spyrou *et al.* (2012, 2014). Spyrou, *et al*. (2014a) used both methods to calculate the celerity; see Figure 21.

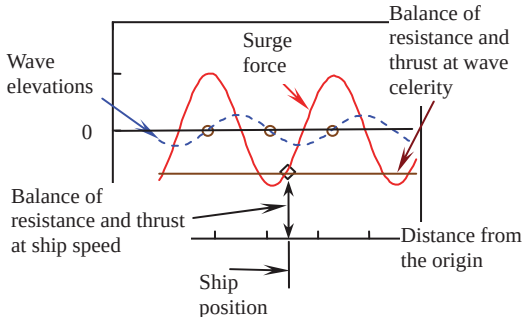

Figure 20: "Spatial snapshot" for t=150s (Belenky *et al.* 2012)

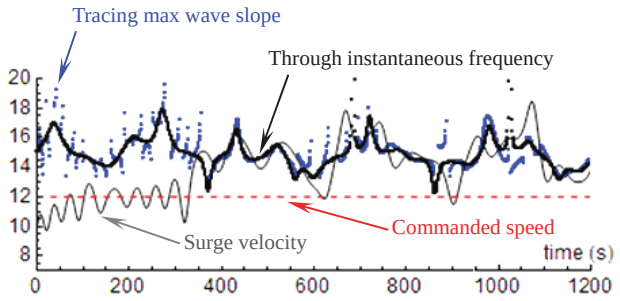

Figure 21: Time histories of surge velocity and celerity calculated with max wave slope and instantaneous frequency (Spyrou *et al.* 2014a)

Both methods of the wave celerity calculation seem to identify surf-riding instance in the same way, which is not surprising considering the similarity in the results of the two methods (Figure 14).

5.3 Phase Space in Irregular Waves

The position and type of the equilibria defines the topology of the phase plane, so the evolution of surf-riding equilibria in space and time is a logical starting point for analyzing surf-riding in irregular waves. Figure 22 shows the calculated loci of equilibria for the tri-chromatic case described above. The result is remarkably consistent with the notional topology presented in Figure 7.

The accuracy of the evaluation of the equilibrium stability was not always sufficient near the points where the equilibria appeared or disappeared, so the stability status of those point was corrected based on geometric considerations. Correct points are shown as two-color symbols. The inset in Figure 22 shows a close-up where the geometrical correction was applied.

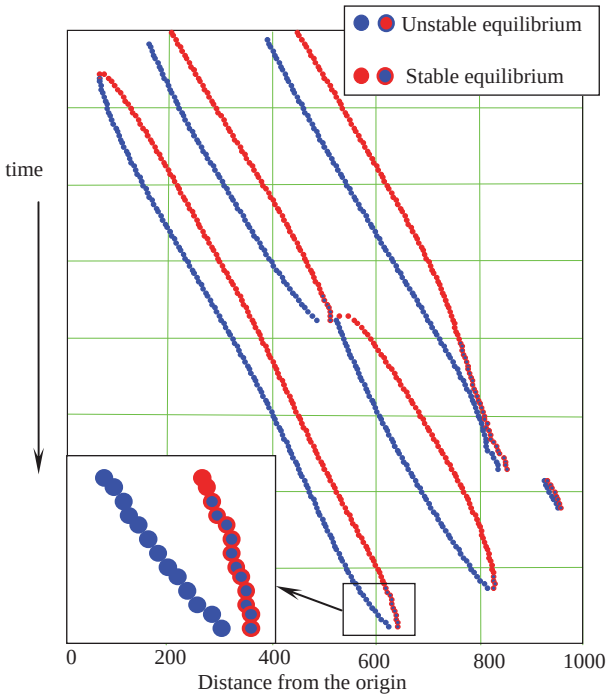

Figure 22: Calculated traces of equilibria

The unsteady motion of the equilibria qualitatively changes the phenomenon. A frame of reference moving with the equilibrium is no longer inertial. Also, the dynamical system cannot stay at the equilibrium position, even if the initial conditions correspond exactly to the equilibrium, because the equilibrium will move away. As an analogy, imagine a small heavy ball in a wine glass that is being moved in a circular motion. The ball will continuously "chase" a quasi-equilibrium point that moves around the inside of the glass.

The phase plane is also changing with time; strictly speaking, the phase plane by itself does not make sense beyond the "spatial snapshot". The phase trajectory becomes a 3D line in hybrid phase-time coordinates (Kontolefas and Spyrou 2015). Projecting to a plane, the set of trajectories behaves as a non-stationary fluid flow. Spyrou *et al.* (2014a) describe an application of the concept of a Feature Flow Field (Theisel and Seidel 2003), which addresses the problem of feature tracking in non-stationary flow fields. The Feature Flow Field (FFF) method has been proposed for the tracking of a variety of different local features, including critical points of vector fields (such

as, in our case, the surf-riding equilibria). Figure 23 shows an example plot for surf-riding, where "saddle and focus-like" structures are present.

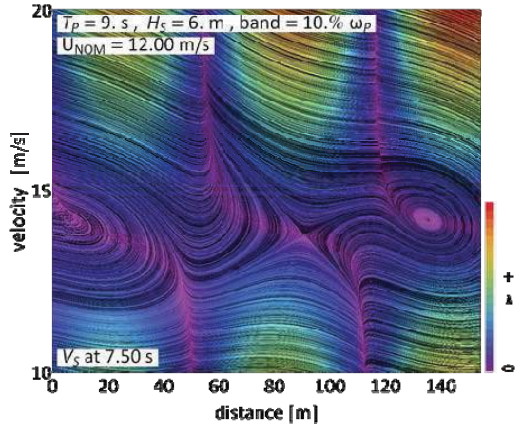

Figure 23: Streamlines and magnitude of forward velocity; JONSWAP Spectrum (Spyrou *et al.* 2014a)

Further developments towards the understanding of this time-dependent phase plane are described in Kontolefas and Spyrou (2015). Here is discussed a combined consideration of the feature flow field concept for tracking surf-riding states with the concept of hyperbolic Lagrangian Coherent Structures which can be seen as the finite-time generalization of the manifolds.

5.4 Statistics of High-Runs

The study of surf-riding in irregular waves requires the capability to characterize observations from simulations or model tests. However, the identification of surf-riding events in irregular waves is not trivial, particularly if the wave celerity cannot be calculated, which will generally be the case in a model test. It therefore makes sense to also look at the statistics of significant exceedances of the nominal speed by the surge velocity, also known as "high-runs". Themelis *et al.* (2015) studied the statistics of high-runs depending on spectrum and sea state.

The idea of high-runs is not new. As pointed out in that work, Grim (1963) had looked into the probabilistic quantification of the occurrence and duration of high-runs ("long run") in a following irregular sea, taking into account the strongly nonlinear character of surge motion when the phenomenon occurs. Themelis *et al.* (2015) also examined the relation between the high-run occurrences and the instantaneous wave celerity (Figure 24).

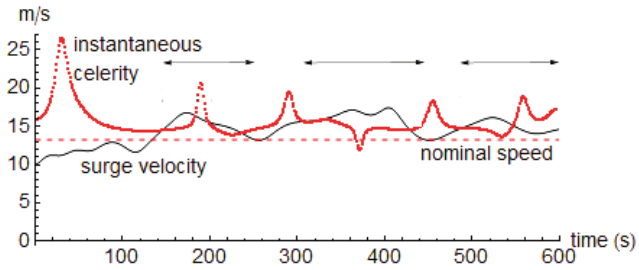

Figure 24: Schematic definition of high-run with the superimposed instantaneous wave celerity (Themelis *et al.* 2015)

The conclusion was that the velocity of the high-run shows good correlation with the mean instantaneous celerity when an error metric combining errors of amplitude and phase is applied.

5.5 Metric for Likelihood of Surf-Riding

As described at the beginning of this paper, a central element in the implementation of the split-time method is developing a metric for the likelihood of a rare event which can be evaluated at the occurrence of an intermediate event of some sort. An initial proposal for a metric of the likelihood of surf-riding can be found in Spyrou *et al.* (2014a) and is illustrated in Figure 25. The idea is to compute a "critical distance" in the phase plane between the ship's state (position and velocity) at up-crossing and a critical state (point in the phase plane) from which the ship would be captured into surf-riding.

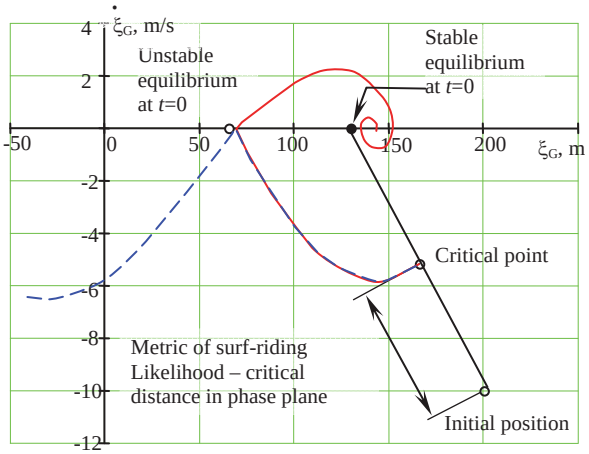

Figure 25: Initial idea for the metric of the likelihood of surf-riding

The critical point would lie on the line between the initial position of a ship (state at upcrossing) and the position of the stable quasi-equilibrium at the initial instant. A series of "rare" simulations would be performed for initial conditions corresponding to points along this line, and these simulations would determine the conditions that led to surf-riding.

This metric was initially tested with a slowly changing regular wave for which it is possible to explicitly consider the motion of the equilibria. The critical distance could be calculated, but the point to which the system was attracted and, once the critical point was reached, captured into surf-riding was different from the stable equilibrium at the initial moment.

A method of calculating wave celerity based on instantaneous frequency allowed the metric to be tried in irregular waves. The observed picture was more complex. The acceleration of the equilibria is not small and, as a result, the actual attraction does not occur. Instead, the dynamical system moves around the equilibrium path, similar to the picture on Figures 13 and 24. Figure 26 shows the phase plane computed for a moving frame of reference. The velocity of this frame of reference is constant and corresponds to a velocity of the stable equilibrium at the initial moment.

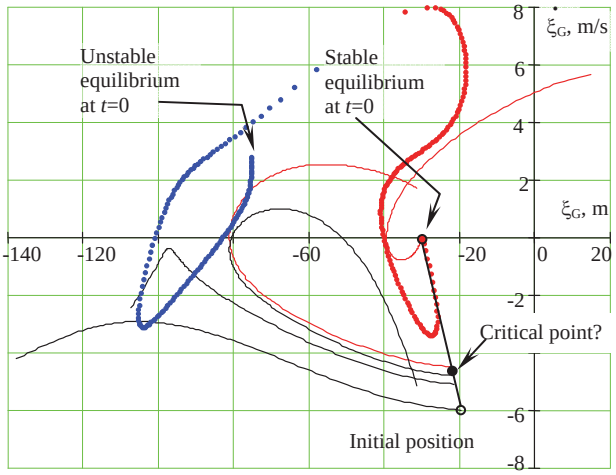

Figure 26: Phase plane trajectories for the critical point determination in calculating a metric for the likelihood of surf-riding in irregular waves

The main difference is that the dynamical system does not follow the stable equilibrium, even if it was placed exactly in the equilibrium position at the initial moment. Furthermore, the equilibria can move toward each other and disappear, releasing the ship from the surf-riding. This means that the criterion for attraction to equilibrium is not as evident as in the case shown in Figure 25. While it is possible to find the critical point visually, the development of a formal criterion of attraction remains for the future work.

6. CONCLUSIONS AND FUTURE WORK

This paper has reviewed work related to surf-riding and broaching-to that has been and continues to be performed under the ONR project entitled "A Probabilistic Procedure for Evaluating the Dynamic Stability and Capsizing of Naval Vessels". The present work focusses on how irregular waves influence the phenomenon. The review addressed three major areas:

- Simulation of surf-riding and broaching-to by advanced hydrodynamic codes and the applicability of nonlinear dynamics tools
- Celerity of irregular waves
- Properties of time-dependent phase space of surging and surf-riding in irregular seas and their characterization.

The results of the studies may be summarized in the following conclusions:

- Surf-riding and broaching-to responses predicted via hybrid hydrodynamic codes are consistent with theoretical results, and the concepts and tools developed from ODE-based analysis can applied to simulation tools as well
- The introduction of irregular waves leads to qualitative changes in surf-riding and broaching-to, including:
  - Problem must be considered in space and time
  - Surf-riding equilibria moves in an unsteady (accelerating) manner, and can appear and disappear in time
  - Surf-riding modes exist for a limited period of time
  - The system attracted to an equilibrium cannot stay with the equilibrium, but instead moves around it.

Problems to be addressed in the next stage of the research project include:

- Formulation of convergence criteria for the metric of likelihood of surf-riding
- Inclusion of sway and yaw into the simplest mathematical model, and study of the uncontrolled turn in irregular waves
- Formulation of the metric of likelihood of broaching-to and capsizing caused by broaching-to.

Solution of these problems is aimed at the developing the procedure for a physics-based statistical extrapolation using a limited data set from nonlinear time-domain numerical simulation. It is envisioned that the procedure will consist of the following steps:

- Prepare an extrapolation data set of simulation data
- Set an intermediate threshold providing a reasonable number (thousands) of upcrossings to be observed
- For each upcrossing, compute a metric of the likelihood of surf-riding, broaching-to, or capsizing due to broaching
- Fit a Generalized Pareto Distribution (GPD) to the metric data and evaluate the estimate of the capsizing rate and its confidence interval from the extrapolation of the metric to the level at which capsizing is inevitable.

7. ACKNOWLEDGEMENTS

The work described in this paper has been funded by the Office of Naval Research, under Dr. Patrick Purtell, Dr. Ki-Han Kim, and Dr. Thomas Fu, and by ONR Global under Dr. Richard Vogelsong and Dr. Woei-Min Lin. The authors greatly appreciate their support.

Many colleagues have influenced and contributed to our work. The authors would like to acknowledge Prof. Pol Spanos (Rice University); Dr. Art Reed, Mr. Tim Smith, and Mr. Brad Campbell (NSWCCD, David Taylor Model Basin); Dr. Nikos Themelis and Mr. Ioanis Kontolefas (National Technical University of Athens); and Profs. Ross Leadbetter and Vladas Pipiras (University of North Carolina Chapel Hill).

8. REFERENCES

Belenky, V.L., Weems, K.M., Lin. W.M., and Spyrou, K.J. 2010, "Numerical Evaluation of Capsizing Probability in Quartering Seas with Split Time Method," Proc. 28th Symp. on Naval Hydrodynamics, Pasadena, California, USA.

Belenky, V., Spyrou, K., and Weems, K.M. 2011, "Split-Time Method for Surf-Riding and Broaching-To," Proc. 12th Intl. Ship

Stability Workshop, Washington D.C., USA, pp. 163-168.

Belenky, V., Spyrou, K., and Weems, K. 2012, "Evaluation of the Probability of Surf-Riding in Irregular Waves with the Time-Split Method," Proc. 11th Intl. Conf. on Stability of Ships and Ocean Vehicles STAB *2012*, Athens, Greece, pp. 29-37.

Bishop, B., Belknap, W., Turner, C., Simon, B., and Kim, J. 2005, Parametric Investigation on the Influence of GM, Roll Damping, and Above-Water Form on the Roll Response of Model 5613, Report NSWCCD-50-TR-2005/027, Naval Surface Warfare Center/Carderock Division, West Bethesda, Maryland.

Grim, O. 1963, "Surging motion and broaching tendencies in a severe irregular sea," Ocean Dynamics, Vol. 16, No 5, Springer Berlin/Heidelberg, pp. 201-231.

Kontolefas, I, and Spyrou, K.J. 2015, "Coherent Phase-space Structures Governing Surge Dynamics in Astern Seas," Proc. 12th Intl. Conf. on Stability of Ships and Ocean Vehicles (STAB 2015), Glasgow, UK.

Lin, W.M., and Yue, D.K.P. 1990, "Numerical Solutions for Large Amplitude Ship Motions in the Time-Domain," Proc. 18th Symp. on Naval Hydrodynamics, Ann Arbor, Michigan, USA, pp. 41–66.

Lin, W.M., Zhang, S., Weems, K., and Luit, D. 2006, "Numerical simulations of Ship Maneuvering in Waves," Proc. of 26th Symp. on Naval Hydrodynamics, Rome, Italy.

Spyrou, K.J. 1996, "Dynamic instability in quartering seas: The behavior of a ship during broaching," J. of Ship Research, Vol. 40, No 1, pp46-59.

Spyrou, K.J. 1997, "Dynamic instability in quartering seas-Part III: Nonlinear effects on periodic motion," J. of Ship Research, Vol. 41, No 3, pp210-223.

Spyrou, K.J. 2006, "Asymmetric Surging of Ships in Following Seas and its Repercussions for Safety," Nonlinear Dynamics, Vol. 43, pp. 149-172.

Spyrou, K., Weems, K.M., and Belenky V. 2009, "Patterns of Surf-Riding and Broaching-to Captured by Advanced Hydrodynamic Modeling," Proc. 10th Intl. Conf. on Stability of Ships and Ocean Vehicles STAB2009, St. Petersburg, Russia, pp. 331-346.

Spyrou, K., and Tigkas, I. 2011, "Nonlinear Surge Dynamics of a Ship in Astern Seas: "Continuation Analysis" of Periodic States with Hydrodynamic Memory," J. Ship Research, Vol. 55 No 1, pp 19-28.

Spyrou, K., Belenky, V., Themelis, N., and Weems, K. 2012, "Conditions for Surf-riding in an Irregular Seaway," Proc. 11th Intl. Conf. on Stability of Ships and Ocean Vehicles STAB 2012, Athens, Greece, pp. 323-336.

Spyrou, K.J., Belenky, V., Themelis, N., and Weems, K. 2014, "Detection of Surf-riding Behavior of Ships in Irregular Seas," Nonlinear Dynamics, Vol. 78, No. 1, pp 649-667.

Spyrou, K.J., Belenky, V., Reed, A., Weems, K., Themelis, N., and Kontolefas, I. 2014a, "Split-Time Method for Pure Loss of Stability and Broaching-To," Proc. 30th Symp. Naval Hydrodynamics, Hobart, Tasmania, Australia.

Theisel, H., and Seidel, H. P. 2003, "Feature Flow Fields," Data Visualization 2003. Proc. VisSym 03, pp. 141–148.

Themelis, N., Spyrou, K., and Belenky, V. 2015, "Surf-riding in Multi-chromatic Seas: "High-runs" and the Role of Instantaneous Celerity," Proc. 12th Intl. Conf. on Stability of Ships and Ocean Vehicles (STAB 2015), Glasgow, UK.

Yen, T.-G., Zhang, S., Weems, K., and Lin,

W.M. 2010, “Development and Validation of Numerical Simulations for Ship Maneuvering in Calm Water and in Waves,” Proc. of 28th Symposium on Naval Hydrodynamics Pasadena, California USA.

The Effect of Ship Speed, Heading Angle and Wave Steepness on the Likelihood of Broaching-To in Astern Quartering Seas

Pepijn de Jong, *Delft University of Technology*, pepijn.dejong@tudelft.nl

Martin. R. Renilson, *Higher Colleges of Technology, UAE, and Australian Maritime College*, martin@renilson-marine.com

Frans van Walree, *Maritime Research Institute Netherlands*, f.v.walree@marin.nl

ABSTRACT

A time domain simulation method that has been developed to investigate the non-linear behaviour of fast ships in waves is applied to following and astern quartering seas. The basis for the simulation method is a panel method employing linearization of some aspects of the hydrodynamics, combined with semi-empirical viscous models to enable faster computations and enabling a range of parameters to be studied in a realistic time frame.

This paper describes the application of the simulation method to the behaviour a fine form displacement hull shape in following and astern quartering seas. The effects of: vessel speed; wave length; heading angle to the waves; and wave steepness are investigated, and the implications on the likelihood of broaching-to in a realistic irregular seaway are inferred.

Keywords: *broaching-to, seakeeping and manoeuvring, time-domain panel method*

NOMENCLATURE

Roman

B	Beam	(m)
c	Wave celerity	(m/s)
Fr	Froude number	(-)
GM	Metacentric height	(m)
H	Wave height	(m)
L	Length	(m)
K,N	Manoeuvring moments	(Nm)
m	Ship mass	(kg)
r	Yaw rate	(rad/s)
R	Resistance	(N)
S	Wetted surface area	(m^2)
T	Draught	(m)
U	Forward speed	(m/s)
x,y,z	Spatial reference coordinates	(m)
X,Y,Z	Manoeuvring forces	(N)

Greek

β	Drift angle	(deg)
δ	Rudder deflection	(deg)
φ	Heel angle	(deg)
λ	Wave length	(m)
ρ	Density of sea water	(kg/m^3)
ξ	Long. position in the wave	(m)
ψ	Yaw (course deviation)	(deg)
ψ_w	Desired heading	(deg)
ζ	Wave elevation	(m)

An over-dot denotes a derivative with respect to time.

Non-dimensional parameters

$$Y' = \frac{Y}{\frac{1}{2}\cdot\rho\cdot U^2\cdot L^2} \qquad N' = \frac{N}{\frac{1}{2}\cdot\rho\cdot U^2\cdot L^3}$$

$$r' = \frac{r\cdot L}{U} \qquad v' = \frac{v}{U} \qquad m' = \frac{m}{\frac{1}{2}\cdot\rho\cdot L^3}$$

1. INTRODUCTION

The control of vessels operating in severe following or astern quartering seas can be difficult, and in many cases can lead to broaching-to. Broaching occurs when a vessel is forced to yaw, and turns away from the wave direction, and towards a direction parallel to the waves. Often, the yaw is particularly violent, which, when combined with the rolling moment due to the counter rudder, and the wave induced rolling moment, can result in a sudden capsize (du Cane and Goodrich, 1962 and Renilson, 1980).

A time domain simulation model, termed PANSHIP, has been developed to investigate the broaching of a fast rescue craft (de Jong *et al.*, 2013). The results from this work showed that the method was able to predict the tendency of this vessel to broach in regular waves of varying length and steepness over range of forward speeds.

The current paper describes the application of the simulation model to investigate the broaching of a high speed fine form displacement vessel. In particular the influence of: ship speed; heading angle to the waves; wave length; and wave steepness have been investigated.

2. SIMULATION MODEL

The simulation of broaching in stern to stern-quartering waves is more complex than simulating ship motions in head to beam seas. One of the main difficulties is that in stern to stern-quartering seas a vessel's speed is likely to vary substantially due to the large longitudinal wave force, and the low encounter frequency. As the ship's hydrodynamic characteristics are functions of its longitudinal position in the wave, it is not normally possible to assume an "average" value, as is the usual practice in head seas. Thus, the situation is complicated by a substantial non-linearity, which must be taken into account carefully. This is unlike the behaviour in head seas, where to a large extent it is enough to consider the average position of the vessel in the wave.

On the other hand, as the encounter frequency is low it is often possible to assume quasi-steadiness, which can considerably simplify the situation. This low encounter frequency has inspired some authors to deal with surf-riding and broaching problems in a quasi-steady fashion, see for instance Renilson and Driscoll (1982). As a result of these low encounter frequencies potential flow damping is only slight and viscous forces due to friction and flow separation are important.

As the steepness of the waves increases, so does the tendency to broach, requiring simulation methods to deal with non-linear effects both in the waves and in the body motions. The resulting large variations in the instantaneous submerged body have an influence on the hydrostatic forces, the wave exciting forces, and the hydrodynamic disturbance forces. In extreme cases the large relative motions may lead to deck immersion, requiring incorporation of the dynamics of water on deck.

To completely deal with the above requires a fully non-linear simulation method, preferably including viscous flow effects. Up to now, these methods require a prohibitive amount of computational time and effort for a full time-domain simulation. Consequently, computational techniques, together with captive model experiments, are mostly used to derive manoeuvring coefficients for use in time domain simulations based on differential equations to simulate manoeuvring performance.

Here a time domain panel method is used, employing a linearization of part of the hydrodynamic problem combined with semi-empirical viscous models to enable faster computations and enabling full time domain simulation. This method, termed PANSHIP, is

described in detail in van Walree (2002) and de Jong (2011), and can be characterized by:

- Three-dimensional transient Green function to account for linearized free surface effects, exact forward speed effects, mean wetted surface, mean radiated and diffracted wave components along the hull and a Kutta condition at the stern;
- Three-dimensional panel method to account for Froude-Krylov forces on the instantaneous submerged body;
- Cross flow drag method for viscosity effects;
- Resistance obtained from pressure integration at each time step combined with empirical viscous drag;
- Propulsion using propeller open water characteristics or a semi-empirical water jet model;
- Motion control and steering using semi-empirical lifting-surface characteristics, water jet steering, and propeller-rudder interaction coefficients;
- Empirical viscous roll damping; and
- Autopilot steering and motion control.

The method has partly been developed and validated in the FAST2 and FAST3 research projects. The participants of these projects are Damen Shipyards (NL), Defence Science Technology Organisation (AUS), Royal Netherlands Navy (NL), Marin (NL) and Delft University of Technology (NL). The method has been validated using a range of physical model experiments, some of which are described in de Jong *et al.* (2013), including:

- Prediction of calm water running attitude and resistance;
- Steering moments from water jet propulsion; and
- Sway, yaw and roll manoeuvring forces/moments due to sway and yaw velocities.

3. APPLICATION

3.1 Fine form displacement vessel

The method was applied to the simulation of the motions of a fine form displacement vessel in following to quartering regular waves. This particular hull shape was used earlier in work published by Renilson and Driscoll (1982). They experimentally determined the manoeuvring coefficients for this hull form in slowly overtaking following and quartering regular waves. This was done by performing forced oscillations with the model mounted under a PMM in a circulating water channel outfitted with a wavedozer. The set of coefficients reported in that paper were used in this work to determine whether the current simulation model reflects a realistic manoeuvring behaviour for this type of vessel.

Figure 1 shows the body plan of the fine form displacement vessel and Table 1 presents the main particulars of the vessel. The hull lines were obtained by digitizing the body plan given in the original paper. For the purpose of this paper the main dimensions were scaled to a length between the perpendiculars of 120 m. The experiments were not performed at the design waterline (DWL) of the vessel, but at a larger draught of 5.28 m, denoted EXPWL in **Figure 1**.

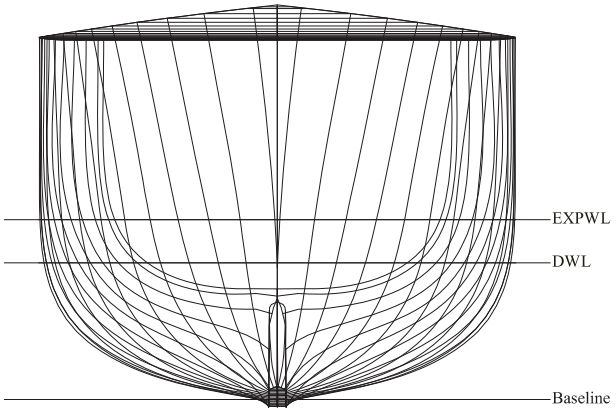

Figure 1 Section plan

Due to the conversion process from a two-dimensional section plan and a lack of longitudinal hull shape information, the displacement and the centre of buoyancy location of the final design differed from the original design. As the intention of the current work was to investigate the behaviour of a generic slender vessel in following waves no further attempt was made to correct the differences in hull parameters.

The propeller and rudder arrangement were not described in the original paper other than the specification of a twin rudder, twin screw arrangement. For this work, a rudder area was chosen of 1% of the lateral area formed by the length between the perpendiculars and the design draught. This is at the lower limit of the usual rudder area for this type of vessel. The propellers were placed at a short distance in front of the rudders, with a diameter of 3.00 meters and a P/D ratio of 1.2.

Table 1 Main particulars

Description	Unit	1982 Value	Current Value
Length between perpendiculars	m	3.660	120.00
Beam	m	0.417	13.67
Draught (EXPWL)	m	0.161	5.28
Draught (DWL)	m	0.122	4.00
Longitudinal centre of buoyancy aft of amidships	m	0.012	6.36[1]
Displacement at EXPWL	kg	127.65	4499054[1]
Radius of gyration about vertical axes	m	0.218 L	0.218 L
Stern arrangement	-	Twin rudder, twin screw	Twin rudder, twin screw
Metacentric height	m	Unknown	1.50
Rudder area	%	Unknown	1%

[1] The center of buoyancy and the displacement given in the original paper were not achievable with the lines provided.

3.2 Numerical modelling details

The forces obtained from the rudders, propellers, and the propeller shafts were determined by using semi-empirical formulations. The rudder formulations accounted for the actual disturbed inflow velocity at the rudder based on the potential flow solution taking into account the orbital velocity from the wave. Rudder emergence was taken into account by determining the wetted span and chord of the rudder below the disturbed water surface and adjusting the forces accordingly. The steering angle was controlled by an autopilot. The settings of the autopilot that were used are given in Table 2.

The propulsion force was determined by the constant rpm setting of the propellers, combined with the inflow velocity at the propeller plane. The rpm setting was determined for the corresponding nominal forward speed in calm water and kept constant during the simulation, The centreline skeg was modelled using combined source and doublet elements combined with a wake sheet extending from its trailing edge. To avoid unrealistic large induced velocities at the hull surface above the skeg, the skeg was extended to the waterline inside the vessel using dummy panels.

Table 2 Auto-pilot settings for course keeping

Description	Symbol	Unit	Value
Damping coefficient	$b_{\delta\psi}$	deg/(deg/s)	9.00
Proportional coefficient	$c_{\delta\psi}$	deg/deg	3.00
Max deflection angle	$\delta_{\max}$	deg	35
Max deflection speed	$\dot{\delta}_{\max}$	deg/s	6.00

Care was taken to ensure fully converged solutions with respect to panel size, time step, wake sheet length, and memory effect length and resolution. Typically around 1300 panels were used on the submerged part of the geometry. The memory effect contributions were truncated at 150 history time steps, and the wake sheet extending from the centre skeg was truncated at 150 panels as well. Time steps

were chosen equivalent to the time necessary to travel 1/50 of the ship length L and kept constant during each simulation.

3.3 Simulation setup

To study the behaviour in following waves, a series of time domain simulations were performed in regular waves. Table 3 presents an overview of the conditions that were simulated. The three different initial headings were tested at the intermediate wave steepness of 1/20 and the three wave steepness were tested at the intermediate initial heading of 20 degrees. This led to a total of 280 individual regular wave time domain simulations of 200 seconds each, requiring about 28 hours in total on a regular desktop computer.

Table 3 Parameter ranges investigated

Description	Parameter	Range	# Variations
Nominal forward speed	Fr	$0.30-0.44$	7
Wave length	λ/L	$0.5-3.0$	8
Wave steepness	H/λ	$1/25, 1/20, 1/17$	3
Initial heading	λ/L	$10°, 20°, 30°$	3

At the start of each simulation the vessel was set to sail at the nominal forward speed with the corresponding rpm setting. The vessel was placed with a wave trough amidships. The wave height and consequently the ship motions were ramped up over 100 time steps. Each time trace was analysed and categorized into one of the following:

- Surf-riding;
- Marginal surf-riding;
- Broaching; or
- None of the above.

The definitions of these characterisations are given in Table 4 and **Table 5**, based on the work of Renilson and Tuite (1998). For the current work no distinction was made between marginal broaching or full broaching, which is the same as the approach taken in an earlier paper (de Jong *et al.*, 2013). The distinction was not found to be very meaningful for this type of simulation and in some cases rather arbitrary.

Table 4 Surf-riding

Description	Surf-riding	Marginal surf-riding
Forward speed	$U = c$	$U \geq 0.9 \cdot c$

Table 5 Broaching (Renilson and Tuite, 1998)

Description	Broach	Marginal broach
Heading deviation	$\psi \geq 20°$	$\psi \geq 20°$
Rudder angle	$\delta = \delta_{max}$	$\delta = \delta_{max}$
Yaw rate	$r > 0$	$r > 0$
Yaw acceleration	$\dot{r} > 0$	-

Prior to the full six degrees of freedom time domain simulations, a number of more basic simulations were carried out. First, a series of calm water runs were performed in order to iteratively determine the calm water trim and sinkage (or rise), as well as the rpm setting necessary for each of the nominal forward speeds. The calm water trim and sinkage were used for determining the mean wetted surface geometry to be used for the linearized radiated and diffracted wave solution.

Second, captive time domain simulations were performed in calm water conditions to capture the manoeuvring coefficients and the steering forces of the vessel and to determine the directional stability over the range of forward speeds of the vessel.

The captive manoeuvring and free running broaching results that are presented in the next section are defined using the axis system given in **Figure 2**. The origin of the ship-fixed frame lies at the centre of gravity of the vessel in the calm water plane. The system is similar to that used for calm water manoeuvring studies. The wave definitions relative to the vessel are used in the free running simulations.

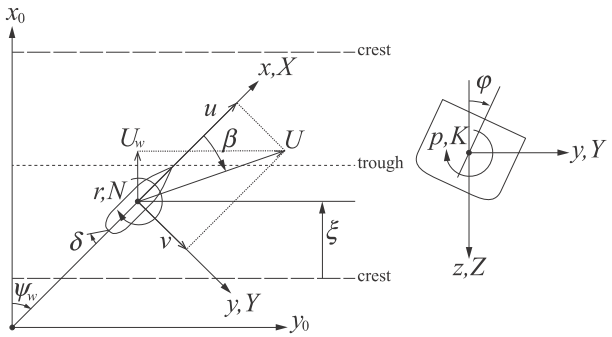

Figure 2 Axis system used for the manoeuvring forces

4. RESULTS

4.1 Manoeuvring

Calm water captive simulations were performed to ensure that the method captured the manoeuvring characteristics of the slender displacement vessel in a realistic manner. The predicted forces and moments in calm water at Froude number 0.40 are compared to those measured by Renilson and Driscoll (1982) at Froude number 0.41 in **Figure 3** to **Figure 6**, and the resulting hydrodynamic coefficients given in **Table 6**.

The dotted blue lines in the figures denote the non-dimensional forces as predicted. The blue solid lines represent the linear component of the fitted polynomial to these forces. The slope of these lines corresponds to the value of the corresponding linear manoeuvring derivative. Deviations between the measured force and the linear fit indicate non-linear contributions to that force component. The slope of green dashed lines represent the value of the calm water manoeuvring coefficients that were reported in the 1982 paper.

The results of the steady drift predictions in Figure 3 and Figure 4 show that both the Y_v and N_v coefficients compare well between prediction and measurement. The results of the yaw oscillations also show a good agreement for N_r in Figure 6. However, the results for the (Y_r-m)-derivative in Figure 5 do not match very well. A possible explanation for this is that this coefficient is the result of the side force distribution over the length of the vessel. For yaw oscillations the contributions to the side force of fore ship and aft ship counteract each other. The difference in their absolute value determines the relatively small magnitude of the resultant side force. The significant mismatch in the longitudinal centre of buoyancy between the original hull and the reconstructed one could cause a relatively large difference, particularly in (Y_r-m).

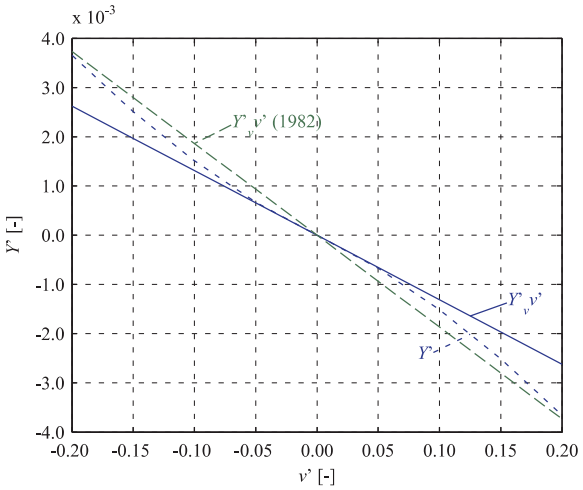

Figure 3 Steady drift: side force computed at three forward speeds and the 1982 measured results

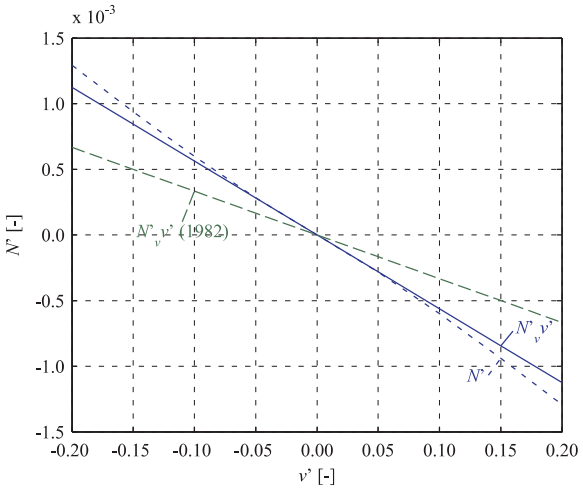

Figure 4 Steady drift: yawing moment computed at three forward speeds and the 1982 measured result

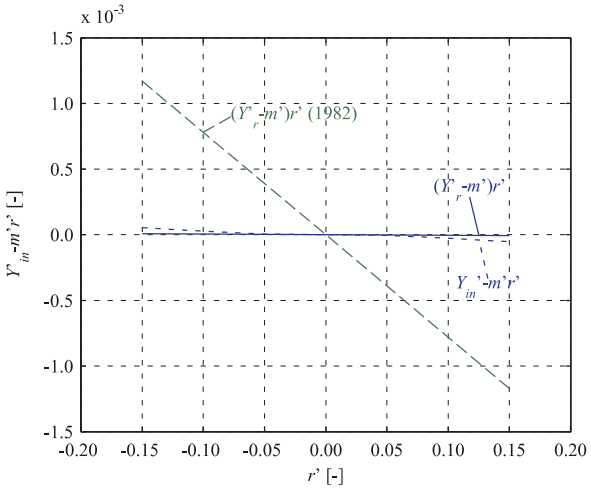

Figure 5 Yaw oscillations: in-phase side force computed at three forward speeds and the 1982 measured results

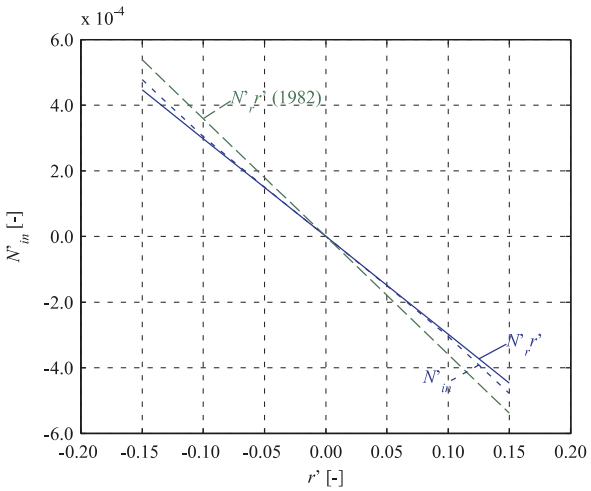

Figure 6 Yaw oscillations: in-phase yawing moment computed at three forward speeds and the 1982 measured results

Table 6 shows the values of the linear manoeuvring coefficients for the 1982 measurement and the current predictions. Also the value of *C*, given by Eq. (1), is reported.

$$C = Y_v' N_v' - N_r' \left(Y_r' - m' \right) \qquad (1)$$

The quantity *C* is considered the discriminator for determining whether a ship possesses control-fixed straight-line stability (Lewis, 1989). A positive value for *C* means, in most cases, that a ship is dynamically stable in the horizontal plane, and will resume on a straight-line path after a disturbance has ended.

Table 6 Results for manoeuvring

	Measured	**Computed**
Fr	**0.412**	**0.400**
Y_v'	-1.87E-02	-1.28E-02
N_v'	-3.33E-03	-5.49E-03
$Y_r' - m'$	-7.81E-03	-5.07E-05
N_r'	-3.59E-03	-2.98E-03
C	+4.09E-05	+3.78E-05

Table 6 indicates that despite the deviation in Y_r'-m', the value of *C* agrees well between the 1982 measured value and the prediction. The main reason is that the contribution of the first term in Eq. (1) is at least an order of magnitude larger than the contribution of the second term. It can be concluded that both hulls have similar controls-fixed directional stability.

Finally, in **Figure 7** a comparison of the predicted and the 1982 measured steering forces is presented. Although the side force agrees well between computation and measurement, the predicted steering moment was found to be slightly lower than in the 1982 measurements. As the 1982 rudder size could not be recovered, the comparison seems to confirm the chosen relatively small rudder area for the computations. The deviation in steering moment arm can only partly be explained by the deviation in longitudinal centre of buoyancy between original and reconstructed hull.

Although not presented here, turning circle manoeuvres were simulated resulting in predicted turning circles diameters in the order of 4 to 6 times *L* at full rudder, depending on the nominal forward speed.

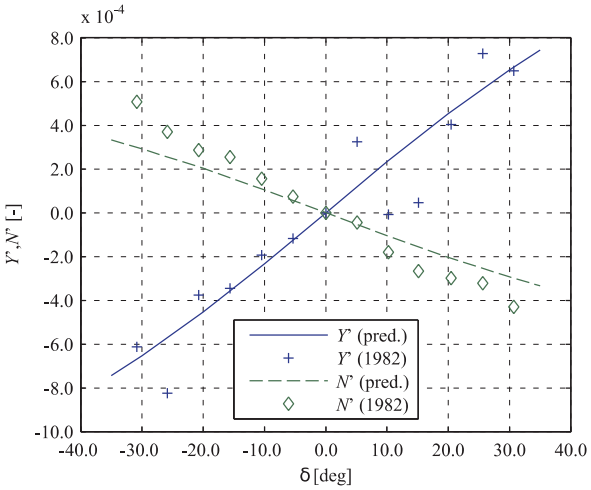

Figure 7 Steering forces: side force and steering moment

4.2 Broaching

The results of the full six degrees of freedom time domain simulations are presented in **Figure 8** to **Figure 13**. First, in **Figure 8** an overview plot is presented for a heading of 20 degrees and wave steepness of 1/20 as an example. Each symbol in the figure represents the outcome of one 200 second time domain simulation. The shape of the symbol indicates categorization of that time trace, using the definitions presented in the previous section.

Furthermore, the figure shows two additional lines. One is marked 'broaching zone' and demarcates the region within which broaches were detected. The other line, marked '$U = c$', indicates the line of zero frequency of encounter, based on the nominal forward speed and wave heading. Below this line, the vessel is initially overtaking the waves, above this line initially the waves are overtaking the vessel.

In both cases the vessel can become entrapped between two wave crests. When the waves are initially overtaking the vessel, this is known as surf-riding. The vessel rides on the front face of the wave, leading to a wave induced moment that tends to force the vessel off course, possibly leading to a broach. The situation where the vessel is initially overtaking the waves has been termed wave-blocking (Maki *et al.*, 2013). In this case the vessel is travelling on the back face of a wave and there is much less risk of upsetting wave forces being built up.

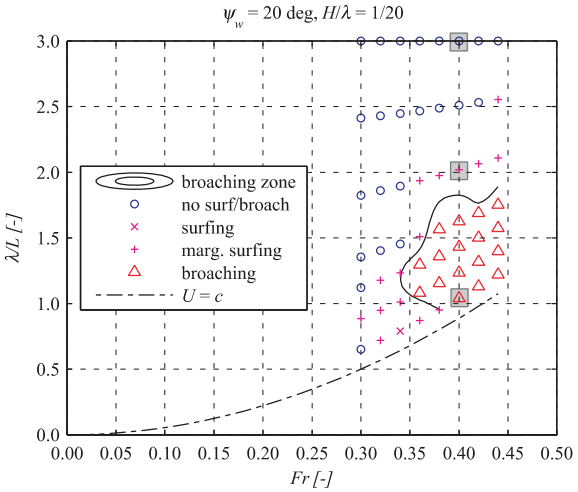

Figure 8 Broaching plot (ψw = 20°, H/λ = 1/20)

Figure 9 to **Figure 11** show relevant time traces of three particular individual time domain simulations performed at Froude number 0.40. The top time trace in each of these figures shows the component of the forward speed of the vessel in the direction of the wave, denoted U_w. The two horizontal red dotted lines mark the wave celerity and 90% of the wave celerity (the threshold for marginal surf-riding). The fourth time trace in each of these figures shows the yaw motion, and the red dotted line indicates a course deviation of 20 degrees (the main threshold value for broaching). The red lines in the last time trace indicate the maximum steering angle. The red circles in the first figure mark the broaches that were detected.

Figure 9 shows the time traces of a run in which broaches were detected. The broaching behaviour is cyclic: within the simulation two broaches occurred. **Figure 10** shows marginal surf-riding, characterised by asymmetric surging with the vessel spending relatively more time close to the wave crest.

Figure 11 shows a situation without surfing or broaching. Although there is still significant

asymmetry in the surge motion, the forward speed in the direction of the wave does not exceed 90% of the wave celerity.

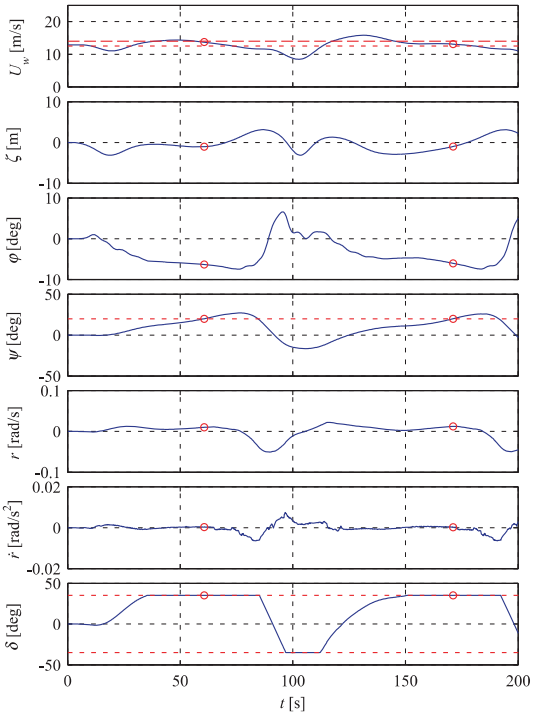

Figure 9 Time traces showing broaching (Fr = 0.40, ψw = 20°, H/λ = 1/20, λ/L = 1.04)

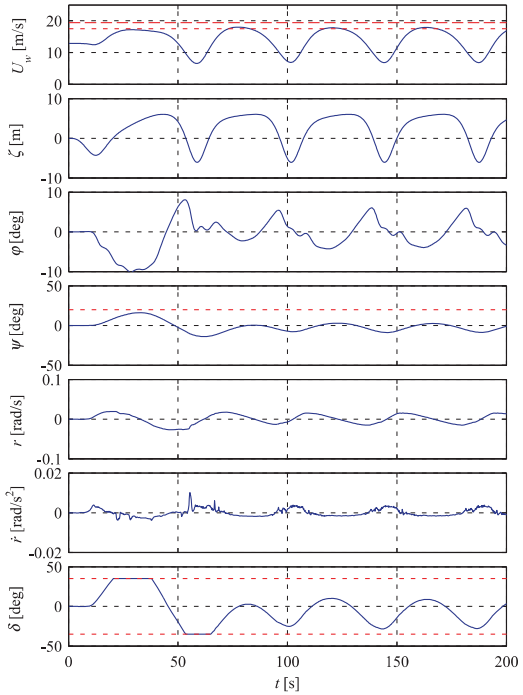

Figure 10 Time traces showing marginal surf-riding (Fr = 0.40, ψw = 20°, H/λ = 1/20, λ/L = 2.02)

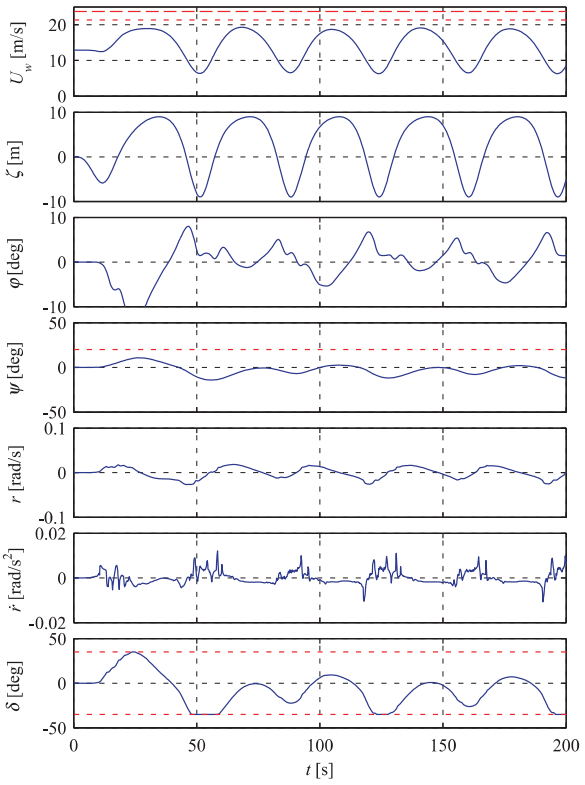

Figure 11 Time traces of no broaching/surf-riding (Fr = 0.40, ψw = 20°, H/λ = 1/20, λ/L = 3.00)

The broaching zones for the variations in initial heading angle are presented in **Figure 12** and the broaching zones for the variations in wave steepness in **Figure 13**. Both figures also show the zero frequency of encounter lines for reference. There is no broaching zone for the smallest heading of 10 degrees in **Figure 12**. For this heading, although surf-riding took place over a significant region, no broaches were detected.

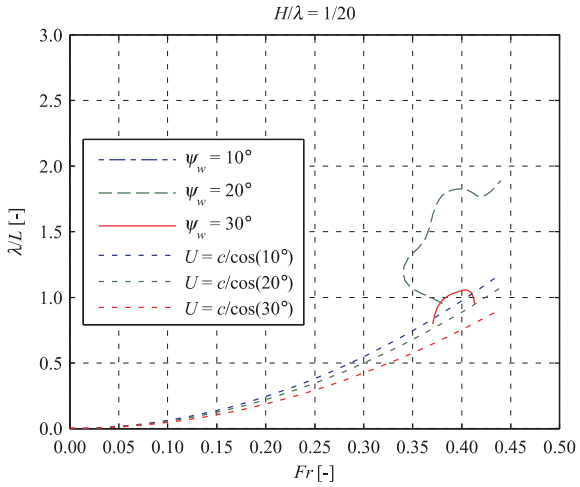

Figure 12 Broaching zones for varying headings

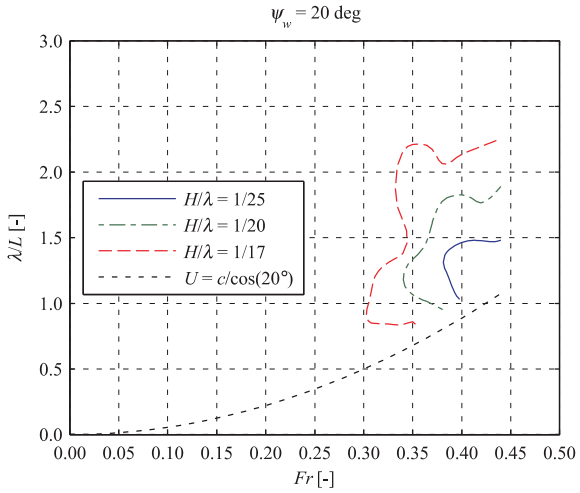

Figure 13 Broaching zones for varying values of the wave steepness

There seems to be a clear progression from no broaching at 10 degrees heading, to a significant broaching region for 20 degrees heading, before diminishing again towards 30 degrees of heading. The fact that the broaching zone is smaller for an initial heading of 30 degrees is counterintuitive, as the wave induced yaw moment at 30 degrees is larger than at 20 degrees. However, this is due to the lower component of the ship velocity in the wave direction when the heading is 30 degrees, resulting in a much lower likelihood of surf-riding.

Figure 13 confirms the expected outcome that the broaching zone expands significantly with increasing wave steepness.

5. DISCUSSION

For a broach to occur there are two conditions to be satisfied: (1) the upsetting wave induced yaw moment should exceed the available restoring steering moment; and (2) this should happen for enough time for the course deviation to build up – hence the link of broaching with surf-riding. The upsetting yaw moment increases with an increasing heading angle, whereas the tendency to surf diminishes with increasing heading angle. This appears to be confirmed by the results presented in this work, showing the largest broaching zone at the intermediate heading.

To compare the results presented in this work with experimental work use was made of results reported by Renilson and Driscoll (1982) and by Nicholson (1974) for similar fine form displacement vessels. Despite differences in hull design and control parameters with these free running experimental investigations, very similar broaching zones were found. The work of Nicholson seems to tend to larger zones at smaller values of the initial heading. Design parameters as metacentric height, rudder size, maximum rudder turning speed and control parameters can have a significant impact on the broaching behaviour and possibly can explain this difference.

De Jong *et al.* (2013) used the same simulation method applied to a water jet powered small rescue craft. Some simulations were carried out at a wave steepness of 1/17 and an initial heading of 20 degrees, allowing a comparison with **Figure 13** in this paper. Although the broaching zones were similar shaped, the rescue craft showed less tendency to broach, with broaching zones starting at slightly larger Froude numbers (0.32 and above) and longer wave lengths (1.1*L* and above).

Although broaching zones are an useful tool for obtaining a systematic overview of the broaching behaviour of a vessel, and for

comparing the relative performance of alternative designs, the question remains how to use the broaching zone plots for predicting the chance of occurrence and the severity of broaches in realistic irregular seas with directional spreading. Aided by the low frequency of encounter and near quasi-steady behaviour, it might be possible to identify an equivalent regular wave with its own length, height and heading for each passing irregular wave crest and subsequently using the broaching plot to determine the consequences of that wave. The authors are planning to investigate this approach, and compare the results with those obtained in irregular waves, in the future.

6. CONCLUDING REMARKS

Time domain simulations were performed for a fine form displacement vessel with semi-nonlinear panel method with empirical viscous flow corrections. The broaching in regular following to astern quartering waves was simulated to study the effect of: vessel speed; wave length; heading angle to the waves; and wave steepness.

To ensure realistic manoeuvring and course keeping characteristics the results of captive manoeuvring simulations in calm water were compared with earlier experimental data, showing good agreement, despite some differences and unknowns in the design parameters. The deviations found in the side force due to yaw oscillations were shown not to significantly influence the horizontal plane dynamic stability.

The results of time domain simulations were presented as broaching zones, showing the influence of wave heading and wave steepness.

It was found that the broaching zone was larger for a heading of 20 degrees compared to headings of both 10 degrees and 30 degrees. This is due to a greater wave upsetting moment occurring at the greater heading angle, but a lower component of ship speed in the wave direction, and hence less surf-riding at the higher wave heading.

As expected, the tendency to broach was shown to increase with increasing wave steepness.

The broaching zones were found to be similar to zones based on previous free running experimental work with comparable vessels. The question remains how to use these plots for studying the behaviour in realistic irregular seas, and the authors plan to address this in the future.

REFERENCES

Cane, P. du and Goodrich G.J., 1962, “The following sea, broaching and surging”, Transactions of the Royal Society of Naval Architects, Vol. 104, pp. 221-228.

Jong, P. de, 2011, “Seakeeping behaviour of high speed ships - An experimental and numerical study”, Ph.D. Thesis, Delft University of Technology.

Jong, P. de, Renilson, M.R. and Walree, F. van, 2013, “The broaching of a fast rescue craft in following seas”, Proceedings of the 12th International Conference of Fast Sea Transportation, Amsterdam, The Nether-lands.

Lewis, E.V. (ed.), 1989, “”Motions in Waves and Controllability”, In Principles of Naval Architecture, Vol. 3, The Society of Naval Architectures and Marine Engineers, NJ, USA.

Maki, A., Umeda, N., Renilson, M.R., and Ueta, T., 2013, “Analytical methods to predict the surf-riding threshold and the wave-blocking threshold in astern seas”, Journal of Marine Science and Technology, Vol.19(4), pp. 415-424.

Nicholson, K., 1974, “Some parametric model experiments to investigate broaching-to”, International Symposium on the Dynamics

of Marine Vehicles and Structures in Waves, London, UK, pp. 171-177.

Renilson, M.R., 1980, "Broaching in a heavy following sea", The Motor Ship.

Renilson, M.R. and Driscoll, A., 1982, "Broaching – An investigation into the loss of directional stability in severe following seas", Transactions Royal Institution of Naval Architects, Vol. 124, pp. 253-273.

Renilson, M.R. and Tuite, A.J., 1998, "Broaching-to – A proposed definition and analysis method", Proceedings of the 25th American Towing Tank Conference, Iowa, USA.

Walree, F. van, 2002, "Development, Validation and Application of a Time Domain seakeeping method for High Speed Craft with a Ride Control System", Proceedings of the 24th Symposium on Naval Hydrodynamics, Fukuoka, Japan, pp. 475-490.

Session 13.2 – LIQUEFACTION

Computation of Pressures in Inverse Problem in Hydrodynamics of Potential Flow

Potential Assessment of Cargo Liquefaction Based on an UBC3D-PLM Model

Coupled Granular Material and Vessel Motion in Regular Beam Seas

This page is intentionally left blank

Computation of Pressures in Inverse Problem in Hydrodynamics of Potential Flow

Ivan Gankevich, *Saint Petersburg State University* igankevich@yandex.com

Alexander Degtyarev, *Saint Petersburg State University* deg@csa.ru

ABSTRACT

The inverse problem in hydrodynamics of potential flow consists of finding velocity and wave pressures under assumption that a wavy surface elevation is known beforehand. The solution to this problem in both two and three dimensions is known but is based on theory of small-amplitude waves. Since some hydrodynamic problems involve waves of arbitrary amplitudes a more general solution is needed. In the paper such solution is given for two and three dimensions and it is shown that it is efficient from computational point of view and more accurate than the solution for small-amplitude waves.

Keywords: *inviscid flow, irrotational flow, analytical solution*

1. INTRODUCTION

A potential flow is the flow of inviscid incompressible fluid which is described by the system of equations (Kochin et al, 1966)

$$\begin{aligned} &\nabla^2\varphi = 0, \\ &\varphi_t + \frac{1}{2}\left|\vec{\upsilon}\right|^2 + g\varsigma = -\frac{p}{\rho}, \quad \text{on } \varsigma = \varsigma(x,y,t), \\ &D\varsigma = \nabla\varphi\cdot\vec{n}, \qquad\qquad \text{on } \varsigma = \varsigma(x,y,t), \end{aligned} \tag{1}$$

where φ is velocity potential, ζ is wavy surface elevation, p is wave pressure, ρ is water density, $\upsilon=(\varphi_x,\varphi_y,\varphi_z)$ is velocity vector, g is gravitational acceleration and D is a substantial derivative. The first two equations are equation of continuity and equation of motion (the so called dynamic boundary condition) and both are derived from Navier-Stokes equations for incompressible inviscid fluid. The last one is kinematic boundary condition for free wavy surface which states that rate of change of wavy surface elevation equals to the change of velocity potential derivative along the wavy surface normal.

In previous paper (Degtyarev & Gankevich, 2012) the solution to inverse problem is given for small-amplitude waves when wave length is much larger than wave height ($\lambda >> h$). It is shown that the inverse problem is linear and can be reduced to a Laplace equation with a mixed boundary condition with equation of motion being used only to determine wave pressure. The assumption of small amplitudes means the slow decay of wind wave coherence function, i.e. a small change of a local wave number in time and space compared to the wave elevation. This assumption allows the use of special derivative formula $\zeta_z=k\zeta$, where k is the wave number; using this formula the solution is constructed. In two-dimensional case the solution is given by

$$\begin{aligned} &\frac{\partial\varphi}{\partial x}\Big|_{x,t} = -\frac{1}{\sqrt{1+\alpha^2}}e^{-I(x)}\int_0^x \frac{\partial\dot{z}/\partial z + \alpha\dot{\alpha}}{\sqrt{1+\alpha^2}}e^{I(x)}dx, \\ &I(x) = \int_0^x \frac{\partial\alpha/\partial z}{1+\alpha^2}dx, \end{aligned} \tag{2}$$

where α is the wave slope. In three-dimensional case the solution is given by

$$\frac{\partial^2\varphi}{\partial x^2}\left(1+\alpha_x^2\right)+\frac{\partial^2\varphi}{\partial y^2}\left(1+\alpha_y^2\right)+2\alpha_x\alpha_y\frac{\partial^2\varphi}{\partial x\partial y}+$$
$$\left(\frac{\partial\alpha_x}{\partial z}+\alpha_x\frac{\partial\alpha_x}{\partial x}+\alpha_y\frac{\partial\alpha_x}{\partial y}\right)\frac{\partial\varphi}{\partial x}+$$
$$\left(\frac{\partial\alpha_y}{\partial z}+\alpha_x\frac{\partial\alpha_y}{\partial x}+\alpha_y\frac{\partial\alpha_y}{\partial y}\right)\frac{\partial\varphi}{\partial y}+$$
$$\frac{\partial\dot{\varsigma}}{\partial z}+\alpha_x\dot{\alpha}_x+\alpha_y\dot{\alpha}_y=0.$$

Here the formula is not explicit and represents elliptic equation which is intended to be solved by a variety of known numerical methods.

Although, these methods are efficient and work well for a wide range of wavy surfaces some weather conditions produce waves with wave numbers which change frequently in time and space. These are transitions between normal and storm weather, wind wave and swell heading from multiple directions and some others. These weather conditions and a possibility to obtain a more general solution are the main reasons for solving the potential flow problem for arbitrary amplitude waves case.

2. TWO-DIMENSIONAL CASE

For two-dimensional flow equation (1) can be rewritten as follows.

$$\varphi_{xx}+\varphi_{zz}=0,$$
$$\varphi_t+\frac{1}{2}\left(\varphi_x^2+\varphi_y^2\right)+g\varsigma=-\frac{p}{\rho},\ \text{on}\ z=\varsigma(x,y,t),$$
$$\varsigma_t+\varsigma_x\varphi_x=\frac{\varsigma_x}{\sqrt{1+\varsigma_x^2}}\varphi_x+\varphi_z,\ \text{on}\ z=\varsigma(x,y,t),$$

The first step is to solve Laplace equation using Fourier method. The solution can be written as integral similar to Fourier transform:

$$\varphi(x,z)=\int_{-\infty}^{\infty}E(\lambda)e^{\lambda(z+ix)}d\lambda \qquad (3)$$

Then coefficients E can be determined by plugging this integral into kinematic boundary condition and evaluating derivatives. This step gives equation

$$\frac{\varsigma_t\sqrt{1+\varsigma_x^2}}{1-i\varsigma_x\left(\sqrt{1+\varsigma_x^2}-1\right)}=\int_{-\infty}^{\infty}\lambda E(\lambda)e^{\lambda(\varsigma+ix)}d\lambda$$

which represents forward bilateral Laplace transform and thus can be inverted to yield formula for coefficients E:

$$E(\lambda)=\frac{1}{2\pi i\lambda}\int_{-\infty}^{\infty}\frac{\varsigma_t\sqrt{1+\varsigma_x^2}}{1-i\varsigma_x\left(\sqrt{1+\varsigma_x^2}-1\right)}e^{-\lambda(\varsigma+ix)}dx \qquad (4)$$

The third step is to plug (4) into (3) which yields the final result:

$$\varphi(x,t)=\frac{1}{2\pi i}\int_{-\infty}^{\infty}\frac{1}{\lambda}e^{\lambda(\varsigma+ix)}d\lambda \qquad (5)$$
$$\int_{-\infty}^{\infty}\frac{\varsigma_t\sqrt{1+\varsigma_x^2}}{1-i\varsigma_x\left(\sqrt{1+\varsigma_x^2}-1\right)}e^{-\lambda(\varsigma+ix)}dx.$$

When equation (1) is solved that way, wave pressures can be determined from dynamic boundary condition.

Since velocity potential is the only unknown prerequisite for determining wave pressures it is feasible to use it to validate the solution. A comparison was done to the known small-amplitude wave solution (2) and numerical experiments showed good correspondence rate between resulting velocity potential fields.

In order to obtain velocity potential fields the wavy sea surface was generated by auto-regressive model differing only in wave amplitude. In numerical implementation infinite outer and inner integral limits of (5) were replaced by the corresponding wavy surface size (x_0,x_1) and wave number interval (λ_0,λ_1) so that inner integral of (5) converges.

Experiments were conducted for waves of both small and large amplitudes and in case of small-amplitude waves both solutions produced similar results, whereas in case of large-amplitude waves only general solution prduced

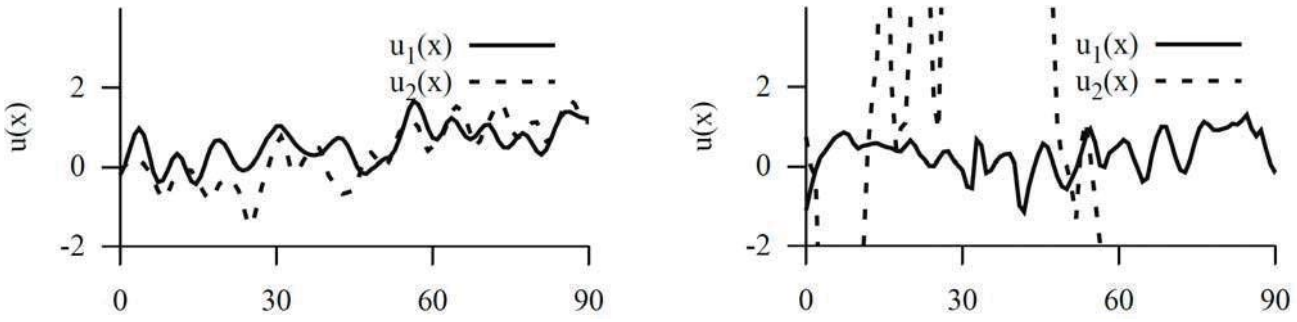

Fig. 1 Comparison of velocity fields produced by general solution (u_1) and solution for small-amplitude waves (u_2). Velocity fields for small-amplitude (left) and large-amplitude (right) wavy sea surfaces.

stable velocity field (Figure 1). The fact that velocity fields for small-amplitude waves are not equal can be explained by stochastic nature of autoregressive wind wave model (i.e. the amplitude is small in a statistical sense only). Therefore, general solution in two-dimensional case works for different wavy sea surfaces without restriction on wave amplitude.

3. SPECIAL TRANSFORM

Three-dimensional problem can be solved with help of special inversion formula which serves as a modified version of Fourier transform. The transform has the following form:

$$F(x,y)=\int_{-\infty}^{\infty}\int f(\lambda,\gamma)e^{i(\lambda x+\gamma y)+\varsigma(x,y)\sqrt{\lambda^2+\gamma^2}}d\lambda d\gamma. \tag{6}$$

In order to derive inversion formula this expression should be reduced to a two-dimensional convolution. By applying transformations

$$\begin{aligned}&(\lambda,\gamma)\to(r,\theta),\lambda=r\cos\theta,\gamma=r\sin\theta,|J|=r,\\&(x,y)\to(\rho,\psi),x=\rho\cos\psi,y=\rho\sin\psi,\end{aligned} \tag{7}$$

the formula is rewritten in polar coordinates for both f and F:

$$F(\rho,\psi)=\int_0^{\infty}\int_0^{2\pi} rf(r,\theta)e^{ir\rho\cos(\psi-\theta)+r\varsigma(\rho,\psi)}d\theta dr.$$

Then applying additional transformations

$$\begin{aligned}&r\to r',r=e^{r'};\rho=\rho',\rho=e^{-\rho'};\\&\varsigma\to\varsigma',\varsigma=e^{\rho'}\varsigma'\end{aligned} \tag{8}$$

to the radius vectors and function ζ a convolution can be obtained:

$$\begin{aligned}&F(\rho',\psi)=f_1*f_2,\\&f_1(r',\theta)=e^{2r'}f(r',\theta),\\&f_2(\rho',\psi)=\exp\left[ie^{-\rho'}\cos\psi+e^{-\rho'}\varsigma'(\rho',\psi)\right].\end{aligned} \tag{9}$$

Since convolution theorem permits any converging integral transform to be applied to a convolution, here a modified polar version of Fourier transform

$$\begin{aligned}&\text{☞}'\{g(r,\theta)\}(r_1,\theta_1)=\int_0^{\infty}\int_0^{2\pi}-e^{-2r}g(r,\theta)\\&\exp\left[-ie^{-r}r_1\cos(\theta_1-\theta)\right]d\theta dr\end{aligned} \tag{10}$$

is used. Applying this transform to the both sides of equation (9) yields the final formula

$$\begin{aligned}&\text{☞}\{F(x,y)\}=\text{☞}\left\{\frac{f(x,y)}{x^2+y^2}\right\}\\&\text{☞}\{\exp[ix+\varsigma(x,y)]\},\end{aligned} \tag{11}$$

where ☞ is ordinary forward Fourier transform.

This formula is useful in two cases. First, it allows inversion of initial modified Fourier transform (6) which is needed when solving three-dimensional problem. Second, it can be used to compute F efficiently with use of fast Fourier transform family of algorithms. So, special transform is the tool to solve three-dimensional problem.

4. THREE-DIMENSIONAL CASE

Three-dimensional problem is solved mostly the same way as its two-dimensional counterpart, however, special transform developed in the previous section should be used instead of bilateral Laplace transform and some terms from system of equations (1) should be rewritten in dimensionless form for convolution to be physically feasible.

4.1 Formula derivation

Consider a square region with a side N where the problem is being solved. Then coordinate transform $(x,y)\to(xN,yN)$ produces system of equations with dimensionless x and y:

$$\frac{1}{N^2}\varphi_{xx}+\frac{1}{N^2}\varphi_{yy}+\varphi_{zz}=0,$$

$$\varphi_t+\frac{1}{2}\left(\frac{\varphi_x^2}{N^2}+\frac{\varphi_y^2}{N^2}+\varphi_z^2\right)+g\varsigma=-\frac{p}{\rho},$$

$$\text{☹♦}=\varsigma(x,y,t),$$

$$\varsigma_t+\frac{\varsigma_x}{N^2}\varphi_x+\frac{\varsigma_y}{N^2}\varphi_y=\frac{\varsigma_x}{Nd}\varphi_x+\frac{\varsigma_y}{Nd}\varphi_y+\varphi_z,$$

$$\text{☹♦}=\varsigma(x,y,t),$$

where $d=\sqrt{N^2+\varsigma_x^2+\varsigma_y^2}$.

The first step is to solve Laplace equation with Fourier method which yields

$$F(x,y,z)=\int_{-\infty}^{\infty}\int E(\lambda,\gamma)e^{M(iN(\lambda x+\gamma y)+z(x,y)\sqrt{\lambda^2+\gamma^2})}d\lambda d\gamma. \quad (12)$$

Here λ and γ represent wave numbers which were made dimensionless with transform $(\lambda,\gamma)\to(\lambda M,\gamma M)$. Then the expression is plugged into the kinematic boundary condition yielding

$$\varsigma_t=\int_{-\infty}^{\infty}\int d\lambda d\gamma E(\lambda,\gamma)e^{M(iN(\lambda x+\gamma y)+\varsigma\sqrt{\lambda^2+\gamma^2})}$$

$$\frac{M}{Nd}\left[N^3\sqrt{\lambda^2+\gamma^2}-i\lambda\varsigma_x(d-N)-i\gamma\varsigma_y(d-N)\right]$$

In order to obtain convolution formula transformations (7) and (8) from the previous section are applied:

$$\varsigma_t=\int_{-\infty}^{\infty}\int d\theta dr' e^{Me^{r'-\rho'}(iN\cos(\theta-\psi)+\varsigma)}\frac{Me^{2r'}}{Nd'}E(r',\theta)$$

$$\begin{bmatrix}N^3-ie^{\rho'}\cos(\theta-\psi)\varsigma_{\rho'}(d'-N)\\ -ie^{\rho'}\sin(\theta-\psi)\varsigma_{\psi}(d'-N)\end{bmatrix},$$

where $d'=\sqrt{N^2+e^{2\rho'}\left(\varsigma_{\rho'}^2+\varsigma_{\psi}^2\right)}$.

Finally, after applying modified Fourier transform (10) to the both sides of this equation the formula for coefficients E can be derived:

$$☞\{\varsigma_t(x,y)\}=☞\left\{\frac{E(\lambda,\gamma)}{\lambda^2+\gamma^2}\right\}☞\{f(x,y)e^{M(iNx+\varsigma)}\},$$

$$f(x,y)=M\frac{N^2+i\varsigma_x\left(\sqrt{N^2+\varsigma_x^2+\varsigma_y^2}-N\right)}{N\sqrt{N^2+\varsigma_x^2+\varsigma_y^2}}.$$

4.2 Numerical implementation

Using formula (11) the integral from (12) can be decomposed into two forward and one inverse Fourier transforms, so the whole solution can be computed efficiently:

$$\varphi(x,y,z)=☞^{-1}\left\{☞\left\{\frac{E(\lambda,\gamma)}{\lambda^2+\gamma^2}\right\}☞\{e^{M(iNx+\varsigma)}\}\right\}.$$

Forward and inverse Fourier transform of E cancel each other:

$$\varphi(x,y,z)=☞^{-1}\left\{\frac{☞\{\varsigma_t(x,y)\}☞\{e^{M(iNx+\varsigma)}\}}{☞\{f(x,y)e^{M(iNx+\varsigma)}\}}\right\}.$$

There is no easy way to derive analogous formula for velocity potential derivatives, however, numerical experiments have shown that there is no need to do it. These derivatives can be obtained numerically via finite difference formulae. Less number of integral transforms means less numerical error and faster computation.

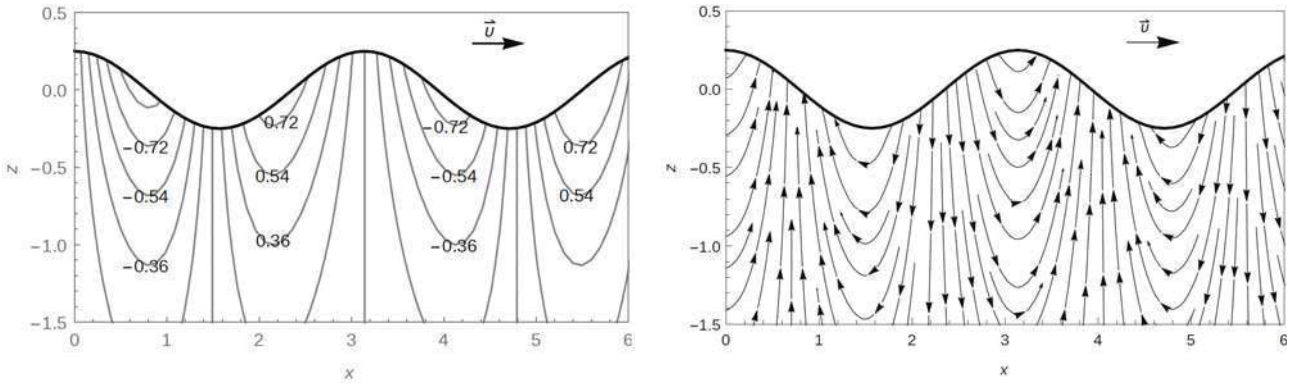

Fig. 2 Slices at *y=3.1; t=0* of propagating waves' velocity potential field (left) and stream lines (right). Here $\varsigma(x,y,t) = \frac{1}{4}\cos(4\pi x - 0.25t)$.

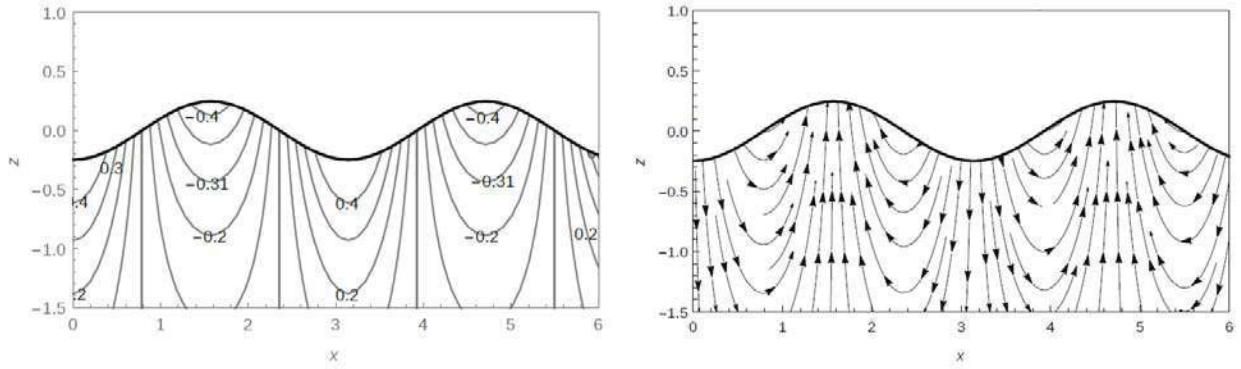

Fig. 3 Slices at *y=3.1; t=1* of standing waves' velocity potential field (left) and stream lines (right). Here $\varsigma(x,y,t) = \cos(4\pi x)\sin(-0.25t)$.

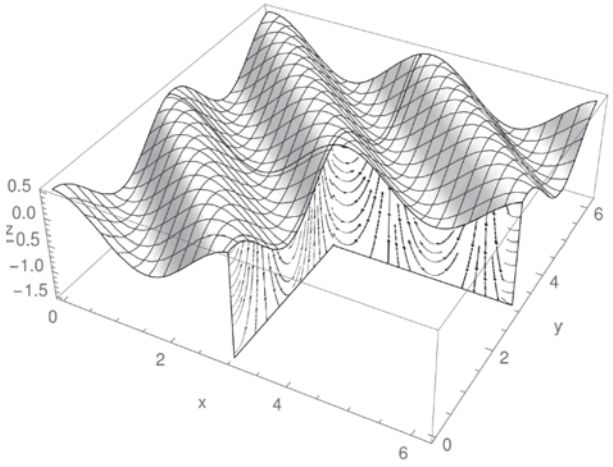

Fig. 4 Slice at y = 3:1; t = 0 of propagating waves' velocity potential stream lines. Here $\varsigma(x,y,t) = \frac{1}{2}\cos(4\pi(x+y) - 0.25t)$.

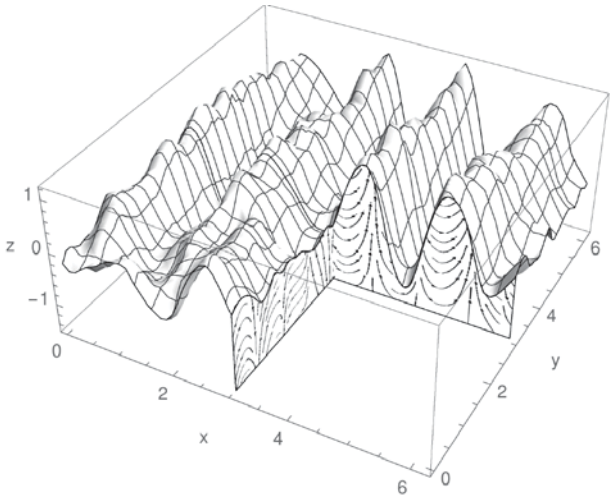

Fig. 5 Slice of a wavy surface with waves of large amplitude generated by autoregressive wind wave model.

So, from computational point of view velocity potential is given by four fast Fourier transforms plus three numerical differentiations (one for each coordinate), in other words its asymptotic complexity is roughly $4n\log_2 n + 3n$, where n is the total number of points in the volume.

4.3 Evaluation

Three-dimensional solution was evaluated on different types of waves: propagating, standing and real ocean waves generated by autoregressive model. For the first two types of waves the shape of velocity potential and velocity field is known and can be found elsewhere (van Dyke, 1982), so they were used to validate the solution. The last type of wave was used to see how the solution behaves in case of large amplitude waves.

Since computation is done with discrete Fourier transforms the resulting data is sometimes perturbed on the edges (Lyons, 2010). In real world those perturbations should be removed from the solution but here they were left for the sake of transparency of results.

Propagating waves are known to have region of negative velocity potential under the front slope and region of positive potential under the back slope while standing waves are known to have region of negative potential under their crests and region of positive potential under their bottoms. Velocity of a water particle is always in the direction of negative potential and it is perpendicular to the contours of velocity potential. This behaviour is fully captured by the solution (Figures 2–4).

For large amplitude waves the solution was tested on the wavy surface generated by autoregressive wind wave model and in this case the shape of stream lines and potential field is asymmetric. As can be seen in Figure 5 stream lines are skewed in the direction which is opposite to the direction of wave propagation.

5. CONCLUSIONS

To sum up, new solution allows determining velocity field for waves of arbitrary amplitudes and is fast from computational point of view. For plain waves the solution gives the same field as previously known solutions and for large-amplitude waves it gives asymmetrical velocity field.

6. ACKNOWLEDGEMENTS

The research was carried out using computational resources of Resource Centre “Computational Centre of Saint Petersburg State University” (T-EDGE96 HPC-0011828-001) within frameworks of grants of Russian Foundation for Basic Research (project no. 13-07-00747) and Saint Petersburg State University (projects no. 9.38.674.2013 and 0.37.155.2014).

7. REFERENCES

A. Degtyarev and I. Gankevich. Evaluation of hydrodynamic pressures for autoregression model of irregular waves. In Proceedings of 11th International Conference on Stability of Ships and Ocean Vehicles, Athens, pages 841–852, 2012.

N. Kochin, I. Kibel, and N. Roze. Theoretical hydrodynamics [in Russian]. FizMatLit, 1966.

Richard G Lyons. Understanding digital signal processing. Pearson Education, 2010.

Milton Van Dyke. An album of fluid motion. 1982.

Potential Assessment of Cargo Fluidization based on an UBC3D-PLM Model

Lei Ju, *Ship Stability Research Centre, University of Strathclyde,* lei.ju@strath.ac.uk

Dracos Vassalos, *Ship Stability Research Centre, University of Strathclyde,* d.vassalos@strath.ac.uk

ABSTRACT

Fluidization of fine particle cargoes, resulting in cargo shift and loss of stability, has caused the loss of many lives in numerous marine casualties over the past decades. Since the dangers of cargo fluidization have long been known to the shipping industry, the question of why the phenomenon is resurfacing now would be a legitimate one. With this in mind, an UBC3D-PLM model based on FEM theory in the commercial software PLAXIS is presented in this paper to consider soil DSS (Direct Simple Shear) test to verify the model. To assess the cargo fluidization potential, an evaluating method is presented in the paper considering cargo fluidization. Shaking table tests with different amplitude, frequency and initial degree of saturation of cargos were studied to predict time-domain characteristics. This method in the paper could be feasibly used as a reference and possibly support a suitable regulatory framework to the fluidization analysis of ship stability.

Keywords: *Cargo Liquefaction; UBC3D-PLM; Ship Stability*

1. INTRODUCTION

Liquefaction of mineral ores, such as ore fines from India and nickel ore from Indonesia, the Philippines and New Caledonia, resulting in cargo shift and loss of stability, has been a major cause of marine casualties over the past few years. Such a transition during ocean carriage can cause a sudden loss of stability of the carrying vessel. While cargoes are loaded on board a vessel, the materiel is exposed to mechanical agitation and energy input in the form of engine vibrations, vessel movement and wave impact, resulting in a gradual settling and compaction of the cargo. The gaps between the particles become smaller in the process, while the pore pressure between particles will increase. The water holding ability or matric suction of particles decreases and the water in the cargos will separate from the cargo. Then cargos turn into a viscous fluid, i.e. fluidization.

The UBC3D-PLM is a powerful constitutive model, which is a 3-D extension of the UBCSAND model introduced by Beaty & Byrne (1998). The Mohr-Coulomb yield condition in a 3-D principal stress space is used. The bulk modulus of water is depended with the degree of saturation, which is specified via PLAXIS input, enabling the prediction of the pore pressure evolution in unsaturated particles.

2. KEY FEATURES OF UBC3D-PLM

2.1 Yield Surface

Mohr-Coulomb yield function generalized in 3-D principal stress space is used in UBC3D-PLM model (Alexandros & Vahid, 2013) as presented in Figure 1.

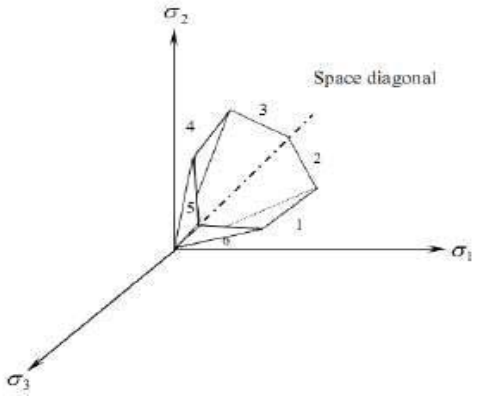

Figure 1 The Mohr-Coulomb yield surface in 3-D principal stress space

The critical yield surface could be defined given by Equation (1):

$$f_m = \frac{\sigma'_{\max} - \sigma'_{\min}}{2} - \left(\frac{\sigma'_{\max} + \sigma'_{\min}}{2} + c' \cot\phi'_p\right)\sin\phi_{mob} \quad (1)$$

Where, $\sigma'_{\max}$ and $\sigma'_{\min}$ are the maximum and minimum principal stresses respectively, c' is the cohesion of the soil, ϕ'_p is the peak friction angle of the soil, ϕ_{mob} is the mobilized friction angle during hardening.

2.2 Elasto-plastic Behaviour

The elastic behaviour which occurs within the yield surface is controlled by two parameters expressed in terms of the elastic bulk modulus K_B^e and the elastic shear modulus K_G^e as shown below:

$$K_B^e = k_B^e P_A \left(\frac{p'}{P_A}\right)^{me} \quad (2)$$

$$K_G^e = k_G^e P_A \left(\frac{p'}{P_A}\right)^{ne} \quad (3)$$

Where, p' is the mean effective stress, P_A is the reference stress (usually equal to 100kPa), k_B^e and k_G^e are the bulk and shear modulus numbers respectively and, *me* and *ne* are the elastic exponents which define the rate dependency of stiffness.

The hardening rule as reformulated by Tsegaye (2011) in UBC3D-PLM model is given as:

$$d\sin\phi_{mob} = 1.5K_G^p \left(\frac{p}{P_A}\right)^{np} \frac{P_A}{P_m}\left(1 - \frac{\sin\phi_{mob}}{\sin\phi_{peak}} R_f\right)^2 d\lambda \quad (4)$$

Where, $d\lambda$ is the plastic strain increment multiplier, np is the plastic shear modulus exponent, ϕ_{mob} is the mobilized friction angle, which is defined by the stress ratio, ϕ_{peak} is the peak friction angle and R_F is the failure ratio n_f / n_{ult}, ranging from 0.5 to 1.0.

2.3 Plastic Potential Function

The plastic potential function specifies the direction of the plastic strain. A non-associated flow rule based on the Drucker-Prager plastic potential function is used in the UBC3D-PLM (Tsegaye, 2011). The plastic potential function is formulated as:

$$g = q - a(p' + c\cot\phi_p) \quad (5)$$

$$a = \frac{\sqrt{3}\sin\psi_{mob}}{\cos\theta + \frac{\sin\theta\sin\psi}{\sqrt{3}}} \quad (6)$$

Where, θ equals 30° cause the Drucker-Prager surface is fixed in the compression point.

2.4 Post-liquefaction Rule and Cyclic Mobility

From the experimental studies, the stiffness degradation of soil due to the post-liquefaction behaviour of loose non-cohesive soils or due to the cyclic mobility of dense non-cohesive sands is occurred. For modelling this, an

equation is implemented in UBC3D-PLM which gradually decreases the plastic shear modulus as a function of the generated plastic deviatoric strain during dilation of the soil element.

This behaviour is presented in Figure 2 picturing the process of cyclic mobility of dense sand. The stiffness degradation is computed as follows:

$$K_G^p = K_{G,primary}^p * e^{E_{dil}} \tag{7}$$

$$E_{dil} = \min(110 * \varepsilon_{dil}, fac_{post}) \tag{8}$$

Where ε_{dil} is accumulation of the plastic deviatoric strain which is generated during dilation of the soil element, the input parameter fac_{post} is the value of the exponential multiplier term.

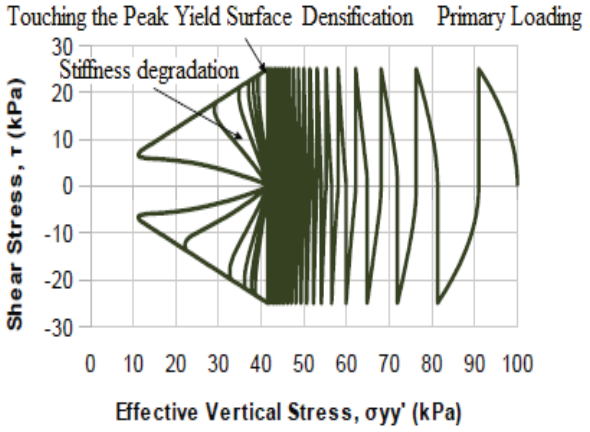

Figure 2 Undrained cyclic shear stress path reproduced with UBC3D-PLM for dense sand. Cyclic mobility, stiffness degradation and soil densification are mentioned on the graph

2.5 Undrained Behaviours

The increment of the pore water pressure is computed by the following equation:

$$dp_w = \frac{K_w}{n} d\varepsilon_v \tag{9}$$

Where K_w is the bulk modulus of the water and n is the soil porosity and $d\varepsilon_v$ is the volumetric strain of the fluid.

The bulk modulus of water is dependent with the degree of saturation of the soil. The bulk modulus of the unsaturated water is defined as follows:

$$K_w^{unsat} = \frac{K_w^{sat} K_{air}}{SK_{air} + (1-S)K_w^{sat}} \tag{10}$$

Where K_w^{sat} is the bulk modulus of the saturated water and K_{air} is the bulk modulus of air which equals 1 *kPa* in this implementation having the minimum value which enables to avoid the generation of pore pressures during modelling a dry sand. S is the degree of saturation in the soil.

3. VALIDATION OF THE UBC3D-PLM IN ELEMENT TEST

3.1 Validation of the UBC3D-PLM in Monotonic Loading

The validation of the UBC3D-PLM in monotonic loading is presented in this section. The input parameters for modelling the tri-axial compression test (TxC) and the direct simple shear test (DSS) on loose Syncrude sand are given in Table 1. The results of the UBC3D-PLM are in a good agreement with the experimental data (Puebla & Byrne & Philips, 1997) as shown in Figure 3 and Figure 4.

Table 1 UBC3D input parameters for all the validation tests

Parameter	Syncrude S. (TxC, DSS)	Fraser S. (Cyclic DSS)	Cargo (FEM)

$\varphi_p(\circ)$	33.7	33.8	31.2
$\varphi_{cv}(\circ)$	33	33	34.6
k_B^e	300	607	720
k_G^e	300	867	1031
$K_G^p(TxC)$	310	-	
$K_G^p(DSS)$	98.3	266	700
$me = ne$	0.5	0.5	0.5
np	0.5	0.4	0.4
R_f	0.95	0.81	0.74
$N1(60)$	8	8	13
fac_{hard}	1	1	0.45
fac_{post}	0	0.6	0.01

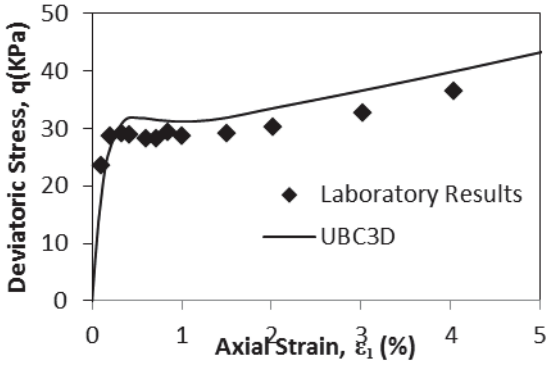

Figure 3 Undrained tri-axial compression

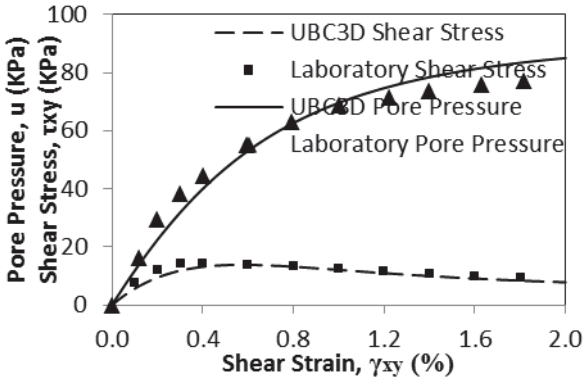

Figure 4 Undrained simple shearing

3.2 Validation of the UBC3D-PLM in Cyclic Loading

The behaviour of loose Fraser sand under cyclic direct simple shear is modelled and the numerical results are compared with experimental data as published by Sriskandakumar (2004). The relative density (RD) of the tested sand is 40%. In Figures 5, the evolution of stress-strain is presented. The applied CSR equals 0.08. The vertical applied stress is 100 *kPa* in all cases. The K0 factor is assumed to be 1 for simplification.

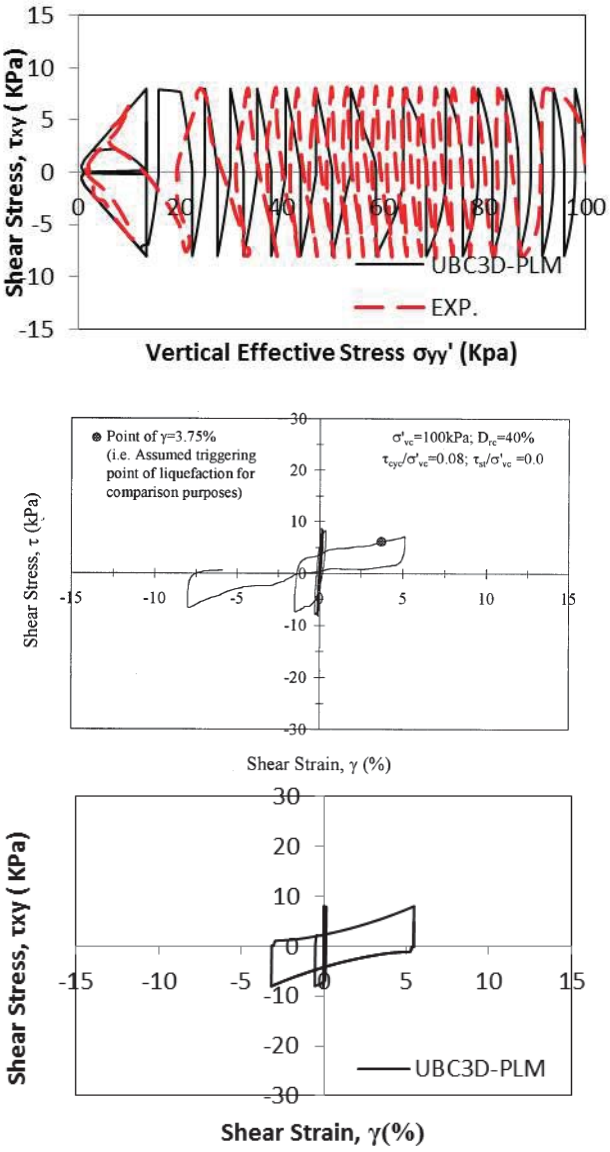

Figure 5 Cyclic DSS stress controlled (RD=0.4 CSR=0.08 σ_v =100kpa)

4. CARGO FLUIDIZATION IN A FINITE ELEMENT SCHEME

4.1 Evaluating cargo fluidization

The soil-water characteristic curve is the basis for estimating the dynamic analysis of particles. Unsaturated particles are composed of three phases; including particle skeleton (solid), pore water (liquid) and pore are (gas). The air-water interface has a surface tension. In the unsaturated particles, the pore air pressure and pore water pressure are unequal and greater than the latter. The interface is under the part pore air pressure of lager pore water pressure. The pressure difference (i.e., pore air pressure minus pore water pressure) across the interface of air and water is called the matric suction. Matric suction is generally the key parameter describing the mechanical property of unsaturated particles.

In the capillary tube, the surface between pore air and pore water displays curved interface. The fluid pressure of sides interface is discontinuous. If the upside of the interface is connected with atmosphere, the pressure upside interface is larger than the water pressure. The pressure difference is called matric suction. S depends on the curvature of the curved interface and surface tension.

$$S = u_a - u_w \tag{11}$$

The soil-water characteristic curve (SWCCs) relates the water content or degree of saturation to matrix suction of a particle. A representative SWCCs is shown in Fig 6. We can see different iron ore has different water holding ability. When the cargo compaction, the volume decreases resulting in increasing pore water pressure and decreasing matric suction of cargos. Cargos cannot hold any water in case of suction equals zero. Water is progressively displaced in the hold base, which may result in some portions or all of the cargo developing a flow state.

For earthquake liquefaction, the acceleration is large and soil could be regarded as un-drained soil, where acceleration for cargo fluidization is small and the water could drain from cargos. When the degree of saturation turns 100% and water comes out from the cargos, the cargos have reflected the nature of fluidization. Therefore, take suction=0 as the onset of cargo fluidization in the paper.

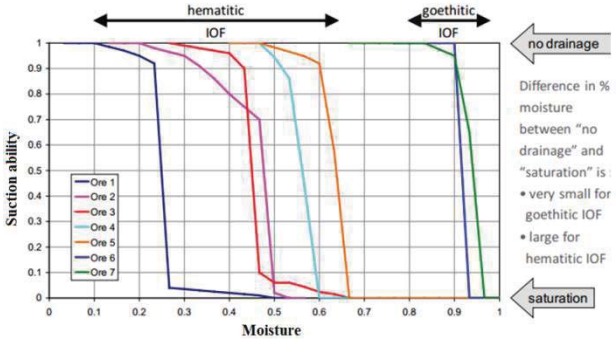

Figure 6 Soil-water characteristic curves

4.2 Centrifuge Test

The influence of degree of saturation on the free field response is investigated. The geometry of layer is shown in Figure 7. Locations L, N, O are monitored through the test. The initial degree of saturation is supposed uniform.

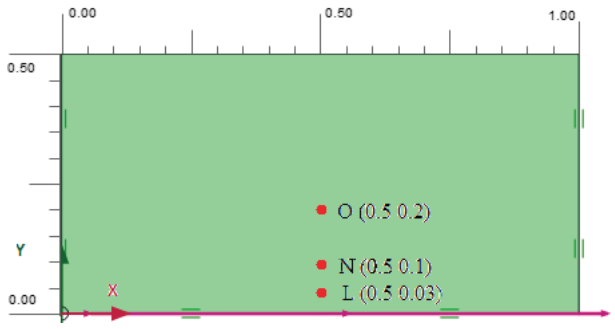

Figure 7 Centrifuge test model

The degree of saturation varies as S=99.0%, 97.0% and 94.0%. The initial stress may have a

great influence on the results and the initial stress used is due to the gravity action during all the tests. The boundary conditions are defined as: at the base of layer, the vertical displacement is blocked, and the input energy is sinusoidal horizontal acceleration with the amplitude $0.02m/s^2$ and the frequency 2HZ. At the lateral boundaries, the horizontal displacement is blocked. The model parameters are listed in Table 1.

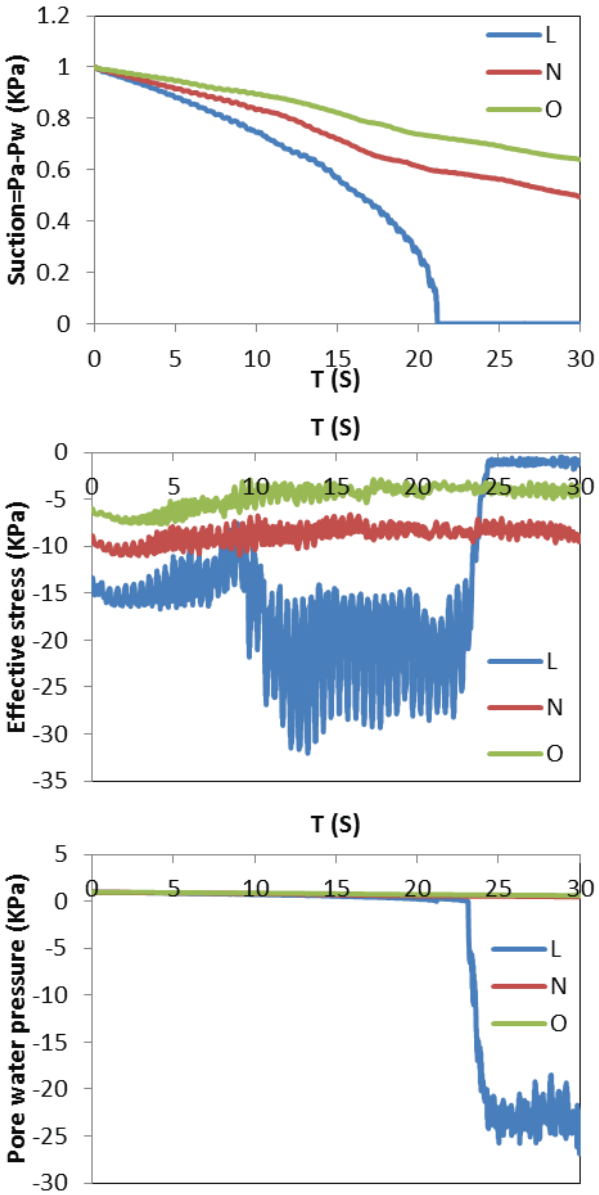

(a) Degree of saturation=94%

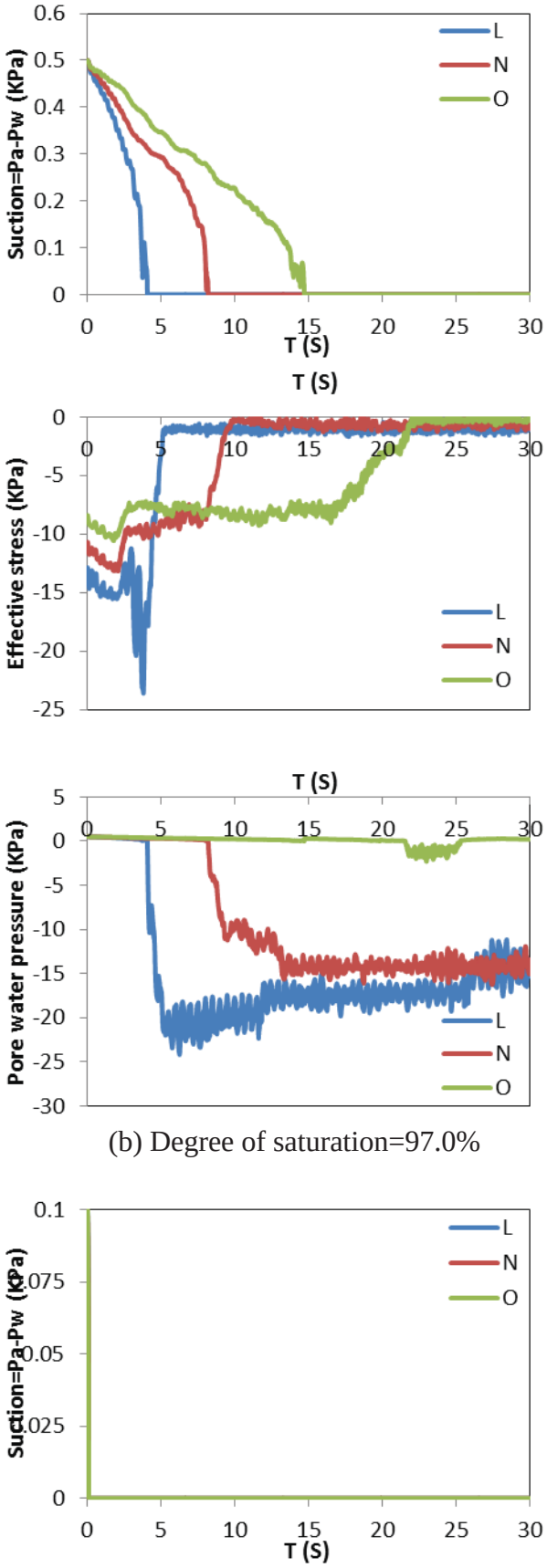

(b) Degree of saturation=97.0%

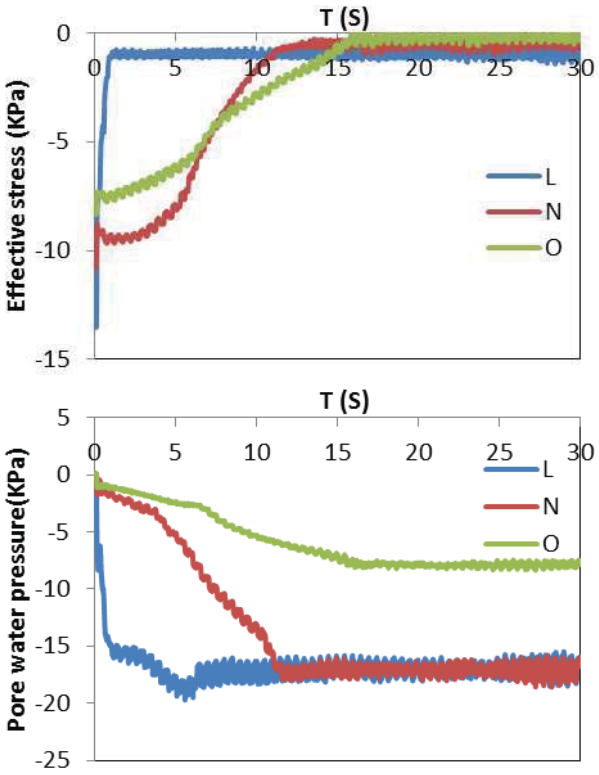

(c) Degree of saturation =99.0%

Figure 8 Evolution of suction, effective stress and pore water pressure of the column during centrifuge test

From Figure 8, we can see that variation of the degree of saturation has a significant influence on matric suction, effective stress and pore water pressure generation. When the matric suction decreases to 0, the degree of saturation turns 100%. From the figure, after full degree of saturation, the pore water pressure increases rapidly and the effective stress decreases to zero and fluidization occurs immediately. when the degree of saturation is less 94%, the onset of fluidization at point L could be delayed to 23s. With the increase in the initial degree of saturation, the onset of fluidization is easier to reach.

4.3 Shaking Table Test

Shaking table tests considering sway motion of ship with different amplitude, frequency and initial degree of saturation of cargos are investigated to predict time-domain characteristics during liquefaction based on UBC3D-PLM Model in commercial software PLAXIS. The geometry of layer is shown in Figure 9. Locations M, L, K, P, O and N are monitored through the test. The initial degree of saturation is supposed uniform and varies as 99%, 95.16% and 92.38%. The frequency varies as 0.25HZ, 0.35HZ and 0.5HZ. The amplitude varies as 0.02m, 0.04m and 0.06m. The boundary conditions are defined as: rigid box is used in the shaking table test; at the base of layer, the vertical displacement is blocked, and the input energy is sinusoidal horizontal displacement condition. At the lateral boundaries, the horizontal displacement is free and has the same motion with the base of box. The initial stress due to the gravity is shown in Figure 10.

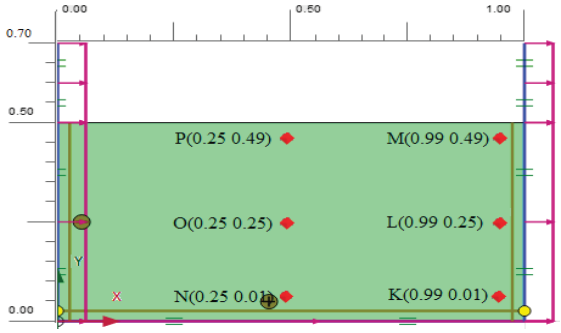

Figure 9 Shaking table test model

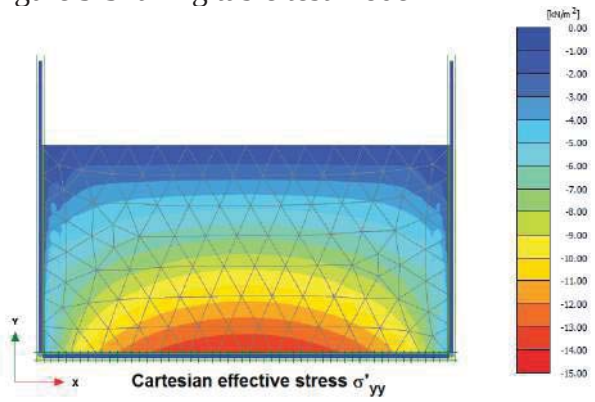

Figure 10 The effective stress contour after gravity action

From Figure 11 in the calculation of amplitude 0.04m, frequency 0.25HZ and degree of saturation 95.16%, we can see the soil near locations L, O and K is at the edge of liquefaction due to severe contraction. Locations M and P occurs dilation and N has a

high effective stress which are difficult to liquefy.

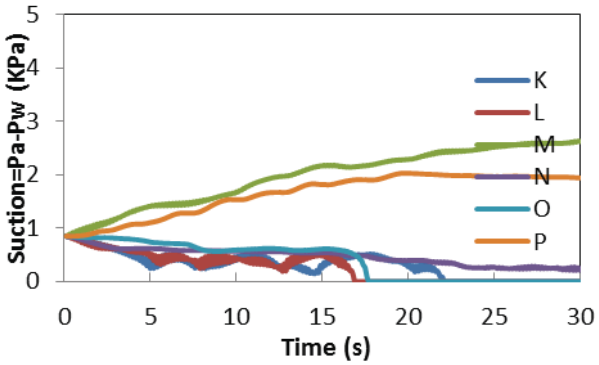

Figure 11 Evolution of suction during shaking table test

Emphasis could be put on the middle column of location O. From Figure 12, we can see that the higher degree of saturation, frequency and amplitude, the easier the onset of liquefaction. Due to the interaction between soil and rigid box, liquefaction of the soil displays more complicated from the curves of effective stress. From (a) to (c), varies of the amplitude and the frequency have small impact on liquefaction, where degree of saturation is just the reverse.

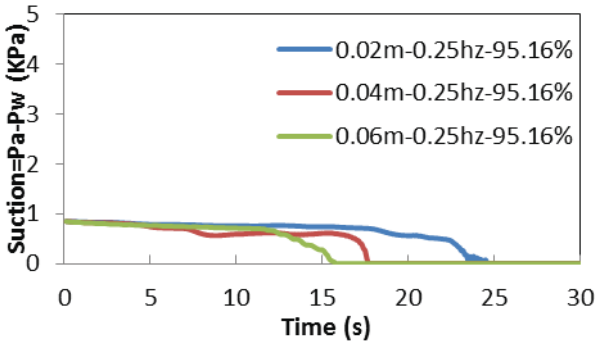

(a) Variation with amplitude

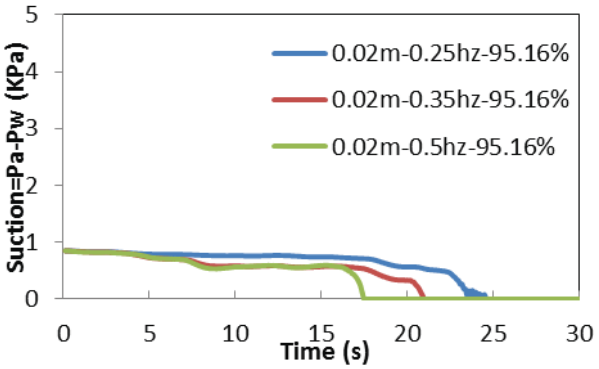

(b) Variation with frequency

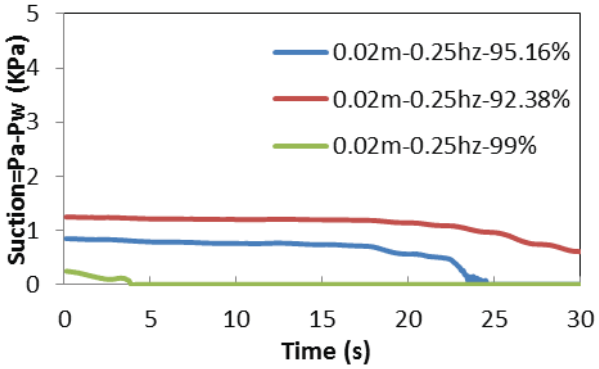

(c) Variation with degree of saturation

Figure 12 Evolution of suction at the middle of the column during shaking table test

5. CONCLUSIONS

Tests for monotonic loading and cyclic loading agree well with experimental data. Finite Element Method combined with UBC3D-PLM model could be used to simulate cargo liquefaction potential assessment. Accurate description for properties of cargos is the key factor to predict cargo liquefaction. In the tests, special properties of soil were used to model the cargo liquefaction.

With the higher degree of saturation, frequency and amplitude, cargo has smaller liquefaction resistance. Among these three factors, the only one we could control is the degree of saturation. Therefore, reducing the degree of saturation of cargos will enormously improve the stability of the cargo ship during transportation. Comparison with centrifuge test of the single vibration source on the base of column, soil liquefaction with shaking table is more complicated due to the interaction between soil and rigid box.

This method in the paper could be feasibly used as a reference and possibly support a suitable regulatory framework based on time domain analysis of cargo liquefaction.

6. REFERENCES

Beaty, M. and Byrne, P., 1998, "An Effective Stress Model for Predicting Liquefaction Behaviour of Sand", ASCE Geotechnical Earthquake Engineering and Soil Dynamics (geotechnical special publication III), Vol. 75(1), pp. 766-777.

Petalas, Alexandros. and Galavi, Vahid., 2013, "Plaxis Liquefaction Model UBC3D-PLM", PLAXIS Report.

Puebla, H., Byrne, M., and P.Philips, P., 1997, "Analysis of canlex liquefaction embankments prototype and centrifuge models", Canadian Geotechnical Journal, Vol. 34, pp. 641-651.

Sriskandakumar, S., 2004, "Cyclic loading response of fraser sand for validation of numerical models simulating centrifuge tests", Master's Thesis, The University of British Columbia, Department of Civil Engineering.

Tsegaye, A., 2011, "Plaxis Liquefaction Model", PLAXIS Report.

G.R. Martin, W.D.L. Finn, and H.B. Seed., 1975, "Fundamentals of liquefaction under cyclic loading", Journal of the Geotechnical Engineering Division, ASCE, 101.

This page is intentionally left blank

Coupled Granular Material and Vessel Motion in Regular Beam Seas

Christos C. Spandonidis & Kostas J. Spyrou

School of Naval Architecture and Marine Engineering
National Technical University of Athens

spandonx@mymail.ntua.gr, k.spyrou@central.ntua.gr

ABSTRACT

The behaviour of granular cargos under the effect of ship motions has not been sufficiently studied and international regulations on bulky cargos' loading and stowage, despite their updating and improvement, remain empirical. In the current work we investigate the interplay of granular material flow with a vessel's motion. The method of molecular dynamics is employed for modelling granular material dynamics, combined with a standard model of ship rolling for regular beam seas. Dry granular materials, spherical particle approximation and non-linear frictional forces are the key assumptions in modelling the cargo's movement. Characteristic simulation results including comparisons against cases of rigid cargo are presented.

Keywords: *granular material, molecular dynamics, ship cargo shift, ship motion*

1. INTRODUCTION

The problem of cargo shift is one of the most important ship safety issues. The recent upgrading of international regulations concerning the loading and stowage of ship cargos in bulky form is based, almost entirely, on empirical considerations (IMO, 2012). Approaches with potential to establish a solid scientific basis for this problem, using micro-scale modelling of cargo particles' motion and their interaction with the moving ship under wind/wave excitations, are still lacking. A possible reason is because such modelling is very demanding and it calls for an interdisciplinary approach, overcoming the often fragmented nature of scientific efforts. As type of problem, cargo shift could be classified along with sloshing; with clear methodological analogies prevalent in particular when, for the latter, a smooth particles hydrodynamics (SPH) modelling approach is applied. As well known, coupled ship motions affected by liquid sloshing have been extensively studied in the past, since high impacting pressures on tank walls constitute a perennial operation hazard. Faltinsen & Timokha (2009) provided an in depth presentation of analytical and numerical models for the coupled fluid motion in a tank. Moreover, in Monaghan (2005) was included a review of commonly applied SPH techniques. When it comes to granular cargos however, the authors could not identify any research effort of similar standing. A category of interesting works have dealt, for example, with the dynamics of sloshing cargos in silo vehicles (e.g. Fleissner et al 2009). But they have not presumed any link to the ship motion problem.

A key element in the coupled roll-granular cargo problem formulation is the feedback from ensemble of discontinuously moving particles to the ship's body. Such abrupt particle movement is a characteristic of container-body motions receiving external excitations predominantly of low frequency, with some higher frequencies appearing in the excitation from time to time. Such sudden

motion of the cargo constitutes the main contributing factor for a ship to acquire large roll bias, a state wherefrom capsize becomes imminent. In general, in terms of dynamics, the particles behave like oscillating masses interacting with each other and also, in unison, with the hold they are transported wherein. As a matter of fact, significant quantities of energy can be exchanged between the particles and the carrying body in a rather intermittent manner. These effects of interaction take the problem out of the convenient field of rigid body dynamics where ship stability studies are customarily performed.

In a line of research initiated at NTUA since 2011 to fill this gap, we have investigated already the excited motion of granular materials when the hold is subjected to series of prescribed oscillations. It was studied in particular the mechanism of formation of the cargo's angle of repose and associated phenomena (Spandonidis & Spyrou 2012 & 2013). In the current paper we take a step further, to study how the ship and the granular material behave, as a system, under the effect of wave excitation on the hull. Our intention is to understand how the coupling between material and ship works, in order to create a suitable tool for assessing the severity of such coupling effect. Although it is aimed to develop, in the longer run, a full ship motion model, at present we have restricted our study to regular beam sea waves in deep water, applied on a prism with rectangular cross section restrained to move only in roll.

2. ASPECTS OF THE BEHAVIOUR OF VIBRATED GRANULAR MATERIAL

As it is intended to combine a ship roll model with a suitable granular material flow model, in this part are reviewed briefly some aspects of their modelling and behaviour. General interest for the study of granular flows is inspired by their several industrial applications as well as by their complex rheological character. A granular material flow typically is comprised of a particulate solid in an interstitial fluid (usually air) subjected to a shearing force. In the most common granular material vibration experiments the considered materials are sand, grain or glass spheres (usually 0.5 – 3 mm diameter with standard deviation 5%). They are placed in a rectangular or cylindrical container mounted on a rigid base which is subjected to multi axial, sinusoidal oscillations. Even these simple systems can exhibit surprisingly complex behaviour that has yet to be fully explained. For example, the particle bed can behave as a "cloud" of particles with little or no structure; and in other cases the particle bed moves as a coherent mass. Depending on the frequency and amplitude of acceleration, vibrated granular materials can give rise to various phenomena such as compaction, convective flow, size segregation and "arching". Particle rearrangements induced by vibrations lead to lower shear strength and higher ability to flow. In the full fluidization regime, there are no permanent contacts between particles and the system behaves as a dissipative gas. When particle accelerations remain below the gravitational acceleration, the system keeps its static nature and the vibrational energy propagates through a rather compact network of inter-particle contacts. On the other hand, vibrations at high frequency and low amplitude lead to slow (logarithmic) decay of the pore space as a function of time. Several theories trying to explain this behaviour have been proposed (e.g. Laroche et al. 1989; Gallas et al. 1992; Corwin et al. 2005); yet none seem to be universally accepted. Another phenomenon that is observed for deep beds is the formation of surface waves. The waves travel from the lowest point of the heap up the slope to the peak but do not interfere with the continuous avalanche of particles associated with the convection pattern. The waves increase in length and decrease in height as they travel up the slope and eventually disappear at the peak. The onset of the travelling surface waves depends on the vibration- amplitude-to-particle-diameter ratio. Standing surface waves form at half the excitation frequency for certain

ranges of the excitation amplitude and frequency, following a mechanism similar to the Faraday instability (Douady & Fauve 1988; Miles & Henderson 1990).

3. EQUATION OF MOTION

The analysis is performed in model scale and a small rectangular hold is considered. It is placed inside a box barge that is allowed to be rotated in roll only, around a specific axis (1-DOF approach). That is, the roll centre is considered fixed (point *P* in Figure 1). Each particle's motion is monitored from another coordinate system, whose origin is placed at the hold's bottom left corner (*ZOY*). This coordinate system remains always horizontal (i.e. it does not follow vessel's rotation). System *yKz* is also placed at the bottom left corner; but it follows the motion of the hold in such a manner that its *z*-axis is always perpendicular to the bottom. The reference system *aPb* is assumed to be at the centre of rotation of the vessel (which in the current study coincides with the middle point of the ideal flat free surface). This coordinate system follows vessel's rotation.

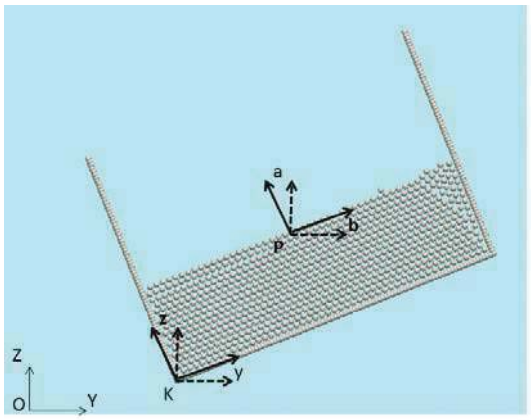

Figure 1 The three different coordinate systems (solid lines) and their irrotational equivalents (dashed lines) are being depicted.

In Figure 1 systems *yKz* and *aPb* are depicted with solid lines. In what follows, only the dynamics on the xy plane is under investigation due to the 2D nature of the developed granular material algorithm. Thus, the barge is assumed to be long enough (2 m) compared to her height (0.3 m) and beam (0.34 m). These dimensions should facilitate direct comparison with the results of experiments in the future.

Two different problems need to be tackled simultaneously: The wave induced ship motion and the motion of the granules inside the hold. On the basis of the so called "molecular dynamics" method we predict the trajectory of each individual particle, assumed to interact with all its neighbouring particles through non-linear elastic and frictional forces. "Molecular dynamics" is the most important among the simulation methods that have been used for granular flows. It involves solution of Newton's equation of motion for every particle. Normally to the line of contact of particle collisions we have considered nonlinear elastic and frictional forces; while transversely we have assumed acting a purely frictional force:

$$F_{nor} = -k_n \xi^{3/2} - \gamma_n \xi^{1/2} \dot{\xi}$$
$$F_{\tan} = -\min\left(\left|\gamma_s u_s\right|, \left|\mu F_n\right|\right) \cdot sign\left(u_s\right) \quad (1)$$

γ_n and γ_s are normal and shear damping constants respectively; k_n is non-linear stiffness coefficient, u_s is the shear velocity component and μ stands for the dynamic friction coefficient (see Spandonidis & Spyrou 2012 for details). Collision forces are computed for each couple and at every time step. From them, the forces that act on the side plates of the hold are obtained.

Newton's equation for ship roll motion is also solved at each time step, with loads considered due to added moment of inertia, hydrodynamic damping, restoring, "Froude-Krylov" moment and the impacting moment due to possible particles' impact with hold's side walls. Vessel's roll motion can be described then by Eq. (2) which is solved in time, coupled with the nonlinear molecular dynamics model of the granular material:

$$(I+\delta I)\ddot{\varphi}+B_1\dot{\varphi}+B_2\dot{\varphi}\left|\dot{\varphi}\right|+M_R = \\ = mg\,GM\,r\,Ak\cos(\omega t)+M_I \quad (2)$$

φ is the roll angle, I and δI are respectively the roll moment of inertial and the added moment of inertia, B_1 and B_2 are the linear and the quadratic roll damping coefficients. δI and B_1 were calculated with a linear BEM code while B_2 was taken as frequency independent. M_R is the restoring moment calculated as the sum of three moments (M_B due to buoyancy, M_S due to ship's weight and M_C due to cargo's weight) calculated around the fixed axis of rotation:

$$M_R = M_B + M_S + M_C \quad (3)$$

Moreover, the impact moment M_I generated by the particles' contact with nonzero relative velocity with hold's walls is calculated.

In order to verify our results we performed reliability tests as proposed by Haile (1997). Different operating systems (Windows 8, Windows XP, Linux RedHat 5.1), hardware configuration and computational software (Microsoft Visual C++, Mathematica, Matlab) were used, in order to calculate the systemic error. Also, several repetitions were performed for each numerical experiment in order to check conservation principles and monitor the statistical error. The algorithm can provide accurate calculations with a statistical and systemic error whose deviation does not exceed 2%. Validation of the coupled motion results could not be done at this stage due to lack of suitable experimental measurements and we relied on separate validation of the two sub-algorithms. For the validation of the molecular dynamics algorithm see Spandonidis & Spyrou (2013). Concerning the ship motion equation, results for "empty hold" and for "hold with solid (frozen) cargo" were compared against similar experimental results obtained by Rogenbake & Faltinsen (2003) and by Murashige & Aihara (1998), indicating that the algorithm performs very well with a standard deviation less than 1%.

4. CASE STUDY

We assumed the hold filled with cellulose acetate particles of diameter 0.3 cm such that the particle parameters (friction, stiffness etc) coincide with these experimentally measured by Forester et al (1994). The draft with the material inside is (in initial position) 0.11 m. The material height-to- width-ratio is 0.36 which corresponds certainly to a "finite" material depth case. The vessel was free to move only in roll, with an external excitation owed to waves that were fixed in amplitude and frequency. Granules were considered as smooth spheres with diameters that could be either fixed or varied in some range and they could be translated (horizontally-vertically) or rotated. At this specific stage we assumed dry granules and the weight of the cargo equalled that of the vessel itself (even though this would not be the real case e.g. for a bulk-carrier). Several tests were performed before beginning the actual numerical experiments, in order to identify the critical parameters. At first step, the material was left to balance in calm water. In this way the draught of the barge and its initial roll angle were calculated for several slightly different initial free surface configurations. The eigenperiod of the barge lies within acceptable, for real case scenario, limits. In addition, following the tilting table method described in the International Maritime Solid Bulk Cargoes code -IMSBC (IMO 2012), we determined the critical angles leading to cargo shift. In Figure 2 is depicted the horizontal displacement of the centre of mass versus the tilting angle, for different tilting rates. As indicated, when relatively slow rates are applied (smaller than 1 rad/s) two angles with values close to 25 and 42 deg are identified.

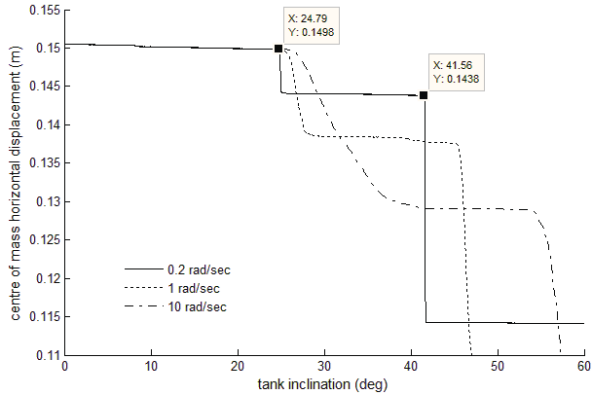

Figure 2 Center of mass displacements versus vessel inclination (the illustration is based on the zKy coordinate system).

The former is the angle where heap formation occurs; while the latter should be considered as the true angle of repose (Spandonidis & Spyrou, 2013). Moreover, it is shown that when a large enough tilting ratio is used, the cargo behaves in a slightly different way. In that case, the flow of the cargo is larger after the first critical value is reached.

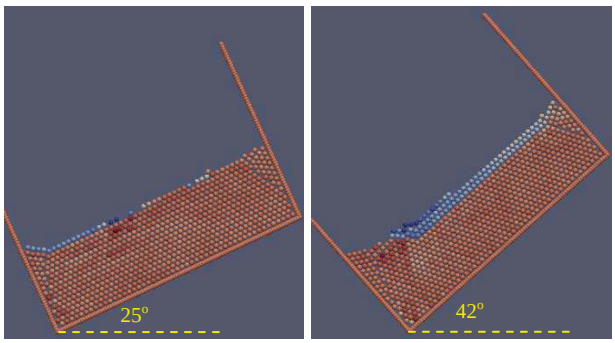

Figure 3 Time shots of inclined vessel when roll angle has a value of 25° (left) and 42° (right).

In Figure 3 is shown cargo's state inside the hold at specific time instants when critical angles are reached. Red colour is used when the particle has kinetic energy close to 0 and blue when it has clearly nonzero kinetic energy. In this way the percentage of material involved in cargo shift can be illustrated. Our main goal was the identification of critical parameters affecting system's dynamic response.

Two kinds of numerical experiments were performed. The first was basically a reference case and the vessel was loaded with *solid cargo*; that is cargo with the same weight and mass centre with the granular but without the ability to move. It was tested in several wave frequencies and amplitudes. Analysis of these results provided a good feeling of the most significant frequency region for further investigation. The second series involved tests with actual granular cargo. The wave frequency and amplitude region of interest were 2.3-6.5 rad/s and 0.005-0.025 m, respectively.

In Figure 4 are shown some examples of comparison of behaviour, for four different frequency values and wave amplitude fixed at 0.01m. The key findings are as follows:

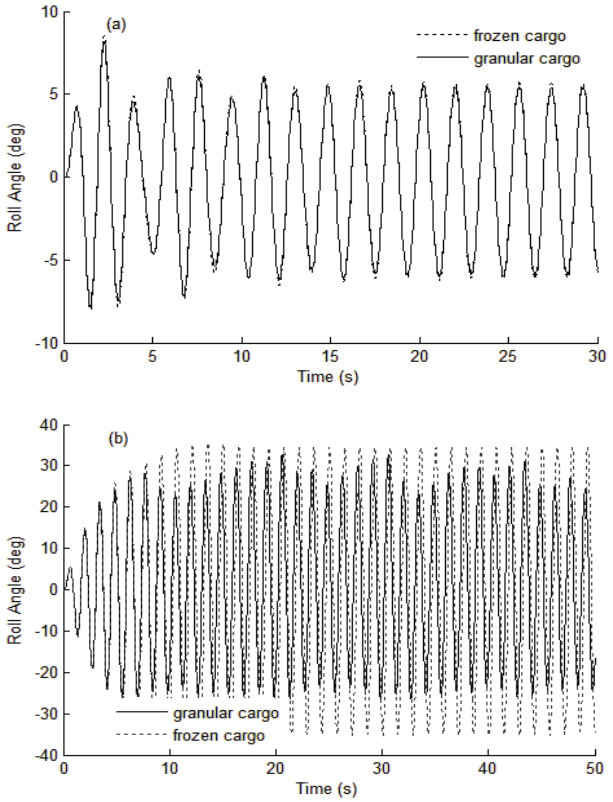

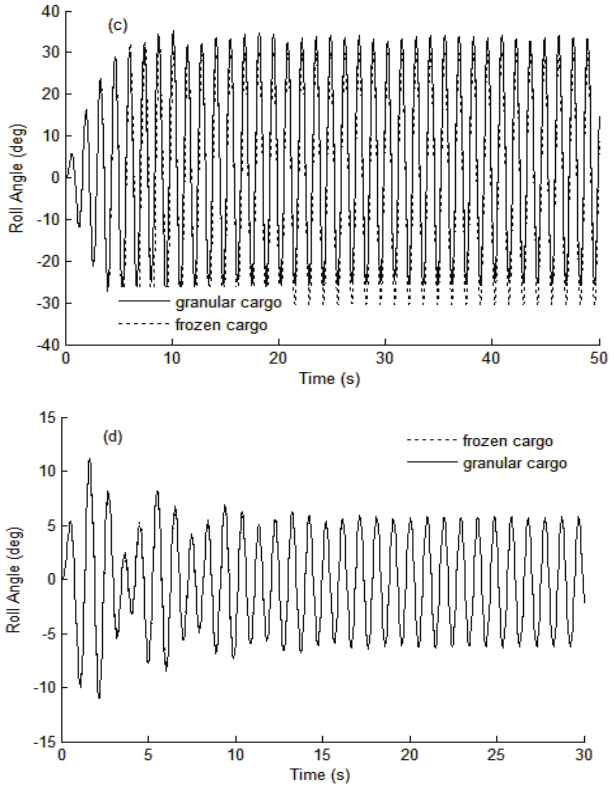

Figure 4 Comparison of response of frozen and granular cargo. The excitation amplitude s fixed at 0.01m and the frequency varies: a) 3.5 rad/s, b) 4.4 rad/s, c) 4.7 rad/s and d) 6.5rad/s.

a) For wave frequency values below 3.5 or above 6 rad/s, barge's response is limited (Fig. 4 (a) and (d)). After a short transient, she reaches a max roll angle less than 5 deg. The behaviour of the barge does not depend on whether she is frozen or with movable cargo (i.e. the granular material does not perform any substantial motion).

b) For wave frequency between 3.5 and 6 rad/s, the barge, in either condition, enters a resonant region. As shown in Figure 4b, the peak response amplitude for the case of frozen cargo appears at frequency 4.4 rad/s and a maximum roll angle about 36 deg is reached. The "unfrozen" system shows smaller response, mainly apparent after a frequency about 4 rad/s. The peak roll angle reached is less than 30 deg. The lower response is because the granular material reaches the first critical angle of heap formation which sets it in motion. As the phase of cargo's movement opposes that of the vessel, the overall motion becomes smaller. Calculation of moments indicates that, the moment due to cargo's mass centre, and not the impact moment, is the primary cause of this effect.

c) Further observation of Figure 4b produces two more, secondary, findings. Firstly, the motion of the vessel with the granular cargo has become asymmetrical. Local movement of cargo occurring around the one corner of the free surface, leads to lower absolute roll peak when the hold rotates clockwise. Secondly, for certain values of wave frequency, the steady-state is characterized by more than one frequency. As confirmed from Figs. 4b and 4d where the simulation was run for 50 s, this phenomenon is not transient but it is true long-term response.

d) Inside the resonant region and after a critical value of 4.7 rad/s the two systems present almost identical mean responses. Despite though their similar behaviour, the initial movement of the granular cargo during the transient stage leads to larger absolute roll amplitude. For the case of 4.7 rad/s (Fig. 4c) both systems oscillate with mean roll amplitude of 30 deg. But for the granular cargo, an almost 2 degree dynamic roll bias is incurred, generating a higher absolute roll peak. These findings are summarized in Fig.5.

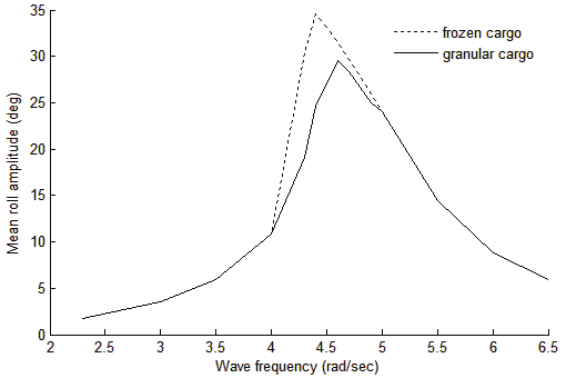

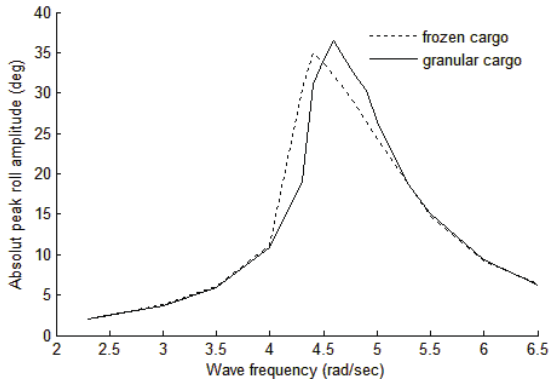

Figure 5 Mean roll amplitude (up) and absolute roll peak (down), for 0.01m excitation.

For wave amplitudes between 0.005 and 0.15 m, our simulations yielded that the behaviour remains qualitatively similar to that obtained for 0.01 m excitation.

In Figure 6 appear comparisons at the two ends of the investigated region of wave amplitude [0.005 m (up) and 0.015 m (down) - wave frequency, respectively, 4.5 and 4.3 rad/s]. Notably, for wave amplitude 0.015 m, the granular cargo case is associated with smaller response but with a "clear" second frequency existing in the steady state due to material's displacement.

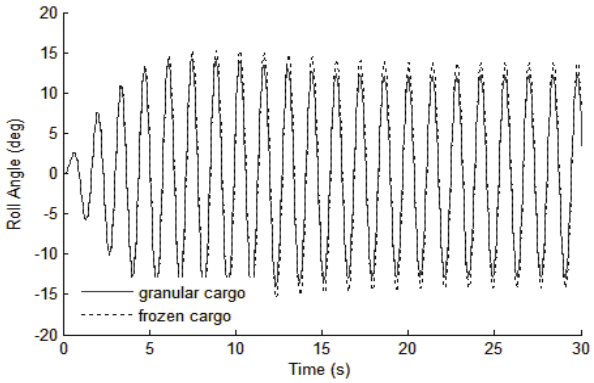

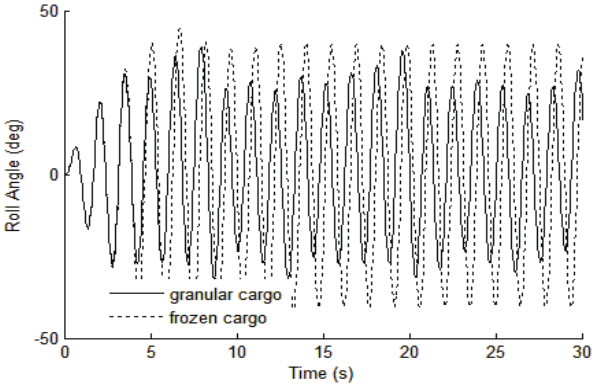

Figure 6 Comparison of response of solid and granular cargo: (up) excitation amplitude 0.005m and frequency 4.5 rad/s; (down) excitation 0.015m and frequency 4.3 rad/s.

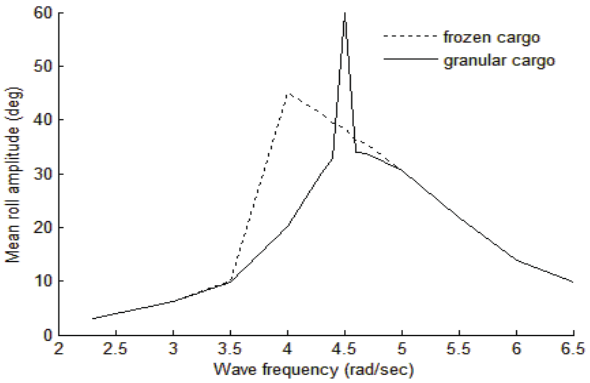

Figure 7 Mean roll amplitude for wave amplitude 0.017 m and frequency 4.3 rad/s

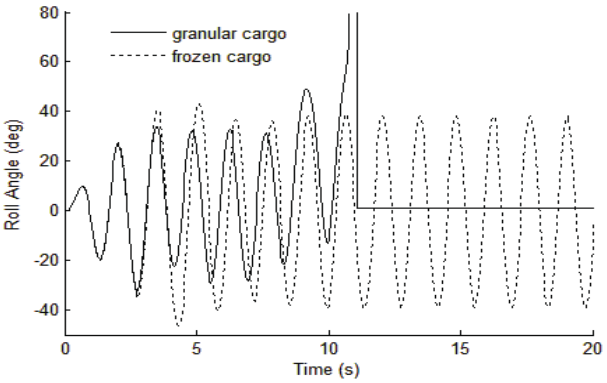

Figure 8 Comparison between frozen and granular cargo for wave amplitude 0.0017m and frequency 4.5 rad/s.

Further increase of the excitation leads however to a substantially different behaviour (Figure 7): for wave amplitude 0.017 m and frequency 4.5 deg/s, the material inside the

hold moves in such a way that the barge cannot return towards the upright position and capsize is finally realized.

To investigate deeper this behaviour we considered the first seconds of motion. Figure 8 depicts in a comparative manner the 20 first seconds for the two systems. At about the 10th second, the barge with the granular cargo capsized. Whilst she initially behaved in a similar to the 0.01m wave amplitude case (that is, smaller mean roll angle and quasi-steady state response), suddenly a large peak value appeared (almost 45 deg). This is above the material's second critical angle associated with its angle of repose. In the ensuing cycle the roll angle grows further and capsize finally occurs. Visual inspection of the cargo inside the hold indicates that, that due to high acceleration, significant amount of material is displaced during the two roll cycles before capsize (Figure 9). Wave amplitudes larger than 0.02m generate qualitatively similar results for material's behaviour.

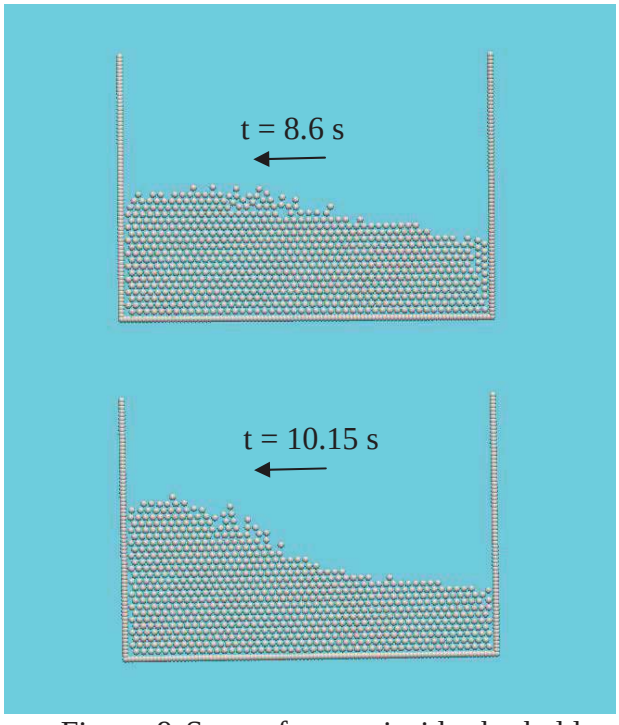

Figure 9 State of cargo inside the hold at two successive passages of the barge from the upright position: (up) seventh roll cycle; (down) 8th roll cycle in which capsize occurs. The arrow indicates the direction of motion (anti-clockwise).

5. CONCLUDING REMARKS

A step towards a systematic investigation of the coupled granular material-and-vessel-motion in regular beam seas, based on numerical procedures, was presented. The vessel was allowed to move only in roll direction performing thus a restricted 1 DOF motion. Several values of wave amplitude and frequency were applied on a scaled container containing spherically shaped particles of granular material in order to capture the response of the system. Special attention was given in the comparison of the results against corresponding cases where the cargo was treated as solid ("frozen").

These results indicated that, although the same resonant region occurs for both systems, in the case of granular cargo and for wave amplitudes below a certain limit, the motion of the system is smaller. This leads to a system that is even more stable that its frozen counterpart, even though it appears to have some difficulty in reaching steady state. For higher wave amplitudes a new region appears where the vessel due to her cargo's movement, shows larger response and in some cases it capsizes. An effort to analyse this behaviour revealed that, this is related with a shift of the roll resonance peak value.

A logical next step in our research would be the experimental examination of these results. In the meantime, several different numerical experiments are executed in a systematic way. Specifically, different material-height-to-hold-width ratios, constant wave steepness, more than one frequency wave packets, different material parameters and different vessel shapes are under study. Furthermore, dynamical analysis tools are being considered for capturing more rigorously vessel dynamics as influenced by the granular material's movement. It is remarked that, a further investigation based on a 3 DOF coupled

motion is currently under verification /validation. Early results indicate some significant effects for higher frequencies.

6. ACKNOWLEDGMENTS

The present work was supported by the Greek General Secretariat for Research and Technology under the General Programme ARISTEIA (EXCELENCE) I, with contract reference number GSRT-252.

7. REFERENCES

Corwin E.I., Jaeger H.M., Nagel S.R., 2005. "Structural signature of jamming in granular media", Nature, 435: 1075-1078.

Douady S., Fauve S., 1988. "Pattern selection in Faraday instability", Europhysics Letters, 6: 221-226.

Faltinsen O.M., Timokha A.N., 2009. "Sloshing", New York: Cambridge University Press.

Fleissner F., Alessandro V., Schiehlen Wand Eberhard P., 2009. "Sloshing cargo in silo vehicles", Journal of Mechanical Science and Technology 23: 968-973.

Foerster S. F, Louge M.Y, Chang H, Allia K., 1994, "Measurements of the collision properties of small spheres", Phys. Fluids 6: l108.

Gallas J. A. C., Herrmann H. J., Sokolowski, S., 1992. "Convection Cells in Vibrating Granular Media", Physics Review Letters, 69:1371-1374.

International Maritime Organization (IMO), 2012. "Solid Bulk Cargoes Code [IMSB Code 268(85)]", IMO publishing, ISBN: 978-92-801-1535-2.

Laroche C., Douady S., Fauve S., 1989. "Convective flow of granular masses under vertical vibrations", Journal de Phyique France, 50: 699-706.

Miles J., Henderson D., 1990. "Parametrically forced surface waves", Annual Review of Fluid Mechanics, 22: 143-165.

Monaghan J.J., 2005. "Smoothed Particle Hydrodynamics", Reports on Progress in Physics, 68: 1703-1759.

Murashige S., Aihara K., 1998. "Coexistence of periodic roll motion and chaotic one in a forced flooded ship", International Journal of Bifurcation and Chaos 8:619-626

Rognebakke O.F, Faltinsen O.M., 2003, "Coupling of sloshing and ship motions", Journal of Ship Research 47, no 3, 208-221.

Spandonidis C., Spyrou K. J., 2013. "Micro-scale modelling of excited granular ship cargos: A numerical approach", Ocean Engineering 74: 22–36.

Spandonidis C., Spyrou J., 2012. "Use of granular material dynamics simulation for the study of cargo shift of ships", Proceedings of 11th International Conference on the Stability of Ships and Ocean Vehicles, Athens, pp. 497-507.

This page is intentionally left blank

Session 13.3 – EXTREME BEHAVIOUR

Numerical Simulation of Ship Parametric Roll Motion in Regular Waves Using Consistent Strip Theory in Time Domain

Validation of Statistical Extrapolation Methods for Large Motion Prediction

Coupled Hydro – Aero – Elastic Analysis of a Multi – Purpose Floating Structure for Offshore Wind and Wave Energy Sources Exploitation

This page is intentionally left blank

Numerical Simulation of Ship Parametric Roll Motion in Regular Waves Using Consistent Strip Theory in Time Domain

Shan Ma, *College of Shipbuilding Engineering, Harbin Engineering University*,
mashan01@hrbeu.edu.cn
Rui Wang, *College of Shipbuilding Engineering, Harbin Engineering University*,
wangrui10653@163.com
Wenyang Duan, *College of Shipbuilding Engineering, Harbin Engineering University*,
duanwenyang@hrbeu.edu.cn
Jie Zhang, *College of Shipbuilding Engineering, Harbin Engineering University*,
pressme@163.com

ABSTRACT

In this paper, a numerical method is proposed to simulate the parametric rolling of ship in regular head seas. The numerical method aims at solving the coupled 3 degrees of freedom heave, pitch and roll together for better modelling of this nonlinear motions. The method is developed in time domain based on strip theory. The concept of impulse response function method is used to take into account the memory effect of fluid due to ship motion generated wave. Via theoretical analysis, a consistent way of estimating the impulse response function using strip theory is presented.

In order to model the nonlinear time variation of restoring force coefficients in wave, the Froude-Krylov forces (incident wave forces) and hydrostatic force are evaluated on the instantaneously wetted surface of the ship. Based on the developed method, the parametrically excited roll motions of C11 containership is simulated and the numerical results are compared with model tests.

Keywords: *Parametric rolling of ship, numerical model, nonlinear ship motions, impulse response function method*

1. INTRODUCTION

In a seaway the parametrically excited roll motion of a ship unexpectedly generated in either following or head sea conditions is quite a dangerous phenomenon due to its occurrence with large rolling amplitudes. Therefore, the quantitative prediction of the parametric roll phenomenon are absolutely essential to ensure the safety of life and property on ships. Authoritative organizations of the maritime industry correspondingly published prediction guidelines (ABS, 2004, ITTC, 2005). The vulnerability criteria on parametric rolling are also under development by the International Maritime Organization (IMO) in the second intact stability criteria.

Parametric rolling in head seas as one of transverse stability problems resulting from time-varying changes in the underwater hull geometry is a nonlinear phenomenon with dynamic pitch and heave motions, which make it difficult to accurately predict parametric rolling in head seas. Before several accidents with ships operating in head seas (France et al., 2003, Hua et al.,2006), parametric rolling is largely handled in the cases of following waves (Kerwin, 1955) or beam waves (Blocki, 1980). In case of following waves the encounter frequency is much lower than the natural frequency of heave and pitch, so that coupling with heave and pitch is not important. As for head seas, however, prediction of parametric rolling is not so easy because parametric roll in head seas is more likely influenced by and coupled with heave and pitch motions, which are typically more pronounced in head waves (Shin et al., 2004). Effect of dynamic heave and pitch motions on parametric rolling was investigated so far by many researchers and is well established that restoring arm variation in head waves depends on dynamic heave and pitch (Taguchi et al., 2006). Nevertheless, the effect of coupling from roll into heave and pitch on parametric rolling in regular head seas is not significant in case the wavelength is equal to the ship length (J. Lu et al., 2012). Naoya Umeda et al. (2003) confirmed that a mathematical model with a roll-restoring moment in waves calculated with the Froude-Krylov assumption could considerably overestimated the danger of capsizing associated with parametric rolling. Neves and Rodriguez (2005) used a two-dimensional analysis for a set of coupled heave, pitch and roll equations of motion with 2nd and 3rd order non-linearities describing the restoring actions. Ahmed et al. (2006, 2008) used a system with 3 degrees of freedom, with the coupled heave and pitch motions providing input to the parametric excitation simulated using a one degree of freedom non-linear roll equation of motion. Levadou and van't Veer (2006) used coupled non-linear equations of motion in the time domain with 3(heave, roll and pitch) and 5 (sway, heave, roll, pitch and yaw) DOF, where nonlinear excitations are evaluated considering the actual submerged surface whereas diffraction forces are considered linear. Hydrodynamics are calculated in the frequency domain and are incorporated in the time domain by adopting the impulse response functions method. More recently, Ahmed et al. (2010) employed a system with 4 DOF (sway, heave, roll, pitch) to investigate parametric rolling in regular waves. The non-linear incident wave and hydrostatic restoring forces/moments are incorporated considering the instantaneous wetted surface while the hydrodynamic forces and moments, including diffraction, are expressed in terms of convolution integrals based on the mean wetted hull surface. Kim et al. (2010) and Park et al. (2013) also used impulse response function method (IRFM) to predict the parametric roll. Ribeiro e Silva and Guedes Soares (2013) described a time-domain non-linear theory model of ship's motions in 6 DOF, with the time variations of the restoring force calculated over the instantaneous submerged hull and hydrodynamic effects based on a potential flow strip theory using Frank's close fit method.

Analysis of parametric roll of container ships in regular head waves has been studied extensively. However, the ships do not encounter regular waves in the ocean. So, it is necessary to study how important parametric roll is in irregular seas. The work conducted by Ribeiro e Silva et al.(2003, 2005, 2013) and Bulian et al.(2006) are examples of investigations in this field. Nonetheless, numerical simulations and experimental measurements in regular waves are a useful way of observing and understanding the physics of the parametric roll phenomenon as well as validating numerical methods. According to past research, it is necessary for parametric roll to occur that four certain conditions need to be satisfied, namely, an encounter frequency equal or close to twice the natural frequency of roll, a wave length of the same order as the ship length, a wave height exceeding a critical level and finally, roll damping to be below a threshold value (France

et al., 2003). As well known, non-linear damping tends to increase with roll velocity, thus, it will eventually exceed the damping threshold leading to stabilization of the roll motion and reaching a steady roll amplitude. It is worth noting the fact that rationally accounting for non-potential roll damping is of substantial importance for an accurate simulation of parametric rolling.

When the impulse response function method (IRFM) is used, the coefficients and the IRF in Cummins's equation (Cummins, 1962) must be estimated in advance. Liapis et al. (1986) and King (1987) established the complete time domain framework of ship motion with forward speed by 3D time domain potential flow theory in which the coefficients are directly calculated by 3D boundary element method in time domain. While in time domain strip theory using IRFM, the impulse response function is often transformed from frequency domain hydrodynamic coefficients without any extra modification. This transformation seems already being a common practice. Although during the transformation, there are some different methods in the way to estimate the hydrodynamic damping and radiation restoring forces. It looks that people seldom noticed that there is some theoretical inconsistency during the transformation. The hydrodynamic radiation and damping coefficients in Cummins's equation is theoretically derived using the conception of strip theory by us and some of the modification to restoring radiation coefficients is proposed to ensure the consistent transformation.

In this work, the effect of parametric resonance on a containership sailing in head seas is investigated using a partly non-linear numerical model with 3 DOF (heave, roll and pitch). In this model, the incident wave and hydrostatic restoring forces/moments are assumed non-linear and are evaluated at every time step considering the instantaneous submerged surface while hydrodynamic forces and moments are assumed linear. Radiation forces and moments are expressed in terms of convolution integrals and diffraction forces and moments are calculated in the frequency domain by strip method and then incorporated in the time domain. The requisite impulse response functions are obtained from Fourier transforms performed on hydrodynamic coefficients evaluated from STF method (Salvesen et al., 1970) in frequency domain based on the mean wetted surface. Comparisons between numerical and experimental results demonstrate the usefulness and accuracy as well as some limitations of the method proposed.

2. MATHEMATICAL MODEL OF PARAMETRIC ROLLING SHIP MOTIONS IN WAVES

2.1 Ship Motion Equations

A right-handed inertial coordinate system fixed with respect to the mean position of the ship oxyz is established with z in the vertical upward direction and passing through the centre of gravity of the ship and x directed to the bow. The origin is in the plane of the undisturbed free surface. This coordinate moves with the ship but remains unaffected by its parasitic motions. Parallel with oxyz, the inertial coordinate system cx1y1z1 with origin at center of gravity of the ship can also be formed. In order to express the large amplitude rolling motions, the right-handed body-fixed coordinate system cxbybzb, with origin c at the center of mass of the ship is also formed.

The unrestrained 3 DOF rigid body motions of a vessel with or without advancing speed are considered. The ship motions in time domain is formed as followed:

$$(M+\mu_{33})\ddot{\eta}_3+b_{33}\dot{\eta}_3+\int_0^t K_{33}(t-\tau)\dot{\eta}_3(\tau)d\tau+(c_{33}+C_{33})\eta_3$$
$$+\mu_{35}\ddot{\eta}_5+b_{35}\dot{\eta}_5+\int_0^t K_{35}(t-\tau)\dot{\eta}_5(\tau)d\tau+c_{35}\eta_5$$
$$=F_3^I+F_3^S+F_3^D-Mg$$

$$(I_{44}+\mu_{44})\ddot{\eta}_4+b_{44}\dot{\eta}_4+\int_0^t K_{44}(t-\tau)\dot{\eta}_4(\tau)d\tau+c_{44}\eta_4 = F_4^I+F_4^S+F_4^D$$

$$\mu_{53}\ddot{\eta}_3+b_{53}\dot{\eta}_3+\int_0^t K_{53}(t-\tau)\dot{\eta}_3(\tau)d\tau+c_{53}\eta_3 + (I_{55}+\mu_{55})\ddot{\eta}_5+b_{55}\dot{\eta}_5+\int_0^t K_{55}(t-\tau)\dot{\eta}_5(\tau)d\tau + c_{55}\eta_5 = F_5^I+F_5^S+F_5^D \quad (1)$$

Where η_3 , η_4 , η_5 are heave, roll and pitch motion respectively where η_3 is given along cz_1, η_4 , η_5 is given along $cx_by_bz_b$ coordinate system. *M, I_{44}, I_{55}* are the mass, inertial moment of the ship along the cx_b and cy_b axis. The radiation forces/moments are expressed by convolution integrals, with accounted for the memory effect. Diffraction forces/moments F_3^D , F_4^D , F_5^D are obtained from strip theory. Both radiation and diffraction forces/moments are represented on $cx_1y_1z_1$ coordinate system.

The incident wave excitations F_3^I , F_4^I , F_5^I and restoring forces/moments F_3^S , F_4^S , F_5^S are referenced to another right-handed body-fixed coordinate system $cx_by_bz_b$, with origin c at the center of mass of the ship.

2.2 Radiation Forces and Moments Modelling

According to Cummins's theory, the added mass and damping coefficients is referenced to an equilibrium axis system, Cummins (1962) showed that the linear radiation forces in time domain can be written as followed:

$$F_{jk}(t) = -\mu_{jk}\ddot{\eta}_k(t) - b_{jk}\dot{\eta}_k - c_{jk}\eta_k(t) - \int_0^t K_{jk}(t-\tau)\dot{\eta}_k(\tau)d\tau \quad (2)$$

where, $\eta_k(t)$ represents the oscillation motion in k -mode and the overdot represents the derivative with respect to time. K_{jk} is the impulse response function (IRF) representing the memory effect of fluid. μ_{jk} and b_{jk} are the asymptotic values of the radiation coefficients at high frequency, and c_{jk} is the radiation restoring force coefficient. The IRF K_{jk} can be directly related to the frequency-domain hydrodynamic coefficient:

$$K_{jk}(\tau) = \frac{2}{\pi}\int_0^\infty (B_{jk}(\omega)-b_{jk})\cos\omega\tau d\omega \quad (3a)$$

$$K_{jk}(\tau) = \frac{2}{\pi}\int_0^\infty \left(\omega\mu_{jk}-\omega A_{jk}(\omega)-\frac{1}{\omega}c_{jk}\right)\sin\omega\tau d\omega \quad (3b)$$

where, ω is the encounter frequency of ship in waves.

By Fourier transformation, Eq. (3) can be written as follows:

$$A_{jk} = \mu_{jk} - \frac{1}{\omega^2}c_{jk} - \frac{1}{\omega}\int_0^\infty K_{jk}(\tau)\sin\omega\tau d\tau \quad (4a)$$

$$B_{jk} = b_{jk} + \int_0^\infty K_{jk}(\tau)\cos\omega\tau d\tau \quad (4b)$$

Eq.3 means that the hydrodynamic impulse response function K_{jk} can be expressed using frequency domain hydrodynamic coefficients without solving the problem directly in time domain. Presently strip theory is used to calculate the hydrodynamic coefficients and estimate IRF. However it's known that this theory is not a fully strict theory to solve the hydrodynamics of ship with forward speed in frequency domain. While Eq. 2 is established using strict 3D hydrodynamic theory in time domain. Because of the discrepant mathematical model described in both domains, the inconsistency may occur if the hydrodynamic coefficients obtained by STF are directly used to calculate the IRF based on Eq. (3a) or Eq. (3b).

With the theoretical analysis followed, the inconsistency can be shown and some modifications are derived.

In the following procedure, the pitch added mass A_{55} and damping B_{55} are taken as example to show the modification. According to STF method, the hydrodynamic coefficients of the ship can be written as follows:

$$A_{55}(\omega) = A_{55}^0(\omega) + \frac{u^2}{\omega^2} A_{33}^0 - \frac{u}{\omega^2} x_A^2 b_{33}^A(\omega) + \frac{u^2}{\omega^2} x_A a_{33}^A(\omega) \tag{5a}$$

$$B_{55}(\omega) = B_{55}^0(\omega) + \frac{u^2}{\omega^2} B_{33}^0 + u x_A^2 a_{33}^A(\omega) + \frac{u^2}{\omega^2} x_A b_{33}^A(\omega) \tag{5b}$$

where, A_{55}^0 and B_{55}^0 represent added mass and damping coefficients at zero speed, a_{33}^A and b_{33}^A are stern sectional added mass and damping coefficient, respectively. x_A is the longitudinal distance between stern section and the gravity center of the ship. According to (3a) and (4a):

$$K_{55}(\tau) = \frac{2}{\pi}\int_0^\infty (B_{55}(\omega) - b_{55})\cos\omega\tau d\omega \tag{6a}$$

$$\mathrm{A}_{55} = \mu_{55} - \frac{1}{\omega^2} c_{55} - \frac{1}{\omega}\int_0^\infty K_{55}(\tau)\sin\omega\tau d\tau \tag{6b}$$

Substituting (6a) into the third term in the right hand side of (6b) leads to the following equation which is not identical to equation (5a) excluding the additional modification term $c_{55\,plus}$.

$$\mathrm{A}_{55} = \mu_{55} - \frac{1}{\omega^2}(c_{55} + c_{55\,plus}) - \frac{1}{\omega}\int_0^\infty K_{55}(\tau)\sin\omega\tau d\tau \tag{7a}$$

$$\mathrm{c}_{55\,plus} = -u^2\frac{2}{\pi}\int_0^\infty \frac{B_{33}^0 + x_A b_{33}^A}{\omega_1^2} d\omega_1 - u x_A^2 \frac{2}{\pi}\int_0^\infty (a_{33}^A(\omega) - \mu_{33}^A) d\omega_1 \tag{7b}$$

From the above, we can see that the direct transformation from strip theory to get IRF will cause the inconsistency between hydrodynamics in time domain and frequency domain. The modification to the hydrodynamic coefficients like radiation restoring coefficients $c_{55\,plus}$ is necessary to assure the transformation consistent. The numerical results to be shown in section 4 will demonstrate the necessity of the modification.

2.3 Diffraction Forces Modelling

Similarly, the diffraction forces/moments contribution can also be represented using convolution integrals (King, 1987, Ahmed et al. 2010), which is what we will study in next step. In the present method, the strip theory in frequency-domain is employed to calculate the diffraction force directly. The diffraction forces/moment can be expressed in time-domain as followed:

$$F_j^D(t) = \zeta_a F_{ja}^D \cos(\omega_e t + \varphi_j) \qquad j = 3,4,5 \tag{8}$$

Where ω_e is the encounter frequency of ship in waves. F_{ja}^D, φ_j are amplitude and phase angle of diffraction force transfer function using strip theory, ζ_a is the amplitude of incident regular wave.

2.4 F-K and hydrostatic restoring forces modelling

In order to capture the ship rolling restoring moment variation in wave, the main cause for parametric rolling, the restoring force/moment should be accurately modelled accounting for the exact ship geometry and the position on waves at each time step. In the method presented here, the non-linear incident wave excitation is also incorporated. Together with the corresponding weight contributions, the fluid loads $F_j^I + F_j^S$ from incident wave excitation and hydrostatic restoring force are determined by integration of the incident wave pressure and hydrostatic pressure over the actual submerged part of the hull as shown in Fig. 1.

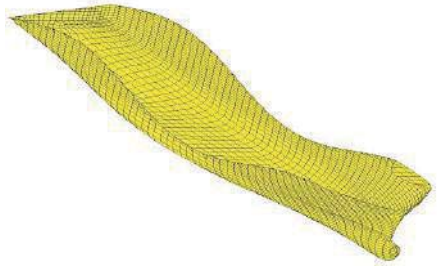

Fig. 1 The instantaneous wetted ship surface under incident wave profile

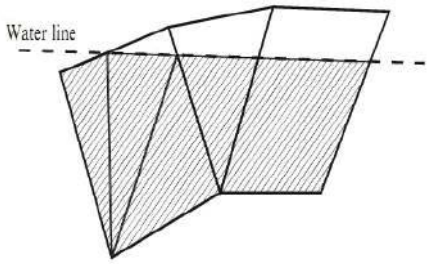

Fig. 2 panels subdivision across the incident wave free surface

The entire surface of the ship hull (up to deck line) is discretised with quadrilateral or triangular panels. At each time step, panels which are above the instantaneous incident wave free surface are directly ignored while panels below the instantaneous free surface are accounted. In particular, panels which are cross the free surface are subdivided and the smaller panels are newly formed, as shown in figure 2. The pressure acting on each panel is assumed uniform and equal to that acting at the centroid of the panel. At each time step, the toll ship rolling moment is given by summing up contributions of all the accounted panels.

2.5 Ship roll damping modelling

In general, ships rolling on the free surface of the sea are subjected to the damping of the water where the viscous effect contributes quite large amount and can't be calculated using traditional potential flow theory. The most accurate way to account for the damping moment is to conduct experiments on models or actual ships. In this study, a series of free-decay experiment with different advancing speed are conducted on a scaled model of C11 class containership.

In order to confine the case to the problem of non-linear roll damping, the following roll equation are considered, where the original damping term is expressed as a series expansion of $\dot{\eta}_4$:

$$(I_{44}+\mu_{44})\ddot{\eta}_4 + b_{44}\dot{\eta}_4 + b_{441}\dot{\eta}_4 + b_{442}\dot{\eta}_4^3 + \int_0^t K_{44}(t-\tau)\dot{\eta}_4(\tau)d\tau + c_{44}\eta_4 = F_4^I + F_4^S + F_4^D \quad (9)$$

where b_{441} is the linear damping term, and b_{442} is the cubic damping term. The terms b_{441} and b_{442} can be determined by analyzing the free-decay rolling experimental data.

3. THE MODEL TEST ABOUT THE PARAMETRIC ROLLING FOR C11 CONTAINERSHIP

The free running experiment with a 1/65.5 scaled model of the post Panamax C11 class containership in regular waves is conducted at the seakeeping basin of China Science Research Center in China, in which the ship model is propelled by one propeller whose revolution is controlled to keep the same mean speed with the tow carriage (J. LU, 2012). The principal particulars and the line plan of the C11 class containership are shown in Table 1 and Fig. 3.

Table 1 Main particulars of C11 class containership

Principal particular	Value
Length between perpendiculars (L_{pp})	262.0 m
Breadth (B)	40.0 m
Mean draught (T)	11.5 m
Block coefficient (C_b)	0.560
Pitch radius of gyration (κ_{yy})	$0.24L_{pp}$
Longitudinal position of center of gravity from amidship (x_{CG})	5.483 m aft

Transverse metacentric height, still water (GM)	1.952 m
Natural roll period (T_φ)	24.20 s

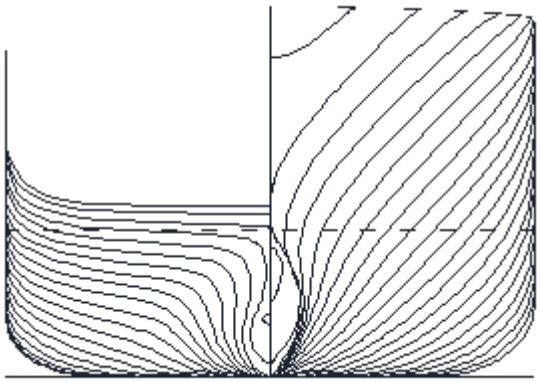

Fig.3. Lines plan for the C11 class containership

The test carried out covering a range of Froude numbers of 0.0, 0.05, 0.1, 0.15 and a range of wave steepness varying from 0.01 to 0.04. And the wavelength is equal to ship length between perpendiculars. Roll damping is determined directly from free roll decay tests at different speed based on extinction curve method. For example, the time history of a free-decay test with Froude number of 0.1 is illustrated in Fig. 4, imposing the largest heeling angle of 19.25°. Then the extinction curve obtained by regressive analysis and demonstrated in Fig. 5 can be calculated as follow:

$$\Delta\eta_4 = a\eta_{4m} + b\eta_{4m}^3 \qquad (10)$$

where η_{4m} and $\Delta\eta_4$ are mean roll amplitude and roll amplitude decrement per half cycle, respectively.

After obtaining the coefficients a and b, the roll damping then can be calculated. The method is based on the concept that the rate of change of the total energy in roll motion equals to the rate of energy dissipated by the roll damping.

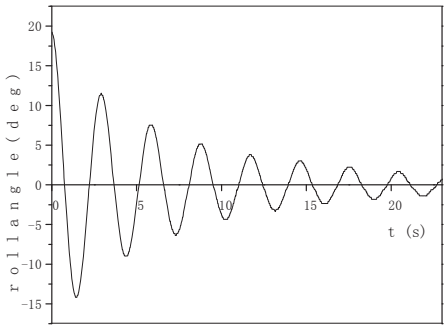

Fig.4. Time history of free roll decay test with Froude number of 0.1

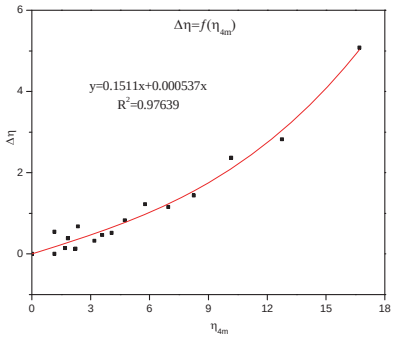

Fig.5. The extinct curve of the corresponding free roll decay test

4. NUMERICAL RESULTS AND DISCUSSIONS

4.1 The numerical results and discussion on the modification of radiation restoring coefficients using IRF method

The comparison of linear hydrodynamics-radiation pitch moment with or without considering the term $c_{55\text{plus}}$ -for C11 containership using Eq. 2 and numerical result using strip theory in frequency domain is illustrated in Fig. 6. In the plot, the results are obtained assumed that the ship is performing harmonic pitch motion with unit amplitude. Obviously, the result from "new transformation" considering the term $c_{55\text{plus}}$

keeps highly consistence with that from STF method.

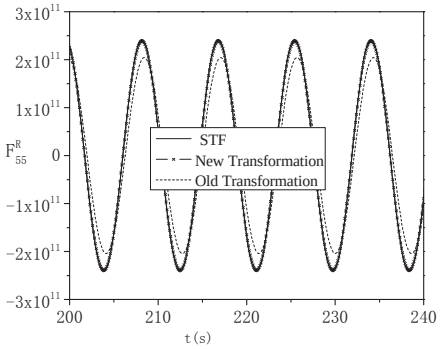

Fig.6 The comparison of radiation pitch moment between strip theory and time domain hydrodynamics using IRF

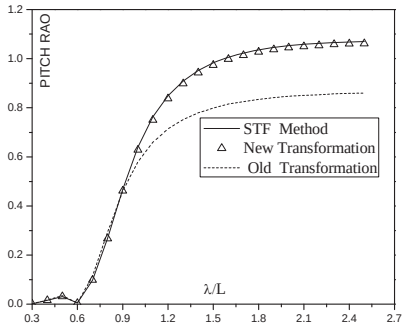

Fig.7 The comparison of pitch motion between strip theory and time domain solution using IRF

To further show the influence of the modification to hydrodynamic coefficients like term c_{55plus} using IRF method, The comparison of linear pitch motion between time domain calculation and strip theory results in frequency domain are demonstrated in Fig. 7. It is evident that the present method can provide consistent results with those from original strip theory.

4.2 The numerical simulation of parametric rolling and compared with model test using 3 DOF coupled method in time domain

Based on the numerical model for parametric rolling prediction, the time-domain simulation of vessel's motions is carried out using fourth order Runge-Kutta method. As mentioned before, only three degrees of freedoms are considered, i.e., heave, roll, pitch.

In table 2, Experimental and numerical results for C11 class containership are presented. The table provides the final steady roll amplitudes comparisons between numerical predictions and experimental data. From the comparison, it's seen that the numerical code generally presents quite well predictions on the steady amplitude of parametric rolling. While it can also be observed that the numerical code fails to predict properly in four cases where three of them fail to predict its occurence and one of them overestimated the steady magnitude. From the discussion by Belenky et. al. (2011) about the influence of roll damping on parametric rolling, it is known that the linear damping will make the instability zone narrower and increase the threshold value of minimum GM variation. Therefore the possible reason of numerical code unable to predict the occurrence of parametric roll is related to damping. The numerical damping used in simulation is a little larger and consequently move the system out of the instability region. For the case Test No. 1 where the numerical code overestimate the experiment value, the possible reason is not clearly yet.

Table 2. Experimental and numerical results for the C11 class containership

Test No.	Fr. #	Wave steepness	Experimental Roll Amp.(deg.)	Numerical Roll Amp.(deg.)
1	0.0	0.01	8.12	30.65
2		0.02	24.77	33.46
3		0.03	28.61	33.91

4		0.04	30.23	34.52
5	0.05	0.01	17.77	0.0
6		0.02	30.6	37.15
7		0.03	34.7	42.87
8		0.04	39.97	44.69
9	0.10	0.01	0.0	0.0
10		0.02	21.16	0.0
11		0.03	31.07	37.1
12		0.04	34.43	48.33
13	0.15	0.01	0.0	0.0
14		0.02	0.0	0.0
15		0.03	21.89	0.0
16		0.04	28.13	36.89

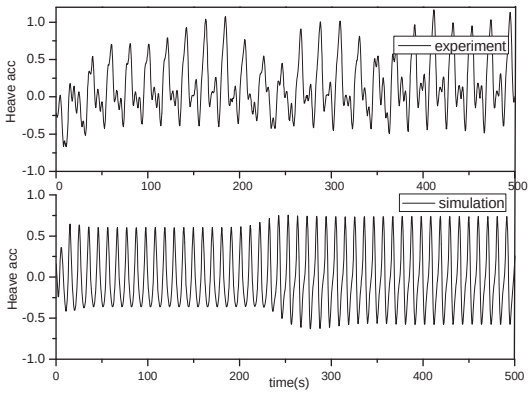

Fig. 8a Time history of heave acceleration

The following Fig. 8 presents the comparison of time history between numerical code and model test. The model test case is referred to Test No.11 in Tab. 2. where the Froude number is 0.1, the wave height is H_w=7.86 m and incident wave period is 12.95s.

As we can see, the parametric roll stabilizes at a roll angle of about 37 degrees, which is close to the experimental result of 31.07 degrees. The successful prediction justifies the usefulness and accuracy of the presented method. The associated heave acceleration and pitch motions are also illustrated. In term of numerical predictions for heave and pitch motions itself, it's seen that there is a increase in heave and a very slight decrease in pitch motions accompanied with parametric rolling compared with those when ship roll motions is not excited. These phenomena should be the influence of non-linearity from fluid loads and coupling between heave-roll-pitch.

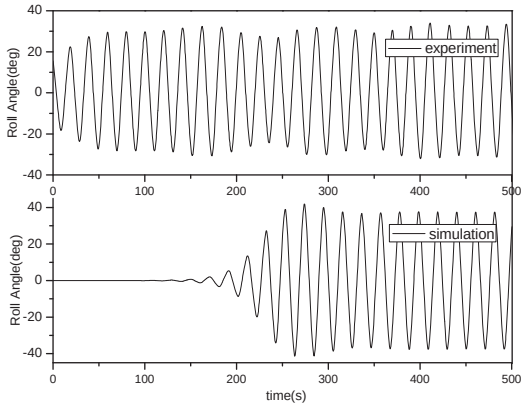

Fig. 8b Time history of roll angle

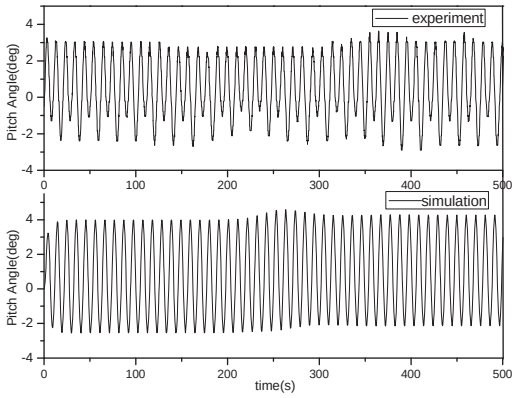

Fig. 8c Time history of pitch angle

Fig. 8. Time history comparison for test No. 11 obtained from numerical simulations and experimental measurements

5. CONCLUSION

In this paper, a partly non-linear time-domain numerical model is presented and utilized to simulate parametric excited rolling resonance in regular head waves. In the present numerical model, the impulse response function method is used to model the time domain radiation forces of ship motions. The impulse response function is obtained from strip theory. Via theoretical analysis, consistent transformation from frequency domain to time domain has been performed. Results obtained for C11 class containership demonstrate that the method succeeds in obtaining steady roll angles of parametric roll that mostly compares reasonably well with experimental data. In addition, it should be noted that the presented model undesirably fails to predict the occurrence of parametric ship rolling under some cases. The possible reason is due to the numerical modelling of rolling damping which will influence the occurrence of parametric rolling. Further developments needed to improve the capability of the presented method will include: considering the hydrodynamic coupling effects from heave and pitch to rolling and vice versa, the numerical modelling of parametric rolling in irregular wave.

6. ACKNOWLEDGEMENT

In this paper, the model test data of parametric rolling for C11 containership is provided by Prof. M. Gu and Dr. J. Lu from CSSRC. The model test data is very useful for validating our numerical code. Their help is gratefully acknowledged.

The present work is supported by the National Natural Science Foundation of China (Grant no. 51079032, 51109040) and Defense Industrial Technology Development Program (Grant no. B2420132001). Young Faculty Academic Supporting Program of Heilongjiang Province (Grant No.1252G017) is also gratefully acknowledged.

7. REFERENCES

Ahmed, T.M., Ballard, E.J., Hudson, D.A., and Temarel, P., 2006, “Prediction of parametric roll resonance in longitudinal regular waves using a non-linear method”, Proceedings of the Ninth International Conference on Stability of Ships and Ocean Vehicles STAB’06, vol. 1, Rio de Janeiro, Brasil, pp.89–97.

Ahmed, T.M., Ballard, E.J., Hudson, D.A., and Temarel, P., 2008, “A non-linear numerical method for the simulation of parametric roll resonance in regular waves”, Proceedings of the ASME 27th International Conference on Offshore Mechanics and Arctic Engineering OMAE 2008, Estoril, Portugal.

Ahmed T M, Hudson D A, Temarel P. 2010, “An investigation into parametric roll resonance in regular waves using a partly non-linear numerical model”, Ocean Engineering, 37(14): 1307-1320

Bulian, G. Francescutto, A.,2006, “On the effect of stochastic variations of restoring moment in long-crested irregular longitudinal seas”, Proceedings of the Ninth International Conference on Stability of Ships and Ocean Vehicles (STAB’06), vol. 1, pp. 131–146.

Blocki W., 1980,“Ship Safety in Connection with Parametric Resonance of the Roll”, International Shipbuilding Progress, 27:36-53.

Cummins, W. E., 1962, “The impulse response function and ship motions”, DTMB-1661. David Taylor Model Basin Washington DC.

France, W.N., Levadou, M., Treakle, T.W., Paulling, J.R., Michel, R.K. and Moore, C. ,2003, " An investigation of head-sea parametric rolling and its influence on container lashing systems", Marine Technology, Vol. 40, pp. 1-19

"Guide for the assessment of parametric roll resonance in the design of container carriers", 2004, American Bureau of Shipping, Houston, TX. USA.

Hua, J., Palmquist, M. and Lindgren, G.,2006, "An analysis of the parametric roll events measured onboard the PCTC Aida", Proc. STAB 2006, pp. 109-118

Kerwin J.E., 1955, "Note on Rolling in Longitudinal Waves",International Shipbuilding Progress, 2(16): 597-614.

Kim, T.Y. and Kim, Y., 2010, "multi-level approach of parametric roll analysis", The 7th International Workshop on Ship Hydrodynamics. ITTC Workshop on Seakeeping, Seoul, Korea, Oct. 19-21

King, B., 1987, "Time-domain analysis of wave exciting forces on ships and bodies.", Ph.D. Thesis, The University of Michigan.

Liapis, S. J., 1986, "Time-Domain Analysis of Ship Motions", Ph.D. Thesis, University of Michigan.

Levadou, M. van ′t Veer, R.,2006, "Parametric roll and ship design". Proceedings of the Ninth International Conference on Stability of Ships and Ocean Vehicles (STAB'06), vol. 1, pp. 191–206.

LU J., GU M., Umeda N., 2012, "Numerical Approaches on Parametric Rolling in Head Seas", 10th International Conference on Hydrodynamics, St. Petersburg, Russia.October 1-4, 2012.

Neves, M., Rodriguez, C., 2005. "A non-linear mathematical model of higher order for strong parametric resonance of the roll motion of ships in waves", Marine Systems & Ocean Technology 1 (2), 69–81 .

Park, D. M., Kim, Y., Song, K. H., 2013. "Sensitivity in numerical analysis of parametric roll", Ocean Engineering, 67, 1-12.

Ribeiro e Silva S, Guedes Soares C. 2013, "Prediction of parametric rolling in waves with a time domain non-linear strip theory model", Ocean Engineering, 72: 453-469.

Ribeiro e Silva, S., Santos, T. Guedes Soares, C. 2003, "Time domain simulation of a fully coupled parametrically excited roll response in regular and irregular head seas", Proceedings of the Eighth International Conference of Ships and Ocean Vehicles (STAB'03), Madrid, Spain, pp. 349–360.

Ribeiro e Silva, S., Santos, T.A., Guedes Soares, C.,2005, "Parametrically excited roll in regular and irregular head seas", International Shipbuilding Progress 52, 29–56.

Salvesen, N., Tuck, E. O., Faltinsen, O. M.. "Ship motions and sea loads", SNAME, 1970

Shin, Y.S., Belenky, V.L., Paulling, J.R., Weems, K.M., Lin, W.M., 2004. "Criteria for parametric roll of large containerships in longitudinal seas". Transactions of SNAME 112, 14–47.

"Testing and Extrapolation Methods Loads and Responses, Stability Predicting the Occurrence and Magnitude of Parametric Rolling", Revision 00, 2005, ITTC-international towing tank conference 7.5-02-07-04.3,

Taguchi H., Ishida S., Sawada H. and Minami, M,2006, "Model Experiment on Parametric Rolling of a Post-Panamax Containership in Head Waves",Proceedings of the 9th

International Conference of Ships and Ocean Vehicles, COPPE Univ Fed Rio de Janeiro, 147-156

Umeda N, Hashimoto H, Vassalos D, et al ,2003, "Nonliner dynamics on parametric roll resonance with realistic numerical modelling", Proceedings of the 8th International Conference on Stability of Ships and Ocean Vehicles, Madrid, pp 281–290.

Belenky V., Bassler C.C., Spyrou K.J., 2011, "Development of Second Generation Intact Stability Criteria", NSWCCD-50-TR-2011/065, Hydromechanics Department Report, Naval Surface Warfare Center, Carderock Division.

Validation of Statistical Extrapolation Methods for Large Motion Prediction

Timothy Smith, *NSWCCD (Naval Surface Warfare Center, Carderock Division)*
timothy.c.smith1@navy.mil
Aurore Zuzick, *NSWCCD (Naval Surface Warfare Center, Carderock Division)*
aurore.zuzick@navy.mil

ABSTRACT

Large amplitude ship motion often results from nonlinear aspects of hull geometry and wave excitation. As a result, large amplitude ship motion occurs infrequently, making direct simulation problematic. Statistical extrapolation is a methodology to assess the probability of large amplitude ship motion from shorter duration simulations or model test data that may not contain such large motion. The validation process involves the fitting of an extreme value distribution to data, generation and identification of a "true value," and formulation of a comparison such that a definitive answer can be made.

This paper presents a worked numerical example of statistical extrapolation considering large amplitude roll, pitch, vertical acceleration, and lateral acceleration. Examining different motions addresses different types and levels of nonlinearity. Data are fit with the Generalized Pareto Distribution to formulate a statistical extrapolation. The generation of a "true value" for comparison is discussed. Lastly, the formulation of three-tier acceptance criteria is demonstrated to fully answer the question of statistical extrapolation accuracy. The paper will stress the desired traits and interactions between the main parts of extrapolation, true value, and acceptance criteria.

Keywords: *statistical extrapolation, validation, non-linear motion*

1. INTRODUCTION

The validation of numerical simulations is addressed by various professional societies and governmental bodies for many engineering disciplines. There are established verification and validation outlines, guides, and processes to follow when performing numerical simulation verification and validation (AIAA, 1998; ASME, 2009; ITTC, 2011). These processes and guides are often generalized with details left to the engineers actually performing the verification and validation. Validation at its core consists of a comparison between the simulation and the "true value," and becomes the basis for a validation decision. The true value comes from scale model testing or higher fidelity simulations and implies enough physical understanding to recognize it as the true value.

Focusing on the phenomena of large motion and capsizing, the true value is at once both non-linear and rare. The simulation of these phenomena requires advanced, hydrodynamic blended method prediction tools due to the non-linearity involved (de Kat and Pauling, 1989; Lin and Yue, 1990; Shin *et al*., 2003). Furthermore, the ITTC parametric roll study (Reed, 2011; ITTC Stability in Waves, 2011) showed the uncertainty can be quite large due to practical non-ergodicity. This further increases the difficulty in understanding the result of the validation effort and achieving a definitive result.

This paper continues Smith (2014) and Smith and Campbell (2013) by providing a complete worked example to demonstrate a

multi-tiered validation approach with large amplitude motions and accelerations including statistical extrapolation of rare events.

2. TEST CASE

This test case considers ship roll and pitch motion and lateral and vertical acceleration for a range of relative wave heading in a high sea state. Extrapolations are made based on a sub-set of time history data and compared to a directly counted true value at a motion level not necessarily seen in the data sub-set.

2.1 Extrapolation Method

Following (Smith, 2014), this paper uses the extrapolation technique based on Generalized Pareto Distribution (GPD) as implemented by Campbell, *et al*, (2014). GPD can be used to approximate the tail of any distribution that makes use of a scale and shape parameter to fit the data. There are various implementation details in terms of selecting a threshold and determining the scale and shape parameter.

The confidence intervals for the extrapolated estimate were calculated using two approaches assuming a normal distribution of the GPD parameters. The first is based on the confidence interval of the GPD parameters and generation of a boundary based on the upper and lower extremes of the possible combinations. The second follows the confidence interval method from Campbell, *et al*, (2014) except the logarithm of the scale parameter was used instead of the scale parameters itself. The use of the logarithm of the scale parameter ensures its positive value. These are referred to as the boundary CI and logarithm CI in this paper.

2.2 True Value

The true value was determined by calculating hundreds of thousands of hours of ship motion simulation using a fully coupled, 3 degree of freedom (DOF) simulation tool based on volume calculation (Weems and Wundrow, 2013, Weems and Belenky, 2015). This model assumes constant radiation and diffraction forces with non-linear hydrostatics on 2D strip hull representation. As such it captures essential hydrostatic non-linearity and maintains very fast computation time. Note that in the case of validation against model test data, the true value is typically characterized by some non-negligible amount of uncertainty related to instrumentation and sampling limitations. By simulating against large amounts of simulated data, this uncertainty can be reduced such that a single true value may be identified.

The appropriateness of the 3DOF simplified simulation tool was checked by comparing various instantaneous roll and pitch parameters to those same parameters as calculated with a higher fidelity, 6 DOF blended simulation tool (Lin and Yue, 1990). The parameters compared dealt with the roll and pitch restoring force such as metacentric height, area under GZ curve, and peak of the GZ curve. The most useful comparison was plotting instantaneous roll angle and GZ value. Due to the difference in degree of freedom, the simulation tools could not be compared time step by time step for the same wave realization. The determination of appropriate and adequate physical representation was based on general agreement between the 3DOF and 6DOF simulations (Weems and Belenky 2015).

The peaks were extracted using an envelope approach (Belenky and Campbell, 2012). This method ensures independent data samples as required to apply GPD. The true value of the exceedance rate is found using a direct counting procedure studied in detail in Belenky and Campbell (2012).

3. VALIDATION APPROACH

This example expands the multi-tier validation approach consisting of a parameter, condition and set criteria to include vertical and lateral acceleration (Smith, 2012). The three tiered structure reflects typical scale model data structures of individual motion channels, a run condition of speed-heading-seaway, and a test consisting of many conditions. Criteria are set to determine an acceptable parameter comparison, and what constitutes an acceptable condition and overall set.

A parameter comparison, Tier I, is the elemental comparison between the simulation and true value. It refers to a single motion or response. Choosing an appropriate parameter-level comparison metric depends largely on the problem under examination. Metric options typically share underlying principles and utilize similar properties of the sample data to draw conclusions. They tend to differ in terms of the specific information they provide about each comparison. Some metrics produce binary outcomes (pass or fail) while others provide quantified measures of correlation. Smith (2012) discusses possible comparisons for motions. Further discussion of comparison methods appears later in this paper.

Tier II is a condition comparison. Typically, a condition is the environment, speed and heading used to define the simulation and the associated motion response. So a set of environmental descriptors (e.g. significant wave height, period, etc.), speed and heading and four motions would be four conditions due to the four motions. Thus, a condition can be defined as a deterministic vector:

$$\vec{S} = \left(H_S, T_m, V_S, \beta, i_{dx}\right) \qquad (1)$$

where H_S is a significant wave height, T_m modal frequency, V_S, forward speed, β-heading, i_{dx} –motion index (say, i_{dx}=4 corresponds to roll). This considers motions or parameters independently and Tier II mirrors Tier I.

Alternatively, motions (parameters) can be considered collectively with all or multiple motions (parameters) being included in the condition definition. Then the number of passing motion (parameter) responses becomes a criterion for a condition passing. This is a more stringent criterion to pass with slightly different bookkeeping. The Tier II criterion defines what constitutes a passing condition in terms of number or combinations of passing Tier I comparisons.

Tier III, the set comparison, defines how many conditions have to pass for the simulation to pass the validation criteria. The condition definition needs to be considered in setting the Tier III validation criteria to avoid an impossible criterion.

There is an inter-relationship between the parameter comparisons, second tier condition definition and third tier acceptance levels. Other parameter comparisons besides confidence interval capture of the true value may be used depending on what is important to the application. For instance, the amount of conservatism or absolute difference may be used as a metric. A change of the parameter comparison could change the condition criteria. The multi-tier validation definition used in this study provides a check on both the extrapolation and the confidence interval formulation as both are included in the parameter comparison.

For this example, the parameter comparison is the comparison of a statistical extrapolation to the true value at a specified critical motion level. The parameter comparison passes the test if the extrapolation confidence interval captures the true value. Multiple extrapolations are made from different data sets all representing the same condition, that is speed-heading-seaway-motion combination. A condition passes if the true value is captured by the confidence interval at a percentage roughly equal to the confidence probability. This is repeated for a number of different conditions.

The extrapolation method is considered valid if a high percentage of conditions pass.

These acceptance criteria assume a valid confidence interval formulation. As two confidence interval calculation methods are assessed, this example also serves as a validation of the confidence interval calculation method.

4. FURTHER PARAMETRIC COMPARISONS

The validation approach described above examines the effectiveness of the method used to calculate the confidence interval on the extrapolated value. If the acceptance criteria are passed, we have demonstrated that the 95% confidence interval for any given population sample set does indeed capture the true population value 95% of the time. Once we have confidence that our methods can accurately calculate the uncertainty associated with an extrapolated value, the extrapolated values and their associated uncertainty can be used to validate the simulation tool's ability to model real ship motions. This section discusses parameter comparisons appropriate for non-rare and rare comparisons between simulation data and model test data as an expansion of Smith (2012, 2014). The comparisons discussed are: confidence interval overlap, hypothesis testing, and quantiles (percentiles).

4.1 Confidence Interval Overlap

Confidence interval overlap is a straightforward comparison metric which provides an unambiguous outcome applicable to both non-rare and rare comparisons. Note that the application of the confidence interval overlap metric described earlier for validation of the confidence interval formulation is distinctly different from its use as validation metric for comparisons between simulation and model test data. When evaluating the confidence interval formulation, a true value is known and there are many sample sets of the population from which to draw conclusions. For model test comparisons, the "true values" from two populations (model and simulation) are being compared, and only one sample set from each population is available. When validating simulation results against model test data, confidence intervals are calculated at a specified confidence probability for both sets of sample data; if the intervals from both sets overlap one another, the comparison is considered successful. However, the existence of overlapping 95% confidence intervals does not necessarily signify a 95% chance that both samples share the same underlying population characteristics. The combined probability that the true population values of both data sets lie within the overlapped interval range is significantly less than 95% and depends on the lengths and relative position of both confidence intervals.

The interval overlap metric also provides no information about the probability of differences between the populations. For example, significant overlap of relatively long intervals (high uncertainty) suggests that both populations lie on the same interval; but if the interval is large, the populations could be very different. Alternatively, if intervals are very small, this metric can reject comparisons when population differences are very (perhaps acceptably) small. A perhaps undesirable characteristic of the interval overlap metric is that comparisons are inherently less likely to pass the criteria as uncertainty is reduced.

The confidence interval on the difference between parameter populations is an extension of the interval overlap method. The level of significance is associated with the comparison (i.e. a form of combined probability), rather than with each individual data set. The extents of the confidence interval on the difference provide information about how similar and how different the populations are likely to be. A 95% confidence interval on difference provides the range of values for which the following is true: there is a 95% probability

that the true difference between the two populations lies within that range. Setting limits on the allowable difference (including uncertainty) forms a pass/fail application of this comparison metric. Unlike the interval overlap method, this criterion does not become more difficult to pass when the data are more well-known (less uncertainty). In addition, the difference (including uncertainty) can be used to quantify the simulation's overall level of accuracy. For example, basic statistics (minimum, mean, etc.) of the observed lower uncertainty limits across Tier I comparisons quantify the amount of under-prediction and provide information on safety margin for simulation results.

Another metric making use of the confidence interval is the maximum conservative distance (MCD) which is the difference between the extrapolation upper confidence level and the true value. The upper confidence level is often the "not to exceed" limit. Maximum conservative distance then provides a direct measurement of accuracy of the important parameter.

4.2 Hypothesis Testing

Hypothesis testing on the difference between population statistics is another way to associate a level of significance with a quantified measure of correlation agreement based on two sets of sample data. Formulation of an appropriate null hypothesis is integral to applying this metric. When attempting to identify evidence of good correlation that cannot initially be assumed to exist, the null hypothesis should be contrary to the outcome desired. Formulated this way, strong evidence must be present in the sample data to reject the null hypothesis (acceptance of desired outcome).

For example, the following null hypothesis for a one-tailed Student's t-test may be well-suited as parameter-level criteria metric: the difference between the population mean significant single amplitude (SSA) values is greater than a specified amount. The level of significance used in the test dictates the probability of wrongly rejecting the null hypothesis. For the given null hypothesis, it is possible to quantify (and set to an acceptably low level) the probability of incorrectly identifying good correlation. The probability of failing to correctly identify good correlation is not associated with a specific probability (often known as the Type II or beta error); while this value is of interest, it is typically of less concern than incorrectly identifying poor correlation as good correlation. By defining both a specific limit on the allowable population difference and a level of significance for the test, the Student's t-test can provide a pass/fail outcome for the comparison.

Alternatively, by specifying the level of significance and solving for the critical value of the limit on the difference allowed to pass the test, a quantified measure of correlation agreement is produced. Similarly, by specifying the limit on the difference and solving for the critical level of significance to pass the test, the probability associated with success of the comparison is produced; see Appendix A. Both the quantified measure of agreement and probability of test success are comparison outcomes which can be used to develop measures of correlation across multiple comparisons. The beta error is not explicitly calculated in this process.

Hypothesis tests rely upon measures of the variance in both populations; for comparison of extrapolated values, the confidence intervals on the extrapolated values can be used to calculate the parameters necessary for hypothesis test calculations.

4.3 Percentiles – Rare Comparisons

To make comparisons farther out on the tail of the motion distribution, a cumulative distribution of the measured peaks is useful. The cumulative distributions or quantiles can

be compared at specific percentiles with uncertainty bands. Uncertainty bands at any percentile can be calculated using the normal approximation to the binomial distribution (Belenky and Campbell, 2012).

Percentiles comparisons across the range of available data (shown as a Quantile-Quantile (Q-Q) plot) provide strong visual indications about model and simulation correlation across the distribution of ship response. However, establishing parameter criteria metrics to quantify correlation (including uncertainty) across a range of percentiles is challenging; applying comparison metrics at one or more discrete percentile of peak values is recommended.

One should be cautious when deciding at which percentile to apply parameter criteria comparison metrics. Data at the highest percentiles are prone to large sampling uncertainties; repetition of an ensemble of runs often leads to very different values of the 99th percentile of roll peaks due to the small number of samples associated with extreme motions. The 90th percentile of ship motion peak responses has been observed to be a stable level at which quasi-rare behavior can be observed without being obscured by very large uncertainty. Note that high percentile of peak values are related to threshold exceedance rate. Both high percentiles of peaks and exceedance rates are useful parameters for which non-rare motion channel criteria may be applied, though percentiles tend to lend themselves more easily to the definition of margins and limits. The authors have not yet attempted to apply this to extrapolations.

5. RESULTS

Ten of thousands of hours simulated ship motions were calculated using the 3DOF simplified simulation tool in large sea states for a range of heading. The seaway was a 9.5 m significant wave height and 15 sec modal period with a Bretschneider spectral shape. The headings ranged from near following (15 deg) to bow seas (135 deg). The headings were 15, 30, 45, 60, 90, and 135 deg. The speed was 12 knots for all cases.

The total exposure time was accumulated by ensembling many half-hour simulations. Each simulation had a unique set of random phases to generate a unique and independent wave realization. Time histories of roll, pitch, vertical acceleration, and lateral acceleration were analyzed to extract peaks. This distribution of peaks is the true value for each heading-motion combination. The length of exposure time varies between headings as a matter of convenience. The difference in exposure time does not affect the validation results beyond potentially limiting the maximum comparison value.

Around 100 extrapolations were made with sub-sets of the total exposure time for each heading-motion combination. The use of multiple extrapolations allows for a direct check on confidence interval formulation and gives understanding of data sub-set dependency. The data sub-set exposure time was either 50 hours or 100 hours depending on the number of peaks extracted, with 50 hours being used for cases with more peaks. This was due to a memory limitation on the analysis software.

The extrapolations were compared to the true value at an evaluation level corresponding to a high motion level in the true data set. The comparison was based on overlap of the 95% confidence interval with the true value. The evaluation level was selected as the highest level in the true data set that had more than 30 data samples. Thirty samples are enough to have meaningful uncertainty. With less than 30 samples, the uncertainty becomes very large and the true value has not stabilized.

Figure 1 shows an example of the roll parameter comparisons for stern seas, 30 deg heading. In this figure, the true value is represented by a solid line (1.1111^{-8}). Each extrapolation confidence interval is represented

by a vertical line and represents a single Tier I comparison. The extrapolation captures the true value if the vertical line crosses the horizontal true value line. The estimate of mean value of crossing rate is denoted by a circle and the most probable crossing rate is denoted by a cross. The confidence intervals are asymmetric relative to the mean or most probable crossing rate. This is a property of GPD and different than the symmetric confidence intervals more commonly seen with the normal distribution.

The entirety of Figure 1 represents a Tier II comparison comprised of 100 Tier I comparisons. The expected passing rate percentage is the same as the confidence interval due to use of confidence interval overlap for the parameter comparison. Due to the finite number of data sets, the passing rate can vary from 90 to 100% and still be acceptable; though the mean rate across all the conditions should be close to the confidence level. Table 1 shows the passing rates for all the conditions for the two different confidence formulations. Conditions that pass are bold; failing conditions are italicized. Smith (2014) indicated both CI approaches were acceptable based on roll and pitch. The addition of lateral and vertical acceleration shows a difference between the two CI approaches. The logarithm CI has many instances where the true value capture rate is less than 90% and fail the Tier I comparison (parameter).

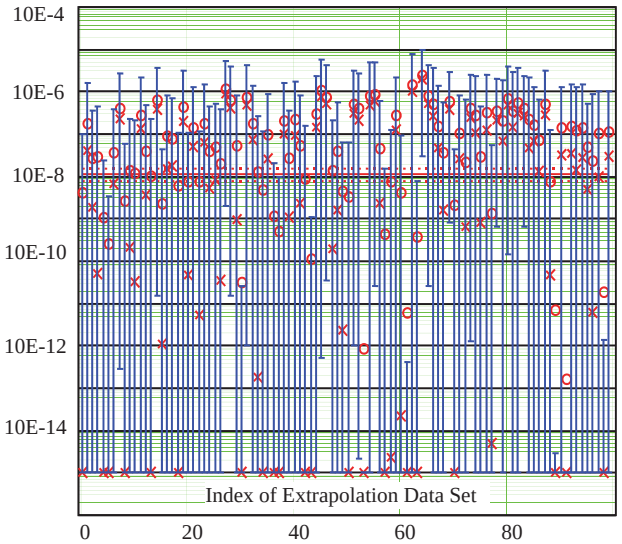

Figure 1 Confidence interval overlap of true value for roll at 30 deg heading at 30 deg comparison level using logarithm CI (91%) (true value 1.111E-08)

As noted in Smith (2014), the GPD can have zero probability which results in asymmetric confidence intervals that have very small lower confidence limits. This can result in automatically capturing the true value if the extrapolation is at all conservative; larger than the true value.

Figure 1 shows roll comparison at 30 deg wave heading for the logarithm boundary CI. The estimates of the mean value are distributed about the true value, while the most probable values are mainly less than the true value. This is a property of the mean value averaging over the entire confidence interval region, whereas the most probable value is selected at a particular point. This difference is discussed in Campbell *et al*. Figure 2 shows the pitch comparison at the same condition where both the mean value estimates and most probable values are greater than the true value. This is indicative of a conservative bias.

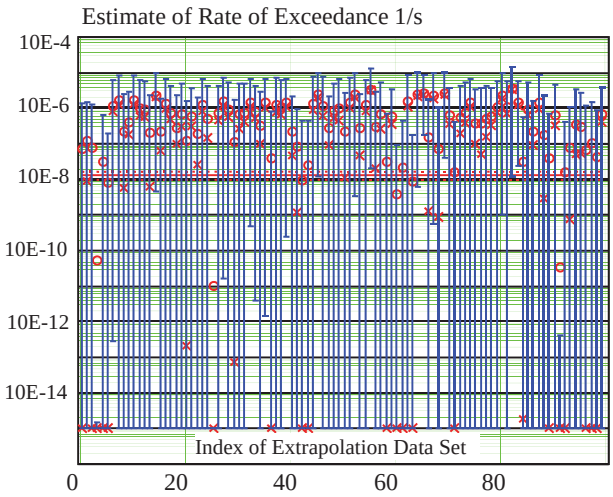

Figure 2 Confidence interval overlap of true value for pitch at 30 deg at 11.5 deg using logarithm CI (97%)

Figures 3 and 4 show the difference in confidence interval method for pitch at 45 deg heading at 11.5 deg comparison level. The

boundary CI method has a higher average upper boundary and a lower boundary always at the lowest value considered (10^{-15}). The logarithm CI method produces smaller confidence intervals.

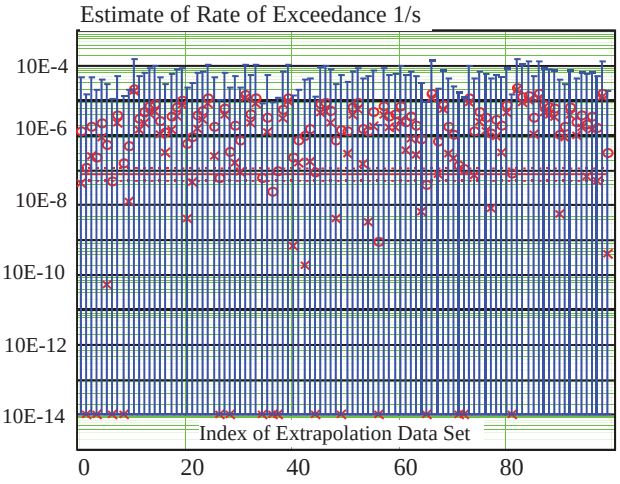

Figure 3 Confidence interval overlap of true value for pitch at 45 deg heading at 11.5 deg comparison level using boundary CI (100%)

Table 1 Confidence interval overlap results

Heading	Motion	Avg GPD Threshold	Comparison Level	# Points at Threshold	Exposure Hours	Boundary CI pass %	Boundary CI MCD	Logarithm CI pass %	Logarithm CI MCD	Shooting Distance
15	roll	6.947	15	53	230000	**96**	119.210	*84*	60.867	1.159
15	pitch	7.359	12	69	230000	**99**	278.512	**94**	166.585	0.653
15	lat accel	No data > 0.2g								
15	vert accel	0.125	0.2	468	230000	**100**	89.878	*86*	49.892	0.607
30	roll	12.877	30	40	100000	**96**	178.616	**91**	101.038	1.330
30	pitch	7.296	11.5	46	100000	**99**	420.751	**97**	244.296	0.576
30	lat accel	0.091	0.2	16	100000	**100**	1061.000	**98**	591.799	1.186
30	vert accel	0.133	0.25	13	100000	**100**	955.188	**96**	484.258	0.877
45	roll	17.094	60	30	230000	**99**	193.110	**94**	112.282	2.510
45	pitch	7.012	11.5	28	230000	**100**	503.342	**98**	269.962	0.640
45	lat accel	0.135	0.3	37	230000	**98**	237.340	**94**	118.744	1.221
45	vert accel	0.158	0.25	518	230000	**99**	74.673	**90**	41.558	0.578
60	roll	18.754	50	49	100000	**100**	276.284	**100**	169.168	1.666
60	pitch	6.257	9.5	71	100000	**100**	330.874	**91**	179.786	0.518
60	lat accel	0.157	0.35	19	100000	**98**	415.630	**97**	213.923	1.227
60	vert accel	0.194	0.3	169	100000	**100**	193.528	*86*	98.556	0.547
90	roll	16.055	32.5	41	230000	**99**	329.773	**99**	192.832	1.024
90	pitch	1.517	2.5	170	230000	**100**	136.716	**94**	68.382	0.648
90	lat accel	0.154	0.25	43	230000	**94**	136.448	*86*	74.551	0.621
90	vert accel	0.270	0.4	287	230000	**100**	98.103	**96**	52.179	0.480
135	roll	12.350	17.5	186	230000	**100**	92.851	**92**	60.694	0.417
135	pitch	4.909	7	172	230000	**100**	134.019	**94**	70.853	0.426
135	lat accel	0.137	0.25	25	230000	**96**	424.676	*88*	232.106	0.827
135	vert accel	0.283	0.4	192	230000	**98**	150.486	**96**	85.572	0.416
Average Value						99		93		

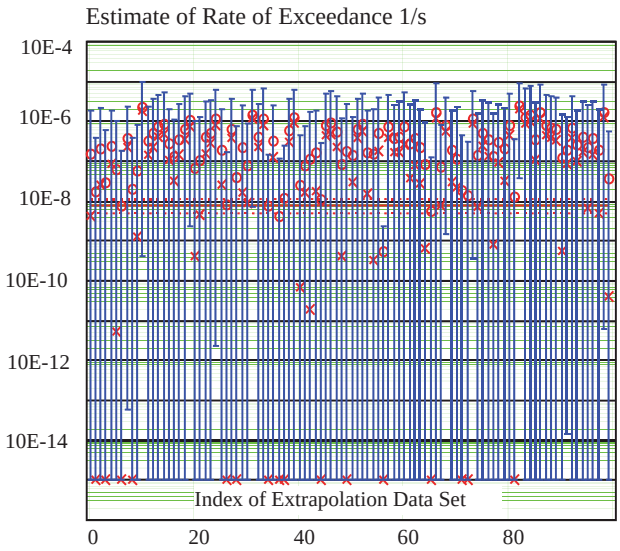

Figure 4 Confidence interval overlap of true value for pitch at 45 deg heading at 11.5 deg comparison level using logarithm CI (98%)

Figure 5 shows asymmetric confidence intervals for the 45 deg heading, lateral acceleration logarithm CI at 0.3 g comparison. At 0.2g comparison level for lateral acceleration at 45 deg heading, Figure 6 shows much smaller confidence intervals and a conservative bias. Although the true value capture rate is very low, the actual difference is small.

Figures 7 and 8 compare the boundary and logarithm CI methods for vertical acceleration at 30 deg heading and 0.2g comparison level. For comparisons at higher levels, both methods have 100% capture rate. The boundary method has larger confidence intervals; both a higher upper bound and many more instances of near zero lower bound. The boundary CI higher upper bound is indicated by the higher MCD; 99.5 vice 54.2. These are similar to the trends seen for pitch in Figures 3 and 4.

Pipiras, *et al.* (2015) compares the boundary and logarithm (lognormal) confidence interval approaches with a preference for lognormal as anti-conservative.

Figure 5 Confidence interval overlap of true value for lateral acceleration at 45 deg heading at 0.3g comparison level using logarithm CI

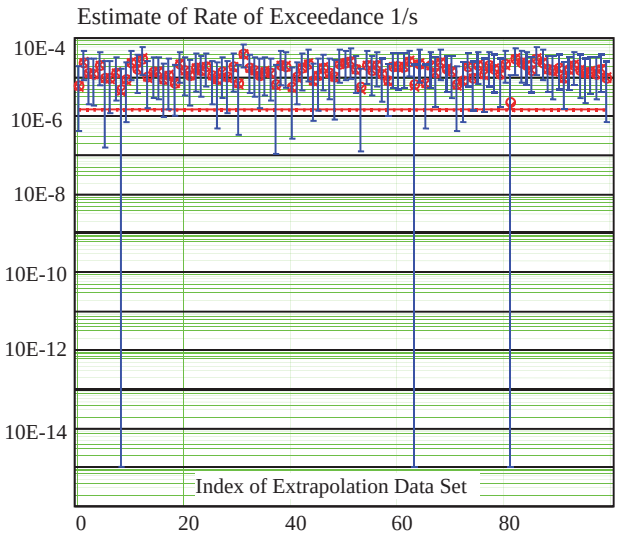

Figure 6 Confidence interval overlap of true value for lateral acceleration at 45 deg heading at 0.2g comparison level using logarithm CI

In terms of acceptance criteria, the boundary CI approach had all the parameter comparisons pass. Therefore, all the Tier II conditions pass and overall acceptance, Tier III, automatically passes if all condition comparisons, Tier II, are acceptable. In this case, even the alternate Tier II definition requiring all the motions to pass for a condition to pass results in overall acceptance.

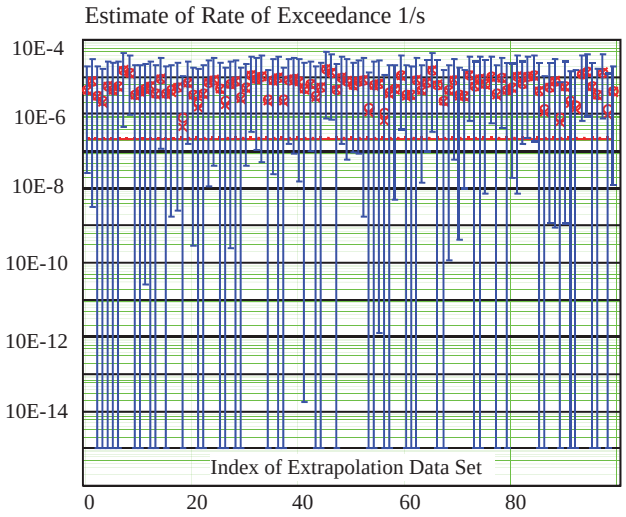

Figure 7 Confidence interval overlap of true value for vertical acceleration at 30 deg heading at 0.2g comparison level using boundary CI

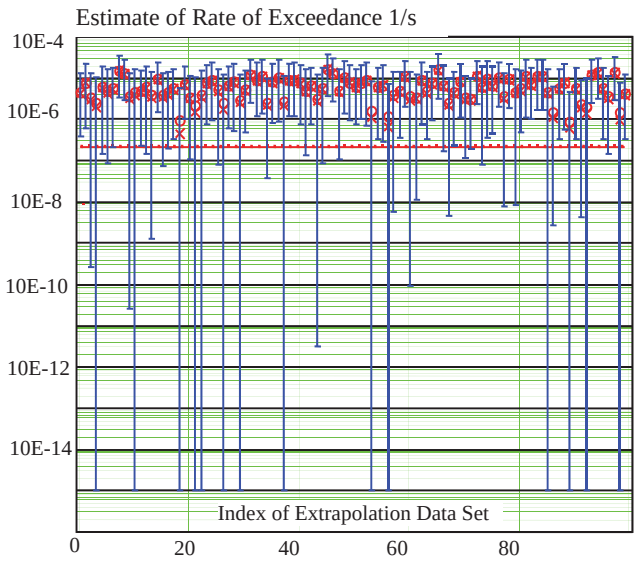

Figure 8 Confidence interval overlap of true value for vertical acceleration at 30 deg heading at 0.2g comparison level using logarithm CI

It is perhaps more instructive to look at the logarithm CI results. Here some of the acceleration parameter comparisons are not acceptable; true value capture rates less than 90%. As a result, some conditions do not pass but the condition pass rate is acceptable for overall acceptance, 18/23 (78%). However, a condition criterion requiring the passing of all motion comparisons is failed for two-thirds the conditions defined by unique speed-heading-seaway combination. There are six such conditions in this example. Overall acceptance fails as well.

However, this does show there is a heading range that is acceptable; aft of beam seas. There could be a limited acceptance with the restricted range of headings. This may also highlight a difference in performance due to behavior of the distribution tail, that is, heavy or light.

As an alternative, the mean conservative distance is a metric which uses the upper confidence limit on an extrapolated sample value. This metric estimates how much conservatism (or over-prediction) is present in the simulation results. For validation of a simulation tool against model data for ship guidance, this quantity may be more important than overall total confidence interval. The difficulty is agreeing to what is an acceptable value. In this example, only one case was over 3 orders of magnitude and almost all were over 2 orders of magnitude. At first glance, this appears to be completely unacceptable as a 100% difference is usually considered unacceptable. However, for exceedance rates of extreme values the uncertainty is inherently high and 1 in a billion is essentially the same as 10 in a billion. The acceptable MCD can be determined by the level at which the over conservatism produces an undesired operational restriction or life time risk level.

The MCD is calculated from the upper confidence limit; the upper confident limit suggests that 95% of the time, the true value is smaller than the limit value. Re-analysis of the existing data would show how successfully both methodologies estimate this quantity. Because this investigation would be focused on only the upper interval limit, the overall methodology validation conclusions may differ from those related to formulation of the entire confidence interval.

This example demonstrates the many factors influencing the comparison: CI method, comparison level, and comparison metric.

6. CONCLUSIONS

This paper demonstrated the applicability of a multi-tier validation approach to the validation of an extrapolated value confidence interval calculation method based on the Generalized Pareto Distribution. The first tier, parameter comparison, was made by comparing the 95% confidence interval from a GPD extrapolation to the true value. This was done 50 to 100 times to determine a passing rate for the Tier II, condition, comparison. Lastly, most of the conditions passed the second tier criterion, which passes the Tier III, or set, comparison. The extrapolation method would be considered validated. A rigorous validation effort would specify passing percentages at Tiers I and II.

Discussion was extended from parameter comparisons of a confidence interval calculation methodology against a known population to comparisons of extrapolated data between simulation and model data. The confidence interval overlap validation approach for these Tier I comparisons requires a validated confidence interval formulation. Other comparison metrics such as maximum conservative distance, mean difference, hypothesis testing, and percentiles were discussed as alternatives to confidence interval overlap. The boundary CI method proved marginally better than the logarithm CI method due to more acceptable conditions and mean value closer to confidence level. Still the boundary CI has many instances of 100 percent capture. This could be indicative of an overly large CI. The logarithm CI method had many failing conditions. Both approaches showed a conservative bias. Extrapolation of acceleration peaks tended to have lower capture rates than for roll or pitch for both CI methods. In terms of the acceptance criteria, the boundary CI method passed when accelerations are included and the logarithm CI method did not. It was shown that the acceptance criteria can indicate the presence of different behavior of distribution tail based on which parameters/motions pass.

The ratio of the GPD threshold and the evaluation level provides a metric for practical use. This ratio was less for accelerations than motions. The conditions with low motions can either have more data added, in the hope of increasing the GPD threshold level, or ignoring the condition as having negligible motions.

7. ACKNOWLEDGEMENT

This work was funded by the Office of Naval Research under Dr. Ki-Han Kim. The authors are grateful to Dr. V. Belenky for providing the data and analysis tools for the numerical example and thorough editing of the manuscript.

8. REFERENCES

AIAA, 1998, Guide for the Verification and Validation of Computational Fluid Dynamics Simulations. American Institute for Aeronautics and Astronautics, Reston, Virginia.

ASME, *2009, Standard for Verification and Validation in Computational Fluid Dynamics and Heat Transfer*, American Society of Mechanical Engineers, NY.

Belenky, V. and Campbell, B. 2012 “Statistical Extrapolation for Direct Stability Assessment”, Proc. 11th Intl. Conf. on Stability of Ships and Ocean Vehicles STAB 2012, Athens, Greece, pp. 243-256.

Belenky, V., Pipiras, V., Kent, C., Hughes, M., Campbell, B. and Smith, T. 2013 " On the Statistical Uncertainties of Time-domain-based Assessment of Stability Failures: Confidence Interval for the Mean and Variance of a Time Series", Proc. 13th Intl.

Ship Stability Workshop, Brest, France, pp. 251-258.

Belenky, V., Pipiras, V. and Weems, K. 2015 "Statistical Uncertainty of Ship Motion Data" Proc. of 12th Intl Conference of the Stability of Ships and Ocean Vehicles STAB 2015, Glasgow, UK

Campbell, B., Belenky, V. and Pipiras, V. 2014, "On the Application of the Generalized Pareto Distribution for Statistical Extrapolation in the Assessment of Dynamic Stability in Irregular Waves," Proc. 14th Intl. Ship Stability Workshop, Kuala Lumpur, Malaysia.

de Kat, J. O. and Paulling, J. R., 1989, "The Simulation of Ship Motions and Capsizing in Severe Seas," Transactions of The Society of Naval Architects and Marine Engineers, vol. 97.

ITTC Loads and Responses Seakeeping, 2011, "Verification and Validation of Linear and Weakly Nonlinear Seakeeping Computer Code," Procedure 7.5-02-07-02.4 Rev 1.

Lin, W.M., & D.K.P. Yue, 1990, "Numerical Solutions for Large Amplitude Ship Motions in the Time-Domain." Proc. 18th Symp. of Naval Hydrodynamics, Ann Arbor, Michigan, pp. 41–66.

Pipiras, V., Glotzer, D., Belenky, V., Campbell, B., Smith, T. 2015 "Confidence Interval for Exceedance Probabilities with Application to Extreme Ship Motions", Journal of Statistical Planning and Inference (Submitted).

Reed, A. M., 2011, "26th ITTC Parametric Roll Benchmark Study," Proc. 11th Intl. Ship Stability Workshop, Washington, DC, USA.

Shin, Y.S., Belenky, V. Lin, W.M. Weems, K.M. and Engle, A.H. 2003, "Nonlinear Time Domain Simulation Technology for Seakeeping and Wave-Load Analysis for Modern Ship Design," SNAME Transactions, Vol. 111.

Smith, T. C., 2012, "Approaches to Ship Motion Simulation Acceptance Criteria" Proc. of 11th Intl Conference of the Stability of Ships and Ocean Vehicles STAB 2012, Athens, Greece pp 101-114.

Smith, T. C., 2014, "Example of Validation of Statistical Extrapolation Example of Validation of Statistical Extrapolation," Proc. of the 14th Intl. Ship Stability Workshop, Kuala Lumpur, Malaysia.

Smith, T. and Campbell, B. 2013, "On the Validation of Statistical Extrapolation for Stability Failure Rate," Proc. 13th Intl. Ship Stability Workshop, Brest, France.

The Specialist Committee on Stability in Waves, 2011, Final Report and Recommendations to the 26th ITTC, Proc. 26th International Towing Tank Conference, Vol II, Rio de Janeiro, Brazil.

Weems, K. and Wundrow, D. 2013, "Hybrid Models for Fast Time-Domain Simulation of Stability Failures in Irregular Waves with Volume-Based Calculations for Froude-Krylov and Hydrostatic Force", Proc. 13th Intl. Ship Stability Workshop, Brest, France.

Weems, K. and Belenky, V. 2015, "Fast Time-Domain Simulation in Irregular Waves With Volume-Based Calculations for Froude-Krylov and Hydrostatic Force" Proc. of 12th Intl Conference of the Stability of Ships and Ocean Vehicles STAB *2015*, Glasgow, UK

9. APPENDIX A: DISCUSSION OF HYPOTHESIS TESTING ERROR

Hypothesis testing involves the formulation of a null hypothesis and has two errors that need to be controlled. The Type I error is associated with rejecting a null hypothesis that should be accepted - false negative. It is characterized with probability α (also known as the level of significance). On the probability

density function (PDF), this is the area in the tails of the distribution. The confidence interval is the area between the tails, 1-α (probability that null hypothesis is accepted correctly).

Type II error is the error associated with accepting a null hypothesis that should be rejected - false positive. It is characterized with probability β. Indeed, 1- β is the probability that the null hypothesis is rejected correctly. Type II error is calculated based on the difference in means between the data sets relative to an allowable or desired difference. The Type II error is overlap area of the original PDF and a PDF shifted by the difference in means.

If the mean shift is large, then it is relatively easy to detect false positives as the means being compared are far apart and β is small. Conversely, if the mean shift is small, then it is difficult to detect false positives and they are more likely to occur. For this case, β would be larger and even greater than 50%. A normal distribution is often used to describe the data probability density function for the Type II comparison.

This example deals with motion data sets with equal number of records and the comparison metric is the standard deviation. The null hypothesis is that the two variances are assumed to come from the same data set or the variances are statistically the same. Probability of Type II error is arbitrarily desired to be less than 50% using 90% confidence probability.

It is possible to check if β < 0.5 without actually calculating β by taking advantage of the fact that once normalized, the mean difference must be greater than 1.645 (90% quintile of a normal distribution with zero mean and unity variance) based on the shift to achieve less than 50% probability with 90% confidence and two-tailed Normal distribution. This critical difference, δ_{cr}, is applicable to all comparisons using the same confidence and β. Using other values of β results in different mean critical differences.

As the comparison metric is related to standard deviation, the starting point is normalizing the allowable mean difference D_A between the variance estimates of the two data samples:

$$\delta_{cr} = \frac{D_A}{\sqrt{Var(\hat{D})}} \qquad \text{(A1)}$$

$\hat{D}$ is the difference between variance estimates of the two samples and $Var(\hat{D})$ is the variance of this difference.

$$\hat{D} = \hat{V}_1 - \hat{V}_2 \qquad \text{(A2)}$$

The samples are independent, thus:

$$Var(\hat{D}) = Var(\hat{V}_1) + Var(\hat{V}_2) \qquad \text{(A3)}$$

Each sample consists of a number of records obtained from simulation or model experiment. Variance estimates of each sample are the result of averaging the variance estimates of each record. Thus, variance of the variance estimate is expressed as:

$$Var(\hat{V}_1) = \frac{Var(\hat{V}_{R1})}{N_1}; Var(\hat{V}_2) = \frac{Var(\hat{V}_{R2})}{N_2} \qquad \text{(A4)}$$

$Var(\hat{V}_{R1})$ and $Var(\hat{V}_{R2})$ are the variances of the variance of a single record.

The validity of the code is the hypothesis being tested. Thus, the code is expected to recover the theoretical variance reflected in a model test. It also means that the variance of the variance estimate of a single record is the same between the code and model test:

$$Var(\hat{V}_{R1}) = Var(\hat{V}_{R2}) = Var(\hat{V}_R) \qquad \text{(A5)}$$

Thus, the theoretical value of the variance of the differences is

$$\begin{aligned} \hat{Var}(D) &= \frac{Var(\hat{V}_{R1})}{N_1} + \frac{Var(\hat{V}_{R2})}{N_2} \\ &= Var(\hat{V}_R)\left(\frac{1}{N_1} + \frac{1}{N_2}\right) \end{aligned} \quad \text{(A6)}$$

The problem is that the theoretical value $Var(\hat{V}_R)$ is not known. Instead, the estimates $\hat{Var}(\hat{V}_{R1})$ and $\hat{Var}(\hat{V}_{R2})$ can be computed using an option for a large number of records, see Belenky, *et al.* (2013, 2015). The best estimate of $Var(\hat{V}_R)$ can be obtained by pooling together the two available estimates:

$$\begin{aligned} &\hat{Var}(\hat{V}_R) \\ &= \frac{(N_1 - 1)\hat{Var}(\hat{V}_{R1}) + (N_2 - 1)\hat{Var}(\hat{V}_{R2})}{N_1 + N_2 - 2} \end{aligned} \quad \text{(A7)}$$

Finally:

$$\begin{aligned} &\hat{Var}(\hat{D}) = \\ &= \frac{(N_1 - 1)\hat{Var}(\hat{V}_{R1}) + (N_2 - 1)\hat{Var}(\hat{V}_{R2})}{N_1 + N_2 - 2} \\ &\times \left(\frac{1}{N_1} + \frac{1}{N_2}\right) \end{aligned} \quad \text{(A8)}$$

Setting δ_{cr} to 1.645 and substituting (A8) into equation (A1)

$$1.645\sqrt{\hat{Var}(\hat{D})} < D_A \quad \text{(A9)}$$

For the case when number of records in each sample is the same: $N_1=N_2=N$:

$$\hat{Var}(\hat{D}) = \frac{\hat{Var}(\hat{V}_{R1}) + \hat{Var}(\hat{V}_{R2})}{N} \quad \text{(A10)}$$

Equal number of records allows producing a simple final formula to assess Type II error:

$$1.645\sqrt{\frac{\hat{Var}(\hat{V}_{R1}) + \hat{Var}(\hat{V}_{R2})}{N}} < D_A \quad \text{(A11)}$$

Coupled Hydro – Aero – Elastic Analysis of a Multi – Purpose Floating Structure for Offshore Wind and Wave Energy Sources Exploitation

Thomas P., Mazarakos, *Laboratory for Floating Structures and Mooring Systems, School of Naval Architecture and Marine Engineering,* tmazarakos@naval.ntua.gr

Dimitrios N., Konispoliatis, *Laboratory for Floating Structures and Mooring Systems, School of Naval Architecture and Marine Engineering,* dkonisp@naval.ntua.gr

Dimitris I., Manolas, *Aerodynamic Laboratory, School of Mechanical Engineering National Technical University of Athens,* manolasd@fluid.mech.ntua.gr

Spyros A., Mavrakos, *Laboratory for Floating Structures and Mooring Systems, School of Naval Architecture and Marine Engineering,* mavrakos@naval.ntua.gr

Spyros G., Voutsinas, *Aerodynamic Laboratory, School of Mechanical Engineering National Technical University of Athens,* spyros@fluid.mech.ntua.gr

ABSTRACT

A coupled hydro–aero–elastic analysis of a multi–purpose floating structure suitable for offshore wind and wave energy sources exploitation is presented. The floating structure encompasses an array of hydrodynamically interacting Oscillating Water Column (OWC) devices consisting of concentric vertical cylinders, which are moored through tensioned tethers as a Tension Leg Platform (TLP) supporting a 5 MW W/T. The solutions of the diffraction and the pressure– and motion– dependent radiation problems around the floating structure and the aerodynamics of the Wind Turbine (W/T) are properly combined in the frequency and time domain. Results are compared at the level of RAOs and consistent results are obtained.

Keywords: *Multi purpose floating structure, Oscillating water column device, Wind turbine*

1. INTRODUCTION

In the last years considerable efforts and advances have been made worldwide in developing renewable energy devices. Among the numerous concepts proposed for wave energy conversion one of the most promising is the multi bodied floating structure based on the oscillating water column principle. Such type of devices have been reported in connection with the wave energy extraction (Konispoliatis & Mavrakos, 2013a) or in composing semi–submersible platforms for renewable electricity generation from the combined wind and wave action (Aubault et al., 2011; Mavrakos et al., 2011).

In the present contribution we consider a system of three identical OWC devices which

are placed at the corners of a triangular floater and can oscillate about their mean equilibrium position moving as a unit. The geometric configuration of each device consists of an exterior partially immersed toroidal oscillating chamber of finite volume supplemented by a concentric interior piston– like truncated cylinder. The wave action causes the captured water column to oscillate in the annular chamber, compressing and decompressing the air above the inner water surface. As a result, there is an air flow moving forwards and backwards through a turbine coupled to an electric generator. In the centre of the platform a solid cylindrical body is arranged in order to support the W/T (Figure 1).

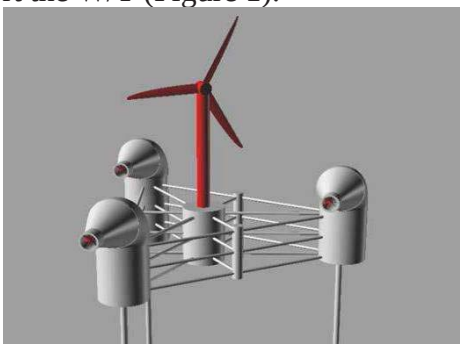

Figure 1: Multi-purpose floating structure with three OWC devices and a W/T

The latter is a typical 5MW horizontal axis turbine which is a variable- speed variable-pitch controlled WT. Detailed data are given in Jonkman et al. 2009. The tower of the WT is cantilevered at an elevation of 10m above the sea water level (SWL) to the top of the main column of the floating platform.

2. FORMULATION OF THE PROBLEM

2.1 Calculation of the velocity potential function

We consider that the group of three OWCs is excited by a plane periodic wave of amplitude $H/2$, frequency ω and wave number k propagating in water of finite water depth d. The distance between each device is L. The outer and inner radii of each device's chamber q, q=1, 2, 3, are denoted by α_q, b_q, respectively, whereas the distance between the bottom of the q device and the sea bed is denoted by h_q. The radius of the interior concentric cylindrical body in each device q, is denoted by $b_{1,q}$ and the distance between its bottom and the sea bed is $h_{1,q}$. The radius of the central cylindrical body that supports the WT is c and the distance between its bottom and the sea bed is h_c (Fig2 & Fig3). Small amplitude waves, inviscid, incompressible and irrotational flow are assumed, so that linear potential theory can be employed. A global Cartiesian co–ordinate system O–XYZ with origin on the sea bed and its vertical axis OZ directed positive upwards and coinciding with the vertical axis of symmetry of the central body is used. Moreover, three local cylindrical co-ordinate systems (r_q,θ_q,z_q), q = 1, 2, 3 are defined with origins on the sea bottom and their vertical axes pointing upwards and coinciding with the vertical axis of symmetry of the q device.

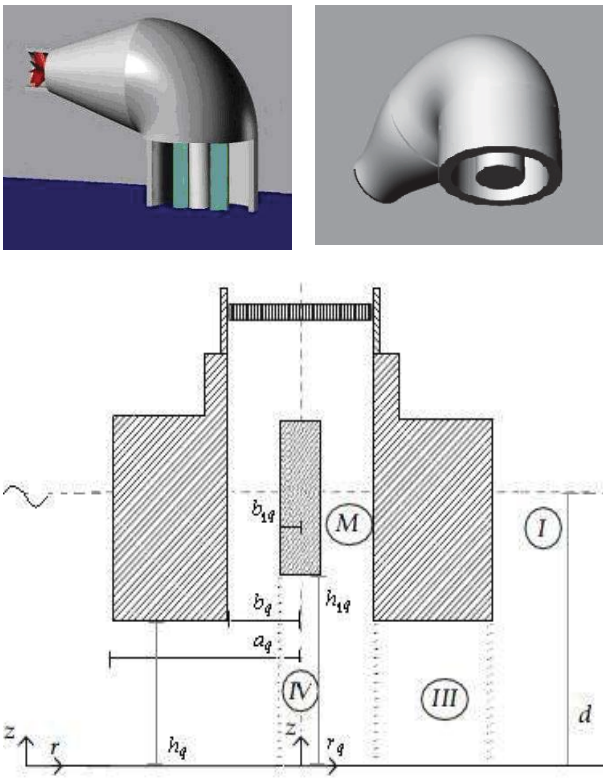

Figure 2: Definition sketch of the q OWC device of the array

The fluid flow around the q = 1, 2, 3, 4 device/body (three OWCs & one solid body) can be described by the potential function:

$$\Phi^q\left(r_q,\theta_q,z;t\right)=\mathrm{Re}\left\{\phi^q\left(r_q,\theta_q,z\right)\cdot e^{-i\omega t}\right\} \qquad (1)$$

Following Falnes (2002) the spatial function ϕ^q can be decomposed, on the basis of linear modelling, as:

$$\varphi^q=\varphi_0^q+\varphi_7^q+\sum_{p=1}^{4}\sum_{j=1}^{6}\dot{x}_{j0}^p\cdot\varphi_j^{qp}+\sum_{i=1}^{3}p_{in0}^i\cdot\varphi_P^{qi} \qquad (2)$$

Here, ϕ_0^q is the velocity potential of the undisturbed incident harmonic wave (Mavrakos & Koumoutsakos, 1987); ϕ_7^q is the scattered potential around the q device/body, when it is considered fixed in waves with the duct open to the atmosphere, so that the pressure in the chamber is equal to the atmospheric one (for the OWCs); ϕ_j^{qp} is the motion–dependent radiation potential around the device/body q resulting from the forced oscillation of the p–th device/body, p=1,2,3,4, moving with unit velocity amplitude, $\dot{x}_j^p=\mathrm{Re}\left\{\dot{x}_{j0}^p\cdot e^{-i\omega t}\right\}$; ϕ_P^{qi} is the pressure–dependent radiation potential around the q–th device/body when it is considered fixed in the wave field and open to the atmosphere (for the OWCs), due to unit time harmonic oscillating pressure head, $P_{in}^i=\mathrm{Re}\left\{p_{in0}^i\cdot e^{-i\omega t}\right\}$, in the chamber of the i=1,2,3 device which is considered fixed in otherwise calm water.

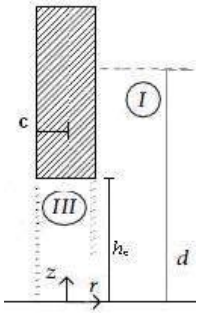

Figure 3: Definition sketch of the central cylindrical body basing the W/T

The diffraction, i.e. $\phi_D^q=\phi_0^q+\phi_7^q$, q=1,2,3,4, the motion– dependent radiation potentials around the isolated q device/body and pressure–dependent radiation potential around the isolated q device, when it is considered alone in the field, are expressed in its own cylindrical co–ordinate system $\left(r_q,\theta_q,z\right)$ as follows:

$$\phi_D^q(r_q,\theta_q,z)=-i\omega\frac{H}{2}\sum_{m=-\infty}^{\infty}i^m\Psi_{D,m}^q(r_q,z)\cdot e^{im\theta_q} \qquad (3)$$

$$\phi_j^{qq}(r_q,\theta_q,z)=-i\omega\sum_{m=-\infty}^{\infty}\Psi_{j,m}^{qq}(r_q,z)\cdot e^{im\theta_q} \qquad (4)$$

$$\phi_P^{qq}(r_q,\theta_q,z)=\frac{1}{i\omega\rho}\sum_{m=-\infty}^{\infty}\Psi_{P,m}^{qq}(r_q,z)\cdot e^{im\theta_q} \qquad (5)$$

Here ρ is the water density.

The potentials ϕ_j^l ($l\equiv q,\ qp$; j=D, 1, …, 6, P; p, q = 1,2,3,4; i=1,2,3) are solutions of Laplace's equation in the entire fluid domain and satisfy the following boundary conditions:

$$\omega^2\phi_j^l-g\frac{\partial\phi_j^l}{\partial z}=\left\{\begin{array}{lll} 0 & \text{for} & r_q\ge a_q;\text{ or } r_q\ge c \\ & & l\equiv q,\ j=D;\quad \text{or} \\ & & l\equiv qp,\ j=1,2,...,6,P \\ 0 & \text{for} & b_{1,q}\le r_q\le b_q; \\ & & l\equiv q,\ j=D;\quad \text{or} \\ & & l\equiv qp,\ j=1,2,...,6 \\ -\delta_{q,i}\dfrac{i\omega}{\rho} & \text{for} & b_{1,q}\le r_q\le b_q; \\ & & l\equiv qi;\ j=P \end{array}\right\} \qquad (6)$$

on the outer and inner free sea surface $\left(z=d\right)$, and the zero normal velocity on the sea bed $\left(z=0\right)$. Moreover, the potentials have to fulfil kinematic conditions on the mean device/body's wetted surface. Finally, a radiation condition must be imposed which states that propagating disturbances must be outgoing.

The unknown potential functions $\Psi_{j,m}^{k,l}$, k=I, III, M, IV, see Eq3 – Eq5, can be established in each fluid region surrounding the q–th device/body (see Figs. 2 and 3) using the method of matched axisymmetric eigenfunction expansions.

Next, the potentials, ϕ_j^{qp}, ϕ_P^{qi}, (j=1, …, 6) around anybody q of the multi – body configuration due to oscillation of body p,

p=1,2,3,4, in otherwise still water (motion – dependent radiation potential) or due to inner time harmonic oscillating pressure head in the air chamber of the device i, i=1,2,3, (pressure – dependent radiation potential), can be expressed in the q–th body's cylindrical coordinate system, as:

$$\phi_j^{qp}(r_q,\theta_q,z) = -i\omega \sum_{m=-\infty}^{\infty} \Psi_{j,m}^{qp}(r_q,z)\cdot e^{im\theta_q} \tag{7}$$

$$\phi_p^{qi}(r_q,\theta_q,z) = \frac{1}{i\omega\rho} \sum_{m=-\infty}^{\infty} \Psi_{p,m}^{qi}(r_q,z)\cdot e^{im\theta_q} \tag{8}$$

In order to express the potentials, ϕ_j^{qp}, ϕ_p^{qi} in the form of Eq7 and Eq8, use is made of the multiple scattering approach (Twersky, 1952; Okhusu, 1974). This method has been further elaborated to solve the diffraction and the motion – dependent radiation problems around arbitrarily shaped, floating or / and submerged vertical axisymmetric bodies by Mavrakos & Koumoutsakos (1987) and Mavrakos (1991) and for the diffraction and the pressure–dependent radiation problems for an interacting array of OWC's devices by Konispoliatis & Mavrakos (2013b); thus, it will be no further elaborated here.

2.2 Volume flow

The time dependent volume flow produced by the oscillating internal water surface in q OWC device, q = 1, 2, 3, is denoted by $Q^q(r_q,\theta_q,z;t) = \mathrm{Re}\left[q^q(r_q,\theta_q,z)\cdot e^{-i\omega t}\right]$, where:

$$q^q = \iint_{S_i^q} u_z\, dS_i^q = \iint_{S_i^q} \frac{\partial \phi^q}{\partial z} r_q\, dr_q\, d\theta_q \tag{9}$$

Here u_z denotes the vertical velocity of the water surface, and S_i^q the inner water surface in the q device, q=1, 2, 3.

Assuming that the Wells turbine is placed in a duct between the q device's chamber and the outer atmosphere and that it is characterized by a pneumatic admittance Λ^q, then the total volume flow is equal to (Evans & Porter; 1996, Falnes; 2002):

$$Q^q(t) = \Lambda^q \cdot P_{in}^q(t) \tag{10}$$

Assuming isentropy so that variations of air density and pressure are proportional to each other with $c_{air}^2 = dp_{in}^q / d\rho_{air}$, c_{air} being the sound velocity in air, the pneumatic complex admittance Λ^q is equal to (Martins–Rivas & Mei, 2010):

$$\Lambda^q = \frac{KD}{\rho_{air} N} + (-i\omega)\frac{V_0^q}{c_{air}^2 \rho_{air}} \tag{11}$$

Where K is constant for a given turbine geometry (independent of turbine size or rotational speed), D is turbine rotor diameter, N is the rotational speed (radians per unit time), ρ_{air} is the atmospheric density and V_0^q the q device's air chamber volume.

Decomposing the total volume flow, q^q, of the q–th device, same as for the velocity potential; see Eq2, into three terms associated with the diffraction, q_D^q, and the motion– and pressure–dependent radiation problems, q_R^q, q_P^q, respectively, we can obtained:

$$q^q = q_D^q + q_R^q + \sum_{i=1}^{3} p_{in0}^i \cdot q_P^{qi} \tag{12}$$

Here:

$$q_R^q = \sum_{p=1}^{4}\sum_{j=1}^{6} \dot{x}_{j0}^p \cdot q_{3,j}^p - \dot{x}_{30}^p \cdot S_i^p \tag{13}$$

Where S_i^p is the inner water surface in the p device, p=1, 2, 3.

The pneumatic admittance Λ^q for the OWCs, for the presented results, was considered as a real and positive number equal to the optimum coefficient Λ_{opt} of the same restrained OWC device but in isolation condition as in Evans and Porter (1996) work.

2.3 Hydrodynamic forces

The various forces on the *q* device/body can be calculated from the pressure distribution given by the linearised Bernoulli's equation:

$$P(r_q,\theta_q,z;t) = -\rho\frac{\partial\Phi^q}{\partial t} = i\omega\rho\phi^q\cdot e^{-i\omega t} \qquad (14)$$

Where ϕ^q is the *q* devices' velocity potential in each fluid domain *I*, *III*, *M* and *IV* (see Figs. 2 and 3). The horizontal and vertical exciting forces and moments acting on an array of OWC devices have been presented in Konispoliatis & Mavrakos (2013b).

The hydrodynamic reaction forces and moments F_{ij}^{qp} acting on the device/body *q*, *q*=1,2,3,4, in the *i*–th direction due to the oscillation of device/body *p*, *p*=1,2,3,4, in the *j*–th direction, can be calculated by the Eq14 and the complex form f_{ij}^{qp} may be written in the form (Newman, 1977):

$$f_{ij}^{qp} = \omega^2(a_{ij}^{qp} + {}^{i}\!/\!_{\omega}\, b_{ij}^{qp})x_{j0}^{p} \qquad (15)$$

Here, a_{ij}^{qp}, b_{ij}^{qp}, are the well–known added mass and damping coefficients.

In the same way, the hydrodynamic pressure forces and moments f_i^{ql} acting on the device/body *q* in the *i*–th direction due to oscillating pressure head in the *l*=1,2,3 device can be written in the form:

$$f_i^{ql} = \left(-e_i^{ql} + id_i^{ql}\right)\cdot p_{in0}^{l} \qquad (16)$$

Here e_i^{ql}, d_i^{ql} are the pressure damping coefficients.

The total hydrodynamic forces on the entire multi–body configuration can be calculated by properly superposing the corresponding forces on each device with respect to the reference point of motion, *G*, of the entire structure. (for details see Mavrakos, 1991).

2.4 Mooring system

The floating structure is moored with a TLP mooring system of three tendons spread symmetrically about the platform Z-axis. The fairleads are located at the base of the offset columns, at a depth of 20.0m below the sea water level. The anchors (fixed to the inertia frame) are located at a water depth of 200m below the sea water level. Each of the 3 tendons has an unstretched length of 180m, a diameter of 0.130m, an equivalent mass per unit length of 104kg/m and a submerged weight per unit length equal to 888.6N/m. The pretension of each tendon is 10800 kN. The mooring line stiffness k_{xx} and k_{zz} of each tendon is 60KN/m and 14700KN/m, respectively.

2.5 Aerodynamic loading

In the frequency domain formulation, the contribution of the W/T is projected on the degrees of freedom of the floater motion. This is carried out in the context of Hamiltonian dynamics with gravity and aerodynamics being the external forcing. The aerodynamic loading is defined from the Blade Element Momentum theory. After a linearization procedure, additional mass, damping and stiffness matrices are defined which contribute the W/T aerodynamic, inertial-gyroscopic and gravitational loading (Papadakis et al. 2014).

2.6 The time domain problem

The time domain simulations are carried out using the advanced full model hydroGAST developed at NTUA (Riziotis et al., 1997, 2004, Manolas et al. 2012). hydroGAST is a multi-body FEM dynamic model of the complete system. The aerodynamic loading is based on BEM modeling, the hydrodynamic loading is based on linear theory, and the mooring tendons as co-rotating non-linear truss elements. The specific model has been verified within the OC4 IEA project (Popko et al., 2012, Robertson et al., 2014a).

3. RESPONSE AMPLITUDE OPERETORS (RAO'S)

The investigation of the dynamic equilibrium of the forces acting on the freely floating array of OWC devices/body without the W/T leads to the following well – know system of differential equations of motions, in the frequency domain, i.e.:

$$\sum_{j=1}^{6}\left[-\omega^2(M_{i,j}+A_{i,j}+\frac{i}{\omega}B_{i,j})+C_{i,j}\right]\cdot x_{j0}-F_{P,i}=F_i \quad (17)$$

for i=1,…,6.

where $M_{i,j}$ and $C_{i,j}$ are elements of the (6x6) mass and stiffness matrices of the entire configuration; $A_{i,j}, B_{i,j}$, are the hydrodynamic masses and potential damping of the entire configuration; F_i are the exciting forces acting on the multi–body system at the i–th direction; $F_{P,i}$ are the pressure hydrodynamic forces acting on the multi–body system at the i–th direction; x_{j0} is the motion displacement of the entire OWC system at the j–th direction with respect to a global co – ordinate system G.

By inserting the TLP mooring system and the W/T characteristics in the multi – body system, Eq17 can be reduced to the following form (Mazarakos et al. 2014a), describing the couple hydro – aeroelastic problem of the investigated moored multi-purpose floating structure in the frequency domain:

$$\sum_{j=1}^{6}\left[\begin{array}{l}-\omega^2(M_{i,j}+A_{i,j}+M^{WT}\\+\frac{i}{\omega}B_{i,j}+\frac{i}{\omega}B_{i,j}^{WT})\\+C_{i,j}+C_{i,j}^{WT}+C_{mooring}\end{array}\right]\cdot x_{j0}= \quad (18)$$
$$=F_i+F_{P,i}$$

where M^{WT}, B^{WT} and C^{WT}, are the mass, damping and stiffness which contribute the W/T aerodynamic, inertial-gyroscopic and gravitational loading respectively, while $C_{mooring}$ is the mooring lines stiffness matrix.

The RAO's can be estimated from time series data from the following equation:

$$RAO(\omega)=\frac{|P_{xy}(\omega)|}{P_{xx}(\omega)} \quad (19)$$

where P_{xx} is the auto power spectral density and P_{xy} is the cross spectral density. P_{xx}, P_{xy} are calculated using Welch's method with a sufficient number of data split and 50% overlap between the split data parts. x refers to the input (wave elevation) and y to the output (each motion). The simulations lasted 3600sec - the first 600sec are excluded – assuming a uniform wind speed and white noise waves of 1m significant wave height.

4. NUMERICAL MODELING

4.1 Eigen values

In Table 1 the first 12 eigenvalues of the coupled system are presented, as provided by hydroGAST. In the flexible case, the flexibility of the W/T's members (tower, shaft, blades) is considered, while in the rigid case the members are stiff. The rigid case corresponds to the frequency domain analysis as well, because

only the 6 rigid modes of the floater are considered.

The main differences, between the two cases, are: the reduction of the roll/pitch eigenvalues from 0.3 Hz to 0.25 Hz and the presence of the tower fore-aft and side-to-side frequencies at ~0.85 Hz. Flexibility is important in the TLP case due to the strong coupling between the roll/pitch motion and the side-to-side/fore-aft bending moments of the tower. The modes of the blades and the shaft are not coupled with the motions of the floater, so they are not expected to appear in the RAOs.

Table 1: Coupled system eigen values [Hz]

Mode description	**flexible**	**rigid**
Platform Surge	0.026	0.026
Platform Sway	0.026	0.026
Platform Yaw	0.028	0.028
Platform Roll	**0.244**	**0.301**
Platform Pitch	**0.245**	**0.301**
Platform Heave	0.569	0.569
1st Drivetrain Torsion	0.585	-
1st Blade Flapwise Yaw	0.634	-
1st Blade Flapwise Pitch	0.653	-
1st Blade Collective Flap	0.702	-
1st Tower Fore-Aft	**0.854**	-
1st Tower Side-Side	**0.861**	-

4.2 RAO's comparison

Frequency and time domain methods consistently predict similar RAOs, in the case of a TLP floating W/T (Mazarakos et al. 2014b). In the present paper, RAOs for the TLP floating W/T with 3 OWC devices predicted by the frequency domain (fd) and the time domain (td) method are compared. Two inflow conditions are modelled; the zero wind speed case where the rotor is still and the 11.4 m/s case

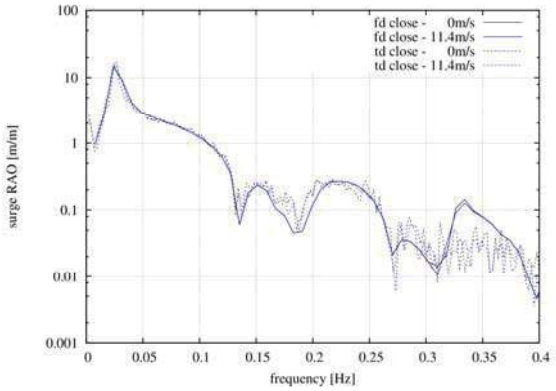

Figure 4: Surge RAO's comparison

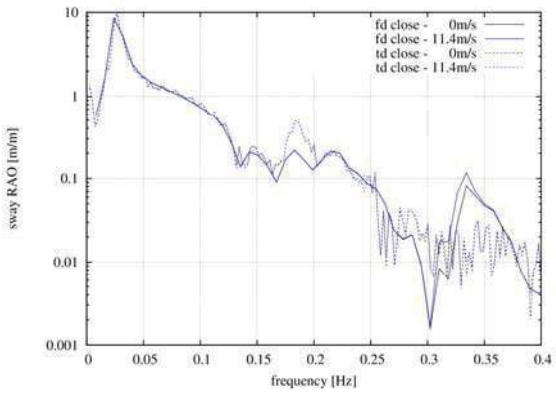

Figure 5: Sway RAO's comparison

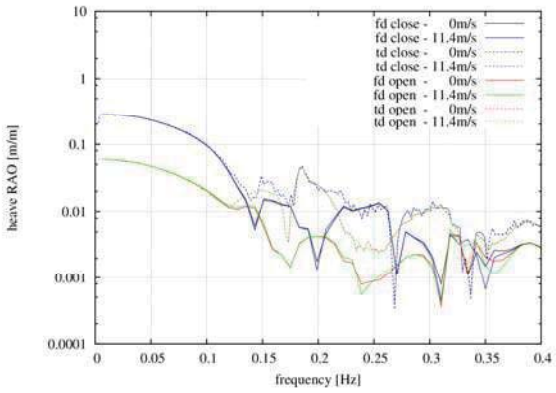

Figure 6: Sway RAO's comparison

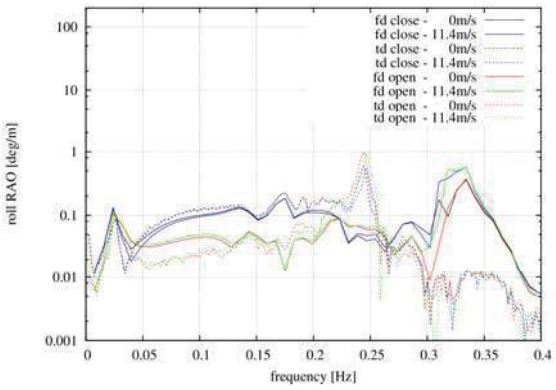

Figure 7: Roll RAO's comparison

which corresponds to the rated wind speed at which the rotational speed is 12 rpm. The wave heading angle is 30 deg.

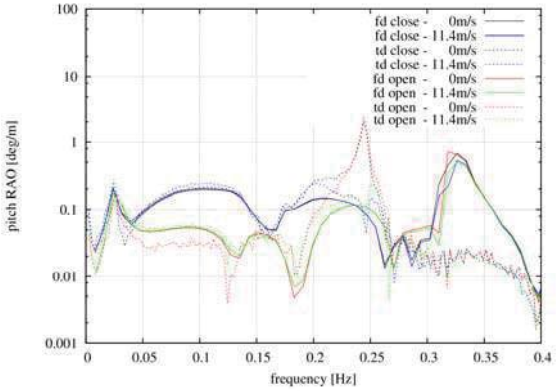

Figure 8: Pitch RAO's comparison

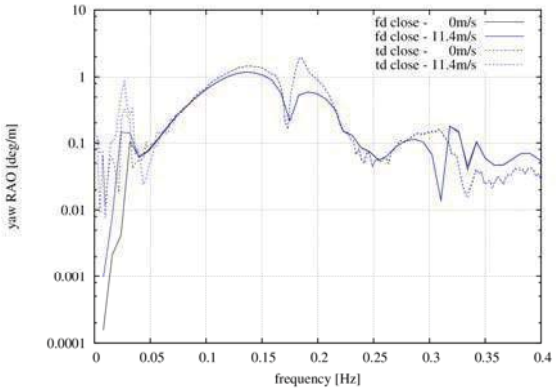

Figure 9: Yaw RAO's comparison

The 'open' case RAOs plots in the heave, roll and pitch motions correspond to the case where the OWC does not contribute additional pressure terms. The surge, sway and yaw RAO's are not affected by the OWC. Time domain simulations consider additional elastic degrees of freedom and nonlinear modeling of the aerodynamics, the complete dynamics, the mooring lines and the viscous term of the Morison's equation. Both methods consider the same linear hydrodynamic theory.

In general both methods predict similar RAOs and the eigen frequencies of table 1 are clearly identified. Focusing on the differences, in the frequency domain results the surge-pitch and the sway-roll coupling at 0.35 Hz are excited, contrary to that shown in the time domain ones (Figures 4, 5). Excellent agreement is observed in the heave motion (Figure 6) up to 0.15 Hz. At higher frequencies the heave exciting force, which is not presented due to space limitation, is almost zero and explains the difference. In the roll and the pitch motions (Figures 7, 8) the reduction of the natural frequency is clearly depicted, as already discussed in section 4.1. Both methods capture the reduction of the roll and pitch amplitudes at the corresponding eigen frequencies due to the aerodynamic damping. The influence of the aerodynamic damping in the time domain predictions is by far more significant due to nonlinear aerodynamics. It is noted that viscous drag could not be the reason, because it is present in the 0 wind case as well, in which the amplitudes are high and comparable to those in the frequency domain results. The OWC also does not seem to influence the peak amplitude, as the roll and pitch eigen frequencies are outside the wave region. In the range of the wave frequencies, the amplitudes of the heave (Figure 6) and the roll/pitch (Figures 7, 8) motions are more excited when the contribution of the OWC is considered. Finally, the time domain method predicts slightly higher yaw amplitude RAOs. Both methods capture the gyroscopic effects at

~0.03 Hz where the rotation of the blade increases the yaw motion.

5. CONCLUSIONS

A TLP floater supporting the NREL 5MW RWT and 3 OWC devices has been analyzed. For this design, RAO's of the complete system have been calculated using frequency as well as time domain simulations.

By comparing the results from the two methods, the following conclusions were drawn:

1 Both methods consistently predict the system RAO's, which gives confidence to the specific frequency domain approach as a preliminary design tool.

2 The frequency domain method does not include structural flexibilities which affect the roll/pitch RAO's. The natural frequency in roll/pitch for the rigid WT is 0.3Hz, while for the flexible WT is 0.25Hz and the tower bending frequencies about 0.85Hz. On the other hand roll and pitch is very small for a TLP - in time domain calculations do not exceed 0.1 deg. - and not within the wave frequency range.

3 As regards the design, it seems difficult to increase the roll/pitch natural frequencies above 0.25 Hz and keep the cost reasonable, due to the strong coupling with the tower that is counteracting.

4 Both methods capture the aerodynamic damping that reduces the amplitude of the roll/pitch motions around resonance and the gyroscope effect affecting the yaw amplitude.

5 The roll and pitch RAO's amplitudes near resonance as predicted by the time domain method are smaller, most probably due to aerodynamic nonlinearities, and not viscous damping as was initially supposed.

6 The action of the OWC devices increase heave, roll and pitch RAO's. In this respect, the IEC load cases should be performed in time domain.

6. ACKNOWLEDMENTS

This research has been co-financed by the European Union (European Social Fund – ESF) and Greek national funds through the Operational Program "Education and Lifelong Learning" of the National Strategic Reference Framework (NSRF) 2007 – 2013: Research Funding Program: ARISTEIA, Program POSEIDON (2041).

7. REFERENCES

Aubault, A., Alves, M., Sarmento, A., Roddier, D., Peiffer, A., 2011. Modeling of an oscillating water column on the floating foundation WINDFLOAT; Proceedings, 30th International Conference on Ocean, Offshore and Arctic Engineering (OMAE2011), Rotterdam, The Netherlands.

Evans, D.V., Porter, R., 1996. Efficient calculation of hydrodynamic properties of OWC type devices; OMAE–Volume I – Part B; p. 123–132.

Falnes, J., 2002. Ocean waves and oscillating systems: linear interactions including wave-energy extraction; Cambridge University Press.

Jonkman, J., Butterfield, S., Musial, W. and Scott G., 2009 Definition of a 5-MW Reference Wind Turbine for Offshore System Development, Technical Report, NREL/TP-500-38060, USA.

Konispoliatis, D.N., Mavrakos, S.A., 2013 a. Hydrodynamics of multiple vertical axisymmetric OWC's devices restrained in waves; Proceedings, 32nd International

Conference Ocean, Offshore and Arctic Engineering (OMAE2013), Nantes, France.

Konispoliatis, D.N., Mavrakos, S.A., 2013 b. Hydrodynamics of arrays of OWC's devices consisting of concentric cylinders restrained in waves; Proceedings, 10th European Wave and Tidal Energy Conference (EWTEC 2013), International Conference Ocean, Aalborg, Denmark.

Manolas, D., Riziotis, V., Voutsinas, S., 2012. Assessment of 3D aerodynamic effects on the behaviour of floating wind turbines, The science of making torque from Wind, TORQUE 2012, Oldenbourg, Germany.

Martins–rivas H. & Mei C.C., 2009. Wave power extraction from an oscillating water column along a straight coast. In: Ocean Engineering 36; p. 426–433.

Mavrakos, S.A. & Koumoutsakos, P., 1987. Hydrodynamic interaction among vertical axisymmetric bodies restrained in waves; Applied Ocean Research, Vol. 9, No. 3.

Mavrakos, S.A., 1991. Hydrodynamic coefficients for groups of interacting vertical axisymmetric bodies; Ocean Engineering, Vol. 18, No. 5, p. 485–515.

Mavrakos, S.A., Chatjigeorgiou, I.K., Mazarakos, T., Konispoliatis, D.N, Maron, A., 2011. Hydrodynamic forces and wave run-up on concentric vertical cylinders forming piston-like arrangements; Proceedings, 26th International Workshop on Water Waves and Floating Bodies, Athens, Greece.

Mazarakos, T.P., Mavrakos, S.A., Konispoliatis, D.N., Voutsinas, S.G., Manolas, D., 2014a. Multi- purpose floating structures for offshore wind and wave energy sources exploitation. COCONET Workshop for Offshore Wind Farms in the Mediterranean and Black Seas, Anavyssos- Greece, *9- 10 June 2014*.

Mazarakos, T.P., Manolas, D.I., Grapsas T., Mavrakos, S.A., Riziotis V.A., Voutsinas S.G., 2014b, Conceptual design and advanced hydro-aero-elastic modeling of a TLP concept for floating wind turbine applications. RENEW 2014, *Lisbon, Portugal*.

Newman, J.N., 1977. The motions of a floating slender torus; J. Fluid Mech, Vol. 83, p. 721–735.

Okhusu, M., 1974. Hydrodynamic forceson multiple cylinders in waves; Int. Symp. on the Dynamics of Marine Vehicles and structures in Waves, University College London, London.

Papadakis, G., Riziotis, V., Voutsinas, S., Mavrakos, S.A., 2014. W/T's reduced order aeroelastic models (in Greek). Technical Report No. D3.2, Program POSEIDON (2014), Greek General Secretariat for Research and Technology.

Popko et al., 2012. Offshore Code Comparison Collaboration Continuation (OC4), Phase I – Results of Coupled Simulations of an Offshore Wind Turbine with Jacket Support Structure, ISOPE 2012, Rhodes, Greece.

Riziotis. V.A., Voutsinas, S.G., 1997. GAST: A general aerodynamic and structural prediction tool for wind turbines. Procerdings of the EWEC' 97, Dublín, Ireland, 1997.

Riziotis, V., S.G. Voutsinas, E.S. Politis, P.K. Chaviaropoulos 2004. Aeroelastic Stability of Wind Turbines: the problem, the methods, the issues", Wind Energy, 7, pp 373-392.

Robertson Amy et al., 2014. Offshore code comparison collaboration, continuation within IEA wind task 30: phase II results regarding a floating semisubmersible wind system, OMAE 2014, San Francisco, USA.

Twersky, V., 1952. Multiple scattering of radiation by an arbitrary configuration of parallel cylinders; J. Acoustical Soc. of America, 24 (1).

This page is intentionally left blank

Session 14 – 40 YEARS OF STABILITY

SOTA on Damage Stability of Cruise Ships – Evidence and Conjecture

SOTA on Dynamic Stability of Ships – Design and Operation

SOTA on Intact Stability Criteria of Ships – Past, Present and Future

This page is intentionally left blank

Damage Survivability of Cruise Ships – Evidence and Conjecture

Dracos Vassalos, *The Ship Stability Research Centre, Department of Naval Architecture, Ocean and Marine Engineering, University of Strathclyde, Glasgow, Scotland, UK,*

d.vassalos@strath.ac.uk

ABSTRACT

This paper delves into damage stability legislation as it applies to passenger ships. The Concordia accident, like many others before it, has shaken the maritime profession once again with many questions being asked without being able to provide credible answers. Old ships have been designed to lower standards (it is common knowledge that new ships are safer than old ships, with the latter comprising the majority of the population), new standards are holistic and goal-based offering knowledge of the standard these ships are designed to, which is not true for old ships, emergency response is an altogether different science in modern ships and many others. Notwithstanding this state of affairs, there is another more fundamental weakness in the regulations for damage stability, perhaps at the heart of most problems with cruise ships safety, old and new. A critical review into damage stability legislation, as it applies to passenger ships, offers compelling evidence that cruise ship characteristics and behaviour have not been accounted for in the derivation of relevant damage stability rules. As a result, the regulatory instruments for damage stability currently in place do not provide the right measure of damage stability for cruise ships and, even more worryingly, the right guidance for design improvement. This leads to a precarious situation where cruise ships are underrated when it comes to assigning a damage stability standard whilst depriving designers of appropriate legislative instruments to nurture continuous improvement. Documented evidence is being presented and the ensuing results and impact discussed. Recommendations are given for a way forward.

Keywords: *damage stability and survivability, cruise ships*

1. INTRODUCTION

SOLAS regulations is the Bible of safety and like the latter, it is considered "holy" by many and it will take endless debates to change a line, even though the former has been written, in the best of circumstances, by naval architects not yet canonised. A passenger ship is a vessel carrying 12 or more passengers (… and is involved in international trade), irrespective of size, shape, age, construction and condition. This state of affairs has served the maritime industry well for over a century, as it has taken half as long for all concerned to realise that current rules are becoming progressively less relevant and amendments have run their course. The Secretary General of the International Maritime Organization (IMO) Koji Sekimizu, realising fully this state of affairs has set 2029 (the 100th anniversary of SOLAS) as the date by which a new, more relevant, SOLAS will be introduced. Sadly, he is leaving in less than a year's time and the chance that another Naval Architect will be filling his shoes is slim. In the interim, we have reached the embarrassing situation of having to conceal knowledge on the fact that treating all IMO-defined passengers ships the same, is alienating the

profession when it comes to developing and setting standards for damage stability. It is certain there are many other "anomalies" in SOLAS concerning all sort of different issues but damage stability is big enough a subject when it comes to passenger ships to consider it in isolation. More specifically, there is documented evidence to demonstrate that passenger ship damage stability rule development to date is based almost 100% on RoRo Passenger vessels and this has led to an unfathomable situation where cruise ship safety is underrated by the rules whilst rendering any attempts to improve damage stability of cruise ships futile, using current IMO cost-effectiveness criteria for decision making. This is a precarious position for the cruise ship industry to be in for both the safety-cultured and the rule-evading owners; the former because the current regulatory framework does not justify improving cruise ship safety, which we know cannot be right, and the latter because newbuildings cruise ships can easily meet the common "passenger ships pool" regulations and are relaxed in this futility. This situation must change. We must change it. As Naval Architects, we owe it to the travelling public, who board these ships by the thousands at a time.

2. PROBABILISTIC CONCEPT OF SHIP SUBDIVISION

2.1 Conceptual Formulation

A direct link between the probabilistic concept of ship subdivision and modern concepts of risk estimation may simplistically be expressed as follows:

$$R_c = P_c \times P_{w/c} \times P_{f/w/c} \times P_{l/f/w/c} \quad (1)$$

Where:

P_c Probability of a collision event, dependent on loading condition, area of operation, geography, topology, bathymetry, route, traffic density, ship type, human factors, etc.;

$P_{w|c}$ Probability of water ingress, conditional on collision event occurring (accounting for all the above);

$P_{f|w|c}$ Probability of failure (capsize / sinking / collapse), conditional on collision and water ingress events occurring – expressed as a function of e.g., sea state, structural strength and time;

$P_{l/f/w/c}$ Consequences (Probability of Loss) deriving from the collision event, conditional on all the foregoing; this accounts for loss of (or injury to) life, property damage / loss and impact to the environment. The former will depend on time to capsize and time to abandon ship (as determined from evacuation analysis – passenger ships) and the latter of e.g., probabilistic oil outflow using relevant models of oil spill damages and results from known accidents or through analysis using first-principles tools.

Considering the above and on the basis of work by (Lutzen, 2001), the relevant probabilities can be calculated from first-principles. Hence, if a more specific analysis is warranted for a novel ship design concept, the probability of collision damage that leads to hull breaching and flooding can be calculated. Moreover, based on work reported in (Jasionowski and Vassalos, 2006) and (Dogliani, et al., 2004), the various terms in [1] could also be addressed for each pertinent scenario from first principles. This allows for complete risk analysis of any damage case.

2.2 Basic Formulation (SOLAS 2009)

One of the fundamental assumptions of the probabilistic concept of ship subdivision in SOLAS 2009 is that the ship under consideration is damaged, i.e. the hull is assumed to be breached and there is (large scale) flooding. This implies that the cause of the breach, the collision event and the circumstances leading to its occurrence are disregarded; hence the interest focuses on the conditional probability of survival. Other pertinent factors, such as size of ship, number of persons on board, life-saving appliances arrangement, and so on, are directly or indirectly accounted for by the Required Index of Subdivision R. Therefore, the probability of ship surviving collision damage is given by the Attained Index of Subdivision, A, using the following expressions:

$$A = \sum_{j=1}^{J} \sum_{i=1}^{I} w_j \cdot p_i \cdot s_i \qquad (2)$$

Where,

j = represents the loading conditions (draught) under consideration

J = is the number of loading conditions considered in the calculation of the attained index (normally 3 draughts)

w_j is weighting factor for each draught;

i represents each compartment or group of compartments under consideration for loading condition j

I is the set of all feasible flooding scenarios, comprising single compartments and groups of adjacent compartments for loading condition j; The sum is taken for all cases of flooding in which one, two, three or more adjacent compartments are involved.

P_i is the probability that, for loading condition j, only the compartment(s) under consideration are flooded weighted by the probability that the space above a horizontal subdivision may not be flooded (note that $\sum p_i = 1$ for each draught considered)

s_i is the (conditional) probability of surviving the flooding of compartment(s) under consideration for loading condition j

The summation in equation (2) covers only flooding scenarios for which both p_i and s_i are positive (i.e., survivable scenarios, which contribute to the summation). In other words, A is the weighted average "s-factor", with "p-factors" being the weights, i.e.:

$$A = \hat{E}(s) \text{ on } I \qquad (3)$$

The Attained Index of Subdivision, A, must be greater than the Required Index, R, as specified by the regulations, i.e.:

$$A > R \qquad (4)$$

Deriving from the above, it is further implied that two different ships achieving the same Attained Index of subdivision are equally safe. The philosophy behind the probabilistic concept is that two different ships with the same index of subdivision have equal *overall* capacity to resist flooding following collision, although these ships may have quite different actual capabilities to withstanding individual damage scenarios (*local*) in addition to being subjected to different collision risk altogether. Therefore, it is this summary statistic that is the key.

Having said this, there is a profound knowledge hidden in the basic formulation of the probabilistic rules for damage stability, especially when the targeted population is

cruise ships, carrying thousands of people onboard. In this case, given that capsize or sinking of any such ship will be catastrophic, the emphasis in the risk model shifts towards damage limitation rather than reducing the probability of such an event taking place. Hence, the emphasis by (Wendel, 1968) on Index-A alone. This is key to understanding Wendel's formulation and to ensuring that no effort will be spared with e.g., large cruise ships to making A as close to 1 as possible.

Considering (1) and (3) and allowing for large time intervals, it is apparent that

$$R_{l/f/w/c} = (1\text{-}A) \qquad (5)$$

This means that Index A is the marginal probability for time to capsize within certain time, assuming that the time being considered is sufficiently long for capsize to have occurred in the majority of cases. This is a key observation, as this can be used to derive the flooding risk contribution, as indicated in the following. However, the assumption on time being sufficiently long is critical.

Finally, the Required Index of Subdivision, R represents the "level of safety" associated with collision and flooding events that is deemed to be acceptable by society, in the sense that it is derived using ships that society considers fit for purpose, since they are in daily operation.

3. STATUTORY A-INDEX CALCULATION (SOLAS 2009)

3.1 Capsize band

Capsize band is a concept describing the transition of sea-states from those at which no capsize is observed (lower boundary) to those at which the probability of capsize equals unity (upper boundary). In simpler terms, it is a band outside which capsize is either unlikely to happen or certain. For a finite observation time, the probability of capsize can be approximated either as a sigmoid function (Tsakalakis et al, 2010) or alternatively as a Gaussian distribution (Jasionowski et al, 2007). Significantly, it can be observed that as the time of observation increases the capsize band contracts towards its lower boundary, becoming a unit step function as time approaches infinity (Figure 1). This property is of major importance, particularly when the focus is cruise ships where the time it takes the vessel to capsize is normally much longer than the current SOLAS-based evaluation of 30 minutes. In this respect, Hs_{Crit}, is associated with the sea state at which the probability of capsize (P_f) is equal to 0.5, based on 30-minute tests.

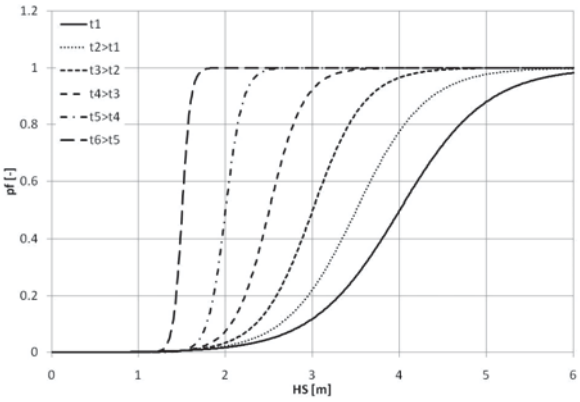

Figure 1: Capsize band as function of the observation time.

3.2 Survival Factor-s (Projects HARDER and GOALDS)

Although it is not explicitly stated in SOLAS, the s-factor is a measure of the probability of survival of a damaged ship in waves, namely:

$$s = \int_0^\infty dH_S \cdot f_{H_S|coll}(H_S) \cdot F_{surv}(H_S) \qquad (6)$$

Where: $f_{H_S|coll}(H_S)$ is the probability density distribution of sea states expected to be encountered during collision and $F_{surv}(H_S)$ is

the probability of survival in that sea state when exposed to a specific flooding case. More importantly, deriving from the observations made in 3.1 above, the probability of survival is in fact a conditional probability:

$$F_{surv}(H_S) \equiv F_{surv}(t = 30\,\text{min} | H_S) \quad (7)$$

This yield:

$$s(t = 30\,\text{min}) = \\ = \int_0^{\infty} dH_S \cdot f_{H_S|coll}(H_S) \cdot F_{surv}(t = 30\,\text{min} | H_S) \quad (8)$$

Furthermore, it has been assumed that the probability of survival, $F_{surv}(H_S)$ can be approximated by a step function centred on the sea state. That is, the Hs_{crit} constitutes the 50th percentile of the significant wave height the vessel, subjected to a particular damage scenario, can survive for 30 minutes (this corresponds to the abscissa of the inflection point of the sigmoid that defines the capsize band, obtained for t=30min). In Project GOALDS, the capsize band itself was substituted by a step function, as outlined next:

$$F_{surv}(H_S) = \begin{cases} 1 \Leftrightarrow H_S \le H_{S\,crit} \\ 0 \Leftrightarrow H_S > H_{S\,crit} \end{cases} \quad (9)$$

On the basis of this, the final formulation becomes:

$$s = \int_0^{H_{S\,crit}} dH_S \cdot f_{H_S|coll}(H_S) = \\ = \exp\left(-\exp\left(0.16 - 1.2 \cdot H_{S\,crit}\right)\right) \quad (10)$$

Where the $H_{S\,crit}$ is given as:

$$H_{S\,crit}\Big|_{t=30\,\text{min}} = \\ = 4\left(\frac{\min\left(GZ_{\max},\ 0.12\right)}{0.12}\frac{\min\left(Range,\ 16\right)}{16}\right) = (11) \\ = 4 \cdot s\left(t = 30\,\text{min}\right)^4$$

In essence, the approach adopted within the GOALDS Project is similar to that of the HARDER project with the main difference stemming from the assumption of Hs_{crit} corresponding to the lower limit of the capsize band, thus allowing for a justified assumption of very long ("infinite") time of survival. Therefore, the limiting assumption of short survival time, implicit in the formulation of HARDER has been addressed properly in GOALDS. This makes the GOALDS s-factor formulation better suited to cruise ships than the current SOLAS formulation.

Moreover, in the analysis of results pertaining to small and large vessels (sample ships in Project GOALDS), it was made apparent that there is a significant effect deriving from scale. Indeed, one of the major concerns related to SOLAS 2009 formulation for the s-factor was that it does not account for the ship size and that it might be inaccurate when applied to vessels deviating significantly from the size of the test vessels used in HARDER as basis for its derivation. In addition, the fact that the SOLAS 2009 s-factor formulation (residual GZ curve characteristics) is limited to relatively small range and maximum GZ values fails to account for the contribution of watertight volume distributed high enough not to be "seen" by the formulation. This, in essence deviates from normal Naval Architecture practice, previously expressed through the explicit demand for and provision of residual/effective freeboard.

Accounting for the above and using a systematic approach based on applying Design of Experiments (DoE), the formulation finally proposed is given by the following expression (Cichowicz, et al. 2011):

$$H_{S\,crit} = \frac{A_{GZ\,E}}{\frac{1}{2}GM_f \cdot Range} V_R^{1/3} \quad (12)$$

And,

$$s(H_S)=\begin{cases} e^{\left(-e^{(0.16-1.2H_{S\,crit})}\right)}, & \forall(A_{GZ},V_R,Range,k>0) \\ 0, & otherwise \end{cases} \quad (13)$$

Where $A_{GZ\ E}$ is an effective area under the GZ curve taken up to the heel angle corresponding to the submersion of the opening in question and VR is the residual volume mentioned above; GM_f is residual metacentric height. This formulation, by incorporating residual volume accounts for the effect of scale on one hand whist on the other incorporates a key feature of the cruise vessels, namely residual volume high up in the vessel, which is a key characteristic of modern cruise vessel design.

The overall improvement between Projects HARDER (SOLAS 2009) and GOALDS, pertaining to cruise ships, is best visualised (hard evidence) in Figure 2 next.

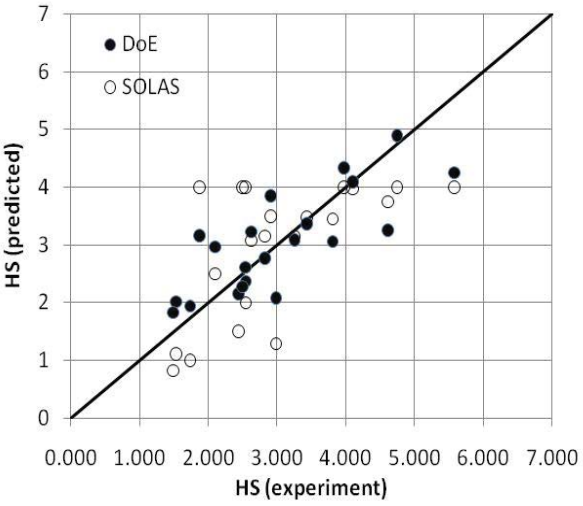

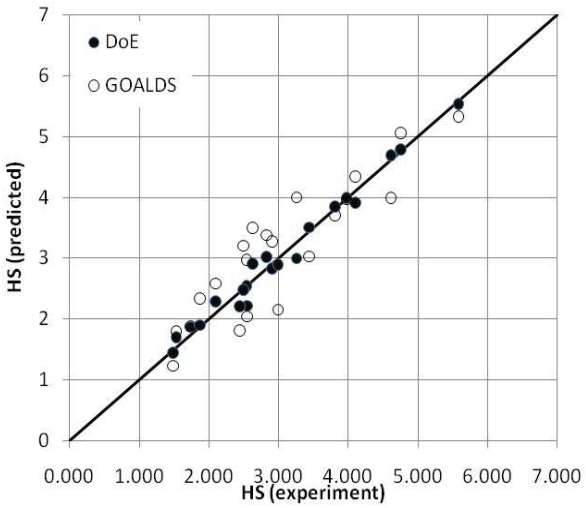

Figure 2: Comparison between predicted and experimental survivability results, using SOLAS 2009 (HARDER - Top) and (GOALDS - bottom) s–factor formulations.

As indicated in the introduction, the formulation for the s-factor in current SOLAS is based almost exclusively on results of either RoPax or cargo ships. The one cruise ship used in GOALDS provides evidence that the SOLAS formulation for s-factors

(a) Does not relate to cruise ships and, this fact leads to another truth, namely that

(b) Current SOLAS does not account for the known survival resilience of cruise ships

Figures 3 and 4 next provide rare evidence.

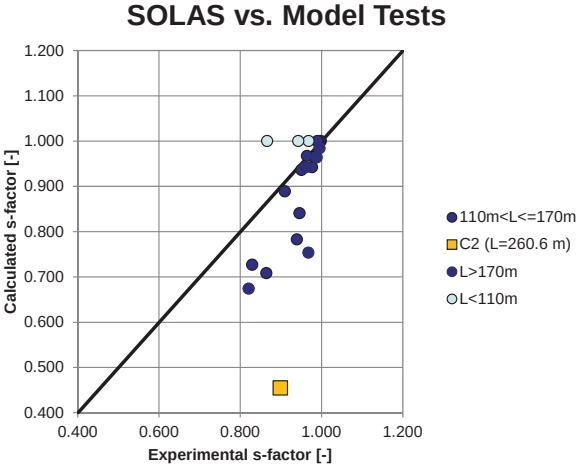

Figure 3: Comparison between predicted and experimental survivability results, using SOLAS 2009 (HARDER) s–factor formulation

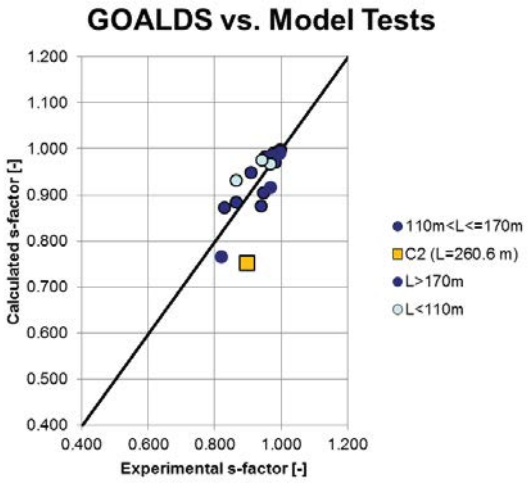

Figure 4: Comparison between predicted and experimental survivability results, using Project GOALDS s–factor formulation

In this light, it is important mentioning here that similar to Project GOALDS, the formulation of the s-factors for the current SOLAS formulation (Project HARDER) contains only one survivability experiment of a cruise ship, which again illustrates higher capsize resilience (Figure 5). The graph also illustrates that the s-factor in current SOLAS is, in fact, based on cargo ships results!

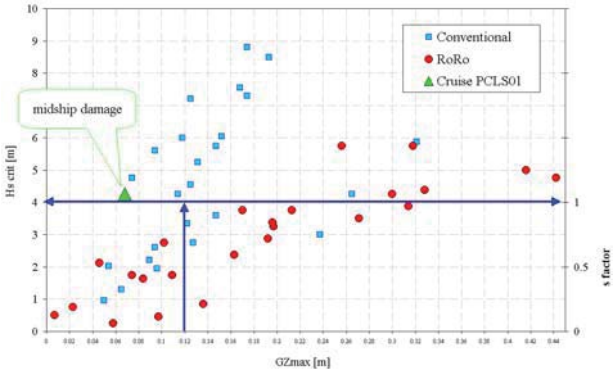

Figure 5: Experimental damage survivability results used to support SOLAS 2009 (HARDER) s–factor formulation

4. DIRECT APPROACH A-INDEX DERIVATION

4.1 Approval of Alternative and Equivalents

With direct influence from regulations, and because of the level of effort that is still needed to implement Risk-Based Design (RBD) in full, the real innovation attributable to RBD is currently witnessed mainly at local level. Known as "Approval of Alternatives and Equivalents" (MSC.1/Circ. 1455, 24 June 2013), it is using the principle of equivalent safety to consider alternative design and arrangements other than those supported by SOLAS legislation. This has taken a more generalised character than initially envisaged, with legislative instruments currently in place to address Fire Safety (SOLAS II-2, Reg. 17, MSC/Circ.1002); Life Saving Appliances (SOLAS III/Reg. 38, MSC/Circ. 1238), Damage Stability (Ch. II-1, Re, 4) and general Approval of Equivalents (MSC/Circ. 1455).

This opens the door to using an equivalent approach to A-Index derivation, as reported in (Vassalos et al, 2008) and highlighted in the following.

4.2 Impact of Time to Capsize

As discussed earlier, the survival factor "s" is estimated based on the assumption that the ship capsizes within half an hour, deriving mainly from work on RoPax. This, however, is not the case with cruise ships and it will be of interest to have another introspective look into this with the view to ascertaining the impact of a more prolonged time to capsize. The time to capsize (tc), is a random variable, hence only known as a distribution determined through probability methods. Moreover, it is dependent upon a number of parameters (e.g. flooding condition, sea state, damage extent) all of which are also random in nature. In this respect, accounting only for the damage case scenarios implicit in SOLAS 2009 (normally

over 1,000 for a typical passenger ship) and considering the 3 loading conditions, also implicit in the rules, and some 10 sea states per damage case, it becomes readily obvious that some form of simplification and reduction will be meritorious. In view of this, two lines of action have been pursued and two methods are currently available. The first relates to the development of a simple (inference) model for estimating the time to capsize, for any given collision damage scenario; the second entails automation of the process using Monte Carlo sampling of the random variables and time domain simulation, as outlined next.

Method 1: Univariate Geometric Distribution

Considerable effort has been expended over many years to develop an analytical expression, which could provide an overall description of the character of the stochastic process of ship capsize when subjected to collision damage in a seaway, (Jasionowski, et. al, 2004, 2006, 2008). The inference model used is based on a Univariate Geometric Probability (UGD) density distribution for time to capsize for each flooding scenario, where the only random variable being considered is the survival factor "s" as defined in SOLAS. Hence, the result will be subjected to the same limiting assumptions, inherent in the rules, e.g., applicable to scenarios where the time to capsize is short. Figure 6 presents a result for a typical ship at scenario level where using this simple inference model, it is possible to predict instantly the likelihood of a vessel to capsize within a given time in any given flooding scenario.

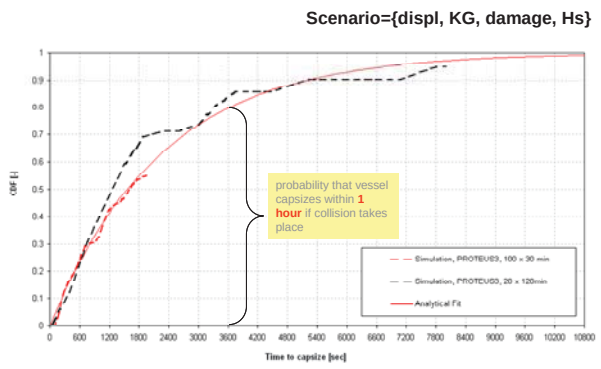

Figure 6: Cumulative probability function for time to capsize (scenario level) - Comparison between analytical model and numerical simulation results

Considering the ease of this operation, tens of thousands of scenarios may be considered to develop pertinent distributions at ship level, see Figure 7. Considering all flooding scenarios of interest for a typical ship, the outcome is the marginal cumulative probability distribution for time to capsize, shown in Figure 7.

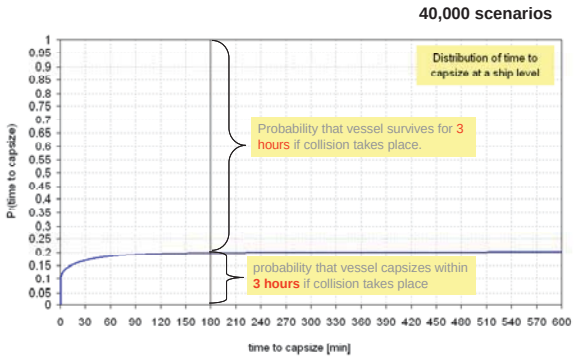

Figure 7: Cumulative marginal probability distribution for time to capsize within a given time

A close examination of Figure 7 reveals the following noteworthy points:

- If a vessel did not capsize within the first hour post-accident, capsize is unlikely, on average.
- The marginal probability distributions for time to capsize tends asymptotically (i.e., after infinite time, in principle) to values defined by (1-A), as indicated earlier.

Method 2 – Monte Carlo Simulation

To overcome problems associated with "averaging" the following approach may be adopted instead:

- Use of actual statistics (e.g., loading, sea state, damage size, survival time);
- Account properly for physical phenomena of ship motion and floodwater dispersion;

- Disclose ship attitude and behaviour as a function of time (including time to capsize);
- Aiming to avoid any "unnecessary" conservatism and other approximations and potential weaknesses embedded in the formulation of the probabilistic rules (e.g., heel limitations, down flooding points, etc.), the random variables distributions comprising loading conditions, sea states and damage characteristics are sampled using Monte Carlo Sampling and each ensuing damage scenario is simulated using explicit dynamic flooding simulation by PROTEUS3, (Jasionowski, 2005);
- Random variables to be considered would involve for collision: location, length, height, penetration according to the damage statistics adopted in the probabilistic rules and sea state. The resolution could be as high as necessary (every second of each scenario) accounting for transient- cross- and progressive-flooding, impact of multi-free surfaces, watertight and semi-watertight doors (relevant to cruise ships).

Applications of this method indicate that 500 scenarios would result in an absolute sampling error for the cumulative probability of time to capsize in the order of 4%-5%. Examples of Monte Carlo simulations setup are shown in Figures 8-9 for collision.

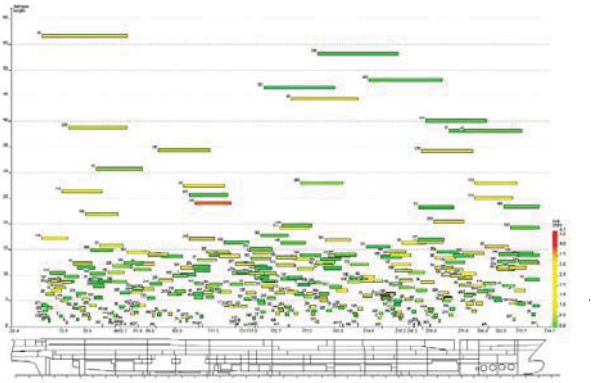

Figure 8: Monte Carlo Simulation Set up – Collision (342 scenarios) – Large Cruise Ship

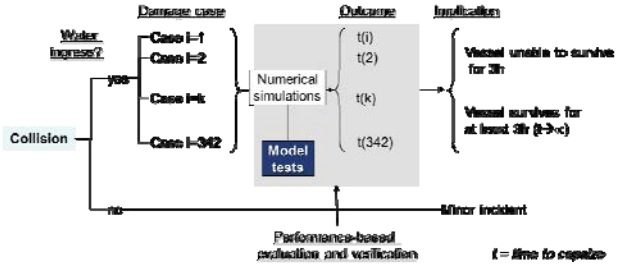

Figure 9: Monte Carlo Simulation and post-processing set up – Collision (342 scenarios) – Large Cruise Ship

Typical results are shown in Figures 10 and 11 for a RoPax and a Cruise Ship respectively as cumulative distribution functions of time to capsize. From the latter it will be seen that differences between the two methods of nearly an order of magnitude have been encountered and this led to renewed scrutiny of the probabilistic rules, as reported in (Vassalos and Jasionowski, 2007) that led to the EC-funded Project GOALDS.

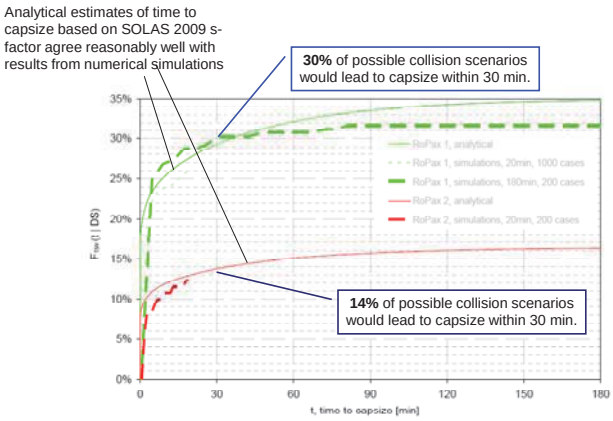

Figure 10: Probability Distributions of Time to Capsize (RoPax) – SOLAS 2009 Vs Direct Approach

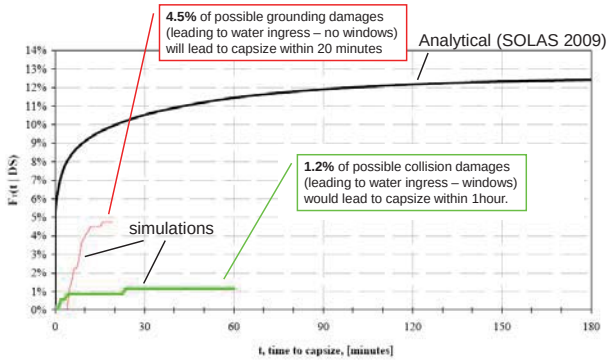

Figure 11: Probability Distributions of Time to Capsize (Cruise Ship) – SOLAS 2009 Vs Direct Approach

The results shown in the above figures offer another piece of evidence that the s-factor in current SOLAS does not represent the survivability of cruise ships by far. The fact that time to capsize for cruise ships is considerably longer than RoPax or indeed cargo ships on which the current SOLAS is based (i.e., half an hour) appears to have much larger impact on the ability to predict survivability of cruise ships than initially envisaged. Efforts to rectify this in Project GOALDS by encompassing cruise ship characteristics in the final formulation appear to have improved this situation as shown in Figure 12. However, the fact that only one data point related to a cruise ship was used in such derivation has not had as full an impact on the final formulation of the s-factor as focusing on cruise ships alone would bring.

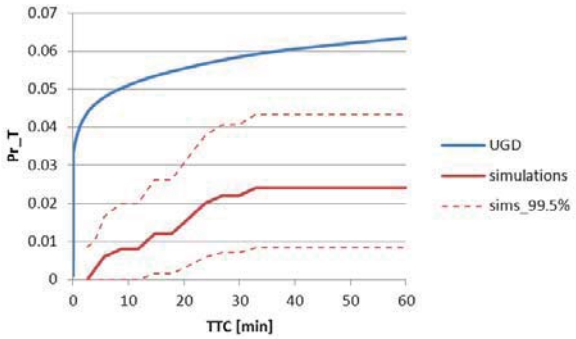

Figure 12: Probability Distributions of Time to Capsize (Cruise Ship) – GOALDS Project s-factor Vs Direct Approach

5. RECOMMENDATIONS FOR A WAY FORWARD

All the evidence available to date strongly suggests that the current SOLAS misrepresents the survivability of cruise ships. Continuing to group these with RoPax is no longer workable and more importantly largely unjustifiable. It is time to address survivability of cruise ships as a separate group of ships from RoPax. This will incentivise research to focus on these ships for the first time ever with the view to understanding the underlying characteristics that define survivability of cruise ships and to attempt to capture these in formulating and proposing a new s-factor for cruise ships. Following verification, application and calibration by the industry, this will lead to a legislative instrument, specifically for cruise ships, that will incentivise industry to seek continuous improvement and to facilitate designers in this quest. This time, it has to be the industry that takes initiative and leadership to put together a Joint Industry Project to target and accomplish this in a relatively short time. This is the only way forward!

6. CONCLUDING REMARKS

- The general formulation of the s-factor for cargo ships was adopted as the harmonised solution for both cargo and passenger ships. This is irrational considering that cruise ships are vastly different to both types of ships on which the formulation is based.

- SOLAS 2009 formulation considerably underestimates cruise ship survivability. This implies that due credit is not given to the damage resilience of cruise ships, which, in turn, affects industry image (ships being seen less safe than they actually are).

- SOLAS 2009 formulation does not support best-practice design, meaning that potential solutions for improving cruise

ship survivability will not be properly rated and hence dismissed. Adding to this is the risk of alienating the designers in that what they know to improve survivability in their designs does not appear to be justifiable.

- Emphasis on continuous safety improvement is, as a result, being hindered and safety culture undermined.

- The general formulation of the s-factor for cargo ships was adopted as the harmonised solution for both cargo and passenger ships. This is irrational considering that cruise ships are vastly different to both types of ships on which the formulation is based.

- SOLAS 2009 formulation considerably underestimates cruise ship survivability. This implies that due credit is not given to the damage resilience of cruise ships, which, in turn, affects industry image (ships being seen less safe than they actually are).

- SOLAS 2009 formulation does not support best-practice design, meaning that potential solutions for improving cruise ship survivability will not be properly rated and hence dismissed. Adding to this is the risk of alienating the designers in that what they know to improve survivability in their designs does not appear to be justifiable.

- Emphasis on continuous safety improvement is, as a result, being hindered and safety culture undermined.

7. REFERENCES

Lutzen, M, 2006, "Damage Distributions, Report No.: 2-22-D-2001-01-1, Task 2.2, EU Project No: GRD1- Harder", November 2001, 66 pp.; also in: Ship collision damage, PhD thesis, Department of Mechanical Engineering, Technical University of Denmark, Lyngby.

Jasionowski, A. and Vassalos, D., 2006, "Conceptualising Risk", STAB 2006, Rio de Janeiro, Brazil

Dogliani, M, Vassalos, D and Strang, T, 2004, "Evacuation Notation – A New Concept to Boost Passenger Evacuation Effectiveness in the Cruise Industry", COMPIT 2004, 3rd Int. Euro-Conference on Computer Applications and Information Technology in the Marine Industries, Parador Siguenza, Spain

Wendel, K, 1968, "Subdivision of Ships", Diamond Jubilee International Meeting, New York, June 1968, pp 12-1 to 12-21.

Tsakalakis, N., Cichowicz, J., Vassalos, D., 2010, "The concept of the capsize band revisited", 11th International Workshop on Stability of Ships and Ocean Vehicles, Wageningen

Jasionowski, A, Dodworth, K, Vassalos, D, 1999, "Proposal for Passenger Survival-Based Criteria for Ro-Ro Vessels", International Shipbuilding Progress, Vol. 46, No 448

Cichowicz, J, Tsakalakis, N, Vassalos, D and Jasionowski, A, 2011, "Survivability of Passenger Vessels - Re-engineering of the s-Factor", Proceeding of the 12th International Ship Stability Workshop, Washington D.C., USA.

Vassalos, D, Jasionowski, A and Guarin, L, 2008, "Risk-Based Design: A Bridge too far?", OC 2008 Seakeeping and Stability, Osaka, Japan.

Jasionowski A, Vassalos D, Guarin L, 2004, "Theoretical Developments on Survival Time Post-Damage", Proc. The 7th Int Ship Stability Workshop, Shanghai.

Jasionowski A, Bulian G, Vassalos D, Francescutto A, Pawlowski, M, Maccari A, 2007, "Modelling survivability", SAFEDOR, D2.1.3, www.safedor.org.

Jasionowski, A, 2005: "An integrated approach to damage ship survivability assessment", PhD, University of Strathclyde.

Vassalos, D and Jasionowski, A, 2007, "SOLAS 2009 – Raising the Alarm", 9th International Stability Workshop, Hamburg, Germany

SOTA on Dynamic Stability of Ships – Design and Operation

Jan Otto de Kat

This page is intentionally left blank

Intact Stability Criteria of Ships – Past, Present and Future

Alberto Francescutto, *University of Trieste*, Italy, francesc@units.it

ABSTRACT

This paper contains a brief excursus of the developments of intact stability of ships through the time from stone age, through historical period, modern age, renaissance, completion of the first intact stability code, beginning of development of 2nd generation intact stability criteria, present status and the foreseeable future developments.

Keywords: *Ship stability, 2nd generation stability criteria, ship safety*

1. INTRODUCTION

Sinking due to insufficient buoyancy and capsizing because of insufficient stability are two of the major threats to ship survivability at sea. The safety from sinking and capsizing is thus an important part of the safety of navigation with the entailed safety of life and protection of the environment in waterborne transportation. The two aspects had an extremely different development through history. As we will see, this is substantially due to the different perception of the immediacy of danger and to the very different entailment of physical and mathematical aspects in the two aspects. An important change in the perception was given by the change in propulsion, in particular the passage from sail ships to mechanical propulsion.

Due to the short time available, the paper is just a working scheme for presentation, mostly composed of quotations from relevant literature. The adopted nomenclature for historical periods doesn't conform to the standard use. It has been adapted by the author (Francescutto 1993, Francescutto 2004, Francescutto 2007) to the slow development of ship stability as a science.

2. FROM THE STONE AGE TO THE BEGINNING OF HISTORY

Man has travelled for thousands of years throughout the oceans without knowing how and why this was possible. Although the basic concepts of floatability and stability will have been known before, the basic laws of hydrostatics of floating bodies were introduced by the great Archimedes in 300 BC. It is well established that he was the first to formulate the basic law of buoyancy and eventually floatability. It was, however, only quite recently that it was found that he had also set the foundations of stability of floating bodies, namely by introducing the concept of the balance of couples of forces or moments.

The part of naval architecture known as buoyancy and stability is directly founded on the roots of Archimedes' principle, but it is not clear whether his early findings about the stability of floating paraboloids were generalized by himself to actual ship forms or not. What is certain, is the fact that, after some great scientific achievements in the Hellenistic era, there was a long silence (Russo, 2004). Gained knowledge remained unexploited for centuries (or was simply ignored and not

referenced) and it is not known what its impact on later developments in ship stability actually was. The development of ship stability as a science, indeed, occurred very late in the 18th century with two different approaches based on the introduction of the metacentre and the righting moment notions respectively. These approaches were developed respectively by Bouguer and Eulero.

3. THE BEGINNING OF HISTORY

Additional details on the similarities and differences between Bouguer and Eulero are contained in references [Nowacki 2001, Nowacki and Ferreiro 2003 and Francescutto and Papanikolaou 2011]. What is important to remark here is that, after the bright but isolated spot of Archimedes, the decisive progress of ship stability, as we know it now, came from the (mostly) geographer Bouguer while he was strolling up-and-down the Andes in search of a proof that Earth shape was following Descartes theories against Newton's theories. The result was the notion of metacentre, i.e. the upper limitation of the position of centre of gravity that guarantees the stability-in-the-small or initial stability.

It is important to note the observation made by Bouguer in the Preface to his book (Bouguer 1746): "Il n'était guére possible que l'Architecture navale, compliquée comme l'est par la multitude des diverses connoissances qu'elle suppose, fit des progrès aussi rapides quel es autres parties de la Marine qui sont incomparablement plus simples. Il falloit non-seulement que les diverse Théories sur le mouvement dont elle dépend, & dont l'époque est assez recente, fussent portées plus loin, il étoit encore nécessaire que l'Analyse même & les methods géométriques qui devoient servir à réfoudre les grandes difficultés qui lui sont propres, parvinnent elles-mêmes à un degré de perfection qu'il ni a pas longtemps qu'elles ont acquis."

This witnesses the intrinsic physical and mathematical difficulties connected with the development of the subject. It is not casual that previous development was due to the best mechanician-mathematician of the ancient Greece (although he flourished in Magna-Grecia, present Italy…).

The work was completed by the Rev. Moseley (Moseley 1850) introducing the coincept of dynamic stability in 1850: "Whence it follows that the work necessary to incline a floating body through any given angle is equal to that necessary to raise it bodily through a height equal to the difference of the vertical displacements of its centre of gravity and that of its immersed part, so that other things being the same, that ship is the most stable the product of whose weight by this difference is the greatest."

Quoting Barnes (Barnes 1861): "The first general theorem for the determination of the measure of a ship's stability was given by M. Bouguer, in his Traité du Navire, about a century ago. This measure of a ship's stability, although only strictly true when the angle of inclination from the upright is extremely small, yet gives the relative stabilities of ships of the usual form for a tolerably large angle of inclination with sufficient exactness for all practical purposes. Bouguer's measure, in consequence of the simplicity of the calculations for obtaining the height of the metacentre and its close approximation to the correct results, is that which is in general use: but a naval architect should also be familiar with the mechanical principles upon which the stability of a ship depends, and be able to determine the exact stability of a ship of any form whatever, at any given finite angle of inclination."

Unfortunately, the idea of Bouguer didn't have real practical applications. Notwith-standing fierce debates, mostly in the frame of the Institution of Naval Architects, as a consequence of the sudden sinking of the monitor Captain (designed by Cole) having a

higher metacentric height but a smaller freeboard giving a smaller range of positive stability with respect to the Monarch (designed by Reed). White and John (White and John 1871) comment: "In 1867 calculations were made at the Admiralty of the stability of two or three low-sided vessels, and the results were embodied in a Paper read by Mr. Reed at the Meetings of this Institution in 1868. With this Paper most of the Members and Associates are doubtless familiar. It showed conclusively that instability would occur in such vessels at a very moderate angle of inclination, and illustrated the contrast, as regards stability and safety, existing between rigged ships with high freeboard and those with low freeboard. … This paper did not succeed, however, in impressing members of the profession with the necessity for more complete calculations of stability, and the subject remained in comparative obscurity until the loss of the Captain forced it into painful prominence."

The reasons for the absence of transformation of Bouguer intuition in practical (stability) rules are well explained by Rahola in his doctoral thesis: "Even the most recent of the fundamental laws that determine the amount of stability for a vessel are already about 200 years old. Consequently, it would seem natural that the estimating of a vessel's stability and the determining of its minimum amount should have drawn attention very early. However, that is by no means the case. Only about a hundred years after forming the principles for the theory of stability one began to understand, by reason of a certain accident having occurred, the great importance the stability qualities of a vessel have for its seaworthiness and non-sinking qualities. This earlier under-valuation of the stability circumstances appears at first sight difficult to explain, particularly when one compares the fortunes of this question with those of its parallel question, the development of the problem of preventing the overloading of vessels. … The slight interest roused for the amount of a vessel's stability can in a way be explained very simply. So long as the wind was the propelling force for the ships, one was obliged, without studying the matter theoretically, generally to have a comparatively high freeboard for the hull. This brought about at the same time that the range of stability became great. The master of a sailing ship was also aware at every moment of the approximate amount of the stability, because when sailing he constantly happened to perform some kind of inclining experiment with his vessel, even if it was primitive. It was therefore easy for the master to avoid imperiling the stability of his ship, and whenever he was tempted to load an excessive deck-cargo or otherwise reduce the stability, he probably did so well aware of the risk he was causing his vessel. … The construction of a diverging type of vessel led to a flagrant violation of the building rules for well tested sailing vessels.

4. THE BEGINNING OF THE MODERN AGE

This is situated in the '30s of last century and is substantially based on two papers. First of all, Pierrottet (Pierrottet 1935) laid the foundations of what later will be the weather criterion. During his presentation in front of the Royal Institution, the following debate, illuminating about the general conception of stability at that time, was recorded: "The CHAIRMAN: I do not wish in the least to detract from the good work that Professor Pierrottet has done. I think the Paper will be very useful to us, but I do hope it will be a long time before it is made the basis for new Board of Trade regulations by the Classification Societies. The number of losses from capsizing is so exceedingly small, even more tiny than he says, that it would be a very stiff to impose these regulations. After all, when you had imposed them, the skipper might upset them all by his loading of the ship. There is the difficulty. I hope Professor Pierrottet will not assume that I am pouring too much cold water on his scheme, for I think you will agree with me that he has devoted his energy, brains and ability to producing an interesting and, I

believe, a useful Paper, and that we ought to accord him a very hearty vote of thanks"

PIERROTTET: "To Sir Archibal Denny I would say that I think the problem of stability is rather neglected by ship designers. I can see danger in his recommendations of empirical, rather than scientific methods. If the proportions of bridges across rivers were decided empirically, I am sure that sooner or later there would be many a disaster. The limits of the field over which empirical methods can safely be applied are very vague. It is my opinion, therefore, that no effort should be spared to study scientifically the stability of ships, and to ensure that designers do not neglect its consideration. I am rather doubtful, moreover, if this object can be attained without the application of binding regulations. I quite agree that at 50° inclination nothing would remain still on deck, but that is not the problem : when a ship is unfortunate enough to acquire a list of 50°, the problem is not so much of how to keep all the passengers safely on board, but rather to prevent her from capsizing. I should not be adverse, though, to reducing the proposed 50° to some smaller figure."

Second came the PhD Thesis of Rahola (Rahola 1939). It is a too important contribution to be summarized here, but it is important to consider at least the following couple of sentences from the introduction: "The object of the present investigation is to find a procedure by means of which it may be possible to judge with adequate certainty the amount of the stability of a certain vessel which may come to navigate under the conditions prevailing on the lakes and the waters adjacent to our country, and to decide whether it is sufficient or not." … "With regard to stability circumstances we must clearly make a distinction between the determining and the judging of stability."

Almost contemporarily, the first issue of the Principles of Naval Architecture (Vincent 1939), in line with the thinking of the time, considering that still paid more attention to comfort that to safety from capsizing: "Suitable Metacentric Height. Metacentric height is one of the fundamental features of a design and should have such a value that it will meet the following requirements:

(a) Large enough in passenger ships to prevent capsizing or an excessive list in case of flooding a portion of the ship during an accident.

(b) Large enough to prevent listing to unpleasant or dangerous angles in case all passengers crowd to one side. This may require considerable GM in light displacement vessels, such as excursion steamers, carrying large numbers of passengers.

(c) Large enough to minimize the possibility of a serious list under pressure from strong beam winds.

(d) Small enough to prevent violent rolling in waves. As explained in Chapter I, Volume 2, an excessive GM results in unpleasant rolling that may even be dangerous should the period of roll approximately synchronize with that of the waves. The traveling public is inclined to avoid vessels known to roll badly. Several large ships that were unpopular because they rolled badly have undergone costly major alterations to improve the condition."

And following: "Damaged stability considerations may occasionally require excessive metacentric heights. Recognizing this, several formulas have been devised to establish the maximum GM that need be provided in the interest of safety. In the light condition modern passenger vessels ordinarily have very little positive GM, often not over 1 per cent of the beam, and many of the older liners have negative GM when light. For all classes of vessels there is an advantage in having at least positive GM in this condition, as such a vessel does not require as careful handling as one that has a negative GM. A few authorities insist upon at least positive GM in the light condition. The above views on the

maximum GM acceptable for passenger vessels are those of the author (S. A. Vincent) but not those of all naval architects and others interested in shipping. Some believe that a higher load GM should be used, if necessary to give adequate stability in the flooded condition."

It is worth Noting that at the time, no substantial progress was still made by SOLAS, still involved in the development of subdivision rules after Titanic's sinking, in addressing the issue of stability. Finally, concerning dynamic stability, in spite of the tremendous work done, mostly published in the Proceedings of the Institution of Naval Architects (PNA 1988) following Moseley: "The dynamical stability of a ship at a given inclination is defined as the work done in heeling the vessel to that inclination. Dynamical stability is rarely calculated in practical merchant ship design work, but is used in investigations of the motion of a vessel among waves, the list due to firing guns and similar problems."

The far-looking intuitions of Rahola and Pierrottet, not to speak of Bouguer and Moseley, had to wait long time, respectively 30 and 50 years, and the birth of IMCO (later IMO), before becoming international regulations. Only starting with the 1988 edition the Principles of Naval Architecture dedicates due attention to minimum standards of intact stability: "In Chapter II more attention is given to stability curves and to criteria for acceptable stability based on them."

5. THE FIRST GENERATION INTACT STABILITY CRITERIA

Provisions concerning intact ship stability have been introduced at a late stage in international regulations of ship safety. The need of intact stability rules was indeed uncertain until SOLAS 1948, where it was stated, in the Recommendations contained in Annex D:

"The Conference examined the need and the practical possibility of adopting rules relative to the intact ship stability. Considering that the rules adopted relatively to the damage stability have an influence on the intact stability of the ship, the Conference believes that, before establishing additional rules concerning intact stability, further experience to establish the extent to which such rules are necessary is needed. The Conference recommends therefore to the Administrations to examine in more detail the intact ship stability and to exchange information on such subject.".

We have not to forget that the adopted rules for damage stability practically consisted in: "In the case of symmetrical flooding the residual metacentric height shall be positive, except that, in special cases, the Administration may accept a negative metacentric height (upright) provided the resulting heel is not more than seven degrees."

The first international intact ship stability rule was originated by a recommendation contained in the conclusions of SOLAS'60: "The Conference, having considered proposals made by certain governments to adopt as part of the present Convention regulations for intact stability, concluded that further study should be given to these proposals and to any other relevant material which may be submitted by international Governments.

The Conference therefore recommends that the Organization should, at a convenient opportunity, initiate studies on the basis of the information referred to above, of:

a) intact stability of passenger ships;

b) intact stability of cargo ships;

c) intact stability of fishing vessels, and

d) standards of stability information…"

As a result, the General Stability Criteria based on righting arm characteristics was adopted by IMCO in 1968 as Res. A.167. Following Kobyliński (Kobyliński 1975): "In 1962 IMCO started its work towards the development of stability criteria for fishing vessels for small passenger and cargo vessels of less than 100 metres in length. The work was completed in 1968 the criteria were introduced by IMCO as recommendations"

The Weather Criterion was adopted in 1985 as Res. A.562. Again, this rule originated as an answer to a recommendation given in the conclusions of SOLAS'74: "(IMO) Recommends that steps be taken to formulate improved international standards on intact stability of ships taking into account, inter alia, external forces affecting ships in a seaway which may lead to capsizing or to unacceptable angles of heel".

Weather Criteria were already enforced in several countries including Japan (Yamagata 1959) and Australia. We just mention here that present weather criterion was obtained merging the Japanese standard, which still constitutes the backbone, with the Russian standard especially for the evaluation of roll-back angle and the effect of appendages on roll damping.

Both criteria were based on ideas, concepts and ship typologies/dimensions, existing long before their adoption.

6. THE "RENAISSANCE"

The renaissance of Ship Stability in general and Intact Ship Stability in particular can be identified with the mid '70s of past century due to the intuition of Prof. Kuo from Strathclyde University that there was a diffuse greater sensitivity to the subject. In 1975 he organized *The* International Conference on Stability of Ships and Ocean Vehicles which was an unprecedented event with many consequences. In addition to gathering the experts on the subject, he organized a Questionnaire which is of great interest to understand the feeling of that time. Almost all contributions to the Conference and to the Questionnaire should be mentioned in this paper, which is out of possibility. It is however important to remind the answers to selected questions:

Existing criteria (IMO Res. A.167): only 29% of respondents felt that the existing stability criteria based on the use of the righting arm curve met practical needs. Almost 50% felt that the criteria were unsatisfactory;

Main priorities: the two main priorities for research were seen as: (a) the effects of waves, and (b) the development of fresh methods for relating motion characteristics to stability criteria;

Metacentric height: a large majority of respondents considered such knowledge to be very important whereas the remainder thought that it was not important as long as it had a positive value. Of the respondents to the question on minimum metacentric height 55% of all respondents opted for 300 mm or more.

Several critical paper were developed to the existing Stability Criteria (mostly to the so-called statistical one represented by Res. A. 167, but also to the Weather Criterion, Res. A. 562, although its being partly a physical approach). Among these, since the beginning, there was Kobiliński (Kobiliński 1975), calling for "rational criteria": "At the time IMCO started its work towards elaborating international stability criteria several countries introduced stability criteria going beyond the requirements of I960 SOLAS Convention, All national requirements and regulations were carefully analysed, but the main source of inspiration for the evaluation of IMCO-Criteria was an analysis of casualty records and a comparison of the various stability parameters for vessels which capsized with those which were found safe in service. From all the stability parameters which could be used as stability criteria, the ones chosen for further analysis were those which lead to the lowest

position of KG. This was decided on the basis of statistics. … It should be underlined, however, that the approach was a pure statistical one. Its main drawback was that the available data constituted only a small population of vessels. In consequence, the statistical analysis was not satisfactory. During the discussions at IMCO, the view was expressed several times that in future more rational stability criteria are needed. Rational stability criteria are understood to be those that can take into account the physical phenomena occurring during the ship's service and all external forces exerted on them. The development of such rational criteria is a long-term task and for this reason simpler statistical approaches are first adopted at IMCO."

This objective was futher-on proposed by Francescutto (Francescutto 1993): "As we have seen, too often we assist the attempt to circumvent the actual stability rules, whose inadequacy and arbitrariness, on the other hand, has been declared by different authorities. It is difficult to change mental habits, but it is possible to intervene in the rules, not only to strengthen them, but to change the approach to ship safety. The conclusion is that the only way to overcome the many difficulties lies in the development of a system for the time domain simulation of ship motions in a seaway, including a detailed description of the environment and taking into account the non-linearities present and the dynamic effect of liquids with free surface in tanks, or on board as a result of deck wetness or damage. This will be called the *Physical Approach* to the hydrodynamic aspects of ship safety. Of course, it is a long term program involving the solution of many aspects connected with non-linear dynamics of motions and with the development of the non-linear hydrodynamics necessary to deal with large amplitude, transient asymmetric motions. The reason for the use of such a system as part of the design process from the beginning is to improve ship safety. This allows a further step in a procedure that usually uses optimization taking into account resistance, propulsion and seakeeping only. In this way, the hydrodynamic aspects of ship safety could be treated in a probabilistic way, as pertains to their very nature, overcoming the actual approach based on 'simple, certain, rules'. This could allow the introduction of the concept of 'safety performance' and the development of training tools for safety. It is not clear at this point if this approach leads to much more restrictive rules, but it is clear that the rules will be more realistic and defendable.";

Spyrou (Spyrou 1998): "Whilst one might think of many different methods for assessing the behaviour of a system, there is little doubt that the most reliable are those which are based on sufficient understanding of the system's key properties. For ship stability assessment however the application of this principle has been, so far at least, less than straightforward; because the behaviour of a ship in an extreme wave environment, where stability problems mostly arise, is often determined by very complex, hydrodynamic or ship dynamic, processes."; and by Spyrou and Papanikolaou (Spyrou and Papanikolaou 2000): "Is it possible to use in ship design the latest findings from the modern analyses of capsize based on the theory of nonlinear dynamics? This is the question which we are attempting to address in the present paper. Our goal is the establishment of a rigorous scientific basis for quantitative assessment of dynamic stability which will cover all the known types of ship capsize. Our approach will be comprised of two levels: The first refers to a very early stage of design where it is desirable to have simple analytical predictors of dynamic stability (or, for a certain standard of stability, of the required values of influential parameters such as damping), while our knowledge about the ship is still limited. The detailed account of a ship's form takes place at a second level where the stability analysis is performed with suitable numerical methods. It is remarked that the presented measures of stability could be relevant also for the operational side of the problem which however should be the subject of another publication. We think that a rational approach

about ship safety entails the best available scientific knowledge to be "infused" with the current practices of design, operation and rule setting. These notwithstanding, we are urged to note the profound lack of a proper methodological framework of ship stability assessment which would exploit the recent progress in understanding the dynamic origins of capsize and play the role of an interface between practice and research. The development of such a framework is nontrivial because the process of ship capsize is often determined by nonlinear phenomena and is not a simple task to develop scientifically sound and yet simple-to-understand and practical, quantitative measures of dynamic stability covering all possible types of capsize. Recent advances in the study of ship dynamics have allowed us to develop a two-level framework for a rigorous quantitative assessment of ship stability. This framework can be useful to a designer who wants to determine, along with other design considerations, a hull geometry and appendages that maximize safety against capsize."

It is worth noting that both call, in some way, for layered approach to stability regulations, an approach later-on adopted in the development of Second Generation Intact Stability Criteria.

7. THE SECOND GENERATION INTACT STABILITY CRITERIA

The revision process started in 2001 (Francescutto 2004, Francescutto 2007) with a critical analysis submitted by Italian delegation to IMO (IMO 2001, Francescutto et al. 2001) concerning the need of updating and tuning some coefficients of the Weather Criterion in view of its excessive weight in determining the limiting KG for ships with large values of B/d. This was considered a good opportunity to "shake" the ISC foundations putting them on a more physical basis through the development of new *performance based criteria* (PBC) originally intended to replace the old ones. These last were indeed identified as a source of difficulties due to their partly or totally empirical character which originated a non-uniform distribution of safety among different ship typologies. At the same time, their structure rendered these criteria quite difficult to modify without a possible significant loss of safety level of covering of present world fleet. The first part of the long work undertaken in the revision of the IMO Intact Stability Code in 2001 with the establishment of an ad-hoc Working Group (WGIS) operating during the Sessions of the Sub-Committee on Stability and Load Lines and on Fishing Vessel Safety (SLF) and intersessionally between them, was completed in 2008.

This part of the WGIS activity was mostly devoted to restructuring the previous Intact Stability Code (IMO 1993) in several parts and making Part A of the new International Code on Intact Stability, 2008 (IS Code 2008) mandatory under the provisions of both SOLAS and ILLC Conventions. This action was partly a consequence of the development of an FSA study, made by the German Delegation at IMO (IMO 2003), proving the potential cost-effectiveness implied in this change of legal status. The Code was also subject to some polishing and clarification, elimination of some ambiguities. In addition explanatory notes to the 2008 IS Code have been issued mostly consisting in a review of history of intact stability leading to present regulatory situation. It is however noteworthy that explanatory notes also contain guidance for an alternative application of "criteria regarding righting lever curve properties", in particular the rule requiring the position of the maximum of GZ to be above 25 deg. The new Part A contains mandatory instruments for passenger and cargo ships, while Part B contains recommendations for other ship typologies. An originally planned "Part C" containing nomenclature, an historical part describing the origins and the developments of intact stability criteria and explanatory notes to the new International Intact Stability Code 2008, has been finalized as an MSC Circular

(MSC.1/Circ.1281). Although what is now Part A was previously made de-facto mandatory under umbrellas different from IMO (European Directives, Classification Societies rules, etc.), the fact that after its adoption by SOLAS/ILLC the Code will become mandatory erga-omnes, constitutes a big change, because no attenuation to its standards is acceptable unless the "equivalent level of safety" with existing regulations is proved to the satisfaction of Administrations. This in turn is made difficult by the lack of knowledge of the actual safety level of present regulations. There is in fact the strong feeling that they provide an unequal distribution of safety among different typologies and, even within the same typologies, to different ship size. As a result, the revision made necessary the request and subsequent implementation of some important changes in the two basic design criteria.

As to the Weather Criterion, an alternative way of assessment, completely or partially based on experiments on scale models in towing tank/wind tunnel, was approved, based on both the obsolescence of the existing Weather Criterion due to the variations in ship forms and loading, and to correct some inconsistencies in the original formulation.

Notwithstanding the importance of this work, the most important part of the initial scope of the revision, i.e. the formulation and implementation of a new generation intact stability criteria performance-based was still to a large extent lying on the carpet. The time flown was in any case important for proving the potential cost-effectiveness implied in the new criteria and for the maturation of some important concepts connected with the dangerous phenomena to be covered, the basic structure and dictionary, and the philosophy of application of the new criteria.

It was subsequently decided that the following five possible stability failures should be individually addressed (IMO 2007, IMO 2010, Bassler et al. 2009, Francescutto and Umeda 2010, Peters et al., 2011,):

- dead ship conditions;

- following/stern quartering seas associated with matters related to stability variation in waves, in particular reduced righting levers of a ship situated on a wave crest;

- parametric resonance, including consideration of matters related to large accelerations and loads on cargo and stability variation in waves;

- broaching including consideration of matters related to manoeuvrability and course keeping ability as they affect stability;

- excessive accelerations.

Moreover the new generation intact stability criteria should be structured in three levels:

- Vulnerability 1st level;

- Vulnerability 2nd level;

- Direct assessment.

Specific Operational Guidelines should be added as a sort of "fourth level", in the acknowledgement that not all dangerous situations can be avoided only by design prescriptions.

After an initial good starting, the development of the procedures for the assessment of all the identified failure modes, mostly for the first two levels assessment, slightly diverged in a number for alternatives. During the last meeting of the Working Group, at SDC 2 (IMO 2015) last February, however, several choices were made concerning the application, the resolving of the alternatives for some failure modes, the development of explanatory notes and the development of "ways-out", in the form of operational limitations or operational guidelines (IMO 2013) at the different levels.

Work is in progress at inter-sessional level to arrive at next meeting of SDC 3 in 2016 with a polished text for all the identified failure modes, ready for thorough checks. It is encouraging that both the remaining failure modes for which alternatives were present are presently converging towards an agreed text.

8. REFERENCES

PNA, 1988, “Principles of Naval Architecture - II Revision”, Lewis, E. V., Vol. I, Stability and Strength, SNAME.

Barnes, F. K., 1861, “On a New Method of Calculating the Statical and Dynamical Stabilities of a Ship”, Trans. INA, Vol. II, pag. 163

Bassler, C., Belenky, V., Bulian, G., Francescutto, A., Spyrou, K., and Umeda, N., 2009, “A review of available methods for application to second level vulnerability criteria”, Proceedings of the 10th International Conference on Stability of ships and ocean vehicles - STAB 2009, Saint Petersburg, pp. 111–128.

Bouguer, P., 1746, “Traité du Navire, de sa Construction et de ses Mouvemens (Treatise of the Ship, its Construction and Movements”, Jombert, Paris.

Francescutto, A, Umeda, N., 2010, “Current Status of New Generation Intact Stability Criteria Development”, Proceedings 11th International Ship Stability Workshop, Wageningen, pp. 1-5.

Francescutto, A., 2004, "Intact Ship Stability - The Way Ahead", Marine Technology, Vol. 41, pp. 31-37.

Francescutto, A., 2007, “Intact Stability of Ships: Recent Developments and Trends”, Proc. 10th International Symposium on Practical Design of Ships and Other Floating Structures – PRADS’07, Houston, Vol. 1, pp. 487-496.

Francescutto, A., 1993, "Is it Really Impossible to Design Safe Ships?", Transactions Royal Institution of Naval Architects, Vol. 135, pp. 163-173.

Francescutto, A., Papanikolaou, A. D., 2011, “Buoyancy, Stability and Subdivision: From Archimedes to SOLAS2009 and the Way Ahead”, International Journal of Engineering for the Maritime Environment (Proceedings Institution of Mechanical Engineers, Part M), Vol. 225, pp. 17-32.

Francescutto, A., Serra, A., Scarpa, S., 2001, "A Critical Analysis of Weather Criterion for Intact Stability of Large Passenger Vessels", Proceedings 20th International Conference on Offshore Mechanics and Arctic Engineering - OMAE'2001, Rio de Janeiro, Vol. 1, pp. 829-836.

IMO, 1993, “Code of Intact Stability for all Ships Covered by IMO Instruments”, Res. A. 749.

IMO, 2001, “Weather criterion for large passenger ships”, Submitted by Italy, SLF44/INF.6.

IMO, 2003, “Revision of the Code on Intact Stability”, MSC78/24/1, Submitted by Germany,.

IMO, 2007, “Framework for the development of new generation criteria for intact stability, submitted by Japan, the Netherlands and the USA”, IMO SLF50/4/4.

IMO, 2010, “Development of new generation intact stability criteria – Report of the Working Group (Part 1)”, SLF52/WP.1.

IMO, 2013, “Development of Second Generation Intact Stability Criteria - Comments on present status of development of second generation intact

stability criteria", Submitted by Italy, SLF 55/3/7

IMO, 2015, "Development of Second Generation Intact Stability Criteria - Development of Amendments To Part B of The 2008 IS Code on Towing, Lifting and Anchor Handling Operations - Report of the working group (Part 1)", SDC 2/WP.4.

IS Code, 2008, "International Code on Intact Stability, 2008", IMO, London.

Kobyliński, L., 1975, "Rational Stability Criteria and the Probability of Capsizing", Proceedings (1st) International Conference on Stability of Ships and Ocean Vehicles, Kuo, C., Paper 1.4.

Moseley, H., 1850, "On the Dynamical Stability and on the Oscillations of Floating Bodies", Phil. Trans. of the Royal Society of London, Vol. 140, pp. 609-643.

Nowacki, H. and Ferreiro, L. D., 2003, "Historical roots of the theory of hydrostatic stability of ships", Proceedings of the 8th International Conference on Stability of Ships and Ocean Vehicles - STAB 2003, Madrid.

Nowacki, H., 2001, "Archimedes and ship stability", Proceedings of the Euro-Conference on Passenger ship design, operation and safety, Anissaras-Chersonissos, Crete, 2001.

Pierrottet, E., 1935, "Standards of Stability for Ships", Transactions Institution of Naval Architects, Vol. 77, pp. 208-222.

Rahola, J., 1939, "The Judging of the Stability of Ships and the Determination of the Minimum Amount of Stability Especially Considering the Vessels Navigating Finnish Waters", Ph.D. Thesis, Technical University of Finland, Helsinki.

Russo, L., 2004, "The forgotten revolution: how science was born in 300 BC and why it had to be reborn", Springer, Berlin.

Spyrou, K. J., 1998, "Ship Capsize Assessment and Nonlinear Dynamics", Proceedings 4th International Workshop on Theoretical Advances in Ship Stability and Practical Impact, St John's, Newfoundland, Canada.

Spyrou, K. J., Papanikolaou, A. D., 2000, "Ship Design for Dynamic Stability", Proceedings of the 7th International Marine Design Conference - IMDC2000, KS Min & J-J Kim, Kyongju, Korea, pp. 167-178.

Vincent, S. A., 1939, "Transverse Stability", Principles of Naval Architecture – Written by a Group of Authorities, Rossell, H. E. & Chapman, L. B., Vol. I, Chapter III, SNAME, pp. 99-137.

Peters, W., Belenky, V., Bassler, C., Spyrou, K. Umeda, N., Bulian, G.,. Altmayer, B., 2011, "The Second Generation Intact Stability Criteria: An Overview of Development", Transactions - The Society of Naval Architects and Marine Engineers, Vol. 119, pp. 225-264.

White, W. H., John, W., "On the Calculation of the Stability of Ships, and some Matters of Interest Connected Therewith", Transactions Institution of Naval Architects, Vol. XII, 1871, pp. 76-127.

Yamagata, M., 1959, "Standard of stability adopted in Japan", Transactions of Institution of Naval Architects, Vol. 101, pp. 417–443.

This page is intentionally left blank

ISBN-13: 978-1-909522-13-8 (print)

ISBN-13: 978-1-909522-14-5 (ebook)